WILEY

Polyolefin Composites

Edited by
Domasius Nwabunma
Thein Kyu

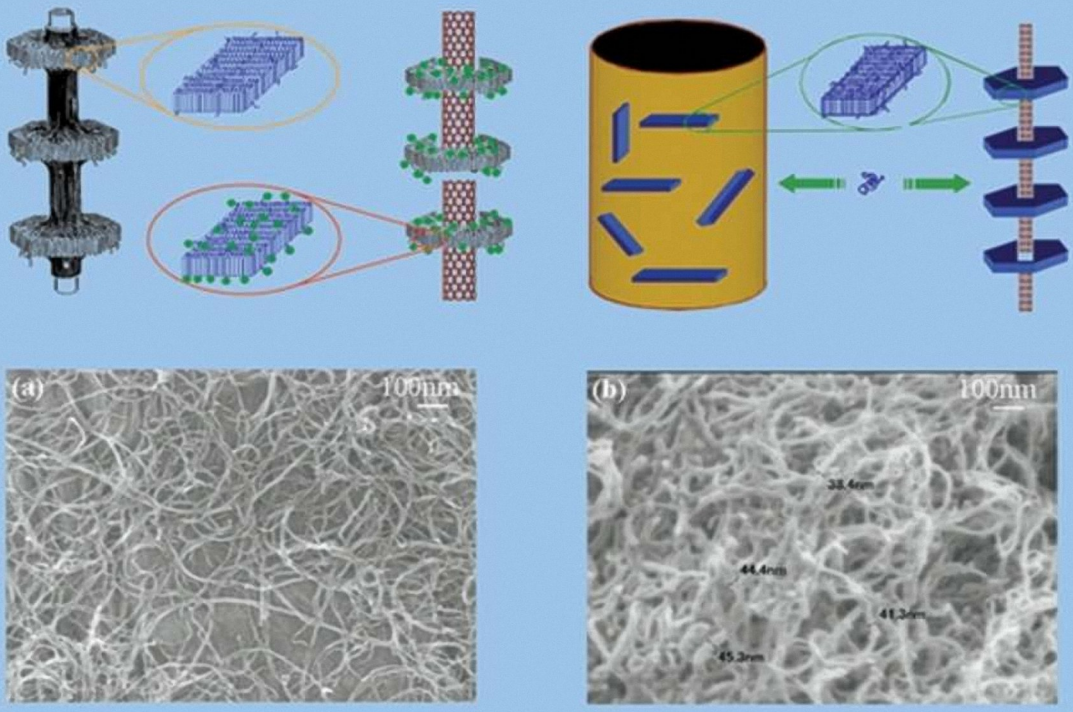

POLYOLEFIN COMPOSITES

The Wiley Bicentennial–Knowledge for Generations

Each generation has its unique needs and aspirations. When Charles Wiley first opened his small printing shop in lower Manhattan in 1807, it was a generation of boundless potential searching for an identity. And we were there, helping to define a new American literary tradition. Over half a century later, in the midst of the Second Industrial Revolution, it was a generation focused on building the future. Once again, we were there, supplying the critical scientific, technical, and engineering knowledge that helped frame the world. Throughout the 20th Century, and into the new millennium, nations began to reach out beyond their own borders and a new international community was born. Wiley was there, expanding its operations around the world to enable a global exchange of ideas, opinions, and know-how.

For 200 years, Wiley has been an integral part of each generation's journey, enabling the flow of information and understanding necessary to meet their needs and fulfill their aspirations. Today, bold new technologies are changing the way we live and learn. Wiley will be there, providing you the must-have knowledge you need to imagine new worlds, new possibilities, and new opportunities.

Generations come and go, but you can always count on Wiley to provide you the knowledge you need, when and where you need it!

William J. Pesce
President and Chief Executive Officer

Peter Booth Wiley
Chairman of the Board

POLYOLEFIN COMPOSITES

Edited by

Domasius Nwabunma
3M Company

Thein Kyu
University of Akron

WILEY-INTERSCIENCE
A JOHN WILEY & SONS, INC., PUBLICATION

Published by John Wiley & Sons, Inc., Hoboken, New Jersey
Published simultaneously in Canada

Library of Congress Cataloging-in-Publication Data:

Nwabunma, Domasius.
Polyolefin composites/edited by Domasius Nwabunma, Thein Kyu.
p. cm.
Includes index.
ISBN 978-0-471-79057-0 (cloth)
1. Polyolefins. 2. Polymeric composites. I. Kyu, Thein, 1948- II. Title.

TP1180.P67N93 2007
668.4'234–dc22 2007021316

Printed in the United States of America
10 9 8 7 6 5 4 3 2 1

Contents

Preface xv

Contributors xvii

Part I Introduction 1

1. Overview of Polyolefin Composites 3

1.1 Introduction 3
1.2 Olefinic Monomers 4
1.3 Polyolefin Homopolymers, Copolymers, and Terpolymers 5
1.4 Polyolefin Composites 7
1.5 Trends in Polyolefin Composites 14
Nomenclature 16
References 17

Part II Polyolefin Micro Composites 29

2. Polypropylene Natural Cellulosic Fiber Composites 31

2.1 Introduction 31
2.2 Applications of Polypropylene Composites 32
2.3 Preparation Techniques for Polypropylene Composites 33
2.4 Fiber Surface and Polypropylene Modifications 36
2.5 Forming of Polypropylene Composite 38
2.6 Composite Morphology and Polypropylene Crystallization 38
2.7 Mechanical Properties 39
2.8 Additives and Complementary Structures 40
2.9 Conclusions 41
Nomenclature 42
References 42

3. Polyolefin/Natural Fiber Composites 44

3.1 Introduction 44
3.2 Structure and Properties of Plant Fibers 46

3.2.1 Chemical Structure and Applications 47
3.2.2 Cellulose Microfibrils 48
3.3 Surface Modification of Plant Fibers 50
3.3.1 Physical Treatments 50
3.3.2 Physicochemical Treatments 51
3.3.3 Chemical Modification of Plant Fibers 54
3.4 Polyolefin Composites 63
3.4.1 Processing of Polyolefin/Natural Fiber Composites 63
3.4.2 Mechanical Properties of Polyolefin/Natural Fiber Composites 64
3.4.3 Dynamic Mechanical Properties of Polyolefin/Natural Fiber Composites 71
3.4.4 Rheological Properties of Polyolefin/Natural Fiber Composites 72
3.4.5 Thermoanalytical Properties of Polyolefin/Natural Fiber Composites 72
3.4.6 Electrical Properties of Polyolefin/Natural Fiber Composites 73
3.4.7 Water Absorption by Polyolefin/Natural Fiber Composites 75
3.4.8 Nanocomposites 76
3.5 Characterization of Polyolefin/Fiber Interfaces 77
3.6 Applications of Polyolefin Composites 78
3.7 Conclusions 81
Nomenclature 81
References 82

4. Composites of Polyolefins and Some Polyolefin/Polyamide Blends as Matrices and Calcium Carbonate, Wood Flour, Sisal Fiber, Hydroxyapatite, and Montmorillonite as Fillers 87

4.1 Introduction 87
4.2 Composites of Polypropylene and High Density Polyethylene with Calcium Carbonate 88
4.2.1 Mechanical Properties 88
4.2.2 Influence of the Mixing Conditions on the Dispersion of the Filler 89
4.2.3 Surface Modifiers for Calcium Carbonate 90
4.2.4 Thermal Properties 94
4.3 Composites of Polypropylene and High Density Polyethylene with Wood Flour and Sisal Fibers 95
4.3.1 Mechanical Properties 96
4.3.2 Thermal Properties 101
4.3.3 Influence of the Gamma Radiation on the Behavior of the Composites 104
4.4 Composites of Polypropylene and High Density Polyethylene with Hydroxyapatite 106
4.4.1 Influence of the Composite Preparation Methods on Its Mechanical Properties 107
4.4.2 Modification of the HA Particles Surface and Its Influence on the Tensile Properties 111

4.4.3 Influence of Gamma Radiation on the Composites 113
4.5 Composites of Polyolefins/Polyamide 6 with Montmorillonite 116
4.5.1 Mechanical Properties 118
4.5.2 Influence of Different Compatibilizing Agents 118
4.5.3 Analysis of the Physical, Mechanical, Thermal, and Morphological Properties of Composites 119
4.6 Conclusions 123
Nomenclature 124
References 125

5. Ethylene–Propylene–Diene Rubber/Carbon Black Composites 129

5.1 Introduction 129
5.2 Composite Preparation 130
5.3 Characterization of Composites 131
5.3.1 ^{129}Xe-NMR Studies 131
5.3.2 ^{1}H NMR Studies 132
5.4 Morphology of Composites 134
5.5 Mechanical and Viscoelastic Properties 135
5.5.1 Mechanical Properties 135
5.5.2 Viscoelastic Properties 137
5.6 Rheological Properties 138
5.7 Conductive Properties 140
5.8 Aging Properties 144
5.9 Applications 145
5.10 Conclusions 146
Nomenclature 146
References 147

6. Selected Topics on Polypropylene/Wood Flour Composites: Thermal, Mechanical, and Time-Dependent Response 150

6.1 Introduction 150
6.2 Interfacial Compatibilization: Addition of Maleated Polypropylene and Chemical Modification of Wood Flour 152
6.3 Composite Preparation: Processing Methods 154
6.4 Thermal Behavior: Thermal Degradation and Dynamic Mechanical Properties 157
6.5 Mechanical Behavior: Tensile, Flexural, and Impact Properties 162
6.6 Time-Dependent Response: Short- and Long-Term Creep 167
6.6.1 Effect of Processing Conditions and Wood Flour Concentration 167
6.6.2 Effect of Interfacial Modification 170
6.6.3 Effect of Temperature 170
6.7 Conclusions 173
Nomenclature 174
References 175

7. Deformation and Fracture Behavior of Natural Fiber Reinforced Polypropylene **178**

7.1 Introduction 178
7.2 Effect of Loading Conditions 181
7.3 Microstructural Effects 181
7.3.1 Fiber Breakage 183
7.3.2 Fiber Agglomeration 184
7.3.3 Fiber Orientation 185
7.3.4 Transcrystallinity 186
7.4 Deformation Behavior 187
7.5 Fracture Behavior 191
7.5.1 Quasistatic Loading Conditions 191
7.5.2 Impact Loading Conditions 192
7.6 Failure Mechanisms 195
7.7 Conclusions 199
Nomenclature 200
References 201

Part III Polyolefin Nano Composites **205**

8. Metallocene Catalyzed Functionalized Polyolefins in Composites **207**

8.1 Introduction 207
8.2 General Functionalization Approaches 208
8.3 Functionalized Polyolefins through Metallocene Catalysis 209
8.4 Compatibilization of Polyolefin Composites 211
8.4.1 Background 211
8.4.2 Functionalized Olefin Copolymers in Melt Compounding 212
8.4.3 *In situ* Polymerization 219
8.5 Conclusions 223
Nomenclature 224
References 224

9. Polyethylene/Layered Silicate Nanocomposites: Preparation and Properties **228**

9.1 Introduction 228
9.2 Preparation Strategies and Morphological Study 229
9.2.1 Melt Intercalation 230
9.2.2 *In situ* Polymerization Method 231
9.3 Properties of Polyethylene/Layered Silicate Nanocomposites 234

9.3.1 Tensile Properties 234
9.3.2 Dynamic Mechanical Analysis 236
9.3.3 Gas Barrier Properties 237
9.3.4 Thermal Stability 238
9.3.5 Flammability Properties 239
9.3.6 Photooxidative Degradation 240
9.3.7 Thermal Expansion and Thermal Conductivity 241
9.4 Polyethylene/Clay Nanocomposites Exposed to High Energy Irradiation 242
9.5 Crystallization Behavior of Polyethylene-Based Nanocomposites 243
9.6 Rheological Properties and Processability 245
9.7 Conclusions 248
References 248

10. Polypropylene/Clay Nanocomposites 251

10.1 Introduction 251
10.2 Structure and Properties of Clay 252
10.3 Typical Morphologies of Polymer/Clay Hybrids 253
10.4 Preparation of PP/Clay Nanocomposites 254
10.4.1 Clay Modification 254
10.4.2 Fabrication of PP/Clay Nanocomposites 257
10.5 Characterization of PP/Clay Nanocomposites 264
10.5.1 Microstructures 264
10.5.2 Thermal Transitions and Stability 267
10.5.3 Mechanical Properties 268
10.5.4 Thermomechanical Behaviors 272
10.5.5 Rheological Behaviors 275
10.5.6 Other Properties 276
10.6 Applications of PP/Clay Nanocomposites 277
10.7 Conclusions and Future Trends 278
Nomenclature 279
References 279

11. Polyolefin/Layered Double Hydroxide (LDH) Nanocomposites: Preparation, Structure, and Properties 283

11.1 Introduction 283
11.2 Synthesis and Characterization of Organomodified LDH 286
11.3 Preparation of Polyolefin/LDH Nanocomposites 290
11.4 Structure and Morphology of Polyolefin/LDH Nanocomposites 292
11.5 Rheological Properties of Polyolefin/LDH Nanocomposites 295
11.6 Thermal Properties of Polyolefin/LDH Nanocomposites 298
11.7 Thermal Stability of Polyolefin/LDH Nanocomposites 300
11.8 Mechanical Properties of Polyolefin/LDH Nanocomposites 302
11.9 Flame-Retardant and Gas Barrier Properties of Polyolefin/LDH Nanocomposites 305

11.10 LDH Versus MMT in Polyolefin Nanocomposites 305
11.11 Conclusions 306
Nomenclature 307
References 309

12. Effect of Nanofillers on Crystallization, Phase Transformation, and Thermomechanical Behavior of Poly(1-Butene) 311

12.1 Introduction 311
12.1.1 Crystallization and Phase Transformation of PB 312
12.1.2 Polymer Nanocomposites 313
12.1.3 Preparation of PB Nanocomposites 314
12.2 PB/Clay Nanocomposites 315
12.2.1 Clay 315
12.2.2 Structure Evaluation 317
12.2.3 Nonisothermal Crystallization 318
12.2.4 Isothermal Crystallization 321
12.2.5 Optical Microscopy 323
12.2.6 Phase Transformation 323
12.2.7 Dynamic Mechanical Analysis (DMA) 325
12.2.8 Thermogravimetric Analysis 326
12.3 PB/MWCNT Nanocomposites 327
12.3.1 Carbon Nanotubes 327
12.3.2 Morphology 328
12.3.3 Nonisothermal Crystallization 328
12.3.4 Isothermal Crystallization 329
12.3.5 Optical Microscopy 329
12.3.6 Phase Transformation 331
12.3.7 Dynamic Mechanical Analysis 332
12.3.8 Thermogravimetric Analysis 334
12.4 PB/$BaTiO_3$ Nanocomposites 334
12.4.1 Nanoparticles 334
12.4.2 Morphology 335
12.4.3 Nonisothermal Crystallization 335
12.4.4 Isothermal Crystallization 336
12.4.5 Optical Microscopy 337
12.4.6 Phase Transformation 337
12.4.7 Dynamic Mechanical Analysis 338
12.4.8 Thermogravimetric Analysis 339
12.5 Effect of Nanofillers on the Rate of Phase Transformation 340
12.6 Conclusions 341
Acknowledgments 343
Nomenclature 343
References 343

13. Toward Polyethylene Nanocomposites with Controlled Properties 346

13.1 Introduction 346
13.2 Optimizing Dispersion of Nanofillers 349
13.3 Characterizing Dispersion in Polyethylene Nanocomposites 352
13.3.1 Conventional Techniques: X-ray Diffraction and Electron Microscopy 352
13.3.2 Small-Angle Scattering 353
13.4 Conclusions 359
Acknowledgments 360
Nomenclature 360
References 361

14. Polyolefin–Silicate Nanocomposites: Mechanical Properties and Fracture Mechanics 365

14.1 Introduction 365
14.2 Structure of Polyolefin/Silicate Nanocomposites 369
14.2.1 Polyethylene/Montmorillonite Nanocomposites 371
14.2.2 Polypropylene/Montmorillonite Nanocomposites 378
14.2.3 Polyolefin/Vermiculite Nanocomposites 380
14.2.4 Effect of Elastomer Additions 384
14.3 Mechanical Properties 389
14.4 Patent Processes 399
14.5 Essential Work of Fracture (EWF) 402
14.6 Conclusion 410
Nomenclature 410
References 411

Part IV Advance Polyolefin Nano and Molecular Composites 415

15. Polyolefin/Clay Nanocomposites: Theory and Simulation 417

15.1 Introduction 417
15.2 Nanocomposite Morphology, Thermodynamics, and Phase Behavior 419
15.2.1 Exfoliated, Intercalated, and Immiscible Nanocomposite Morphologies 420
15.2.2 Tailoring Polymers and Clays to Promote Exfoliation 422
15.2.3 Modeling Macroscopic Phase Behavior of Polymer–Clay Mixtures 427
15.2.4 Interpreting Morphology Using X-ray Scattering Data 430
15.3 Nanocomposite Rheology and Dynamics 431
15.3.1 Intercalation Dynamics 431
15.3.2 Nanocomposite Rheology 434

15.4 Prediction of Nanocomposite Properties 436
15.4.1 Common Features Between Predictive Methods 436
15.4.2 General Classes of Predictive Methods 438
15.4.3 Thermoelastic Property Modeling 440
15.4.4 Transport Property Modeling 443
15.5 Conclusions 444
Acknowledgment 445
Nomenclature 445
References 446

16. Monte Carlo Modeling of Polyethylene Nanocomposites Using a High Coordination Lattice 449

16.1 Introduction 449
16.1.1 Computer Simulations of Spherical Nanocomposites 453
16.2 Simulation Method 454
16.2.1 Second Nearest Neighbor Diamond Lattice 454
16.2.2 Simulation Setup 463
16.3 Simulation Results 466
16.3.1 Chain Structure (Static Properties) 467
16.3.2 Chain Dynamics 473
16.3.3 Adsorption–Desorption Dynamics 477
16.4 Conclusions 482
Nomenclature 483
References 484

17. Characteristics of Multiwall Carbon Nanotube and Polyethylene Composites Prepared by Gelation/Crystallization from Solutions 486

17.1 Introduction 486
17.2 Characteristics of UHMWPE, EMMA, and Two Kinds of MWNTs 488
17.3 Advantage of Preparing UHMWPE–MWNT Composite by Gelation/Crystallization 489
17.4 Characteristics of UHMWPE–MWNT Composites 494
17.4.1 Morphology of the Drawn UHMWPE–MWNT Composite Film 494
17.4.2 Mechanical Property of the Undrawn and Drawn Composite Films 497
17.4.3 Electrical Conductivity of UHMWPE–MWNT Composite Films Dependent on the Temperature 499
17.4.4 Effect of Iodine Doping on the Electrical and Thermal Properties of UHMWPE–MWNT Composites 501
17.5 Uniform Mixing of UHMWPE and Rigid MWNTs with Ordered Graphene Sheets 509
17.6 Conclusions 519
Nomenclature 520
References 521

18. Crystallization Behavior of Polyethylene/Carbon Nanotube Composites **523**

18.1 Introduction 523
18.1.1 Structure and Properties of Carbon Nanotubes 523
18.1.2 Carbon Nanotube Nanocomposites 525
18.2 Experimental 526
18.2.1 Materials 526
18.2.2 Experimental Procedure 526
18.3 Results and Discussions 527
18.3.1 PE/CNT Nanohybrid Shish-Kebabs Via Solution Crystallization 527
18.3.2 PE CNT Nanohybrid Shish-Kebabs Via Physical Vapor Deposition 533
18.3.3 PE/CNT Nanocomposites 537
18.4 Conclusions 547
Acknowledgment 547
Nomenclature 547
References 548

19. Formation of Shish-Kebab Structures in Ultrahigh Molecular Weight Polyethylene (UHMWPE)/Low Molecular Weight Polyethylene (LMWPE) Composites Under Shear Flow **552**

19.1 Introduction 552
19.2 Experimental 554
19.2.1 Materials 554
19.2.2 DPLS Measurements 554
19.2.3 SAXS Measurements 555
19.2.4 SANS Measurements 555
19.3 Results and Discussion 556
19.3.1 Depolarized Light Scattering Measurements 556
19.3.2 Small-Angle X-Ray Scattering Measurements 561
19.3.3 Small-Angle Neutron Scattering Measurements 567
19.4 Conclusions 572
Nomenclature 573
References 574

20. Template Crystallization of Ultrahigh Molecular Weight Polypropylene Induced by Chain Orientation of Cocrystallized Ultrahigh Molecular Weight Polyethylene **577**

20.1 Introduction 577
20.2 Materials and Methods 579
20.2.1 Sample Preparation 579
20.2.2 Characterization 580

20.3 Results and Discussion 581
20.3.1 Thermal Characterization of Melting Transitions of Gelation-Crystallized UHMW Polyolefins 581
20.3.2 Structure of Gelation-Crystallized UHMWPE 584
20.3.3 Characterization of Gelation-Crystallized UHMWPP 587
20.3.4 *In Situ* Template Crystallization of Gelation-Crystallized UHMWPE–UHMWPP Blends 589
20.4 Conclusions 593
Acknowledgment 593
Nomenclature 593
References 594

Index **597**

Preface

Polyolefins are the most widely used commodity thermoplastics. The polyolefin field remains the most vibrant area in polymer research largely driven by the synthesis of novel polyolefins using single-site catalysts. Today, it is possible to design novel polyolefin homopolymers, copolymers, and terpolymers with precise control of chain architecture (e.g., linear chain with regular side-branching, comblike, or star-shaped topologies), microstructures, and molecular weight distributions that are hard to come by in conventional Ziegler–Natta olefin polymerization.

Polyolefin composites are a subset of polymer composites that emerged as a result of the need to meet application requirements not satisfied by synthesized neat polyolefins. In comparison to other subsets of polymer composites, polyolefin composites have distinct advantages of lower density, lower cost, processing ease, and good combination of chemical, physical, and mechanical properties. In the last several years, the research and usage of polyolefin composites have increased dramatically due to new application opportunities (e.g., in construction and transportation) and the synthesis of novel polyolefins.

To the best of the editors' knowledge, there is currently no single book that focuses exclusively on polyolefin composites. Moreover, it is important to capture in a book format the latest developments in nanostructured polyolefin composites such as polyolefin/clay nanocomposites, polyolefin nanofiber composites, and polyolefin/carbon nanotube composites. These are the two motivations to publish this book.

The chapters are organized as follows: Chapter 1 provides an overview of polyolefin composites by first introducing polyolefins as a significant class of soft materials, preparation, and reinforcement through incorporation of inorganic and organic particles and fibers. This introductory chapter further examines emerging trends in polyolefin composites research and development. The contributed chapters are divided fairly evenly among three categories, namely microcomposites (Chapters 2–7), nanocomposites (Chapters 8–14), and advanced nano- and molecular composites (Chapters 15–20). All of these chapters cover preparation, characterization, and properties of polyolefin composites at various structural levels. Chapters 15 and 16 provide new insights into fundamental theoretical understanding of nanostructured polyolefin composites from molecular perspectives through advanced modeling and simulation.

The book covers several aspects of polyolefin composites such as processing, morphological characterization, crystallization, structure and properties, and performance evaluation at micro- and nanostructural levels. Processing covers *in situ* reactive blending, functionalization, compatibilization, and addition of micro- or nanosized inorganic or organic additives of natural or synthetic origin having different functional capabilities to improve performance or to aid processing.

This book is intended to serve as a valuable reference for academic and industrial professionals engaged in research and development activities in the specific area of polyolefin composites or in the general area of polymer composites. Some review chapters are written at an introductory level to attract newcomers including senior undergraduate and graduate students and to serve as a reference book for professionals from other disciplines. Since this book is the first of its kind devoted solely to polyolefin composites, it is hoped that it will be sought after by a broader technical audience. Some knowledge of polymer chemistry, physics, and engineering, although are not strictly essential, would be helpful to better appreciate the technical contents of some chapters.

All chapters were contributed by renowned professionals from academia, industry, and government laboratories from various countries and were peer reviewed in accordance with guidelines utilized elsewhere by top-rated polymer journals. The editors would like to thank all contributors for believing in this endeavor, sharing their views and precious time, and obtaining supporting documents. Finally, the editors would like to express their gratitude to the external reviewers whose contributions helped improve the quality of this book.

Domasius Nwabunma

Thein Kyu

Contributors

Yvonne A. Akpalu, Department of Chemistry & Chemical Biology and Rensselaer Nanotechnology Center, Rensselaer Polytechnic Institute, Troy, NY 12180, USA. akpaly@rpi.edu

Carmen Albano, Laboratorio de Polímeros, Centro de Química, Instituto Venezolano de Investigaciones Científicas (IVIC); Caracas, Venezuela.
Escuela de Ingeniería Química, Facultad de Ingeniería, Universidad Central de Venezuela (UCV), Caracas, Venezuela. calbano@ivic.ve

Mirta I. Aranguren, INTEMA-Facultad de Ingeniería; Universidad Nacional de Mar del Plata, Juan B. Justo 4302, B7608FDQ Mar del Plata, Argentina. marangur@fi.mdp.edu.ar

Anna C. Balazs, Department of Chemical and Petroleum Engineering, University of Pittsburgh, Pittsburgh, PA 15261, USA. balazs1@engr.pitt.edu

Celina R. Bernal, Advanced Materials Group, INTECIN (UBA-CONICET), Department of Machanical Engineering, Engineering Faculty, University of Buenos Aires, Av. Paseo Colón 850, C106 3ACV, Buenos Aires, Argentina. crbernal@fi.mdp.edu.ar

Jozef Bicerano, Bicerano & Associates Consulting, Inc., 1208 Wildwood Street, Midland, MI 48642, USA. bicerano@polymerexpert.biz

Yuezhen Bin, Department of Clothing and Apparel Science, Nara Women's University, Nara, Women's University, Nara 630–8263, Japan. yuezhen@cc.nara-wu.ac.jp

Qingyun Chen, Department of Clothing and Apparel Science, Nara Women's University, Nara 630–8263, Japan. eak.chin@cc.nara-wu.ac.jp

Yang C. Chua, Institute of Materials Research & Engineering, 3 Research Link, Singapore 117602. chuayc@imre.a-star.edu.sg

Peter J. Dionne, Department of Mechanical, Aerospace and Nuclear Engineering, Rensselaer Polytechnic Institute, Troy, NY 12180, USA. dionnp@rpi.edu

Soney C. George, Amal Jyothi College of Engineering, Koovapally, Kottayam 686518, Kerala, India. soneygeo@sancharnet.in

Valeriy V. Ginzburg, The Dow Chemical Company, Core Research and Development, Building 1710, Midland, MI 48674, USA. vvginzburg@dow.com

Ulla Hippi, Laboratory of Polymer Technology, Polymer Science Centre, Helsinki University of Technology, P.O. Box 3500, 02015 TKK, Finland. ulla.hippi@tkk.fi

Yuan Hu, State Key Laboratory of Fire Science, University of Science and Technology of China, Hefei, Anhui 230026, China. yuanhu@ustc.edu.cn

Jyoti P. Jog, Polymer Science and Engineering Division, National Chemical Laboratory, Dr. Homi Bhabha Road, Pashan, Pune 411008 India. jp.jog@ncl.res.in

Toshiji Kanaya, Institute for Chemical Research, Kyoto University, Uji, Kyoto-fu 611–0011, Japan. kanaya@scl.kyoto-u.ac.jp

Steve L. Kodjie, Arkema Inc., Analytical & Systems Research, King of Prussia, PA 19406, USA. tephen.kodjie@arkemagroup.com

Thein Kyu, Department of Polymer Engineering, University of Akron, Akron, OH 44325–0301, USA. tkyu@uakron.edu

Bing Li, A. J. Drexel Nanotechnology Institute and Department of Materials Science and Engineering, Drexel University, Philadelphia, PA 19104, USA. bl56@drexel.edu

Christopher Y. Li, A. J. Drexel Nanotechnology Institute and Department of Materials Science and Engineering, Drexel University, Philadelphia, PA 19104, USA. chrisli@drexel.edu

Lingyu Li, A. J. Drexel Nanotechnology Institute and Department of Materials Science and Engineering, Drexel University, Philadelphia, PA 19104, USA. 1168@drexel.edu

Barbro Löfgren, Laboratory of Polymer Technology, Polymer Science Centre, Helsinki University of Technology, P.O. Box 3500, 02015 TKK, Finland. barbro.lofgren@tkk.fi

Hongdian Lu, State Key Laboratory of Fire Science, University of Science and Technology of China, Hefei, Anhui 230026, China. Department of Chemical and Material Engineering, Hefei University; Hefei, Anhui 230022, China. hdlu@mail.ustc.edu.cn

Xuehong Lu, School of Materials Science and Engineering, Nanyang Technological University, Nanyang Avenue, Singapore 639798 asxhlu@ntu.edu.sg

Adriaan S. Luyt, Department of Chemistry, University of the Free State, (Qwagwa Campus), Private Bag X13; Phuthaditjhaba 9866, South Africa. luytas@qwa.uovs.ac.za

Rockliffe St. J. Manley, Department of Chemistry, McGill University, Montreal, Quebec, Canada H3A 2A7. jim.manley@mcgill.ca

Norma E. Marcovich, INTEMA-Facultad de Ingeniería; Universidad Nacional de Mar del Plata, Juan B. Justo 4302, B7608FDQ Mar del Plata, Argentina. marcovic@fi.mdp.edu.ar

Go Matsuba, Institute for Chemical Research, Kyoto University, Uji, Kyoto-fu 611–0011, Japan. gmatsuba@scl.kyoto-u.ac.jp

Masaru Matsuo, Department of Clothing and Apparel Science, Nara Women's University, Nara 630–8263, Japan. m-matsuo@cc.nara-wu.ac.jp

Koji Nishida, Institute for Chemical Research, Kyoto University, Uji, Kyoto-fu 611–0011, Japan. knishida@scl.kyoto-u.ac.jp

Domasius Nwabunma, 3M Company, Safety, Security, and Protection Business Services Laboratory, St. Paul, MN 55144, USA. dnwabunma@mmm.com

Rahmi Ozisik, Department of Materials Science and Engineering, Rensselaer Polytechnic Institute, Troy, NY 12180, USA. ozisik@rpi.edu

Rosestela Perera, Departmento de Mecánica, Universidad Simón Bolivar (USB), Caracas, Venezuela. rperera@usb.ve

Catalin R. Picu, Department of Mechanical, Aerospace and Nuclear Engineering, Rensselaer Polytechnic Institute, Troy, NY 12180, USA. picuc@rpi.edu

Laly A. Pothan, Department of Chemistry, Bishop Moore College, Mavelikkara 690101, Kerala, India. lalyaley@yahoo.co.uk

María M. Reboredo, INTEMA-Facultad de Ingeniería, Universidad Nacional de Mar del Plata, Juan B. Justo 4302, B7608FDQ Mar del Plata, Argentina. mrebored@fi.mdp.edu.ar

Noora Ristolainen, Laboratory of Polymer Technology, Polymer Science Centre, Helsinki University of Technology, P.O. Box 3500, 02015 TKK, Finland. noora.ristolainen@tkk.fi

Jukka Seppälä, Laboratory of Polymer Technology, Polymer Science Centre, Helsinki University of Technology, P.O. Box 3500, 02015 TKK, Finland. jukka.seppala@tkk.fi

Robert A. Shanks, CRC for Polymers, School of Applied Sciences, RMIT University, GPO Box 2476V, Melbourne, Vic 3001, Australia. robert.shanks@rmit.edu.au

Lei Song, State Key Laboratory of Fire Science, University of Science and Technology of China, Hefei, Anhui 230026, China. leisong@ustc.edu.cn

Sabu Thomas, School of Chemical Sciences, Mahatma Gandhi University, Priyadarshini Hills, Kottayam 686560, Kerala, India. sabut@sancharnet.in; sabut552001@yahoo.com

Sie C. Tjong, Department of Physics and Materials Science, City University of Hong Kong, Tat Chee Avenue, Kowloon, Hong Kong. aptjong@cityu.edu.hk

José I. Velasco, Centre Català del Plàstic, Departament de Ciències dels Materials i Enginyeria Metallúrgica, Universitat Politècnica de Catalunya, C. Colom 114, E-08222 Terrassa (Barcelona), Spain. jose.ignacio.velasco@upc.edu

Ke Wang, Institute of Materials Research & Engineering, 3 Research Link, Singapore 117602. k-wang@imre.a-star.edu.sg

Santosh D. Wanjale, Polymer Science and Engineering Division, National Chemical Laboratory, Dr. Homi Bhabha Road, Pashan, Pune 411008, Maharashtra, India. sd.wanjale@ncl.res.in

Atsuko Yamanaka, Department of Clothing and Apparel Science, Nara Women's University, Nara 630–8263, Japan. atsu0038@yahoo.co.jp

Part I

Introduction

Chapter 1

Overview of Polyolefin Composites

Domasius Nwabunma[1]

1.1 INTRODUCTION

Polyolefins are synthetic polymers of olefinic monomers. They are the largest polymer family by volume of production and consumption. Several million metric tons of polyolefins are produced and consumed worldwide each year, and as such they are regarded as commodity polymers. Polyolefins have enjoyed great success due to many application opportunities, relatively low cost, and wide range of properties. Polyolefins are recyclable and significant improvement in properties is available via blending and composite technologies.

Polyolefins may be classified based on their monomeric unit and chain structures as ethylene-based polyolefins (contain mostly ethylene units), propylene-based polyolefins (contain mostly propylene units), higher polyolefins (contain mostly higher olefin units), and polyolefin elastomers (1). Ethylene-based polyolefins are normally produced either under low pressure conditions using transition metal catalysts resulting in predominantly linear chain structure or under high pressure conditions using oxygen or peroxide initiators resulting in predominantly branched chain structures of various densities and crystallinity levels.

Propylene-based polyolefins are normally produced with transition metal catalysts resulting in linear chain structures with stereospecific arrangement of the propylene units or special stereoblock structures from a single-site catalyst. Higher polyolefins are normally produced using transition metal catalysts resulting in linear and stereospecific chain structures. Polyolefin elastomers based mainly on a combination of ethylene and propylene may be produced using metal or single-site catalysts with or without the inclusion of dienes (for cross-linking) and are mostly amorphous

[1]3M Company, Safety, Security, and Protection Business Services Laboratory, St. Paul, MN 55144, USA

Polyolefin Composites, Edited by Domasius Nwabunma and Thein Kyu

with high molecular weights and heterogeneous in phase structures. One may conclude that a given polyolefin may be a homopolymer, copolymer, or terpolymer depending on the number of monomers used in making the polyolefin, crystalline or amorphous depending on their chain conformation, configuration, and processing conditions.

Today polyolefins and polyolefin-based materials are used in many applications. These applications include transportation (automotive, aerospace), packaging, medical, consumer products (toys, appliances, etc.), electronics, cable and wire coating, thermal and acoustic insulation, and building and construction. Polyolefins can be extruded as filaments (fibers), films (cast and blown), and pipes/profiles. They can be molded into parts of various shapes. They can be foamed with physical and chemical foaming/blowing or/and can be coated onto other materials.

1.2 OLEFINIC MONOMERS

The alkenes having one or more unsaturated double bonds in their structures are the monomers used to synthesize polyolefins. They have the general formula C_nH_{2n}, $n \geq 2$. Table 1.1 shows the first 10 members of the olefinic monomers with one double bond, which are often called α-olefins.

The monomers in Table 1.1 form a homologous series of hydrocarbon compounds. Thus, apart from having the same general formula, all compounds in the series have the same functional groups. Each member of the group differs from the next in the series by the CH_2 group equivalent to 14 relative molecular mass units.

All members of the series have similar chemical properties. The physical properties of the compounds in the series show a progressive change with increasing relative molecular mass. The first three members of the alkenes homologous series are gases at room temperature. Those containing between 5 and 15 carbon atoms are colorless liquids and the higher compounds are waxy solids at room temperature. These α-olefinic monomers may be obtained as products of the cracking of gas–oil and naphtha fractions of petroleum distillations. They can also be obtained from synthetic organic chemistry methods.

Table 1.1 Alkene Monomers Having One Double Bond Used in the Synthesis of Polyolefins.

No. of carbon atoms (n)	Formula (C_n>H_{2n}, $n \geq 2$)	Name (other name)
2	C_2H_4	Ethene (ethylene)
3	C_3H_6	Propene (propylene)
4	C_4H_8	Butene-1 (butylene)
5	C_5H_{10}	Pentene-1
6	C_6H_{12}	Hexene-1
7	C_7H_{14}	Heptene-1
8	C_8H_{16}	Octene-1
9	C_9H_{18}	Nonene-1
10	$C_{10}H_{20}$	Decene-1

1.3 POLYOLEFIN HOMOPOLYMERS, COPOLYMERS, AND TERPOLYMERS

Polyolefin homopolymers, copolymers, and terpolymers are foundation materials for polyolefin blends. They may be obtained via radical or ionic chain growth polymerization of alkenes using conventional free radicals (e.g., from peroxides) and organometallic complexing (Ziegler–Natta and metallocenes) catalyst systems. Polyolefin polymerization technologies and novel catalyst systems have enabled the rapid development of polyolefins with a wide range of molecular chain structures, morphologies, properties, and particle size and shape.

Polyolefin homopolymers include polyethylene (PE), polypropylene (PP), polybutene-1 (PB), polymethylpentene-1 (PMP), and higher polyolefins. Table 1.2 shows the structures of commercial polyolefin homopolymers.

Table 1.2 Structures of Commercial Polyolefin Homopolymers.

Name (other name)	Chemical structure (repeat unit)
Polyethylene (polyethene, polymethylene)	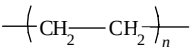
Polypropylene (polypropene)	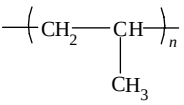
Polybutylene (polybutene-1)	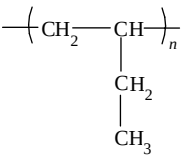
Polyisobutylene (polysobutene-1)	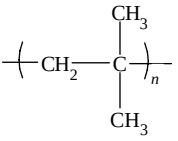
Polybutadiene	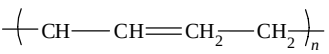
Poly-4-methylpentene-1	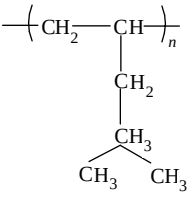
Polyisoprene	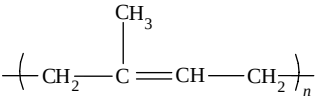

Of these, PE and PP are the largest by amount produced yearly by the global polyolefin companies (1). PE comes in various forms differing in chain structures, crystallinity, and density levels. These are high density polyethylene (HDPE), low density polyethylene (LDPE), linear low density polyethylene (LLDPE), ultralow density polyethylene (ULDPE), and ultrahigh molecular weight polyethylene (UHMWPE). PP and higher polyolefins come in three stereo specific forms of varying densities: isotactic, syndiotactic, and atactic forms.

Polyolefin copolymers involve two olefinic monomers. The process of copolymerization is normally used to control the properties of the polyolefins. Some of the consequences of copolymerization are reduced crystallinity, melting point, modulus, strength, hardness, and low temperature impact. Polyolefin copolymers are either random or block copolymers of same or different monomers and may be a single phase or heterophasic depending on the amount of comonomer, the polymerization catalyst, and the process. For polyolefin copolymer of same monomers, this can be achieved by having different segments of the copolymer with different tacticities. One can have polyolefin block copolymers of same block or of varying block lengths. One can also have polyolefin copolymers consisting of both block and random segments together in the same macromolecule. Polyolefin copolymers are usually not homogeneous in composition but are actually mixtures of copolymers of varying compositions. It is also possible with polyolefins to have block copolymers with only one monomer. These are called stereoblock copolymers and can be achieved by having sections of the polyolefin copolymer possess different tacticities.

Polyolefin copolymers started with LLDPE and ethylene–propylene rubber (EPR). Today there are polyolefin copolymers of ethylene with butene-1, hexene-1, octene, cyclopentene, and norbornene and copolymers of propylene with butene-1, pentene-1, and octene-1 in addition to ethylene. There are copolymers of butene-1 with pentene-1, 3-methylbutene-1, 4-methylpentene-1, and octane in addition to its copolymers with ethylene and propylene. There are copolymers of 4-methyl-pentene-1 with pentene-1 and hexane-1 in addition to its copolymers with butene-1 and propylene. The function of the comonomers is to reduce crystallinity, as compared to the homopolymers, resulting in copolymers that are highly elastomeric with very low glass transition temperatures, high impact strength, low modulus, low density, and often optical transparency. The most widely used multiphase polyolefin copolymer is polypropylene impact copolymer. These copolymers are typically composed of isotactic polypropylene (iPP) and EPR. Impact polypropylene copolymers are produced by various processes, but they are generally characterized by the synthesis of iPP in the first reactor and EPR in the second reactor. Therefore, these systems are typically reactor blends. Postreactor blending can be done, but the starting material is most often the reactor blend polypropylene copolymer. Polyolefin copolymers are often used for film applications or as impact modifiers.

Polyolefin terpolymers contain three olefinic monomers in their structures. A well-known example is ethylene propylene diene monomer (EPDM). The diene

(double bond) monomer is usually ethylidene norbornene or 1,4-hexadiene. EPDM was introduced because of the difficulty in cross-linking saturated polyolefin homopolymers and copolymers.

There are also functionalized polyolefins. These are usually copolymer or terpolymer containing functional groups like epoxide, anhydride, hydroxyl, acrylate, and carboxylic acid. These functional groups are either grafted onto the polyolefin after polymerization or added directly *in situ* during polymerization reactions involving olefins and functional groups bearing polar monomers such as vinyl acetate, methyl acrylate, butyl acrylate, glycidyl methacrylate, and acrylic acid. Functionalized polyolefins are useful compatibilizers and impact modifiers in blends and composites containing polyolefins and nonpolyolefins. In this sense, functionalized polyolefins may be considered as additives rather than matrix materials in the formulation of polyolefin composites.

Commercial polyolefins often contain additives such as colorants, flame retardants, antioxidants, light stabilizers, nucleating agents, antistatic agents, and lubricants (microcrystalline waxes, hydrocarbon waxes, stearic acid, and metal stearates). These additives aid the processing and fabrication of products from polyolefins. Detailed treatments about specific polyolefins, polymerization systems/mechanism/processes, structures, properties, processing, and applications may be found in References (2–9).

1.4 POLYOLEFIN COMPOSITES

Polyolefin composites are a subset of polymer composites (10–14). They emerged as a result of the need to meet the increasing application demands not satisfied by synthesized neat polyolefins. Polyolefin composites may be defined as polyolefin-based materials containing at least one functional nonpolymeric additive of organic or inorganic origin. Polyolefin composites may be consolidated, void containing, with random or oriented additives. Additives of interest in the formulation of polyolefin composite may be of natural or synthetic origin, different sizes, continuous (long) or discontinuous (short) in length, fibrous, flaky, disc-like or spherical.

Additives in polyolefin composites may be classified according to their functions as modifiers (e.g., fillers, plasticizers, blowing agents, coupling agents, impact modifier, and nucleating/clarifying agents), property extenders (e.g., heat stabilizer, antioxidants, flame retardants, light stabilizers, antistatic agents, and biocides), and processing aids (e.g., lubricants, slip agents, and antiblocking agent). In terms of specific chemical names, additives used in polyolefin composites include, but not limited to, the following: glass fibers, hollow glass bubbles, clay minerals, carbon black, carbon nanotubes, carbon fibers, graphite, wollastonite, magnesium hydroxide, aluminum trihydroxide, attapulgite, titanium dioxide, hydroxyapatite, calcium carbonate, silica, and natural fibers.

In addition to the polyolefin and the additives, polyolefin composites may contain other thermoplastics or thermosetting polymers. The characteristics of polyolefin

composites are determined by the properties of their components, compositions, structures, and interactions, as is case with any multicomponent material. Table 1.3 lists the typical polyolefin composites studied in the literature (15–396). These composites involve the following polyolefins: PP, PE (LLDPE, LDPE, HDPE, and UHMWPE), EPR, EPDM, and PB.

Polyolefin composites may be prepared by processes that involve mixing and/or melting the components of the composites in a batch or in continuous mixers (single and twin screw extruders), followed by fabrication (molding, thermoforming) into the desired shape. The mixing process may be physical or accompanied by chemical reactions in situations where chemical or reactive modifiers are used.

There are plenty of publications (journal articles and patents) on polyolefin composites in the literature. To illustrate the abundant publications in the field, Tables 1.4 shows the total number of journal articles and patents published each year during the 6-year period from 2000 to 2005.

The date range is arbitrarily chosen. The number of journal articles for each year was electronically searched and obtained from polymer and polymer-related journals using the keywords polyolefin and composite. Within the polyolefin keyword, the subkeywords used in the search are polyethylene (PE, LLDPE, LDPE, HDPE, UHMWPE, PE, etc.), polypropylene (PP, iPP, sPP, aPP, etc.), polybutene-1 (PB), poly-4-methyl pentene-1 (PMP), ethylene–diene monomer (EPDM), ethylene–propylene–diene terpolymer(EPDM), ethylene–propylene rubber (EPR), thermoplastic olefins (TPO), natural rubber, polybutadiene, polyisobutylene, polyisoprene, and polyolefin elastomer (POE). Within the keyword composite, subkeywords used are clay (kaolin, talc, mica, smectite, (bentonite (montmorillonite) and hectorite)), alumina, hydroxyapatite, carbon black, carbon nanotube, carbon fiber, natural fiber (flax, jute, silk, wool, cotton, linen, kenaf, cashmere, sisal, bamboo, hemp, coconut, etc.), wood flakes, flour, fiber, ammonium polyphosphate, aluminum trihydroxide (aluminum trihydrate), magnesium hydroxide, graphite, attapulgite, cellulosic flour, wollasonite, silica, titanium dioxide, mica, calcium carbonate, glass beads, glass fiber, glass bubbles, and so on.

Regarding the patent search, polymer indexing codes and manual codes were used to search for the patents in Derwent World Patent Index based on the above keywords. Table 1.4 shows a growing trend in the number of publications in the polyolefin composites. It should be noted that in the preparation of Table 1.4, it is possible that some publications were missed in the reference search period (2000–2005).

Polyolefin composites research involves many issues such as the following:

i. Effect of additives (e.g., coupling agent, fillers, and impact modifier).

ii. Batch and continuous mixing/compounding and molding.

iii. Morphological characterization using techniques such as scanning electron microscopy (SEM), transmission electron microscopy (TEM), atomic force microscopy (AFM), and polarized light microscopy (PLM).

Table 1.3 Polyolefin Composites Studied in the Literature.

Polyolefin composites		
PE/calcium carbonate (35, 200, 228, 235, 238, 242, 243, 247, 250, 258)	PP/PS/montmorillonite (177)	PP/PET/glass beads (55, 109, 346)
PE/wood flour (42, 48, 56, 101, 138, 192, 259, 395)	PP/polyamide 6/glass fiber (107, 249, 335, 382)	PP/lignocellulosic flour (145)
PE/PA6/montmorillonite (175)	PP/PA6/talc (110)	PP/PMMA/calcium carbonate (118)
PE/PA6/glass fiber (128)	PP/PA6/calcium carbonate (110)	PP/SBR/calcium carbonate (143)
PE/alumina (148)	PP/PA6/ammonium polyphosphate (110)	PP/EPDM/wollasonite (45)
PE/Ethylene-co-ethyl acrylate/carbon black (164)	PP/glass beads (42, 70, 203, 224, 312, 383)	PP/EPDM/clay (33, 351)
PE/silica (171)	PP/PA6/montmorillonite (68, 82, 147, 360)	PP/EPDM/glass beads (157)
PE/EVA/montmorillonite (26)	PP/sisal fiber (285, 318, 338, 379)	PP/EPDM/glass fiber (333)
PE/carbon nanotube (91)	PP/carbon black (16, 209, 276, 295, 339)	PP/EPDM/calcium carbonate (187)
PE/titanium dioxide (137)	PP/HDPE/wood flour (287)	PP/EPDM/antimoniumntrioxide (257)
PE/glass fiber (309, 310, 317)	PP/magnesium–aluminum silicate (60)	PP/EPDM/flax fiber (41, 172)
PE/LCP fiber/glass fiber (326)	PP/SBS/glass fiber (324, 325)	PP/flax fiber (321)
PE/hydroxyapatite (161)	PP/alumina (132)	PP/copper wire/glass fiber fabric (327)
PE/magnesium hydroxide (254, 278, 394)	PP/magnesium hydroxide (47, 86, 103, 134, 262)	PP/EPDM/talc (158)
PE/graphite (72, 286, 329, 350, 366)	PP/basalt fiber (112)	PP/EPDM/white rice husk (220, 241, 244)
PE/natural fiber(252)	PP/PET/montmorillonite (114)	Polybutadiene/montmorillonite (263)
PE/jute fiber (229)	PP/natural rubber/rice husk ash (245)	Polybutadiene/carbon black (377)
PE/glass fiber/sisal fiber (359)	PP/talc (51, 65, 160, 169, 170, 214, 362, 380, 389)	Poly(butene-1)/montmorillonite (74)
PE/sisal fiber (199, 305)	PP/aluminum trihydroxide (42, 43, 186)	Poly(4-methyl-1-pentene)/ montmorillonite (364)
PE/montmorillonite (18, 22, 30, 37, 46, 67, 73, 75, 85, 100, 119, 135, 136, 151, 154, 156, 173, 175, 183, 191, 197, 198, 225, 261, 266, 272, 274, 337, 341, 342, 365)	PP/glass fiber (102, 211, 221, 237, 281, 296, 298, 301, 304, 306, 328, 330, 332)	EPR/silica (106, 293)

Table 1.3 (*Continued*)

Polyolefin composites		
PE/wood fiber (267, 386)	PP/carbon nanotube (21, 34, 134, 144)	EPR/wollasonite (182)
PE/wood flake (292)	PP/EVA/calcium carbonate (57)	EPR/carbon fiber (96)
PE/PP/glass fiber (230)	PP/natural fiber/magnesium hydroxide (265)	EPDM/silica (375)
PE/red phosphorus (278)	PP/HDPE/EPR/calcium carbonate (284)	EPDM/white rice husk (375)
PE/PP/calcium carbonate (64, 284)	PP/PE/magnesium hydroxide (277)	EPDM/melamine fiber (275, 315)
PE/carbon black (23, 72, 79, 104, 126, 129, 279, 282, 289, 290, 349, 361)	PP/carbon fiber (202, 295, 322, 331)	EPDM/clay (52, 210, 255, 357, 373)
PE/calcite/zeolite (387)	PP/calcium carbonate (32, 80, 84, 120, 152, 184, 201, 204, 207, 246, 302, 311, 334, 336, 371)	EPDM/butyl rubber/carbon black (193)
PE/magnesium–aluminum double hydroxide (194)	PP/wood fiber (58, 14, 208, 222, 299–300)	EPDM/aluminum trihydroxide (291)
PP/talc/calcium carbonate (264)	PP/silica (77, 78, 117, 353, 363, 390)	EPDM/carbon black (49, 196, 268, 291)
PP/kenaf fiber (58)	PP/ethylene-co-octene/clay (99)	Natural rubber/oil palm wood flour
PP/cotton fibers/wood flakes (111)	PP/polyhedral oligomeric silsesquioxanes (89)	Natural rubber/aluminium powder (280)
PP/wood flour (59, 138, 162, 181, 248, 294)	PP/graphite (176)	Natural rubber/ montmorillonite (205, 358)
PP/kaolin (240)	PP/SBS/glass fiber (323, 324)	Natural rubber/silica (206, 212, 227, 233, 283, 354, 368)
PP/clay/calcium carbonate (142)	PP/montmorillonite (19, 15, 17, 25, 27, 29, 31, 38–40, 44, 54, 61, 63, 66, 69, 71, 75, 76, 81, 83, 87, 88, 92–95, 98, 108, 113, 115, 116, 121, 124, 130, 131, 133, 153, 155, 159, 165–167, 178, 179, 190, 194, 213, 226, 231, 232, 256, 260, 266, 269–271, 273, 297, 308, 340, 342, 343, 345, 347, 352, 355, 367, 385, 393, 395)	Natural rubber/bamboo fiber (216)

PP/natural fiber (234, 303)
PP/rice husk powder (214, 353)
PP/silver (370)

PP/HDPE/sisal fiber (379)
PP/HDPE/EPR/sisal fiber (379)
PP/PC/attapulgite (150, 391)
PP/calcite/zeolite (387)

PP/ethylene-co-octene/magnesium hydroxide (123)
PP/EPDM/paper sludge (253)
PP/natural rubber/white husk powder (245)

PP/EPR/talc (24)
PP/EPR/silica (90)
PP/EPR/montmorillonite (50, 174)
PP/epoxy/glass fiber/carbon black (127)

Natural rubber/rubber wood fiber (384)
Natural rubber/kenaf (236)
Natural rubber/carbon black (215, 218, 223, 239, 283, 368, 374, 376, 388)
Natural rubber/calcium carbonate (239)
Natural rubber/lead (316)
Natural rubber/carbon fiber (374, 390)
Natural rubber/lignocellulosic (251)

Table 1.4 Summary of Number of Electronic Articles on Polyolefin Composites Published between 2000 and 2005 in English Language-Based Polymer and Polymer-Related Journals in Comparison to the Number of Patents.

	Journal articles						
Year	2000	2001	2002	2003	2004	2005	Total
Number of articles	34	53	44	57	95	99	382
	Patents						
Year	2000	2001	2002	2003	2004	2005	Total
Number of patents	244	259	379	374	407	442	2105

iv. Structural characterization using radiation scattering and diffraction techniques such as X-ray scattering (XRS), X-ray diffraction (XRD), electron diffraction, and small-angle neutron scattering (SANS).

v. Structural characterization using spectroscopic techniques such as nuclear magnetic resonance (NMR) and Fourier transform infrared (FTIR).

vi. Rheological characterization.

vii. Thermal transitions and thermal stability.

viii. Isothermal and nonisothermal crystallization behavior under quiescent and nonquiescent conditions.

ix. Mechanical (static and dynamic) behavior under tensile, shear, compressive, or impact mode.

x. Plastic deformation.

xi. Thermomechanical behavior and thermal stability.

xii. Adhesion, interfacial, and interphase behavior.

xiii. Fire resistance/flammability behavior.

xiv. Barrier and transport properties.

xv. Surface/tribological properties.

xvi. Electrical/dielectric properties.

xvii. Ageing effects (time–temperature-dependent behavior).

xviii. Modeling and simulation via the use of phenomenological, atomistic, molecular dynamics, and Monte Carlo methods and comparisons with experimental results.

Of these issues, investigation of the effect of the use of coupling agents on interfacial adhesion between the hydrophobic polyolefin and the hydrophilic additive (particulate or fibrous) appears to be the most important. Poor polyolefin–additve interaction gives rise to poor properties, in particular mechanical property. The function of the coupling agent is to reduce the interfacial tension between a polymer and the nonviscoelastic particulate or fibrous additive and hence improve the desired composite properties. Table 1.5 shows a list of coupling agents used in the formulation of

Table 1.5 Polymeric and Nonpolymeric Coupling Agents Used in the Formulation of Polyolefin Composites.

Coupling agent	Polyolefin composite
PE-g-maleic anhydride	PE/montmorillonite (18, 30, 37, 46, 53, 67, 75, 100, 153, 173, 175, 183)
Ethylene-co-vinyl acetate	PE/montmorillonite (26)
Ethylene-co-glycidyl methacrylate	PE/montmorillonite (53)
Hydroxyl (OH) functionalized PE	PE/montmorillonite (53)
Ethylene-co-methacrylic acid	PE/montmorillonite (100)
PE-g-maleic anhydride	PE/PA6,6/montmorillonite (175)
PE-g-maleic anhydride	PE/wood flour (42)
Stearic anhydride	PE/wood flour (48)
PP-g-maleic anhydride	PE/wood flour (48)
Ethylene-co-methacrylic acid	PE/wood flour (101)
PE-g-acrylic acid	PE/wood flour (395)
PE-g-maleic anhydride	PE/wood fiber (267)
2-Hydroxy ethyl methacrylate	PE/jute fiber (229)
PE-g-maleic anhydride	PE/calcium carbonate
PP-g-maleic anhydride	PP/montmorillonite (19, 25, 27, 44, 62, 66, 76, 83, 92–94, 98, 116, 121, 125, 159, 165–167, 178, 179, 213, 269, 270, 308, 342, 395)
Styrene-co-maleic anhydride	PP/montmorillonite (83)
Hydroxyl (OH) functionalized PP	PP/montmorillonite (87)
Hydroxyl (OH) and amine (NH_2) Functionalized PP	PP/montmorillonite (115)
Hexamethylene modified PP-g-maleic anhydride	PP/montmorillonite (131)
PP-g-acrylic acid	PP/montmorillonite (159)
PP-g-maleic anhydride	PP/PA6/montmorillonite (147)
EPR-g-maleic anhydride	PP/PA6/montmorillonite (68, 147)
PP-g-maleic anhydride	PP/ethylene-co-octene/montmorillonite (99)
PP-g-maleic anhydride	PP/EPDM/montmorillonite (33, 63)
PP-g-maleic anhydride	PP/PET/montmorillonite (114)
PP-g-maleic anhydride	PP/EPDM/flax fiber (41)
PP-g-maleic anhydride	PP/PET/glass bead (55)
PP-g-maleic anhydride	PP/wood flour (59, 138, 162, 181, 248)
Styrene-co-ethylene-co-butadaiene-co-styrene-g-maleic anhydride	PP/wood flour (138)
PP-g-maleic anhydride	PP/wood flour (294)
PP-g-maleic anhydride	PP/wood fiber (222, 300)
PP-g-maleic anhydride	PP/natural fiber (234)
PP-g-maleic anhydride	PP/kenaf fiber (121, 323)
PP-g-monomethyl itaconate	PP/rice husk
PP-g-succinyl-fuoresceine	PP/talc (65)
PP-g-maleic anhydride	PP/silica (90)
Ethylene-co-butyl acrylate	PP/silica (90)
Ethylene-co-butyl acrylate-co-maleic anhydride	PP/silica (90)

Table 1.5 (*Continued*)

Coupling agent	Polyolefin composite
PP-g-monomethyl itaconate	PP/silica (353)
Styrene-co-ethylene-co-butadaiene-co-styrene	PP/glass fiber (306)
Styrene-co-ethylene-co-butadaiene-co-styrene-g-maleic anhydride	PP/glass fiber (306)
PP-g-maleic anhydride	PP/PA6/glass fiber (107)
PP-g-acrylic acid	PP/PA6/glass fiber (382)
4,4′-Diphenylmethane carbodiimide	PP/PA6/glass fiber (249)
4,4′-Diphenylmethane bismaleimide	PP/PA6/glass fiber (249)
2,2′-(1,4-Phenylene) bisoxazoline	PP/PA6/glass fiber (249)
PP-g-maleic anhydride	PP/PET/glass beads (109)
PP-g-maleic anhydride	PP/silicon dioxide (117)
PP-g-maleic anhydride	PP/calcium carbonate (204)
PP-g-acrylic acid	PP/calcium carbonate (334)
PP-g-maleic anhydride	PP/graphite (176)
PP-g-maleic anhydride	PP/graphite oxide (176)
PP-g-maleic anhydride	PP/EPDM/paper sludge (253)
PP-g-acrylic acid	PP/magnesium hydroxide (47)
1, 3-Phenylene dimaleimide	PP/magnesium hydroxide (103)
PP-g-maleic anhydride	PP/aluminum trihydroxide (185)
Hydroxyl (OH) functionalized PP	PP/aluminum trihydroxide (185)
EPDM-g-maleic anhydride	EPDM/montmorillonite (255)
PP-g-maleic anhydride	EPR/carbon fiber (96)
Ethylene diamine dilaurate	Natural rubber/silica (229)
Propylene-co-ethylene-g-acrylic acid	Natural rubber/LLDPE/white rice husk ash (219)
PP-g-maleic anhydride	Natural rubber/kenaf fiber (236)

polyolefin composites. These coupling agents are either polymer based (high molecular weight) or low molecular weight.

1.5 TRENDS IN POLYOLEFIN COMPOSITES

The first trend and perhaps the most important one is the addition of nanosized additives to form polyolefin nanocomposites. This trend has begun to gain wider acceptance and utility. Polyolefin nanocomposites are expected to be used in applications such as automotive, packaging, electronics, and electrical industries. The nanosized additives include layered clay minerals such as smectite, (bentonite (montmorillonite), vermiculite, kaolinite, hectorite), carbon nanotubes/nanofibers, and silica nanoparticles. The layered nanoclays and nanofibers/nanotubes have large aspect ratio, whereas other nanoparticles have large surface areas. In polyolefin nanocomposites, properties such as strength and stiffness, flame retardation/char

formation, barrier, heat distortation temperature, electrical and thermal conductivities can be improved significantly at low (typically < 5 wt%) nanosized additive loadings, compared with composites of macro- and microsized additives. Methods to make polyolefin nanocomposites include *in situ* polymerization, melt blending, solution blending, and ultrasonic mixing. In the nanocomposites containing layered clay, the clay may be exfoliated, intercalated, or in tactoid form. It is preferred to have the clay in the exfoliated form to obtain the desired property improvement. The main application of polyolefin nanocomposites is in the automotive industry with rising demand in packaging, building and construction, appliances, electrical and electronics, tools, sporting equipment, and so on.

The second trend is the growing use of certain functional additives. These additives improve either processing or performance of polyolefin composites. For example, there is a growing importance of the use of flame retardants, particularly nonhalogenated flame retardant such as nitrogen/phosporus-based compounds (ammonium polyphosphates, melamine, melamine cyanurate, melamine phosphates, etc.), metal oxides (e.g., aluminum oxide and antimonum oxides), hydroxides (e.g., alumnum trihydroxide and magnesium hydroxide), and metal hydrates (e.g., zinc borate). Flame retardant polyolefin composites find applications in electrical and electronics, transportation (motor vehicles, aircraft, and rail), building and construction, plastic-based consumer goods, and wire and cables. There is a growing use of block copolymers containing amine, epoxy, anhydride, and acid functionality as coupling agents in polyolefin composites formulation, in contrast to maleic anhydride-grafted polyolefins, which comparatively are not very efficient. This leads to polyolefin composites with improved impact. Reinforced/filled polyolefin composites with improved impact are increasingly replacing low end engineering polymers such as ABS and polyamides. Other functional additives that are increasingly used in the development polyolefin composites are stabilizers that improve long-term heat and light stability, high molecular weight antioxidants that address yellow discoloration caused by conventional phenolic antioxidants, surface modifiers that render polyolefin surface hydrophilic, processing aids (silica, flouropolymers, hydrocarbon waxes, and metal stearates) that improve flow properties, dispersants for better distribution of the additives within the polyolefin matrix, antimicrobials/biocides to inhibit the growth of bacteria, fungi, molds, mildews, and hollow glass bubbles/foaming agents for density reductions.

The third trend is particularly important from the standpoint of the development of polyolefin composites that are environmentally sustainanble, recyclable, renewable, and reusable. Example is the increasing modification of polyolefins (notably PE, PP, and EPDM) with biodegradable additives such as flax, jute, silk, wool, cotton, linen, kenaf, cashmere, sisal, bamboo, hemp, coconut, ramie, bagasse, abaca, corn starch, tapioca, and sago to form the so-called ecocomposites or green composites. The most widely used ''ecocomposites'' is polyolefin/wood flour or fiber composite. The challenge in polyolefin/biodegradable additive composites is the improvement of adhesion between the additives and the polyolefin and the dispersion of additives within the polyolefin matrix. These two challenges are being addressed by the use of coupling agents and chemical pretreatment of the biodegradable additives. There are

other advanatages of ‘‘ecocomposites’’ apart from their recyclability and potential biodegradability. They are usually cheap since the natural additives are obtained from abundant plants (often from waste). From a processing standpoint, they are less abrasive to processing equipment and pose less inhalation hazards than glass fibers. They usually have good thermal and acoustic insulating properties. Finally, they are of low density compared to mineral-filled polyolefin composites, and with a proper and careful choice of coupling agents and processing aids, they can provide an aesthetic appeal and good mechanical properties.

The fourth trend is the increasing use of novel processing methods, particularly for polyolefin nanocomposites processing. For example, there is a growing use of supercritical fluids (e.g., supercritical carbon dioxide and nitrogen gases) such as dispersants to aid distribution and exfoliation of nanoclays or to reduce composites density in general. There is the use of ultrasound to exfoliate nanoclays during the preparation of polyolefin/layered clay nanocomposites. There is the use of solid-state shear processing to delaminate layered clay.

In conclusion, interest in polyolefin composites is growing and will continue to grow as new polyolefins are made and as new applications are sought for these materials.

NOMENCLATURE

AFM	Atomic force microscopy
BR	Butyl rubber
DSC	Differential scanning calorimetry
ED	Electron diffraction
EPDM	Ethylene propylene diene monomer
EPR	Ethylene propylene rubber
EVA	Ethylene-co-vinyl acetate
EVOH	Ethylene-co-vinyl alcohol
FTIR	Fourier transform infrared
HDPE	High density polyethylene
LCP	Liquid crystal polymer
LDPE	Low density polyethylene
LLDPE	Linear low density polyethylene
MLDPE	Medium density polyethylene
NBR	Nitrile butadiene rubber
NMR	Nuclear magnetic resonance
NR	Natural rubber
PA	Polyamide
PA12	Polyamide 12
PA6	Polyamide 6
PA66	Polyamide 66
PB	Polybutene-1
PBT	Polybutylene terephthalate

PC	Polycarbonate
PCL	Polycaprolactone
PE	Polyethylene
PEN	Polyethylene naphthalate
PET	Polyethylene terephthalate
PIB	Polyisobutylene
PLM	Polarized light microscopy
PMMA	Polymethylmethacrylate
PMP	Polymethylpentene-1
PP	Polypropylene
iPP	Isotactic polypropylene
sPP	Syndiotactic polypropylene
aPP	Atactic polypropylene
POE	Polyolefin elastomer
PPE	Poly(2,6 dimethyl-1,4-phenylene ether)
PPO	Polyphenylene oxide
PPS	Polyphenylene sulfide
PS	Polystyrene
PTT	Polytrimethylene terephthalate
PVC	Polyvinyl chloride
SAN	Styrene-co-acrylonitrile
SB	Styrene-co-butadiene
SBR	Styrene butadiene rubber
SBS	Styrene-co-butadiene-co-styrene
SEM	Scanning electron microcopy
SEBS	Styrene-co-ethylene-co-butadiene-co-styrene
SEP	Styrene-co-ethylene-co-propylene
SEPs	Styrene-co-ethylene-co-propylene-co-styrene
TEM	Transmission electron microscopy
TPE	Thermoplastic elastomer
TPO	Thermoplastic olefin
TPU	Thermoplastic polyurethane
TPV	Thermoplastic vulcanizate
TREF	Temperature rising elution fractionation
UHMWPE	Ultrahigh molecular weight polyethylene
ULDPE	Ultralow density polyethylene
VLDPE	Very low density polyethylene
XRD	X-ray diffraction
XRS	X-ray scattering

REFERENCES

1. M. Gahleitner, *Prog. Polym. Sci*., **26**, 895 (2001).
2. J. L. White, *Polyolefins*, Hanser Gardener, Munich, 2005.

3. N. Pasquini (ed.), *Polypropylene Handbook*, Gardener, Munich, 2005.
4. G. K. Harutun (ed.), *Handbook of Polypropylene and Polypropylene Composites*, Marcel Dekker, New York, 2003.
5. C. Vasile (ed.), *Handbook of Polyolefins*, Marcel Dekker, New York, 2000.
6. A. J. Peacock (ed.), *Handbook of Polyethylene*: *Structures, Properties, and Applications*, Marcel Dekker, New York, 2000.
7. O. Olagoke, *Handbook of Thermoplastics*, Marcel Dekker, New York, 1997.
8. E. P. Moore (ed.), *Polypropylene Handbook*, Hanser, Munich, 1996.
9. J. Karger-Kocsis (ed.), *Polypropylene: Structure, Blends, and Composites*, Chapman & Hall, 1995.
10. G. K. Harutun (ed.), *Handbook of Polypropylene and Polypropylene Composites*, Marcel Dekker, New York, 2003.
11. C. Vasile and A. K. Kulshreshtha (eds.), *Handbook of Polymer Blends and Composites*, Rapra Technology Limited, 2003.
12. T. Araki, Q. Tran-Cong, and M. Shibayama (eds.), *Structure and Properties of Multi-Phase Polymeric Materials*, Marcel Dekker, New York, 1998.
13. I. S. Miles and S. Rostani (eds.), *Multi-Component Polymer Systems*, Longman Scientific, Essex, 1992.
14. J. Manson and L. H. Sperling (eds.), *Polymer Blends and Composites*, Plenum Press, New York, 1976.
15. Sz. Molnár, B. Pukánszky, C.O. Hammer, and F.H.J. Maurer, *Polymer*, **41**, 1529 (2000).
16. M. Mucha, J. Marszalek, and A. Fidrych, *Polymer*, **41**, 4137 (2000)
17. X. Liu and Q. Wu, *Polymer*, **42**, 10013 (2001).
18. K. H. Wang, M. H. Choi, C. M. Koo, Y. S. Choi, and I. J. Chung, *Polymer*, **42**, 9819 (2001).
19. P. H. Nam, P. Maiti, M. Okamoto, T. Kotaka, N. Hasegawa, and A. Usuki, *Polymer*, **42**, 9633 (2001).
20. X. Liu, Q. Wu, L. A. Berglund, J. Fan, and Z. Qi, *Polymer*, **42**, 8235 (2001).
21. T. Kashiwagi, E. Grulke, J. Hilding, K. Groth, R. Harris, K. Butler, J. Shields, S. Kharchenko, and J. Douglas, *Polymer*, **45**, 4227 (2004).
22. S. Hotta and D.R. Paul, *Polymer*, **45**, 7639 (2004).
23. K.-M. Jäger and S. S. Eggen, *Polymer*, **45**, 7681 (2004).
24. W. J. Choi and S. C. Kim, *Polymer*, **45**, 2393 (2004).
25. R. Nowacki, B. Monasse, E. Piorkowska, A. Galeski, and J.M. Haudin, *Polymer*, **45**, 4877 (2004).
26. M. Zanetti and L. Costa, *Polymer*, **45**, 4367 (2004).
27. R. Toth, A. Coslanich, M. Ferrone, M. Fermeglia, S. Pricl, S. Miertus, and E. Chiellini, *Polymer*, **45**, 8075 (2004).
28. H. Li, X. Zhang, Y. Duan, D. Wang, L. Li, and S. Yan, *Polymer*, **45**, 8059 (2004).
29. J. H. Kim, C. M. Koo, Y. S. Choi, K. H. Wang, and I. J. Chung, *Polymer*, **45**, 7719 (2004).
30. J. A. Lee, M. Kontopoulou, and J. S. Parent, *Polymer*, **45**, 6595 (2004).
31. G. Galgali, S. Agarwal, and A. Lele, *Polymer*, **45**, 6059 (2004).
32. Q. X. Zhang, Z.-Z. Yu, X.-L. Xie, and Y.-W. Mai, *Polymer*, **45**, 5985 (2004).
33. J. K. Mishra, K.-J. Hwang, and C.-S. Ha, *Polymer*, **46**, 1995 (2005).
34. T. E. Chang, L. R. Jensen, A. Kisliuk, R. B. Pipes, R. Pyrz, and A. P. Sokolov, *Polymer*, **46**, 439 (2005).
35. A. Lazzeri, S.M. Zebarjad, M. Pracella, K. Cavalier, and R. Rosa, *Polymer*, **46**, 827 (2005).
36. L. Wang and J. Sheng, *Polymer*, **46**, 6243 (2005).
37. A. Ranade, K. Nayak, D. Fairbrother, and N. A. D'Souza, *Polymer*, **46**, 7323 (2005).
38. T. Z. Sen, M. A. Sharaf, J. E. Mark, and A. Kloczkowski, *Polymer*, **46**, 7301 (2005).

39. S. Pavlková, R. Thomann, P. Reichert, R. Mülhaupt, A. Marcinčin, and E. Borsig, *J. Appl. Polym. Sci.*, **89**, 604 (2003).
40. Thomas S. Ellis and Joseph S. D'Angelo, *J. Appl. Polym. Sci.*, **90**, 1639 (2003).
41. M.A. López Manchado, M. Arroyo, J. Biagiotti, and J. M. Kenny, *J. Appl. Polym. Sci.*, **90**, 2170 (2003).
42. N. E. Marcovich, and M. A. Villar, *J. Appl. Polym. Sci.*, **90**, 2775 (2003).
43. I. L. Dubnikova, S. M. Berezina, and A. V. Antonov, *J. Appl. Polym. Sci.*, **94**, 1917 (2004).
44. S.-Y. Gu, J. Ren, and Q.-F. Wang, *J. Appl. Polym. Sci.*, **91**, 2427 (2004).
45. I. Šmit, V. Musil, and I. Švab, *J. Appl. Polym. Sci.*, **91**, 4072 (2004).
46. G. Liang, J. Xu, S. Bao, and W. Xu, *J. Appl. Polym. Sci.*, **91**, 3974 (2004).
47. Z. Lin, Y. Qiu, and K. Mai, *J. Appl. Polym. Sci.*, **91**, 3899 (2004).
48. Y. Geng, K. Li, and J. Simonsen, *J. Appl. Polym. Sci.*, **91**, 3667 (2004).
49. J. Yun and A. I. Isayev, *J. Appl. Polym. Sci.*, **92**, 132 (2004).
50. S. Mehta, F. M. Mirabella, K. Rufener, and A. Bafna, *J. Appl. Polym. Sci.*, **92**, 928 (2004).
51. M. Abdouss, N. S. Sanjani, F. Azizinejad, and M. Shabani, *J. Appl. Polym. Sci.*, **92**, 2871 (2004).
52. W. Li, Y. D. Huang, and S. J. Ahmadi, *J. Appl. Polym. Sci.*, **94**, 440 (2004).
53. K. Motha, U. Hippi, K. Hakala, M. Peltonen, V. Ojanperä, B. Löfgren, and J. Seppälä, *J. Appl. Polym. Sci.*, **94**, 1094 (2004).
54. S. Xie, S. Zhang, and F. Wang, *J. Appl. Polym. Sci.*, **94**, 1018 (2004).
55. D. Arencón, J. I. Velasco, M. A. Rodríguez-Pérez, and J. A. de Saja, *J. Appl. Polym. Sci.*, **94**, 1841 (2004).
56. N. M. Stark and L. M. Matuana, *J. Appl. Polym. Sci.*, **94**, 2263 (2004).
57. M. Öksüz and H. Yildirim, *J. Appl. Polym. Sci.*, **96**, 1126 (2005).
58. F. P. La Mantia, M. Morreale, and Z. A. Mohd Ishak, *J. Appl. Polym. Sci.*, **96**, 1906 (2005).
59. N. Sombatsompop, C. Yotinwattanakumtorn, and C. Thongpin, *J. Appl. Polym. Sci.*, **97**, 475 (2005).
60. Y. Chen and H. Li, *J. Appl. Polym. Sci.*, **97**, 1553 (2005).
61. J. Ma, S. Zhang, Z. Qi, G. Li, and Y. Hu, *J. Appl. Polym. Sci.*, **83**, 1978 (2002).
62. W. Xu, G. Liang, W. Wang, S. Tang, P. He, and W.-P. Pan, *J. Appl. Polym. Sci.*, **88**, 3225 (2003).
63. C. H. Hing, Y. B. Lee, J. W. Bae, J. Y. Jho, B. U. Nam, G. J. Nam, and K. J. Lee, *J. Appl. Polym. Sci.*, **97**, 2375 (2005).
64. J. González, C. Albano, M. Ichazo, and B. Díaz, *Eur. Polym. J.*, **38**, 2465 (2002).
65. J. M. García-Martínez, O. Laguna, S. Areso, and E. P. Collar, *Eur. Polym. J.*, **38**, 1583 (2002).
66. D. García-López, O. Picazo, J. C. Merino, and J. M. Pastor, *Eur. Polym. J.*, **39**, 945 (2003).
67. J. Morawiec, A. Pawlak, M. Slouf, A. Galeski, E. Piorkowska, and N. Krasnikowa, *Eur. Polym. J.*, **41**, 1115 (2005).
68. W. S. Chow, A. Abu Baker, Z. A. Mohd Ishak, J. Karger-Kocsis, and U. S. Ishiaku, *Eur. Polym. J.*, **41**, 687 (2005).
69. D. H. Kim, J. U. Park, K. H. Ahn, and S. J. Lee, *Macromol. Rapid Commun.*, **24**, 388 (2003).
70. J.-Z. Liang, *Macromol. Mater. Eng.*, **286**, 714 (2001).
71. W. Xu, M. Ge, and P. He, *J. Polym. Sci. B Polym. Phys.*, **40**, 408 (2001).
72. W. Thongruang, C. M. Balik, and R. J. Spontak, *J. Polym. Sci. B Polym. Phys.*, **40**, 1013 (2002).
73. K. H. Wang, M. H. Choi, C. M. Koo, M. Xu, I. J. Chung, M. C. Jang, S. W. Choi, and H. H. Song, *J. Polym. Sci. B Polym. Phys.*, **40**, 1454 (2002).
74. S. D. Wanjale and J. P. Jog, *J. Polym. Sci. B Polym. Phys.*, **41**, 1014 (2002).
75. S. C. Tjong and Y. Z. Meng, *J. Polym. Sci. B Polym. Phys.*, **41**, 1476 (2003).

76. Gi. Gorrasi, L. Tammaro, M. Tortora, V. Vittoria, D. Kaempfer, P. Reichert, and R. Mülhaupt, *J. Polym. Sci. B Polym. Phys.*, **41**, 1798 (2003).
77. J. Weng, R. H. Olley, D. C. Bassett, and P. Jääskeläinen, *J. Polym. Sci. B Polym. Phys.*, **41**, 2342 (2003).
78. H. Nakajima, K. Yamada, Y. Iseki, S. Hosoda, A. Hanai, Y. Oumi, T. Teranishi, and T. Sano, *J. Polym. Sci. B Polym. Phys.*, **41**, 3324 (2003).
79. Y. Song, Q. Zheng, and X.-S. Yi, *J. Polym. Sci. B Polym. Phys.*, **42**, 1212 (2003).
80. L. Zhang, C. Li, and R. Huang, *J. Polym. Sci. B Polym. Phys.*, **42**, 1656 (2003).
81. W. Zheng, X. Lu, C. L. Toh, T. H. Zheng, and C. He, *J. Polym. Sci. B Polym. Phys.*, **42**, 1810 (2003).
82. M. Feng, F. Gong, C. Zhao, G. Chen, S. Zhang, M. Yang, and C. C. Han, *J. Polym. Sci. B Polym. Phys.*, **42**, 3428 (2004).
83. F.-C. Chiu, S.-M. Lai, J.-W. Chen, and P.-H. Chu, *J. Polym. Sci. B Polym. Phys.*, **42**, 4139 (2004).
84. S. Mishra, S. H. Sonawane, and R. P. Singh, *J. Polym. Sci. B Polym. Phys.*, **43**, 107 (2004).
85. S. C. Tjong and S. P. Bao, *J. Polym. Sci. B Polym. Phys.*, **43**, 253 (2004).
86. J. Yin, S. Wang, Y. Zhang, and Y. Zhang, *J. Polym. Sci. B Polym. Phys.*, **43**, 1914 (2005).
87. N. Ristolainen, U. Vainio, S. Paavola, M. Torkkeli, R. Serimaa, and J. Seppälä, *J. Polym. Sci. B Polym. Phys.*, **43**, 1892 (2005).
88. K. Wang, S. Liang, Q. Zhang, R. Du, and Q. Fu, *J. Polym. Sci. B Polym. Phys.*, **43**, 2005 (2005).
89. A. Fina, D. Tabuani, A. Frache, and G. Camino, *Polymer*, **46**, 7855 (2005).
90. R. Uotila, U. Hippi, S. Paavola, and J. Seppälä, *Polymer*, **46**, 7923 (2005).
91. T. McNally, P. Pötschke, P. Halley, M. Murphy, D. Martin, S. E. J. Bell, G. P. Brennan, D. Bein, P. Lemoine, and J. P. Quinn, *Polymer*, **46**, 8222 (2005).
92. E. M. Benetti, V. Causin, C. Marega, A. Marigo, G. Ferrara, A. Ferraro, M. Consalvi, and F. Fantinel, *Polymer*, **46**, 8275 (2005).
93. H. Qin, S. Zhang, C. Zhao, G. Hu, and M. Yang, *Polymer*, **46**, 8386 (2005).
94. M. Modesti, A. Lorenzetti, D. Bon, and S. Besco, *Polymer*, **46**, 10237 (2005).
95. V. G. Gregoriou, G. Kandiloiti, and S. T. Bollas, *Polymer*, **46**, 11340 (2005).
96. A. Kelarakis, K. Yoon, R. H. Somani, X. Chen, B. S. Hsiao, and B. Chu, *Polymer*, **46**, 11591 (2005).
97. F.-C. Chiu, S.-M. Lai, Y.-L. Chen, and T.-H. Lee, *Polymer*, **46**, 11600 (2005).
98. F. Perrin-Sarazin, M.-T. Ton-That, M. N. Bureau, and J. Denault, *Polymer*, **46**, 11624 (2005).
99. H.-S. Lee, P. D. Fasulo, W. R. Rodgers, and D. R. Paul, *Polymer*, **46**, 11673 (2005).
100. K. Chrissopoulou, I. Altintzi, S. H. Anastasiadis, E. P. Giannelis, M. Pitsikalis, N. Hadjichristidis, and N. Theophilou, *Polymer*, **46**, 12440 (2005).
101. M. Sedláčkoá, I. Lacík, and I. Chodák, *Macromol. Symp.*, **170**, 157 (2001).
102. O. Benevolenski and J. Karger-Kocsis, *Macromol. Symp.*, **170**, 165 (2001).
103. C. M. Liauw, V. Khunova, G. C. Lees, and R. N. Rothon, *Macromol. Symp.*, **170**, 205 (2001).
104. M. Omastová, J. Prokeš, S. Podhradská, and I. Chodák, *Macromol. Symp.*, **170**, 231 (2001).
105. R. Sciamanna, G. Arribas, C. Albano, V. Merola, and C. Pacheco, *Macromol. Symp.*, **176**, 31 (2001).
106. E. Passaglia, W. Bertuccelli, and F. Ciardelli, *Macromol. Symp.*, **176**, 299 (2001).
107. N. Abbacha and S. Fellahi, *Macromol. Symp.*, **178**, 131 (2002).
108. U. Wagenknecht, B. Kretzschmar, and G. Reinhardt, *Macromol. Symp.*, **194**, 207 (2003).
109. D. Arencón, M. L. Maspoch, and J. I. Velasco, *Macromol. Symp.*, **194**, 225 (2003).
110. X. Almeras, M. Le Bras, F. Poutch, S. Bourbigot, G. Marosi, and P. Anna, *Macromol. Symp.*, **198**, 435 (2003).
111. P. Anna, E. Zimonyi, A. Márton, A. Szép, Sz. Matkó, S. Keszei, Gy. Bertalan, and Gy. Marosi, *Macromol. Symp.*, **202**, 245 (2003).

112. Sz. Matkó, P. Anna, Gy. Marosi, A. Szép, S. Keszei, T. Czigány, and K. Pölöskei, *Macromol. Symp.*, **202**, 255 (2003).
113. A. Korakianiti, V. Papaefthimiou, T. Daflou, S. Kennou, and V. G. Gregoriou, *Macromol. Symp.*, **205**, 71 (2004).
114. J. I. Velasco, M. Ardanuy, L. Miralles, S. Ortiz, M. L. Maspoch, M. Sánchez-Soto, and O. Santana, *Macromol. Symp.*, **221**, 63 (2005).
115. Z. M. Wang, H. Han, and T. C. Chung, *Macromol. Symp.*, **225**, 113 (2005).
116. K. C. Cole, F. Perrin-Sarazin, and G. Dorval-Douville, *Macromol. Symp.*, **230**, 1 (2005).
117. D. N. Bikiaris, A. Vassiliou, E. Pavlidou, and G. P. Karayannidis, *Eur. Polym. J.*, **41**, 1965 (2005).
118. K. Renner, M. S. Yang, J. Móczó, H. J. Choi, and B. Pukánszky, *Eur. Polym. J.*, **41**, 2520 (2005).
119. J.-T. Xu, Q. Wang, and Z.-Q. Fan, *Eur. Polym. J.*, **41**, 3011 (2005).
120. Y. W. Leong, M. B. Abu Bakar, Z. A. Mohd. Ishak, and A. Ariffin, *J. Appl. Polym. Sci.*, **98**, 413 (2005).
121. C. H. Hong, Y. B. Lee, J. W. Bae, J. Y. Jho, B. U. Nam, and T. W. Hwang, *J. Appl. Polym. Sci.*, **98**, 427 (2005).
122. M. Tajvidi, *J. Appl. Polym. Sci.*, **98**, 665 (2005).
123. J. Yin, Y. Zhang, and Y. Zhang, *J. Appl. Polym. Sci.*, **98**, 957 (2005).
124. J. Yang, Y. Lin, J. Wang, M. Lai, J. Li, J. Liu, X. Tong, and H. Cheng, *J. Appl. Polym. Sci.*, **98**, 1087 (2005).
125. L. W. Jang, E. S. Kim, H. S. Kim, and J.-S. Yoon, *J. Appl. Polym. Sci.*, **98**, 1229 (2005).
126. Y.-J. Wang, Y. Pan, X.-W. Zhang, and K. Tan, *J. Appl. Polym. Sci.*, **98**, 1344 (2005).
127. Y. Li, S. Wang, Y. Zhang, and Y. Zhang, *J. Appl. Polym. Sci.*, **98**, 1142 (2005).
128. T. Baouz and S. Fellahi, *J. Appl. Polym. Sci.*, **98**, 1748 (2005).
129. Y. Song and Q. Zheng, *J. Polym. Sci. B Polym. Phys.*, **43**, 2484 (2005).
130. M. M. Dudkina, A. V. Tenkovtsev, D. Pospiech, D. Jehnichen, L. Häuβler, and A. Leuteritz, *J. Polym. Sci. B Polym. Phys.*, **43**, 2493 (2005).
131. J.-Y. Wu, T.-M. Wu, W.-Y. Chen, S.-J. Tsai, W.-F. Kuo, and G.-Y. Chang, *J. Polym. Sci. B Polym. Phys.*, **43**, 3242 (2005).
132. H. Zhao and R. K. Y. Li, *J. Polym. Sci. B Polym. Phys.*, **43**, 3652 (2005).
133. H. Qin, S. Zhang, C. Zhao, and M. Yang, *J. Polym. Sci. B Polym. Phys.*, **43**, 3713 (2005).
134. M. Sarno, G. Gorrasi, D. Sannino, A. Sorrentino, P. Ciambelli, and V. Vittoria, *Macromol. Rapid Commun.*, **25**, 1963 (2004).
135. J.-T. Xu, Y.-Q. Zhao, Q. Wang, and Z.-Q. Fan, *Macromol. Rapid Commun.*, **26**, 620 (2005).
136. M. A. Osman and J. E. P. Rupp, *Macromol. Rapid Commun.*, **26**, 880 (2005).
137. Z. Wang, G. Li, G. Xie, and Z. Zhang, *Macromol. Chem. Phys.*, **206**, 258 (2005).
138. H. Nitz, P. Reichert, H. Römling, and R. Mülhaupt, *Macromol. Mater. Eng.*, **276/277**, 51 (2000).
139. C. M. Liauw, V. Khunová, G. C. Lees, and R. N. Rothon, *Macromol. Mater. Eng.*, **279**, 34 (2000).
140. S. Houshyar and R. A. Shanks, *Macromol. Mater. Eng.*, **288**, 599 (2003).
141. V. Hristov and S. Vasileva, *Macromol. Mater. Eng.*, **288**, 798 (2003).
142. Y. Tang, Y. Hu, R. Zhang, Z. Wang, Z. Gui, Z. Chen, and W. Fan, *Macromol. Mater. Eng.*, **289**, 191 (2004).
143. X. Su, Y. Hua, J. Qiao, Y. Liu, X. Zhang, J. Gao, Z. Song, F. Huang, and M Zhang, *Macromol. Mater. Eng.*, **289**, 275 (2004).
144. M.-K. Seo and S.-J. Park, *Macromol. Mater. Eng.*, **289**, 368 (2004).
145. M. E. Malainine, M. Mahrouz, and A. Dufresne, *Macromol. Mater. Eng.*, **289**, 855 (2004).
146. S. Houshyar, R. A. Shanks, and A. Hodzic, *Macromol. Mater. Eng.*, **290**, 45 (2005).
147. W. S. Chow, Z. A. Mohd Ishak, and J. Karger-Kocsis, *Macromol. Mater. Eng.*, **290**, 122 (2005).

148. X. Zhang and L. C. Simon, *Macromol. Mater. Eng.*, **290**, 573 (2005).
149. L. Shavit-Hadar, R. L. Khalfin, Y. Cohen, and D. M. Rein, *Macromol. Mater. Eng.*, **290**, 653 (2005).
150. X. Gao, L.-X. Mao, R.-G. Jin, L.-Q. Zhang, and M. Tian, *Macromol. Mater. Eng.*, **290**, 899 (2005).
151. R. Ozisik, J. Zheng, P. J. Dionne, C. R. Picu, and E. D. von Meerwall, *J. Chem. Phys.*, **123**, 134901-8 (2005).
152. T. Kairn, P. J. Daivis, I. Ivanov, and S. N. Bhattacharya, *J. Chem. Phys.*, **123**, 194905-7 (2005).
153. G. Galgali, C. Ramesh, and A. Lele, *Macromolecules*, **34**, 852 (2001).
154. C. M. Koo, H. T. Ham, S. O. Kim, K. H. Wang, I. J. Chung, D.-C. Kim, and W.-C. Zin, *Macromolecules*, **35**, 5116 (2002).
155. L. A. Utracki and R. Simha, *Macromolecules*, **37**, 10123 (2004).
156. P. J. Dionne, R. Ozisik, and C. R. Picu, *Macromolecules*, **38**, 9351 (2005).
157. J. Z. Liang, R. K. Y. Li, and S. C. Tjong, *Polym. Eng. Sci.*, **40**, 2105 (2000).
158. Y. Obata, T. Sumitomo, T. Ijitsu, M. Matsuda, and T. Nomura, *Polym. Eng. Sci.*, **41**, 408 (2001).
159. K.-N. Kim, H. Kim, and J.-W. Lee, *Polym. Eng. Sci.*, **41**, 1963 (2001).
160. M. J. Oliveira, C. A. Bernardo, and D. A. Hemsley, *Polym. Eng. Sci.*, **42**, 146 (2002).
161. R. Joseph, W. J. McGregor, M. T. Martyn, K. E. Tanner, P. D. Coates, and W. Bonfield, *Polym. Eng. Sci.*, **42**, 326 (2002).
162. A. J. Nuñez, J. M. Kenny, M. M. Reboredo, M. I. Aranguren, and N. E. Marcovich, *Polym. Eng. Sci.*, **42**, 733 (2002).
163. S.-B. Kwak and J.-D. Nam, *Polym. Eng. Sci.*, **42**, 1674 (2002).
164. G. J. Lee, M. G. Han, S. C. Chung, K. D. Suh, and S. S. Im, *Polym. Eng. Sci.*, **42**, 1740 (2002).
165. S. Hambir, N. Bulakh, and J. P. Jog, *Polym. Eng. Sci.*, **42**, 1800 (2002).
166. P. Maiti, P. H. Nam, M. Okamoto, T. Kotaka, N. Hasegawa, and A. Usuki *Polym. Eng. Sci.*, **42**, 1864 (2002).
167. P. H. Nam, P. Maiti, M. Okamoto, T. Kotaka, T. Nakayama, M. Takada, M. Ohshima, A. Usuki., N. Hasegawa, and H. Okamoto, *Polym. Eng. Sci.*, **42**, 1907 (2002).
168. S. I. Farid, M. T. Kortschot, and J. K. Spelt, *Polym. Eng. Sci.*, **42**, 2336 (2002).
169. Y. Zhou and P. K. Mallick, *Polym. Eng. Sci.*, **42**, 2449 (2002).
170. Y. Zhou and P. K. Mallick, *Polym. Eng. Sci.*, **42**, 2461 (2002).
171. M. Q. Zhang, M. Z. Rong, H. B. Zhang, and K. Friedrich, *Polym. Eng. Sci.*, **43**, 490 (2003).
172. J. Biagiotti, M. A. López-Manchado, M. Arroyo, and J. M. Kenny, *Polym. Eng. Sci.*, **43**, 1031 (2003).
173. C. Y. Lew, W. R. Murphy, and G. M. McNally, *Polym. Eng. Sci.*, **44**, 1027 (2004).
174. P. D. Fasulo, W. R. Rodgers, R. A. Ottaviani, and D. L. Hunter, *Polym. Eng. Sci.*, **44**, 1036 (2004).
175. M. Mehrabzadeh and M. R. Kamal, *Polym. Eng. Sci.*, **44**, 1152 (2004).
176. T. G. Gopakumar and D. J. Y. S. Pagé, *Polym. Eng. Sci.*, **44**, 1162 (2004).
177. J. G. Ryu, H. Kim and J. W. Lee, *Polym. Eng. Sci.*, **44**, 1198 (2004).
178. M. Kato, M. Matsushita, and K. Fukumori, *Polym. Eng. Sci.*, **44**, 1205 (2004).
179. M.-T. Ton-That, F. Perrin-Sarazin, K. C. Cole, M. N. Bureau, and J. Denault, *Polym. Eng. Sci.*, **44**, 1212 (2004).
180. J. J. Strebel, F. Mirabella, C. Blythe, and T. Pham, *Polym. Eng. Sci.*, **44**, 1588 (2004).
181. A. J. Nuñez, N.E. Marcovich, and M. I. Aranguren, *Polym. Eng. Sci.*, **44**, 1594 (2004).
182. A. Dasari, R. D. K. Misra, and J. Rohrmann, *Polym. Eng. Sci.*, **44**, 1738 (2004).
183. Y. Zhong and D. D. Kee, *Polym. Eng. Sci.*, **45**, 469 (2005).
184. C. G. Ma, M. Z. Rong, M. Q. Zhang, K. Friedrich, *Polym. Eng. Sci.*, **45**, 529 (2005).
185. M. Rezaei, N. G. Ebrahimi, and M. Kontopoulou, *Polym. Eng. Sci.*, **45**, 678 (2005).

186. N. Ristolainen, U. Hippi, J. Seppälä, A. Nykänen, and J. Ruokolainen, *Polym. Eng. Sci.*, **45**, 1568 (2005).
187. M. Zheng and H. Li, *J. Appl. Polym. Sci*., **91**, 1635 (2004).
188. J. Zhou and F. Yan, *J. Appl. Polym. Sci*., **93**, 948 (2004).
189. K. J. Yao, M. Song, D. J. Hourston, and D. Z. Luo, *Polymer*, **43**, 1020 (2002).
190. L. Százdi, B. Pukánszky Jr., E. Földes, and B. Pukánszky, *Polymer*, **46**, 8010 (2005).
191. M. A. Osman, J. E. P. Rupp, and U. W. Suter, *Polymer*, **46**, 8209 (2005).
192. N. M. Stark, L. M. Matuana, and C. M. Clemons, *J. Appl. Polym. Sci.*, **93**, 1021 (2004).
193. F. Abd-El Salam, M. H. Abd-El Salam, M. T. Mostafa, M. R. Nagy, and M. I. Mohamed, *J. Appl. Polym. Sci.*, **90**, 1539 (2003).
194. W. Xu, G. Liang, W. Wang, S. Tang, P. He, and W.-P. Pan, *J. Appl. Polym. Sci.*, **88**, 3093 (2003).
195. F. R. Costa, M. Abdel-Goad, U. Wagenknecht, and G. Heinrich, *Polymer*, **46**, 4447 (2005).
196. P. Ghosh and A. Chakrabarti, *Eur. Polym. J.*, **36**, 607 (2000).
197. P. J. Dionne, R. Ozisik, and C. R. Picu, *Macromolecules*, **38**, 9351 (2005).
198. R. Ozisik, J. Zheng, P. J. Dionne, C. R. Picu, and E. D. von Meerwall, *J. Chem. Phys.*, **123**, 134901 (2005).
199. F. G. Torres and M. L. Cubillas, *Polym. Test.*, **24**, 694 (2005).
200. S. C. S. Teixeira, M. M. Moreira, A. P. Lima, L. S. Santos, B. M. da Rocha, E. S. de Lima, R. A. A. F. da Costa, A. L. N. da Silva, M. C. G. Rocha, and F. M.B. Coutinho, *Polym. Test.*, **24**, 983 (2005).
201. M. C. G. Rocha, A. H. M. F. T. Silva, F. M. B. Coutinho, and A. L. N. Silva, *Polym. Test.*, **24**, 1049 (2005).
202. D. Nai-Xiu, Z. Mao-Sheng, and W. Peng-Xiang, *Polym. Test.*, **24**, 635 (2005).
203. W. Yang, Z.-Y. Liu, G.-F. Shan, Z.-M. Li, B.-H. Xie, and M.-B. Yang, *Polym. Test.*, **24**, 490 (2005).
204. G. Gong, B.-H. Xie, W. Yang, Z.-M. Li. W. Zhang, and M.-B. Yang, *Polym. Test.*, **24**, 410 (2005).
205. J. Sharif, W. M. Z. W. Yunus, K. Z. Hj. M. Dahlan, and M. H. Ahmad, *Polym. Test.*, **24**, 211 (2005).
206. H. Yan, K. Sun, Y. Zhang, and Y. Zhang, *Polym. Test.*, **24**, 32 (2005).
207. R. Dangtungee, J. Yun, and P. Supaphol, *Polym. Test.*, **24**, 2 (2005).
208. V. N. Hristov, R. Lach, and W. Grellman, *Polym. Test.*, **23**, 581 (2004).
209. D. Nai-Xiu and Z. Mao-Sheng, *Polym. Test.*, **23**, 523 (2004).
210. H. Zheng, Y. Zhang, Z. Peng, and Y. Zhang, *Polym. Test.*, **23**, 217 (2004).
211. S. Cabral-Fonseca, M. C. Paiva, J. P. Nunes, and C. A. Bernardo, *Polym. Test.*, **22**, 907 (2003).
212. H. M. da Costa, T. A. S. Abrantes, R. C. R. Nunes, L. L. Y. Visconte, and C. R. G. Furtado, *Polym. Test.*, **22**, 769 (2003).
213. J. Li, C. Zhou and W. Gang, *Polym. Test.*, **22**, 217 (2003).
214. H. G. B. Premalal, H. Ismail, and A. Baharin, *Polym. Test.*, **21**, 833 (2002).
215. S.-S. Choi, *Polym. Test.*, **21**, 741 (2002).
216. H. Ismail, M. R. Edyham, and B. Wirjosentono, *Polym. Test.*, **21**, 139 (2002).
217. H. Ismail and S. M. Nasir, *Polym. Test.*, **20**, 819 (2001).
218. H. Ismail, Z. Ahmad, and Z. A. Mohd. Ishak, *Polym. Test.*, **20**, 607 (2001).
219. H. Ismail, J. M. Nizam, and H. P. S. Abdul Khalil, *Polym. Test.*, **20**, 125 (2001).
220. S. Siriwardena, H. Ismail, and U. S. Ishiaku, *Polym. Test.*, **20**, 105 (2001).
221. N. Sombatsompop and W. Chaiwattanpipat, *Polym. Test.*, **19**, 713 (2000).
222. T. H. S. Costa, D. L. Carvalho, D. C. S. Souza, F. M. B. Coutinho, J. C. Pinto, and B. V. Kokta, *Polym. Test.*, **19**, 419 (2000).
223. H. Ismail and H. Anuar, *Polym. Test.*, **19**, 349 (2000).
224. J. Z. Liang, R. K. Y. Li, and S. C. Tjong, *Polym. Test.*, **19**, 213 (2000).

225. L. Wei, T. Tang, and B. Huang, *J. Polym. Sci. A Polym. Chem.*, **42**, 941 (2004).
226. Y. Tang, Y. Hu, B. Li, L. Liu, Z. Wang, Z. Chen, and W. Fan, *J. Polym. Sci. A Polym. Chem.*, **42**, 6163 (2004).
227. H. Ismail, Suryadiansyah, and B. Azhari, *Polym. Plast. Technol. Eng.*, **44**, 1657 (2005).
228. S. Wu, Q. Ran, and Z. Liu, *Polym. Plast. Technol. Eng.*, **44**, 1467 (2005).
229. M. J. Miah, F. Ahmed, A. Hossain, and A. H. Khan, *Polym. Plast. Technol. Eng.*, **44**, 1443 (2005).
230. A. P. Gupta, U. K. Saroop, and M. Verma, *Polym. Plast. Technol. Eng.*, **43**, 937 (2004).
231. N. Othman, H. Ismail, and M. Jaafar, *Polym. Plast. Technol. Eng.*, **43**, 713 (2004).
232. A. A. Abd El-Hakim, A. S. Badran, and H. A. Essawy, *Polym. Plast. Technol. Eng.*, **43**, 555 (2004).
233. H. Ismail and R. Nordin, *Polym. Plast. Technol. Eng.*, **43**, 285 (2004).
234. H. Li and M. M. Sain, *Polym. Plast. Technol. Eng.*, **42**, 853 (2003).
235. F. Petraru, M. Popa, and R. Tudose, *Polym. Plast. Technol. Eng.*, **42**, 555 (2003).
236. J. K. Sameni, S.H. Ahmad, and S. Zakaria, *Polym. Plast. Technol. Eng.*, **42**, 345 (2003).
237. A. P. Gupta, U. K. Saroop, G. S. Jha, and M. Verma, *Polym. Plast. Technol. Eng.*, **42**, 297 (2003).
238. F. Petraru, M. Popa, and R. Tudose, *Polym. Plast. Technol. Eng.*, **41**, 877 (2002).
239. H. Ismail, R. Nordin, and A. Md. Noor, *Polym. Plast. Technol. Eng.*, **41**, 847 (2002).
240. S. N. Maiti, B. H. Lopez, and M. N. Ibrahim, *Polym. Plast. Technol. Eng.*, **41**, 663 (2002).
241. S. Siriwardena, H. Ismail, and U. S. Ishiaku, *Polym. Plast. Technol. Eng.*, **41**, 419 (2002).
242. Q. Wang, H. Chen, and Y. Liu, *Polym. Plast. Technol. Eng.*, **41**, 215 (2002).
243. F. Petraru, R. Tudose, and M. Popa, *Polym. Plast. Technol. Eng.*, **40**, 653 (2001).
244. S. Siriwardena, H. Ismail, and U. S. Ishiaku, *Polym. Plast. Technol. Eng.*, **40**, 519 (2001).
245. H. Ismail and L. Mega, *Polym. Plast. Technol. Eng.*, **40**, 463 (2001).
246. K. Premphet and P. Horanont, *Polym. Plast. Technol. Eng.*, **40**, 235 (2001).
247. F. Petraru, M. Popa, and R. Tudose, *Polym. Plast. Technol. Eng.*, **40**, 145 (2001).
248. T. Q. Li and R. K. Y. Li, *Polym. Plast. Technol. Eng.*, **40**, 1 (2001).
249. M. B. Andreeva, T. N. Novotortzeva, E. V. Kalugina, V. A. Tochin, L. N. Gurinovich, T. I. Andreeva, I. G. Kalinina, K. Z. Gumargalieva, and G. E. Zaikov, *Polym. Plast. Technol. Eng.*, **39**, 513 (2000).
250. F. Petraru, M. Popa, and R. Tudose, *Polym. Plast. Technol. Eng.*, **39**, 469 (2000).
251. M. N. Ismail, G. M. Turky, and A. M. A. Nada, *Polym. Plast. Technol. Eng.*, **39**, 249 (2000).
252. J. B. Naik and S. Mishra, *Polym. Plast. Technol. Eng.*, **44**, 687 (2005).
253. S. H. Ismail and A. Abu Bakar, *Polym. Plast. Technol. Eng.*, **44**, 863 (2005).
254. M. A. Hassan, *Polym. Plast. Technol. Eng.*, **43**, 1487 (2004).
255. S. Morlat-Therias, B. Mailhot, J.-L. Gardette, C. Da Silva, B. Haidar, and A. Vidal, *Polym. Degrad. Stabil.*, **90**, 78 (2005).
256. F. G. Ramos Filho, T. J. A. Mélo, M. S. Rabello, and S. M. L. Silva, *Polym. Degrad. Stabil.*, **89**, 383 (2005).
257. L. Yu, W. Wang, and W. Xiao, *Polym. Degrad. Stabil.*, **86**, 69 (2004).
258. N. S. Allen, J. M. Pena, M. Edge, and C. M. Liauw, *Polym. Degrad. Stabil.*, **67**, 563 (2000).
259. N. M. Stark and L. M. Matuana, *Polym. Degrad. Stabil.*, **86**, 1 (2004).
260. H. Qin, S. Zhang, C. Zhao, M. Feng, M. Yang, Z. Shu, and S. Yang, *Polym. Degrad. Stabil.*, **85**, 807 (2004).
261. M. Zanetti, P. Bracco, and L. Costa, *Polym. Degrad. Stabil.*, **85**, 657 (2004).
262. A. B. Shehata, *Polym. Degrad. Stabil.*, **85**, 577 (2004).
263. S. Su, D. D. Jiang, and C. A. Wilkie, *Polym. Degrad. Stabil.*, **84**, 279 (2004).
264. Y. W. Leong, M. B. Abu Bakar, Z. A. Mohd Ishak, and A. Ariffin, *Polym. Degrad. Stabil.*, **83**, 411 (2004).

265. M. Sain, S. H. Park, F. Suhara, and S. Law, *Polym. Degrad. Stabil.*, **83**, 363 (2004).
266. S. Su, D. D. Jiang, and C. A. Wilkie, *Polym. Degrad. Stabil.*, **83**, 321 (2004).
267. B. Li and J. He, *Polym. Degrad. Stabil.*, **83**, 241 (2004).
268. F. Delor-Jestin, J. Lacoste, N. Barrois-Oudin, C. Cardinet, and J. Lemaire, *Polym. Degrad. Stabil.*, **67**, 469 (2000).
269. B. Mailhot, S. Morlat, J.-L. Gardette, S. Boucard, J. Duchet, and J.-F. Gérard, *Polym. Degrad. Stabil.*, **82**, 163 (2003).
270. A. Tidjani, O. Wald, M.-M. Pohl, M. P. Hentschel, and B. Schartel, *Polym. Degrad. Stabil.*, **82**, 133 (2003).
271. Y. Tang, Y. Hu, L. Song, R. Zong, Z. Gui, Z. Chen, and W. Fan, *Polym. Degrad. Stabil.*, **82**, 127 (2003).
272. H. Qin, C. Zhao, S. Zhang, G. Chen, and M. Yang, *Polym. Degrad. Stabil.*, **81**, 497 (2003).
273. D. Wang and C. A. Wilkie, *Polym. Degrad. Stabil.*, **80**, 171 (2003).
274. J. Zhang and C. A. Wilkie, *Polym. Degrad. Stabil.*, **80**, 163 (2003).
275. R. S. Rajeev, S. K. De, A. K. Bhowmick, and B. John, *Polym. Degrad. Stabil.*, **79**, 449 (2003).
276. M. Miraftab, A. R. Horrocks, and J. Mwila, *Polym. Degrad. Stabil.*, **78**, 225 (2002).
277. J.-P. Gibert, J.-M. Lopez Cuesta, A. Bergeret, and A. Crespy, *Polym. Degrad. Stabil.*, **67**, 437 (2000).
278. Z. Wang, G. Wu, Y. Hu, Y. Ding, K. Hu, and W. Fan, *Polym. Degrad. Stabil.*, **77**, 427 (2002).
279. M. Liu and A.R. Horrocks, *Polym. Degrad. Stabil.*, **75**, 485 (2002).
280. V. S. Vinod, S. Varghese, and B. Kuriakose, *Polym. Degrad. Stabil.*, **75**, 405 (2002).
281. L. Ferry, J. M. Lopez Cuesta, C. Chivas, G. Mac Way Hoy, and H. Dvir, *Polym. Degrad. Stabil.*, **74**, 449 (2001).
282. V. M. Goldberg, N. N. Kolesnikova, N. G. Paverman, S. M. Kavun, P. E. Stott, and M. E. Gelbin, *Polym. Degrad. Stabil.*, **74**, 371 (2001).
283. C. M. Liauw, N. S. Allen, M. Edge, and L. Lucchese, *Polym. Degrad. Stabil.*, **74**, 159 (2001).
284. J. González, C. Albano, M. Ichazo, M. Hernández, and R. Sciamanna, *Polym. Degrad. Stabil.*, **73**, 211 (2001).
285. C. Albano, J. Reyes, M. Ichazo, J. González, and M. I. Chipara, *Polym. Degrad. Stabil.*, **73**, 225 (2001).
286. R. Xie, B. Qu, and K. Hu, *Polym. Degrad. Stabil.*, 313 (2001).
287. C. Albano, J. Reyes, J. González, M. Ichazo, R. Poleo, and E. Davidson, *Polym. Degrad. Stabil.*, **73**, 39 (2001).
288. D. Raghavan and A. Emekalam, *Polym. Degrad. Stabil.*, **72**, 509 (2001).
289. J. M. Peña, N. S. Allen, M. Edge, C. M. Liauw, I. Roberts, and B. Valange, *Polym. Degrad. Stabil.*, **70**, 437 (2000).
290. J. M. Peña, N. S. Allen, M. Edge, C. M. Liauw, and B. Valange, *Polym. Degrad. Stabil.*, **72**, 163 (2001).
291. C. Canaud, L. L. Yuan Visconte, M. A. Sens, and R. C. R. Nunes, *Polym. Degrad. Stabil.*, **70**, 259 (2000).
292. R. Li, *Polym. Degrad. Stabil.*, **70**, 135 (2000).
293. C. S. Reddy, C. K. Das, and M. Narkis, *Polym. Compos.*, **26**, 806 (2005).
294. S. Zhang, D. Rodrigue, and B. Riedl, *Polym. Compos.*, **26**, 731 (2005).
295. M. Drubetski, A. Siegmann, and M. Narkis, *Polym. Compos.*, **26**, 454 (2005).
296. C. Mobuchon, P. J. Carreau, M.-C. Heuzey, M. Sepehr, and G. Ausias, *Polym. Compos.*, **26**, 247 (2005).
297. S. Parija, S. K. Nayak, S. K. Verma, and S. S. Tripathy, *Polym. Compos.*, **25**, 646 (2004).
298. M. N. Bureau and J. Denault, *Polym. Compos.*, **25**, 622 (2004).

299. R. Seldén, B. Nyström, and R. Långström, *Polym. Compos.*, **25**, 543 (2004).
300. V. N. Hristov, S. T. Vasileva, M. Krumova, R. Lach, and G. H. Michler, *Polym. Compos.*, **25**, 521 (2004).
301. H. Kiratisaevee and W. J. Cantwell, *Polym. Compos.*, **25**, 499 (2004).
302. Y. Wang and W.-C. Lee, *Polym. Compos.*, **25**, 451 (2004).
303. J. Biagiotti, S. Fiori, L. Torre, M. A. López-Manchado, and J. M. Kenny, *Polym. Compos.*, **25**, 26 (2004).
304. D. Trudel-Boucher, M. N. Bureau, J. Denault, and B. Fisa, *Polym. Compos.*, **24**, 499 (2003).
305. A. R. Martin, F. S. Denes, R. M. Rowell, and L. H. C. Mattoso, *Polym. Compos.*, **24**, 464 (2003).
306. S. C. Tjong, S.-A. Xu, and Y. W. Mai, *Polym. Compos.*, **24**, 437 (2003).
307. S. Ratner, A. Weinberg, and G. Marom, *Polym. Compos.*, **24**, 422 (2003).
308. L. Jian, C. Zhou, W. Gang, Y. Wei, T. Ying, and L. Qing, *Polym. Compos.*, **24**, 323 (2003).
309. A. Somnuk, N. Yanumet, J. W. Ellis, B. P. Grady, and E. A. O'Rear, *Polym. Compos.*, **24**, 171 (2003).
310. S. A. R. Hashmi, T. Kitano, and N. Chand, *Polym. Compos.*, **24**, 149 (2003).
311. Y. Wang and W.-C. Lee, *Polym. Compos.*, **24**, 119 (2003).
312. K. W. Kwok, Z. M. Gao, C. L. Choy, and X. G. Zhu, *Polym. Compos.*, **24**, 53 (2003).
313. G. Toriz, F. Denes, and R. A. Young, *Polym. Compos.*, **23**, 806 (2002).
314. M. A. López-Manchado, J. Biagiotti, and J. M. Kenny, *Polym. Compos.*, **23**, 779 (2002).
315. R. S. Rajeev, A. K. Bhowmick, S. K. De, G. J. P. Kao, and S. Bandyopadhyay, *Polym. Compos.*, **23**, 574 (2002).
316. S. E. Gwaily, M. Madani, and H. H. Hassan, *Polym. Compos.*, **23**, 495 (2002).
317. S. A. R. Hashmi, T. Kitano, and N. Chand, *Polym. Compos.*, **23**, 500 (2002).
318. X. L. Xie, R. K. Y. Li, S. C. Tjong, and Y.-W. Mai, *Polym. Compos.*, **23**, 319 (2002).
319. C. Wang and C.-C. Chen, *Polym. Compos.*, **23**, 104 (2002).
320. S. S. Tripathy, G. Levita, and L. Di Landro, *Polym. Compos.*, **22**, 815 (2001).
321. T. Aurich and G. Mennig, *Polym. Compos.*, **22**, 680 (2001).
322. R. J. Kuriger and M. Khairul Alam, *Polym. Compos.*, **22**, 604 (2001).
323. D. Feng, D. F. Caulfield, and A. R. Sanadi, *Polym. Compos.*, **22**, 506 (2001).
324. C. Saujanya and S. Radhakrishnan, *Polym. Compos.*, **22**, 232 (2001).
325. C. Saujanya, S. Sainkar, and S. Radhakrishnan, *Polym. Compos.*, **22**, 221 (2001).
326. S. A. R. Hashmi, T. Kitano, and N. Chand, *Polym. Compos.*, **22**, 213 (2001).
327. K. B. Cheng, S. Ramakrishna, and K. C. Lee, *Polym. Compos.*, **22**, 185 (2001).
328. S.-J. Liu, I.-T. Chang, and S.-W. Hung, *Polym. Compos.*, **22**, 132 (2001).
329. Q. Wang, J. Gao, R. Wang, and Z. Hua, *Polym. Compos.*, **22**, 97 (2001).
330. P. Punchaipetch, N. A. D'Souza, W. Brostow, A. E. Akinay, and J. Reed, *Polym. Compos.*, **22**, 32 (2001).
331. R. Taipalus, T. Harmia, and K. Friedrich, *Polym. Compos.*, **21**, 396 (2000).
332. E. Mäder and E. Pisanova, *Polym. Compos.*, **21**, 361 (2000).
333. S. E. Barbosa, N. J. Capiati, and J. M. Kenny, *Polym. Compos.*, **21**, 377 (2000).
334. F. Rahma and S. Fellahi, *Polym. Compos.*, **21**, 175 (2000).
335. Y. J. Maeng, B. S. Yoon, M. H. Suh, W. B. Im, and S. H. Lee, *Polym. Compos.*, **21**, 41 (2001).
336. Y. Wang and M.-J. Yu, *Polym. Compos.*, **21**, 1 (2000).
337. S. H. Ryu and Y.-W. Chang, *Polym. Bull.*, **55**, 385 (2005).
338. C. Albano, J. González, M. Ichazo, N. Velasco, J. Guevara, and F. La Mantia, *Polym. Bull.*, **51**, 245 (2003).
339. F. Hernández-Sánchez and P. J. Herrera-Franco, *Polym. Bull.*, **45**, 509 (2001).

340. J. W. Lee, Y. T. Lim, and O. O. Park, *Polym. Bull.*, **45**, 191 (2000).
341. H. Lu, Y. Hu, Q. Kong, Z. Chen, and W. Fan, *Polym. Adv. Technol.*, **16**, 688 (2005).
342. Z. Mlynarčíková, D. Kaempfer, R. Thomann, R. Mülhaupt, E. Borsig, and A. Marcinčin, *Polym. Adv. Technol.*, **16**, 362 (2005).
343. N. Xu, W. Zhou, and W. Shi, *Polym. Adv. Technol.*, **15**, 654 (2004).
344. H. Lu, Y. Hu, Q. Kong, Y. Cai, Z. Chen, and W. Fan, *Polym. Adv. Technol.*, **15**, 601 (2004).
345. W. Wang, M. Fu, and B. Qu, *Polym. Adv. Technol.*, **15**, 467 (2004).
346. Q. Yuan, W. Jiang, L. An, and R. K. Y. Li, *Polym. Adv. Technol.*, **15**, 409 (2004).
347. Y. Tang, Y. Hu, S. Wang, Z. Gui, Z. Chen, and W. Fan, *Polym. Adv. Technol.*, **14**, 733 (2003).
348. D. M. Rein, L. Vaykhansky, and Y. Chen, *Polym. Adv. Technol.*, **13**, 428 (2002).
349. J. Chen and N. Tsubokawa, *Polym. Adv. Technol.*, **11**, 101 (2000).
350. G. Chen, J. Lu, W. Lu, D. Wu, and C. Wu, *Polym. Int.*, **54**, 1689 (2005).
351. E. Passaglia, R. Sulcis, F. Ciardelli, M. Malvaldi, and P. Narducci, *Polym. Int.*, **54**, 1549 (2005).
352. S. M. Lomakin, I. L. Dubnikova, S. M. Berezina, and G. E. Zaikov, *Polym. Int.*, **54**, 999 (2005).
353. P. Toro, R. Quijada, O. Murillo, and M. Yazdani-Pedram, *Polym. Int.*, **54**, 730 (2005).
354. A. R. R Menon, C. K. S Pillai, W. S. Jin, and C. Nah, *Polym. Int.*, **54**, 629 (2005).
355. W. Shao, Q. Wang, and H. Ma, *Polym. Int.*, **54**, 336 (2005).
356. S. Jia, Z. Zhang, Z. Wang, X. Zhang, and Z. Du, *Polym. Int.*, **54**, 320 (2005).
357. K. G. Gatos, R. Thomann, and J. Karger-Kocsis, *Polym. Int.*, **53**, 1191 (2004).
358. M. A. López-Manchado, B. Herrero, and M. Arroyo, *Polym. Int.*, **53**, 1766 (2004).
359. G. Kalaprasad, B. Francis, S. Thomas, C. R. Kumar, C. Pavithran, G. Groeninckx, and S. Thomas, *Polym. Int.*, **53**, 1624 (2004).
360. M. Feng, F. Gong, C. Zhao, G. Chen, S. Zhang, and M. Yang, *Polym. Int.*, **53**, 1529 (2004).
361. Y. Song and Q. Zheng, *Polym. Int.*, **53**, 1517 (2004).
362. G. Wu, B. Wen, and S. Hou, *Polym. Int.*, **53**, 749 (2004).
363. M. Z. Rong, M. Q. Zhang, S. L. Pan, B. Lehmann, and K. Friedrich, *Polym. Int.*, **53**, 176 (2004).
364. S. D. Wanjale and J. P. Jog, *Polym. Int.*, **53**, 101 (2004).
365. D. Martin, P. Halley, R. Truss, M. Murphy, O. Jackson, and O.-Y. Kwon, *Polym. Int.*, **52**, 1774 (2003).
366. B. Qu and R. Xie, *Polym. Int.*, **52**, 1415 (2003).
367. Y. Tang, Y. Hu, S. Wang, Z. Gui, Z. Chen, and W. Fan, *Polym. Int.*, **52**, 1396 (2003).
368. S.-S. Choi, C. Nah, and B.-W. Jo, *Polym. Int.*, **52**, 1382 (2003).
369. J. Kim, T. Oh, and D. Lee, *Polym. Int.*, **52**, 1203 (2003).
370. S. Y. Yeo, S. H. Jeong, *Polym. Int.*, **52**, 1053 (2003).
371. N. Kao, A. Chandra, and S. Bhattacharya, *Polym. Int.*, **51**, 1385 (2002).
372. A. M. Y. El Lawindy, K. M. Abd El-Kade, W. E. Mahmoud, and H. H. Hassan, *Polym. Int.*, **51**, 601 (2002).
373. Y.-W. Chang, Y. Yang, S. Ryu, and C. Nah, *Polym. Int.*, **51**, 319 (2002).
374. N. C. Das, T. K. Chaki, and D. Khastgir, *Polym. Int.*, **51**, 156 (2002).
375. S. Siriwardena, H. Ismail, and U.S. Ishiaku, *Polym. Int.*, **50**, 707 (2001).
376. H. Ismail, Z. Ahmad, and Z. A. Mohd. Ishak, *Polym. Int.*, **50**, 612 (2001).
377. R. Mansencal, B. Haidar, A. Vidal, L. Delmotte, and J.-M. Chezeau, *Polym. Int.*, **50**, 387 (2001).
378. Q. Zhang, Q. Fu, L. Jiang, and Y. Lei, *Polym. Int.*, **49**, 1561 (2000).
379. M. N. Ichazo, C. Albano, and J. González, *Polym. Int.*, **49**, 1409 (2000).
380. D. Lu and R. Guan, *Polym. Int.*, **49**, 1389 (2000).
381. H. Ismail, R. M. Jaffri, and H. D. Rozman, *Polym. Int.*, **49**, 618 (2000).

382. F. Rahma and S. Fellahi, *Polym. Int.*, **49**, 519 (2000).
383. J. Z. Liang and R. K. Y. Li, *Polym. Int.*, **49**, 170 (2000).
384. J. K. Sameni, S. H. Ahmad, and S. Zakaria, *Adv. Polym. Technol.*, **23**, 18 (2004).
385. M. Avella, S. Cosco, G. D. Volpe, and M. E. Errico, *Adv. Polym. Technol.*, **24**, 132 (2004).
386. H. Zhang, G. M. Rizvi, and C. B. Park, *Adv. Polym. Technol.*, **23**, 263 (2004).
387. P. P. Kundu, J. Biswas, H. Kim, S. E. Shim, S. Choe, and D. S. Lee, *Adv. Polym. Technol.*, **23**, 230 (2004).
388. N. C. Das, T. K. Chaki, D. Khastgir, and A. Chakraborty, *Adv. Polym. Technol.*, **20**, 226 (2001).
389. G. Guerrica-Echevarría, J. I. Eguiazábal, and J. Nazábal, *J. Macromol. Sci. B Phys.*, **39**, 441 (2000).
390. V. P. Privalko, R. V. Dinzhos, E. G. Privalko, and A. A. Usenko, *J. Macromol. Sci. B Phys.*, **43**, 859 (2004).
391. L. Wang, J. Sheng, and S. Wu, *J. Macromol. Sci. B Phys.*, **43**, 935 (2004).
392. Š. Chmela, A. Kleinová, A. Fiedlerová, E. Borsig, D. Kaempfer, R. Thomann, and R. Mülhaupt, *J. Macromol. Sci. A Pure Appl. Chem.*, **42**, 821 (2005).
393. M. A. Sharaf, A. Kloczkowski, and J.E. Mark, *Comput. Theor. Polym. Sci.*, **11**, 251 (2001).
394. A. L. Kelly, M. Woodhead, P.D. Coates, D. Barnwell, and K. Martin, *Int. Polym. Process.*, **15**, 361 (2000).
395. Y. Wang, H.-C. Chan, S.-M. Lai, and H.-F. Shen, *Int. Polym. Process.*, **16**, 100 (2001).
396. D. Merinska, M. Chmielová, A. Kalendova, Z. Weiss, P. Capkova, and J. Šimoník, *Int. Polym. Process.*, **18**, 133 (2003).

Part II

Polyolefin Micro Composites

Chapter 2

Polypropylene Natural Cellulosic Fiber Composites

Robert A. Shanks[1]

2.1 INTRODUCTION

Polypropylene (PP) is a commodity polymer that has properties that can be extended into the applications of high performance polymers. PP has become a universal polymer, and it is applied in each of the areas where special properties are required: moldings, extrusions, sheets, films including cast and blown, thermoformed containers, foamed materials, and fibers. PP has higher strength than other polyolefins, low density, and acceptable thermal resistance and is available in many grades differing in molar mass and copolymer type and distribution. It has two main restrictions: PP is brittle at lower temperatures and it has only moderate strength and is subject to creep. The properties of PP can be enhanced to make it competitive with typically higher performing polymers by increasing its strength and creep resistance with fillers and toughening with rubber particle inclusions (1). Natural fibers of many varieties have been used to form ecocomposites, or green composites, with recycled polyethylene (2).

Many fillers are used in PP composites (3). Typical mineral fillers are talc, calcium carbonate, barium sulfate, calcium silicate (wollastonite), and kaolin. Glass fiber is typically used for high performance. Natural fibers are increasingly gaining interest due to their high specific modulus strength, wide availability, and suitability for the type of applications of PP composites in which the performances of nylon, polycarbonate, and polyester composites with glass and carbon fibers are not achievable. The specific modulus and strength refer to the corresponding absolute value divided by the density, which reflects the modulus and strength relative to the mass of the structure. Natural fibers are almost entirely cellulose based. Some

[1]CRC for Polymers, School of Applied Sciences, RMIT University, GPO Box 2476V, Melbourne, Vic 3001, Australia

Polyolefin Composites, Edited by Domasius Nwabunma and Thein Kyu

Table 2.1 Comparative Mechanical Performance and Cost of Fibers.

Natural fiber	Tensile strength, MPa	Tensile modulus, GPa	Cost \$ kg^{-2}
Cotton	287–597	5.5–12.6	3.5–4
Glass	2000–3500	70	7
Flax	345–1035	27.6	1–2
Ramie	400–938	61–128	0.7
Jute	393–773	26.5	0.6
Hemp	690	—	1–2
Kenaf	11,900	60	—
Bagasse	170–290	15–29	—
Sisal	511–635	9.4–22	0.9

examples of cellulose fibers that will be considered in this chapter are wood flour, wood fibre, bast fibers such as flax, hemp, jute, rami, and kenaf, rice and wheat husks and straw, cotton, bagasse, sisal, waste paper, and many other fibrous materials that are available as by-products from crops (see Table 2.1 for examples of properties). With the exception of wood, the fibers are obtained from fast-growing crops. The high performance of microcrystals of cellulose or cellulose whiskers in various matrices in considered to be due to the percolation effect (4). Cellulose can be used in microfiber pulp to form structural forms without use of external bonding agents (5).

The relative ease of preparation, formability, or recycling suitability and the performance to cost consideration make PP–natural fibre composites useful for many structural and cladding materials. This review will provide a summary of current and future applications. The preparation techniques are diverse compared with typical thermoplastic composites because of the availability of low fibers and the adaptability of PP. PP is hydrophobic, while natural fibers are hydrophilic, so some compatibilization or modification of the interface is usually needed. The fibers contain extraneous plant material that can be removed to provide composites with better performance and stability. The fibers and PP coexist and create an interdependence of morphology, particularly with polypropylene crystallinity. The main requirement is mechanical properties, and these will be reviewed. Each individual application provides its own challenge for additional requirements, so the additives and properties will be considered for specific examples.

2.2 APPLICATIONS OF POLYPROPYLENE COMPOSITES

PP is a convenient thermoplastic with a balance between processing and performance. The melting temperature ($T_m = 162 - 165°C$) is high enough to resist boiling water yet low enough to permit ease of thermoforming composite sheets. PP is available in grades intended for extrusion into film, sheet and profiles, injection

molding, and thermoforming. PP is non polar and therefore lacks interaction with cellulose fibers; however, grafted forms of PP with polar functionality are available, and blended polar compatibilizers can be added. Automotive lining panels are a significant volume application for natural fibers and wood flour PP composites. Similar composites can be used for building panels, acoustic materials, furniture, biodegradable containers, plant pots, and geotextiles. Water-resistant lumber is available for outdoors uses. Wood texture can be included to provide materials that appear like timber and can be sawn and nailed. Rice husks have been combined with high density polyethylene to form decking boards that may undergo swelling and bowing with changes in humidity and temperature, analogous to behavior expected of PP composites (6).

The use of bio fibers in automotive applications has been reviewed. Composites mainly based on polypropylene are used in interior and exterior components. Uses include door panels, seat backs, headliners, package trays, dashboards, and trunk liners. Typical fibers include jute, flax, hemp, kenaf, and wood. A significant advantage of these composites is the weight reduction of the components. A concept car has been developed called the EcoCar. The EcoCar is constructed from bio fiber composite panels (7).

2.3 PREPARATION TECHNIQUES FOR POLYPROPYLENE COMPOSITES

The fibers and polypropylene must be combined uniformly into conveniently formable structures, non woven fiber mats, powder impregnation, film laminates, and extrusion mixing with wood flour. The most direct method of preparation is extrusion where PP, wood flour, or chopped fibers, together with compatibilizer and any other additives are directly dispersed, typically using a twin-screw extruder. The extrudate can be used directly or pelletized and injection molded or re-extruded into a final form. PP and PP-g-MA were melt mixed with cellulose fibers and the mixture was hot pressed into composite sheets. In this example, the cellulose was derived from Dwarf Cavendish banana tree, and it was purified by mechanical isolation, milling to 60–140 mesh, and extraction with multiple solvents (8).

Rheology of cellulose suspensions in melted PP is important for processing. Wood flour–PP melt suspensions have been studied using dynamic rheology, and the results were scalable with respect to filler content and superimposed onto a single master curve. The data were modeled using several functions that describe viscosity in relation to volume fraction: Poslinski equation, Carreau–Yasuda model, and a generalized Maxwell model (9). In another study, the Doolittle equation was used to describe the rheological behavior of polymer melts with natural fibers, using low density polyethylene and polystyrene with cotton, flax, and hemp (10).

PP fiber can be combined with natural fiber, typically long fibers such as flax or hemp, by needle punching to form an intimately intermingled felted mat

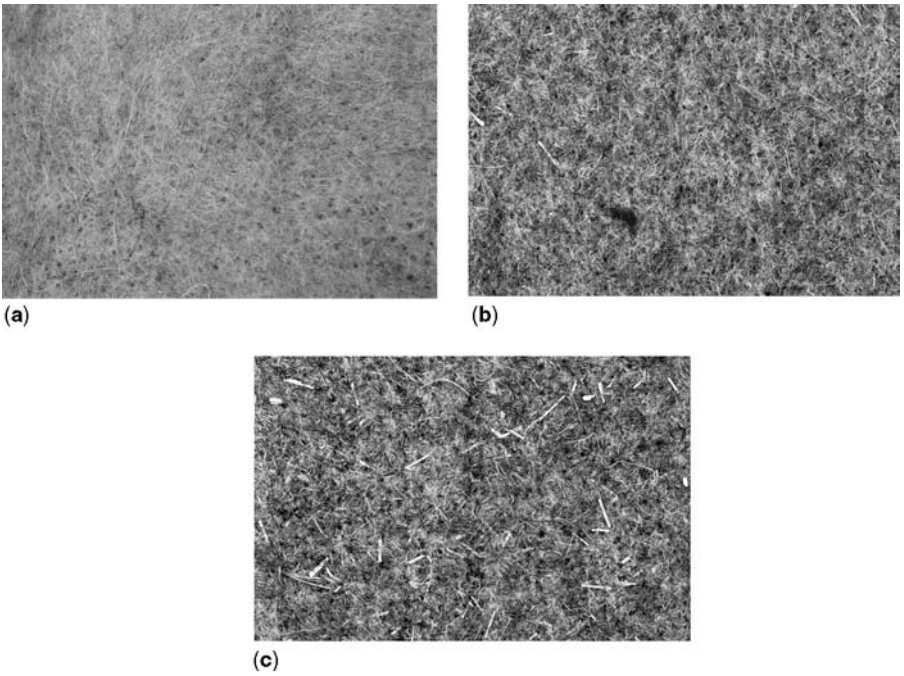

Figure 2.1 Nonwoven mats of black polypropylene and flax fibers: (**a**) finely intermingled fibers, (**b**) typical composite quality flax, and (**c**) lower quality flax including stalks.

(Figure 2.1). The mat is then hot pressed to melt the PP fibers and consolidate the composite (Figure 2.2), though voids remain that provide lower bulk density to the final composite board (Figure 2.3). Melting of the PP fibers is usually incomplete due to low thermal conductivity of the mat and the need to limit temperature to

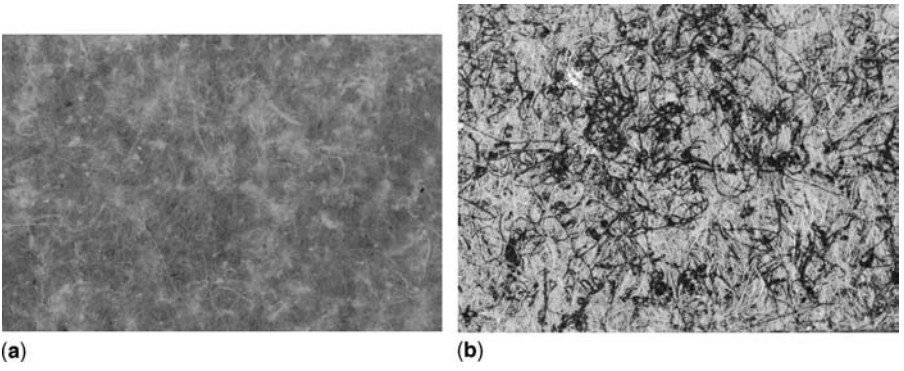

Figure 2.2 Composites prepared by compression molding of non woven fiber mats as shown in (**a**) Fig. 2.3 and (**b**) Fig. 2.4a.

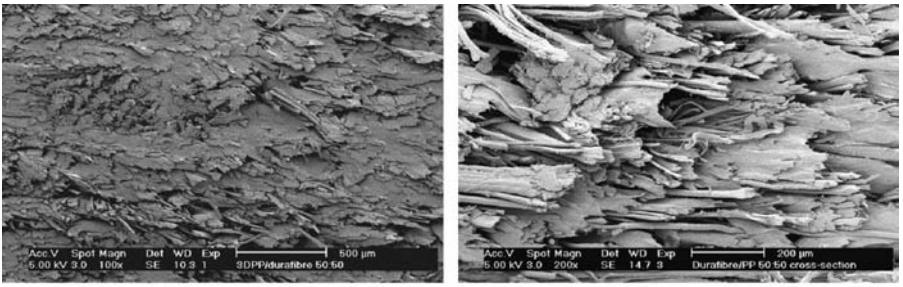

(a) (b)

Figure 2.3 Polypropylene–flax composite (**a**) hot pressed under high pressure to form a densely consolidated structure and (**b**) hot pressed under relatively low pressure to give voided low density structure.

about 200°C and use a short heating time of about 1–2 min to avoid embrittlement of the cellulose due to dehydration or degradation. The composite board is then cut and thermoformed to the required shape for application such as automotive interior and trunks storage lining to support upholstery and carpet coverings. PP fibers and kenaf fibers were spread into layers with alternating fiber direction and then hot pressed to form composite boards. The effect of number of kenaf layers, heating time, and kenaf mass fraction on the flexural modulus of the composites was measured (11).

The natural fibers can be needle punched or woven into a mat which is then impregnated with powdered polymer by distribution over the surface while the mat is vibrated. The powdered polymer is then fused by heating with hot rollers or a press to achieve a composite the one board similar to derived from the intermingled fibers described above. An alternative method is to form the laminate from the fiber mat laminated with polymer film, where the film is melted and diffused through the fibers in a heated press or by passing through heated rollers to form the composite.

PP is adaptable to each of the above composite formation methods since it is available as pellets, fiber, film, or powder. The extrusion of pellets is suitable for short fibers, while the other methods are suitable for long fibers that are co mingled via felting or weaving. The latter methods form composites that have high tensile strength. Compressive and tensile forces on the upper and lower surfaces largely determine the flexural strength during loading. The surfaces are most consolidated during compression molding and maximum strength is developed in the surface layers, while the core will have lower bulk density which will provide a favorable overall low composite density.

PP–cellulose whisker (cellulose mono crystals) nanocomposites have been prepared from toluene solution of PP. A nonionic surfactant (polyoxyethylene-9-nonylphenyl ether) was used as a dispersant. PP-g-MA was used as a compatibilizer and a high shear disperser was used to ensure flocculation did not take place (12).

2.4 FIBER SURFACE AND POLYPROPYLENE MODIFICATIONS

Three approaches may be used to increase adhesion between PP and cellulose fibers: modify PP, modify the fibers, or add a compatibilizer. The most common way to modify PP is by grafting with maleic anhydride (MA), and the MA residues are assumed to bond with cellulose either by esterification or hydrogen bonding. Another grafting monomer is glycidyl methacrylate, though self-polymerization is likely in this case. The grafted PP will likely have properties different from the original PP due to chain scissions and different crystallization, so grafted PP may be added to the PP chosen for the specific application (13). PP-g-MA waxes are available, though these may be seen as additive compatibilizer. This approach may not be suitable for PP fiber intermingling methods, since maleated PP fibers may not be available and the grafted PP will not be optimal for fiber formation.

PP-g-MA of normal molar mass ($M_w = 52,000\,g\,mol^{-1}$) and a wax ($M_w = 9100\,g\,mol^{-1}$) were used as compatibilizer for PP–jute composites. The jute was a bidimensional fabric, and the composites were prepared by a film lamination method using films containing PP blended with PP-g-MA (14).

Cellulose fibers are too hydrophilic for adhesion to PP, and they absorb about 10% moisture, which will cause changes in the composite with humidity. Cellulose fibers are impure in that they contain varying amounts of hemicellulose, lignin, pectins, and waxes. Native cellulose exists in the cellulose I crystal form, and the fibers are assembled in vascular bundles (15). Various pretreatments are used to extract the cellulose from the plant, such as biological degradation of other plant materials, called retting, and mechanical disruption of the plant. The fibers may be washed or extracted with water in the first instance. Extraction with sodium hydroxide (20% aqueous), mercerization, is used to remove hemicelluloses, lignin, and pectins (Figure 2.4). In addition, the alkali treatment causes disruption of intermolecular cellulose hydrogen bonds giving swelling and crystal–crystal transition to cellulose II crystals. The cellulose II has different mechanical properties and water absorption. A further purification step is acetone extraction of the waxes. Pulping conditions have been shown to modify the crystal structure of cotton linters (16). Alkali treatment and extraction have been cornstalks used to produce high quality cellulose fibers from cornstalks (17). Lignins have been separated from sugarcane bagasse using ultrasonication (18). Bioscouring has been used to remove pectins from hemp fibers, and the method is suitable for other natural fibers using pectic lyase (Scourzyme L) (19).

The purified cellulose is still too polar for adhesion to PP, but it is ready for reactive or additive reduction of hydrophilicity. A common treatment is to process with fatty acids such as stearic acid. Silanization has been used as a reactive treatment where trimethylsilyl, vinyltrimethoxysilane (VTMO), or methacrylated silanes are bonded to the cellulose hydroxy groups (20). Acrylonitrile has been absorbed into the pores of purified, dry hemp and graft polymerized to control moisture sorption and limit dimensional changes (21). Dialkyltitanate dicarboxylates are another coupling agent that can be used with cellulose fibers. Cellulose fibers have been grafted with

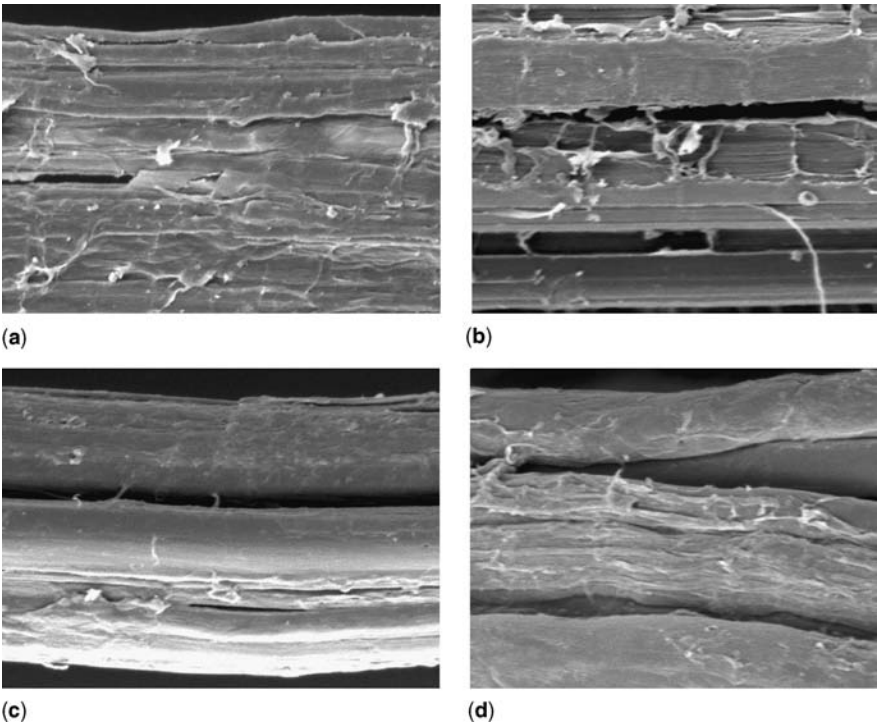

Figure 2.4 Hemp fibers after various treatments: (**a**) untreated, (**b**) acetone extracted, and (**c**) with sodium hydroxide solution, 8% and (**d**) 20%.

acrylate, acrylonitrile, and styrene monomers where the grafted polymer may reside inside the fibers and/or as a coating on the fiber surface (22). PP has been grafted with glycidyl methacrylate (GMA) and the grafted polymer used to prepare hemp composites in a batch mixer. Separately, hemp was reacted with GMA and the hemp–GMA was compounded with PP in the presence of a radical initiator to form grafts with the PP (23).

PP composites with short flax fiber have been prepared by modifying both the PP, using PPg-MA, and the flax, by using VTMO. Hygroscopicity of the flax–VTMO decreased by about 8–40% and the flax–VTMO was more thermally stable (24). Hydrocarbon crystalline wax addition and peroxide initiation of grafting has been used to prepare composites of short sisal fibers with low density polyethylene (25). PP–wood flour composite moisture uptake and transport properties were investigated using a two-level full-factorial experimental design. The variables were coupling agent (PP-g-MA), wood flour content, wood flour particle size, and surface removal. The wood flour content was the most significant variable, though significant interactions were found between variables such as wood flour content and surface treatment (26).

The next approach is to add a blended polymer compatibilizer. The blended polymer will be chosen to have both hydrophobic and hydrophilic components. Some examples are as follows: poly(ethylene-co-vinyl acetate), poly(ethylene-co-vinyl alcohol), poly(ethylene-co-methyl acrylate), poly(ethylene-co-methacrylic acid), and its ionomers adducts. The selection is based on polyethylene, not polypropylene, because polar polypropylene copolymers are not generally available.

2.5 FORMING OF POLYPROPYLENE COMPOSITE

The composite will be prepared as pellets or sheet. In the case of pellets, a separate thermoplastic molding or extrusion operation will prepare the final product. Composite sheets need to be cut by blade or high velocity water-jet. The composite sheet will then be laminated with the desired surface finish. This may be a vinyl sheet with textured finish, a fabric, or a carpet. Other finishes such as wood veneer, aluminum foil, various paperboards, or laminates with melamine–formaldehyde and phenol–formaldehyde resins are suitable to provide attractive and protective finishes. The laminated composite sheet can then be shaped by thermoforming so that it can be fitted to curved locations. The laminated composite sheets are suitable for various building applications where they could be saw-cut and fastened with screws or nails in a traditional fashion.

The feasibility of recycling of PP–flax composites was investigated by subjecting the composites to multiple extrusion cycles. PP suffered significant degradation, though the composites showed acceptable mechanical response. The elastic modulus and impact strength of the composites gave suitable performance that may be, in part, attributed to improved dispersion and distribution of the fibers (27).

PP–wood composites were produced for injection molding using soft wood fiber and an endothermic foaming agent to obtain a microcellular, foamed texture. At a processing temperature of 160°C, the composites showed a finer microcellular structure when molded into box parts or panels for automotive use. The microcellular injection-molded parts provided suitable tensile and flexural strength together with low density consistent with the objective of weight reduction in automotive components (28).

2.6 COMPOSITE MORPHOLOGY AND POLYPROPYLENE CRYSTALLIZATION

The fiber content of the composites will determine its properties. A typical composite may contain up to 50% fibers, above this value it is difficult to ensure adequate fiber wetting and bonding by polymer. After forming the PP, the matrix must crystallize. The crystallinity, crystal size, and orientation of PP crystals are a key determinant of composite properties. In addition to PP, the matrix often contains voids that lower the density, though at the expense of some properties. Maleic anhydride grafting of PP composites with wood flour will lead to an increase in PP crystallinity, but a decrease

in lamella thickness. The results will depend on the wood flour particles size and the content of maleic anhydride grafted PP (29).

PP has been observed to nucleate on the cellulose fiber surface with consequential epitaxial growth leading to transcrystallinity. The effect of transcrystallinity on properties is a vexed question, with some researchers providing evidence of decreased properties, while others finding better adhesion giving improved properties.

The complete fusion and continuity of the surface layers is most important. The surfaces provide a disproportionate contribution to strength, both tensile and flexural. Surface layers of many moldings differ in morphology from the bulk since the surface is usually the first to solidify in the mold or upon exiting from an extruder or contacting a chilled roller set. This phenomenon is present in the PP–cellulose fiber composites.

PP–wood flour composite morphology and properties were enhanced by using a specific betanucleating agent based on *N*,*N*′-dicyclohexylnaphthalene-2,6-dicarboxamide and a compatibilizer of PP-g-MA. The β-PP crystals in the matrix provided improved ductility, though yield stress and break strain were decreased (30). PP-g-MA improved properties by increasing interfacial adhesion.

2.7 MECHANICAL PROPERTIES

The important mechanical properties of PP–cellulose fiber composites are tensile, flexural, and impact. The tensile properties are derived from the tensile properties of the fibers and the fiber–matrix adhesion. Long fibers will provide the best tensile modulus and strength, with typically low break strain. The tensile strength of composites made from felted or woven mats is high because the fiber entanglements reduce dependence on adhesion to the matrix. Typical fiber volume theoretical approaches have been found to describe the tensile properties, including fiber orientation effects. In each of the mechanical properties, the bast fibers are superior to short fibers and in particular to wood flour.

Strain hardening has been induced in regenerated cellulose fibers (Viscose and Lyocell types) after repeated straining and unloading in a cyclic tensile test. The strain hardening, which was more pronounced in Lyocell, was attributed to orientation of the crystalline cellulose (31).

Flexural properties are often more important since the composites must retain their shape and support the surface finish. They may need to support loads that press against or lean upon them. Cellulose fibers are relatively stiff and increasingly so when felted or woven together. Thus, they are able to support the flexible PP in typical applications. The surface compaction and presence of fibers in the surface layers is important since flexure requires extension–compression of the surfaces.

Impact strength is needed for all applications involving molded laminates sheets. The composite must protect other parts of a vehicle or people in automotive applications, and undergo little or limited damage in building applications. PP has poor impact resistance at low temperature, though this is increased in the fiber

composites especially if some voids are present. Tensile, flexural, and impact behavior have been found to be improved when PP-g-MA was used as a compatibilizer in conjunction with PP, or when fiber bundles were treated with PP-g-MA. Water uptake increased with fiber content but decreased when pp-g-MA was included. These enhancements of properties were interpreted as caused due to increased adhesion between flax fibers and PP. Both degree of grafting and molar mass were important in determining the effectiveness of compatibilization (32).

Dynamic mechanical properties of PP composites with wood flour, rice husks, kenaf, and waste newsprint have shown higher storage and loss modulus than pure PP. The glass transition was shifted to slightly lower temperatures and the α-transition was higher, implying that defects in the crystalline regions increased when fibers were added (33).

Composites of jute and hemp with PP were studied using micromechanical and nondestructive acoustic emission analyses. Variables were the presence of PP-g-MA and treatment of the fibers using sodium hydroxide, thermal and silane coupling agent (vinylbenzyl(trimethylsilyl)propylethanediamine hydrochloride (34). Wetability and surface energy measurements were used to compare fiber treatments. Interfacial shear strength (IFSS) was measured using a micromechanical fiber pullout test, and the results were clarified using a nondestructive acoustic emission technique. The data were analyzed using unimodal and bimodal Weibull distribution statistics based on defects in the structures.

2.8 ADDITIVES AND COMPLEMENTARY STRUCTURES

Moisture adsorption–desorption is a problem with hydrophobic cellulose fibers (35). Moisture can cause fungal and mold growth on the fibers, leading to discoloration, adverse odors, and decreased mechanical properties. Fungal and mold inhibitors are available in emulsion and solutions. The additives can be sprayed onto the fibers or adsorbed from immersion in water during other fiber treatments. A further consideration is to limit moisture absorption by fibers treatments or additives, such as stearates, waxes, or plasticizers that coat the cellulose or absorb into the fiber voids excluding water. PP dispersion in itself decreases moisture absorption since the cellulose is not directly exposed to the environment. These treatments and additives decrease biodegradability, though this is necessary for structural materials with suitable lifetimes. Cellulose can still ultimately biodegrade to form products totally compatible with the environment. Gravimetric and dielectric measurements have been used to compare moisture sorption in glass, jute, and washed jute fibers, and a Fickian model was found to be suitable to describe the data (36). The diffusion properties of PP–wood flour composites have been related to material parameters using a factorial design experiment set. While wood flour content had the largest effect as expected, the surface treatment of the wood flour often predominated (37).

All polymer composites, and particularly those of thermoplastics, are flammable. Composites with organic fibers are more flammable than those with glass fibers or other mineral fillers. Flame retardants may be obligatory for automotive and

building components. Halogen-containing flame retardants, such as decabromodiphenyl ether (Decabrom) with antimony oxide (Sb_2O_3), are suitable but not consistent with biodegradability to natural materials. Phosphate esters are suitable and some are available in water emulsions for direct addition to the fibers as well as the pure material being dispersible in PP. The composites will typically have high fiber loading so many non halogen flame retardants will not be suitable when they need to be used in high concentration. Ammonium polyphosphate (APP) has been used to provide flame retardancy to linear low density polyethylene composites with wood flour. Wood flour was limited to 30 pphr, while APP levels of 22–40 pphr were used. Some other flame retardants such as Decabrom–Sb_2O_3, and melamine phosphate (MP) were used for comparison, and pentaerythritol (PER) was added as a synergist for APP (38). Fire retardancy of polypropylene–flax fiber blends has been enhanced using APP with different synergist materials and expandable graphite (EG). Flax fiber content was 30% and either 25% of APP or 15–25% EG were used and tested using thermogravimetry and cone calorimetry (39).

Other fillers are often included. For example, poly(ethylene-co-octene) was used to make wood flour nanocomposites where the nano filler was montmorillonite clay. The polymer was grafted with MA and melt mixing was used for preparation. Composites with up to 50% wood flour had improved mechanical properties when montmorillonite was present (40).

The surface appearance of the composites is not directly suitable for cladding applications. Films of other materials can be laminated onto the composites to provide surface finish or a protective layer. Examples of such films are wood veneers, flexible vinyl sheets that may have embossed patterns, metal foils such as of aluminum, textiles, or carpets that may be woven or felted.

The surface layers contribute to the tensile and flexural properties disproportionately, so that strengthening layers may be added to improve mechanical properties. Polyester or nylon film or woven mats can be laminates to the surfaces. Compression molding usually provides greater consolidation of the matrix and fibers near the surface so there is inherent strengthening of the composite at the surfaces while the interior may be of lower density.

2.9 CONCLUSIONS

Thermoplastic composites are gaining increasing importance, and polypropylene is a central polymer for new developments, combining a typical thermoplastic with natural products. Natural fibers are available from many sources and after purification quality cellulose fibers are available with high reinforcement capacity for composites. Polypropylene can be combined with natural fibers in several ways: by extrusion with short fibers, by powder impregnation into the fibers and fusion, by fiber–fiber felting followed by fusion, by film lamination with fibers and then fusion, and specialized extrusion texturing and injection molding. The composites can be further molded or thermoformed into the final product, or in some cases recycled into the production process. There are many other natural fiber composites formed from

other polymers that have not been considered in this review. The composites with thermosetting polymers are a separate class, with unsaturated polyesters, epoxy resins, phenol, and urea formaldehyde resins as representative polymers.

Fiber modification or polypropylene grafting, typically with maleic anhydride are used to increase fiber–matrix adhesion. Flame retardants, anti fungal, antioxidant, and moisture-resistant additives are included. The composites may be toughened with dispersed elastomers. Natural fibers can have nucleation action with polypropylene that can be expressed as transcrystallinity or decreased crystal size. Voids are often present and may be preferred where low density is required. Modulus, tensile, and flexural strength are high, with useful toughness, rigidity, and thermal resistance suitable for many applications. Automotive, building paneling, and wood substitutes are typical applications.

Applications will continue to expand as new compositions and forms become available. Natural fibers suitable for composite preparation are becoming increasingly available, and the technologies for handling the materials, manufacturing, and distributing the composites are being installed. The concept of natural fiber composites is sound and the uses are increasing as particular compositions meet materials specifications and building codes.

NOMENCLATURE

APP	Ammonium polyphosphate
Decabrom	Decabromodiphenyl ether
EG	Expandable graphite
GMA	Glycidyl methacrylate
IFSS	Interfacial shear strength
MA	Maleic anhydride
MP	Melamine phosphate
PER	Pentaerythritol
PP	Polypropylene
PP-g-MA	Polypropylene grafted with maleic anhydride
Sb_2O_3	Antimony oxide
VTMO	Vinyltrimethoxysilane

REFERENCES

1. J. Karger-Kocsis (ed.), *Polypropylene Structure, Blends and Composites, Vol 3: Composites*, Chapman and Hall, London, 1995, Chapters 1–10.
2. F. P La Mantia and M. Morreale, *Polym. Eng. Sci.*, **46**, 1131 (2006).
3. S. C. Tjong, *Mater. Sci Eng. Rep.*, **53**, 73 (2006).
4. M. M. De Souza Lima and R. Borsali, *Macromol. Rapid Commun.*, **25**, 771 (2004).
5. H. Dopfner, M. Ernegg, and R. Bramsteidl, *US Patent* 6,379,594 B1 (2002).
6. W. Wang, M. Sain, and P. A. Cooper, *Polym. Degrad. Stabil.*, **90**, 540 (2005).

7. A. K. Bledzki, O. Faruk, and V. E. Sperber, *Macromol. Mater. Eng*., **291**, 449 (2006).
8. H. Faria, N. Condeiro, M. N. Belgacem, and A. Dufresne, *Macromol. Mater. Eng*., **291**, 16 (2006).
9. N. E. Marcovich, M. M. Reboredo, J. Kenny, and M. I. Arauguren, *Rheol. Acta*, **43**, 293 (2004).
10. R. T. Steller, *J. Appl. Polym. Sci*., **97**, 1401 (2005).
11. S. Shinichi, Y. Cao, and I. Fukumoto, *Polym. Test*., **25**, 142 (2006).
12. N. Ljungberg, J. Y. Cavaille, and L. Heux, *Polymer*, **47**, 6285 (2006).
13. W. Qiu, T. Endo, and T. Hirotsu, *Eur. Polym. J*., **42**, 1059 (2006).
14. B. A Acha, M. Reboredo, and N. E. Marcovich, *Polym. Int*., **55**, 1104 (2006).
15. H. Yu, R. Liu, D. Shen, Y. Jiang, and Y. Huang, *Polymer*, **46**, 5689 (2005).
16. E. Gumuskaya, M. Usta, and H. Kirci, *Polym. Degrad. Stabil*., **81**, 559 (2003).
17. N. Reddy and Y. Yang, *Polymer*, **46**, 5494 (2005).
18. J. X. Sun, F. Xu, X. F. Sun, R. C. Sun, and S. B. Wu, *Polym. Int*., **53**, 1711 (2004).
19. S. Ouajai and R. A. Shanks, *Macromol. Biosci*., **5**, 124 (2005).
20. A. Hodzic, R. A. Shanks, and M. Leorke, *Polym. Polym. Compos.*, **10**, 281 (2002).
21. S. Ouajai, A. Hodzic, and R. A. Shanks, *J. Appl. Polym. Sci*., **94**, 2456 (2004).
22. R. A. Shanks, A. Hodzic, and D. Ridderhof, 2006, *J. Appl. Polym. Sci*., **99**, 2305 (2006).
23. M. Pracella, D. Chionna, I. Anguillesi, Z. Kulinski, and E. Piorkowska, *Compos. Sci. Technol.*, **66**, 2218 (2006).
24. A. Arbelaiz, B. Fernandez, J. A. Ramos, and I. Mondragon, *Thermochim. Acta*, **440**, 111 (2006).
25. A. S. Luyt and M. E. Malunka, *Thermochim. Acta*, **426**, 101 (2005).
26. V. Steckel, C. M. Clemons, and H. Thoemen, *J. Appl. Polym. Sci*., **103**, 752 (2006).
27. J. Moran, V. Alvarez, R. Petrucci, J. Kenny, and A. Vazquez, *J. Appl. Polym. Sci*., **103**, 228 (2007).
28. A. K. Bledzki and O. Faruk, *Macromol. Mater. Eng*., **291**, 1226 (2006).
29. M. G. Salemane and A. S. Luyt, *J. Appl. Polym. Sci*., **100**, 4173 (2006).
30. J. Kotek, I. Kelnar, H. Synkova, Z. Stary, and J. Baldrian, *J. Appl. Polym. Sci*., **103**, 506 (2007).
31. W. Gindl and J. Keckes, *Compos. Sci. Technol*., **66**, 2049 (2006).
32. A. Arbelaiz, B. Fernandez, J. A. Ramos, A. Retegi, R. Llano-Ponte, and I. Mondragon, *Compos. Sci. Technol*., **65**, 1582 (2005).
33. T. Mehdi, R. H. Falk, and J. C. Hermanson, *J. Appl. Polym. Sci*., **101**, 4341 (2006).
34. J. M. Park, S. T. Quang, B. S. Hwang, and K. L. DeVries, *Compos. Sci. Technol*., **66**, 2686 (2006).
35. S. Okubayashi, U. J. Griesser, and T. Bechtold, *J. Appl. Polym. Sci*., **97**, 1621 (2005).
36. A. N. Fraga, E. Frullloni, O. de la Osa, J. M. Kenny, and A. Vazquez, *Polym. Test.*, **25**, 181 (2006).
37. V. Steckel, C. M. Clemons, and H. Thoemen, *J. Appl. Polym. Sci*., **103**, 752 (2007).
38. B. Li and J. He, *Polym. Degrad. Stabil*., **83**, 241 (2004).
39. B. Schartel, U. Braun, U. Schwarz, and S. Reinemann, *Polymer*, **44**, 6241 (2003).
40. H. T. Liao and C. S. Wu, *Macromol. Mater. Eng*., **290**, 695 (2005).

Chapter 3

Polyolefin/Natural Fiber Composites

Laly A. Pothan,[1] Adriaan S. Luyt,[2] and Sabu Thomas[3]

3.1 INTRODUCTION

Over the years, humankind has learned that cellulose, the most dynamic material used by nature for its own sustenance, can be used for a better life while maintaining harmony with nature itself. A number of researchers have involved themselves in investigating the use of cellulosic fibers as load-bearing constituents in composite materials. The use of these materials in composites has increased over the last few years owing to the relatively low cost of these materials compared to conventional materials such as glass fiber or aramid fiber. Another attraction is the fact that it is recyclable. They compete well in terms of strength per weight of material (1). Natural fibers are classified according to their source: plants, animals, or minerals. Generally, plant fibers are used to reinforce plastics in the composites industry. There are many varieties of plant fibers such as hairs (cotton and kapok), fiber sheafs of dicotyl plants or vessel sheafs of monocotyl plants (e.g., flax, hemp, jute, and ramie), and hard fibers (sisal, henequen, and coir), not to mention the large variety of fibers obtained from trees. By far, the most abundant is wood fiber sourced from trees (see Table 3.1). Other fiber types are also in common use.

The biofiber world is full of examples where cells or groups of cells are ''designed'' for strength and stiffness. Sparing use of resources has resulted in the optimization of cell functions. Cellulose is a natural polymer with high strength

[1]Department of Chemistry, Bishop Moore College, Mavelikkara 690101, Kerala, India

[2]Department of Chemistry, University of the Free State (Qwaqwa Campus), Private Bag X13, Phuthaditjhaba, 9866, South Africa

[3]School of Chemical Sciences, Mahatma Gandhi University, Priyadarshani Hills, Kottayam 686560, Kerala, India

Polyolefin Composites, Edited by Domasius Nwabunma and Thein Kyu

Table 3.1 Commercially Important Fiber Sources.

Fiber source	Species	World production (10^3 tons)	Origin
Wood	(>10,000 species)	1,750,000	Stem
Bamboo	(>1250 species)	10,000	Stem
Cotton lint	*Gossypium* sp.	18,450	Fruit
Jute	*Corchorus*	2300	Stem
Kenaf	*Hibiscus cannabinus*	970	Stem
Flax	*Linum usitatissimum*	830	Stem
Sisal	*Agave sisilana*	378	Leaf
Roselle	*Hibiscus sabdariffa*	250	Stem
Hemp	*Cannabis sativa*	214	Stem
Coir	*Cocos nucifera*	100	Fruit
Ramie	*Boehmeria nivea*	100	Stem
Abaca	*Musa textiles*	70	Leaf
Sunhemp	*Crorolaria juncea*	70	Stem

Reprinted from Reference 4 with permission from Springer/Kluwer Academic Publishers.

and stiffness per weight, and it is the building material of long fibrous cells. These cells can be found in the stems, leaves, and seeds of plants. In general, the fiber consists of a wood core surrounded by a stem. Within the stem there are a number of fiber bundles that contain individual fiber cells or filaments. The filaments are made of cellulose and hemicellulose, bonded together by a matrix that can generally be lignin or pectin. Pectin surrounds the bundles, thus holding them onto the stem (2).

The lack of raw material is also a concern for the manufacturing industry, and the pressures on the industry to use ever more ''greener'' technologies have made this area of research of worldwide interest. The main reasons for this current interest in these natural materials are their (i) environmental friendliness, (ii) easy availability, and (iii) intrinsic properties. Their relatively lower density and easy processability are the other important factors that have made them potential candidates as materials for reinforcement in various polymeric matrices. Compared to traditional synthetic fillers, natural fibers have lower density, less abrasiveness, and lower cost, and they are renewable and biodegradable. Moreover, their mechanical performance can be compared to that of synthetic fibers used nowadays, and they have good thermal properties (3). The fact that they are fibers obtained directly from natural resources makes them even more attractive in terms of sustainability and environmental friendliness. Plant fibers obtained from various parts of the plant, namely bast, stem, and seed, are being used in the preparation of composites. Fibers derived from banana plant, sisal, flax, hemp, pineapple leaf, oil palm seed, and coconut husk have been tried out as reinforcement in thermoplastic, thermoset, and rubber matrices.

Polyolefins are interesting materials that find application in various fields. Polyolefin polymers, such as polyethylene (PE) and polypropylene (PP), are

widely used in the automotive industry and for domestic applications where ductility and low cost have to be combined. Various thermoplastics, including polyethylene, polypropylene, and poly(vinyl chloride) (PVC), have been used for research and development, both on laboratory and on industrial scales. In addition, mineral fillers and fibers are now extensively used in the plastics industry to achieve desired properties or to reduce the price of the finished article. Compared to thermoset matrices, polyolefinic matrices have the additional advantage of being recyclable.

This chapter gives an overview of plant fibers and the modification techniques most commonly employed when these plant fibers are used as reinforcement in polymeric matrices. Both physical and chemical methods employed to modify the plant fibers, and the major observations of some of the researchers including the suggested mechanism in a few cases, are represented in this chapter. The modifications are usually limited to the superficial OH groups to preserve the integrity of the fibers and thus their mechanical strength. Detailed reviews of literature available on polyolefinic composites of various natural fibers and their applications are discussed.

3.2 STRUCTURE AND PROPERTIES OF PLANT FIBERS

With the exception of synthetic polymers, most economically important products such as paper, cordage (cords and rope), and textiles are derived from plant fibers. Fibers are elongated cells with tapering ends and very thick, heavily lignified cell walls. The lumen or cavity inside mature and dead fiber cells is very small when viewed in cross section. Plant fibers vary widely in terms of chemical composition, structure, and dimensions, and originate from different parts of the plant. Based on the part of the plant from which they are obtained, plant fibers are classified as seed fibers (cotton and ramie), bast fibers (jute, banana, and flax), and leaf fibers (sisal and abaca). Figure 3.1 shows the longitudinal section and cross section of a fiber cell. Table 3.1 gives the world production figures of certain commercially important fiber sources.

Bast fibers or some of the ''hard'' leaf fibers are extracted from stems (or leaves) after a process called retting (4).

In retting, anaerobic bacteria, especially *Clostridium*, bring about the gradual decomposition of the pectin material forming the middle lamella of the cell wall, so that the fiber bundles are released from the tissues around them. The bark is removed from the retted stems and beaten until the fiber bundles are separated from phloem, cortex, and epidermal tissues (5).

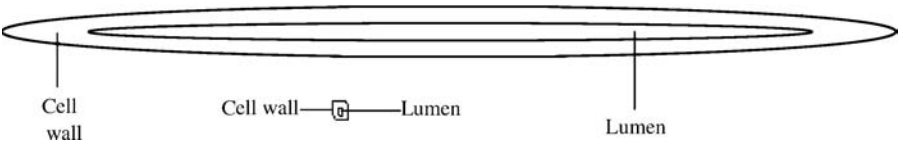

Figure 3.1 Longitudinal section and cross section of a fiber cell.

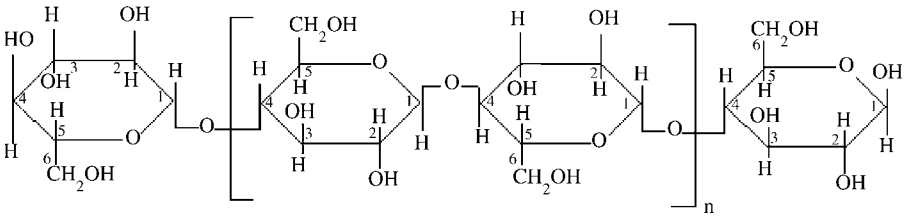

Figure 3.2 Haworth projection formula for cellulose.

3.2.1 Chemical Structure and Applications

The essential component of all plant fibers is cellulose. The term cellulose was first used by Payen (6) in 1838. Since then it has been generally accepted that cellulose is a linear condensation polymer consisting of D-anhydroglucopyranose units, joined together by β-1-4-glycosidic bonds. The Haworth projection formula for cellulose is given in Fig. 3.2. In another sense, cellulose can be considered as a syndiotactic polyacetal of glucose. Terminal hydroxyl groups are present at both ends of the cellulose chain molecule. However, these groups are quite different in nature. The C(1) hydroxyl at one end of the molecule is an aldehyde hydrate group with reducing activity and originates from the formation of the pyranose ring through an intermolecular hemiacetal reaction. In contrast to this, the C(4) hydroxyl on the other end of the chain is an alcoholic hydroxyl and is nonreducing.

The chemical character of the cellulose molecule is determined by the sensitivity of the glucosidic linkages, between the glucose repeating units, to hydrolytic attack, and by the presence of three reactive hydroxyl groups—one primary and two secondary—in each of the base units. These reactive hydroxyl groups are able to undergo etherification and esterification reactions. The main cause for the relative stiffness and rigidity of the cellulose molecule is the intramolecular hydrogen bonding, which is reflected in its high viscosity in solution, its high tendency to crystallize, and the ability to form fibrillar strands. The glucosidic linkage further favors chain stiffness.

The molecular structure of cellulose is responsible for its supramolecular structure and this, in turn, determines many of its physical and chemical properties. In the fully extended molecule, their mean planes are at an angle of 180° to each other and oriented adjacent to chain units. The mechanical properties of natural fibers also depend on the cellulose type, because each type of cellulose has its own cell geometry and the geometrical conditions determine the mechanical properties. The crystal structure of natural and regenerated cellulose is known as cellulose I and II, respectively. In cellulose I the chains within the unit cell are in parallel configuration (7), while they have an antiparallel configuration (8) in cellulose II. In addition to the cellulose component, natural fibers contain hemicellulose, which consists of a group of polysaccharides that remain associated with the cellulose after lignin has been removed. The hemicelluloses differ from cellulose, in that they contain several sugar units, whereas cellulose contains only glucopyranose units.

Hemicellulose also exhibits considerable chain branching whereas cellulose is strictly linear. Also, the degree of polymerization of native cellulose is 10–100 times higher than that of hemicellulose. Unlike cellulose, the constituents of hemicelluloses differ from plant to plant (9). Lignins, complex hydrocarbons with aliphatic and aromatic components, are the other constituents of plant fibers. Lignin is a little-understood hydrocarbon polymer with a highly complex structure consisting of aliphatic and aromatic constituents (10) and forms the matrix sheath around the fibers that holds the natural structure (e.g., trees) together.

Lignin is an aromatic biopolymer, an integral cell constituent in all vascular plants including the herbaceous varieties. It is built up by oxidative coupling of three major C6–C3 (phenylpropanoid) units, namely syringyl alcohol, guaiacyl alcohol, and *p*-coumaryl alcohol, which form a random structure in a tridimensional network inside the cell walls (11). The major interunit linkage is an aryl–aryl ether type. Besides the 20 different types of bonds present within the lignin itself, lignin seems to be particularly associated with the hemicellulosic polysaccharides (12). Their chief monomer units are various ring-substituted phenyl propanes, linked together in ways that are not fully understood. Lignin forms the matrix sheet around the fibers that hold the natural structure together. The mechanical properties of lignin, however, are lower than those of cellulose (13). In addition to these, pectin and waxes make up parts of the fiber (14). Pectins are a collective name for heteropolysaccharides, which consist of β-1,4-linked galacturonic acid units, sugar units of various composition, and their respective methyl esters (15). Finally, the waxes consist of various alcohols and form a small percentage of the structure. Cellulose is found not to be uniformly crystalline.

3.2.2 Cellulose Microfibrils

The ordered regions are extensively distributed throughout the material and these regions are called crystallites. The threadlike entity, which arises from the linear association of these components, is called the microfibril. It forms the basic structural unit of the plant cell wall. These microfibrils are found to be 10–30 nm wide, less than this in width, and indefinitely long containing 20,000–30,000 cellulose molecules in cross section. Their structure consists of a predominantly crystalline cellulose core. This is covered with a sheath of paracrystalline polyglucosan material surrounded by hemicelluloses (16). In most natural fibers, these microfibrils orient themselves at an angle to the fiber axis called the microfibril angle.

The ultimate mechanical properties of natural fibers are found to be dependent on the microfibrillar angle. Cellulose exists in the plant cell wall in the form of thin threads with an indefinite length. Such threads are cellulose microfibrils, playing an important role in the chemical, physical, and mechanical properties of plant fibers and wood. Microscopists' and crystallographers' studies have shown the green algae *Valonia* to be an excellent material for the ultrastructural study of the cellulose microfibril (17). A discrepancy in the size of the crystalline regions of cellulose, obtained by X-ray diffractometry and electron microscopy, led to differing concepts

on the molecular organization of microfibrils. Frey-Wyssling (18) regarded the microfibril itself as being made up of a number of crystallites, each of which was separated by a paracrystalline region and later termed ''elementary fibril.'' The term ''elementary fibril'' is therefore applied to the smallest cellulosic strand.

Reports on the characterization and makeup of the elementary fibrils and their association while establishing the fiber structure—usually called fibrillar or fringed fibril structure—are found in the literature (19). According to this concept, the elementary fibril is formed by the association of many cellulose molecules that are linked together in repeating lengths along their chains. In this way, a strand of elementary crystallites is held together by parts of the long molecules reaching from one crystallite to the next, through less ordered interlinking regions. Molecular transition from one crystallite strand to an adjacent one is possible, in principle. Apparently, in natural fibers this occurs only to a limited extent, whereas in man-made cellulosic fibers such molecular transitions occur more frequently.

The internal cohesion within the elementary fibrils is established by the transition of the long cellulose chain molecules from crystallite to crystallite. The coherence of the fibrils in their secondary aggregation is provided either by hydrogen bonds at close contact points or by diverging molecules. Access into this structure is given by large voids formed by the imperfect axial orientation of the fibrillar aggregates, by interspaces of nanometer dimensions between the fibrils in the fibrillar aggregations, and by the less ordered interlinking regions between the crystallites within the elementary fibrils.

Dufresne (20) has reported on whiskers obtained from a variety of natural and living sources. Cellulose microfibrils and cellulose whisker suspensions were obtained from sugar beet root and from tunicin. A typical electron micrograph obtained from a dilute suspension of sugar beet is shown in Fig. 3.3. Individual

Figure 3.3 Transmission electron micrograph of a dilute suspension of sugar beet cellulose. (From Reference 20 with permission from Springer.)

microfibrils are almost 5 nm in width while their length is of a much higher value, leading to a practically infinite aspect ratio of this filler. They can be used as a reinforcing phase in a polymer matrix.

3.3 SURFACE MODIFICATION OF PLANT FIBERS

Though researchers, industrialists, and environmentalists have accepted natural cellulosic fibers as reinforcement in polymeric matrices, these fibers also have some disadvantages. A major disadvantage of cellulose fibers is their highly polar nature, which makes them incompatible with nonpolar polymers such as polyolefins. Several techniques have been used to modify the surface of natural fibers in order to reduce the hydrophilicity and to minimize the interfacial energy with nonpolar polyolefinic matrices.

Plant fibers have an external surface that is coated with waxy substances. This surface usually has a low surface tension that prevents strong bonding with polymeric matrices. The bond strength can be improved effectively by one or more operations that include

- cleaning the surface by dissolving the waxy layer and the cuticle,
- allowing the fiber to react with reagents that make it hydrophobic, and
- grafting the surface with suitable reagents.

Belgacem and Gandini have given a detailed review on the various strategies adopted in modifying cellulose fibers for use as a reinforcing element in composite materials (21). They have classified the major approaches of fiber treatments, as (i) physical treatments such as solvent extraction, (ii) physicochemical treatments, like the use of corona and plasma discharges or laser, X-ray, and ultraviolet (UV) bombardment, and (iii) chemical modifications, both by the direct condensation of the coupling agents onto the cellulose surface and by various grafting strategies including polycondensations and free radical or ionic polymerizations.

3.3.1 Physical Treatments

The physical methods used for surface modification involve methods such as stretching (22), calendaring (23), thermal treatment (24), and production of hybrid yarns (25). These methods do not change the chemical composition of the fiber. However, they change the structural and surface properties of the fiber and thereby influence the mechanical bonding to polymers. Simple treatment of the lignocellulosics with a solvent has been reported by several researchers (26,27).

Different types of cellulose fibers obtained from various sources were subjected to solvent extraction (mostly Soxhlet extraction) with solvents like acetone, ethanol/toluene mixture, diethyl ether, and cold and hot water. Comparison of the data related to the surface characteristics of the fibers after solvent extraction showed that at least part of the aliphatic and aromatic impurities that were originally present on the

surface were removed. The surface energy of the fibers determined by inverse gas chromatography (IGC) increased from 32 to 47 mJ m^{-2} as a result of the removal of small molecules with low surface energy (28). The acid–base characteristics of the treated fibers were also found to increase by these treatments.

Boufi and Gandini (29) have reported on a novel approach to envelop cellulose fibers with a thin sleeve of polymer without any chemical interaction at the interface. Cationic surfactants were made to adsorb on the surface of fibers suspended in water to form admicellar configurations, and subsequently water-insoluble monomers like styrene and acrylates were included on the surface of the fibers. Free radical polymerization of the adsorbed monomer generated a thin layer of polymer on the fiber surface reducing the surface free energy of the fibers as well as their hydrophilicity. The method seems to be appropriate in tailor-making the surface polarity of fiber surfaces to have proper interaction with the polymer of our choice.

3.3.2 Physicochemical Treatments

Physicochemical treatment methods of fiber modification involve methods such as corona treatment, surface fibrillation, γ-ray irradiation, UV treatment, and so on. This treatment is aimed at purifying, oxidizing, and activating the surface of plant fibers. These physicochemical treatments change the structural and surface properties of the fiber and thereby influence the mechanical bonding with the polymer.

3.3.2.1 Corona Treatments

Sakata et al. (30) reported on the oxidation of hydrophilic constituents of the surface of different types of wood through corona treatments. In the case of wood fibers, surface activation increases the number of aldehyde groups. Gassan and Gutowski (31) treated tossa jute fibers by corona discharge and UV rays to improve the properties of natural fiber epoxy composites. Corona-treated fibers exhibited significantly higher polar components of the free surface energy with increasing treatment energy output. It was observed that at optimum treatment conditions, an increase of about 30% in the composite flexural strength was observed. Gassan et al. (32) studied the surface characteristics of corona-treated jute fibers by dynamic contact angle measurements. They showed that treatment increased the polarity of the fiber surface. The fiber surface changes depended on the corona energy output.

3.3.2.2 Plasma Treatments

Plasma treatment offers a new approach to the modification of natural fiber surfaces. Cold plasma techniques are dry, clean processes that do not involve

environmental concerns (33). Plasmas can be defined as partially ionized gases that have a collective behavior. One of the main advantages of this approach is that the modification is confined to the surface of the materials without interfering with their bulk properties. Energetic species present in the discharge—such as electrons, ions, free radicals, and photons—have energy levels high enough to alter all chemical bonds in the surface layers of natural polymeric substrates. Proper selection of starting compounds and external plasma parameters (e.g., power, pressure, and treatment time) allows the creation of desired characteristics on lignocellulosic substrate surfaces. In a cold plasma treatment system, depending on the type and nature of the gases used, a variety of surface modifications can be achieved. Surface energy can be increased or decreased, cross-linking can be introduced, and reactive free radicals and groups can be produced. In the case of wood surface activation, this process has been reported to increase the amount of aldehyde groups (34).

Yuan et al. (35) have reported on the effect of argon and plasma treatment on the surface of wood fiber to improve the compatibility between the fiber and polypropylene. Surface characterization by X-ray photoelectron spectroscopy (XPS) showed an increase in the oxygen–carbon ratio of wood fiber after chemical modification in the composites leading to failure by delamination. They tried to achieve adequate adhesion at desirable levels across the interface by better wetting and chemical bonding between the fiber and matrix.

Some typical effects of plasma treatment on the appearance of wood fibers have been reported by Yuan et al. (35). Figure 3.4a shows the scanning electron micrograph (SEM) of the untreated wood fiber surface. The surface morphology reveals that the untreated wood fiber surface is relatively smooth, but after Ar plasma treatment, it becomes rougher (Fig. 3.4b). It is also interesting to note that the pits in the untreated fiber surface are either closed or partially open (Fig. 3.4a).

However, the pits on the surface of Ar plasma treated wood fiber have been practically opened, most likely by the etching mechanism of the plasma. Low temperature plasma treatment causes mainly chemical implantation, etching, polymerization, free radical formation, and crystallization, whereas sputter etching brings about chiefly physical changes such as surface roughness, which leads to better fiber–matrix interaction (36). Low temperature plasma can be generated under atmospheric pressure in the presence of helium. The action of these plasmas involves abstraction of protons and creation of unstable radicals that convert functional groups such as alcohols, aldehydes, ketones, and carboxylic acids.

3.3.2.3 γ-Irradiation

Khan et al. (37) studied the effect of γ- and UV irradiation on the mechanical properties of jute composites. Jute yarn treated with methyl methacrylate (MMA) + methanol (MeOH) solutions was used for irradiation. In γ-irradiation, the polymer loading of MMA onto jute increased quite substantially. However, the strength of the composite decreased sharply after 15% polymer loading. The tensile strength of the UV-cured jute yarn composite was found to increase with an increase

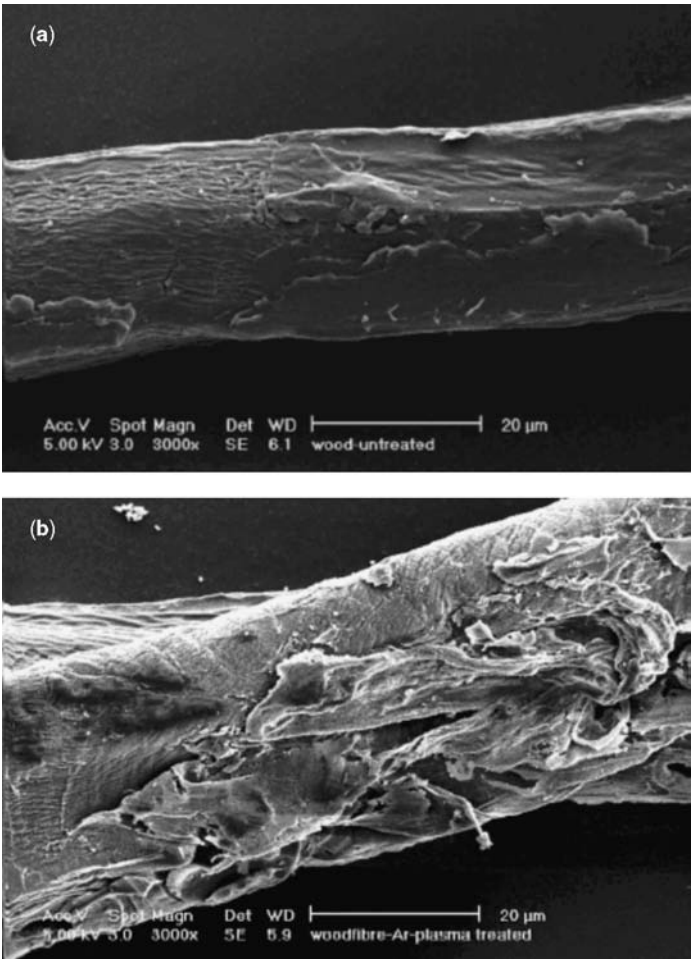

Figure 3.4 (**a**) SEM of the untreated wood fiber surface. (From Reference 35 with permission from Elsevier Ltd.) (**b**) SEM of the argon plasma treated wood fiber surface. (From Reference 35 with permission from Elsevier Ltd.)

of grafting level, in contrast to the behavior observed with γ-irradiated jute composite samples.

It has been mentioned by Belgacem Gandini (21) that the extremely high energies associated with γ-irradiation are not conducive to polymeric materials, since the high energy radiations are likely to degrade the fiber. Sreekala and Thomas (38) have reported on the effect of γ-irradiation on oil palm fibers. The properties of the composites prepared using the treated fibers, however, were found to decrease while the resistance to water uptake increased. Belgacem and Gandini (39), in their review article, have mentioned treatments with laser beam and also UV radiations on natural fibers.

3.3.3 Chemical Modification of Plant Fibers

The chemical modification of plant fibers involve

- chemical treatment,
- chemical coupling, and
- direct surface activation

3.3.3.1 Chemical Treatment

In chemical treatment, as discussed earlier, the surface impurities are removed, improving the surface's adhesive characteristics. Treatment with alkali is one of the oldest methods used to modify natural fibers. The natural and artificial impurities from the surface of the fiber get removed on treatment with alkali, which brings about improved surface tension, improved wettability, and thereby improved bonding. Alkali treatment has varying effects on different fibers. A few important observations of alkali treatment are mentioned.

Martins et al. (40) carried out alkali treatment for sisal fibers and investigated the effect of alkali concentration on the surface of the fiber under varying time and concentration conditions. Usually, the effects of mercerization on the properties of natural fibers depend on the type and concentration of the alkali solution as well as the temperature and time of treatment (41). Alkali treatment has been reported to dissolve and leach out the fatty acids and their condensation products that form the waxy cuticle layer (42). SEM studies of alkali-treated sisal fibers under varying conditions gave interesting results. It was shown that the parenchyma cells were only partially removed and that the morphological changes were independent of the treatment conditions used (43). Fibers submitted to less severe treatment conditions showed more significant changes than those submitted to severe conditions. These results were observed for all the fibers studied under all the different mercerization conditions, indicating that it was possible to use less drastic and more economical treatment conditions. Gravimetric results obtained after the mercerization treatment showed that the mass loss depended more on the temperature than on the time.

Ray et al. (44) studied the effect of alkali treatment on jute fibers. It was observed that treatment of jute fibers with 5% NaOH for varying periods of time showed an overall improvement in properties both as fibers and as reinforced composites. Ray and Sarkar (45) studied the changes occurring on the surface of jute fibers treated with alkali of different concentration. They observed an improvement in tenacity and modulus of the fibers by about 45% and 79%, respectively. They attributed the improvement in mechanical properties to the reduction of linear density of the fiber after treatment. In addition, a weight loss of 9.63% was observed during a 2-h treatment, with a drop in hemicellulose content from 22% to 12.9%. X-ray diffractograms showed an increase in the crystallinity of the fibers after 6 h of treatment.

Owolabi et al. (46) reported on the effect of preirradiation and alkali treatment on coir fibers. In general, this treatment reduces the cementing material followed by

the escape of volatile products with the rupture of bonds. Optimal conditions of mercerization ensure the improvement of tensile properties. It is believed that the increase in the crystallinity index measured by wide-angle X-ray scattering (WAXS) is in fact an increase in the order of the crystallite packing rather than an increase in the intrinsic crystallinity. The modification of cellulose fibers, therefore, develops into changes in morphology and increase in hydroxyl groups. These changes will effectively result in improved surface tension, wetting ability, swelling, adhesion, and compatibility with polymeric materials (47).

The structural features and fracture morphology of raw and chemically treated pineapple leaf fibers (PALFs) have been studied by Saha et al. (48) using SEM. Surface morphology progressively changes with gradual removal of non cellulosic constituents like lignin and hemicellulose by alkali treatment. XPS studies of alkali-treated banana fibers (49) revealed that aluminosilicates as well as Mg present in raw fiber have been dissolved by NaOH. In the case of aluminosilicates containing magnesium, NaOH would destroy the silicate lattice and remove the formed aluminum and silicon ions, but usually the magnesium will remain on the sample surface. The loss in the [N]:[C] ratio shows that the organic matrix of the fiber surface is affected in the strong basic environment. The small decrease in the [O]:[C] ratio can be attributed to the dissolution of hemicellulose and lignin after alkali treatment. The dissolution of the lignin component with a high [O]:[C] ratio results in an overall lowering of the same.

3.3.3.2 Chemical Coupling

The chemical coupling reactions used in modifying cellulose fiber surfaces can mainly be classified as (i) etherification, (ii) esterification, (iii) urethane formation, and (iv) siloxane formation. All these strategies are based on using molecules bearing one or several functions capable of reacting with the cellulose surface OH groups and thus append long hydrophobic grafts, which play the double role of protecting the fiber surface from water uptake and making it more compatible with nonpolar matrices like polyolefins. Other than the above-mentioned strategies, surface grafting is an efficient strategy. Grafting reaction introduces functions capable of polymerizing with the matrix, thus giving a continuous pathway of covalent bonds between the cellulose fibers and the matrix macromolecules and hence ensuring optimum interfacial adhesion.

Etherification Zadorecki and Ronnhult (50) synthesized C18-T (2,4-dichloro-6-*n*-octadecyloxy-s-triazine) and grafted it onto cellulose fibers. The chlorotriazine derivative was used to treat different plant fibers (51). Pothan et al. (52) treated banana fibers with C18-T and characterized the surface using solvatochromism, zeta potential measurements, and XPS. These results showed the fiber surface to be acidic. The proposed reaction path is shown in Fig. 3.5.

Cellulosic fibers derived from flax and purified by steam explosion were etherified with ethyl iodide (53). The fibers were characterized using techniques like Fourier transform infrared spectroscopy (FTIR), WAXS, and time-of-flight

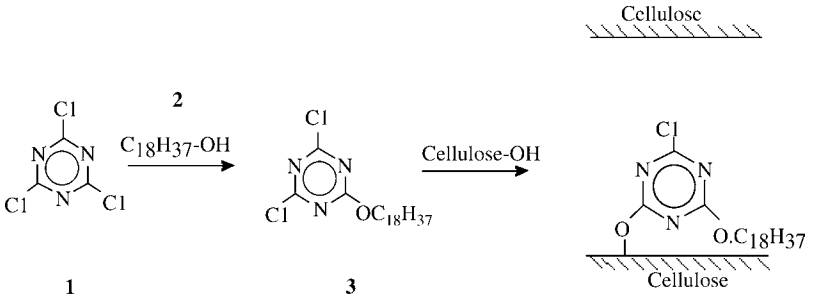

1 – Trichloro-s-triazine
2 – Stearyl alcohol
3 – 2,4-Dichloro-6-*n*-octadecyloxy-s-triazine

Figure 3.5 Reaction path of banana fibers treated with trichloro-s-triazine. (From Reference 50 with permission from Wiley Interscience.)

secondary ion mass spectrometry (ToF-SIMS). The reduction of the water absorption of cellulose fibers and their composites treated with triazine derivates was explained by reducing the number of cellulose hydroxyl groups that are available for water uptake, and restraint of the swelling of the fiber, by creating a cross-linked network due to covalent bonding (54).

Esterification Cellulose acetate is the first compound prepared as a result of the esterification of cellulose. The reagents most intensively explored for acetylation are acetic anhydride, alkyl ketene dimer, alkenyl succinic anhydride, and different fatty acids (with *n* varying from 6 to 22) or their chlorides. The acetylation of the C–OH groups of the cellulose not only prevents the formation of inter- and intramolecular hydrogen bridge linkages, but is also a way to lower the polarity and enhance the compatibility to polyolefin matrices.

To improve the moisture resistance of sisal fiber, Chand et al. (55) have taken acetylated sisal fiber and studied its tensile strength. It was shown that acetylation can reduce the moisture content from 11% to 5.45%. However, the tensile strength of acetylated sisal fiber is reduced from 445 to 320 MPa due to the loss of the hemicelluloses in the fiber during acetylation. Acetylation has been reported to be an effective modification method for natural fibers by several other authors (56,57).

Cellulose fibers derived from flax and purified by steam explosion were heterogeneously esterified by acetic anhydride using sulfuric acid catalyst. After modification, the fibers were recovered by filtration, washed with water, and dried at 50°C (58). The fibers were characterized using FTIR, SEM, and WAXS. It was found that the structure of the fibers, as well their biodegradability, was maintained.

Albano et al. (59) studied the effect of acetylated and nonacetylated sisal fiber on the thermal degradation of blends of PP and polyolefins. Acetylated fiber stability was found to have improved. Zafeiropoulus et al. (60) studied the effect of acetylation and stearation on flax fibers. The effect of two surface treatments (acetylation and stearation) upon the tensile strength of flax fibers was studied. The results were

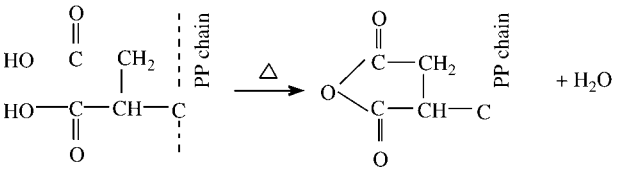

Figure 3.6 Activation of the copolymer by heating. (From Reference 62 with permission from Elsevier Ltd.)

discussed in terms of Gaussian statistics and it was found that the treatments did not significantly change the flax fiber tensile strength. In addition, SEM examination of the fractured surfaces revealed that acetylated fibers exhibit a different mode of failure from the other fibers, suggesting that the treatment altered the bulk properties along with the surface properties.

Trifluoroacetic anhydride has recently been identified as an esterification agent for cellulose, both in the gaseous and in the liquid state. The CF_3 groups proved to be hydrophobic but were prone to hydrolysis (61). Joseph et al. (62) treated sisal fibers with maleic anhydride grafted polypropylene (MAH-PP) in order to improve the interfacial adhesion between the fiber and the PP matrix in a sisal/PP composite. The beneficial effect of maleated PP on the strength properties of sisal/PP composites has been attributed to the esterification reaction between cellulosic fiber hydroxyl groups and the anhydride functionality of maleated PP. The mechanism of the reaction can be divided into two steps (Figs. 3.6 and 3.7).

In a recent interesting study, Zheng et al. (63) modified the surface of bagasse fibers (BF) with benzoic acid. A mixture of PVC, BF, benzoic acid, and other processing additives were dry-blended in a two-roll mill followed by compression molding. The experimental results indicated that the ratio of PVC/BF, the content of benzoic acid, and the processing temperature had a significant effect on the mechanical properties of the composite. The interface modifier significantly improved the tensile strength and had little effect on the impact strength of the composite.

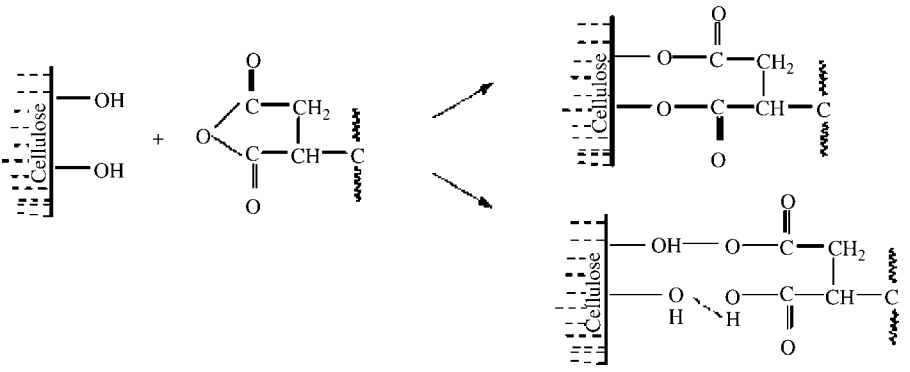

Figure 3.7 Esterification of cellulose. (From Reference 62 with permission from Elsevier Ltd.)

Urethane Formation The mechanical properties of composites reinforced with wood fibers and PVC or PS as the resin can be improved by an isocyanate treatment of the cellulose fiber or the polymer matrix (64). Polymethylene polyphenyl isocyanate (PMPPIC) in the pure state or in solution in the plasticizer can be used. PMPPIC is chemically linked to the cellulose matrix through strong covalent bonds (65). Both PMPPIC and PS contain benzene rings and their delocalized π electrons provide strong interactions, so that there is an adhesion between PMPPIC and PS. Equivalent results are obtained when PMPPIC is used for the modification of the fibers or the polymer matrix.

Mishra (66) carried out cyanoethylation of natural fibers to modify the surface. The presence of different functional groups such as —OH, —COOH, >CO, —CN (in cyanoethylated fiber), and aromatic moieties is indicated by the FTIR spectra of the chemically modified fibers.

Sisal fibers were treated with a urethane derivative of toluene diisocyanate/poly(propylene glycol) (TDI/PPG) and PMPPIC by Joseph et al. (67) with the objective of improving the dynamic mechanical properties of sisal/PP composites. The better performance is due to the formation of a urethane linkage between the —OH group of the fiber and the —NCO group of PMPPIC or TDI/PPG, as shown in Fig. 3.8.

In an interesting study, Karmarkar et al. (68) used a novel compatibilizer (*m*-TMI-g-PP) with an isocyanate functional group. This was synthesized by grafting *m*-isopropenyl-a,a-dimethylbenzyl isocyanate (*m*-TMI) onto isotactic polypropylene in a twin-screw extruder. The proposed mechanism of interaction of *m*-TMI-g-PP on wood fiber is shown in Fig. 3.9.

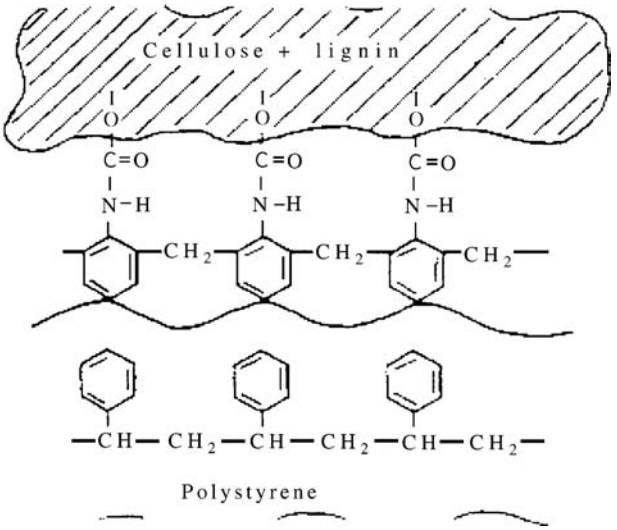

Figure 3.8 Hypothetical chemical structure of the PMPPIC–PS interface area. (From Reference 67 with permission from Elsevier Ltd.)

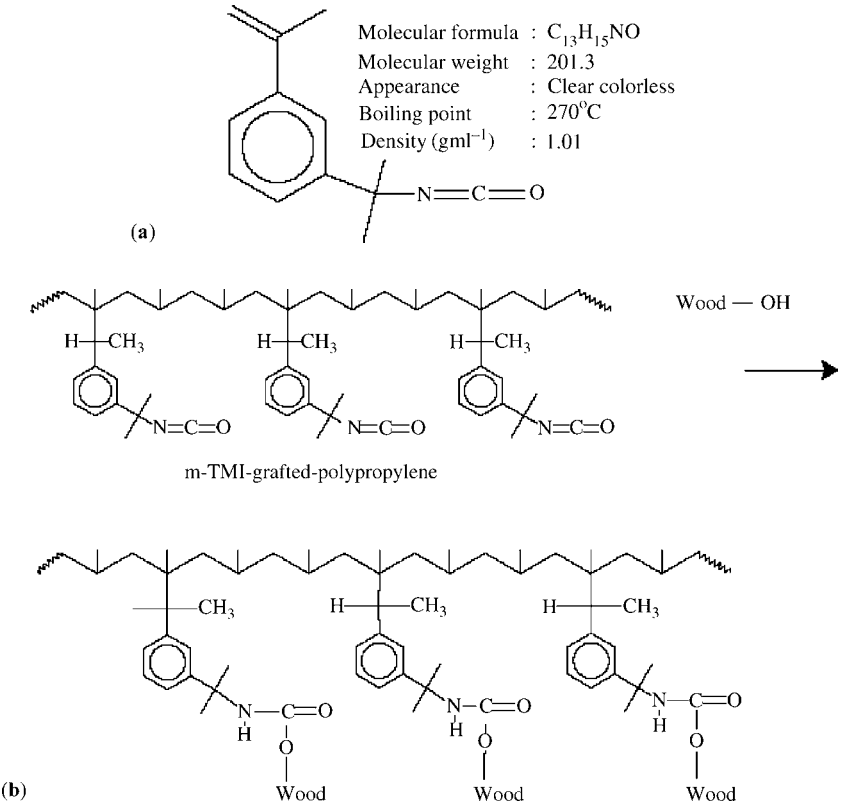

Figure 3.9 (**a**) Structure and physical properties of *m*-TMI. (From Reference 68 with permission from Elsevier Ltd.) (**b**) Proposed mechanism of interaction of *m*-TMI-g-PP on wood fiber. (From Reference 68 with permission from Elsevier Ltd.)

The effect of filler concentration on the mechanical properties of wood fiber filled composites, prepared by using *m*-TMI-g-PP as the compatibilizer, was investigated. The addition of the compatibilizer resulted in greater reinforcement of the composites, as indicated by the improvement in mechanical properties. The tensile strength of the composites so prepared increased by almost 45%, whereas an 85% increase in flexural properties was observed.

Siloxane Formation Silanes that have been proved effective coupling agents in the case of glass fibers have been found to be also effective in the case of natural fibers. This family of grafting agents was tested on different lignocellulosic substrates, under different conditions. In the presence of moisture, coupling takes place with the silanol, which indicates that the chemical modification of cellulose fibers by siloxanes must be mediated by their preliminary (partial) hydrolysis. Even then it will only occur to a measurable extent if the temperature is raised.

Different authors have reported on the effect and mechanism of silane treatment. The general mechanism that has been suggested is shown in Fig. 3.10 (69).

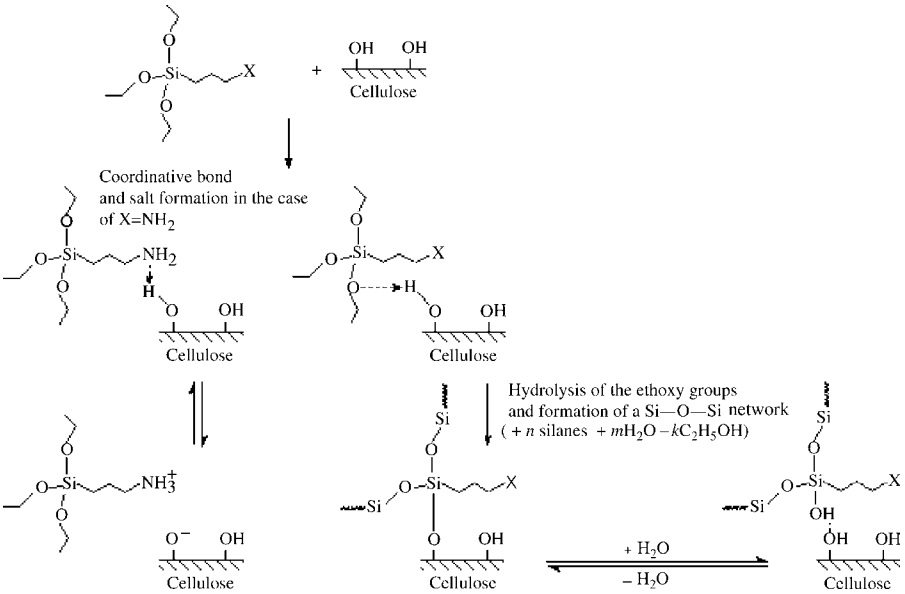

Figure 3.10 Scheme of interaction of silane with cellulose. (From Reference 69 with permission from ACS.)

The reaction of the hydrolyzed compounds with cellulose was shown by FTIR spectroscopy to occur, as proved by the bands at 1134 and 1038 cm^{-1} associated with Si—O—C. Other typical bands, characteristic of a siloxane, were detected at 1712 and 1637 cm^{-1} attributed to C=O and C=C, respectively (70).

Singh et al. (71) carried out FTIR spectroscopic studies of various coupling agent treated sisal fibers. The coupling agents used were γ-methacryloxypropyltrimethoxysilane (A-174), neopentyl(diallyl)oxytri(dioctyl)pyrophosphato titanate (LICA-38), neopentyl(diallyl)oxytriacryl zirconate (NZ-39), and *N*-substituted methacrylamide (QB-012). The presence of precipitated oligomers on the surface was confirmed by the appearance of hydrogen-bonded carbonyl group and unsaturation bands. The results showed an irregular physisorption/chemisorption of coupling agents, their penetration beyond the surface, and a decrease in the hydrophilicity of fibers. SEM and dynamic contact angle studies on the fibers supported these findings. FTIR microscopy in its reflectance mode was more effective in ascertaining the chemical nature and structure of adsorbed layers onto sisal fiber surfaces compared with DRIFT and transmission spectroscopy. The difference in the properties of untreated and chemically treated fibers has also been verified in the polymer composites.

The effect of various silane coupling agents on short natural fiber reinforced polyethylene and natural rubber composites was reported by Abdelmouleh et al. (72). Low density polyethylene (LDPE) and natural rubber were used as matrices. Cellulose fibers were treated with three different silanes. The mechanical properties were

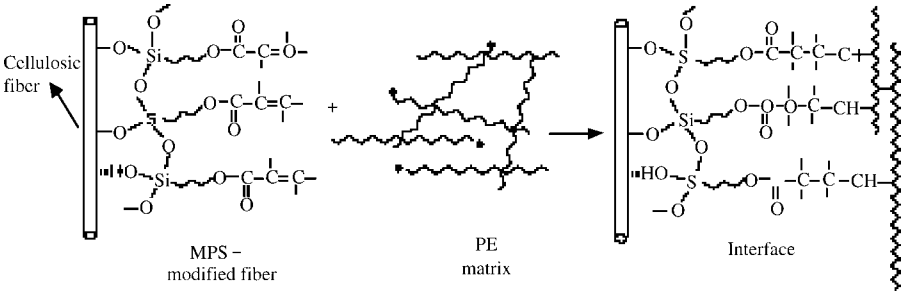

Figure 3.11 Schematic illustration of the interfacial zone in LDPE-based composites containing MPS-modified cellulose fibers (the relative sizes of the fibers and of the chemical species are not on scale.) (From Reference 72 with permission from Elsevier Ltd.)

found to increase with increasing fiber length and with chemical modification. The authors explained the improvement in properties as follows: Both methacryloxypropyltrimethoxysilane (MPS) and mercaptopropyltrimethoxysilane (MRPS) contain functional groups that can react with radical species to generate a covalent bond, either by an addition reaction with the π bond (for MPS) or through a transfer reaction with the mercapto moiety. The radical species may be generated through peroxide decomposition, which arises from the thermal oxidation likely to occur during the processing of the composite. The resulting reaction gives rise to chemical bonding between the fibers and the matrix, which enhances interfacial adhesion. Possible reactions between MPS grafts and the LDPE matrix, where the radical species result from thermal degradation during the mixing and compression processes, are shown in Fig. 3.11.

3.3.3.3 Graft Copolymerization

Graft copolymerization of monomers is one of the universal, effective, and accessible methods of chemical modification of high molecular weight compounds, particularly natural polymers (73). The studies on the effect of grafting on the performance of composites are a challenging field of research, which is yet to be established by research workers. Graft copolymerization of acrylonitrile (AN) onto chemically modified PALF has been studied by Mohanty et al. (74) using a Ce(IV) and *N*-acetylglycine (NAG) combination as initiator in the temperature range 40–60°C. Tripathy et al. (75) studied the Cu(II)-IO_4-initiated graft copolymerization of MMA from defatted PALF. Effects of variation of time and temperature, concentration of Cu(II), KIO_4, and MMA, the amount of PALF, and also the effects of some inorganic salts and organic solvents on the percentage of graft yield have been investigated. On the basis of these experimental findings, a reaction mechanism (Fig. 3.12) has been proposed. It has been shown that grafting improved the thermal stability of PALF. Samal and Bhuyan (76) studied the graft copolymerization of AN and MMA onto PALF, using a ceric ion as an initiator at varying concentrations of monomer, initiator, and mineral acid at a number of temperatures for various time intervals.

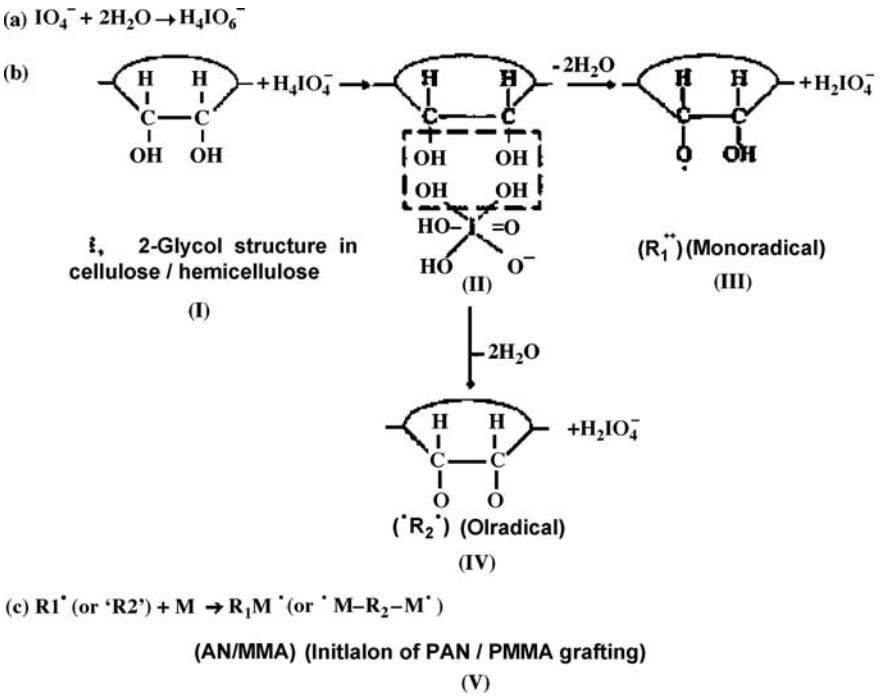

Figure 3.12 Reaction mechanism of grafting. (From Reference 77 with permission from John Wiley Sons, Inc.)

Graft copolymerization of AN onto chemically modified sisal fiber has been carried out by Mishra (77) with a view to improving the surface, as well as the bulk mechanical properties, for its potential use as a reinforcing fiber for polymer composites. It has been concluded that there is an optimum concentration of the fiber and the grafting agent, which will produce the best results. The best water absorption and tensile properties are obtained with a low percentage (5%) of fiber grafting. The AN-grafted sisal fibers are expected to act as compatible reinforcing fibers with several hydrophobic resin systems, including thermoplastics and thermosets, for the preparation of high performance composites.

Initiation by free radicals is one of the most common methods used for the grafting of vinylic monomers onto cellulose (78). These free radicals are produced as a result of a reaction of the cellulosic chain in a redox system. In this reaction, oxidation of the anhydroglucose units occurs along the cellulosic chains and macrocellulosic radicals are generated on the surface of the fiber. These reactions modify the properties of the fiber, and one of the roles of the cellulose fibers in composites is to give stiffness and strength to the polymeric matrix. It has been shown that cyanoethylation followed by grafting with AN and MMA brings about a significant reduction in the moisture regain (enhanced hydrophobicity) of PALF. The dye uptake ability of PALF is progressive with the time of cyanoethylation. Wood dust or strips

from *Pinus sylvestris* were grafted with propionic, crotonic, and methacrylic anhydrides, using pyridine as reaction medium and a catalyst at 60°C, with reaction times of 2, 4, and 6 h (79).

3.4 POLYOLEFIN COMPOSITES

3.4.1 Processing of Polyolefin/Natural Fiber Composites

Natural fiber–thermoplastic composites are normally processed through melt or solution mixing, extrusion, compression molding, and/or injection molding. In melt mixing, the fiber is added to a melt of thermoplastics and mixing is performed using a mixer at a specified temperature and speed for a specified time. The mix is then taken out from the mixer while hot and molded using a hand-operated injection molding machine into long and thick rods. In the solution mixing method, the fibers are added to a viscous solution of the thermoplastic in a solvent in a stainless steel beaker with a stainless steel stirrer. The temperature is maintained for some time and the mix transferred to a flat tray and kept in a vacuum oven to remove the solvent. The solution mixing procedure avoids fiber damage that normally occurs during blending of fiber and thermoplastic by melt mixing (80). Joseph et al. (81) used a solution mixing method, followed by injection or compression molding, to prepare their LDPE–short sisal fiber composites. Short fibers were added to a viscous slurry of LDPE and toluene, after which the toluene was evaporated and the samples injection or compression molded. Several papers on polyolefin–natural fiber composites describe this composite processing method (82,91). Several polyolefin–natural fiber composites were investigated, where the composites were prepared through melt mixing of the polymer with short fibers (35,89,92–97).

Bledzki and Gassan (98) summarized previous work done on the processing of wood–thermoplastic composites. According to them, the main problem in processing wood–thermoplastic composites is the tendency of untreated wood to form large aggregates, due to a high intermolecular bonding among fibers. Therefore, the dispersion of the fibers in the polymer matrix is small and the reinforcing ability of the fiber is reduced to a remarkable extent. The better the advance dispersion of the fibers in the polymer matrix, the better its uniformity. The mixing time can then be shortened, leading to a reduction in fiber breakage (by shearing) during the mechanical mixing process (99–104). The dispersion of wood fibers can be improved by pretreatment with lubricants or thermoplastic polymers. Impregnation or encapsulation of wood particles with chemicals, compatible with the polymer matrix (105,106), produces an insulating film of hydrophobic polymer on the surface, thus preventing agglomerization and in some cases improving the thermoplasticity of wood.

Another problem is that the rate of thermal decomposition of lignocellulosics increases exponentially with an increase in temperature. At normal processing temperatures (180–200°C), critical values of decomposition are realized (104). Decomposition of the pulp components creates voids inside the composite, causing

a decrease in mechanical properties. Optimization of processing temperature and time is therefore necessary. The suggested mixing and molding temperature for wood–HDPE is 170°C (107).

Bledzki and Gassan (98) also refer to an ''express'' process. The extrusion press processing (express processing) was developed for the production of flax fiber reinforced PP at the research center of Daimler Benz, Ulm, Germany (108). In this process natural fiber nonwovens and thermoplastic melt films are alternatively deposited and molded in a tempered mold. The thermoplastic melt films are laid on by a mobile extruder. If this process is optimally adapted to the element, a single passage by the extruder suffices. The structural order consists of three layers: two layers of nonwovens at the bottom and one on the top, with the melt film in between. Singleton et al. (109) also used a film stacking and compression molding method to prepare recycled HDPE–flax fiber composites. Torres and Cubillas (110) prepared long sisal fiber polyethylene composites through compression molding.

3.4.2 Mechanical Properties of Polyolefin/Natural Fiber Composites

Natural fibers are generally incompatible with polyolefins, because of their hydrophilic character compared to the hydrophobic character of polyolefins. Most of the previous studies were therefore aimed at investigating the influence of different fiber treatments on the mechanical properties of the composites. In these studies it was mostly the fibers that were treated before composite processing (81–91,96,97), but in certain studies where peroxide treatment was used, the peroxide was added to the molten polymer–fiber mixture (94,95). In the case of LDPE–sisal composites the treated fibers gave rise to improved tensile strength and modulus, while the elongation at break decreased (81). Alkali-treated fiber composites showed better tensile properties than untreated composites due to their rough surface topography and increased aspect ratio. These property improvements were, however, marginal. For example, the presence of 30% sisal fiber (5.8 mm length) in LDPE gave tensile strength values of 34.3 MPa for alkali-treated fiber composites and 31.1 MPa for untreated fiber composites, compared to 9.2 MPa for pure LDPE. It is observed that there is an enhancement in tensile strength and Young's modulus with increasing concentration of sodium hydroxide (82). The maximum tensile strength and modulus can be observed at 5% NaOH. This may be due to the increase in surface roughness of the sisal fiber as a result of leaching out of alkali-soluble components such as lignin, wax, and fatty acids. On further increase of concentration there is a reduction in tensile properties, due to the extensive leaching out of lignin, which forms the backbone of sisal fiber.

The following fiber treatments gave rise to tensile strengths of around 40 MPa. Isocyanate-treated LDPE composites exhibited superior mechanical properties, probably because of the —N=C—O functional group that is highly reactive to the —OH groups of cellulose and lignin. This gives rise to the development of a urethane linkage. The cardanol derivative of toluene diisocyanate (CTDIC) was especially

effective, which may be due to the fact that the long-chain structure of CTDIC linked to the cellulose fibers makes the fiber hydrophobic, compatible, and highly dispersible in the PE matrix. Peroxide-treated composites showed an enhancement in tensile properties due to peroxide-induced grafting. The proposed grafting mechanism looks as follows:

$$\mathrm{RO{-}OR} \rightarrow 2\mathrm{RO}^{\bullet}$$
$$\mathrm{RO}^{\bullet} + \mathrm{PE{-}H} \rightarrow \mathrm{ROH} + \mathrm{PE}^{\bullet}$$
$$\mathrm{RO}^{\bullet} + \mathrm{cellulose{-}H} \rightarrow \mathrm{ROH} + \mathrm{cellulose}^{\bullet}$$
$$\mathrm{PE}^{\bullet} + \mathrm{cellulose}^{\bullet} \rightarrow \mathrm{PE{-}cellulose}$$

Although this mechanism had been assumed for a number of years, it is only recently that grafting between the polymer matrix and the cellulose in sisal fiber has been proved beyond any doubt.

Malunka et al. (95) showed through gel content determination, porosimetry measurements, SEM, surface free energy, and FTIR microscopy that grafting between the ethylene–vinyl acetate copolymer (EVA) chains and sisal fibers does take place. Gel content determinations showed that in the presence of dicumyl peroxide (DCP) there was a substantial increase in gel content with increasing fiber content, despite the fact that in the absence of fiber the polymer showed almost no cross-linking under the same conditions. Hg porosimetry showed the following substantial decrease in the volumes of all pore sizes: sisal fiber > EVA–fiber composite > DCP-treated EVA–fiber composite. This indicates a very strong EVA–sisal interaction. The FTIR microscopy results showed a decrease in the peak sizes of the −C=O and −OH peaks at the EVA–sisal interfaces, while SEM clearly showed fiber delamination at the fractured surfaces of DCP-treated EVA–sisal composites (84,94).

In an investigation of linear low density polyethylene (LLDPE)–sisal composites (94), where DCP was added to the LLDPE–short sisal fiber mixture during melt mixing, composites prepared in the presence of DCP showed higher tensile strength values for a given PE–sisal composition. This was also attributed to DCP-induced PE–sisal grafting. The composites with 3% DCP showed lower tensile strength values than those with 1%, for one specific sisal concentration. Melt pressing of the sheets in the presence of higher DCP concentrations induced besides cross-linking, significant degradation of the matrix, which consequently reduces tensile strength. The combined effects of cross-linking and grafting lead to an increase in the elongation at break. At low sisal content levels, when the effects of cross-linking are more pronounced, elongation at break was significantly higher than that in the pure composite. Further increase in sisal content reduced elongation at break, but still the values were higher than those of the untreated material. Introduction of the higher modulus sisal fibers into the PE matrix enhanced the modulus of the resultant material. Up to 30% of fiber, the tensile modulus of samples treated with 1% of DCP was close to that of the untreated composite. At higher sisal loadings (>30%) the modulus of the untreated samples started to decrease, probably as a result of poor wetting of the fibers by the matrix. The

samples melt pressed with 3% DCP also showed lower elastic modulus values than the pure samples and the samples with 1% DCP. Reducing the crystal fraction, induced by high DCP concentration, could be responsible for the lower moduli of these samples, especially at low fiber contents.

In the beginning of (up to 100 s) stress relaxation measurements on LLDPE–sisal composites (94), stress decay was fast but gradually slowed down with time. The initial stresses also followed the changes in the elastic modulus with an increase in sisal content. Stress relaxation in a semicrystalline polymer, such a polyethylene, can be well explained in terms of a two-process model. This model treats the stress relaxation in semicrystalline polymers as a superposition of two thermally activated processes, each connected to one phase of the material, crystal or amorphous. It is assumed that in the beginning of stress relaxation, taut tie chains, which actually carry the applied load, are pulled out from the crystal lamellae because they impose large local stresses. Taut tie molecules are, in fact, defects in the crystal structure at the point where they enter lamellae, and the stress concentration in these points is very high. Stress concentration induces propagation through the lamellae, so-called *c*-axis slip. As a consequence of this crystal process, the average distance between the lamellae increases until stretching of formerly loose tie molecules takes place. Since the applied stress is now redistributed over a large number of tie chains, their propagation will be partially reduced and relaxation will start to slow down. This can explain the presence of fast and slow relaxation processes in this system. In principle, the above approach can also be applied to polymer composites if one treats the fibers as ''crystals'' embedded in an amorphous matrix. However, instead of a crystal process or *c*-axis slip, a matrix fiber debonding process should be considered. It is possible that sisal fibers in the polyethylene matrix act like a shield, which prevents to some extent defects propagating through the lamellae. As long as the interaction between the fibers and the polyethylene chains is good, it will stabilize the stress decay and the stress will also increase. At higher sisal loadings (40% and 50%), poor wetting of fibers by the matrix enables easier conformational rearrangements of PE chains during stress relaxation. As a result, the stress decay will be more pronounced. The composites with DCP showed similar relaxation behavior as the untreated ones. The composites, melt pressed in the presence of 1% DCP, showed higher values of normalized stress than the untreated composites, because of the strong interaction between the phases. Stress relaxation also depends on the viscosity coefficient of the material, which depends on chain mobility. After fiber–matrix debonding, the mobility of chains increases, which reduces the viscosity and leads to a more intense cold flow. Debonding effects will obviously be reduced after grafting between sisal fibers and PE chains during melt pressing with 1% DCP, which will improve the stability of the material on loading.

Permanganate-treated composites showed a similar trend due to permanganate-induced grafting (81). Among the various types of treatments, CTDIC and DCP treatment showed the best properties. Tensile properties are also improved through acetylation of sisal fibers, where the presence of $-CH_3$ groups in acetylated sisal fiber contributes to better interaction with polyethylene, and through stearic acid treatment, where there is an enhancement in tensile strength and

modulus with increasing stearic acid concentration, with the maximum tensile strength at 4% concentration (82). Maleic anhydride treatment of PE also improves the tensile properties of PE–sisal composites, due to the dipolar interactions between anhydride groups and cellulosic —OH groups. Silane treatment of sisal fibers also strongly improves the tensile properties of the composites, because the vinyl groups present in the silane undergo polymerization in the presence of DCP and form a long hydrophobic polymeric chain on the fiber surface that interacts with the polyethylene matrix through van der Waals type of bonding. Thus, silanes form a bridge at the interface of sisal and polyethylene and act like a compatibilizer, which binds two incompatible polymers. Generally, it was found that the efficiency of the different treatments varies in the following order: alkali < acetylation < stearic acid < $KMnO_4$ < maleic anhydride polymer treatment < silane < dicumyl peroxide < dibenzoyl peroxide.

The effect of fiber length also plays an important role in determining the tensile properties of polyolefin–natural fiber composites (82,84). In short fiber reinforced polymer composites, the applied load is transmitted from the matrix to the fiber through a shearing action at the fiber–matrix interface. Consequently, the tensile strength of these composites is greatly influenced by the interfacial shear strength (IFSS). This interfacial shear strength in turn depends on the critical fiber length or critical aspect ratio of the fiber, which is given by the following equation:

$$L_c = \frac{\sigma_f r}{2\tau} \tag{3.1}$$

where σ_f is the fracture strength of the fiber, r is the radius, τ is the shear strength, and L_c is the critical length of the fiber. In the case of a short fiber reinforced composite, there exists a critical aspect ratio for the fiber at which the mechanical properties of the composite are maximized. But there are some conditions for a fiber to exhibit a critical aspect ratio in the composite. They are as follows: (i) the shape of the fiber should be cylindrical; (ii) all fibers should be perfectly aligned in the load (longitudinal) direction; and (iii) fiber-to-fiber contact should be absent in the composite. It has been observed that, in the case of LDPE–sisal composites, tensile strength increases with increasing fiber length and reaches a maximum at 6–8 mm fiber length. With further increase in fiber length, the tensile strength decreases. As the length of sisal fiber increases, the chance of its curling increases. The curly nature of fibers prevents the proper alignment of fibers in the longitudinal direction.

The reinforcement effects of natural fiber depend largely on matrix ductility, that is, the resistance to crack propagation. Thus, in order to obtain a maximum reinforcement effect, it is necessary to use matrices with a high ductility. However, most of the commercial plastics do not have high ductility and when filled with 40–50% fiber, they become brittle and lose strength considerably. Polyethylene has higher ductility than thermoset matrices and thereby offers a better reinforcement effect. In addition to this, the fiber-to-matrix strength/modulus ratio of an LDPE–sisal system is much higher than those of the thermoset–sisal systems. Therefore, superior reinforcing effects can be obtained by incorporating sisal fiber in a polyethylene matrix (84).

When comparing the tensile properties of short sisal fiber–reinforced LDPE composites with those predicted by theoretical composite models such as the parallel and series, Hirsch, Cox, Halpin–Tsai, modified Halpin–Tsai, and modified Bowyer and Bader models, it was found that the Hirsch (Eqs. 3.2 and 3.3), and modified Bowyer and Bader (Eqs. 3.4 and 3.5) models best fit the experimental results for longitudinal and randomly oriented fibers (85).

$$M_c = x(M_m V_m + M_f V_f) + (1 - x)\left(\frac{M_f M_m}{(M_m V_f + M_f V_m)}\right) \tag{3.2}$$

$$T_c = x(T_m V_m + T_f V_f) + (1 - x)\left(\frac{T_f T_m}{(T_m V_f + T_f V_m)}\right) \tag{3.3}$$

$$T_c = T_f K_1 K_2 V_f + T_m V_m \tag{3.4}$$

$$M_c = M_f K_1 K_2 V_f + M_m V_m \tag{3.5}$$

with M the modulus, T the tensile strength, V the particle volume fraction, K_1 the fiber orientation factor, and K_2 the fiber length factor. The subscripts f and m denote fiber and matrix, respectively.

In an investigation of aging on the physical and mechanical properties of untreated and treated LDPE–sisal composites (90) it was found that the surface of the CTDIC-treated sisal fiber is irregular or rough. This leads to strong physical interaction between the fiber and the matrix. Therefore, treated natural fibers are likely to offer greater resistance to pullout from the matrix than man-made fibers and this results in superior mechanical properties. However, the untreated sisal fiber composites show inferior properties. The tensile strength values of both untreated and CTDIC-treated sisal–LDPE composites decrease steadily with exposure time in boiling water. The decrease in modulus with exposure time observed in sisal–LDPE composites is associated with water absorption. This has been explained as being due to the softening of the desorbed zones of the cellulose microfibrils. After an exposure of 7 h in boiling water, the modulus values of CTDIC-treated sisal fiber filled LDPE composites increase with fiber loading, whereas untreated sisal fiber filled LDPE composites showed a decreasing tendency. This is because of the variation in the hydrophilic nature of the fibers. The decrease is sharper in the case of untreated composites. This can be attributed to the fact that the rate of diffusion of water into the composite is time and temperature dependent. The decreases in properties are marginal in the case of CTDIC-treated composites, because the CTDIC treatment reduces water absorption. In the case of CTDIC-treated sisal fibers, the functional group —N=C=O reacts with the cellulose —OH group and thereby the hydrophilic nature of the cellulose fiber is reduced. After exposure for 7 h in boiling water, the tensile strength of untreated sisal–LDPE composites is unaffected by fiber loading. At all levels of fiber loading the tensile strength is almost the same. However, the CTDIC-treated composites showed a different trend; that is, tensile strength increases with fiber loading. When the fiber–matrix composites are accessible to moisture from the environment, wood fibers tend to swell. This results in the development of shear stress at the interface, which leads to the ultimate debonding of fibers.

Although composites of cellulose are supposed to remain stable up to 160°C, the degradation reaction may initiate slowly for prolonged heating at 80°C. The decomposition of fiber will develop voids at the interface and this leads to poor fiber–matrix adhesion. The modulus increases steadily with fiber loading. Since the modulus of the matrix is constant, the relative packing efficiencies of the fiber and the fiber–matrix adhesion are the important factors in determining the modulus of the composite. At higher fiber loading (>20%), the CTDIC-treated composites exhibit the maximum modulus values. As expected, the untreated composites show the lowest modulus values. In all cases, elongation at break decreases with an increase in fiber loading due to the lower elongation at break values of the fiber. Moreover, the addition of brittle fiber makes the matrix more rigid by decreasing the flexibility of the polymer chains.

Use of MAPP as coupling agent improved mechanical properties of composites by enhancing the adhesion between flax fiber bundles and PP (92). Besides, fiber bundle surface treatment with MAPP or matrix modification with MAPP had similar effects on the mechanical properties of composites. Both acid number and molecular weight of MAPP are important parameters in order to determine its effectiveness. Results suggest that there is a critical amount of compatibilizer, dependent upon its constitution and molecular weight, at which the strongest interactions between lignocelluloses fibers and a PP matrix occur. Stiffness of unmodified and MAPP-modified composites increases with increasing fiber bundle content, with the modulus values for the MAPP-modified composite slightly higher. However, the strength of the unmodified flax fiber–PP composites decreases with flax fiber bundle content, as a consequence of poor interfacial adhesion, while for MAPP-modified composites the opposite trend is observed. After passing MAPP-modified flax fiber–PP composites several times through an injection molding machine, the mechanical properties only slightly changed. So the mechanical recycling of flax fiber–PP composites is one feasible option to reuse this type of material.

A flax–HDPE (10% fiber by volume) composite shows a lower strain to failure, about 5% compared to 20% or more for recycled HDPE (109). While there a modest increase only in yield stress and tensile strength, the tensile modulus increases from 1.8 to 8 GPa. As fiber content increases so does yield stress, tensile modulus, and tensile strength, the latter by as much as 25%. In a corresponding manner, but in opposing fashion, the ductility falls with increasing fiber reinforcement. This effect is related to the clumping of flax fibers and inadequate impregnation of the fiber bundle by the polymer during the molding process. These experimental results agree well with theoretical predictions based on a simple rule of mixture and a 3/8 fiber orientation correction factor for in-plane random fiber orientations. Using a fiber modulus of 60 GPa and a matrix modulus of 1.2 GPa, the composite stiffness for random flax fiber composites with different fiber volume fractions can be predicted. Theoretical values predicted using such a first approximation are 2.7, 4.9, and 7.1 GPa for fiber volume fractions of 10%, 20%, and 30% respectively, which agree well with experimental observations. A significant increase in toughness of the composites by 50 kJ m^{-2} over that of recycled HDPE indicates that the flax fiber plays an important role in the toughening processes.

Studies on the interfacial shear strength of PE–sisal composites show that there is an important variation in fiber diameter among sisal fibers of the same batch (110). The high variation in tensile strength among sisal fibers is clearly an important source of error in the calculation of the interfacial shear strength. Sisal fibers, like many other natural fibers, differ not only geometrically but also morphologically, depending on how the individual fibrils are organized in the fiber. This certainly affects tensile strength in this type of fiber. Fiber pretreatment with stearic acid improves the interfacial shear strength by 23% with respect to untreated fibers. These results need to be treated carefully, partly due to the fact that adhesion is variable along the fiber–matrix interface. Reduced fiber pullout indicates higher interfacial shear strength for the treated specimens.

In the case of PP–wood fiber composites the tensile strength decreases after adding 10 mass% of wood fibers, but then gradually increases with the addition of wood fibers until 30 mass% is reached, whereas the tensile modulus increases monotonically up to its maximum value at 30 mass% of wood fibers (35). It is hypothesized that up to 20 mass% of wood fibers there is a sufficient concentration of wood fibers to form a network with significant mechanical interlocking. Beyond 30% there are more wood fibers; however, the quantity of matrix encapsulating and holding the wood fiber network in place decreases below the optimal level. Tensile strengths increase by about 20% for air plasma and 12% for Ar plasma treatments. Additionally, the tensile strengths of both plasma-treated wood fiber composites are consistently higher than that of the pure polypropylene, whereas without any treatment the average tensile strength of the composite actually decreases. For tensile modulus, the improvements after adding wood fibers (treated, untreated) are even more significant. For untreated fibers it is 78% larger than that for pure PP, whereas Ar plasma and air plasma treatments give 100% and 128% larger values of tensile moduli, respectively (35).

The strength of silane-modified PP–wood pulp composites is not changed appreciably, while treatment with PMPPIC leads to increased strength (111–114). Shear and tensile strengths increase by about 100% and 25%, respectively, for flax–polypropylene composites, when a MAH-PP coupling agent is applied to the flax fiber before the composite is processed. These values depend on the grafting rate and on the average molar mass of the graft copolymer, as well as on application parameters. Similarly, increased values can be obtained with a polypropylene matrix material modified with MAH. The acidic anhydride groups of the MAH coupling agent lead to hydrogen and chemical bonds with the hydroxyl groups of the flax fiber, anchored strongly by the coupling agent onto the fiber surface. The long polypropylene chains of the MAH-PP coupling agent lead to an adaptation of the very different surface energies of matrix and reinforcement fiber, which allows a good wetting of the fiber by the viscous polymer and increases adhesion strength by an increased work of adhesion.

MAPP treatment also improves wetting of filter paper, wheat straw, and jute fibers (115,116), resulting in better fiber–PP matrix adhesion compared to those of unmodified fiber–matrix systems. An increase in the composite strength with increasing cellulose content is achieved by the covalent bond due to the addition

of a coupling agent. The chemical bonding between the anhydride and the hydroxyl groups causes a better stress transfer from the matrix into the fibers, leading to a higher tensile strength. For PP–jute composites improved fiber–matrix adhesion due to a coupling agent such as MAPP leads to a distinctly higher dynamic strength, that is, stress at fracture measured in a load increasing test, than for the composites with untreated jute fiber (115). Progress of damage for unmodified PP–jute composites is nearly independent of the fiber content, which results in independent maximum stresses, due to the improved fiber–matrix adhesion, caused by the MAH-PP coupling agent and thereby improved force transfer. In contrast to untreated PP–jute composites, a 40% increase of dynamic strength, at comparable fiber contents, is attained through the use of the coupling agent. Impact investigations of PP–jute composites show that the damaging initiations can be shifted to higher forces with a strong fiber–matrix adhesion, as composites with a weak fiber–matrix adhesion at smaller forces break down at a load perpendicular to the fiber. When the composites have no coupling agent, a part of the impact energy is degraded in the fiber–matrix interface, for example, by debonding and friction effects.

3.4.3 Dynamic Mechanical Properties of Polyolefin/Natural Fiber Composites

Dynamic mechanical properties of short sisal fiber reinforced PP composites are influenced by fiber loading, fiber length, chemical treatment, frequency, and temperature (96). The presence of sisal fiber in pure PP increases the storage modulus E' from 2.54×10^8 Pa for pure PP to 3.13×10^8 Pa for composites containing 20% fiber. This is due to the reinforcement imparted by the fiber that allows stress transfer from the matrix to the fiber. Loss modulus E'' also increases with increasing fiber loading. An optimum fiber length of 2 mm gave a maximum dynamic modulus and loss modulus. E' and E'' of chemically treated composites are higher than those of the untreated composites due to improved fiber–matrix interfacial adhesion. For composites containing 20% fiber, E' is 3.88×10^8 Pa for maleic anhydride and $KMnO_4$ treated composites. Both storage modulus and loss modulus decrease with increasing temperature, which is associated with softening of the matrix at higher temperature. The glass transition temperatures and dynamic moduli increase with increasing frequency due to reduced segmental mobility.

The storage and loss moduli of wood fiber–PP composites are higher than those of pure polypropylene in the entire temperature rage (−60 to 160°C), especially at higher temperatures (35). This is due to the higher wood fiber stiffness relative to the PP, but transcrystallinity and fiber orientation may also influence the stiffness. Plasma treatment has a more pronounced effect on composites. The storage moduli of plasma-treated wood fiber composites are higher than those for untreated fiber composites. Air plasma treatment shows greater improvement than Ar plasma treatment. There is no significant change in T_g shown from storage and loss moduli.

3.4.4 Rheological Properties of Polyolefin/Natural Fiber Composites

Chemical treatment of fiber increases the viscosity of sisal/glass LDPE hybrid composites because of the increased fiber–matrix interaction. The viscosity values decrease with increasing temperature, except for peroxide-treated composites where there is an increase because of grafting of fiber to the LDPE matrix and cross-linking of the matrix chains (83). In the case of LDPE–short pineapple leaf fiber composites (86), the viscosity of the system increases with the fiber loading. The increase in viscosity is more predominant at a lower shear rate than at higher shear rates. The fiber-filled systems exhibit higher viscosity than the pure polymer at all shear rates. In the filled system, fibers will perturb the normal flow of polymer and hinder the mobility of chain segments in flow. At low shear rate, fibers are disoriented. The probability of fiber–fiber collision is much higher for misaligned fibers. This collision increases with fiber loading and as a result viscosity increases. But as the shear rate increases, most of the shearing of fibers takes place closer to the tube wall and the fibers will align strongly along the tube axis. Therefore, the probability of fiber–fiber collision is much lower and so the increase in viscosity with the fiber content is less at high shear rates. Viscosity marginally increases upon the increase of fiber length from 2 to 10 mm. At higher fiber length, the dispersion of fibers is not so good and at the same time it is difficult to orient in the direction of flow. This is associated with the fiber entanglement at higher fiber loading. Fibers having shorter length are more easily aligned and distributed along the direction of flow than longer fibers. The viscosity of the composite increases after DCP-initiated silane treatment as a result of improved interfacial adhesion, as well as after peroxide and NaOH treatments, as a result of, respectively, fiber–matrix grafting and mechanical interlocking effects.

3.4.5 Thermoanalytical Properties of Polyolefin/Natural Fiber Composites

The lower thermal stability of up to 230°C for natural fibers limits the number of thermoplastics to be considered as matrix material for natural fiber thermoplastic composites. Only those thermoplastics are usable for natural fiber reinforced composites, whose processing temperature does not exceed 230°C. These are, most of all, polyolefins. Technical thermoplastics, like polyamides, polyesters, and polycarbonates, require processing temperatures >250°C and are therefore not usable for such composite processing without fiber degradation (117).

Thermogravimetric analysis of PP–sisal composites shows that sisal fiber degrades before the PP matrix (97). In the case of sisal fiber, most of the cellulose decomposes at a temperature of 350°C, whereas PP decomposes at a temperature of 398°C. The thermal stabilities of the PP–sisal composites are higher than those of the PP and fiber individually. DSC analyses show that the incorporation of sisal fiber in PP causes an apparent increase in crystallization temperature and

percentage crystallinity. The morphology of the PP matrix is changed by the addition of fiber. When PP melt is allowed to cool in contact with sisal fiber, which is a source of nucleating centers, the proximity of these sites on the surface inhibits lateral growth of the resultant spherulites; thus, the crystallization develops only in one direction, and only to the fiber surface. The development of such a layer has been termed ''transcrystallization.'' The crystal growth changes from the radial direction of spherulites to the direction normal to the fiber surface when nucleation occurs with a sufficiently high density along the fiber surface, that is, transcrystalline growth.

In an investigation of LLDPE–sisal composites (94), where DCP was added to the LLDPE–short sisal fiber mixture during melt mixing, the melting temperatures of untreated composites increased with the amount of sisal fiber, while samples with 3% of DCP showed the opposite behavior. The presence of the sisal fibers in the untreated composite obviously favors lamellar thickening, probably as a result of reduced mobility of the PE chains. Regardless of the amount of sisal in the composite, introduction of DCP led to a decrease in the melting temperature due to cross-linking of the matrix as well as grafting of PE chains onto the fibers.

3.4.6 Electrical Properties of Polyolefin/Natural Fiber Composites

In the investigation of the electrical properties of treated and untreated LDPE–sisal composites, it was found that the untreated composites show higher dielectric constants at all frequencies than pure LDPE or its treated composites (87). In the case of NaOH-treated fibers, this is probably the result of a decrease in polarity of the fibers. In the case of acetylation and CTDIC treatment the hydrophilic nature of the fiber decreases, giving rise to a decrease in the orientation polarization due to the presence of water molecules. The stearic acid treated cellulose fiber has a hydrophobic chain of stearic acid molecules, which imparts water resistance to the composites. Owing to the decrease of polar water molecules as a result of stearic acid treatment, the orientation polarization decreases and the dielectric constant values correspondingly decrease. As a result of peroxide treatment, the hydrophilicity of the fibers decreases, giving rise to a decrease in polar water molecules and orientation polarization in the fiber, and hence the dielectric constant also decreases.

The dielectric constant for 1% permanganate-treated sisal fiber–LDPE composites is higher than that for composites of untreated sisal fiber at all frequencies. Permanganate-induced grafting of polyethylene onto sisal fibers takes place as a result of permanganate treatment of the sisal fibers. As a result of permanganate treatment, the hydrophilic tendency of sisal fibers is reduced, and therefore water absorption decreases. The part of the orientation polarization due to polar water molecules decreases, resulting in a decrease in the dielectric constant of the permanganate-treated sisal fiber–LDPE composites. But at higher concentration of

$KMnO_4$, there are chances for the degradation of cellulose fiber resulting in the formation of polar groups. The orientation polarization increases with the concentration of $KMnO_4$. Hence, the dielectric constant values increase as the concentration of $KMnO_4$ increases.

For coir–LDPE composites, the dielectric constant increases with fiber content over the entire rage of frequencies (91). The increase is higher for low frequencies, lower for medium frequencies, and very small for high frequencies. Since LDPE is a nonpolar molecule, it has only atomic and electronic polarization, which is instantaneous; so there should be no variation in the dielectric constants with frequency. The dielectric constants of LDPE are almost the same over a wide range of frequencies, but are slightly different at very low frequencies and very high frequencies. The increase of dielectric constant with increase in sisal fiber content (91) can be explained by considering the chemical nature of sisal fiber, and also by the heterogeneous nature of the composite.

The dielectric constant of the polymer depends upon the polarization of the molecules. If there is greater polarizability of the molecules, the dielectric constant of the material will be higher. The overall polarizability of a molecule is the sum of electronic, atomic, and orientation polarizations. Of these, atomic and electronic polarizations are instantaneous polarization components. The effects of such instantaneous polarization are seen only at very high frequencies. Dipole or orientation polarization is due to the presence of polar groups in the fibers. The degradation of cellulose during the processing affects the properties of the cellulose-containing composites. Changes in the chemical structure of cellulose and possibly oxidation of the polyethylene matrix both contribute to the characteristic properties of the composites. Since the composite is heterogeneous, interfacial polarization also exists. Interfacial polarization influences the dielectric properties at low frequencies. The effect of orientation polarization and interfacial polarization will depend upon the concentration of fillers. Hence, the dielectric constant values increase with the concentration of fibers at all the frequencies, especially at low frequencies.

At constant fiber loading, the number of interfaces per unit volume is greater for 1 mm fiber length. Hence, the contribution of interfacial polarization is at a maximum, and therefore the dielectric constant values are at a maximum for 1 mm fiber length. The number of interfaces decreases with an increase in fiber length. However, when the fiber length is increased to 6 mm, the fibers undergo bending and curling. This results in an increase in the number of interfaces. Hence, the dielectric constant values again increase slightly. It is known that in any polymeric material, the current flows mainly through the crystalline regions, and that the noncrystalline regions allow current to pass through mainly due to the presence of moisture. Since sisal fiber is lignocellulosic, it absorbs moisture. The presence of moisture and impurities increases the conduction. A fiber embedded in a thermoplastic melt can act as a nucleate for the growth of spherulites. If there are many nucleation sites along a fiber surface, the resulting spherulite growth will be restricted in the lateral direction so that a columnar layer known as transcrystallinity will develop and enclose the fiber. This also increases electrical conduction.

3.4.7 Water Absorption by Polyolefin/Natural Fiber Composites

For hydrophilic fillers such as cellulose fibers, an increase in water absorption can be expected (88). Cellulosic fibers are difficult to dissolve because of their higher crystallinity; however, they tend to retain liquids in the interfibrillar space. Initially, the absorption is linear, subsequently gradual, and finally reaches a plateau. The initial rate of water absorption and equilibrium uptake of water increases with increasing fiber content. Since polyethylene is hydrophobic and PALF hydrophilic, the absorption of water is by virtue of the fiber alone. As the fiber loading increases, the cellulose content increases, which in turn results in the absorption of more water.

The hydrophilicity of the fiber can be reduced to a considerable extent by suitable chemical treatment. In the case of treated fiber composites, the water absorption rate decreases considerably compared to that of the untreated fiber composites. However, the extent of reduction depends on the nature of the treatment. This can be explained by enhanced bonding between fiber and matrix through chemical treatment. As a result of chemical treatment, the hydroxyl groups of the cellulose react with the functional groups of the coupling agent, which in turn bonds with the polymer matrix and thus good fiber–matrix bonding is established. Therefore, the chances of hydroxyl groups coming in contact with water molecules are reduced considerably. Alkali treatment reduces the polarity of PALF. The location of some lignin, a ''disturbing'' component, near the boundaries of the crystallites prevents the penetration of water molecules. The increase in crystallinity as a consequence of alkaline treatment will result in a reduction in the sorption capacity of the fiber. To understand the mechanism of sorption, the moisture uptake data of PALF–LDPE composites were fitted to the equation

$$\log(Q_t/Q_\infty) = \log k + n \log t \tag{3.6}$$

where Q_t is the mol% increase in uptake at time t, Q_∞ is the mol% increase in uptake at equilibrium, and k is a constant characteristic of the sample that indicates the interaction between the sample and water. For a Fickian mode of diffusion, the value of n is equal to 0.5. When the value falls between 0.5 and 1, the diffusion is anomalous. The moisture equilibration may or may not follow the classical Fickian process where diffusion is driven only by a concentration gradient. In the case of PALF–LDPE composites, n approaches 0.5 with increasing temperature and k correspondingly decreases for treated fiber composites.

Immersion in water may lead to rapid debonding, delamination, and loss of structural integrity. As the immersion time increases, the composite tensile strength decreases. This is true for all fiber loadings. Property changes may be due to combinations of plasticization and mechanical damage from moisture-induced swelling. The absorption of moisture will plasticize the system and this leads to a reduction in strength. Although the treated fiber composites show higher strength, the relative extent of the decrease is greater in treated composites and it increases with fiber loading. The relatively small decrease in properties of the untreated fiber composites can be explained by the thermal shrinkage of the polyethylene. The

thermal shrinkage of the matrix results in voids surrounding the fibers. The fiber can swell to fill this gap and may even produce some radial pressure. In treated fiber composites the voids are filled by small particles of adhesive and coatings, which will hinder the rate of absorption of water. However, the radial pressure developed between the fibers and matrix is correspondingly less. The trapped water acts as a plasticizer and decreases the tensile strength. The modulus of the composites increases with fiber loading. But as the exposure time in water increases, the modulus decreases owing to the plasticization effect. Treated composites also exhibit a similar trend. Because of the absorption of water, the interfacial adhesion between fiber and matrix becomes weak.

PP–sisal composites show the same water absorption characteristics (89). By the introduction of sisal fiber into the PP matrix, the extent of PP degradation during UV irradiation can be reduced. The extent of degradation for neat PP after 3 months is 92.6% whereas that for 10% fiber loading is 58%, that for 20% fiber loading is 37%, and that for 30% fiber loading is 23%. With an increase in fiber loading, the extent of retention in tensile properties increases. Chemically treated composites show a decrease in tensile strength with increase in UV exposure time. Although the treated fiber composites show higher strength, the relative extent of decrease is greater in treated composites. In the case of chemically treated PP–sisal composites, the surface is badly damaged and fibers lying near the surface become exposed upon UV irradiation. The extent of degradation after 3 months in the case of MAPP-treated composites is 49.6%, urethane derivative of polypropylene glycol treated composites 40%, benzoylated composites 38%, and untreated composites 37%. The decrease in tensile properties is greater for chemically treated composites than for untreated composites.

For PP–flax composites water uptake increases with fiber bundle content (92). MAPP-modified composites exhibit a remarkable reduction in water uptake rates. Due to a better interfacial bonding between flax fiber bundles and the PP matrix, the equilibrium water uptake shows a small reduction. Although the use of MAPP slightly decreases composites' affinity to water, long periods of water immersion degrade the fibers' mechanical properties and subsequently the composites' properties. Therefore, flax fiber–PP composites should not be used in applications where water uptake is of critical importance.

In an investigation of LLDPE–sisal composites (94), the sisal–PE composites, prepared in the presence of DCP, show reduced water absorption, although the mass% of the absorption has the same dependence on time as the untreated composites. Significantly lower values of the mass% changes are obtained in the case of DCP-treated composites, compared to untreated ones. Improved interfacial bonding is the probable reason for the behavior. Grafting reactions reduce the number of voids between sisal and the PE matrix, and partially prevent fibers coming into contact with water.

3.4.8 Nanocomposites

Studying tunicin whiskers reinforced PVC composites, Chazeau (118) claimed the presence of an immobilized polymeric matrix layer in the vicinity of the filler. The

changes in the shear loss modulus induced by the cellulosic filler were discussed using a mean field approach and assuming a three-phase system.

3.5 CHARACTERIZATION OF POLYOLEFIN/FIBER INTERFACES

Several techniques have been suggested by various researchers in characterizing the interface of a composite. The single-fiber pullout test is a popular method suggested by researchers to measure the IFSS. Li and Mai carried out a single-fiber pullout test to determine the interfacial strength of sisal/HDPE composites (119). Silane and permanganate treatments were carried out for the sisal fibers. The improvement in interfacial strength in the case of γ-methacryloxypropyltrimethoxysilane has been explained as being due to van der Waals interaction that could have been set up between the HDPE matrix and the silane. Improvement in the case of $KMnO_4$ treatment has also been explained as being due to the etching of the fiber surface by oxidation giving a rougher surface. Interfacial shear strength of sisal fibers before and after chemical treatments was compared. It was concluded from the studies that interfacial shear strength can be considerably improved by chemical modification of the fiber surface.

Paiva et al. (120) reported on the morphological and interfacial characterization of alfa fibers. Alfa fibers are bleached soda pulps from the Tunisian annual plant esparto (*Alfa tenassissima*). They had a specific surface (in a dry state) of 3 $m^2\,g^{-1}$ and an average length about 500 μm. The interface of the fibers with the PP matrix was evaluated using fragmentation tests on single-filament composites. Experiments were conducted for dry and humid fibers. The specimens were then stretched in a Zwick-Roell Z005 universal testing machine, equipped with a load cell of 5 kN, at a speed of 0.5 mm min^{-1}, until the matrix yields to the maximum, and to induce repeated breakage of the fibers until the saturation of the fragmentation process. The specimens were kept under strain by holding them in a metal frame, and the lengths of the fiber fragments were measured by means of transmission optical microscopy. Shorter fiber length was obtained for dry fibers compared to humid fibers. The smaller fragment lengths correspond to higher interfacial shear strength, considering as a first approximation that the tensile strength of the fibers was not considerably affected by the humidity content. This observation of poorer interfacial strength for the composites with humid fibers may be interpreted as resulting from the formation of voids and flaws along the interface during compression molding, due to the release of water vapor.

Park et al. (121) carried out interfacial evaluation of untreated and treated jute and hemp fiber reinforced polypropylene–maleic anhydride grafted polypropylene copolymer (PP–MAPP) composites by a micromechanical technique combined with acoustic emission (AE) and dynamic contact angle measurement. The IFSS of jute and hemp fiber–PP composites was measured by the microdroplet test. The natural fibers were fixed in an equidistant series in a steel frame. Microdroplets of PP were formed on each natural fiber using a tip pin. The microdroplet specimen was fixed by

a microvice using a specially designed micrometer. The IFSS was calculated from the measured pullout force. Figure 3.13a shows the photographs of the typical microfailure modes of the jute and hemp fiber–PP systems before and after microdroplet pullout testing.

The microdroplet appeared on the matrix crack modes and thus became out of shape due to less strong interfacial adhesion. The micrographs showed that the fiber failures indicated a typically weak interfacial bond, and even though fiber breakage occurred, the matrix did not fail and the weak interfacial bond was evident from the debonding that occurred through the matrix/fiber interface. Figure 3.13b shows typical microfailure modes in tension of the combinations of the natural fiber–PP composites for (A) jute and (B) hemp fibers. It is also clear that while the microfailure for jute occurred by splitting for jute, the microfailure modes for hemp fiber showed final fiber fracture.

Doan et al. (122) studied the effect of matrix modification on the interfacial adhesion and mechanical properties of jute–PP composites. Single jute fibers were embedded in PP droplets blended with and without MAPP. From each force–displacement curve, the maximum force F_{max} and the embedded length were determined. It was found that the addition of 2% MAPP increases the tensile strength of the composite significantly. The fracture surfaces of the fibers were examined using atomic force microscopy. The difference in surface morphology suggests improved interaction in the case of the treated fiber composites as shown in Fig. 3.14.

3.6 APPLICATIONS OF POLYOLEFIN COMPOSITES

Current environmental awareness coupled with societal needs requires that we produce materials that are less toxic and are recyclable. Natural fiber composites with the fiber material as the main component provide a good basis for such concepts. Natural fiber composites are a viable alternative to synthetic fiber reinforced composites and they have an edge over conventional materials used in the building as well as automobile industries. The automotive industry has been using biofibers for interior components for several years; now biofiber composites are also used in exterior components. Figure 3.15 shows the underfloor protection trim of a Mercedes A class made from banana fiber reinforced composites. Biofiber composites in the automotive industry both reduce material waste and increase fuel efficiency. If glass fiber composites are replaced by natural fiber composites, there will be a reduction in the weight of 10–20 kg. This can bring about a significant reduction in fuel consumption leading to a positive effect on the environment. Although the automobile industry has taken the lead in the large-scale deployment of natural fibers, their use has by and large been limited to upholstery and paneling applications, where their acoustic and thermal insulation properties, low cost, and environment-friendly image are advantages.

New biobased structural composite materials for use in housing and infrastructure applications can play a significant role. Biofiber reinforcement in blended thermoplastics or resinated thermoset compression moldings is now generally

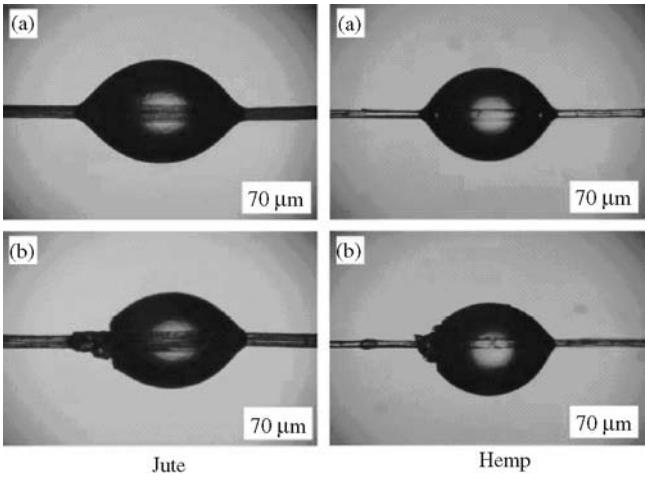

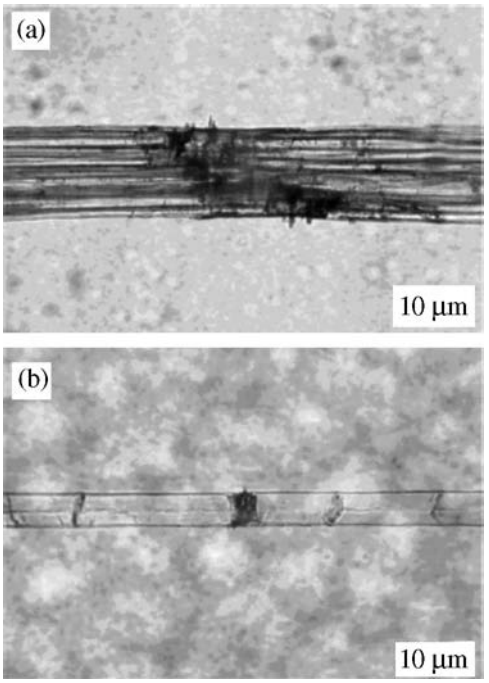

Figure 3.13 (**a**) Microfailure modes of untreated natural fibers/PP systems under tension for (A) jute fiber and (B) hemp fiber. (From Reference 121 with permission from Elsevier Ltd.) (**b**) Photographs of the typical microfailure modes of jute and hemp fibers/polypropylene systems before and after microdroplet pullout testing. (From Reference 121 with permission from Elsevier Ltd.)

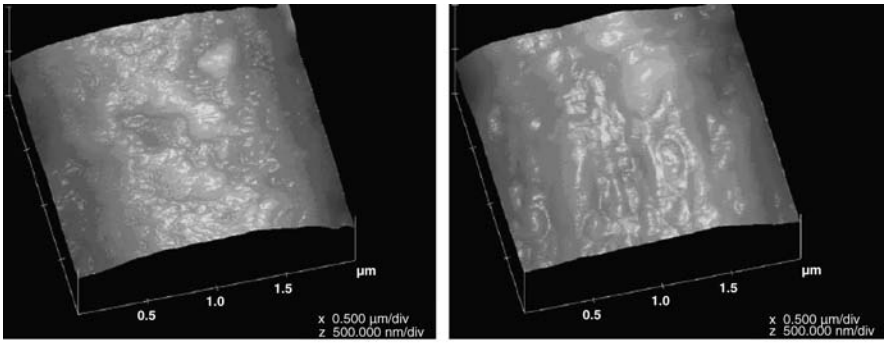

(a) (b)

Figure 3.14 AFM topographies of (**a**) an as-received jute fiber surface and (**b**) a pulled out fracture fiber surface from PP with 2 wt% MAH-PP. (From Reference 122 with permission from Elsevier Ltd.)

accepted for applications as door liners/panels, parcel shelves, and boot liners (123). Daimler Chrysler's innovative application of the abaca fiber in exterior underfloor protection for passenger cars has been recently recognized (123). Another product, FlexForm, includes a natural fiber composite made by using a carding system to vary natural and synthetic fiber formulations (124). FlexForm's natural fiber composites have been used in vehicle areas such as rear package trays, A-, B-, and C-pillar covers, center consoles, door panel inserts, and headliners for heavy-duty trucks. In addition to automotive interior trim, FlexForm Technologies' natural fiber composites are also suitable for heavy-duty truck, trailer, recreational vehicle, office furniture, ceiling tile, and packaging applications.

Another area where natural fiber composites are finding wide applications is construction. Biobased construction materials and composites include polyurethane made from a soybean oil polyol. Hundreds of applications can employ these materials. They range from carpet backing to foam cushions, pads for furniture, automotive seats, and dashboards; molded cases and covers for appliances, telephones, computers, rigid insulating foams used to insulate refrigerators, freezers, coolers, and appliances. Highly engineered blends of recycled paper products, biobased resins, and color additives can combine to provide a strong, durable

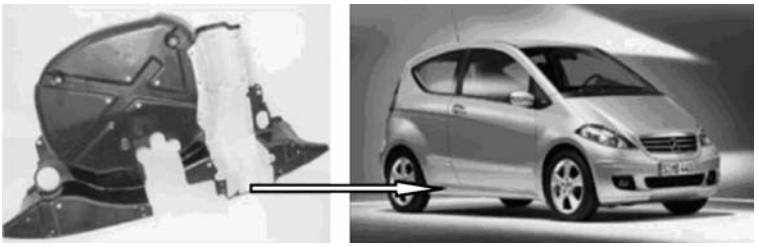

Figure 3.15 Underfloor protection trim of Mercedes A class made from banana fiber reinforced composites. (From Reference 123 with permission from John Wiley Sons, Inc.)

composite that is functionally similar to wood. It can be used where the appearance of stone and the workability of wood are desired. The grain pattern is present throughout the material, which allows for three-dimensional shaping.

These biobased products can be fabricated, sawed, sanded, fastened, milled, drilled, routed, inlaid, engraved, glued, and jointed with similar tools and techniques used in working with traditional hardwoods. Applications include furniture, tabletops, trim, store fixtures, awards, plaques, trophies, indoor signage, and other interior, nonstructural uses. Biobased composites can be used to make hay baler panels, harvester walls, and tractor parts. Soy-based resins are being used with natural fiber, chicken feather, flax, and glass reinforcements for automobile body panels and truck parts (125,126). The high stiffness and the ecofriendly composition make natural fiber composites also an ideal choice for molded houseware and cosmetics packaging, besides decking and railing systems.

3.7 CONCLUSIONS

Growing environmental awareness has resulted in a paradigm shift in the use of natural fibers. Recyclability and sustainability being the buzzwords today, natural fibers from different sources are being experimented with by researchers from various fields all over the world. Several fibers have been found to be potential candidates for use as reinforcement in various polymeric matrices.

Among the major issues that are to be handled in the preparation and use of natural fibers, its hydrophilicity and incompatibility with hydrophobic matrices are the most important. Several strategies have been suggested for modifying the surfaces. More serious work can be done in that direction, and interfacial characterization of the composites prepared after chemical modification is also an area that is gaining importance. Natural fiber based polyolefin composites have been prepared using different natural fibers and various matrices. Several ways have been suggested by researchers to improve the interaction between the fiber and the various polymeric matrices and also to characterize the interface.

NOMENCLATURE

AE	Acoustic emission
AN	Acrylonitrile
Ar	Argon
BF	Bagasse fibers
C18-T	2,4-Dichloro-6-*n*-octadecyloxy-s-triazine
CTDIC	Cardanol derivative of toluene diisocyanate
DCP	Dicumyl peroxide
E'	Storage modulus
E''	Loss modulus
EVA	Ethylene–vinyl acetate copolymer

F_{max}	Maximum force
FTIR	Fourier transform infrared spectroscopy
γ	Gamma
IFSS	Interfacial shear strength
IGC	Inverse gas chromatography
LDPE	Low density polyethylene
LLDPE	Linear low density polyethylene
MAH-PP or MAPP	Maleic anhydride grafted polypropylene
MeOH	Methanol
Mg	Magnesium
MMA	Methyl methacrylate
MPS	Methacryloxypropyltrimethoxysilane
MRPS	Mercaptopropyltrimethoxysilane
m-TMI-g-PP	*m*-Isopropenyl-a,a-dimethylbenzyl isocyanate grafted polypropylene
NAG	*N*-Acetylglycine
NaOH	Sodium hydroxide
PALF	Pineapple leaf fiber
PE	Polyethylene
PMPPIC	Polymethylene polyphenyl isocyanate
PP	Polypropylene
PS	Polystyrene
PVC	Poly(vinyl chloride)
SEM	Scanning electron microscopy
T_g	Glass transition temperature
TDI/PPG	Toluene diisocyanate/poly(propylene glycol)
ToF-SIMS	Time-of-flight secondary ion mass spectrometry
UV	Ultraviolet
WAXS	Wide-angle X-ray scattering
XPS	X-ray photoelectron spectroscopy

REFERENCES

1. S. V. Prasad, C. Pavithran, and P. K. Rohatgi, *J. Mater. Sci.*, **18**, 1443 (1983).
2. A. K. Bledzki, O. Faruk, and V. E. Sperber, *Macromol. Mater. Eng.*, **291**, 449 (2006).
3. C. Cockcroft, *The Guardian*, Manchester, UK, 10 May 2001.
4. J. Bolton, *Outlook Agric.*, **24**, 85 (1995).
5. L. S. Cobley, *An Introduction to the Botany of Tropical Crops*, Longman Group, UK, 1976.
6. A. Payen and C. R. Hebd, *Seances Acad. Sci.*, **7**, 1052 (1838).
7. C. Woodcock and A. Sarko, *Macromolecules*, **13**, 1183 (1980).
8. A. Sarko and R. Muggli, *Macromolecules*, **7**, 480 (1974).
9. R. K. Samal, M. Mohanty, and B. B. Panda, *J. Polym. Mater.*, **12**, 235 (1995)
10. G. Buschle-Diller, C. Fanter, and F. Loth, *Text. Res. J.*, **69**, 244 (1999).

11. E. Ammalahti, G. Brunow, M. Bardet, D. Robert, and I. Kipelainen, *J. Agric. Food Chem.*, **46**, 5113 (1998).
12. B. Xiao, X. F. Sun, and R. C. Sun, *Polym. Degrad. Stabil.*, **74**, 307 (2001).
13. J. Gassan and A. K. Bledzki, *Seventh International Techtextil Symposium*, Frankfurt, 20–22 June 1995.
14. A. K. Bledzki and J. Gassan, *Prog. Polym. Sci.*, **24**, 221 (1999).
15. G. E. Kritschewsky, *Chemische Technology von Textilmaterialien*, Moskau, Legprombitisdat, 1985.
16. P. J. Roe and M. P. Ansell, *J. Mater. Sci.*, **20**, 4015 (1985)
17. N. David, S. Hon, and N. Shiraishi, *Wood and Cellulose Chemistry*, Marcel Dekker, New York, 1991.
18. A. Frey-Wyssling, *Science*, **119**, 80 (1954).
19. H. A. Krassig, *Cellulose*, Gordon and Breach Science Publishers, Philadelphia, 1992.
20. A. Dufresne, *Recent Res. Dev. Macromol. Res.*, **3**, 455 (1998).
21. M. N. Belgacem and A. Gandini, *Compos. Interface*, **12**(1–2), 41 (2005).
22. S. H. Zeronian, H. Kawabata, and K. W. Alger, *Text. Res. Inst.*, **60**, 3 (1990).
23. P. K. Ray, A. C. Chakravarty, and S. B. Bandyopadhyay, *J. Appl. Polym. Sci.*, **20**, 1765 (1976).
24. A. N. Shah and S. C. Lakkard, *Fiber Sci. Technol.*, **15**, 41 (1981).
25. M. N. Belgacem, P. Bataille, and S. Sapieha, *J. Appl. Polym. Sci.*, **53**, 379 (1994).
26. D. P. Kamdem, S. K. Bose, and P. Luner, *Langmuir*, **9**, 3039 (1993).
27. M. N. Belgacem, G. Czeremuszkin, S. Sapieha, and A. Gandini, *Cellulose*, **2**, 145 (1995).
28. J. Simonsen, Z. Hong, and T. G. Rials, *Wood Fiber Sci.*, **29**, 75 (1997).
29. S. Boufi and A. Gandini, *Cellulose*, **8**, 303 (2001).
30. I. Sakata, M. Morita, N. Tsuruta, and K. Morita, *J. Appl. Polym. Sci.*, **49**, 1251 (1993).
31. J. Gassan and V. S. Gutowski, *Compos. Sci. Technol.*, **60**, 2857 (2000).
32. J. Gassan, V. S. Gutowski, and A. K. Bledzki, *Macromol. Mater. Eng.*, **283**, 132 (2000).
33. F. Denes, L. D. Nielsen, and R. A. Young, *Lignocellulosic-Plast. Comp.*, **1**, 61 (1997).
34. A. K. Bledzki and J. Gassan, *Prog. Polym. Sci.*, **24**, 221 (1999).
35. X. Yuan, K. Jayaraman, and D. Bhattacharyya, *Composites A*, **35**, 1363 (2004).
36. T. Wakida and S. Tokino, *Ind. J. Fiber Text. Res.*, **21**, 69 (1996).
37. M. A. Khan, M. Hossain, and K. M. Idriss Ali, *J. Appl. Polym. Sci.*, **74**, 900 (1999).
38. M. S. Sreekala and S. Thomas, *Compos. Sci. Technol.*, **63**, 861 (2003).
39. M. N. Belgacem and A. Gandini, *Compos. Interface*, **12**, 41 (2005)
40. M. A. Martins, P. Kunihiro Kiyohara, and I. Joekes, *J. Appl. Polym. Sci.*, **94**, 2333 (2004).
41. M. Z. Rong, M. Q. Zhang, Y. Liu, G. C. Yang, and H. M. Zeng, *Compos. Sci. Technol.*, **61**, 1437 (2001).
42. L. Y. Mwaikambo and M. P. Ansell, *J. Appl. Polym. Sci.*, **84**, 2222 (2002).
43. M. A. Martins and I. Joekes, *J. Appl. Polym. Sci.*, **89**, 2507 (2003).
44. D. Ray, B. K. Sarkar, A. K. Rana, and N. R. Bose, *Composites A*, **32**, 119 (2001).
45. D. Ray and B. K. Sarkar, *J. Appl. Polym. Sci.*, **80**, 1013 (2001).
46. O. Owolabi, T. Ozvikovzki, and I. Kovacs, *J. Appl. Polym. Sci.*, **30**, 1827 (1985).
47. J. M. Felix and P. Gatenholm, *J. Mater. Sci.*, **29**, 3043 (1994).
48. S. C. Saha, B. K. Das, P. K. Ray, S. N. Pandey, and K. Goswami, *J. Appl. Polym. Sci.*, **43**, 1885 (1991).
49. L. A. Pothan, C. Bellmann, L. Kailas, and S. Thomas, *J. Adhes. Sci. Technol.*, **16**, 157 (2002).
50. P. Zadorecki and T. Ronnhult, *J. Polym. Sci. A Polym. Chem.*, **24**, 737 (1986).
51. C. Joly, M. Kofman, and R. Gauthier, *J.M.S. Pure Appl. Chem. A*, **33**, 1981 (1996).

52. L. A. Pothan, Y. Zimmermann, S. Thomas, and S. Spange, *J. Polym. Sci. B Polym. Phys.*, **38**, 2534 (2000).
53. M. Baiardo, G. Frisoni, M. Scandola, and A. Licciardello, *J. Appl. Polym. Sci.*, **83**, 38 (2002).
54. P. Zadorecki and P. Flodin, *J. Appl. Polym. Sci.*, **31**, 1699 (1986).
55. N. Chand, S. Varma, and A. C. Khazanchi, *J. Mater. Sci. Lett.*, **8**, 1307 (1989).
56. L. A. Pothan, J. George, and S. Thomas, *Compos. Interface*, **9**, 335 (2002).
57. P. V. Joseph, K. Joseph, and S. Thomas, *Compos. Interface*, **9**, 171 (2002).
58. G. Frisoni, M. Baiardo, M. Scandola, D. Lednicka, M. C. Cnockaert, J. Mergaert, and J. Swings, *Biomacromolecules*, **2**, 476 (2001).
59. C. Albano, J. Gonzalez, M. Ichazo, and D. Kaiser, *Polym. Degrad. Stabil.*, **66**, 179 (1999).
60. N. E. Zafeiropoulos, G. G. Dijon, and C. A. Baillie, *Composites A*, **38**, 621 (2007)
61. C. S. R. Freire, A. G. Cunha, A. J. D. Silvestre, C. Pascoal Neto, and A. Gandini, Surface treatment of cellulose fibers with perfluoro-reagents, *J. Colloid Interface Sci.*, submitted.
62. P. V. Joseph, K. Joseph, S. Thomas, C. K. S. Pillai, V. S. Prasad, G. Groeninckx, and M. Sarkissova, *Composites A*, **34**, 253 (2003).
63. Y. T. Zheng, D. R. Cao, D. S. Wang, and J. J. Chen, *Composites A*, **38**, 20 (2007).
64. D. Maldas, B. V. Kokta, and C. Daneaulf, *J. Appl. Polym. Sci.*, **37**, 751 (1989).
65. D. Maldas, B. V. Kokta, and C. Daneault, *J. Vinyl Technol.*, **11**(2), 90 (1989).
66. S. Mishra, Sisal fiber composites, *Ph.D. thesis*, Utkal University, Vani Bihar, Orissa, India, 2001.
67. P. V. Joseph, K. Joseph, S. Thomas, C. K. S. Pillai, V. S. Prasad, G. Groeninckx, and M. Sarkissova, *Composites A*, **34**, 253 (2003).
68. A. Karmarkar, S. S. Chauhan, J. M. Modak, and M. Chanda, *Composites A*, **38**, 227–233 (2007).
69. L. A. Pothan, F. Simon, S. Spange, and S. Thomas, *Biomacromolecules*, **7**, 892 (2006).
70. S. U. A. Redondo, E. Radovanovic, M. E. Goncalves, and I. V. P. Yoshida, *J. Appl. Polym. Sci.*, **85**, 2573 (2002).
71. B. Singh, M. Gupta, A. Verm, and O. S. Tyagi, *Polym. Int.*, **49**, 1444 (2000).
72. M. Abdelmouleh, S. Boufi, M. N. Belgacem, and A. Dufresne, Short natural-fiber reinforced polyethylene and natural rubber composites: effect of silane coupling agents and fibers loading, *Compos. Sci. Technol.* Forthcoming.
73. Z. A. Rogovin and L. S. Galbraykh, *Chemical Conversions and Modification of Cellulose*, Khimiya Publications, Moscow, 1979.
74. A. K. Mohanty, S. Parija, and M. Misra, *J. Appl. Polym. Sci.*, **60**, 931 (1996).
75. P. C. Tripathy, M. Misra, S. Parija, S. Mishra, and A. K. Mohanty, *Polym. Int.*, **48**, 868 (1999).
76. R. K. Samal and B. L. Bhuyan, *J. Appl. Polym. Sci.*, **52**, 1675 (1994).
77. S. Mishra, M. Misra, S. S. Tripathy, S. K. Nayak, and A. K. Mohanty, *Macromol. Mater. Eng.*, **286**, 107 (2001).
78. G. Canché-Escamilla, J. I. Cauich-Cupul, E. Mendizabal, J. E. Puig, H. Vázquez-Torres, and P. J. Herrera-Franco, *Composites A*, **30**, 349 (1999).
79. N. S. Cetin and C. A. S. Hill, *J. Wood Chem. Technol.*, **19**, 247 (1999).
80. Y. Li, Y. W. Mai, and L. Ye, *Compos. Sci. Technol.*, **60**, 2037 (2000).
81. K. Joseph, S. Thomas, and C. Pavithran, *Polymer*, **37**, 5139 (1996).
82. G. Kalaprasad, B. Francis, S. Thomas, C. R. Kumar, C. Pavithran, G. Groeninckx, and S. Thomas, *Polym. Int.*, **53**, 1624 (2004).
83. G. Kalaprasad and S. Thomas, *J. Appl. Polym. Sci.*, **89**, 443 (2003).
84. K. Joseph, S. Varghese, G. Kalaprasad, S. Thomas, L. Prasannakumari, P. Koshy, and C. Pavithran, *Eur. Polym. J.*, **32**, 1243 (1996).
85. G. Kalaprasad, K. Joseph, S. Thomas, and C. Pavithran, *J. Mater. Sci.*, **32**, 4261 (1997).

86. J. George, R. Janardhan, J. S. Anand, S. S. Bhagawan, and S. Thomas, *Polymer*, **37**, 5421 (1996).
87. A. Paul, K. Joseph, and S. Thomas, *Compos. Sci. Technol.*, **57**, 67 (1997).
88. J. George, S. S. Bhagawan, and S. Thomas, *Compos. Sci. Technol.*, **58**, 1471 (1998).
89. P. V. Joseph, M. S. Rabello, L. H. C. Mattoso, K. Joseph, and S. Thomas, *Compos. Sci. Technol.*, **62**, 1357 (2002).
90. K. Joseph and S. Thomas, *Compos. Sci. Technol.*, **53**, 99 (1995).
91. A. Paul and S. Thomas, *J. Appl. Polym. Sci.*, **63**, 247 (1997).
92. A. Arbelaiz, B. Fernández, J. A. Ramos, A. Retegi, R. Llano-Ponte, and I. Mondragon, *Compos. Sci. Technol.*, **65**, 1582 (2005).
93. T. J. Keener, R. K. Stuart, and T. K. Brown, *Composites A*, **35**, 357 (2004).
94. M. A. Mokoena, V. Djoković, and A. S. Luyt, *J. Mater. Sci.*, **39**, 3403 (2004).
95. M. E. Malunka, A. S. Luyt, and H. Krump, *J. Appl. Polym. Sci.*, **100**, 1607 (2006).
96. P. V. Joseph, G. Mathew, K. Joseph, G. Groeninckx, and S. Thomas, *Composites A*, **34**, 275 (2003).
97. P. V. Joseph, K. Joseph, S. Thomas, C. K. S. Pillai, V. S. Prasad, G. Groeninckx, and M. Sarkissova, *Composites A*, **34**, 253 (2003).
98. A. K. Bledzki and J. Gassan, *Prog. Polym. Sci.*, **24**, 221 (1999).
99. R. G. Raj and B. V. Kokta, *Polym. Eng. Sci.*, **31**, 1358 (1991).
100. R. G. Raj, B. V. Kokta, F. Dembele, and B. Sanschagrain, *J. Appl. Polym. Sci.*, **38**, 1987 (1989).
101. R. G. Raj, B. V. Kokta, and C. Daneault, *J. Mater. Sci.*, **25**, 1851 (1990).
102. M. M. Sain and B. V. Kokta, *J. Appl. Polym. Sci.*, **54**, 1545 (1994).
103. P. Bataille, P. Allard, P. Cousin, and S. Sapieha, *Polym. Compos.*, **11**, 5301 (1990).
104. R. G. Raj, B. V. Kokta, D. Maldas, and C. Daneault, *J. Appl. Polym. Sci.*, **37**, 1098 (1989).
105. D. Maldas, B. V. Kokta, and C. Daneault, *J. Appl. Polym. Sci.*, **37**, 571 (1989).
106. P. Gatenholm, H. Bertilsson, and A. Mathiasson, *J. Appl. Polym. Sci.*, **49**, 197 (1993).
107. K. L. Yam, B. K. Gogoi, C. C. Lai, and S. E. Selke, *Polym. Eng. Sci.*, **30**, 693 (1990).
108. Th. Schlösser and Th. Fölster, *Kunststoffe*, **85**, 319 (1995).
109. A. C. N. Singleton, C. A. Baillie, P. W. R. Beaumont, and T. Peijs, *Composites B*, **34**, 519 (2003).
110. F. G. Torres and M. L. Cubillas, *Polym. Test.*, **24**, 694 (2005).
111. D. Maldas, B. V. Kokta, and C. Daneault, *J. Vinyl Technol.*, **11**, 90 (1989).
112. R. G. Raj and B. V. Kokta, *Polym. Eng. Sci.*, **31**, 1358 (1991).
113. B. V. Kokta, R. Chen, C. Daneault, and J. L. Valade, *Polym. Compos.*, **4**, 229 (1983).
114. R. G. Raj, B. V. Kokta, and C. Daneault, *J. Appl. Polym. Sci.*, **40**, 645 (1990).
115. J. Gassan and A. K. Bledzki, *Composites A*, **28**, 1001 (1997).
116. M. Avella and R. dell'Érba, *Proceedings of the Ninth International Conference on Composite Mater*, Vol. II, Madrid, 1993, p. 864.
117. H. Baumgartl and A. Schlarb, *Symposium Nachwachsend Rohstoffe-Perpektiven für die Chemie*, Frankfurt, 5–6 May 1993.
118. L. Chazeau, *Ph.D. thesis*, Joseph Fourier University, Grenoble, France, 1998.
119. Y. Li and Y. W. Mai, *J. Adhes.*, **82**, 527 (2006).
120. M. C. Paiva, I. Ammar, A. R. Campos, R. B. Cheikh, and A. M. Cunha, Alfa fibers: mechanical, morphological and interfacial characterization, *Compos. Sci. Technol.* Forthcoming.
121. J. M. Park, S. T. Quang, B. S. Hwang, and K. L. De Vries, *Compos. Sci. Technol.*, **66**, 2686-2699 (2006).
122. T. T. L. Doan, S. L. Gao, and E. Mäder, *Compos. Sci. Technol.*, **66**, 952 (2006).
123. A. K. Bledzki, O. Faruk, and V. E. Sperber, *Macromol. Mater. Eng.*, **291**, 449 (2006).

124. K. Buchholz, A natural material choice, *Mater. Innovations*, **55** (2005).
125. USDA Biobased Products Sourcebook Outreach: An Evaluation of Industry Perspectives on Proposed Biobased Product Content Guidelines, Final Report, April 2002.
126. M. A. Dweib, B. Hu, A. O_Donnell, H. W. Shenton, and R. P. Wool, *Compos. Struct.*, **63**, 147 (2004).

Chapter 4

Composites of Polyolefins and Some Polyolefin/Polyamide Blends as Matrices and Calcium Carbonate, Wood Flour, Sisal Fiber, Hydroxyapatite, and Montmorillonite as Fillers

Carmen Albano[1,2] and Rosestela Perera[3]

4.1 INTRODUCTION

Over the last few years, the development of new materials has been oriented toward composites, because they are more attractive systems with great significance for research and industrial applications. Incorporation of fillers in plastics is a common practice, as it typically reduces the costs and modifies their physical and mechanical properties. This alteration of properties in plastics depends on the nature of fillers as well as of the plastics.

[1] Laboratorio de Polímeros, Centro de Química, Instituto Venezolano de Investigaciones Científicas (IVIC), Caracas, Venezuela

[2] Escuela de Ingeniería Química, Facultad de Ingeniería, Universidad Central de Venezuela (UCV), Caracas, Venezuela

[3] Departamento de Mecánica, Universidad Simón Bolívar (USB), Caracas, Venezuela

Polyolefin Composites, Edited by Domasius Nwabunma and Thein Kyu

Polyolefins such as polyethylene (PE) and polypropylene (PP) are widely accepted for their commodity applications. Thus, their composites represent an important class of engineering materials. The degree of improvement of the mechanical and physical properties of these composites depends on the judicious choice of filler origin, particle size and shape, the amount or fraction of filler, their surface characteristics, degree of dispersion, and its surface treatment which promotes interaction between the polymer matrix and filler (1).

Composites made from particulate fillers are macroscopically isotropic, and the fillers can be either organic or inorganic. The inclusion of stiff inorganic fillers into polymeric materials enhances their physical and mechanical properties, such as modulus, hardness, creep resistance, and processability, and improves the dimension stability of the polymer. On the contrary, natural fibers based on lignocellulose can be considered as an interesting alternative for glass fibers as reinforcements in engineering polymeric materials. Natural fibers like flax, hemp, kenaf, jute, and sisal have a number of techno-economical and ecological advantages over glass fibers.

Generally, the addition of organic and inorganic fillers will have an embrittlement effect on polymers and decrease their impact energy (2). The filler can change the characteristics of a polymer system in two ways. First, the properties of the particles themselves (size, shape, and modulus) can have a profound effect, especially on the mechanical properties. Second, the particles may change the micro morphology of the polymer. The surface of the filler may act as a nucleating agent, thereby altering the amount of crystallinity or type of crystalline structure.

4.2 COMPOSITES OF POLYPROPYLENE AND HIGH DENSITY POLYETHYLENE WITH CALCIUM CARBONATE

4.2.1 Mechanical Properties

The mechanical properties of the polyolefin-based composites with calcium carbonate ($CaCO_3$) have been determined by changing the filler content, particle size, mixing conditions, adding surface modifiers, using elastomers, and, under plasma (3–21).

The Youngs modulus increases almost in 80% with the addition of 60 wt% of the filler, and the tensile strength and elongation at break decrease indicating that there is no chemical interaction between the inorganic phase ($CaCO_3$) and the organic phase (PP) in the composites of PP with $CaCO_3$ with an average particle size of 5.5 μm. These results are attributed to the fact that the polymeric matrix is stiffened by the particulated second phase of $CaCO_3$. The particles restrict the mobility and deformability of the matrix by introducing a mechanical restraint, the degree of which depends on the interparticulate spacing and the properties of the particles and the matrix (3). It can also be suggested that this tensile behavior is the result of a physical interaction, for example, surface adsorption (22). There is also a restriction in polymer molecular diffusion in the presence of solid particles due to an effective

attraction potential between segments of the chain sequential to the repulsive potential that the polymer is subjected to when it approaches the solid particles (23).

The impact strength of these composites increases at lower contents of $CaCO_3$ (e.g., 26 wt%) and their toughness increases. This fact unfolds as a consequence of the local micro plastic deformation arising from the microscopic cavities around the poorly bonded particles. The reduction in toughness at high filler contents was found to be due to the limited plastic flow of the PP matrix, because the more ductile matrix was replaced by the more rigid dispersed particles (4).

Similar works were carried out by Albano et al. (13) using a $CaCO_3$ with a very similar particle size. A value of the Young's modulus of 1592 MPa was obtained for composites with 30 wt% of the filler. This value was 35% higher than that for pure PP. However, there were no changes in the tensile strength and the elongation at break.

One of the factors playing an important role in the tensile behavior of composites is the particle size of the $CaCO_3$. Using particle sizes of about 0.7 μm (11), a higher increase (46%) in the stiffness (from 1840 MPa without filler to 2700 MPa) can be obtained, and if the particle size is even smaller, that is, 0.1 μm, an increase in the stiffness of PP composites with 10 wt% of the filler is reached. There is an interval for the optimal particle size in $CaCO_3$ that induces the presence of β-spherulites, and these spherulites increase the rate of crack initiation, but the rate of crack propagation is smaller and proceeds with more difficulty. Some authors concluded that the optimal particle size must be between 1 and 0.1 μm (18).

The Young's modulus of the PP composites with nanoparticles of $CaCO_3$ (0.044 μm) increase from 1600 to 2600–3000 MPa with filler contents ranging from 0 to 30 wt%. This significant increase in the modulus can be attributed to two counterbalanced forces that affect the mechanical properties: reinforcing and nucleation effects of the $CaCO_3$ nanoparticles (17). Even though a smaller particle size of the $CaCO_3$ increases the Young's modulus of the composites, it is possible to achieve a change from 1400 to 2700 MPa for composites of 0.07 μm particle size and from 1400 MPa to 3060 MPa for composites with a particle size of 3.5 μm (16). These results indicate that larger particle sizes could substantially increase the Young's modulus, depending on the dispersion as well as the presence of agglomerates and their sizes.

4.2.2 Influence of the Mixing Conditions on the Dispersion of the Filler

The mixing conditions and the extruder configuration characteristics are important to obtain a good dispersion and smaller agglomerate sizes. Gendron and Binet (9) and Bories et al. (10) studied the effects of the configuration of the elements of the screw, screw speed, flow rate, position of the feeding port, and barrel temperature profiles on the dispersion of $CaCO_3$ into PP. In general, the agglomerate relative fraction increases with the flow rate. Furthermore, the increase in the flow rate decreases the residence time, leaving less time and specific energy to break the agglomerates. The processing conditions must be such that the decrease in the agglomerate sizes is

possible, because there is a critical size of approximately 10 μm, from where the fracture initiates. However, the dispersion levels improve as the screw speed increases, even though the mean residence time tends to diminish. The shearing action, beneficial for the break up of the aggregates and agglomerates, is proportional to the rotation speed of the screw, and appears to be the dominant variable in that case. Additionally, the amount of agglomerates decreases as the rotor frequency increases and as the polymer viscosity decreases when the barrel temperature profile increases, as a consequence of a better wetting and dispersion. Optimal conditions for dispersion may however be detrimental for the polymer matrix, where the viscosity of the polymer is strongly decreased and degradation may take place.

Changes in mixing conditions, as well as in the screw configuration affect the mechanical behavior of the composites. For instance, the tensile strength and elongation at break decrease as the agglomerates fraction increases, showing the importance of dispersion for the mechanical performance. The Young's modulus however is enhanced slightly by increasing agglomerate concentration. This is consistent with the fact that the volume of agglomerates is larger than that expected from the mineral density. In fact, the agglomerates are composed of mineral as well as entrapped air and polymer. The presence of agglomerates therefore increases the apparent solid content in the composite.

4.2.3 Surface Modifiers for Calcium Carbonate

Agglomerates are formed as the $CaCO_3$ content in PP composites increases. Therefore, there are different ways of improving the polymer–filler interaction and dispersion. Among the different ways of improving the polymer–filler interactions, the following can be cited: the use of coupling agents (5,6,12,13,15,21,23–25), the use of some elastomers (13,26,27), and surface modification of $CaCO_3$ particles by plasma-polymerized acetylene (7) among others.

The use of isopropyltriisostearoyl titanate (Lica 12) as a coupling agent in the treatment of the $CaCO_3$ (0.8 μm) particle's surface in PP/$CaCO_3$ composites improves their fracture toughness and impact resistance. Additionally, it produces a better dispersion and a decrease in the amount of filler agglomerates. The highest value of the impact strength obtained was 3 kJ m^{-2} with 20 wt% of treated filler (5). The increase in the toughness at low concentrations of the filler may be due the local micro plastic deformation arising from the microscopic cavities around the poorly bonded particles. The reduction in toughness at high filler concentrations is attributed to limited plastic flow of the PP matrix because the more ductile matrix is replaced by the more rigid dispersed particulates. However, composites made from blends of polyolefin (PP/HDPE, 80/20) with 30 wt% of $CaCO_3$ of two different particle sizes (3.0 and 1.8 μm) treated with Lica 12 show impact strength values of 13 and 16 J m^{-1} for the indicated filler sizes. Moreover, the use of 0.3–0.5 wt% of Lica 12 increases the tensile strength and the Young's modulus of the composites. Other coupling agents of the titanate type, such as Lica 01 and Lica 9, zirconates (NZ12), and a mixture of Lica 01 and Lica 12 in a 1:1 proportion were also analyzed. These agents

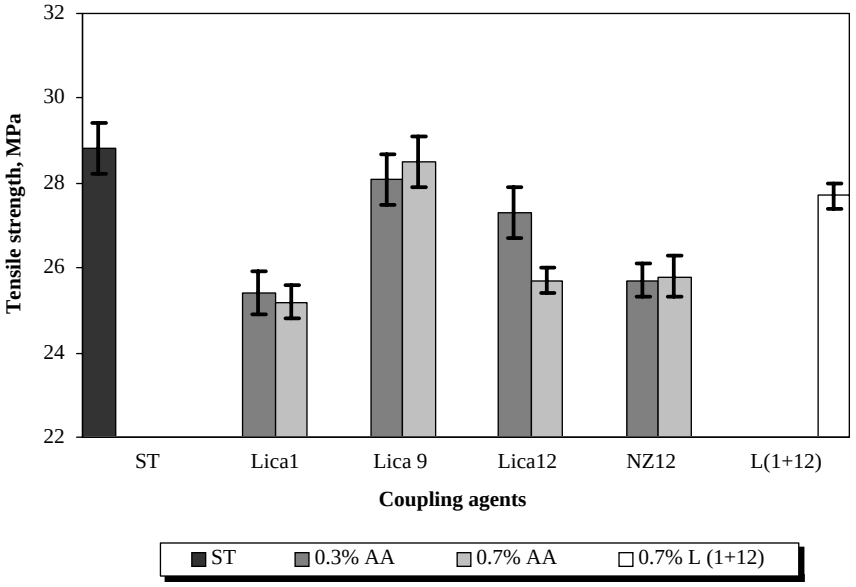

Figure 4.1 Tensile strength of PP/HDPE with 30 wt% filler treated with different coupling agents. (From Reference 15 with permission from Elsevier.)

were used in amounts of 0.3 and 0.7 wt% of the filler content. It was reported that none of these agents increase the tensile strength value when it was compared to that of the untreated composite (Fig. 4.1). Nonetheless, Lica 12, Lica 01, and NZ12 increased the elongation at break, showing a plasticizing effect of these coupling agents. Only the blending of Lica 01 and Lica 12 caused a large increment in the impact strength of the composites (Fig. 4.2) (15).

However, researchers from Kenrich Petrochemicals (24), who have 30 years of experience in the coupling agent's field, recommend the use of neoalkoxy titanates and zirconates. The results of their researches showed, for example, that the use of tridodecylbenzene sulfonyl titanate in PP composites with 40 wt% of $CaCO_3$ reduces the injection molding cycle time in 35.5% and the temperature of the injection process in 22%. Another group of silane-type coupling agents has been used (23) in composites of PP/$CaCO_3$. However, not all of them produce an increase in the yield stress and tensile strength when compared to the composite with untreated filler. A reactive coupling agent performs its action in a fashion different from that of an agent that only acts as a plasticizer. The high energy surface of the filler will be covered by an organic substance here, too, reducing the surface tension. However, the reduced reversible work of adhesion will be compensated and exceeded by stronger—probably covalent—bonds between the functional group of the coupling agent and the polymer matrix. In general, when a coupling agent is reactive, the yield stress and tensile strength increase, while the corresponding deformations decrease owing to the enhanced strength and rigidity of the interphase. On the contrary, the effect of the

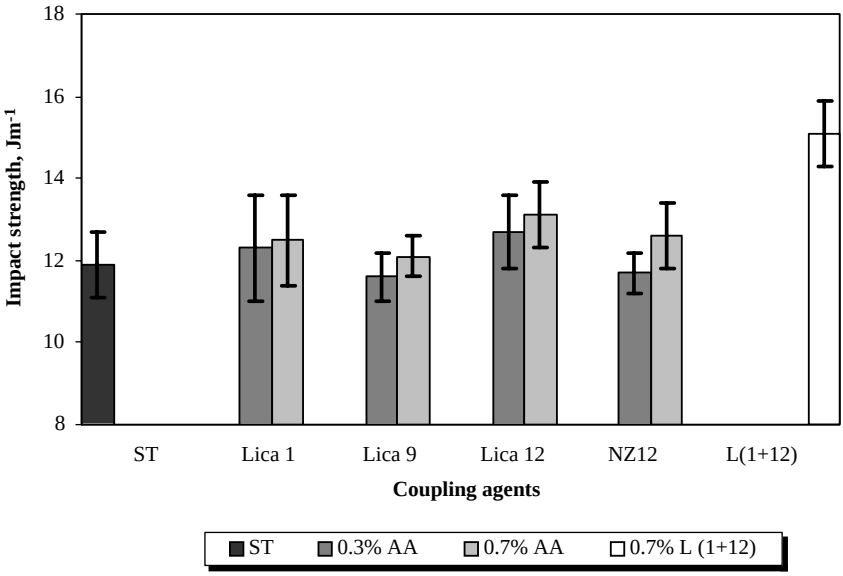

Figure 4.2 Impact strength of PP/HDPE with 30 wt% filler treated with different coupling agents. (From Reference 15 with permission from Elsevier.)

surface treatment on the Young's modulus values is almost negligible. The lack of a significant effect of the treatment on the stiffness can be explained by the fact that the Young's modulus is theoretically measured at zero deformation, thus displacements must not be taking place at the interface. As a consequence, the strength of interfacial interaction, which may be influenced by the coupling agents, plays no role in the actual value of the modulus. Tensile yield stress and tensile strength are affected much more by the surface treatment, since at large deformations, the mobility of the interfacial region influences the performance of the composite. Hence, there must be a relationship between the effect of the coupling agent and its chemical structure which indicates that the length of the organofunctional group of the coupling agents plays a major role in their efficiency.

On the matter of using an elastomer in composites with $CaCO_3$ with the purpose of improving the impact strength, some studies were performed by Wang (4), Albano et al. (13), and Zhang et al. (27), among others.

Composites of PP/PS (70/30) blends with 5 wt% of SBS, 50% of $CaCO_3$, and a titanate as a coupling agent show a slight change in the impact strength values, from 60 J m^{-1} for the blend without $CaCO_3$ to 75 J m^{-1} for the composite with 30 wt% of the filler (4). This synergistic phenomenon is caused by several factors acting simultaneously: (1) the recovery of chain mobility of the interfacial layers; (2) the change in morphology of the interfacial layers; (3) the removal of additional relaxation processes that follow the bounding of filler particles to polymer; (4) the change in the localization of zones of plastic deformation; (5) the formation of pores, which

contributes to the macroscopic strain of the samples; (6) the fibrillation of pore walls; (7) the reorientation of anisotropy filler particles; (8) the better heat subtraction; and (9) the better physical contact between filler particles and the polymer (28). In composites prepared from a blend of PP/HDPE (80/20) with 5 wt% of ethylene–propylene (EPR) with respect to the polyolefin blend and with 30 wt% of $CaCO_3$ treated with Lica 12 at 1 wt% with respect to the filler, both the Young's modulus and elongation at break decreased (from 2855 to 2065 MPa, and from 17% to 13 %, respectively) and the tensile strength increased (from 26.7 to 29.5 MPa), but the impact strength remained constant (28–29 $J\,m^{-1}$) (13). However, in blends of a copolymer of PP and high density propylene (HDPE) with 50 wt% of $CaCO_3$ and 0.5wt% of a coupling agent of the titanate type, an increase in the impact strength from 60 $J\,m^{-1}$ in the pure copolymer to 328 $J\,m^{-1}$ in the composite with treated filler was obtained (4).

An ethylene–octene copolymer has also been used in PP composites containing $CaCO_3$ of particle sizes of about 1.0, 0.6, and 0.05 μm. The toughening of PP with the elastomer and filler led to a system with higher stiffness and higher impact energy. At the same time, the smaller particle size (0.05 μm) was the most effective for the toughening of the polymeric matrix. From these studies of composites based on PP/elastomer/$CaCO_3$, it was found that the ligament thickness between neighboring elastomer particles is the key parameter determining whether the material would be brittle or tough.

Lei and Zhou (29) used a low molecular weight HDPE modified by UV (uHDPE) as compatibilizer and tested the use of up to 5 wt% of modified HDPE in substitution of HDPE. They found increased impact strength and yielding strength, from 210 to 400 $J\,m^{-1}$ and from 16.7 to 26.4 MPa, respectively. On the contrary, as the amount of the compatibilizer was increased further, the impact strength decreased and the yielding strength remained constant (Table 4.1). This

Table 4.1 Mechanical Properties of HDPE/uHDPE/$CaCO_3$.

Composition of the samples of HDPE/uHDPE/$CaCO_3$	Yielding strength, MPa	Impact strength, $J\,m^{-1}$
70/0/30	16.7	210
69/1/30	25.3	354
67/3/30	25.2	431
65/5/30	26.4	400
60/10/30	26.4	221
50/20/30	26.5	135
40/30/30	27.1	79
30/40/30	27.0	73
20/50/30	27.0	55
10/60/30	27.0	32
0/70/30	28.7	32

From Reference (29) with Permission from Elsevier.

behavior is attributed to chemical reactions between carboxyl groups of the modified HDPE with $CaCO_3$ particles during mixing in preparation of the filled material.

Other ways of modifying the $CaCO_3$ particle's surface is by polymerized acetylene plasma, which gives rise to a better composite system with increased toughness compared to that of the unmodified filler. The plasma polymer product possibly contains both hydrophobic and hydrophilic groups with properties similar to those of the polypropylene matrix and to the filler surfaces, and hence it can be effective in improving interfacial/interphase properties between filler particles and the matrix polymer (7).

4.2.4 Thermal Properties

Studies on the crystallization behavior (30) and thermodegradative analysis of these composites (14) have also been performed. Mitsuishi et al. (30) demonstrated that the particle size (1.0, 4.5, and 30 μm) strongly affects the crystallization temperature (T_c) of the PP in the composites. The increase in T_c was found to be due to the fact that the activity of the particle surface increases with a decrease in the particle size. However, the use of a surface modifier in the $CaCO_3$ particles (alkyl dihydrogen phosphates) reduces the increase in T_c with the filler content. This fact was attributed to the relaxation of the resistance of the polymer chain movement at the PP–$CaCO_3$ interface and the restriction of rapid crystallization. Hence, it can be inferred that the crystallization effectiveness is the result of the interactive adhesion of the particle surface and polymer matrix.

The overall crystallization rates of PP nanocomposites containing 1–3 wt% of $CaCO_3$ were analyzed under isothermal conditions by differential scanning calorimetry. The experimental data of the isothermal bulk crystallization rate were analyzed according to the theory of phase transformation proposed by Avrami, which relates the time dependence of the overall change in crystallinity. The values of Avrami index are equal to 2, independent of both temperature and composition. This value suggests a heterogeneous nucleation coupled with dimensional growth of the crystals (31).

Thermodegradative studies of polyolefin composites (PP/HDPE (80/20)) with 30 wt% of $CaCO_3$ treated with Lica 12 at 1 wt%, as well as the use of an EPR were carried out by González et al. (14). They determined that if EPR is not introduced into the composites, the values of the E_a (activation energy) are higher when compared with those of the composites to which EPR was added. The reported values of E_a are 198 kJ mol^{-1} for the composite of PP/HDPE and untreated filler and 218 kJ mol^{-1} for the composite with the treated filler. When EPR was incorporated into the composite, the Ea values were 160 and 192 kJ mol^{-1} for the composites of PP/HDPE/EPR with treated and untreated filler, respectively. A very important factor determining the Ea values was found to be the degree of dispersion of the filler. This work proved that when the filler is loaded through different feeding ports into the extruder, the Ea values increase from 160 to 198 kJ mol^{-1}.

4.3 COMPOSITES OF POLYPROPYLENE AND HIGH DENSITY POLYETHYLENE WITH WOOD FLOUR AND SISAL FIBERS

During the last years, there has been a considerable increase in the use of composites made with organic fillers and plastic matrices, specially because of their low costs and multiple applications such as in interior panels of automobiles and aerospace industry (32–38). This growth is attributed to the fact that the organic fillers have some advantages. Among them, the following deserve attention: lower density, less processing equipment abrasion, and renewable resources.

The use of wood flour (WF) as a filler is a choice offering an economical solution for the increasing costs of wooden products and construction materials. There is a considerable commercial interest in thermoplastic composites filled with wood flour due to the potential opportunities of combining the attractive characteristics and properties of both components. The product developed has the aesthetical appearance of wood and the processing capability of thermoplastics. The material can be considered as an easily attainable (natural) option, is competitive as far as price is concerned, and is convenient for a wide range of applications. In addition, sisal is a highly resistant and rigid natural fiber, mainly used in applications ranging from manufacturing of ropes and yarns for carpets, to different textiles and handicrafts.

Thanks to their high tensile strength, cellulose fibers are excellent reinforcing elements for the preparation of polymer composite materials. In addition, given their elastic nature, they can be more easily processed than some more rigid fibers such as fiberglass. Among the main tensile properties of these organic filler, the following can be mentioned (39,40): (a) sisal fiber displays a tensile strength of 510 MPa and a Young's modulus of 28 GPa; and (b) wood flour shows a compression modulus of 3.94 GPa.

As a result, wood flour, wood fibers, sisal fibers, cane trash, and so on, are taking an increasing share on the market of reinforced plastics and filled polymers, thus displacing fiberglass and other mineral reinforcements (41).

Disadvantages associated with the use of natural fibers as reinforcement in thermoplastics are the result of a lack of good interfacial adhesion and a poor resistance to humidity absorption, since cellulose fibers are hydrophilic and thermoplastics are hydrophobic.

For this reason, it is important to perform some chemical treatments to the filler with the suitable and easy-to-use substances. Some researchers (15,34,37,38,42–45) have tested treatments with alkalis, silane, filler acetylation, as well as the use of some compatibilizing agents that can help improve the physical and mechanical properties of the composites.

Chemical modification of these fillers involves various chemical treatments with the aim of reducing the number of –OH groups of the fillers or to introduce cross-linking by physical and chemical bonds between the fillers and the matrix. The stability of new structures depends on the nature of the bonds. It has an important influence on the mechanical properties of the composites.

4.3.1 Mechanical Properties

The vast majority of the studies reported in the literature analyze the mechanical behavior of composites containing untreated wood flour, as well as the treatment of the wood flour or the addition of compatibilizing agents or maleic anhydride-functionalized polyolefins (34–38,43,45–50).

The mechanical behavior of composites of PP with WF of different average particle sizes indicates that the Young's and flexural modulus increase with the wood flour content, but change in these parameters with particle size is not significant (34,36–38,46,50). This is the common behavior of composites filled with natural fillers (Fig. 4.3). Fillers are said to be much stiffer than polymer matrices and consequently they add stiffness to the final product. Figure 4.4 unfolds a general decrease in the tensile strength (stress at break) due to poor interaction between the polymer and the filler (Fig. 4.5a) and dispersion (Fig. 4.5b). Interfacial adhesion is low in those composites, and the material losses its toughness. It is known that the matrix adds toughness to a composite, and therefore an increase in filler content will result in a decrease in matrix content, resulting in a smaller amount of matrix to withstand the applied stress.

As Fig. 4.5 shows, the addition of wood flour to a polymer gives rise to a concentration of holes, which were left after the filler particles are de bonded from the matrix. The proximity of the holes indicates that the filler exists in the form of bubbles, which could not provide efficient stress transfer from the matrix. In natural filler composites, weak adhesion may result from incompatibility between the hydrophilic natural fillers and the hydrophobic polymer. The use of different chemical treatments to modify the interface can improve adhesion and thus enhance the tensile properties. These changes are observed when the filler is treated in different

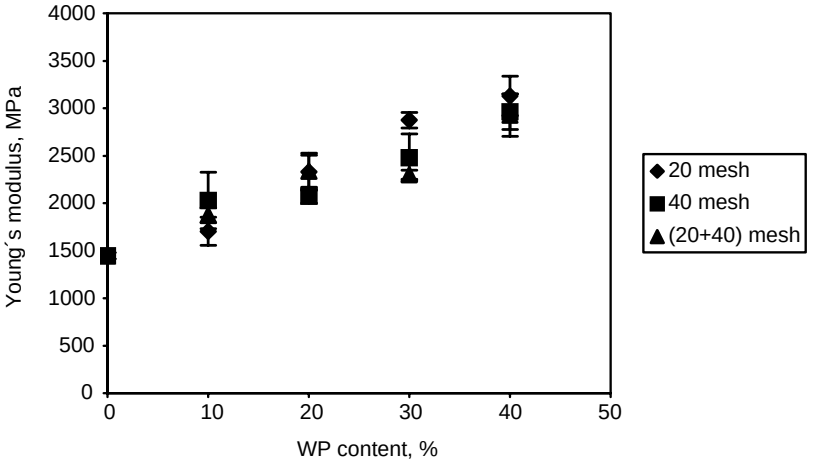

Figure 4.3 Young's modulus behavior of PP/wood flour at different content of wood flour and different particle sizes. (From Reference 46 with permission from Innovación Tecnológica.)

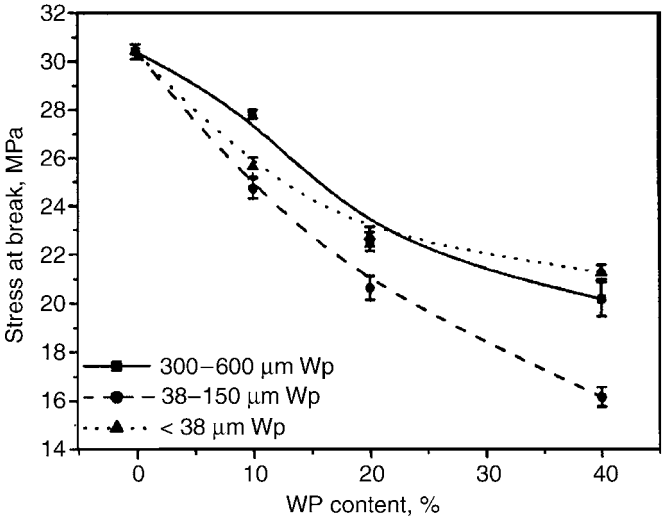

Figure 4.4 Tensile strength (stress at break) behavior of PP/wood flour at different content of WF and different particle size of filler. (From Reference 50 with permission from Wiley Periodicals.)

ways: sodium hydroxide at different immersion times, acetylation, vinil-tris-(2-metoxietoxi)-silane, and use of polypropylenes functionalized with maleic anhydride (PP-g-MA) as compatibilizers (34,35,43,48,50,51).

Table 4.2 shows the effect that the different treatments and compatibilizers produce on the mechanical properties of the composites. All the treatments showed the same tendency of slight increase in the tensile modulus and the tensile strength of the composites. Morphological studies showed that the use of PP-g-MA and silanes

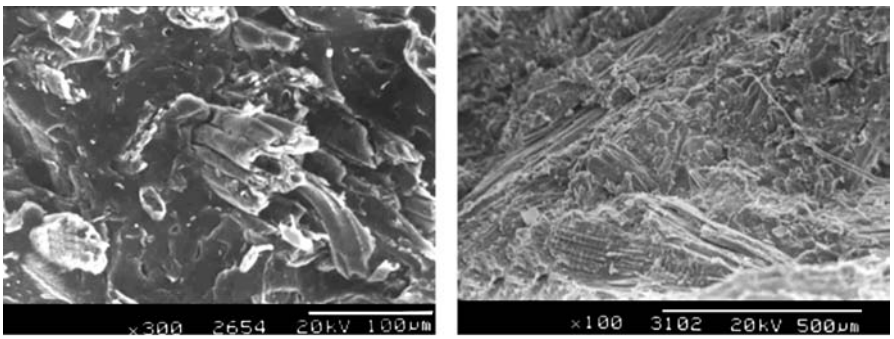

(a) (b)

Figure 4.5 SEM micrographs of the fracture surface of PP with 40 ppc of wood flour. This wood flour is a mixture of particle size of 50 wt% of 20 and 40 mesh. (**a**) Adhesion, and (**b**) Dispersion. (From Reference 46 with permission from Innovación Tecnológica.)

Table 4.2 Results of the Mechanical Tests on PP and PP/WF[a] Composites.

Simple	E MPa	σ_r MPa	ε_r %	IS, J m^{-1}
PP	1448 ± 33	25 ± 1	23.4 ± 8.7	26 ± 2
PP/untreated WF	3016 ± 193	37 ± 1	3.1 ± 0.1	15 ± 1
PP/treated WF with NaOH (1/2 h)	3211 ± 89	38 ± 1	2.7 ± 0.3	15 ± 1
PP/treated WF with NaOH (1 h)	3125 ± 141	38 ± 1	2.6 ± 0.1	16 ± 1
PP/treated WF with silane	3177 ± 310	36 ± 1	2.7 ± 0.1	12 ± 1
PP/WF/Polybond 3150	3270 ± 159	39 ± 1	1.2 ± 0.1	13 ± 1
PP/WF/Polybond 3200	3010 ± 228	43 ± 1	2.1 ± 0.1	11 ± 1

From Reference 45 with permission from Elsevier.

improved the polymer–WF adhesion and the dispersion of the particles, while the alkaline treatment only improved their dispersion (34).

When the WF surface was treated with silane, the alkoxy groups of the silane form silanols, which form many hydrogen bonds with the –OH groups of the cellulosic filler polymer. The remaining active groups R of the silanes can adhere to the PP only with weak Van der Waals forces. Both hydrogen bonds and Van der Waals forces are insufficient to provide strong interactions between the filler and the polymer (36).

When PP-g-MA was used, interactions between the anhydride groups of the maleated PP and the hydroxyl groups of the natural fillers can overcome the incompatibility problem. Mechanical interlocking may occur between the wood flour and coupler (PP-g-MA) and between the polymer and coupler. In view of the results showed in Table 4.2, it can be inferred that only a PP-g-MA with a proper balance of grafting degree and molecular weight can achieve a better performance in the tensile behavior, because the maleated coupler needs enough acid functionality to attract the filler and enough molecular weight to entangle or crystallize into the base polymer (50).

In the wood flour acetylation, a possible reaction of the wood flour hydroxyl groups with the carbonyl groups of the anhydride can take place. The acetylation alters the specific configuration of the wood component due to the substitution of the hydroxyl groups. The acetyl groups would replace hydroxyl groups on the filler surface. Thus, this would produce more hydrophobic surface as compared to that of the unmodified wood flour, and therefore, more kindred to the polymer (43).

The alkaline treatment improves the characteristics of the particle surface of the filler by removing impurities, thus producing a rougher topography, which results in a sort of polymer–filler interaction.

As discussed in the different ways of modifying the interface to improve the polymer–filler interactions, other additional factors are necessary in order to have an effective interaction and a substantial improvement in the mechanical behavior. Among them, the following are worth noting: formation of a silane monolayer in the WF particles' surface, acetylation of the surface and its degree, grafting degree, and molecular weight in the PP-g-MA.

Another variable affecting the mechanical behavior is the water absorption by the composite. This absorption is modified by the treatment performed on the wood flour surface. The functionalized PP, the acetylation, and the use of silane displayed lower rates of water absorption compared to those of the untreated WF composites. The alkaline treatments favored the water absorption, since the wood particles became more hygroscopic. According to Marcovich et al. (52), moisture sorption is mainly due to hydrogen bonding of water molecules to the hydroxyl groups on the cell walls of the wood. In fact, mercerization increases the accessibility of the water molecules to reactive regions through the enlargement of the specific surface area; thus, the hygroscopicity of the filler is increased.

As it is the case in wood flour, the treatment of the sisal fiber surface is important to modify the interactions between the polymer and the filler, to achieve improvements in the tensile behavior of the composites. A comparative analysis of the effects of the indicated different treatments (immersion in NaOH, filler treatment with silane, use of PP-g-MA) on the mechanical properties of the PP/WF composites (40 phr of WF) and PP/sisal fiber (20 phr of sisal fiber) was made by Albano et al. (34). The composites with sisal fiber showed a lower Young's modulus, higher elongation at break, and high impact strength (Figs. 4.6–4.8). In composites of low density polyethylene (LDPE) filled with sisal fiber, it has been determined that there is an optimum in the fiber length (5.8 mm) that remained independent of the type of treatment performed on the sisal fiber. The studied treatments were immersion of the fiber in NaOH, use of isocianates, dicumil peroxide, benzoil peroxide, and potassium permanganate. The tensile behavior, specifically the tensile strength and Young's modulus values, followed the order following: dicumil per-

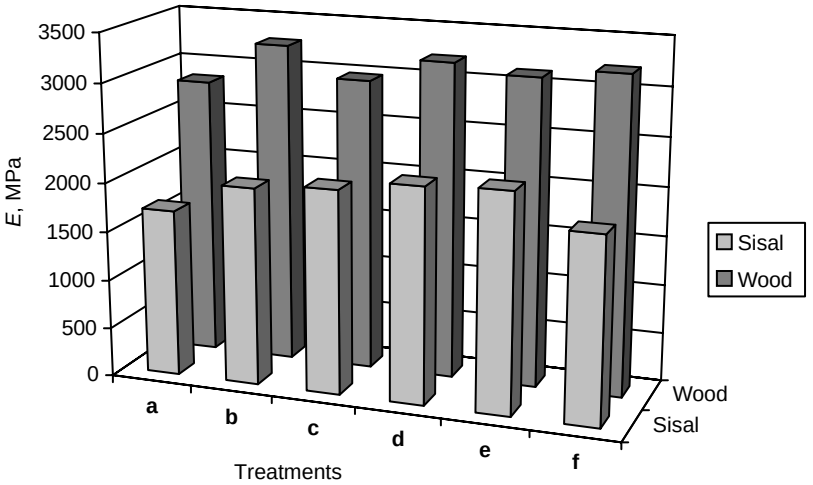

Figure 4.6 Comparative effect of various treatments on the tensile modulus for PP/sisal fiber and PP/wood flour composites: (**a**) PP/untreated filler; (**b**) PP/filler/Polybond 3150; (**c**) PP/filler/Polybond 3200; (**d**) PP/filler treated with NaOH for half 12; hour; (**e**) PP/filler treated with NaOH for 1 h; and (**f**) PP/filler treated with silane. (From Reference 34 with permission from Springer-Verlag.)

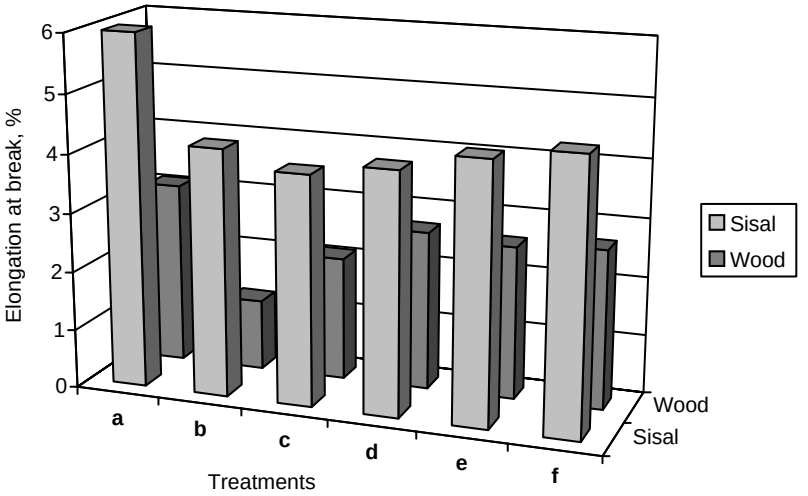

Figure 4.7 Comparative effect of various treatments on the elongation at break for PP/sisal fiber and PP/wood flour composites: (**a**) PP/untreated filler; (**b**) PP/filler/Polybond 3150; (**c**) PP/filler/Polybond 3200; (**d**) PP/filler treated with NaOH for half hour; (**e**) PP/filler treated with NaOH for 1 hour; and (**f**) PP/filler treated with silane. (From Reference 34 with permission from Springer-Verlag.)

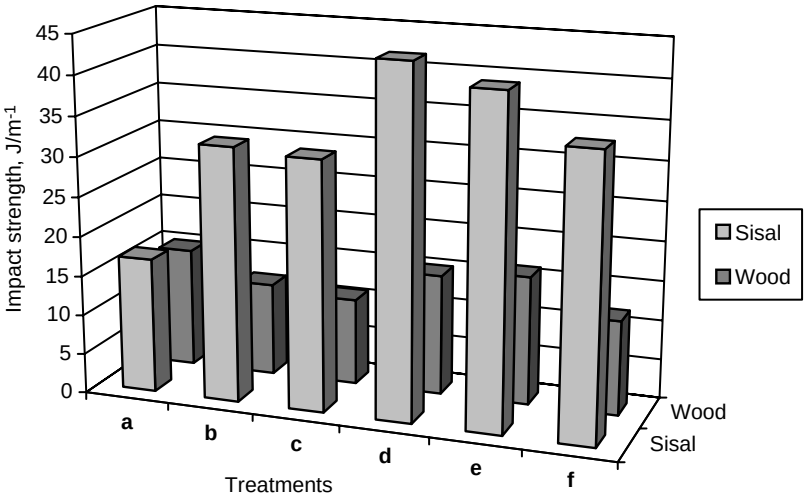

Figure 4.8 Comparative effect of various treatments on the impact strength for PP/sisal fiber and PP/wood flour composites: (**a**) PP/untreated filler; (**b**) PP/filler/Polybond 3150; (**c**) PP/filler/Polybond 3200; (**d**) PP/filler treated with NaOH for half hour; (**e**) PP/filler treated with NaOH for 1 h; and (**f**) PP/filler treated with silane. (The composites with sisal fiber showed a hinge type fracture and probes of the composite with wood flour showed full fracture.) (From Reference 34 with permission from Springer-Verlag.)

oxide > isocianate > benzoil peroxide > potassium permanganate, indicating that the differences found between the peroxides used were a consequence of their relative decomposition rates (33–34).

The blending of PP with HDPE is very important, since each of these polyolefins has attractive properties. Albano et al. (53) demonstrated that it is possible to use up to 30 wt% of HDPE in blends with PP without producing any significant detriment in the mechanical properties. From the tensile behavior of composites of PP/HDPE/sisal fiber, it was inferred by these and other authors (51) that the fiber acetylation gives rise to an increase in the Young's modulus and the tensile strength of the composites. Figure 4.9b and c shows how the fiber surface adhesive characteristics are improved by removing natural and artificial impurities. Figure 4.9c also shows formation of microfibers from the acetylated sisal fiber. This treatment produced an improvement in the wettability property and increased the effective surface area available for the contact with the matrix. It also reduced the fiber diameter, thereby increasing the aspect ratio.

4.3.2 Thermal Properties

Studies on the crystallization behavior and analysis of the thermodegradative characteristics of these composites were also performed (46,50,54,55).

In PP–wood flour composites, an increase in the WP content leads to higher enthalpy values. This fact indicates an increase in the crystallinity degree of the material. When WP is introduced into the PP matrix, it settles in the amorphous region, and as a result new zones are formed around the WP particles through epitaxial crystallization on their surface. The melting peak temperatures of the composites are somewhat lower than that of pure PP, indicating a decrease in the lamellar thickness, which may also be the result of epitaxial crystallization on the WP surface (50). The wood flour addition also increases the crystallization temperature of the PP from 113 to 119°C for WF contents up to 40 wt%, indicating a nucleating ability of the WF surface in the crystallization process of PP (46). Thermodegradative studies of these PP and PP/HDPE composites with 20 wt% of acetylated and non acetylated sisal fibers were carried out using the kinetic models of Horowitz–Metzger (56) and Reich–Stivala (57) to understand their degradative process (54). The acetylated sisal fiber showed an activation energy (Ea) value of 119–171 kJ mol^{-1}, which is higher than that of the material without acetylated sisal fiber (98–148 kJ mol^{-1}). The values depended on the kinetic model used. This fact was attributed to the replacement of the OH groups of the fiber by bulkier groups, which restrict the segmental mobility, increasing the main chain stiffness of the cellulose (one of the main components of the sisal fiber).

A decrease in the Ea values of PP with the addition of sisal fibers was also reported. This effect is less pronounced when the fiber was acetylated. The values of Ea changed from 259 kJ mol^{-1} for the pure polymer to 178 kJ mol^{-1} for the composite and to 187 kJ mol^{-1} when the fiber was acetylated. A similar behavior was observed for composites of PP/HDPE with filler, with and without the addition of EPR rubber.

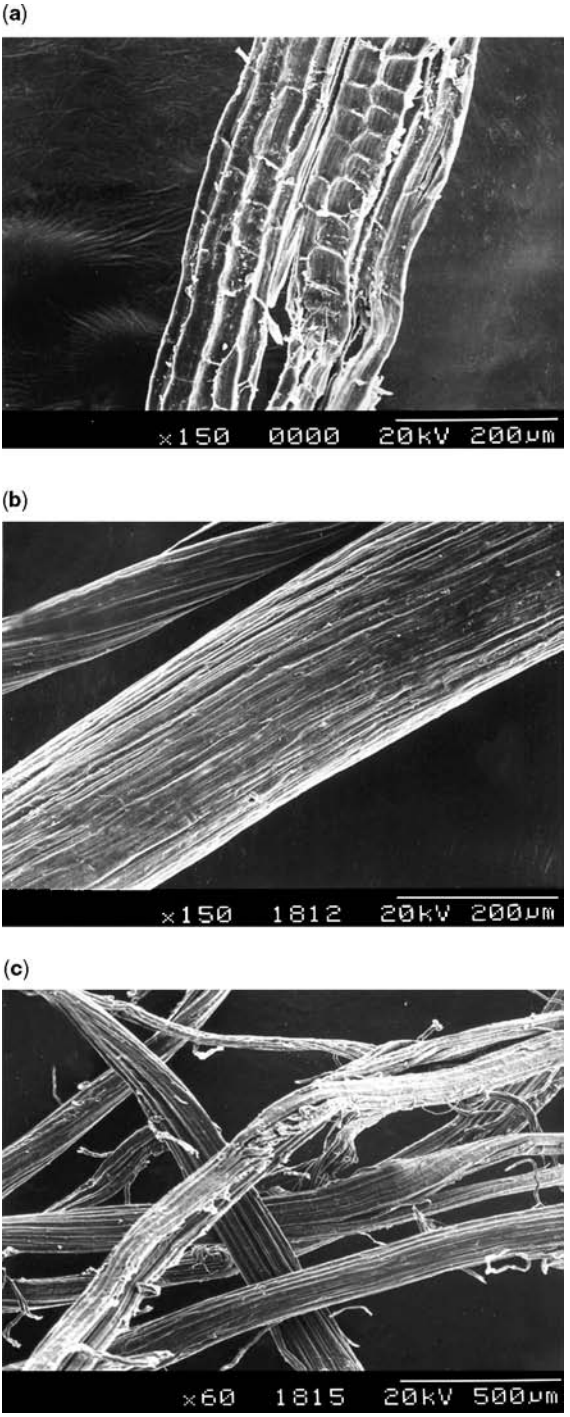

Figure 4.9 SEM micrograph showing untreated (**a**) and treated (**b**, **c**) sisal fiber, at different magnifications. (From Reference 51 with permission from Society of Chemical Industry.)

Table 4.3 Activation Energy (E_a) and Pre-exponential Factor (A) Values at Constant Conversion, Using Romero–García Method for the PP with Untreated Sisal Fiber.

Conversion (adm)	E_a, kJ mol^{-1}	A min^{-1}
0.1	99	5.2×10^4
0.3	213	6.6×10^{14}
0.5	224	4.1×10^{15}
0.7	187	9.6×10^{12}
0.9	145	1.1×10^{10}

(From Reference 55 with permission from Springer–Verlag.)

A more thorough study of the thermal stability in PP composites with non acetylated and acetylated sisal fibers was carried out using the kinetic model of Romero–García (58) to determine the probable decomposition mechanisms that could be taking place in the composites (55). The initial decomposition temperature (T_{id}) varies between 590 and 650K for the composites, being slightly higher for those composites made with acetylated sisal fiber, due to the presence of functional groups in its surface. Tables 4.3 and 4.4 show the Ea values of composites of PP with acetylated and non acetylated sisal fibers, at different conversions. It can be seen that the Ea values increase and then decrease as a function of conversion, and that a low value of Ea (99 kJ mol^{-1}) is detected at 0.1% of conversion, which is in agreement with the corresponding Ea value of the sisal fiber obtained by Albano et al. (54). The variation in conversion as a function of temperature clearly implies that there is a change in the decomposition mechanism as a function of conversion. The change in the reaction mechanism is a reflex of the existence of multiple competing steps in the polymer degradation. Additionally, they found that Ea values of the composite of PP with untreated sisal fiber and of untreated fiber alone are lower than that of the composite with treated fiber and of treated fiber alone, at the different conversion levels.

Table 4.4 Activation Energy (E_a) and Pre-exponential Factor (A) Values at Constant Conversion, Using Romero–García Method for the PP with Treated Sisal Fiber.

Conversion (adm)	E_a, kJ mol^{-1}	A min^{-1}
0.1	99	7.2×10^5
0.3	299	4.9×10^{20}
0.5	255	2.5×10^{17}
0.7	205	5.6×10^{13}
0.9	154	1.1×10^{10}

(From Reference 55 with permission from Springer-Verlag.)

The dominant decomposition mechanisms are as follows:

PP/treated sisal fiber: F1 (first-order random nucleation), D3 (diffusion three-way transport), and R3 (limiting surface reaction between both phases three dimensions), from which it could be inferred that the decomposition process starts with a nucleation in the active sites (F1) and then continues with reaction processes in three dimensions on the limiting surface (R3) and diffusion on the smaller molecules (D3), which would correspond to the gases formed in the interface during the decomposition process.

PP/untreated sisal fiber: F1, D2 (diffusion two-way transport), and R3.

4.3.3 Influence of the Gamma Radiation on the Behavior of the Composites

The gamma radiation effect is another important aspect that could be analyzed in these composites of wood flour and sisal fiber. It is well known that gamma radiation modifies the chemical structure of the components that form the composites and consequently affects their mechanical and thermal behavior, the formation of radicals determined by ESR, and the kinetic analysis of the decomposition process.

Through ESR, the development of the carbonyl group of aldehyde type on the PP/sisal fiber and PP/wood flour composites (at 20 and 40 wt%, respectively) in the dose interval from 10 to 70 kGy at a dose rate of 4.8 kG h^{-1} in air and room temperature is analyzed. The formed radicals increase with the radiation doses and are produced in larger proportions in the sisal fiber composites. This is attributed to a chainscission process, which is the main mechanism of decomposition of the PP (59).

The tensile properties (tensile strength (MPa), elongation at break (%), and impact strength (J m^{-1})) of both types of composites (PP/sisal fiber; PP/wood flour) showed a similar behavior. In other words, initially there is an increase of 38% and 35% the tensile strength and elongation at break, respectively, for the PP/wood flour composite values and an increase of 24% and 25%, respectively, for the PP/ sisal fiber composite at low radiation doses (<10 kGy). Studies carried out by Slovokhatova et al. (60) on irradiated PP showed that the consumption of unsaturated groups at low irradiation doses is related to a slight cross-linking. However, Guan (61) revealed that irradiated PP exhibits higher hydrophilicity than nonirradiated PP due to the oxygen content in the irradiated samples. This could give rise to a higher polymer–filler interaction, since the filler has a high concentration of OH groups which may produce interactions of the hydrogen-bonding type between the filler and the PP. This interaction is revealed through the widening of the band in the 3300 and 3400 cm^{-1} region of the infrared spectrum of PP. Thus, surface oxidation of the PP could increase its adhesion to the filler. Differential scanning calorimetry studies determined that lower doses (<10 kGy) do not produce changes in the melting (Tm) and crystallization (T_c) temperatures. On the contrary, changes in T_m from 165 to 157°C for the composite with wood flour and from 165 to 154°C in the PP/sisal fiber composite was found as the absorbed dose was increased (59).

Generally, when macromolecules are irradiated (polymers, composites), the total energy deposited in the sample by the irradiation is responsible for the modifications occurring within the material. As a consequence, the evolution of physicochemical properties of theses systems is controlled by the integral dose (D_i) and the irradiation rate (D_r). Since the radiation rate was constant, it was not consider as a variable and was not taken into consideration in the presented model. Therefore, if degradation criteria are represented by the modification of a physical property P, then the modification law of the property can be represented as $P = \alpha P_o\, g(D_i)$, where P_o is the value of the property of the material not subjected to radiation and is α an adjustment factor. The deviation of α from unity is a measure of the linear contribution to the degradation process and g is a function of the radiation or absorbed doses (D_i).

According to Chipara et al. (62,63), a different behavior such as degradation and cross-linking can be observed in both matrix and filler during irradiation, which can be represented by means of the relatively simple expressions capable of describing or indicating the type of process taking place when the composite is submitted to the effects of irradiation.

Through simple models (mathematical adjustments), the kinetic behavior of the mechanical properties and the concentration of free radicals in PP/wood flour and PP/sisal fiber composites irradiated at low doses (<10 kGy) are indicative of a complex degradation process, implying the possibility of cross-linking and chain-scission reactions, both in the polymer and in the filler. Consequently, it can be concluded that the cross-linking reactions are predominant. The behavior observed at higher irradiation doses means that both types of reactions, cross-linking and chain scission, occur, the latter reactions being the prevailing ones. The analysis of the tensile properties, elongation at break, tensile strength, and Young's modulus show that there is a predominance of the cross-linking reactions at low doses and coexistence of both mechanisms (cross-linking and chain scission) at higher doses (64).

In composites made of blends of polyolefins PP/HDPE (80/20) with 40 wt% of wood flour (50/50 mixture of 20 and 40 mesh), the generation of free radicals by ESR, the tensile behavior, and also the kinetic analysis (65–67) is analyzed. The Young's modulus decreased when the samples were irradiated at doses equal or lower than 50 kGy (Fig. 4.10) especially as a consequence of chain scissions in PP and due to the destruction of crystallites in HDPE, which act as ''physical cross-links'' (68,69). The behavior of the Young's modulus is very similar to that of the density. Initially, a drop occurs, which is consistent with the destruction of the crystalline region in the polymer, and when almost all crystalline zones have been destroyed, density rises again as a result of the structural change in the HDPE, that is, the formation of double bonds and cross-links, which bind the molecules more closely together and lead to a tighter packing of the polymer chains (68). Therefore, Young's modulus adjusts to a cubic polynomial equation, indicating a more complex dependency of this property on the radiation dose. A similar behavior was found in the elongation at break. This indicates that polymers have influence not only on the composite behavior against radiation but also on the filler characteristics and the filler–polymer adhesion.

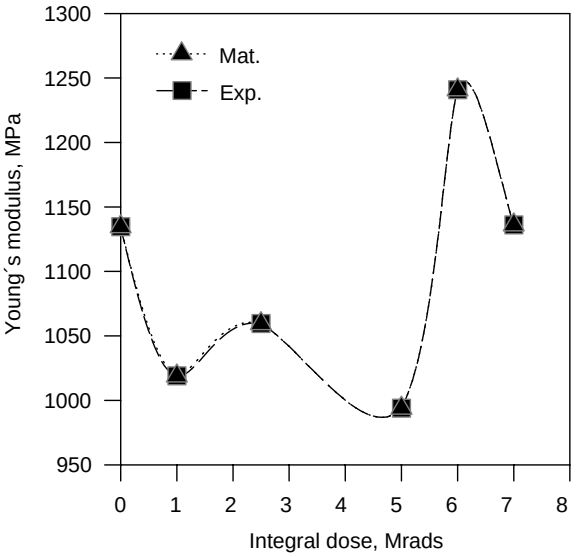

Figure 4.10 Young's modulus behavior of PP/v-HDPE/wood flour at different integral doses of irradiation. Exp.: experimental values; Mat: mathematical modeling. (From Reference 65 with permission from Elsevier.)

Allyl, alkyl, and carbonyl radicals are generated due to the radiation of the PP/HDPE/wood flour composites. The ESR spectra, the radical concentration, the Hpp factors (peak-to-peak resonant line width), and K (shape factor) were analyzed. The position and structure of the resonance line, as well as the high stability at room temperature of the radicals observed in the samples, support the identification of the peaks. No resonance signal at $g = 4$ ascribed to free radical pairs was recorded, suggesting that their concentration (if they exists) is fairly low. No resonance signal near $g = 2$ ascribed to free radicals formed in gamma-irradiated cellulose (69) was recorded, suggesting that there were no grafting processes or chemical interactions between polymers and wood flour. The resonance line parameters (line, widths, and line shape factor) suggested that dipolar interactions among free radicals were dominant as gamma irradiation doses increase (67).

4.4 COMPOSITES OF POLYPROPYLENE AND HIGH DENSITY POLYETHYLENE WITH HYDROXYAPATITE

The demand in the market for devices made of biomaterials for medical applications is growing fast nowadays. This fact has created the necessity of making products with specific characteristics to compete in the market. At present, the tendency in the field of biomaterials is to combine two materials with different properties to obtain a product with different characteristics. Composite systems based on a polymeric matrix and ceramic fillers present advantages due to their low cost and weight and improved processability.

The preparation of composites based on polyolefins and a biocompatible ceramic, such as hydroxyapatite (HA), is important due to their potential application. HA is a material that can be used as a substitute of human bones and teeth because it is one of their major constituents. Hydroxyapatite is a calcium phosphate whose composition is $(Ca_{10}(PO_4)_6(OH)_2)$ with a calcium/phosphorus ratio (Ca/P) of 1.67. It is a material that shows osteoconductive characteristics, so it is considered a bioactive material (70). However, it has an important disadvantage, which is its low tensile, compression, and fatigue strengths (Young's modulus: 85 GPa; tensile strength: <1MPa), when compared to human bone's properties (Young's modulus: 7–30 GPa; tensile strength: 50–150 MPa).

However, polyolefins such as HDPE show Young's modulus values that vary between 1000 and 1400 MPa depending on the polymer characteristics. HDPE can be used in composites with HA for biomedical applications due to its low toxicity.

4.4.1 Influence of the Composite Preparation Methods on Its Mechanical Properties

Composites of HDPE with commercial HA, varying in particle sizes and using the filler in its sintered and non sintered versions, were obtained by melt mixing in an extruder which generated high shear forces to disperse the filler particles into the polymeric matrix. The Young's modulus of the composites shows a significant increase when a HA of particle size of approximately 4 μm was used. This increase varies from 4290 to 6500 MPa with the HA volumetric fraction (0–40 vol%). However, the tensile strength remains approximately around 19 MPa. The necking of the specimens disappeared at filler contents higher than 20 vol%, unfolding a ductile–brittle transition at fracture. This was detected by the flaw type fracture surface (70–75).

The mechanical behavior in flexion of these composites, specifically their modulus values, increases in even higher proportions if high molecularweight PEs are used as matrices (M_w of 250,000 and 270,000) or if those PEs are cross-linked. The modulus increased with the HA content (two different particle sizes, 4.14 and 7.32 μm) varying from 440 to 930 MPa for pure polyethylenes to 4920 and 6700 MPa for the composites with 45 vol% of HA. The flexural strength varied from 20 to 40 MPa. Therefore, the molecular HDPE weight of, as well as the HA particle size, significantly influences the mechanical properties of the composites (76).

In general, the above-mentioned works point out the need of obtaining a good dispersion to improve the behavior of the final product, from where a biomedical application could be possible. In general terms, most of the cited works reported the preparation of the HA composites by melt mixing in an extruder. Hence, it is necessary to evaluate other mixing techniques to analyze the possibility of achieving a better performance of these materials.

The tensile behavior of composites obtained by different methods of mixing to achieve a better dispersion of the HA into the HDPE matrix with HA of nanometric

Table 4.5 Tensile Properties of HDPE/HA Composites Obtained by Extrusion.

Filler content, %	Young's modulus, MPa	Tensile strength, MPa	Elongation at break %
0	1012 ± 79	10.1 ± 0.6	1166 ± 57
10	1032 ± 132	25.7 ± 1.7	7.2 ± 0.8
20	1028 ± 154	23.3 ± 1.9	7.2 ± 0.7
30	1166 ± 183	21.9 ± 1.6	4.9 ± 0.3

size (20×60 nm) synthesized in house was analyzed (77–80). Tables 4.5 and 4.6 show the tensile properties of HDPE/HA composites obtained either by solution or by extrusion. The Young's modulus values are higher in composites prepared by solution compared to those obtained by extrusion. The difference was found to be about 11% for the 10 and 30 wt% composites, having a maximum of 35% in the case of HDPE with 20 wt% of HA. A similar behavior was noticed in the tensile strength, which is the difference between the two mixing methods about 22%, 36%, and 21% for the 10, 20, and 30 wt% composites, respectively.

From the observed behavior of the Young's modulus and tensile strength, it can be inferred that the use of the solution method of blending provides a better dispersion and, as a consequence, an improved homogenization of the blend. At the same time, agglomerates began to form at concentrations of HA higher than 20 wt% due to the amount and dimensions of the filler. This phenomenon caused a decrease in the tensile parameters. Figure 4.11 shows the micrograph of such composites with 20 wt% of HA prepared in solution. The HA particles are very homogeneously distributed. Figure 4.12 shows the micrograph of composites with 20 wt% of HA prepared by extrusion. Some agglomerates of approximately 0.4 μm are clearly seen, homogeneously distributed into the material. Figure 4.12b shows an enlargement of a region of Fig. 4.12a, where these agglomerates can be clearly noticed. This morphology is consistent with the tensile behavior obtained in the composites. The results show that 20 wt% of HA is the optimum filler content where agglomerates are not formed when the composite is made in solution.

The values of the Young's modulus and tensile strength of the composites obtained through extrusion (71,72) were compared with those obtained by solution (79). The tensile strength of the latter showed a higher value (17 MPa versus 32 MPa)

Table 4.6 Tensile Properties of HDPE/HA Composites Obtained by Solution.

Filler content, %	Young's modulus, MPa	Tensile strength, MPa	Elongation at break, %
0	1108 ± 72	11.0 ± 2.2	249 ± 92
10	1141 ± 56	31.3 ± 2.5	11.9 ± 1.5
20	1384 ± 108	31.8 ± 1.8	7.0 ± 1.1
30	1315 ± 20	26.9 ± 2.3	5.4 ± 0.8

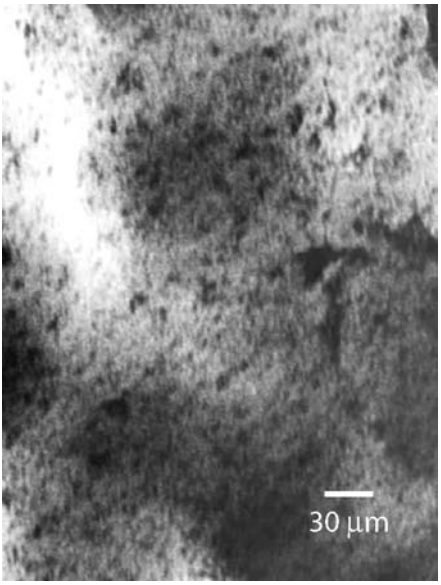

Figure 4.11 TEM micrographs of the composite with 20 wt% of HA obtained by solution. (From Reference 77 with permission from Society of Plastics Engineers.)

due to a better dispersion of the filler into the HDPE matrix. The Young's modulus values showed similar trends when the standard deviations are considered, being 1400 and 1600 MPa. If an injection molding equipment that induces an orientation in the composites is used, the Young's modulus values obtained are up to 225% higher than those of samples injection-molded traditionally (5900 MPa versus 1600 MPa, respectively) (81).

HDPE/HA nanocomposites were also prepared using an internal mixer (78), where the temperature conditions, the rotors frequency, and the mixing time (160°C, 90 rpm, and 5 min) were optimized to obtain a good dispersion (Fig. 4.13), to evaluate the possibility of neglecting the mixing via solution to eliminate the detrimental effects of the residual decalin in the composites. Decalin has a negative influence on toxicity, thereby hindering possible applications as biomedical materials. At the same time, coupling agents are usually soluble in decalin. The values of the Young's modulus and the tensile strength of the composite with 20 wt% of HA obtained by internal mixing were 1365 and 18.9 MPa versus 1380 and 32 MPa for the same composites obtained by solution.

The different tensile behaviors showed and analyzed were obtained in composites with HA particle sizes in the order of microns (70–74,76,81–83) and nanometers (77–80), which form agglomerates of up to 20 μm. This could explain why the modulus values obtained by the latter authors are not as high as expected.

Recently, Lim et al. (84) carried out a similar study in ultrahigh molecular weight polyethylene filled with HA (2–20 μm) using an internal mixer at190°C and

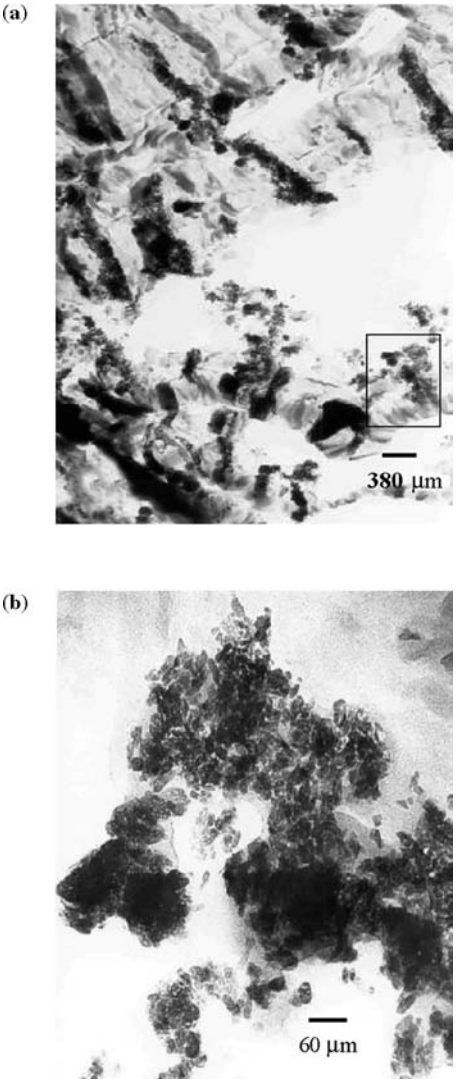

Figure 4.12 (**a**) TEM micrographs of the composite with 20 wt% of HA obtained by extrusion, (**b**) magnified detail. (From Reference 77 with permission from Society of Plastics Engineers.)

30 rpm. The Young's and flexural modulus values found in composites with 22 vol% of HA were 2.5 and 3 GPa, respectively. The tensile strength varies between 21 and 23 MPa in the HA range contents. Fang et al. (85,86) employed a different mixing procedure based on the use of paraffin as a swelling agent for the preparation of a HDPE/HA composite. Then, the composite slurry was homogenized in an ultrasonicator and the mixture was compounded using a twin-screw extruder twice at 5 and 30 rpm. The Young's modulus and tensile strength values

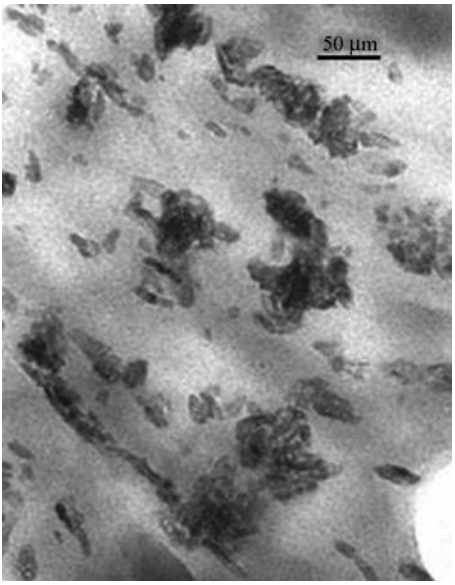

Figure 4.13 Micrograph for HDPE/HA composite prepared at 160°C and 90 rpm (obtained by internal mixer). (From Reference 78 with permission from Taylor & Francis.)

obtained in composites with 20 vol% of HA were 6.8 GPa and 26.6 MPa, respectively. These values are the highest reported so far and show a significant enhancement of the stiffness, which was close to the lower bound of cortical bones (7–30 GPa and 50–150 MPa).

4.4.2 Modification of the HA Particles Surface and Its Influence on the Tensile Properties

In any HDPE/HA composite there are two distinct phases, one is the dispersed phase and the other is the continuous phase or matrix. Therefore, only physical coupling that has resulted from shrinkage of the polyethylene around hydroxyapatite particles during composite processing is achieved between the HA reinforcement and the polyethylene matrix. Polyethylene is non polar and hydrophobic and the introduction of a polar group is mandatory to achieve an affinity between polyethylene and the hydroxyapatite. The use of silanes as HA surface treatment and the functionalization of HDPE with acrylic acid in composites of HDPE with HA gives rise to a positive effect on the mechanical behavior, especially on the Young's modulus and the tensile strength. These values could vary from 1.60 to 1.81 GPa and from 17.7 to 19.9 MPa, respectively. This effect was not significant in composites with a high content of HA (40 vol%) (87,88), where a slight decrease is actually found (from 4.29 to 3.87 GPa and from 22.7 to 23.2 MPa, respectively). There are some factors that affect the mechanical behavior of the composites of HDPE with silane-treated HA. They are as

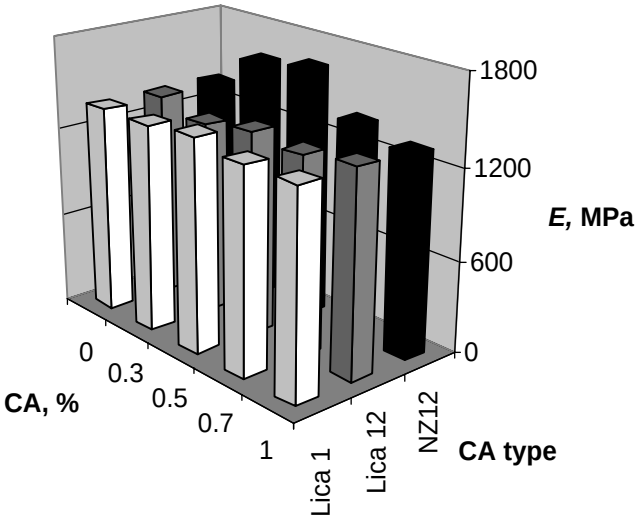

Figure 4.14 Young's modulus (*E*) of the coupled composites (CA: coupling agent).

follows: the organofunctional chemistry, the pH of the treatment solution, as well as the adoption or not of acrylic acid grafting (89,90).

Less toxic coupling agents like titanates (Lica 12) and zirconates (NZ12) as well as acrylic acid to functionalize the polyethylene have been used (78,79,89,91). These coupling agents produce a better HDPE–HA interaction, but do not produce significant changes in the tensile behavior of the composites. Using treated HA with particle sizes of the order of microns and an injection-molding equipment producing a highly oriented melt (89,91), variations of 5.9 to 6.5 GPa in the Young's modulus for composites with 0.25–0.5 wt% of titanates and of 81–86 MPa in the tensile strength for 0.75 wt% of NZ12 was reported. On the contrary, when the treated HA particle sizes are nanometric, increases in the Young's modulus and tensile strength of approximately 20–30% in composites with filler contents of 20 wt% and 0.3 and 0.5 wt% of NZ12 are obtained (Fig. 4.14 and 4.15) (78,79). Figure 4.16 shows the effect of NZ12 on the dispersion of the HA.

To analyze in a more detailed fashion whether an interaction between the HA and the HDPE matrix does exist when the NZ12 coupling agent is present, XPS studies were performed by Albano et al. (80) in those composites where the coupling agents were used at concentrations of 0.5 wt%. The analysis of the results indicates that the NZ12 possess more electronic density available to interact with HA sites. In consequence, the hydrophilic part of the NZ12 coupling agent must be covering the HA surface in a better way, thus improving the HA–NZ12 interaction. Zirconium in NZ12 is richer in electronic density than Ti in Lica, meaning that it could transfer more electron density to the hydrophobic part of the NZ12 chain, rendering it less polar and thus more alike the polymeric matrix. In this way, it can interact better with HDPE than the hydrophobic part of the Lica coupling agents.

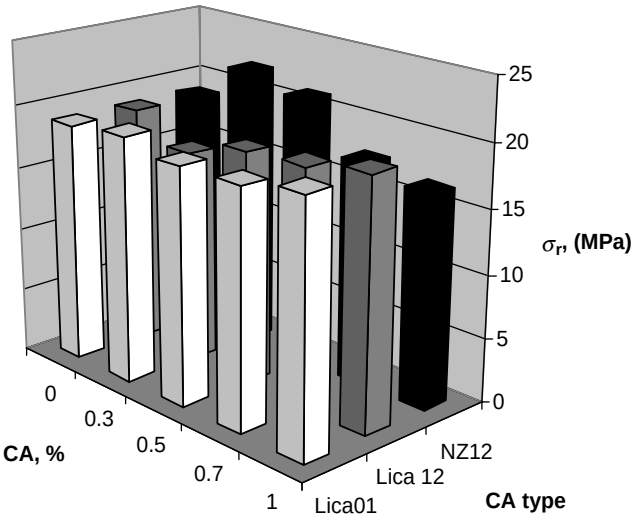

Figure 4.15 Tensile strength (σ_r) of the coupled composites (CA: coupling agent).

4.4.3 Influence of Gamma Radiation on the Composites

Radiation is widely used in material science, either to modify properties or to sterilize. The energy sources most commonly used in the radiation of biomaterials are high energy electrons, gamma radiation, ultraviolet (UV), and visible light.

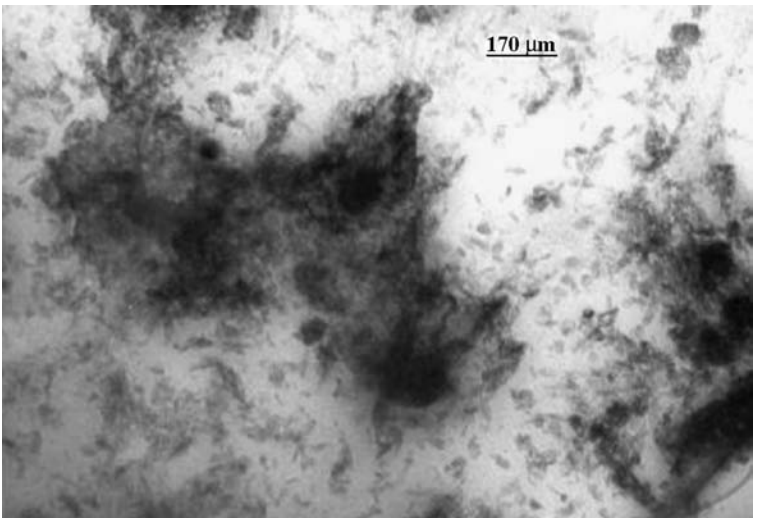

Figure 4.16 TEM micrograph of HDPE/HA composites coupled with NZ12 at a concentration of 0.3 wt%.

The exposure of a polymer to radiation, especially ionizing radiation, can lead to chain scission or cross-linking, with changes in its bulk and surface properties.

Suwanprateeb et al. (74) studied the affect of gamma radiation at a dose of 25 kGy and thermal aging (annealing) on the thermal properties and the creep of HDPE in composites with 20 and 40 vol% of HA. They observed that the thermal aging produces larger increases in the modulus than when radiation was used. These increases are 36% and 16% at 37°C, respectively. They also indicate that the radiation at that dose does not produce changes in the crystallinity degree but the thermal aging increases the crystallinity by about 4%.

Albano et al. (92) evaluated the mechanical and thermal behavior of a composite of a high molecular weight HDPE and a synthesized HA of nanometric particle size. Their composites were obtained by extrusion and also irradiated at 25 kGy with a ^{60}Co source at a dose rate of $5\,\mathrm{kGy\,h^{-1}}$ in an air atmosphere. They observed an increase in the crystallinity degree of the HDPE due to the nucleating effect of HA. However, they reported a decrease in the crystallinity degree with the applied radiation dose. They also showed a decrease in the composite's thermal stability with the absorbed dose, because the activation energy values decreased from 572 to $412\,\mathrm{kJ\,mol^{-1}}$ for the irradiated and non irradiated composites, respectively. Moreover, they found a decrease in MFI, tensile strength, and elongation at break and a slight increase in the Young's modulus values.

Albano et al. (79) studied the effect of gamma radiation on the mechanical, rheological, and thermal behavior of HDPE/HA composites that were prepared in solution, using a PE with a weight-average molecular weight of $70,000\,\mathrm{g\,gmol^{-1}}$. The applied doses varied from 0 to 100 kGy. The performance of these composites was different from that of extruded ones due to the effect of the presence of decalin traces that gave rise to an increase in the MFI values with the radiation. This behavior was more pronounced when HA contents less than or equal to 20 wt% were tested (Fig. 4.17). This fact evidenced that decalin traces help the chain-scission mechanisms of the HDPE. The lowering of the HDPE's molecular weight was demonstrated by gel permeation chromatography (GPC) of pure HDPE subjected to the same treatments. The decrease in the HDPE molecular weight was almost of 50%. This phenomenon of molecular weight decay was slower in the composites. Hence, the addition of HA have a stronger effect on the molecular weight decay than the radiation doses tested. This fact was attributed to the very high linear character of the HDPE showed by SSA studies (successive self-nucleation and annealing technique) since they did not show significant variations when thermograms of the irradiated polymer were compared to those of the non irradiated one. However, the crystallinity degree showed a slight increase with filler addition, but when samples were exposed to gamma radiation, a decrease in crystallinity was observed in all the materials, probably due to the interruption of the more linear sequences of the polyethylene resulting from the chain scission process and/or cross-linking. Regarding the thermal stability of these irradiated and non irradiated composites, a tendency similar to that of the degree of cristallinity was found. This indicates that the composites irradiated at different absorbed doses are less stable and more prone to thermal degradation.

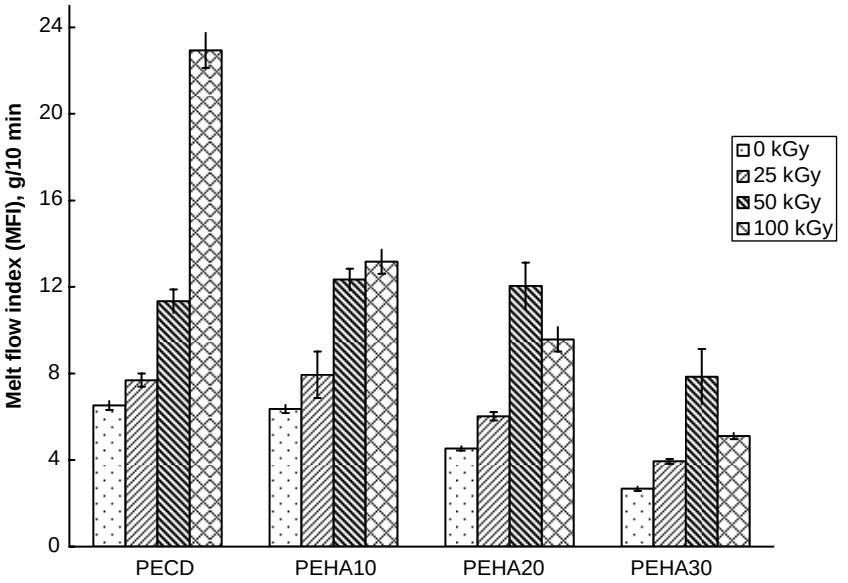

Figure 4.17 Melt flow index of irradiated HDPE/HA composites. (From Reference 79 with permission from Elsevier.)

Studies of composites of PP with 20 and 30 wt% of HA irradiated at 10 and 25 kGy were made by Ramírez et al. (93). They showed that the tensile strength does not display significant variations with the radiation doses. On the contrary, the elongation at break decreased as the doses were increased, this decrease being slower in the composites containing more HA. A slight decrease in the melting temperature (Table 4.7) as well as in the initial temperature of the decomposition process (T_{id}) and in the activation energy (Table 4.8) are indicative of the predominance of chain-scission reactions over cross-linking PP as a consequence of the irradiation process.

Table 4.7 Thermal Properties of PP With and Without HA Filler Irradiated at Different Doses.

	Irradiation dose, kGy								
	$T_c(\pm 2)$, °C			$T_m(\pm 2)$, °C)			$X_c(\pm 5)$, %		
Sample	0	10	25	0	10	25	0	10	25
PP-0 wt% HA	120	121	120	165	162	160	56	58	56
PP-20 wt% HA	119	120	119	165	164	163	54	58	53
PP-30 wt% HA	120	120	119	166	164	163	54	56	58

(From Reference 93 with permission from Elsevier.)

Table 4.8 Thermodegradative Parameters of PP/HA Composites Irradiated at Different Doses.

	Irradiation dose, kGy					
	$T_i(\pm 2)$, °C			$E_a(\pm 5)$, kJ mol^{-1}		
Sample	0	10	25	0	10	25
PP-0 wt% HA	426	427	398	163	158	140
PP-20 wt% HA	442	447	397	168	165	113
PP-30 wt% HA	420	427	407	149	123	101

(From Reference 93 with permission from Elsevier.)

4.5 COMPOSITES OF POLYOLEFINS/POLYAMIDE 6 WITH MONTMORILLONITE

In recent years, nanocomposites of polymer/layered silicates have drawn great interest due to their improved properties when compared to those of the respective pure polymers or conventional micro composites and macrocomposites. These better properties include higher tensile moduli, increased mechanical strength, heat resistance and biodegradability, and decreased gas permeability and flammability. The research dealing with the preparation of a polyamide 6/montmorillonite (MMT) nanocomposite reported by the Toyota research group in 1990, for which very small amounts of layered silicate loadings resulted in significant improvements in the mechanical and thermal properties, and the fact that it is possible to obtain such composites by melt mixing polymers with layered silicates (94), set a turning point in this field (95).

Polymer/layered nanocomposites are based on the preparation "*in situ*" of composites of a polymeric matrix with silicate particles with a high aspect ratio, where at least one of the dimensions of the dispersed particle lies in the nanometric range. The uniform dispersion of these nanoscopic particles brings about an enormous interfacial area per volume unit, which is of 700 mm^2 cm^{-3}, approximately. These particularities, along with the nanoparticle dimensions and small amount of filler used (usually lower than 5 %, are the main characteristics that make this type of composites different from the traditional ones. A polymeric matrix and the inorganic filler with a nanometric size forming the dispersed phase are the main components of a nanocomposite. A coupling agent could also be used to improve the compatibility of the matrix with the nanoscale filler. The high area/volume ratio obtained by the uniform dispersion of the particles causes a great deal of interfaces, which implies that the majority of the polymeric chains are located near an inorganic surface, which in turn, limits the number of conformational structures adopted by the polymeric molecules. Thus, the molecular mobility and hence the free volume and the relaxation behavior are hindered.

The addition of any type of filler to semicrystalline polymers modifies the ordering degree and the packing perfection and, hence, the crystallinity degree and

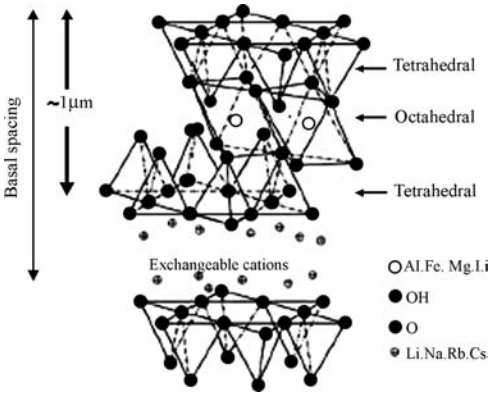

Figure 4.18 Structure of phyllosilicates. (From Reference 95 with permission from Elsevier.)

the crystalline front growth. However, the spatial ordering of the nanoparticles, spherical, roll-shaped, or layered, will give rise to a large number of systems. As a conclusion, the final properties of the nanocomposite depend on both the individual properties of the components of each phase and the relative disposition and synergy between the phases.

The most extensively studied layered silicates are those known as 2:1 phyllosilicates. These inorganic nanoclays are made of hydrated aluminum silicates. Among them, the hectorite, the saponite, and the montmorillonite are the most commonly used, the last one reportedly being the most extensively. In its natural form, MMT has the form of stacked layers. Each layer has a thickness of at least 10 Å, but its lateral dimensions are 200 times larger (Fig. 4.18).

Under proper conditions, the spaces between the layers can be occupied by monomer, oligomer, or polymer molecules, which then increases the distance between them. [This depends on a number of variables such as the nature of the interlayer cation and of the polymer, clay packing density, functionalization of the polymer, or the length of the coupling agents or the clay-modifier molecules, as well as on the process of preparation of the nanocomposite.] Some chemical modifications must be made to the interlayer cation through ion-exchange reactions with organic and inorganic cations to produce polar interactions between the polymer and the filler. This last step is vital to improve the degree of dispersion as well as the degree of intercalation and/or exfoliation of the layered silicate in a given polymer matrix.

There are many different methods for obtaining nanocomposites of polymer/layered silicates. The "*in situ*" polymerization of a monomer in the presence of the clay, the intercalation of the polymer from a solution, and the melt intercalation during melt mixing are the most widely reported. The last method will be dealt with in this section. During melt intercalation, polymer and clay are heated above the softening point of the former, usually under shear. The polymer chains diffuse from the bulk into the galleries between the silicate layers. A range of composites with structures from intercalated to exfoliated can thus be obtained, depending on the degree of penetration of the polymer chains into the galleries. Vaia et al. (96), explained that this process is allowed even though there is an entropy loss associated

with the confinement of a polymer melt because there is an entropy gain associated with the layer separation, resulting in a net entropy change near to zero.

4.5.1 Mechanical Properties

Nanocomposites of polymeric matrices offer an unusual combination of stiffness and toughness which is difficult to obtain from its individual components. Liu et al. (97) added different amounts of MMT ranging from 1 to 18 wt% to polyamide 6 and reported improved mechanical properties in nanocomposites of polyamide 6 with less than 10 wt% of the clay when compared to those of the neat polymer. This fact was attributed to the efficient dispersion of the MMT that allowed obtaining a smaller particle size through melt intercalation. They found that exfoliated structures were produced at clay contents lower than 10 wt%, whereas only intercalated structures were produced at higher contents. They also obtained a higher reinforcement effect, tensile and flexural moduli, tensile strength, and heat distortion temperature in the nanocomposites at the expense of lower impact energy values in notched specimens.

Ji et al. (98) explained that a better reinforcement effect obtained when a nanoclay is used in polyamide 6 nanocomposites is attributed to a decreased particle size and/or to an enlargement in the interfacial specific area when it is well dispersed and exfoliated. As a result, the interactions between the clay and the polymeric matrix are improved and the volume fraction of the interfacial region becomes comparable to that of the matrix.

Other authors have reported that the addition of small amounts of nanoclay increases the fragile–ductile transition temperature in nanocomposites of polyamide 6. Cho and Paul (99) reported that a fragile-ductile transition is observed in nanocomposites as well as in the polyamide as the temperature reaches T_g. Above T_g, the nanocomposites become very tough and show high levels of ductility. However, when the amount of clay is increased above a certain level, the material loses its ductile character and a fragile fracture takes place as a consequence of the fragile–ductile temperature increasing above the T_g of the polyamide. The same authors reported that the Young's modulus increases from 2.66 GPa in the pure polyamide to 3.66 GPa in the composites, whereas the tensile strength increases from 64.2 to 83.4 MPa. Both properties are higher than those of a conventional fiberglass-reinforced polyamide. The main reason for the drastic improvement in the tensile modulus in polyamide 6 nanocomposites is the strong interaction between the matrix and the silicate layers via formation of hydrogen bonds, though the improvement directly depends on the aspect ratio (95). However, the elongation at break decreases significantly from 200% to 126% with the use of clay, and the Izod impact strength values remain at approximately $38\,J\,m^{-1}$.

4.5.2 Influence of Different Compatibilizing Agents

Likewise, nanocomposites based in polyolefins show substantial reinforcements in their properties. Nonetheless, since they are non polar in nature, their direct

intercalation into the silicate galleries is almost impossible. It is then necessary to employ mechanisms that improve the interfacial adhesion between them and the clay. One of these mechanisms is the grafting of the polyolefins with polar monomers having functional groups such as maleic anhydride (MA) or diethyl maleate (DEM). The dispersion of the clays depends heavily on the hydrophilic character of the functionalized polyolefin and on the hydrophobic character of the alkylammonium—organically modified clay. Both processes, the polymer functionalization and the clay modification, are mandatory to achieve the proper adhesion between the phases.

Kawasumi et al. (100), Hasegawa et al. (101), and Nam (102) have reported evenly dispersed and intercalated and exfoliated structures in nanocomposites prepared by melt mixing using maleic anhydride grafted polypropylene and clays modified with alkylammonium. Varela et al. (103) studied the effects of three different types of compatibilizers on nanocomposites of clay/PP: diethyl maleate grafted PP, maleic anhydride grafted PP and carbamyl maleamic acid grafted PP. The clay was modified in an acidic medium with octadecylamine. The nanocomposites were prepared in an internal mixer using 20% and 40% of the compatibilizing agent and 5 wt% of the organophilic clay. Tactoid, intercalated and exfoliated structures were observed by TEM in all the samples (Fig. 4.19). Improved mechanical properties were obtained with tensile modulus values as much as three times that of pure PP. They also found that the melting temperature of the PP did not vary significantly with the addition of the clay. However, an increase in the crystallization temperature accompanied by a slight decrease in the crystallinity degree was measured due to the nucleating effect of clay. The best results were obtained when maleic anhydride was used as the polar grafting monomer. Intermediate properties were the result of using carbamyl maleamic acid, followed by diethyl maleate as grafting agents. The best mechanical properties were obtained when 40% of modified PP was used, because the stresses are much more efficiently transferred from the matrix to the filler when functional groups are incorporated into the polymer (Table 4.9).

4.5.3 Analysis of the Physical, Mechanical, Thermal, and Morphological Properties of Composites

Liu and Wu (104) found that there is a sharp increase in the tensile modulus with the clay content at clay loadings less than or equal to 3 wt%, followed by a much slower increase in clay loadings of 4 wt% or higher (Fig. 4.20). Wang et al. (105) prepared maleated polyethylene/clay nanocomposites using the melt intercalation technique. They found that the extent of exfoliation and intercalation depended on the hydrophilicity of the grafted polyethylene and the number of methylene groups in the alkylamine. Gopakumar et al. (106) reported an increase of 30% in the Young's modulus in a polyethylene grafted with maleic anhydride with the addition of 5% of organically modified montmorillonite (OMMT), making evident the significant contribution of the functionalization step in improving the interfacial adhesion between polymer and clay, because in the absence of this step, the improvement in modulus was only of 9%. These authors explain that the significant improvements in

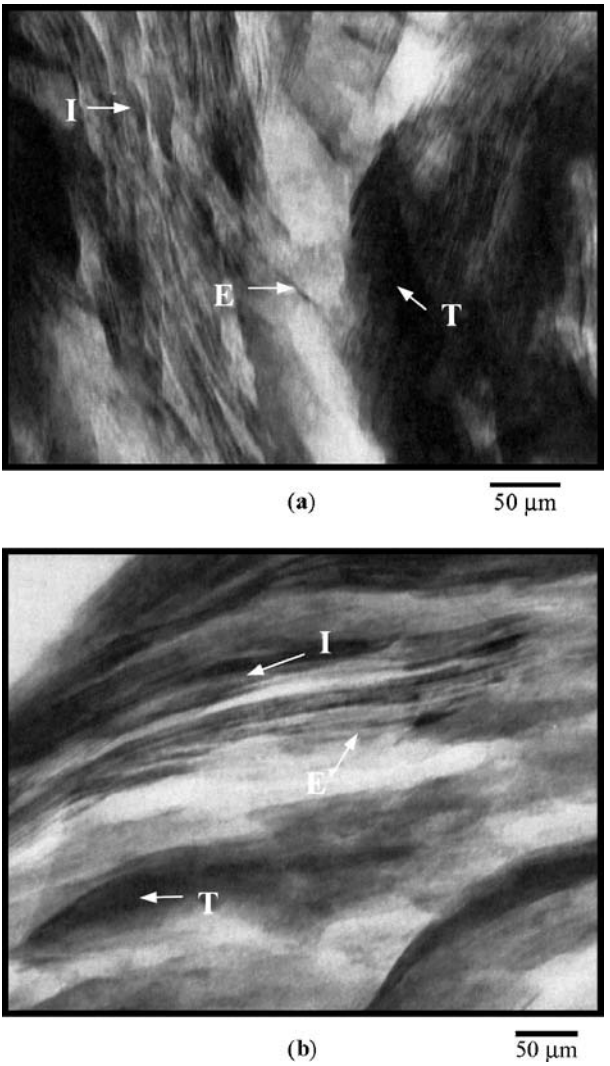

Figure 4.19 TEM microphotographs of PP hybrid: PP + IMt + 40 wt% of PP-g-MA (**a**) 100K and (**b**) 120K. (From Reference 103 with permission from Wiley Interscience.)

mechanical properties are attributed to the clay exfoliation. Nonetheless, they consider that the crystallinity degree is also an important factor in determining the mechanical properties. In this sense, they propose that the silicate layers act as nucleating agents, which, in turn, increase the rate and temperature of crystallization and decrease the crystallinity degree.

Wang et al. (107) found that the Young's modulus and the yield stress are more dependent on the aspect ratio of the silicate layers than on the crystallinity degree of

Table 4.9 Tensile Properties of Nanocomposites of PP/MMT with Different Compatibilizers.

Sample	Material	Young's modulus, GPa	Tensile strength, MPa	Elongation at break, %
1	PP + IMt	1.4 ± 0.3	15 ± 2	15 ± 4
2	PP + 40 wt% PP-g-DEM	1.1 ± 0.1	20 ± 3	445 ± 26
3	PP + IMt + 20 wt% PP-g-DEM	1.7 ± 0.3	24 ± 4	4 ± 1
4	PP + IMt + 40 wt% PP-g-DEM	2.9 ± 0.3	28 ± 3	4 ± 1
5	PP + 40 wt% PP-g-UMA	1.1 ± 0.2	22 ± 4	501 ± 41
6	PP + IMt + 20 wt% PP-g-UMA	2.5 ± 0.3	26 ± 5	5 ± 1
7	PP + IMt + 40 wt% PP-g-UMA	3.5 ± 0.4	30 ± 4	4 ± 1
8	PP + 40 wt% PP-g-MA	1.1 ± 0.2	20 ± 3	476 ± 62
9	PP + IMt + 20 wt% PP-g-MA	2.9 ± 0.4	29 ± 4	4 ± 1
10	PP + IMt + 40 wt% PP-g-MA	4.0 ± 0.5	34 ± 6	4 ± 1
11	PP-g-DEM	0.94 ± 0.16	13 ± 2	5 ± 1
12	PP-g-UMA	1.00 ± 0.20	16 ± 3	5 ± 1
13	PP-g-MA	0.96 ± 0.17	15 ± 2	5 ± 1
14	PP	13 ± 0.3	22 ± 3	563 ± 23

[MA: maleic anhydride, DEM: diethyl maleate, UMA: carbamyl maleamic acid. (From Reference 103 with permission from Wiley Interscience.]

the polyethylene matrix, because the latter decreases with an increase in the amount of filler. The nanocomposites of maleic anhydride grafted polyethylene prepared by these authors display a high tensile strength due to the high aspect ratio of the OMMT, the nanometric scale dispersion, and the strong interfacial adhesion between the functionalized matrix and the filler surface. Finally, they found that the addition of OMMT increases the crystallization and melting temperatures at filler contents

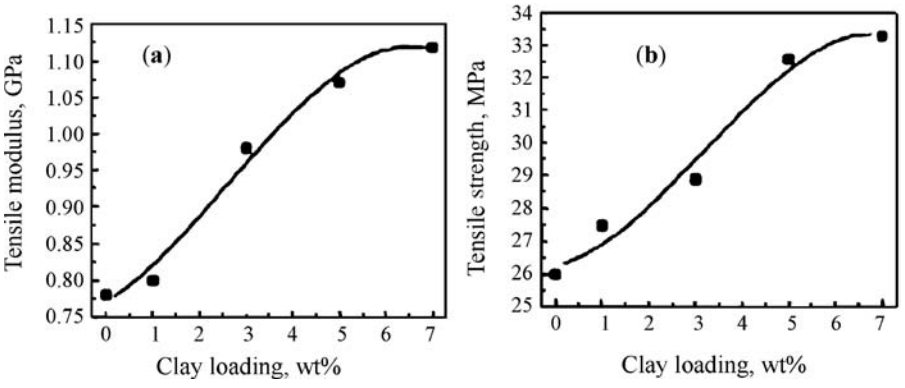

Figure 4.20 Effect of clay loading on (**a**) tensile modulus and (**b**) tensile strenght of PP/MMT. (From Reference 104 with permission from Elsevier.)

lower than 3%, because at higher contents, both parameters decrease due to an increased melt viscosity.

As it has already been mentioned, even though there is an improvement in the tensile modulus and strength, in general, with the use of a nanoclay, there is also a decrease in the elongation at break of the polymer. One way to overcome this disadvantage is to blend the polymeric matrix with another polymer with a more elastomeric behavior. Yu et al. (108) blended a polyamide 6 with polyethylene–octene elastomers. However, polyamides and polyethylenes are incompatible and immiscible. When this last component is highly dispersed into the polyamide matrix, it acts as an efficient stress concentrator and improves the dissipation of energy by promoting crazing and shear yielding in the matrix and a sharp fragile–ductile transition at a critical particle size of the dispersed phase or when the distance between particles reaches a specific value (109). As both processes allow dissipating large amounts of energy, there is a significant increase in the toughness of the polyamide.

It is well established that the phase morphology of immiscible polymer blends can be controlled by the addition or ''*in situ*'' formation of compatibilizers that act as interfacial agents. A suitable morphology could be achieved by selecting a good balance of the viscosity and melt elasticity ratios of the components at the processing conditions, and a certain level of grafting of the dispersed phase, in order to reduce the interfacial tension, increase the adhesion between the phases, and obtain a finer dispersion and a more stable morphology.

The functionalization of the polyolefins is a very successful way to enhance the interfacial adhesion between the above-mentioned polymeric phases, also promoting the reduction of the particle size of the dispersed phase due to the ''*in situ*'' formation of a grafted copolymer at the interface during the melt-blending process. Such blends exhibit excellent toughness and high notched Izod impact properties at room temperatures and low temperatures, without significantly decreasing their tensile strength.

However, the main shortcoming of rubber-toughened blends is the significant reduction of the Young's modulus caused mainly by the addition of the elastomeric phase. Then, if those polyolefins are blended with polyamide 6 nanocomposites with enhanced modulus, this could be overcome.

Perera et al. (110) studied the effectiveness of using grafted metallocene copolymers and styrene/ethylene–buthlene/styrene rubbers (SEBS) as toughening materials in binary and ternary blends with a polyamide 6 nanocomposite as the matrix phase. The effect of viscosity, comonomer content, and grafting degree of the metallocene polyethylenes in the nanocomposites characteristics was also evaluated. The different possibilities of functionalizing the polymer in their laboratory allowed them to control and optimize the process. Diethyl maleate and maleic anhydride were used as grafting monomers. Their results showed that ternary blends prepared with metallocene polyethylenes are tougher than binary ones and the polyamide 6 nanocomposite. The results are related to the degree of clay dispersion and the type of morphology developed in the different blends. Nonetheless, despite the presence of the nanometric filler, a significant decrease in the tensile modulus and strength was obtained when incorporating the elastomeric phase. The grafting with

MA unfolded a stress–strain behavior that is better than that obtained when DEM was used as the grafted monomer, and the latter yielded better tensile properties than blends prepared with non functionalized polyethylenes.

However, Contreras et al. (111) analyzed the effectiveness of using MA-grafted SEBS as toughening material in ternary blends with two different polyamide 6 nanocomposites as matrix phases. Two metallocene polyethylenes and two polypropylenes were used as dispersed phases. Results showed that blends prepared with metalloce polyethylenes are tougher than those prepared with PP, and no significant changes in tensile modulus or strength were observed when changing the type of polyethylene used. When a blend of SEBS and AM-grafted SEBS instead of pure AM-grafted SEBS was used as compatibilizing agent in ternary blends of polyamide 6 nanocomposites, major decreases in the Young's modulus and the tensile strength, and also a higher toughness, were observed. Blends prepared with PPs of different molecular weights as matrices exhibited individual elongated polyamide–OMMT particles with MA-grafted SEBS encapsulation. The formation of clusters of the polyamide nanocomposite seems to improve the toughness/stiffness balance of the material. The results depend on the degree of clay dispersion in the polyamide and the type of morphology developed in the different blends.

4.6 CONCLUSIONS

In composites of polyolefins/$CaCO_3$, it has been detected that the most important subject is related to their mechanical properties due to their potential applications. The use of nanoparticles of $CaCO_3$, as well as some additives to improve the interactions at the interface, has slight influence on the tensile behavior of these composites. Hence, new tendencies must point to polyolefins/nano$CaCO_3$.

The mechanical behavior of polyolefins/WF and polyolefins/sisal fiber composites is affected by the filler treatment. Consequently, new routes aiming to improve the filler–polymer interaction and dispersion are necessary to produce changes in tensile and impact properties. However, it seems interesting to use other fibers, such as coconut fibers, and analyze their influence on composites of polyolefins.

In polyolefins/HA composites, the current and future trends point to modification of the mixing mechanisms to improve the dispersion of the filler and, hence, their tensile and impact properties. These properties are most relevant in applications in the biomedical field. Additionally, the affect of the irradiation on the composites is very important because it is a widely used sterilization method that could produce structural changes, thereby modifying the mechanical behavior.

In the preparation of the present review, it was clear that polyolefins remain as the most used matrices in polymer composites with the different fillers dealt with in this work, in applications in fields such as textile, medical, among others.

NOMENCLATURE

$CaCO_3$	Calcium carbonate
DEM	Diethyl maleate
D_i	Integral dose
D_r	Radiation rate
D_3	Diffusion-three-way transport
D_2	Diffusion two-way transport
EPR	Ethylene–propylene copolymer
ESR	Electron paramagnetic resonance
D_a	activation energy
F1	First-order random nucleation
HA	Hydroxyapatite
HDPE	High density polyethylene
Hpp	Peak-to-peak resonance line
K	Shape factor
Lica 12	Neopentyl(diallyl)oxy, tri(dioctyl)phosphato titanate
Lica 01	Neopentyl(diallyl)oxy, trineodecanonyl titanate
MA	Maleic anhydride
MMT	Montmorillonite
M_w	Average molecular weight
NaOH	Sodium hydroxide
NZ12	Neopentyl(diallyl)oxy, trineodecanoyl zirconate
OH	Hydroxyl group
OMMT	Organically modified montmorillonite
P	Physical properties
PP	Polypropylene
PP-g-MA	Polypropylene functionalized with maleic anhydride
PS	Polystyrene
Po	Property not subjected to radiation
R3	Limiting surface reaction between both phases three dimensions
SBS	Styrene–butylene–styrene copolymer
SSA	Successive self-nucleation and annealing technique
T_g	Transition temperature
T_{id}	Initial decomposition temperature
T_m	Melting temperature
vol%	Volumetric fraction
TEM	Transmission electron microscopy
SEBS	Styrene–ethylene–butylene–styrene rubber
UV	Ultraviolet radiation
WF	Wood flour
XPS	X-ray photoelectron spectroscopy
g	Function
phr	Part per hundred

uHDPE	High density polyethylene modified by ultraviolet
wt%	Weigth percentage
α	Adjustment factor

REFERENCES

1. H. S. Hatz and J. Milewski (eds.), *Handbook of Fillers for Plastics*, VNR, New York, 1987.
2. Z. Bartzack, *Polymer*, **40**, 2347 (1999).
3. S. N. Maiti and P. K. Mahapatro, *J. Appl. Polym. Sci.*, **42**, 3101 (1991).
4. Z. Wang, *J. Appl. Polym. Sci.*, **60**, 2239 (1996).
5. Y. Wang and J. S. Huang, *J. Appl. Polym. Sci.*, **60**, 1779 (1996).
6. Y. Wang and Y. J. Wang, *Polym. Eng. Sci.*, **39**, 190 (1999).
7. G. Akovali and M. A. Akman, *Polym. Int*., **42**, 195 (1997).
8. J. Suwanprateeb, S. Tiemprateeb, S. Kangwantrakool, and K. Hemachandra, *J. Appl. Polym. Sci.*, **70**, 1717 (1998).
9. R. Gendron and D. Binet, *J. Vinyl Additive Technol.*, **4**, 54 (1998).
10. M. Bories, M. A. Huneault, and P. G. Lafleur, *Int. Polym. Process. XIV*, **3**, 234 (1999).
11. W. C. J. Zuiderduin, C. Westzaan, H. Huetink, and R. J. Gaymans, Toughening of polypropylene with calcium carbonate particles, in: *Proceedings of the Antec 2001*, Society of Plastics Engineers Dallas, Texas, USA, 2001, p. 2848.
12. K. Premphet and P. Horanont, *Polym. Plastic Technol. Eng.*, **40**, 235 (2001).
13. C. Albano, J. González, M. Ichazo, C. Rosales, C. Urbina de Navarro, and C. Parra, *Compos. Struct.*, **48**, 49 (2000).
14. J. González, C. Albano, M. Ichazo, Hernández M, and R. Sciamanna, *Polym. Deg. Stabil.*, **73**, 211 (2001).
15. J. González, C. Albano, M. Ichazo, and B. Díaz, *Eur. Polym. J.*, **38**, 2465 (2002).
16. Y. S. Thio, A. S. Argon, R. E. Cohen, and M. Weinberg, *Polymer*, **43**, 3661 (2002).
17. Ch. M. Chan, J. Wu, J. X. Li, and Y. K. Cheung, *Polymer*, **43**, 2981 (2002).
18. T. Labour, G. Vigier, R. Séguéla, C. Gauthier, G. Orange, and Y. Bomal, *J. Polym. Sci. B Polym. Phys.*, **40**, 31 (2002).
19. S. C. S. Teixeira, M. M. Moreira, A. P. Lima, L. S. Santos, B. M. da Rocha, E. S. de Lima, R. A. A. F. da Costa, A. L. N. da Silva, M. C. G. Rocha, and F. M. B. Coutinho, *J. Appl. Polym. Sci.*, **101**, 2559 (2006).
20. P. Supaphol and W. Harnsiri, *J. Appl. Polym. Sci.*, **100**, 4515 (2006).
21. R. Doufnoune, N. Haddaoui, and F. Riahi, *Int. J. Polym. Mater.*, **55**, 815 (2006).
22. J. A. Manson and L. H. Sperling, *Polymer Blends and Composites*, Plenum, New York, 1976.
23. Z. Demjen, B. Pukanszky, and J. Nagy, *Composites A*, **29**, 323 (1998).
24. S. J. Monte, Injection molding unfilled and filled polymers with titanates and zirconates, in: *Proceedings of the Antec 2001* (*SPE's 59 Annual Technical Conference*), Society of Plastics Engineers Dallas, Texas, USA, 2001, p. 774.
25. Z. H. Liu, K. W. Kwok, R. K. Y. Li, and C. L. Choy, *Polymer*, **43**, 2501 (2002).
26. L. Zhang, C. Li, and R. Huang, *J. Polym. Sci. B Polym. Phys.*, **42**, 1656 (2004).
27. L. Zhang, C. Li, and R. Huang, *J. Polym. Sci. B Polym. Phys.*, **43**, 1113 (2005)
28. A. Galeski, M. Kryazewski, and T. Kowalewski, *Polym. Eng. Sci.*, **32**, 1217 (1992).
29. J. Lei and R. Zhou, *Polym. Eng. Sci.*, **40**, 1529 (2000).
30. K. Mitzuishi, S. Ueno, S. Kodama, and H. Kawasaki, *J. Polym. Sci. B Polym. Phys.*, **43**, 2043 (1991).

31. M. Avella, S. Cosco, M. L. Di Lorenzo, E. DiPace, M. E. Errico, and G. Genlile, *Eur. Polym. J.*, **42**, 1548 (2006).
32. J. Kuruvilla, T. Sabu, C. Pavithran, and M. Brahmakumar, *J. Appl. Polym. Sci.*, **47**, 1731 (1993).
33. J. Kuruvilla, T. Sabu, and C. Pavithram, *Polymer*, **37**, 5139 (1996).
34. C. Albano, M. Ichazo, J. González, M. Delgado, and R. Poleo, *Mater. Res. Innovat.*, **4**, 284 (2001).
35. A. Bledzki, O. Faruk, and M. Huque, *Polym. Plastic Technol. Eng.*, **41**, 435 (2002).
36. D. Maldas and B. V. Kokta, *J. Appl. Polym. Sci.*, **40**, 917 (1990).
37. D. Maldas and B. V. Kokta, *Int. J. Polym. Mater.*, **27**, 77 (1994).
38. G. E. Myers, I. S. Chahyadi, C. A. Coberty, and D. S. Erme, *Int. J. Polym. Mater.*, **15**, 21 (1991).
39. J. George, M. S. Sreekala, and S. Thomas, *Polym. Eng. Sci.*, **41**, 1471 (2001).
40. D. Nabi Saheb and J. P. Job, *Adv. Polym. Technol.*, **18**, 351 (1999).
41. A. Paul and S. Thomas, *J. Appl. Polym. Sci.*, **63**, 247 (1997).
42. C. Joly, M. Kofman, and R. Gauthier, *J. Macromol. Sci. Pure Appl. Chem.*, **A33**, 1981 (1996).
43. H. P. S. Abdul Klalil, H. D. Rozman, H. Ismael, and A. N. N. Rosfaizal, *Polym. Plast. Technol, Eng.*, **41**, 453 (2002).
44. M. J. Zaini, M. Y. A. Fuad, Z. Ismael, M. S. Marisor, and J. Mustafah, *Polym. Int.*, **40**, 51 (1996).
45. M. N. Ichazo, C. Albano, J. González, R. Perera, and M. V. Candal, *Compos. Struct.*, **54**, 2007 (2001).
46. J. González, C. Albano, M. Ichazo, L. Espejo, and K. Molina, *Revista de la Facultad de Ingeniería de la UCV*, **17**, 67 (2002).
47. M. Bengtsson and K. Oksman, *Composites A*, **37**, 752 (2006).
48. A. K. Bledzki, M. Letman, A. Viksne, and L. Rence, *Composites A*, **36**, 789 (2005).
49. M. Tajvidi, R. H. Falk, and J. C. Hermanson, *J. Appl. Polym. Sci.*, **101**, 4341 (2006).
50. M. G. Salemane and A. S. Luyt, *J. Appl. Polym. Sci.*, **100**, 4173 (2006).
51. N. N. Ichazo, C. Albano, and J. González, *Polym. Int.*, **49**, 1409 (2000).
52. N. E. Marcovich, M. M. Roboredo, and M. I. Aranguren, *J. Appl. Polym. Sci.*, **68**, 2069 (1998).
53. C. Albano, G. Sánchez, and A. Ismael, *J. Macromol. Sci. Pure Appl. Chem.*, **A35**,1349 (1998).
54. C. Albano, J. González, M. Ichazo, and D. Kaiser, *Polym. Deg. Stabil.*, **66**, 179 (1999).
55. C. Albano, J. González, M. Ichazo, N. Velasco, J. Guevara, and F. La Mantia, *Polym. Bull.*, **51**, 245 (2003).
56. H. M. Horowitz and G. Metzger, *Anal. Chem.*, **35**, 1464 (1963).
57. L. Reich and S. Stivale, *Thermochim. Acta*, **24**, 9 (1978).
58. G. Romero and E. García, *Anal. Quím.*, **58**, 464 (1988).
59. C. Albano, J. Reyes, M. Ichazo, J. González, M. Brito, and D. Moronta, *Polym. Degrad. Stabil.*, **76**, 191 (2002).
60. N. A. Slovokhatova, Z. F. Ilïcheva, L. A. Valisiev, and V. A. Kargin, *Polym. Sci. USSR*, **6**, 671 (1964).
61. R. Guan, *J. Appl. Polym. Sci.*, **76**, 75 (2000).
62. M. I. Chipara, D. Barb, M. Cojocaru, D. Tudor, M. D. Chipara, and M. Rogalski, *Polym. Degrad. Stabil.*, **37**, 61 (1992).
63. M. I. Chipara, *Nuclear Instrum. Methods Phys. Res. B*, **131**, 188 (1997).
64. C. Albano, R. Poleo, J. Reyes, J. González. M. Brito, and M. Ichazo, *E-polymers*, **022**, 11 (2004).
65. C. Albano, J. Reyes, J. González, M. Ichazo, R. Poleo, and E. Davidson, *Polym. Degrad. Stabil.*, **73**, 39 (2001).
66. J. Reyes, C. Albano, E. Davidson, R. Poleo, J. González, M. Ichazo, and M. Chipara, *Mater. Res. Innovat.*, **4**, 294 (2001).
67. J. Reyes-Romero, E. Davidson, C. Albano, D. Moronta, and P. Reyes-Turcu, *Mol. Cryst. Liq. Cryst.*, **416**, 351 (2004).

68. A. Chapiro (ed.), *Radiation Chemistry of Polymeric Systems*, Wiley Interscience, New York, 1962.
69. M. Dole (ed.), *The Radiation Chemistry of Macromolecules*, Academic Press, New York, 1972.
70. M. Wang, D. Porter, and W. Bonfield, *Br. Ceram. Trans.*, **93**, 91 (1994).
71. M. Wang, C. Berry, M. Braden, and W. Bonfield, *J. Mater. Sci. Mater. Med.*, **9**, 621 (1998).
72. M. Wang, R. Joseph, and W. Bonfield, *Biomaterials*, **19**, 2357 (1998).
73. J. Suwanprateeb, K. E. Tanner, S. Turner, and W. Bonfield, *J. Mater. Sci. Mater. Med.*, **6**, 804 (1995).
74. J. Suwanprateeb, K. E. Tanner, S. Turner, and W. Bonfield, *J. Biomed. Mater. Res.*, **39**, 16 (1998).
75. S. N. Nazhat, R. Joseph, M. Wang, R. Smith, K. E. Tanner, and W. Bonfield, *J. Mater. Sci. Mater. Med.*, **11**, 621 (2000).
76. M. Wang, L. Y. Leung, P. K. Lai, and W. Wonfield, *Bioceramics*, **254–256**, 611 (2004).
77. C. Albano, A. Karam, G. González, N. Domínguez, Y. Sánchez, J. González, M. Ichazo, and P. Joskowicz, Effect of the mixing on the mechanical and thermal behavior HDPE/hydroxyapatite composites, in: *Proceedings of the Antec 2004* (*SPÉs 62nd Annual Technical Conference*), Society of Plastics Engineers Chicago, Illinois, USA, 2004, p. 3371.
78. C. Albano, A. Karam, N. Domínguez, Y. Sánchez, J. Puerta, R. Perera, and G. González, *Mol. Cryst. Liq. Cryst.*, **448**, 251 (2006).
79. C. Albano, A. Karam, R. Perera, G. González, N. Domínguez, J. González, and Y. Sánchez, *Nucl. Instrum. Methods Phys. Res. B*, **247**, 331 (2006).
80. C. Albano, R. Perera, A. Karam, G. González, J. Puerta, N. Domínguez, Y. Sánchez, and J. Brito, *Macromol. Symp.*, **27**, 197 (2007).
81. R. A. Sousa, J. F. Mano, R. L. Reis, A. M. Cunha, and M. J. Bevis, *Bioceramics*, **14**, 218 (2002).
82. R. Joseph, W. J. McGregor, M. T. Martyn, K. E. Tanner, and P. D. Coates, *Biomaterials*, **23**, 4295 (2002).
83. R. Joseph, W. J. McGregor, M. T. Martyn, K. E. Tanner, P. D. Coates, and W. Bonfield, *Polym. Eng. Sci.*, **42**(2), 326 (2002).
84. K. L. K. Lim, Z. A. Mohd Ishak, U. S. Ishiaku, A. M. Y. Fuad, A. H. Yusof, T. Czigany, B. Pukanzsky, and D. S. Ogunniyi, *J. Appl. Polym. Sci.*, **100**, 39931 (2006).
85. L. Fang, Y. Leng, and P. Gao, *Biomaterials*, **26**, 3471 (2005).
86. L. Fang, Y. Leng, and P. Gao, *Biomaterials*, **27**, 3701 (2006).
87. M. Wang and W. Bonfield, *Biomaterials*, **22**, 1311 (2001).
88. S. Deb, M. Wang, K. E. Tanner, and W. Bonfield, *J. Mater. Sci. Mater. in Medicine*, **7**, 191 (1996).
89. R. A. Sousa, R. L. Reis, A. M. Cunha, and M. J. Bevis, *J. Mater. Sci. Mater. Med.*, **14**, 475 (2003).
90. M. Wang, S, Deb, and W. Wonfield, *Mater. Lett.*, **44**, 119 (2000).
91. R. A. Sousa, R. L. Reis, A. M. Cunha, and M. J. Bevis, *J. Appl. Polym. Sci.*, **86**, 2873 (2002).
92. C. Albano, A. Karam, G. González, N. Domínguez, Y. Sánchez, F. Manzo, and C. Guzmán-García, *Polym. Adv. Technol.*, **16**(2–3), 283 (2005).
93. C. Ramírez, C. Albano, A. Karam, N. Dominguez, Y. Sánchez, and G. González, *Nuclear Instrum. Methods Phys. Res. B*, **236**, 531 (2005).
94. R. A. Vaia, H. Ishii, and E. P. Giannelis, *Chem. Mater.*, **5**, 1694 (1993).
95. S. Sinha-Ray and M. Okamoto, *Prog. Polym. Sci.*, **28**, 1539 (2003).
96. R. A. Vaia and E. P. Giannelis, *Macromolecules*, **30**, 7990 (1997).
97. L. M. Liu, Z. N. Qi, and X. G. Zhu, *J. Appl. Polym. Sci.*, **71**, 1133 (1999).
98. X. L. Ji, J. K. Jing, W. Jiang, and B. Zheng, *Polym. Eng. Sci.*, **42**, 983 (2002).
99. J. W. Cho and D. R. Paul, *Polymer*, **42**, 1083 (2001).
100. M. Kawasumi, N. Hasegawa, M. Kato, A. Usuki, and A. Okada, *Macromolecules*, **30**, 6333 (1997).
101. N. Hasegawa, M. Kawasumi, M. Kato, A. Usuki, and A. Okada, *J. Appl. Polym. Sci.*, **67**, 87 (1998).
102. P. H. Nam, P. Maiti, M. Okamoto, T. Kotaka, N. Hasegawa, and A. Usuki, *Polymer*, **42**, 9633 (2001).

103. C. Varela, C. Rosales, R. Perera, M. Matos, T. Poirier, J. Blunda, and H. Rojas, *Polym. Compos.*, **27** (4), 451 (2006).
104. X. Liu and Q. Wu, *Polymer*, **42**, 10013 (2001).
105. K. H. Wang, M. H. Choi, C. M. Koo, Y. S. Choi, and I. J. Chung, *Polymer*, **42**, 9819 (2001).
106. T. G. Gopakumar, J. A. Lee, M. Kontopoulou, and J. S. Parent, *Polymer*, **43**, 5483 (2002).
107. K. H. Wang, M. H. Choi, C. M. Koo, M. Xu, I. J. Chung, M. C. Jang, S. W. Choi, and H. H. Song, *J. Polym. Sci. B Polym. Phys.*, **40**, 1454 (2002).
108. Z. Yu, Y. Ou, and G. Hu, *J. Appl. Polym. Sci.*, **69**, 1711 (1998).
109. S. Wu, *Polym. Eng. Sci.*, **27**, 335 (1987).
110. R. Perera, C. Rosales, M. Matos, J. Palacios, S. Quintana, M. Cafiero, and S. Da Silva. To be published.
111. V. Contreras, M. Cafiero, S. Da Silva, C. Rosales, R. Perera, and M. Matos, *Polym. Eng. Sci*. **46** (8), 1111–1120 (2006).

Chapter 5

Ethylene–Propylene–Diene Rubber/Carbon Black Composites

Soney C. George[1] and Sabu Thomas[2]

5.1 INTRODUCTION

Polymer composites have gained greater attention during the past few decades in different technological applications due to their light weight, easy processability, corrosion resistance, cost reduction, and improved mechanical properties (1,2). Among them particle-filled elastomers are the most commonly used classes of polymeric composites. Carbon black (CB) filled elastomeric composites are widely used in tire industries and lot of studies have been done related to their structure and properties (3–5). Carbon black is also used to impart conductivity in elastomeric composites. This is because polymers generally have very low concentration of free charge carriers. They are electrically nonconductive and transparent to electromagnetic radiation. To provide conductivity and shielding from electromagnetic interference (EMI) (6), the incorporation of fillers of high intrinsic conductivity such as carbon black, carbon and graphite fibers, or metal powder to the polymers is required (7,8). Carbon black filled conductive rubbers have wide applications such as flooring material to dissipate static electric charge (9,10), pressure sensitive sensors that can be used for shockproof switches (11), sensors for vehicle weight measurement to collect toll tax on roads (12), and electromagnetic shielding materials (13,14) apart from the conventional application of semiconducting materials for dissipation of static electricity (15,16). Various rubbers are used for the preparation of such

[1]Amal Jyothi College of Engineering, Koovapally, Kottayam 686518, Kerala, India.
[2]School of Chemical Sciences, Mahatma Gandhi University, Priyadarshini Hills, Kottayam 686560, Kerala, India.

Polyolefin Composites, Edited by Domasius Nwabunma and Thein Kyu

composites, for example, silicone rubber, nitrile rubber, butyl rubber, natural rubber, and ethylene–propylene–diene rubber (EPDM) rubber (17). Blends of rubbers having different polarities are also very useful for achieving a high degree of conductivity, particularly because of their well-defined interface (18). EPDM elastomer has proved to be a useful material in the automotive, electrical, and construction industries (19,20) due to its unique mechanical and chemical properties. EPDM exhibits excellent resistance to weather, ozone, acids, and alkalies while accommodating high volume fractions of filler and liquid plasticizers and retaining desirable physical and mechanical properties. These characteristics have allowed EPDM to be employed as automobile tire sidewalls, automotive tubes, window sealing in cars (21), gaskets, conveyer belts, appliance parts, membrane (22–24), and in roofing (25,26).

This chapter is intended to describe the type of interaction existing between the carbon black filler and the EPDM matrix. It also brings out the dependence of properties of composites, especially the conductive properties, on carbon black loading and its nature. Finally, the potential applications of these composites are also furnished here.

5.2 COMPOSITE PREPARATION

The mixing or compounding of EPDM with carbon black and other additives is often carried out in a laboratory two-roll mill by following the conventional technique. Proper mixing is essential to ensure uniform and efficient dispersion of the filler particles in the elastomer matrix. Carbon black loading is selectively varied. The vulcanization or curing characteristics of the filled EPDM compounds have been studied in a Monsanto rheometer at 160°C. Vulcanizates from the appropriately compounded elastomers are prepared in a compression molding machine under pressure to the optimum cure time. The chemical composition and properties of EPDMs used are given in Table 5.1 (27). The different types of carbon black mainly

Table 5.1 Chemical Composition and Properties of the EPDMS.

	EPDM-1	EPDM-2
1. Composition, %		
Ethylene	44.6	46
Propylene	45.4	49
Ethylidene norbornene	10.0	5
2. Mooney viscosity ML (1+4) 125°C		30[a]
3. Molar mass ($\times 1000\,g\,mol^{-1}$)		
M_n		32
M_w		132
M_z		517
4. Long-chain branching Parameter, $\Delta\delta$		9.8

[a]In Mooney units

From Reference 27 with the permission of American Chemical Society.

Table 5.2 Physical Properties of the Carbon Blacks.

Properties	Vulcan XC-72[a] (N472)	Acetylene black	High abrasion furnace (HAF, N330)	Semireinforcing furnace (SRF, N660)
Particle size, nm	29	42	23	60
N_2 surface area, $m^2\,g^{-1}$	180	70		
DBP[b] absorption value, ml/100g	178	250[c]	102	90
Iodine absorption value, mg g^{-1}	270		82	36
CTAB[d] surface area, $m^2\,g^{-1}$	86		83.4	

[a]Highly conducting carbon black.
[b]Dibutyl phthalate.
[c]m^3/100g.
[d]Cetyl trimethyl ammonium bromide.

used in EPDM matrix are Vulcan XC-72, acetylene black, high abrasion furnace (HAF) black, and semireinforcing furnace black (SRF). The physical properties of these carbon blacks are given in Table 5.2.

5.3 CHARACTERIZATION OF COMPOSITES

5.3.1 ^{129}Xe-NMR Studies

^{129}Xe-NMR spectroscopy has been found to be a valuable tool for the study of microporous solids. Xe atoms with their diameter of 4.4 Å can be absorbed in many porous materials, ranging from crystalline materials such as silicates to amorphous polymers (28). The advantage of Xe as a Nuclear magnetic resonance (NMR) probe is the extraordinary sensitivity of the Xe chemical shift to the interaction between the Xe atoms and the material in which they are adsorbed. The Xe atom is not small compared to the local free volume of the polymers, and the mobility of the Xe atoms is largely determined by the polymer chain mobility. It is reported that ^{129}Xe-NMR is a powerful tool to investigate carbon black and carbon black filled elastomers (29). Figure 5.1 shows the ^{129}Xe spectra of three EPDM samples N110, N330 and N550 filled with the carbon blacks that have aggregate sizes of 18, 30, and 56 nm, respectively. In these spectra no xenon resonances in the carbon black region are found. In spite of the high concentration of carbon black (85 phr), the only observable effect of carbon black in the spectra of Fig. 5.1 is a slight broadening of the EPDM line at 205 ppm. The line width increases from 164 Hz for pure EPDM to 250 Hz for EPDM/N550. The temperature dependence of the EPDM chemical shift and line width, however, are slightly dependent on the presence and the type of carbon black. At around 240 K the sample filled with N110 with the smallest aggregate size has the

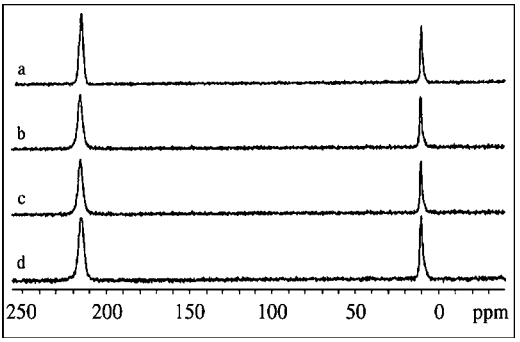

Figure 5.1 ^{129}Xe NMR spectra of Xenon in (**a**) unfilled EPDM, (**b**) EPDM/N110, (**c**) EPDM/N330, and (**d**) EPDM/N550 at room temperature. (From Reference 29 with the permission of Sociedade Brasileira de Quimica.)

highest line width. In spite of the high concentration of carbon black, no direct evidence of xenon adsorbed at the carbon black aggregates is found in the spectra of Fig. 5.1. The xenon atoms in the bound EPDM fraction exchange rapidly on the NMR timescale between a state in which they are adsorbed on the carbon black surface and a state in which they are absorbed in the EPDM layer. This would imply that the carbon black aggregates are not completely covered with EPDM chains.

5.3.2 ^{1}H NMR Studies

The low resolution proton NMR method is one of the few successful techniques used for the study of elastomer–filler interactions and was used in a carbon black filled natural rubber and a fumed silica filled silicon rubber (30,31). Proton T2 relaxation experiments were reportedly used to study the EPDM/carbon black interface (27). It was shown that two microregions with significantly different local chain mobility are observed in the filled EPDM: a thin layer of immobilized (semirigid) EPDM chain units covering the surface of the carbon black and a mobile EPDM matrix outside of the EPDM/carbon black interface (Fig. 5.2). The thickness of the interfacial layer is in the range of one to two diameters of the monomer unit. The interface provides adsorption junctions at the sites of interaction between the carbon black and the EPDM. These junctions interconnect the neighboring carbon black particles and aggregates. The spatially heterogeneous, ''bimodal''-like distribution of the adsorption junctions provides a good representation of the structure of the physical network (Fig. 5.3) in the rubber matrix. There is an EPDM fraction that is loosely bound to the carbon black by adsorption interactions. This loosely bound rubber has numerous adsorption network junctions, similar to those of the bound rubber. The other fraction of EPDM, the extractable (unbound) rubber, has a relatively low number of adsorption network junctions and can apparently be extracted from the compound. The fraction of loosely bound EPDM chains, as measured by NMR, increases as the maximum possible EPDM/carbon black contact area per unit volume of the

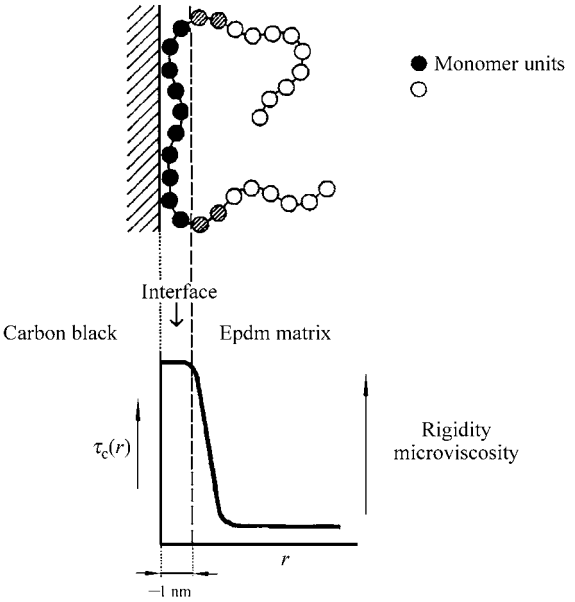

Figure 5.2 A simplified graphic representation of EPDM chains at the carbon black surface. Low mobile monomer units in the interface and mobile chain units outside of the interface are shown by solid and open points, respectively. (From Reference 27 with the permission of American Chemical Society.)

elastomer increases, regardless of the type of carbon black, and is relatively close to the content of the bound rubber. One fraction of the EPDM matrix, the loosely bound rubber, has numerous adsorption interactions with the surface of the carbon black, similar to the interactions in the bound rubber. These network chains are characterized by the relaxation time. The other fraction is known as tightly bound rubber. This kind of heterogeneous nature is due to the agglomeration of carbon black. Carbon black aggregates are not randomly distributed in the elastomer matrix because of the difference between elastomer/carbon black and carbon black/carbon black interactions, which is supposed to be the intrinsic origin of agglomeration of carbon blacks.

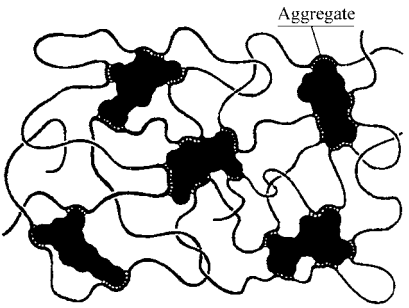

Figure 5.3 A schematic drawing of the physical network structure in a carbon black filled elastomer. (From Reference 27 with the permission of American Chemical Society.)

Therefore it may be assumed that a three-dimensional heterogeneous elastomer–carbon network exists in the EPDM matrix.

5.4 MORPHOLOGY OF COMPOSITES

The morphology of EPDM vulcanizates having different carbon black loadings (10–50 phr) emanating from Scanning electron microscopy (SEM) micrographs is shown in Fig. 5.4 (32). SEM micrograph (Fig. 5.4a) of a low carbon black loading (10 phr) shows closely packed, broad, and nearly parallel strands or clusters of the EPDM phase interspaced with the distributed carbon black phase. As the carbon black loading is increased over the percolation concentration range (20–35 phr or slightly beyond), the distribution of the carbon black phase becomes more uniform through breakdown of the parallel strands and clusters of the EPDM phase into finer strands with carbon black particles. Development of a filler–matrix co-continuous phase morphology is observed with increase in carbon black loading over the percolation concentration range (Fig. 5.4b and c). For carbon black loading (50 phr) much above the percolation concentration range, the phase morphology becomes notably different indicating masking, interpenetration, and overlapping of the two phases (Fig. 5.4d).

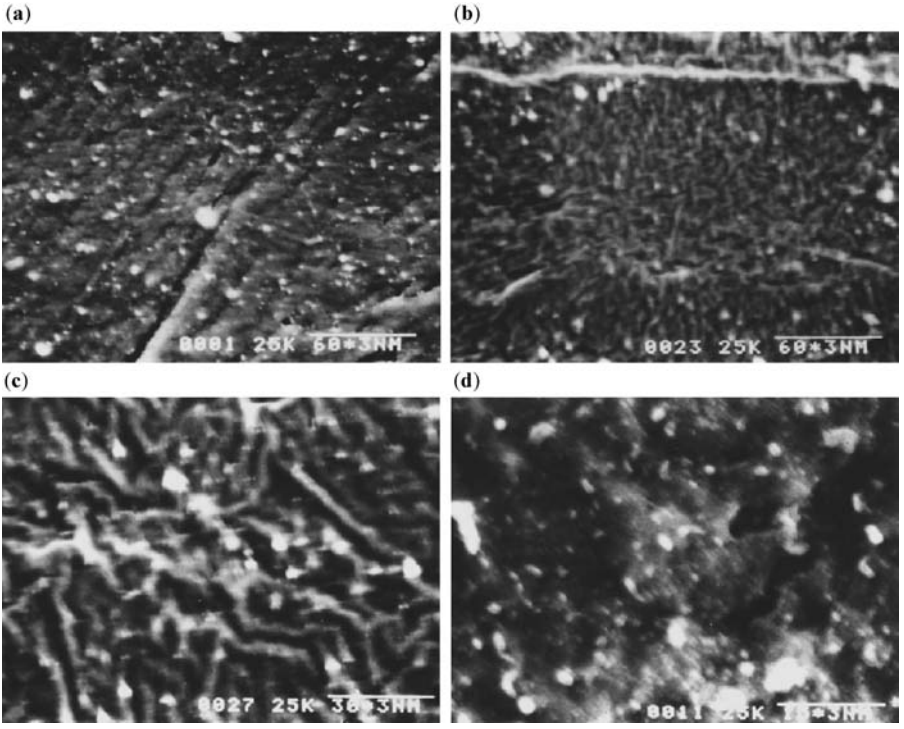

Figure 5.4 Scanning electron micrographs of EPDM vulcanizate having conducting carbon black loadings of (**a**) 10 phr, (**b**) 20 phr, (**c**) 35 phr, and (**d**) 50 phr. (From Reference 32 with the permission of Elsevier Science Ltd.)

5.5 MECHANICAL AND VISCOELASTIC PROPERTIES

5.5.1 Mechanical Properties

Bantjes and coworkers (33) reported that mechanical properties of carbon black filled EPDM changed drastically in multistep peroxide vulcanization. The elongation at break decreased whereas the tensile strength increased due to this vulcanization method. A compound cured with 1.0 phr peroxide and 300% strain during the second step had the same mechanical properties as a compound cured with 7.0 phr peroxide, but without strain during the vulcanization. The effects of incorporation of different extents of extra conducting carbon black as filler on selected physical and mechanical properties of vulcanizates of EPDM-based compounds have been reported (32). Increasing the carbon black loading caused a monotonic increase in density and hardness (Fig. 5.5) and in tensile strength with a leveling-off trend corresponding to carbon black filler loading greater than 40 phr.

Elongation at break of the initial EPDM vulcanizates, however, passes through a maximum corresponding to 20 phr carbon black loading. The mechanical properties of modified *in situ* EPDM vulcanizates filled with carbon black by unsaturated hydroxyl fatty acids were reported (34). The addition of unsaturated hydroxyl fatty acid had obvious effects on EPDM vulcanizate. The modulus at 300% decreased slowly with the increase of unsaturated hydroxyl fatty acid, whereas tensile strength and tear strength showed opposite trends. The elongation at break passed through a maximum as the concentration of unsaturated hydroxyl fatty acid increased. The flexure fatigue properties of the composites were enhanced remarkably by the addition of unsaturated fatty acids. The experimental and theoretical investigations of the mechanical properties of an EPDM elastomer reinforced with carbon black have been reported (35). The material constants of the testing material were determined by plotting the stress–strain experimental curve in a reduced stress versus the inverse stretch diagram (Fig. 5.6). It was found that the EPDM-reinforced elastomer

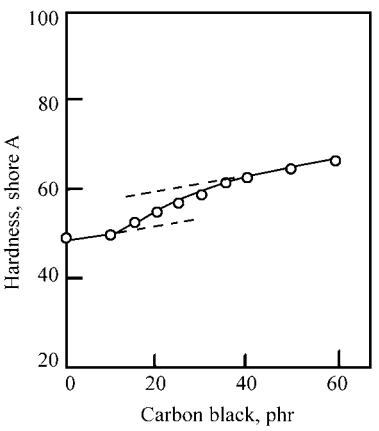

Figure 5.5 Plot of hardness (shore A) versus conducting carbon black loading (phr) at 25°C for EPDM vulcanizates. (From Reference 32 with the permission of Elsevier Science Ltd.)

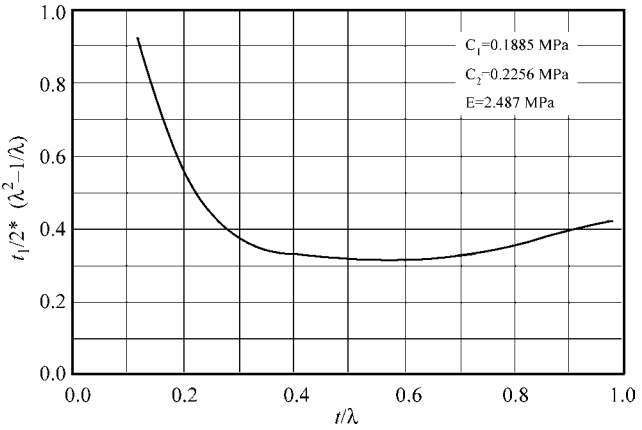

Figure 5.6 Reduced stress versus principal stretch for the carbon black filled EPDM sample. (From Reference 35 with the permission of John Wiley & Sons, Inc.)

depicts a highly nonlinear dependence of the stress on the deformation of the testing specimens under simple tension conditions. The Ogden equation, which was used for the strain energy function to fit uniaxial experimental stress–strain curves, is represented as (35,36)

$$W = \sum_{j=1}^{M} \mu_j \sum_{i=1}^{3} \frac{(\lambda_i^j - 1)}{\alpha_j} \tag{5.1}$$

where W is the strain energy function, M denotes the number of terms in the series expansion, λ is the extension ratio, and $i, j = 1, 2, 3$ with $i \neq j$.

The physicomechanical properties of EPDM rubber samples loaded with SRF have been investigated (37). It is observed that tensile strength increases and elongation at break decreases with the increase of SRF content. The properties such as hardness, modulus, tear strength, hysteresis, and abrasion resistance of zinc sulfonated EPDM were improved by the addition of HAF (38). The incorporation of the filler improves the retention of stress–strain properties of the polymer at elevated temperatures, although the room temperature tensile strength of the filled polymer is similar to that of the neat polymer. In zinc sulphonated EPDM, incorporation of carbon black strengthens the physical cross-links arising from ionic aggregates, thereby increasing the high temperature strength properties. Therefore, the tension set values gradually decreased with increase in filler loading. Incorporation of carbon black in EPDM increases the room temperature stress–strain properties due to the weak rubber–filler interactions, but at higher test temperatures the properties drop sharply. This is in sharp contrast to the observation made with carbon black filled zinc sulfonated EPDM.

The improvement in tear strength is due to the deviation in tear path, as well as the formation of knotty tear. The increase in hysteresis on addition of filler is due to

additional energy dissipation mechanisms, such as motion of filler particles, chain slippage or breakage, and dewetting at high strains.

5.5.2 Viscoelastic Properties

Elastomers are generally complex viscoelastic materials and their mechanical response behavior depends strongly on the loading procedure, loading history, time (frequency), and temperature (39,40). Normally, the viscoelastic relaxation of a polymeric material extends over several decades of time- or frequency scale at a particular temperature. By using time–temperature superposition principle, it is possible to measure the viscoelastic data of a polymeric system at different temperatures over a limited period of time or/frequency. Eberhard and coworkers (41) have investigated the effect of porosity on the dynamic mechanical properties of rubber in compression. It was observed that nonlinear stress–strain curves of porous rubber blocks produced a dependence of dynamic properties on the mode of testing. Both storage and loss moduli as well as tan δ depended on the levels of porosity. The loss modulus increased with higher strain levels in porous samples, while the storage modulus changed because of reduced sample stiffness. The dynamic data were in agreement with the results of flexometer tests on porous and solid samples. The results suggest that the introduction of porosity reduces service life of rubber parts by providing stress raisers for crack initiation, rather than throughly changing the dynamic properties. The viscoelastic behavior of gum and highly filled EPDM at 138 carbon black was investigated (42) as function of time, temperature, strain, and frequency. The tensile strain relaxation and recovery results of the gum system show time dependent but strain-invariant behavior, whereas the filled system shows both strain and time dependence. The relaxation time spectrum of the filled system reveals nonlinear viscoelastic behavior. The networks of carbon black formed at high loading contribute significantly to the relaxation process. For short-term testing, the highly filled system appears to be time–temperature superposable. Filler aggregates adsorb a part of the molecular chain between, and within, the filler aggregate agglomerates and isolate and reduce the mobility of a part of the chain segment. The effects of vulcanizing system and cross-link density on strain-dependent isothermal dynamic mechanical properties of carbon black filled EPDM have been studied (43). The concept of filler–polymer interaction and the interaggregate attraction for filler was used to explain the observed variations. Dynamic mechanical properties of elastomer filled with polymeric and nonpolymeric fillers have been described in terms of mechanical models (44). In the case of a two-component series model, equations were developed to predict the individual strain in each phase when testing under position control. Utilizing the loss modulus and the square of the dynamic strain amplitude of each phase, it is possible to calculate the hysteresis in each section. On the basis of the assumption that the model hysteresis is a weighted average of individual hysteretic contributions, the energy loss per cycle of the series model may be predicted. This approach could be used in the case of a two-component parallel model.

5.6 RHEOLOGICAL PROPERTIES

The rheological character and the flow behvaior of carbon black filled elastomers are useful in rubber compounding and rubber processing industries. Such reinforcing fillers will (i) enhance the melt viscosity (45,46) with a prominent development in thixotropic character (47,48) and (ii) reduce the die swell and extrudate distortion (49) in elastomer compounds. Li (50) measured the shear viscosity, creep, and constant shear rate transients for 0.20 volume fraction compounds of an EPDM with carbon black and other particulate fillers at 100°C. All the compounds exhibited enhanced viscosities and yield values. Muller (51) has investigated the influence of changing temperature conditions on longtime behavior of carbon black filled rubbers. It was reported that shear creep and relaxation processes of carbon black filled EPDM rubber used as bearing materials increased with increasing temperature. On the contrary, the freezing and crystallization effects below 0°C retarded or stopped the response of rubber elastic. An experimental investigation has been carried out to study the rheological behavior of EPDM compounds in extrusion containing blowing agent (52). The apparent shear stress increases with the increase in shear rate. On the contrary, the apparent shear stress value is found to decrease with the addition of the blowing agent for both gum and carbon black filled compounds. There is a significant reduction in stress and viscosity with the blowing agent in the presence of a curing agent compared to the absence of the curing agent. The viscosity reduction factor (VRF) is decreased with the blowing agent loading, shear rate, and temperature (Fig. 5.7). With VRF data one can predict the viscosities of the mixture of EPDM compound and blowing agent with information on the viscosities of virgin compound alone at the desired shear rate and temperature.

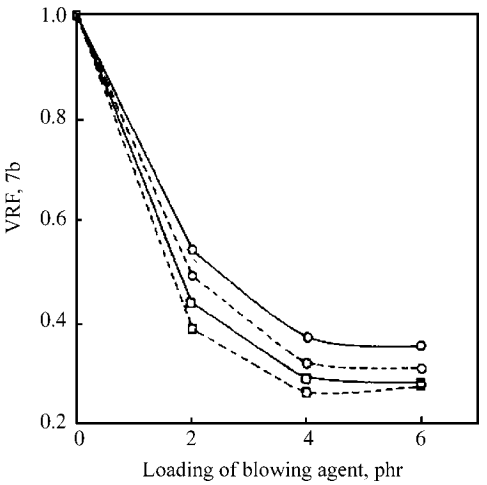

Figure 5.7 The viscosity reduction factor (VRF) at different shear rates in carbon black filled compounds with blowing agent loading at different extrusion times in absence of curing agent at 140°C: (—) 3 min; (– – –) 6 min; (○) 3.074 s^{-1}; (□) 23.055 s^{-1}. (From Reference 52 with the permission of Elsevier Science Ltd.)

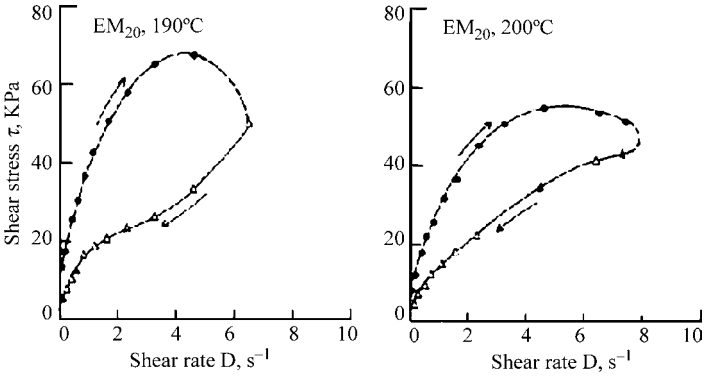

Figure 5.8 Thixotropic character of conducting carbon black filled EPDM compound at 190 and 200°C: plots of shear stress developed versus shear rate applied over shear loading and unloading cycles in each case. (From Reference 53 with the permission of Elsevier Science Ltd.)

The effect of incorporation of different doses of extra conducting carbon black filler on melt rheology and relaxation behavior of EPDM system at 190 and 200°C was reported (53). Melts of both unfilled EPDM and carbon black filled EPDM compounds showed pseudoplastic or shear thinning flow behavior (Fig. 5.8). Increasing the carbon black loading caused a monotonic increase in the pseudoplastic character of EPDM. Higher incorporation of carbon black as filler imparted a decreasing trend in rupture shear rate (Dr) (Fig. 5.9) and in shear hysteresis loss up to the rupture point; however, other rheological parameters

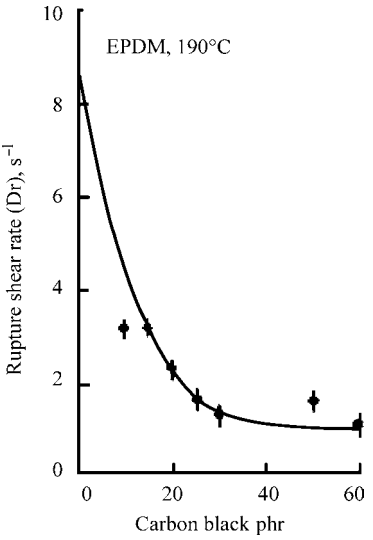

Figure 5.9 The effect of different loadings of conducting carbon black as filler on rupture shear rate (Dr) for EPDM at 190°C. (From Reference 53 with the permission of Elsevier Science Ltd.)

such as limiting shear viscosity (η_L), rupture shear viscosity (η_r), yield stress (τ_0), and relaxation time (t_R) followed increasing trends with increasing filler loading. The trend of changes of different rheological property parameters with increasing carbon black loading is mainly because of the clustering of filler particles, ultimately leading to filler networking. Carbon black filler induced structural modification of the elastomer chain segments mostly through physical interactions including occlusion within the pores of the filler particles and partly through chemical anchorage of the elastomer chain molecules or segments on the surface of the conducting carbon black filler particles, utilizing the traces of functional groups present in them.

5.7 CONDUCTIVE PROPERTIES

The electrical conductivity in polymer–carbon black composites depends on particle size, high structure, high porosity, and low volatile content of carbon blacks (54). The conductivity of carbon black is mainly related to structure and/or porosity, which can be inferred from the DBPA (dibutyl phthalate absorption) (55) number as a measure of the structure of the carbon black aggregate. Generally, higher DBPA means higher structure and bulkiness, resulting in an increase of conductivity (56). High structure is referred to as an aggregate of carbon black containing up to 200 elementary particles of carbon black (57). EPDM is used in a diverse range of electrical applications because of its superior electrical properties, its flexibility over a wide temperature range, and its resistance to moisture and weather (58). Dielectric properties of elastomer have been investigated during microwave curing process (59,60). Ganchev et al. (61) have used completely filled short-circuited wave guide techniques to conduct extensive dielectric constant measurement of rubber compounds (61). The influence of carbon black content on rubber was investigated and at all frequencies the dielectric constant increases as a function of increasing carbon black content. The variation of dielectric constant values decreases as frequency increases. The results showed that the real and imaginary parts of rubber dielectric constant increase as a function of increasing percentage of carbon black. The influence of curatives on uncured rubber compounds with different carbon black volume percentages was also detected. With small volume content of curatives, the detection of dielectric constant of the rubber compound is possible. The sensitivity of detection increases with decreasing frequency. Application of electrochemical impedance spectroscopy (EIS) in the investigations of the anodic properties of conductive polymeric composites, based on the EPDM and the mixture of carbon black designated for cathodic protection, has been reported (62). Elastomeric polymeric anodes are relatively new materials used in impressed current cathodic protection systems. They have been applied in the protection of reinforced concrete structures and underground steel pipelines. Their lifetime is estimated to be 10 years and even up to 25 years; however, there are reports of cases of damage caused by excessive local current density (63,64). It was found for low carbon black content composite that a significant increase in the resistance of the anode current flow occurs in time (62).

Thus, it is beneficial to introduce larger amounts of conductive carbon material. On the contrary, too high carbon black content will damage the processing properties of the polymeric mixture. For composites containing a given type of carbon black, the partial resistance of the anodic reaction does not change significantly. However, electric properties of anodes, expressed as an increase in the resistance of the polymeric layer, may deteriorate, especially in the zone directly in contact with the electrolytic environment. It is greater, if the carbon black content in the composite is less and the density of the polarizing current is high. The EIS technique allows elaboration in a short time of new composites containing modified conductive components, making easier the evolution of oxygen or chlorine and limiting the process of carbon oxidation. This should lead to composites characterized by greater anodic stability and smaller susceptibility to greater current loads and at the same time should have an advantageous effect on cathodic protection systems with polymeric anodes.

DC electrical conductivity measurements of the filled EPDM vulcanizate indicate a percolation concentration range over 15–30 phr of conducting carbon black loading (32). Trends of change in voltage (V) developed with increase in the current (I) applied for the carbon black filled EPDM vulcanizate at different temperatures commonly indicate ohmic behavior for application of current up to a critical level. Beyond the critical current (IC), the developed voltage practically becomes insensitive to large enhancements in the applied current; the filled vulcanizates, thus, exhibit nonohmic character for $I >$ IC. Electromagnetic interference (EMI) shielding effectiveness (SE) generally increases on increasing the carbon black loading. Vulcanization substantially contributes to the enhancement in the EMI SE of the filled EPDM compounds. Influences of alumina trihydrate (ATH) and carbon black content on the tracking resistance of EPDM compounds have been reported (65). Tracking and erosion resistance of EPDM/ATH compounds significantly improves with the increase of ATH content. Carbon black content up to 1.5 phr has a positive effect on improving the tracking resistance before and after weathering in UV-B lamp. It could be due to the fact that carbon provides a more linear voltage distribution, that is, mitigation of concentration of the electric field due to conductivity of carbon black. The positive temperature coefficient (PTC) effects of carbon black filled semicrystalline and amorphous EPDM composites were reported (66). The semicrystalline EPDM/CB composite exhibited a low PTC effect followed by a pronounced negative temperature coefficient (NTC) effect, while the amorphous EPDM/CB composite exhibited only an NTC effect. By the effect of γ-ray irradiation, not only was the NTC effect of the composites eliminated but also a high PTC effect appeared. The PTC intensity reached as high as six orders of magnitude even for an amorphous EPDM/CB composite, and the PTC transition temperature decreased with the irradiation dose. The preparation of new thermistors based on EPDM/TiC composites with new double negative and positive temperature coefficients of conductivity (NTCC/PTCC) has been reported (67). EPDM composites loaded with 50 phr HAF carbon black and different concentrations of TiC were developed. Figure 5.10 shows the effect of TiC content on the electrical conductivity of EPDM composites. It was found that the conductivity increases slightly up to 40 phr, followed by a very sharp increase after

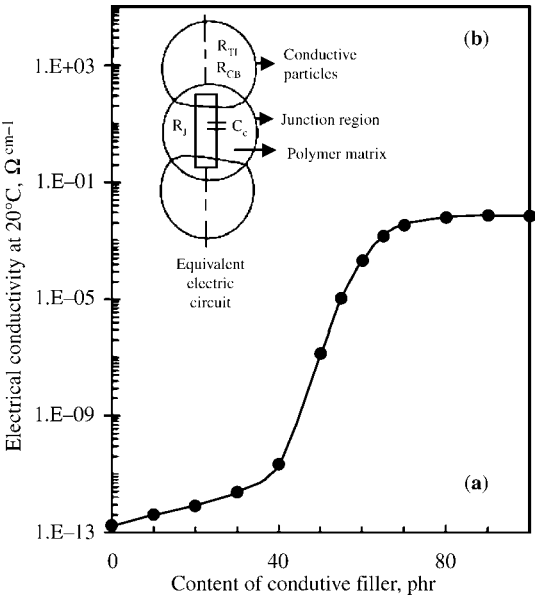

Figure 5.10 Shows the effect of TiC content on (**a**) the electrical conductivity of EPDM composites at room temperature, and (**b**) the equivalent resistor–capacitor circuit in the junction region of conductive particles in an EPDM composites. (From Reference 67 with the permission of Elsevier Science Ltd.)

reaching the percolation threshold. For low HAF black loading, the conducting particles in the rubber matrix are widely separated and the large gap distance between conductive phases acts as barrier to the flow of mobility carrier through the matrix resulting in a lower level of electrical conductivity value. In the percolation concentration zone (20–50 phr), the conductive particle concentration increases and leads to a decrease in gap distance between conductive particles. Thereafter a sharp increase in the electrical conductivity was observed. The electrical properties of EPDM composites are strongly affected by TiC content and exhibit hopping conductivity and p-type semiconductor behavior. The effects of TiC on the NTCC and PTCC intensities are given in Table 5.3. NTCC and PTCC values increased with increasing TiC content. This indicates that TiC increases the ordering and/or the texturing of the rubber matrix. This reveals that EPDM/TiC composites are good NTCC and PTCC thermostats for practical applications. The dielectric constant increases linearly with temperature, without any remarkable change in behavior. TiC improves the thermal stability and the microstructure core of the rubber matrix.

Zabicky and Adler (68) have investigated the effect of various carbon blacks on the dielectric properties of composites. It was found that EPDMs with XC-72 and intermediate superabrasion furnace (ISAF) have higher tensile strength, lower dielectric properties, and lower tracking resistance with increasing carbon black concentration. For the samples with fast extruding furnace (FEF) and SRF, the tensile

Table 5.3 Values of NTCC and PTCC Intensities.

Sample code[a]	NTCC 10^3 °C^{-1}	PTCC 10^3 °C^{-1}
F0	−5.2436	5.002
F5	−6.7430	5.6754
F10	−1.7771	6.5432
F15	−8.7498	7.9876
F20	−9.2636	8.7980

[a]0, 5, 10, 15, and 20 stands for the loading of TiC content in the composite, respectively.
From Reference 67 with the permission of Elsevier Science Ltd.

strength moderately increases and the dielectric properties moderately decrease with increasing carbon black concentration. EPDM with medium thermal (MT) black does not change the mechanical and dielectric properties at concentrations up to 20 phr and improve the tracking resistance up to 10 phr. The lower dielectric properties of composites with XC-72 and ISAF are due to the presence of high concentration of oxidized groups in their surfaces, such as quinone (=O), phenol (—OH), carboxylic acid (—COOH), and lactone (—COO—) (55), which result in a higher chance of static energy accumulation and higher polarity. Addition of up to 1.5 phr of SRF black has a positive effect, improving both tracking and weathering resistance. The enhancement of tracking resistance could be due to the fact that conductivity of carbon black suppresses the electrical field, leading to a linear voltage distribution during the tracking test. Thus, tracking resistance and erosion resistance are improved by adding a small amount of carbon black.

Common conductive fillers other than carbon black are carbon and graphite fibers, metal-coated inorganic oxide particles, and metal powders; But carbon black is the most widely used material for rubber matrices. It not only provides high degree of conductivity but also imparts good reinforcement to the rubber matrix. However, for many applications high conductivity is the main requirement and the mechanical properties of the system are a secondary consideration. Short carbon fiber (SCF) as conductive filler is a better choice than conductive carbon black, as it can provide higher conductivity at lower loading. SCF-filled rubber composite provides high level of conductivity and the percolation limit can be reached at relatively much lower loading than that with conductive carbon black (69). SCF may be considered as a long chain of carbon black particles, and this aids in the formation of a continuous conductive network through aggregation of SCF in the matrix.

Owning to the brittle nature of carbon fiber, extensive breakage occurs during mixing and processing with rubber, and the extent of breakage increases with increase in matrix viscosity and fiber loading. The degree of reinforcement achieved through incorporation of SCF is marginal due to the poor fibre–rubber interaction as well as the large particle size of SCF.

5.8 AGING PROPERTIES

A very serious problem related to polymer materials is aging and degradation in long-term applications, especially in severe environmental conditions. Several methods such as tensile strength and elongation at break testing (70), density testing (71), oxidation induction time (OIT) testing by watching for the exothermic peak that occurs during isothermal exposures in a differential scanning calorimeter (72), and indenter modulus testing (73) have been developed to monitor the aging condition of wire and cable materials. Recently, Micro-ATR spectroscopy has been shown to be a useful method for studying the aging properties of EPDM/carbon black composites (74). The oxidation profile obtained from the aging study conducted at 70°C for 4, 8, and 9 days are shown in Fig. 5.11. After 4 days, oxidation is detected only for the surface regions with relative position width of about 0.05 that corresponds to just over 0.1 mm. After 8 days, oxidation is detected up to a relative position of about 0.25 into the sample from both faces. This corresponds to oxidation into the sample of about 0.6 mm from both faces. The 9-day profile is a little different to that measured after 8 days. The shape of the oxidation profile shows that EPDM starts oxidizing suddenly from the surface after consumption of the antioxidant. The reaction proceeds very fast at the higher temperature and is severely diffusion-limited resulting in the steep U-shaped profile. Wong and coworkers (75) reported that the resistivity measurements are good as nondestructive test to monitor the aging process in EPDM composites. It was observed that carbon black filled EPR composite had large changes in resistivity by the time the mechanical failure of the material was reached. Figure 5.12 shows the effect of aging time on the variation of resistivity change, volume shrinkage, volume fraction change of carbon black, and

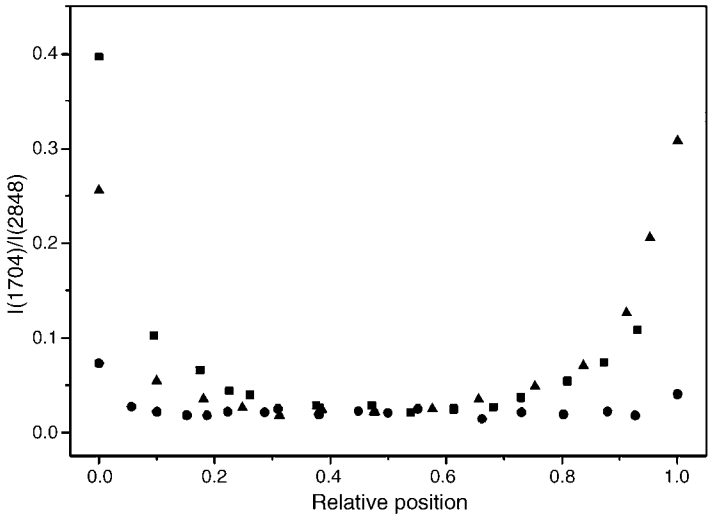

Figure 5.11 Oxidation profiles of EPDM at 170°C: (●) 4 days; (▲) 8 days; (■) 9 days. (From Reference 74 with the permission of Elsevier Science Ltd.)

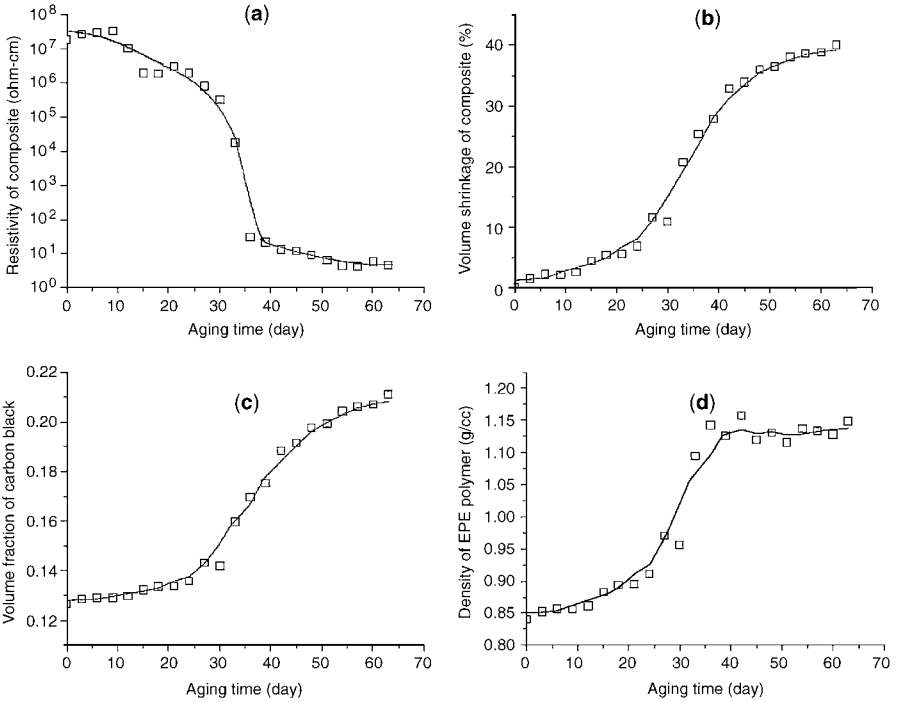

Figure 5.12 Analysis of 25-CB sample changed (**a**) resistivity change, (**b**) volume shrinkage, (**c**) volume fraction change of carbon black, and (**d**) density change of the EPR polymer component versus the aging time. (From Reference 75 with the permission of Elsevier Science Ltd.)

density change of the EPR component of the composite. Analyses of weight and density changes indicate that the resistivity decrease was due to the increase in volume fraction of the conductive carbon black caused by the mass loss of polymer matrix and the sample shrinkage during the thermal aging process.

5.9 APPLICATIONS

Carbon black filled EPDM rubber is found to be suitable for manufacturing microwave shielding materials in the X-band frequency (76). Major applications of EPDM composites are as weather-resistant rubber moldings (77) and weather seals (78). The other important areas are in the production of rubber springs (79) and conductive rubbers (80). The NTCC effects of EPDM composites are useful in a number of other applications such as self-controlled heaters, current limiters, over current protectors, and sensors (81,82) The PTCC effect can be used in antistatic materials, electromagnetic shielding, and electromagnetic interface shielding (32,83). It is also used as reinforced elastomer joint, especially for use as glazing seal in buildings or transportations.

5.10 CONCLUSIONS

In this chapter, we have provided an overview of research in EPDM/carbon black composites and insights into the factors that will ultimately control their properties. The properties of composites depend on a multitude of factors that include the type, the particle size of carbon black, the composition of the EPDM matrix, the interaction between the carbon black and the EPDM matrix, and the morphology of the composites. A uniform morphology is observed as the carbon black loading is increased over the percolation concentration range. The trend of changes of different rheological property parameters with increasing carbon black loading is mainly because of the clustering of filler particles, ultimately leading to filler networking. Carbon black and black in presence of TiC have demonstrated their capability as conductive filler in EPDM matrix. The NTCC and PTCC effects of these composites have potential application in various electrical fields.

In conclusion, EPDM/carbon black composites offer both a great potential and a vibrant area of work for years to come.The significant progress in the understanding of these composite systems within the past few years points toward a bright future.

NOMENCLATURE

ATH	Alumina trihydrate
ATR	Attenuated total reflectance microscopy
CB	Carbon black
DBPA	Dibutyl phthalate absorption
EIS	Electrochemical impedance spectroscopy
EMI	Electromagnetic interference
EPDM	Ethylene–propylene–diene rubber
FEF	Fast extruding furnace
HAF	High abrasion furnace
I	Current
ISAF	Intermediate superabrasion furnace
MT	Medium thermal
NMR	Nuclear magnetic resonance
NTCC	Negative temperature coefficient of conductivity
OIT	Oxidation induction time
PTCC	Positive temperature coefficient of conductivity
SCF	Short carbon fibre
SE	Shielding effectiveness
SEM	Scanning electron microscopy
SRF	Semireinforcing furnace
V	Voltage
VRF	Viscosity reduction factor
Dr	Rupture shear rate

η_L Limiting shear viscosity
η_r Rupture shear viscosity
τ_0 Yield stress
t_R Relaxation time

REFERENCES

1. H. R. Clauser, *Industrial and Engineering Materials*, McGraw-Hill, New York, 1975.
2. J. V. Masi, D. S. Dixon, and M. Avoux, in: *Proceedings of IEEE International Symposium on EMC*, IEEE, Atlanta, 1987, p. 183.
3. A. I. Medalia, *Rubber Chem. Technol.*, **51**, 437 (1978).
4. S. Wolff, in: *Carbon Black Science and Technology*, 2nd Edition, J.-B. Donnet, R. C. Bansal, and M.-J. Wang (eds.), Marcel Dekker, New York, 1993, p. 289.
5. M. Gerspacher, in: *Carbon Black Science and Technology*, 2nd edition, J.-B. Donnet, R. C. Bansal, and M.-J Wang (eds.), Marcel Dekker, New York, 1993, p. 377.
6. N. C. Das, T. K. Chaki, D. Khastgir, and A.Chakraborty, *Adv. Polym. Technol.*, **20**, 226 (2001).
7. D. M. Bigg, *Polym. Eng. Sci.*, **19**, 1188 (1979).
8. S. Lipatov, Y. P. Mayunyia, N. A. Gladyreva, and Y. V. Lebedev, *Polym. Sci. USSR*, **25**, 714 (1983).
9. R. H. Norman, *Conductive Rubber and Plastics*, Elsevier, London, 1970.
10. V. E. Grew, *A Study of Electrically Conductive Polymers and their Applications*, Yokogawa Shobo, 1970.
11. K. Kanamari, Japan Patent, 52-68437 (1977).
12. K. Kanamari, *Int. Polym. Sci. Technol.*, **13**(2), T47 (1991).
13. J. Regan, in: *Polymer Plastic Technology and Engineering*, Vol. 3, L. Natureman (ed.), Marcel Dekker, New York, p. 47.
14. D. M. Bigg, W. Merik, and D. E. Stutz, *Polym. Test.*, **5**, 169 (1985).
15. A. Sternfield, *Mod. Plast. Int.*, **13**(2), 48 (1982).
16. K. Kakizawa, *Int. Polym. Sci. Technol.*, **13**(2), T-40 (1986).
17. K. Kanamori, *Int. Polym. Sci. Technol.*, **13**(2), T-4 (1986).
18. P. A. Marsh, A. T. Voet, L. D. Price, and T. J. Mullens, *Rubber Chem. Technol.*, **141**, 344 (1968).
19. H. F. Mark, N. M. Bikales, C. G. Overberge and G. Menges, *Encyclopedia of Polymer Science and Engineering*, Vol. 6, Wiley, New York, 1986.
20. Y. Suzuki, M. Owaki, M. Mouri, N. Sato, H. Honda, and K. Nakashima, *Toyota Tech. Rev.*, **48**, 53 (1998).
21. E. K. Easterbrook and R.D. Allen, in: *Rubber Technology*, M. Morton (ed.), Van Nostrand Reinhold, New York, 1987, p. 260.
22. E. E. B. Meuleman, B. Bosch, M. H. V. Mulder, and H. Strathmann, *AIChE J.*, **45**, 2153 (1999).
23. C. C. Pereira, A. C. Habert, R. Nobrega, and C. P. Borges, *J. Membr. Sci.*, **138**, 227 (1998).
24. R. Y. M. Huang, G. Y. Moon, and R. Pal, *Ind. Eng. Chem. Res.*, **41**, 531 (2002).
25. A. G. Strong, *Elastomerics*, **116**, 19 (1984).
26. R. Kidd, *Elastomerics*, **116**, 37 (1984).
27. V. M. Litvinov and P. A. M. Steeman, *Macromolecules*, **32**, 8476 (1999).
28. D. Raftery, B. F. Chmelka, in: *NMR Basic Principles and Progress*, Vol. 30, D. Fluck, G. Kosfeld and Seelig (eds.), Springer Verlag, Berlin, Heidelberg, 1994, p. 111.
29. K. Sperling-Ischinsky and W. S. Veeman, *J. Braz. Chem. Soc.*, **10**, 299 (1999).

30. V. M. Litvinov, in: *Organosilicon Chemistry: From Molecules to Materials*, Vol. II, N. Auner and J. Weis (eds.), VCH, Weinheim, 1996, p. 779.
31. V. J. McBrierty and J. C. Kenny, *Kautsch. Gummi Kunstst.*, **47**, 342 (1994).
32. P. Ghosh and A. Chakrabarti, *Eur. Polym. J.*, **36**, 1043 (2000).
33. J. L. M. Verschuren, R. Zeeman, L. V. D. Doss, and A. Bantjes, *Kuatsch. Gummi Kunst.*, **49**, 336 (1996).
34. Q.-B. Jiang, D.-M. Jia, J. Yang, *Tanxingti*, **14**, 25 (2004).
35. P. A. Kakavas, *Polym. Eng. Sci.*, **41**, 589 (2001).
36. R. W. Ogden, *Proc. R. Soc. Lond.*, **326**, 565 (1972).
37. A. F. Younan, A. M. Choneim, A. A. A. Tawfik, and K. N. Abd-El-Nour, *Polym. Degrda. Stabil.*, **49**, 215 (1995).
38. T. Kurian, P. P. De, D. Khastgir, D. K. Tripathy, S. K. De, and D. G. Peiffer, *Polymer*, **36**, 3875 (1995).
39. N. G. McCrum, B. E. Read, and G. Williams, *An elastic and Dielectric Effects in Polymeric Solids*, Wiley, New York, 1967.
40. J. D. Ferry, *Viscoelastic Properties of Polymer*, 3rd edition, Wiley, New York, 1980.
41. A. I. Kasner and E. A. Meinecke, *Rubber Chem. Technol.*, **69**, 223 (1996).
42. M. G. Makovic, N. K. Dutta, M. Dimopoulos, N. R. Choudhury, and J. G. Matisons, *Thermochim. Acta*, **357**, 211 (2000).
43. C. S. S. Namboodiri and D. K. Tripathy, *Plasti. Rubber Comp. Proc. Appl.*, **17**, 171 (1992).
44. J. Luthern, *Polymer*, **34**, 4241 (1993).
45. J. L. White and J. W. Crowder, *J. Appl. Polym. Sci.*, **18**, 1013 (1974).
46. S. Toki and J. L. White, *J. Appl. Polym. Sci.*, **27**, 3171 (1982).
47. L. Mullins, *J. Phys. Colloid Chem.*, **54**, 239 (1950).
48. Y. Suetsugu and J. L. White, *J. Non-Newtonian Fluid Mech.*, **114**, 121 (1984).
49. J. L. Leblanc, *Rubber Chem. Technol.*, **54**, 905 (1981).
50. L. Li, *Rubber Chem. Technol.*, **69**, 628 (1996).
51. F. A. Muller, in: *Proceedings of the 5th Conference of the European Plastic Caoutch*, C. R., Vol. 2, pp. D17-1-D17–3 (1978).
52. K. Ch. Guriya, A. K. Bhattachariya, and D. K. Tripathy, *Polymer*, **39**, 109 (1998).
53. P. Ghosh and A. Chakrabarti, *Eur. Polym. J.*, **36**, 607 (2000).
54. J. F. Rabek, *Photodegradation of Polymers*, Elsevier Applied Sciences, London, 1990, p. 196.
55. E. K. Sichel, *Carbon Black–Polymer Composite*s, Marcel Dekker, New York, 1982, p. 9.
56. J. E. Mark, B. Erman, and F. R. Eirich, *Science and Technology of Rubber*, Academic Press, New York, 1994, p. 434.
57. J. L. Leblanc, *Prog. Polym. Sci.*, **27**, 627 (2002).
58. M. Brown, *IEEE Electr. Insul. Mag.*, **10**, 16 (1994).
59. B. Terselius and B. Ranby, *J. Microwave Power.*, **13**, 327 (1978).
60. H. F. Schwarz, R. G. Rosisio, M. R. Wertheimer, and D. Couderc, *J. Microwave Power.*, **8**, 303 (1973).
61. S. I. Ganchev, J. Bhattacharyya, S. Bakhtiari, N. Qaddoumi, D. Brandenburg, and R. Zoughi, *IEEE Trans. on Microwave Theor. and Tech.*, **42**, 1 (1994).
62. J. Walaszkowski, J. Orlikowski, and R. Juchniewicz, *Corros. Sci.*, **37**, 1143 (1995).
63. B. S. Wyatt, in: *Cathodic Protection Theory and Practice*, V. Ashworth and C. Googan (eds.), Ellis Horwood Ltd., Chichester, 1993.
64. W. F. Gibson and J. L. Pikas, *Mater. Perform.*, **32**(3), 24 (1993).
65. C. H. Lee and S. W. Kim, in: *Proceedings of International Symposium on Electrical Insulating Materials*, Toyohashi, Japan, 1998, p. 297.

66. X. He, L. Wang, and X. Chen, *J. Appl. Polym. Sci.*, **80**, 1571 (2001).
67. F. El-Tantawy, *Eur. Polym. J.*, **38**, 567 (2002).
68. R. Alder and J. Zabicky, Electrically conducting carbon black and Its composites, *Thesis*, July 2002.
69. K. P. Sau, T. K. Chaki, and K. Khastgir, *Polymer*, **39**, 6461 (1998).
70. C. S. Shah, M. J. Patni, and M. V. Pandya, *Polym. Sci. Symp. Proc. Polym.*, **1**, 405 (1991).
71. K. T. Gillen, M. Celina, and R. L. Clough, *Radiat. Phys. Chem.*, **56**, 429 (1999).
72. L. R. Mason and A. B. Reynolds, *J. Appl. Polym. Sci.*, **66**, 169 (1997).
73. T. A. Shook and J. B. Gardener, EPRI Technical Report NP-5920, EPRI Publication, CA, USA, 1988, p. 68.
74. T.-T. Do, M. Celina, and P. M. Fredericks, *Polym. Degrad. Stabil.*, **77**, 417 (2002).
75. Y. Sun, S. Luo, K. Watkins, and C. P. Wong, *Polym. Degrad. Stabil.*, **86**, 209 (2004).
76. P. Annadurai, A. K. Mallick, and D. K. Tripathy, *J. Appl. Polym. Sci.*, **83**, 145 (2002).
77. I. Tadanobu and U. Mitsuo Ger.Offen, A1 19840105 (1984).
78. O. Robert, US Patent, WO2006083506.
79. N. Naven, J. Vittoser, Z. Gilmakn, and S. Puuter, *Rubber Chem. Technol.*, **75**, 265 (2002).
80. O. Tomoaki and F. Kiyoshi, Japan Patent, JP 8134294.
81. D. Saraydin, *Polym. J.*, **29**, 631 (1997).
82. F. El-Tantawy. *Eur. Polym. J.*, **37**(3), 565 (2001).
83. H. Tagachi, *Physica B*2, **70**, 325 (1999).
84. S. J. Pierre, Euopean Patent, FR2764032.

Chapter 6

Selected Topics on Polypropylene/Wood Flour Composites: Thermal, Mechanical, and Time-Dependent Response

María M. Reboredo,[1] Mirta I. Aranguren,[1] and Norma E. Marcovich[1]

6.1 INTRODUCTION

The need for materials for specific purposes with environment-friendly characteristics is growing, due to limited natural resources and increasing environmental regulations (1–3). Demands for saving fossil resources and for relieving the strain on disposal sites and atmosphere must be taken into account when developing and using new materials (4). For a wide variety of applications in the field of low and medium mechanical loads, renewable raw materials are increasingly used as strengthening components for innovative products, as an alternative to the use of established fibers (glass fiber and carbon fiber) (5). Moreover, the use of lignocellulosic materials in thermoplastic composites may contribute to reduce the waste of vegetal biomass (6). Recently, Guillet (7) showed that plastics have the lowest energy costs of all comparable materials and cause less environmental pollution in their production and fabrication. The technology of photodegradable plastics and experimental studies of the biodegradation of conventional and photodegradable polyethylene (PE), polypropylene (PP), and poly(ethylene terephthalate) may lead

[1]INTEMA-Facultad de Ingeniería, Universidad Nacional de Mar del Plata, Juan B. Justo 4302, 7600 Mar del Plata, Argentina

Polyolefin Composites, Edited by Domasius Nwabunma and Thein Kyu

to thermoplastic/cellulosic filler composites even more environment friendly, since these reinforcing fillers derive from renewable sources, are biodegradable, and can reduce squandering of many valuable cellulosic fibers (7).

Wood fiber reinforced plastic profiles are growing rapidly in nonstructural wood replacement applications like decking.

Suitable matrix materials for natural fiber reinforced polymers are resin systems, thermoplastic starch, and polyolefins (PE and PP), while polypropylene provides most of the advantages with regard to economic (price), ecological (recycling behavior), and technical requirements (higher thermal stability than polyethylene) (7). Moreover, among commodity thermoplastics, polypropylene possesses outstanding properties like low density, good flex life, sterilizability, good surface hardness, very good abrasion resistance, and excellent electrical insulation properties. There are environmental and economical advantages in producing wood flour (WF) thermoplastic composites. Commonly, the main purpose for the addition of cellulose-based fillers to thermoplastics is to reduce costs per unit volume and improve stiffness (8). Low price cellulose-based fibers such as wood flour, wood fibers, and cellulose fibers have high stiffness and low density, and are recyclable and nonabrasive. Contrary to PP, cellulosic fibers are highly hygroscopic, due to the presence of polar groups on its different components. In particular, wood fibers have a natural tendency to absorb moisture, due to their overall structure made of cellulose fibers in an amorphous matrix of hemicellulose and lignin, all three components containing numerous hydroxyl groups that are strongly hydrophilic (9,10).

Reinforced PP combines fiber composite mechanical properties with thermoplastic versatility of manufacturing allowing its use in several industrial sectors characterized by mass production: cars, sports, domestic appliances, and so on. The excellent processability is a key characteristic of short fiber/particulate-reinforced PP; thus, the utilization of almost the same plastic processing/molding methods developed for unreinforced polymers is adequate. Moreover, wood fibers are less abrasive to molds and mixing equipments than mineral fillers.

Recent studies have demonstrated the feasibility of developing microcellular structures in polymer–wood fiber composites. The wood fiber reinforced polypropylene microfoams, a new trend in wood fiber strengthened plastic racks made by injection molding process, are now being studied. Bledzki and Faruk (11) examined in a very recent work, the influence of the different types of chemical foaming agents, wood fiber types and contents, as well as the use of a compatibilizer on the physicomechanical properties of wood fiber–PP microfoamed composites.

The renaissance of the cellulose fiber composites, however, has been greatly hindered by the available forms of the cellulose fibers. Rather than providing continuous cellulose filaments, which would be the essence of the reinforcement, present techniques produce fibers or fabrics consisting of discontinuous waved cellulose fibers (12). The situation makes the wood flour a competitive substitute for the cellulose fibers, especially when extrusion compounding and injection molding are adopted as processing methods. This is clearly so, when polypropylene is considered as the matrix polymer (13). The promise of using a cellulosic

reinforcement, in combination with the possibility of plastics recycling, has made the subject of polypropylene–wood fiber or flour blends one of the most widely studied systems in this research area.

6.2 INTERFACIAL COMPATIBILIZATION: ADDITION OF MALEATED POLYPROPYLENE AND CHEMICAL MODIFICATION OF WOOD FLOUR

In order to improve the interaction between the otherwise incompatible surfaces, the addition of a compatibilizer or the surface modification of the fibers (or the matrix) is envisaged. The hydrophilization of PP is possible (14), but most often treatments are performed on the lignocellulosic reinforcements (15–18). The addition of small quantities of maleic anhydride–polypropylene copolymer (MAPP) improved the interfacial adhesion, thereby leading to improved properties of the final composites (8,16,19–23). Generally, dry blending of MAPP with the wood and the isotactic PP provides a processing cost advantage over other coupling methods that rely on the pretreatment of the wood (24,25). One of the examples regarding chemical modification of cellulosic filler is the work of Mishra and Naik (26), who esterified several lignocellulosic fibers with maleic anhydride (MAN) and used them to prepare composites with polystyrene as matrix material. They found that the treatment reduced the moisture sorption of both fibers and resulting composites with respect to the untreated systems. Clemons et al. (27) found the same behavior comparing the response of composites made from PP and esterified aspen fibers. Felix and Gatenholm (28) modified cellulose fibers with several surface modifying agents in order to compatibilize them with PP. The interfacial interactions between polypropylene and treated cellulose fibers increased with an increasing molecular weight of the coupling agent, but the properties of the final composite were not evaluated. More recently, Ichazo and coworkers (9) treated wood flour with sodium hydroxide and with silane and also used two maleated polypropylenes to improve the adhesion between filler and PP matrix. They found that both the silane treatment and MAPPs addition improved the polymer–WF adhesion and the dispersion of the particles, while the alkaline treatment only improved the dispersion. An interesting summary regarding chemical and physical modification of cellulosic fibers can be found in one of the works of Bledzki and Gassan (12).

In our work, wood flour from *Eucalyptus* sp. (Entre Rios, Argentina) was used as reinforcing filler. Only particles that pass through a sieve of mesh 100 (Tyler series) were utilized. Thus, the maximum particle average diameter was 147 μm; particles below this size were used in the study.

To chemically modify the filler, wood flour was dried at 70°C up to constant weight in a vacuum oven and then immersed in a 0.6 mol l^{-1} solution of MAN in xylene and heated at reflux temperature (140°C) for 4 h. Subsequently, the esterified wood particles were separated from the xylene solution and intensively washed with distilled water in order to eliminate the unreacted anhydride. Finally, the wood flour was dried again at 70°C in a vacuum oven until constant weight was achieved. The

MAN content of the treated wood flour was determined using analytical techniques (29), and corresponded to 23.47 g MAN/100 g neat wood flour.

The polymeric matrix was polypropylene Moplen powder, kindly provided by Himont (Italy), with a density of 0.91 g cm^{-3}, a melt flow index (MFI) of 17.2 ± 1.3 (at 230°C, according to ASTM 1238), a melting temperature $T_m = 163.5$°C (determined by dynamic scanning calorimetry at 10°C min^{-1} under nitrogen atmosphere), and a glass transition temperature $T_g = 9.7$°C (from dynamic mechanical analysis (DMA) at 10°C min^{-1}). Maleic anhydride modified polypropylene, MAPP (modified J 300, kindly provided by University of Simon Bolivar, Venezuela), was also used as compatibilizing agent. Determination of the degree of grafting was conducted by a method of acid–base titration suggested by different authors (30–32). The MAN content of the copolymer was 0.3 ± 0.05 wt%. Other characteristics of the selected MAPP were as follows: density = 0.82 g cm^{-3}; MFI = 6.6 ± 1.4 (at 230°C, according to ASTM 1238), melting temperature $T_m = 162.5$°C (determined by dynamic scanning calorimetry at 10°C min^{-1} under nitrogen atmosphere), and glass transition temperature $T_g = 3.0$°C (from dynamic mechanical analysis at 10°C min^{-1}). The compatibilizing agent was added in the proportion of 5 g of MAPP for each 100 g of untreated wood flour.

Natural and synthetic polymers suffer the degradation of their mechanical properties under the influence of increasing temperatures. Thus, it is very important to have some knowledge about the effect of the working temperatures on the processing duration, since these variables can contribute to the generation of thermal stresses during the manufacturing of the reinforced thermoplastic composites and can also trigger the thermal degradation of the materials. Essential information regarding the thermal stability of the natural fibers to be processed can be obtained from the thermogravimetric analysis (TGA) (4).

TGA dynamic scans (at 10°C min^{-1}) allowed to prove the efficiency of the MAN treatment in reducing the moisture sorption of the wood flour (percent loss at 105°C), since the absorbed water represented less than 1.5% of the weight of the sample, while the untreated wood flour contained more than 6% of moisture (33). This result agrees with the observations made by different researchers, regarding differently esterified lignocellulosic samples (10,26,27). Table 6.1 shows the results of isothermal thermogravimetric measurements performed at 200°C on treated and untreated wood flour under air and nitrogen atmosphere. It is clearly seen that the loss of mass suffered by the MAN-treated wood flour is larger compared with that of the

Table 6.1 Percentage of Weight Lost in TGA Isothermal (200°C) Measurements for Untreated and MAN-Treated Wood Flour.

Sample	Atmosphere	15 min	1 h	2 h
Untreated wood flour	Nitrogen	0.62	1.59	2.48
	Air	0.92	3.02	5.62
MAN-treated wood flour	Nitrogen	3.64	6.00	7.48
	Air	4.20	7.87	10.71

untreated reinforcement, even in the first minutes of the tests. As expected, the mass lost in nitrogen atmosphere is, in all cases, lower than the mass lost in an oxidative atmosphere (air). Unfortunately, during processing of PP and PP composites, a relatively high temperature is needed in order to decrease the melt viscosity. The low thermal stability of MAN-treated wood flour might generate volatiles during the extrusion and injection steps and thus generate voids in the final composites.

The use of a chemical treatment on wood flour particles or the addition of a compatibilizer had an obvious effect on the interface fiber–matrix as can be seen in the SEM micrographs of the fractured composites (34). Figure 6.1 shows the SEM micrographs of the surface of wood flour particles observed after fracture of different composites. Untreated wood flour exhibits a rather smooth surface (Fig. 6.1a) with almost no remains of the attached polymer. On the contrary, the particle surfaces show a very similar appearance if they were previously treated with MAN (Fig. 6.1b) or when untreated wood flour was used but MAPP was added as coupling agent (Fig. 6.1c). In the last two cases, the surface of the wood flour after the composite fracture shows a coating layer, evenly distributed on the entire surface as the result of the PP or MAPP attachment.

6.3 COMPOSITE PREPARATION: PROCESSING METHODS

The final properties of WF/PP composites to a large extent depend on the type of compounding process and processing conditions. Effective mixing is crucial for achieving optimal dispersion of WF and optimizing the properties of the composites. It must also be kept in mind that WF is temperature sensitive and the high shear stresses developed during compounding can add to the heating of the mixture. Therefore, the preparation process can result in thermal degradation of WF, which can further alter the mechanical properties of the composite (35).

Wood fibers are mixed with the polymer matrix in different melt blending equipments, most frequently twin-screw extruder (35). Injection molding and extrusion are established processes for manufacturing wood fiber–thermoplastic composites, usually, in prismatic or sheet forms (36). Injection molding is one of the most important commercial fabrication processes for molding a broad spectrum of thermoplastics. A great deal of attention has been given to defining the engineering aspects of the operation for maximizing production rates and for controlling part strength, brittleness, shrinkage, and appearance characteristics (37,38). Nowadays, commercial equipments that offer corotating, intermeshing compounding twin-screw extrusion are being advertised as able to process a ''wide variety of plastic compounds including wood–plastic composite materials, such as PVC, polyethylene, and polypropylene, in combination with most woods including pine, maple, and oak'' (39).

Bledzki et al. (35) tested three compounding techniques (two-roll mill, high speed mixer and twin-screw extruder) for preparation of WF/PP composites. The best mechanical strength and lowest values of absorbed water were exhibited by composites compounded in the extruder. They also noticed (from microscopical

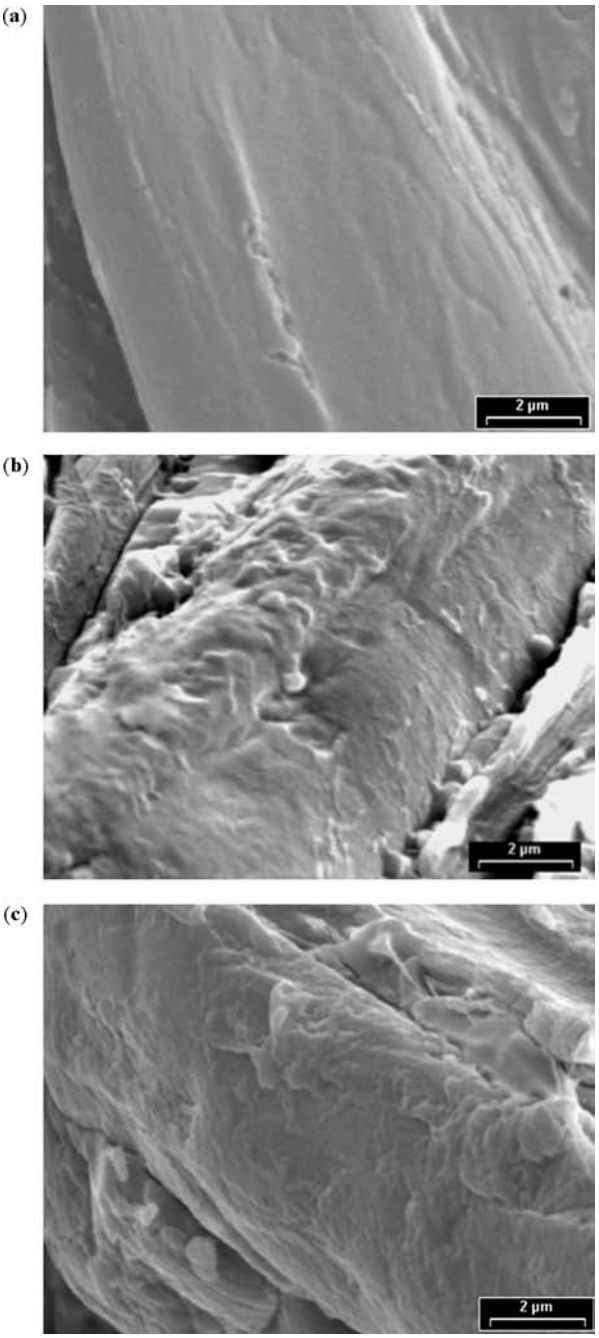

Figure 6.1 SEM micrographs of the wood flour surface in (**a**) WFC, (**b**) MWFC, and (**c**) PWFC. (From Reference 34 with permission from John Wiley & Sons, Inc.)

observations) an important breakage of WF when WF/PP composites were compounded in two-roll mill and extruder, but this did not affect negatively the mechanical strength of composites.

Thermoforming of preconsolidated wood fiber–thermoplastic composite sheets into three-dimensional shapes is a logical and needed next step for product manufacturing (40). One of the most relevant pieces of research regarding thermoforming is the work of Igl and Osswald (41), in which material behavior of wood flour filled polypropylene sheets was studied to develop a computer simulation of thermoforming under various conditions. Balatinecz et al. (42) and Karmaker and Youngquist (43) have noted fiber attrition during high shear mixing, such as thermokinetic processes used in injection molding and extrusion. Furthermore, true ''fibers'' can have orientations and the ability to overlap and interlock, giving better mechanical properties than particulate fillers. These factors significantly affect the formability of the composite sheets and cannot be addressed by considering the same features of ''wood flour'' reinforced thermoplastic composites.

In our work, plaques were obtained in two different ways: extrusion followed by injection molding and intensive mixing followed by compression molding of wood flour/PP mixtures, using the conditions described below.

Injection-molded samples: Plaques of the composite were obtained by injection, using a Sandretto Series 8 model 60t machine. The barrel temperature profiles were chosen as 180, 200, and 220°C (extrusion zone) and 220°C (injection zone) and the pressure was maintained at 125 bar in the extrusion zone and 50 bar in the injection zone.

Compression-molded samples: Treated or untreated wood flours were mixed with PP (and MAPP in some cases) in an intensive mixer at 180°C for 10 min. Small chunks were cut from these mixtures and placed into an aluminum mold. Plaques of the composites were obtained by compression at 180°C and 5 ton for 15 min. Natural air cooling of the samples was carried out in the mold and under pressure.

In both cases, the filler was dried overnight before compounding because the tendency of WF to absorb moisture leads to void formation during the processing, which can be further detrimental to the mechanical properties of the composites.

Three different series of wood flour/plastic composites were prepared:

(a) composites with wood flour incorporated without treatment (WFC);

(b) composites with wood flour pretreated with MAN (MWFC);

(c) composites with wood flour incorporated without treatment, but with the addition of 5% of MAPP (with respect to the wood flour weight) as compatibilizer agent (PWFC).

In all cases the weight percentage of filler is indicated between brackets; for example, WC(40) indicates a composite made with untreated wood flour in a 40:60 (filler:PP) or (filler:PP + MAPP) proportion.

The following sections describe the results obtained for these composites prepared by injection. The effect of the mixing/molding conditions on the properties of these composites was analyzed from creep measurements (see Section 6.6).

6.4 THERMAL BEHAVIOR: THERMAL DEGRADATION AND DYNAMIC MECHANICAL PROPERTIES

The thermal stability of the wood flour/PP composites was studied by thermogravimetry. Figure 6.2 shows the derivative (DTG) curves of WC as a function of the temperature for different weight percentages of wood flour. Application of thermal energy to PP initially induces the breakup of macromolecular chains and the formation of low molecular mass products. The initiation of the degradation consists of the cleavage of the carbon–carbon bonds of the macromolecules to form free radicals. In the PP molecular chain, the cleavage occurs at the bonds adjacent to the tertiary carbons, weakest bond (44, 45). The thermal degradation of neat PP takes place in one step (only one peak is observed in the DTG curve), which begins approximately at 340°C and finishes at 490°C. Composites begin to degrade at lower temperature (approximately at 256, 246, 234, and 218°C for composites containing 10%, 26%, 40%, and 50% of wood flour, respectively), because the filler is less stable thermally than neat PP. Clearly, composites degrade in at least three step processes (three peaks appear in the DTG curves), with the first two corresponding to those of the untreated wood flour (they appear in the same temperature range as that observed in wood flour degradation) and the last due to PP degradation. As expected, the first two peak areas in the DTG curves increase and the third peak area decreases as the wood flour content increases. No evidence of thermal interaction between PP and wood flour was found; that is, the experimental DTG thermograms of the composites could be obtained as the weighted sum of the experimental DTG curves of untreated wood flour and PP. The residual char at 500°C increases as the filler content increases (33). This is the result of the pyrolysis of the wood flour, added in larger amounts, and also

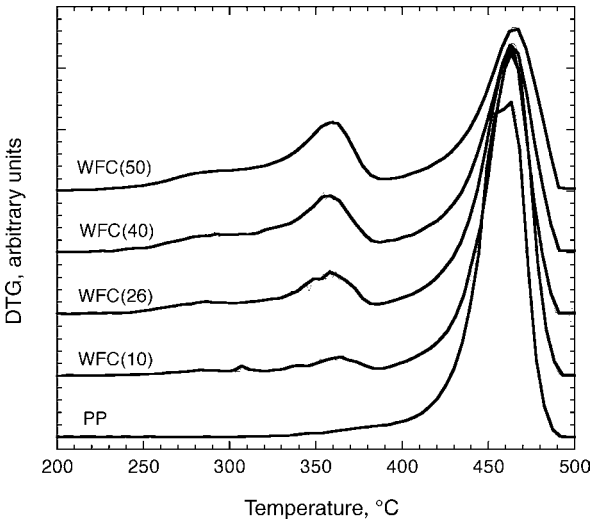

Figure 6.2 Derivative thermogravimetric (DTG) curves of WFC as a function of the temperature for different weight percent of wood flour.

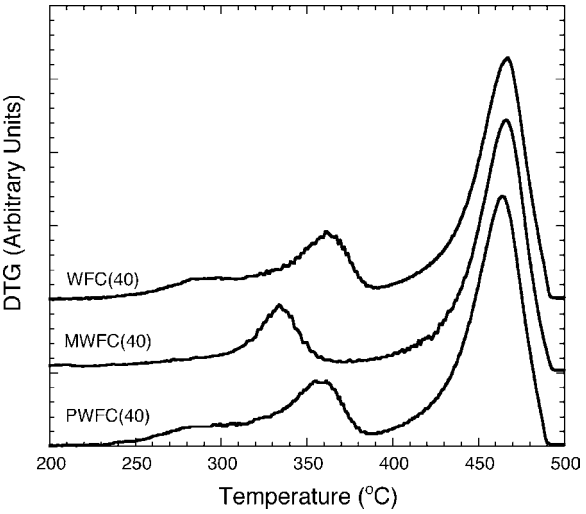

Figure 6.3 Derivative thermogravimetric (DTG) curves of WFC(40), MWFC(40), and PWFC(40) as a function of the temperature.

of the insulating effect of the char originated during the process, which protects the remaining composite from further thermal degradation.

Figure 6.3 compares the DTG thermograms of WFC(40), MWFC(40), and PWFC(40). No significant differences were observed in the performance of PWFC with respect to the behavior of WFC. However, the thermal degradation pattern of MWFC is quite different, since the region associated with the WF degradation appears as a single peak with the maximum at 334°C, a lower temperature than the main WF degradation peak of the other two samples (about 360°C). This difference is attributed to the lower thermal stability of the esterified wood flour. Besides, since no filler–polypropylene interaction was observed, the weight percent remaining after degradation of the wood flours (at about 383°C) is approximately the same for the three different composites (74%, 73%, and 73% for MWFC(40), PWFC(40), and WFC(40), respectively).

The foreseen applications of natural fiber reinforced composites, commonly, interior lining of cars and commercial vehicles, pose requirements on strength and stiffness that have to be satisfied in a temperature range of approximately −20 to 100°C. For acquiring such temperature-dependent material data, the DMA offers an excellent tool (46).

The structural or material damping of a composite can also be investigated by this technique, through the use of tan δ, which is the ratio of the loss modulus to the storage modulus or the ratio of the energy dissipated to the energy stored during a dynamic loading cycle (47). This magnitude is associated with damping properties of the composite matrix (48). The peak appears in the glass transition region, where the material changes from the rigid to the rubbery state. The change is associated with increased molecular mobility that permits configurational rearrangements of polymer chain backbones, all of which are initially extremely low (49,50). The fractional

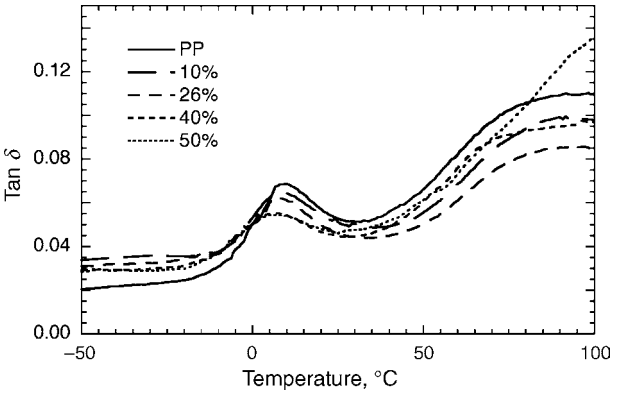

Figure 6.4 Temperature scans of tan δ of neat PP and WFC composites. (From Reference 33 with permission from John Wiley & Sons, Inc.)

energy lost in a system due to deformation is often proportional to the imperfections in the elastic structure of a polymer (51). Damping is a sensitive indicator of all kinds of molecular motions and phase transitions. In a composite system, damping is affected by the incorporation of fibers. This is mainly due to shear stress concentrations at the fiber ends added to the viscoelastic energy dissipation in the matrix material (50).

Figure 6.4 shows the temperature dependence of tan δ for untreated WF composites and unfilled PP. In the range of temperature analyzed, the tan δ curve of neat PP exhibits two relaxations located in the vicinity of 10 and 100°C. The lower temperature peak corresponds to the relaxation related to the glass–rubber transition of the amorphous phase of PP and the temperature of its maximum was representative of the glass transition temperature (T_g). The high temperature relaxation peak can be attributed to a lamellar slip mechanism and rotation in the crystalline phase (52). The location of the low temperature transition is shifted toward lower temperatures as the wood flour content increases, as it was also observed in talc-filled polypropylene composites (53). The wood flour acts as a nucleating agent, leading to a faster crystallization of the PP. That speedup of the crystallization generates an amorphous phase with bigger mobility in the WF–PP composites, resulting in a lower T_g value. These results are also supported by dynamic scanning calorimetry tests (33). As expected, the height of the tan δ peak decreases as wood flour content increases since the PP fraction is reduced correspondingly.

The storage modulus G' is a measure of the capacity of a material to store elastic energy during one cycle. Table 6.2 summarizes the values of the storage modulus measured at −50°C (glassy region) and at 80°C (rubbery plateau region, high above the glass transition temperature) for WFC. It is evident that addition of WF increases the modulus of the neat PP in the whole temperature range, except in the case of WC(50) sample. The improvement in stiffness with wood flour content is the expected effect caused by the addition of a rigid filler into a semirigid matrix. The $\Delta G'$ change of the composites during the transition $(G'_{glass} - G'_{rubber})$ appears smaller

Table 6.2 Storage Modulus and *C* Values for Untreated Wood Flour–PP Composites.

	WF, wt%				
	0	10	26	40	50
G' (−50°C), GPa	1.214	1.333	1.577	1.450	1.031
G' (80°C), GPa	0.193	0.273	0.370	0.485	0.319
C	—	0.77	0.67	0.47	0.51

than that for the unfilled PP. The decrease of the storage modulus of the WFC(50) composite with respect to that of the neat PP in the glassy region could be attributed to the agglomeration of particles due to the high concentration of WF incorporated. However, the rubbery storage modulus of WFC(50) is still higher than that of neat PP, because the particles have a much higher modulus than the matrix in that temperature range and they also introduce an elevated degree of mechanical restraint, which reduces the mobility and deformability of the rubber matrix.

Above T_g, the difference in dynamic modulus becomes more pronounced because of the larger modulus ratio of the components when the polymer is in the rubbery state compared to the glassy state. Figure 6.5 illustrates this observation as the temperature variation of the relative modulus calculated according to Equation (6.1):

$$G'_{rel} = \frac{G'_c}{G'_m} \tag{6.1}$$

where G_{rel}, G_c, and G_m are the relative modulus, the storage modulus of the composite, and the storage modulus of the neat polymer, respectively. The increase

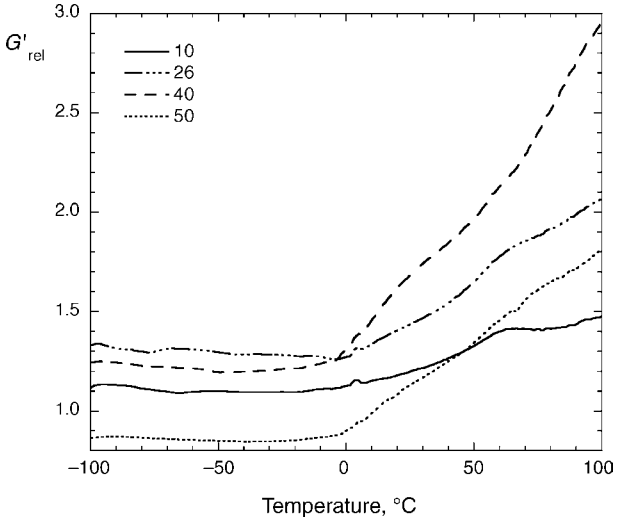

Figure 6.5 Relative storage modulus (G'_r) of WFC as a function of the temperature for different weight percent of wood flour.

in relative modulus with temperature suggests that WF controls the values of G'. Nielsen and Lewis (54) hypothesized that the changes in relative modulus with temperature for particulate-reinforced composites are also a consequence of thermally induced stresses in the polymer. The thermal stresses result from differences in thermal coefficients, as the composites cool from the molding temperature. Thus, the stressed polymer surrounding the filler particles will have a lower modulus than the bulk polymer. Therefore, the increase in relative modulus at higher temperatures is due to the reduction in thermal stresses, in addition to the obvious decrease in modulus of the polymer at T_g.

The effectiveness of fillers on the modulus of the composites can be represented by a coefficient C such as (50,55)

$$C = \frac{(G_g/G_r)_{comp}}{(G_g/G_r)_{resin}} \tag{6.2}$$

where G_g and G_r are the storage modulus values in the glassy and rubbery regions, respectively. The higher the value of the constant C, the lower the effectiveness of the filler. The measured G' values at -50 and 80°C (arbitrarily selected) were used as G'_g and G_r, respectively. The C values obtained for untreated WF composites, listed in Table 6.2, decrease as WF content increases, reaching a minimum for WFC(40), and then increase for WFC(50). This tendency indicates that the effectiveness of the filler increases only up to a WF content of 40 wt%. It was already mentioned that the difficulty in dispersing the WF at 50 wt% reduced the efficiency of the addition of the filler and thus the properties deteriorated.

Table 6.3 summarizes the values of the storage modulus observed at -50 and 80°C for WFC(40), MWFC(40), and PWFC(40). The PWFC composite presents slightly higher G' at low temperature than that of the WFC sample. This behavior is the result of the MAPP attached at the wood flour surface, which can form entanglements with the PP chains of the matrix. Moreover, the beneficial effects of maleated polypropylene on the strength properties of cellulosic fiber–PP composites have been attributed to the esterification reaction of the hydroxyl groups of the fiber with the anhydride functionality of maleated PP (56,57). This interaction improves the interfacial adhesion in the composite. These conclusions are also supported by similar observations made by other authors, for example, Liang et al. (58) in their studies on effects of glass bead size and content on the viscoelasticity of filled polypropylene. These authors hypothesized that for a thermoplastic composite filled

Table 6.3 Storage Modulus and T_g Values for 40 wt% WF Composites.

Composite	WFC	MWFC	PWFC
G' (−50°C), GPa	1.450	0.989	1.823
G' (80°C), GPa	0.485	0.311	0.488
T_g^a (°C)	6.60	7.02	7.13

[a]The temperature at which the maximum in tan δ occurs.

with rigid inorganic particles, the morphological structure of the interface influences the viscoelastic properties of the composites, besides the dependence on interfacial adhesion strength, filler size, and filler concentration.

On the contrary, the G' value of the MWFC sample is the lowest in the whole range of temperatures. This behavior could be attributed to the presence of voids in the MWFC composites, which was confirmed by density measurements (33). These voids are thought to be generated during the processing step: the MAN-treated wood flour begins to degrade at lower temperature than the untreated one. The thermal degradation of the fibers also results in the production of volatiles at the processing temperatures, leading to porous polymeric products with lower densities and inferior mechanical properties. However, the position of the maximum in the tan δ curve of the resulting PP composites is unaffected by the chemical treatment of the filler (33). This indicates that the washing step after treatment of the wood flour was efficient in removing any unreacted MAN. In other words, the modifier became firmly attached to the wood flour and was not solubilized in the bulk matrix, which would have lead to the plastification of the PP phase. Moreover, this result also indicates that the degree of interaction between treated or untreated WF and PP was not strong enough to modify the activation temperature for molecular relaxations in the polymer.

6.5 MECHANICAL BEHAVIOR: TENSILE, FLEXURAL, AND IMPACT PROPERTIES

Figure 6.6 illustrates the effect of the wood flour concentration on the tensile properties of the composites. Figure 6.6a shows the ratio of composite tensile modulus to neat PP modulus (1.22 ± 0.16 GPa) as a function of WF content. In all cases, the modulus increases with wood flour content, but the increase is larger for WFC, except when high wood flour concentrations are considered. The modulus of short fiber reinforced composites depends mainly on fiber loading, fiber length, and moduli: of matrix and fiber. The WF content and PP matrix are the same, regardless of the composite system. Addition of 5 wt% MAPP, which has lower modulus in comparison with PP, did not affect the tensile modulus of the composite. On the contrary, the improved dispersion obtained by using MAN-treated wood flour or by MAPP addition was responsible for increasing the Young's modulus of the composites up to high wood flour contents. Contrarily, the WFC tensile modulus reached a maximum at about 40 wt% and then decreased. For untreated wood flour contents higher than 40 wt%, filler particles form aggregates. Direct physical bonds between filler particles are weak, and thus easily broken during tensile loading, which explains the decrease in the modulus of elasticity at high particle contents.

Figure 6.6b shows the relative tensile strength of the different composites. The strength of WFC samples is higher than that of the MWFC specimens (except for samples containing 50 wt% of wood flour). It is interesting that the PWFC(50) shows higher modulus and strength, as well as larger ultimate deformation than the untreated or esterified wood flour composites (Fig. 6.6c). As a result of the filler addition, the ultimate strain decreases due to the decreased deformability of the

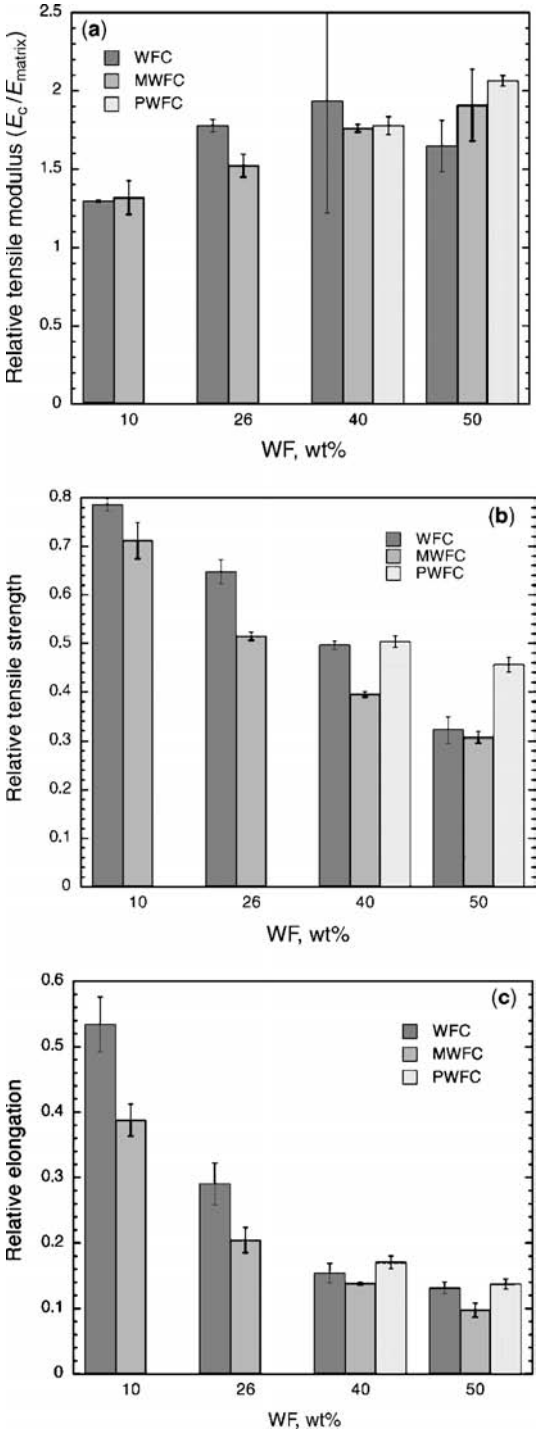

Figure 6.6 Effect of the wood flour concentration on the tensile properties of the composites. (**a**) Relative modulus, **(b)** relative strength, and (**c**) relative ultimate deformation.

matrix (restricted by the rigid particles). Fillers with larger stiffness than the matrix can increase the modulus of the composites, but generally causing a dramatic decrease in the elongation at break, because almost all of the elongation occurs in the matrix. This effect was observed for all the wood flour composites (Fig. 6.6c). The yield stress dependence on composition shows a similar trend.

Figure 6.7 shows the relative bending modulus (E_b, Fig. 6.7a) and the yield stress (σ_{b_y}, Fig. 6.7b) of the different composites, as a function of the filler content. The flexural modulus shows an increase with the weight percentage of filler, as observed

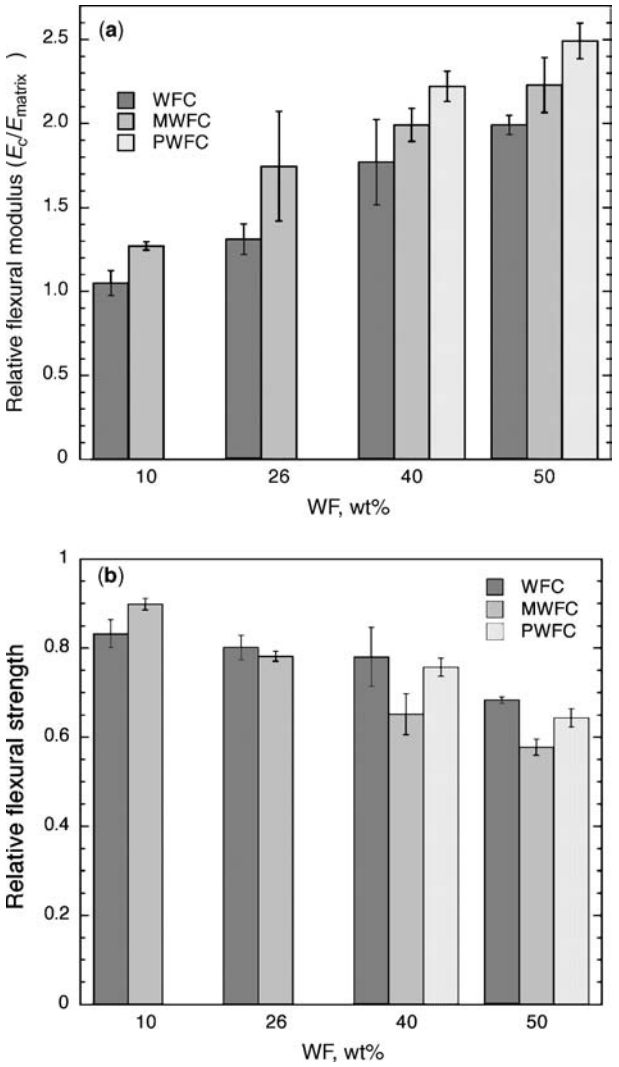

Figure 6.7 Effect of the wood flour concentration on the flexural properties of the composites. (**a**) Relative bending modulus and (**b**) relative yield stress.

in the tensile tests, but the increase is larger for MWFC and even more for PWFC. Similarly, all the composites present a lower flexural yield stress than that of the pure PP, and the yield stress decreases as a function of the filler content.

The increase in the flexural modulus of PWFC samples with respect to that of the WFC composites can be explained on the basis of the increased compatibility between filler and matrix. The dispersion of the wood flour in the PP matrix was consequently improved, and thus, the reinforcing effect of the wood flour is more effective than it was found in WFC. It is known that strong interactions can cause a stiffening effect on the polymer matrix adjacent to the filler particles interphase (59). Hence, it is expected that the improved interaction between wood flour and PP due to the addition of MAPP would cause the increase of the composite modulus with respect to the WFC one. This effect is clearer in flexural than in tensile tests, since some shearing stress components are present in bending tests.

Although wood flour was MAN treated to increase its affinity for the PP matrix (in MWFC) and to improve its dispersion, it also accelerated thermal degradation, which was evident in the darker color of the injected samples. Degradation leads to samples with reduced properties, and this effect (such as pores formation) is more evident in tensile than in flexural tests.

Void formation during MWFC injection can also explain the decrease of flexural and tensile yield stress of MWFC samples compared with WFC. Furthermore, the contribution of a loose interphase formed between esterified wood flour and PP should also be considered, since MAN moieties in the wood flour surface cannot form entanglements with the PP matrix. Felix and Gatenholm (60), who worked with different molecular weight modifiers, indicated that the longer is the modifier chain, the strongest is the achieved interface. Esterification with MAN improves the compatibility (wettability) between the filler and the matrix, but does not improve the interfacial strength.

Most of the published works on the use of MAPP compatibilizers in lignocellulosic PP systems report the improvement of the mechanical response (23,61) because the polypropylene chains of MAPP are compatible with the matrix and long enough to form entanglements with the matrix chains. In the present case, the benefits of using the compatibilizer are more visible at the highest filler content, where the good compatibility leads to higher tensile strength and modulus. The untreated fiber composite at 50 wt% is beyond the wetting possibilities of the matrix and the modulus drops below the maximum value.

The notched Izod impact energy of composites is plotted against the weight percent of wood flour in Fig. 6.8. The composite Izod strength exceeds that of the neat PP at WF contents as low as 10%, because of the additional mechanisms of energy absorption effective during fracture in the filled systems. However, the impact strength of reinforced PP decreased as wood flour content was further increased, whereas stiffness simultaneously increased. Although impact resistance of reinforced thermoplastics usually decreases with increasing amount of filler, quite frequently a maximum is observed at low or intermediate ($<$15% volume) filler contents. The maximum is most probably the combined result of different competitive micromechanical deformation processes influenced by polymer–filler

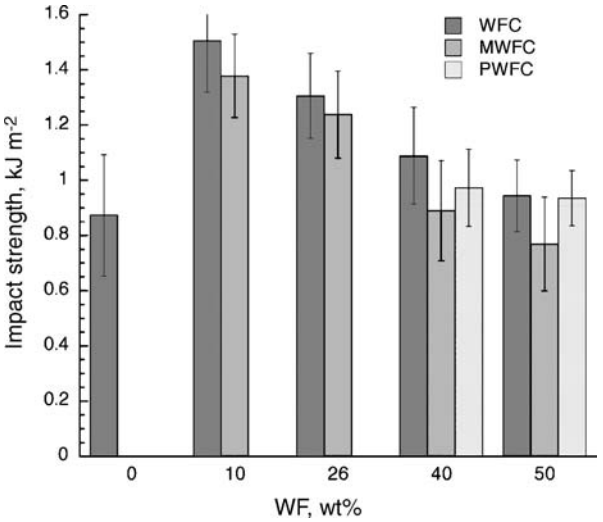

Figure 6.8 Notched Izod impact energy of composites as a function of the weight percent of wood flour.

interaction and particle–particle interactions (62). As the concentration of wood flour increases, the material becomes more rigid and the impact strength is reduced. As the wood flour content increases, there is a change from ductile to more brittle fracture behavior, due to the restrictive presence of the rigid WF particles. On the contrary, and although the addition of rigid particles to a polymer matrix tends to cause a reduction of the strength of the filled material, it is well established that crack propagation becomes more difficult in such materials (63). In this work, the decrease of the impact strength with wood flour concentration was attributed to the increase in fiber ends within the composites, which could cause crack initiation and hence potential fracture of the composite (64). Besides, at high filler contents the probability for fiber agglomeration (65) also increases, creating regions of stress concentration that require less energy to initiate or propagate a crack.

It is observed that the impact energy values measured in MWFC samples are always lower than those corresponding to WFC, in agreement with the higher void volume fraction of these composites. Notched impact behavior is controlled to a great extent by factors affecting the propagation of fracture initiated at the location of the predominant stress concentration around the notch tip. The fracture propagation process absorbs less energy as it finds voids at the crack tip. Moreover, since the adhesion between fibers and matrix was improved with WF esterification, the interface fiber–matrix in MWFC is stronger than that corresponding to the WFC. The debonding between the cellulosic fibers and their sheath that occurs mainly in WFC also suggests additional energy absorbing mechanisms. The larger Izod strength noticed for WFC is thus in agreement with the accepted fact that a weak interface results in higher impact resistance (66,67).

The MAPP compatibilizer has little or no effect on the notched impact strength. Different results are reported in the literature. Myers et al. (23) reported that MAPP did not improve the impact strength but instead reduced it with increasing MAPP content. Järvelä et al. (68) indicated that MAPP located at the interlayer between the matrix and the filler plays the role of a cross-linking agent because MAN groups of MAPP chains may react with —OH groups of wood flour, resulting in hardening of the interlayer. In addition, a polypropylene segment of MAPP is the same as the one of PP; thus, MAPP increases interaction between the matrix and the filler. Such interaction could also inhibit polymer mobility and thereby lower the ability of the system to absorb energy during fracture propagation. The hardening of the interlayer leads to an increase in modulus, but reduces the impact strength of the composites. Other authors have reported just the opposite behavior when testing unnotched samples (21,61,69). Rana and coworkers (69) attributed this behavior to the compatibilizer migration around the fibers, which acted as a damper to the shock wave produced during the impact that was transmitted evenly onto the fibers. In the present case, there are negligible differences with respect to those of untreated WF composites.

6.6 TIME-DEPENDENT RESPONSE: SHORT- AND LONG-TERM CREEP

6.6.1 Effect of Processing Conditions and Wood Flour Concentration

Polymers used in engineering applications are often subjected to stress or to high temperatures for prolonged periods of time or changing temperatures. These factors trigger time-dependent responses, and thus, a detailed knowledge of the viscoelastic properties of the material is needed to predict or at least estimate its behavior under such conditions (70). Creep is the time-dependent deformation of materials subjected to a continuous stress. This deformation can be elastic, viscoelastic, and plastic, and, therefore, it can be partially nonrecoverable when the load is removed. When subjected to a constant load, the material suffers an instantaneous elastic deformation followed by a rapid creep rate decrease with time. Then, the creep rate reaches a steady-state value, and finally, the creep rate increases rapidly and the material fractures. Thus, creep can lead to unacceptable deformation in use and eventually structural failure and it is, therefore, an important property for engineering plastics and composites (1,71,72). Particularly in polymers, the deformation process under load is strongly dependent on the mobility of the chains, and this is not only temperature dependent, but also time dependent.

The short-term creep response of untreated wood flour/neat polypropylene composites (WFC) prepared by injection molding is shown in Fig. 6.9. As expected, neat polypropylene shows the highest creep during test. When a small amount of wood flour (10 wt%) was added, the creep decreased and it continued decreasing with increasing wood flour content up to approximately 40%wt. Samples prepared

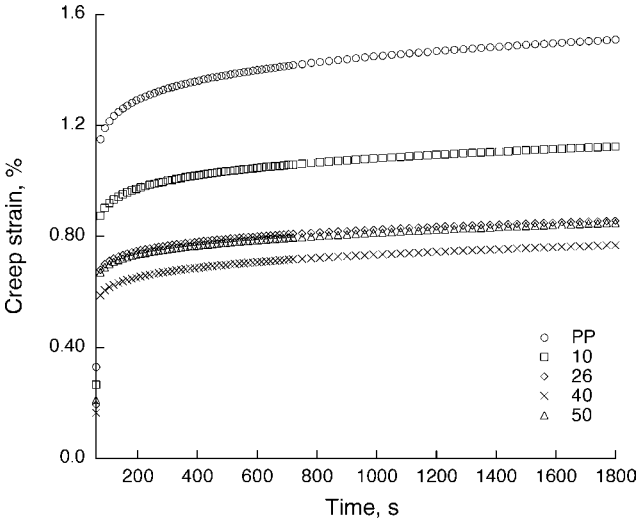

Figure 6.9 Short-term creep response of untreated wood flour/neat polypropylene composites (WFC) prepared by injection molding. Tested at 20°C. (From Reference 34 with permission from John Wiley & Sons, Inc.)

with 50 wt% showed a larger deformation than those prepared with 40 wt% of wood flour. As it was previously pointed out, at this high concentration the amount of polymer is not enough to completely wet the reinforcement, and thus, particle agglomerates are formed, reducing the mechanical properties of the composite.

WFC composites prepared by intensive mixing followed by compression molding were also subjected to short-term creep tests. Although the dependence of the creep deformation with wood flour concentration is formally that described for the injected samples, two different features are worth to be noticed. First of all, composites with higher wood flour content could be prepared (up to 60% wood flour) and what is more, the creep deformations of all the compression-molded samples (even the neat PP) are lower than those corresponding to the injected counterparts. As it was indicated previously, as the filler concentration increases, the deformation decreases, as it should be expected from the increased rigidity of the composites.

Regarding intensive-mixed–compression-molded samples, the upper concentration limit for adequate wettability is achieved at 60 wt% wood flour. At this high concentration, the creep resistance is decreased by the presence of direct particle–particle interactions, which generate only physical or mechanical bonds, easily broken during deformation. Moreover, the intensive-mixed–compression-molded WFC shows lower creep deformation at 50% wood flour than at 40% filler, in agreement with the observed improved dispersion obtained by the use of the intensive mixer. Thus, the effect of the wood flour addition is the stiffening of the composite, at least if filler wetting and dispersion are efficiently accomplished.

To facilitate comparison, Fig. 6.10 presents the creep response at 20°C of WFC containing 0, 40, and 50 wt% wood flour and obtained by the two processing conditions. Composites made from semicrystalline thermoplastics and rigid fillers

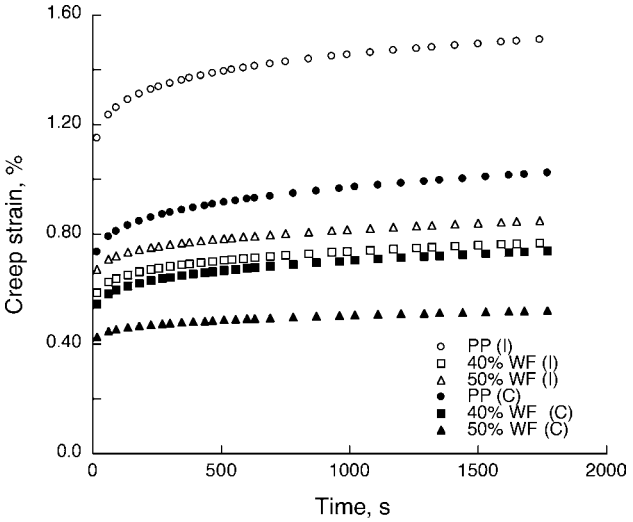

Figure 6.10 Creep response at 20°C of WFC containing 0, 40, and 50 wt% wood flour and obtained from different processing conditions. (I) Injected samples; (C) compression-molded samples.

show a great variety of mechanical properties, depending on the composition and the processing conditions. The final properties of the composites are highly dependent on the rheological conditions during the processing (73) and are also governed by the individual properties of the components as well as by the interactions developed at the matrix/filler interface. Moreover, it is worth noting that not only the improved filler dispersion is responsible for the differences in creep behavior, since the neat polymer also shows very different strain–time curves. In a partially crystalline polymer, the mobility of the amorphous tie molecules is highly hindered by the reinforcing effect of the crystalline phase (70). The injection-molded polymer and composites present a peculiar multilayer structure, in which the type, size, structure, and orientation of the amorphous and crystalline phases of the polymer change continuously from the skin to the core (73–76). The explanation of this result must also be related to the different amorphous contents of specimens obtained with different processing conditions. Injection-molded samples present a thicker skin, that is, a higher content of polymer that was cooled very quickly from the melt. Because of that, samples obtained by injection are expected to have a higher amorphous content, as indicated in similar works (77). Moreover, in injection-molded specimens, both polymer phases and anisometric filler particles remain highly oriented. The inner structure of the sample is also far from being homogeneous or isotropic as it was pointed out in other works (77–79). On the contrary, compression-molded samples were air cooled slowly in the press and thus have a relative high crystalline content. Comparing both processing methods, the advantages of the time-intensive consolidation with long cooling times come to the fore. The economically important advantage of saving time when using an injection

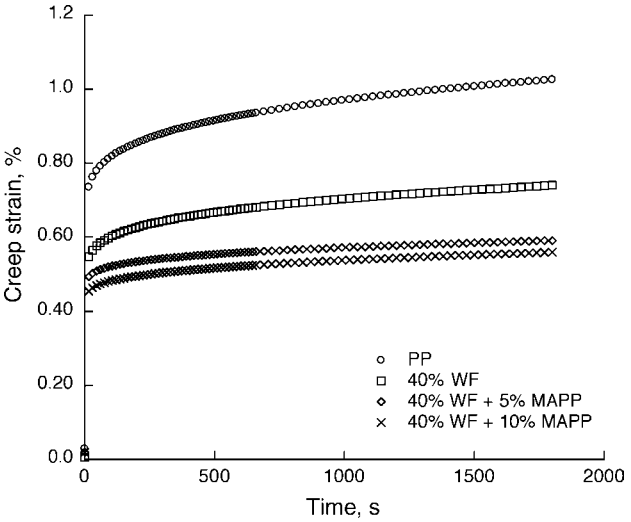

Figure 6.11 Creep behavior at 20°C of neat PP and 40 wt% wood flour composites prepared by intensive mixing and compression molding. (From Reference 70 with permission from John Wiley & Sons, Inc.)

molding machine must be weighed against the improved creep performance of the composites prepared in two steps.

6.6.2 Effect of Interfacial Modification

The effect of varying the adhesion between matrix and reinforcement, by addition of a compatibilizing agent, on the creep behavior of intensive-mixed samples was also analyzed. Figure 6.11 shows the creep behavior at 20°C for the different 40 wt% wood flour composites. All composites show less deformation with respect to the matrix at the same applied stress (10 MPa). An important reduction in creep deformation is observed when MAPP compatibilizer (5 wt% with respect to WF content) is added to the formulation. A further decrease of creep is observed for 10% MAPP addition, although the difference with the 5% MAPP addition is very slight and probably the economy of the process does not justify the use of higher amount of compatibilizer. The figure shows that samples prepared with 10 wt% of MAPP showed a reduction of creep deformation of 45% compared to the matrix and 24% if compared to that of the untreated composite at the end of the test.

6.6.3 Effect of Temperature

Figure 6.12 shows the strong temperature dependence of the creep behavior of the 26 wt% untreated wood flour composites prepared by intensive mixing and compression molding. At the final test time, the strains reached at 50 and 80°C are

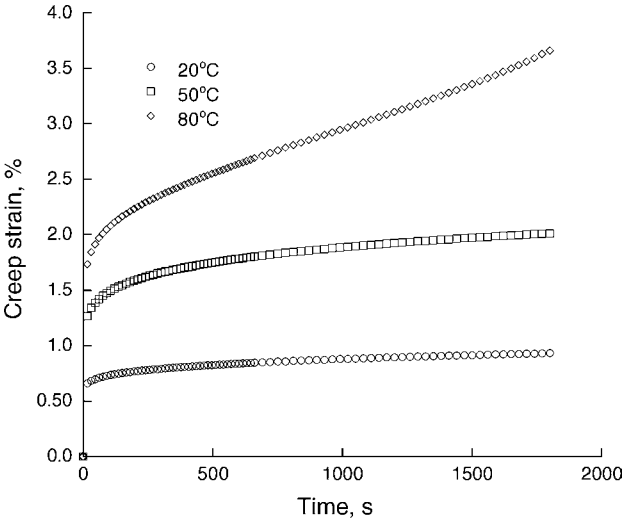

Figure 6.12 Temperature dependence of the creep behavior of the 26 wt% untreated wood flour composites prepared by intensive mixing and compression molding. (From Reference 70 with permission from John Wiley & Sons, Inc.)

2.15 and 3.93 times the strain at 20°C, respectively. At 80°C, the end of the creep curve insinuates the beginning of the last stage where the strain rate increases with time, eventually leading to the final material failure.

In partially crystalline polymers, the creep response, viscoelastic in nature, depends on the material structure, which is a strong function of the temperature of the test. In the range of temperatures analyzed, below the melting temperature, no changes in the crystalline phase are expected. On the contrary, changes in the mobility of amorphous bulk and tie molecules occur. As the temperature increases, the mobility of the chains increases and this results in increased creep deformation at the same applied stress (80–82).

Long-term creep behavior might be predicted from short-term test data if the time–temperature superposition (TTS) principle is applicable to the studied material. Thus, master curves can be constructed to obtain information over a longer period of time than the experimental interval covered by the test. The superposition technique exploits the sensibility of the molecular relaxation process to temperature. Under certain simplifying assumptions, a quantitative equivalence between time and temperature can be established. Thus, a longtime prediction can be obtained from shorter test data obtained at higher temperature. Although this technique cannot be assumed to be applicable *a priori* for multiphased systems, it has been shown to be effective in the characterization of different composite materials (70,83–86). Nuñez et al. (70) generated a master curve from creep strain data measured at various temperatures, after shifting them according to the TTS principle. The reference temperature selected was 60°C. Figure 6.13 shows the ''master curve'' constructed from the

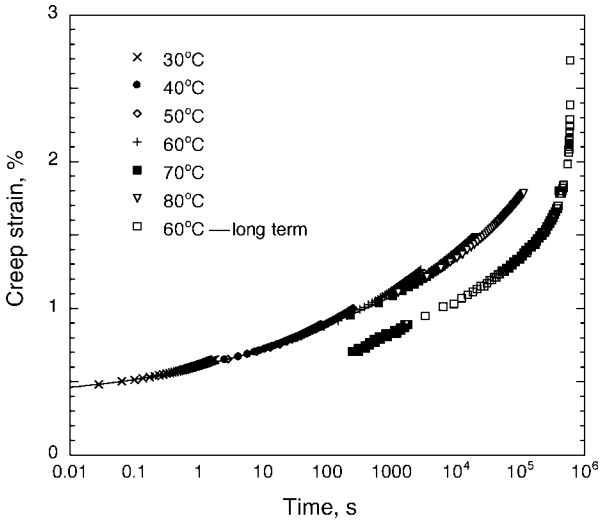

Figure 6.13 Long-term creep data experimentally measured at 60°C and master curve (reference temperature = 60°C) obtained from short-term creep data measured at different temperatures, for a composite containing 40% untreated wood flour and 10% MAPP prepared by intensive mixing and compression molding.

short-term data obtained for a composite containing 40% untreated wood flour and 10% MAPP and prepared by intensive mixing and compression molding.

Although a ''master curve'' was successfully constructed, that is not a sufficient condition to validate the TTS principle. One reason for the occasional differences found between experimental data and master curves is physical aging (82,85,87,88). In completely amorphous polymers, the glass rubber transition occurs in a relatively narrow temperature range, below which aging occurs. This is not the case in semicrystalline polymers, where the amorphous fractions close to the crystalline regions contain chains that may be partially incorporated in both phases and consequently are strongly hindered in their mobility. These chains require a significantly higher activation energy for relaxation. The same is true for ''tie molecules'' that belong to different crystals, and thus present intermediate amorphous sections. The result is that the transition for these polymeric fractions occurs at higher temperatures. This kind of transition occurs around 80°C in PP, and aging of the polymer can take place at room temperature. Heating of the samples near this transition effectively erases the previous history of the material, ''rejuvenating'' it. Pioneer work had already detected changes in polypropylene properties at room temperature; the studies showed no changes in the crystallinity of the samples, but a steadily increasing density. Gas sorption and diffusion experiments allowed to identify the amorphous phase as the responsible for these changes (89–93).

Thus, if aging takes place during creep it would result in a lower than expected deformation. Physical aging that can take place during the experiment can be neglected in the short-term tests, because of the short length of time involved. On

the contrary, during long-term tests, the material can suffer physical aging while the material creeps. Thus, the ''master curve'' obtained from short-term creep data may not represent the experimental behavior of the composite for long-term creep. To check this behavior, experimental long-term creep tests (on intensive-mixed composite with 40% untreated wood flour and 10% MAPP) were carried out up to the rupture of the material, which occurred at 6.87 days at 60°C. Figure 6.13 shows the long-term creep data experimentally measured at 60°C, together with the master curve obtained from short-term creep data measured at different temperatures. The figure clearly illustrates the fact that the predicted curve overestimates the creep deformation of the material because it does not take into account the aging of the material, which occurs below the 80°C transition. The prediction is actually much better for temperatures close to the transition because in those conditions the aging is negligible (70).

6.7 CONCLUSIONS

It is clear that wood flour–PP composites do not possess strengths and moduli as high as those of conventional high performance composites (i.e., reinforced with aramid and carbon fibers); however, they do have better strengths than some neat plastics and medium performance composites (i.e., glass fiber reinforced plastics) and also have interesting properties if compared with wood (i.e., reduced moisture sorption).

Composite tensile and flexural properties can be improved using MAPP coupling agents. The adequate amount of coupling agent is a function of the studied material (i.e., depends on the amount of fiber surface —OH groups, MAPP or MAN content, PP and MAPP molar masses, etc.). After the fiber surface is saturated with the compatibilizer, its excess migrates around the fibers causing the self-entanglement among compatibilizer chains rather than between compatibilizer and polymer matrix chains, resulting in reduced mechanical properties. It is also important to notice that an excess of coupling agent is also not profitable, since MAPP is much more expensive than PP. On the contrary, composites prepared from wood flour treated with MAN displayed reduced mechanical properties as a result of the low thermal stability of the filler.

The creep deformation can be reduced increasing the wood flour concentration whereas the polymeric matrix is enough to effectively wet the fibers. Addition of MAPP and/or improving dispersion by intensive mixing increases the critical concentration for complete wetting.

Since PP is a semicrystalline polymer, the processing conditions greatly influence its crystallization behavior and the amount and perfection of the formed crystals, and in consequence the mechanical performance of the resulting composites.

There are already many commercial applications for wood flour–PP composites, and it is expected that the acceptance of these products continues growing at the same time that new applications are envisioned for these materials. Since the reinforcing material is ecofriendly, nontoxic, nonhealth hazardous, low in cost, and easily

available as compared to conventional fibers like glass, Kevlar, and asbestos, the composites are a good substitute for wood in indoor applications such as shelves, partitions, wash basins, and tabletops, and may also be suitable for outdoor uses such as roofing, drainage pipes, automobile components, electrical fittings as well as larger items such as lightweight fishing boats.

Moreover, other considerations have to be taken into account in the design of natural fiber/PP composites. One of the most important issues is the degradation behavior of the composites exposed to outdoor environmental conditions, and the effect of external factors such as humidity, sunlight, or the action of microorganisms. The poor resistance of the wood flour to water absorption can have undesirable effects on the mechanical properties and the dimensional stability of the composites. Hence, future research should focus on achieving equivalent or superior technical performance and component lifetime than the synthetic materials that are substituting.

NOMENCLATURE

C	Coefficient, which represents the effectiveness of fillers on the modulus of the composites
DMA	Dynamic mechanical analysis
DTG	Derivative signal of the thermogravimetric curve
E_b	Relative bending modulus
G'	Storage modulus
G_c	Composite storage modulus
G_g	Storage modulus in the glassy region
G_m	Storage modulus of the neat polymer
G_r	Storage modulus in the rubbery region
G_{rel}	Relative storage modulus
MAN	Maleic anhydride
MAPP	Maleic anhydride–polypropylene copolymer
MFI	Melt flow index
MWFC	Composites with wood flour pretreated with MAN
PE	Polyethylene
PP	Polypropylene
PVC	Poly(vinyl cloride)
PWFC	Composites with nontreated wood flour, but with the addition of MAPP as compatibilizer agent
SEM	Scanning electronic microscopy
TGA	Thermogravimetric analysis
T_g	Glass transition temperature
T_m	Melting temperature
TTS	Time–temperature superposition principle
WF	Wood flour
WFC	Composites with wood flour incorporated without treatment
δ	Phase angle

$\Delta G'$ Change in the storage modulus during the transition $(G'_{\text{glass}} - G'_{\text{rubber}})$
σ_{b_y} Flexural yield stress

REFERENCES

1. S.-Y. Lee, H.-S. Yang, H.-J. Kim, C.-S. Jeong, B.-S. Lim, and J.-N. Lee, *Compos. Struct.*, **65**, 459 (2004).
2. J. Son, H.-J. Kim, and P. W. Lee, *J. Appl. Polym. Sci.*, **82**, 2709 (2001).
3. J. Son, H.-S. Yang, and H.-J. Kim, *J. Thermoplast. Compos. Mater.*, **17**, 509 (2004).
4. B. Wielage, Th. Lampke, G. Marx, K. Nestler, and D. Starke, *Thermochim. Acta*, **337**, 169 (1999).
5. Th. Kretschmer and J. Kohlhoff, *Werkstoffe in der Fertigung*, **5**, 3 (1997).
6. F. M. B. Coutinho and T. H. S. Costa, *Polym. Test.*, **18**, 581 (1999).
7. J. Guillet, *Macromol. Symp.*, **123**, 209 (1997).
8. K. Oksman and C. Clemons, *J. Appl. Polym. Sci.*, **67**, 1503 (1998).
9. M. N. Ichazo, C. Albano, J. González, R. Perera, and M. V. Candal, *Compos. Struct.*, **54**, 207 (2001).
10. N. E. Marcovich, M. M. Reboredo, and M. I. Aranguren, *J. Appl. Polym. Sci.*, **68**, 2069 (1998).
11. A. K. Bledzki and O. Faruk, *Composites A*. **37**(9), 1358 (2006).
12. A. K. Bledzki and J. Gassan, *Prog. Polym. Sci.*, **24**, 221 (1999).
13. J. Karger-Kocsis, in: *Polypropylene: Structure, Blends, and Composites*, J. Karger-Kocsis (ed.), Chapman & Hall, London, 1995.
14. R. Karnani, M. Krishnan, and R. Narayan, *Polym. Eng. Sci*., **37**, 476 (1997).
15. R. Gauthier, C. Joly, A. C. Coupas, H. Gauthier, and M. Escoubes, *Polym. Compos.*, **19**, 287 (1998).
16. M. Avella, L. Casale, R. Dell'erba, B. Focher, E. Martuscelli, A., and J. Marzetti, *J. Appl. Polym. Sci.*, **68**, 1077 (1998).
17. B. Pukánszky, F. Tudos, J. Jancar, and J. Kolarik, *J. Mater. Sci. Lett.*, **8**, 1040 (1989).
18. F. M. B. Coutinho, T. H. S. Costa, and D. L. Carvalho, *J. Appl. Polym. Sci.*, **65**, 1227 (1997).
19. S. Takase and N. Shiraishi, *J. Appl. Polym. Sci.*, **37**, 645 (1989).
20. X. Chen, Q. Guo, and Y. Mi, *J. Appl. Polym. Sci.*, **69**, 1891 (1998).
21. A. R. Sanadi, D. F. Caulfied, R. E. Jacobson, and R. M. Rowell, *I&EC Res.*, **34**, 1889 (1995).
22. H. D. Rozman, G. B. Peng, and Z. A. Mohd Ishak, *J. Appl. Polym. Sci.*, **70**, 2647 (1998).
23. G. E. Myers, I. S. Chahyadi, C. A. Coberly, and D. S. Ermer, *Int. J. Polym. Mater.*, **15**, 21 (1991).
24. D. Harper and M. Wolcott, *Composites A*, **35**, 385 (2004).
25. J. Z., Q. Lu, and H. S., McNabb, *Wood Fiber Sci*., **32**, 88 (2000).
26. S. Mishra and J. B. Naik, *J. Appl. Polym. Sci.*, **68**, 681 (1998).
27. C. Clemons, R. A. Young, and R. M. Rowell, *Wood Fiber Sci.*, **24**(3), 353 (1992).
28. J. M. Felix and P. Gatenholm, Evaluation of surface treatments for cellulose fibers and interfacial interactions in composites, in: *Controlled Interphases in Composite Materials*, H. Ishida (ed.), Elsevier, New York, 1990.
29. J. Urbanski, in: *Handbook of Analysis of Synthetic Polymers and Plastics*, J. Urbanski, W. Czerwinski, K. Janicka, F. Majewska, and H. Zowall (eds.), Wiley, Poland, 1977.
30. C.-W. Lin and W.-L. Lee, *J. Appl. Polym. Sci.*, **70**, 383 (1998).
31. N. G. Gaylord, M. Mehta, and R. Mehta, *J. Appl. Polym. Sci.*, **33**, 2549 (1987).
32. N. G. Gaylord, R. Mehta, V. Kumar, and M. Tazi, *J. Appl. Polym. Sci.*, **38**, 359 (1989).
33. A. J. Nuñez, J. M. Kenny, M. M. Reboredo, M. I. Aranguren, and N. E. Marcovich, *Polym. Eng. Sci.*, **42**, 733 (2002).

34. A. J. Nuñez, P. C. Sturm, J. M. Kenny, M. I. Aranguren, N. E. Marcovich, and M. M. Reboredo, *J. Appl. Polym. Sci.*, **88**, 1420 (2003).
35. A. K. Bledzki, M. Letman, A. Viksne, and L. Rence, *Composites: A*, **36**, 789 (2005).
36. D. Nabi Saheb and J. P. Jog, *Adv. Polym. Technol.*, **18**, 351 (1999).
37. Baer E, *Engineering Design for Plastics*, *SPE Polymer Science and Engineering Series*, Reinhold, New York, 1964.
38. E. C. Bernhardt, *Processing of Thermoplastics Materials*, *SPE Plastics Engineering Series*, Reinhold, New York, 1959.
39. NFM Welding Engineers, www.nfm.net/products/products.aspx.
40. D. Bhattacharyya, M. Bowis, and K. Jayaraman, *Compos. Sci. Technol.*, **63**, 353 (2003).
41. S. A. Igl and T. A. Osswald, A study of the thermoformability of wood fibre-filled polyolefin composites, wood-fibre/polymer composites: fundamental concepts, processes, and material options, Forest Products Society, Madison, WI, USA, 1993.
42. J. J. Balatinecz, B. D. Park, R. T. Woodhams, R. A. Fructl, P. R. Garand, and S. Iaboni, Reactive processing of wood fibre composites. Wood-fibre/polymer composites: fundamental concepts, processes and material options, Forest Products Society, Madison, WI, USA, 1993.
43. A. C. Karmaker and J. A. Youngquist, Fibre attrition during injection moulding and its effect on the mechanical performance of natural fibre-reinforced polypropylene composite, in: *Proceedings of the Conference on Woodfibre–Plastic Composites: Virgin and Recycled Wood Fibre and Polymers for Composites*, Forest Products Society, Madison, WI, USA, 1995, pp. 96–98.
44. M. Y. Fuad, J. Mustafah, M. S. Mandor, Z. A. Mohd Ishak, and A. K. Mohd Omar, *Polym. Int.*, **38**, 33 (1995).
45. R. G. Gann, R. A. Dipert, and M. J. Drews, Flammability, in: *Encyclopedia of Polymer Science and Engineering*, Vol. 7, 2nd edition J. I. Kroschwitz (ed.) 2nd Wiley, New York, 1985.
46. B. Wielage, Th. Lampke, H. Utschick, and F. Soergel, *J. Mater. Process. Technol.*, **139**, 140 (2003).
47. A. O'Donnell, M. A. Dweib, and R. P. Wool, *Compos. Sci. Technol*., **64**, 1135 (2004).
48. S. H. Aziz and M. P. Ansell, *Compos. Sci. Technol*., **64**, 1231 (2004).
49. J. D. Ferry, The nature of viscoelastic behavior, in: *Viscoelastic Properties of Polymers*, Wiley, New York, 1980.
50. L. A. Pothan, Z. Oommen, and S. Thomas, *Compos. Sci. Technol.*, **63**, 283 (2003).
51. L. E. Nielsen and R. F. Landrel, *Mechanical Properties of Polymers and Composites*, Vol. 2, Marcel Dekker, New York, 1994.
52. A. Amash and P. Zugenmaier, *J. Appl. Polym. Sci.*, **63**, 1143 (1997).
53. S. Díez-Gutiérrez, M. A. Rodríguez-Pérez, J. A. De Saja, and J. I. Velasco, *Polymer*, **40**, 5345 (1999).
54. L. E. Nielsen and T. B. Lewis, *J. Polym. Sci.*, **7**, 1705 (1969).
55. B. A. Acha, N. E. Marcovich, and J. Karger-Kocsis, *Plast. Rubber Compos.*, **35**(2), 73 (2006).
56. M. Kazayawoko, J. J. Balatinecz, and R. T. Woodhams, *J. Appl. Polym. Sci*, **66**, 1163 (1997).
57. P. V. Joseph, G. Mathew, K. Joseph, G. Groeninckx, and S. Thomas, *Composites A*, **34**, 257 (2003).
58. J. Z. Liang, R. K. Y. Li, and S. C. Tjong, *Polym. Test.*, **19**, 213 (2000).
59. F. Stricker, M. Bruch, and R. Mülhaupt, *Polymer*, **38**, 5347 (1997).
60. M. Felix and P. Gatenholm, *J. Appl. Polym. Sci.*, **50**, 699 (1993).
61. H. Dalväg, C. Klason, and H. E. Strömvall, *Int. J. Polym. Mater.*, **11**, 9 (1985).
62. B. Pukánszky, in: *Polypropylene. Structure, Blends and Composites*, Vol. 3, 1st edition, J. Karger-Kocsis (ed.), Chapman & Hall, Cambridge, 1995.
63. A. J. Kinloch and R. J. Young, *Fracture Behavior of Polymers*, Applied Science Publishers, London, 1983.
64. M. J. Folkes, in: *Short Fibre Reinforced Thermoplastics*, M. J. Devis (ed.), John Wiley & Sons, Ltd, Herts, UK, 1982.

65. L. Mascia, *The Role of Additives in Plastics*, Edwar Arnold, London, 1974, Chap.3.
66. T. Q. Li, C. N. Ng, and R. K. Y. Li, *J. Appl. Polym. Sci.*, **81**, 1420 (2001).
67. V. N. Hristov and R. Lach, W. Grellmann, *Polym. Test.*, **23**, 581 (2004).
68. P. A. Järvelä, L. Shucai, and P. K. Järvelä, *J. Appl. Polym. Sci.*, **65**, 2003 (1997).
69. K. Rana, A. Mandal, B. C. Mitra, R. Jacobson, R. Rowell, and A. N. Banerjee, *J. Appl. Polym. Sci.*, **69**, 329 (1998).
70. A. J. Nuñez. N. E. Marcovich, and M. I. Aranguren, *Polym. Eng. Sci.*, **44**, 1594 (2004).
71. D. P. N. Vlasveld, H. E. N. Bersee, and S. J. Picken, *Polymer*, **46**, 12539 (2005).
72. B.-D. Park and J. J. Balatinecz, *Polym. Compos.*, **9**, 377 (1998).
73. S. Díez-Gutiérrez, M. A. Rodríguez-Pérez, J. A. De Saja, and J. I. Velasco, *Polymer*, **40**, 5345 (1999).
74. J. P. Trotignon and J. Verdu, *J. Appl. Polym. Sci.*, **35**, 29 (1987).
75. M. Fujiyama, T. Wakino, and Y. Kawasaki., *J. Appl. Polym. Sci.*, **35**, 29, (1988).
76. P. Singh and M.R. Karmal, *Polym Compos*., **10**, 344 (1989).
77. J. I. Velasco, C. Morhain, A. B. Martínez, M. A. Rodríguez-Pérez, and J.A. de Saja, *Polymer*, **43**, 6813 (2002).
78. M. Fujiyama and T. Wakino, *J. Appl. Polym. Sci.*, **42**, 2739 (1991).
79. M. Fujiyama, *Int. Polym. Process*., **7**, 165 (1992).
80. B. E. Read and P. E. Tomlins, *Polym. Eng. Sci.*, **37**, 1572 (1997).
81. P. E. Tomlins and B. E. Read, *Polymer*, **39**, 355 (1998).
82. D. S. Matsumoto, *Polym. Eng. Sci.*, **28**, 1313 (1988).
83. V. P. Cyras, J. F. Martucci, S. Iannace, and A. Vázquez, *J. Thermoplast. Compos. Mater.*, **15**, 253 (2002).
84. A. Vázquez, V. A. Dominguez, and J. M. Kenny, *J. Thermoplast. Compos. Mater.*, **12**, 253 (1999).
85. C. Marais and G. Villoutreix, *J. Appl. Polym. Sci*., **69**, 1983 (1998).
86. M. Sumita, T. Shizuma, K. Miyasaka, and K Ishikawa, *J. Macromol. Sci. Phys*., **B22**, 601 (1983).
87. D. Dean, M. Husband, and M. Trimmer, *J. Polym. Sci. B Polym. Phys.*, **70**, 2971 (1998).
88. L. C. Brinson and T.S. Gates, *Int. J. Solid Struct*., **32**, 827 (1995).
89. J. Fiebig, M. Gahleitner, C. Paulik, and J. Wolfschwenger, *Polym. Test.*, **18**, 257 (1999).
90. G. W. Schael, *J. Appl. Polym. Sci.*, **10**, 901 (1966).
91. S. Kapur and C.E. Rogers, *J. Polym. Sci. A-2*, **10**, 2107 (1972).
92. M. K. Agarwal and J. M. Schultz, *Polym. Eng. Sci.*, **21**, 776 (1981).
93. V. Vittoria, *Polymer*, **29**, 1118 (1988).

Chapter 7

Deformation and Fracture Behavior of Natural Fiber Reinforced Polypropylene

Celina R. Bernal[1]

7.1 INTRODUCTION

Over the recent years, reinforcing thermoplastic polymers with natural fibers (lignocellulosics) has become very attractive mainly because of the good mechanical properties that can be obtained at relatively low cost (1). Natural fiber reinforced thermoplastics have light weight, adequate strength and stiffness, and low cost and can be easily produced by conventional plastics processing techniques such as extrusion molding and injection molding (2). Currently, natural fibers are being used as reinforcements of polymers in many applications such as building, automotive, packaging, furniture, and even aerospace applications. The use of natural fibers as an alternative of the use of glass fibers in polymer matrices is driven by ecological reasons and also because natural fibers have several advantages compared to their inorganic counterparts (3). They are low cost fibers, highly available and renewable, with low density and high specific properties as well as biodegradable and less abrasive to expensive molds and mixing equipments. Nevertheless, their potential use as reinforcement is greatly reduced because of their incompatibility with the hydrophobic polymer matrix (especially polyolefins) (4), their poor resistance to moisture and their tendency to form aggregates during processing (5,6). In addition, the most important disadvantage of natural fibers is their quality, which depends on many external factors such as climate, soil, plant cultivation, and fiber extraction (7).

[1]Advanced Materials Group, INTECIN (UBA-CONICET), Department of Mechanical Engineering, Engineering Faculty, University of Buenos Aires, Av. Paseo Colón 850, C1063ACV, Buenos Aires, Argentina.

Polyolefin Composites, Edited by Domasius Nwabunma and Thein Kyu

Poor mechanical and physical properties of natural fiber reinforced composites are frequently attributed to a weak fiber–matrix interface as a result of the low compatibility between both components mentioned before. Therefore, an efficient mean of improving the compatibility is a major area of investigation (8).

Several matrix resin modifications as well as different fiber surface treatments have been considered in the literature to improve the fiber/matrix compatibility in natural fiber reinforced polymers (1,4,6,9–16). It has been reported that the fiber/matrix interfacial adhesion may be increased, and the mechanical properties of the composites may be improved after such fiber and matrix modifications. Furthermore, chemical treatment on natural fibers not only modifies the matrix/fiber interface but also induces different changes on the interphase between elementary fibers, as well as on the roughness and density of the technical fibers (17,18). Other factors derived from the intrinsic complex composite structure of the natural fiber complicate the dependence of mechanical properties on fiber treatment methods (19–21).

In addition, the most commonly used thermoplastics in industry are polyolefins. Among them, a useful commodity polymer having outstanding properties is polypropylene (PP). It is characterized for having low density, sterilizability, good surface hardness, very good abrasion resistance, excellent electrical properties, as well as good mechanical and barrier properties to water. It also has low cost, worldwide production, simplicity of processing, capability to burn without producing toxic emissions, working security, and recyclability. However, its use as structural material is still limited because it is quite brittle at room temperature and exhibits poor resistance to crack propagation (22,23). PP has received considerable attention for the production of natural fiber reinforced thermoplastic composites (24–37).

In the case of glass fiber, it is well established in the literature (38) that the interfacial shear strength between glass fiber and PP is very low, therefore wetting is poor and shrinkage during crystallization also contributes to this lack of wetting. Moreover, the surface roughness of glass fiber does not offer sites for mechanical anchoring. Interfacial adhesion has been successfully improved in this case by using polymeric coupling agents such as grafted polyolefins and elastomers. It has been observed that while stiffness is independent of the coupling, strength values are greatly affected by it. Besides, coupling has an adverse effect on toughness, owing to restricted matrix deformation. What is more, by incorporating a third elastomeric component to the binary system of PP-g-AA with filler, the toughness may be increased or decreased, depending on whether the filler is encapsulated by the elastomer or not (38).

For natural fiber reinforced polypropylene composites, the addition of coupling agents (especially maleic anhydride grafted PP (MAPP)) has been demonstrated to improve interfacial adhesion and hence the material properties. In the case of maleic anhydride grafted on the backbone of PP, both covalent ester and hydrogen bonds are formed when reacting with hydroxyl groups at the cellulose surface (2). Many works have been done regarding this issue (2,14,15,39–42) and there is extensive evidence for the positive role of MAPP in the improvement of mechanical properties of PP wood-filled composites. However, the structural details of interfacial interactions are less understood and little work has been

reported about the morphological changes and the deformation and fracture mechanisms associated with this improvement (2).

Furthermore, many works have been focused on the effect of silane coupling agents on the physical and mechanical properties of natural fiber/polypropylene composites. It has been established in the literature that the hydrophilic group of a silane coupling agent is expected to react chemically with the functional groups on the wood fiber surface. The hydrophobic group should react or have relatively high compatibility with the polymer matrix (8).

In addition, it is well known that the macroscopical behavior of heterogeneous materials depends on many factors such as composition, behavior of each component, geometrical arrangement of the phases, and interface properties. In the case of natural fiber reinforced polymers, the intrinsic complex composite structure of the technical fiber even complicates the scenario. Technical fiber is multicellular with a nonuniform crystalline structure (43) called cellulose. It is composed of ordered regions (crystallites) extensively distributed throughout the material. Cellulose is the most important chemical component of natural fiber, especially in composites manufacturing (44). The other components are hemicellulose and lignin. This forms the matrix sheath around the fibers holding the structure together. In addition, a small percentage of the structure is formed by waxes. The linear association of these components leads to a threadlike entity called microfibril, which can be seen at an intermediate range of electron microscopy (45). It has a structure consisting on a crystalline cellulose core surrounded by hemicelluloses. In most natural fibers, these microfibrils orient themselves at an angle with respect to the fiber axis called the microfibril angle (43). Both cellulose and the noncellulosic components (e.g., lignin and hemicellulose) play an important role in determining the characteristic properties of the fibers (46).

The structural features of the cell walls have recently been taken into account to predict the mechanical properties of natural fibers through the use of several models. These models consider the spiral angle of the cellulose fibrils and the content of cellulose and noncrystalline regions (46,47).

Natural fibers are commonly used in the form of discontinuous reinforcements, although natural fiber reinforced polymers do not offer such high stiffness and strength values as those of conventional continuous-fiber composites. Their low cost and easy processing make them preferred for many applications (48). However, natural fibers have also been used in continuous form as reinforcement of polymers (15,49,50).

In the case of discontinuous fiber reinforced composites, different energy dissipation mechanisms can be identified depending on the fiber length. In short fiber reinforced composites, a large number of inelastic failure mechanisms in the vicinity of an advancing crack become active. These mechanisms contribute to the creation of the fracture process zone with a concomitant substantial slow crack growth preceding unstable fracture (51,52). In short fiber reinforced thermoplastics, the fibers of subcritical length are pulled out rather than broken, as they are too short to reach their strength. In this case, the relevant energy dissipation mechanisms such as debonding, sliding, restricted pullout, and brittle or ductile matrix fracture are well

described elsewhere (48). Other failure mechanisms such as fiber splitting into ultimate cells, stretching and uncoiling of microfibrils in the cells of fibers, transverse microcracking, and multiple ultimate cell fracture have also been described in natural fiber reinforced polymers (53–55).

Over the last years, many investigations have been done concerning the use of natural fibers with polypropylene (4–5,7,14–16,24–37,56) as well as regarding the fracture and failure behavior of fiber-reinforced polymers (57–61). However, there are relatively few works on both issues simultaneously: the fracture and failure behavior of natural fiber reinforced thermoplastics (3,62,63). Moreover, fewer investigations have been developed on this subject in the case of natural fiber reinforced polypropylene (2,8,39,64,65).

In this chapter, recent works about the mechanical and fracture behavior of natural fiber reinforced polypropylene composites are presented with special emphasis on the deformation characteristics and the fracture and failure mechanisms exhibited by these materials.

7.2 EFFECT OF LOADING CONDITIONS

It has been well established in the literature (66) that the mechanical and fracture behavior of polymer composites is greatly affected by loading conditions such as temperature and strain rate.

Recently, Coutinho et al. (67) studied the effect of testing rate on the deformation behavior of sawdust-reinforced PP composites. They found the expected result that the effect of increasing test velocity was analogous to decreasing the temperature. At high test speeds (400 mm min^{-1}), both PP and the composites exhibited brittle behavior with significantly smaller elongation at break (Fig. 7.1), whereas at low test speeds (5 and 0.1 mm min^{-1}) PP presented cold drawing and at 0.1 mm min^{-1} the composite develops necking rupture. The mode of fracture was dependent on the test speed. When test speed was high, the material exhibited brittle behavior through the formation of planes of crazes. In contrast, at low test speed the matrix underwent large plastic deformation evidenced by the existence of fibrils and the fracture was entirely ductile. At intermediate test speed, mixed mode of fracture with ductile and brittle fracture areas existed.

In addition, Cabral et al. (56) observed the effect of test speed on the mechanical behavior of natural fiber reinforced polypropylene composites. They found that jute/PP composites broken in quasistatic tension displayed some matrix yielding as suggested by the rough surfaces and the stress whitening observed (Fig. 7.2a). On the contrary, composites broken in Izod impact tests did not exhibit any signs of plastic deformation of the matrix material (Fig. 7.2b).

7.3 MICROSTRUCTURAL EFFECTS

In the case of short fiber reinforced thermoplastics, a complex microstructure exists. This is a consequence of the fiber length and orientation distribution in the molding

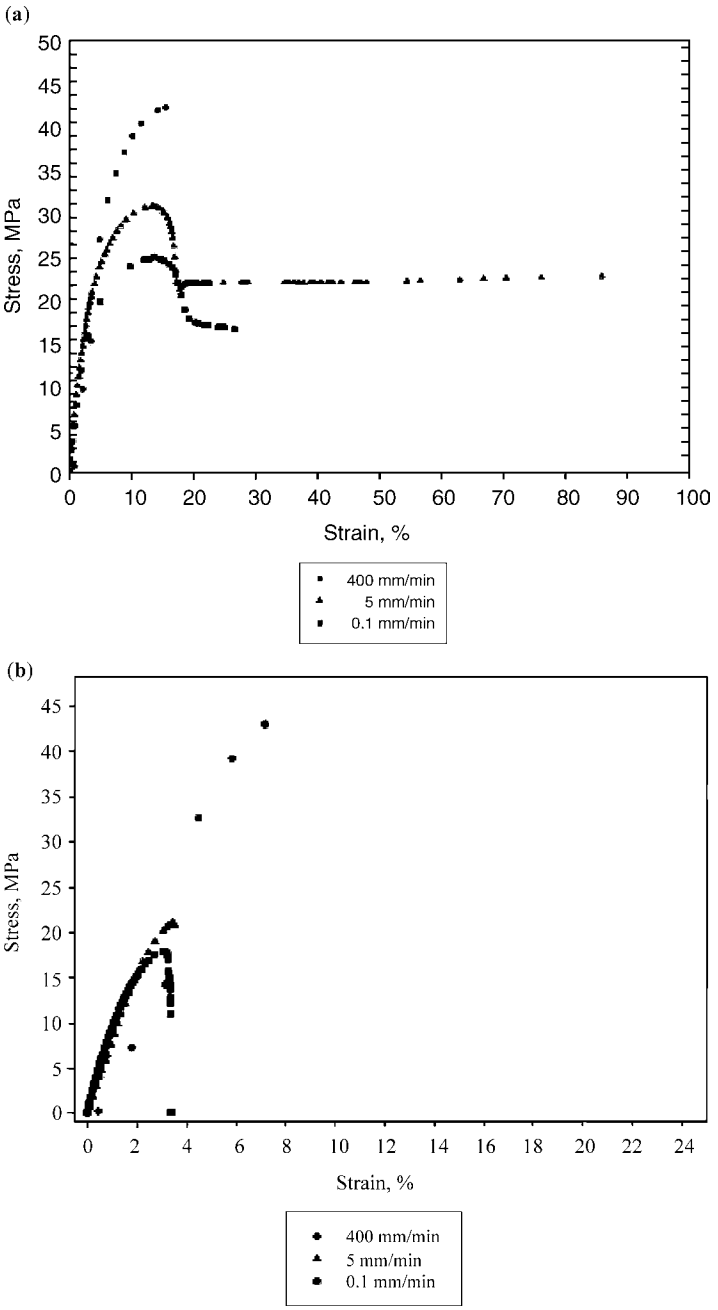

Figure 7.1 Stress–strain curves of sawdust-reinforced PP at different test speeds. (**a**) Neat PP; (**b**) 20 wt% sawdust/PP composite. (From Reference 67 with permission from Elsevier.)

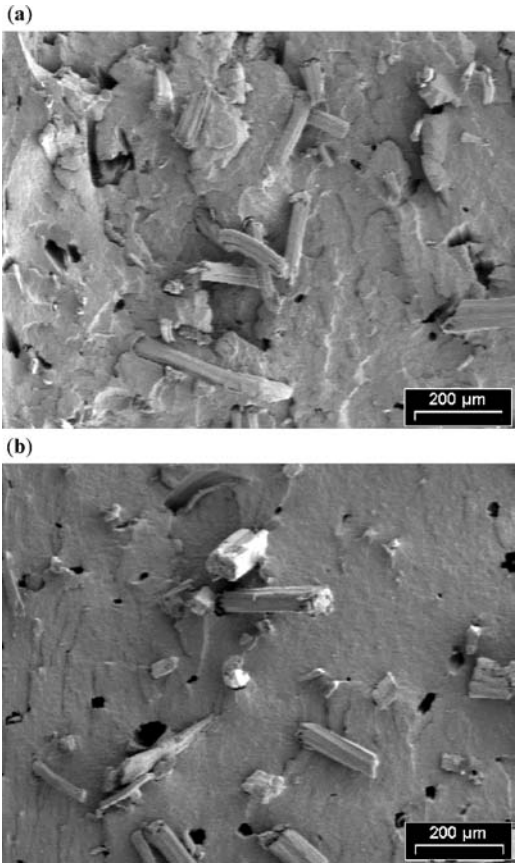

Figure 7.2 Global view of fracture surfaces of samples of a composite with 6 vol% of jute. (**a**) Sample broken in tension under static loading conditions obtained by SEM. (**b**) Sample broken in Izod impact tests obtained by SEM. (From Reference 56 with permission from SAGE.)

and the existence of the interface, which affects the mechanical properties as well as the stress concentrations at the fiber ends.

7.3.1 Fiber Breakage

A very important microstructural effect that influences the mechanical response of composites is the gradual fiber breakage that is observed when composites are prepared by extrusion processes (3,68,69). This effect is found to be more pronounced as the fiber content increases. Within the extruder, higher fiber loaded composites develop higher shear stresses due to their higher viscosity. Hence, higher processing temperatures are generated (energy dissipation is proportional to viscosity). The combination of higher stresses and higher temperatures results in higher degradation of the composites with higher fiber loading.

Table 7.1 Fiber Volume Fraction and Fiber Aspect Ratio for Jute–PP Composites.[a]

Fiber volume fraction, v_f	Fiber aspect ratio, *l/d*
0.06	11.4
0.12	10.9
0.18	9.2
0.23	8.4
0.29	8.1
0.34	7.2
0.45	6.2

[a]From Reference 56 with permission from SAGE.

In the case of natural fibers, as they mainly consist on cellulose fibrils embedded on a lignin–hemicellulose matrix as described before, fiber degradation also leads to defibrillation. This in turn may account for an important reduction in the fiber diameter (70). Doan et al. (71) observed on jute–PP composites that the distribution curves of fiber length moved toward smaller values with increasing fiber content. They attributed this phenomenon to the more damaging fiber–fiber interactions promoted by a higher fiber concentration. A decrease in fiber aspect ratio with fiber content was also observed for extrusion and subsequently injection-molded jute/PP composites by Cabral et al. (56) (Table 7.1). A decreasing trend of fiber pullout length with fiber loading due to the shorter initial fiber length, as a result of the processing induced fiber breakage was also observed by these authors. Similar results were previously found by Vázquez et al. (27) on bagasse fiber–PP composites.

In addition, Joseph et al. (26) studied the effect of processing variables on the mechanical properties of sisal fiber reinforced PP composites. They found a maximum in tensile properties with the mixing time due to the competition between the enhancement of fiber dispersion and the fiber breakage. A maximum in tensile strength with mixing temperature was also observed by these authors. At low temperatures, the high viscosity and shear stresses generated in the mixture led to fibers break down. At high temperatures, thermal degradation and poor dispersion of fibers were observed. The effect of mixing speed was similar to the effect of mixing time.

It is important to note that in synthetic fibers, fiber attrition is directly related to a decrease in the aspect ratio and hence in the mechanical properties. In natural fibers, on the other hand, mechanical degradation may also be accompanied by defibrillation. Therefore, shorter fiber lengths may not necessarily imply smaller aspect ratios. Consequently, some care should be taken when analyzing the effect of fiber breakage on the mechanical properties of composites reinforced with natural fibers.

7.3.2 Fiber Agglomeration

Another important microstructural effect is the agglomeration of natural fibers. Dissimilarity between the surface polarity of polypropylene and natural fibers, leads

to poor dispersion of the fibers in the PP matrix. The nonpolar hydrophobic polypropylene surface repels the polar groups (hydroxyl) on the surface of the natural fiber that is hydrophilic in nature (5). Therefore, polar groups on natural fibers are attracted to each other, leading to the formation of agglomerates. This tendency to form agglomerates may cause an undesirable effect on the mechanical properties. Fiber agglomerates act more like a discontinuity within the matrix structure rather than as a reinforcing material. Doan et al. (71) observed on jute–PP composites a significant improvement of the tensile properties with increasing fiber content, whereas the impact toughness was found to decrease slightly. This result was attributed by these authors to a change from ductile to brittle fracture behavior with increasing fiber content as well as to the increase in the probability for fiber agglomeration at higher fiber content. The probability for fiber agglomeration also increased at higher fiber content, creating regions of stress concentration that require less energy to initiate or propagate a crack. Nuñez et al. (14) also observed that for untreated wood flour/PP composites with filler contents higher than 40%, the filler particles formed aggregates. Cabral et al. (56) also considered the formation of aggregates as a contributing factor to a decrease in the mechanical properties of jute/PP composites.

7.3.3 Fiber Orientation

Fiber orientation is another important factor to be taken into account when analyzing the composite mechanical behavior, irrespective of the nature of the reinforcement.

From optical microscopic observation of polished samples obtained from the longitudinal midsection of injection-molded specimens (Fig. 7.3), Cabral et al. (56) observed a processing induced orientation effect. Fibers were oriented along the mold filling direction in the outer layers, whereas they aligned more randomly in the core region. It has been well established in literature (72,73) that injection-molded

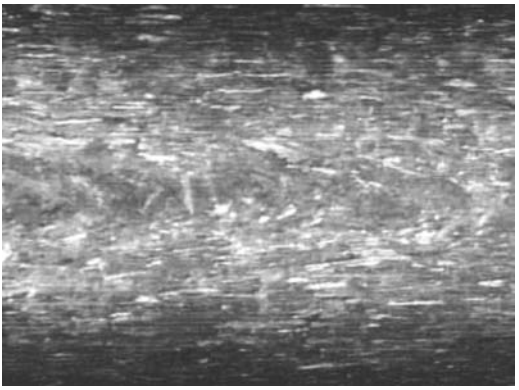

Figure 7.3 Optical micrograph of midsection view along the mold filling direction of an injection-molded specimen of a composite with 45 vol% of jute. (From Reference 56 with permission from SAGE.)

short fiber reinforced polymer composites usually have a processing induced three-layer structure. In the skin layers, fibers are mainly oriented parallel to the mold filling direction, whereas in the core layer, fibers are mainly oriented perpendicular to the mold filling direction. This effect was found to be more pronounced as the fiber content increases and was also considered by Cabral et al. (56) as an influencing factor in the mechanical properties.

Joseph et al. (26) also investigated the effect of fiber orientation on natural fiber reinforced polypropylene. They observed that the strength of unidirectionally aligned fiber composites transverse to the fiber alignment was lower than that of the randomly oriented fiber composites. In the former, the fibers were aligned normal to the direction of loading and they did not contribute to the matrix in increasing the composite strength. In contrast, the strength along the axis of the fiber alignment was higher than that of randomly oriented composites that exhibited intermediate values of strength. Similar results were also found by Alvarez et al. (63) on sisal-reinforced starch-based composites and by Hornsby et al. (40) on PP composites reinforced with wheat and flax straw fibers.

Furthermore, as it has been established in the literature (38), fiber orientation also affects the composite toughness. Moreover, fiber structuring (layering and orientation with respect to the crack path) may be used to improve the toughness of injection-molded items. Interrelated factors such as the effects of fiber structuring, molding-induced enrichment or depletion of the reinforcement, and the aspect ratio and its distribution all influence toughness. Therefore, they are included in empirical expressions to estimate the critical stress intensity factor of short fiber reinforced thermoplastics (38).

Recently, Czigany (65) observed on flax fiber reinforced polypropylene composites that parallel directional K_{IC} values were higher than the similar data in perpendicular direction. These data were close to the values of the matrix as no reinforcement was achieved in the loading direction. Similar results were reported by Alvarez et al. (63) for sisal fiber/starch-based composites.

In natural fiber reinforced polypropylene, it appears that the effect of fiber orientation has characteristics similar to those observed in composites reinforced with inorganic fibers.

7.3.4 Transcrystallinity

Finally, in semicrystalline polymers, the reinforcement may act as a nucleating site for heterogeneous crystallization and may lead to the phenomenon called transcrystallization (38). For transcrystallization to occur, a high density of active nuclei on the surface of the reinforcement is needed in order to restrain the lateral extension of spherulites. Then, they grow perpendicular to the surface of the reinforcement. This is named ‘‘oriented crystallization’’ and if the density of nuclei is higher on the substrate than in the bulk polymer, the morphology is columnar. The effect of transcrystallinity on the mechanical properties of composites still appears controversial in the literature. While many researchers support evidence for improved mechanical properties

with the presence of a transcrystallinity layer (74,75), other authors state that it does not have a significant effect on the performance of the composites (38). Therefore, further work should be done to give more light on this issue.

7.4 DEFORMATION BEHAVIOR

Bledzki and Gassan (1) presented a very complete review article on composites reinforced with cellulose-based fibers. Some of the topics they developed in their work are the most remarkable results about the effect of different coupling agents on the mechanical properties of natural fiber reinforced polymers. They reported that significant improvements in the tensile strength and Young's modulus of polypropylene composites reinforced with natural fibers (i.e., flax, wood pulp, cellulose, wheat straw fibers, jute) using different coupling agents (dimethylurea, polymethylene polyphenylisocyanate, maleic anhydride–polypropylene copolymers) were found in the literature.

Very recently, Doan et al. (71) observed for jute/PP systems without coupling agent that the fiber acted as a filler in the resin matrix weakening the composite as a result of poor interfacial adhesion. The incorporation of 2 wt% of coupling agent (MAPP) in the matrix led to improved tensile strength values and also an opposite trend of these values with fiber loading. A negative effect of the fiber incorporation to PP on strength has also been found in the literature (14,27,33,67) for sawdust, bagasse fiber, and sisal fiber reinforced PP composites. However, the addition of more than 10% of MAPP to sawdust/PP composites (76) allowed improving the composites tensile strength with a small change in ductility. Vazquez et al. (27) also obtained enhanced tensile properties when isocyanate and mercerization treatments were applied onto bagasse fibers.

On the contrary, a trend of increasing Youngs modulus and/or tensile strength with fiber content has been found in many lignocellulosic-filled PP, irrespective of the presence of any matrix or fiber modification (39,56). Acha et al. (15) found that the modulus of PP–jute fabric composites increased with jute content but the strain at break decreased, due to the restriction to matrix deformation imposed by the fibers. They also observed an increase in tensile strength with jute content up to 25% jute. In addition, composites compatibilized with two commercial maleic anhydride grafted polypropylenes exhibited higher tensile strength values than uncompatibilized composites or neat matrix. Elongation at break of the compatibilized composites, on the contrary, was lower in agreement with the results of others (5,77,78).

Sain et al. (79) observed that tensile strength increased as the concentration of low molecular weight maleated PP as a coupling agent increased, and leveled out at higher concentration of the coupling agent. This result suggested that the low molecular coupling agent they used was able to improve the wettability of the fiber with the matrix, leading to improved dispersion. Hence, there was better stress transfer efficiency from the matrix to the fiber.

Recently, Xie et al. (64) investigated the effect of the incorporation of maleic anhydride grafted styrene–(ethylene–co-butylene)–styrene copolymer as a

compatibilizer to improve interfacial bonding between PP and sisal fibers. They reported a slight reduction of Young's modulus of PP/SEBS-g-MA/sisal fiber composites with the increase in SEBS-g-MA content due to the reduction in the matrix modulus with the increase of rubber content. In contrast, they also found that tensile strength of the PP/SEBS-g-MA/sisal fiber composites was higher than that of PP/sisal fiber composite. This was attributed (64) to the improvement in interfacial bonding between sisal fiber and PP promoted by the presence of SEBS-g-MA and evidenced by scanning electron microscopy (SEM) analysis.

Fung et al. (80) proposed a preimpregnation process for the injection molding of sisal fiber reinforced polypropylene. It allowed reducing the injection molding temperature and improving interfacial bonding between sisal fiber and PP. Consequently, higher reinforcement efficiency could be achieved by this processing technique. Maleic anhydride grafted polypropylene was extruded with dry sisal fiber yarns. Then, they were well impregnated by the compatibilizer as they were drawn out during extrusion as a result of the strong wettability between both components.

From the above results, a generalization about the effect of the incorporation of natural fibers to PP on the mechanical properties seems to be very difficult. While some authors reported improvements and increasing trends of Young's modulus and tensile strength with fiber loading, others observed the opposite trend. The great number of factors influencing the mechanical behavior of fiber-reinforced composites is still greater in the case of natural reinforcements due to the complex composite structure of the technical fiber itself. In general, the addition of compatibilizers leads to improved mechanical properties in comparison to unmodified systems due to improved wetting, chemical interaction, better dispersion of the reinforcement or a combination of them. In addition, the intrinsic mechanical behavior of the compatibilizer is also an influencing factor to be taken into account. Introducing an elastomeric component in the coupling agent seems to be a very promising mean of improving fracture properties in natural fiber reinforced polypropylene, as it will be explained later.

It should also be noted that many of the works mentioned above are mostly focused on the changes in the mechanical properties rather in the detailed description of the deformation behavior of natural fiber reinforced PP. An attempt to give more light in this issue is made in the following paragraphs by presenting relevant papers on this topic.

In general, neat PP displays ductile behavior under uniaxial tensile loading characterized by a decrease in stress after yield (strain softening) and exhibiting substantial plastic deformation until failure occurs (22,23,81). On the contrary, natural fiber reinforced PP composites (27,56) frequently do not exhibit significant plastic deformation. They display less ductility than pure PP as a result of the restriction to matrix plastic deformation imposed by the fibers. This is independent of the processing route or the fiber treatment used as indicated by the results of Vazquez et al. (27).

Li et al. (39) reported the tensile behavior of sawdust/recycled PP composites with different filler content (Fig. 7.4). They observed that except the

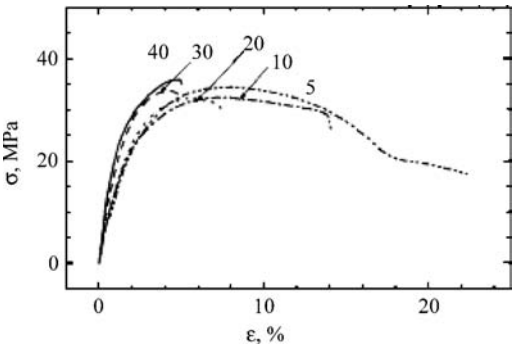

Figure 7.4 Stress–strain curves for PP/MAPP/wood composites (numbers denote filler content). (From Reference 39 with permission from John Wiley & Sons, Inc.)

composite with 5% filler, all PP–wood flour composites showed intensive stress whitening and failed after yielding in a semibrittle fashion. In agreement with Cabral et al. (56), no necking or drawing were observed by Li et al. (39) when filler content was equal to or higher than 10%. Irrespective of the presence of MAPP compatibilizer, they found an increasing trend of tensile modulus with filler content. On the contrary, tensile strength showed opposite trends depending on whether the composites contain MAPP or not. Yield strain and the strain at break were higher when MAPP was incorporated. Li et al. (39) pointed out the role of MAPP in enhancing filler dispersion as well as in promoting a better interfacial wetting.

On jute fabric–PP composites, Acha et al. (15) found significant differences in the stress–strain curves of uncompatibilized and compatibilized composites. In uncompatibilized composites, the stress gradually decreased after maximum point due to the existence of some amount of fiber pullout. In compatibilized composites, however, as a result of the better inferfacial adhesion obtained when using modified matrices, the stress drop suddenly to zero after failure.

It is also interesting to note that Cabral et al. (56) from macroscopic observation of uniaxial samples after failure (Fig. 7.5) found that PP samples developed a well-defined stress whitened neck that stabilized and fractured after significant plastic deformation. In the jute–PP composites specimens, in contrast, no neck could develop and white lines perpendicular to the loading direction were seen. Acha et al. (15) also observed white lines perpendicular to the tensile axis. The concentration of these lines decreased as the jute content increased in agreement with the results of Cabral et al. (56) (Fig. 7.5). This indicated that the amount of matrix yielding decreased with fiber content due to the restriction imposed by the fibers mentioned before. Coutinho et al. (67) on 20 wt% sawdust/PP composites found similar results. While neat PP presented cold drawing at low test speeds (5 mm min^{-1}), the composite only presented necking rupture at very low test speeds (0.1 mm min^{-1}). The presence of fibrils showed that the matrix of the composite underwent a large plastic deformation at this very low test speed.

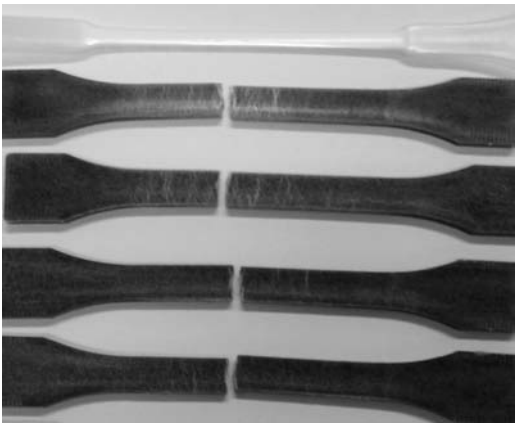

Figure 7.5 Jute/PP tensile samples with 0, 6, 12, 18, and 23 vol% jute from Cabral et al. (unpublished results). (Fiber content increases from the top to the bottom.)

Recently, Hristov et al. (2) studied the effect of grafting level of maleic anhydride in the maleated polypropylene used as a coupling agent on the deformation mechanisms of PP/wood flour composites. They found that the addition of maleated polypropylene increased the tensile properties of the composites in agreement with the results of others. They also observed an optimal level of grafted MA in the compatibilizer that gave maximum tensile strength. Further increase in the MA-grafted level reduced the tensile strength almost to that of the unmodified PP wood flour composite. These authors observed that low concentrations of maleic anhydride conduced to the formation of a thin interfacial layer from which polymer fibrils were readily stretched out during deformation, while the bulk PP matrix underwent voiding and brittle fracture. A higher concentration of MA groups attached on the PP chains led to stronger interaction between PP and wood flour, probably by formation of chemical bonds between MA groups from MAPP and cellulose hydroxyl groups. Consequently, brittle fracture characterized by cohesive failure in both PP and wood particle and reduced ductility of the matrix were observed. Regarding the elongation at break, the same authors found the expected results that the addition of fillers stiffer than the matrix caused a dramatic decrease in the elongation at break. However, the incorporation of maleated polypropylene led to an increase in ductility that was also more pronounced at a critical value of MA in the compatibilizer. The composites with low MA concentration deformed plastically during the test with intensive stress whitening, while the composite with higher MA concentration deformed and fractured predominantly in a brittle fashion without significant plastic deformation before fracture.

Previously, Wu et al. (8) investigated the tensile properties of PP reinforced with wood fibers with different pretreatments. They observed that generally, wood fiber/PP composites exhibited improved tensile modulus, yield stress, and tensile strength in comparison to pure PP or PP/SEBS-g-MA blends. In addition, the tensile properties of the composites containing plain wood fibers displayed the lowest values very close to that of pure PP, suggesting a significant effect of the fiber pretreatment

condition on these properties. Wu et al. (8) also stated that silane coupling agents improved the adhesion by forming a thin interfacial layer that bridges the two components through chemical and physical interactions among the coupling layer, fiber, and polymer matrix. The same authors also investigated the incorporation of a styrene–ethylene–butylene–styrene copolymer grafted with maleic anhydride (SEBS-g-MA) as a compatibilizer in the composite preparation. They observed that the strengthening effect of the wood fiber slightly compensated the softening effect of the SEBS-g-MA copolymer, resulting in composites with tensile properties close to those of pure PP. However, a significant increase in the notched Charpy impact strength was observed when both SEBS-g-MA and wood fiber were added to the composites as it will be described later. Very complete descriptions of the failure mechanisms of the composites were presented by Hristov et al. (2) and Wu et al. (8). These will be discussed in Section 7.6.

7.5 FRACTURE BEHAVIOR

7.5.1 Quasistatic Loading Conditions

Usually in quasistatic fracture experiments, neat polypropylene exhibits nonlinear load–displacement behavior with some amount of slow crack growth preceding unstable fracture (22,23,82). At initial steps stable crack propagation is observed and at a certain point in the load–displacement curve, the propagation mode suddenly changes. Crack propagation becomes unstable and samples separate into two halves (22,23). The *J*-integral parameter at instability (*Jc*) that can be used for quasibrittle fracture characterization (83) was adopted by Montoya et al. (23) to characterize fracture in this material. They found a value of around of 10 kJ m^{-2} (22,23) that was well within the range of values reported for PP homopolymer by other authors (22,84).

In the case of many polymers and composites, the failure occurs via crack propagation; therefore, the application of the linear elastic fracture mechanics (LEFM) is strongly limited for these materials. The fracture behavior is still more complicated in the case of thermoplastic composites reinforced with textile fabrics due to the large damage zone that may even change its shape during crack growth (85). In order to properly characterize the fracture behavior of such systems, the corresponding resistance curves (fracture parameter as a function of crack growth) have to be determined by tracing the crack tip and crack growth during loading. Visual inspection and compliance calibration techniques are not appropriate in this case. Acoustic emission (AE) and heat development using the technique of infrared thermography (IT) have been successfully used in the literature to trace the crack growth during loading. Recently, Romhany et al. (85) determined crack propagation on thermoplastic starch composites containing crossed quasi-unidirectional flax fiber reinforcement by adopting the AE localization method. They also used the IT technique to verify the results derived from the experiments via mathematical treatise. These techniques appear very promising to determine crack propagation on natural fiber reinforced PP.

More recently, Czigany (65) studied the resistance to crack propagation and determined the size of the damage zone in flax fiber reinforced polypropylene composites. They reported fracture toughness values for these composites comparable to those of conventional fiberglass and carbon fiber reinforced composites (K_{IC} values between 5.1 and 13.8 MPa $m^{1/2}$). However, the size of the damage zone was found to be smaller than that in the case of synthetic composites. It was attributed by this author to a lack of adequate adhesion between matrix and fibers, as the connection of both components was very difficult because difference in neither polarity nor reactive groups existed. Significantly smaller damage zone size in comparison with that of synthetic composites was previously reported by Hughes et al. (86) for polyester reinforced with chopped jute fibers. It was considered by these authors to be responsible for the lower fracture toughness of natural fiber reinforced polymers in comparison to their synthetic counterparts.

7.5.2 Impact Loading Conditions

Li et al. (39) studied the impact fracture toughness of sawdust/recycled PP composites. They observed that under impact loads, neat PP and the composites exhibited completely brittle behavior characterized by an abrupt decrease of load to zero after its maximum value. LEFM was applied through the critical strain energy release rate, G_c, by Li et al. to characterize the materials impact fracture. They observed that G_c values for the composites were always lower than that of neat PP (Fig. 7.6). They attributed this result to the lower level of plastic flow ahead of the crack tip. In the absence of compatibilizer, G_c was much lower than that of PP and did not depend on filler content. If maleic anhydride grafted PP was added to the composites, G_c values increased with filler content but still remained lower than that of the matrix. Fracture toughness, K_c, was also obtained by Li et al. (39) from the measured maximum dart stress. They found an increase in K_c with filler content irrespective of the presence of

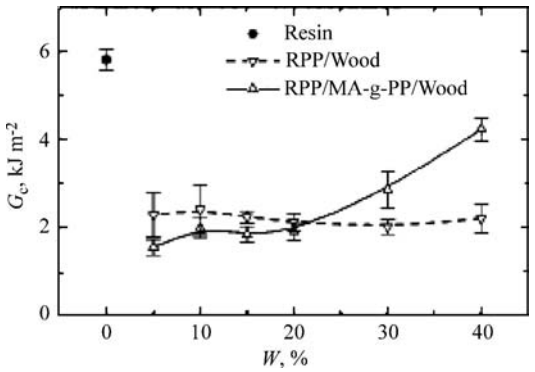

Figure 7.6 G_c versus filler content for PP/MAPP/wood composites. (From Reference 39 with permission from John Wiley & Sons, Inc.)

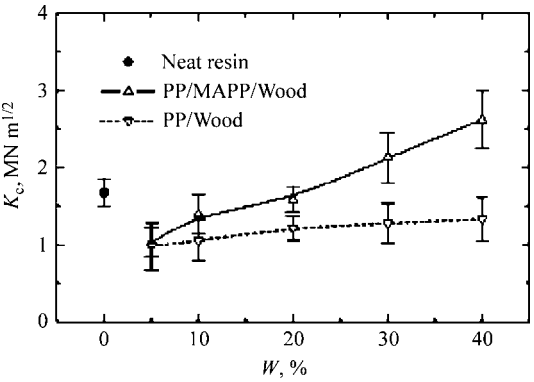

Figure 7.7 K_c versus filler content for PP/MAPP/wood composites. (From Reference 39 with permission from John Wiley & Sons, Inc.)

compatibilizer, as a result of the reinforcing effect of wood filler (Fig. 7.7). Always larger K_c values for compatibilized composites also indicated the enhanced interaction across the interface during impact. The critical stress intensity factor can be viewed as providing a measure of the material strength in the presence of a defect (86). Therefore, it is expected to increase with increasing content of the reinforcement with higher strength and also to depend on interfacial adhesion. Li et al. (39) also observed larger areas of the plastic process zone ahead of the crack tip for composites with MAPP, which probably accounted for the observed improvement of G_c. However, the increase in the process zone size induced by the incorporation of MAPP seemed to be insufficient to counteract the negative effect of the presence of the fibers, as the G_c values still remained lower than that of the matrix.

Furthermore, Hristov et al. (2) reported the impact Charpy load–deflection curves of PP wood flour composites compatibilized with maleated polypropylene with different maleic anhydride concentrations. Unmodified composites displayed brittle fracture, characterized by an almost linear loading curve with a precipitous fall of load after peak load, limited plastic deformation at the notch tip and, unstable crack growth in agreement with Li et al. (39) results. The plateau at the maximum load became broader with increasing concentration of MA in the compatibilizer due to the plastic deformation at the notch tip. However, in the case of the composite with 1.5% MA in the coupling agent the plateau at the maximum load shortened as a result of the reduced ductility of the composite. The Charpy notched impact strength of the composites decreased with respect to the matrix mainly because of the change in the local stress distribution and the lower impact energy dissipated by the PP (2). Maleated polypropylene provided better adhesion between the matrix and wood flour, leading to enhanced impact strength. The maximum impact strength was found for the composite containing 1 wt% MA in the compatibilizer. The slightly reduced impact strength for 1.5 wt% MA was caused by very strong interfacial bond strength. When this composite was subjected to impact loading, plastic deformation of PP matrix was depressed by the high strain rate as well as the

constraint imposed by the rigid filler. The material in front of the crack tip was in a state of plane strain and the crack propagated through the PP matrix with little plastic deformation (2).

Sain et al. (79) investigated the effect of maleated PP content on the notched and unnotched Izod impact of old newsprint-filled PP composites. They observed that notched impact strength was always lower than the corresponding unnotched value as expected. This was due to the additional energy required for crack initiation in the latter. Notched impact strength slightly decreased with the incorporation of the coupling agent and it was almost independent of its content. The unnotched impact strength, in contrast, increased with the coupling agent content. This was attributed by the authors to the more homogeneous dispersion of the fiber derived from the increasing wettability of the fiber with increasing concentration of the coupling agent. This led to a more uniform distribution of the applied stress and required more energy for fiber debonding and subsequent fiber pullout. The crack initiation process that was greatly affected by the coupling agent was the main factor in the unnotched impact strength.

Xi et al. (64) observed that the Izod specific impact energy increased significantly with the SEBS-g-MA content for PP/SEBS-g-MA/sisal fiber composites. These authors also observed from drop-weight dart-impact tests that the incorporation of SEBS-g-MA in PP/sisal fiber composites delayed the crack initiation and propagation, prolonged the crack initiation and propagation time, and increased the energy of impact fracture, hence improving the composite toughness.

In the case of short fiber reinforced polymers with ductile matrices, such as polypropylene, the major source of toughness derives from the matrix-related energy absorption mechanisms such as matrix shear deformation (8). In addition, if fiber–matrix debonding is operative at the end of a single fiber where maximum shear stresses exist (59), local matrix yielding will be induced. On the contrary, in the absence of debonding, the triaxial stress in the matrix may be sufficient to suppress matrix plastic deformation and, subsequently, the material undergoes brittle fracture. The detrimental effect of the incorporation of natural fibers to polypropylene on the impact fracture properties can be explained by the combined effect of the matrix embrittlement that occurs under impact load and the restriction to matrix yielding imposed by the natural fibers. Similar results have been recently reported in the literature for high impact polystyrene reinforced with sisal fibers (3). In addition, interfacial adhesion also influences the material fracture behavior. If a relatively weak interfacial bonding exists, fiber–matrix debonding will induce local shear yielding of the PP matrix and the subsequent increase of toughness. In contrast, if fiber–matrix debonding is suppressed as a result of an excessively strong interface, brittle fracture will occur and toughness will not be improved.

It should also be noted that the number of detailed studies of the fracture behavior of natural fiber reinforced polypropylene composites is still limited. Moreover, only a little data on the fracture toughness values on both quasistatic and impact loading conditions have been reported in the literature. Adequate values of fracture toughness will be required in addition to stiffness and strength, if this family of materials is used in structural or semistructural applications.

7.6 FAILURE MECHANISMS

It is well known that the most important energy dissipation mechanisms in fiber-reinforced polymer composites are fiber–matrix debonding, fiber pullout, matrix shear yielding, and fracture of matrix and fibers that are fiber-, interface-, or matrix-related mechanisms. Their presence depends on several factors such as nature of reinforcement, matrix characteristics, interfacial properties, geometrical arrangement of reinforcement, and loading conditions. In the case of short fiber reinforced ductile matrices, the matrix-related mechanisms including the matrix shear deformation are the major sources of toughness (8) as stated before. However, under appropriate conditions (38), fiber-related energy dissipation mechanisms such as debonding, pullout, and fracture may promote or restrict matrix-related ones. Matrix crazing may be terminated by fiber pullout induced shear yielding, with the subsequent toughness improvement. On the contrary, the impact strength may also be reduced as a result of the loss of ductility derived from the presence of the reinforcement (plastic constraint imposed by the rigid fibers). Stress concentrations at the fiber ends, fiber crossing, or unwetted sites may also decrease toughness, depending on whether or not their effect is counteracted by matrix deformation resulting in an increased damage zone. Frequently, the negative or positive effect of the presence of the fibers is related to the fiber–matrix interface that has to be neither very strong nor very weak to lead to fracture toughness improvement (8). The mechanisms of toughening in fiber-reinforced materials are very complex as both the matrix deformation and fiber-related failure events are always involved (38).

Recently, Romhany et al. (87) studied by SEM and acoustic emission (AE) the failure mode and sequence during loading of technical flax fibers. They found that the failure sequence (axial splitting of the technical fiber along its elementary constituents, radial cracking of the elementary fibers, and multiple fracture of elementary fibers) reflected the hierarchical buildup of natural fibers. Furthermore, during single-fiber fracture two kinds of load–displacement curves were observed by these authors. Some curves displayed a monotonous load increase, whereas other curves displayed a sudden drop of load (''pop-in'') superimposed on a monotonous increasing force. This was attributed to crack bifurcation during which an earlier secondary crack became the major one. In addition, several changes in the plane and direction of the running crack were expected as a result of the complex microstructure of the natural fiber. Romhany et al. (87) also observed by SEM that the failure of natural fiber started by axial debonding and fibrillation along the boundaries of the elementary fibers, which they attributed to the combined effect of the Poisson ratio of the fiber and its microstructure. They also observed that the spiral alignment of microfibrils within the elementary fibers along the fiber axis at a fixed angle caused the breakup of the polysaccharide glue with considerably lower strength than that of the crystalline entities (elementary fibers, microfibrils). Then, radial microcracking in the elementary fibers was found to occur. As a result of this process and fiber fibrillation, local stresses were redistributed and a weak site remote from the initial failure site was created. A zigzag crack advance tearing-type process throughout the split, fibrillated

elementary fibrils was observed. Multiple fracture of the elementary fibers and their constituting microfibrils were found to complete the failure (87).

The very complex failure mechanisms developed during loading of natural fibers and clearly described by Romhany et al. (87) for flax fibers complicate the failure behavior exhibited by natural fiber reinforced polymers and also by natural fiber reinforced polypropylene. Several failure mechanisms that are present in natural fiber reinforced PP are shown in Fig. 7.8.

Coutinho et al. (67) studied the effect of the addition of MAPP to PP–sawdust composites on the material failure behavior. They found that it did not change the matrix fracture mechanism as surface roughness and conic marks were always observed. However, differences between the tensile fracture morphology of PP/MAPP and PP composites were found. The failure of the composites mainly occurred by transversal fracture in the matrix plane. When sufficiently high fiber–matrix adhesion could not be achieved, the composite showed a tendency for fiber pullout. Otherwise, simultaneous fiber pullout and fiber breakage were the basic modes of failure.

In addition, Acha et al. (15) observed that neat PP exhibited entirely brittle fracture in out-of-plane instrumented falling weight impact tests. With the addition of jute fabrics, other energy consumption mechanisms were introduced. Hence, the total energy absorbed during the impact significantly increased. The impact damage mechanism was very complex, different failure mechanisms were involved such as matrix cracking and plastic deformation, surface buckling, delamination, fiber shear-out, and fiber fracture. Furthermore, in the presence of a coupling agent, debonding of fibers was greatly suppressed and the composites behavior was similar to the behavior of a one-phase material. From macroscopic views of impacted samples, Acha et al. (15) also observed that neat PP only exhibited radial cracking, whereas the composites showed a rhombus-shaped delamination pattern aligned with the fabric warp and weft directions. Delamination growth caused by mismatching of the bending stiffness was restrained by the uneven and crimped surface of the woven fabric caused by the interlaced yarns. The same authors also found that irrespective of the presence of compatibilizer, the composites exhibit fiber pullout. However, the fiber length of the pulled fibers was longer and the fracture surface was rougher when no compatibilizer existed. Compatibilized composites also presented fiber breakage confirming an improvement at the interfacial region.

Recently, from SEM analysis of tensile fractured surfaces, Hristov et al. (2) observed in unmodified PP wood flour composites, poor adhesion between the matrix and wood particles. On the fractured surface, many wood particles pulled out of the matrix were seen by Hristov et al. The fracture was found to occur concomitantly within the PP matrix and wood particles without plastic deformation. They attributed the premature brittle fracture to the intensive voids formation in the bulk matrix and their subsequent coalescence in larger voids and cracks. For modified composites with 0.5% of MA in maleated polypropylene as a coupling agent, there were no significant differences in the fracture mode to that of the unmodified composite. However, the fracture occurred selectively at the interfacial regions. Little plastic deformation and a very small gap between the cavitated PP matrix and wood particles

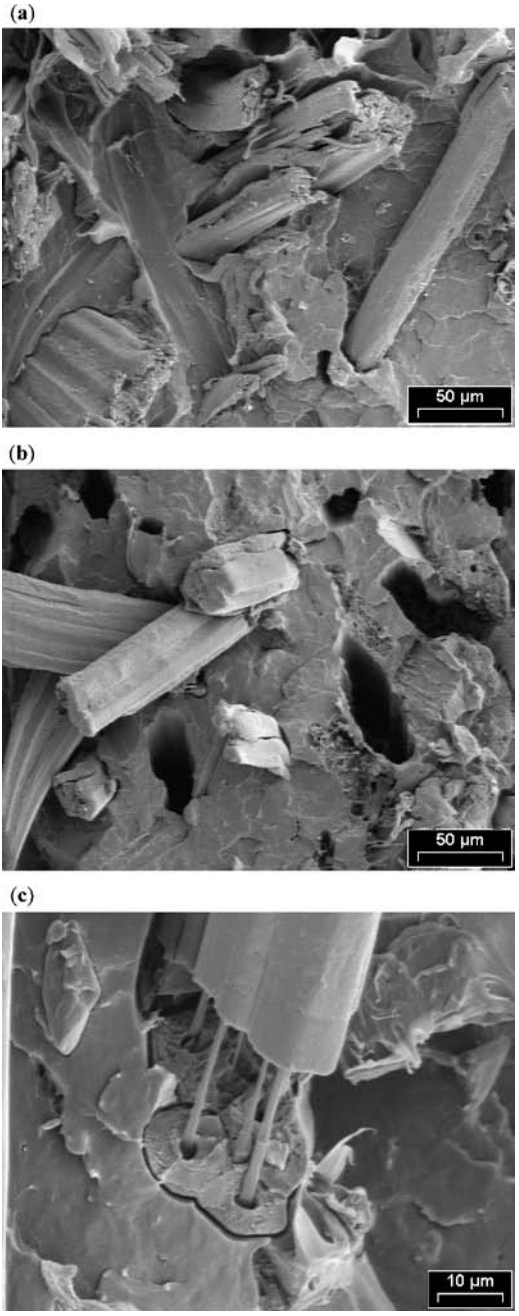

Figure 7.8 SEM micrographs of jute/PP composite samples from Cabral et al. (unpublished results) showing failure mechanisms of natural fiber reinforced polypropylene. (**a**) Fiber splitting into ultimate cell, fiber–matrix debonding, and technical fiber pullout. (**b**) Pullout of technical fibers. (**c**) Pullout of elementary fibers and local matrix yielding.

indicated improved adhesion, probably due to some kind of physical interaction between the compatibilizer and the wood flour (2). On the contrary, there was a significant difference in the deformation mechanism of the PP wood flour composite containing compatibilizer with 1 wt% grafted MA. The wood particles were probably coated with a thin and irregular polymer layer able to deform plastically, and fibrils were stretched between wood particles and PP. These fibrils were formed at some stage of the deformation process, and the tendency to get orientated during the tensile testing created a plastic deformation zone around the wood particles. Thus, the failure mainly occurred at the interfacial regions rather than within the PP matrix or wood particles. The plastic deformation zone mostly developed around the wood particles, while the bulk matrix underwent void formation and brittle fracture. In the case of the composite with 1.5% MA in the coupling agent, the main deformation mechanism was voids formation and brittle fracture of the matrix. Interfacial strength between the matrix and wood particles was very strong, causing fracture of the wood particles rather than being debonded or pulled out of the matrix.

From the observations of Hristov et al. (2), it can be concluded that the interfacial adhesion can be tailored by using the appropriate compatibilizer. The degree of adhesion may even induce slight changes in the mode of failure as demonstrated from the above results.

Finally, the incorporation of an elastomeric component to the coupling agent appears as the most promising mean of improving the material toughness without sacrificing other important mechanical properties such as stiffness and strength.

Xie et al. (64) observed that in the unmodified PP/sisal fiber composites, poor fiber/matrix adhesion was found and long pullout length was observed. Matrix fracture, fiber/matrix debonding and fiber pullout appeared as the main energy absorption mechanisms. When SEBS-g-MA rubber was incorporated, fiber/matrix debonding and fiber pullout were suppressed. Deformation of SEBS-g-MA particles, SEBS-g-MA interface between PP and sisal fibers, and fiber breakage were expected to be the major failure mechanisms.

Wu et al. (8) studied the effect of different pretreatments of the fiber with a silane coupling agent (vinyl-trimethoxy silane) on the failure mechanisms of wood flour/PP composites. They observed that when PP particles are adhering onto the fibers indicating strong interfacial bonding, cohesive failure within the PP matrix was found and it tended to fail in a rather brittle fashion. On the contrary, when gaps between the natural fibers and matrix were seen suggesting a weak fiber–matrix interface, some fibers were pulled out with little plastic deformation of the surrounding matrix. The same authors also observed that mixing of fibers with different surface treatments alone with the PP matrix or using SEBS-g-MA alone to modify the PP only provided a slight improvement in the material impact strength. A synergistic toughening effect, on the contrary, was achieved when both SEBS-g-MA copolymer and the wood flour were incorporated to PP. The incorporation of SEBS-g-MA into the wood fiber/PP composites led to the formation of a ductile polymeric and rubbery coupling layer between the wood fiber and the matrix. The MA segment of the copolymer could react with the hydroxyl groups on the wood fiber surface and the copolymer formed a thin encapsulating layer on the fiber

surface. The SEBS could diffuse into the PP phase resulting in a good interfacial adhesion with PP. As a result of the interactions among the PP, wood fiber, and SEBS-g-MA, the copolymer was anchoraged at the fiber–matrix interface. The SEBS rubbery interface was highly ductile and under plane strain conditions was able to relax laterally and undergo debonding cavitation through chain disentanglement. This interface relaxation prevented premature brittle failure of the fiber–matrix interface or the matrix. Depending on the interfacial bond strength, mechanical properties could be optimized. From SEM observations Wu et al. (8) confirmed the proposed mechanism.

Previously, Oksman and Lindberg (16) reported a beneficial effect of SEBS-g-MA as a compatibilizer between wood particles and matrix on the mechanical properties of LDPE/woodflour composites. They attributed the compatibilizer mechanism between SEBS-g-MA and the wood surface as dependent on chemical bonding (esterification) and hydrogen bonding between the MA and OH groups on the surface of the wood particle. The same considerations are expected to be valid for composites with PP as the matrix material.

On the basis of the above observations, it is evident that natural fiber reinforced polypropylene composites exhibit the same failure mechanisms of their synthetic counterparts. Additional energy absorption mechanisms derived from the intrinsic complex composite structure of natural fibers (fiber splitting into ultimate cells, stretching and uncoiling of microfibrils in the cells of fibers, transverse microcracking, and multiple ultimate cell fracture) are also observed in these composites (87).

7.7 CONCLUSIONS

In this chapter, recent works about the deformation and fracture and failure behavior of natural fiber reinforced polypropylene were presented.

The effect of loading conditions on the mechanical properties of natural fiber reinforced polypropylene composites is similar to that observed in their inorganic counterparts. This is due to the fact that this effect is mostly governed by the matrix characteristics rather than those of the fibers.

Microstructural effects, exhibit some distinctive features when natural reinforcements are used. In the case of synthetic fibers, fiber attrition is directly related to a decrease in the aspect ratio and, hence, in the composite mechanical properties. In the case of natural fibers, on the contrary, mechanical degradation may also lead to defibrillation that may counteract the effect of fiber breakage on the aspect ratio. Consequently, some care should be taken when analyzing the effect of fiber breakage on the mechanical properties of polypropylene reinforced with natural fibers.

The effect of fiber orientation on the mechanical and fracture properties of natural fiber reinforced polypropylene composites has also similar characteristics to those observed in polypropylene reinforced with inorganic fibers.

In addition, further work should be done to give more light on the effect of transcrystallinity on the mechanical properties of the composites analyzed, as it appears still controversial in the literature.

On the basis of the results reported in the literature, a generalization about the effect of the incorporation of natural fibers to PP on the mechanical properties seems to be very difficult. While some authors reported improvements and increasing trends of Young's modulus and tensile strength with fiber loading, others observed the opposite trend. The great number of factors influencing the mechanical behavior of fiber-reinforced composites is still greater in the case of natural reinforcements due to the complex composite structure of the technical fibers themselves.

In general, the addition of compatibilizers leads to improved mechanical properties in comparison to unmodified systems due to improved wetting, chemical interaction, better dispersion of the reinforcement or their combination. Furthermore, interfacial adhesion can be modified by using the appropriate compatibilizer that is even able to induce slight changes in the mode of failure.

In addition, the intrinsic mechanical behavior of the compatibilizer is also an influencing factor to be taken into account. Introducing an elastomeric component in the coupling agent, appears as the most promising mean of improving fracture properties in natural fiber reinforced polypropylene. With this method, other important mechanical properties such as stiffness and strength are not sacrificed.

It should also be noted that many of the works mentioned in this chapter are mostly focused on the changes in the mechanical and fracture properties of natural fiber reinforced PP. A lack of detailed descriptions of the deformation and failure behavior of these composites is frequently observed. Consequently, further effort should be done regarding this topic.

Moreover, only a few data of fracture toughness values on both quasistatic and impact loading conditions have been reported in the literature. These values will be needed if this family of materials is used in structural or semistructural applications. In addition to stiffness and strength, adequate toughness is required for these applications.

Finally, natural fiber reinforced polypropylene composites exhibit the same failure mechanisms of their synthetic counterparts. However, other energy absorption mechanisms derived from the intrinsic complex composite structure of natural fibers (fiber splitting into ultimate cells, stretching and uncoiling of microfibrils in the cells of fibers, transverse microcracking, and multiple ultimate cell fracture) exist. Their presence complicates the failure behavior of these composites.

NOMENCLATURE

AE	Acoustic emission
G_c	Critical energy release rate
IT	Infrared thermography
J_c	*J*-integral
K_{IC}	Critical stress intensity factor
LEFM	Linear elastic fracture mechanics
MA	Maleic anhydride
MAPP	Maleic anhydride grafted PP

PP	Polypropylene
SEBS	styrene–(ethylene-co-butylene)–styrene rubber
SEBS-g-MA	Maleic anhydride grafted styrene–(ethylene-co-butylene)–styrene copolymer
SEM	Scanning electron microscopy

REFERENCES

1. A. K. Bledzki and J. Gassan, Composites reinforced with cellulose based fibres, *Prog. Polym. Sci.*, **24**, 221–274 (1999).
2. V. N. Hristov, M. Krumova, St. Vasileva, and G. H. Michler, *J. Appl. Polym. Sci.*, **92**, 1286 (2004).
3. P. Antich, A. Vazquez, I. Mondragon, and C. Bernal, *Composites A*, **37**, 139 (2006).
4. N. E. Zafeiropoulos, D. R. Williams, C. A. Baillie, and F. L. Matthews, *Composites A*, **33**, 1083 (2002).
5. H. D. Rozman, G. B. Peng, and Z. A. Mohd Ishak, *J. Appl. Polym. Sci.*, **70**, 2647 (1998).
6. D. N. Saheb and J. P. Jog, *Adv. Polym. Technol.*, **18**, 351 (1999).
7. G. Romhany, J. Karger-Kocsis, and T. Czigany, *J. Appl. Polym. Sci.*, **90**, 3638 (2003).
8. J. Wu, D. Yu, C.-M. Chan, J. Kim, and Y.-W. Mai, *J. Appl. Polym. Sci.*, **76**, 1000 (2000).
9. Y. Li, Y.-W. Mai, and L. Ye, *Compos. Sci. Technol.*, **60**, 2037 (2000).
10. L. Y. Mwaikambo and M. P. Ansell, *J. Appl. Polym. Sci.*, **81**, 2222 (2002).
11. G. Mehta, L. T. Drzal, A. K. Mohanty, and M. Misra, *J. Appl. Polym. Sci.*, **99**, 1055 (2005).
12. D. Ray, B. K. Sarkar, and N. Bose, *Composites A*, **33**, 233 (2002).
13. J. George, M. S. Sreekala, and S. Thomas, *Polym. Eng. Sci.*, **41**, 1471–1485 (2004).
14. A. J. Nuñez, P. C. Sturn, J. M. Kenny, M. I. Aranguren, N. E. Marcovich, and M. M. Reboredo, *J. Appl. Polym. Sci.*, **88**, 1420 (2003).
15. B. A. Acha, M. M. Reboredo, and N. E. Marcovich, *Polym. Int.*, 2006. Forthcoming.
16. K. Oskman and H. Lindberg, *J. Appl. Polym. Sci.*, **68**, 1845 (1998).
17. J. Gassan and A. K. Bledzki, *Compos. Sci. Technol.*, **59**, 1303 (1999).
18. D. Plackett and A. Vazquez, Biopolymers and biocomposites, in: *Green Composites: Polymer Composites and the Environment*, C. Baille (ed.), Woodhead Publishers, 2004, Chapter 5.
19. V. P. Cyras, C. Vallo, J. M. Kenny, and A. Vazquez. *J. Compos. Mater.*, **38**, 1387 (2004).
20. A. Mukherjee, P. K. Ganguly, and D. J. Sur, *J. Text. Inst.*, **84**, 348 (1993).
21. M. Z. Rong, M. Q. Zhang, Y. Lui, G. C. Yang, and H. M. Zeng, *Compos. Sci. Technol.*, **61**, 1437 (2001).
22. P. M. Frontini and A. Fave, *J. Mater. Sci.*, **30**, 2446 (1995).
23. M. Montoya, M. J. Abad, L. Barral Losada, and C. Bernal, *J. Appl. Polym. Sci.*, **98**, 1271 (2005).
24. P. R. Hornsby, E. Hinrichsen, and K. Traverdi, *J. Mater. Sci.*, **32**, 1009 (1997).
25. H. D. Rozman, K. W. Tan, R. N. Kumar, A. Abubakar, and Z. A. Mohd Isaac, *Eur. Polym. J.*, **36**, 1483 (2000).
26. P. J. Joseph, K. Joseph, and S. Thomas, *Compos. Sci. Technol.*, **59**, 1625 (1999).
27. A. Vazquez, V. A. Dominguez, and J. M. Kenny, *J. Thermoplast. Compos.*, **12**, 477 (1999).
28. M. N. Ichazo, C. Albano, J. Gonzalez, R. Perera, and M. V. Candal, *Compos. Struct.*, **54**, 207 (2001).
29. K. L. Fung, R. K. Y. Li, and S. C. Tjong, *J. Appl. Polym. Sci.*, **85**, 169 (2002).
30. K. Jayaraman, *Compos. Sci. Technol.*, **63**, 367 (2003).
31. K. Van de Velde and P. Kiekens. *J. Thermoplast. Compos.*, **14**, 244 (2004).
32. K. Van de Velde, *J. Thermoplast. Compos.*, **15**, 281 (2002).

33. M. A. Lopez-Machado, J. Biagiotti, and J. M. Kenny, *J. Thermoplast. Compos.*, **15**, 337 (2002).
34. I. Taha and G. Ziegmann, *J. Compos. Mater.*, (2006). Available online.
35. H. Li, S. Law, M. Sain, *J. Reinf. Plas. Compos.*, **23**, 1153 (2004).
36. D. N. S. Hon and S. Ren, *J. Reinf. Plas. Compos.*, **22**, 957 (2003).
37. G. Cantero, A. Arbelaiz, F. Mugika, A. Valea, and I. Mondragon, *J. Reinf. Plas. Compos.*, **22**, 37 (2003).
38. J. Karger-Kocsis, Reinforced polymer blends, in: *Polymer Blends, Volume 2: Performance.* D. R. Paul, and C. B. Bucknall (eds.), Wiley, New York, 2000.
39. T. Q. Li, C. N. Ng, and R. K. Y. Li. *J. Appl. Polym. Sci.*, **81**, 1420 (2001).
40. P. R. Hornsby, E. Hinrichsen, and K. Tarverdi, *J. Mater. Sci.*, **32**, 1009 (1997).
41. A. K. Bledzki, H. P. Fink, and K. Specht, *J. Appl. Polym. Sci.*, **93**, 2150 (2004).
42. A. Rana, A. Mandal, B. C. Mitra, R. Jacobson, R. Rowell, and A. N. Banerjee, *J. Appl. Polym. Sci.*, **69**, 329 (1998).
43. S. J. Eichhorn, C. A. Baillie, N. Zafeiropoulos, L. Y. Mwaikambo, M. P. Ansell, A. Dufresne, K. M. Entwistle, P. J. Herrera-Franco, G. C. Escamilla, L. Groom, M. Hughes, C. Hill, T. G. Rials, and P. M. Wild, *J. Mater. Sci.*, **18**, 2107 (2001).
44. L. Y. Mwaikambo and M. P. Ansell, *J. Appl. Polym. Sci.*, **84**, 2222 (2002).
45. Kh. M. Mannan and M. A. I. Talukder, *Polymer*, **38**, 2493 (1997).
46. C. Gassan and A. Bledzki, *J. Appl. Polym. Sci.*, **71**, 623 (1998).
47. J. Gassan, A. Chate, and A. J. K. Bledzki, *J. Mater. Sci.*, **36**, 3715 (2001).
48. B. Lauke, *J. Polym. Eng.*, **11**, 103 (1992).
49. T. Munikenche Gowda, A. C. B. Naidu, and R. Chhaja, *Composites A*, **30**, 277 (1999).
50. P. J. Herrera-Franco and A. Valadez-Gonzalez, *Composites A*, **35**, 339 (2004).
51. B. Lauke and W. Pompe, *Compos. Sci. Technol.*, **26**, 37 (1986).
52. B. Lauke and W. Pompe, *Compos. Sci. Technol.*, **31**, 25 (1988).
53. G. Romhány, J. Karger-Kocsis, and T. Czigány, *Macromol. Mater. Eng.*, **288**, 699 (2003).
54. X. Lu, M. Q. Zhang, M. Z. Rong, G. Shi, and G. C. Yang, *Polym. Compos.*, **23**, 624 (2002).
55. J. Karger-Kocsis, *J. Appl. Polym. Sci.* (2002).
56. H. Cabral, M. Cisneros, J. M. Kenny, A. Vazquez, and C. Bernal, *J. Compos. Mater.*, **39**, 51 (2005).
57. S.-C. Wong and Y.-W. Mai, *Polym. Eng. Sci.*, **39**, 356 (1999).
58. D. E. Mouzakis, T. Harmia, and J. Karger-Kocsis, *Polym. Polym. Compos.*, **8**, 167 (2000).
59. S.-C. Wong, G.-X. Sui, C.-Y. Yue, and Y.-W. Mai, *J. Mater. Sci.*, **37**, 2659 (2002).
60. G.-X Sui, S.-C Wong, and C.-Y Yue, *Compos. Sci. Technol.*, **61**, 2481 (2001).
61. S.-C. Tjong, S.-A. Xu, R. K.-Y. Li, and Y.-W. Mai, *Compos. Sci. Technol.*, **62**, 831 (2002).
62. V. Alvarez, C. Bernal, and A. Vazquez, *Polym. Compos.*, **26**, 316 (2005).
63. V. Alvarez, A. Vazquez, and C. Bernal, *J. Compos. Mater.*, **40**, 21 (2006).
64. X. L. Xie, K. L. Fung, R. K. Y. Li, S. C. Tjong, and Y.-W. Mai, *J. Polym. Sci. B Polym. Phys.*, **40**, 1214 (2002).
65. T. Czigany, *J. Compos. Mater.*, **38**, 769 (2004).
66. J. Karger-Kocsis, Microstructural aspects of fracture in polypropylene and in its filled, chopped fiber and fiber mat reinforced composites, in: *Polypropylene. Structure, Blends and Composites*, J. Karger-Kocsis (ed.), Chapman and Hall, London, 1995.
67. F. M. B. Coutinho, T. H. S. Costa, J. C. M. Miguez Suarez, and D. P. Melo, *Polym. Test.*, **19**, 625 (2000).
68. P. Haijji, J. Y. Cavaille, V. Favier, C. Gauthier, and G. Vigier, *Polym. Compos.*, **17**, 612 (2004).
69. A. Dani and A. A. Ogale, *Compos. Sci. Techn.*, **56**, 911 (1996).

70. J. Moran, V. Alvarez, R. Petrucci, J. Kenny, and A. Vazquez, *J. Appl. Polym. Sci.*, (2006). Available online.
71. T. T. L. Doan, S.-L Gao, and E. Mader, *Compos. Sci. Techn.*, **66**, 952 (2006).
72. D. Hull, *An Introduction to Composite Materials*, Cambridge University Press, Cambridge, 1981, p. 80.
73. T. Harmia and K. Friedrich, *Compos. Sci. Techn.*, **53**, 423 (1995).
74. S. Mukhopadhyay, B. L. Deopura, and R. Alagiruswamy, *J. Thermoplast. Compos.*, **16**, 479 (2003).
75. N. E. Zafeiropoulos, C. A. Baillie, and F. L Matthews, *Composites A*, **32**, 525 (2001).
76. J. C. Miguez Suarez, F. M. B. Coutinho, and T. H. Sydenstricker, *Polym. Test.*, **22**, 819 (2003).
77. J. M. Felix and P. Gatenholm, *J. Appl. Polym. Sci.*, **42**, 609 (1991).
78. K. P. Mieck, A. Nechwatal, and C. Knobelsdorf, *Melliand Textilberichte* **75**, 892 (1994).
79. M. Sain, P. Suhara, S. Law, and A. Bouilloux, *J. Reinf. Plast. Compos.*, **24**, 121 (2005).
80. K. L. Fung, X. S. Xing, R. K. Y. Li, S. C. Tjong, and Y.-W. Mai, *Compos. Sci. Technol.*, **63**, 1255 (2003).
81. M. Montoya, M. J. Abad, L. Barral Losada, and C. Bernal, *Eur. Polym. J.*, **42**, 265 (2006).
82. E. Santarelli and P. Frontini, *Polym. Eng. Sci.*, **41**, 1803 (2001).
83. L. Fasce and P. Frontini, *J. Macromol. Sci. B Phys.*, **B41**, 1231 (2002).
84. J. M. Hodgkinson, A. Savadori, and J. G. Williams, *J. Mater. Sci.*, **18**, 2319 (1983).
85. G. Romhany, T. Czigány, and J. Karger-Kocsis, *Compos. Sci. Technol.*, (2005). Available online.
86. M. Hughes, C. A. S. Hill, and J. R. B. Hague, *J. Mater. Sci.*, **37**, 4669 (2002).
87. G. Romhany, J. Karger-Kocsis, and T. Czigany, *J. Appl. Polym. Sci.*, **90**, 3638 (2003).

Part III

Polyolefin Nano Composites

Chapter 8

Metallocene Catalyzed Functionalized Polyolefins in Composites

Ulla Hippi,[1] Noora Ristolainen,[1] Barbro Löfgren,[1] and Jukka Seppälä[1]

8.1 INTRODUCTION

Polyolefins are by far the most common commercial polymers that we encounter in day-to-day life. A number of disadvantages prevent their even wider use. These include the lack of functional groups and polarity, which result in poor adhesion and incompatibility between polyolefins and other materials, such as glass fibers, clays, metals, pigments, fillers, and most polymers. The properties of polyolefins are modified through the introduction of fillers, but the components are not compatible as such. To reduce the interfacial tension between the matrix and the filler, fillers are often coated with fatty acids. Alternatively, functionalized polyolefins can be employed as compatibilizers.

Conventionally, functional groups are introduced to polyolefins by free-radical grafting. The drawbacks of this method are the degradation of the polyolefin chain, cross-linking, and possible monomer residuals in the product. Despite some limitations, another attractive way to produce functionalized polyolefins is by direct metallocene-mediated copolymerization. Differing dramatically from the previous generations of catalysts, the metallocenes offer a new route to higher value added products. The shortfalls associated with the classical Ziegler–Natta catalysts are also avoided since the metallocenes are more tolerant of monomers with Lewis base properties. Furthermore, as compared with earlier catalysts, metallocenes offer better

[1]Laboratory of Polymer Technology, Polymer Science Centre, Helsinki University of Technology, P.O. Box 3500, 02015 TKK, Finland

Polyolefin Composites, Edited by Domasius Nwabunma and Thein Kyu

control of polymer tacticity, molar mass, and polydispersities, as well as copolymer microstructure and composition.

Functionalized polyolefins prepared with metallocene catalysts are rarely used as compatibilizers in polyolefin-based blends and composites. This is probably due to the still limited commercial availability of metallocenes as catalysts for bulk polyolefins. The preparation of functionalized polyolefins and their use in polyolefin composites is the focus of this chapter. The main techniques employed in the preparation are melt compounding and *in situ* polymerization.

8.2 GENERAL FUNCTIONALIZATION APPROACHES

The introduction of a polar functional group into a polyolefin is highly attractive for improving the properties and for broadening the scope of applications of polyolefins. There are three main approaches to the synthesis of functionalized polyolefins, as illustrated in Fig. 8.1. The commercial high pressure free-radical process produces copolymers of ethylene with vinyl acetate, acrylic acid, and acrylate-type comonomers (1,2). An important limitation is that propylene cannot be used due to rapid chain transfer reactions.

Postpolymerization chemical modification of polyolefins by melt free-radical grafting, or reactive extrusion, is a widely used technique. The most frequently used monomers are maleic anhydride, vinyl silanes, and methacrylates. Radical-generating species such as peroxides are used to initiate the grafting. Unfortunately, the undesired side reactions such as homopolymerization of the monomer, polymer degradation, and cross-linking compete with the grafting in the reactive extrusion (3–6). An additional drawback is the presence of residual monomer in the final product.

The direct copolymerization of olefins with polar comonomers (7,8) is a straightforward procedure to achieve functionalized polyolefins. The chief advantage of this approach is that it enables a random distribution of the incorporated polar groups along the polyolefin chain. Usually direct copolymerization suffers to some degree from catalyst deactivation. An alternative way to copolymerize functionalized

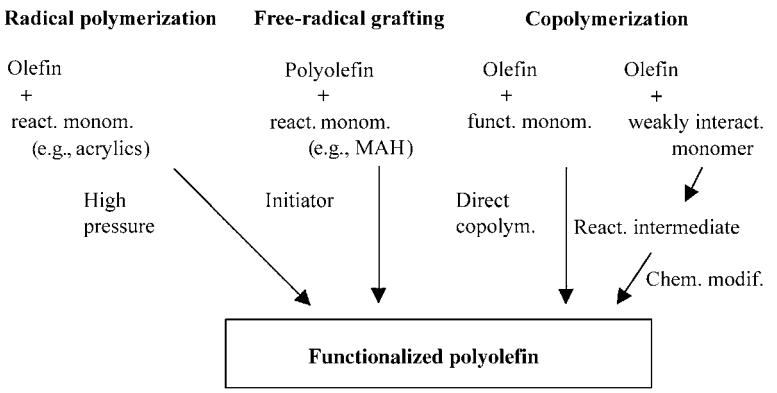

Figure 8.1 Functionalization techniques for polyolefins.

polyolefins is postpolymerization functionalization. In this method, precursors with pendant reactive groups are synthesized from Lewis acidic borane monomers (9–11), dienes (12–15), silanes (16–18), *p*-methyl styrene (19), or divinylbenzene (20,21), and the reactive groups are transformed to a variety of polar groups in the postpolymerization step.

8.3 FUNCTIONALIZED POLYOLEFINS THROUGH METALLOCENE CATALYSIS

Metallocene catalysts have been used in the commercial manufacture of polyolefins since the early 1990s, though metallocenes combined with aluminum alkyls for olefin polymerization have been known since the fifties. The real breakthrough occurred in the early 1980s when the metallocene catalyst was combined with methylaluminoxane (MAO) cocatalyst (22,23). A great deal of effort has since gone into the development of highly stereospecific metallocenes of interest, both in research and in industry. Metallocene catalyst systems will not be discussed here since they are well covered elsewhere (24–39).

The coordination polymerization by metallocene catalysts is a versatile method for preparing linear polyolefins under mild and controlled conditions. Unfortunately, the direct copolymerization of olefins with polar monomers suffers from catalyst poisoning caused by the interaction of the polar groups with the catalyst center. Several strategies have been devised to circumvent this problem. Among these strategies are insertion of a spacer between the polymerizable vinyl double bond and the functional group (40–42); shielding of the heteroatom with sterically demanding groups (43–47) or by silyl protection (48,49) in order to weaken the electron-donating character of the heteroatom through attachment of electron-withdrawing substituents on or adjacent to it; and precomplexing of the polar monomer with a Lewis acid, typically an organoaluminum compound (Fig. 8.2)

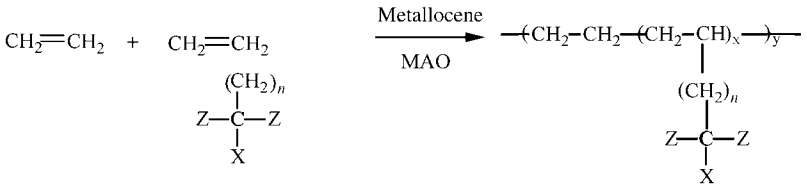

Figure 8.2 Direct copolymerization of olefins with functional monomers with required protection of the functional group.

(7,8,50–54). Deactivation can be minimized by protecting both the functional group and the active sites of the catalyst (55).

As mentioned above, another versatile method to exploit the characteristic features of metallocenes is postpolymerization functionalization. This differs from direct copolymerization in that the olefin does not react directly with the functional monomer and catalyst poisoning is avoided. In the first step, a substituted olefin monomer containing a reactive group is copolymerized to give a polyolefin copolymer with pendant reactive groups. In the second step, the intermediate copolymer is converted by chemical modification to give polar functionalized groups in the polyolefin. Postpolymerization functionalization greatly benefits from the capability of certain metallocenes to effectively copolymerize a broad variety of comonomers. Moreover, the copolymers synthesized with metallocenes have narrow molar mass and composition distributions, giving uniform distribution of the reactive groups in the reactive intermediate. Evidently, Chung and coworkers were the first to describe this reactive polyolefin intermediate approach to synthesize side group functionalized polyolefins, though at that time it was developed for conventional Ziegler–Natta catalysts (56–58). Borane groups do not interfere with metallocene-mediated olefin polymerization and are chemically stable against metallocene catalysts as well as their cocatalysts. Other types of precursor monomers are dienes, silanes, *p*-methylstyrenes, and divinylbenzenes.

Copolymerization of olefins with dienes is an emerging area in metallocene-based polymerizations. This process results in pendant double bonds that like boranes can be converted into functional groups by standard organic chemical reactions. Such functional groups can then act as ''active sites'' for the synthesis of graft copolymers. Copolymerization with dienes is complicated by the occurrence of cross-linking, particularly in the case of symmetrical dienes (59). On the contrary the high reactivity of the more strained endocyclic double bond in a bicyclic olefin, such as 5-vinyl-2-norbornene, leads to a copolymer in which enchainment occurs selectively and leaves a reactive pendant unsaturation free for further functionalization (60). Chung et al. (61) adopted a two-step approach that included the synthesis of unsaturated ethylene–diene copolymer and subsequent functionalization by borane reagents.

The electropositive character of silanes enables the incorporation of vinyl-terminated polar silane monomers without loss of catalyst activity. Intermediates with a reactive phenylsilane group have been synthesized and used to produce functional groups in polyolefins (16–18).

The copolymerization of olefins with *p*-methyl styrene also enables the introduction of a variety of functional groups in the polyolefin backbone (19). The incorporated *p*-methyl styrene units can even be transformed to stable anionic initiators for living anionic ''graft-form'' polymerization reactions.

Metallocene technology makes it possible to control the incorporation of divinylbenzene, which selectively reacts with only one of the two vinyl groups. The pendant styrenic moieties along the polymer chain are reactive in many chemical reactions, including free radical, cationic, and anionic reactions (20,21).

Yet another approach is the functionalization of double bonds at the chain ends of polyolefins (62–66). With the use of metallocene/MAO catalyst systems, several different chain transfer reactions are available. Terminal functional groups offer an opportunity to prepare multisegmented polymers. In general, three methods can be used to synthesize such polymers: (i) chemical modification of chain-end unsaturated polyolefins, (ii) living polymerization, and (iii) *in situ* chain transfer reaction by chain transfer agent containing either a polar group or its precursor. Among these approaches, the chain transfer method is the most effective and also the most widely applied for the synthesis of chain-end functionalized polyolefins.

As made clear above, a variety of routes are available to introduce functional groups into polyolefins or to produce block and graft copolymers. Given the typically reduced oxophilicity of late transition metals, vis-à-vis the early metals, late transition metal catalysts are, in the context of functional monomers, highly promising for the future since they are not as sensitive as metallocene catalysts to polar groups. This makes them suitable for catalyzing the direct copolymerization of olefins with functional monomers (67).

8.4 COMPATIBILIZATION OF POLYOLEFIN COMPOSITES

8.4.1 Background

A common way to alter the properties of polyolefins is through the introduction of fillers. In general, fillers increase stiffness, provide abrasion resistance, and reduce shrinkage of molded parts. Disadvantages include deterioration in toughness and difficulties in processing. Since fillers are often hydrophilic, adhesion between the filler surface and the polyolefin matrix tends to be poor. The achievement of properties such as color, conductivity, and flame retardancy nevertheless usually requires the introduction of fillers, sometimes in high concentration (68).

Nanoparticles, which are objects smaller than 100 nm, offer a means to improve stiffness and thermal and barrier properties with low loadings, while keeping processability at a comparable level to that for the neat polymer. The large functional and active surfaces of nanoparticles means that they can act as heterogeneous catalysts or photocatalysts, or introduce conductivity or antibacterial properties to polymer composites. Nanoparticles are smaller than the wavelength of visible light, and conductive, transparent nanocomposites may possess interesting electro-optical properties. Nanofillers are characterized by large specific surface area, and challenges are to disperse them without losing this property and to ensure good interfacial adhesion with the polymer matrix so that their unique properties are transferred to the composites (69–71).

The properties of filler surfaces, whether micro- or nanosized, are often modified through application of coatings, which reduce the interfacial tension at the boundary of the filler surface and the polyolefin matrix. Typical coating agents for the fillers used with polyolefins are fatty acids such as stearic acid and their salts, which can react with

the hydroxyl groups on the filler surfaces (70,71). In the case of layered silicates, the penetration of a polymer matrix is aided by making the interlayers of the sheets more organophilic. Usually this is carried out by cation exchange with an alkyl amine.

As an alternative to coatings as a means of improving the adhesion between filler particles and polyolefin matrix, functionalized polyolefins are added as compatibilizers (72–75). Reactive groups of the functionalized polyolefin readily interact with the functional groups on the filler surface, while long hydrocarbon tails are anchored to the polymer matrix through physical entanglements and van der Waals interactions (75,76). Durable linkages between the filler and the matrix are thereby formed. Improved adhesion is expected to influence the mechanical properties of the composites, and in fracture processes this may result in cohesive failure within the polyolefin instead of an adhesive failure taking place between the filler and the polymer (77).

Functionalized olefin copolymers produced with Ziegler-type catalysts have been suggested to possess better adhesion properties than other polymers and fillers. However, only a few studies report experimental results in this area. Hydroxyl-functionalized polypropylene has been used as an interfacial agent in polypropylene/aluminum and in polypropylene/glass laminates (78,79). Indications of strong interactions between the functionalized polypropylene and the aluminum or glass were observed as a failure mode of mostly cohesion type and an increase in peel strength. Chemical reaction between the free silanol groups of the glass and the hydroxyl groups of the polypropylene was also verified.

Improvement in adhesion to an aluminum sheet was recently reported for functionalized olefin copolymers produced with metallocene catalysts (80). The copolymers have only rarely been used as compatibilizers in polyolefin-based blends and composites, although the use of polymeric additives in these applications is well established. In the following sections, the use of polyolefins containing polar groups, synthesized with metallocene catalysts, in polyolefin composites is discussed based on the method of producing the composite. The methods are melt compounding and *in situ* polymerization, which are used for both conventional microsized fillers and nanofillers. In the discussion of melt compounding, the preparation of the polyolefin composites is presented according to the type of filler, in either particle or layered form. The *in situ* polymerization method is described in general, and its application in the preparation of polyolefin composites is discussed.

8.4.2 Functionalized Olefin Copolymers in Melt Compounding

The effectiveness of polyethylene-based compatibilizers to act as adhesion promoters in polyethylene/metal hydroxide composites has been studied by Hippi et al. (81). The composites were polyethylene/aluminum trihydroxide (PE/ATH) and polyethylene/magnesium hydroxide (PE/MH) composites with composition 60/40, while the compatibilizers were hydroxyl and carboxylic acid functionalized copolymers prepared with ansa-indenyl zirconocene catalysts and commercial polyethylenes functionalized with butyl acrylate, maleic anhydride, epoxy, and acrylic

acid. In composites without compatibilization, the particles were not attached to the matrix, as shown in Fig. 8.3a. Similarly, when the particles were coated with stearic acid, debonding occurred between the particles and the matrix. Addition of any one of the polymeric compatibilizers improved the adhesion to such an extent that the fracture mechanism changed from adhesion failure to cohesion failure (Fig. 8.3b).

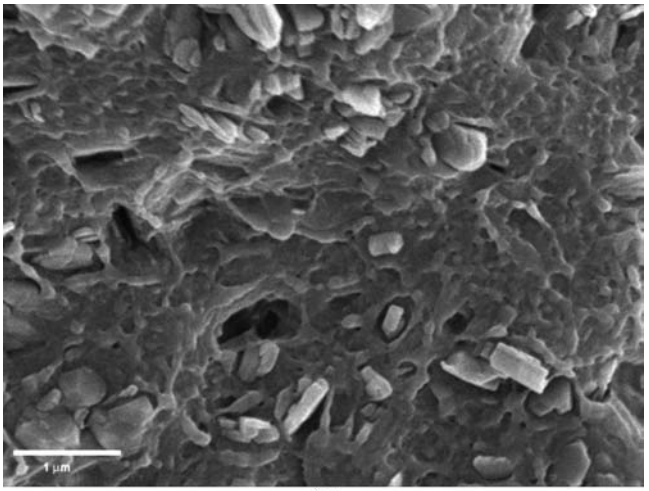

(a)

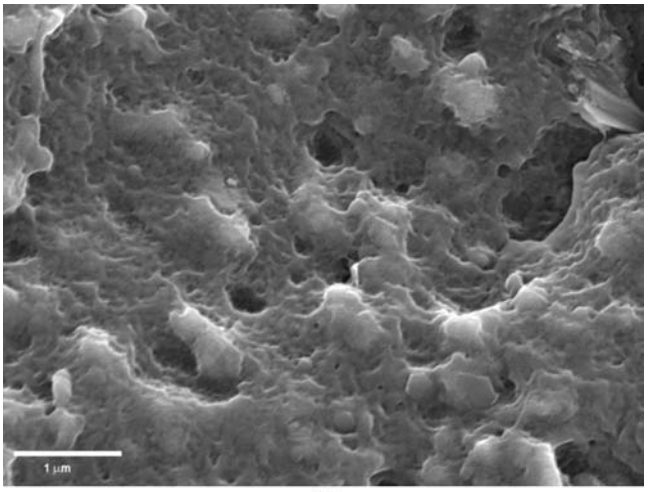

(b)

Figure 8.3 Scanning electron microscopy images of PE/ATH (60/40) composites with (**a**) no compatibilizer and (**b**) 10 wt% of carboxylic acid functionalized PE. (From Reference 81 with the permission from Elsevier.)

Improvement in both stiffness and toughness of the composites was obtained. Improvements in flammability properties achieved with ATH or MH were also preserved.

The behavior of functionalized polyethylenes at the boundary of filler and matrix in PE/ATH 60/40 composites was further studied by Lipponen and Seppälä (18). The compatibilizers were copolymers of ethylene and phenylsilane that were posttreated into chloro-, fluoro-, or alkoxysilanes (16). Comparison was made with a commercial ethylene/butyl acrylate copolymer. The polyethylenes containing reactive silane groups formed a strong bond between filler and matrix resulting in a highly crystalline PE phase as observed by thermal analysis. Even with very low functionality content in the polyethylene phase, 1/10 that of the butyl acrylate functionalized polyethylene, impact strength of the composites was markedly improved. Tensile modulus was increased. Ethylene/phenyl silane copolymer also interacted weakly with the filler.

Control of the microstructure of polypropylene/microsilica composites by adding functionalized polyolefins and the effect of this addition on thermal and mechanical properties were studied by Uotila et al. (82). The matrix was an impact modified PP containing ethylene/propylene rubber inclusions, and the fillers were precipitated silica and silica fume. Commercial polypropylene and polyethylene/butyl acrylate functionalized with maleic anhydride and hydroxyl-functionalized ethylene and propylene copolymers prepared with metallocene catalysts were used as compatibilizers. Unfunctionalized polyethylene/butyl acrylate tended to move toward the rubber phase. When the elastomer was functionalized with maleic anhydride, it interacted with the filler and dragged the particles along with it bringing about an increase in the total surface area of the elastomer phase. The structure resembled a core–shell microstructure. The filler particles acted as nucleating agent in the elastomer phase and increased its crystallization temperature. The increase in the total surface area of the elastomer phase resulted in the threefold increase in impact strength, but as there was less filler particles present in the matrix, the tensile modulus decreased. With maleic acid grafted polypropylene as compatibilizer, the particles were coated and dispersed throughout the polypropylene matrix, forming predominately a phase-separated microstructure. The crystallization temperature of the polypropylene phase increased due to interaction between the filler and the matrix. This led to improved toughness and enhanced stiffness as well. The application of hydroxyl-functionalized polypropylene prepared with metallocene catalyst improved the nucleating activity even further and stiffened the composite.

Nanocomposites based on layered silicates are widely studied because of their high aspect ratio and because the addition of a small amount of silicate has been found to provide excellent mechanical, thermal, flame-retardant, and barrier properties. A disadvantage is the difficulty of obtaining nanostructures with polyolefins during melt blending. Layered silicates have a sheet structure where layers are held together by weak van der Waals forces. Polymer nanocomposite is obtained when a polymer chain penetrates between the layers (intercalated structure) or when the sheets are completely embedded by polymer and lose their organized structure (exfoliated structure) (69).

A hydroxyl group associated with the polyolefin chain is less polar than the more commonly employed maleic anhydride grafted polyolefins (83,84). Intercalation with hydroxyl group takes place through hydrogen bonding between the hydroxyl group of the compatibilizer and the oxygen group on the layer surface. Hydroxyl-functionalized olefin copolymer is sufficiently polar to penetrate between the layered sheets, and an exfoliated nanocomposite is obtained. A minimum of functionality content must be defined for each polyolefin/clay nanocomposite separately. However, too high content of functionality affects the exfoliation negatively (85,86).

Motha et al. (87) studied the compatibilization of polyethylene nanocomposites with conventional maleic anhydride grafted polyethylenes and with hydroxyl-functionalized ethylene copolymers prepared with metallocene catalysts. Both types of compatibilizers yielded intercalated and exfoliated structures, and the tensile properties were improved. Change in molar mass or in functionality content appeared to have no effect on the mechanical properties in the case of the hydroxyl-functionalized compatibilizers. For the maleic anhydride grafted polyethylenes, however, lower molar mass and higher maleic anhydride content gave a better stiffness–toughness combination. Permeability of oxygen and water vapor was reduced when layered silicate was added to the polyethylene. Further decrease was obtained with the addition of compatibilizer, especially hydroxyl-functionalized copolymer. The control of the functionalization reaction achieved with metallocene catalyst decreased the concentration of compatibilizer required as compared with maleic anhydride grafted polyethylene compatibilizer, while the matrix properties were unchanged.

The effectiveness of a series of hydroxyl-functionalized propylene copolymers (PP-co-OH) prepared with metallocene catalysts in PP/layered silicate nanocomposites has been studied (86). Hydroxyl-functionalized polypropylenes with functionality content of 0.4–0.6 mol% were compared with a commercial maleic anhydride grafted polypropylene (PP-g-MA). The molar masses of the PP-co-OH compatibilizers varied, and they were also significantly lower than the molar mass of the commercial PP-g-MA compatibilizer. Intercalated and exfoliated structures were achieved in melt blending with both types of compatibilizers. Even though a wider space between the layers resulted when cation exchange was carried out with an alkyl ammonium containing 18 (organoclay18) carbons in the alkyl chain than with an alkyl ammonium containing 11 (organoclay11) carbons, nanostructure was achieved.

The PP-co-OH compatibilizer interacted more with the outer surface of the clay particles than with the interlayers. PP-g-MA compatibilizer, on the contrary, interacted more with the interlayers of layered clays (Fig. 8.4). More exfoliated structure was achieved when PP-co-OH concentration was twice the concentration of the modified clay than when it was the same. The ratio of compatibilizer to organomodified clay determined the success of the formation of nanostructure. Nanoscale characterization by transmission electron microscopy and X-ray diffraction analysis confirmed that PP-co-OH, just as PP-g-MA compatibilizer, was able to penetrate between the organomodified clay sheets to form intercalated and exfoliated nanostructures.

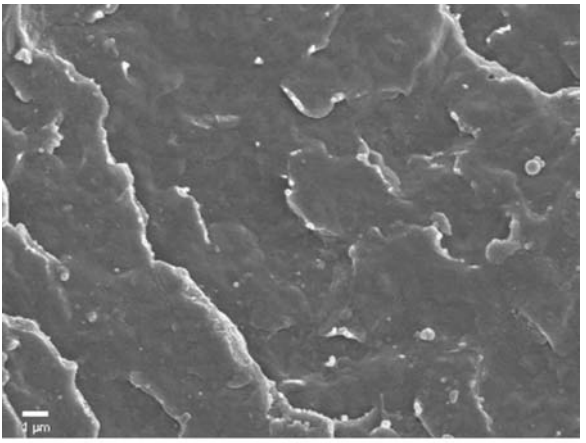

(a)

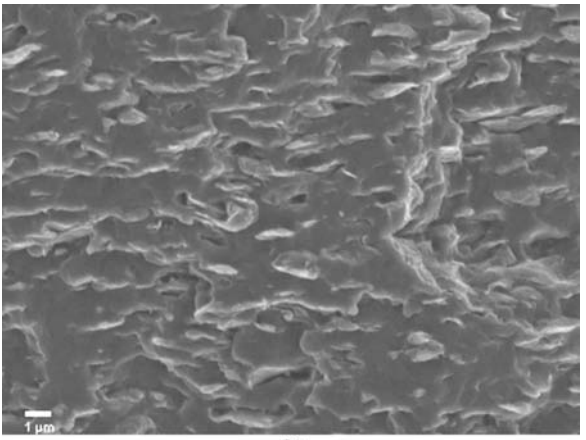

(b)

Figure 8.4 Scanning electron microscopy images of fracture surfaces of (**a**) PP/PP-co-OH/organoclay11 (90/5/5) and (**b**) PP/PP-g-MA/organoclay18 (70/20/10). (From Reference 86 with the permission from John Wiley & Sons, Inc.)

Flame retardancy of layered silicates is based on two phenomena: sheets absorb and bind volatile molecules, and a long diffusion path is created by the so-called labyrinth effect. In addition, layered silicates form char during combustion and the char acts as a thermal insulator and a barrier against mass transport. The flame retardancy of aluminum trihydroxide particles is based on water release and absorption of heat. Synergy in fire retardancy can be obtained by combining ATH and nanoclays in a polyolefin matrix.

Partial substitution of ATH with layered clay without losing the fire retardancy properties was successfully achieved by Ristolainen et al. (88). Commercial maleic

anhydride grafted polypropylene and hydroxyl-functionalized polypropylene were used as compatibilizers. It was shown that the adhesion between filler and matrix was improved with both compatibilizers and exfoliated nanostructure was achieved. The two compatibilizers acted in different ways in the composites: PP-g-MA preferably interacted with the organoclay producing an exfoliated and intercalated structure, whereas PP-co-OH embedded the ATH particles more deeply, and the structure of the organoclay was less exfoliated (Fig. 8.5).

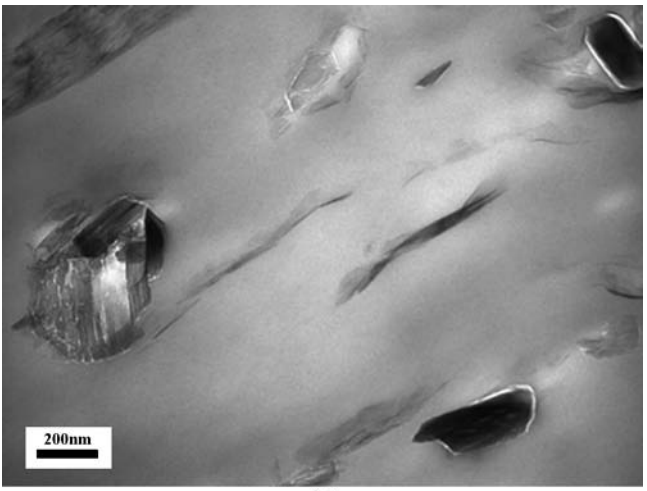

(a)

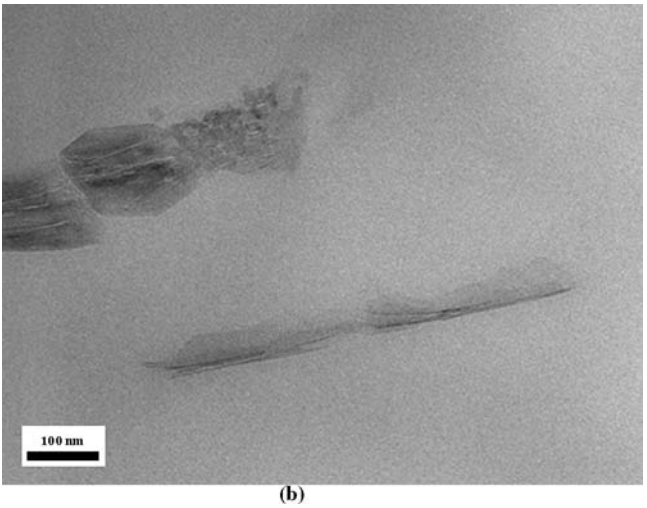

(b)

Figure 8.5 Transmission electron microscopy images of PP/ATH (stearic acid coated)/organoclay nanocomposites with (**a**) PP-*g*-MA compatibilizer and (**b**) PP-co-OH compatibilizer. (From Reference 88 with the permission from John Wiley & Sons, Inc.)

ATH particles can be used without a coating layer in a polyolefin/ATH/nanoclay composite because the compatibilizer also lowers the surface energy between the ATH particles and the matrix. However, the ATH particles and the layered clays compete for interaction with the compatibilizer, and an adequate amount of compatibilizer is therefore essential (89).

Final properties of the polymer nanocomposites are influenced by the crystallinity and the crystalline structure. Nanoparticles act as nucleating agents, which can be detected as an increase in crystallization temperature (87). Partial substitution of organoclay for the ATH particles in PP/ATH/compatibilizer composites resulted in decreased crystallization temperature, whether or not the ATH particles were surface treated. The decrease may have been due to an insufficient amount of compatibilizer to effectively bind the ATH particles and the organoclay to the matrix. However, coating agents on ATH particles reduce the need for PP-co-OH compatibilizer.

The fire-retardant properties were retained and in some cases improved when layered silicates were partially substituted for ATH particles (Fig. 8.6). Other properties, in addition to the flame retardancy, of the PP/ATH/clay composite depended on the degree of exfoliation of the layered clay. Stiffness was at maximum when degree of exfoliation was at maximum. Maximum exfoliation can be achieved by using a coating agent on ATH particles and sufficient PP-co-OH compatibilizers.

The purpose of applying functionalized polyolefin to a layered silicate is to facilitate penetration of the polymer between the interlayer by rendering them more organophilic. The organic surfactant ion-exchange step becomes unnecessary if similar properties are introduced to the polyolefin chain, that is, by replacing the organic surfactant with a polyolefin containing terminal end group $-Cl$, $-OH$, or $-NH_2$. In the studies of Chung (64), functionality content was significantly lower in chain-end functionalized polyolefins than in copolymerized or grafted polyolefins, and exfoliated structure was achieved with the chain-end functionalized

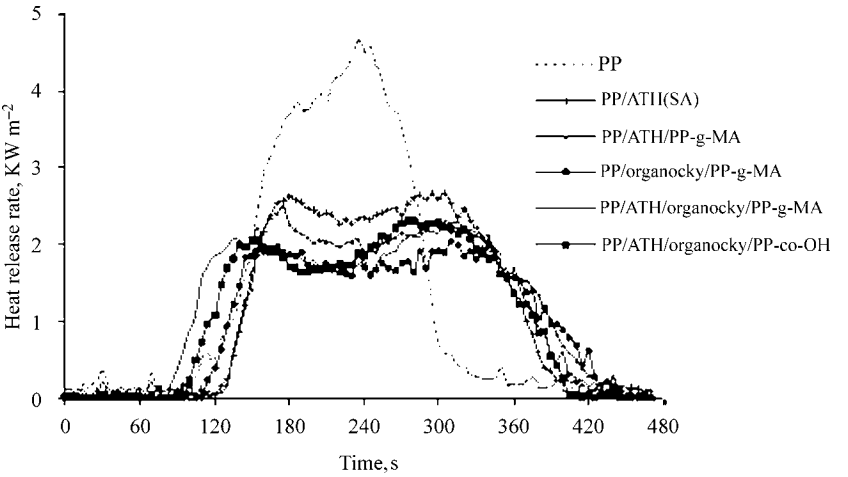

Figure 8.6 Comparison of the heat release rate of neat PP and PP/ATH/organoclay composites of different compositions. (From Reference 88 with the permission from John Wiley & Sons, Inc.)

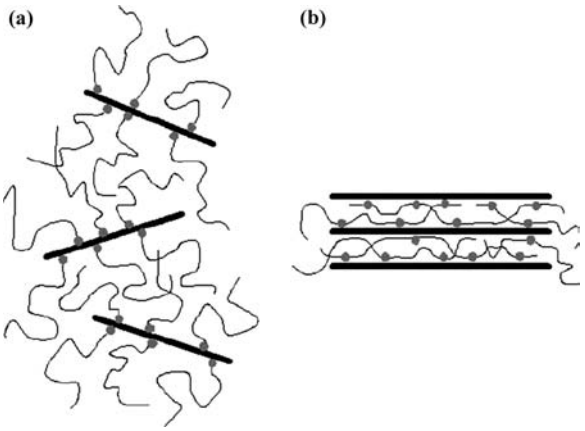

Figure 8.7 Illustration of the molecular structures of (**a**) chain-end functionalized and (**b**) side chain functionalized polyolefin located between clay interlayers. (From Reference 64 with the permission from Elsevier.)

polypropylenes. The terminal functional group reacted with the interlayer surface of the clay, while the rest of the chain was orientated toward the matrix. As illustrated in Fig. 8.7, random copolymers can align parallel to the clay surface forming intercalated structure, but this cannot occur with a chain-end functionalized polymer.

8.4.3 *In situ* Polymerization

Most polyolefin composites are prepared by mechanical compounding above the melting temperature of the polyolefin matrix. The challenges are to disperse the filler particles and get them attach to the matrix polymer. Other techniques available for the preparation of polyolefin composites are solution blending (90) and preparing either the filler particles or the polymer matrix in the presence of the other component (91). Solution blending and preparing the filler particles in the presence of the polymer require the polymer to be soluble, which makes these techniques poorly applicable to polyolefins. Polymerization in the presence of the filler has gained more attention lately, particularly in response to developments in catalyst technology (92). This technique, called *in situ* polymerization or polymerization-filling technique (PFT), consists of attaching a catalyst to the surface of a filler before proceeding with the polymerization. Through this technique, composites with high filler loadings, much more uniform filler distribution, and considerably enhanced interfacial adhesion can be achieved. Improved mechanical properties of the composites may follow (93).

Metallocene catalysts can be covalently bonded onto filler surfaces through their aluminum alkyls. Thus all active species for the polymerization are located on the filler surface, and the filler is homogeneously dispersed in the composite. Unlike Ziegler–Natta catalysts, which can only be anchored to acidic surfaces of fillers, the cocatalyst methylaluminoxane (MAO) used in metallocene catalyst systems can be attached to a wide variety of surfaces such as acidic, basic, organic, and metallic

(94). A further advantage of metallocene catalysts is their versatility and thus the possibility to tailor the microstructure of the polyolefin matrix.

Over 20 years ago, Kaminsky et al. (95) produced filled polyolefins by *in situ* polymerization with metallocene catalysts. The inorganic fillers were calcium sulfate, calcium carbonate, and mica. Since then, many fillers, both microsize and nanosize, have been used to prepare polyethylene composites (94,96–99). Aluminum powder, aluminum bronze, and zinc powder were covered with polyethylene or polypropylene when treated with methylaluminoxane and metallocene catalyst before polymerization (96). With high filler loadings, the composites showed thermal conductivity combined with electrical resistivity. The result was attributed to a closed shell of polyolefin around each aluminum particle preventing the metal particles from forming electrically conductive paths. Dubois et al. (94) used fillers with different surface properties in the preparation of polyethylene composites by *in situ* polymerization. Acidic surface (kaolin, glass beads, silica), basic surface (magnesium hydroxide, wollastonite), graphite, and nickel particles were studied. The encapsulation of the filler particles resulted in good dispersity, which was promotive of the tensile and impact properties of the composites, especially as compared with composites prepared by melt compounding. In polyethylene/graphite composites the deagglomeration of the filler particles considerably increased the percolation threshold (98). Propylene has also been polymerized *in situ* onto carbon fillers: carbon black, carbon nanofiber, and multiwalled carbon nanotubes (100). Polypropylene nanocomposites with homogeneous filler distribution at low filler loadings were achieved by sonication of the fillers before polymerization. Thermal degradation of the polypropylene matrix shifted to higher temperatures, and carbon nanofillers were shown to act as nucleating agents.

Dispersing nanofillers with layered structure requires exfoliation or at least intercalation of the layers to obtain desired properties in the nanocomposite. In melt compounding the matrix polymer needs to be intercalated between the layers, which can be achieved with polar polymers such as polyamides. In the case of polyolefins a third component, such as maleic anhydride grafted polyolefin, needs to be added to improve polyolefin–filler interactions (101,102). In *in situ* polymerization the monomer diffuses into the interlayer spacing and intercalates more easily than the respective polymer. Once there, together with the active species of the catalyst, it is polymerized to create polyolefin chains within the interlayers.

The preparation of polyolefin nanocomposites of layered silicates by *in situ* polymerization with metallocene catalyst was first studied by Tudor et al. (103). Metallocene catalyst, dicyclopentadienyl zirconium dichloride, was intercalated into clay interlayer galleries by ion exchange of the interlamellar cations. In the presence of methylaluminoxane (MAO), propylene was polymerized into low molar mass atactic polypropylene. Bergman et al. (104) intercalated layered silicate with alkyl ammonium cations before adding late transition metal catalyst. *In situ* polymerization of ethylene led to exfoliated nanocomposite as shown by X-ray diffraction analysis and transmission electron microscopy. When MAO was allowed to react with organomodified layered silicate before the addition of metallocene catalyst and subsequent polymerization, polypropylene nanocomposites with layered silicate were obtained (105). The propagation of the polymerization further separated and dispersed the sheets.

Heinemann et al. (106) prepared nanocomposites by *in situ* polymerization and compared them with nanocomposites prepared by melt compounding. Ethylene was homo- and copolymerized with 1-octene using MAO activated rac-dimethylsilylene-bis(2-methyl-benzindenyl) zirconium dichloride in the presence of organomodified layered silicate. Improved dispersion of the nanocomposites prepared by *in situ* polymerization as compared with those prepared by melt compounding was clearly visible, as evidenced by larger interlayer spacings and by the formation of exfoliated anisotropic nanosilicates with high aspect ratio. Polyethylene nanocomposites have been successfully prepared from nonmodified layered silicate by *in situ* polymerization using constrained geometry catalyst by Dow Chemical Company (107). With a large amount of methylaluminoxane to impart sufficient activity to the catalyst, polyethylene nanocomposites with exfoliated structure were achieved. In the absence of a chain transfer agent, ultrahigh molar mass polyethylene with poor tensile properties was produced. Upon hydrogen addition, the molar masses decreased with simultaneous improvement in the tensile and the shear modulus.

Recently, polyethylene nanocomposites were prepared by *in situ* polymerization with functional monomer 10-undecen-1-ol (108). Layered silicate was first reacted with an aluminum compound through the hydroxyl groups in clay galleries. Undecenol was reacted with the aluminum compound through the hydroxyl groups to further enhance intercalation and the organophilic character of the inorganic clay. Then copolymerization of ethylene and the undecenol attached to the clay was performed with a late transition metal catalyst. The polymerization led to exfoliation of the layered silicate and to polyethylene chains chemically bonded to the silicate surface.

A similar procedure was used in the preparation of polyethylene/alumina nanocomposites (109,110). Alumina was treated with triisobutylaluminum and undecenol to create grafted vinyl groups on the surface of the nanoparticles

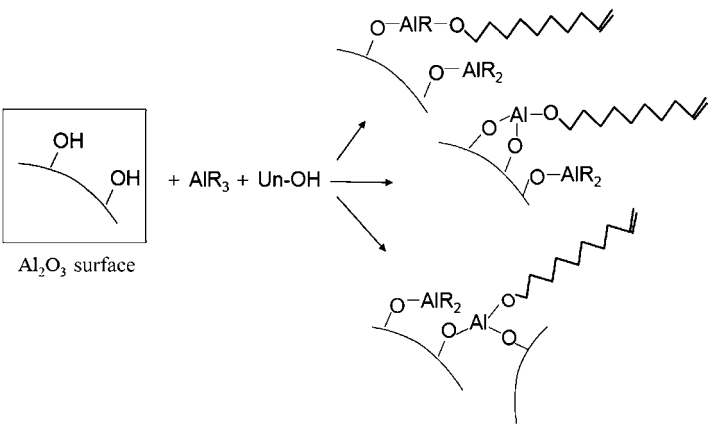

Figure 8.8 Model for modification of alumina surface with polar comonomers. (From Reference 109 with permission from Wiley-VCH Verlag GmbH & Co. KG and author.)

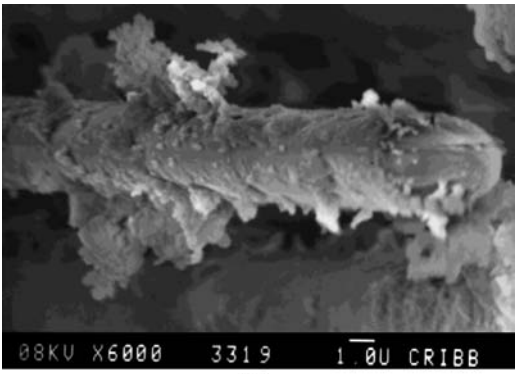

Figure 8.9 Scanning electron microscopy images of polypropylene/glass fiber composites with (**a**) 0.4 % and (**b**) 4% decenol concentration of the total olefin amount. (From Reference 111 with permission from John Wiley & Sons, Inc.)

(Fig. 8.8). The strong tendency of alumina nanoparticles to agglomerate was thereby diminished. The particles were then copolymerized with ethylene using a late transition metal catalyst to obtain a relatively uniform particle distribution inside the polyethylene matrix. Covalent bonding between the polyethylene and the alumina nanoparticles created a composite with good interaction between the matrix and the dispersed phase. Mechanical properties were improved relative to those of the homopolyethylene synthesized under the same conditions.

Copolymerization of propylene with 9-decen-1-ol covalently bonded to glass fiber surface has also been performed with metallocene catalyst using *in situ* polymerization (111). The glass fibers were allowed to react with MAO, further reacted with decenol, and then the decenol was copolymerized with propylene. Morphology studies showed that the polypropylene matrix was attached to the glass fiber surface, as depicted in Fig. 8.9. This structure remained after elimination of physically

bonded polypropylene by solvent extraction, which was an indication of chemical bonding between the matrix and the glass fiber. The result was the different morphologies of the grafted polypropylene—clusters or more uniform layer on the glass fiber—according to the use of low or high concentration of decenol. The composition of the composites was studied by energy disperse X-ray microanalysis and Fourier transform infrared spectroscopy, which gave further evidence of the chemical structure between the substances.

Polyhedral oligomeric silsesquioxane (POSS) nanoparticles have drawn attention because they are easier to disperse in a polyolefin matrix and have lower density and higher thermal stability than that of layered silicate nanofillers. In addition, POSS contains no trace metals and the interfacial properties are tailorable. Poorly controllable radical, condensation, and ring-opening polymerization techniques were employed until metallocene catalysts made it possible to copolymerize POSS macromolecules with olefins.

Polypropylene and polyethylene containing POSS nanoparticles have been synthesized with metallocene catalysts (112). Novel hybrid copolymers were obtained via direct polymerization in a wide range of POSS concentrations. In addition, the molar mass and distribution were controlled. Low loadings of POSS particles with propylene and ethylene copolymers improved thermal and tensile properties. The copolymers can be utilized in high temperature applications. However, the direct olefin polymerization in the presence of POSS is still in the developmental stage.

8.5 CONCLUSIONS

Polyolefins are major commodity thermoplastics, increasingly valued for their versatility, low cost, and relatively favorable environmental impact. Although basic grades of polyolefins are competitive with many other engineering plastics, they are characterized by poor adhesion, low stiffness, and high permeability. Functionalization of polyolefins and polyolefin blends and composites offer feasible approaches to overcoming these disadvantages.

Compatibilization is the key technology in the production of polyolefin blends and composites. Essential prerequisites for obtaining these materials are well-prepared dispersions, even down to nanoscale, and good interfacial adhesion. Compatibilization is based either on physical secondary interactions or on interfacial chemical bonding. In general, the controlled phase structures lead to favorable final material properties.

The activities and flexibility of metallocene catalyst systems offer enormous potential for the development of new polymer structures, which will extend the applications of polyolefins still further. Metallocene catalysts make available polyolefins containing functional groups that earlier were difficult or even impossible to prepare. The significance of these new compatibilizers in polyolefin composites has been demonstrated in the higher stiffness and the better barrier properties achieved for polyolefins.

Catalytic system attached to particle or fiber surfaces enables *in situ* production of polyolefin composites. This technology promises to be of increasing interest in the preparation of polyolefin nanocomposites containing well-dispersed and well-attached particles.

NOMENCLATURE

ATH	Aluminum trihydroxide
Cl	Chloro
MA	Maleic acid anhydride
MAO	Methylaluminoxane
MH	Magnesium hydroxide
NH_2	Amido
OH	Hydroxyl
PE	Polyethylene
PFT	Polymerization-filling technique
POSS	Polyhedral oligomeric silsesquioxane
PP	Polypropylene
PP-co-OH	Hydroxyl-functionalized propylene copolymer
PP-g-MA	Maleic anhydride grafted polypropylene

REFERENCES

1. H. F. Mark, N. M. Bikales, C. G. Overberger, and G. Menges (eds.), *Encyclopedia of Polymer Science and Engineering*, Vol. 6, Wiley, New York 1986, p. 383.
2. M. Buback, L. Wittkowski, S. A. Lehmann, and F. O. Mähling, *Macromol. Chem. Phys.*, **200**, 1935 (1999).
3. G. Moad, *Prog. Polym. Sci.*, **24**, 81 (1999).
4. S. B. Brown, in: *Reactive Extrusion: Principles and Practice*, M. Xanthos (ed.), Hanser, Munich, 1992, p. 75.
5. K. E. Russell, *Prog. Polym. Sci.*, **27**, 1007 (2002).
6. M. van Duin, *Macromol. Symp.*, **202**, 1 (2003).
7. P. Aaltonen and B. Löfgren, *Macromolecules*, **28**, 5353 (1995).
8. P. Aaltonen, G. Fink, B. Löfgren, and J. Seppälä, *Macromolecules*, **29**, 5255 (1996).
9. T. C. Chung and W. Janvikul, *J. Org. Chem.*, **581**, 176 (1999).
10. G. Xu and T. C. Chung, *J. Am. Chem. Soc.*, **121**, 6763 (1999).
11. G. Xu, J. Y. Dong, and T. C. Chung, *Polym. Prepr.*, **41**, 1926 (2000).
12. S. Marathe and S. Sivaram, *Macromolecules*, **27**, 1083 (1994).
13. M. Hackmann, T. Repo, G. Jang, and B. Rieger, *Macromol. Chem. Phys.*, **199**, 1511 (1998).
14. T. Uozumi, G. Tian, C.-H. Ahn, J. Jin, S. Tsubahi, T. Sano, and K. Soga, *J. Polym. Sci. A Polym. Chem.*, **38**, 1844 (2000).
15. M. Arnold, S. Bornemann, T. Schimmel, and T. Heinze, *Macromol. Symp.*, **181**, 5 (2002).
16. S. Lipponen and J. Seppälä, *J. Polym. Sci. A Polym. Chem.*, **40**, 1303 (2002).
17. S. Lipponen and J. Seppälä, *J. Polym. Sci. A Polym. Chem.*, **42**, 1461 (2004).

18. S. Lipponen and J. Seppälä, *J. Polym. Sci. A Polym. Chem.*, **43**, 5597 (2005).
19. H. L. Lu, S. Hong, and T. C. Chung, *Macromolecules*, **31**, 2028 (1998).
20. T. C. Chung and J. Y. Dong, *Macromolecules*, **35**, 2868 (2002).
21. J. Y. Dong, H. Hong, and T. C. Chung, *Macromolecules*, **36**, 6000 (2003).
22. H. Sinn, W. Kaminsky, H.-J. Vollmer, and R. Woldt, *Angew. Chem.*, **92**, 396 (1980).
23. W. Kaminsky, in: *Transition Metal Catalyzed Polymerizations—Alkenes and Dienes*, R. P. Quirk (ed.), Vol. 4, Harwood, New York, 1983, p. 225.
24. R. Mülhaupt, *Nachr. Chem. Technol. Lab.*, **41**, 1341 (1993).
25. P. Silverberg, *Chem.Eng.*, **104**, 37 (1997).
26. W. Kaminsky, *Macromol. Symp.*, **134**, 63 (1998).
27. W. Kaminsky, *Pure Appl. Chem.*, **70**, 1229 (1998).
28. W. Kaminsky, *J. Chem. Soc., Dalton Trans.*, 1413 (1998).
29. M. Bochmann, G. J. Pindado, and S. J. Lancaster, *J. Mol. Catal. A Chem.*, **146**, 179 (1999).
30. M. Bochmann, *Top. Catal.*, **7**, 9 (1999).
31. K. B. Sinclair, *Pop. Plast. Packg.*, **42**, 58 (1997).
32. N. Kashiwa and T. Shinozaki, *Plast. Eng.*, **40**, 273 (1997).
33. J. A. Ewen, *Stud. Surf. Sci. Catal.*, **25**, 271 (1986).
34. J. A. Ewen, *J. Mol. Catal. A Chem.*, **128**, 103 (1998).
35. J. A. Ewen, *Sci. Am.*, **276**, 86 (1997).
36. M. Hackmann and B. Rieger, *CATTECH*, **1**, 79 (1997).
37. H.-H. Brintzinger, D. Fisher, R. Mülhaupt, B. Rieger, and R. M. Waymouth, *Angew. Chem. Int. Ed. Engl.*, **34**, 1143 (1995).
38. W. Kaminsky, *Rapra Rev. Rep.*, **10**, 1 (1999).
39. B. Löfgren, E. Kokko, and J. Seppälä, *Adv. Polym. Sci.*, **169**, 1 (2004).
40. P. Aaltonen and B. Löfgren, *Eur. Polym. J.*, **33**, 1187 (1997).
41. L. Ahjopalo, B. Löfgren, K. Hakala, and L.-O. Pietilä, *Eur. Polym. J.*, **35**, 1519 (1999).
42. K. Hakala, B. Löfgren, and T. Helaja, *Eur. Polym. J.*, **34**, 1093 (1998).
43. B. Löfgren and J. Seppälä, in: *Metallocene-based Polyolefins: Preparation, Properties, and Technology*, Vol. 2, J. Scheirs and W. Kaminsky (eds.), Wiley, Chichester, 2000, p.143.
44. K. Hakala, T. Helaja, and B. Löfgren, *J. Polym. Sci. A Polym. Chem.*, **38**, 1966 (2000).
45. K. Hakala, T. Helaja, and B. Löfgren, *Polym. Bull.*, **46**, 123 (2001).
46. S. Paavola, R. Uotila, B. Löfgren, and J. Seppälä, *React. Funct. Polym.*, **61**, 53 (2004).
47. S. Paavola, B. Löfgren, and J. Seppälä, *Eur. Polym. J.*, **41**, 2861 (2005).
48. M. R. Kesti, G. W. Coates, and R. M. Waymouth, *J. Am. Chem. Soc.*, **114**, 9679 (1992).
49. M. J. Schneider, R. Schäfer, and R. Mülhaupt, *Polymer*, **38**, 2455 (1997).
50. R. Goretzki and G. Fink, *Macromol. Rapid Commun.*, **19**, 511 (1998).
51. R. Goretzki and G. Fink, *Macromol. Chem. Phys.*, **200**, 881 (1999).
52. K. Radhakrishnan and S. Sivaram, *Macromol. Rapid Commun.*, **19**, 581 (1998).
53. M. M. Marques, S. G. Correia, J. R. Ascenso, A. F. G. Ribeiro, P. T. Gomes, A. R. Dias, P. Foster, M. D. Rausch, and J. C. W. Chien, *J. Polym. Sci. A Polym. Chem.*, **37**, 2457 (1999).
54. H. Hagihara, K. Tsuchihara, K. Takeuchi, M. Murata, H. Ozaki, and T. Shiono, *J. Polym. Sci. A Polym. Chem.*, **42**, 52 (2004).
55. J. Imuta, Y. Toda, and N. Kashiwa, *Chem. Lett.*, **30**, 710 (2001).
56. S. Ramakrishnan, E. Berluche, and T. C. Chung, *Macromolecules*, **23**, 378 (1990).
57. T. C. Chung and D. Rhubright, *Macromolecules*, **24**, 970 (1991).
58. T. C. Chung and D. Rhubright, *Macromolecules*, **26**, 3019 (1993).

59. K. Radhakrishnan and S. Sivaram, *Macromol. Chem. Phys.*, **200**, 858 (1999).
60. S. Marathe and S. Sivaram, *Macromolecules*, **27**, 1083 (1994).
61. T. C. Chung, H. L. Lu, and C. L. Li, *Macromolecules*, **27**, 7533 (1994).
62. R. Mühlhaupt, T. Duschek, and B. Rieger, *Macromol. Chem., Macromol. Symp.*, **48–49**, 317 (1991).
63. T. C. Chung, G. Xu, Y. Lu, and Y. Hu, *Macromolecules*, **34**, 8040 (2001).
64. T. C. Chung, *J. Organomet. Chem.*, **690**, 6292 (2005).
65. J.-Y. Dong and Y. Hu, *Coord. Chem. Rev.*, **250**, 47 (2006).
66. T. C. Chung, *Prog. Polym. Sci.*, **27**, 39 (2002).
67. S. D. Ittel, L. K. Johnson, and M. Brookhart, *Chem. Rev.*, **100**, 1169 (2000).
68. G. Pritchard, Additives are essential, in: *Plastics Additives: An A–Z Reference*, G. Pritchard (ed.), Chapman & Hall, London, 1998.
69. M. Alexandre and P. Dubois, *Mater. Sci. Eng.*, **28**, 1 (2000).
70. M. Gilbert, Surface Treatment for Particulate Fillers in Plastics, in: *Plastics Additives: An A–Z Reference*, G. Pritchard (ed.), Chapman & Hall, London, 1998.
71. G. Wypych, *Handbook of Fillers*, ChemTec Publishing, Toronto, 1999.
72. R. N. Rothon, Surface Modification and Surface Modifiers, in: *Particulate-Filled Polymer Composites*, R. N. Rothon (ed.), Rapra Technology Ltd., Shrewsbury, UK, 2003.
73. P. R. Hornsby and C. L. Watson, *J. Mater. Sci.*, **30**, 5347 (1995).
74. K. Hausmann and V. Flaris, *Polym. Polym. Compos.*, **5**, 113 (1997).
75. F. Rahma and S. Fellahi, *Polym. Compos.*, **21**, 175 (2000).
76. J. Jancar and J. Kucera, *Polym. Eng. Sci.*, **30**, 714 (1990).
77. L. H. Sperling, *Polymeric Multicomponent Materials*, Wiley, New York, 1997.
78. W. Chinsirikul, T. C, Chung, and I. R. Harrison, *J. Thermoplast. Compos. Mater.*, **6**, 18 (1993).
79. S. H. Lee, C. L. Li, and T. C. Chung, *Polymer*, **35**, 2980 (1994).
80. J. Imuta, N. Kashiwa, S. Ota, S. Moriya, T. Nobori, and K. Mizutani, EP 1186619 (2002).
81. U. Hippi, J. Mattila, M. Korhonen, and J. Seppälä, *Polymer*, **44**, 1193 (2003).
82. R. Uotila, U. Hippi, S. Paavola, and J. Seppälä, *Polymer*, **46**, 7923 (2005).
83. P. Reichert, H. Nizt, S. Klinke, R. Brandsch, R. Thomann, and R. Mülhaupt, *Macromol. Mater. Eng.*, **277**, 8 (2000).
84. K.-N. Kim, H. Kim, and J.-W. Lee, *Polym. Eng. Sci.*, **41**, 1963 (2001).
85. M. Kato, A. Usuki, and A. Okada, *J. Appl. Polym. Sci.*, **66**, 1781 (1997).
86. N. Ristolainen, U. Vainio, S. Paavola, M. Torkkeli, R. Serimaa, and J. Seppälä, *J. Polym. Sci. B Polym. Phys.*, **43**, 1892 (2005).
87. K. Motha, U. Hippi, K. Hakala, M. Peltonen, V. Ojanperä, B. Löfgren, and J. Seppälä, *J. Appl. Polym. Sci.*, **94**, 1094 (2004).
88. N. Ristolainen, U. Hippi, J. Seppälä, A. Nykänen, and J. Ruokolainen, *Polym. Eng. Sci.*, **45**, 1568 (2005).
89. R. N. Rothon, Effects of Particulate Fillers on Flame Retardant Properties of Composites, in: *Particulate-Filled Polymer Composites*, R. N. Rothon (ed.), Rapra Technology Ltd., Shrewsbury, UK, 2003.
90. H. G. Jeon, H.-T. Jung, S. W. Lee, and S. D. Hudson, *Polym. Bull.*, **41**, 107 (1998).
91. L. Wei, T. Tang, and B. Huang, *J. Polym. Sci. A Polym. Chem.*, **42**, 941 (2004).
92. T. F. McKenna, J. B. P. Soares, and L. C. Simon, *Macromol. Mater. Eng.*, **290**, 507 (2005).
93. P. Dubois, M. Alexandre, F. Hindryckx, and R. Jerome, *J. Macromol. Sci. Rev. Macromol. Chem. Phys.*, **C38**, 511 (1998).
94. P. Dubois, M. Alexandre, and R. Jerome, *Macromol. Symp.*, **194**, 13 (2003).

95. W. Kaminsky, J. Dutschke, H. Maedler, M. Miri, and M. Schlobohm, DE 3240382 (1984).
96. W. Kaminsky and H. Zielonka, *Polym. Adv. Technol.*, **4**, 415 (1992).
97. M. Alexandre, E. Martin, P. Dubois, M. Garcia-Marti, and R. Jerome, *Macromol. Rapid Commun.*, **21**, 931 (2000).
98. M. Alexandre, M. Pluta, P. Dubois, and R. Jerome, *Macromol. Chem. Phys.*, **202**, 2239 (2001).
99. M. Pluta, M. Alexandre, S. Blacher, P. Dubois, and R. Jerome, *Polymer*, **42**, 9293 (2001).
100. K. Wiemann, W. Kaminsky, F. H. Gojny, and K. Schulte, *Macromol. Chem. Phys.*, **206**, 1472 (2005).
101. M. Kawasumi, N. Hasegawa, M. Kato, A. Usuki, and A. Okada, *Macromolecules*, **30**, 6333 (1997).
102. N. Hasegawa, M. Kawasumi, M. Kato, A. Usuki, and A. Okada, *J. Appl. Polym. Sci.*, **67**, 87 (1998).
103. J. Tudor, L. Willington, D. O'Hare, and B. Royan, *Chem. Commun.*, 2031 (1996).
104. J. S. Bergman, H. Chen, E. P. Giannelis, M. G. Thomas, and G. W. Coates, *Chem. Commun.*, 2179 (1999).
105. J.-M. Hwu and G.-J. Jiang, *J. Appl. Polym. Sci.*, **95**, 1228 (2005).
106. J. Heinemann, P. Reichert, R. Thomann, and R. Mülhaupt, *Macromol. Rapid Commun.*, **20**, 423 (1999).
107. M. Alexandre, P. Dubois, T. Sao, J.M. Garces, and R. Jerome, *Polymer*, **43**, 2123 (2002).
108. S.-Y. A. Shin, L. C. Simon, J. B. P. Soares, and G. Scholz, *Polymer*, **44**, 5317 (2003).
109. J. X. Zhang and L. C. Simon, *Polym. Mat. Sci. Eng.*, **91**, 705 (2004).
110. X. Zhang and L. C. Simon, *Macromol. Mater. Eng.*, **290**, 573 (2005).
111. S. E. Barbosa, M. L. Ferreira, D. E. Damiani, and N. J. Capiati, *J. Appl. Polym. Sci.*, **81**, 1266 (2001).
112. L. Zhen, R. J. Farris, and W. B. Coughlin, *Macromolecules*, **34**, 8034 (2001).

Chapter 9

Polyethylene/Layered Silicate Nanocomposites: Preparation and Properties

Yuan Hu,[1] Hongdian Lu,[1,2] and Lei Song[1]

9.1 INTRODUCTION

Polymer/layered silicate nanocomposites (PLSNs) are nanoscale organic–inorganic hybrid materials, in which the inclusions have at least one dimension smaller than 100 nm. The layered silicate frequently used for the preparation of PLSN is the smectite group mineral such as montmorillonite (MMT), which belongs to the general family of 2:1 phyllosilicates. Their crystal lattice consists of 1-nm thin layers, with a central octahedral sheet of either aluminum or magnesium hydroxide fused between two silica tetrahedral sheets. Isomorphic substitution within the layers (e.g., Al^{3+} replaced by Mg^{2+} or Fe^{2+}) generates negative charges, defined through the cationic exchange capacity (CEC), which are counterbalanced by alkali or alkaline earth cations situated between the layers. Stacking of these layers leads to regular Van der Waals gaps in a parallel fashion called interlayers or galleries.

Since the Toyota group developed a nylon 6/montmorillonite nanocomposite with excellent mechanical properties, there has been considerable academic, government, and industrial interests in the investigation on various polymer system based nanocomposites (1–3) because these PLSNs exhibit markedly improved mechanical performance, higher thermal stability, improved flame retardancy, and decreased gas

[1]State Key Laboratory of Fire Science, University of Science and Technology of China, Hefei, Anhui 230026, China
[2]Department of Chemical and Material Engineering, Hefei University, Hefei, Anhui 230022, China

Polyolefin Composites, Edited by Domasius Nwabunma and Thein Kyu

permeability even with low loadings of layered silicates ($\leq 5\%$) when compared to neat polymers or conventional micro- and macrocomposites (4–19).

Polyolefins, such as polyethylene (PE), polypropylene (PP), and ethylene propylene diene methylene rubber (EPDM), defined as polymers constituted of alkene-1 or α-olefins, are the most widely used group of thermoplastic polymers. For the past decades, as one of the most widely used polyolefins, PE nanocomposites containing layered silicates have emerged due to their promising enhanced performances in transportation, wire and cable, food packaging, and building industries.

In this chapter, recent developments in syntheses, properties, crystallization, and rheology behaviors of polyethylene/layered silicate nanocomposites are reviewed, with an aim to deepen the understanding of their structure–property relationships.

9.2 PREPARATION STRATEGIES AND MORPHOLOGICAL STUDY

In general, PLSNs can be classed into two types: (a) intercalated nanocomposites, which correspond to well-ordered multilayered structures where the polymer chains are inserted into the spacing between the silicate layers, and (b) exfoliated nanocomposites, for which the individual silicate layers are separated within the polymer matrix and are no longer close enough to interact with the gallery cations. These two classes of the structure of polymer/layered silicate nanocomposites can be characterized by X-ray diffraction (XRD) and transmission electron microscopy (TEM). XRD is the most straightforward way to evaluate the spacing between the silicate layers, reflecting the relationship of the clay layers with themselves. However, one should be careful with the interpretation of the XRD results, because it can only detect the periodically stacked silicate layers, not reveal how well dispersed the clay is throughout the polymer. TEM is therefore a necessary complement for evaluating nanocomposite structure, since it allows a qualitative understanding of the internal structure, spatial distribution of the various phases, and observations of the defect structure through direct visualization.

Intercalation of polymer chains into silicate galleries has been verified to be a successful method to prepare intercalated or exfoliated PLSNs. Four main approaches have been developed to prepare PLSN: exfoliation–adsorption, *in situ* intercalative polymerization, melt intercalation, and template synthesis.

PLSNs have been obtained successfully through these strategies in a large variety of polymer systems with layered silicates. However, synthesis of polyethylene/layered silicate nanocomposites remains a scientific challenge because of the weak interaction between nonpolar polyethylene chains and hydrophilic clay surfaces. Two methods are most commonly used to synthesize polyethylene/layered silicate nanocomposites according to the starting components and processing techniques: melt intercalation method and *in situ* intercalative polymerization. In the following sections, an overview of the advances that have been made in the intercalation and the exfoliation of layered silicates in polyethylene matrix are given.

9.2.1 Melt Intercalation

The melt intercalation technique first reported by Vaia et al. in 1993 has been widely used to prepare PLSNs, since this method makes an environment-friendly and economically viable alternative for application in industry (20). During melt process, the layered silicate and polymer matrix are mixed in the molten state, the polymer then crawls into the interlayer space and forms either an intercalated or an exfoliated nanocomposite. Furthermore, in 1997, Vaia and Giannelis developed a mean-field statistical lattice model to understand the thermodynamic issue associated with the contributions of entropic and energetic factors to the free energy of the system on polymer/layered silicate formation (21,22). In general, although there is a decrease in the conformational entropy of the polymer chains during the intercalation, this process is allowed because entropy loss can be compensated by enthalpic interactions between the polymer matrix and the silicates. From the model, the authors pointed out that the formation of nanocomposites via melt intercalation primarily depended on the surface energies of the polymer and silicates.

A wide range of polar thermoplastics, such as polyimide, poly(methyl methacrylate), poly(butylenes terephthalate), and poly(ethylene-*co*-vinyl acetate) (EVA), have been successfully prepared by this method; however, polyethylene has so far only been successfully intercalated to a limited extent since it has no polar groups in the chain (23–26).

It is impossible to directly intercalate polyethylene chains into silicate galleries. During fabrication of polyethylene/layered silicate nanocomposites, the layered silicates must exchange with organic ions to render their hydrophilic surface compatible with the hydrophobic polyethylene and facilitate the intercalation. Osman et al. reported the influence of several organically modified montmorillonites (OMT), which were prepared from the Na^+-montmorillonite with different CEC exchanged with alkyl ammonium ions where 1-4 octadecyl chains were attached to the nitrogen atom, with different interlayer *d*-spacing from 1.8 to 4.0 nm on the morphology of high density polyethylene (HDPE) nanocomposites (27,28). The XRD patterns and TEM observations collectively revealed that complete exfoliated nanostructure was not achieved, regardless of the chemical structure of the organic monolayer.

To further enhance the interfacial strength between polyethylene and OMTs, a third component, such as functionalized polymer and polar polymer is usually used as compatibilizing agent. Typically, maleic anhydride (MAH) grafted polyolefin has been used as polymer matrix to combine with OMT to understand the intercalation mechanism. For example, Hasegawa et al. reported the preparation of polyolefin–clay nanocomposites based on MAH-modified polyolefins (PE and PP) with OMT (29,30).

It was found that when polyolefins and OMT were blend without MAH-modified polyolefins, no increase in the *d*-spacing of OMT was observed, but when using MAH-modified polyolefins and OMT, the exfoliated nanocomposites were obtained. Therefore, the authors suggested that the driving force of the MAH-modified polyolefins intercalation originated from the strong hydrogen bonding between MAH groups and the polar layered silicate surfaces. In the dispersion process of the silicate

in MAH-modified polyolefins it is believed that the modified polyolefins are first intercalated into the organophilic silicate during melt blending to increase the interlayer spacing of the silicate while the interaction of the layers is weakened, then the layered structures of the intercalation compound are disordered by shear force during the kneading, and the silicate layers are finally exfoliated into the polyolefin matrix.

For the case of polyethylene system, Wang et al. prepared MAH-grafted linear low density polyethylene (LLDPE-g-MAH)/OMT nanocomposites. It was found that the generation of intercalated and exfoliated nanostructure increased the hydrophilicity of LLDPE-g-MAH and the chain length of organic modifier in the clay (19). Zhang and Wilkie studied the low density polyethylene (LDPE)/OMT nanocomposites with and without PE-g-MAH as a compatibilizer. XRD patterns and TEM studies revealed that all hybrids had a mixed immiscible–intercalated structure and there was better intercalation when PE-g-MAH was combined with LDPE (31). Zanetti and Costa prepared the LDPE/layered silicate nanocomposites in the presence of EVA; the resulting XRD patterns and TEM images indicated the effectiveness of EVA as a compatibilizer to facilitate the formation of intercalated nanocomposites (32).

According to the Vaia study, the interaction between polymer and layered silicate determined the formation of PLSNs. Furthermore, the interaction between silicate layers also influences the morphology of PLSNs. Koo et al. reported in detail the morphological evolution of PE-g-MAH/clay nanocomposites with 6, 18, 24, and 36 vol% OMT concentration (33). The TEM images confirmed that the final morphology of the nanocomposites evolved with increasing OLS content via four stages: disordered exfoliation, ordered exfoliation, dual morphologies of intercalation, and exfoliation and intercalation in sequence with the content of silicate. On the basis of the results, the authors deduced that the relative magnitude of these competing processes between the steric interaction of anisotropic silicate plates and the interaction between silicate plate and polymer chains were crucial for the morphological evolution of the nanocomposite. Particularly, when the distance between silicate layers was smaller than a certain value, the interaction between layers would get dominant, which then resulted in the transition from exfoliation to intercalation of nanocomposites.

Intercalated HDPE/OMT nanocomposite has been obtained successfully via a novel compounding process, namely, ''one-step'' melt intercalation, which directly starts from Na^+-montmorillonite by a melt intercalation technique, using hexadecyl trimethyl ammonium bromide as a reactive compatibilizer (34). XRD patterns and TEM observations clearly indicates the intercalation of montmorillonite layers in polymer matrix. It is postulated that the intercalation mechanism of this technique involves static adsorption of surfactant on the layers of clay and the resultant expansion of interlayer distance.

9.2.2 *In situ* Polymerization Method

Although intercalation of polyolefin into multilayered silicates via melt intercalation technique has been widely used, *in situ* polymerization approach, in which the

layered silicate is swollen within the liquid monomer or a monomer solution and polymerization takes place in the galleries, holds high promise for synthesis of polyolefin/clay nanocomposites. This is because by controlling the polymerization conditions, both intercalated nanocomposites with few polymers outside the clay layers and fully exfoliated nanocomposites can be achieved, which provide perfect models for the investigation of structure and properties of two different types of PLSNs.

In situ polymerization was the first method developed to synthesize polyamide 6/layered silicate nanocomposite by the Toyota research group (35). It was reported that the high surface energy of Na^+-MMT modified with ω amino acids (COOH–$(CH_2)_{n-1}$–NH_2^+, with $n = 2$, 3, 4, 5, 6, 8, 11, 12, 18) attracts the ε-caprolactam monomer molecules to diffuse between the interlayer, then swell the clay at 100°C, and subsequently initiate its ring opening polymerization to obtain nylon 6/clay nanocomposite.

Polyolefins do not include any polar groups in their backbone; it is therefore difficult to overcome the problem associated with poor phase adhesion in polyolefin/clay systems. A mended approach by the intercalation of an initiator or catalyst into a silicate has been widely used in *in situ* polymerization to facilitate the formation of nanostructure because it can eliminate both entropic and enthalpic barriers associated with intercalating polar silicates with nonpolar polyolefins.

In a typical synthesis, Tudor et al. first used the *in situ* intercalative polymerization method for the preparation of PP/clay nanocomposites (36). They demonstrated the ability of soluble metallocene catalysts to intercalate inside silicate layers and to promote the coordination polymerization of propylene. Accordingly, a synthetic hectorite was first treated with methylaluminoxane (MAO) to remove the acidic protons and to prepare the interlayer spacing for receiving the transition metal catalyst. It should be noted that MAO is commonly used in association with metallocenes to produce coordination catalysts active in olefin polymerizations. During this first treatment step, WAXD analysis showed no noticeable increase in the layer spacing, although the diffraction peak broadened slightly, but the increase in Al content and complete disappearance of Si–OH signals from IR spectra agree with MAO reaction/adsorption inside the layered silicate galleries. Upon the addition of the metallocene catalyst ($[Zr(h\text{-}C_5H_5)Me(THF)]^+$), a cation exchange reaction occurred between the Na^+ in the MAO-treated hectorite and the metallocene catalyst, as demonstrated by an increase of 0.47 nm in the interlayer spacing, consistent with the size of the species.

For the synthesis of polyethylene/clay nanocomposites, Kuo et al. developed three different routes of *in situ* blends of metallocene polyethylene (m-PE) with cetyl pyridinium chloride (CPC) pretreated MMT (CPC-MMT), the ansa-metallocence catalyst $Et(Indenyl)_2ZrCl_2$, and the MAO cocatalyst (37). In Route 1, the CPC-MMT was mixed directly with the ethylene monomer, catalyst, and MAO to begin the polymerization at room temperature. In Route 2, the CPC-MMT was mixed initially with the MAO at 30°C for 1.5 h and then mixed with the metallocene catalyst at 55°C for another 0.5 h; the catalyst/clay mixture was then mixed with ethylene monomer to begin the polymerization for 1 h under ambient conditions. In Route 3, the

CPC-MMT was first mixed and agitated with MAO at 30°C for 2.5 h, and then mixed with the metallocene catalyst at 55°C for another 2 h; the catalyst–clay mixture was then mixed with ethylene to begin the polymerization for 1 h under ambient condition. XRD patterns and TEM image suggested that the MMT has been exfoliated in m-PE when the pretreated MMT content was less than 10 wt%, whereas intercalated structure was formed when MMT content was greater than 10 wt%. The polymerization activity using the different polymerization Routes 1–3 has also been compared and found that the polymerization activity can be improved substantially through sequential addition of the clay, MAO, the metallocene catalyst, and the ethylene monomer, as well as by changes in the reaction temperature and the amount of MAO.

An exfoliated polyethylene/clay nanocomposite has been synthesized successfully when an organically modified fluorohectorite intercalated by a well-defined cationic palladium complex was exposed to ethylene gas via an *in situ* ''ship-in-the-bottle'' polymerization approach (38). The authors employed Brookhart's single-component palladium-based complex {**1**;[{2,6-$Pr^i_2C_6H_3N{=}C(Me)C{-}(Me){=}NC_6H_3$ Pr^i_2-2.6}$Pd(CH_2)_3CO_2Me$][$B(C_6H_3(CF_3)_2$-3,5)$_4$]} as the polymerization catalyst and the well-studied synthetic silicate fluorohectorite (**2**) as the inorganic component, respectively. They first prepared the modified fluorohectorite (Pd-2) by the intercalation of the catalyst into the galleries of 1-tetra-decylammonium modified fluorohectorite (C_{14}N-2), and then the dry Pd-2 was exposed to ethylene gas. Over a 2-h period, they observed monomer consumption and a dramatic increase in the size of the silicate-catalyst composite. After 12 h, the Pd-2 material could not be seen; in the place of a small amount of orange, Pd-2 powder was a large mass of colorless, rubbery polymer. Analysis of the toluene-extracted polyethylene by gel-permeation chromatography (GPC) revealed a high molecular weight polymer. Although the catalytic activity was quite low, the XRD pattern of the polyethylene composite formed after 24 h demonstrated the complete absence of diffraction peak, suggesting the formation of an exfoliated polymer nanocomposite.

Recently, Wei et al. developed a new approach to prepare *in situ* polymerized nanocomposites by a simple supporting method to immobilize a common zirconocene on the surface of montmorillonite/silica hybrid (MT-Si) (39). First, MT-Si was prepared by depositing silica nanoparticles between galleries of the MT; then a common zirconocene catalyst [bis(cyclopentadienyl)zirconium dichloride/methylaluminoxane] was fixed on the MT-Si surface, forming supported catalysts (MT-Si-Cat) by a simple method. Finally, the ethylene polymerization was initiated with MT-Si-Cat, and the nanocomposite with two classes of nanofillers (clay layers and silica nanoparticles) dispersed concurrently in the polymer matrix was obtained. This approach allowed for the exfoliation and good dispersion of the clay layers and silica nanoparticles among the PE matrix.

Polyethylene/clay nanocomposites have also been prepared by the so-called polymerization-filling technique (PFT) (17). This method consists in anchoring, in the first step, a Ziegler–Natta type catalyst or any other coordination catalysts, which include MAO activated metallocenes, onto a filler surface, and then *in situ* polymerizing ethylene directly from the surface-treated fillers. The hydrogen, which acts as transfer agent, has a key role in determining the molecular weight of the resulting

polymer. In the absence of a chain transfer agent, ultra high molecular weight (HMW) polyethylene was produced. Upon hydrogen addition, the molecular weight of the polyethylene was decreased. XRD patterns and TEM observations confirmed the formation of exfoliated nanostructure.

9.3 PROPERTIES OF POLYETHYLENE/LAYERED SILICATE NANOCOMPOSITES

The silicate layers dispersed in PLSNs offer a combination of high aspect ratio and large surface area, which have consequences for the hybrid properties. It is believed that the synergistic effects of nanoscale structure and strong interfacial interaction between the polymer matrix and silicate layers impart the PLSN superior properties.

9.3.1 Tensile Properties

The tensile properties of polyethylene have been found to be improved when nanocomposites are formed with silicates, particularly the tensile modulus. Gopakumar et al. reported that Young's modulus of the exfoliated PE-g-MAH/1.44PA nanocomposites increased as clay content increased from 5% to 10%, while the tensile stress at yield exhibited only a marginal increase (18). The authors suggested that the variations in the mechanical properties are influenced by not only the extent of silicate content but also the crystallinity of the polymer matrix. Further, study on the crystallization behavior confirmed that the high interfacial adhesion between PE-g-MAH and clay decreased the mobility of crystallizable chains, leading to reduced crystallinity, which counteracted the reinforcement potential of intercalated and/or exfoliated clay in polymer.

Several studies reported the mechanical properties of polyethylene/clay nanocomposites as a function of clay content and PE-g-MAH compatibilizer (40–43). In the case of LLDPE/PE-g-MAH/clay nanocomposites prepared by melt intercalation using a Haake corotatin twin-screw extruder at the 200°C, the influence of two types of organoclay, one having two alkyl tails $M_2(HT)_2$ and the other having one alkyl tail $M_3(HT)_1$, on the improvement of the mechanical properties of the nanocomposites has been investigated by Hotta and Paul (40). The increase in tensile modulus with addition of organoclay is much higher for $M_2(HT)_2$ than for $M_3(HT)_1$, since the former increases the LLDPE modulus by threefold whereas the latter increases it by 1.75-fold with the filler loadings located in the range of 6.5–6.9%, when the weight ratio of LLDPE-g-MAH/organoclay is fixed as 1. According to the present authors, this behavior is due to the better dispersion of $M_2(HT)_2$ within the matrix than that of $M_3(HT)_1$. The evolution of the tensile modulus and strength for the LLDPE with different content of LLDPE-g-MAH is also studied. There seemed to be no advantage of adding LLDPE-g-MAH for building modulus or strength at low filler content, while there is a clear advantage at higher filler contents. However, in PE/layered silicate nanocomposites, there is a decrease in strength for organoclay content beyond 2.5% in the absence of LLDPE-g-MAH. Therefore, the authors deduced that these characteristics reflect that the LLDPE-g-MAH promote adhesion to the clay particles.

Table 9.1 Tensile Properties of HDPE-Based Nanocomposites Prepared by Polymerization-Filling Technique.

Sample	Filler (loading), wt%	Strain at yield, %	Stress at yield, MPa	Strain at break, %	Stress at break, MPa	Young's modulus, GPa
LD1	0′	~6.0	23.0 ± 1.0	244 ± 13	25.2 ± 1.1	0.69 ± 0.05
LD2	k (2.3)	None	None	225 ± 17	36.6 ± 2.1	0.60 ± 0.01
LD3	h (4.2)	None	None	132 ± 5	28.1 ± 1.3	0.35 ± 0.01
LD4	m (3.3)	None	None	147 ± 8	30.4 ± 1.3	0.72 ± 0.08
LD5	h (3.8)	None	None	205 ± 32	34.8 ± 2.5	0.64 ± 0.10
LD6	h (4.0)	None	None	230 ± 10	39.7 ± 0.7	0.63 ± 0.05
LD7	m (3.9)	None	None	145 ± 37	29.8 ± 0.2	0.66 ± 0.10
LD8	m (4.1)	None	None	178 ± 13	32.0 ± 0.5	0.59 ± 0.03
LD9[a]	h (3.4)	~6.5	27.4 ± 0.4	467 ± 47	27.9 ± 2.4	1.28 ± 0.01
LD9[a,b]	h (3.4)	~6.5	26.4 ± 0.4	458 ± 33	29.7 ± 1.0	0.89 ± 0.13
LD10[a]	h (4.5)	~7.8	26.8 ± 0.3	228 ± 13	25.7 ± 0.9	1.11 ± 0.02
LD10[a,c]	h (4.5)	~7.4	27.1 ± 0.5	373 ± 2	33.2 ± 0.5	1.28 ± 0.18
LD12	h (13.0)	Cannot be shaped				
LD13	h (11.4)	none	none	3.1 ± 0.9	34.2 ± 2.2	2.48 ± 0.24

h = hectorite, m = montmorillonite, k = kaolin. (From Reference 17 with permission from Elsevier.)

[a]Synthesized in the presence of hydrogen.

[b]Premelting at 190°C with a two-roll mill.

[c]Added with Irganox 1010.

Mechanical properties of HDPE/clay nanocomposites prepared by polymerization-filling technique have been investigated by Alexandre (17). The tensile properties of these nanocomposites summarized in Table 9.1 can be classified into two types depending on the addition or not of hydrogen as chain transfer agent. Tensile properties of the first group of samples, LD2–8, ultra-HMW polyethylenes obtained in the absence of hydrogen, were poor, indicating that they were essentially independent of the nature of the matrix but not of the nature and content of the clay. In contrast, addition of hydrogen decreased the molecular weight of PE (LD 9–13) and lead to nanocomposites with improved Young's and shear moduli and an improved strain behavior, reflecting the existence of a nanocomposite structure.

In Reference 39, high tensile modulus and tensile strength were observed for all PE nanocomposites with MT-Si-Cat, and the nanocomposite achieved the highest tensile modulus of 1665 MPa with the low nanofiller content (5.43 wt%). This helps the nanocomposites to compete with costly engineering resins, due to its lighter weight and easier processability than conventional microcomposites with high filler content.

The variation of the mechanical properties of HDPE/clay nanocomposites as a function of their *d*-spacing has been carried out by Osman et al. in Reference 28. The authors found that the large *d*-spacing led to decreased attraction between silicate layers and resulted in more exfoliated silicate layers, because of which the relative

elastic modulus of 2.8 vol% HDPE/clay nanocomposites steadily increased with augmenting *d*-spacing. Meanwhile, as the clay was not fully exfoliated, there was a principal drop in the stress at break followed by further small decrease with increasing *d*-spacing. On the contrary, the nanocomposites showed to be less ductile with increasing exfoliation, and it was evident that there was a monotonous increase in the yield stress and decrease in the stress at break. The authors suggested that the former was attributed to the weak attraction forces between the HDPE matrix and clay, while the decrease in the latter was caused by the local strain amplification in the polymer confined between the clay particles. Also, increased filler loading enhanced the elastic modulus but decreased all other tensile properties, and the tensile properties of the materials correlated to the volume fraction of the inorganic part of the clay and not to the total volume of the clay. It believed that the changes in the tensile properties are due to the presence of the inorganic inclusions, especially the highly anisotropic exfoliated silicate layers.

9.3.2 Dynamic Mechanical Analysis

Dynamic mechanical analysis (DMA) measures the response of a given material to an oscillatory deformation (usually tension or three-point flexion type deformation) as a function of temperature. DMA results are composed of three main parameters: the storage modulus (G'), corresponding to the elastic response to the deformation; the loss modulus (G''), corresponding to the plastic response to the deformation, and tan δ the ratio (G''/G'), useful for determining the occurrence of molecular mobility transitions, such as the glass transition temperature (T_g). In general, polyolefin nanocomposites often exhibit enhancement of the G' than polymer matrix. This is because when materials become soft above T_g, the reinforcement effect of the clay becomes prominent because the strong interfacial strength between polymer and clay surfaces restricts the movement of the polymer chains.

DMA has been used to study temperature dependence of the storage modulus of LDPE nanocomposites with different types of clay, crude Na^+-montmorillonite, dioctadecyldiethylammonium chloride modified montmorillonite (DOM), and trimethylchlorosilane modified montmorillonite (TMD), which were abbreviated as PE/MMT, PE/DOM, and PE/TMD, respectively (41). The measurements were carried out using a Perkin-Elmer DMA-7 with a vibration frequency of 1 Hz with temperature from −150 to 100°C in three-point bending mode. For the three hybrids of the same clay content of 5 wt%, the G' values increased in the order PE/TMD>PE/DOM>PE>PE/MMT. This behavior indicated that nanocomposites were more effective than conventional composites in reinforcement. On the contrary, the tan δ peaks, which represent the T_g, for the nanocomposites were shifted toward higher temperatures, showing that the temperatures were −129.3, −129.6, −126.1, and −125.3°C for PE, PE/MMT, PE/DOM, and PE/TMD, respectively. This confirmed that the polymer chains were confined by the addition of organoclays.

The temperature dependence of G' and tan δ of various polyethylene nanocomposites prepared by the polymerization-filling technique has been tested. The

exfoliated nanocomposite LD9 displayed higher G' than that of LD5 that consisted an ultra-HMW polyethylene matrix although its filler content was lower. The storage modulus dramatically increased as clay content was increased (LD10 and LD13), especially below approximately 80°C. Typical values of moduli at −50°C, thus in the plateau region between the γ and β transitions, are 0.83, 0.95, 1.26, and 2.05 GPa for LD5, LD9 and LD13, respectively. The large increase in moduli is a common characteristic feature of layered silicate based nanocomposites in which a small amount of layers having a high aspect ratio is enough to improve the mechanical properties remarkably. The nanocomposites showed three transition peaks in tan δ, observed at approximately −115, −25, and 70°C, which correspond to the γ, β, and α relaxations of polyethylene, respectively. The γ relaxation is commonly ascribed to the glass transition of the amorphous portion of polyethylene. The β relaxation is related to the glass–rubber transition of constrained noncrystalline chain segments, and the α process is related to the phenomena such as intracrystalline relaxation and sliding of tied chains within crystalline blocks. All these relaxations change with the filler content, suggesting that the nanoclay influences not only the properties of the amorphous polyethylene but also the crystalline regions. The small α transition observed for the LD5 sample can be directly related to the lower crystallinity.

9.3.3 Gas Barrier Properties

Incorporating layered silicate in polymeric matrix is found to substantially improve the permeation-barrier behavior since the silicate layers with high aspect ratio create a maze or ''tortuous path'' that retards the gas molecules to diffusion progress through the PLSNs. The advantage of the tortuous path in PLSNs was first reported by the Toyota research groups. It was found that their nylon 6/clay nanocomposite had a 40% reduction in the rate of water absorption when compared to the neat polymer (44). Later, they also reported that the gas permeability in rubber/clay nanocomposite was decreased by 30% at 4 vol% clay loading (45).

The oxygen gas permeability of HDPE/clay nanocomposites with montmorillonite having different surface coverage and alkyl chain packing density has been found to have decreased with increasing d-spacing and is in line with the assumption that the reinforcement is due to the presence of the inorganic inclusions (27). The nanocomposite formation leads to a lower oxygen permeability coefficient than pure HDPE (54 mm m^3 day^{-1} $mmHg^{-1}$), but varied slightly (the coefficients varied between 31 and 46 mm m^3 day^{-1} $mmHg^{-1}$) with different types of surface-treated clay at the same clay volume fraction. The benefit of the partial orientation of silicate layers to the decrease in permeation coefficient has been confirmed in the study. Similar behavior of the decreased nitrogen gas permeability in PE/clay nanocomposites using PE-g-MAH as compatibilizer has been observed (41). The gas permeability coefficient is found to have decreased by 30–40% as compared to polymer matrix.

9.3.4 Thermal Stability

The thermal stability of materials is often studied by thermogravimetric analysis (TGA), in which the mass loss caused by the volatilization of degradation products is monitored as a function of temperature. A nonoxidative degradation occurs when TGA processes in an inert gas flow, while oxidative degradation occurs in an air or oxygen atmosphere. Generally, the increase in thermal stability by the formation of nanocomposites is attributed to the labyrinth effect of the silicate layers in the polymer matrix that acts as a superior insulator and mass transport barrier. Zhai et al. studied the thermal degradation characterization of HDPE/OMT and HDPE-g-MAH/OMT nanocomposites (46). The TGA results revealed that the onset of the degradation temperature for HDPE/OMT nanocomposites with OMT content of 1–5 wt% was increased from 426.5 to above 453.4°C for HDPE. However, for the temperature at which 50% degradation occurs, only HDPE/OMT (1%) exhibited obvious improved thermal stability, while the nanocomposites having 3% and 5% OMT showed almost no change. The authors suggest that the better thermal properties of HDPE containing 1 wt% OMT than the ones with 3% and 5% OMT is responsible for better dispersion of clay in the former. Further analyses showed that the HDPE-g-MAH/OMT nanocomposites exhibited similar thermal features to those of HDPE/OMT nanocomposites, but the variation in the degradation temperature with the addition of content of OMT is small compared with HDPE-g-MAH. The reason is that the thermal stability of HDPE-g-MAH is quite better than that of HDPE; therefore, the addition of OMT does not much improve its thermal degradation temperature.

Recently, Zanetti et al. conducted detailed thermal analyses of PE/clay nanocomposites prepared by melt intercalation using EVA as compatibilizer (47). The thermal degradation behavior of PE nanocomposite (PE/EVA/MTC18), microcomposite (PE/MTC18), and polymer blend (PE/EVA) was studied by TGA and the chemical evolution in the solid residue with Fourier transfer infrared spectra (FTIR). The degradation of the three samples displays a two-stage degradation process under nitrogen. The first degradation step of the nanocomposite takes place at 280°C, which is lower than that of polymer blend, because the deacylation of EVA is accelerated by catalytic effects of the organoclay. Previous study on the thermal behavior of EVA–OMT nanocomposites has reported the catalytic effects of the OMT on the deacylation of EVA in nitrogen atmosphere. Details regarding this acceleration mechanism are presented in Reference 48. However, the second stage of weight loss is similar to pure polymer blend. FTIR results confirm that the presence of acetic acid intercalated in the MTC18 dispersed in the polymer matrix arises from the deacylation of EVA during the compounding. On the contrary, thermooxidation of the nanocomposite exhibited significant delay in weight loss, and the presence of 5 wt% MTC18 is enough to increase its stability. This protective effect is believed to be due to two facts: the barrier effect of clay layers increases during volatilization owing to ablative reassembly of the reticular silicate layers on the surface of the polymer; and the charring process of non-char-forming PE during oxidation, since the intimate

contact between the polymer chains and the clay platelets in nanocomposites can promote aromatization reactions efficiently leading to the formation of an amount of char, which help to link the clay platelets to form a continuous material, then acts as an excellent insulator and mass transport barrier that slows the escape of the volatile product generated during decomposition.

9.3.5 Flammability Properties

The Cone calorimeter is one of the most effective bench-scale methods for evaluating the fire retardant properties of materials. In a typical experiment, the sample is exposed to a given heat flux, and the heat release rate (HRR), specific extinction area (SEA), and CO_2 yield, as well as the mass loss rate, are recorded as a function of time. It is worth noting that reduction of the HRR and, in particular, the peak HRR measured by cone calorimetry has been found to be the most clear-cut evidence of the efficiency of a flame retardant.

Since the first report on the potential flame retardant properties of nylon 6–clay nanocomposites in 1976, many detailed investigations on flame retardant properties of various types of nanocomposite materials have been done. Gilman et al. have investigated in detail the flame retardant properties of nanocomposites since 1997 (7,8,49,50). It has been shown that the flame retardant mechanism of nanocomposites is mainly caused by the formation of a high performance carbonaceous silicate char built on the matrix surface during burning, which insulates efficiently the underlying material and slows the mass loss rate of degradation products.

Reduction in peak HRR has been observed for PE-based nanocomposites. For example, 30–40% reduction in the peak HRR is observed for all LDPE nanocomposites with different organically modified MMT in comparison with pure LDPE (31). Furthermore, the final flammability properties of the polyethylene/clay nanocomposites prepared by one-step melt intercalation method showed similar feature to that of conventional PE nanocomposite prepared by compounding with OMT. Wang et al. confirmed that the peak HRR of HDPE/OMT nanocomposites prepared by one-step melt intercalation method showed 32% reduction compared to that of pure HDPE, as presented in Fig. 9.1 (34).

Zanetti and Costa reported the fire retardant properties of PE/5% clay nanocomposites prepared by melt intercalation using different amount of EVA as compatibilizer.(32) The mass loss rate (MLR) of the nanocomposite, the primary parameter responsible for the lower heat release rate of the nanocomposites, exhibited the typical behavior of many nanocomposites with an earlier mass loss when compared with the polymer matrix and the microcomposite, which is attributed to the release of the thermal degradation product at the organic treatment of the clay. More recently, Lu et al. found that the improvement in flame retardancy of HDPE/EVA/clay nanocomposites strongly depends on the OMT loading (51). It is noted that all the nanocomposites show lowered peak HRR, but the rates of change of their HRR are different, as shown in Fig. 9.2. HRR curve of the 10% sample changes more gently than that of the 2% and 5% samples and an obvious flat appears from 110 to 230 s.

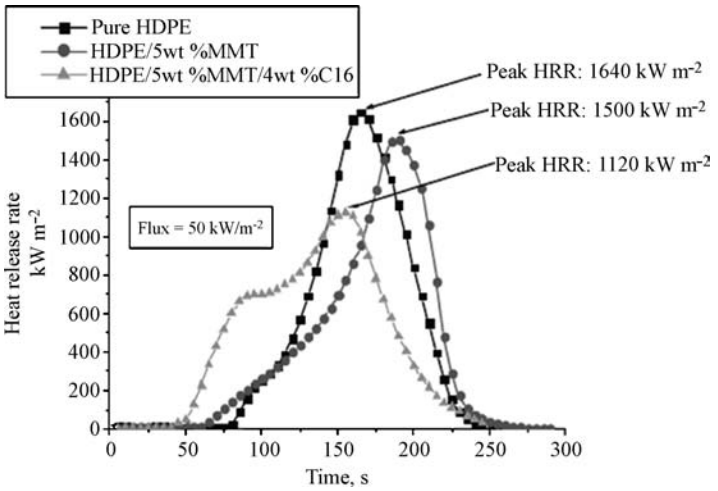

Figure 9.1 Heat release rate data for pure HDPE, HDPE/MMT (5%), and HDPE/MMT (5%)–C16 (4%). (From Reference 34 with permission from Elsevier.)

9.3.6 Photooxidative Degradation

In the presence of silicate, PLSNs show many improvements in most general polymeric properties; however, photooxidative degradation of nanocomposites, such as PP and PA nanocomposites, under photo exposure will be accelerated

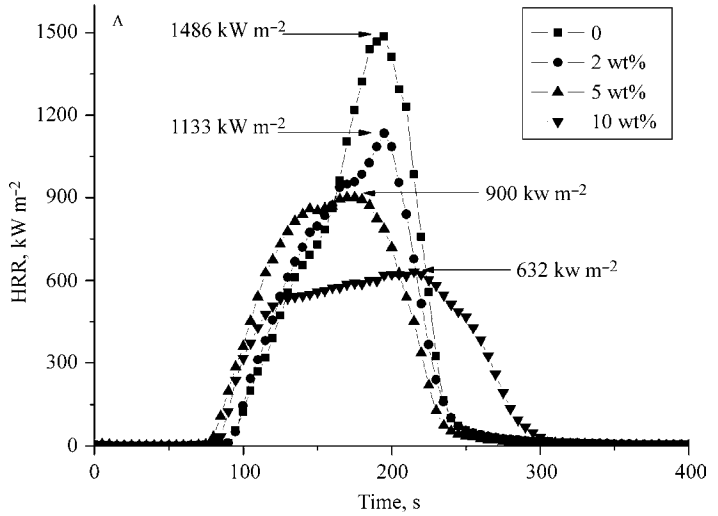

Figure 9.2 The HRR curves for HDPE nanocomposites with different OMT content. (From Reference 51 with permission from John Wiley & Sons, Inc.)

(52–54). Since photooxidative degradation is critical to polymer materials for their processes and usage, therefore this behavior is investigated.

Qin et al. compared the ultraviolet (UV) photooxidative degradation of LDPE/OMT nanocomposites, LDPE microcomposites with MMT, *n*-butylamine modified MMT (C4-MMT), and protonic MMT (H-MMT). The UV exposure tests were carried out on the thin films with a thickness of ~50 μm, and the photooxidative rate was characterized by measuring carbonyl absorbance through FTIR spectra. It was found that the photooxidation rate increased in the order LDPE < LDPE/MMT < LDPE/ C4-MMT < LDPE/ H-MMT < LDPE/OMT, and it increased linearly with the content of OMT for LDPE/OMT nanocomposites. It is known that ammonium catalytic active sites in the aluminosilicate and the corresponding olefin will be generated according to Hoffmann degradation mechanism for OMT. The authors therefore postulated that the acceleration of photooxidative degradation of the nanocomposites was caused because of two reasons. One is the nature of MMT, since the catalytic active sites could accept single electrons from donor molecules of LDPE matrix with low ionization potential, formed free radicals and thus accelerated the photooxidative degradation of the polymer matrix upon UV irradiation. The second is the influence of interlayer ammonium ions, since the decay olefin products can easily form free radicals, and the authors suggested that this is the primary reason for the acceleration of UV photooxidative degradation.

9.3.7 Thermal Expansion and Thermal Conductivity

Thermophysical properties of PE-g-MAH/OMT nanocomposites including thermal expansion and thermal conductivity were studied by the TMA and 3ω methods (56). The TMA experiments were carried out using Setaram TMA92 under an argon gas atmosphere in the temperature range from 20 to 80°C, on $5 \times 5\,mm^2$ plaques. The thermal expansion value was calculated by the ratio of the elongation length to the initial length. For the PE-g-MAH/OMT nanocomposites with OMT content varying from 0.5 to 5 vol%, the coefficient of thermal expansion (CTE) was almost unaffected when the OMT content varied from 0.5 to 3 vol%, but exhibited a clear decrease to a value lower than that of PE-g-MAH when the content increased to 5 vol%. The authors attributed the effective reduction in CTE in the nanocomposites to the nature of clay, that is, high modulus, high aspect ratio, two-dimensional reinforcement, and low CTE. Interestingly, the thermal conductivity of the nanocomposites decreased linearly with an increase in temperature and with an increase of OMT; this is in contrast to the expectation since the silicate particles have a higher thermal conductivity than that of polymer matrix. The authors suggested that the crystallinity and the crystal morphology of the PE-g-MAH/OMT nanocomposites might be the reasons for this unusual result.

9.4 POLYETHYLENE/CLAY NANOCOMPOSITES EXPOSED TO HIGH ENERGY IRRADIATION

Irradiation-induced intermolecular cross-linking of polymers in the presence of high energy irradiation (gamma or electron beam) has been employed to upgrade their properties (57–61). It is well known that the clay commonly used to produce nanocomposites is montmorillonite, which has stable crystal structure, can accumulate high doses of irradiation without distinct damage, and has long been used as engineering barriers in storages of radioactive wastes (62). Since the decrease in radiolytic damage is one of the most important properties of clay, the results of some of the most recent studies on properties of PE/clay nanocomposites exposed to gamma rays are reported in this section.

Lu et al. reported on a study of the morphology evolution of the exfoliated PE-g-MAH/clay nanocomposites exposed to gamma rays (63). TEM images shown in Fig. 9.3 demonstrate that the morphology of the nanocomposite evolved via three stages under irradiation: ideally face-to-face ordered exfoliation, followed by a completely disordered dispersion of stacked layers, and relative ordered distribution of stacked layers. Considering the influences of the mobility of macroradicals, steric interaction between clay layers, and cross-linking of polymer chains induced by gamma rays, the authors deduced that the mechanism of the morphology evolution strongly depends on the relative magnitude of these competing processes between the steric interaction of clay layers and the development of intermolecular cross-linking.

The influence of gamma irradiation on the properties, including thermal degradation, flammability, and tensile properties of HDPE/OMT nanocomposites using EVA as compatibilizer, has also been studied by Lu et al. (51,64). The nanocomposites exhibit interesting material properties of the pure polymer matrix during

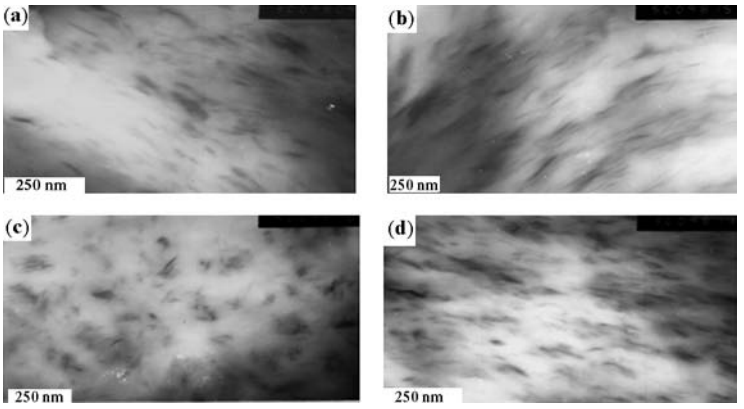

Figure 9.3 TEM micrographs of MAPE/5 wt% OMT nanocomposites with irradiation doses: (**a**) nonirradiated, (**b**) 50 kGy, (**c**) 100 kGy, and (**d**) 150 kGy. (From Reference 63 with permission from Elsevier.)

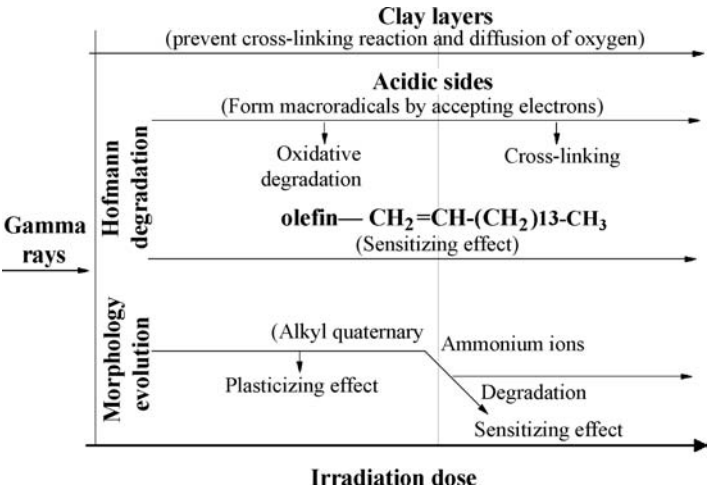

Figure 9.4 Schematic representation of the influence of OMT on the interactions between polymeric matrix and gamma rays. (From Reference 64 with permission from John Wiley & Sons, Inc.)

irradiation and superior irradiation-resistant properties. They suggested that three prominent facts determine the structure–properties relationship of gammairradiated nanocomposites: the segregation of clay layers, the morphology evolution induced by gamma rays, and the effect of Hofmann degradation of OMT. These effects interacted as well as competed with others; the properties of nanocomposites strongly depend on the prevalent effect, developing with increasing irradiation doses. The influence of OMT on the interactions between polymeric matrix and gamma rays is shown in Fig. 9.4.

9.5 CRYSTALLIZATION BEHAVIOR OF POLYETHYLENE-BASED NANOCOMPOSITES

Crystallization is one of the most important behaviors of crystalline polymer, since the resulting properties of polymeric materials in engineering applications are critically dependent on the extent of crystallinity and the nature of crystalline morphology. For nanocomposites, investigations on their crystallization behaviors are helpful for the understanding of the fundamentals associated with the extent of intercalation of polymer chains into clay galleries and the valuable insight into the development of new materials with remarkably enhanced material properties. Differential scanning calorimeter has provided a quick and practical way to study the crystallization behavior of polyethylene/clay nanocomposites prepared by melt intercalation or *in situ* polymerization (42,46,65–68).

The isothermal crystallization behaviors of polymeric materials have been studied intensively, since the experimental conditions are easy to handle and the

problems relating to cooling rates and thermal gradients within specimens are avoided. The isothermal crystallization kinetics is described by the Avrami equation:

$$1 - X(t) = \frac{\Delta H^c_{t=\mathring{a}} - \Delta H^c_t}{\Delta H^c_{t=\mathring{a}} - \Delta H^c_{t=0}} = \exp(Kt^n) \tag{9.1}$$

where $X(t)$ is the relative crystallinity at time t, and $\Delta H^c_{t=\infty}$ and ΔH^c_t are the crystallization enthalpies at complete crystallization time t and after time t, respectively. Xu et al. first compared the isothermal crystallization behaviors of intercalated PE/MMT nanocomposite and fully exfoliated PE/MMT nanocomposite synthesized by *in situ* polymerization (65). They found that the intercalated nanocomposite has longer induction period, longer crystallization half time, and larger crystallization activation energy than the exfoliated sample, revealing the confinement effect of MMT layers. Avrami crystallization kinetics analyses indicated that Avrami exponent (n) increased gradually with crystallization temperature, but the maximal value of n reached 2.0 and 3.0 for the intercalated and exfoliated samples, respectively. It implies that the growth of PE crystals in the intercalated sample is two dimensional and the PE stems are parallel to the MMT layers, because of the smaller lateral surface of the PE crystals that are confined in the MMT layers. On the basis of the depression of melting temperature, the specific free energy of the PE–MMT interface was estimated. It was found that the specific free energy of the PE–MMT interface was much smaller than that of the lateral surface and folding surface of PE crystals. PE crystals parallel to the MMT layers in the intercalated nanocomposite are shown in Fig. 9.5.

In practice, the crystallization processes of materials in a continuously changing thermal environment, namely, under nonisothermal conditions, are of great importance in polymer industries. Several methods, such as that by Ozawa et al., have been developed on the basis of the Avrami equation.

The nonisothermal crystallization kinetics of HDPE/OMT and HDPE/PE-g-MAH/OMT nanocomposites has been investigated in detail by Xu et al. (43,68). They found that in HDPE/OMT system, the nanocomposites exhibited faster crystallization rate than in pure HDPE at a given cooling rate, and nonisothermal kinetic crystallization complied tridimensional growth with heterogeneous nucleation. Similar features have been found in other systems. However, it should be noted

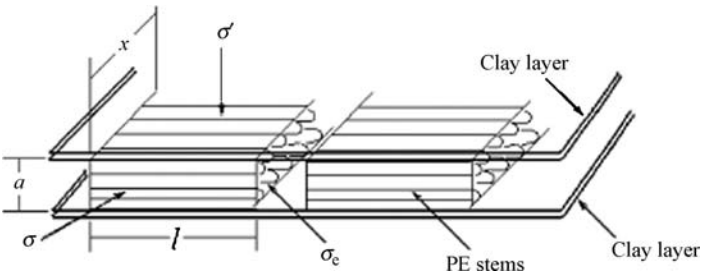

Figure 9.5 Schematic of PE crystals in the intercalated PE/MMT nanocomposite prepared by *in situ* polymerization. (From Reference 65 with permission from Elsevier.)

Table 9.2 Comparison of the Nonisothermal Crystallization Kinetics Parameters for HDPE, HDPE/OMT, and HDPE/PE-g-MAH/OMT Nanocomposites.

Sample	Φ, K min^{-1}	n	Z_c	$t_{1/2}$, min	T_p (°C)	ΔE, kJ mol^{-1}
PE	1	3.37	0.044	2.44	121.62	96.54
	2	3.41	0.416	1.41	120.68	
	5	3.65	1.193	0.74	119.15	
	10	3.88	1.315	0.49	117.44	
PE/Org-MMT = 99/1	1	5.78	0.007	2.33	122.50	111.59
	2	4.87	0.641	1.21	121.78	
	5	5.67	2.184	0.66	120.60	
	10	5.08	1.685	0.44	119.29	
PE/Org-MMT = 97/3	1	6.93	0.005	2.36	122.57	123.28
	2	5.47	0.423	1.39	121.82	
	5	5.43	2.266	0.62	120.80	
	10	4.97	1.773	0.43	119.63	
PE/Org-MMT = 95/5	1	7.19	0.003	1.76	122.74	102.07
	2	7.00	0.246	1.19	121.91	
	5	4.95	1.646	0.63	120.66	
	10	5.37	1.641	0.42	119.21	
HDPE	5	1.51	0.94	45.0	390.3	304.6
	10	1.51	1.04	33.6	387.9	
	20	1.57	1.05	22.2	384.7	
	40	1.60	1.06	18.0	381.8	
PE/PE-g-MAH/org-MMT	5	1.76	0.96	35.4	392.8	223.7
	10	1.73	1.05	26.4	389.2	
	20	1.74	1.06	19.8	386.4	
	40	1.80	1.09	15.0	382.5	

From Reference 43 with permission from John Wiley & Sons and from Reference 68 with permission from Springer.

that the crystallization activation energies of HDPE/OMT were larger than that of HDPE because the increase in viscosity prevented the rearranging of polyethylene chains in a nanocomposite; whereas HDPE/PE-g-MAH/OMT showed a contrary tendency because the MMT layers and the carboxyl groups attached to PE-g-MAH makes the crystallization of nanocomposite easier. Comparison of the nonisothermal crystallization kinetic parameters for the two kinds of nanocomposites with pure HDPE is summarized in Table 9.2.

9.6 RHEOLOGICAL PROPERTIES AND PROCESSABILITY

Besides the concern about the enhancement of material properties of PLSN, much attention has been placed on the processability of these materials in polymer industries. Investigation on the rheological behavior, the primary parameter responsible

for the processability in the molten state, is beneficial for deeper understanding of the complex structure–property relationships in nanocomposites. Commonly, the rheology of polymer melts mainly depends on temperature, where the measurement of elastic modulus (G'), loss modulus (G''), and complex viscosity (η^*) is carried out. It has been established that for thermorheological materials, bilogarithmic plots of the isotherms of G', G'', and η^* can be superimposed.

Rheological behaviors of PE-g-MAH and its micro composites and nanocomposites evaluated by dynamic oscillatory shear measurements are presented in Reference 18. The η^* of the nanocomposites increased dramatically at low frequencies and showed very strong non-Newtonian behavior as clay content increased above 5 wt%. Comparison of the rheological properties of microcomposite (1.44PA/PE) and nanocomposite (1.44PA/PE-g-MAH) revealed that the former demonstrated a modest increase in η^* and Newtonian behavior at low frequencies, while the nanocomposite showed a contrary tendency. The tan δ of the nanocomposites decreased significantly with increasing clay content over the whole experimental frequency range, indicating a substantial deviation from terminal flow behavior and a more elastic response as clay content increased. However, tan δ of the microcomposites containing different clay content decreased slightly and maintained a viscous-like response.

Figure 9.6 shows the time-dependent evolution of the elastic modulus (G') and viscous modulus (G'') for PE-g-MAH and PE-g-MAH/clay (5 wt%) nanocomposites (69). The oscillation time sweep measurements revealed that the PE-g-MAH

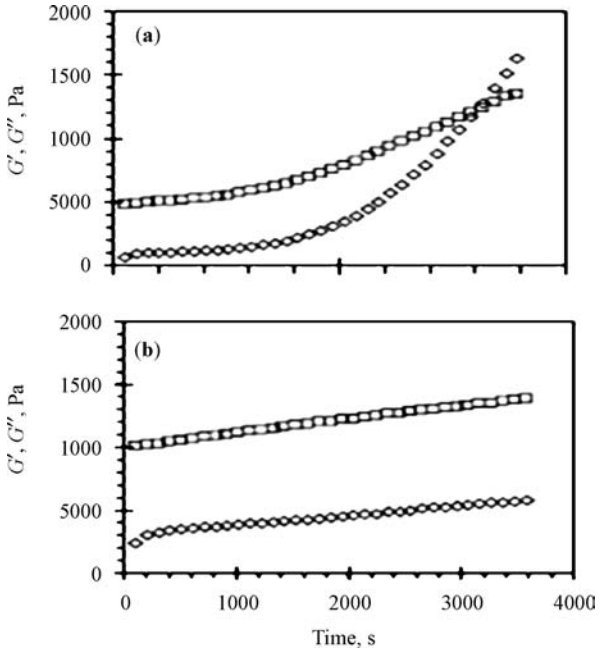

Figure 9.6 G' and G'' as a function of time at 150°C for (**a**) PE-g-MAH and (**b**) 5 wt% NR4C-MM/PE-g-MAn, where (◇) G' and (□) G''. (From Reference 69 with permission form Elsevier.)

showed a typical behavior of cross-linking processes, where the intersection of G' and G'' denotes the point of gelation. When 5 wt% exfoliated clay was presented, the viscoelastic properties of the nanocomposite improved substantially. The G' increased at a much lower rate than polymer matrix, and no crossover point between G' and G'' was observed. The authors suggested that the rheological response of nanocomposite was governed by both polymer–polymer and polymer–clay interactions, since the latter reduced the intensity of intermolecular functional group associations that establish a physical polymer network within PE-g-MAH. Also, the evolution of G' showed a similar feature to that of G'', indicating that while functional group interactions within PE-g-MAH affect its rheological behavior at low shear stresses, a range of additives, including the montmorillonite-based fillers, can disrupt these labile associations.

Hatzikiriakos et al. reported the effect of organically modified nanoclays on the processability of polyolefins (70). Figure 9.7 shows the shear rate dependence of the apparent shear stress for metallocene LLDPE (m-LLDPE) and the corresponding nanocomposites with the addition of several nanoclays, where PGV and PGW are unmodified nanoclays and 1.44PA is organically modified nanoclay. It can be seen that most nanoclays have no effect on the flow curve of the matrix except for the addition of 0.5 wt% 1.44PA modified with onium ions. The results of the critical shear rates for the appearance of sharkskin melt fracture exhibited that the 1.44PA containing nanocomposite showed the best performance as the critical shear rate for the onset of the appearance of sharkskin melt fracture increased from $38\,s^{-1}$ to 375^{-1} for pure m-LLDPE, while addition of PGV and/or PGW without organically modifier has no effect on the processability. The authors suggested that the organically modified nanoclay can work as a very effective and powerful solid lubricant for the extrusion processes to suppress the development of extensional stresses to such high levels that can cause melt fracture phenomena. Photos of extrudates obtained in the capillary

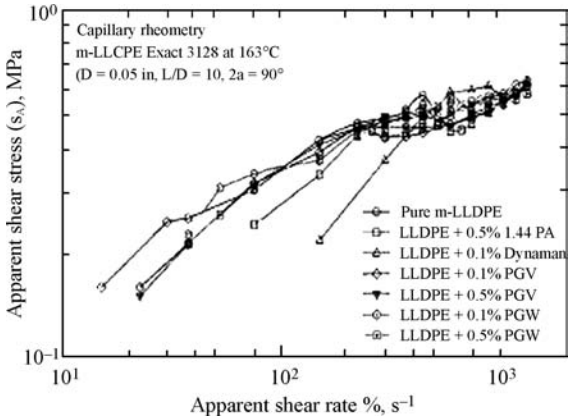

Figure 9.7 The apparent flow curve of resin m-LLDPE loaded with several additives in capillary extrusion at 163°C. (From Reference 70 with permission from John Wiley & Sons, Inc.)

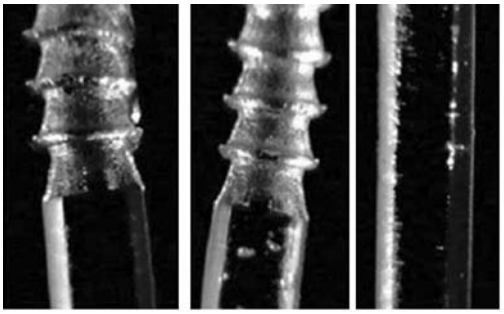

Figure 9.8 Extrudates obtained in capillary extrusion of resin m-LLDPE loaded with several additives at the apparent shear rate of 300 s^{-1} and 163°C. (From Reference 70 with permission from John Wiley & Sons, Inc.)

extrusion of m-LLDPE loaded with several additives confirmed the above suggestion (Fig. 9.8). Similar features observed in the case of HDPE, LLDPE and PP have been reported in the study. Finally, they found that the combination of nanoclays with traditional processing aids can enhance the critical shear rates for the onset of melt fracture than the individual constituents when they are used independently.

9.7 CONCLUSIONS

Polyethylene/clay nanocomposites have experienced an important development over the past 20 years in academics and industries across the world. The nanocomposites possess several advantages, such as improved mechanical properties compared to conventional composites, remarkable increase in thermal stability and flame retardancy, as well as improved gas barrier behavior. These improved properties are achieved at a small clay content ($\leq$ 5 wt%), which make the nanocomposites lighter in weight than conventional composites. As the twenty-first century engineering materials with wide range of markets, they are already commercially available and applied as high performance materials, such as transportation apparatus, electrical and electronics insulation, food packaging materials and building materials, and as high functional materials, such as barrier-functional materials, weathering resistant materials, and so on.

REFERENCES

1. Y. Kojima, A. Usuki, M. Kawasumi, A. Okada, Y. Kukushima, T. Karauchi, and O. Kamigaito, *J. Mater. Res.*, **6**, 1185 (1993).
2. Y. Kojima, A. Usuki, M. Kawasumi, A. Okada, Y. Kukushima, T. Karauchi, and O. Kamigaito, *J. Mater. Res.*, **8**, 1179 (1993).
3. Y. Kojima, A. Usuki, M. Kawasumi, A. Okada, Y. Kukushima, T. Karauchi, and O. Kamigaito, *J. Polym. Sci. A Polym. Chem.*, **31**, 983 (1993).

4. X. H. Liu and Q. J. Wu, *Polymer*, **42**, 10013 (2001).
5. T. Kashiwagi, R. H. Harris Jr., X. Zhang, R. M. Briber, B. H. Cipriano, S. R. Raghavan, W. H. Awad, and J. R. Shields, *Polymer*, **45**, 881 (2004).
6. R. S. Sinha, K. Yamada, M. Okamoto, A. Ogami, K. Ueda, *Chem. Mater.*, **15**, 1456 (2003).
7. J. W. Gilman, C. L. Jackson, A. B. Morgan, *Chem. Mater.*, **12**, 1866 (2000).
8. J. W. Gilman, *J. Appl. Clay Sci.*, **15**, 31 (1999).
9. P. B. Messersmith and E. P. Giannelis, *Chem. Mater.*, **6**, 1719 (1994)
10. Y. K. Kim, Y. S. Choi, K. H., Wang, and I. J. Chung, *Chem. Mater.*, **14**, 4990 (2002).
11. J. H. Chang, Y. U. An, S. J. Kim, and S. Im, *Polymer*, **44**, 5655 (2003).
12. P. Maiti and M. Okamoto, *Macromol. Mater. Eng.*, **288**, 440 (2003).
13. Y. Tang, Y. Hu, R. Zhang, Z. Gui, Z. Z. Wang, Z. Y. Chen, and W. C. Fan, *Polymer*, **45**, 5317 (2004).
14. R. S. Sinha, K. Yamade, M. Okamoto, and K. Ueda, *Polymer*, **44**, 857 (2003).
15. C. M. Koo, M. J. Kim, M. H. Choi, S. O. Kim, and I. J. J. Chung, *Appl. Polym. Sci.*, **88**, 1526 (2003).
16. K. H. Wang, I. J. Chung, M. C. Jang, J. K. Keum, and H. H. Song, *Macromolecules*, **35**, 5529 (2002).
17. M. Alexandre, P. Dubois, T. Sun, J. M. Garces, and R. Jerome, *Polymer*, **43**, 2123 (2002).
18. T. G. Gopakumar, J. A. Lee, M. Kontopoulou, and J. S. Parent, *Polymer*, **43**, 5483 (2002).
19. K. H. Wang, M. H. Choi, C. M. Koo, Y. S. Choi, and I. J. Chung, *Polymer*, **42**, 9819 (2001).
20. R. A. Vaia, H. Ishii, and E. P. Giannelis, *Chem. Mater.*, **5**, 1694 (1995).
21. R. A. Vaia and E. P. Giannelis, *Macromolecules*, **30**, 7990 (1997).
22. R. A. Vaia and E. P. Giannelis, *Macromolecules*, **30**, 8000 (1997).
23. D. F. Wu, C. X. Zhou, H. Zheng, *J. Appl. Polym. Sci.*, **99**, 1865 (2006).
24. C. C. Zeng and L. J. Lee, *Macromolecules*, **34**, 4098 (2001).
25. Y. K. Kim, Y. S. Choi, K. H. Wang, and I. J. Chung, *Chem. Mater.*, **14**, 4990 (2002).
26. Y. Tang, Y. Hua,, S. F. Wang, Z. Gui, Z. Y. Chen, and W. C. Fan, *Polym. Degrad. Stabil.*, **78**, 555 (2002).
27. M. A. Osman, J. E. P. Rupp, and U. W. Suter, *J. Mater. Chem.*, **15**, 1298 (2005).
28. M. A. Osman, J. E. P. Rupp, and U. W. Suter, *Polymer*, **46**, 1653 (2005).
29. N. Hasegawa, H. Okamoto, M. Kawasumi, M. Kato, A. Tsukigase, and A. Usuki, *Macromol. Mater. Eng.*, 280–281, 76, (2000).
30. N. Hasegawa, M. Kawasumi, M. Kato, A. Usuki, and A. Okada, *J. Appl. Polym. Sci.*, **67**, 87 (1998).
31. J. G. Zhang and C. A. Wilkie, *Polym. Degrad. Stabil.*, **80**, 163 (2003).
32. M. Zanetti and L. G. Costa, *Polymer*, **45**, 4367 (2004).
33. C. M. Koo, H. T. Ham, S. O. Kim, K. H. Wang, I. J. Chung, D. C. Kim, and W. C. Zin, *Macromolecules*, **35**, 5116 (2002).
34. S. F. Wang, Y. Hu, Z. K. Qu, Z. Z. Wang, Z. Y. Chen, and W. C. Fan, *Mater. Lett.*, **57**, 2675 (2003).
35. A. Okada, M. Kawasumi, A. Usuki, Y. Kojima, T. Kurauchi, and O. Kamigaito, *Mater. Res. Soc. Symp. Proc.*, **171**, 45 (1990).
36. J. Tudor, L. Willington, D. O'Hare, and B. Royan, *Chem. Commun.*, **17**, 2031 (1996).
37. S. W. Kuo, W. J. Huang, S. B. Huang, H. C. Kao, and F. C. Chang, *Polymer*, **44**, 7709 (2003).
38. J. S. Bergman, H. Chen, E. P. Giannelis, M. G. Thomas, and G. W. Coates, *Chem. Commun.*, **21**, 2179 (1999).
39. L. M. Wei, T. Tang, and B. T. Huang, *J. Polym. Sci. A Polym. Chem.*, **42**, 941 (2004).
40. S. Hotta and D. R. Paul, *Polymer*, **45**, 7639 (2004).
41. C. G. Zhao, M. Feng, F. L. Gong, H. L. Qin, and M. S. Yang, *J. Appl. Polym. Sci.*, **93**, 676 (2004).
42. M. Kato, H. Okamoto, N. Hasegawa, A. Tsukigase, and A. Usuki, *Polym. Eng. Sci.*, **43**, 1312 (2003).
43. G. D. Liang, J. T. Xu, and W. B. Xu, *J. Appl. Polym. Sci.*, **91**, 3054 (2004).

44. A. Okada, M. Kawasumi, A. Usuki, Y. Kojima, T. Kurauchi, and O. Kamigaito, *Mater. Res. Soc. Proc.*, **171**, 45 (1990).
45. Y. Kojima, K. Fukumori, A. Usuki, A. Okada, and T. Kurauchi, *J. Mater. Sci. Lett.*, **12**, 889 (1993).
46. H. B. Zhai, W. B. Xu, H. Y. Guo, Z. F. Zhou, S. J. Shen, and Q. S. Song, *Eur. Polym. J.*, **40**, 2539 (2004).
47. M. Zanetti, P. Bracco, and L. Costa, *Polym. Degrad. Stabil.*, **85**, 657 (2004).
48. M. Zanetti, G. Camino, R. Thomann, and R. Mülhaupt, *Polymer*, **42**, 4501 (2001).
49. S. Bourbigot, M. L. Bras, F. Dabrowski, J. W. Gilman, and T. Kashiwagi, *Fire Mater.*, **24**, 201 (2000).
50. J. W. Gilman, T. Kashiwagi, A. B. Morgan, R. H. Harris Jr., L. Brassell, M. VanLandinghan, and C. L. Jackson, NISTIR 6531, Gaithersburg, MD, 2000.
51. H. D. Lu, Y. Hu, Q. H. Kong, Y. B. Cai, Z. Y. Chen, and W. C. Fan, *Polym. Adv. Technol.*, **15**, 601 (2004).
52. S. Morlat, B. Mailhot, D. Gonzalez, and J. L. Gardette, *Chem. Mater.*, **16**, 377 (2004).
53. A. Tidjani and C. A. Wilkie, *Polym. Degrad. Stabil.*, **74**, 33 (2001).
54. H. L. Qin, Z. C. G. Zhao, S. M. Zhang, G. M. Cheng, and M. S. Yang, *Polym. Degrad. Stabil.*, **81**, 497 (2003).
55. H. L. Qin, Z. G. Zhang, M. Feng, F. L. Gong, S. M. Zhang, and M. S. Yang, *J. Polym. Sci. B Polym. Phys.*, **42**, 3006 (2004).
56. S. H. Lee, J. E. Kim, H. H. Song, and S. W. Kim, *Int. J. Thermophys.*, 25, 1585 (2004).
57. V. G. Barkhudaryan, *Polymer*, **41**, 575 (2000).
58. D. L. Si and W. X. Chen, *J. Appl. Polym. Sci.*, **86**, 553 (2001).
59. S. Chattopadhyar, T. K. Chaki, A. K. Bhowmick. *Radiat. Phys. Chem.*, **59**, 501 (2000).
60. D. Gheysari, A. Behjat and M. S. Haji, *Eur. Polym. J.*, **37**, 295 (2001).
61. A. Singh, *Radiat. Phys. Chem.*, **56**, 375 (1999).
62. A. Negron, S. Ramos, A. L. Blumenfeld, G. Pacheco, and J. J. Fripiat, *Clays Clay Miner.*, **50**, 35 (2002).
63. H. D. Lu, Y. Hu, J. F. Xiao, Q. H. Kong, Z. Y. Chen, and W. C. Fan, *Mater. Lett.*, **59**, 648 (2005).
64. H. D. Lu, Y. Hu, Q. H. Kong, Z. Y. Chen, and W. C. Fan, Polym. Adv. Technol., **16**, 688 (2005).
65. J. T. Xu, Y. Q. Zhao, Q. Wang, and Z. Q. Fan, *Polymer*, **46**, 11978 (2005).
66. J. T. Xu, Y. Q. Zhao, Q. Wang, Z. Q. Fan, *Macromol. Rapid Commun.*, **26**, 620 (2005).
67. J. Morawiec, A. Pawlak, M. Slouf, A. Galeski, E. Piorkowsk, and N. Krasnikow, *Eur. Polym. J.*, **41**, 1115 (2005).
68. W. B. Xu, H. B. Zhai, H. Y. Guo, Z. F. Zhou, N. Whitely, and W. P. Pan, *J. Therm. Anal. Calorim.*, **78**, 101 (2004).
69. J. A. Lee, M. Kontopoulou, and J. S. Parent, *Polymer*, **45**, 6595 (2004).
70. S. G. Hatzikiriakos, N. Rathod, and E. B. Muliawan, *Polym. Eng. Sci.*, **45**, 1098 (2005).

Chapter 10

Polypropylene/Clay Nanocomposites

Xuehong Lu,[1] Ke Wang,[2] and Yang C. Chua[2]

10.1 INTRODUCTION

The emerging field of polymer/clay nanocomposites has driven much vigorous research in the past decade. These materials are called nanocomposites because of the nanometer thickness (less than 100 nm) of the clay sheets when they are delaminated into individual layers in the polymer matrix. Due to their high aspect ratio, high surface area, and high strength, the uniform dispersion of clay in polymer matrices at the nanometer length scale has often resulted in dramatic enhancements in the mechanical, physical, and thermal properties of the polymers at relatively low inorganic loadings (typically under 5 wt%), and without the property trade-offs typically associated with the formation of composites (1,2). In addition to the unique combination of properties exhibited by polymer/clay nanocomposites, the possibility by which such nanocomposites can be prepared by a simple melt-compounding process (3) also provides a potentially commercially viable route for their large-scale production.

Polypropylene (PP) is one of the most commercially important commodity polymers due to its reasonably good combination of mechanical and thermal properties, low cost, light weight, and favorable processing and recycling characteristics. In meeting the increasing demands of current or new applications, however, the performance of PP often falls short. The development of PP/clay nanocomposites (PPCNs) thus presents a very promising approach, by which the performance of PP may be enhanced, at reasonable cost, well beyond that of traditional

[1]School of Materials Science and Engineering, Nanyang Technological University, Nanyang Avenue, Singapore 639798

[2]Institute of Materials Research & Engineering, 3 Research Link, Singapore 117602

Polyolefin Composites, Edited by Domasius Nwabunma and Thein Kyu

microcomposites. The relatively low clay loadings by which the property enhancements can be realized also allow the desired performance to be achieved without compromising the processing advantages and light weight that are inherent to PP. It is this combination of significantly enhanced performance at favorable cost, processing, and weight profiles that has motivated much research and development of PPCNs in both academia and industries in the past decade.

This chapter reviews the major advancements in the field of PPCNs in the past decade. The main approaches that have been adopted for the preparation of PPCNs, as well as significant aspects of their structures, behaviors, and properties, will be discussed.

10.2 STRUCTURE AND PROPERTIES OF CLAY

Clays are crystalline materials consisting of layers made up of an octahedral sheet of alumina fused to two tetrahedral sheets of silica (Fig. 10.1). Stacking of the layers leads to a regular van der Waals' gap between the layers called the interlayer or gallery. Although the thickness of each layer is only 1 nm, the lateral dimensions of the layers may range from 30 nm to as large as several microns (1,4). Isomorphic substitutions (e.g., Al^{3+} replaced by Mg^{2+} or Mg^{2+} replaced by Li^{+}) within the layers lead to a net negative charge that must be counterbalanced by cations that are situated in the interlayer space, such as Na^{+} or K^{+} ions.

Montmorillonite (MMT) is the most common type of clay used in polymer/clay nanocomposites. Its chemical structure is given by $(Na,Ca)_x(Al_{4-x}Mg_x)Si_8O_{20}(OH)_4$, where x refers to the degree of isomorphous substitution (between 0.5 and 1.3). In the following sections, clay refers to MMT in most cases.

Clays are good candidates for the preparation of inorganic–organic nanocomposites because they are abundant in nature, inexpensive, chemically stable, and possess high aspect ratio and high strength—all of which are important indices for application as reinforcing agents. In addition, two important characteristics of clay

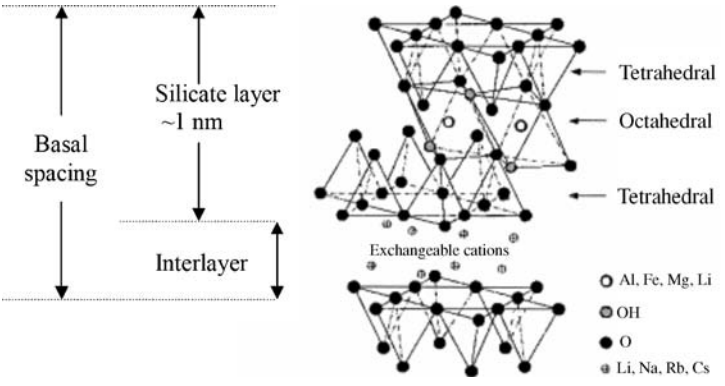

Figure 10.1 Structure of clay. (From Reference 4 with permission from Springer, Heidelberg, Germany.)

make them a natural choice of selection for the preparation of nanocomposites (1,2). First, their layered structure means that it is possible to separate them into individual sheets, each of which is only 1 nm thick. For fully dispersed clays, an aspect ratio of as high as 1000 can be achieved. Second, the possibility of ion exchange within the interlayers provides clay with a rich intercalation chemistry. The surface chemistry of clays can be fine-tuned through ion exchange with various organic or inorganic cations to make them compatible with a wide range of polymers.

10.3 TYPICAL MORPHOLOGIES OF POLYMER/CLAY HYBRIDS

When clay is added to a polymer matrix, three types of structures can be expected—a phase-separated microcomposite, an intercalated nanocomposite, and an exfoliated nanocomposite (Fig. 10.2) (1,2).

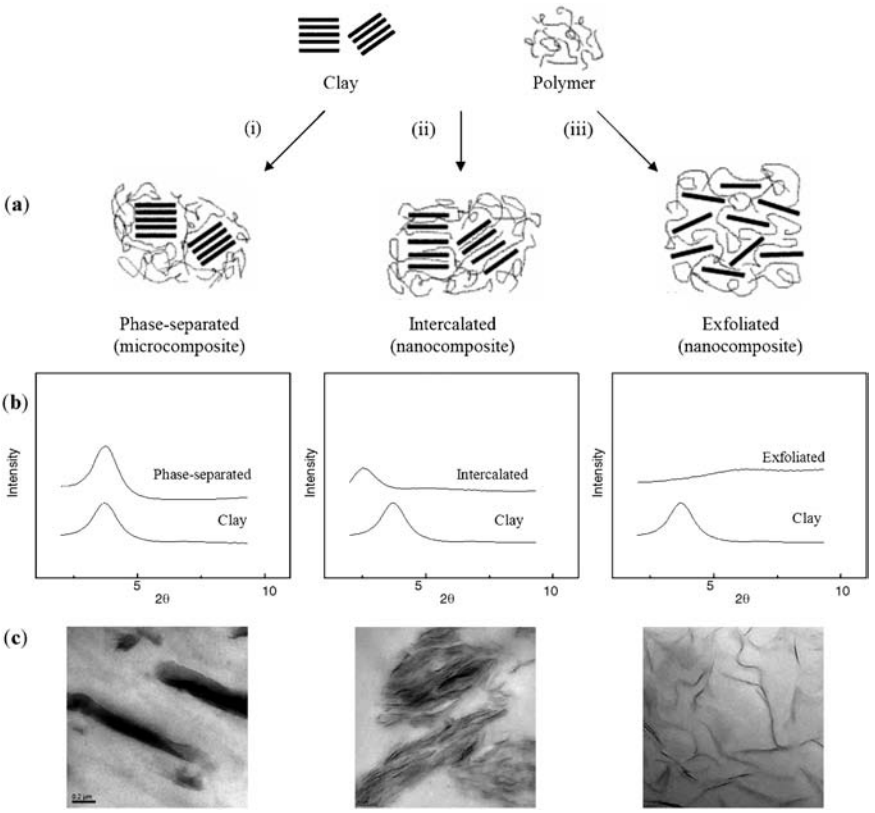

Figure 10.2 (**a**) Schematic illustration of the morphologies of polymer/clay hybrids: (i) phase-separated microcomposite; (ii) intercalated nanocomposite; and (iii) exfoliated nanocomposite, and typical (**b**) XRD patterns and (**c**) TEM images corresponding to each type of morphology. (From Reference 1 with permission from Elsevier Science Ltd., UK.)

When the polymer is unable to enter the spaces between the clay layers, and the clay still remains in the form of large stacks known as tactoids, a phase-separated microcomposite results. The properties of such composites remain in the same range as conventional microcomposites. When the extended polymer chains are inserted into the spaces between the clay layers, an intercalated nanocomposite is obtained. In this state, the clay preserves its well-ordered multilayered morphology, although the separation between the individual layers is often increased due to the presence of the polymer that is sandwiched between the clay layers. With extensive penetration of the polymer chains into the clay galleries, the clay can be completely delaminated into individual nanometer-thick layers. When the clay loses its regular layer register and becomes disordered and uniformly suspended in a continuous polymer matrix, an exfoliated nanocomposite results. In reality, however, polymer/clay nanocomposites often exhibit a mixed morphology, in which a combination of these three types of dispersion states coexists within the same material.

The degree of clay dispersion in the hybrids is often evaluated by a combination of X-ray diffraction (XRD) and transmission electron microscopy (TEM). XRD is used to determine the interlayer spacing of the clay in the clays, as well as in the hybrids. The measured diffraction angle (θ) is related to the average interlayer spacing of clay (d) by Bragg's relation: $\lambda = 2d \sin \theta$, where λ corresponds to the wavelength of the X-ray radiation used. In addition, the width of the peak provides an assessment of the degree of order in the stacked sheets while the intensity of the peak provides statistical information about the number of multilayer stacks. The clay layers can only be detected by XRD if they remain parallel and evenly spaced. In an exfoliated nanocomposite, the extensive layer separation associated with the delamination of the original clay layers in the polymer matrix results in the eventual disappearance of any coherent X-ray diffraction from the distributed clay layers. For an intercalated nanocomposite, the intercalation of polymer into the intergallery spaces results in a shifting of the basal reflection to a position corresponding to a larger interlayer spacing. In the case where the clay is incompatible with the polymer matrix, the diffraction peak will be observed at the same position as that seen for the clay in the absence of the polymer (Fig. 10.2b). Although XRD provides a quick and convenient way for the determination of the clay interlayer spacing in the clays and in the resulting hybrids, no conclusive information can be derived about the spatial distribution of the clay layers or any structural inhomogeneities in the hybrids based on just the XRD pattern. For this reason, TEM is often used in complement with XRD to directly observe the level of dispersion that has been achieved in the hybrids at the nanoscale.

10.4 PREPARATION OF PP/CLAY NANOCOMPOSITES

10.4.1 Clay Modification

Due to the absence of any polar groups in the PP backbone, clays, in their pristine hydrophilic state, are too incompatible with PP to be dispersed in it at the nanoscale. To improve the compatibility of clays with PP, it is essential to convert the

hydrophilic surfaces of clays to organophilic ones, by replacing the interlayer alkali ions with organic cationic surfactants, such as alkylammonium cations (5–11). The surfactants in the resulting ''organoclays'' help to lower the surface energy of the clays, improve the wetting characteristics of the PP matrix, as well as facilitate the intercalation of PP chains into the clay galleries.

10.4.1.1 Alkylammonium Modifiers

The most common cationic surfactants that are used to modify clay for the preparation of PPCNs are primary, secondary, tertiary, and quaternary alkylammonium cations. The alkyl chain length and molecular structure of the alkylammonium modifiers have been found to have important effects on the morphology of the nanocomposites.

Reichert et al. (6) have examined the influence of the alkyl chain length of protonated alkyl-substituted primary amines on the exfoliation behavior of synthetic clay. It was found that in order for the clay modification to be effective, alkyl chains that are longer than eight carbon atoms are required. Alkyl chain lengths that have only eight carbon atoms or fewer tend to give only a limited expansion of interlayer space. On the contrary, when alkyl chains of longer lengths are used, the *d*-spacing is found to increase significantly (Fig. 10.3a). When compounded with maleic anhydride modified PP (MAPP), only the clays modified with long alkyl amine chains (more than eight carbon atoms) exhibit good dispersion in the matrix, as evidenced by the broadening and diminishing of the intensity associated with the clay peak (Fig. 10.3b) in these hybrids.

Kim and White (11) have also found that organoclays modified with quaternary ammoniums tend to have relatively better compatibility with PP in comparison to their primary, secondary, or tertiary counterparts. Quaternary ammonium salts that contain four long alkyl chains can create a larger organic surface and interlayer spacing in the clay galleries, which helps to facilitate the penetration of polymer chains into the clay layers. The type of alkylammonium surfactants affects the dispersion of the organoclay through not only organic surface coverage and interlayer spacing, but also the thermal stability of the organoclay, since the melt compounding of PP usually proceeds at temperatures above 180°C. Lee et al. (7) studied the importance of the thermal stability of the organoclays by using two organoclays that are modified with different alkylammonium cations. After melt compounding, the organoclays modified with alkylammonium cations of poorer thermal stability exhibit a reduction in their interlayer spacings, which is attributed to the release of organic molecules by thermal desorption of organic ion, as well as the thermal decomposition of the organic molecule itself. In addition, the release of organic ions may make the surface of the organoclay less organophilic, which may also affect the melt intercalation of PP into the clay galleries as a result of the ensuing poorer compatibility.

In addition to the architecture of the alkylammonium surfactants, the loading of the surfactants in the organoclays has also been found to exert an important influence on the clay dispersion in the PP matrix. In particular, incomplete exchange of the

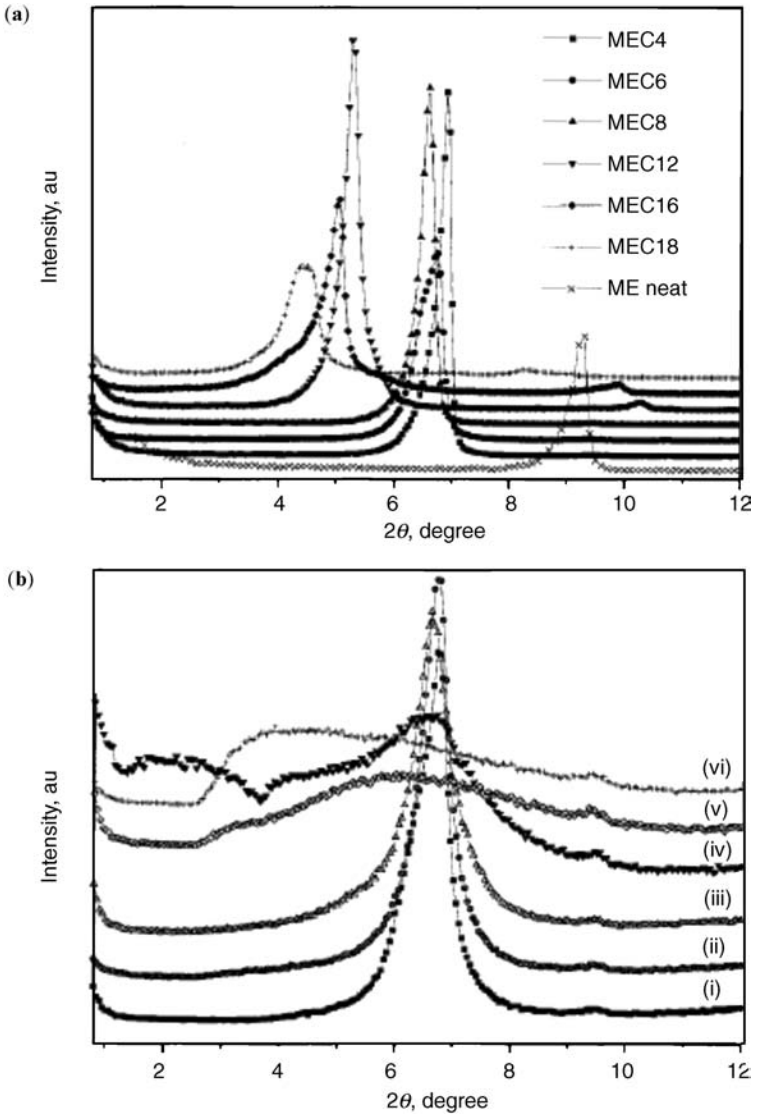

Figure 10.3 XRD patterns of (**a**) clays treated with protonated primary alkyl amines of different lengths. The clays are denoted by MEC*n*, where *n* represents the number of carbon atoms in the alkyl amine substituent; and (**b**) PP/clay hybrids prepared with the clays and 20 wt% of Hostaprime HC5 (20H) compatibilizer: (**i**) PP/MEC4; (**ii**) PP/MEC6; (**iii**) PP/MEC8; (**iv**) PP/MEC12; (**v**) PP/MEC16; (**vi**) PP/MEC18. (From Reference 6 with permission from Wiley-VCH Verlag GmbH, Germany.)

interlayer alkali ions has been found to have a beneficial effect on clay dispersion (12). This is attributed to the increase in the density of the surfactants on the clay surfaces with an increase in the surfactant loading, which tends to weaken favorable interactions between the polymer and the clay.

10.4.1.2 Other Intercalants and Additives

Although the use of alkylammonium surfactants has achieved a certain extent of success in facilitating the dispersion of clay in PP, their lack of thermal stability at the processing temperature of PP has been identified as a potential problem. The need for an additional ''compatibilizer'' to improve the clay dispersion in the PP matrix, even with the use of alkylammonium-modified clays, is also a cause of concern (Section 10.4.2.1). For these reasons, there have been various attempts to develop novel intercalants that can potentially bypass the above problems (13–17).

To allow PPCNs to be prepared with unmodified clays and to minimize the amount of compatibilizers incorporated in PPCNs, Moad et al. have explored the use of PEO-based nonionic surfactants as intercalants (13). The results show that the clay was partially intercalated by the nonionic surfactants, with the PEO-based surfactants of longer PEO blocks providing greater expansion of the clay layers. The resulting nanocomposites also exhibit significantly improved thermal stability and mechanical properties. Wilkie and coworkers (15–17) have also investigated the feasibility of using polymeric ammonium salts as a clay intercalant. Vinylbenzyl chloride was copolymerized with other vinyl monomers such as styrene and methyl methacrylate, and the copolymer was reacted with *N*,*N*-dimethylhexadecylamine to form the polymeric ammonium salt. Sodium clay was then modified with the ammonium salt and melt compounded with PP without using any compatibilizers. Exfoliated PPCNs, which also displayed improved thermal stability and mechanical properties, were obtained with this method. Manias et al. (18) have also suggested the use of semifluorinated surfactants, as they tend to have even more unfavorable interactions with the clay compared to the alkylammonium cations. By rendering PP–clay interactions to be more thermodynamically favorable, a coexisting intercalated and exfoliated structure can be achieved with PP, without the need for any compatibilizing agents.

Besides intercalants, attempts have also been made to incorporate other additives, such as antioxidants (19), silane coupling agents (20), and titanate coupling agents (21), into the system to improve the dispersion of clay.

10.4.2 Fabrication of PP/Clay Nanocomposites

Approaches that have been adopted to fabricate PPCNs include melt compounding (5–21), solution compounding (22–25). *in situ* polymerization (26–30), and solid-state shear compounding (31). The discussion in this section will be mainly focused on the melt-compounding route as it has been the most popular approach for the preparation of PPCNs due to its flexibility and compatibility with current industrial processes such as extrusion and injection molding. In addition, this method is environmentally benign as no organic solvents are required.

Melt compounding involves mixing the clay with PP and heating the mixture above the melt temperature of PP, usually above 180°C, in an extruder or mixer under shear. The success of the melt-compounding method in delaminating the clay depends on an interplay of both entropic and enthalpic factors. Although confinement

of the polymer within the clay galleries results in a decrease in the overall entropy of the polymer chains, this entropic penalty may be compensated by the greater conformational freedom of the tethered surfactant chains when the clay layers separate. For small increases in interlayer spacing, the total entropy change is expected to be small; thus, changes in the system's total enthalpy play a crucial role in determining whether intercalation is thermodynamically possible. Favorable enthalpy of mixing is achieved when the polymer/clay interactions are more enhanced in comparison to the surfactant/clay interactions (32,33).

Modification of the hydrophilic clay surface with organic surfactants (Section 10.4.1) enables the clay to be more organophilic and hence more compatible with PP. However, due to the absence of any polar groups in the PP backbone, unless an additional ''compatibilizer'' is incorporated into the matrix, there will still be no favorable excess enthalpy to promote the dispersion of the organoclay in the PP matrix (18,34). In this case, even the application of high shear intensity during melt processing will not be effective in delaminating the clay layers (34,35).

In the following section, the effects of the compatibilizers, PP matrix, and compounding process on the morphologies of the resulting PPCNs will be discussed to gain a greater understanding of their roles on the dispersion of clays in PPCNs.

10.4.2.1 Compatibilizer

10.4.2.1.1 Maleic Anhydride Grafted Polypropylene Maleic anhydride grafted polypropylene (PP-g-MA) is the most widely used compatibilizer for the preparation of PPCNs. It has been suggested that the compatibilizing effect of PP-g-MA originates from the strong hydrogen bonding between the maleic anhydride (MA) groups (or the COOH groups generated from the hydrolysis of the MA group) and the oxygen groups of the clay (22, 34, 36, 37). The intercalation of PP-g-MA into the clay layers helps to expand the clay gallery spacing as well as weaken the interactions between the clay layers. When the PP-g-MA-intercalated clays contact PP under a strong shear field, the delamination of the intercalated clay can occur if the miscibility of PP-g-MA with PP is good enough for it to be dispersed at the molecular level. It is, however, well known that natural smectite clay surfaces have –OH groups only at their edges, and with their contents being generally low, it seems improbable that interactions with them would lead to exfoliation (38). Mulhaupt et al. have suggested that anhydride groups may react with octadecylamine and lead to strong hydrogen bridges between the *N*-octadecyl-succinimide-grafted polypropylene and silanol groups at the clay surface (39). Pukanszky et al. (35), however, pointed out that the formation of hydrogen bridges between the functionalized PP and the clay surface is not the most important factor. Through model reactions, they found that the chemical reaction between the PP-g-MA and the surfactant plays an important role in determining the level of clay dispersion achieved. If the surfactant does not contain any active hydrogen groups, then no chemical reactions can take place and only a microcomposite will be formed.

The effectiveness of PP-g-MA as a compatibilizer is dependent on its molecular structure, as well as its molecular weight. In order to achieve good dispersion of clay

in PP, the oligomers must contain sufficient polar groups so that it can be intercalated into the clay layers via hydrogen bonding. Excessive MA in PP-g-MA will, however, hamper diffusion of PP into the clay galleries because of the large polarity difference between PP and MA. Furthermore, oligomers possessing high MA contents will tend to interact with the organoclay instead and be trapped within the clay interlayers. Such kinetic limitations will preclude further intercalation of other molecules. The amount of polar functional groups in PP-g-MA must thus be optimized in order for well-dispersed PPCNs to be obtained (34). In particular, Marchant and Jayaraman (40) have suggested that the molar ratio of functional groups to compatibilizer chains is a better parameter for ranking the compatibilizer effectiveness than the acid number, which is a weight ratio. With a higher value of the molar ratio, a lower concentration of compatibilizer will be required to achieve a similar extent of clay dispersion.

The dispersion in PPCNs can also be greatly influenced by the molecular weight of the PP-g-MA. The use of PP-g-MA with a low molecular weight and high grafting content can lead to relatively good and uniform intercalation with clay (41). However, the lack of miscibility with the PP matrix will preclude further delamination. On the contrary, PP-g-MA with a higher molecular weight tends to provide only limited intercalation with clay, as its low grafting content will limit intercalation with the clay. However, because of the longer chain length and better miscibility with PP, a greater level of interaction with the PP matrix can be achieved, which will facilitate the formation of a partially exfoliated structure. The effect of molecular weight is also related to rheological factors because the shear viscosity of PP-g-MA is sensitive to its molecular weight. PP-g-MA of low molecular weight is unable to generate sufficient torque for extensive exfoliation of organoclay. On the contrary, nanocomposites prepared from PP-g-MA of low melt flow index (corresponding to a medium-to-high molecular weight) and a moderate degree of grafting can exhibit a large extent of clay delamination under the same processing conditions (42–44).

10.4.2.1.2 Chain End Functionalized PP Although grafted functional PPs are most commonly employed as compatibilizers for the preparation of PPCNs, they possess several serious shortcomings, such as the tendency for severe molecular weight reduction as a result of chain degradation during the grafting process. To overcome the problems associated with their use, several groups have attempted to prepare side chain functionalized PPs for potential applications as compatibilizers. The functional groups that have been explored include hydroxyl, chlorine, and sulfochloride groups (45–47).

More recently, Manias and Chung (48–50) have synthesized a new type of end-functionalized PP that contains a terminal functional group (such as OH, COOH, NH_2, anhydride, etc.) and at the same time maintains a well-controlled molecular weight as well as a narrow molecular weight distribution. In particular, the ammonium group terminated PP (PP-t-NH_3^+) has been directly compounded with untreated clay and an organoclay. Although the end-functionalized PP possesses only a low concentration of functional groups, it exhibits a distinct advantage over other functionalized PP polymers containing side chain functional groups or long functional blocks, as a result of its unique structure and the high molecular weight of

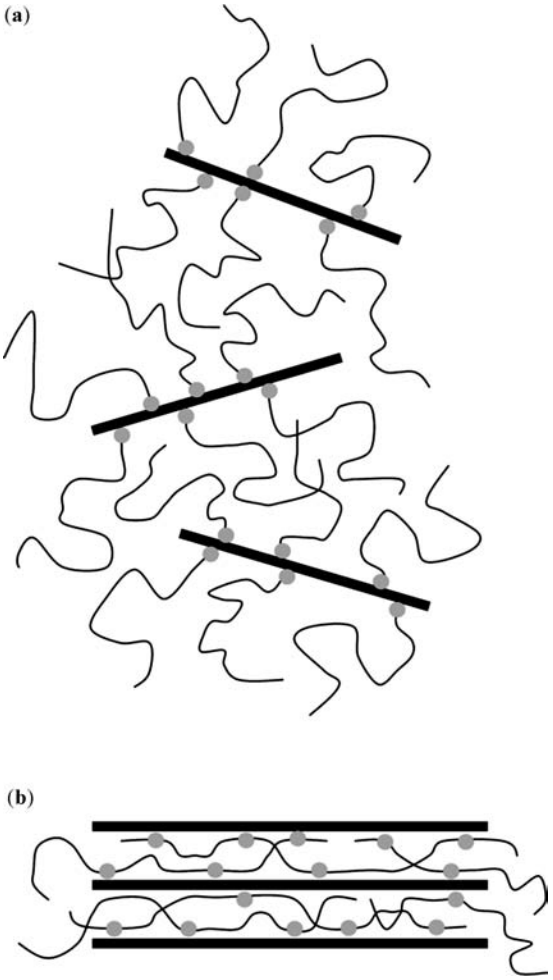

Figure 10.4 Illustration of the molecular structures of (**a**) chain end functionalized PP and (**b**) side chain functionalized PP located between the clay interlayers. (From Reference 48 with permission from American Chemical Society, USA.)

the main chain. As shown schematically in Fig. 10.4a (48), the terminal hydrophilic NH_3^+ cations, with good mobility and reactivity, effectively ion exchange with the cations (Li^+, Na^+, or the alkylammonium surfactants) located between the clay interlayers and anchor the PP chain to the clay surfaces. At the same time, the remaining unperturbed, end-tethered, high molecular weight PP tail helps to exfoliate the clay layers. This exfoliated structure is maintained even after further mixing with neat PP. In contrast, side chain functionalized or block copolymer PPs form multiple contacts with each of the clay surfaces (Fig. 10.4b), which not only aligns the polymer chains parallel to the clay surfaces but also bridges consecutive clay platelets, thus promoting the formation of intercalated structures.

In addition to its effectiveness in promoting clay exfoliation, the fact that an organic surfactant is not required to promote compatibility between the end-functionalized PP and the untreated clay also eliminates previous concerns associated with the thermal stability of the compatibilizers during high temperature melt processing and the long-term stability of the organic surfactants in the PPCNs under various application conditions.

10.4.2.2 PP Matrix

The effect of the PP molecular weight on the intercalation behavior and final morphology of the PPCNs is complicated. On one hand, a matrix of higher molecular weight can impose a greater shear stress during melt compounding (due to its higher viscosity), which will facilitate the delamination of the clay platelets. On the other hand, increasing the length of the PP chains will further increase the thermodynamic barrier for the intercalation of the PP polymer into the clay galleries. In the PP system, the second effect is more dominant over the first; thus, PP polymers with a lower molecular weight and higher melt flow rate are more favorable for clay delamination (51).

10.4.2.3 Melt-Compounding Process

10.4.2.3.1 One-Step Compounding Most PPCNs are produced via a one-step compounding route in a twin-screw extruder, in which neat PP, the compatibilizer, and the organoclay are premixed in the solid state before being introduced into the extruder. In addition to the composition of the PPCNs, the processing conditions, such as the configuration and *L*/*D* ratio of the screw, the screw speed, the barrel temperature, the feeding speed as well as the residence time, are also important factors controlling the final morphology of the PPCNs.

Modesti et al. (52) have found that the shear stress exerted on PP during melt compounding has a greater influence on the extent of clay intercalation and delamination than the residence time. As the viscosity of a polymer melt is inversely proportional to the temperature, the barrel temperature is a very important parameter that controls the clay dispersion. A lower processing temperature will increase the apparent melt viscosity and the shear stress imposed by the melt, which will be more favorable for achieving a greater extent of clay exfoliation.

The shear rate is another factor that is often considered. Hasegawa and Usuki (44) examined the effect of shear rate by sandwiching a PPCN premix in a cone plate viscometer and applying shear to the samples at constant shear rates. As shown in Fig. 10.5, the clay dispersion is not changed significantly after shearing at a rate of 20 s^{-1} for 10 min; at a higher shear rate of 50 or 100 s^{-1}, however, most of the clay layers are homogeneously dispersed after 2 min.

Lertwimolnun and Vergnes (53,54) have investigated the effects of feed rate and screw speed on the degree of clay dispersion achieved in a twin-screw extruder. The degree of exfoliation is enhanced when the feed rate is reduced and the screw speed is increased. The authors also suggested that the melt yield stress, which tends to

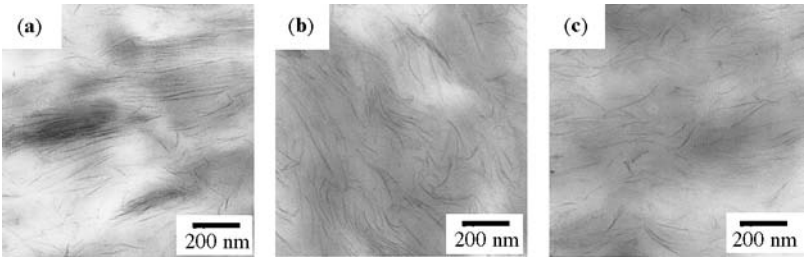

Figure 10.5 TEM images of PPCN samples after being sheared at rates of (**a**) 20 s^{-1}, (**b**) 50 s^{-1}, and (**c**) 100 s^{-1}. (From Reference 44 with permission from John Wiley & Sons, Inc., USA.)

decrease with increasing feed rate/screw speed ratio, is the most important parameter controlling the level of exfoliation.

The effects of feed location and the order of feeding were also considered by Wang et al. (55). In particular, "hopper feed," in which the PP matrix was fed upstream through the main hopper and the premixed clay/PP-g-MA powder was fed downstream at the second barrel, was compared with "side feed" in which the premixed clay/PP-g-MA powder was fed upstream and PP was fed downstream at the fourth barrel. XRD, TEM, and rheological characterization indicated that the PPCNs prepared with side feed achieved a better dispersion compared to those prepared with hopper feed. It was suggested that, in the hopper feed process, the PP melt together with the PP-g-MA and interfere with the wetting of the clay tactoids by the compatibilizer. In the side feed process, however, PP-g-MA can be melted in the first mixing section without the presence of PP; hence, a longer time is available for mixing the clay and the PP-g-MA to achieve a more complete wetting of the organoclay by PP-g-MA.

10.4.2.3.2 Two-Step Compounding To improve the versatility of PPCNs, as well as to enhance the dispersion of clay in PP, a two-step masterbatch compounding process has often been employed. The process involves the preparation of a higher concentration PPCN masterbatch, which is then diluted with neat PP in a second compounding cycle to give the desired composition. Zhu and Xanthos (56) compared the clay dispersion achieved in a two-step compounding process with that obtained in a one-step process. It was found that the two-step mixing process helps to achieve a better exfoliation of clay; however, it was also pointed out that the structures of the clay platelets were mostly determined during the preparation of the masterbatch, and the improvement brought about by the dilution is actually quite small. A similar conclusion was also obtained by Hong et al. (57) who stated that the clay dispersion was mostly achieved during the first compounding step, and further exfoliation of clays did not occur in the second step.

10.4.2.3.3 Reactive Compounding Reactive compounding, which makes use of the driving force of reactions to peel apart the clay layers, has also been explored by several groups as a potential route for the preparation of PPCNs. Liu and

Wu (58) have prepared PPCNs via grafting–melt compounding, by using a novel organoclay that was cointercalated by a common alkylammonium, an unsaturated monomer (epoxypropyl methacrylate), as well as a free radical initiator. The organoclay has a significantly larger interlayer spacing (2.98 nm) compared to the conventional organoclay (1.96 nm). In addition, one of its cointercalation monomers is unsaturated, which allows it to be attached to the PP backbone by a grafting reaction. XRD and TEM verify that the larger interlayer spacing and strong interaction arising from the grafting reaction help to improve the dispersion of clay in the PP matrix.

Tjong et al. (59) explored the use of maleic anhydride as a reactive reagent for the *in situ* formation of PP/vermiculite nanocomposites during extrusion. The MA acts as both a swelling agent for the clay and a modifying agent for PP. The results show that the MA molecules can easily enter the galleries of acid-treated clay and effectively extend the gallery spacing. At the same time, it can be readily melt grafted onto the PP chains and improve the affinity between the resulting MAPP and vermiculite. This method thus allows the preparation of PP/vermiculite nanocomposites by simple melt mixing of PP and MA-modified clay.

More recently, Wang et al. (60–62) have proposed another masterbatch-related reactive compounding approach to obtain PP/clay nanocomposites. The masterbatch was prepared by a ''slurry compounding'' method (63,64) with epoxy oligomer as the carrier resin. PP and the masterbatch were then melt compounded in the presence of PP-g-MA. The MA on the PP was expected to react with the epoxy group on the oligomers, to form a block copolymer of PP and epoxy during the melt-compounding process. This copolymerization process has double impact on the structure and property of the nanocomposites: the copolymer acts as a compatibilizer between PP and epoxy, which helps to promote the dispersion of the clay layers; at the same time, the copolymerization helps to minimize the adverse effect due to the low molecular weight components, including the PP-g-MA and epoxy oligomers, on the performance of the final material.

10.4.2.3.4 Special Compounding Methods To further improve the efficiency of the melt-compounding process, several groups have also attempted to incorporate additional accessories in the processing equipment, which are specially designed to facilitate the dispersion of clay. Guo et al. (65,66) have prepared PPCNs via an ''ultrasonic extrusion technology,'' in which the extrusion system was equipped with a special cylinder die that generates ultrasonic oscillations during the compounding process. The oscillations produce local shear in the melt, which helps to further disperse the clay. Although intercalated nanostructures are formed in both the conventional and ultrasonicated PPCNs, a finer dispersion of clay, with smaller aggregates and several exfoliated layers, is observed in the ultrasonicated PPCN. Improved clay dispersion was also reported by Lee et al. (67), who applied a similar method of *in situ* ultrasonication of the polymer melt phase via an ultrasonic horn.

Dynamic packing injection molding (DPIM) was also investigated by Wang et al. (68) in the preparation of PPCNs. In DPIM, shear stresses are applied to the

PPCN melt during the packing stage of injection by means of hydraulically actuated pistons that force the melt to move repeatedly with the same frequency as the solidification progressively occurs from the mold wall to the core part. The degree of exfoliation is found to dramatically increase from the skin to the core of the prepared samples, which is attributed to the continuous improvement of shear stress from the skin to the core during melt solidification. The results thus also indicate that there is a critical shear stress, which needs to be applied in order for clay to be delaminated effectively.

Finally, Kato et al. (69,70) have developed a direct compounding method for the preparation of PPCNs, which does not require any pretreatment of clay with organic surfactants. In this method, a specially designed twin-screw extruder, in which the screw is equipped with four geometrical sections and a much longer length-to-diameter (*L*/*D*) ratio (77:1), is used. PP, PP-g-MA, untreated clay, and the alkylammonium salt are fed into the extruder in the first section and premixed. Water is injected into the second section of the extruder to disperse the clay into a slurry state in PP. Water is then evaporated in the third and fourth sections of the extruder. With this method, clay can be exfoliated and uniformly dispersed in PP. In addition, they exhibit mechanical properties that are as good as PPCNs prepared by the conventional method.

10.5 CHARACTERIZATION OF PP/CLAY NANOCOMPOSITES

The structures and properties of PPCNs are often profoundly influenced by the dispersion of clay at the nanoscale. In this section, the structures and properties exhibited by the PPCNs, as well as the underlying mechanisms responsible for the changes, will be discussed. As PP is often mixed with PP-g-MA in the preparation of PPCNs, the structural and property changes are often compared against the MAPP instead of the PP homopolymer.

10.5.1 Microstructures

As PP is a semicrystalline polymer, the presence of the dispersed clay phase may exert an important influence on the crystal structure, morphology, and orientation that develops in the PP crystalline phase. An understanding of the microstructures exhibited by PPCNs is thus an important aspect by which their properties may be better predicted and controlled.

10.5.1.1 Crystal Structure

Isotactic PP (iPP) can exist in three different crystalline forms—α, β, and γ. Zheng et al. have studied the effects of clay on the polymorphism behavior of iPP under various thermomechanical conditions (71). It was found that under compression at 200°C and subsequent crystallization at 120°C, significant β-phase crystallites can

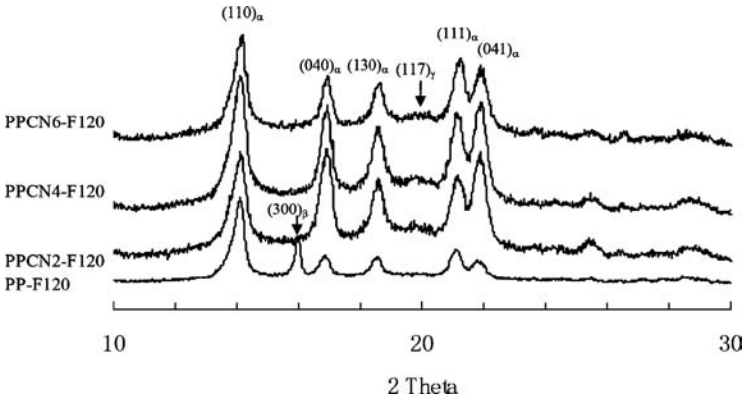

Figure 10.6 X-ray diffraction patterns of PP and PPCN film samples prepared by isothermal crystallization at 120°C on the hot press. (From Reference 71 with permission from John Wiley & Sons, Inc., USA.)

develop in neat PP. Under the same crystallization conditions, however, no trace of β-crystallites was detected in the nanocomposites (Fig. 10.6). The results thus indicate that clay strongly inhibits the formation of the β-crystal form in iPP. It was proposed that the clay may greatly speed up the crystallization process of the α-crystallites, while it has an insignificant effect on the crystallization rate of the β-crystal form. Once the α-crystallites develop to a significant amount and size, the growth of the β-crystallites becomes inhibited, so that when they are nucleated, they become unstable.

The presence of a very weak (117)γ peak in the diffractograms of the PPCNs also suggests that the presence of clay may slightly promote the formation of the γ-crystal phase in PP. As the γ-phase PP crystallites are nucleated on the α-phase lamellae, the fact that clay tends to enhance α-phase formation justifies the possibility that clay may also slightly promote the formation of the γ-crystal form. The enhancement of the formation of the γ-crystal form in PPCNs is also observed by Nam et al. (72); however, they proposed that this phenomenon is due to the narrow space surrounding the dispersed clay particles in the nanocomposite, and the intercalation of the PP chains in the clay galleries, which tend to reduce the mobility of the PP chains.

10.5.1.2 Crystalline Morphology

Figure 10.7 displays the typical spherulitic textures exhibited by MAPP and the PPCNs after crystallization at 130°C for 12 h. The presence of clay results in the formation of smaller spherulites with a broader spherulitic region. Furthermore, in contrast to the positive spherulites observed in MAPP, the spherulites in the PPCNs exhibit negative birefringence, which is attributed to the sufficiently low proportion of crosshatched lamellae in comparison to the radial lamellae (73).

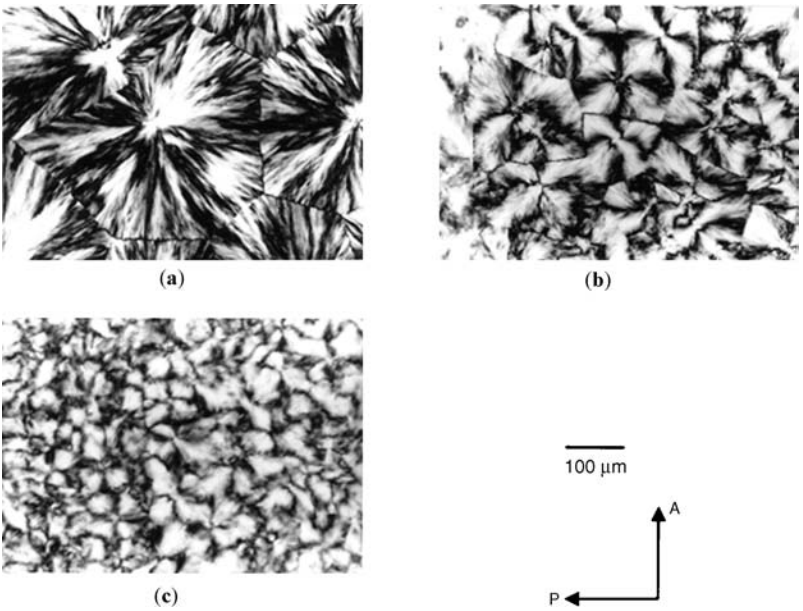

Figure 10.7 Polarized optical micrographs of MAPP and PPCNs after complete solidification at 130°C: (**a**) MAPP, (**b**) PPCN2, and (**c**) PPCN7.5. The numbers following the PPCN indicate its clay content in wt%. (From Reference 73 with permission from American Chemical Society, USA.)

Light scattering further reveals that although MAPP exhibits a four-leaf-clover pattern, the scattering patterns of the PPCNs were smeared, or even rodlike with increasing clay content, which indicates the formation of less-ordered spherulites in the PPCNs. In particular, the rodlike scattering pattern is ascribed to the parallel arrangement of radiating primary lamellae and the disordered arrangement of cross-hatched lamellae (72,73).

Morphological parameters derived from small-angle X-ray scattering (SAXS) indicate that the long period and average lamellar thickness of the PPCNs are in the same order of magnitude as the average thickness and correlation length of the dispersed clay particles (72). Based on these results, it was suggested that the lamellae structure of the PPCNs develops mainly in the space surrounded by the dispersed clay particles. The presence of clay in the interfibrillar position causes the spherulites formed in the PPCNs to be disordered.

10.5.1.3 Orientation

The orientation behavior of PPCNs during uniaxial drawing was investigated by Koo et al. (74). Two-dimensional X-ray diffraction (2D XRD) and TEM indicate that the high aspect ratio clay platelets tend to be aligned parallel to the specimen surface during uniaxial drawing. 2D XRD further shows that the c and a^* axes of the PP

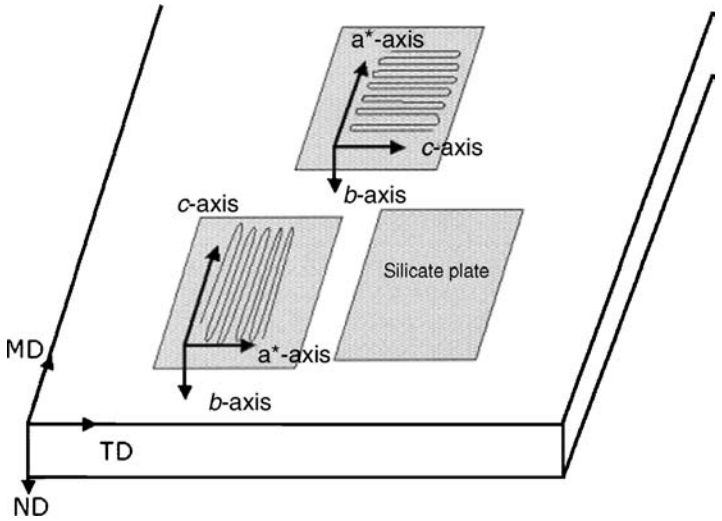

Figure 10.8 Schematic illustration of the orientations of clay and PP crystallites. (From Reference 74 with permission from John Wiley & Sons, Inc., USA.)

crystallites are bimodally oriented to the flow direction, while the *b* axes are oriented along the thickness direction of the specimens. Figure 10.8 schematically illustrates the orientations of the clays and the PP crystallites in the PPCNs.

10.5.2 Thermal Transitions and Stability

10.5.2.1 Glass Transition Behavior

Table 10.1 displays a comparison of the glass transition temperatures (T_g) of a PPCN along with its matrix materials, as derived from dynamic mechanical analysis (DMA) (34). The slightly lower T_g of the PPCN is probably attributed to the lower T_g of the MAPP matrix that is used to prepare the nanocomposite. The presence of organic surfactants in the organoclay could also give rise to some plasticization effect and lead to some reduction in the T_g of the PPCN.

Table 10.1 Glass Transition Temperatures of a 5 wt% PPCN and the Related Matrix Materials.

Sample	PP	MAPP	PPCN
T_g, °C[b]	13	10	8

From Reference 34 with permission from American Chemical Society, USA.

[b]As derived from the peak in the tan δ versus temperature curve in DMA.

10.5.2.2 Crystallization and Melting Behaviors

Isothermal crystallization studies on the differential scanning calorimetry (DSC) (75) indicate that the presence of clay can significantly reduce the crystallization time of PP. Together with the polarized optical microscopy observations, it was proposed that clays enhance the crystallization rate of the matrix by acting as heterogeneous nuclei during the nucleation of PP crystallites (73,75).

The effect of clay content on the melting temperature (T_m) of MAPP was investigated by Kim et al. (76). It was found that the T_m of MAPP is relatively independent of the clay content, and that there is effectively no difference between the T_m of a phase-separated PP/clay hybrid and an exfoliated PPCN. A similar conclusion is obtained by Maiti et al., who found no difference in the equilibrium melting temperatures of MAPP and the PPCNs by carrying out a Hoffman–Weeks plot (73).

10.5.3 Mechanical Properties

10.5.3.1 Tensile and Flexural Properties

PPCNs often exhibit tremendously improved stiffness and strength at relatively low clay loadings (under 5 wt%). This is a major strength of PPCNs over many conventional composite systems because this indicates that the mechanical property enhancements can often be achieved without the penalty of an increased density. For example, the tensile and flexural moduli exhibited by a 4 wt% PPCN are comparable to those of a 20 wt% talc-filled PP (77). Specific gravity measurements further indicate that the PPCNs exhibit a 12% mass saving compared to the talc-filled PP. In addition, PPCNs do not display the property trade-offs that are typically associated with traditionally filled systems. For instance, although the addition of talc can enhance the modulus of PP, this is obtained with the accompanying loss of yield strength and fatigue strength. On the contrary, PPCNs display concurrent enhancements in their yield strength and fatigue strength along with their modulus increase (78), while exhibiting only a small decrease in the maximum strain at break (18).

The reinforcing effectiveness of nanoclay in PPCNs is mainly dependent on its dispersion state in the matrix, as well as the interfacial interactions between the clay and the matrix. A greater extent of clay delamination increases the aspect ratio as well as the interfacial area of the dispersed clay phase, which allows the stress transfer from the matrix to the clay to be more effective. Because of this correlation between dispersion state and mechanical properties, the mechanical behavior of PPCNs exhibits a strong dependence on the type and amount of surfactants used to modify the clay surface, the type and amount of compatibilizers used, as well as the processing conditions employed for the preparation of the PPCNs.

The impact of the alkyl chain length of the interlayer ammonium cation on the tensile properties of the PPCNs is studied by Reichert et al. (6). Figure 10.9 indicates that when the number of carbon atoms in the alkyl chain increases from 8 to 12, a sharp jump is observed in the Young's modulus and yield stress exhibited by the PPCNs. This sharp improvement corresponds to the length of alkyl chain that is

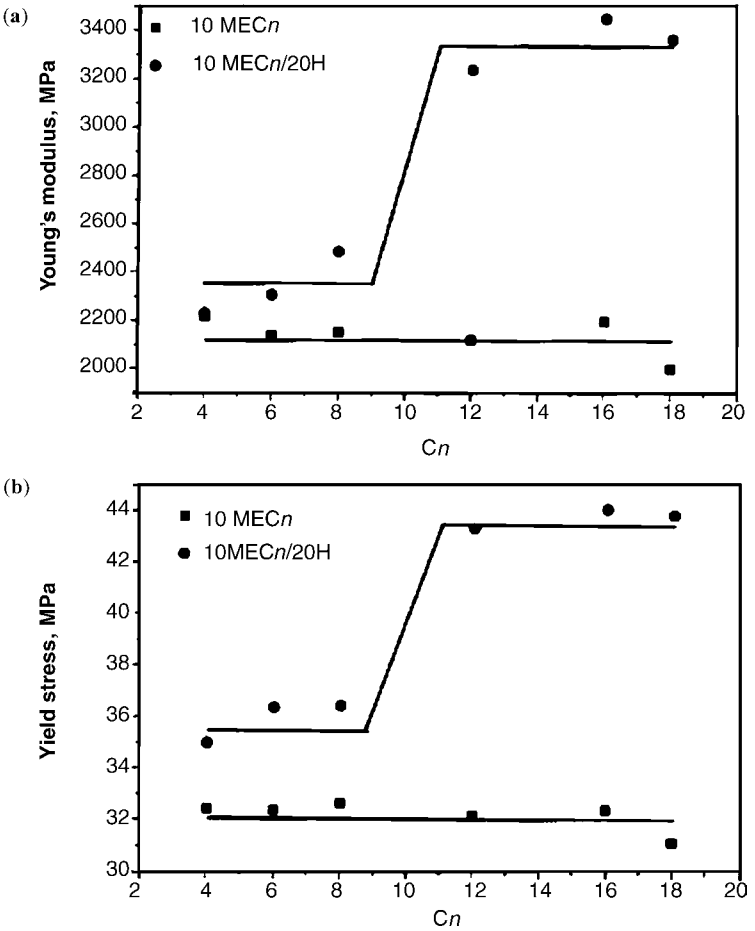

Figure 10.9 (**a**) Young's modulus and (**b**) yield stress as a function of the chain length of the interlayer ammonium cation (C*n*, where *n* refers to the number of carbon atoms in the alkyl chain). The comparison is made between PPCNs prepared in the absence and presence of 20 wt% of Hostaprime HC5 compatibilizer (abbreviated as 20H). (From Reference 6 with permission from Wiley-VCH Verlag GmbH, Germany.)

required in order for the clay modification to be effective to achieve good dispersion in the PPCNs (Section 10.4.1.1). Excess surfactants have, however, been found to be deleterious to the mechanical properties, which is attributed to the plasticization effect of the surfactant chains on the polymer matrix. When excess modifiers are removed by Soxhlet extraction, an improvement in the flexural modulus is observed (79).

The use of compatibilizers also has a significant influence on the mechanical properties exhibited by the PPCNs. In the absence of compatibilizers, a much smaller improvement in the Young's modulus and yield stress is achieved (Fig. 10.9). The addition of compatibilizers helps to enhance the interfacial coupling between PP and

the organoclay; as a result of the better dispersion of clay and stronger organoclay–matrix interactions, a corresponding increase in the Young's modulus and yield stress is observed (6,52,80). The mechanical enhancement brought about by the addition of compatibilizers is also dependent on the chemistry of the compatibilizers employed. The use of PP-g-MA with a low molecular weight and a high MA content is usually not favored because of their poorer intrinsic mechanical property, poor thermal stability at the processing temperature, as well as their relatively poorer compatibility with the PP matrix. On the contrary, the use of high molecular weight PP-g-MA helps to significantly improve the tensile and flexural properties of PPCNs (81), because of their high molecular weight and thermal stability, as well as their good compatibility with both PP and organoclays, which helps in the formation of a stronger interface (81,82). The amount of PP-g-MA added must also be carefully controlled—sufficient PP-g-MA compatibilizers must be added to ensure that adequate interactions between PP and the organoclay are achieved; however, excessive PP-g-MA will lead to a deterioration of the PPCN properties. Xu et al. have found that the maximum values for the tensile strength are achieved when the PP-g-MA content is 10 wt% (83).

The mechanical properties exhibited by the PPCNs can also be affected by their processing conditions. The greatest tensile and flexural moduli are observed when a higher screw speed (i.e., higher shear rate) and a lower barrel temperature profile are employed during melt compounding (52). Furthermore, the tensile strength and modulus of PPCNs prepared via a masterbatch or thermokinetic mixer tend to be higher than those prepared with the traditional one-step extruder compounding, due to the better clay dispersion that is achieved using these methods (57,81).

Additional enhancement in the mechanical properties of the PPCNs can be achieved by further enhancing the adhesion between the matrix and clay. When MA functional groups are incorporated into the PP backbone, a greater increase in the tensile properties (compared to PPCNs with the same clay loading) is observed because the stresses can be more effectively transferred from the polymer matrix to the clay (18). A greater increase in the Young's modulus and yield stress is also observed in a PPCN, in which the hydroxyl edges of the clay have been replaced by nonpolar organic silane (20). The silane groups not only help to reduce the attractive interactions between the clay edges, but also enhance the interactions between the polymer and the platelet edges, so that a better dispersion of clay and a more profound improvement in the tensile properties is attained.

10.5.3.2 Impact Strength and Fracture Toughness

The incorporation of nanoclay at low concentrations (0.5–2 wt%) has been found to improve the impact strength of PP (84,85). Modesti et al. (52) suggested that exfoliated or intercalated clay layers may help to hinder the crack path caused by impact. During impact, the stress in the sample may be dispersed by the intercalated or exfoliated clay layers, which possess higher strength and modulus than the matrix. This effect is further enhanced when the interaction between the clay and matrix is strengthened. A further increase in the clay concentration, however, results in a

reduction in the impact strength, which is probably due to the aggregation of clay and poor intercalation. The crystalline morphology of the PPCNs may also contribute to its impact performance—Svoboda et al. observed a reduction in the impact strength of a well-dispersed PPCN system, in which the spherulite size remains almost the same. On the contrary, a less well-dispersed system displays a slight increase in its impact strength, which is attributed to the smaller size of the spherulites formed (82). Further studies are, however, required to clarify the length scale and size at which toughening can take place in clays, as well as the possible part that could be contributed by the PPCN crystalline morphology.

Chen et al. (86,87) have reported a simultaneous substantial increase in the tensile strength, modulus, and initiation fracture toughness in a PPCN containing 2.5 wt% clay. Further increase in the clay content only leads to stiffening and strengthening at the expense of the fracture toughness. A plot of the *J*-integral initiation fracture toughness versus the plastic zone size indicates that the toughness increase in the nanoclay-reinforced MAPP arises from the increase in the plastic zone, which results from the plastic deformation in the reinforced matrix. The macroscale three-point bend fracture data were supported by TEM observations of the subcritically loaded crack tip deformation zone, which show that microvoids are generated near the crack tips, as well as SAXS examinations of deformed tensile specimens, where the PPCN with a 2.5 wt% clay concentration exhibits the highest equatorial scattering (a measure of the concentration of craze deformation and voiding in the matrix). Further increase in the clay loading above 2.5 wt% reduces the scattering, the matrix plasticity, and thus the fracture toughness. The results thus provide evidence that nanoclays toughen the PP matrix by enhancing the energy-absorbing mechanisms in front of the crack tip.

Based on essential work of fracture (EWF) testing and fractographic analysis, Bureau et al. (80) have also found that the fracture toughness and fracture surface features exhibited by PPCNs are dependent on the microscopic distribution of clay in the PPCNs. Micron-sized clay particles are found to act as void nucleation sites within the PP matrix, which gives rise to higher void nucleation, reduced void growth, and rapid void coalescence in the matrix, along with extensive fibrillation. This not only results in an important reduction in the fracture toughness with respect to PP, but also gives rise to an increase in the plastic work dissipation. PPCNs prepared via a one-step compounding route in the presence of a PP-g-MA compatibilizer display an improvement in the fracture toughness in comparison to uncompatibilized PPCNs, along with an increase in the plastic work dissipation. The results demonstrate that effective coupling of the particles is obtained with the use of compatibilizers. Precompounding of clay in PP results in a different microscopic distribution of clay, which is characterized by a very large surface particle density, compared to PPCNs prepared via a one-step compounding route. The fracture toughness exhibited by these PPCNs is similar to those of unfilled PP, and considerably higher than those obtained for the one-step PPCNs. It is surmised that the very high average surface particle density leads to more extensive void nucleation than in neat PP, but not as extensive as in the one-step PPCNs. It is thus suggested that the considerably higher number of particles with good clay–matrix

adhesion in the PPCNs gives rise to intermediate void nucleation and further fibrillation, which probably accounts for the higher fracture toughness observed for these PPCNs.

Some studies have, however, reported a reduction in the impact strength of PP with the addition of clay. This effect has been attributed to the degradation of the organic clay modifiers (81), or the high content of the PP-g-MA compatibilizer added (6,57). At high PP-g-MA content, the free radical MA grafting process is accompanied by chain scission, which results in the production of low molecular mass PP-g-MA. A high content of such oligomers is detrimental to the impact performance. Incompatibility may also arise with a high MA content, which can also contribute to the lower impact strength observed. To summarize, until now, the reports on the effects of clay addition on the impact strength of PP are still controversial and more studies are required in order to better understand the micro-deformation and fracture mechanisms of PPCNs.

For most applications, an optimum balance of stiffness and toughness is desired. To improve the impact strength and fracture toughness of PPCNs, attempts have also been made to incorporate elastomers such as polyethylene–octene copolymer (POE) (88–90), styrene–butadiene–styrene copolymer (SBS) (91), and MAH-g-SBS (92) into PPCNs.

10.5.4 Thermomechanical Behaviors

10.5.4.1 Thermodynamic Mechanical Properties

The thermomechanical behavior of a polymeric material is typically studied by DMA. In DMA, the response of a material when subjected to an oscillatory deformation is measured as a function of temperature. From DMA, three important parameters can be obtained: the storage modulus (E'), which indicates the elastic response to the deformation, the loss modulus (E''), which indicates the plastic response to the deformation, and the loss tangent (tan δ), which is derived from the ratio of E''/E'. In particular, the storage modulus is of special interest, because the stiffness of a polymer is strongly dependent on its E' value.

The dynamic mechanical behaviors of PPCNs prepared from MAPP matrices containing different amounts of maleic anhydride groups (PP-g-MA-1001, acid value = 26 mmol KOH g^{-1}; PP-g-MA-1010, acid value = 52 mmol KOH g^{-1}) were investigated by Kawasumi et al. (34) (Fig. 10.10). Table 10.2 summarizes the storage moduli of the PPCNs and related materials at various temperatures.

It was observed that the storage modulus of PPCH-C18-Mt/1010 is higher than that of PP below 120°C, while that of PPCH-C18-Mt/1001 is higher than that of PP below 140°C. The lower moduli of the PPCNs above these temperatures are attributed to the lower softening points of the MAPPs with respect to PP. In addition, it was observed that the modulus improvement below T_g (~10°C) is relatively small (~1.3 times that of PP); above T_g, however, a greater improvement in the storage modulus (~1.6–1.7 times that of PP) is obtained. Above T_g, the amorphous part of the matrix softens; hence, the reinforcement effect exerted by

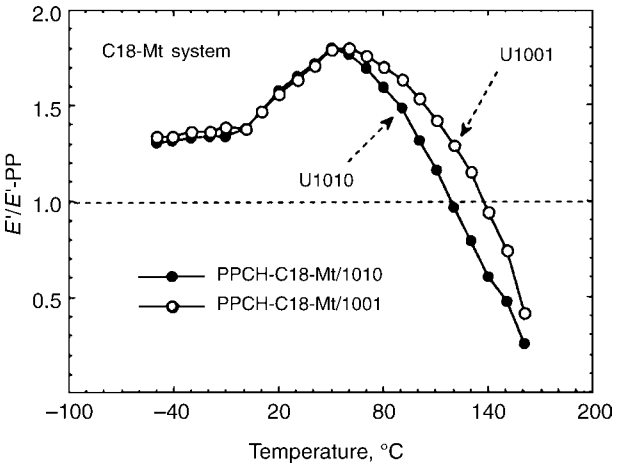

Figure 10.10 Variation of the relative dynamic storage moduli (E'/E'-PP) of PPCNs to that of PP as a function of temperature. PPCH-C18-Mt/1001 and PPCH-C18-Mt/1010 denote the PPCNs prepared using PP-g-MA-1001 and PP-g-MA-1010 as compatibilizers, respectively. The organoclay used is stearylammonium-modified MMT (C18-Mt). (From Reference 34 with permission from American Chemical Society, USA.)

clay becomes more prominent. In particular, the higher relative moduli of PPCH-C18-Mt/1001 with respect to PPCH-C18-Mt/1010 above 60°C can be attributed to the higher softening point of PP-g-MA-1001 in comparison to PP-g-MA-1010, as well as the better dispersibility of the clays in the MAPP-1001 matrix (due to its better miscibility with PP).

The effects of clay content and crystallization temperature (T_c) on the dynamic mechanical properties have also been studied by Maiti et al. (73). In particular, the storage moduli improvements of PPCNs crystallized at two extreme temperatures of

Table 10.2 Dynamic Storage Moduli of PPCNs and Related Materials at Various Temperatures (the Inorganic Content of the PPCNs is Fixed at 5 wt%).

	Storage modulus,[b] GPa		
Samples	−40°C	20°C	80°C
PPCH-C18-Mt/1010	5.15 (1.31)	3.12 (1.58)	1.03 (1.59)
PPCH-C18-Mt/1001	5.26 (1.34)	3.09 (1.56)	1.10 (1.70)
PP/C18-Mt	4.50 (1.15)	2.36 (1.19)	0.82 (1.26)
MAPP-1010	3.92 (1.00)	1.99 (1.01)	0.60 (0.92)
MAPP-1001	4.04 (1.03)	2.02 (1.02)	0.55 (0.85)
PP	3.92	1.98	0.65

From Reference 34 with permission from American Chemical Society, USA.
[b]Values in parentheses are obtained by taking the ratio of the storage modulus of the material to that of PP (E'-PP).

Table 10.3 Storage Modulus of MAPP and PPCNs Crystallized at 70 and 130°C, at 50°C (the Numbers Following the PPCN Refer to Their Clay Contents in wt%).

System	T_c, °C	Storage modulus, GPa	Percent increase
MAPP	70	0.292	9.9
	130	0.321	
PPCN2	70	0.479	−6.1
	130	0.450	
PPCN4	70	0.516	30.6
	130	0.674	
PPCN7.5	70	0.749	13.3
	130	0.849	

From Reference 73 with permission from American Chemical Society, USA.

70 and 130°C were compared (Table 10.3). From Table 10.3, it was clearly observed that the improvement in the storage modulus increases with the amount of clay present. More interestingly, Table 10.3 indicates that the effect of T_c on the improvement in the storage modulus increases in the order PPCN4 > PPCN7.5 > PPCN2. This phenomenon is related to the degree of intercalation that takes place in the PPCNs during the crystallization process. For PPCN2, the lower storage modulus of the sample crystallized at 130°C is due to the lower degree of intercalation achieved at 130°C than at 70°C. On the contrary, both PPCN4 and PPCN7.5 display an increase in their degree of intercalation from 70 to 130°C. PPCN4, in particular, achieves a much higher efficiency of intercalation at 130°C than PPCN7.5, which explains why it also exhibits the greatest modulus improvement as the crystallization temperature changes from $T_c = 70$ to 130°C. (The degree of crystallinity is eliminated as a possible factor contributing to the modulus improvement at 130°C, because the degree of crystallinity increases by about the same amount for MAPP and PPCN4.)

Another reason that contributes to the greater modulus improvement at 130°C is related to the segregation of the dispersed clay particles to the interspherulitic regions at 130°C, due to the slower rate of PP crystallization at this temperature. As the modulus of a semicrystalline polymer is determined by the stiffness of its intercrystalline regions, the higher concentration of clay at the interspherulitic region may also give rise to the greater modulus enhancement observed in the PPCNs crystallized at 130°C.

10.5.4.2 Heat Distortion Temperature

The heat distortion temperature (HDT) of a polymeric material is the temperature at which it undergoes an arbitrary deformation under a constant load. HDT is one of the key indicators of the load-bearing capabilities of the polymer at elevated temperatures. The incorporation of clays in PP has been found to increase its HDT (Table 10.4) (18). Table 10.4 also shows that the HDT improvement in the PPCNs

Table 10.4 Heat Distortion Temperatures (HDT) of PPCNs and Neat PP.

	HDT, °C	
Organoclay loading, wt%	PP/f-MMT[b]	PP/alkyl-MMT
0 (Neat PP)	109 ± 3	109 ± 3
3	144 ± 5	130 ± 7[c]
6	152 ± 5	141 ± 7[d]
9	153 ± 5	

[b] PPCN loaded with MMT, which is treated with a mixture of hydrogenated and fluorinated-alkyl surfactants.

[c] PPCN loaded with MMT, which is treated with octadecylammonium and processed with an extruder.

[d] PPCN loaded with MMT, which is treated with dimethyldioctadecylammonium and processed with a twin-head mixer.

tends to vary with the type of clays used. This indicates that the HDT improvement in PPCNs is also related to the level of clay dispersion in the PP matrix. The improvement in HDT originates from the more enhanced mechanical stability of the PPCNs, as no increase in the melting point is observed in the PPCNs. It is essential to note that the increase in HDT in PPCNs is a very significant property improvement, as it is very difficult to achieve similar HDT improvements by chemical modifications or reinforcement by conventional fillers (18).

10.5.5 Rheological Behaviors

An understanding of the rheological properties of PPCNs is an important aspect by which their melt processing can be better controlled. In addition, the rheological behaviors of PPCNs can provide useful clues on the mesostructure of the nanocomposites.

Solomon et al. have performed both linear and nonlinear rheological measurements on PPCNs in the melt state (93). Comparison of the linear viscoelastic response of the PPCNs with that of pure MAPP reveals that the addition of clay has a significant effect on both the storage (G') and loss (G'') moduli, especially at low frequencies. In particular, the G' and G'' values of the PPCNs were significantly enhanced with respect to neat MAPP. In addition, no terminal linear viscoelastic behavior was observed in the PPCNs beyond a clay loading of 2 wt%. The transition in viscoelastic behavior from liquidlike in the pure polymer (i.e., $G' \propto \omega^2$ and $G'' \propto \omega^1$) to solidlike in the PPCNs (i.e., G' and $G'' \propto \omega^0$) is attributed to the formation of a percolated network structure of the clay layers. Similar solidlike rheological behavior of the PPCNs has also been observed by Galgali et al. (94). The similar flow activation energies obtained for the pure MAPP and the PPCN further reveal that the solidlike behavior is attributed to the strong frictional interactions between the clay layers above the percolation limit, rather than the immobilization of confined polymer chains between the clay layers (94).

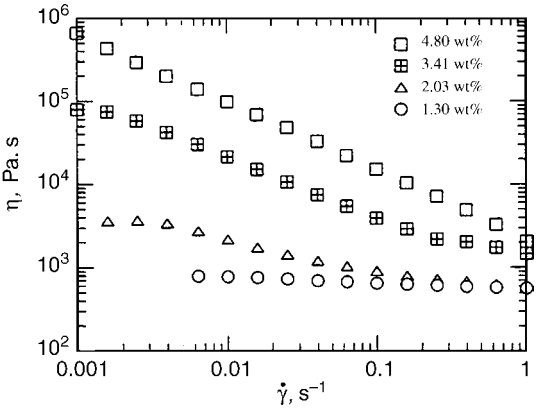

Figure 10.11 Shear rate dependence of the steady-state viscosity of PPCNs at various clay contents. The measurements were performed at 180°C. (From Reference 93 with permission from American Chemical Society, USA.)

The nonlinear dynamic response of the PPCNs (Fig. 10.11) indicates that the low shear rate steady viscosity of the PPCNs tends to increase monotonically with clay concentration. However, at high shear rates, a strong shear thinning behavior is observed, especially at higher clay loadings, which is attributed to the rupture of the agglomerated network of clay under the effect of shear. A similar phenomenon has also been reported by Gu et al. (95) who observed that at low shear rates, the addition of clay gives rise to a significant increase in the viscosity; but at high shear rates, the viscosities of the PPCNs become comparable to or even lower than that of neat MAPP, due to their shear thinning behaviors. The rheological behaviors exhibited by PPCNs thus indicate that they can enhance mechanical performance of PP without seriously compromising its processability.

10.5.6 Other Properties

10.5.6.1 Flame Retardancy

By itself, PP burns rapidly with a relatively smoke-free flame and without leaving a char residue because of its wholly aliphatic hydrocarbon structure. The incorporation of clays has been found to promote the flame retardancy of PP. Figure 10.12 displays the mass loss rate plots obtained for neat MAPP and PPCNs with 2 and 4 wt% of clay, under controlled combustion conditions with a cone calorimeter (96). A 4 wt% PPCN, for instance, exhibits a 75% reduction in flammability in comparison with the neat MAPP. The enhanced flame retardancy of the PPCNs is attributed to the formation of a carbonaceous char, which develops on the outer surface during combustion. The surface char contains a high content of clays and thus acts as an excellent insulator and mass transport barrier in slowing down the in-diffusion of oxygen and the out-diffusion of volatile combustion products.

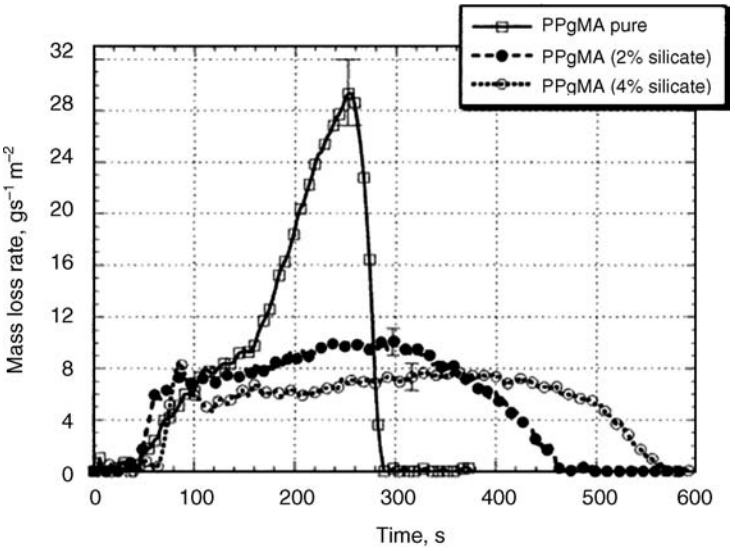

Figure 10.12 Mass loss rate plots during cone calorimetry combustion of pure MAPP and PPCNs containing 2 and 4 wt% clay. (From Reference 96 with permission from American Chemical Society, USA.)

Zanetti et al. (97) have also investigated the combustion behaviors of PPCNs in which conventional vapor phase fire retardants (FR), namely decabromodiphenyl oxide (DB) and antimony trioxide (AO), have been added. It was found that when DB and/or AO is present in the PPCN, a synergistic effect can be observed, which does not occur in the pure polymer under identical testing conditions.

10.5.6.2 Barrier Properties

The dispersion of clays in the PP matrix also results in a reduction of its permeability to gas and water vapor. Gas permeability reductions range from 24% for oxygen and 47% for carbon dioxide for a 6 wt% PPCN (98). This is attributed to the more tortuous diffusion path that needs to be taken by the diffusing molecules as they are forced to bypass the impenetrable clay platelets. As PP is already a low water vapor transmitter, the reduction in the water vapor transmission rate (14%) is more modest compared to the reductions in the oxygen and carbon dioxide transmission rates.

10.6 APPLICATIONS OF PP/CLAY NANOCOMPOSITES

The unique combination of properties exhibited by PPCNs has already found their applications in the automotive industry. The higher cost of the PPCNs is offset by its considerable lighter weight and other cost savings associated with its better processability and performance. General Motors introduced the first commercial PPCN

automotive exterior on the step assist of its GMC Safari and Chevrolet Astro vans in 2002. In January 2004, General Motors further expanded the use of PPCN, by applying it on the body side molding for the '04 Chevrolet Impala. The next commercial automotive applications planned for PPCNs will be in exterior claddings, interior parts, and nonsupport trim (99).

PPCNs have also been used in flame-retardant cables, electrical enclosures, and housings. Although the presence of clay can slow down burning and enhance char formation, they are unable to reduce ignition tendency or after-flaming properties, hence, for fire-retardant applications, they must still be used in combination with other flame retardants; however, because of the synergistic effect observed when clays are used in conjunction with traditional FR agents, they can be used to reduce the amount of FR required to reach a satisfactory degree of retardancy. A 40% reduction in halogen-based FR can, for instance, be achieved by the use of just 5% of clay (100). This not only allows for the use of less halogen-based additives, which are costly and harmful to the environment, but also helps to enhance the mechanical performance of the component, due to less dilution caused by FR addition and also greater mechanical reinforcement provided by the clay itself.

10.7 CONCLUSIONS AND FUTURE TRENDS

The addition of clays to PP presents a promising avenue by which the properties of PP may be enhanced to satisfy increasingly more demanding specifications for current or new applications. The nanoscale dispersion of clay has been successfully achieved through the introduction of polar groups into PP, either by blending it with a compatibilizing copolymer (such as PP-g-MA) or by incorporating polar functional groups into the PP backbone, in combination with the use of suitably organically modified clays. The resulting PPCNs not only display significantly improved mechanical properties, such as a higher stiffness and strength without a concurrent reduction in impact resistance and toughness, but also exhibit other performance attributes that are not typically achieved with the use of other fillers, such as a higher HDT, an increased flame retardancy, and enhanced barrier properties. As these improvements in properties are generally attained at relatively low inorganic loadings, PPCNs also hold the potential for significant weight and material savings. The unique suite of properties offered by PPCNs, coupled with their ease of processing via common processing techniques, make them extremely promising for a wide range of applications. Already, they have been commercialized as interior and exterior trim in the transportation industry, as well as appliance and power tool housings.

Much progress has been made in the field of PPCNs in the past decade. Nevertheless, there are several aspects that must be addressed in order for their potential to be further realized. As PP does not have the inherent advantage of the well-established nylon-6 system in regard to their polymerization techniques and polarity, maintaining good adhesion and stress transfer from the PP matrix to the nanoclay filler remains a great challenge and is currently a very important factor limiting the

level of reinforcement that can be achieved in PPCNs (101). Furthermore, a more fundamental understanding of their structure–property relationships is imperative in order for the physicomechanical properties of the PPCNs to be better predicted and controlled. By further enhancing the performance of PPCNs beyond its current level through better materials design and process control, and developing economies of scale for their production, PPCNs will be better positioned for acceptance in the mainstream of global plastics processing.

NOMENCLATURE

2D XRD	Two-dimensional X-ray diffraction
AO	Antimony trioxide
DB	Decabromodiphenyl oxide
DMA	Dynamic mechanical analysis
DSC	Differential scanning calorimetry
E'	Storage modulus (measured in DMA)
E''	Loss modulus (measured in DMA)
EWF	Essential work of fracture
FR	Flame retardant
G'	Storage modulus (measured in linear viscoelastic measurements)
G''	Loss modulus (measured in linear viscoelastic measurements)
HDT	Heat distortion temperature
iPP	Isotactic polypropylene
MA	Maleic anhydride
MAPP	Maleic anhydride modified polypropylene
MMT	Montmorillonite
PP	Polypropylene
PPCN	Polypropylene/clay nanocomposite
PP-g-MA	Maleic anhydride grafted polypropylene
SAXS	Small-angle X-ray scattering
tan δ	Loss tangent
TEM	Transmission electron microscopy
T_c	Crystallization temperature
T_g	Glass transition temperature
T_m	Melting temperature
ω	Radial frequency
XRD	X-ray diffraction

REFERENCES

1. M. Alexandre and P. Dubois, *Mater. Sci. Eng. R Rep.*, **28**, 1 (2000).
2. S. Sinha Ray and M. Okamoto, *Prog. Polym. Sci*, **28**, 1539 (2003).
3. R. A. Vaia, H. Ishii, and E. P. Giannelis, *Chem. Mater.*, **5**, 1694 (1993).

4. E. P. Giannelis, R. Krishnamoorti, and E. Manias, *Adv. Polym. Sci.*, **138**, 108 (1999).
5. A. Leuteritz, D. Pospiech, B. Kretzschmar, M. Willeke, D. Jehnichen, U. Jentzsch, K. Grundke, and A. Janke, *Adv. Eng. Mater.*, **5**, 678 (2003).
6. P. Reichert, H. Nitz, S. Klinke, R. Brandsch, R. Thomann, and R. Mulhaupt, *Macromol. Mater. Eng.*, **275**, 8 (2000).
7. J. W. Lee, Y. T. Lim, and O. O. Park, *Polym. Bull.*, **45**, 191 (2000).
8. P. Kodgire, R. Kalgaonkar, S. Hambir, N. Bulakh, and J. P. Jog, *J. Appl. Polym. Sci.*, **81**, 1786 (2001).
9. M. J. Chung, L. W. Jang, J. H. Shim, and J. S. Yoon, *J. Appl. Polym. Sci.*, **95**, 307 (2005).
10. L. W. Jang, E. S. Kim, H. S. Kim, and J. S. Yoon, *J. Appl. Polym. Sci.*, **98**, 1229 (2005).
11. Y. Kim and J. L. White, *J. Appl. Polym. Sci.*, **96**, 1888 (2005).
12. Z. F. Zhao, T. Tang, Y. X. Qin, and B. T. Huang, *Langmuir*, **19**, 7157 (2003).
13. G. Moad, K. Dean, L. Edmond, N. Kukaleva, G. X. Li, R. T. A. Mayadunne, R. Pfaendner, A. Schneider, G. P. Simon, and H. Wermter, *Macromol. Mater. Eng.*, **291**, 37 (2006).
14. A. Sasaki and J. L. White, *J. Appl. Polym. Sci.*, **91**, 1951 (2004).
15. S. P. Su, D. D. Jiang, and C. A. Wilkie, *Polym. Degrad. Stabil.*, **83**, 321 (2004).
16. J. G. Zhang, D. D. Jiang, and C. A. Wilkie, *Polym. Degrad. Stabil.*, **91**, 641 (2006).
17. S. P. Su, D. D. Jiang, and C. A. Wilkie, *Polym. Degrad. Stabil.*, **83**, 333 (2004).
18. E. Manias, A. Touny, L. Wu, K. Strawhecker, B. Lu, and T. C. Chung, *Chem. Mater.*, **13**, 3516 (2001).
19. J. H. Kim, C. M. Koo, Y. S. Choi, K. H. Wang, and I. J. Chung, *Polymer*, **45**, 7719 (2004).
20. J. W. Lee, M. H. Kim, W. M. Choi, and O. O. Park, *J. Appl. Polym. Sci.*, **99**, 1752 (2006).
21. G. Mani, Q. G. Fan, S. C. Ugbolue, and Y. Q. Yang, *J. Appl. Polym. Sci.*, **97**, 218 (2005).
22. A. Usuki, M. Kato, A. Okada, and T. Kurauchi, *J. Appl. Polym. Sci.*, **63**, 137 (1997).
23. J. Y. Wu, T. M. Wu, W. Y. Chen, S. J. Tsai, W. F. Kuo, and G. Y. Chang, *J. Polym. Sci. B Polym. Phys.*, **43**, 3242 (2005).
24. F. C. Chiu and P. H. Chu, *J. Polym. Res.*, **13**, 73 (2006).
25. M. Avella, S. Cosco, and M. E. Errico, *Macromol. Symp.*, **228**, 147 (2005).
26. A. H. He, L. M. Wang, J. X. Li, J. Y. Dong, and C. C. Han, *Polymer*, **47**, 1767 (2006).
27. A. H. He, H. Q. Hu, Y. J. Huang, J. Y. Dong, and C. C. Han, *Macromol. Rapid Commun.*, **25**, 2008 (2004).
28. J. S. Ma, Z. N. Qi, and Y. L. Hu, *J. Appl. Polym. Sci.*, **82**, 3611 (2001).
29. J. M. Hwu and G. J. Jiang, *J. Appl. Polym. Sci.*, **95**, 1228 (2005).
30. T. Sun and J. M. Garces, *Adv. Mater.*, **14**, 128 (2002).
31. W. G. Shao, Q. Wang, and H. Ma, *Polym. Int.*, **54**, 336 (2005).
32. R. A. Vaia and E. P. Giannelis, *Macromolecules*, **30**, 7990 (1997).
33. R. A. Vaia and E. P. Giannelis, *Macromolecules*, **30**, 8000 (1997).
34. M. Kawasumi, N. Hasegawa, M. Kato, A. Usuki, and A. Okada, *Macromolecules*, **30**, 6333 (1997).
35. L. Szazdi, B. Pukanszky Jr., E. Foldes, and B. Pukanszky, *Polymer*, **46**, 8001 (2005).
36. M. Kato, A. Usuki, and A. Okada, *J. Appl. Polym. Sci.*, **66**, 1781 (1997).
37. N. Hasegawa, H. Okamoto, M. Kawasumi, M. Kato, A. Tsukigase, and A. Usuki, *Macromol. Mater. Eng.*, **280–281**, 76 (2000).
38. K. A. Carrado, L. Xu, R. Csencsits, and J. V. Muntean, *Chem. Mater.*, **13**, 3766 (2001).
39. P. Walter, D. Mader, P. Reichert, and R. Mulhaupt, *J. Macromol. Chem.*, **A36**, 1613 (1999).
40. D. Marchant and K. Jayaraman, *Ind. Eng. Chem. Res.*, **41**, 6402 (2002).
41. F. Perrin-Sarazin, M. T. Ton-That, M. N. Bureau, and J. Denault, *Polymer*, **46**, 11624 (2005).
42. Y. Wang, F. B. Chen, K. C. Wu, and J. C. Wang, *Polym. Eng. Sci.*, **46**, 289 (2006).
43. Y. Wang, F. B. Chen, and K. C. Wu, *J. Appl. Polym. Sci.*, **97**, 1667 (2005).

44. N. Hasegawa and A. Usuki, *J. Appl. Polym. Sci.*, **93**, 464 (2004).
45. Y. Kim and J. White, *J. Appl. Polym. Sci.*, **90**, 1581 (2003).
46. J. Kotek, I. Kelnar, M. Studenovsky, and J. Baldrian, *Polymer*, **46**, 4876 (2005).
47. N. Ristolainen, U. Vainio, S. Paavola, M. Torkkeli, R. Serimaa, and J. Seppala, *J. Polym. Sci. B Polym. Phys.*, **43**, 1892 (2005).
48. Z. M. Wang, H. Nakajima, E. Manias, and T. C. Chung, *Macromolecules*, **36**, 8919 (2003).
49. Z. M. Wang, H. Han, and T. C. Chung, *Macromol. Symp.*, **225**, 113 (2005).
50. T. C. Chung, *J. Organomet. Chem.*, **690**, 6292 (2005).
51. W. Gianelli, G. Ferrara, G. Camino, G. Pellegatti, J. Rosenthal, and R. C. Trombini, *Polymer*, **46**, 7037 (2005).
52. M. Modesti, A. Lorenzetti, D. Bon, and S. Besco, *Polymer*, **46**, 10237 (2005).
53. W. Lertwilmolnun and B. Vergnes, *Polymer*, **46**, 3462 (2005).
54. W. Lertwilmolnun and B. Vergnes, *Polym. Eng. Sci.*, **46**, 314 (2006).
55. Y. Wang, F. B. Chen, and K. C. Wu, *J. Appl. Polym. Sci.*, **93**, 100 (2004).
56. L. J. Zhu and M. Xanthos, *J. Appl. Polym. Sci.*, **93**, 1891 (2004).
57. C. H. Hong, Y. B. Lee, J. W. Bae, J. Y. Jho, B. U. Nam, and T. W. Hwang, *J. Appl. Polym. Sci.*, **98**, 427 (2005).
58. X. H. Liu and Q. J. Wu, *Polymer*, **42**, 10013 (2001).
59. S. C. Tjong, Y. Z. Meng, and A. S. Hay, *Chem. Mater.*, **14**, 44 (2002).
60. K. Wang, C. B. He, L. Chen, M. L. Toh, and K. Y. Mya, PCT/SG2005/000006 (2005).
61. L. Chen, K. Wang, M. L. Toh, and C. B. He, *Macromol. Mater. Eng.*, **290**, 1029 (2005).
62. L. Chen, K. Wang, M. Kotaki, C. Hu, and C. B. He, *J. Nanosci. Nanotechnol.,* **6**, 3969 (2006).
63. K. Wang, L. Chen, J. S. Wu, M. L. Toh, C. B. He, and A. F. Yee, *Macromolecules*, **38**, 788 (2005).
64. K. Wang, L. Wang, J. S. Wu, L. Chen, and C. B. He, *Langmuir*, **21**, 3613 (2005).
65. J. Li, L. J. Zhao, and S. Y. Guo, *Polym. Bull.*, **55**, 217 (2005).
66. L. J. Zhao, J. Li, S. Y. Guo, and Q. Du, *Polymer*, **47**, 2460 (2006).
67. E. C. Lee, D. F. Mielewski, and R. J. Baird, *Polym. Eng. Sci.*, **44**, 1773 (2004).
68. K. Wang, S. Liang, Q. Zhang, R. N. Du, and Q. Fu, *J. Polym. Sci. B Polym. Phys.*, **43**, 2005 (2005).
69. N. Hasegawa, H. Okamoto, M. Kato, A. Usuki, and N. Sato, *Polymer*, **44**, 2933 (2003).
70. M. Kato, M. Matsushita, and K. Fukumori, *Polym. Eng. Sci.*, **44**, 1205 (2004).
71. W. Zheng, X. Lu, C. L. Toh, H. Z. Tong, and C. He, *J. Polym. Sci. B, Polym. Phys.*, **42**, 1810 (2004).
72. P. H. Nam, P. Maiti, M. Okamoto, T. Kotaka, N. Hasegawa, and A. Usuki, *Polymer*, **42**, 9633 (2001).
73. P. Maiti, P. H. Nam, M. Okamoto, N. Hasegawa, and A. Usuki, *Macromolecules*, **35**, 2042 (2002).
74. C. M. Koo, J. H. Kim, K. H. Wang, and I. J. Chung, *J. Polym. Sci. B Polym. Phys.*, **43**, 158 (2005).
75. J. Ma, S. Zhang, Z. Qi, G. Li, and Y. Hu, *J. Appl. Polym. Sci.*, **83**, 1978 (2002).
76. B. Kim, S.-H. Lee, D. Lee, B. Ha, J. Park, and K. Char, *Ind. Eng. Chem. Res.*, **43**, 6082 (2004).
77. T. S. Ellis and J. S. D'Angelo, *J. Appl. Polym. Sci.*, **90**, 1639 (2003).
78. Y. X. Zhou, V. Rangari, H. Mahfuz, S. Jeelani, and P. K. Mallick, *Mater. Sci. Eng. A*, **402**, 109 (2005).
79. A. B. Morgan and J. D. Harris, *Polymer*, **44**, 2313 (2003).
80. M. N. Bureau, F. Perrin-Sarazin, and M. T. Ton-That, *Polym. Eng. Sci.*, **44**, 1142 (2004).
81. M. T. Ton-That, F. Perrin-Sarazin, K. C. Cole, M. N. Bureau, and J. Denault, *Polym. Eng. Sci.*, **44**, 1212 (2004).
82. P. Svoboda, C. C. Zeng, H. Wang, L. J. Lee, and D. L. Tomasko, *J. Appl. Polym. Sci.*, **85**, 1562 (2002).
83. W. B. Xu, G. D. Liang, W. Wang, S. P. Tang, P. S. He, and W. P. Pan, *J. Appl. Polym. Sci.*, **88**, 3225 (2003).
84. Q. Zhang, Q. Fu, L. X. Jiang, and Y. Lei, *Polym. Int.*, **49**, 1561 (2000).

85. C. Ding, D. M. Jia, H. He, B. C. Guo, and H. Q. Hong, *Polym. Test.*, **24**, 94 (2005).
86. L. Chen, S. C. Wong, and S. Pisharath, *J. Appl. Polym. Sci.*, **88**, 3298 (2003).
87. L. Chen, S. C. Wong, T. X. Liu, X. H. Lu, and C. B. He, *J. Polym. Sci. B Polym. Phys.*, **42**, 2759 (2004).
88. H. S. Lee, P. D. Fasulo, W. R. Rodgers, and D. R. Paul, *Polymer*, **46**, 11673 (2005).
89. J. W. Lim, A. Hassan, A. R. Rahmat, and M. U. Wahit, *Polym. Int.*, **55**, 204 (2006).
90. J. W. Lim, A. Hassan, A. R. Rahmat, and M. U. Wahit, *J. Appl. Polym. Sci.*, **99**, 3441 (2006).
91. Y. M. Li, G. X. Wei, and H. J. Sue, *J. Mater. Sci.*, **37**, 2447 (2002).
92. S. C. Tjong, S. P. Bao, and G. D. Liang, *J. Polym. Sci. B Polym. Phys.*, **43**, 3112 (2005).
93. M. J. Solomon, A. S. Almusallam, K. F. Seefeldt, A. Somwangthanaroj, and P. Varadan, *Macromolecules*, **34**, 1864 (2001).
94. G. Galgali, C. Ramesh, and A. Lele, *Macromolecules*, **34**, 852 (2001).
95. S.-Y. Gu, J. Ren, and Q.-F. Wang, *J. Appl. Polym. Sci.*, **91**, 2427 (2004).
96. J. W. Gilman, C. L. Jackson, A. B. Morgan, J. R. Harris, E. Manias, E. P. Giannelis, M. Wuthenow, D. Hilton, and S. H. Philips, *Chem. Mater.*, **12**, 1866 (2000).
97. M. Zanetti, G. Camino, D. Canavese, A. B. Morgan, F. J. Lamelas, and C. A. Wilkie, *Chem. Mater.*, **14**, 189 (2002).
98. T. Lan, J. Cho, Y. Liang, J. Qian, and P. Maul, Applications of Nanomer® in nanocomposites: from concept to reality, in: *Proceedings of the Nanocomposites 2001*, Chicago, IL, USA, 25–27 June 2001.
99. GM's 2005 Hummer H2 Features Nanocomposite Components. *The A to Z of Nanotechnology.* Accessed 11 May 2006. URL: http://www.azonano.com/details.asp?ArticleID=1017.
100. Flame Retardant Case Study. *Nanocor Technical.* Accessed 11 May 2006. URL: http://www.nanocor.com/Cases/case_FlameRet.asp.
101. D. Jarus, J. DeWerth, and J. Qian, Polyolefin nanocomposites in TPOs, in: *Proceedings of the Automotive TPO Conference 2005*, Detroit, MI, USA, 10–12 October 2005.

Chapter 11

Polyolefin/Layered Double Hydroxide (LDH) Nanocomposites: Preparation, Structure, and Properties

José I. Velasco[1]

11.1 INTRODUCTION

During the last years, several and thorough studies have been done on the efficiency of inorganic nanoparticles as a way to improve the properties of polymers. Polymer composites containing finely dispersed inorganic platelet like particles in the nanometer range are referred to as polymer–clay nanocomposites. They are commonly prepared from organophillized layered silicates (organoclay). Among other properties, these materials show improved mechanical, gas permeation, and flammability characteristics for low concentration loadings of silicate particles (5–10%) (1–3). Polyolefin–clay nanocomposites have been well described (4–7), and the results published in the literature have stimulated widespread research efforts in industry. Polyolefin nanocomposites are expected to be mostly used in the near future in different fields, such as automotive, household, packaging, electronics, and electrical industries.

In addition to layered silicates, nanoparticles of silica (8), zinc oxide (9), boehmites (10), and layered double hydroxides (LDH) (11) can be used, among many others, as inorganic phase to promote nanostructured polymeric composites. A review concerning the utilization of LDH materials in polymer nanocomposites, in comparison to smectite-type materials, has been realized by Leroux (12).

Centre Català del Plàstic, Department of Materials Science and Metallurgy, [1]Universitat Politècnica de Catalunya, C. Colom 114. E-08222 Terrassa, Barcelona, Spain

Polyolefin Composites, Edited by Domasius Nwabunma and Thein Kyu

Hydrotalcite $[Mg_6Al_2(OH)_{16}](CO_3)\cdot 4H_2O$ is the most common layered double hydroxide used in the preparation of organic–inorganic hybrid compounds. In 1988, Sugahara et al. (13) described the synthesis of an MgAl LDH–polyacrilonitrile (PAN) hybrid using *in situ* polymerization. Direct synthesis of hybrids LDH with poly(acrylic acid) (PAA), poly(vinyl sulfonate) (PVS), and poly(styrene sulfonate) (PSS) (14,15) were also reported. Multilayer composite films of the exfoliated LDH nanosheets and poly(sodium styrene 4-sulfonate) were assembled in a layer-by-layer fashion (16). Magnetic circular dichroism measurements demonstrated that Co-Al LDH nanosheets acted as nanoscale ferromagnetic layers at room temperature, and their multilayer assemblies exhibited significant magneto-optical response in the ultraviolet(UV)–visible region. Whilton et al. (17) compared the formation of LDH–polyaspart hybrids applying *in situ* polymerization and direct intercalation of the biopolymer. Recently, layered double hydroxide–polymer nanocomposites have been prepared with poly(ε-caprolactone) (PCL) (18), polyimide (19), epoxy resins (20–22), polyethylene oxide (23), poly(ethylene glycol diacrylate) (24), poly(methyl methacrylate) (PMMA) (25,26), polystyrene (PS) (27–30), polymer-dispersed liquid crystal (31), ethylene–maleic anhydride copolymers (32), and poly(propylene carbonate) (PPC) (33). In these works, both *in situ* polymerization and solution intercalation methods were employed. Tammaro et al. (18) compared three different methods of preparation of composites of poly(ε-caprolactone) and a modified MgAl LDH. Microcomposite systems were obtained by the solution mixing of modified LDH with high molecular weight poly(ε-caprolactone) (HMWPCL), an intercalated PCL oligomer in the inorganic layers was obtained by the *in situ* polymerization of ε-caprolactone in the modified LDH lamella; and nanocomposites, containing exfoliated LDH lamellae, were obtained by the solution mixing of HMWPCL with the oligomer of PCL partially intercalated into the 12-hydroxydodecanoate-intercalated LDH.

The disorderly exfoliated PMMA/LDH nanocomposites (26) with various contents of 10-undecenoate intercalated LDH were successfully synthesized in a two-stage process by the *in situ* bulk polymerization. The thorough dispersion of the LDH nanolayers enhanced the thermal properties of PMMA. In addition, the strong interfacial adhesion between the dispersed LDH layers and the PMMA matrix significantly improved the tensile properties as compared to that of the polymer.

Qiu and Qu (30) have recently demonstrated that exfoliated PS/LDH nanocomposite can be achieved by a soap-free emulsion polymerization method without the aid of any surfactant. Due to the absence of organic surfactant, the PS/LDH nanocomposite shows improvement on the onset decomposition temperature compared with the virgin polymer. This technique has been proposed as an alternative to prepare other exfoliated polymer/LDH nanocomposites, such as polyacrylate/LDH and poly(methylmethacrylate)/LDH nanocomposites. LDH mixed with nematic liquid crystal and photopolymer was studied by Tsai et al. (31) as a new emerging optical application. The redistribution of charges was enhanced as the polymer-dispersed liquid crystal was hybridized with the inorganic layers, which provided extra trapping sites. The combination of light interference pattern and the applied dc electric field produced a space-charge field, which led to molecular reorientation and

refractive-index grating in the device. Therefore, the diffraction efficiency was improved.

Lee and Nam (34) incorporated LDH nanoparticles into a Nafion (DuPont) polyelectrolyte membrane in order to investigate direct methanol fuel cell performance at high feed concentrations of methanol up to 7 M. The open circuit voltage was increased by virtue of a decrease in methanol cross-over through the modified Nafion/LDH membranes, and an optimum balance between the diffusion coefficient and the ionic conductivity was found.

From a practical point of view, the melt-mixing method appears as an accurate way to prepare LDH nanocomposites with polyolefins and other thermoplastic polymers. Electrostatic attractive forces and surfactant layer density between the layers may play an important role in the exfoliation mechanism. Shear, together with the exchange capacity, seems to be the key factor for the delamination of LDH. However, the decrease in LDH plate size in the nanocomposite may reveal the breakage of LDH layers during melt compounding, due to fragility and/or partial dehydroxylation of the LDH.

An *in situ* bubble-stretching model can be applicable to the dispersion of solid granular aggregates in polymer melts because the dispersed phase itself serves as a nucleation agent, giving rise to bubbles that expand at the surface of the microgranules and their aggregates (35). In terms of bidirectional stretching, such process can increase the degrees of freedom of granule dispersion, which favors more homogeneous dispersion. According to theoretical predictions and indirect experimental estimations of the dispersion of nanoscale $CaCO_3$ and hydrotalcite in high density polyethylene (HDPE), when the bubble expands, the stretching rate of the polymer melt on the bubble wall can reach 10^5–$10^6\ s^{-1}$. The granular size of dispersed $CaCO_3$ and hydrotalcite in HDPE was about two orders of magnitude smaller than that attained with a shearing rate of $10^3\ s^{-1}$ in a capillary rheometer (35). The efficiency of the *in situ* bubble-stretching model to exfoliate nanoclay platelets has also been proved in the preparation of low density polyethylene (LDPE)/hectorite nanocomposite foams (36, 37).

Exfoliated LDH-based PA6 nanocomposites could be prepared by melt processing when suitable organic-modified LDH with appropriate anionic exchange capacity values were synthesized (38). A reduction in the onset of thermal decomposition temperature was observed in PA6/LDH nanocomposites as compared to pure PA6, which is most likely related to a nucleophilic attack mechanism. Dodecylsulfate-modified MgAl LDH provided good compatibility with PET molecules, resulting in exfoliated nanocomposites having enhanced thermal and mechanical properties as compared to other nanocomposites prepared with dodecylbenzene sulfonate and octylsulfate-modified LDH, as well as the homopolymer (39). Wang et al. (40) have recently prepared a new nanostructured flame-retardant compound from hydrotalcite dispersed in brominated polystyrene solution. On the basis of LOI values, improvement in the fire retardancy of poly(ethylene terephthalate) was achieved after melt compounding with the modified hydrotalcite.

Concerning polyolefin/LDH nanocomposites prepared by melt-mixing technique, LDPE/MgAl LDH nanocomposites have been synthesized using maleic

anhydride grafted polyethylene as compatibilizer (41–43). LDH was previously modified by sodium dodecylbenzene sulfonate (SDBS) using the reconstruction method. The transmission electron microscopy (TEM) analysis showed a complex nature of particle dispersion in the polymer matrix with wide distribution of particles sizes and shapes. Changes observed in rheological properties are related to the LDH–polymer chains interactions resulting in a networklike structure.

Linear low density polyethylene (LLDPE)/LDH nanocomposites have been prepared by both the solution and the melt intercalation methods (44,45). All nanocomposites show significantly enhanced thermal stability compared with virgin LLDPE. Qiu and et al. (44) compare LLDPE/MMT and LLDPE/LDH nanocomposites. Both LLDPE/MMT and LLDPE/MgAl LDH materials exhibit mixed intercalated–exfoliated structures, whereas the LLDPE/ZnAl LDH nanocomposites exhibit completely exfoliated structures due to higher weakness of the ZnAl LDH platelets. LDH nanocomposites show much higher thermal degradation temperatures than montmorillonite nanocomposites with the same filler content.

Completely exfoliated HDPE/LDH nanocomposites can be obtained by controlling the organomodified LDH loading via melt intercalation (46). The effect of LDH loading on the gel content of UV-irradiated nanocomposites shows that the LDH materials can greatly absorb the UV irradiation and thus decrease the cross-linking efficiency.

The thermal and photooxidative behaviors of exfoliated polypropylene (PP)/LDH nanocomposites have been characterized by Ding and Qu (47) and compared to those of PP/MMT nanocomposites. The photooxidation mechanism of PP in PP/LDH materials is not modified compared with that of virgin PP. However, photooxidation rate of PP/LDH materials results much lower than that of PP and PP/montmorillonite samples, indicating better UV stability. In this sense, Duan and co workers intercalated (48,49) a large anionic pigment (the calcium salt of 4-((5-chloro-4-methyl-2-sulfophenyl)azo)-3-hydroxy-2-naphthalene-carboxylic acid) and an organic UV absorber (the sodium salt of 5-benzotriazolyl-4-hydroxy-3-sec-butyl-benzenesulfonic acid) into a LDH host by ion exchange of an MgAl LDH precursor. After intercalation of the pigment and the UV absorber, the interlayer distance in the LDH increased from 0.86 to 1.72 nm and 2.32 nm, respectively. The intercalated LDHs exhibited much higher thermostability and photostability to UV light than the pristine compounds, in the case of both the pure solids and their composites with polypropylene.

In the following sections a review of various melt-mixing preparation processes of polyolefin–LDH nanocomposites as well as their structure, morphology, and properties are presented.

11.2 SYNTHESIS AND CHARACTERIZATION OF ORGANOMODIFIED LDH

LDH are a family of layered compounds also called anionic clays or hydrotalcite-type compounds. The LDH platelets (typical thickness 0.5 nm) are brucitelike,

$Mg(OH)_2$, where the partial replacement of divalent cations with trivalent ones produces a positive charge, compensated by the presence of anions in the interlayer spacing. They are normally represented by the following global formula: $[M^{2+}_{1-x}M^{3+}_{x}(OH)_2][A^{n-}_{x/n} \cdot mH_2O]$ $(0.2 \leq x \leq 0.33)$, where M^{2+} and M^{3+} are the metallic cations placed on hydroxyl octahedral positions and A^{n-} is the anion that, together with some water molecules, positions between the referred layers (50).

Three main benefits are normally obtained in the LDH by means of organomodification, related to potential use as nanocomposites precursors in polymer matrices: Firstly, the LDH basal space increases, making possible the intercalation of macromolecular segments or molecules within the interlayer galleries. Secondly, the attractive forces between contiguous platelets decrease. As a consequence, the exfoliation of the platelets can be achieved more easily by means of shearing forces during the melt mixing with the polymer. Finally, it gives organophilic character to the LDH particles, making them more compatible with polymer matrices.

Thus, the first step to prepare LDH–polyolefin nanocomposites was the LDH organophillization. It could be realised by anionic exchange reaction with organic anions. Afterwards, the modified LDH was melt blended with the polyolefins. Polymer intercalation within the LDH lamellar structure and dispersion of LDH particles determine the two possible nanocomposite morphologies: intercalated and exfoliated.

Both Ciba Specialty Chemicals and Süd-Chemie, among other producers, provide commercial hydrotalcite. In first stage, an intermediate compound named LDH(Cl) was prepared by hydration of the previously calcined LDH in a sodium chloride solution. Due to the specific reconstitution behavior of LDH, chloride anions can be located instead of the carbonate ions in the interlamellar space. This intermediate compound in known to show higher tendency to exchange the chloride anions (e.g., by sulfate anions) than the carbonate anions present in the original LDH (51–53). After washing the intermediate LDH(Cl) compound, it was placed in a sodium dodecylsulfate solution for 72 h at room temperature in order to promote the second ion exchange reaction. The obtained compound was named LDH(DS). It contains dodecylsulfate anions in the interlamellar space, and thus higher basal spacing. Finally, this organomodified LDH was washed, dried under vacuum at 65°C for 24 h, and milled to obtain powdery LDH(DS).

Composition and structure of the modified hydrotalcite were analyzed by using different instrumental techniques. Wide-angle X-ray diffraction (WAXD) spectra were obtained with a Siemens D-500 diffractometer using CuK_α radiation ($\lambda = 0.154$ nm). FTIR spectra were obtained using a Nicolet 510 apparatus on samples prepared with 3 wt% of LDH in dry KBr. A Setaram TG-DTA 92 thermobalance was used to analyze the thermal stability by heating the samples at 5°C min^{-1} to 1000°C. Density was measured with a helium picnometer (AccPyc 1330) and the specific surface area was determined using a Micrometrics ASAP 2000 machine.

Some physicochemical characteristics of the LDH used to prepare the polyolefins nanocomposites are compiled in Table 11.1. As can be seen, anionic exchange

Table 11.1 Physicochemical Characteristics of Layered Double Hydroxides.

Sample code	Density g cm^{-3}	$d_{(003)}$, Å	Weight loss, %	Specific surface area, m^2 g^{-1}
LDH(Cl)	2.10	7.74	35.0	27.3
LDH(DS)	1.54	28.6	55.0	6.8

of chloride ions by dodecylsulfate (DS^-) ions considerably reduced the density of the compound. This change is related to a expansion of the LDH crystalline structure because of increase in basal spacing. Hydrotalcite crystal (003) diffraction peak appears (Fig. 11.1) at significantly lower diffraction angle when DS^- anions are present $(2\theta = 3.28^\circ)$ compared to that of the LDH and LDH(Cl) sample $(2\theta = 11.43^\circ)$. As a consequence, interlamellar distance (d_{003}) increased from 0.774 to 2.86 nm. These values were in good agreement with those reported in literature, obtained empirically from X-ray measures (52,53) or determined from theoretical models (54). Figure 11.2 illustrates how the DS^- anions are placed within the hydrotalcite interlamellar space. The higher distance would be the main cause of the reduction in density, even though DS^- anions have higher molecular weight than the chloride and carbonate anions present in LDH(Cl).

Fourier transform infrared spectroscopy (FTIR) analysis firstly showed that the reconstitution of hydrotalcite in the chloride solution did not result in a compound totally free of carbonate anions. In sight of the spectra (Fig. 11.3), a relatively high concentration of residual carbonates are expected to be present in the sample LDH(Cl). Therefore, the intermediate LDH(Cl) have both carbonates and chloride ions. So, the experimental conditions applied for the hydrotalcite re hydration should be optimized in order to promote the maximum ion exchange ratio possible. In LDH(DS) sample, a lower residual carbonate concentration was evidenced from the FTIR spectra, since the intensity of 1372 cm^{-1} peak, which is associated with the

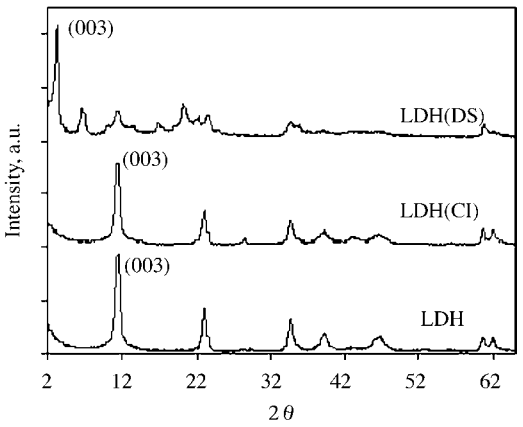

Figure 11.1 WAXD spectra of unmodified and modified layered double hydroxides.

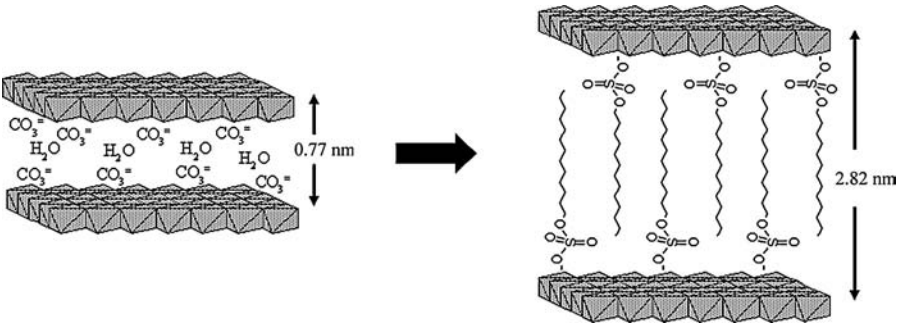

Figure 11.2 Schematic diagrams of unmodified and dodecylsulfate modified layered double hydroxide.

vibrational modes of carbonate, was remarkably reduced. As expected from the presence of dodecylsulfate ion in LDH(DS) sample, the characteristic IR bands appeared at 2925 and 2852 cm^{-1}, corresponding to C–H bond, as well as at 1212 cm^{-1} (S=O bond).

The weight loss suffered by LDH(DS) by heating up to 850°C in the TG analyzer was 55% (Fig. 11.4), which means a relative increment of 57% with respect to the weight loss of LDH(Cl). This remarkable difference is attributed to the differences in the molecular weight between the exchanged anions, DS^- (266 g mol^{-1}), chloride (35.5 g mol^{-1}) and carbonate (60 g mol^{-1}), and to the concentration in each sample. The ionic exchange ratio obtained could be estimated from the average hydrotalcite formula and the weight lost differences between the unmodified LDH and the LDH(DS) sample. It was accepted that for each carbonate, two dodecylsulfate anions

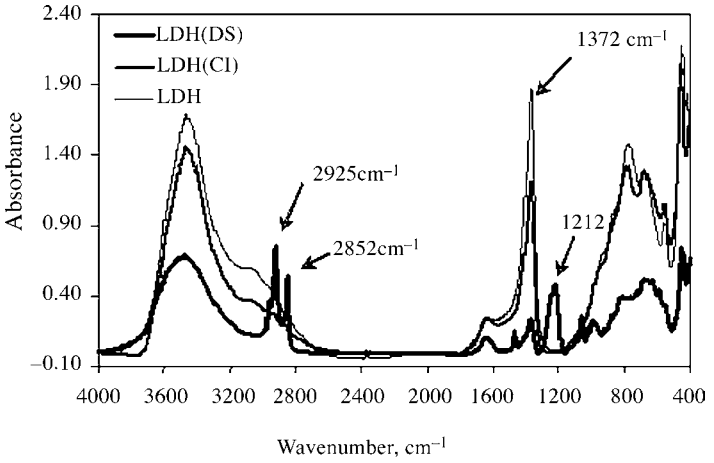

Figure 11.3 FTIR spectra of unmodified and modified layered double hydroxides.

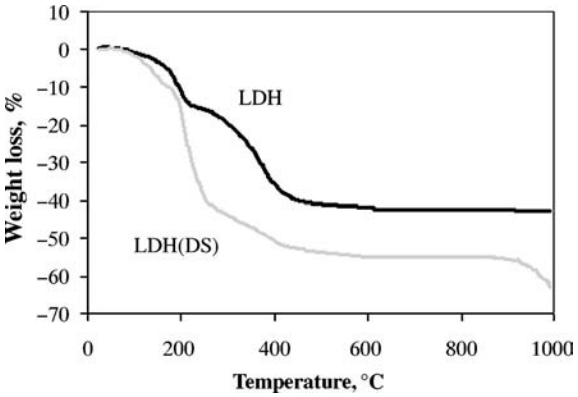

Figure 11.4 TGA plots of unmodified and modified layered double hydroxides.

were exchanged. The measured weight lost corresponded to dehydration and decarbonizing stages in LDH sample, as well as to the decomposition of the aliphatic chain of DS^- in LDH(DS). The sulfate groups start to decompose at temperature higher than 850°C and thus are not considered. A value of 58% could be estimated as ion exchange ratio reached in the modified hydrotalcite with respect to the original one.

The LDH modification resulted in lower values of the specific surface area for the particles (Table 11.1). Jaynes and Vance (55) found a similar result after the intercalation of long chained cationic surfactants in natural clays. The long-chain surfactants would limit the nitrogen absorption onto the modified LDH particle. That would be the cause for the lower values of surface area obtained with the BET method.

Costa et al. (41) modified MgAl hydrotalcite by the reconstruction method with SDBS after calcination. WAXD showed an increase in interlayer spacing of the modified SDBS–LDH ($d_{003} = 2.96$ nm) with respect to the synthesized MgAl LDH ($d_{003} = 0.76$ nm). FTIR comparison between the original MgAl LDH and SDBS-modified LDH showed the carbonate ion characteristic peak (1356 cm^{-1}) present in the first but almost absent in the second, indicating that, alongside the WAXD observations, the rehydration method produced SDBS intercalated layered materials, almost carbonate free, with a large interlayer distance.

11.3 PREPARATION OF POLYOLEFIN/LDH NANOCOMPOSITES

It has been shown that it is possible to prepare nanocomposites with organomodified LDH and different polyolefins by melt-mixing methods (41–43, 45–47, 56). A polypropylene homopolymer (PP) and a HDPE, both manufactured by Repsol-YPF (Puertollano, Spain), were used in the other (56). A maleic anhydride–PP copolymer (PP-g-MAH) manufactured by Eastman Chemical SA, a

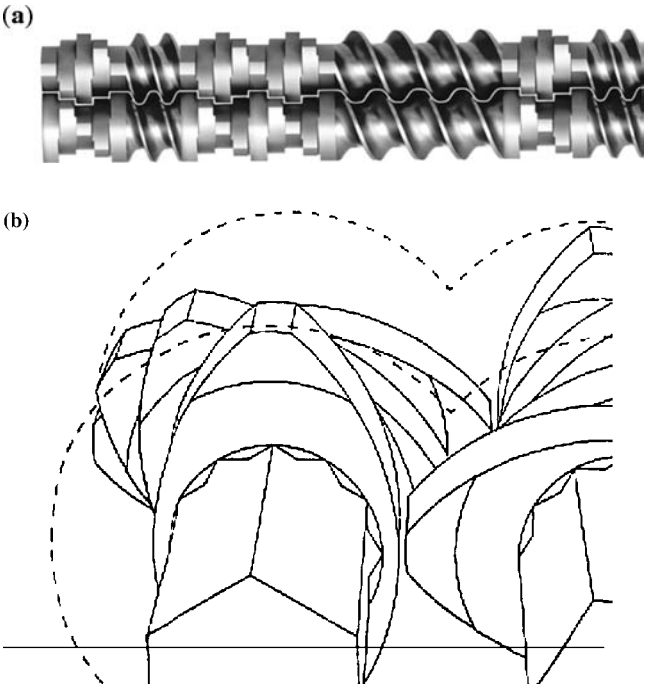

Figure 11.5 Screws of the co rotating twin-screw extruder used for the nanocomposite preparation (**a**) and schematic detail of the kneading bocks inserted in the screw to promote dispersive mixing (**b**).

maleic anhydride–SEBS copolymer (SEBS-g-MAH) supplied by AKElastomer, and a polyethylene–methacrylic acid (EMMA) ionomer (DuPont) were used as compatibilizers.

Compounding was carried out in a Collin ZK-35 co rotating twin-screw extruder (Fig. 11.5a) of 25 mm diameter and $L/D = 36$. Nominal temperature profile in the extruder was established at 120°C at the feeding port up to 190°C at the die exit. The screw speed was fixed at 100 rpm. During the processing, the maximum temperature of the polymer melt measured in the circular die (diameter 3 mm) was never higher than 195°C. Under these conditions, and thanks to the special geometry configuration of the screws containing kneading discs (Fig. 11.5b), the LDH particles were well dispersed and homogenized into the respective polyolefin melt. The extrudate was cooled under water and pelletized. In Table 11.2, the composition of all the materials prepared is compiled.

Plates of thickness 1, 2, and 3 mm were compression molded in a hot-plate press. Standard specimens were prepared for tensile testing (type IV, ASTM D-638), vertical combustion testing, and limiting oxygen index (LOI) determination. Ultramicrotomed sheets were taken for TEM observation, and specimens of $25 \times 25 \times 3\ \text{mm}^3$ for X-ray diffraction analysis were cut off from the molded plates.

Table 11.2 Chemical Composition and Mechanical Characteristics of the Pure Polyolefins As Well as HDPE/layered Double Hydroxides and PP/Layered Double Hydroxides Microcomposites and Nanocomposites.

Sample code	Composition, wt %	E, MPa	σ_{max}, MPa	ε_{max}, %
PP	PP (100)	1360	28.4	9.8
PPHT	PP/LDH (90/10)	1380	25.1	7.3
PPHTDS	PP/LDH(DS) (90/10)	1410	26.0	6.0
PPMHTDS	PP/PP-g-MAH/LDH(DS) (88/2/10)	1640	28.2	6.2
PPSHTDS	PP/SEBS-g-MAH/LDH(DS) (88/2/10)	1440	26.0	8.7
PE	HDPE (100)	1210	20.2	11.5
PES	HDPE/EMMA (98/2)	1170	19.7	10
PEHT	HDPE/LDH (90/10)	1430	18.7	9.2
PESHT	HDPE/EMMA/LDH (88/2/10)	1360	19.8	9.3
PEHTDS	HDPE/LDH(DS) (90/10)	1180	19.5	8.4
PESHTDS	HDPE/EMMA/LDH(DS) (88/2/10)	1270	19.8	9.1

11.4 STRUCTURE AND MORPHOLOGY OF POLYOLEFIN/LDH NANOCOMPOSITES

WAXD spectra of PP/LDH and HDPE/LDH nanocomposites are displayed in Fig. 11.6. Firstly, when comparing the LDH crystal (003) diffraction peak in the spectrum of LDH(DS) with the one for the PP and HDPE nanocomposites spectra, a general marked decrease in intensity and width is observed (Fig. 11.6a). Intensity reduction is partially explained by the dilution effect. Nevertheless, a detailed observation of this diffraction signal shows subtle additional differences regarding the shape and position of the peak for the different materials (Fig. 11.6b). Different interaction effects between both polyolefin macromolecules and the organophillized hydroxide platelets should be associated with these small changes. The position of the peak at slightly lower angles observed for some nanocomposites (particularly for PEHTDS) could be the result of macromolecule intercalation within the interlayer spacing, resulting in an additional expansion of the distance between hydroxide layers in the crystal. The widening and/or decreasing of that peak's intensity observed in the WAXD spectra of nanocomposites could come from decrease in the content of LDH particles having crystal structure similar to that of the original LDH, as a consequence of partial exfoliation during the melt-mixing step. The incorporation of compatibilizer copolymers within the PP nanocomposites formula resulted in reduced intensity of the crystal diffraction signal in the nanocomposites, due to increase polyolefin surface energy that would promote stronger interactions and higher adhesion with the surface of LDH particles, favoring their delamination at similar shear mixing stresses.

However, in HDPE/LDH nanocomposites, the intensity of the LDH crystal (003) diffraction peak seems to slightly decrease and move to lower angles for the sample without compatibilizer (PEHTDS) when compared to the sample containing

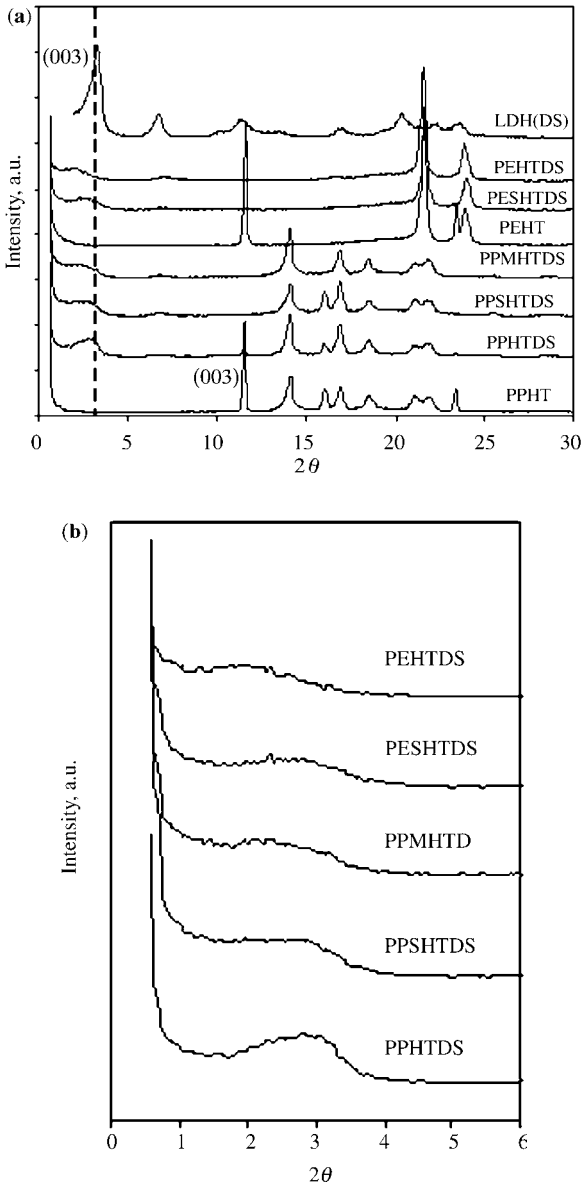

Figure 11.6 WAXD spectra of the nanocomposites (sample codes as in Table 11.2). (**a**) Full spectra, (**b**) Details of the first diffraction signal.

poly(ethylene-co-methacrylic acid) (EMAA) ionomer (PESHTDS). From this result, this copolymer would not enhance the LDH exfoliation.

Typical morphologies in polyolefin/LDH nanocomposites are displayed in Fig. 11.7. Particles formed by stacking of platelets alongside the exfoliated ones

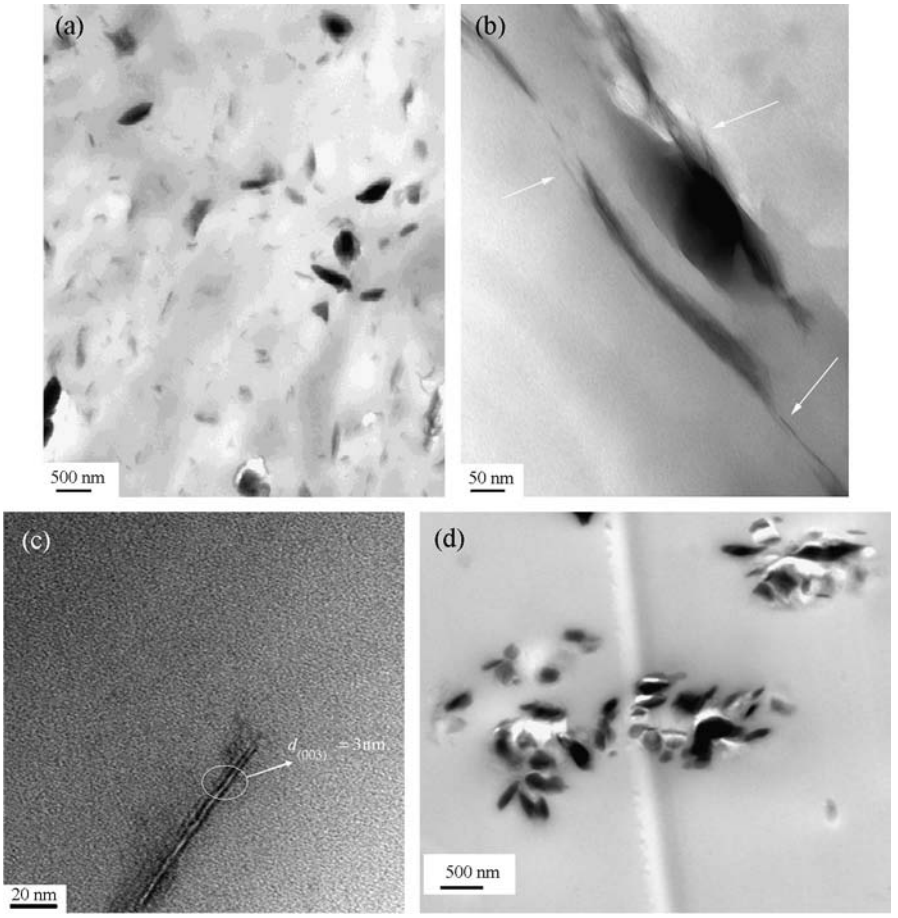

Figure 11.7 TEM pictures showing the morphology of the nanocomposites at three different magnifications: (**a**) general view displaying a distribution of tactoids, platelets, and stacks of platelets; (**b**) magnification of tactoids displaying individual platelets coming off of them due to exfoliation; (**c**) details of a pair of exfoliated platelets in a PP/LDD(DS) nanocomposite, showing the interlamellar spacing; and (**d**) platelets aggregation in a EMAA/LDH(DS) nanocomposite.

are discussed. In addition (Fig. 11.7d), high tendency of platelet aggregation can be observed in the TEM pictures of exfoliated EMAA/LDH(DS) nanocomposites (57). This effect should be related to the ionic aggregation behavior of EMAA ionomers (58).

The effects of UV irradiation on the HDPE/LDH nanocomposites (46) show that the photoinitiated cross-linking can destroy a completely exfoliated structure to form a partially exfoliated structure, which decreased the thermal stability of the nanocomposites.

LDPE/MgAl LDH nanocomposites were prepared by melt mixing using LDPE-g-MAH (41) and HDPE-g-MAH (42) as compatibilizer, with previously modified LDH by SDBS. LDPE had a MFI value of 3.52 dg min^{-1}. The dispersed LDH particles showed a tendency to form structural aggregates with the increasing concentration of LDH. At low LDH concentration (0.5–1 phr), no characteristic WAXD peaks were noticed, due to a highly exfoliated degree, confirmed via TEM. Nevertheless, the dispersion of the LDH particles changed with increase in the loading (appearance of the LDH basal peak and sometimes of weak higher order peaks in WAXD spectra). The short-range ordering of the stacked LDH layers is maintained (confirmed by the unmodified position of the (003) basal peak and the broadening of the higher order peaks), as well as the decrease in the average number of layers in a single stack (59), with a lowering of the intensity indicating a certain loss in symmetry arrangement. WAXD and TEM results indicated an intercalated LDH structure for high loadings. The LDH particles appeared dispersed in the form of single platelets on both matrices. Occasional delamination of individual layers after SDBS LDH modification (expanded intergallery, with weakening of the LDH interlayer bonds) and fragmentation during melt mixing was observed. Nevertheless, normally multiple numbers of LDH layers composed these thin layers obtained after melt mixing, with thicknesses ranging from 50 nm to a few hundred nanometers.

DS-modified ZnAl LDH was also used to prepare LLDPE nanocomposites by solution intercalation in xylene (44). Characteristic WAXD (001) diffraction peak disappeared completely when the LDH concentration was increased from 2.5 to 10 wt%, indicating a possible complete exfoliation of the LDH particles, which was confirmed by TEM pictures.

11.5 RHEOLOGICAL PROPERTIES OF POLYOLEFIN/LDH NANOCOMPOSITES

Rheological properties, both linear and nonlinear, of LDPE/LDH nanocomposites were studied (42). Dynamic oscillatory shearing using a sinusoidal input strain function with the strain amplitude γ_0 maintained below 5% to ensure linear viscoelastic regime was used

$$\gamma(t) = \gamma_0 \sin(\omega t) \tag{11.1}$$

The evolution of the complex viscosity at low frequency was studied in the range of temperatures from 180 to 260°C (Fig. 11.8). The dependence of rheological properties on temperature was found to be reduced for the nanocomposites with regard to the pure LDPE, especially beyond a certain LDH loading, meaning a deviation of the liquidlike low frequency flow behavior toward a pseudosolid one. HDPE-g-MAH nanocomposites showed this shifting behavior at much lower LDH loadings (around 5 phr) when compared to the LDPE/compatibilizer composites (changes in viscosity regarding temperature were still observed at a 10 phr LDH concentration), meaning that the nature of the polymer matrix strongly affected the

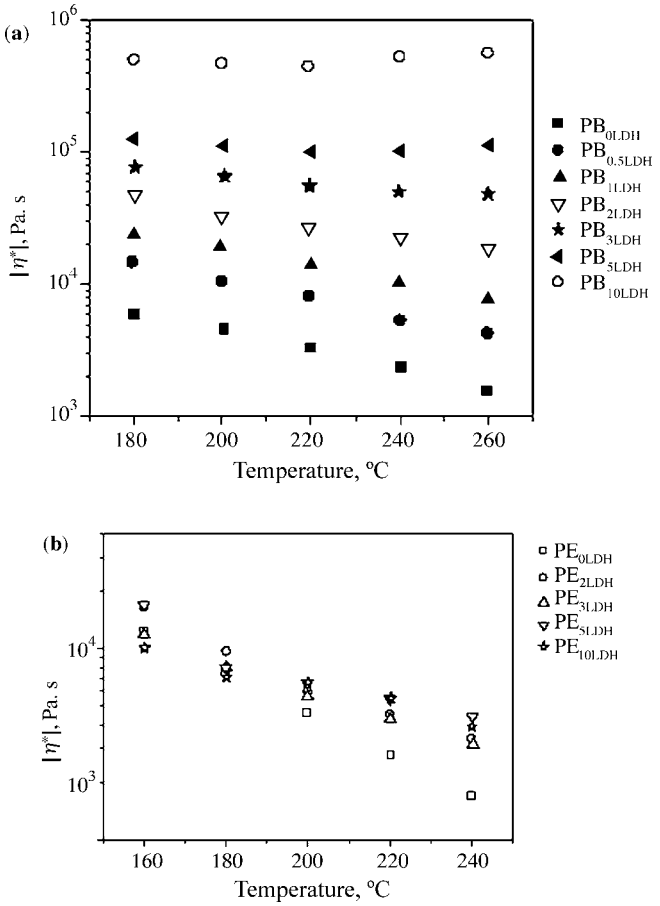

Figure 11.8 Effects of LDH loading on the temperature dependence of complex viscosity at low frequency (0.177 rad s^{-1}) of polyethylene/LDH nanocomposites. (**a**) Nanocomposite series based in HDPE-g-MAH (PB_{XLDH} series, where X represents the weight concentration of LDH in phr). (**b**) Nanocomposite series based in LDPE with LLDPE-g-MAH as compatibilizer, prepared with a weight ratio of LDH to compatibilizer 1:2 (PE_{XLDH} series). (From Reference 42 with permission from Elsevier.)

effect of increasing LDH concentration on the rheological behavior of the nanocomposites.

Low frequency measures revealed a monotonic increase in the storage modulus (G') with increasing LDH loading. The higher increase in HDPE-g-MAH showed that the polarity of the modified matrix increased the dispersion of the LDH particles. The tendency to obtain plateaulike G' versus frequency plots was reached at lower LDH loadings for the more polar matrix, indicating an increasingly incomplete polymer chain relaxation.

The complex viscosity ($|\eta^*|$) versus frequency plots showed the typical transition from Newtonian flow (low frequency regime) to shear thinning (high frequency

regime) for the unfilled materials. With the increasing nanoparticle concentration, the low frequency response shifted to a shear thinning mode, with a similar behavior for both nanocomposites. Two factors could explain this behavior: first, the polarity difference of the two matrices, and second, the presence of a low molecular weight compatibilizer in one of the composites.

Both unfilled and conventional particulate polyolefin microcomposites melts normally show a Newtonian liquidlike behavior at low frequency. However, LDPE/LDH nanocomposites presented a shear thinning behavior that is a higher shear thinning exponent and lower relaxation exponent. As shown in Fig. 11.9, both

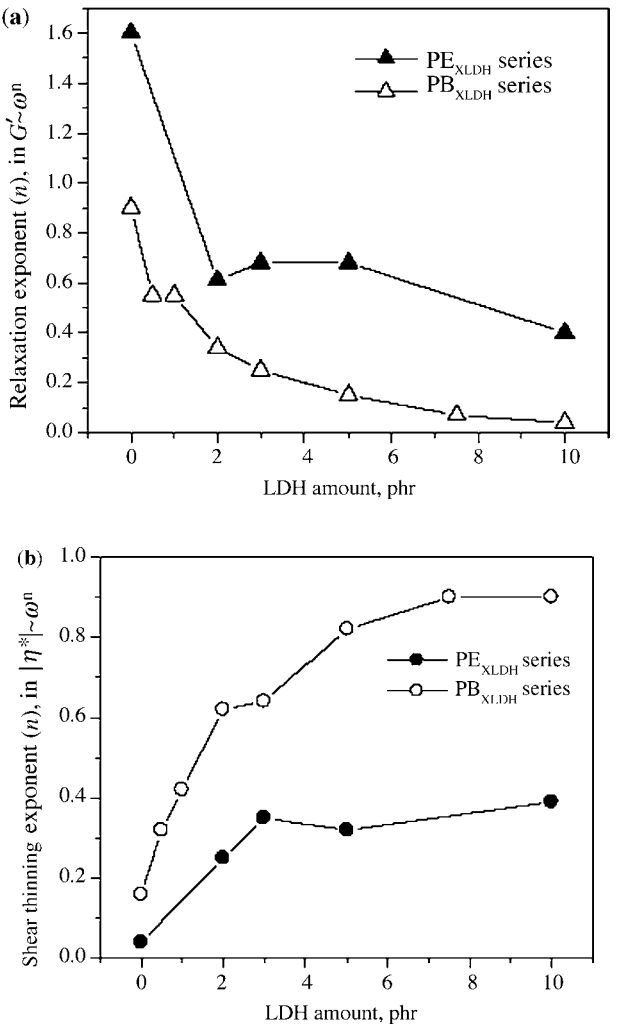

Figure 11.9 Variation in the terminal slopes of the flow curves ($|\eta^*|$ versus ω (**a**) and G' versus ω (**b**)) with LDH loading in the nanocomposites. (From Reference 42 with permission from Elsevier.)

exponents become nearly independent of LDH concentration for higher values of loading. Shear thinning exponent (n) values can give a semiquantitative measurement of the degree of clay delamination in polymer nanocomposites (60). Although higher negative values of n are normally related to higher clay exfoliation, in LDPE/LDH nanocomposites, the higher shear thinning exponent values were related to polymer chains or segments constraining, thus delaying the relaxation process. Higher LDH loadings would enhance this effect, with G' increasing and being less frequency dependent. Also, as the average distance between the dispersed platelets decreases, their tendency to interlock acting as an energetic barrier against the relaxation would be magnified.

In order to study and predict morphological changes during the processing of LDPE/LDH nanocomposites, the melts were subjected to a non linear shearing process (42). A constant shear rate was applied till steady state was reached, then the shear was stopped and restarted at the same initial shear rate in the opposite direction. Stress developed on the nanocomposites during the re-shearing step was studied as a function of time. A stress overshoot (maximum), related to weak agglomerated networklike structures, which ruptured during the first shearing step and restructured after the rest period, was observed. Steady viscosity was reached for very high times, with the ruptured particles starting to align in the flow direction.

Due to the fact that the networklike LDH structures were not delaminated during linear viscoelastic shearing, the previously mentioned regeneration was studied, analyzing the variations in the storage modulus with time under small frequency and strain amplitude conditions. It was noticed that G' increases steadily with time and for higher LDH loadings (Fig. 11.10). It was explained due to lower average distance between the particles and consequent faster regeneration. Moreover, as in the linear viscoelastic oscillatory shearing experiences, the low molecular weight compatibilizer (LLDPE-g-MAH) deteriorated the elasticity of the matrix after the destruction of the network by shearing and the alignment of the polymer chains in the flow direction, resulting in lower G'. High LDH loadings and long rest periods could allow sufficient structural recovery, overcoming this situation.

11.6 THERMAL PROPERTIES OF POLYOLEFIN/LDH NANOCOMPOSITES

Eventual changes in the melting and crystallization characteristics of polypropylene and polyethylene in the nanocomposites, due to LDH platelets presence, were studied by means of differential scanning calorimetry (DSC). A Perkin-Elmer Pyris 1 calorimeter was used with samples weighting around 10 mg. The nanocomposites samples were initially heated from room temperature until 200°C at 10°C min^{-1} and held for 2 min to erase the thermal history before cooling at 10°C min^{-1} from 200 to 20°C. Next, the samples were heated a second time at 10°C min^{-1} from 20 to 200°C to analyze the melting signal of the polymer. Crystallinity percentages for both polyolefins in the nanocomposites were determined from the crystallization (T_c) and

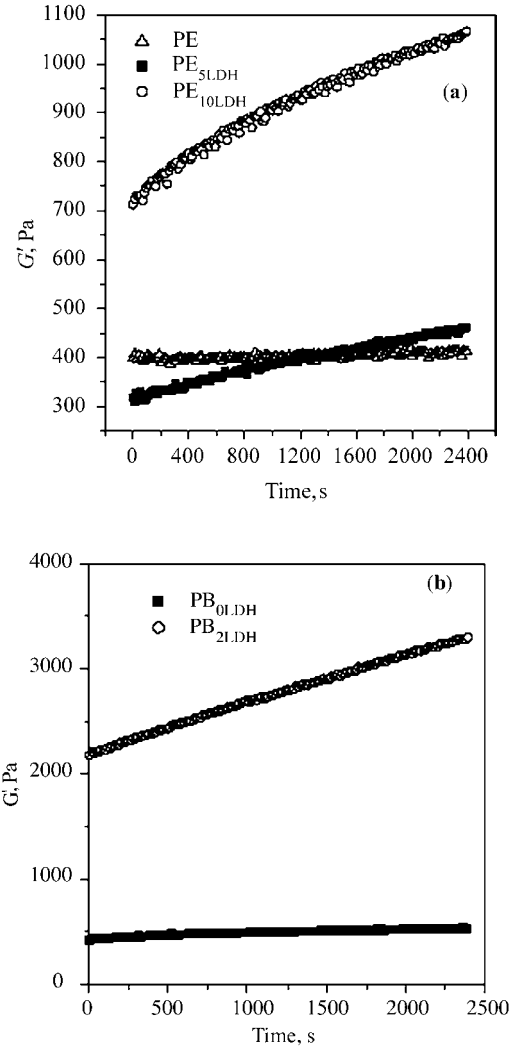

Figure 11.10 The effect of structural regeneration of the dispersed LDH particles on the storage modulus (G') of the melt during the "rest period" in the non linear shearing experiment (frequency 1 rad s^{-1} and strain 1%). Sample codes are same as in Fig. 11.8. (From Reference 42 with permission from Elsevier.)

melting (T_m) peak temperatures, as well as the respective enthalpies (ΔH_c and ΔH_m). Theoretical by, 100% crystalline values of enthalpy for polypropylene and polyethylene (ΔH_m°) were respectively taken as 207.1 and 293 J g^{-1}.

Melting and crystallization characteristics of PP and HDPE in the nanocomposites are compiled in Table 11.3. For HDPE, both melting and crystallinity peak temperatures, as well as crystallinity, seemed unaffected by the presence of LDH particles. Nonetheless, polypropylene nanocomposites showed interesting effects

Table 11.3 Thermal, Rheological, and Flammability Characteristics of the Pure Polyolefins As Well as HDPE/layered Double Hydroxides and PP/Layered Double Hydroxides Microcomposites and Nanocomposites.

Sample code	T_m, °C	T_c, °C	X_m, %	X_c, %	MFI, $^{-1}$ dg min	Vicat, °C	TFBD, s	LOI, %
PP	164.2	113.5	52.7	55.8	5.8	97.2	6	18.2
PPHT	163.5	116.1	51.3	55.8	6.1	97.9	9	19.2
PPHTDS	163.5	119.1	54.0	56.9	5.4	92.6	15	18.8
PPMHTDS	165.3	126.7	65.2	60.0	5.8	103.6	21	19.3
PPSHTDS	163.9	119.0	63.4	61.6	5.7	95.2	17	18.9
PE	130.0	116.4	79.9	83.3	1.03	75.4	12	18.4
PES	130.7	116.7	82.0	85.1	0.94	71.9	13	18.5
PEHT	130.6	116.6	83.8	82.6	1.01	71.6	19	18.7
PESHT	131.2	116.5	84.2	83.8	0.84	72.8	15	18.5
PEHTDS	131.3	116.4	86.6	82.3	0.75	70.2	26	19.2
PESHTDS	131.5	116.1	80.2	79.2	0.75	71.0	20	18.3

MFI: melt flow index determined with a load of 2160 g and at 230°C (for PP) and at 190°C (for PE). Vicat: softening temperature determined at 50°C min^{-1} (Vicat B). TFBD: time to the first burning drop determined under UL-94 test geometry.

regarding the crystallinity values and crystallization temperature due to the presence of LDH particles. LDH particles remarkably increased the crystallization temperature of PP, thus showing the LDH particles have a notable effect as nucleation agent for this polyolefin. This effect is found to be more relevant in PP nanocomposites (particularly in PPMHTDS sample) than in PP/LDH microcomposites (PPHT sample). It has to be noted that previous studies using PP-g-MAH as compatibilizer in particulate-filled PP showed efficiency as a nucleation accelerator during the crystallization of the polyolefin. Thus, this effect would be reinforcing the effect caused by the LDH platelets.

For all the PP-based samples studied, the polypropylene was found to develop: a tendency for the crystallization temperature versus the crystallinity the composite sample in which nucleation agent is present should display a higher crystalline fraction, as the polymer crystallization started at higher temperatures during the cooling stage inside the calorimeter.

The DSC data show that exfoliated LDH layers increase the endothermic peak temperature of LLDPE by about 5°C when 5 wt% of MgAl LDH(DS) is added (45).

11.7 THERMAL STABILITY OF POLYOLEFIN/LDH NANOCOMPOSITES

The thermal stability and thermo-oxidative degradation of LLDPE/LDH nanocomposites was studied (44). The thermal stability was enhanced for the nanocomposites

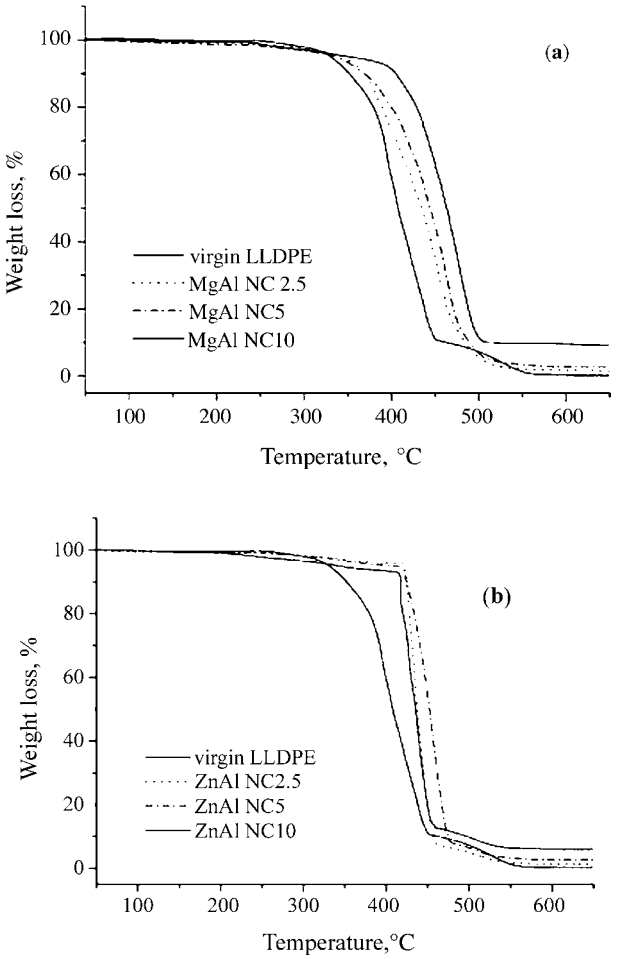

Figure 11.11 Change of TGA profiles with different contents of MgAl LDH (**a**) and ZnAl LDH (**b**) in the LLDPE nanocomposites. (From Reference 44 with permission from Elsevier.)

compared to the pure LLDPE, as seen in the thermogravimetric analysis (TGA) curves (Fig. 11.11).

The isoconversional kinetic analysis of the thermo-oxidative behavior of the LLDPE/LDH nanocomposites showed that at the beginning of the degradation (conversion extent, $\alpha = 0.03$) the activation energy (E_α) of pure LLDPE and LDH nanocomposites was similar, indicating that degradation initiated by similar reactions. Pure LLDPE showed a slight increase in E_α until $\alpha = 0.2$, which is consistent with common oxygen-initiated chain scission. The nanocomposites showed higher activation energies with increasing α. The LLDPE/MgAl and LLDPE/ZnAl LDH nanocomposites showed a shift between peroxide radical

decomposition and random scission decomposition that started at low α values (0.1 and 0.2, respectively). These results were consistent with the barrier model mechanism, where the inorganic layers act as an effective oxygen-diffusional barrier.

By analyzing the absorbance FTIR peaks (Fig. 11.12), as well as their relative peak intensities of absorbance at 925 cm^{-1} assigned to the $-CH_2-$ or $-CH_3$ asymmetric vibration in the LLDPE and its nanocomposites, it was concluded that thermal degradation of the LLDPE/LDH nanocomposites mainly lead to alkene-type products; meanwhile, the thermo-oxidative degradation of pure LLDPE resulted in characteristic carbonyl peaks, which could be explained on the basis of an oxygen barrier effect of the LDH platelets.

The data from TGA show that the HDPE/LDH nanocomposites have much higher thermal stability than HDPE sample (46). When the 50% of weight loss is selected as a comparison point, the decomposition temperature of HDPE/LDH sample with 5 wt% LDH loading is 40°C higher than that of HDPE sample. Similarly, the thermal degradation temperature of the exfoliated PPC/MgAl LDH nanocomposites with 1 wt% of modified LDH is 10°C higher than that of pure poly(propylene carbonate) at 20% of weight loss (33).

PP/LDH nanocomposites have enhanced thermal stability compared not only with virgin PP but also with the corresponding PP/montmorillonite nanocomposites (47), especially in high temperature range during the thermal decomposition of the samples.

11.8 MECHANICAL PROPERTIES OF POLYOLEFIN/LDH NANOCOMPOSITES

The mechanical behavior of the nanocomposites was studied by tensile tests, at room temperature and a constant speed of 10 mm min^{-1}. Strain was measured with a video-extensometer. Both PP/LDH and HDPE/LDH nanocomposites displayed similar tensile behavior compared to the respective neat polyolefins. Stress–strain curves were quite similar to those of the neat polymers. Only slight differences were observed in the yield and the maximum stresses, as well as in the strain at break (Table 11.2). HDPE-based composites showed increased stiffness with the presence of unmodified LDH particles (samples PEHT and PESHT), explained by the own rigidity of untreated hydrotalcite particles, which should be higher than that of the polymer. According to the values compiled in Table 11.2, Young's modulus value (E) of unmodified HDPE/LDH microcomposites was approximately 1.4 GPa, which is higher than those of LDH(DS) nanocomposites (PEHTDS and PESHTDS) and pure HDPE ($E \approx 1.2$ GPa). On the basis of these values, a plasticizing effect on polyethylene was attributed to the modified LDH(DS).

The tensile strength (σ_{max}) did not decrease for LDH(DS) nanocomposites, but decreased slightly for the unmodified LDH ones. These small differences between micro composites (PEHT) and nanocomposites (PEHTDS) should be

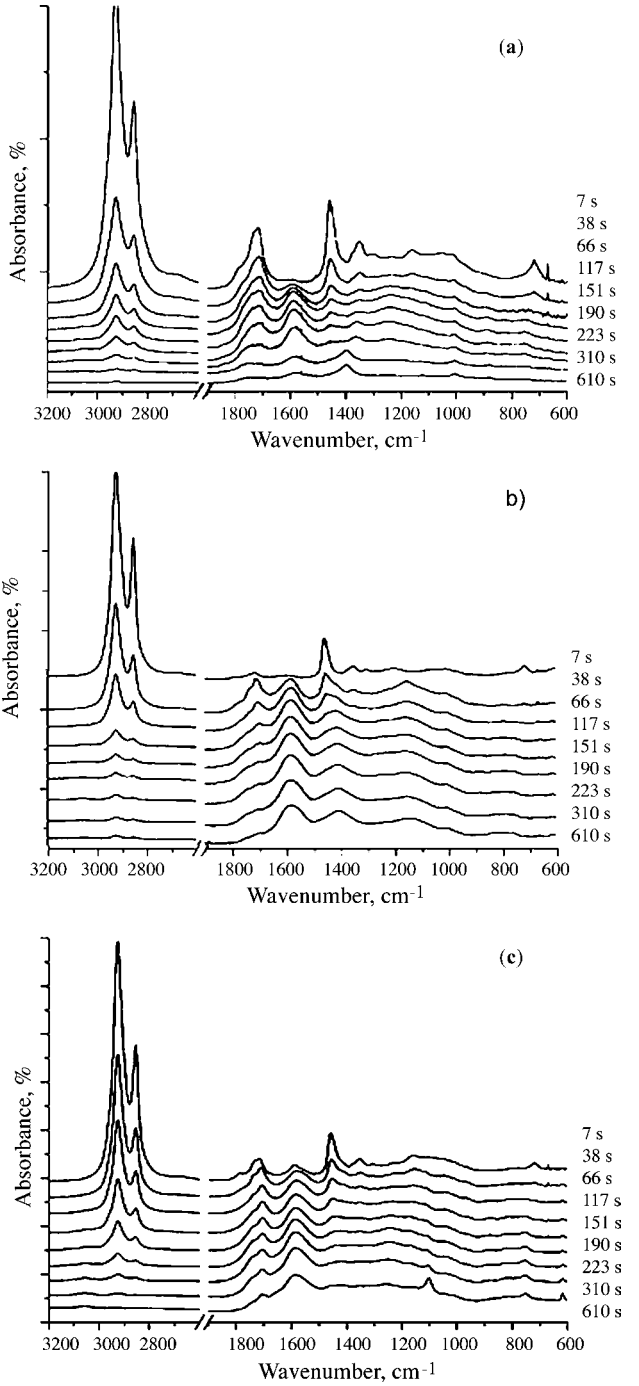

Figure 11.12 Dynamic FTIR spectra with different thermo-oxidative time at 400°C: (**a**) virgin LLDPE, (**b**) MgAl NC10, and (**c**) ZnAl NC10. (From Reference 44 with permission from Elsevier.)

attributed to the size of the dispersed LDH particles. In this sense, primary particles of average size 0.7 μm were mainly observed by TEM for unmodified HDPE/LDH samples. However, individual and stacks of few platelets (typical thicknesses 1 nm) were mainly observed for the LDH(DS) nanocomposites (Fig. 11.7c). The higher the aspect ratio of the particle, the higher the tensile strength of the composite. In this sense, as the concentration of individual exfoliated platelets increases in the nanocomposites, its tensile strength also increases.

As for HDPE/LDH composites, slight differences were noticed in tensile properties for PP/LDH composites. Only LDH(DS) nanocomposite prepared with compatibilizer showed significantly higher stiffness (Table 11.2) than the rest of samples. The cause would be the effect of increased crystallinity developed by polypropylene.

Regarding the tensile strength of PP/LDH samples, as expected from a polymer containing micrometric-sized particles, tensile strength of PPHT microcomposite (25.1 MPa) resulted lower than that of the unfilled polymer (28.4 MPa). The values of PP/LDH(DS) nanocomposites were closer to those of the unfilled PP. In these nanocomposites, the compatibilizer copolymer promoted higher interfacial adhesion, increasing the maximum tensile stress.

The plastic strain of the nanocomposites was found to be lower than that of the microcomposites and the pure polyolefins. The cause of which should be related to the restraining of the polymer chain mobility at the particle interface.

Fracture behavior of polyethylene (LDPE)/MgAl LDH based nanocomposites has been studied by essential work of fracture approach (43). A maximum in the nonessential work of fracture was observed at 5 wt% LDH, demonstrating enhanced resistance to crack propagation compared to pure LDPE. Morphological analyses show that the dispersed LDH platelets are partially exfoliated and also forms clusters with polymer chains remaining entrapped within. At 5 wt% LDH, a ductile-to-brittle transition has been observed. Fracture surface investigation by SEM reveals the arresting of the plastic crack growth by the LDH particle clusters, which is more significant at 5 wt% LDH content. At higher LDH concentrations, the number of clusters increases, causing decrease in the average distance between them. As a result, large-scale plastic deformation of the LDPE matrix at higher LDH concentration is effectively arrested, favoring small strain failure. The resistance against crack initiation (essential work of fracture) and crack propagation (non essential work of fracture) in these nanocomposites was correlated with the matrix behavior and the nanocomposite morphology (state of LDH particle dispersion) respectively.

Mechanical properties of PPC are also found to be remarkably improved when nanocomposites of this polymer are prepared with LDH. It has been reported (33) that the tensile strength value of PPC/MgAl LDH nanocomposites containing 5 wt% of LDH is 36.9 MPa, which is 72% and 30% higher than those of the pure PPC sample and the simply mixed sample, respectively, with the same content of LDH. Its Young's modulus is 1303 MPa, which is 57% and 21% higher than those of the same two samples, respectively.

11.9 FLAME-RETARDANT AND GAS BARRIER PROPERTIES OF POLYOLEFIN/LDH NANOCOMPOSITES

Like polyolefin/clay nanocomposites, polyolefin/LDH nanocomposites could penetrate different industrial fields. For example, they could be used as an alternative or synergist component in flame-retardant polymer formulations as well as in gas barrier polymer films. That is why it is important to characterize these materials by technical parameters commonly used in the plastic industry, such as the melt flow index and the Vicat softening temperature. Values of some of these common parameters have been compiled in Table 11.3. In general, decrease in Vicat values could be assigned to LDH plasticizing effect, while higher Vicat values could come from higher polymer crystallinity.

The MFI values indicated higher apparent viscosity for the nanocomposites compared to the respective pure polymers and LDH microcomposites, and they are in agreement with the rheological properties of these kind of nanocomposites. The high viscosity at low strain rates of polymer nanocomposites is found to influence the flame behavior, limiting dripping of the burning polymer. Although a 10 wt% of LDH in the studied nanocomposites did not result in increased LOI value (oxygen percentage needed for the combustion), it promoted a considerable increase in the time needed to start dripping after the flame application on the material specimen (TFBD), measured by vertical flammability tests (UL-94 standard). As shown in Table 11.3, nanocomposites displayed the highest values.

The TGA profiles of LLDPE/MgAl LDH(DS) nanocomposites show (45) a faster charring process between 210 and 370°C, as well as a higher thermal stability above 370°C, than LLDPE. The decomposition temperature of the nanocomposites with 10 wt% of modified LDH was 42°C higher than that of LLDPE at 40% of weight loss. Dynamic FTIR spectra reveal that this nanocomposite has a slower thermo-oxidative rate than LLDPE between 200 and 320°C. The exfoliated LDH layers promote the charring process and, thus, this kind of nanocomposite is a promising flame retardant for polyolefin materials.

Finally, the oxygen permeability of polypropylene films was found to be reduced in the PP/LDH nanocomposites in the same extension than PP/MMT nanocomposites. So, the oxygen transmission rate (OTR) value for pure PP was 500 cc m^{-2} per day, while for PP nanocomposites prepared with 5 wt% of organophillized LDH and with 5 and 10 wt% of organophillized montmorillonite the OTR values were 210, 260, and 220 cc m^{-2} per day, respectively (61). Thus, LDH nanocomposites could be used in low concentration to reduce the oxygen permeation of polyolefins.

11.10 LDH VERSUS MMT IN POLYOLEFIN NANOCOMPOSITES

Polyolefin/LDH nanocomposite compare favorably with those of cationic clays, like montmorillonite. LDHs can be prepared with simple procedures with a high level of purity, are cheap, and can be organically modified with a variety of organic anions,

which are generally much more numerous than organic cations. Compared with polyolefin/MMT nanocomposites prepared with similar concentration of particles, polyolefin/LDH ones display lower stiffness and mechanical strength. LDH platelet does not cause as much mechanical reinforcing as one of the MMT or other cationic clays. This would be due to lower inherent mechanical properties of LDH platelet in comparison with that of the cationic clays. As a consequence, polyolefin/LDH nanocomposites can be used in functional applications where it is important to maintain the mechanical properties of the polyolefin (e.g., films and coatings, etc.).

As in polyolefin/MMT nanocomposites, the oxygen permeability through polyolefin/LDH films is reduced in comparison with that of the pure polyolefin. Values in PP nanocomposites seem to indicate better performance of LDH than MMT for a similar weight fraction. The cause of such improvement could be related with both lower density and platelet thickness of LDH compared with MMT.

In flame-retardant polyolefin formulations, MgAl LDH can effectively compete with micrometric aluminum and magnesium hydroxides. These compounds act by lowering the flame energy and diluting the combustible gases because of endothermic decomposition and liberation of water. The nano-oxide residue could promote a more homogeneous protective layer for the condensed phase. Even ZnAl LDH could have a smoke-suppressant effect similar to that of the zinc oxide. LDH does not compete with cationic nanoclays due to the different action mechanisms. Therefore, nano-LDH can be effectively used in combination with silicates and/or other flame-retardant additives and fillers. Synergistic effects concerning LDH nanoplatelets have still to be studied.

11.11 CONCLUSIONS

The interlayer spacing of layered double hydroxides is increased by ionic exchange of dodecylsulfate and dodecylbenzene sulfonate anions. Different polyolefin/LDH nanocomposites have been prepared by melt mixing organophillized LDH with different polyethylenes and polypropylenes. In general, their structure is formed by a mixture of individual platelets and stacks of them obtained by exfoliation due to the melt-mixing shearing forces. These nanocomposites are mainly characterized by higher melt shear viscosity, improved flame retardancy, and slightly higher elasticity modulus than the pure polyolefins.

Polypropylene/LDH nanocomposites display improved thermal and mechanical properties when compared with pure PP and conventional LDH microcomposite. The crystallization rate is slightly increased and a higher crystallinity degree results. Both moderate increase in stiffness and decrease in ductility are found. The tensile strength of PP/LDH nanocomposites remains almost unaffected in pure PP. It has been shown that compatibilizer polymers like PP-g-MAH and SEBS-g-MAH are not

essential to prepare exfoliated PP/LDH nanocomposites. Nevertheless, they slightly improve the LDH dispersion and play an important role in promoting variations in the structure and properties of the composite material.

In polyethylene/LDH nanocomposites, the use of compatibilizer copolymers generally also improves the LDH dispersion. However, the final structure and properties of these nanocomposites are quite different, depending not only on the compatibilizer but also on the type of polyethylene (LDPE, HDPE, and LLDPE), layered double hydroxide (MgAl LDH and ZnAL LDH), interlamellar organic anion (DS and DBS), as well as on the nanocomposite preparation method (melt mixing and, solution intercalation). Crystalline characteristics of polyethylene are found to be hardly affected by LDH nanoparticles. However, polyethylene rheological properties are notably improved, as well as its thermal stability.

At present, LDH appears as a promising new kind of component in polyolefin composites for halogen-free flame-retardant cables and gas barrier films among other functional applications. Polyolefin/LDH nanocomposites are going to be studied in greater detail in the near future.

NOMENCLATURE

$d_{(003)}$	Interplanar distance of the layered double hydroxide (003) diffraction plane
DBS	Dodecylbenzene sulfonate ion
dc	Direct current
DS	Dodecylsulfate ion
DTA	Differential thermal analysis
E	Young's modulus.
E_α	Activation energy
EMAA	Poly(ethylene-co-methacrylic acid)
FTIR	Fourier transform infrared spectroscopy
G'	Storage shear modulus
HDPE	High density polyethylene
HDPE-g-MAH	High density polyethylene-graft-maleic anhydride
HMWPCL	High molecular weight poly(ε-caprolactone)
LDH	Layered double hydroxide
LDH(Cl)	Chloride containing layered double hydroxide
LDH(DS)	Dodecylsulfate containing layered double hydroxide
LDPE	Low density polyethylene
LLDPE	Linear low density polyethylene
LDPE-g-MAH	Low density polyethylene-graft-maleic anhydride
LOI	Limiting oxygen index
L/D	Length-to-diameter ratio

MFI	Melt flow index
MgAl NC	Magnesium and aluminum LDH-based nanocomposite
MMT	Montmorillonite
n	Shear thinning exponent
OTR	Oxygen transmission rate
PAA	Poly(acrylic acid)
PAN	Polyacrilonitrile
PA6	Polyamide (Nylon) 6
phr	Parts per hundred parts of resin
PCL	Poly(ε-caprolactone)
PMMA	Poly(methyl methacrylate)
PP	Polypropylene
PPC	Poly(propylene carbonate)
PP-g-MAH	Polypropylene-graft-maleic anhydride
PS	Polystyrene
PSS	Poly(styrene sulfonate)
PVS	Poly(vinyl sulfonate)
rpm	Revolutions per minute
SDBS	Sodium dodecylbenzene sulfonate
SEBS	Poly(styrene–ethylbutylene–styrene)
SEBS-g-MAH	Poly(styrene–ethylbutylene–styrene)-graft-maleic anhydride
T_c	Crystallization peak temperature
TEM	Transmission electron microscopy
TFBD	Time to first burning drop
TGA	Thermogravimetric analysis
T_m	Melting peak temperature
UL-94	Underwriter's Laboratory test for flammability
UV	Ultraviolet
Vicat	Softening temperature
WAXD	Wide-angle X-ray diffraction
X_c	Crystallinity determined from the DSC crystallization signal
X_m	Crystallinity determined from the DSC melting signal
ZnAl NC	Zinc and aluminium LDH-based nanocomposite
α	Extent of reaction
ΔH_c	Enthalpy of crystallization
ΔH_m	Enthalpy of melting
ΔH_m	Melting enthalpy value for 100% crystalline polymer
ε_{max}	Strain at maximum load
γ_0	Shear strain amplitude
$\gamma(t)$	Shear strain function
σ_{max}	Maximum stress
ω	Shear strain frequency
$\lvert\eta^*\rvert$	Complex viscosity

REFERENCES

1. T. J. Pinnavia and G. W. Beall (eds.), *Polymer–Clay Nanocomposites*, Wiley, New York, 2000.
2. E. P. Giannelis, *Adv. Mater.*, **8**, 29 (1996).
3. R. A. Vaia, S. Vasudevan, W. Krawiec, L. G. Scanlon, and E. P. Giannelis, *Adv. Mater.*, **7**, 154 (1995).
4. J. Heinemann, P. Reichert, R. Thomann, and R. Mülhlhaupt, *Macromol. Rapid Commun.*, **20**, 423 (1999).
5. P. Kodgire, R. Kalgaonkar, S. Hambir, N. Bulakh, and J. P. Jog, *J. Appl. Polym. Sci.*, **81**, 1786 (2001).
6. J. I. Velasco, M. Ardanuy, V. Realinho, M. Antunes, A. I. Fernández, J. I. González-Peña, M. A. Rodríguez-Pérez, and J. A. de Saja, *J. Appl. Polym. Sci.*, **102**, 1213 (2006).
7. U. N. Ratnayake and B. Haworth, *Polym. Eng. Sci.*, **46**, 1008 (2006).
8. Y. Liu and M. Kontopoulou, *Polymer*, **47**, 7731 (2006).
9. H. Zhao and R. K. Y. Li, *Polymer*, **47**, 3207 (2006).
10. R. Xalter, T. S. Halbach, and R. Mülhaupt, *Macromol. Symp.*, **236**, 145 (2006).
11. F. Leroux and J. P. Besse, *Chem. Mater.*, **13**, 3507 (2001).
12. F. Leroux, *J. Nanosci. Nanotechnol.*, **6**, 1 (2006).
13. Y. Sugahara, N. Yokoyama, K. Kuroda, and C. Kato, *Ceram. Int.*, **14**, 163 (1988).
14. O. C. Wilson Jr., T. Olorunyolemi, A. Jaworski, L. Borum, D. Young, A. Siriwat, E. Dickens, C. Oriakhi, and M. Lerner, *Appl. Clay Sci.*, **15**, 265 (1999).
15. C. O. Oriakhi, I. V. Farr, and M. M. Lerner, *J. Mater. Chem.*, **6**, 103 (1996).
16. Z. Liu, R. Ma, M. Osada, N. Iyi, Y. Ebina, K. Takada, and T. Sasaki, *J. Am. Chem. Soc.*, **128**, 4872 (2006).
17. N. T. Whilton, P. J. Vickers, and S. Mann, *J. Mater. Chem.*, **7**, 1623 (1997).
18. L. Tammaro, M. Tortora, V. Vittoria, U. Costantino, and F. Marmottini, *J. Polym. Sci. A Polym. Chem.*, **43**, 2281 (2005).
19. H. B. Hsueh and C. Y. Chen, *Polymer*, **44**, 1151 (2003).
20. H. B. Hsueh and C. Y. Chen, *Polymer*, **44**, 5275 (2003).
21. M. Zammarano, M. Franceschi, S. Bellayer, J. W. Gilman, and S. Meriani, *Polymer*, **46**, 9314 (2005).
22. R. Gensler, P. Gröppel, V. Muhrer, and N. Müller, *Part. Part. Syst. Charact.*, **19**, 293 (2002).
23. F. Leroux, P. Aranda, J. P. Besse, and E. Ruiz-Hizky, *Eur. J. Inorg. Chem.*, **6**, 1242 (2003).
24. M. S. Cho, B. Shin, S. D. Choi, Y. Lee, and K. G. Song, *Electrochim. Acta*, **50**, 331 (2004).
25. G. A. Wang, C. C. Wang, and C. Y. Chen, *Polymer*, **46**, 5065 (2005).
26. G. A. Wang, C. C. Wang, and C. Y. Chen, *Polym. Degrad. Stabil.*, **91**, 2443 (2006).
27. F. Leroux, L. Meddar, B. Mailhot, S. Morlat-Thérias, and J. L. Gardette, *Polymer*, **46**, 3571 (2005).
28. P. Ding and B. J. Qu, *J. Appl. Polym. Sci.*, **101**, 3758 (2006).
29. F. A. He, L. M. Zhang, F. Yang, L. S. Chen, and Q. Wu, *J. Polym. Res.*, **13**, 483 (2006).
30. L. Qiu and B. J. Qu, *J. Colloid Interface Sci.*, **301**, 347 (2006).
31. T. Y. Tsai, S. W. Lu, Y. P. Huang, and F. S. Li, *J. Phys. Chem. Solids*, **67**, 938 (2006).
32. W. Chen and B. Qu, *Chem. Mater.*, **15**, 3208 (2003).
33. L. Du, B. J. Qu. Y. Meng, and Q. Zhu, *Compos. Sci. Technol.*, **66**, 913 (2006).
34. K. Lee and J. D. Nam, *J. Power Sources*, **157**, 201 (2006).
35. W. Daming, M. Quigyun, L. Ying, D. Yumei, C. Weihong, X. Hong, and R. Dongyun, *J. Polym. Sci. B Polym. Phys.*, **41**, 1051 (2003).
36. J. I. Velasco, M. Antunes, O. Ayyad, J. M. López-Cuesta, P. Gaudon, C. Sáiz-Arroyo, M. A. Rodríguez-Pérez, and J. A. de Saja, *Polymer*, **48**, 2098 (2007).

37. J. I. Velasco, M. Antunes, O. Ayyad, C. Sáiz-Arroyo, M. A. Rodríguez-Pérez, F. Hidalgo, and J. A. de Saja, *J. Appl. Polym. Sci.* **105**, 1658 (2007).
38. M. Zammarano, S. Bellayer, J. W. Gilman, M. Franceschi, F. L. Beyer, R. H. Harris, and S. Meriani, *Polymer*, **47**, 652 (2006).
39. W. D. Lee, S. S. Im, H. M. Lim, and K. J. Kim, *Polymer*, **47**, 1364 (2006).
40. M. Wang, M. F. Zhu, and B. A. Sun, *J. Macromol. Sci. A*, **43**(11), 1867 (2006).
41. F. R. Costa, M. Abdel-Goad, U. Wagenknecht, and G. Heinrich, *Polymer*, **46**, 4447 (2005).
42. F. R. Costa, U. Wagenknecht, D. Jehnichen, M. Abdel-Goad, and G. Heinrich, *Polymer*, **47**, 1649 (2006).
43. F. R. Costa, B. K. Satapathy, U. Wagenknecht, R. Weidisch, and G. Heinrich, *Eur. Polym. J.*, **42**, 2140 (2006).
44. L. Qiu, W. Chen, and B. J. Qu, *Polymer*, **47**, 922 (2006).
45. L. C. Du and B. J. Qu, *J. Mater. Chem.*, **16**, 1549 (2006).
46. P. Ding and B. J. Qu, *J. Polym. Sci. B Polym. Phys.*, **44**, 3165 (2006).
47. P. Ding and B. J. Qu, *Polym. Eng. Sci.*, **46**, 1153 (2006).
48. S. Guo, D. Li, W. Zhang, M. Pu, D. G. Evans, and X. Duan, *J. Solid State Chem.*, **177**, 4597 (2004).
49. D. Li, Z. Tuo, D. G. Evans, and X. Duan, *J. Solid State Chem.*, **179**, 3114 (2006).
50. A. de Roy, C. Forano, and J. P. Besse, Layered double hydroxides: Syinthesis and post-synthesis modification, in: *Layered Double Hydroxides: Present and Future*, V. Rives (ed.), Nova Science Publishers, New York, 2001, Chapter 1.
51. M. Tanaka, I. Y. Park, K. Kuroda, and C. Kato, *Bull. Chem. Soc. Jpn.*, **62**, 3442 (1989).
52. F. Leroux, M. Adachi-Pagano, M. Intissar, S. Chauvière, C. Forano, and J. P. Besse, *J. Mater. Chem.*, **11**, 105 (2001).
53. R. Trujillano, M. J. Holgado, and V. Rives, *Stud. Surf. Sci. Catal.*, **142**, 1387 (2002).
54. M. A. Drezdon, *Inorg. Chem.*, **27**, 4628 (1998).
55. W. F. Jaynes and G. F. Vance, *Soil Sci. Soc. Am. J.*, **60**, 1742 (1996).
56. J. I. Velasco, M. Ardanuy, I. Chainho, F. Picca, A. Briz, A. Gordillo, A. B. Martínez, L. Miralles, and A. I. Fernández, Nanocompuestos de poliolefinas con hidróxidos dobles laminares, in: *Proceedings of the VIII Congreso Nacional de Materiales*, SPUPV Valencia, Spain, 2004, pp. 1163–1170.
57. M. Ardanuy, PhD dissertation, Technical University of Catalonia, UPC, Barcelona, (2006).
58. Y. Tsujita, M. Yasuda, M. Takei, T. Kinoshita, A. Takizawa, and H. Yoshimizu, *Macromolecules*, **34**, 2220 (2001).
59. R. A. Vaia and W. Liu, *J. Polym. Sci. B Polym. Phys.*, **40**, 1590 (2002).
60. R. Wagner and T. J. G. Reisinger, *Polymer*, **44**, 7513 (2003).
61. J. I. Velasco, Internal Report, Centre Català del Plàstic, Barcelona (2004).

Chapter 12

Effect of Nanofillers on Crystallization, Phase Transformation, and Thermomechanical Behavior of Poly(1-Butene)

Santosh D. Wanjale[1] and Jyoti P. Jog[1]

12.1 INTRODUCTION

Poly(1-butene) (PB) is one of the members of polyolefin family. It is synthesized by polymerization of butene-1 with a stereospecific Ziegler–Natta catalyst to produce a linear, high molecular weight and isotactic semicrystalline polymer. It has excellent mechanical properties superior to those offered by other members of polyolefin family.

A major application area for polybutene resins is seal-peel or easy-open packaging. The pipes produced from PB are being used in modern domestic and institutional heating and plumbing systems due to the inherent flexibility, excellent creep, and burst pressure resistance. It is also used in heavy-duty bags, pressure-sensitive tapes, agricultural films, gaskets, and diaphragms. In applications where high impact resistance is required at low temperature, PB is preferred over isotactic polypropylene (iPP) and poly(4-methyl-1-pentene) (PMP). However, its applications are limited compared to other polyolefins such as polyethylene (PE) and polypropylene

[1]Polymer Science and Engineering Division, National Chemical Laboratory, Dr. Homi Bhabha Road, Pashan, Pune 411008, Maharashtra, India

Polyolefin Composites, Edited by Domasius Nwabunma and Thein Kyu

Table 12.1 Crystalline Forms of PB and Their Properties.

Form	Crystal lattice	Helix	T_m, °C	Density, g cm^{-3}
I	Hexagonal (twinned)	3_1	125–138	0.95
I′	Hexagonal (untwined)	3_1	90–100	—
II	Tetragonal	11_3	110–120	0.90
III	Orthorhombic	4_1	90–100	0.90

(PP) because of the slow room temperature phase transformation, which complicates the production of goods with stable mechanical properties.

PB exhibits very complex polymorphic behavior and can crystallize in four polymorphic forms depending on the conditions of crystallization and the presence of other components. The characteristics of the various forms and their chain conformations are presented in Table 12.1. After melting, PB crystallizes in the tetragonal crystal form II with 11_3 helix and then it transforms into stable twined hexagonal crystal form I of 3_1 helix. As a result, the chain packing is improved with a substantial increase in the density from 0.90 g cm^{-3} to approximately 0.95 g cm^{-3}. These structural changes are also associated with significant changes in the mechanical properties such as tensile strength, stiffness, and hardness. Form I generally melts at 125–138°C, whereas form II melts at low temperature around 110–120°C. The phase transformation process from form II to form I starts soon after the crystallization of form II and is generally completed in about 10 days. The third form with an orthorhombic unit cell with 4_1 helix can be obtained by precipitating the polymer from various solvents. Form III melts at about 100°C. The fourth form is I′ with untwined hexagonal form of 3_1 helical structure and melts at around 90–100°C (1).

12.1.1 Crystallization and Phase Transformation of PB

The crystallization of poly(1-butene) is of great interest because of its spontaneous, kinetically favored (PBII) to thermodynamically stable (PBI) phase transformation in solid state. It is well known that the crystal form PBI shows superior mechanical properties than the PBII. As the phase transformation takes place over a period of 10 days, the slow kinetics hampers the commercial development of the PB. As a result, there is tremendous interest in finding the novel routes to accelerate the rate of phase transformation from form II to form I. It is thus indispensable to study the kinetics of spontaneous time-dependent crystalline transformation from tetragonal form II to twinned hexagonal form I. Researchers have tried different techniques to study the rate of phase transformation, such as differential scanning calorimetry (DSC), X-ray diffraction (XRD), and IR spectroscopy (2–5).

Hong and Spruiell (6) examined the effects of cold rolling, orientation produced in film blowing, and some additives on the rate of phase transformation by XRD and density measurements. They revealed that the cold rolling was an effective method as

it causes a rapid partial transformation to form I followed by further transformation at enhanced rates. The molecular orientation induced during melt processing also enhances the rate of transformation. The mechanical blending of PP (5–10 wt%) resulted in acceleration of the phase transformation process, whereas addition of 1-naphthylacetamide, a known nucleating agent, did not increase the rate when added at 0.1%. A special attempt has been made to enhance the phase transformation rate by increasing the tie molecules or tie fibrils population by controlling the crystallization process, and the authors claimed (7) that the major effect of variation of the crystallization conditions is the change in the number of interactions of crystalline segments with the amorphous phase.

Pressure (8), temperature (9), and mechanical deformation (1) were found to influence the kinetics. In the case of PP/PB blend system, the transformation rate for 75 wt% PB composition was found to be higher than those for the other compositions and surprisingly form I was not observed in the case of 15 wt% PB (10).

The nucleating agents such as pimelic acid, azelaic acid, the quinacridone dye permanent red E3B, and the mixture of calcium carbonate and pimelic acid have been found to be effective in accelerating the isothermal crystallization and form II to form I transformation in PB. Among these E3B, calcium carbonate–pimelic acid mixture was found to be most efficient as reported by Zhang et al. (11).

The isothermal crystallization and phase transformation kinetics at various temperatures have been studied by Rybnikar et al. (12). The crystallization rate was found to increase or decrease as a result of addition of various solid additives. The crystallization rate was increased by 100% in the presence of sodium salicylate while with talc the rate was unexpectedly decreased by about 300%. The most important observation of this study was that the nucleating agents had no effect on the phase transformation rate.

12.1.2 Polymer Nanocomposites

Nanocomposites is an emerging area in the industries as well as academia. Recently, the polymer composites with nanofillers are studied due to the significant enhancement in physical and mechanical properties compared to the microcomposites with very small amount of nanofillers than the microfillers. The main property improvements include higher modulus at low loading of the nanofillers, higher heat distortion temperature (HDT), dramatic decrease in coefficient of thermal expansion (CTE), improved dimensional stability, flame retardancy, and improved barrier properties. Since the loading of the nanofillers required to bring about significant changes in the physical properties of the polymers is generally less than 5%, these nanocomposites are amenable to most of the common processing techniques and these are more recyclable. These nanocomposites are easily dyeable and exhibit better appearance of painted parts. The nanofillers that are generally used include layered silicates, nanotubes, and various nanoparticles (13–30).

In this chapter, the results of the crystallization, crystal-to-crystal phase transformation, and dynamic mechanical behavior of PB in the presence of nanofillers such as clay, nanotubes, and nanoparticles have been discussed.

12.1.3 Preparation of PB Nanocomposites

12.1.3.1 Materials

Poly(1-butene) with molecular weight of $570,000\,g\,mol^{-1}$ procured from Aldrich was used for the present investigation.

Nanoclay: Organically modified layered silicate, Nanocor (octadecylamine-treated MMT), was generously supplied by Nanocor Inc.

Multiwalled carbon nanotubes (MWCNTs) (internal diameter 5–10 nm, outer diameter 10–20 nm, length 0.5–200 μm, and with 95% purity) and $BaTiO_3$ nanoparticles (30–50 nm) were procured from Aldrich Chemicals.

12.1.3.2 Compounding and Characterization

Melt compounding was carried out in a Thermo Haake Polylab batch mixer at 150°C with 60 rpm for 7 min. The films were compression molded using Carver press model F-15181 and used for further characterization. The sample codes for the nanocomposites are given in Table 12.2. The structure of the PB/clay nanocomposites was evaluated using Rigaku X-ray diffractometer, model Dmax 2500 with Cu $K_{\alpha 1}$ ($\lambda = 0.154$ nm) radiation operated at 40 kV and 100 mA. The samples were scanned in the 2θ range of 2–15°. The basal spacing of the clay was estimated from the d_{001} peak in the XRD pattern.

The dispersion of clay in the polymer matrix was evaluated using transmission electron microscopy. The nanocomposite film was microtomed using Leica Ultracut UCT ultramicrotome with diamond knife and a 100-nm-thick sample was taken on copper grid (400 mesh) to view under a JEOL (JEM 1200 EX) transmission electron microscope.

The fractured surface morphology was viewed using Leica-440 scanning electron microscope, for the dispersion of multiwalled carbon nanotubes and $BaTiO_3$ nanoparticles in the polymer matrix.

Nonisothermal and isothermal crystallization were studied by using a Perkin-Elmer DSC-2 with TADS, in nitrogen atmosphere. The energy and temperature

Table 12.2 Sample Codes for the Nanocomposites.

Nanofiller	Concentration, wt%	Code
Nanocor clay	3	PB3N
	5	PB5N
	7	PB7N
Multiwalled carbon nanotubes	3	PB3C
	5	PB5C
	7	PB7C
Barium titanate	5	PB5$BaTiO_3$
	7	PB7$BaTiO_3$

scales were calibrated using indium as a standard. Nonisothermal crystallization was studied for different cooling rates. The sample was heated at a rate of 10°C min^{-1} up to 150°C and held for 2 min to ensure complete melting, and then crystallization peaks were recorded at different cooling rates. In isothermal crystallization, the sample was heated at a rate of 40°C min^{-1} up to 150°C and held for 2 min, and then quenched at a cooling rate of 160°C min^{-1} to the desired crystallization temperature (T_c), and the isothermal peak was recorded. The spherulitic morphology of PB and nanocomposites was studied with a Leica Laborlux 12 Pol S polarized light microscope. The samples were prepared by melt pressing at 160°C between a glass slide and a coverslip and kept for a minute to ensure uniform melting. The slide was then transferred to the hot stage maintained at 80°C. The photomicrographs were taken under cross-polarizers with a Cannon Powershot S 50 digital camera.

The phase transformation of PB was studied using Perkin-Elmer DSC-7. The temperature and energy scales were calibrated using standard procedures. The samples for this study were prepared by melting the polymer in DSC at a rate of 10°C min^{-1} up to 150°C and cooling it at a rate of 40°C min^{-1} up to room temperature. This step was carried out to ensure identical thermal history for each sample. The samples were then stored at room temperature for various time intervals ranging from 30 min to about 9 days. Dynamic mechanical properties of the samples were studied on compression-molded films using rheometric dynamic mechanical analyzer model IIIE in the tensile mode. The samples were tested in a temperature range from −50 to 100°C and at a frequency of 10 rad s^{-1} and 0.02% strain.

Thermogravimetric analysis was carried out using Perkin-Elmer thermal analysis system model TGA 7. The TGA scans were recorded at a heating rate of 10°C min^{-1} under nitrogen atmosphere in a temperature range from 50 to 550°C.

12.2 PB/CLAY NANOCOMPOSITES

12.2.1 Clay

Montmorillonite clay (MMT) is used in the preparation of nanocomposites. MMT belongs to phyllosilicate class (2:1 layered structure) having flat thin morphology with extremely high surface area of about 750 $m^2 g^{-1}$. MMT consists of two fused silica tetrahedral sheets and an edge-shared octahedral sheet of either magnesium or aluminum hydroxide sandwiched between them making the thickness of 1 nm. One of the important properties of MMT is the ion-exchange capacity. The intergallery ions such Al^{3+} and Mg^{2+} can be easily exchanged by the organic molecules such as quaternary amine and ammonium salts to make the MMT organophilic and consequently to improve the interactions with the polymer matrix.

12.2.1.1 Organic Modification of Clay

MMT is treated with organic modifiers to make them organophilic. The organo-modified clays are prepared by reacting more voluminous organic onium cations

with the montmorillonite clay. The reaction results in the exchange of relatively small sodium ions with organic counterions. This ion exchange results in an increase of the clay interlayer space, enabling organic cation chains to move in between them, and secondly, the surface properties of each clay sheet are changed from hydrophilic to hydrophobic. Such a modification is sufficient to facilitate intercalation in polar polymers such as Nylons. However, in the case of polyolefins, use of organoclay only is not sufficient to obtain intercalated or exfoliated nanocomposites. This is mainly due to the low polarity of these polymers, which makes it difficult for intercalation and homogeneous dispersion of the silicate layers. Thus, the use of a third component, a compatibilizer, becomes necessary to facilitate the formation of an intercalated or exfoliated polymer/clay nanocomposite. A lot of work has been reported on the use of compatibilizers for polyethylene and polypropylene. However, unlike other polyolefins, PB can be intercalated into the clay layers without use of any compatibilizers as shown in the following section.

12.2.1.2 Melt Intercalation

The process of melt intercalation depends mainly on two factors, first is the interaction between the polymer chains and the host silicate layers and second is the transport of polymer chains. The organically modified clay provides such interactions and under the action of shear the intercalation of polymer takes place. The intercalated polymer chains occupy the interlayer space in the organically modified clay and this finite layer expansion results in a new basal reflection corresponding to larger *d* spacing as observed in the XRD patterns. The process of melt intercalation is schematically shown in Fig. 12.1.

Depending on the interactions of the layered silicates with the polymer matrix, three different structures can be defined for the nanocomposites, namely immiscible (microcomposites), intercalated, and exfoliated. In the immiscible structure, the layered silicate remains as such without any infiltration of polymeric chains. The intercalated structure is the one in which the polymer chains infiltrate into the clay galleries and increase the gallery height but the layers remained stacked without losing the ordered structure. In the exfoliated structure, the clay layers are well separated as individual layers without any ordered structure and are well dispersed in

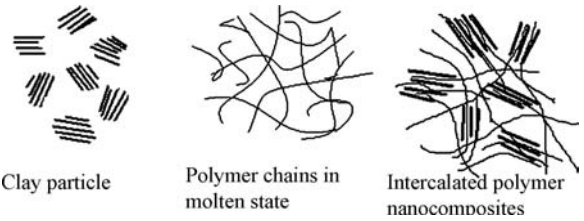

Figure 12.1 Schematic representation of the melt intercalation process.

the polymer matrix. In the melt intercalation process, however, a combination of intercalated and exfoliated structures is generally obtained.

12.2.2 Structure Evaluation

The intercalation of polymer matrix into the layered silicates can be directly probed by X-ray diffraction patterns. The interactions of polymer matrix with the layered silicates govern the changes in the diffractions patterns of the composites. An increase in *d* spacing generally suggests an intercalated structure, while the complete disappearance of the peaks suggests delamination of the clay layers leading to the exfoliated structures. The XRD pattern of Nanocor clay shows a characteristic peak at a 2θ value of 3.6° corresponding to a basal spacing of 2.4 nm. The nanocomposites exhibit well-defined diffraction peaks with the increase in *d* spacing of about 0.4, 0.54, and 0.32 nm for PB3N, PB5N, and PB7N, respectively. The increase in *d* spacing as a function of clay content is shown in Fig. 12.2. The increase in the *d* spacing for all the three compositions confirms the intercalation of polymer in clay layers and thus the formation of intercalated structures in PB/clay nanocomposites.

Dispersion of the clay layers in PB is studied using transmission electron microscopy (TEM). Figure 12.3 shows the TEM micrograph for the PB5N nanocomposites. The nanoscale dispersion of the clay layers (dark lines) in the polymer matrix is clearly discernible.

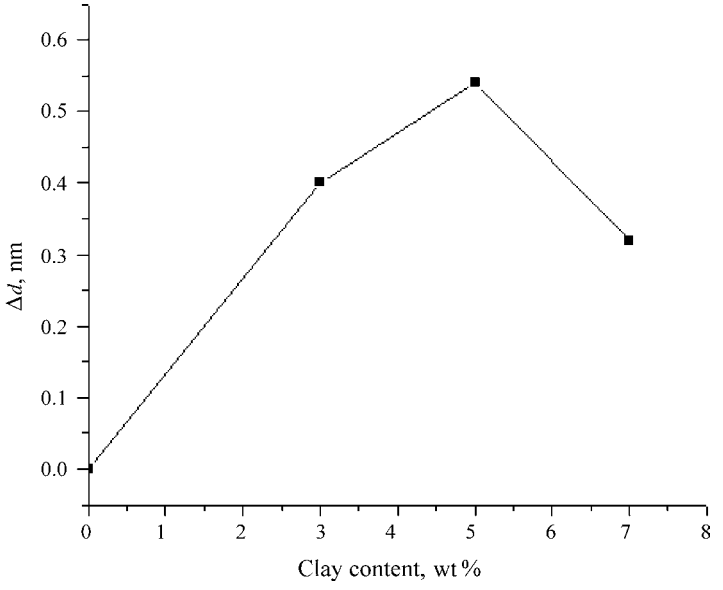

Figure 12.2 Change in *d* spacing (Δd) for PB/clay nanocomposites as a function of clay content.

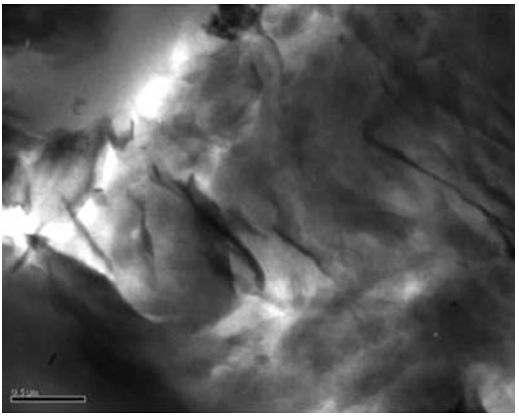

Figure 12.3 TEM micrograph for PB5N (scale bar: 0.5 μm).

12.2.3 Nonisothermal Crystallization

The presence of nanoscale clay layers is known to bring about significant changes in the crystallization behavior and polymorphic nature in semicrystalline polymers. In Nylon 6 (PA), the γ-form is predominantly observed in the presence of layered silicates, while Priya et al. reported the piezoelectric β-form in polyvinylidine fluoride (PVDF) for intercalated nanocomposites with organically modified layered silicates (31,32). It was thus interesting to study the effect of clay layers on the crystallization behavior of PB.

Nonisothermal crystallization behavior of PB and nanocomposites with clay was studied to investigate the effect of cooling rate. Different cooling rates of 2.5, 5, 10, and 20°C min^{-1} were used. The crystallization parameters for PB and nanocomposites for different cooling rates are shown in Table 12.3. It can be seen that the crystallization peak temperature (T_p) for both PB and nanocomposites was shifted to lower temperatures as the cooling rate was increased. However, it was observed that at a given cooling rate, T_p of PB7N nanocomposite was higher than that of pristine PB. This clearly suggested that incorporation of clay results in enhanced nucleation for the PB matrix.

The nonisothermal crystallization peaks were further analyzed for the total crystallization time. For this purpose, the temperature scale was converted to time-scale as follows:

$$t_c = (T_i - T_f)/\varphi \tag{12.1}$$

where T_i is the initial crystallization temperature, T_f is the final crystallization temperature, and ϕ is the cooling rate. From the observed data of crystallization peak temperature and the time required for crystallization in the case of PB and PB/clay nanocomposites, it can be concluded that the crystallization process was enhanced due to incorporation of clay in the PB matrix and clearly suggested the heterogeneous nucleation.

Table 12.3 Nonisothermal Crystallization Parameters by Avrami for PB and PB Nanocomposites.

Sample	ϕ, K min^{-1}	$t_{1/2}$ (min)	T_p, K	n	Z_t
PB	2.5	1.5	352.4	4.2	4.99×10^{-3}
	5	1.1	347.3	4.5	5.28×10^{-2}
	10	1.0	342.8	4.6	0.54
	20	0.9	335.9	4.2	3.48
PB7N	2.5	1.3	356	3.7	2.47×10^{-2}
	5	1.0	351	4.3	6.99×10^{-2}
	10	0.9	347	4.2	0.725
	20	0.9	341.5	4.5	8.89
PB7C	2.5	1.3	365.8	4.7	0.02
	5	1.0	362.6	4.8	0.08
	10	0.9	357.9	4.6	1.07
	20	0.8	352.3	4.1	7.75
PB7BaTiO$_3$	2.5	1.4	356.5	4.2	1.02×10^{-2}
	5	1.0	352.4	4.5	9.39×10^{-2}
	10	0.9	348.0	4.1	1.296
	20	0.9	340.8	3.9	8.097

12.2.3.1 Nonisothermal Crystallization Kinetics

The nonisothermal crystallization kinetics was studied using Avrami theory by converting temperature scale into the timescale for various degrees of cooling rates. For isothermal crystallization kinetics (33–35), the Avrami equation was used as given below.

$$1 - X_t = \exp(-Z_t t^n) \tag{12.2}$$

Converting Equation 12.1 into logarithmic form as follows:

$$\log[-\ln(1 - X_t)] = n \log t + \log Z_t \tag{12.3}$$

where X_t is the relative degree of crystallinity at time t, n is the Avrami exponent, and Z_t is a rate constant, signifies the nucleation and growth rate kinetics. The Z_t values are being corrected for the nonisothermal purpose, which converts the temperature scale into the timescale by

$$\log Z_c = \frac{\log Z_t}{\varphi} \tag{12.4}$$

The plot of log $[-\ln(1 - X_t)]$ versus log t gave straight lines; the Avrami exponent (n) and growth rate parameter (Z_t) were calculated from the slope and intercept, respectively.

The crystallization half-time ($t_{1/2}$) was calculated using the following equation:

$$t_{1/2} = \left(\frac{\ln 2}{Z_c}\right)^{1/n} \tag{12.5}$$

The $t_{1/2}$, n, and Z_t values are given in Table 12.3. As the cooling rate increased, the Z_t value also increased in both PB and PB7N; however, the nanocomposite showed higher values compared to pristine PB. The $t_{1/2}$ values for nanocomposites are found to be slightly lower than those for PB. The above results signify that the rate of crystallization is enhanced in the nanocomposite.

Ozawa (36) introduced the combined Avrami–Ozawa equation for the determination of nonisothermal crystallization kinetics.

$$\log Z_t + n \log t = \log K(T) - m \log \varphi \tag{12.6}$$

The above equation is converted to

$$\log \varphi = \log F(T) - a \log t \tag{12.7}$$

where $F(T) = [K(T)/Z_t]^{1/m}$ and a is the ratio between the Avrami and Ozawa exponents, that is, n/m. $F(T)$ refers to the value of the cooling rate chosen at unit crystallization time, when the system has a defined degree of crystallinity.

The plots of log ϕ versus log t yielded a straight line at a defined crystallinity with log $F(T)$ and $-a$ determined by intercept and slope, respectively. From the plots of log ϕ versus log t at different degrees of crystallinities, the values of $F(T)$ and a are determined, as shown in Table 12.4. It is revealed from the data that the values of

Table 12.4 Nonisothermal Crystallization Parameters by Combined Avrami–Ozawa Equation for PB and PB Nanocomposites.

Sample	X_t, %	$F(T)$	a
PB	20	8.1	1.3
	40	10.3	1.3
	60	12.2	1.3
	80	14.7	1.3
PB7N	20	6.6	1.4
	40	8.5	1.4
	60	10.4	1.4
	80	12.4	1.4
PB7C	20	6.1	1.4
	40	7.9	1.4
	60	9.3	1.4
	80	11.5	1.5
PB7$BaTiO_3$	20	6.3	1.2
	40	8.1	1.2
	60	9.5	1.2
	80	11.2	1.3

$F(T)$ were increased with the relative degree of crystallinity, signifying that the time required for reaching the defined degree of crystallinity increased for the given cooling rate. In the case of nanocomposite, the values of $F(T)$ are found to be lower than those for PB, suggesting time required to attain the certain degree of crystallinity is lowered compared to the time required for the same degree of crystallinity for the pristine polymer.

12.2.3.2 Nucleating Activity

The nucleating activity of the clay was determined by the method used by Dobreva and Gutzow (37), where the cooling rate and the degree of supercooling were taken into consideration. For homogeneous nucleation, the following equation was used:

$$\log \varphi = A - \frac{B}{2.303\Delta T_{\mathrm{p}}^2} \tag{12.8}$$

For the heterogeneous system in which the foreign particles help in crystallization, the following equation was used:

$$\log \varphi = A - \frac{B^*}{2.303\Delta T_{\mathrm{p}}^2} \tag{12.9}$$

where ϕ is the cooling rate, ΔT_{p} is the degree of supercooling ($T_{\mathrm{m}} - T_{\mathrm{p}}$), and A, B, and B^* are constants. B is a parameter that can be calculated using the following equation:

$$B = \frac{\omega\sigma^3 V_{\mathrm{m}}^2}{nkT_{\mathrm{m}}\Delta S_{\mathrm{m}}^2} \tag{12.10}$$

where ω is a geometrical factor, σ is the specific surface energy, V_{m} is the molar volume of the crystallizing substance, n is the Avrami exponent, ΔS_{m} is the entropy of melting, and k is the Boltzman constant. Φ, the nucleating activity, is determined from the ratio of B^* to B, the slopes of linear function $\log \phi$ as a function of $1/\Delta T_{\mathrm{p}}^2$. It has been stated that as Φ tends to zero more is the active surface, while if it tends to 1 the surface is considered as an inert surface for nucleation (38). The nucleating activity was calculated from the crystallization temperatures at various cooling rates for 7% clay nanocomposites and found to be 0.897, which suggest that in this system clay is acting as nucleating agent.

12.2.4 Isothermal Crystallization

The isothermal crystallization of PB and PB/clay nanocomposites was studied to determine the effect of incorporation of layered silicates. The measurements were carried out over a temperature range from 80 to 90°C. The Avrami equation was used

to analyze the isothermal curves for the crystallization kinetics in PB and PB/clay nanocomposites.

$$X_t = 1 - \exp(-Kt^n) \tag{12.11}$$

where X_t is the relative degree of crystallinity at different crystallization times, n is the Avrami exponent that gives dimensionality of the crystal, and K is the rate constant related to nucleation and growth parameters. Equation (12.11) can be written as follows:

$$\log[-\ln(1 - X_t)] = n \log t + \log K \tag{12.12}$$

By plotting log $[-\ln(1 - X_t)]$ versus log t, a straight line could be obtained if the crystallization kinetics obeys Avrami theory. The Avrami exponent (n) and the crystallization kinetic constant (K) were obtained from the slope and the intercept of the straight lines, respectively. The total crystallization time (t_c) and the rate constant were calculated from the plots. The rate constant at 86°C for PB was 1.03×10^{-4}, while for PB7N it increased to 2.1×10^{-4}. Nanocomposites exhibit narrow isothermal crystallization peaks compared to PB and the total crystallization time was found to depend on the content of layered silicates. Figure 12.4 illustrates the temperature dependence of t_c calculated at each crystallization temperature for PB and PB/clay nanocomposites. From the figure it can be seen that the values of t_c for nanocomposites were found to be lower than those for PB. The effect of layered silicates on the crystallization was clearly seen at higher crystallization temperature compared to the lower one. At 86°C, t_c for PB was 301 s, while for PB7N it was decreased to 216 s. At 90°C, t_c for PB was 816 s, which has been drastically reduced

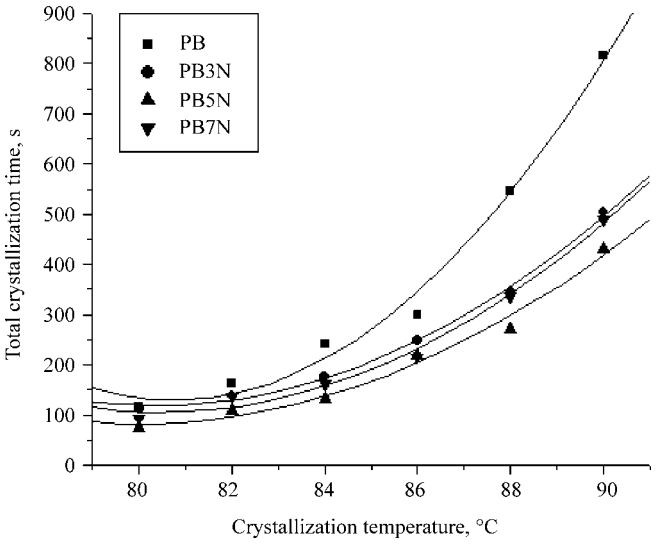

Figure 12.4 Total crystallization time for PB and PB/clay nanocomposites.

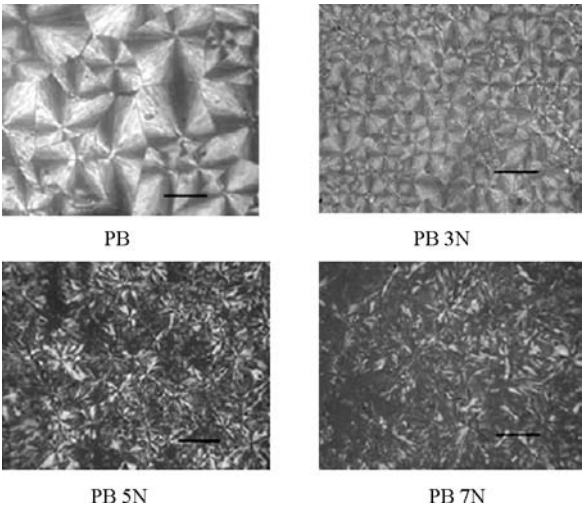

Figure 12.5 Optical micrographs for PB and PB/clay nanocomposites (scale bar: 100 μm).

to 491 s. The lower values of t_c suggest acceleration of the crystallization process in nanocomposites as compared to PB.

12.2.5 Optical Microscopy

As can be seen from Fig. 12.5, pristine PB shows well-defined spherulitic morphology. In the case of nanocomposites, however, a disturbed morphology was observed because of the introduction of layered silicates. As the clay percent increased, the Maltese cross gradually disappeared. The optical micrographs clearly show the effect of layered silicates on the spherulitic morphology. From the figure it can be envisaged that the silicate layers diffuse into an interfibrillar region and appear dark because of optical extinction. However, the size of the spherulites slightly reduced for PB3N, as can be seen from the micrographs. Generally in case of polymer/clay nanocomposites, the clay layers serve as seeds for spherulitic growth and resulted in fine, uniform, and very small sized spherulites (32,39).

12.2.6 Phase Transformation

Differential scanning calorimetry was used to study the phase transformation of PB and PB/clay nanocomposites. As stated earlier, DSC easily differentiates the various polymorphic forms of PB by the melting points. The endothermic peaks at about 128 and 114°C correspond to PBI and PBII, respectively. Figure 12.6 shows the DSC thermograms for PBI and PBII.

The phase transformation was studied by measuring the heat of fusion at various time intervals upon aging at room temperature. As time increases, a fraction of form

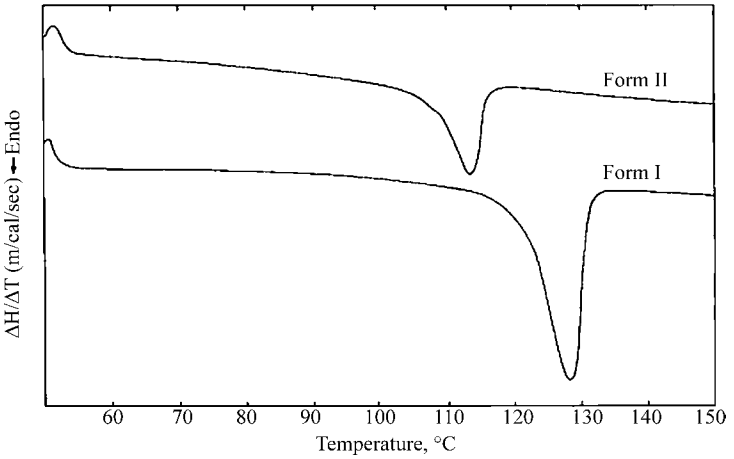

Figure 12.6 DSC thermograms for crystalline form I and form II of PB.

II transforms to form I, as evidenced by the heat of fusion. For 100% crystalline PBI, the heat of fusion was 125.4 J g^{-1}, and 75.2 J g^{-1}, for PBII (40).

Figure 12.7 shows the phase transformation as a function of time. From the figure it is revealed that in early stages of transformation the formation of form I

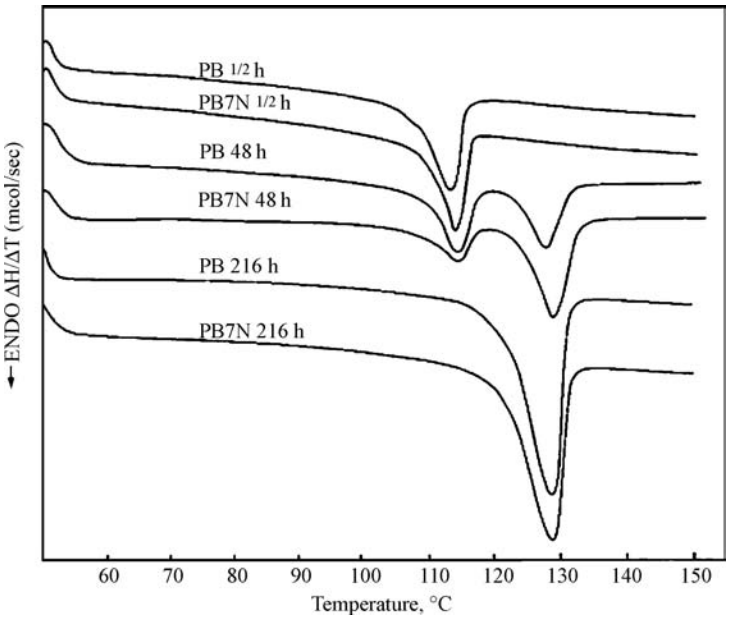

Figure 12.7 DSC thermograms illustrating the phase transformation for PB and PB7N nanocomposites.

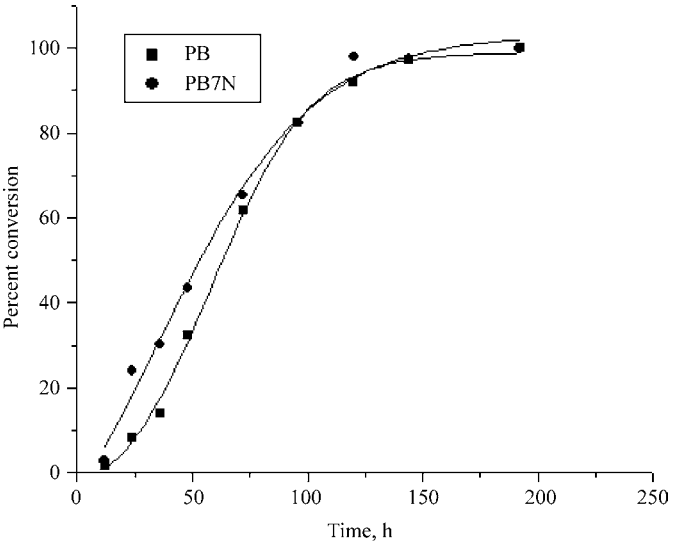

Figure 12.8 Percent conversion of form I for PB and PB7N nanocomposites.

from form II is faster in the case of the nanocomposites. The phase transformation kinetics was studied by applying Avrami theory and the kinetic parameters were determined. The time required for 50% transformation was 58 and 54 h for PB and PB7N, respectively. The rate constant was found to be about 1.6×10^{-3}, while the Avrami constant (n) was about 1.4 for PB. In the case of the nanocomposite with clay, the rate constant increased slightly to 2.1×10^{-3}, while the Avrami constant remained almost same, about 1.5. These data clearly indicate that the transformation of PB from form II to form I takes place faster in the presence of the silicate layers. Figure 12.8 shows the percent conversion of form I as a function of time. For example, after 24 h, the conversion is 8.2% for PB as compared to 24% for PB7N. While at 48 h, the conversion for PB is about 32%, whereas it is about 44% for PB7N.

12.2.7 Dynamic Mechanical Analysis (DMA)

DMA is a suitable technique to study the dynamic response of the polymers under a given set of conditions. The storage modulus, loss modulus, and tan δ curves are used to generate information on the crystalline as well as amorphous nature in polymers. At -15°C, the storage modulus (E') for PB is about 1.84×10^9 Pa, which decreases as the temperature increases, and at 50°C it drops down to 3.55×10^8 Pa. The sharp decrease in storage modulus at about -10°C corresponds to the onset of micro-Brownian motion with the short-range diffusional motion in the polymer. Figure 12.9 depicts the improvement in storage modulus for nanocomposites as a function of clay content. The nanocomposites show higher

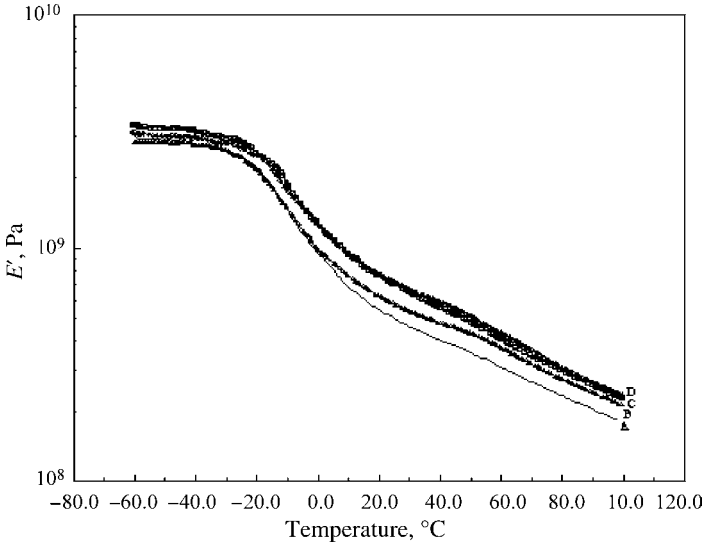

Figure 12.9 Storage modulus (E') curves for PB (**a**), PB3N (**b**), PB5N (**c**), and PB7N (**d**) nanocomposites.

values for the storage modulus over the entire temperature range studied. It is observed that as the clay percent increases, the storage modulus also increases. The increase in the storage modulus at 100°C was about 16%, 25%, and 29% for the PB3N, PB5N, and PB7N nanocomposites, respectively. The organophilic clay layers get expanded as a result of intercalation of the polymer, thereby increasing the apparent aspect ratio of the clay layers. This increase in the storage modulus of the nanocomposites clearly illustrates the reinforcing effect of clay, which in turn could be ascribed to the higher aspect ratio of the clay layers. Similar increase in storage modulus was found for other polymer nanocomposites (41–43).

12.2.8 Thermogravimetric Analysis

The thermogravimetric analysis of PB and PB/clay nanocomposites was carried out in nitrogen atmosphere. Figure 12.10 shows the TGA thermograms for nanocomposites with different contents of clay. It is observed that the temperature at the onset of degradation increases by about 23°C for 3% clay to about 33°C for 7% clay. The increase in the temperature at the onset of degradation suggests delay in degradation of PB/clay nanocomposites and can be ascribed to the higher thermal stability of the clay and its layered structure that exhibits barrier effect to the evaporation of the small molecules generated in the thermal decomposition of the PB. Similar results have been reported for other polymer/clay nanocomposites (44,45).

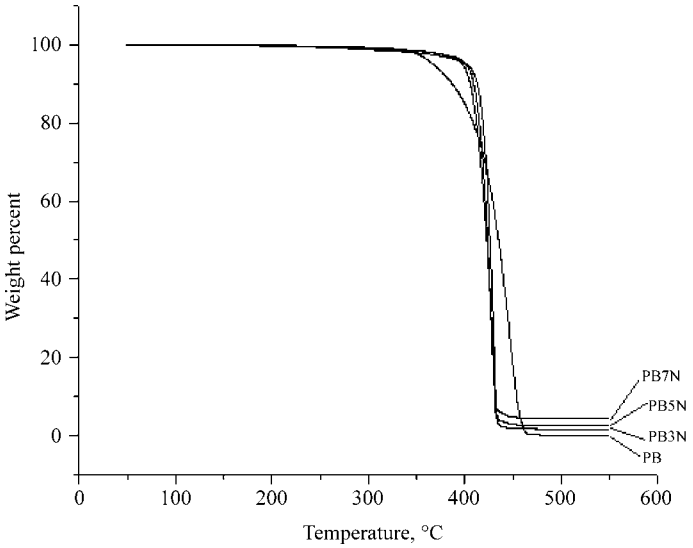

Figure 12.10 TGA thermograms for PB and PB/clay nanocomposites.

12.3 PB/MWCNT NANOCOMPOSITES

12.3.1 Carbon Nanotubes

Carbon nanotubes are the graphite (hexagonal lattice of carbon) sheets having a cylindrical shape. CNTs are classified according to the number of cylindrical sheets as single (SWCNT), double, and multiwalled and possess very broad range of thermal, electronic, elastic, and structural properties depending on different kinds of nanotubes. The unique structure and properties of carbon nanotubes offer promising potential for developing various novel, smart, and advanced materials (46–49).

There are different synthetic methods to produce CNTs, such as arc discharge, laser ablation, and chemical vapor deposition (CVD). CVD is one of the promising synthetic methods for the production of CNTs. Nanotubes naturally align themselves into ropes held together by Van der Waals forces. MWCNTs are reported to exhibit lower mechanical properties as compared to those of SWCNTs (50). However, MWCNTs can be produced in much larger quantities and thus can be used for large-scale applications. CNTs are considered to be multi-beneficial in reinforcement due to the improvement in mechanical properties, thermal stability, barrier properties, and flow properties of the polymer matrix and significantly influence the crystallization behavior of the polymers (19–24).

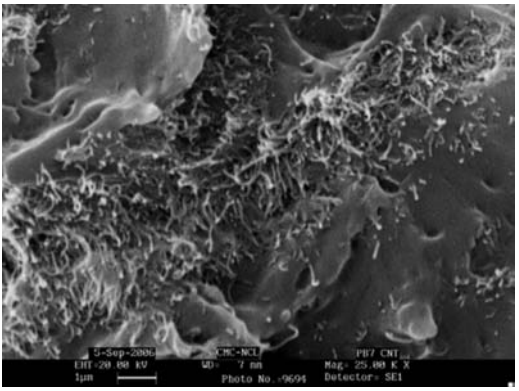

Figure 12.11 Scanning electron micrograph for the PB7C nanocomposite.

12.3.2 Morphology

Nanotubes have a tendency to bundle due to the substantial Van der Waals attractions between them. This and the large aspect ratio cause them to agglomerate into microscopic bundles and even microscopic particles. Figure 12.11 depicts the scanning electron micrograph for PB7C. The fractured surface of the nanocomposites reveals the agglomeration of nanotubes in bundles, which dispersed in the matrix.

12.3.3 Nonisothermal Crystallization

The effect of different cooling rates and the MWCNT content on the nonisothermal crystallization of PB was studied. The crystallization parameters at different cooling rates are shown in Table 12.3. It can be revealed from the table that the crystallization peak temperature (T_p) is lowered for both PB and nanocomposites as the cooling rate is increased. However, T_p for the nanocomposites was higher than that for pristine PB at a given cooling rate and found to increase with the MWCNT content.

12.3.3.1 Nonisothermal Crystallization Kinetics

Nonisothermal crystallization kinetics was studied as discussed earlier in Section 12.2.3.1. The nonisothermal crystallization parameters calculated from the plots of $\log[-\ln(1 - X_t)]$ versus $\log t$ are presented in Table 12.3. The value of Z_t was found to increase with increase in the cooling rates for both PB and PB/MWCNT nanocomposites, while the value of $t_{1/2}$ was found to decrease as the cooling rate increased. The higher values of Z_t and the lower values of $t_{1/2}$ for the nanocomposites as compared to pristine PB signify the enhanced rate of crystallization of PB in the nanocomposites.

The $\log \phi$ versus $\log t$ gave linear relationship at the given degree of crystallinity. Table 12.4 presents values of $F(T)$ and a calculated from the graphs. It can be

observed that $F(T)$ values for PB and the nanocomposites were increased with increase in the relative degree of crystallization, suggesting the time required for reaching the finite degree of crystallization increased for a given cooling rate. However, in the case of nanocomposites, the values of $F(T)$ were lower than those for the pristine PB. This clearly suggests that the time required for reaching certain degree of crystallization was lowered in the case of nanocomposites compared to the time required for the same degree of crystallization in pristine PB. The values of Avrami–Ozawa exponent a were 1.3 and 1.4–1.5 for all the cooling rates for PB and PB7C nanocomposites, respectively.

12.3.3.2 Nucleating Activity

Nucleating activity of the MWCNT can be determined by the method used by Dobreva and Gutzow as explained in Section 12.2.3.2. The nucleating activity was found to be 0.479 for PB7C nanocomposite, which signifies the active surface for nucleation.

12.3.4 Isothermal Crystallization

Isothermal crystallization was studied for PB and PB/MWCNT nanocomposites in the temperature range of 82–90 and 86–94°C for PB and PB/MWCNT nanocomposites, respectively. Isothermal crystallization of PB and the nanocomposites was strongly affected by temperature of crystallization (T_c). As T_c increased, the exothermic peak shifted to higher value, broadened, and the time required to reach the maximum degree of crystallization increased. This signifies that the rate of crystallization decreased with increasing T_c. The influence of T_c was similar for both PB and the nanocomposites; however, because of the presence of MWCNTs, the time required for reaching the maximum degree of crystallization was reduced in nanocomposites, signifying enhanced crystallization rate.

Figure 12.12 depicts the variation of t_c with T_c. It can be seen from the figure that t_c increased with increasing T_c for PB as well as PB/MWCNT nanocomposites. However, it can be observed that at comparable temperatures of crystallization, the t_c value for the nanocomposites was much lower than that observed for pristine PB. This reduction in the total crystallization time indicates enhanced crystallization rate in the presence of MWCNT. The values of rate constant K at 86°C for PB and PB7C were 1.03×10^{-4} and 2.84×10^{-3}, respectively. The t_c value for PB at 86°C was 301 s, while it reduced to 70 s for PB7C. These results confirm the enhanced crystallization of PB in the presence of MWCNT.

12.3.5 Optical Microscopy

Figure 12.13 shows the optical micrographs for PB and PB/MWCNT nanocomposites. The micrographs indicate that the pristine PB shows well-defined spherulitic morphology. In the case of nanocomposites very small crystalline structures are

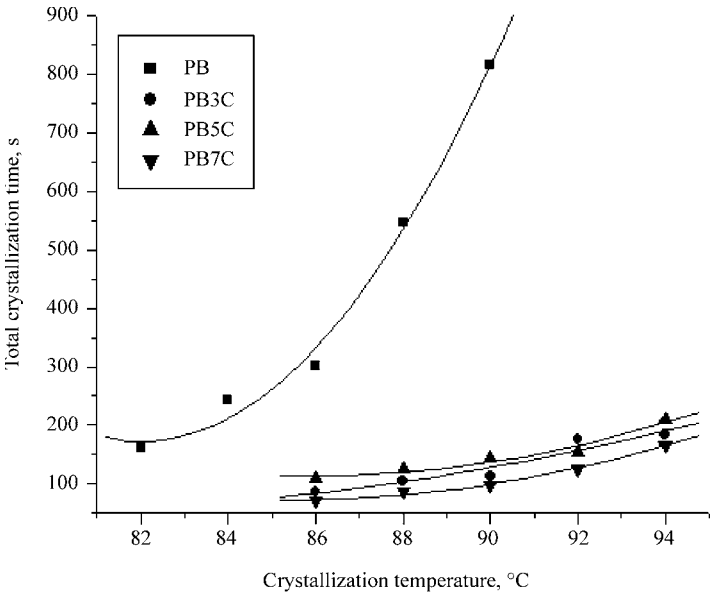

Figure 12.12 Total crystallization time for PB and PB/MWCNT nanocomposites.

observed, suggesting that the dispersion of MWCNT in the polymer matrix hinders the formation of ordered crystallites of form II and does not allow enough time to attain the inherent morphology of the spherulite of the pristine polymer due to heterogeneous nucleation.

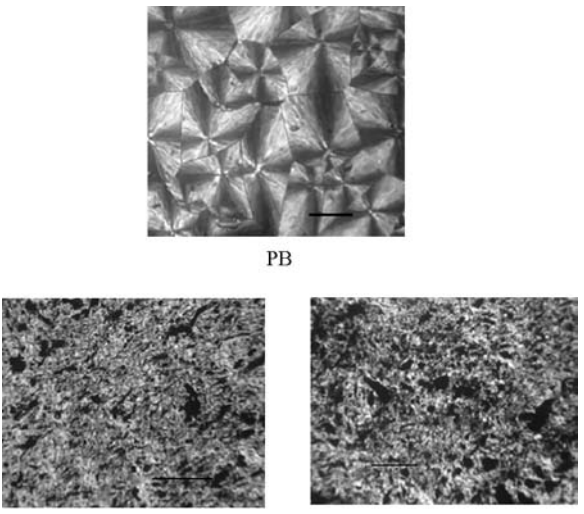

Figure 12.13 Optical micrographs for PB and PB/MWCNT nanocomposites (scale bar: 100 μm).

12.3.6 Phase Transformation

The effect of the presence of various solvents and different temperatures has been used to study the phase transformation of PB (4,51). It has been reported that the rate of phase transformation is maximum at room temperature (25°C) (4). The mechanism of this transformation is yet not fully understood. However, it was proposed that form I grows by pulling in the molecular chains from the surrounding form II crystals, creating new stems of form I rather than growing stem by stem (52).

Here we have studied the phase transformation of PB and PB7C nanocomposite at room temperature by measuring the heat of fusion for the two forms at various time intervals. The heating scans for melt-crystallized PB and PB7C samples show a melting peak at 114°C corresponding to form PBII. As the aging time increases, the area under the lower temperature peak decreases and the area under the higher temperature peak (128°C, which corresponds to PBI) increases. The fractional conversion for each form was calculated by taking the ratio of the heat of fusion observed to the heat of fusion reported for 100% crystalline forms.

Figure 12.14 shows the phase transformation for PB and PB7C at different time intervals of 24, 72, and 144 h. It clearly indicates that the rate of phase transformation is higher in the case of the nanocomposite. For example, the crystallinity of form I for PB at 48 h was 33%, while it significantly increased to 82.9% in the presence of 7% MWCNT, suggesting significant enhancement in the rate of phase transformation in the presence of MWCNT. The Avrami equation was used to study the phase transformation kinetics. The rate constant for phase transformation was found to be about 0.042 in the case of PB7C, suggesting enhanced rate of phase transformation. The Avrami exponent was found to be 0.87 for PB7C, which clearly explains that the process of nucleation as well as growth is different for PB/MWCNT

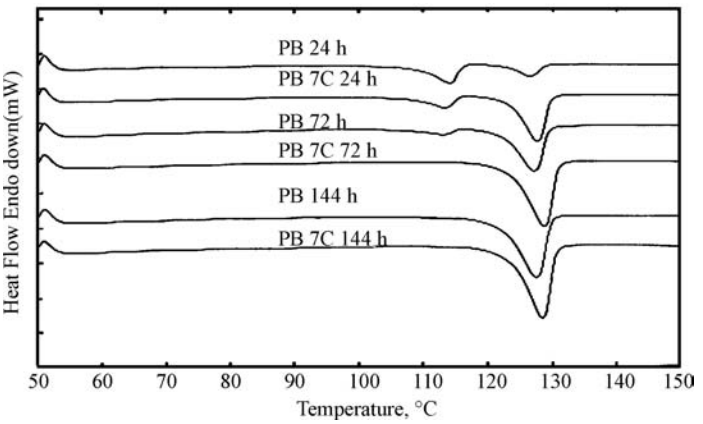

Figure 12.14 DSC thermograms illustrating the phase transformation for PB and PB7C nanocomposites.

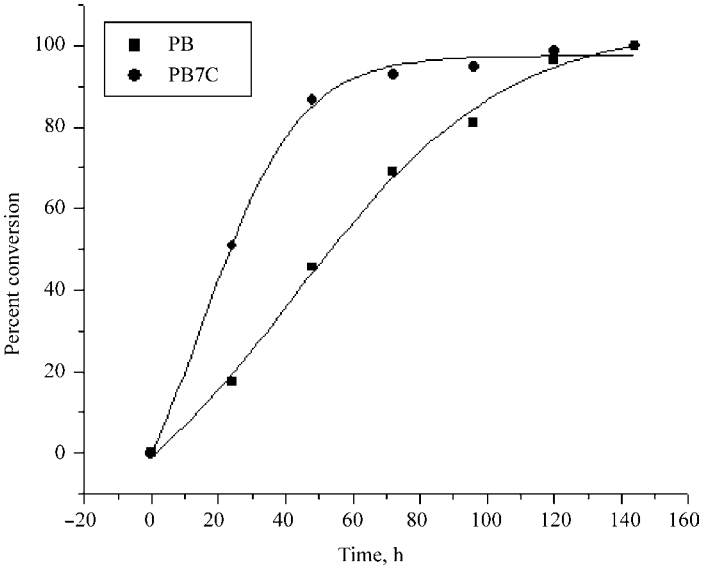

Figure 12.15 Percent conversion of form I for PB and PB7C nanocomposites.

nanocomposites. The half-time for phase transformation (50% conversion to form I) of PB was about 58 h and it significantly reduced to 25 h for PB7C. As discussed in an earlier section for PB/clay nanocomposites, the half-time for phase transformation was found to be about 54 h, which was comparatively very high with respect to PB7C nanocomposite. The above results clearly indicate that the MWCNT acts as a nucleating agent for PB, as it enhances the nucleation as well as the rate of phase transformation from metastable form to stable form. The percent conversion is given in Fig. 12.15.

12.3.7 Dynamic Mechanical Analysis

Figure 12.16 shows the improvement in storage modulus with the content of MWCNT. At 100°C, the E'_{nc}/E'_{p} (E'_{nc} is storage modulus for the nanocomposite, and E'_{p} is storage modulus for PB) values for PB3C, PB5C, and PB7C are found to be about 1.36, 1.42, and 1.61, suggesting an increase in E' by 36%, 42%, and 61% for 3, 5 and 7 wt% MWCNT loading, respectively. It is interesting to note that there is a significant increase in storage modulus when the polymer chains are highly mobile; this reveals that the reinforcement of MWCNT in the polymer matrix forms a network that hinders the molecular motions at high thermal energy and also lowers the dissipation of energy. As the interfacial interactions in unmodified MWCNT and nonpolar polymer are weak, there is no change in glass transition temperature of the polymer but the effect of reinforcement of MWCNT is clearly seen on the tan δ values. Due to internal friction and molecular motions the energy

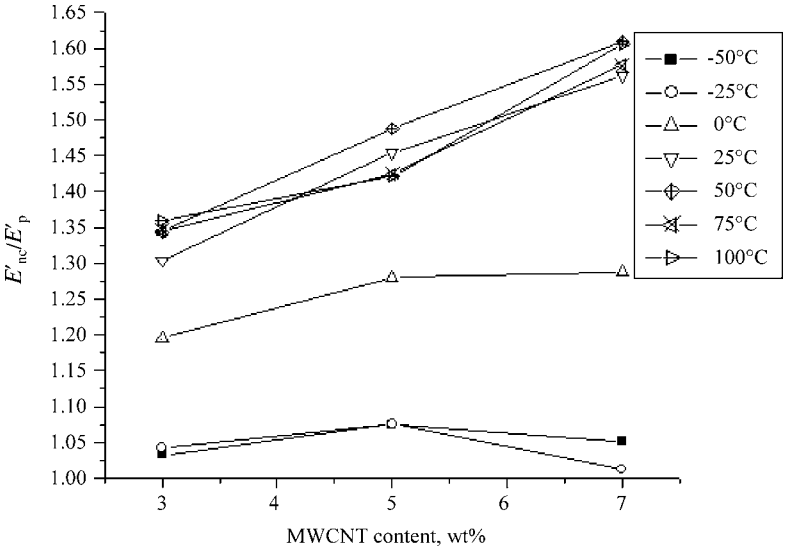

Figure 12.16 E'_{nc}/E'_p for PB and PB/MWCNT nanocomposites.

gets dissipitated as heat, which signify the tan δ values. The tan δ values for the nanocomposites are found to be lower compared to pristine PB and dependent on the content of MWCNT, which suggest the damping is lowered for the nanocomposites (Fig. 12.17).

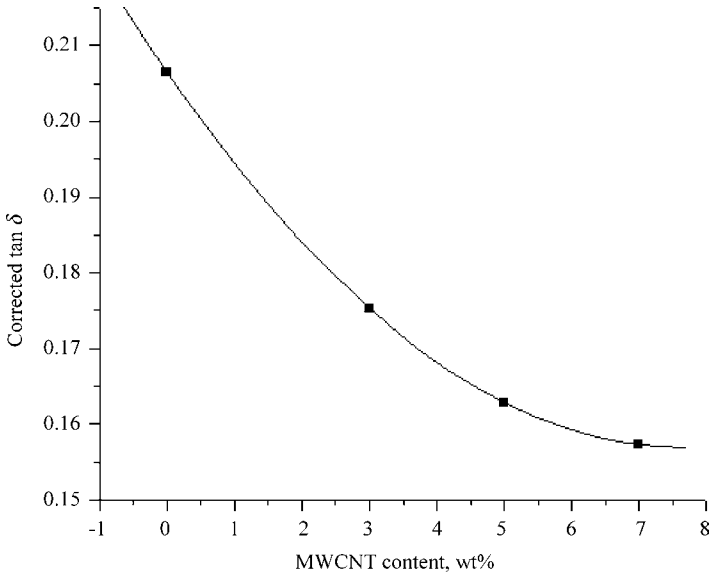

Figure 12.17 The tan δ values for PB and PB/MWCNT nanocomposites.

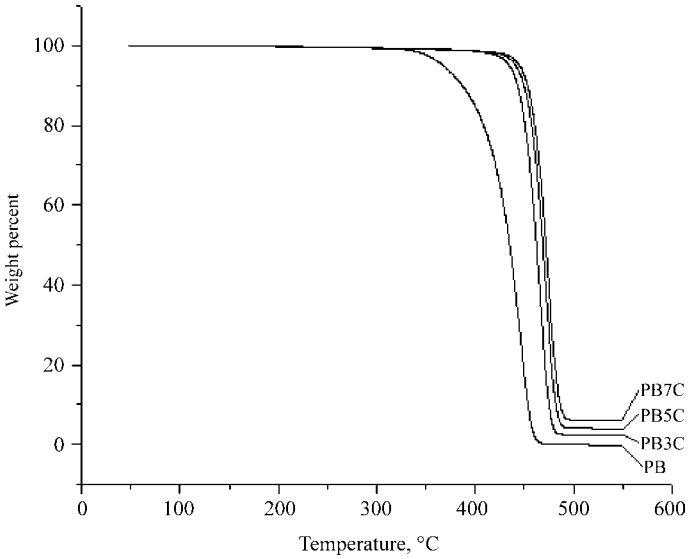

Figure 12.18 TGA thermograms for PB and PB/MWCNT nanocomposites.

12.3.8 Thermogravimetric Analysis

Thermal stability of the nanocomposites was studied using thermogravimetric analysis. Figure 12.18 demonstrated the TGA thermograms for PB/MWCNT nanocomposites. It can be clearly seen that because of reinforcement of MWCNTs in the polymer matrix, the thermal stability of PB was significantly improved. The constant weights of the composites were found at 483°C for 3% and increased with respect to the loading, suggesting that the PB matrix degraded completely and the residue left was of only nanotubes. This might be due to the higher thermal stability of the nanotubes. There are two reasons given in the literature for the improvement in the thermal stability of the composites, the first is the barrier effect due to well dispersion of nanotubes, which hinders the formed degradation products, and the second is due to the strong physical adsorption of matrix molecules on the surface of nanotubes and these adsorbed molecules are much less active than those far from the nanotube surface and thus their volatilization is delayed. Dondero and Gorga (22) have reported about 80°C increase in thermal stability for PP/MWCNT nanocomposites with just 3% MWCNT content, prepared by melt compounding. In HDPE/SWNT nanocomposites, the thermal stability was found to be increased by about 70°C in nitrogen atmosphere and 115°C in air (23).

12.4 PB/$BaTiO_3$ NANOCOMPOSITES

12.4.1 Nanoparticles

Particles having at least one dimension of less than 100 nm are called as nanoparticles. These are mainly synthesized by gas-phase and sol–gel processing as well as

generated by evaporation and condensation in an inert atmosphere, while the sol–gel is a wet process to synthesize nanoparticles using gelation, precipitation, and hydrothermal treatment.

In polymer nanoparticle composites, the polymer matrix shows significant differences in physical properties as compared to the pristine. In crystallization study, reinforcement of nanomaterials in the polymer matrix shows various results including enhancement and retardation of crystallization, crystal structure modification, and different spherulitic morphologies (25–27).

12.4.2 Morphology

The scanning electron micrograph of PB7$BaTiO_3$ nanocomposite is presented in Fig. 12.19. In the case of the nanocomposites with 7% $BaTiO_3$, a reasonably homogeneous dispersion of nanoparticles is seen. Some of the nanoparticles in the form of agglomerates of the size around 1–4 μm are also observed. The agglomeration of the size about 5–10 μm for the treated SiO_2 nanoparticles has been observed in the case of LLDPE nanocomposites (53).

12.4.3 Nonisothermal Crystallization

The effect of $BaTiO_3$ nanoparticles on the crystallization of PB at different cooling rates was studied. The crystallization temperature decreased as the cooling rate is increased; similar behavior is observed in nanocomposites. The nanocomposites with $BaTiO_3$ show higher values of crystallization temperature than pristine PB.

As described earlier in Section 12.2.3.1, the Avrami equation was used to determine n and Z_t for the nanocomposites. The value of Z_t was increased with increase in cooling rate for PB as well as for nanocomposite and is presented in Table 12.3.

Table 12.4 shows the values of $F(T)$ and a calculated from the plots. $F(T)$ values signify the time required to reach the finite degree of crystallinity. These are found to

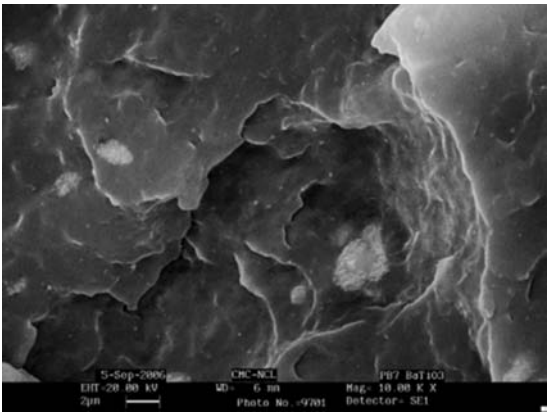

Figure 12.19 Scanning electron micrograph for PB7$BaTiO_3$ nanocomposite.

be slightly lower for the nanocomposite than that of pristine PB, suggesting time required to reach the defined degree of crystallinity is lowered as compared to pristine PB in the presence of nanoparticles.

12.4.3.1 Nucleating Activity

Nucleating activity of the $BaTiO_3$ nanoparticles was determined from the nonisothermal crystallization data. The detailed analysis of this method has been described in Section 12.2.3.2. Nucleating activity for 7% $BaTiO_3$ was found to be about 0.821, suggesting that nanoparticles act as a nucleating agent.

12.4.4 Isothermal Crystallization

Isothermal crystallization was studied in the temperature range from 76 to 86°C for PB and PB/$BaTiO_3$ nanocomposites. The total crystallization time was calculated from the isothermal curves shown in Fig. 12.20. It can be seen from the figure that at higher crystallization temperatures such as 82°C, the total crystallization time for the nanocomposite was lower than that for the pristine PB; similarly, at 86°C the t_c value for PB7$BaTiO_3$ nanocomposite was reduced to 180 s, suggesting enhanced crystallization due to the incorporation of $BaTiO_3$ nanoparticles.

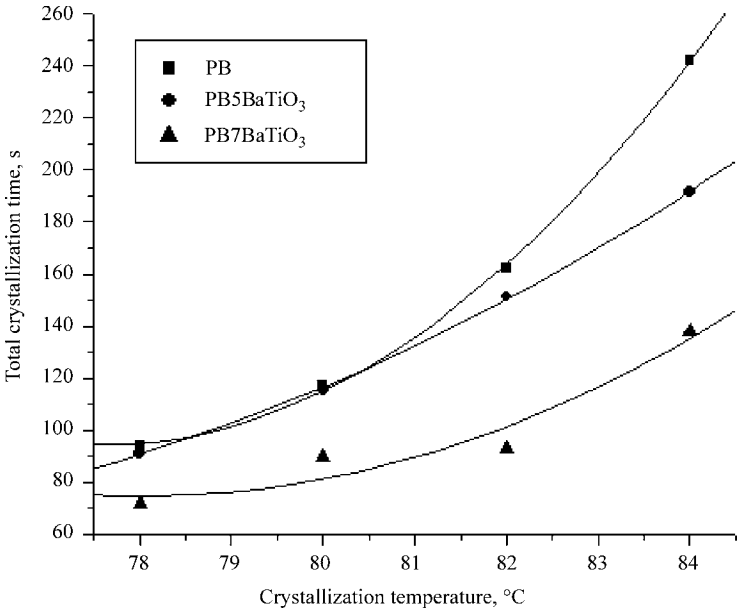

Figure 12.20 Total crystallization time for PB and PB/$BaTiO_3$ nanocomposites.

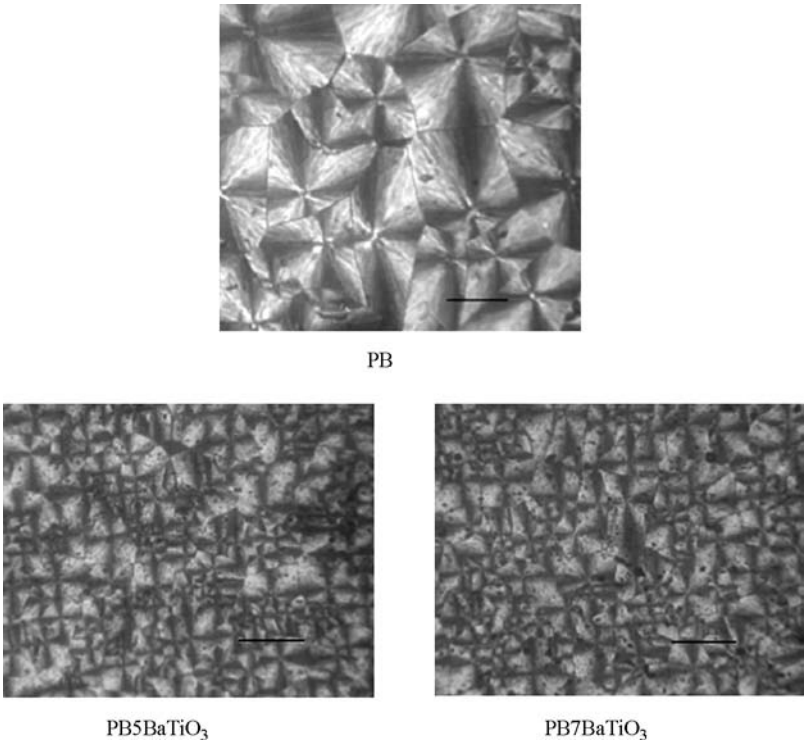

Figure 12.21 Optical micrographs for PB and PB/$BaTiO_3$ nanocomposites (scale bar: 100 μm).

12.4.5 Optical Microscopy

Figure 12.21 shows the optical micrographs for PB and PB/$BaTiO_3$ nanocomposites. The micrographs indicate that the pristine PB as well as the nanocomposites shows well-defined spherulitic morphology. The size of the spherulites for the $BaTiO_3$ nanocomposites was found to be slightly smaller than that for PB. This observation is in contrast with the nanocomposites synthesized using organically modified clay and MWCNT.

12.4.6 Phase Transformation

As mentioned above, the phase transformation using DSC was studied in the presence of nucleating agents. So far, there is no report on this system using fillers with all the dimensions in nanometer scale. Phase transformation studies have been described in detail in Section 12.2.6. It can be seen from Fig 12.22 that the area under the curve for PBII decreases with time suggesting that it transforms into form I, which is stable. The percent conversion (Fig. 12.23) for each form was calculated using the heat of fusions. The rate of phase transformation was found to be about

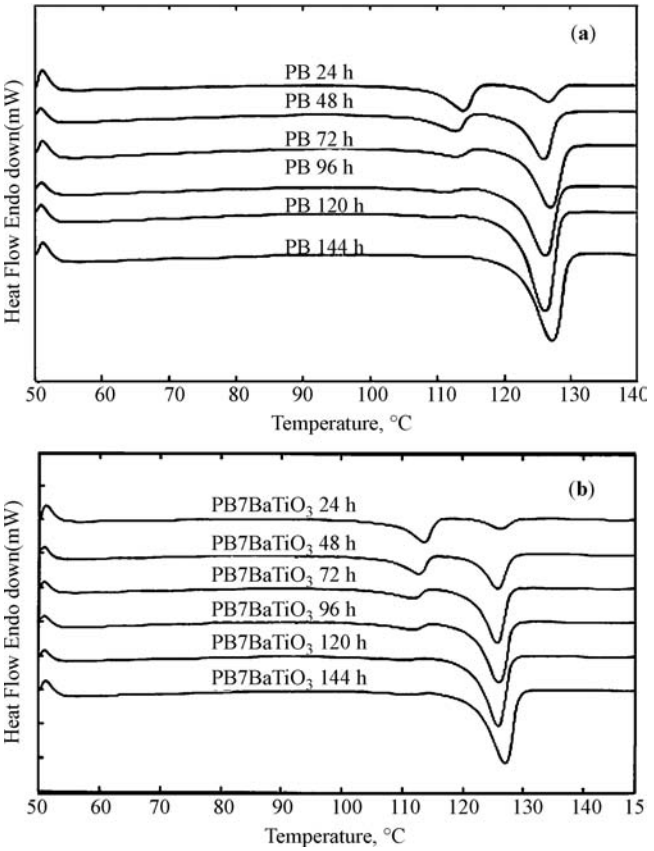

Figure 12.22 DSC curves illustrating the phase transformation for PB (**a**) and PB7$BaTiO_3$ nanocomposite (**b**) at various time intervals.

6.01×10^{-4}, while the Avrami constant was about 1.6. The degree of crystallinity for the nanocomposite was found to be lowered as compared to pristine PB up to 72 h, which suggests that $BaTiO_3$ nanoparticles retard the rate of phase transformation. The important observation of this study is that the $BaTiO_3$ nanoparticles enhance the crystallization rate but slightly reduce the rate of phase transformation.

12.4.7 Dynamic Mechanical Analysis

Figure 12.24 depicts the curves of storage modulus for PB and PB/$BaTiO_3$ nanocomposites. In the sub-glass transition region the storage modulus was found to be slightly increased by about 5–6% as that for PB, while in the rubbery regime it was increased by 22% at 100°C for the 5% nanocomposite. As the $BaTiO_3$ content increased to 7%, the increase in storage modulus remained almost same as that for the 5% nanocomposite.

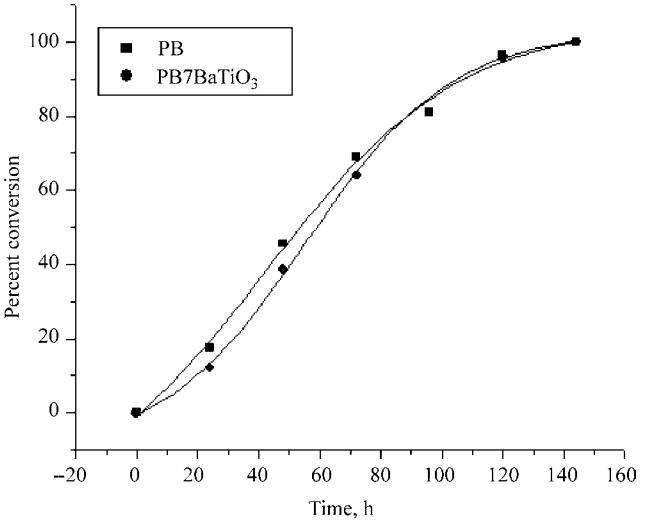

Figure 12.23 Percent conversion of form I for PB and PB7$BaTiO_3$ nanocomposites.

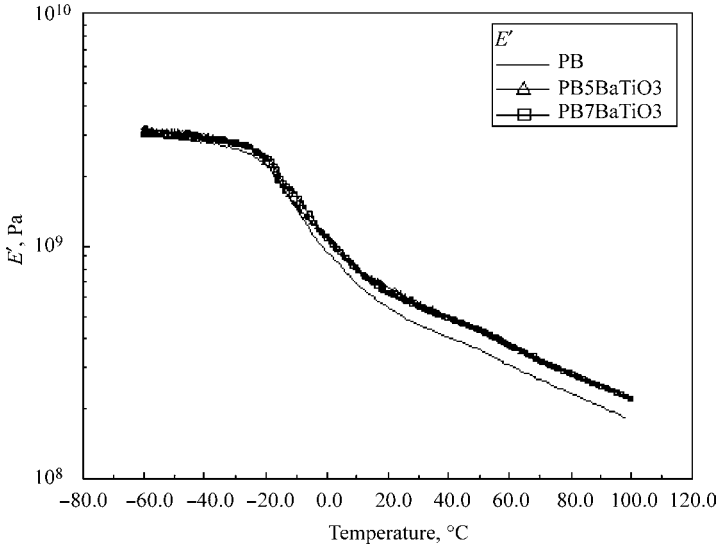

Figure 12.24 Storage modulus curves (E') for PB and PB/$BaTiO_3$ nanocomposites.

12.4.8 Thermogravimetric Analysis

The effect of inorganic $BaTiO_3$ nanoparticles on the thermal stability of PB was studied. The percent weight loss in nitrogen atmosphere is shown in Fig. 12.25. The onset of degradation initiation temperature of the PB/$BaTiO_3$ nanocomposites was

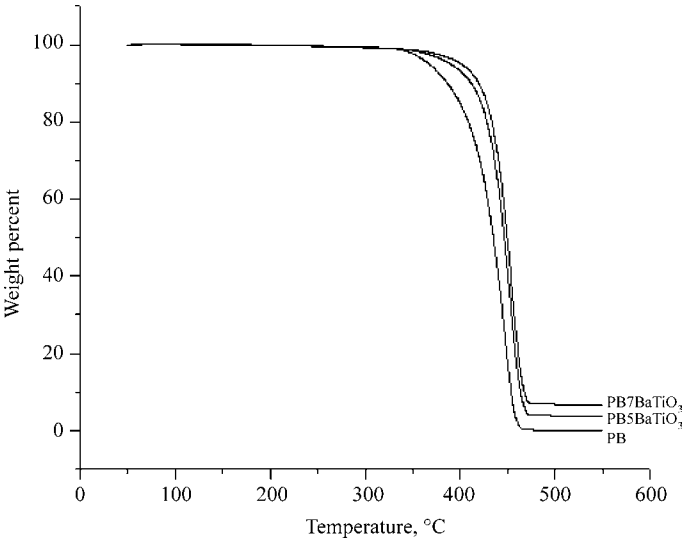

Figure 12.25 TGA thermograms for PB and PB/$BaTiO_3$ nanocomposites.

found to be higher than that of pristine PB. This suggests the enhancement in thermal stability due to the retardation effect of the inorganic nanoparticles. Residual weight after complete degradation of PB was found to be dependent on the content of $BaTiO_3$ nanoparticles.

12.5 EFFECT OF NANOFILLERS ON THE RATE OF PHASE TRANSFORMATION

The effect of nanofillers such as clay, multiwalled carbon nanotubes, and $BaTiO_3$ nanoparticles on the crystallization and phase transformation of PB is evaluated and explained in the following section.

The crystallization studies revealed enhanced crystallization rates for nonisothermal as well as isothermal crystallization in the case of nanocomposites with all the fillers. The nonisothermal crystallization studied using Avrami and Avrami–Ozawa theories revealed enhanced crystallization rates as evidenced by the higher values of Z_t and lower values of $t_{1/2}$ and $F(T)$ for the nanocomposites as compared to PB. The nucleating activity of the nanocomposites was found to be about 0.897, 0.480, and 0.821 for PB7N, PB7C, and PB7$BaTiO_3$ nanocomposites, respectively, signifying that the MWCNTs offer most active surface for crystallization. In isothermal crystallization study, MWCNTs were found to be more effective than clay and $BaTiO_3$ nanoparticles. For example, the total crystallization time (t_c) at 86°C for PB was found to be about 301 s, while it decreased to 216, 70, and 180 s for PB7N, PB7C, and PB7$BaTiO_3$ nanocomposites, respectively, indicating heterogeneous nucleation of PB in the presence of nanofillers.

The important endeavor of this study was to elucidate the effect of the various nanofillers on the kinetics of the phase transformation of PB. Phase transformation was studied using differential scanning calorimetry by monitoring the crystallinity of the two forms at various time intervals. The half-time for conversion, $t_{1/2}$ (50% conversion to form I), for phase transformation was found to be about 58, 54, 25, and 60 h for PB, PB7N, PB7C, and PB7$BaTiO_3$ nanocomposites, respectively. As can be seen from these results, the nanocomposites with MWCNT showed lowest half-time for conversion, $t_{1/2}$, exhibiting significant improvement in the rate of phase transformation in MWCNT nanocomposites in comparison with other nanofillers. The observed differences in the rate of phase transformation can be explained as follows.

In the case of PB/MWCNT nanocomposites, increase in crystallinity was observed (54). Thus, the decrease in the amorphous fraction might lead to an increase in rate of phase transformation as explained by Azzurri et al. (55). It has also been observed that during the process of phase transformation, additional stress acting on the molecular chains through the crystal–amorphous interphase favors the chain extension that is required for the transformation to form I. Similarly, Gohil et al. (56) have also explained that the additional tensile stress induced because of the tightening of the tie molecules on the chain segments through the crystal–amorphous interphase. This additional stress augments the extension of the 11/3 helix to 3/1 helical conformation and facilitates the nuclei formation, which results in the higher rate of phase transformation. As reported earlier, the nanocomposites with MWCNTs showed almost same crystallinity for all the compositions but the rate of phase transformation was found to increase with the MWCNT content. This signifies that in addition to the increase in the crystallinity, other factors also contribute to enhance the rate of phase transformation.

Azzurri et al. (57) and Causin et al. (58) have observed that the disordered crystallite of form II also enhances the rate. In the present case, as can be seen from the optical micrographs, the pristine PB shows well-defined spherulitic morphology. The nanocomposites of PB with clay and $BaTiO_3$ nanoparticles exhibited spherulitic morphology as that for pristine PB. However, at higher clay content the nanocomposites exhibited disturbed spherulitic morphology. Interestingly, the nanocomposites with MWCNTs demonstrate very small and disordered crystallites. The optical micrographs revealed that the dispersion of clay and MWCNTs hinders the formation of well-defined spherulitic morphology of PB. Thus, the present results reveal that the decrease in amorphous content and the disordered morphology of the crystallite play a significant role in enhancing the rate of phase transformation.

12.6 CONCLUSIONS

Poly(1-butene) nanocomposites with different nanofillers such as clay, MWCNTs, and $BaTiO_3$ nanoparticles were prepared using melt-compounding technique. The structure, morphology, isothermal and nonisothermal crystallization, crystal-to-crystal phase transformation, and thermomechanical behavior of the nanocomposites were investigated using various techniques.

PB/clay nanocomposites showed intercalated structures with nanoscale dispersion of clay layers in the polymer matrix, as evidenced by the XRD and TEM results. The scanning electron microscopy of PB/MWCNT nanocomposites exhibited bundles of MWCNTs dispersed in the matrix, while in the case of PB/ $BaTiO_3$ nanocomposites, a uniform dispersion with some agglomerates of the size about 1–4 μm was observed.

In crystallization study, all the three nanocomposites exhibited enhanced crystallization rates for both the non-isothermal and isothermal crystallization due to nucleating effect. The nanocomposites with MWCNTs exhibited highest enhancement in the rate of crystallization as compared to the other nanofillers. This was attributed to the presence of active surface for crystallization offered by MWCNT. This contention was also supported by the values of nucleating activity determined from nonisothermal crystallization. The optical microscopy exhibited well-defined spherulitic morphology for pristine PB, while a disturbed morphology was observed at higher clay content for PB/clay nanocomposites and the nanocomposites with $BaTiO_3$ nanoparticles revealed smaller size spherulites with well-defined morphology. However, the spherulitic morphology was completely destroyed in MWCNT nanocomposites as substantiated by the presence of very small and disordered crystallites.

In the dynamic mechanical analysis, all the nanocomposites showed improvement in storage modulus compared to that of pristine PB, but the highest improvement was found for the nanocomposites with MWCNTs. This effect could be ascribed to the inherent higher aspect ratio of MWCNTs.

The thermogravimetric analysis also showed enhanced thermal stability for the nanocomposites with all the fillers, while the extent of enhancement was maximum (about 90°C) for nanocomposites with MWCNT.

The important aspect of the present study was the effect of nanofillers on the kinetics of phase transformation from metastable tetragonal form (form II) to stable twinned hexagonal form (form I). Avrami theory was used to examine the kinetics of phase transformation. The half-time for transformation was lower for the nanocomposites with clay and MWCNTs suggesting that these two fillers are effective in enhancing the rate of transformation. In contrast, the rate was found to be lower than that for pristine PB in the case of $BaTiO_3$ nanocomposites. The observed difference in the variations for the rate of phase transformation with different nanofillers was explained on the basis of differences observed in the values of crystallinity and the spherulitic morphology of the nanocomposites. It was noted that not only decrease in the amorphous content but also the enhanced nucleation of form I in the presence of MWCNT increases the phase transformation rate. From the Avrami exponent for PB/MWCNT nanocomposites, it is suggested that the mechanism for nucleation and growth of form I is different from that of pristine PB and other nanocomposites. In conclusion, our results demonstrate that the nanofillers clay, MWCNTs, and $BaTiO_3$ nanoparticles provide active nucleation sites for the crystallization of PB; however, MWCNTs play a significant role in enhancing the rate of phase transformation.

ACKNOWLEDGMENTS

The authors would like to thank Mrs. Anuya Harkare for TEM and Mr. A. B. Gaikwad for SEM micrographs. SDW thanks the Council of Scientific and Industrial Research (CSIR), New Delhi, India, for research fellowship.

NOMENCLATURE

a	Avrami–Ozawa exponent (n/m)
A	Constant used for calculating Φ
B	Constant used for calculating Φ
B^*	Constant used in calculating Φ for the nanocomposite
$F(T)$	Value of cooling rate chosen at unit crystallization time when the system has a defined degree of crystallinity
K	Crystallization rate constant
$K(T)$	Avrami–Ozawa rate constant
MWCNTs	Multiwalled carbon nanotubes
n	Avrami exponent
PB	Poly(1-butene)
PMP	Poly(4-methyl-1-pentene)
iPP	Isotactic polypropylene
$t_{1/2}$	Crystallization half-time
t_c	Total crystallization time
T_c	Crystallization temperature (isothermal crystallization)
T_f	Final crystallization temperature
T_i	Initial crystallization temperature
T_p	Crystallization peak temperature (nonisothermal crystallization)
X_t	Relative degree of crystallinity at time t
Z_c	Corrected Z_t for various cooling rates
Z_t	Rate constant for nonisothermal crystallization
ϕ	Cooling rate
Φ	Nucleating activity

REFERENCES

1. K. Nakamura, T. Aoike, K. Usaka, and T. Kanamoto, *Macromolecules*, **32**, 4975 (1999).
2. Q. Fu, B. Heck, G. Strobl, and Y. Thomann, *Macromolecules*, **34**, 2502 (2001).
3. J. Samon, J. Schultz, B. Hsiao, J. Wu, and S. Khot, *J. Polym. Sci. B Polym. Phys.*, **38**, 1872 (2000).
4. M. Kaszonyiova, F. Rybnikar, and P. Geil, *J. Macromol. Sci. B Phys.*, **B43**, 1095 (2004).
5. C. Armeniades and E. Baer, *J. Macromol. Sci.*, **B1**, 309 (1967).
6. K. Hong and J. Spruiell, *J. Appl. Polym. Sci.*, **30**, 3163 (1985).
7. C. Beatty and C. Rogers, *Polym. Prep. Div. Polym. Chem.*, **18**, 641 (1977).
8. C. Nakafuku and T. Miyaki, *Polymer*, **24**, 141 (1983).

9. A. Tanaka, N. Sugimoto, T. Asada, and S. Onogi, *Polymer J.*, **7**, 529 (1975).
10. Y. Shieh, M. Lee, and S. Chen, *Polymer*, **42**, 4439 (2001).
11. X. Zhang, X. Zhang, and G. Shi, *Thermochim. Acta*, **205**, 245 (1992).
12. M. Kaszonyiova, F. Rybnikar, and P. Geil, *J. Macromol. Sci. B Phys.*, **B43**, 1095 (2004).
13. L. Zhao, J. Li, S. Guo, and Q. Du, *Polymer*, **47**, 2460 (2006).
14. J. Hwu and G. Jiang, *J. Appl. Polym. Sci.*, **95**, 1228 (2005).
15. S. Parija, S. Nayak, S. Verma, and S. Tripathy, *Polym. Compos.*, **25**, 646 (2004).
16. K. Wang, M. Choi, C. Koo, Y. Choi, and I. Chung, *Polymer*, **42**, 9819 (2001).
17. D. Marchant and K. Jayaraman, *Ind. Eng. Chem. Res.*, **41**, 6402 (2002).
18. M. Ton-That, F. Perrin-Sarazin, K. Cole, M. Bureau, and J. Denault, *Polym. Eng. Sci.*, **44**, 1212 (2004).
19. M. Cadek, J. Coleman, V. Barron, K. Hedicke, and W. Blau, *Appl. Phys. Lett.*, **81**, 5123 (2002).
20. M. Sarno, G. Gorrasi, D. Sannino, A. Sorrentino, P. Ciambelli, and V. Vittoria, *Macromol. Rapid. Commun.* **25**, 1963 (2004).
21. K. Wiemann, W. Kaminsky, F. Gojny, and K. Schulte, *Macromol. Chem. Phys.* **15**, 1472 (2005).
22. W. Dondero and R. Gorga, *J. Polym. Sci. B Polym. Phys.*, **44**, 864 (2006).
23. S. Kodjie, L. Li, B. Li, W. Cai, C. Li, and M. Keating, *J. Macromol. Sci. B Phys.*, **45**, 231 (2006).
24. O. Breuer and U. Sundararaj, *Polym. Compos.*, **25**, 630 (2004).
25. H. Zhao, K. Robert, and Y. Li, *J. Polym. Sci. B Polym. Phys.*, **43**, 3652 (2005).
26. X. Xia, S. Cai, and C. Xie, *Mater. Chem. Phys.*, **95**, 122 (2006).
27. J. Weon and H. Sue, *J. Mater. Sci.*, **41**, 2291 (2006).
28. D. Chae, K. Kim, and B. Kim, *Polymer*, **47**, 3609 (2006).
29. M. Joshi and B. Butola, *Polymer*, **45**, 4953 (2004).
30. Z. Xiao, Y. Li, D. Ma, L. Schadler, and Y. Akpalu, *J. Polym. Sci. B Polym. Phys.*, **44**, 1084 (2006).
31. X. Liu and Q. Wu, *Polymer*, **43**, 1933 (2002)
32. L. Priya and J. Jog, *J. Polym. Sci. B Polym. Phys.*, **40**, 1682 (2002).
33. M.A. Avrami, *J. Chem. Phys. A*, **7**, 1103 (1939).
34. M.A. Avrami, *J. Chem. Phys. A*, **8**, 212 (1940).
35. M.A. Avrami, *J. Chem. Phys. A*, **9**, 177 (1941).
36. T. Ozawa, *Polymer*, **12**, 150 (1971).
37. A. Dobreva and I. Gutzow, *J. Non-Cryst. Solids*, **13**, 162 (1993).
38. S. Kim, S. Ahn, and T. Hirai, *Polymer*, **44**, 5625 (2003).
39. Z. Wu, C. Zhou, and N. Zhu, *Polym. Test.*, **21**, 479 (2002).
40. S. Cimmino, M. Lorenzo, E. Pace, and C. Silvestre, *J. Appl. Polym. Sci.*, **67**, 1369 (1998).
41. P. Messersmith and E. Giannelis, *Chem. Mater.*, **6**, 1719 (1994).
42. K. Yano, A. Usuki, T. Kurauchi, and O. Kamigaito, *J. Polym. Sci. Polym. Chem.*, **31**, 2493 (1993).
43. S. Hambir, N. Bulakh, P. Kodgire, R. Kalgaonkar, and J. Jog, *J. Polym. Sci. B Polym. Phys.*, **39**, 446 (2001).
44. S. Burnside and E. Giannelis, *Chem. Mater.*, **7**, 1597 (1995).
45. Z. Wang and T. Pinnavaia, *Chem. Mater.*, **10**, 1820 (1998).
46. G. Vasilios, T. Vasilios, G. Dimitrios, and P. Dimitrios, *Chem. Mater.*, **17**, 1613 (2005).
47. D. Mitchell, S. Lee, L.Trofin, N. Li, T. Nevanen, H. Soderlund, and C. Martin, *J. Am. Chem. Soc.*, **124**, 11864 (2002).
48. T. Sreekumar, T. Liu, B. Min, H. Guo, S. Kumar, R. Hauge, and R. Smalley, *Adv. Mater.*, **16**, **58** (2004).
49. J. Sandler, M. Shaffer, T. Prasse, Q. Bauhofer, K. Schulte, and A. Windle, *Polymer*, **40**, 5967 (1999).
50. Z. Jin, K. Pramoda, G. Xu, and S. Goh, *Chem. Phys. Lett.*, **337**, 43 (2001).

51. M. Kaszonyiova, F. Rybnikar, and P. Geil, *J. Macromol. Sci. B Phys.*, **B44**, 377 (2005).
52. M. Tosaka, T. Kamijo, M. Tsuji, S. Kohjiya, T. Ogawa, S. Isoda, and T. Kobayashi, *Macromolecules*, **33**, 9666 (2000).
53. E. Kontou and M. Niaounakis, *Polymer*, **47**, 1267 (2006).
54. S. Wanjale and J. Jog, *Polymer*, **47**, 6414 (2006).
55. F. Azzurri, A. Flores, G. Alfonso, and B. Calleja, *Macromolecules*, **35**, 9069 (2002).
56. R. Gohil, M, Miles, and J. Petermann, *J. Macromol. Sci. Phys.*, **B21**, 189 (1982).
57. F. Azzurri, G. Alfonso, M. Gomez, M. Marti, G. Ellis, and C. Marco, *Macromolecules*, **37**, 3755 (2004).
58. V. Causin, C. Marega, A. Marigo, G. Ferrara, G. Idiyatullina, and F. Fantinel, *Polymer*, **47**, 4773 (2006).

Chapter 13

Toward Polyethylene Nanocomposites with Controlled Properties

Yvonne A. Akpalu[1]

13.1 INTRODUCTION

Polymer nanocomposites are polymers that contain nanofillers (inorganic and metallic materials) or fillers of nanometer dimensions. In the past 10 years, they have emerged as a new class of materials that have demonstrated vastly improved properties without the drawbacks associated with conventional polymer composites (polymers filled with micronsized particulates), unfilled polymers, or polymer blends. Advantages of polymer nanocomposites include dramatic improvements in the addition of small amounts of nanoparticles (<5 wt%) causing substantial changes in barrier, mechanical, electrical, optical, and thermal properties of the polymers (1–4) without the trade-offs and the higher particle loadings required for traditional composites. Thus, using such methods it is possible to create polymer nanocomposites with a range of desirable engineering properties. In crystalline polyethylene nanocomposites (5–24), these changes in properties result because the nanoparticles alter the crystalline structure and the morphology of the polymer. While these benefits have been proposed in the literature and have even been realized in several cases, it is evident that proper characterization of the nanofiller morphology can provide systematic understanding for further improvements in properties. Unfortunately, determining the structure and dispersion of nanoparticles in a crystalline or amorphous polymer matrix is a formidable task, which requires a complete quantitative description of the elastic scattering arising from

[1]Department of Chemistry & Chemical Biology and Rensselaer Nanotechnology Center, Rensselaer Polytechnic Institute, Troy, NY 12180, USA

Polyolefin Composites, Edited by Domasius Nwabunma and Thein Kyu

the distribution of agglomerates of spherical nanoparticles and ''bundles'' of nanofibers over atomistic to micrometer length scales. Such a distinction must consider: (a) the fundamental unit/particle and (b) the spatial and the orientation correlation of the units, which vary with concentration over these scales. In nanofibers, one may have mixtures of individual and stacked layers. Because of the high aspect ratio, they most probably exhibit a complex superposition of spatial–orientational correlations (i.e., a grainy texture) that may be difficult to characterize at a level that makes it possible to identify what aspects of the bundle structure influence the formation of crystals. Thus, morphology characterization of nanocomposites requires information not only on the nanoscale (1–100 nm) but also on the meso-and microscale (0.01–100 μm), reflecting orientation correlation and concentration fluctuations. For nanostructured gels, melts, or fluids, a complex temporal aspect, ranging from molecular motions to collective network relaxation modes, must also be considered. Experiments (25–29) have conclusively demonstrated that enhanced mechanical properties of nanocomposites result when the dispersion of nanoparticles in the polymer matrix is good. In spite of the importance of such information, the improvement of techniques for detailed morphology analysis has lagged behind the substantial progress made in the application of chemical modification of nanoparticle surfaces (30–33) and fabrication methods (34–38) to achieve ''dispersion.'' In addition to these efforts, recent reviews (39–42) describe the considerable interest in theory and the simulations of the properties of polymer nanocomposites.

Although these synthetic, preparation theory, and modeling efforts are paramount to improving the properties of polymer nanocomposites, developing an understanding of the influence of the polymer–nanofiller interface region on the relative arrangement of nanoparticle and polymer constituents and, ultimately, its relationship to the nanocomposites properties is a current research frontier in nanotechnology. Equally important is the development of a general understanding of how the structure and morphology of particles influence properties that can be used to enhance the previously described modeling and simulation efforts for predicting the properties of polymer nanocomposites. In polyethylenes, which constitute over 60% of global polymer production, the macroscopic behavior is strongly dependent on the underlying microstructure (Fig. 13.1), consisting of molecules arranged in the unit cell, lamellar crystals, and the aggregation of these lamellae into superstructures such as spherulites and axialites (43,44). In small-scale applications and thin films, in particular, the macroscopic mechanical properties are dominated by this microstructure. The desire to design materials with favorable properties and control their performance has led to increased interest in building quantitative relationships between the microstructure of materials and their macroscopic behavior. The relatively new field of multiscale modeling of materials shows great promise (45–54). Materials are modeled on a scale that is larger than the atomic but smaller than the continuum level. In polyethylenes, the microstructural or morphological features that need to be considered typically act on the scale of the lamellar stacks or fibrils (several hundred nanometers) to spherulites (several micrometers) (Fig. 13.1).

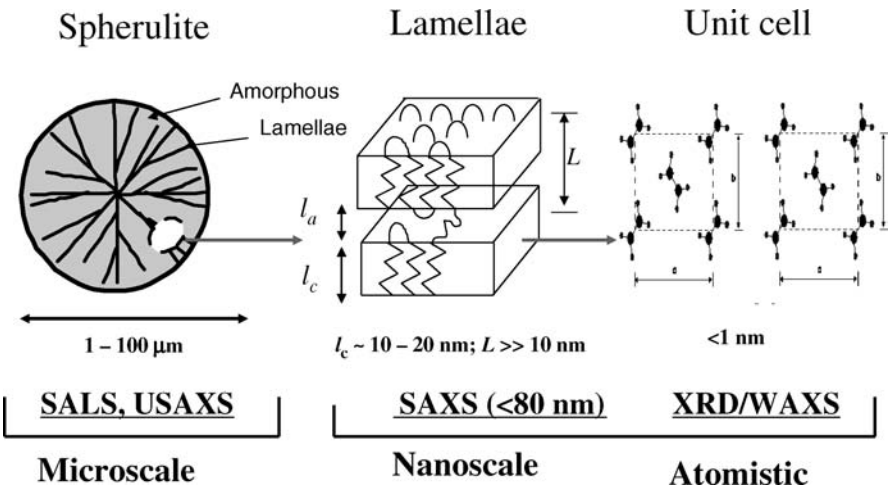

Figure 13.1 Schematic representation of the morphology of semicrystalline polymers and techniques used to obtain structural variables during crystallization and melting. See text for explanation of symbols and abbreviations.

Scattering measurements provide a means to quantify the fractions and sizes of morphological units such as the unit cell (atomistic), lamellar (nanometer scale), fibrillar (several hundred nanometers), and spherulitc (micrometer scale) during crystallization and melting (55–66). Small-angle X-ray scattering (SAXS) (62,64,67,68) can be used to determine the average distance between crystals (L), the average crystal thickness (l_c), the average amorphous thickness (l_a), and the fraction of crystals within lamellar stacks (x_{CL}). Wide-angle X-ray scattering (WAXS) gives the unit cell dimensions and the average size of the crystal (lamella) (61). Ultrasmall-angle X-ray scattering (USAXS) probes the internal structure of spherulites on sizes on the order of several hundred nanometers, organization of lamellar stacks into spherulites, and other micrometer scale fluctuations that may be present. From small-angle light scattering (SALS) (65,66) and USAXS (69), the volume fraction of spherulites (x_S), the volume fraction of lamellar stacks (x_L), and the crystalline fraction within spherulites ($x_{CS} = x_L x_{CL}$) can be obtained. Thus, integrated light and X-ray scattering measurements can provide essential information for building multiscale models that predict polymer properties.

As mentioned previously, when polyethylenes that include high density polyethylene (HDPE), linear low density polyethylene (LLDPE), and low density polyethylene (LDPE) are mixed with particles, significant changes in the mechanical, barrier, and thermal properties result because the nanoparticles can change crystalline structure and/or morphology of the polyethylene matrix (Fig. 13.1). Nanoparticles can also influence overall crystallinity (70,71), the fraction of amorphous and crystalline phases in these structural/morphological units (72–81), the rate of crystallization (82–91), and the relative stability of the

thermodynamic crystalline phase (92–95). As we have shown recently (73,81), the influence of nanoparticles on the crystalline structure and morphology of polyethylenes strongly depends on the size of nanoparticle agglomerates, the polymer–nanoparticle interaction, and dispersion of the particles. Thus, for polyethylene/nanoparticle systems, if the agglomerate structure and dispersion of nanoparticles are well characterized, they can be used to control the folding of the polyethylene chains and the organization of these chains into lamellar crystals, stacks, and spherulites. In effect, knowledge of the dispersion of particles can be used to control the organization of polyethylene crystals and hence the resulting properties of the nanocomposite.

Not only the mean distance between the nanofiller elements but also the spatial and the orientation distribution can be as complex as those found in semicrystalline polymers.

In spite of the nanocomposite preparation and the structural and morphological characterization challenges for polyethylene nanocomposites, a significant progress has been made toward understanding the influence of particles and nanocomposite preparation conditions on the properties of these nanocomposites. Thus the aim of this review is to motivate the combined use of small-angle scattering with X-ray diffraction and electron microscopy to characterize the dispersion of nanofillers mixed in polyethylene matrices as a robust approach for obtaining structural and morphological information of the particles and their agglomerate structures over all relevant size scales (angstroms to several micrometers) that influence the thermomechanical properties of polyethylene nanocomposites.

13.2 OPTIMIZING DISPERSION OF NANOFILLERS

To date, polymer nanocomposites based on clay and layered silicates have been more widely investigated and extensively reviewed (6,38,96,97), probably because the clay starting materials are easily available and because their intercalation chemistry has been studied for a long time (98). The intercalation of polymers in clays can be achieved via intercalation of a suitable monomer and subsequent polymerization, via polymer intercalation from solution, or via melt intercalation. As shown in Fig. 13.2, depending on the nature of the components used (layered silicate, organic cation, and polymer matrix) and the method of preparation, three main types of composites may be obtained when layered clay is associated with a polymer.

When the polymer is unable to intercalate between the silicate sheets, a phase-separated composite (Fig. 13.2a) is obtained, whose properties stay in the same range as traditional microcomposites. Beyond this classical family of composites, two types of nanocomposites can be recovered. Intercalated structure (Fig. 13.2b) in which a single (and sometimes more than one) extended polymer chain is intercalated between the silicate layers resulting in a well-ordered multilayer morphology built up with alternating polymeric and inorganic layers. When the silicate layers are completely and uniformly dispersed in a continuous polymer matrix, an exfoliated or delaminated structure is obtained (Fig. 13.2c).

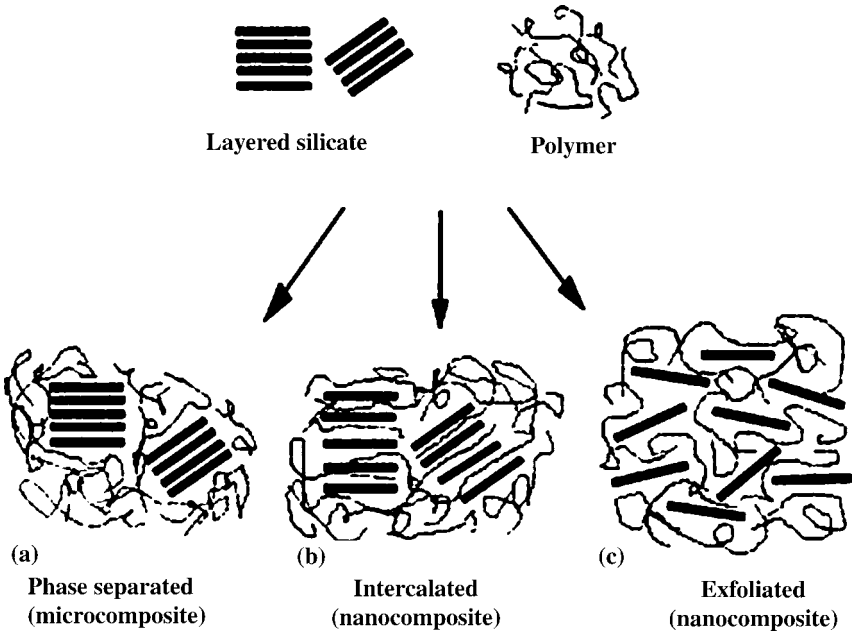

Figure 13.2 Scheme of different types of composites arising from the interaction of layered silicates and polymers: (**a**) phase-separated microcomposite, (**b**) intercalated nanocomposite, and (**c**) exfoliated nanocomposites. (From Reference 6 with permission from Elsevier Science S.A.)

As first demonstrated by Kojima and coworkers (99–101), nylon–clay nanocomposites exhibiting an intercalated morphology can be obtained by polymerizing the ε-caprolactam in the presence of clay. It was shown that improvements in properties can include, for example, increased moduli, strength, and heat resistance, and decreased gas permeability and flammability. Polymer melt intercalation has also been shown to be a good method for obtaining an intercalated morphology. For example, Vaia and coworkers (97,102) have demonstrated that the polymer melt intercalation method results in organically modified clay/polystyrene nanocomposites with nanosized dispersion of the clay platelets. In general, these methods can be used to prepare composites from polymers with polar functional groups such as polyamides, polystyrene, and polyesters. For these polymers, since polymer–clay interactions are more favorable than polymer–polymer or clay–clay interactions, a spontaneous diffusion of polymer chains from the bulk into the channels between the clay nanolayers can occur. Polymer intercalation results because this spontaneous diffusion process forces the spacing between clay nanolayers to increase. The dispersion of isolated nanolayers in the whole polymer matrix usually occurs when the polymer–clay interactions are highly favorable and if the melt blending conditions promote the delamination (exfoliation) of the clay stacks by the intercalated chains. For polyethylene/clay nanocomposites, functionalized clays are required for preparing nanocomposites because clay and polyethylenes are chemically incompatible.

During the last decade, several routes have been developed to disperse a few weight percents of clay nanolayers into PE, particularly HDPE, to prepare high performance nanocomposites. These efforts have been extensively reviewed by Alexandre and Dubois (6). However, until very recently, achieving the polymer nanofiller chemical compatibility required for ideal dispersion of nanofillers (e.g., clays) in polyethylenes via synthesis has been elusive. For instance, Mainil and coworkers (103) have prepared HDPE/clay nanocomposites using three different functionalized polyethylene compatibilizers: an ethylene/vinyl acetate copolymer, a polyethylene grafted with maleic anhydride functions and a (styrene-b-ethylene/butylene-b-styrene) block copolymer. The nanocomposites were prepared via the dispersion in HDPE of a masterbatch prepared from the compatibilizer and clay and by direct melt blending of the three components. These processes resulted in intercalated nanocomposites. It was shown that the significant increase in the stiffness and flame resistance of the nanocomposites can be attributed to the dispersion of thin intercalated stacks within the polymer matrix.

For spherical nanoparticles, surface modification of particles has also resulted in ideally dispersed nanocomposites. For example, Monteil et al. (17) synthesized PE/modified silica nanocomposites by using *in situ* polymerization method. The transmission electron microscopy (TEM) images indicated that the surface-modified silica nanocomposite showed a much better dispersion compared with the unmodified silica composite (Fig. 13.3). It was shown that by improving the compatibility between the polymer and the nanoparticles, the dispersion of the nanoparticles in the polymer matrix can be dramatically improved.

Rong et al. (104) have shown that higher tensile strengths can be obtained in polypropylene/silica nanocomposites prepared by using silica nanoparticles grafted with polystyrene beforehand. This result is significant because polypropylene composites prepared with unmodified silica exhibit a reduced tensile strength and elongation to break due to weak interfacial adhesion. Using dimethylcyclotrisiloxane (DMC) modified TiO_2 nanoparticles, Zan et al. (19) synthesized the LDPE/TiO_2 nanocomposites. It was shown that the presence of TiO_2 nanoparticles in the LDPE films greatly promotes the photocatalytic degradation of the composites.

In summary, the recent development of effective chemical modification of nanofiller surfaces and the improvements in methods for mixing polyethylenes and nanofillers have increased the polyethylene–nanofiller compatibility. As a result, the nanometer-scale dispersion of nanofillers in polyethylenes can be achieved. Despite this progress, the typical sizes of the nanofiller-rich domains obtained are usually several hundred nanometers in size. In the light of the recent improvements in the chemical compatibility of polyethylene and nanofillers through synthesis and preparation methods, it is reasonable to assume that further improvements in these methods may result in intercalated morphologies composed of nanosized filler domains and characteristic of nylon, polystyrene, and polyester nanocomposites. Ultimately, achieving this goal will require the use of structural and morphological information of the nanofillers and their agglomerate structure over atomistic to submicron and/or micrometer size scales.

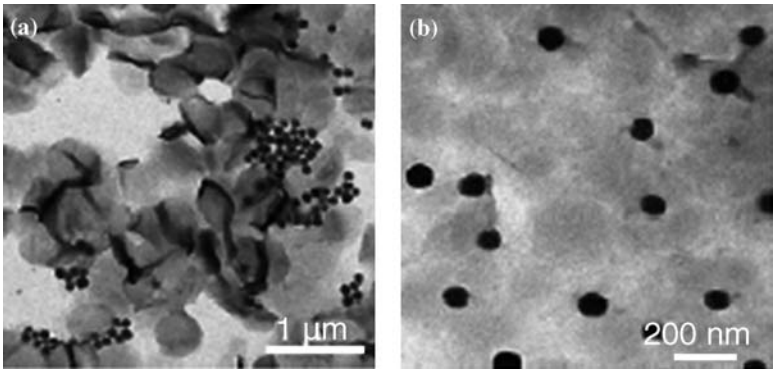

Figure 13.3 TEM images of silica/polyethylene composite dispersions prepared with (**a**) an unmodified silica and (**b**) an octyl-modified silica. (From Reference 17 with permission from the American Chemical Society.)

13.3 CHARACTERIZING DISPERSION IN POLYETHYLENE NANOCOMPOSITES

13.3.1 Conventional Techniques: X-ray Diffraction and Electron Microscopy

Two complementary techniques are routinely used in order to characterize the dispersion of nanofillers in polymer nanocomposites. X-ray diffraction (XRD) is used to identify intercalated structures. In such nanocomposites, the repetitive multilayer structure is well preserved, allowing the interlayer spacing (a few angstroms in size) to be determined. The intercalation of the polymer chains usually increases the interlayer spacing, in comparison with the spacing of the organoclay used (Fig. 13.4), leading to a shift of the diffraction peak toward lower angle values (angle and layer spacing values being related through the Bragg's relation: $\lambda = 2d \sin\theta$, where λ corresponds to the wavelength of the X-ray radiation used in the diffraction experiment, d the spacing between diffractional lattice planes, and θ is the measured diffraction angle or glancing angle).

For exfoliated structures no more diffraction peaks are visible in the XRD diffractograms either because of a too large spacing between the layers (i.e., exceeding 8 nm in the case of ordered exfoliated structure) or because the nanocomposite does not present any atomistic ordering. Besides an intercalated and an exfoliated nanocomposite, other intermediate morphologies can exist presenting both intercalation and exfoliation. In this case, a broadening of the diffraction peak is often observed. For structures where there is no atomistic ordering and/or intermediate morphologies, researchers usually rely on TEM observation to define the overall structure. Alternatively, one can use small-angle scattering by X-rays, neutrons, and light to obtain a quantitative description of nanocomposites morphology. One major advantage of small-angle scattering is that it provides statistical

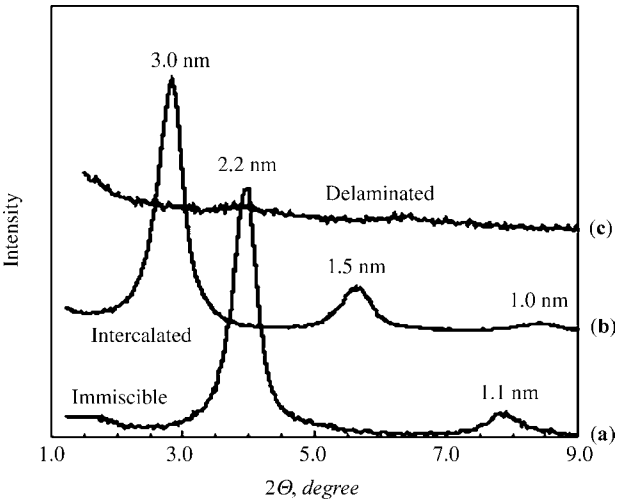

Figure 13.4 XRD patterns of (**a**) phase-separated microcomposite (organomodified fluorohectorite in a HDPE matrix), (**b**) intercalated nanocomposite (same organomodified fluorohectorite in a PS matrix), and (**c**) exfoliated nanocomposite (the same organomodified fluorohectorite in a silicone rubber matrix). (From Reference 115 with permission from Springer-Verlag.)

information on the size distribution of particles in contrast to techniques such as TEM that can evaluate only an extremely small volume of sample.

13.3.2 Small-Angle Scattering

The technique of small-angle scattering (SAS) is used to study the structures of sizes on the order of 10 Å or larger. Information such as the typical size, shape, and arrangement of structure is contained in the intensity of the scattering X-rays, neutrons, and light at small angles, typically $2\theta < 2^{\circ}$. In general, data from SAS measurements can provide information on the average size and distribution of the scattering unit or heterogeneity as long as the wavelength of the incident radiation is comparable to the size of the scattering unit or heterogeneity (105). The analysis of the scattering profiles can provide information on the nature of the interfaces, and the size, shape, and distribution of domains. Furthermore, contrast variation using isotopic substitutions allows one to distinguish between the shape and the spatial correlation of the different polymeric domains: ion rich or ion poor, crystalline, or amorphous. However, to allow for reliable model fitting to experimental data, it is important to explore the largest possible range of scattering angles that span all structures present. Thus, small-angle scattering studies of the structure of multicomponent and multiphase materials such polymer nanocomposites, whose structure and morphology can exhibit features with length scales varying from nanometers to micron, necessitate the use of multiple techniques to span these scales of structure.

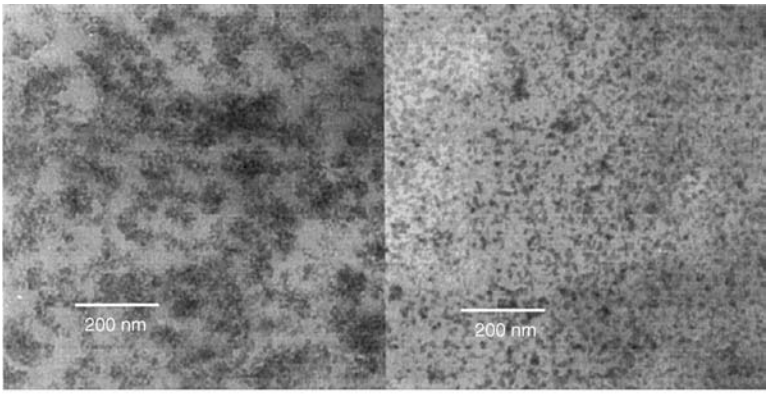

Figure 13.5 TEM micrograph of a poly(methyl methacrylate-co-2-hydroxyethyl methacrylate) (PMH) nanocomposite with (**a**) 59 vol% uncoated and (**b**) 55 vol% MPTS-coated SiO_2 particles, $d = 10$ nm. (From Reference 106 with permission from Kluwer Academic Publishers.)

Although very few SAXS and small-angle neutron scattering (SANS) studies have been previously performed for polymer nanocomposites, these methods have been successfully used to investigate the dispersion of the nanofillers in polymers with polar functional groups (106–110). By combining with TEM or other techniques, SAXS and SANS can provide quantitative information about the aggregates of the nanofillers. For example, using TEM and SAXS, Becker et al. (106) characterized the dispersion of thermoplastic nanocomposites based on a thermoplastic matrix of a copolymer of methyl methacrylate (MMA) and 2-hydroxyethylmethacrylate (HEMA) with spherical 10 nm silica particles as filler. Samples with filler content 2, 5, and 10 vol% were studied. For nanocomposites with uncoated filler particles, aggregates with diameters up to 100 nm could be observed by TEM (Fig. 13.5a). For nanocomposites containing coated particles, TEM showed that the particles were better dispersed in the polymer matrix, only forming aggregates comprised of two or three primary particles (Fig. 13.5b). The small-angle X-ray scattering (Fig. 13.6) for both nanocomposites showed features consistent with TEM observations. For nanocomposites filled with uncoated silica particles, the upturn in the scattering intensity in the very low angle ($\mathbf{q} \ll 0.1\ \text{Å}^{-1}$) region reflects the long-range correlations and structures of large-sized silica agglomerates in the sample, while the shoulder near ($\mathbf{q} \sim 0.1\ \text{Å}^{-1}$) can be attributed to local ''crystalline-like'' ordering of the dispersed silica particles in the matrix (Fig. 13.6b). The monomodal volume-weighted particle size distribution (Fig. 13.7a) calculated from the monotonically decreasing SAXS profiles (Fig. 13.6a) of the nanocomposites filled with uncoated silica particles is consistent with the more uniform size distribution of aggregates measured by TEM and shows particle sizes in the range of primary silica particles. However, for the nanocomposites with coated particles, a bimodal size distribution with particle sizes comparable with those measured by TEM were observed (Fig. 13.7b).

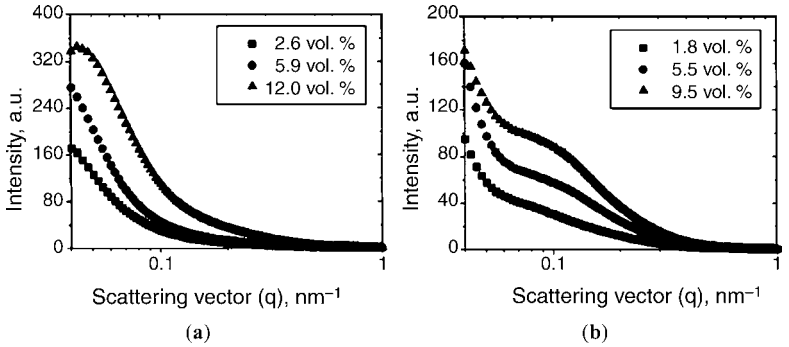

Figure 13.6 SAXS spectra of PMH nanocomposites with (**a**) uncoated and (**b**) MPTS-coated 10-nm SiO_2 particles for different filler volume fractions. (From Reference 106 with permission from Kluwer Academic Publishers.)

Although these SAXS and TEM results (Fig. 13.5–13.7) are in good agreement, ultrasmall-angle scattering using X-rays or neutrons is required to determine the size and distribution of larger aggregates (several hundred nanometers to micrometers in size), and their influence on the properties of the nanocomposite. For polyethylenes, the convolution of crystalline peaks with peaks characteristic of the spacing between nanofiller domains or layers hinders the use of SAXS for characterizing the dispersion of polyethylene nanocomposites. Although SANS can be used to characterize structures on this size range, it is likely that the need for expensive deuteration to provide sufficient contrast has also made it difficult to routinely characterize many commercial polyethylene nanocomposites. On the contrary, light scattering (LS) is an excellent means to probe the structure of agglomerates and other aggregate structures.

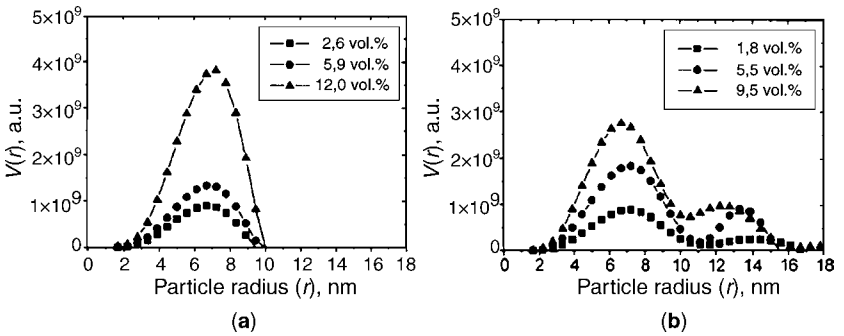

Figure 13.7 Calculated volume-weighted particle size distributions $V(r)$ of the (**a**) uncoated and (**b**) MPTS-coated SiO_2 particles from the SAXS spectra for PMH nanocomposites containing different volume fractions of silica using the program ITP 92 developed by Glatter assuming spherical shape and a limit of calculation of 50 nm. (From Reference 106 with permission from Kluwer Academic Publishers.)

Light scattering is a small-angle scattering technique that is sensitive to the size and the state of aggregation of nanoparticle agglomerates, thereby enabling the characterization of hierarchical structures as well as the agglomerate size distribution. The analysis of light scattering can be treated by solving the Maxell's equations with appropriate boundary conditions (111–113). For example, Mie theory provided a rigorous solution for the problem of light scattering by a homogeneous isotropic sphere (111–112). However, for most practical applications, the exact solutions are difficult to achieve or the exact theories are not applicable. Thus, approximate theories are generally applied. For the case of nanofillers dispersed in a medium, three approximations have generally been used depending on the ratio of refractive indices of the particulates and the medium m, defined as $m = n_p/n_m$, and the size parameter a describing scattering phenomenon, which is defined as $\alpha = 2\pi R/\lambda$, where R is the characteristic dimension of the particulates (for spheres R will be the radius), λ is the wavelength of the light in the medium (111–112). When the size parameter a, fall within the Rayleigh-Gans-Debye limit, i.e $2\alpha|m-1| \ll 1$ the absolute scattered intensity from a small-angle scattering measurement is related to the particle form factor $P(q)$ and the structure factor $S(q)$ as follows:

$$I(q) = N_p V_p^2 (\rho_{partcle} - \rho_{polymer})^2 P(q) S(q) \tag{13.1}$$

where q is the scattering wave vector defined as $q = 4\pi \sin\theta/\lambda$ (λ is the wavelength of the probe and 2θ is the scattering angle), N_p is the number density of particles, V_p is the volume of the scattering particle, $\rho_{particle}$ and $\rho_{polymer}$ are the scattering length densities of the nanoparticle and the polymer, respectively. For nanocomposites, the observed intensity arises from the density fluctuations due to different levels of aggregates of particles in the polymer matrix. In a dilute system such as nanocomposites with less than 5 wt% nanofillers, it is reasonable to assume that interparticle correlations will be very low, and therefore $S(q)$ can be assumed to be 1. At higher particle loadings, the effects of $S(q)$ in the low q region can be observed in the light scattering due to a significantly higher population of aggregates and enhanced interparticle correlations. By combining light scattering with USAXS data, one can learn about the structural features at different levels of organization (tens of micrometers to several hundred nanometers) such as aggregation and agglomeration of nanofillers using the unified fit to light scattering and USAXS data. This method is illustrated below for spherical particles.

For spherical nanoparticles (e.g., silica and titania), the primary particles form one length scale, their aggregates form a second length scale, and cluster of aggregates, namely agglomerates, forms a third length scale. When hierarchical structures are present, the question arises as to how the particles are organized at each level and their correlation in terms of polydispersity or fractal scaling, if any. Such information can be derived using the unified fit analysis (114) of the small-angle scattering intensity. At each level, contributions to $P(q)$ in Equation 13.1 can be used to derive an average radius of gyration (R_g) from a q region where $q_{max}R_g \sim 1$ using the Guinier law

$$I(q) = G\exp\left(-\frac{q^2R_g^2}{3}\right) \tag{13.2}$$

and a power law (P) from a q region where $qR_g \gg 1$.

$$I(q) \sim q^{-P} \tag{13.3}$$

The same procedure can be extended for different length scales at corresponding q ranges in the LS and USAXS data for aggregates and agglomerates. The value of P can be used to interpret the shape of the particles or the fractal nature of the aggregates or agglomerates (105). However, a careful examination of information from other complementary techniques is needed for its proper interpretation. For instance, rods and disks will produce scattering intensity that varies with exponents $P = 1$ and 2, respectively. In the case of mass fractals P that relates to mass M and length R as $M \sim R^P$: P can assume noninteger values from 1 to 3 depending on the density of particles in the aggregate or agglomerate. On the contrary, for a particle with a distinct surface, the scattering arising from the surface of the particle leads to the following intensity variation:

$$I(q) \sim q^{d_s-6} \tag{13.4}$$

where d_s is the surface fractal dimension (105) and is based on the relationship of the surface area (S) to the sphere radius $S \sim R^{d_s} : d_s$ is the measure of the roughness of the surface and varies between 2 and 3, and correspondingly the power-law slope P at $qR_g \gg 1$ will lie between 4 and 3. It must be noted that if the particle size distribution itself follows a power-law behavior, the scattering intensity will also exhibit similar power-law scaling and, invariably for such systems, P has been observed to fall in the range from 3 to 4. Note that $d_s = 2$ pertains to the smooth surface of a sphere as shown by Porod (115). It is clear from the above discussion that $P(q)$ at each level of the hierarchy can be represented by a combination of exponential and power-law regions. This is the basic motivation for the unified fit approach to small-angle scattering proposed by Beaucage (114,116):

$$I(q) = \sum_{i=1}^{n} \left(G_i \exp(-q^2R_{g_i}^2/3) + B_i \exp(-q^2R_{g_{i+1}}^2/3) \times \{[\mathrm{erf}(qR_{g_i}/6^{1/2})]^3/q\}^{P_i}\right) + \gamma \tag{13.5}$$

Here $i = 1$ refers to the smallest size structural level and γ is the flat background scattering. G_i is the Guinier prefactor and is related to the average particle volume (19) V_p through the relationship

$$G_i = N_P r_e^2 (\rho_{\mathrm{particle}} - \rho_{\mathrm{polymer}})^2 V_p^2 \tag{13.6}$$

r_e is the classical electron radius. B_i is the power-law prefactor and is related to the average surface area (19) S of the particle via the following relation:

$$B_i = 2\pi r_e^2 N_p (\rho_{particle} - \rho_{polymer})^2 S \tag{13.7}$$

A successful unified fit analysis for small-angle scattering of the aggregate structure of nanofillers usually requires data that span the angular range (from several micrometers to hundreds of nanometers). For polyethylene nanocomposites, light scattering is required to observe scattering that describes the morphology of the nanofiller agglomerates because these nanofillers are usually several hundred nanometers in size or larger. We have recently shown (81) that our vertical SALS instrument can be used to characterize the structure and dispersion of TiO_2 nanoparticle agglomerates in low density polyethylene. In Fig. 13.8, scanning electron microscopy (SEM) micrographs for dry TiO_2 agglomerates exhibited submicron nanoparticle dispersion in the polymer matrix, even though some micrometer-sized agglomerates were observed. *N*-(2-Aminoethyl) 3-aminopropyl-trimethoxysilane-modified TiO_2 (AEAPS-TiO_2) formed much larger agglomerates (several micrometers) in the polymer matrix, even though individually dispersed particles and clusters of several particles and large micrometer agglomerates were observed in both samples. As shown in Fig. 13.9; the SALS (no polarizers) of AEAPS-TiO_2/LDPE is more concentrated and more intense at lower scattering angles, indicating the presence of larger nanoparticle aggregates in the AEAPS sample and confirming the relative size information from SEM.

It must be noted that the dispersion in these composites is far from ideal, although they represent some of the "good" dispersions of nanofillers that can be achieved with polyethylenes. Thus it is anticipated that with continued improvements in dispersion of nanofillers in polyethylenes through synthesis and preparation

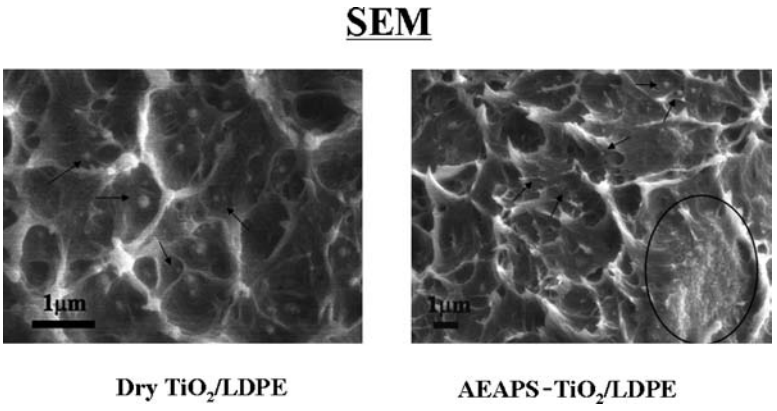

Figure 13.8 Field emission SEM images showing the dispersion of (**a**) dry TiO_2 nanoparticles and (**b**) AEAPS-coated TiO_2 nanoparticles in LDPE. The ellipse represents an agglomerate and arrows point to particles. (From Reference 81 with permission from the American Chemical Society.)

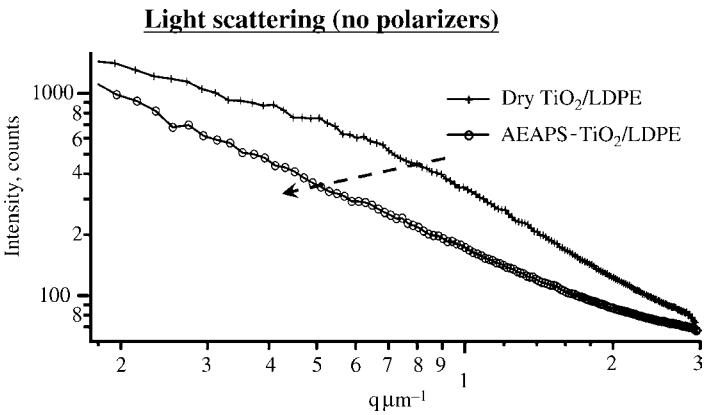

Figure 13.9 Dispersion of TiO_2 nanoparticles by light scattering (no polarizers). The arrow indicates the shift of the scattering curve to larger angles, which is expected as the particle size increases.

methods, the combined use of light and X-ray scattering can provide the morphological insight into tailoring these approaches toward achieving ideal dispersion of nanofillers in polyethylene matrices. This is because the low and the high q scatterings necessary to perform a unified fit analysis can be easily obtained from light scattering measurements (117). In effect, light scattering can greatly enhance any efforts to improve the chemical compatibility of these composites via synthesis since quantitative information on the agglomerate structure can be obtained from the technique. More importantly, our results are significant because it is shown that using light, size and shape features that correlate well with our SEM observations of nanoparticle dispersion can be obtained using our unique vertical light scattering setup. For layered nanofiller domains that are too large for SAXS and SANS, classical small-angle scattering equations (105) for stacked or lamellar structures can be applied to the light scattering of these systems to obtain variables that describe their agglomerate structure and morphology. To date, this application remains relatively unexplored as an alternative method for characterizing polymers filled with anisotropic nanofillers at concentrations where optical transparency of the nanocomposites film is preserved.

13.4 CONCLUSIONS

In this review, it is shown that by combining light with electron microscopy and X-ray diffraction, the dispersion of nanofillers can be characterized on the atomistic to micrometer length scales that influence the properties of polyethylene nanocomposites. This information can provide a foundation for building a robust molecular-level understanding of the influence of the dispersion of nanofillers on the properties of polyethylene nanocomposites.

ACKNOWLEDGMENTS

Y. A. A. would like to acknowledge support of this work by NSF CMMI under Award # 0600317 and DOE-BES under Award # FG02–06ER46349. The light scattering instrumentation cited in this work was developed with NSF support under NSF Award Number DMR-0108976. Y. A. A. would like to thank Mr. Z. Xiao for help in preparing the manuscript.

NOMENCLATURE

AEAPS	3-Aminopropyl-trimethoxysilane
B_i	Power law prefactor
d	Spacing between diffractional lattice planes
d_s	Surface fractal dimension
DMC	Dimethylcyelotrisiloxane
G_i	Guinier prefactor
HDPE	High density polyethylene
HEMA	2-Hydroxyethyl methacrylate
$I(q)$	Scattering intensity at given q value
L	Average distance between crystals
l_a	Average amorphous thickness
l_c	Average crystal thickness
LDPE	Low density polyethylene
LLDPE	Linear low density polyethylene
LS	Light scattering
M	Mass of mass fractal
MMA	Methyl methacrylate
N_p	Number density of particles
PE	Polyethylene
P	Mass fractal dimension or power law slope
$P(q)$	Particle form factor
$\mathbf{q}$	Scattering vector
R	Length of mass/surface fractal
r_e	Classical electron radius
R_g	Radius of gyration
S	Surface area
SALS	Small-angle light scattering
SANS	Small neutron light scattering
SAS	Small-angle scattering
SAXS	Small-angle X-ray scattering
SEM	Scanning electron microscopy
$S(q)$	Structure factor
TEM	Transmission electron microscopy
USAXS	Ultrasmall angle X-ray scattering

V_p	Volume of the scattering particle
WAXS	Wide-angle X-ray scattering
x_{CL}	Fraction of crystals within lamella stacks
x_L	Volume fraction of lamella stacks
x_S	Volume fraction of spherulites
x_{CS}	Crystalline fraction within spherulites
XRD	X-ray diffraction.
λ	Wavelength of the probe (light or X-ray radiation)
θ	Measured diffraction angle or glancing angle for X-ray scattering; 2θ is the scattering angle for light scattering
$\rho_{particle}$	Scattering length density of the nanoparticles
$\rho_{polymer}$	Scattering length density of the polymers
γ	Flat background scattering

REFERENCES

1. R. Krishnamoorti and R. A. Vaia (eds.), *Polymer Nanocomposites: Synthesis, Characterization, and Modeling*, American Chemical Society, Distributed by Oxford University Press, Washington, DC, 2002.
2. R. A. Vaia and E. P. Giannelis, *MRS Bull.*, **26** 394 (2001).
3. T. J. Pinnavaia and G. W. Beall (eds.), *Polymer–Clay Nanocomposites*, Wiley, Chichester, England, 2000.
4. E. P. Giannelis, *Adv. Mater.*, **8**, 29 (1996).
5. M. Kato, A. Usuki, and A. Okada, *J. Appl. Polym. Sci.*, **66**, 1781 (1997).
6. M. Alexandre and P. Dubois, *Mat. Sci. Eng. R Rep.*, **28**, 1 (2000).
7. L. Wang, L. X. Feng, and T. Xie, *Polym. Int.*, **49**, 184 (2000).
8. J. F. Rong, H. Q. Li, Z. H. Jing, X. Y. Hong, and M. Sheng, *J. Appl. Polym. Sci.*, **82**, 1829 (2001).
9. J. Morawiec, A. Pawlak, M. Slouf, A. Galeski, E. Piorkowska, and N. Krasnikowa, *Eur. Polym. J.*, **41**, 1115 (2005).
10. H. M. Yang, Y. H. Song, B. Xu, and Q. Zheng, *Chem. Res. Chin. Univ.*, **22**, 383 (2006).
11. J. G. Zhang and C. A. Wilkie, *Polymer*, **47**, 5736 (2006).
12. J. Zhang, R. K. Gupta, and C. A. Wilkie, *Polymer*, **47**, 4537 (2006).
13. S. H. Ryu and Y. W. Chang, *Polym. Bull.*, **55**, 385 (2005).
14. S. P. Gubin, *Colloids Surf. A Physicochem. Eng. Aspects*, **202**, 155 (2002).
15. J. I. Hong, K. S. Cho, C. I. Chung, L. S. Schadler, and R. W. Siegel, *J. Mater. Res.*, **17**, 940 (2002).
16. J. I. Hong, L. S. Schadler, R. W. Siegel, and E. Martensson, *Appl. Phys. Lett.*, **82**, 1956 (2003).
17. V. Monteil, J. Stumbaum, R. Thomann, and S. Mecking, *Macromolecules*, **39**, 2056 (2006).
18. X. Zhang and L. C. Simon, *Macromol. Mater. Eng.*, **290**, 573 (2005).
19. L. Zan, W. J. Fa, and S. L. Wang, *Environ. Sci. Technol.*, **40**, 1681 (2006).
20. F. Zhang, T. Karaki, M. Adachi, and S. X. Li, *Jpn. J. Appl. Phys. 1 Regular Papers Brief Commun. Revi. Papers*, **45**, 1873 (2006).
21. L. M. Fang, Y. Leng, and P. Gao, *Biomaterials*, **27**, 3701 (2006).
22. L. Zheng, R. J. Farris, and E. B. Coughlin, *Macromolecules*, **34**, 8034 (2001).
23. L. Zheng, A. J. Waddon, R. J. Farris, and E. B. Coughlin, *Macromolecules*, **35**, 2375 (2002).
24. Y. Tong, X. J. He, and H. M. Cheng, *New Carbon Mater.*, **19**, 261 (2004).

25. P. H. T. Vollenberg and D. Heikens, *Polymer*, **30**, 1656 (1989).
26. P. H. T. Vollenberg, J. W. Dehaan, L. J. M. Vandeven, and D. Heikens, *Polymer*, **30**, 1663 (1989).
27. S. S. Sternstein and A. J. Zhu, *Macromolecules*, **35**, 7262 (2002).
28. C. A. Mitchell, J. L. Bahr, S. Arepalli, J. M. Tour, and R. Krishnamoorti, *Macromolecules*, **35**, 8825 (2002).
29. B. J. Ash, R. W. Siegel, and L. S. Schadler, *Macromolecules*, **37**, 1358 (2004).
30. T. von Werne and T. E. Patten, *J. Am. Chem. Soc.*, **123**, 7497 (2001).
31. D. Ma, T. A. Hugener, R. W. Siegel, A. Christerson, E. Martensson, C. Oenneby, and L. S. Schadler, *Nanotechnology*, **16**, 724 (2005).
32. D. Garcia-Lopez, O. Picazo, J. C. Merino, and J. M. Pastor, *Eur. Polym. J.*, **39**, 945 (2003).
33. V. Castelvetro and C. De Vita, *Adv. Colloid Interface Sci.*, **108–109**, 167 (2004).
34. K. Akamatsu and S. Deki, *J. Colloid Interface Sci.*, **214**, 353 (1999).
35. N. Behan and C. Birkinshaw, *Macromol. Rapid Commun.*, **22**, 41 (2001).
36. C. S. Lee, J. S. Lee, and S. T. Oh, *Mater. Lett.*, **57**, 2643 (2003).
37. E. C. Lee, D. F. Mielewski, and R. J. Baird, *Polym. Eng. Sci.*, 44, 1773 (2004).
38. S. S. Ray and M. Okamoto, *Prog. Polym. Sci.*, **28**, 1539 (2003).
39. R. S. Fertig and M. R. Garnich, *Compos. Sci. Technol.*, **64**, 2577 (2004).
40. M. S. Ozmusul, C. R. Picu, S. S. Sternstein, and S. K. Kumar, *Macromolecules*, **38**, 4495 (2005).
41. P. K. Valavala and G. M. Odegard, *Rev. Adv. Mater. Sci.*, **9**, 34 (2005).
42. G. J. Papakonstantopoulos, K. Yoshimoto, M. Doxastakis, P. F. Nealey, and J. J. de Pablo, *Phys. Rev. E* 72 (2005).
43. P. H. Geil, *Polymer Single Crystals*, Wiley Interscience, Chichester, 1963.
44. D. C. Bassett, *Principles of Polymer Morphology*, Cambridge University Press, Cambridge, 1981.
45. C. Charbon and S. Swaminarayan, *Mat. Sci. Eng. A–Struct. Mater. Prop. Microstruct. and Process.*, **238**, 166 (1997).
46. S. Swaminarayan and C. Charbon, *Polym. Eng. Sci.*, **38**, 634 (1998).
47. C. Charbon and S. Swaminarayan, *Polym. Eng. Sci.*, **38**, 644 (1998).
48. R. M. Nieminen, *J. Phys. Condensed Matter*, **14**, 2859 (2002).
49. G. C. Rutledge, *J. Macromol. Sci. Phys. B*, **41**, 909 (2002).
50. N. Sheng, M. C. Boyce, D. M. Parks, G. C. Rutledge, J. I. Abes, and R. E. Cohen, *Polymer*, **45**, 487 (2004).
51. J. Crawshaw and A. H. Windle, *Fiber Diffr. Rev.*, **11**, 52 (2003).
52. J. A. W. van Dommelen, D. M. Parks, M. C. Boyce, W. A. M. Brekelmans, and F. P. T. Baaijens, *Polymer*, **44**, 6089 (2003).
53. D. D. Vvedensky, *J. Phys. Condens. Matter*, **16**, R1537 (2004).
54. M. J. Ko, N. Waheed, M. S. Lavine, and G. C. Rutledge, *J. Chem. Phys.*, **121**, 2823 (2004).
55. S. Go, L. Mandelkern, R. Prud'homme, and R. S. Stein, *J. Polym. Sci. B Polym. Phys.*, **12**, 1485 (1974).
56. L. Mandelkern and J. Maxfield, *J. Polym. Sci. B Polym. Phys.*, **17**, 1913 (1979).
57. J. Koberstein, T. P. Russell, and R. S. Stein, *J. Polym. Sci. B Polym. Phys.*, **17**, 1719 (1979).
58. R. S. Stein, J. Cronauer, and H. G. Zachmann, *J. Mol. Struct.*, **383**, 19 (1996).
59. B. Goderis, M. Peeters, V. B. F. Mathot, M. H. J. Koch, W. Bras, A. J. Ryan, and H. Reynaers, *J. Polym. Sci. B Polym. Phys.*, **38**, 1975 (2000).
60. Z.-G. Wang, B. S. Hsiao, E. B. Sirota, P. Agarwal, and S. Srinivas, *Macromolecules*, **33**, 978 (2000).
61. K. Jokela, A. Vaananen, M. Torkkeli, P. Starck, R. Serimaa, B. Lofgren, and J. Seppala, *J. Polym. Sci. B Polym. Phys.*, **39**, 1860 (2001).

62. Y. A. Akpalu and E. J. Amis, *J. Chem. Phys.*, **111**, 8686 (1999).
63. Y. Akpalu, L. Kielhorn, B. S. Hsiao, R. S. Stein, T. P. Russell, J. van Egmond, and M. Muthukumar, *Macromolecules*, **32**, 765 (1999).
64. Y. A. Akpalu and E. J. Amis, *J. Chem. Phys.*, **113**, 392 (2000).
65. Y. A. Akpalu and Y. Y. Lin, *J. Polym. Sci. B Polym. Phys.*, **40**, 2714 (2002).
66. Y. Li and Y. A. Akpalu, *Macromolecules*, **37**, 7265 (2004).
67. B. Goderis, H. Reynaers, and M. H. J. Koch, *Macromolecules*, **35**, 5840 (2002).
68. B. Crist, *Macromolecules*, **36**, 4880 (2003).
69. G. Beaucage, S. Sukumaran, S. Rane, and D. J. Kohls, *J. Polym. Sci. B Polym. Phys.*, **36**, 3147 (1998).
70. J. Ma, S. Zhang, Z. Qi, G. Li, and Y. Hu, *J. Appl. Polym. Sci.*, **83**, 1978 (2002).
71. M. N. Bureau, J. Denault, K. C. Cole, and G. D. Enright, *Polym. Eng. Sci.*, **42**, 1897 (2002).
72. A. Bafna, G. Beaucage, F. Mirabella, and S. Mehta, *Polymer*, **44**, 1103 (2003).
73. D. L. Ma, Y. A. Akpalu, Y. Li, R. W. Siegel, and L. S. Schadler, *J. Polym. Sci. B Polym. Phys.*, **43**, 488 (2005).
74. A. S. Vaughan, Y. Zhao, L. L. Barre, S. J. Sutton, and S. G. Swingler, *Eur. Polym. J.*, **39**, 355 (2003).
75. M. M. Ueki and M. Zanin, *IEEE Trans. Dielectr. Electr. Insulat.*, **6**, 876 (1999).
76. Y. Yamano and H. Endoh, *IEEE Trans. Dielectr. Electr. Insulat.*, **5**, 270 (1998).
77. Q. Wang, Q. Xue, H. Liu, W. Shen, and J. Xu, *Wear*, **198**, 216 (1996).
78. Q. Wang, J. Xu, W. Shen, and Q. Xue, *Wear*, **209**, 316 (1997).
79. C. J. Schwartz and S. Bahadur, *Wear*, **237**, 261 (2000).
80. W. G. Sawyer, K. D. Freudenberg, P. Bhimaraj, and L. S. Schadler, *Wear*, **254**, 573 (2003).
81. Z. C. Xiao, Y. Li, D. L. Ma, L. S. Schadler, and Y. A. Akpalu, *J. Polym. Sci. B Polym. Phys.*, **44**, 1084 (2006).
82. L. S. Schadler, R. Gobran, S. C. Park, and M. Gleason, *J. Vinyl Additive Technol.*, **1**, 190 (1995).
83. E. Petrovicova, R. Knight, L. S. Schadler, and T. E. Twardowski, *J. Appl. Polym. Sci.*, **78**, 2272 (2000).
84. C. Saujanya and S. Radhakrishnan, *J. Mater. Sci.*, **35**, 2319 (2000).
85. L. Priya and J. P. Jog, *J. Polym. Sci. B Polym. Phys.*, **40**, 1682 (2002).
86. V. Krikorian, M. Kurian, M. E. Galvin, A. P. Nowak, T. J. Deming, and D. J. Pochan, *J. Polym. Sci. B Polym. Phys.*, **40**, 2579 (2002).
87. Z. G. Wu, C. X. Zhou, R. R. Qi, and H. B. Zhang, *J. Appl. Polym. Sci.*, **83**, 2403 (2002).
88. W. Xu, M. Ge, and P. He, *J. Polym. Sci. B Polym. Phys.*, **40**, 408 (2002).
89. T. G. Gopakumar, J. A. Lee, M. Kontopoulou, and J. S. Parent, *Polymer*, **43**, 5483 (2002).
90. T. D. Fornes and D. R. Paul, *Polymer*, **44**, 3945 (2003).
91. W. Xu, G. Liang, H. Zhai, S. Tang, G. Hang, and W.-P. Pan, *Eur. Polym. J.*, **39**, 1467 (2003).
92. Y. Kojima, A. Usuki, M. Kawasumi, A. Okada, Y. Fukushima, T. Kurauchi, and O. Kamigaito, *J. Mater. Res.*, **8**, 1185 (1993).
93. Y. Kojima, A. Usuki, M. Kawasumi, A. Okada, T. Kurauchi, O. Kamigaito, and K. Kaji, *J. Polym. Sci. B Polym. Phys.*, **32**, 625 (1994).
94. C. Saujanya and S. Radhakrishnan, *Polymer*, **42**, 6723 (2001).
95. P. Bhimaraj, *Materials Science & Engineering*, Rensselaer Polytechnic Institute, Troy, 2004.
96. A. Usuki, N. Hasegawa, and M. Kato, *Inorganic Polymeric Nanocomposites and Membranes*, Vol. 179 2005, p. 135.
97. R. A. Vaia and E. P. Giannelis, *Macromolecules*, **30**, 8000 (1997).
98. B. K. G. Theng, *The Chemistry of Clay—Organic Reactions*, Wiley, New York, 1974.

99. A. Okada, M. Kawasumi, A. Usuki, Y. Kojima, T. Kurauchi, and O. Kamigaito, *Mater. Res. Soc. Symp. Proc.*, **171**, 45 (1990).
100. A. Usuki, Y. Kojima, M. Kawasumi, A. Okada, Y. Fukushima, T. Kurauchi, and O. Kamigaito, *J. Mater. Res.*, **8**, 1179 (1993).
101. K. Yano, A. Usuki, A. Okada, T. Kurauchi, and O. Kamigaito, *J. Polym. Sci. A Polym. Chem.*, **31**, 2493 (1993).
102. R. A. Vaia, K. D. Jandt, E. J. Kramer, and E. P. Giannelis, *Macromolecules*, **28**, 8080 (1995).
103. M. Mainil, M. Alexandre, F. Monteverde, and P. Dubois, *J. Nanosci. Nanotechnol.*, **6**, 337 (2006).
104. M. Z. Rong, M. Q. Zhang, Y. X. Zheng, H. M. Zeng, and K. Friedrich, *Polymer*, **42**, 3301 (2001).
105. R. J. Roe, *Methods of X-Ray and Neutron Scattering in Polymer Science*, University Press, Oxford, 2000.
106. C. Becker, B. Kutsch, H. Krug, and H. Kaddami, *J. Sol-Gel Sci. Technol.*, **13**, 499 (1998).
107. C. Karlsson, A. S. Best, J. Swenson, J. Kohlbrecher, and L. Boerjesson, *Macromolecules*, **38**, 6666 (2005).
108. A. H. Tsou and M. B. Measmer, *Rubber Chem. Technol.*, **79**, 281 (2006).
109. Y. Xu, W. J. Brittain, R. A. Vaia, and G. Price, *Polymer*, **47**, 4564 (2006).
110. M. Yoonessi, H. Toghiani, T. L. Daulton, S. Jar, Y.-S. Lin, and C. U. Pittman Jr., *Macromolecules*, **38**, 818 (2005).
111. van der Hulst HC: *Light Scattering by Small Particles*, 1981, Dover, New York.
112. Bohren CF, Huffman DR: *Absorption and Scattering of Light by Small Particles*, 1983, Wiley, New York
113. Born M, Wolf E: *Principles of Optics*, 1999, Cambridge University Press, New York.
114. G. Beaucage, *J. Appl. Crystallogr.*, **28**, 717 (1995).
115. O. Glatter and O. Kratky, *Small Angle X-Ray Scattering*, Academic Press, New York, 1982.
116. G. Beaucage, H. K. Kammler, and S. E. Pratsinis, *J. Appl. Crystallogr.*, **37**, 523 (2004).
117. M. Kerker, *The Scattering of Light and Other Electromagnetic Radiation*, Academic Press, New York, 1969.
118. E. P. Giannelis, R. Krishnamoorti, and E. Manias, *Polymers in Confined Environments*, Vol. **138** Springer, Berlin, 1999, p. 107.

Chapter 14

Polyolefin–Silicate Nanocomposites: Mechanical Properties and Fracture Mechanics

Sie C. Tjong[1]

14.1 INTRODUCTION

The incorporation of nanoparticles to enhance polymer performance has generated considerable research interest in the past decade. Polymer–clay nanocomposites are particularly attractive because they exhibit markedly improved properties including tensile strength, heat resistance, gas permeability, and flame retardancy over conventional microcomposite counterparts. These properties are improved by the incorporation and dispersion of low loading levels of inexpensive clay minerals (usually less than 5 wt%) as platelets with dimensions of the order of a few nanometers in polymer matrices. The lower clay loadings facilitate processing and reduce component weight. The high aspect ratio and large surface area of the clay nanolayers offer high reinforcing efficiency and good barrier properties. The polymer–clay nanocomposites find potential applications as ideal materials for automotive parts, packaging films, household appliances, beverage containers, and medical products (1–3).

The clay minerals used for these purposes are 2:1 phyllosilicates including mica, smectite, vermiculite, and chlorite. Smectite group can be further divided into montmorillonite (MMT), saponite, and hectorite (5,6). The structure of 2:1

[1]Department of Physics and Materials Science, City University of Hong Kong, Tat Chee Avenue, Kowloon, Hong Kong

Polyolefin Composites, Edited by Domasius Nwabunma and Thein Kyu

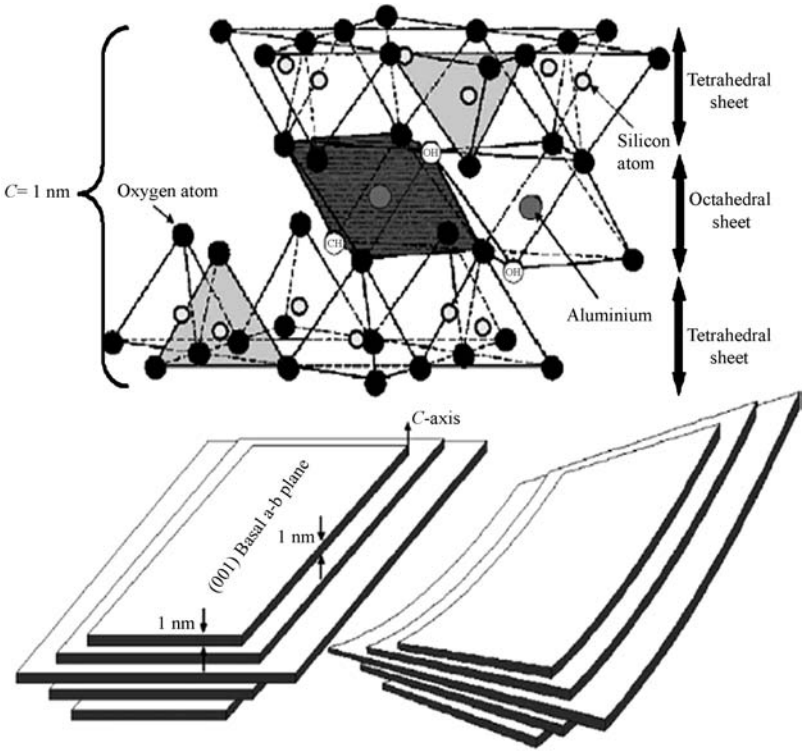

Figure 14.1 Structure of phyllosilicates. (Reprinted from Reference 5 with permission of Elsevier.)

phyllosilicates consists of a central sheet of octahedral alumina sandwiched between two silica tetrahedral sheets, as shown in Fig. 14.1 (4,5). Accordingly, 2:1 phyllosilicates form stacks of layers or platelets. Each platelet has a thickness of ~1 nm thick and a width of ~30 nm (laponite) to 500 nm (vermiculite). The gaps or spaces between these platelets are referred to as ''galleries.'' These stack layers are held together by a combination of electrostatic and van der Waals forces. The sheets layers are stacked along the *c*-axis either regularly with 0° rotation between the successive layers, semi random stacking with random degree of rotations, or turbostratic stacking with completely random rotations and translation between the layers. The structure generally lacks long-range, three-dimensional translational order. This implies that the structure is turbostratic, with little or no correlation between the stacked layers (7). For example, the MMT crystal structure is monoclinic with lattice parameters, $a = 0.52\,\text{nm}$, $b = 0.89\,\text{nm}$, $c = 0.95\text{–}1.00\,\text{nm}$ and $\beta = 95\text{–}100°$ (8). The (*hkl*)-type reflections are absent in the XRD pattern of MMT. Only (*hk*0) and (00*l*) reflections occur (9). The clays are characterized by negative surface charge defined by the cationic exchange capacity (CEC) in which three-valent Al^{3+} cations are replaced by divalent Mg^{2+} cations in the individual layers. This negative charge

Table 14.1 Chemical Formula and Cation Exchange Capacity of 2:1 Phyllosilicates.

Silicate	Formula	CEC, meq./100 g
Montmorillonite	$M_x(Al_{4-x}Mg_x)Si_8O_{20}(OH)_4$	92.6–120 (depending on mineral sources)
Hectorite	$M_x(Mg_{6-x}Li_x)Si_8O_{20}(OH)_4$	120
Saponite	$M_xMg_6(Si_{8-x}Al_x)Si_8O_{20}(OH)_4$	86.6
Vermiculite	$(Mg,Fe,Al)_3[(A1,Si)_4O_{10}](OH)_2M_x \cdot nH_2O$	150

M represents exchangeable cation and x is the layer charge.

is balanced by alkali cations (Na^+, Li^+, or Ca^2) resided at the galleries. Typical CEC values of 2:1 phyllosilicates are listed in Table 14.1. The 2:1 phyllosilicates are produced in several countries from the clay minerals having different impurity contents via purification and modification. The composition of clay minerals varies greatly depending on the ores from which the silicates have been obtained. Thus, it is rather difficult to achieve aluminosilicates with very high purity, controlled particle size distribution, and aspect ratio from the raw clay minerals. In this respect, synthetic clays with desired physical properties have been synthesized in the laboratories accordingly.

Layered silicates are hydrophilic and only compatible with hydrophilic polymers such as polyethylene oxide (PEO) and polyvinyl alcohol. To facilitate compatibility with other hydrophobic polymers, the silicate surfaces must be rendered organophilic by cation exchange of the alkali counterions with organic surfactants such as alkylammoniums or alkylphosphoniums. The resulting organically modified clays are commonly referred to as ''organoclays.'' Three main approaches have been used to disperse organoclays in the polymeric matrices of the nanocomposites. These include solution intercalation, *in situ* polymerization and melt intercalation (6–15). The solution intercalation involves the dispersion of the organoclay and the polymer in water or polar organic solvent. Water-soluble polymer such as PEO can be intercalated into the clay gallery spacing using this technique. The high polarity of water results in swelling of Na^+-MMT (8). *In situ* polymerization involves the incorporation of a monomer into the clay galleries of silicates such that the interlayer spaces are expanded during polymerization. The disadvantages of solution intercalation and *in situ* polymerization routes include suitable monomers and solvents are that they are not always commercially available and the cost of monomers or solvents is relatively high. In contrast, melt compounding is more attractive in terms of the cost effectiveness to prepare polymer–silicate nanocomposites. It is a widely used industrial process to fabricate various thermoplastics into desired products with high productivity using injection molders or extruders. In the case of nanocomposites, the high shear force encountered during melt compounding can assist in delamination or exfoliation of the clay platelets. The low loading levels of clays would

reduce the abrasive effects on the processing facilities. However, alkylammonium surfactant tends to decompose when exposed to high temperatures during melt compounding (16). An alternative is to use phosphonium salts with higher thermal stability.

In general, the structures of polymer–clay nanocomposites can be classified into two categories: (a) intercalated nanocomposites where polymer chains are intercalated into the galleries of organoclays, producing adequate expansion of the gallery spaces, and (b) exfoliated nanocomposites in which the insertion of polymer chains causes the galleries to swell to such an extent that the resulting individual clay platelets are no longer organized into stacks. Instead, the clay platelets are delaminated and dispersed as 1 nm thick layers in the polymeric matrices. It is generally known that the exfoliated structure yields better mechanical properties than intercalated ones. Formation of the intercalated and exfoliated polymer–clay nanocomposites depends greatly on the organic surfactant structure, especially the length of the carbon chain, type and polarity of polymeric matrix as well as appropriate processing conditions. Exfoliated nanocomposites can be readily achieved by blending the layered silicates with polar polyamides (PA) irrespective of the synthesis routes (9,10,17–24). Owing to the polar nature of PA6, clay exfoliation can be simply attained by melt compounding with suitable organoclays. However, exfoliated and homogenous dispersion of the silicate layers in nonpolar polyolefins is more difficult to achieve compared to PA. In this case, addition of suitable compatibilizers such as maleic anhydride (MA) (25–39) or hydroxylfunctionalized polyolefin (40) is needed to improve the compatibility between layered silicates and polyolefins. A compatibilizer grafted with polar functional group can be intercalated into the galleries of the clays via strong hydrogen bonding, leading to an increase in interlayer space. Consequently, the dispersion of silicate platelets in polyolefin matrices can be much improved by applying high shearing forces during melt compounding. In some studies, MA is used as a swelling agent for the clay silicates and as a compatibilizer for the polyolefin–clay nanocomposites (41–45).

In general, the level of tensile stiffness and strength enhancements of the polymer–clay nanocomposites relates to the degree of exfoliation of layered silicates which in turn depends on the surfactant used to prepare the organoclay and on the processing conditions. Paul and coworkers reported that the alkylammonium compound consisting of one alkyl tail is more effective than the quaternary cation having two alkyl tails in forming exfoliated polyamide nanocomposites (20). They attributed this to the competition between effects of the platelet–platelet interactions and the interaction of the polymer with the organoclay platelet. Because of its polarity or strong hydrogen-bonding characteristic PA6, has some affinity for the pristine clay surface. The organic modifier consisting of two alkyl tails shields more silicate surface than one alkyl tail, thereby precluding desirable interactions between the polyamide and the clay surface. On the contrary, nanocomposites made from linear low density polyethylene (LLDPE) showed complete opposite trends. In this case, the two-tailed organoclay formed nanocomposites exhibit better exfoliation and mechanical properties than a one-tailed organoclay (18).

In spite of the fact that the clay additions enhance the mechanical strength and stiffness of polymers, their tensile elongation and impact strength appear to decrease significantly. Consequently, polymer–silicate nanocomposites are vulnerable to brittle fracture damage. Little is known on the mechanism responsible for inferior tensile ductility of the polymer–clay nanocomposites. Recently, impact modifiers or elastomer particles have been incorporated into polymer–clay nanocomposites to improve their tensile ductility and impact toughness (42,46–53). In the case of (PA6,6-SEBS-g-MA)-organoMMT nanocomposites, Mai and coworkers found that the clay platelets are dispersed either in the PA6,6 matrix, SEBS elastomeric phase, or both the PA6,6 and SEBS phases depending on the blending sequence adopted during the melt-mixing process (49). They indicated that the best microstructure for toughness and other mechanical properties is to have the maximum percentage of exfoliated organoclay in the PA6,6 matrix rather than to have it in the dispersed SEBS-g-MA phase. This chapter provides an overview on the structure–mechanical property relationship and fracture behavior of the polyolefin–clay nanocomposites prepared by melt-compounding process.

14.2 STRUCTURE OF POLYOLEFIN/SILICATE NANOCOMPOSITES

For melt intercalation, thermal transport of polymer chains from the bulk melt into the silicate galleries and the mechanical shearing action play crucial roles in the dispersion of clay platelets. Thermal transport is favored by modifying the clay surfaces with appropriate organic surfactants, rendering the galleries more compatible with the polymer molecules (23). The thermodynamics of melt intercalation have been interpreted in terms of the interplay between enthalpic and entropic contributions to the free energy (54). The entropy loss due to the polymer confinement between the silicate layers must be compensated by the entropy gain associated with the increased conformational freedom of the surfactant tails as the gallery increases with polymer intercalation. Favorable enthalpy of mixing can be achieved readily for polar polymers due to the interactions between the polar group of polymers with the oxygen group on silicate clay layers (54,55). For polyolefins, there is no favorable excess enthalpy to promote the dispersion of silicate clay platelets because of the absence of any strong interactions. In this case, grafting of a polar functional group to polyolefins is needed to improve the compatibility between the polyolefins and the clay surfaces. In general, MA compatibilizer creates favorable polymer–clay interaction via hydrogen bonding between the oxygen group of the silicates and the OH or COOH groups of MA functional group (after hydrolysis). This leads to the formation of intercalated, exfoliated, or mixed intercalated/exfoliated polyolefin nanocomposites. The formation of either structure depends on several factors: (a) type and molecular structure of the surfactants employed, (b) type and content of compatibilizer used, and (c) processing conditions such as temperature, screw speed, and shear rate (36,56,57).

X-ray diffraction (XRD) is a versatile tool to characterize the crystalline structure of nanomaterials. The interlayer spacing of clay silicate, d_{001}, can be determined from the Bragg's law, that is, $d_{001} = \lambda/(2\sin\theta)$ where λ is the X-ray wavelength employed. For intercalated nanocomposites, the (001) characteristic peak of the clays tends to shift to lower angle region owing to the expansion of the basal spacing. This implies that the polymer chains are readily inserted into the clay galleries during compounding. Individual clay platelets are still organized into an ordered structure despite swelling of the galleries. In other words, the layers of the clay still retain their structural registry. In contrast, diffracting peaks are absent from the XRD pattern of exfoliated nanocomposites due to loss of the ordered structure of the clay layers. It is worth noting that the absence of Bragg diffraction peaks in the XRD patterns should not be used as the sole evidence for the formation of an exfoliated structure. Further transmission electron microscopic (TEM) observation is needed to confirm the formation of exfoliated nanocomposites (58). In addition, several factors such as clay dilution, peak broadening, and preferred orientation make XRD characterization of polymer nanocomposites susceptible to errors. Clay dilution and peak broadening can yield false result that exfoliation has occurred. Conversely, preferred orientation effects can result in the false conclusion that exfoliation has not occurred (59). TEM can provide useful information in a small localized area of the nanocomposites regarding their morphology, structure, and spatial distribution of the dispersed clay platelets. Thus, XRD and TEM techniques are considered to complement each other for structural characterization of the polymer–clay nanocomposites. In general, complete exfoliation of silicate platelets is scarce, and most nanocomposites display a combination of intercalated and exfoliated structure.

Paul and coworkers used TEM to perform quantitative analysis for the dispersion of clay pellets in polymer matrix (21). The dispersive particle length, number platelets per particle, and plate thickness can be determined semiautomatically from the image analysis using TEM micrographs. In the process, a typical TEM image is electronically scanned and converted into a grayscale tagged-image file format (TIFF) image file. This file is fed into the image analysis program that converts the TIFF image into a black and white image, creates a duplicate of the image, assigns each particle a numerical label, and exports the particle's length to a separate file (Fig. 14.2a). To count the number of platelets per particle, transparency film is placed over the TEM micrograph. The number of platelets per particle is counted and the resulting number is labeled on top of particle (Fig. 14.2b). Figure 14.3a and b shows the typical histograms of MMT particle length and number of platelets per particle for PA6–MMT nanocomposites. High resolution transmission electron microscopy (HRTEM) is generally known as a powerful tool to observe the morphology and structure of nanoparticles. This is due to its atomic resolution capabilities to observe spatially resolved chemistry at nanoscale. Vaia et al. obtained the lattice image from the MMT using the phase contrast method, that is, controlling the defocus effect of the objective lens of TEM to maximize the contrast. Figure 14.4 is a typical HREM image of an organoMMT sheet dispersed in an epoxy matrix. The HREM image matches closely with that of molecular model (60).

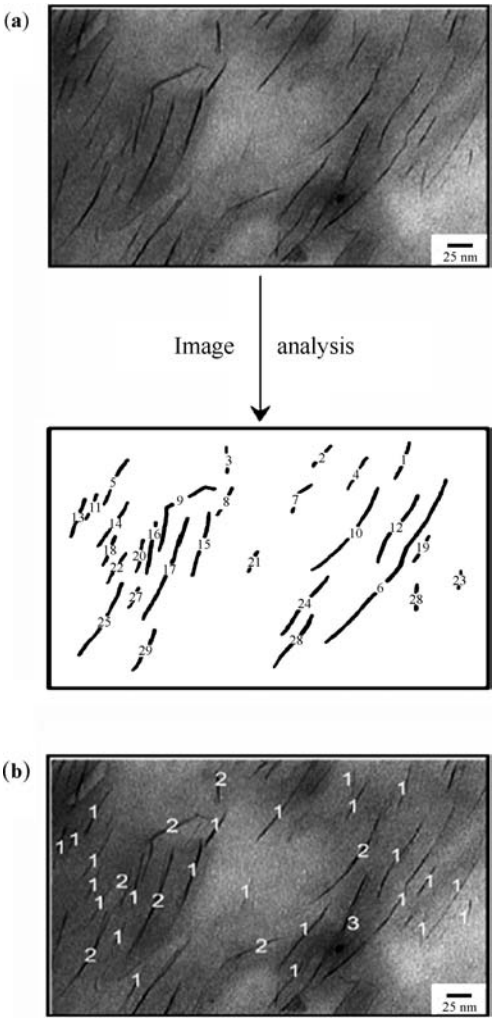

Figure 14.2 Semi automated analysis TEM images for determining (**a**) dispersed particle lengths and (**b**) the number of platelets per particle. (Reprinted from Reference 21 with permission of Elsevier.)

14.2.1 Polyethylene/Montmorillonite Nanocomposites

The molecular structure of the alkylammonium surfactants plays a crucial role in the structure and morphology of polyolefin–clay nanocomposites prepared via melt–intercalation. Therefore, the length and number of alklammonium groups would affect the intercalation of polyolefin chains into the galleries of silicates. Generally, phyllosilicates can be treated with quaternary or other ammonium salt of a primary, secondary, or tertiary linear organic amine in the presence of a dispersing medium

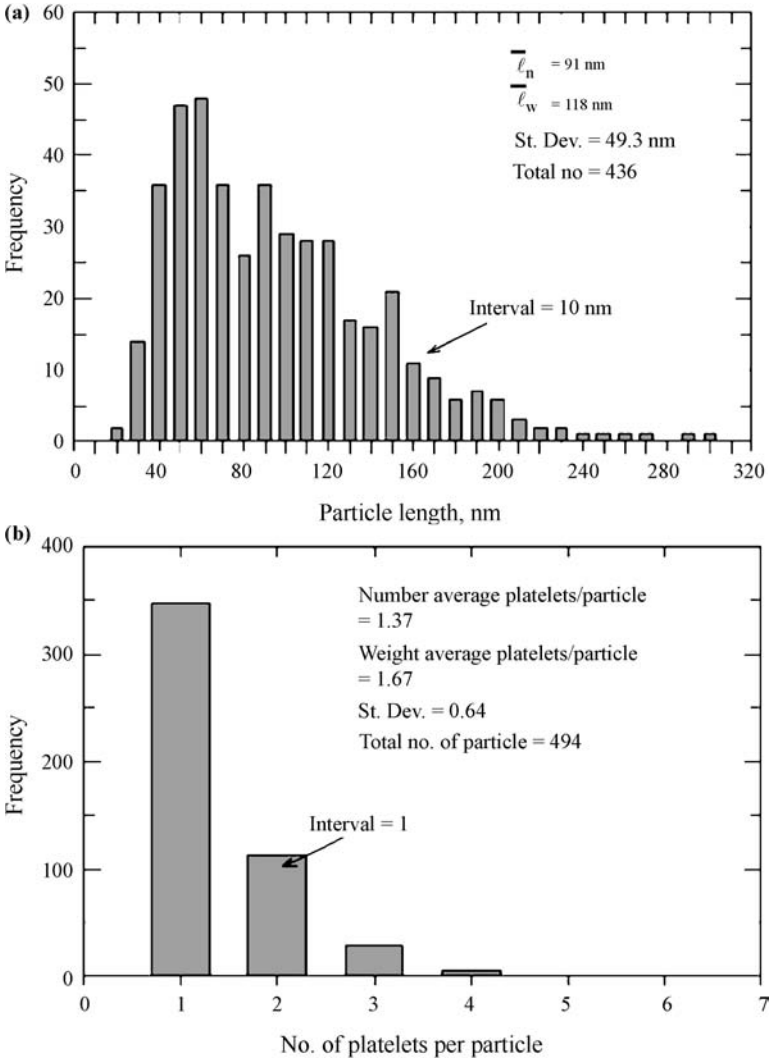

Figure 14.3 Histograms of MMT (**a**) particle length and (**b**) number of platelets per particle for PA6–MMT nanocomposites. (Reprinted from Reference 21 with permission of Elsevier.)

(61–64). Osman et al. (65) used XRD and other spectroscopic techniques such as IR, NMR to study the structure and chain dynamics of self-assembled monolayers of mono-, di-, tri-, and tetraalkylammonium cations of varying length (C, C_8, and C_{18}) on MMT platelets. On the basis of XRD results, the dependence of the (001) basal spacing of MMT on the number of alkyl chains of different length is depicted in Fig. 14.5. At a chain length of four carbon atoms (C4), there is nearly no change in the basal spacing of MMT. In the octyl series (C8–4C8), the *d*-spacing increases linearly with increase in the number of chains. In the octadecyl series (C18–4C18), the *d*-spacing increases markedly and nonlinearly.

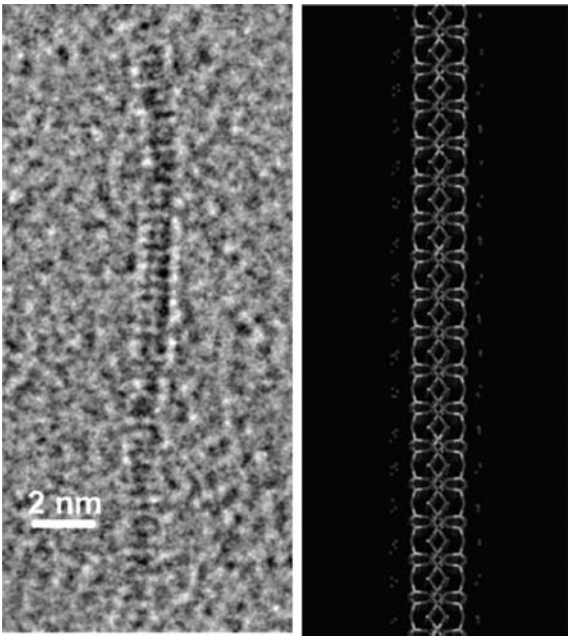

Figure 14.4 HREM image of an organoMMT sheet embedded in an epoxy matrix, compared with an [350] projection MMT molecular model. Atom color codes: Si, orange; Al, light purple; O, red; H, white; Mg, green; Na, dark purple. (Reprinted from Reference 60 with permission of The American Chemical Society.)

The length of the alkyl chains of organically modified silicates can be tailored via proper selection of the alkylammonium salts based on octadecylammine (C18), hexadecyamine (C16), or dodecylamine (C12) (36). The commercial MMT modified with alkylammonium amines are generally composed of two long alky chains and

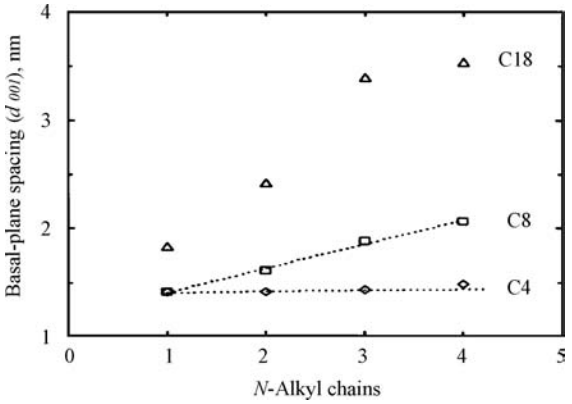

Figure 14.5 Dependence of the basal-plane spacing on the number of alkyl chains of different length, in the organic cation at room temperature. (Reprinted from Reference 65 with permission of The American Chemical Society.)

two short methyl groups. Typical examples are Cloisite 15A and 20A, produced from Southern Clay Products (USA) (66), and Dellite 72T, supplied by Laviosa Chimica Mineraria (Livorno, Italy). Other organoclays are commercially available from a variety of sources globally.

Cloisite 15A and 20A are apolar Na^+-MMT clays modified with quaternary ammonium compounds, that is, dimethyl, dihydrogenatedtallow, quaternary ammonium (2M2HT). HT stands for a tallow-based compound (~65% C18, ~30% C16, ~5% C14) in which a majority of the double bonds have been hydrogenated. These organoclays are available commercially at relatively low cost. The cation molecular structure of Cloisite 15A and 20A is given as follows:

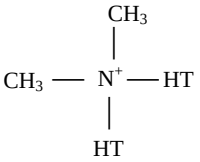

Cloisite 15A and 20A have different ion exchanged quantities, though they all use the same base clay with a CEC between 92 and 95 meq./100g. The modifier concentrations of Cloisite 15A and 20A are 125 and 95 meq./100g clay, respectively. The basal spacings (d_{001}) of the Cloisite 15A and 20A are 3.23 and 2.42 nm. In the case of polar organoclay, Cloisite 30B is available from Southern Clay Products with the organic modifier methyl tallow bis-2-hydroxyethyl ammonium (MT2EtOH) having the formula:

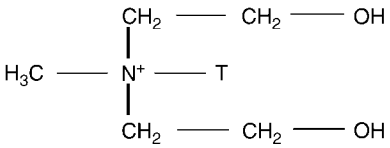

where T stands for tallow. The d_{001} spacing of Cloisite 30B is 1.85 nm (66).

Wang et al. studied the effects of the chain length of alkyl groups of cationic modifier molecules and MA content on the formation of exfoliated PE–MMT nanocomposites. Commercial Cloisite 20A and self-synthesized MMTs having different number of methylene groups in alkylamine chains were used as the reinforcing fillers (36). The authors reported that exfoliated PE/MMT nanocomposites can be formed when the number of methylene groups in alkylamine chains is more than 16 and MA grafting level to PE is higher than 0.1 wt%. Figure 14.6a–d shows the XRD patterns of MA compatibilized PE–MMT nanocomposites prepared from melt compounding of commercial MA modified PE (PEMA, 0.85 wt% MA grafted) with different types of organoclays. The XRD patterns of the Cloisite 20A, and other MMT clays modified with octadecylammonium (C18M), hexadecylammonium (C16M), and dodecylammonium (C12M) are also presented in these figures. The interlayer spacings of C12M, C16M, C18M, and Cloisite 20A are determined to be 1.36, 1.79, 1.85, and 2.47 nm, respectively. It is obvious that the interlayer spacing of

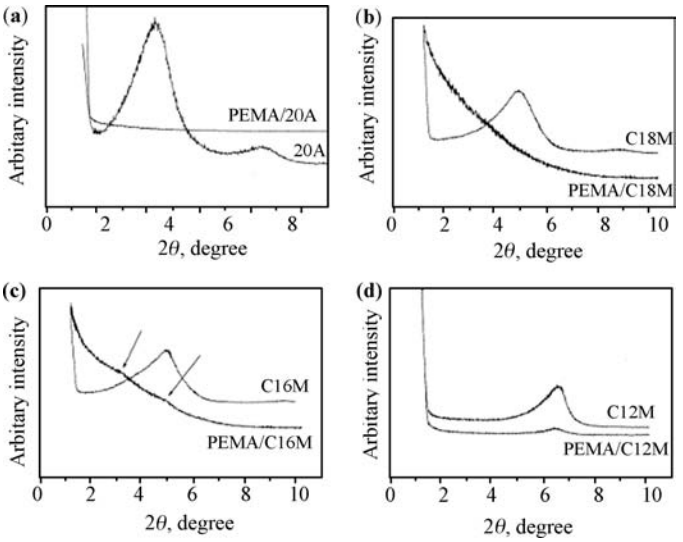

Figure 14.6 XRD patterns of MA compatibilized PE–5% MMT composites prepared from melt compounding of commercial MA-modified PE (PEMA, 0.85 wt% MA grafted) with various organoclays: (**a**) Closite 20A, (**b**) MMT modified with octadecylammonium (C18M), (**c**) MMT modified with hexadecylammonium (C16M), and (**d**) MMT modified with dodecylammonium (C12M). (Reprinted from Reference 36 with permission of Elsevier.)

organoclays increases with increase in the length of akylamine chains and the number of long alkyl chains. It is noted that the interlayer spacings for the C18M and Cloisite 20 determined by Wang et al. are in good agreement with those reported by Osman et al., as shown in Fig. 14.5. For the PEMA/MMT nanocomposites reinforced with Cloiste 20A or C18M, no basal (001) diffracting peak can be detected (Fig. 14.6a and b. The absence of basal diffracting peak of these clays implies the formation of an exfoliated structure associated with the disordered state of silicate platelets. TEM micrographs also provide a substantial evidence for the formation of exfoliated nanocomposites in which the silicate platelets are dispersed homogeneously in the PEMA matrix. In contrast, very faint (001) diffracting peak located at $\sim 3.2^{\circ}$ appears in the XRD pattern of PEMA/C16M nanocomposite. The shift of the (001) diffracting peak of C16M from $\sim 4.9^{\circ}$ to lower angle of $\sim 3.2^{\circ}$ for the PEMA/C16M nanocomposite indicates that PE molecular chains have intercalated in to the galleries of C16M. Compared to C12M clay, the basal peak position of the PEMA/C12M composite clay remains unchanged, indicating that maleated polyethylene cannot intercalate into the galleries of C12M. In another study, Zhai et al. also reported that exfoliated PE/MMT nanocomposites can be prepared via melt intercalation of maleated PE into the MMT modified with C18 alkyl trimethyl ammonium chloride (38). Recently, Hotta and Paul demonstrated that the linear low density polyethylene (LLDPE) clay nanocomposites derived from the organoclay having two alkyl tails, $M_2(HT)_2$, exhibited better dispersion and improvement of mechanical properties than nanocomposites based on the organoclay having an alkyl tail $M_3(HT)_1$ (18).

In addition to the length and number of alkyammonium chains, the extent of functionality or the quantity of compatibilizing agent grafted is also a key parameter in controlling final structure of the polyolefin nanocomposites. Chrissopoulou et al. investigated the effect of PE-g-MA content on the formation of intercalated, exfoliated, or mixed structures for PE–clay nanocomposites reinforced with 10 wt% organoclay Dellite 72T ($d = 3.04$ nm) (37). The PE-g-MA ranges from 2.5 wt%, where it acts as an additive, up to 100 wt%, where it becomes the polymer matrix. For the PE-g-MA content below 5 wt%, the XRD patterns reveal that the diffracting peaks of the composites at lower angles are similar to those of the organoclay (Fig. 11.7). At the PE-g-MA content above 8 wt%, the (001) peak tends to shift in the range $2\theta = 2.70$–$2.45°$, indicating formation of intercalated composites with an interlayer distance of 3.27–3.60 nm. At PE-g-MA content of 30 wt%, the (001) diffracting peak becomes a shoulder. Above 30 wt%, the (001) diffracting peak of organoclay disappears, implying the formation of an exfoliated structure. Chrissopoulou et al. concluded that it is the ratio of PE-g-MA and organoclay that determines the structure of nanocomposites on the basis of XRD and TEM examinations. For ratios of PE-g-MA and organoclay between 0 and 0.45:1, there is no

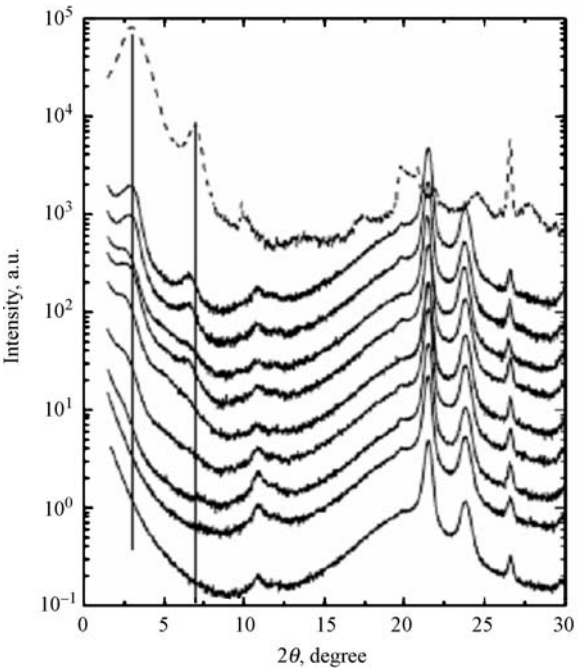

Figure 14.7 XRD patterns of PE-clay nanocomposites containing PE-g-MA and 10 wt% organoclay (Dellite 72T) with different relative compositions of PE to PE-g-MA. Dellite 72T is a ditallow-dimethyl-ammonium ion modified MMT supplied by Laviosa Chimica Mineraria (Livorno, Italy). The XRD pattern of organoclay is presented in dash line. The solid lines from top to bottom corresponds to PE/PE-g-MA = 97.5/2.5, 95/5, 92/8, 85/15, 82/18, 80/20, 70/30, 51/49, and 0/100. (Reprinted from Reference 37 with permission of Elsevier.)

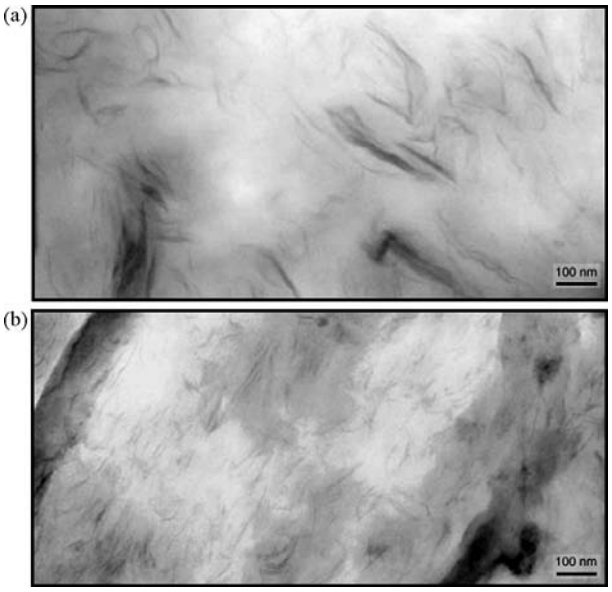

Figure 14.8 TEM images of PE–clay nanocomposites containing PE-g-MA and 10 wt% organoclay (Dellite 72T): (**a**) PE/PE-g-MA = 85/15 and (**b**) PE/PE-g-MA = 51/49. (Reprinted from Reference 37 with permission of Elsevier.)

change in the structure of organoclay. For ratios from 0.72:1 to 2.2: 1, mixed intercalated/exfoliated structure predominates. For ratios above 4.5:1, an exfoliated structure is formed. Figure 14.8a shows the typical TEM image of maleated PE–clay nanocomposite having the PE-g-MA to organoclay ratio of 1.35:1, indicating formation of an intercalated structure. For the PE-g-MA to organoclay ratio of 4.5:1, exfoliate nanocomposite is produced as evidenced by uniform dispersion of silicate platelets in the polymeric matrix (Fig. 14.8b).

Apart from the molecular structure of organoclays and compatibilizing agent content, it is recognized that the delamination and dispersion of silicate platelets in polymeric matrix depend on appropriate processing conditions. Exfoliated polymer–clay nanocomposites can be achieved more readily for polar polyamide matrix via melt compounding. Paul and coworkers demonstrated that the extruder and screw configuration affect the degree of delamination and dispersion of Cloisite 15A in PA6 matrix (23). These factors affect the residence time of polymers in extruders. Dispersion of silicate platelets is poor using a single-screw extruder in spite of the relatively long residence time. In contrast, non-intermeshing twin-screw extruder yields the best delamination and dispersion. Moreover, excellent delamination and dispersion can be achieved with both corotating and counterrotating, intermeshing types of extruders when a fully optimized screw configuration is used. Modesti et al. indicated that the shear stress exerted on maleated polyolefin-clay composites much more influence has on the extent of intercalation and delamination than on the residence time. Shear stress can be maximized by lowering the barrel profile

temperature and increasing the screw speed (57). More recently, Lertwimolnun and Vergnes reported that the proportion of exfoliation of Cloisite 20A platelets in maleated PP/C20A nanocomposite can be estimated by rheological measurements. It increases when the feed rate decreases and the screw speed increases (56).

14.2.2 Polypropylene/Montmorillonite Nanocomposites

Since the successful *in situ* polymerization of PA6–clay nanocomposites at the Toyota research center (Japan) in 1993 (9,10), PP–MMT nanocomposites have also been extensively studied by their researchers (25–28). The presence of a compatibilizer such as MA-grafted PP (PP-MA) oligomer is needed to achieve the desired structural and mechanical properties. PP–clay nanocomposites have been prepared by simple melt mixing of PP, PP-g-MA, and octadecylammonium-exchanged MMT (C_{18}-MMT). Kawasimi et al. reported that the achievement of exfoliated and homogeneous dispersion of the silicate layers in PP matrix depends on two factors: (a) the intercalation capability of the oligomers in the layers and (b) the miscibility of the oligomers with PP (25).

Recently, Chiu et al. studied the combined effects of clay modifications and compatibilizers on the structures of PP–clay nanocomposites. The organoclays employed were apolar Cloisite 20A and polar Closite 30B organoclays. The compatibilizers used were MA-g-PP containing 0.24 mol% MA and styrene-co-maleic anhydride (SMA) containing 50 mol% MA. The clay content was fixed at 5 wt% and the compatibilizers were loaded at 5 and 10 wt% (67). Figure 14.9a shows the XRD patterns of the Cloisite 20A, PP/C20A, and PP/C20A/PP-g-MA nanocomposites with different MA contents melt compounded at 190°C. The characteristic (001) diffracting peak of the Cloisite 20A clay appears at ~3.7°, corresponding to a *d*-spacing of 2.38 nm. Blending the Cloisite 20A with PP does not produce a shift of the (001) peak position to lower angles. The characteristic peak is located at ~3.6°, corresponding to a *d*-spacing of 2.44 nm. In contrast, the (001) peak disappears by adding 5 or 10 wt% PP-g-MA into the PP/Cloisite 20A composite. This implies that the PP-g-MA compatibilizer facilitates the insertion of PP molecular chains into the galleries of Cloisite 20A, leading to the formation of an exfoliated structure. It can also be seen that the (001) diffracting peak of the PP/C20A/SMA nanocomposite shifts to ~2.8° (*d*-spacing of 3.08 nm), indicating formation of an intercalated structure. It is obvious that the addition of SMA to PP/C20A composite yields poorer compatibilizing effect compared to the addition of PP-g-MA due to a higher degree of polarity of SMA. The SMA contains much higher MA content (50 mol%) compared to PP-g-MA (0.24 mol%). Thus, the nonpolar PP molecules exhibit lower compatibility with SMA. However, the addition of 5 wt% SMA to PP/C30B sample leads to the absence of (001) diffracting peak as shown in Fig. 14.9b. This result clearly indicates that the higher degree of polarity of SMA produces an effective compatibilizing effect to PP in forming an exfoliated nanocomposite. It is apparent from Fig. 14.9b that the (001) peak position of the PP/C30B, PP/C30B/PP-g-MA(5%) and PP/C30B/PP-g-MA(10%) shifts to higher angle regimes instead of lower angle regions. This means

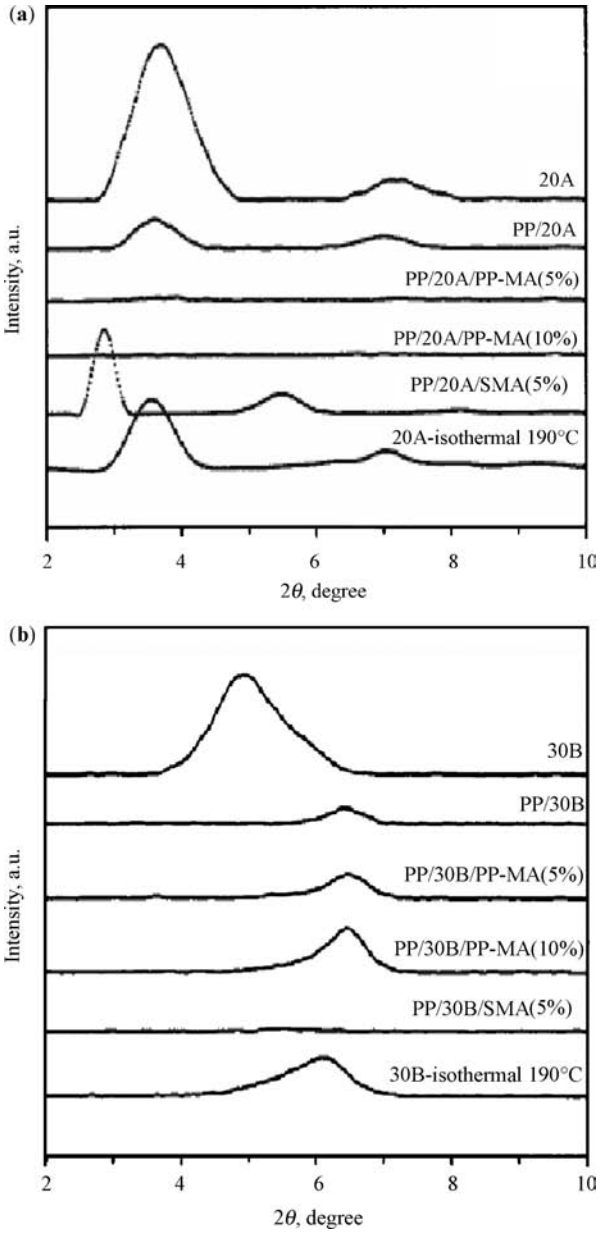

Figure 14.9 XRD patterns of (**a**) Cloisite 20A and its nanocomposites and (**b**) Cloisite 30B and its nanocomposites prepared by melt compounding at 190°C. (Reprinted from Reference 67 with permission of John Wiley & Sons.)

that the interlayer spacing of Cloisite 30B is reduced by compounding with PP or maleated PP. It appears that PP-g-MA fails to play an adequate compatibilizer role for higher polar Cloisite 30B. A reduction of the clay interlayer spacing is commonly attributed to the partial decomposition of the organic modifier during melt compounding. To substantiate this, the Cloisite 30B was isothermally treated at 190°C. The characteristic peak of isothermally treated Cloisite 30B shifts to higher angle (6.2°) as expected. Generally, TEM examination results for the nanocomposites investigated are in good agreement with the results of the XRD patterns (67).

14.2.3 Polyolefin/Vermiculite Nanocomposites

Vermiculite (VMT) is a hydrated magnesium iron aluminum silicate having a composition of $(Mg,Fe,Al)_3[(A1,Si)_4O_{10}](OH)_2M_x{\cdot}nH_2O$, a high value of aspect ratio, and a crystalline structure similar to MMT. However, the electrostatic charge of the VMT layer is larger than that of MMT due to a higher substitution of Si atoms with Al and Mg atoms (Table 14.1). VMT is abundant and available globally at a relatively lower cost compared to MMT. It is widely used as a material for packaging, attic insulation, texturizer in paint, fire protection construction, among others. In this regards, VMT is an ideal filler to reinforce polymers with the desired physical and mechanical properties. Less information is available in literature relating to the synthesis and physical and mechanical behavior of the polymer–VMT nanocomposites compared to that of the polymer–MMT nanocomposites. Tjong et al. introduced MA functional group into VMT galleries to form MA-intercalated VMT (MAV) (41). In the process, VMT was initially pretreated with hydrochloric acid solution followed by drying at 160°C overnight. The acid-treated VMT is further reacted with MA in the presence of acetic acid to form an organoclay. It is generally known in clay science that hydrochloric or sulfuric acid treatment of clay in appropriate concentrations causes the extraction of lattice metal cations from clay layers. The acid activates the clay by transforming it to the high acidity H^+ form. MAV is then meltblended with the polyolefins to form the nanocomposites. In this case, MA functional group acts as a modifying additive for the polyolefin matrix and as a swelling agent for the vermiculite silicate. Consequently, homogeneous dispersion of the VMT platelets in polyolefin matrices can be realized (41–44). Figure 14.10a and b shows the X-ray diffraction patterns MAV at small-angle and wide-angle regimes. These traces show the absence of vermiculite characteristic peaks, indicating the formation of an exfoliated structure. This implies that MA can easily enter the galleries of acid-treated vermiculite because solvent (acetic acid) can act as a carrier to transport MA into hydrophilic vermiculite. MA has a flat molecular structure in which the greatest length is about 5.126 Å, as depicted in Fig. 14.11. This also reveals that the incorporation of excess MA into acid-treated vermiculite extends its gallery spacing. Accordingly, polyolefin–vermiculite nanocomposites with an intercalated or exfoliated structure can be achieved by direct melt mixing of MAV with the polyolefins.

Figure 14.12 shows the XRD patterns of PP–MAV nanocomposites prepared by direct melt mixing of MAV with PP. Apparently, the diffraction traces show no XRD peaks, indicating formation of an exfoliated structure. However, TEM micrograph

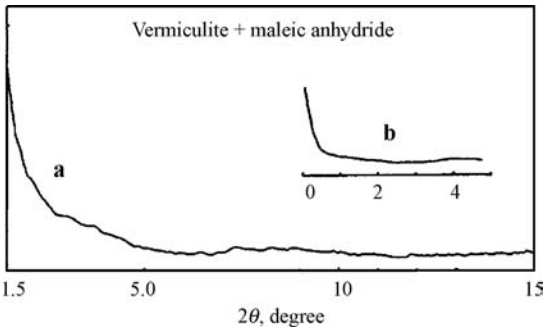

Figure 14.10 XRD patterns of MA-delaminated VMT recorded by (**a**) wide-angle ranging from 1.5° to 15° and (**b**) small-angle ranging from 0° to 5°. (Reprinted from Reference 41 with permission of The American Chemical Society.)

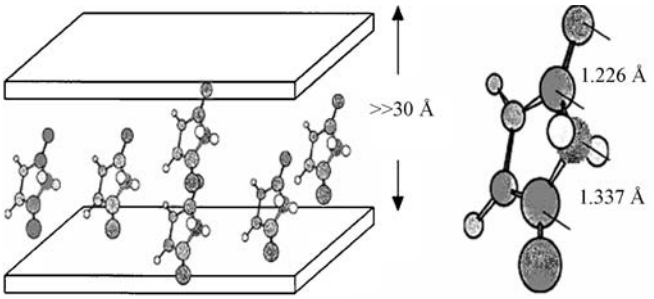

Figure 14.11 Structures for energy-minimized maleic anhydride and MAV. (Reprinted from Reference 41 with permission of The American Chemical Society.)

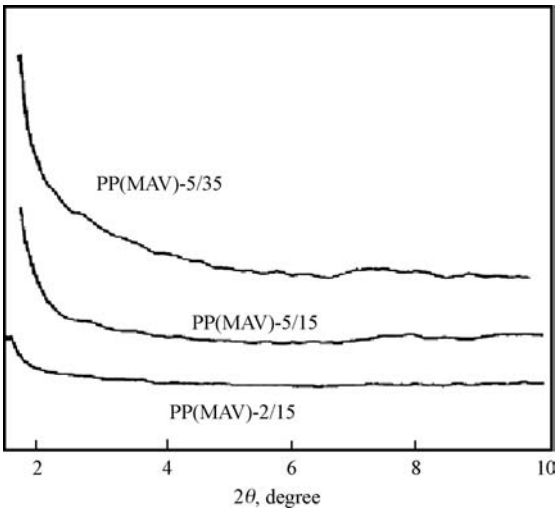

Figure 14.12 XRD patterns for PP nanocomposites reinforced with 2% and 5% maleic anhydride-modified vermiculite (MAV) prepared under melt compounding at a screw speed of 15 or 35 rpm. (Reprinted from Reference 41 with permission of The American Chemical Society).

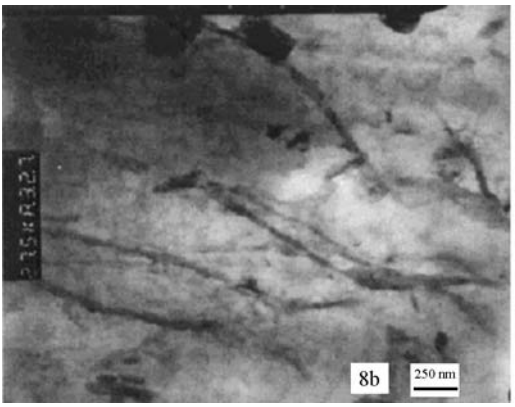

Figure 14.13 TEM micrograph showing formation of a mixed intercalated/exfoliated structure for PP nanocomposite reinforced with 5% maleic anhydride-modified vermiculite (MAV). (Reprinted from Reference 41 with permission of The American Chemical Society.)

shows the formation of a mixed intercalated/exfoliated structure as evidenced by the presence of some stacked silicate platelets and exfoliated layers (Fig. 14.13). It is obvious that X-ray result alone does not accurately predict the dispersion of silicate platelets in polymeric matrix. TEM micrographs can provide useful information relating to the morphology and dispersion of individual platelets in the exfoliated and intercalated states. It appears that nonpolar PP molecular chains can be easily intercalated into the VMT galleries, thereby promoting homogeneous dispersion of VMT platelets in the PP matrix. A schematic diagram showing the intercalation of the PP molecular chain into MAV gallery is depicted in Fig. 14.14.

For the PE/VMT nanocomposites, there are no characteristic X-ray peaks observed from 1.5° to 10°, demonstrating that the VMT platelets are exfoliated (Fig. 14.15). TEM images provide a substantial evidence of the formation of an exfoliated structure (Fig. 14.16a and b). The formation of an exfoliated structure indicates favorable interactions between the PE chains and the layered vermiculite.

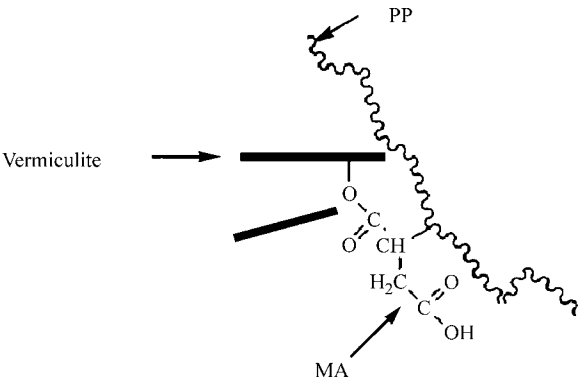

Figure 14.14 Schematic diagram showing intercalation of PP molecular chain into MAV. (Reprinted from Reference 41 with permission of The American Chemical Society.)

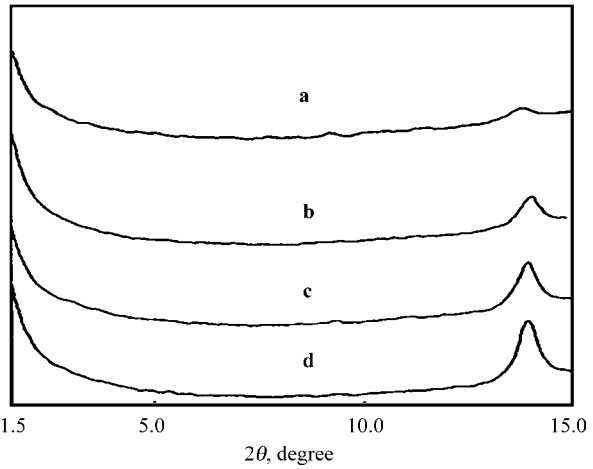

Figure 14.15 XRD patterns of (**a**) PE–2% VMT, (**b**) PE–4% VMT, (**c**) PE–6% VMT, and (**d**) PE–8% VMT nanocomposites. (Reprinted from Reference 43 with permission of John Wiley & Sons.)

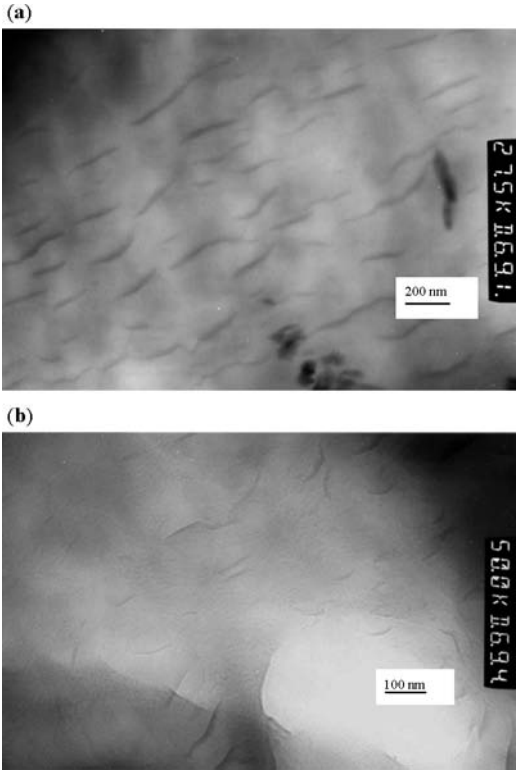

Figure 14.16 TEM micrographs of PE–4%VMT nanocomposite showing (**a**) formation of an exfoliated structure and (**b**) enlarged image of dispersed individual vermiculite platelets. (Reprinted from Reference 43 with permission of John Wiley & Sons.)

As mentioned above, the outcome of polymer–clay melt intercalation is determined by the interplay of entropic and enthalpic factors. The confinement of the polymer inside the interlayers results in a decrease in the overall entropy. This must be compensated by the increased conformational freedom of the tethered surfactant chains as the layer increases. The enthalpy of mixing can be rendered favorable by maximizing the polymer–clay interaction (54,55). However, there exists no favorable enthalpy of mixing for polyolefins and silicate clays due to the absence of interactions between them. The incorporation of MA into VMT surfaces is considered to facilitate favorable interaction between polyolefin molecular chains and VMT. As a result, the insertion of the polyolefin chains into the VMT galleries becomes more thermodynamically favorable.

14.2.4 Effect of Elastomer Additions

It is well recognized that the addition of phyllosilicates into polymers results in significant decreases in tensile ductility and impact toughness. The reason for this is still poorly understood. The effective way to restore the tensile ductility and impact toughness is to add elastomers or impact modifiers into the polymer–clay nanocomposites (42,46–53). Therefore, understanding the effect of the elastomer addition on the microstructure of the resulting polymer–clay nanocomposites under various processing conditions is of considerable importance. Mai and coworkers reported that the blending sequence adopted in the melt-mixing process would affect the dispersion of the clay platelets of PA6,6 nanocomposites toughened with elastomer. On the basis of TEM observation, the clay platelets are found to disperse either in the PA6,6 matrix, SEBS elastomeric phase, or both the PA6,6 and SEBS phases depending on the blending sequence. The best microstructure for toughness and other mechanical properties is to have the maximum percentage of exfoliated organoclay in the PA6,6 matrix rather than to have it in the dispersed SEBS-g-MA phase (49). Lee and Goettler also studied the effect of blending sequence for melt compounding on the mechanical performances of PP nanocomposites toughened with 30–70 wt% ethylene propylene diene terpolymer (EPDM) rubber (68). They reported that the tensile modulus of such nanocomposites shows higher values in the case of selective dispersion of clay platelets in a continuous PP matrix. Mehta et al. studied the microstructure and mechanical properties of thermoplastic olefin (TPO)/clay nanocomposites with clay loadings of 0.6–6.7 wt% clay (69). The commercial TPO employed consisted of about 70 wt% isotactic PP and 30 wt% ethylene–propylene rubber (EPR). TEM examinations revealed that the organoclay (Cloisite 20A) tends to disperse within the PP matrix and at the PP–EPR interfaces as stacks about 10–50 nm thick; each stack having ~5–25 clay platelets. Moreover, the EPR particles were broken into smaller size domains as the clay loading increased from 0.6 to 5.6 wt% (Fig. 14.17). A reduction in the size of EPR domains with increasing clay loadings can be seen more readily in the atomic force microscopic images as shown in Fig. 14.18a–e.

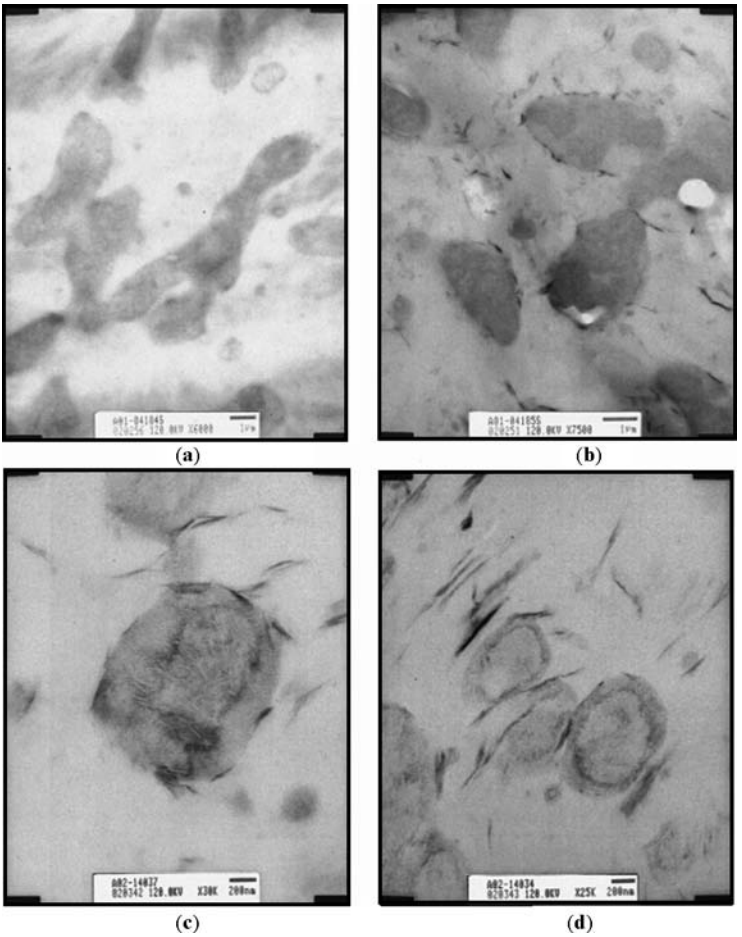

Figure 14.17 TEM micrographs of TPO nanocomposites containing (**a**) 0 wt%, (**b**) 0.6 wt%, (**c**) 2.3 wt%, and (**d**) 5.6 wt% clay. (Reprinted from Reference 69 with permission of John Wiley & Sons.)

In the last few decades, elastomer-toughened PP or TPO materials as well as their microcomposites reinforced with talc fillers have become technologically interesting for use as automotive exterior and interior components. The types of elastomer employed include EPR, EPDM, and polyethylene octane (POE). The elastomer content in TPO can range from 30 to 70 wt%. To achieve the desired mechanical properties, talc filler loadings >20 wt% are incorporated into the TPO matrix. Large filler contents can lead to poor processability and wear of the processing facilities. Compared with conventional olefin compounds, TPO-based nanocomposites show several distinct advantages such as reduce weight, enhanced dimensional stability, improved surface appearance, good scratch resistance,

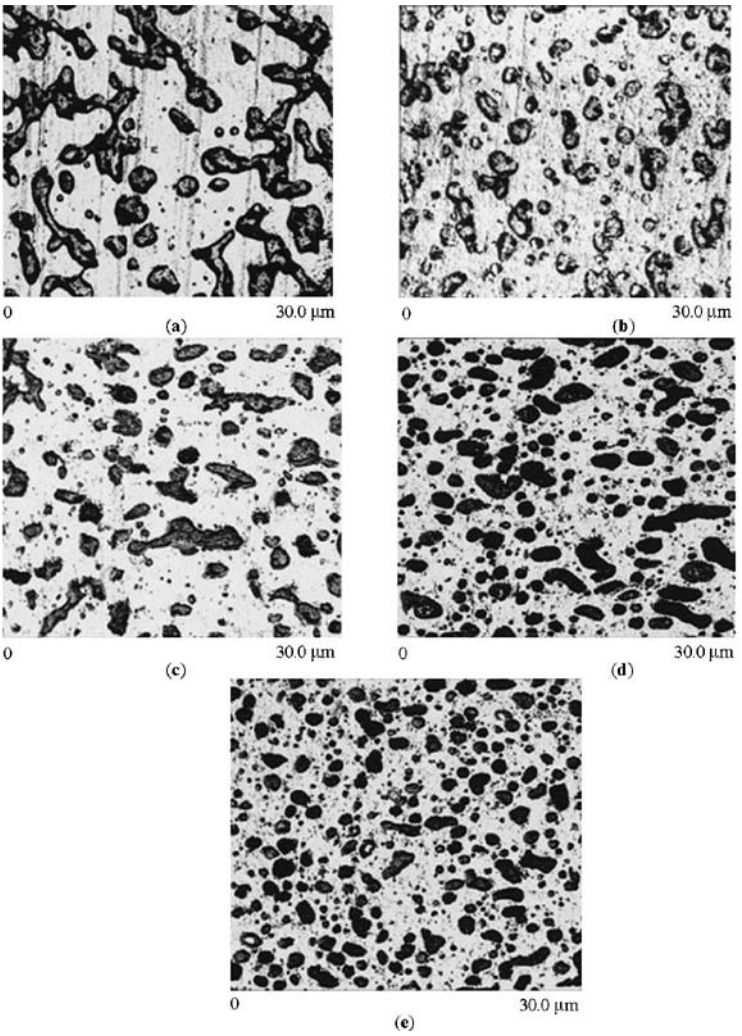

Figure 14.18 AFM images of TPO nanocomposites containing (**a**) 0 wt%, (**b**) 0.6 wt%, (**c**) 2.3 wt%, (**d**) 3.3 wt%, and (**e**) 5.6 wt% clay. (Reprinted from Reference 69 with permission of John Wiley & Sons.)

improved mechanical performance, and so on (51, 68–73). Consequently, General Motors, Basell, and Southern Clay Products have teamed up to produce a nanocomposite TPO-based step-assist for 2002 GMC Safari and Chevrolet Astro vans (74,75).

More recently, Tjong and coworkers reported that the organically modified MMT (Org-MMT) promotes the formation of β-form crystalline structure in PP in the presence of maleated SEBS elastomer (46). The monoclinic α-form PP is the most stable crystalline structure in isotactic PP. The β-form is observed occasionally during crystallization and appears as a minor constituent of PP. The formation of β-form PP depends on the crystallization conditions or the addition of specific

nucleating agents or additives such as quinacridone dye, triphenodithiazine, pimelic acid, or calcium carbonate (76,77). The MMT clays are generally known can induce structural change in polar polyamides (e.g., promote γ-form PA6 formation) (46, 78–80) but not in nonpolar polypropylene. Tjong and coworkers found that the Org-MMT can induce β-form in the PP–Org-MMT nanocomposites only in the presence of SEBS elastomer. For polyamides, the silicate platelets tend to disturb perfect arrangement of hydrogen-bonded sheets of the α-phase, thereby promoting formation of the γ-crystalline structure (46,78, 79).

Figure 14.19 shows the XRD patterns of pure PP and PP–organoMMT nanocomposites toughened with different contents of maleated SEBS elastomer. The XRD patterns of PP–SEBS-g-MA blends (traces (b) and (e)) are also shown for comparison purposes. Five strong characteristic peaks of α-form PP located at 2θ=14.1°, 16.9°, 18.5°, 21.3°, and 21.8°, respectively, can be observed in pure PP and PP–SEBS-g-MA/Org-MMT nanocomposites. However, another distinct diffraction peak at $2\theta = 16.0°$, ascribed to the (300) crystal plane of β-form PP, is also observed in the XRD pattern of PP/SEBS-g-MA/4%Org-MMT hybrid. This demonstrates that the incorporation of high Org-MMT content induces the formation of β-form crystal structure in PP matrix.

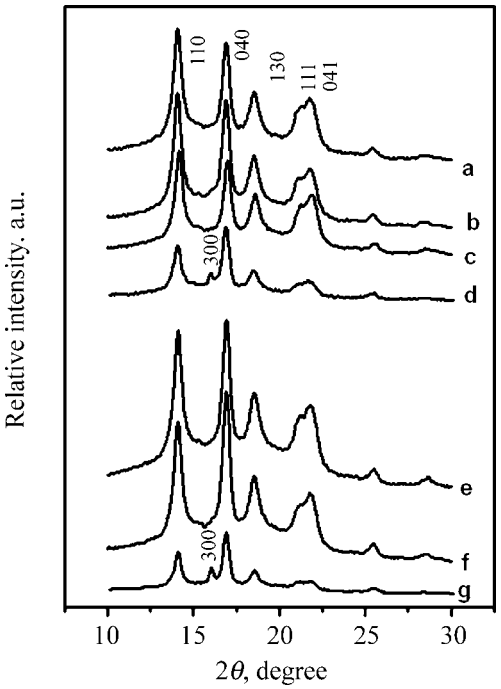

Figure 14.19 XRD patterns of PP, PP/SEBS-g-MA blends, and PP-MMT nanocomposites: (**a**) PP, (**b**) PP–5% SEBS-g-MA, (**c**) PP–5% SEBS-g-MA–2% Org-MMT, (**d**) PP–5% SEBS-g-MA–4% Org-MMT, (**e**) PP–15% SEBS-g-MA, (**f**) PP–15% SEBS-g-MA–2% Org-MMT, and (**g**) PP–15% SEBS-g-MA–4% Org-MMT. (Reprinted from Reference 46 with permission of John Wiley & Sons.)

The polymorphic structures of PP and its elastomer-toughened nanocomposites can be analyzed from the XRD traces in terms of K value. The relative amount of β-form (K value) can be determined from the following equation (77,80):

$$K = I_\beta/(I_{110} + I_{040} + I_{130} + I_\beta) \tag{14.1}$$

where I_β is integrated area of the (300) diffracting of β-form PP peak and I_{110}, I_{040}, and I_{130} are the integrated areas of (110), (040), and (130) peaks of the α-form PP, respectively. The amorphous peak of PP is generally located at $2\theta = 16.30°$. Assuming the diffracting peak shape fits the Gaussian–Lorentz function, then profile fitting method can be used to deconvolute the experimental peak into both the crystalline and amorphous phases. Figure 14.20 shows typical profile

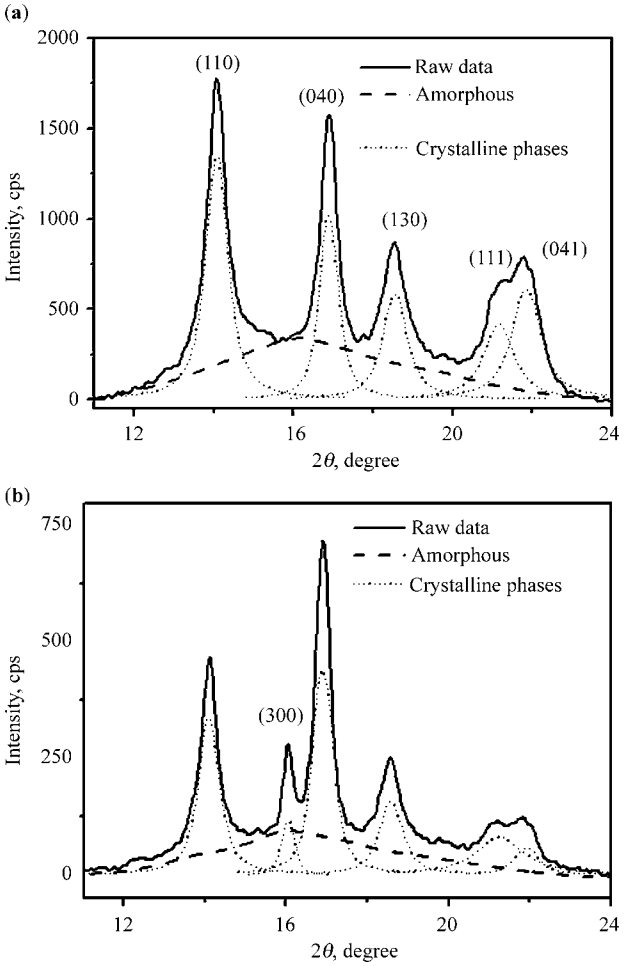

Figure 14.20 Representative XRD patterns of (**a**) PP and (**b**) PP–15% SEBS-g-MA–4% Org-MMT nanocomposite. The profile fitting technique is used to deconvolute the diffracting peaks into crystalline and amorphous phases of PP. (Reprinted from Reference 46 with permission of John Wiley & Sons.)

Table 14.2 Relative Amount of β-Form PP (*K* value) in PP/4%Org-MMT Nanocomposites Containing Different SEBS-g-MA Contents [Reprinted from Reference 46 with permission of John Wiley & Sons.]

SEBS-g-MA (%)	5	10	15	20
K value, %	2.33	3.33	5.23	6

fitting for the diffraction peaks of pure PP and PP/15%SEBS-g-MA/4%Org-MMT nanocomposite. The calculated *K* values for PP/*x*%SEBS-g-MA/4%Org-MMT are listed in Table 14.2. This table reveals that the *K* values of the nanocomposites tend to increase with increasing SEBS-g-MA content, indicating that the elastomer phase favors the formation of β-form PP in the PP/*x*%SEBS-g-MA/4%Org-MMT nanocomposite. It is worth noting that β-form crystal structure is absent in the PP/SEBS-g-MA blends. It is believed that a synergistic effect between Org-MMT and SEBS-g-MA induces the formation of β-form PP crystal structure in the nanocomposites. The molecular chains of maleated SEBS elastomer and PP can intercalate into Org-MMT galleries as evidenced by a shift in the XRD basal reflection (001) peak located at $2\theta = 4.68^\circ$ to lower angles of $2\theta = \sim 2.2^\circ$. This corresponds to an increase in the interlayer spacing from 1.88 to ~3.90 nm (47).

14.3 MECHANICAL PROPERTIES

The introduction of an organoclay into polymers generally leads to enhancements in both their tensile stiffness and strength. Such increases are always higher for the polymers using conventional fillers. However, the tensile ductility and impact toughness of polymers tend to decrease considerably with increasing clay content. Thus, brittle failure mode would occur in polymer–silicate nanocomposites containing higher clay loadings. Restriction on polymer chain rearrangement and mobility exerted by the silicate platelets is considered to partially contribute not only to the enhancement of tensile strength and stiffness but also to the deterioration of tensile ductility and impact strength. Furthermore, crazing cannot be initiated readily in the polymeric matrix of the polymer–clay nanocomposites.

The presence of a notch in mechanical test specimens is well recognized to produce a triaxial state of stress and steep stress gradient known as notch sensitivity. As a result of the triaxial stress produced by the notch, a plastic zone is developed next to the crack tip. For conventional short-fiber reinforced polymer composites, fiber bridging, fiber fracture, debonding, and pullout, as well as matrix deformation in the form of crazing and shear yielding, take place in the plastic zone at a crack tip (81). In the case of polymer–clay nanocomposites, the silicate nanolayers are much smaller than the size of the plastic zone at the crack tip, hence the influence of particles on the crack-tip process such as crack deflection, trapping, and bridging are negligible. Consequently, the ability of polymeric matrix to craze is reduced as the silicate content increases (82). However, Yee and coworkers indicated that

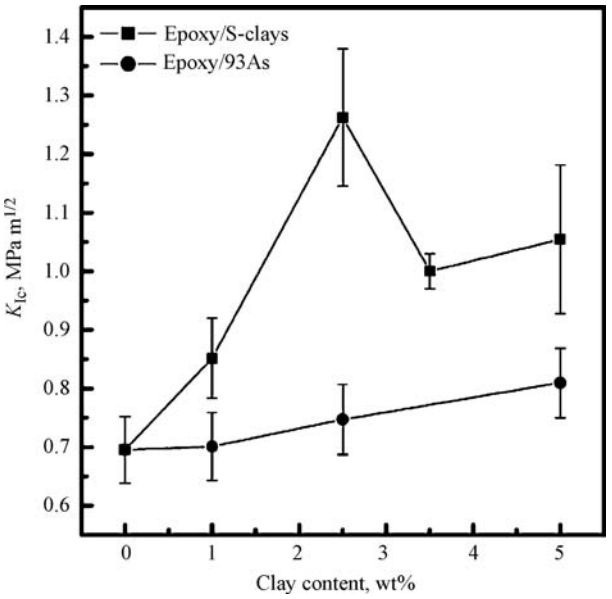

Figure 14.21 Fracture toughness versus clay content for highly exfoliated (■) and poorly intercalated (•) clay–epoxy nanocomposites. (Reprinted from Reference 83 with permission of The American Chemical Society.)

the individual exfoliated clay platelets of the clay–epoxy nanocomposites are very effective to prevent crack propagation (83). The clay–epoxy nanocomposites with highly exfoliated clay were prepared using a so-called slurry-compounding process. TEM observations reveal that most of the microcracks are initiated between clay layers and their propagation is deflected by the clay platelets. Formation of massive microcracks and the increase in fracture surface area due to crack deflection result in toughening of the clay–epoxy nanocomposites. On the contrary, conventionally prepared clay–epoxy nanocomposites exhibit lower fracture toughness due to the poor dispersion of clay platelets in epoxy matrix. Figure 14.21 shows the variation of fracture toughness with clay (MMT) content for the clay–epoxy nanocomposites prepared by different methods. Apparently, the fracture toughness of highly exfoliated clay–epoxy nanocomposites is much higher than that of pure epoxy, particularly for the specimen containing 2.5 wt% clay.

From the above discussion, it is evident that the extent of tensile strength improvement of nanocomposites depends greatly on the degree of dispersion of silicates in polymeric matrix in the form of intercalated or exfoliated platelets. The degree of exfoliation of the organoclay is greatly influenced by the blending conditions and the structure of organoclay. Varlot et al. demonstrated that exfoliated PA6–MMT nanocomposites exhibit larger tensile failure stress but lower tensile failure strain compared to the intercalated samples having a similar MMT content (84). Therefore, optimized processing conditions and proper selection of suitable organic modifiers and compatibilizers to promote good polymer–clay interaction are critical to achieve such improvements in the mechanical properties.

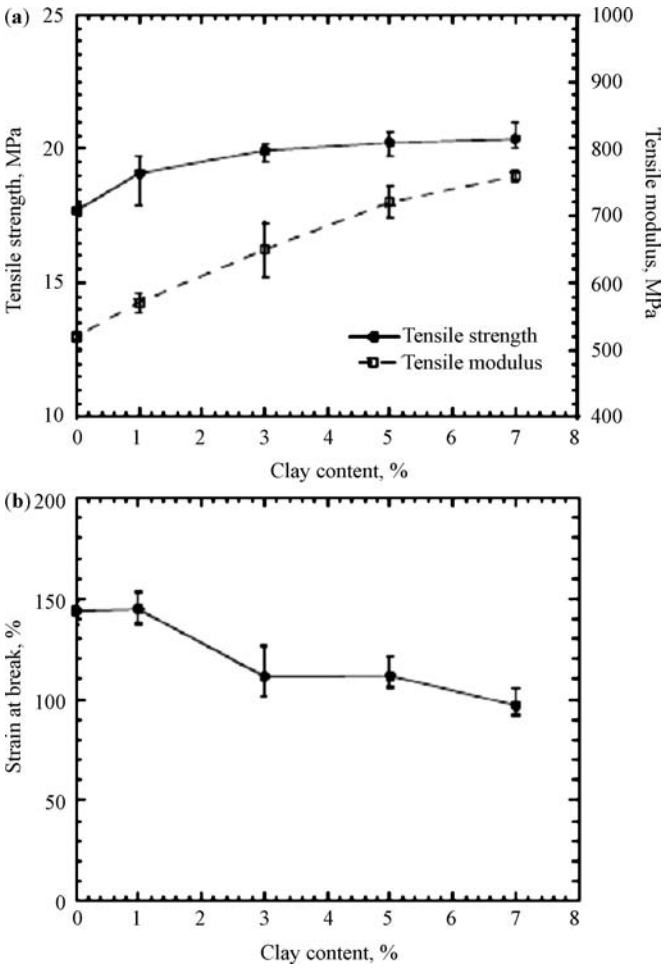

Figure 14.22 Tensile properties of maleated PE–clay nanocomposites: (**a**) modulus and strength, and (**b**) strain at break versus clay content. (Reprinted from Reference 33 with permission of Elsevier.)

Figure 14.22a and b shows the effects of clay loading levels on the tensile strength, modulus, and ductility of the maleated PE/clay nanocomposites having an intercalated structure. The tensile strength and modulus increase significantly with increasing clay content at the expense of strain at break (33). Similar findings are well documented in literature (85). The structure of organic clays also has a dramatic influence on the tensile strength and stiffness of nanocomposites. Figure 14.23 shows the effect of clay content and the number of alkyl tails on the ammonium cation of the organoclay on the tensile properties of LLDPE–clay nanocomposites with and without LLDPE-g-MA compatibilizer (18). The organoclay (Cloisite 20A) having two alkyl tails, $M_2(HT)_2$, exhibits better dispersion and improvement of mechanical properties than nanocomposites based on the organoclay having an alkyl tail $M_3(HT)_1$. Moreover, the LLDPE-g-MA compatibilizer also plays a crucial role in

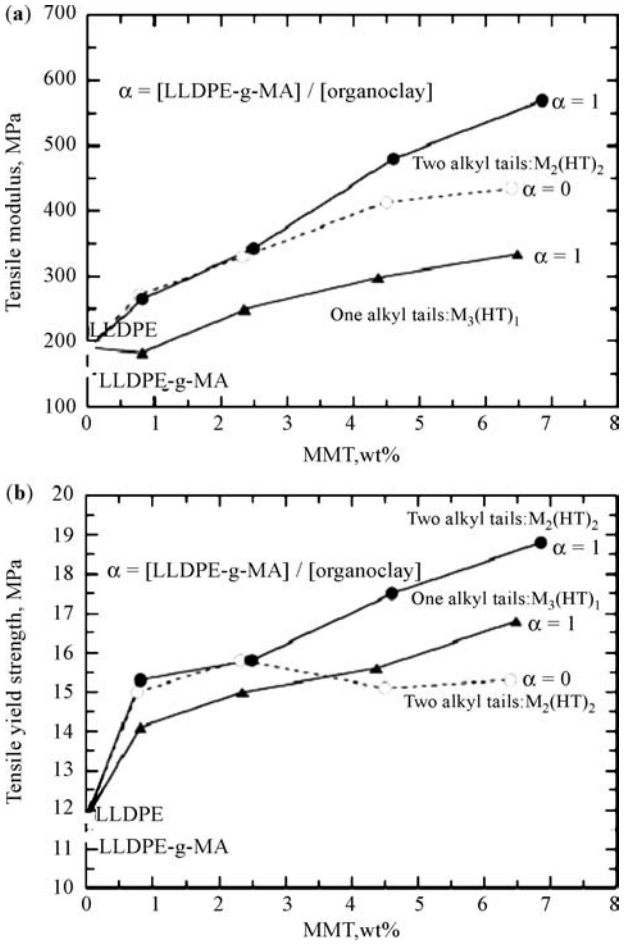

Figure 14.23 Effect of MMT content and the number of alkyl tails on the ammonium cation of the organoclay on (**a**) the modulus and (**b**) the yield strength of LLDPE nanocomposites with and without LLDPE-g-MA. (Reprinted from Reference 18 with permission of Elsevier.)

the dispersion of Cloisite 20A in polymeric matrix. TEM examination reveals that the LLDPE–C20A nanocomposite without LLDPE-g-MA compatibilizer ($\alpha = 0$) contains predominantly unexfoliated clay tatctoids. The nanocomposite containing equal mass of LLDPE-g-MA and organoclay ($\alpha = 1$) is comprised of individually dispersed platelets and unexfoliated clay particles (18).

In the case of PP–clay nanocomposites, Mulhaupt and coworkers (86) investigated the effect of alkyl chain length of alkyl amines, for example, butyl (C_4), hexyl (C_6), octyl (C_8), dodecyl (C_{12}), hexadecyl (C_{16}), and octadecyl (C_{18}), and type of compatibilizers on the tensile properties of nanocomposites. The clay employed was synthetic sodium fluoromica silicate with loading levels of 5 and 10 wt%. In the presence of PP-g-MA compatibilizer having 4.2 wt% MA, the alkyl chain length must exceed eight carbon atoms in order to form nanocomposites. Only 10 wt%

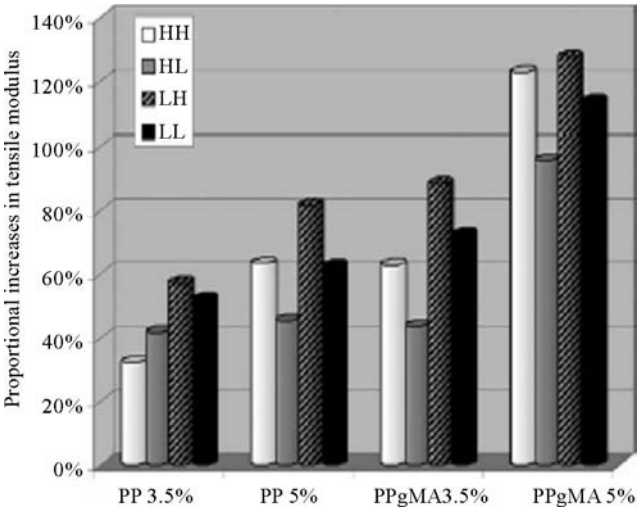

Figure 14.24 Proportional increase of tensile modulus of uncompatibilized and MA compatibilized PP–clay nanocomposites reinforced with 3.5 and 5 wt% organoclay (Dellite 72T) with respect to pure PP. The first letter of sample designation denotes the barrel temperature and the second letter denotes the screw speed. H: high and L: low. (Reprinted from Reference 57 with permission of Elsevier.)

fluoromica modified with C16 amine and compatibilized with 20 wt% PP-g-MA was found to exhibit high yield stress (44 MPa) and Young's modulus (3.46 GPa). More recently, Modesty et al. (57) studied the effect of processing conditions and the role of PP-g-MA compatibilizer on the tensile properties of PP–clay (Dellite 72T) nanocomposites (Fig. 14.24). They reported that exfoliation of clay can be achieved via the addition of PP-g-MA compatibilizer and high shear stress processing condition. Low barrel temperature and high screw speed are the optimum processing conditions that maximize the shear stress exerted on the polymer. In another study, Tjong et al. (41) reported the beneficial effects of high screw speed on the exfoliation of vermiculite clay and on the enhancement of mechanical properties such as storage modulus, tensile strength, and stiffness of the PP/MAV nanocomposites (Fig. 14.25). From Fig. 14.25, it can be seen that the storage modulus of the PP/MAV nanocomposites increases considerably with increasing vermiculite content and screw rotation speed at 25°C.

Brittle fracture of composite materials could lead to catastrophic failure of structural components during their service applications. The low tensile ductility of polyoefin–silicate nanocomposites can be improved by adding suitable impact modifier particles. It is well established in literature that impact modifier additions can alter the stress state in the polymers and induce extensive plastic deformation in polymers via mechanisms such as multiple crazing, cavitation, and shear yielding (87,88). The elastomer particles can act as stress concentrators to initiate crazes or to facilitate internal cavitation to relieve the triaxial stress state ahead of crack tip. Extensive elastomer cavitation and massive crazing can induce shear yielding of the matrix. An improved toughness of PE and PP blends resulting from the elastomer additions is commonly attributed to the cavitation of elastomers followed by shear

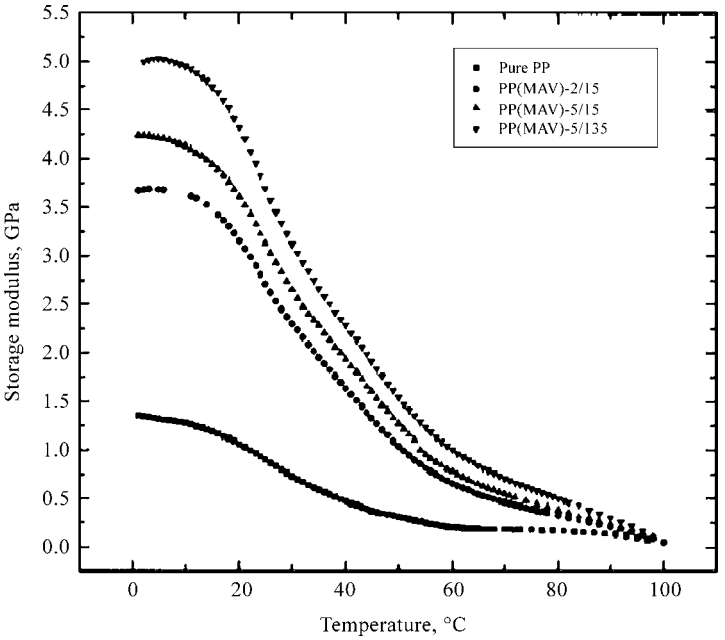

Figure 14.25 Storage modulus versus temperature for pure PP and PP–MAV*x*/*y* nanocomposites (*x* denotes the weight percent of MAV and *y* denotes the screw speed of Brabender Plasticorder in rpm). (Reprinted from Reference 41 with permission of The American Chemical Society.)

yielding of the matrix (89,90). Thus, the phase structure, type, size, interparticle distance of elastomer particles, and interfacial adhesion between modifier and matrix play decisive roles in the toughening mechanism. Several types of elastomers such as SEBS-g-MA, (EPR), and ethylene–propylene–diene-terpolymer (EPDM) are commonly used to toughen polyolefins. Impact modifiers such as SEBS-g-MA (42,47,91), styrene–butadiene–styrene (SBS) (92), and POE (51,52) have been found to effectively improve the tensile ductility and impact strength of the PP–clay nanocomposites. In the former case, the compatibility between SEBS-g-MA and PP phases is good because the chemical structure of PP is close or compatible to the ethylene–butylene (EB) midblock of SEBS-g-MA. POE is a newer type of impact modifier developed by Dow Chemical Company using a metallocene catalyst. The narrow composition and molecular weight distribution of this copolymer offers improved rheological properties. This allows faster mixing and broader compounding conditions with PP compared to the EPR and EPDM (93).

Table 14.3 summarizes the effect of maleated SEBS additions on the tensile strength, stiffness, elongational break, and the storage modulus of PP/4%MAV nanocomposite (42). Apparently, PP/4%MAV nanocomposite exhibits high tensile strength and stiffness, as well as storage modulus. Tensile ductility of the composite in terms of elongation at break is found to decrease by about 90.3% with the incorporation of 4%MAV in compared to pure PP. Addition of 5% maleated SEBS to the PP/4% MAV restores the elongation at break from 12.8% to 88.4%. The

Table 14.3 Tensile Properties of PP and PP/4%MAV Nanocomposites Toughened with SEBS-g-MA Elastomer [Reprinted from Reference 42 with permission of John Wiley & Sons.]

Specimen	Tensile strength, MPa	Tensile Modulus, GPa	Elongation at break, %	Storage modulus[a], GPa
Pure PP	28.1	0.844	132	1.08
PP–4% MAV	36.3	1.208	12.8	3.02
(95% PP–5% SEBS-g-MA)–4% MAV	32.5	0.794	88.4	1.62
(95% PP–10% SEBS-g-MA)–4% MAV	29.9	0.723	127	1.53
(95% PP–15% SEBS-g-MA)–4% MAV	28.1	0.682	168	1.42
(95% PP–20% SEBS-g-MA)–4% MAV	26.6	0.618	231	1.18

[a]Determined from dynamic mechanical analysis at 25°C.

tensile ductility can be further improved by increasing the elastomer content; however, the tensile strength and stiffness appear to drop significantly. From a practical point of point, polymer–silicate nanocomposites are desirable to have high tensile strength and ductility. Therefore, a balance can be maintained between the tensile strength and ductility of PP–MAV nanocomposites by properly controlling the elastomer content. Figure 14.26 shows that the Izod impact strength of PP/4% MAV nanocomposite can be significantly improved by adding impact modifier. The SEBS-g-MA is very effective at converting brittle PP/4%MAV sample into tough nanocomposite. Similar results of maleated additions on the Young's modulus, tensile strength, and impact strength of PP–2%MMT and PP/4%MMT nanocomposites are illustrated in Fig. 14.27a–c. For the purposes of comparison, the variations in Young's modulus, tensile strength, and impact strength with SEBS-g-MA content for PP are shown in Fig. 14.28a–c.

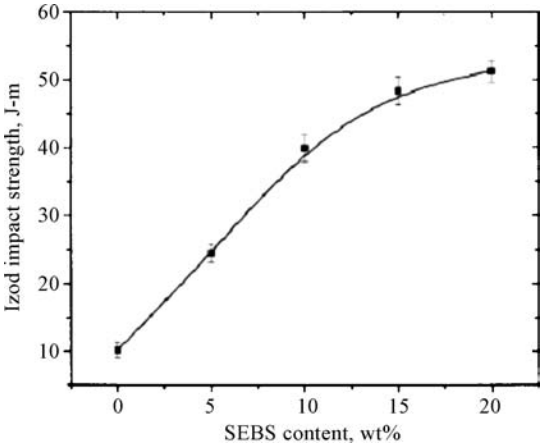

Figure 14.26 Variation of Izod impact strength of PP–4%MAV nanocomposites with SEBS-g-MA content. (Reprinted from Reference 42 with permission of John Wiley & Sons.)

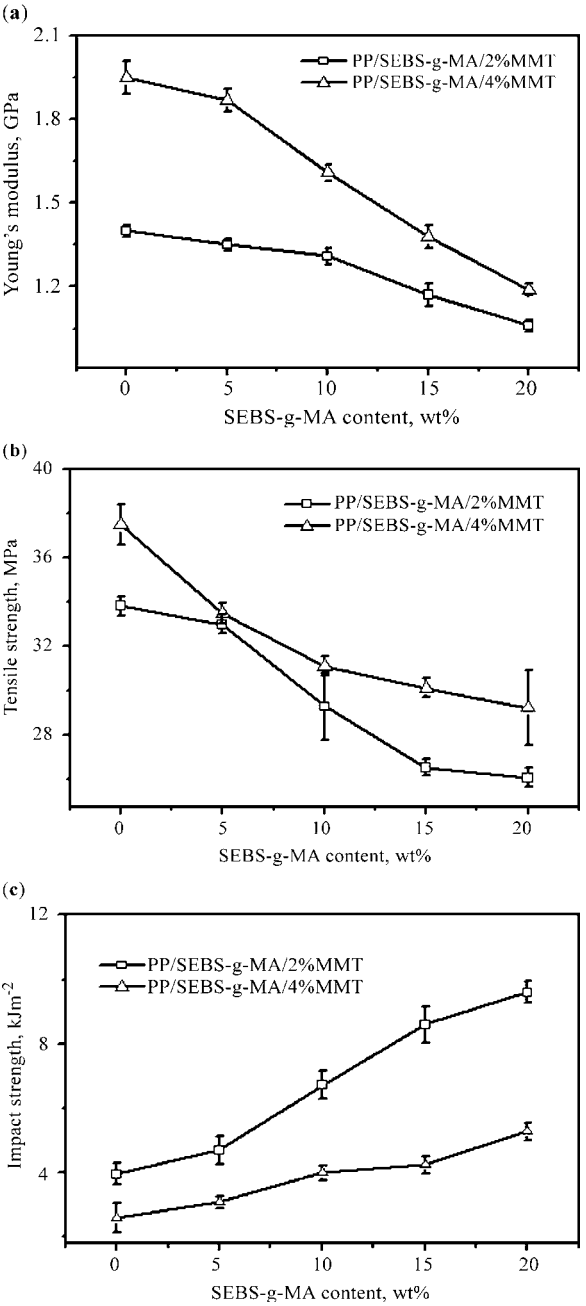

Figure 14.27 Variations of (**a**) Young's modulus, (**b**) tensile strength, and (**c**) Izod impact strength with SEBS-g-MA content for PP–2%MMT and PP–4%MMT nanocomposites. (Reprinted from Reference 46 with permission of John Wiley & Sons.)

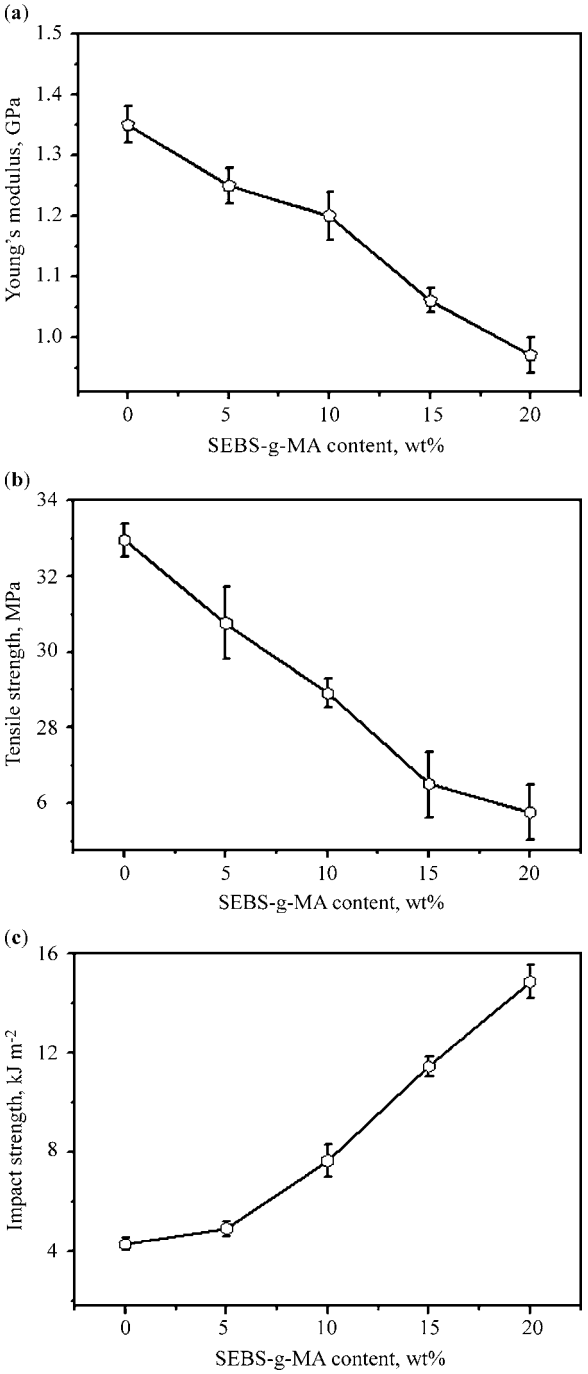

Figure 14.28 Variations of (**a**) Young's modulus, (**b**) tensile strength, and (**c**) Izod impact strength with SEBS-g-MA content for PP blends.

Very recently, Paul and coworkers studied the structure–property relationships of TPO-based nanocomposites (71). On the basis of TEM and AFM observations, they reported that the size of elastomer particles (POE) and aspect ratio of the clay particles tend to decrease with increasing clay content. The effects of addition of organoclay and elastomer on the tensile ductility and impact strength are shown in Figs. 14.29 and 14.30, respectively. The elongation at yield of the nanocomposites containing 10 wt% elastomer decreases considerably with the addition of 1% MMT and then decreases slightly as MMT loading increases. The elongation at yield of the nanocomposites containing 20 and 30 wt% elastomer decreases considerably with the addition of 1% MMT. However, the values increase with further increase in MMT content. From Fig. 14.30a, the addition of MMT leads to a decrease in impact strength for the nanocomposites containing $\leq$10 wt% elastomer. The impact strength increases slightly with increasing MMT content when the elastomer content reaches 20 wt%. Thus, the nanocomposites containing elastomer up to 20 wt% are very brittle (Fig. 14.31). For the nanocomposites containing higher elastomer contents, that is, 30 and 40 wt%, the materials undergo a brittle-to-ductile transition as the MMT content exceeds a certain value (Fig. 14.30b). In other words, nanocomposites containing higher elastomer and MMT contents exhibit supertough characteristics. This is attributed to a reduction in the size of elastomer particles with an increase in the MMT content. The MMT additions increase the melt viscosity and prevent the coalescence of elastomer particles during melt processing. Stress whitening can be readily seen on the surfaces of impact specimens containing higher elastomer and MMT contents (Fig. 14.31).

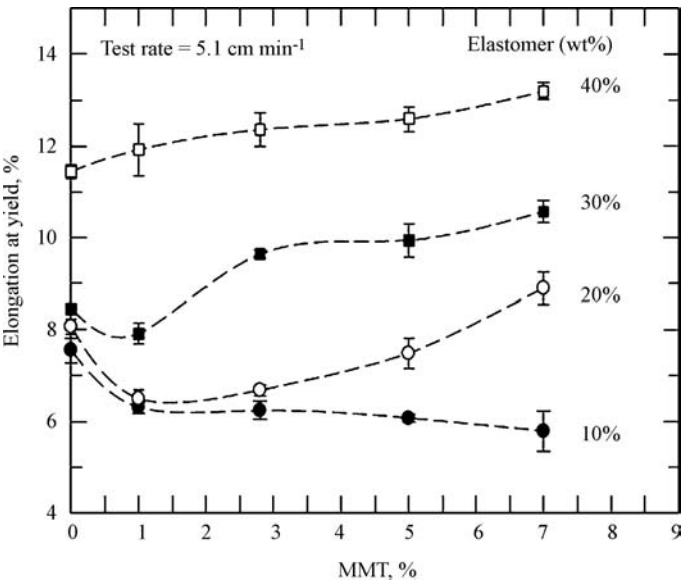

Figure 14.29 Effect of MMT and elastomer content on the elongation at yield of TPO nanocomposites. (Reprinted from Reference 71 with permission of Elsevier.)

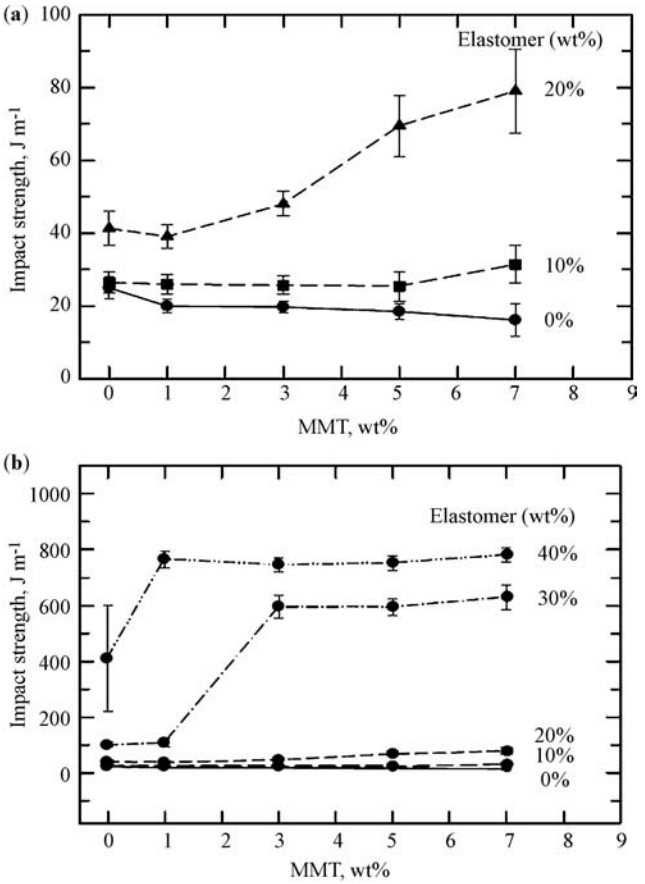

Figure 14.30 Effect of MMT and elastomer content on the notched Izod impact strength of PP nanocomposites: (**a**) nanocomposites containing 0, 10, and 20 wt% elastomer and (**b**) nanocomposites containing 30 and 40 wt% elastomer. (Reprinted from Reference 71 with permission of Elsevier.)

14.4 PATENT PROCESSES

Polymer–clay nanocomposites are experiencing a rapid development in recent years due to their existing and potential applications in a wide variety of technological areas (1–3). Nanocomposites show great promise for use in structural, electronic, food, and medical applications in which enhanced mechanical and physical properties are required. Substantial progress has been made in the commercial development, processing, and characterization of nanocomposites over the recent years (94–102). Several technical processes have been invented by the researchers of chemical companies for possible commercialization of the polymer nanocomposites (Table 14.4). The patents disclose the practices of preparing polymer nanocomposites via *in situ* polymerization and meltcompounding processes. For *in situ*

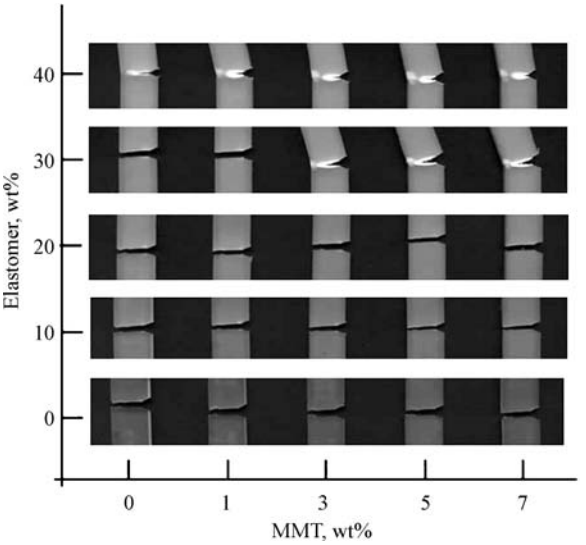

Figure 14.31 Photographs of Izod specimens taken after the notched impact test for PP nanocomposites containing various amounts of elastomer and MMT. (Reprinted from Reference 71 with permission of Elsevier.)

Table 14.4 Patent Processes for Preparing Polymer Nanocomposites.

Patent number and year	Type of nanocomposite	Fabrication process	Inventor	Assignee
US 5,514,734 (1996)	PA or PP	*In situ* polymerization	M. Maxfield, B. R. Christiani, and V. R. Sastri	Allied Signal
US 5,910,523 (1999)	PE or PP	Melt compounding	S. D. Hudson	—
US 6,060,549 (2000)	PA, PC, PPE, PPS, or PEEK thermoplastic elastomer	Melt compounding	D. Li, D. G. Peiffer, C. W. Elspass, and H. C. Wang	Exxon
US 6,465,543 B1(2002)	PE or PP	*In situ* polymerization	M. Alexandre et al.	Dow
US 6,451,897 B1(2002)	PP or TPO	*In situ* polymerization	S. G. Niyogi	Basell
US 6,864,308 B2 (2005)	LLDPE or PP	Melt compounding	J. S. Rosenthal and M. D. Wolkowicz	Basell
EP1268656 B1 (2005)	PP or TPO	Melt compounding	C. J. Chou, E. I. Garcia-Meitin, L. Schilhab, and R. F. Fibiger	Dow

polymerization, US Patent 5,514,734 discloses the dispersion of layered silicates in the polymer matrix that can be a polyester, polyolefin, or polyamide. The clay particles are bonded to organo silanes, organo titanates, or organo zirconates and have one or more moieties bonded to the polymer matrix (95). The fabrication process of the nanocomposites includes two essential steps that may be carried out sequentially or concurrently. The first step comprises forming a swellable layered silicate by intercalating it with organo silanes, organo titatanes, or organo zirconates. The second step comprises polymerizing a polymer precursor with the organo metallic treated layered silicate. In the patent process of Dow Chemical Company, there is no need to exchange ion with the nanofiller particles and to incorporate polar substituents into the polyolefin. The practice involves several steps: (a) dispersing a smectic clay into water to swell the clay, (b) removing the water from the swelled clay by freeze-drying to form an organoclay, and (c) treating the organoclay with an alkyl aluminoxane and subsequently with a catalyst to form a complex that promotes olefin polymerization and platelet dispersion. It is noted that the modification of silicate clays with alkoxysilanes containing reactive group ≡Si—OR has also been conducted in the academic community (103,104).

In the case of the melt-compounded TPO nanocomposites, European Patent 1268656 B1 discloses the melt-mixing process of maleated PP having a weight-average molecular weight of 150,000, PP having a weight-average molecular weight of 150,000, thermoplastic elastomer (AFFINITY 8180 from Dow), and onium treated cation exchanging layered MMT in a Banbury brand polymer mixer at 100 rpm at 150°C for 10 min. The TPO nanocomposite produced can be used to make articles of manufacture such as parts for motor vehicles, appliances, business machines, or construction articles (100). As mentioned above, General Motors, Basell, and Southern Clay Products have used TPO-based nanocomposite as a step-assist for 2002 GMC Safari and Chevrolet Astro vans (74, 75). For the polymer matrix other than polyolefin, US Patent 6,060,549 (Exxon) relates to a process of forming elastomer toughened polymer nanocomposites. The polymers could be PA, PC, PPE, PPS, PEEK, among others. The elastomer employed in the invention is a functionalized, brominates, copolymer of a C_4–C_7 isomonoolefin, such as isobutylene and a *para*-alkylstyrene comonomer (97).

As mentioned previously, polyolefin nanocomposites generally employed PP-g-MA to compatibilize and disperse an organoclay in the polymer matrix. To achieve good intercalation, a minimum PP-g-MA/organoclay ratio of 5:3 is needed. Exfoliation even requires higher 10:3 ratio. The costs of graft copolymer and organoclay are relatively high. Very recently, Rosenthal and Wolkowicz indicated that a solid intercalating agent selected from the group consisting of (a) hydroxyl-substituted carboxylic acid esters, (b) amides, (c) hydroxyl-substituted amides, and (d) oxidized polyolefins can be used to intercalate PP molecular chains into the galleries of an organoclay (Cloisite 20A) during melt blending. The ratio of the intercalating agent and the clay is at least 1:3, based on the ash content of the clay (101). The intercalating agent employed was Adawax 280 ethylene bis-stearamide (EBS), commercially available from Rohm & Haas. The mechanical measurements showed that the melt-compounded PP nanocomposites containing low levels of EBS exhibit

even higher flexural modulus and impact strength than those compatibilized with PP-g-MA. For the nanocomposites containing both EBS and PP-g-MA, there is no synergistic enhancement effect for the flexural modulus. Moreover, EBS did not produce any negative effect on the yield strength and heat distortion temperature of PP nanocomposites.

14.5 ESSENTIAL WORK OF FRACTURE (EWF)

Polymer composites are important structural materials that have found widespread applications in industrial sectors. Failures of polymer composites frequently occur as a result of the exposure to high strain rate impact conditions. Polymers are known to suffer from the strain rate sensitivity in which they are ductile under low strain rate loading and change to brittle mode under high strain rate impact conditions. Understanding the fracture resistance of composites is particularly important because it is directly related to the service life of materials under dynamic deformation. Generally, conventional Izod and Charpy impact tests are used to determine the impact fracture behavior of polymers composites owing to their simplicity, speed, and cost effectiveness. These tests involve the determination of energy required for breaking a notched specimen with a specific notch geometry and a given fracture area. The results simply denote the energy absorption in the notched samples. Thus, they are not reliable indicators of the impact toughness of polymer composites.

In this regard, fracture mechanics is considered to be more appropriate to characterize the fracture toughness of notched specimens. The approach assumes that material fails as a result of initiation and propagation of cracks. Linear elastic fracture mechanics (LEFM) is adopted for the characterization of materials displaying only elastic deformation or materials with only small-scale yielding near the crack tip. The useful LEFM parameters include the critical stress intensity factor (K_c) and critical strain energy release rate (G_c). Failure occurs when the local energy release rate exceeds the critical value. For ductile materials in which a large plastic zone is developed at the crack tip, the fracture criterion of LFEM based on the K_c is invalid. In this case, nonlinear elastic fracture mechanics parameters should be adopted. The *J*-integral concept developed by Rice (105) and the EWF approach proposed by Broberg (106) can be used to characterize the fracture behavior of ductile materials. The determination of a critical value of *J*-integral (J_c) is generally carried out by constructing a resistance curve J–Δa, where Δa is the advanced crack length. The J_c value is determined at the point of intersection between the J–R curve and the blunting line ($J = 2\sigma_y \Delta_a$, where σ_y is the yield stress). The process of determination of J_c value of the ductile material is rather tedious.

In the past decades, the EWF concept has gained widespread acceptance in polymer community over the *J*-integral analysis because of its experimental simplicity (107–113). Broberg assumed that the nonelastic region at the crack tip can be divided into two regions: an inner region, where the fracture process occurs, and the outer region, where plastic deformation takes place. The total fracture work (W_f) can be divided accordingly. The work required to fracture the material in its inner process

zone (W_e) and the work consumed by various deformation mechanisms in the plastic zone (W_p). The former is referred to as the essential work of fracture, whilst the latter is the nonessential work.

For the experimental determination of EWF parameters, a typical double-edge notched tension (DENT) specimen for tensile measurement and a single-edge notched (SEN) specimen for impact loading are commonly employed (Fig. 14.32a and b). From these, the total fracture work (W_f) can be written as

$$W_f = W_e + W_p \tag{14.2}$$

$$W_f = w_e \, L \, t + \beta \, w_p \, L^2 t \tag{14.3}$$

$$w_f = W_f/(Lt) = w_e + \beta w_p L \tag{14.4}$$

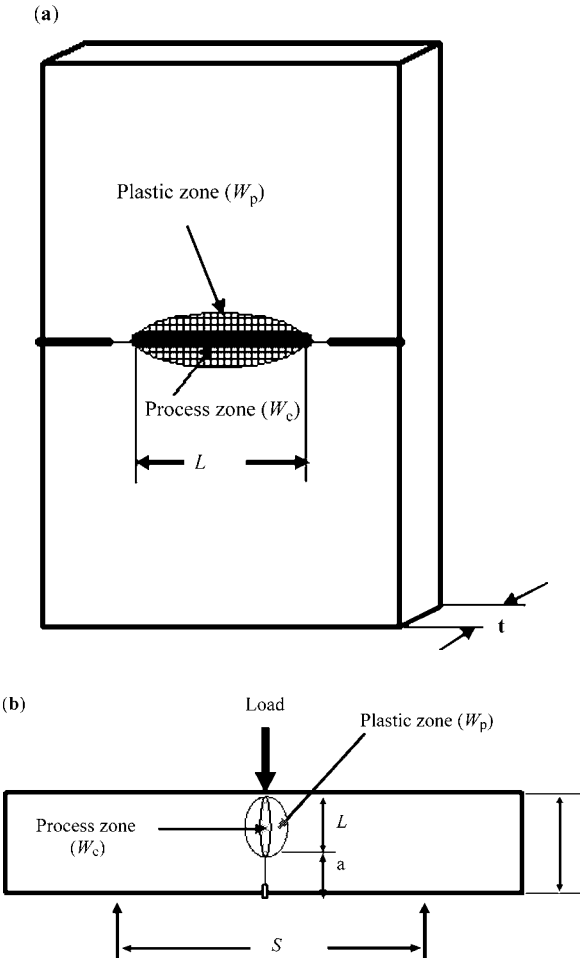

Figure 14.32 Geometries of (**a**) DENT and (**b**) SEN specimens.

where w_f is the specific total fracture work; w_e and w_p are the specific essential fracture work and specific plastic work, respectively; L is the ligament length; t is the sample thickness; and β is a shape factor of the plastic zone. An important prerequisite of EWF approach is that crack propagates only after the ligament has fully yielded and the plastic zone is scaled with the square of the ligament length. The validity range of ligament L under plane stress condition is given by:

$$(3-5)\ t \leq L \leq \min(B/3,\ 2r_p) \tag{14.5}$$

where B is the width of the specimen and $2r_p$ is the size of plastic zone. Apparently, EWF concept is a simple method that consists of testing specimens with different ligament lengths, recording the area under the load displacement curve (W_f), plotting the w_f versus L diagram, and evaluating the best fit linear regression line. This approach has been recently incorporated in the European Structural Integrity Society (ESIS) test protocol for essential work of fracture under quasistatic loading conditions (114).

Figure 14.33a–d shows the tensile load–displacement for pure PP homopolymer, PP/5% SEBS-g-MA blend, PP/5% SEBS-g-MA/2%MMT, and PP/5% SEBS-g-MA/4% MMT hybrids having different ligaments. From Fig. 14.33a,

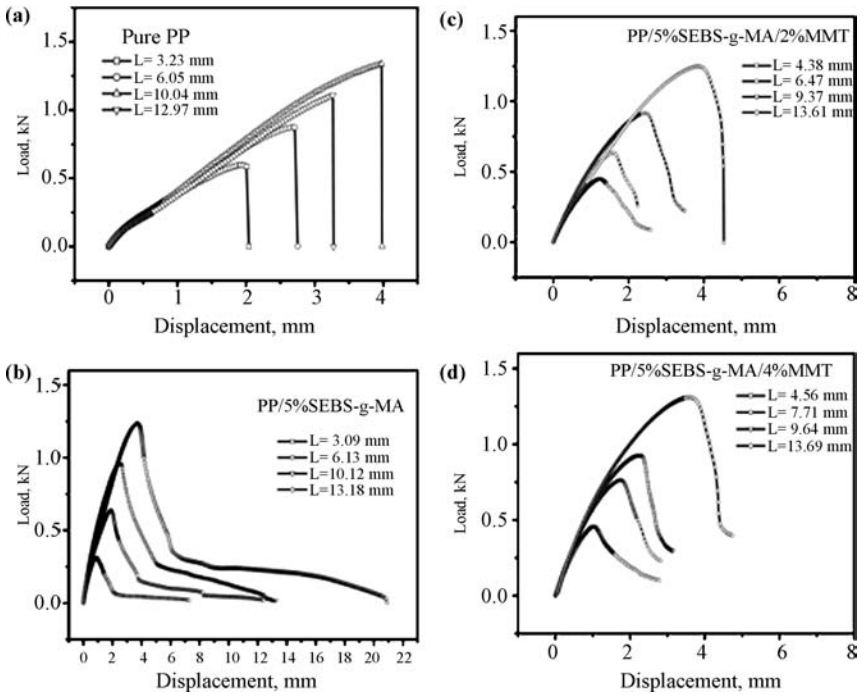

Figure 14.33 Load–displacement curves for (**a**) pure PP, (**b**) PP–5% SEBS-g-MA, (**c**) PP–5% SEBS-g-MA–2% Org-MMT, and (**d**) PP–5% SEBS-g-MA–4% Org-MMT specimens subjected to tensile EWF tests. (Reprinted from Reference 46 with permission of John Wiley & Sons.)

pure PP exhibits typical brittle fracture behavior under employed testing conditions. In this case, the EWF concept cannot be used to determine the fracture toughness of pure PP. However, Fig. 14.33b–d, reveals that gross yielding and necking of various ligaments occur by adding 5% SEBS-g-MA to PP and PP/MMT nanocomposites during tensile deformation process. The results are in accord with the ESIS protocol (114) in which the ligament must be fully yielded prior to crack growth. In this regard, the load–displacement curves of designated specimens having different ligaments should exhibit similar shapes, the so-called self-similarity. It is evident that geometrical self-similarity is maintained for the load–displacement curves as shown in Fig. 14.33b–d. The plots of w_f versus ligament length for PP/5%SEBS-g-MA, PP/5%SEBS-g-MA/2%MMT, and PP/5%SEBS-g-MA/4%MMT samples are depicted in Fig. 14.34a–c. Good linear regression with a high correlation coefficient between the data of w_f and L is obtained for these samples. The results of tensile EWF measurements for pure PP, PP/SEBS-g-MA blend, and PP/SEBS-g-MA/Org-MMT nanocomposite specimens are summarized in Table 14.5. Apparently, the fracture toughness of nanocomposit can be improved by the elastomer as evidenced by their large w_e and βw_p values with increasing SEBS-g-MA content.

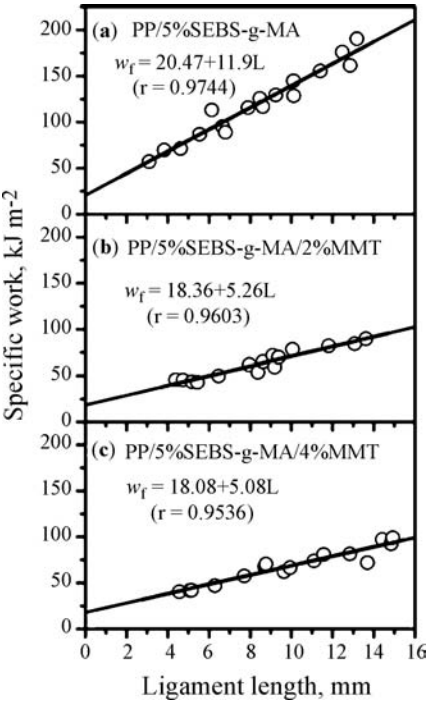

Figure 14.34 w_f versus L plots for (**a**) PP–5% SEBS-g-MA, (**b**) PP–5% SEBS-gMA–2% Org-MMT, and (**c**) PP–5% SEBS-g-MA–4% Org-MMT. (Reprinted from Reference [46] with permission of John Wiley & Sons.)

Table 14.5 Specific Essential Work of Fracture (w_e) and Specific Plastic Work (βw_p) for PP Homopolymer, PP/SEBS-g-MA Blends and PP/SEBS-g-MA/Org MMT Nanocomposites Determined from Tensile EWF Tests [Reprinted from Reference (46) with permission of John Wiley & Sons.]

Specimen	w_e, kJ m^{-2}	βw_p MJ m^{-3}	Correlation coefficient
Pure PP	—	—	—
PP/5% SEBS-g-MA	20.47	11.91	0.9744
PP/10% SEBS-g-MA	22.35	15.96	0.9843
PP/15% SEBS-g-MA	28.18	21.51	0.9846
PP/20% SEBS-g-MA	28.47	25.54	0.9511
PP–5% SEBS-g-MA/2% Org–MMT	18.36	5.26	0.9603
PP–10% SEBS-g-MA/2% Org–MMT	21.23	11.61	0.9832
PP–15% SEBS-g-MA/2% Org–MMT	21.90	16.84	0.9881
PP–20% SEBS-g-MA/2% Org–MMT	26.09	16.96	0.9847
PP–5% SEBS-g-MA/4% Org–MMT	18.08	5.08	0.9536
PP–10% SEBS-g-MA/4% Org–MMT	18.34	8.34	0.9923
PP–15% SEBS-g-MA/4% Org–MMT	20.67	9.81	0.9745
PP–20% SEBS-g-MA/4% Org–MMT	23.77	14.78	0.9854

Figure 14.35 shows the macrographs of pure PP, PP/*x*%SEBS-g-MA blends, and PP/*x*% SEBS-g-MA/*y*% Org-MMT nanocomposites after tensile EWF tests. Stress whitening plastic zone can be clearly seen in the macrographs of PP/*x*% SEBS-g-MA blends and PP/*x*% SEBS-g-MA/*y*%Org-MMT nanocomposites with the exception of pure PP. Figure 14.36a is the SEM micrograph showing the fracture surface feature of PP/5%SEBS-g-MA/4% Org-MMT nanocomposite after EWF measurement. Shear yielding of the PP matrix resulting from cavitation of SEBS-g-MA particles is apparent during the tensile EWF test, leading to the energy dissipation in the outer plastic zone. Fibrillation of the matrix resulting from shear yielding can be readily seen at a higher magnification SEM image (Fig. 14.36b). The results of EWF measurements and SEM observations reveal that cavitation of elastomers

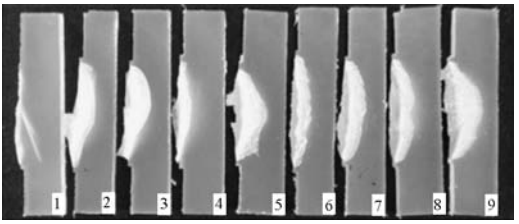

Figure 14.35 Macrographs showing stress whitening for (1) pure PP, (2) PP–5% SEBS-g-MA, (3) PP–15% SEBS-g-MA, (4) PP–5% SEBS-g-MA–2% Org-MMT, (5) PP–15% SEBS-g-MA–2% Org-MMT, (6) PP–5% SEBS-g-MA–4% Org-MMT, (7) PP–10% SEBS-g-MA–4% Org-MMT, (8) PP–15% SEBS-g-MA–4% Org-MMT and (9) PP–20% SEBS-g-MA–4% Org-MMT after EWF tests. (Reprinted from Reference 46 with permission of John Wiley & Sons.)

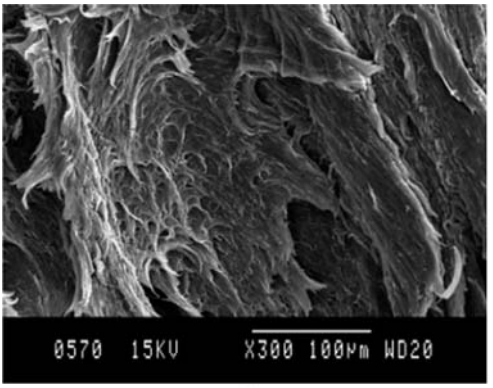

Figure 14.36 SEM micrographs showing fracture surfaces of (**a**) PP–5% SEBS-g-MA–4% Org-MMT with $L = 9.07$ mm after EWF tensile test. (**b**) Higher magnification image showing plastic deformation in the matrix. (Reprinted from Reference 46 with permission of John Wiley & Sons.)

and subsequent shear yielding of the matrix are responsible for the energy dissipation mechanism in the PP/MMT nanocomposites toughened with maleated SEBS elastomers.

On the basis of the successful application of EWF concept under tensile mode, Mai and coworkers extended the EWF methodology to high rate impact testing of polymers (115). Since then, numerous investigations have been carried out using EWF to determine the impact fracture toughness of polymers blends (116,117) and short fiber reinforced composites (111,116–120). Figure 14.37a–c shows the typical plots of impact fracture energy vs ligament length for PP/15wt% SEBS-g-MA blend, PP/15wt% SEBS-g-MA/2wt% Org-MMT, and PP/15wt% SEBS-g-MA/4wt% Org-MMT nanocomposites subjected to EWF impact test. The EWF results were obtained from SEN specimens. It can be seen that good linear regression line with a high correlation coefficient between the data of w_f

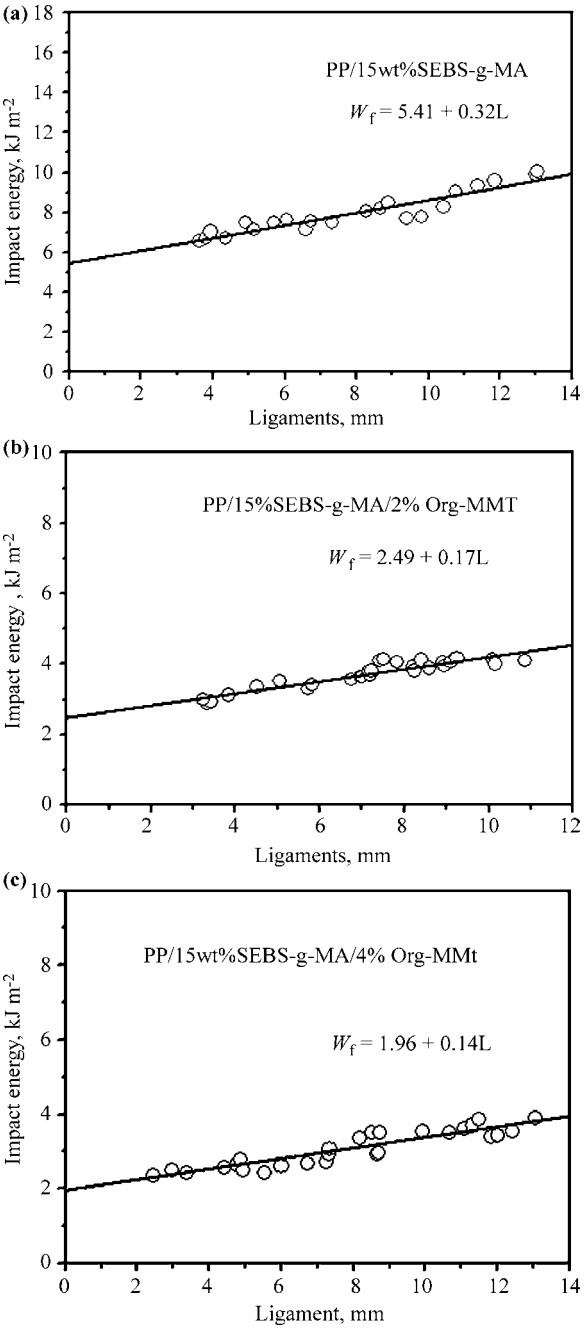

Figure 14.37 Impact fracture energy versus ligament length for (**a**) PP–15wt% SEBS-g-MA, (**b**) PP–15wt% SEBS-g-MA–2wt% Org-MMT, and (**c**) PP–15wt% SEBS-g-MA–4wt% Org-MMT with different ligament lengths. (Reprinted from Reference 91 with permission of Elsevier.)

Table 14.6 Impact-Specific Essential Work of Fracture (w_e) and Specific Plastic Work (βw_p) for PP Homopolymer, PP/SEBS-g-MA blends, and PP/SEBS-g-MA/Org-MMT Nanocomposites at an Impact Velocity of 1.8 m s^{-1} [Reprinted from Reference 92 with permission of Elsevier.]

Specimen	w_e kJ m^{-2}	βw_p MJ m^{-3}	Correlation coefficient
Pure PP	1.32	—	—
PP–5wt% SEBS-g-MA	2.22	0.08	0.917
PP–10wt% SEBS-g-MA	2.67	0.25	0.979
PP–15wt% SEBS-g-MA	5.41	0.32	0.937
PP–20wt% SEBS-g-MA	9.50	0.42	0.910
PP/5wt% SEBS-g-MA/2wt% Org-MMT	1.87	0.07	0.922
PP/10wt% SEBS-g-MA/2wt% Org-MMT	2.46	0.13	0.914
PP/15wt% SEBS-g-MA/2wt% Org-MMT	2.49	0.17	0.921
PP/20wt% SEBS-g-MA/2wt% Org-MMT	4.30	0.30	0.957
PP/5wt% SEBS-g-MA/4wt% Org-MMT	1.27	0.07	0.917
PP/10wt% SEBS-g-MA/4wt% Org-MMT	1.58	0.11	0.912
PP/15wt% SEBS-g-MA/4wt% Org-MMT	1.96	0.14	0.919
PP/20wt% SEBS-g-MA/4wt% Org-MMT	3.19	0.25	0.949

and L is obtained for these samples. The results of impact EWF measurements and the correlation coefficient values for pure PP, PP/SEBS-g-MA blend, and PP/SEBS-g-MA/Org-MMT nanocomposite specimens are listed in Table 14.6. According to the EWF concept, the total fracture energy of pure PP is completely dissipated in the inner region near the fracture surface and no energy is dissipated in the outer plastic zone. This indicates that the impact fracture of pure PP is in brittle mode. For the PP/SEBS-g-MA blends, both the specific essential fracture work (w_e) and nonessential plastic work (βw_p) appear to increase with increasing elastomer content. This implies that the elastomer greatly enhances the energy absorption of crack propagation during the impact loading and consequently enhances the fracture toughness of the blends. The cavitation of elastomers tends to release plastic constraints and trigger mass plastic deformation of the matrix. Similar increasing trends in w_e and βw_p are observed for the PP nanocomposites. Moreover, the addition of 2 wt% Org-MMT to the PP/SEBS-g-MA blends leads to a small decrease in their w_e values. However, the w_e values of the PP/SEBS-g-MA blends appear to decrease considerably by adding 4 wt% Org-MMT in comparison to the corresponding binary blends. As mentioned previously, β-PP phase was induced in the PP/15wt% SEBS-g-MA/4 wt% Org-MMT nanocomposite. The β-PP phase spherulites are known to improve the tensile ductility and impact strength of PP. However, it is considered that the SEBS-g-MA elastomer phase rather than β-PP enhances the impact toughness of nanocomposites due to a minisule amount of β-PP phase induced.

14.6 CONCLUSION

This chapter provides an overview of recent advances in research of the structure, mechanical behavior, and fracture behavior of melt-compounded polyolefin nanocomposites reinforced with low loading levels of silicates derived from montmorillonite and vermiculite. The structure and mechanical properties of such nanocomposites are significantly influenced by the interaction between polyolefin chains and silicate platelets. The hydrophilic silicates are generally pretreated with organic surfactants such as alkylammonium ions to render them more compatible with polyolefins. Owing to nonpolar nature of the polyolefins, a suitable compatibilizer containing MA functional group is further needed to assist the intercalation of the polyolefin molecules into the galleries of organoclays. The MA functional group can be either grafted to the polyolefin matrix or to the silicate clay surfaces. In the later case, MA functional group acts as a swelling agent for the layered silicate and as a modifying additive for the polyolefin matrix. Two types of nanostructures associated with the dispersion of organoclay platelets in polyolefin matrix can be found: intercalated and exfoliated. XRD and TEM techniques are potential tools for the identification and verification of such structures. Formation of an exfoliated structure in polyolefin–clay nanocomposites depends greatly on the molecular structure of organoclay employed, the length of alkyl chain of alkylammonium amine, amount of MA grafted to the polyolefin matrix, barrel temperature of the extruder, screw speed, among others.

The reinforcing effect resulting from the addition of organoclays is confirmed by the static tensile and dynamic mechanical analysis. In general, the tensile stiffness and strength as well as the storage modulus of polyolefin/clay nanocomposites are increased significantly with increasing organoclay contents. However, the tensile ductility and impact strength are sharply reduced with increasing clay contents. Consequently, polyolefin–silicate nanocomposites are vulnerable to brittle fracture. The toughness of the polyolefin–clay nanocomposites can be restored by adding the impact modifiers. However, additions of impact modifier can lead to a large drop in the tensile modulus. A balance between the tensile stiffness and impact strength can be monitored by proper by controlling the volume content of the impact modifiers. The fracture behavior of polyolefin–clay nanocomposites toughened with elastomers under tensile and impact conditions can be well characterized by the EWF concept. The results of EWF measurements and SEM observations demonstrate that cavitation of elastomers and subsequent shear yielding of the matrix are responsible for the energy dissipation mechanism in the PP/MMT nanocomposites toughened with maleated SEBS elastomers under tensile and impact conditions.

NOMENCLATURE

B	Sample width
β	Shape factor of the plastic zone
I_β	Integrated area of (300) diffracting peak of β-PP

I_{110}, I_{040}, and I_{130}	Integrated areas of (110), (040), and (130) peaks of α-PP
K	Content of β-PP phase
L	Ligament length
$2r_p$	Size of plastic zone
t	Sample thickness
w_e	Specific essential fracture work
w_p	Specific plastic work
W_f	Total fracture work

REFERENCES

1. R. Steward, *Plast. Eng.*, **60**, 23 (2004).
2. C. H. Hong, Y. B. Lee, J. W. Bae. Y. Y. Jho, B. U. Nam, and T. W. Hwang, *J. Appl. Polym. Sci.*, **98**, 427 (2005).
3. J. C. Matayabas Jr. and S. R. Turner, Nanocomposite technology for enhancing the gas barrier of polyethylene terephthalate, in: *Polymer–Clay Nanocomposites*, T. J. Pinnavaia and G. W. Beall (eds.), Wiley, New York, 1999, Chapter 11.
4. S. W. Bailey, Structures of layer silicates, in: *Crystal Structures of Clay Minerals and Their X-Ray Identifications*, Monograph No. 5, G. W. Brindley and G. Brown (eds.), Mineralogical Society, London, 1980, pp. 1–123.
5. B. Yalcin and M. Cakmak, *Polymer*, **45**, 6623 (2004).
6. A. Ghosh and E. M. Woo, *Polymer*, **45**, 4749 (2004).
7. J. Mering, Smectites, in: *Soil Components, Vol. 2: Inorganic Components*, J. E. Geiseking (ed.), Springer-Verlag, New York, 1975.
8. G. Brown, *The X-Ray Identification and Crystal Structures of Clay Minerals*, Mineralogical Society, London, 1961.
9. D. M. More and R. C. Reynolds, *X-Ray Diffraction and Identification and Analysis of Clay Minerals*, 2nd edition, Oxford University Press, Oxford, 1997.
10. M. M. Dudkina, A. V. Tenkovtsev, D. Pospiech, D. Jehnichen, L. Haubler, and A. Leuteritz, *J. Polym. Sci. B Polym. Phys.*, **43**, 2493 (2005).
11. Y. K. Kim, Y. S. Choi, K. H. Wang, and I. J. Chung, *Chem. Mater.*, **14**, 4990 (2002).
12. M. Xu, Y. S. Choi, Y. K. Kim, K. H. Wang, and I. J. Chung, *Polymer*, **44**, 6387 (2003).
13. R. A. Vaia, H. Ishii, and E. P. Giannelis, *Chem. Mater.*, **5**, 1694 (1993).
14. R. A. Vaia, K. D. Jandt, E. J. Kramer, and E. P. Giannelis, *Macromolecules*, **28**, 8080 (1995).
15. L. Incarnato, P. Scarfato, L. Scatteia, and D. Acierno, *Polymer*, **45**, 3487 (2004).
16. C. Wan, Y. Zhang, and Y. X. Zhang, *Polym. Test.*, **23**, 299 (2004).
17. T. D. Fornes, D. L. Hunter, and D. R. Paul, *Macromolecules*, **37**, 1793 (2004).
18. S. Hotta and D. R. Paul, *Polymer*, **45**, 7639 (2004).
19. T. D. Fornes, P. J. Yoon, and D. R. Paul, *Polymer*, **45**, 2321 (2004).
20. T. D. Fornes, P. J. Yoon, and D. R. Paul, *Polymer*, **44**, 7545 (2003).
21. T. D. Fornes and D. R. Paul, *Polymer*, **44**, 4993(2003).
22. D. Fornes, P. J. Yoon, D. L. Hunter, H. Keskkula, and D. R. Paul, *Polymer*, **43**, 5915 (2002).
23. H. R. Dennis, D. L. Hunter, D. Chang, S. Kim, J. L. White, J. W. Cho, and D. R. Paul, *Polymer*, **42**, 9513 (2001).
24. K. Masenelli-Varlot, E. Reynaud, G. Vigier, and J. Varlet, *J. Polym. Sci B Polym. Phys.*, **40**, 272 (2002).

25. M. Kawasumi, N. Hasegawa, M. Kato, A. Usuki, and A. Okada, *Macromolecules*, **30**, 6333 (1997).
26. N. Hasegawa, M. Kawasumi, M. Kawasumi, M. Kato, A. Usuki, and A. Okada, *J. Appl. Polym. Sci.*, **67**, 87(1998).
27. N. Hasegawa, H. Okamoto, M. Kato, and A. Usuki, *J. Appl. Polym. Sci.*, **78**, 1918 (2000).
28. P. H. Nam, P. Maiti, M. Okamoto, T. Kotaka, N. Hasegawa, and A. Usuki, *Polymer*, **42**, 9633 (2001).
29. P. Maiti, P. H. Nam, M. Okamoto, N. Hasegawa, and A. Usuki, *Macromolecules*, **35**, 2042 (2002).
30. P. Svoboda, C. Zeng, H. Wang, L. J. Lee, and D. L. Tomasko, *J. Appl. Polym. Sci.*, **85**, 1562 (2002).
31. Y. Q. Zhang, J. J. Lee, H. J. Jang, and C. W. Nah, *Composites B*, **35**, 133 (2004).
32. L. Szazdi, B. Pukanszky Jr., E. Fordes, and B. Pukanszky, *Polymer*, **46**, 8001 (2005).
33. J. H. Lee, D. Jung, C. E. Hong, C. E. Hong, K. Y. Rhee, and S. G. Advani, *Compos. Sci. Technol.*, **65**, 1996 (2005).
34. C. M. Koo, H. T. Ham, S. O. Kim, K. H. Wang, D. C. Kim, and W. C. Zin, *Macromolecules*, **35**, 5116 (2002).
35. T. G. Gopakumar, J. A. Lee, M. Kontopolou, and J. S. Parent, *Polymer*, **43**, 5483 (2002).
36. K. H. Wang, M. H. Choi, C. M. Koo, Y. S. Choi, and I. J. Chung, *Polymer*, **42**, 9819 (2001).
37. K. Chrissopoulou, I. Altintzi, S. H. Anastasiadis, E. P. Giannelis, M. Pitsikalis, N. Hadjichristidis, and N. Theophilou, *Polymer*, **46**, 12440 (2005).
38. H. Zhai, W. Xu, H. Guo, Z. Zhou, S. Shen, and Q. Song, *Eur. Polym. J.*, **40**, 2539 (2004).
39. J. A. Lee, M. Kontopoulou, and J. S. Parent, *Polymer*, **45**, 6595 (2004).
40. N. Ristolainen, U. Vainio, S. Paavola, M. Torkkeli, R. Serimaa, and J. Seppala, *J. Polym. Sci. B Polym. Phys.*, **43**, 1892 (2005).
41. S. C. Tjong, Y. Z. Meng, and A. S. Hay, *Chem. Mater.*, **14**, 44 (2002).
42. S. C. Tjong and Y. Z. Meng, *J. Polym. Sci B Polym. Phys.*, **41**, 2332 (2003).
43. S. C. Tjong and Y. Z. Meng, *J. Polym. Sci B Polym. Phys.*, **41**, 1476 (2003).
44. S. C. Tjong and Y. Z. Meng, *J. Appl. Polym. Sci.*, **86**, 2330 (2002).
45. S. C. Tjong and S. P. Bao, *J. Polym. Sci. B Polym. Phys.*, **43**, 585 (2005).
46. S. C. Tjong, S. P. Bao, and G. D. Liang, *J. Polym. Sci. B: Polym. Phys.*, **43**, 3112 (2005).
47. S. C. Tjong and S. P. Bao, *Compos. Sci. Technol.*, Forthcoming.
48. M. K. Akkapeddi, *Polym. Compos.*, **21**, 576 (2000).
49. A. Dasari, Z. Z. Yu, and Y. W. Mai, *Polymer*, **46**, 5986 (2005).
50. W. S. Chow, A. Abu Bakar, Z. A. Mohd Ishak, J. Karger-Kocsis, and U. S. Ishiaku, *Eur. Polym. J.*, **41**, 687 (2005).
51. J. W. Lin, A. Hassan, A. R. Rahmat, and M. U. Wahit, *J. Appl. Polym. Sci.*, **99**, 3441 (2006).
52. J. W. Lin, A. Hassan, A. R. Rahmat, and M. U. Wahit, *Polym. Int.*, **55**, 204 (2006).
53. C. Y. Wan, Y. Zhang, Y. X. Zhang, X. Y. Qiao, and G. M. Teng, *J. Polym. Sci. B Polym. Phys.*, **42**, 286 (2004).
54. R. A. Vaia and E. P. Giannellis, *Macromolecules*, **30**, 7990 (1997).
55. R. A. Vaia and E. P. Giannelis, *Macromolecules*, **30**, 8000 (1997).
56. W. Lertwimolnun and B. Vergnes, *Polym. Eng. Sci.*, **46**, 314 (2006).
57. M. Modesti, A. Lorenzetti, D. Bon, and S. Besco, *Polymer*, **46**, 10237 (2005).
58. A. B. Morgan and J. W. Gilman, *J. Appl. Polym. Sci.*,, **87**, 1329 (2003).
59. D. F. Eckel, M. P. Balogh, P. D. Fasulo, and W. R. Rodgers, *J. Appl. Polym. Sci.*, **93**, 1110 (2004).
60. L. F. Drummy, H. Koerner, K. Farmer, A. Tan, B. L. Farmer, and R. A. Vaia, *J. Phys. Chem. B*, **109**, 17868 (2005).
61. G. Lagally and A. Weiss, *Z. Naturforschung B*, **24**, 1057 (1969).
62. G. Lagally, M. Fernandez Gonzalez, and A. Weiss, *Clay Miner.*, **11**, 173 (1976).

63. G, Lagally, *Clays Clay Miner.*, **27**, 1 (1979).
64. G. Lagally and R. Malberg, *Colloid Surf.*, **49**, 11 (1990).
65. M. A. Osman, M. Ploetze, and P. Skrabal, *J. Phys. Chem. B*, **108**, 2580 (2004).
66. http://www.nanoclay.com/.
67. F. C. Chiu, S. M. Lai, J. W. Chen, and P. H. Chu, *J. Polym. Sci B Polym. Phys.*, **42**, 4139 (2004).
68. K. Y. Lee and L. A. Goettler, *Polym. Eng. Sci.*, **44**, 1103 (2004).
69. S. Mehta, F. M. Mirabella, K. Rufener, and A. Bafna, *J. Appl. Polym. Sci.*, **92**, 928 (2004).
70. P. D. Fasulo, W. R. Rodgers, and R. A. Ottaviani, *Polym. Eng. Sci.*, **44**, 1036 (2004).
71. H. S. Lee, P. D. Fasulo, W. R. Rodgers, and D. R. Paul, *Polymer*, **46**, 11673 (2005).
72. J. K. Mishra, K. J. Hwang, and C. S. Ha, *Polymer*, **46**, 1995 (2005).
73. M. Maiti, A. Bandyopadhyay, and A. K. Bhowmick, *J. Appl. Polym. Sci.*, **99**, 1645 (2006).
74. http:// www.basell.com.
75. *Plastics Add. Compound.*, **3**, 8 (2001).
76. S. C. Tjong, J. S. Shen, and R. K. Y. Li, *Polym. Eng. Sci.*, **36**, 100 (1996).
77. S. C. Tjong, J. S. Shen, and R. K. Y. Li, *Polymer*, **37**, 2309 (1996).
78. D. M. Lincoln, R. A. Vaia, Z. Wang, and B. S. Hsiao, *Polymer*, **42**, 1621 (2001).
79. X. Liu and Q. Wu, *Polymer*, **43**, 1933 (2002).
80. F. J. Torre, M. M. Cortazar, M. A. Gomez, G. Ellis, and C. Marco, *Polymer*, **44**, 5209 (2003).
81. J. Karger-Kocsis, Microstructural aspects of fracture in polypropylene and its filled, chopped fiber and fiber mat reinforced composites, in: *Polypropylene: Structure, Blends and Composites*, Vol. 3, J. Karger-Kocsis (ed.), Chapman Hall, London, 1995, pp. 142–201.
82. S. Avlar and Y. Qiao, *Composites A*, **36**, 624 (2005).
83. K. Wang, L. Chen, J. Wu, M. L. Toh, C. He, and A. F. Yee, *Macromolecules*, **38**, 788 (2005).
84. K. M. Varlot, E. Reynaud, G. Vigier, and J. Varlet, *J. Polym. Sci B Polym. Phys.*, **40**, 272 (2002).
85. K. H. Wang, M. H. Choi, C. M. Koo, M. Xu, I. J. Chung, M. C. Jang, S. W. Choi, and H. H. Song, *J. Polym. Sci B Polym. Phys.*, **40**, 1454 (2002).
86. P. Reichert, H. Nitz, S. Klinke, R. Brandsch, R. Thomann, and R. Mulhaupt, *Macromol. Mater. Eng.*, **275**, 8 (2000).
87. C. B. Bucknall, *Toughened Plastics*, Applied Science, London, 1977.
88. A. J. Kinloch and R. J. Young, *Fracture Behavior of Polymers*, Applied Science, London, 1983.
89. S. A. Xu and S. C. Tjong, *J. Appl. Polym. Sci.*, **77**, 2024 (2000).
90. G. X. Wei and H. J. Sue, *Polym. Eng. Sci.*, **40**, 1979 (2000).
91. S. P. Bao and S. C. Tjong, *Composites A.* Forthcoming.
92. Y. Li, G. X. Sue, and H. J. Sue, *J. Mater. Sci.*, **37**, 2447 (2002).
93. A. L. Da Silva, M. C. Rocha, F. M. Coutinho, R. Bretas, and C. Scuracchio, *J. Appl. Polym. Sci.*, **75**, 692 (2000).
94. G. W. Beall, S. Tsipsursky, A. Sorokin, and A. Goldman, Intercalates and exfoliates formed with oligomers and polymers and composite materials containing same, *US Patent* 5,552,469 (1996).
95. M. Maxfield, B. R. Christiani, and V. R. Sastri, Polymer nanocomposites comprising a polymer and an exfoliated particulate material derivatized with organo silanes, organo titanates, and organo zirconates dispersed therein and process of preparing Same, *US Patent* 5,514,734 (1996).
96. S. D. Hudson, Polyolefin nanocomposites, *US Patent* 5,910,523 (1999).
97. D. Li, D. G. Peiffer, C. W. Elspass, and H. C. Wang, Rubber toughened thermoplastic resin nanocomposites, *US Patent* 6,060,549 (2000).
98. M. Alexandre, P. G. Dubois, R. J. E. Jerome, M. Garcia-Marti, T. Sun, J. M. Garces, D. M. Millar, and A. Kuperman, Polyolefin nanocomposites, *US Patent* 6,465,543 B1 (2002).

99. S. G. Niyogi, Nanocomposites made from polypropylene graft copolymers, *US Patent* 6,451,897 B1 (2002).
100. C. J. Chou, E. I. Garcia-Meitin, L. Schilhab, and R. F. Fibiger, Thermoplastic olefin nanocomposite based on polypropylene and process for production thereof, Eur. Patent EP1268656 B1 (2005).
101. J. S. Rosenthal and M. D. Wolkowicz, Method for making polyolefin nanocomposites, *US Patent* 6,864,308 B2 (2005).
102. D. B. Redd and R. A. Ottaviani, Nanocomposite color concentrate pellets, WO 2005/087851 A1.
103. V. Antochshuk and M. Jaroniec, *Chem. Mater.*, **12**, 2496 (2000).
104. L. Mercier and T. J. Pinnavaia, *Chem. Mater.*, **12**, 188 (2000).
105. J. R. Rice, *J. Appl. Mech.*, **35**, 379 (1968).
106. K. B. Broberg, *Int. J. Fract.*, **4**, 11 (1968).
107. W. Y. F. Chan and J. G. Williams, *Polymer*, **35**, 1666 (1994).
108. D. E. Mouzakis, F. Stricker, R. Mulhaupt, and J. Karger-Kocsis, *J. Mater. Sci.*, **33**, 2552 (1998).
109. S. C. Wong and Y. W. Mai, *Polym. Eng. Sci.*, **39**, 356 (1999).
110. S. Hashemi, *Polym. Eng. Sci.*, **40**, 798 (2000).
111. S. C. Tjong, S. A. Xu, and Y. W. Mai, *J. Polym. Sci. B Polym. Phys.*, **40**, 1881(2002).
112. S. C. Tjong, S. A. Xu, R. K. Y. Li, and Y. W Mai, *Compos. Sci. Technol.*, **62**, 831 (2002).
113. S. C. Tjong, S. A. Xu, R. K. Y. Li, and Y. W. Mai, *Compos. Sci. Technol.*, **62**, 2017 (2002).
114. E. Clutton, *Fracture Mechanics Testing Methods for Polymers, Adhesives and Composites* A. Pavan and J. G. Williams (eds.), ESIS 28, Elsevier Science, Oxford, 2001, pp. 177–195.
115. J. S. Wu, Y. W. Mai, and B. Cotterell, *J. Mater. Sci.*, **28**, 3373 (1993).
116. L. Fasce, C. Bernal, P. Frontini, and Y. W. Mai, *Polym. Eng. Sci.*, **41**, 1 (2001).
117. K. C. Chiou, F. C. Chang, and Y. W. Mai, *Polym. Eng. Sci.*, **41**, 1007 (2001).
118. S. C. Tjong, S. A. Xu, and Y. W. Mai, *Mater. Sci. Eng. A*, **347**, 338 (2003).
119. E. C. Y. Ching, R. K. Y. Li, S. C. Tjong, and Y. W. Mai, *Polym. Eng. Sci.*, **43**, 558 (2003).
120. S. C. Tjong, S. A. Xu, and Y. W. Mai, *Polym. Compos.*, **24**, 437 (2003).

Part IV

Advance Polyolefin Nano and Molecular Composites

Chapter 15

Polyolefin/Clay Nanocomposites: Theory and Simulation

Anna C. Balazs,[1] Jozef Bicerano,[2] Valeriy V. Ginzburg[3]

15.1 INTRODUCTION

Polyolefin–clay nanocomposites (PNC) represent an interesting new class of materials with potential utility in many areas (automotive, tires and rubber, packaging, etc.) (1–25) Because of the structure and geometry of clay nanofillers (Fig. 15.1), they can provide extremely high surface-to-volume ratio, which is not attainable when more conventional fillers (glass fibers, carbon black, etc.) are used. This, in turn, results in a substantial property modification in a nanocomposite (compared to pristine polymer) at relatively small filler loadings. For example, in the nylon 6–clay nanocomposite, researchers achieved twofold increase in Young's modulus over the pure polymer by adding just 2 wt% clay (1–3). A similar ''stiffening'' effect was observed for several other polymer matrices (polypropylene (PP) (4–11), polyethylene (PE) (11–13), polyurethane (PU) (14,15), and epoxy (16,17)). It is also shown that addition of clay could improve may other properties (gas permeability, flame retardancy, etc.) (18–25).

Despite their initial successes (e.g., Toyota and GM used polypropylene–clay nanocomposites to make parts for automobiles (26)), nanocomposites have not yet found wide application in industry. For polyolefins in particular, preparation of PNCs is extremely challenging. Quite often, adding clay does not increase modulus very much, but instead, dramatically decreases toughness or elongation at break, as

[1]Department of Chemical and Petroleum Engineering, University of Pittsburgh, Pittsburgh, PA 15261, USA
[2]Bicerano & Associates Consulting, Inc., 1208 Wildwood Street, Midland, MI 48642, USA
[3]The Dow Chemical Company, Building 1710, Midland, MI 48674, USA

Polyolefin Composites, Edited by Domasius Nwabunma and Thein Kyu

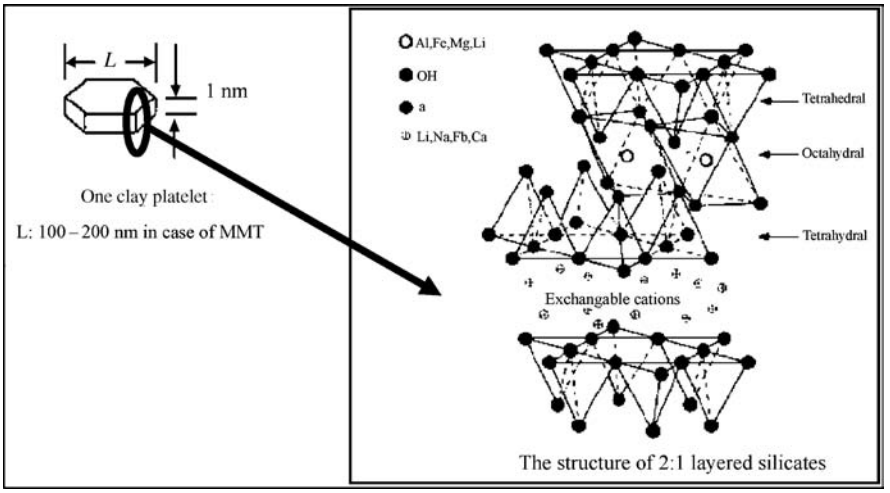

Figure 15.1 Schematic representation of the shape and dimensions of a clay platelet (left) and the chemical structure of the silicate layer (right). (From Reference 25 with permission from Elsevier.)

compared to the original polymer. Most often, this is due to the poor dispersion (distribution on a large scale) and/or poor exfoliation (distribution on a microscale) of clay platelets in the polymer matrix. Because of the strong hydrophilicity of the clay surfaces and the strong hydrophobicity of the polyolefin chains, there is a significant enthalpic driving force for clay platelets to stick together. This is further aggravated by the entropic penalty for putting polymer chains near the surfaces. As a result, unmodified clay tends to remain in stacks when melt mixed with polyolefin polymers. Even if those stacks are broken up by shear forces in a mixer or extruder, it is still thermodynamically favorable for the platelets to reaggregate when shear is removed. Thus, it is necessary to perform costly process of organic modification of the clay platelets, putting small hydrocarbon chains on their surfaces. Even then, thermodynamics of clay platelet mixing with polymer remains often unfavorable, as will be discussed in more detail below.

Why is it so critical to achieve good dispersion and exfoliation? A simple answer is that, once clay platelets assemble into stacks, their behavior begins to resemble that of more conventional, micron-size fillers. Surface-to-volume ratio and effective shape anisotropy become fairly small, and so does any property enhancement (with regards to modulus or gas permeability). However, clay stacks act as stress concentrators, and the material is likely to become more brittle than pure polymer (although this statement is certainly not universal). The influence of incomplete exfoliation on the properties has been modeled very extensively in recent years and will be discussed in detail below, as well.

What, then, are the challenges to successfully prepare polyolefin–clay nanocomposite for any given application? In our view, these are the main three:

- Chemistry—finding the right ''surfactant'' or organic modifier to ensure that clay is thermodynamically compatible with the matrix.

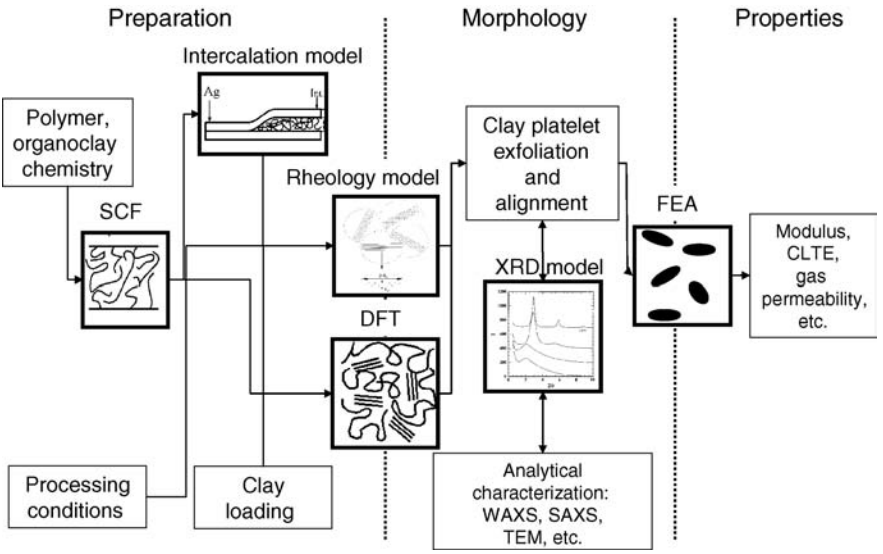

Figure 15.2 Relationship between various models described in this review. SCF: self-consistent field theory; DFT: density functional theory; XRD: X-ray diffraction; FEA: finite-element analysis; CLTE: coefficient of linear thermal expansion; WAXS: wide-angle X-ray scattering; SAXS: small-angle X-ray scattering; TEM: transmission electron microscopy. Boxes with pictures and bold black borders represent various models; boxes with text and thin black borders describe various inputs (experimental conditions) and outputs (morphology or properties to be determined).

- Processing—ensuring that clay platelet exfoliation and alignment is helped ''along the way'' (strong shear, solvent-based processes, etc.).
- Properties–linking the morphology of the nanocomposite (clay volume fraction, degree of exfoliation, and alignment) to the desired property enhancement (modulus increase or gas permeability decrease).

Theory and modeling play important roles in solving those challenges, for polyolefin-based, as well as for many other, systems. Some modeling approaches reviewed here were discussed in our earlier papers (27,28); here, we are trying to give a more comprehensive, if less detailed, picture. The idealized ''flowchart'' of various models reviewed in this chapter is given in Fig. 15.2. Not all pieces are understood equally well, and a lot of work is needed for modeling to become truly predictive. Below, we describe various models and their applications in more detail.

15.2 NANOCOMPOSITE MORPHOLOGY, THERMODYNAMICS, AND PHASE BEHAVIOR

The first major piece in our understanding of the properties of polymer–clay nanocomposites concerns the equilibrium phase behavior of the mixture. Whether or not the system forms a uniform dispersion depends not only on processing but also

ultimately on the thermodynamic considerations. Even if well-separated, isolated clay sheets are intermixed with polymers, these high-aspect ratio platelets can form ordered or crystalline structures, or can phase separate from the matrix material. The task of describing the stability and morphology of polymer–clay mixtures can be divided into two parts: (i) determining the polymer-mediated interactions between the clay sheets and (ii) calculating phase diagrams as a function of the mixture's composition once these interactions are known. In effect, the problem involves analyzing the system on two different length scales. To obtain information about the nanoscale interactions among the organic modifiers, the underlying clay sheets, and the polymer chains, one can treat the sheets as infinite, planar surfaces. To probe the macroscale behavior of the entire system, the clay disks can be treated as rigid particles that are dispersed in an incompressible fluid and interact via excluded-volume and effective long-range potentials. The first problem deals with the properties of polymers confined between the clay surfaces, while the second problem concerns the thermodynamics of anisotropic colloidal particles in a melt or solution. To accurately describe the equilibrium behavior of polymer–clay mixtures, we ultimately must address both these issues.

15.2.1 Exfoliated, Intercalated, and Immiscible Nanocomposite Morphologies

Traditionally, polymer–clay nanocomposites can be divided into three main morphologies: exfoliated, intercalated, and immiscible (Fig. 15.3). Exfoliated morphologies correspond to situation where single-clay platelets are well dispersed in the polymer matrix. Immiscible morphologies are those where large stacks (aggregates) of clay platelets are dispersed in the matrix, so the material becomes almost a conventional composite (with micron-size fillers). Finally, intercalated morphologies represent an ''intermediate'' situation where clay platelets exist in stacks, but polymer molecules penetrate into the ''galleries'' between adjacent platelets.

Qualitative—if not always quantitative—understanding of the driving forces for exfoliation could be obtained by analyzing thermodynamics of polymers confined in the gallery between two parallel clay platelets. As the matrix polymer penetrates into the gallery, its entropy decreases substantially due to confinement; this decrease in entropy needs to be balanced by some gain in enthalpy if exfoliation or intercalation was to occur. The goal of modeling, then, is (i) to develop a formalism to predict free energy of polymers in the galleries and (ii) to use this formalism to suggest the ways of improving the probability of exfoliation or intercalation.

The formalism in question is based on the notion of calculating the free energy of polymers in the gallery, F, as function of the gallery width h. In their pioneering studies, Vaia and Giannelis (29,30) used a simple mean-field lattice model to predict $F(h)$ for a mixture of matrix homopolymer and organically modified silicates. Balazs et al. (31–35) used both numerical and analytical self-consistent field (SCF) theories to calculate such free energy profiles, $F(h)$, for a variety of model systems. As shown

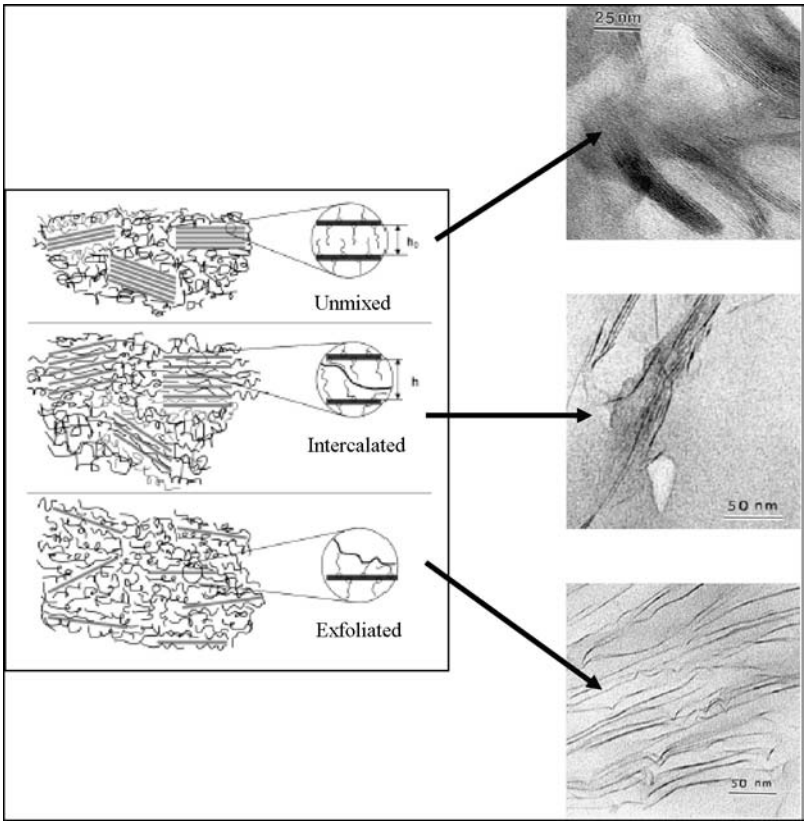

Figure 15.3 Schematic representation (left) and illustrative TEM micrographs (right) of unmixed (immiscible), intercalated, and exfoliated polymer–clay nanocomposites. Micrographs represent: (top) epoxy–organo-MMT nanocomposite (10 wt% clay); (middle) PS–organo-MMT nanocomposite (5 wt% clay); (bottom) PS–organo-MMT nanocomposite (3 wt% clay). (From Reference 64 (cartoons) and Reference 52 (TEM micrographs) with permission from Elsevier and Wiley, respectively.)

in Fig. 15.4, monotonically increasing $F(h)$ corresponds to immiscible morphology; monotonically decreasing $F(h)$ corresponds to exfoliated morphology; and $F(h)$ with a minimum at some finite h represents intercalated morphology. (These predictions, strictly speaking, are exact in the limit of very low clay loadings; at higher clay loadings, clay–clay excluded volume interactions sometimes could dramatically change the morphology.)

As mentioned above, the method mostly used in calculating $F(h)$ is the lattice SCF theory, first proposed by Scheutjens and Fleer (36–38) to study polymers near surfaces and interfaces. Within SCF, polymer melt is assumed to be incompressible, and polymers themselves are treated as ideal Markov chains on a lattice. To reduce a multibody problem to a single-body one, the mean-field approximation is taken, so the free energy of the system is expressed in terms of segment density distribution for segments of various types. We refer the reader to original papers by Scheutjens and

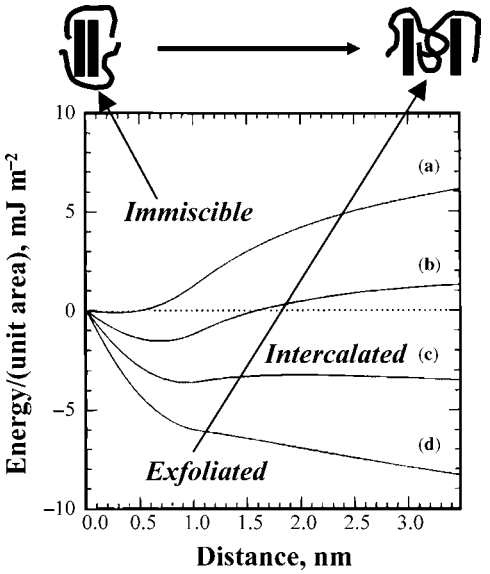

Figure 15.4 Modeling of clay intercalation and exfoliation by mean-field theory of polymers in the "galleries" between adjacent clay platelets in a stack. (From References 28 and 29 with permission from Taylor and Francis and the American Chemical Society, respectively.)

Fleer (37,38) and Balazs and coworkers (31–35) for detailed description of the method and its application to polymer–clay nanocomposites.

15.2.2 Tailoring Polymers and Clays to Promote Exfoliation

SCF-type modeling was used to investigate the properties of three distinct classes of polymer–clay mixtures. First case considered was that of untreated clay particles in a melt of nonfunctionalized polymers. The second case involved a mixture of polymers with pretreated clay particles (where surfactants are grafted on each clay sheet). Finally, the third case corresponded to the dispersion of clay particles (either pristine or organically modified) in a melt of functionalized macromolecules. In such a system, some or all of the matrix polymers have functionalized groups that are strongly attracted to the clay surfaces. Modeling results for all three cases are summarized below.

15.2.2.1 Untreated Clay, Nonfunctionalized Homopolymer

This is the simplest possible scenario, and the one that would be the most useful for practical applications. The two relevant parameters in the problem are the degree of polymerization of the polymer P and the Flory–Huggins interaction parameter

between the polymer and the clay surface, χ_{PC}. Polymer chain length P determines the entropic loss upon polymer confinement; thus, increasing P makes intercalation and/or exfoliation more and more difficult thermodynamically. (Note that we do not discuss dynamic limitations for intercalation as P increases above entanglement length—this is a completely separate topic.) Flory–Huggins parameter χ_{PC} determines the enthalpic gain or loss upon intercalation or exfoliation. If $\chi_{PC} < 0$ (there is preferential attraction of polymer to clay), spontaneous exfoliation is possible, provided that enthalpic gain overcomes entropic loss. If, however, $\chi_{PC} > 0$, free energy profile $F(h)$ is a monotonically increasing function, and intercalation or exfoliation is thermodynamically unfavorable.

Balazs et al. (31) added an important caveat to this thermodynamic analysis. In cases where $\chi_{PC} < 0$, exfoliated state could indeed be the most favorable thermodynamically; however, multiple attraction of various monomers on each chain to the adjacent platelets could lead to bridging intercalation. Thus, achieving fully exfoliated state would become an extremely slow process. This prediction was indeed confirmed by molecular dynamic simulations of Loring and coworkers (39–41). We will discuss the dynamics in more detail in Section 15.3.

Based on the above discussion, it is clear that achieving exfoliated morphology for unmodified clay in a nonfunctionalized homopolymer is fairly difficult task. Unless the polymer is strongly polar and has some attraction to the clay surfaces, the only hope of achieveing reasonable exfoliation is to perform *in situ* polymerization (see, e.g., Reference 4). Achieving exfoliation or even intercalation during melt compounding would be very difficult. Thus, to promote exfoliation, modification of clay, polymer, or both is strongly desired.

15.2.2.2 Organically Modified Clay in a Homopolymer Melt

To improve clay platelet dispersion, one can use the process of organic modification of the clay surface. In this process, short-to-intermediate organic chains are chemically grafted onto the surface of the clay. (For the details of this so-called ion-exchange process, we refer the reader to reviews 19 and 25). The role of these grafted chains is twofold: (i) balance entropic losses of the matrix polymer upon the increase in the interlayer spacing and (ii) provide better chemical compatibility with matrix polymer and reduce enthalpic losses. As Vaia and Giannelis wrote (30), ''The entropy loss associated with confinement of a polymer melt is not prohibitive to hybrid formation because an entropy gain associated with layer separation balances the entropy loss of polymer intercalation, resulting in a net entropy change near zero. Thus, from the theoretical model, the outcome of hybrid formation via polymer melt intercalation depends on energetic factors which may be determined from the surface energies of the polymer and organoclay.''

In a series of papers (31–33), Balazs and coworkers investigated the role of various factors in determining the ''morphology map'' for polymer–organoclay systems. In the first study, they varied the polymer–surfactant interaction parameter, χ_{PS}, while keeping fixed the length of the surfactants at $N_{gr} = 25$, and the grafting density at $\rho_{gr} = 0.04$. Figure 15.5 shows the $F(h)$ profiles for various values of χ_{PS}.

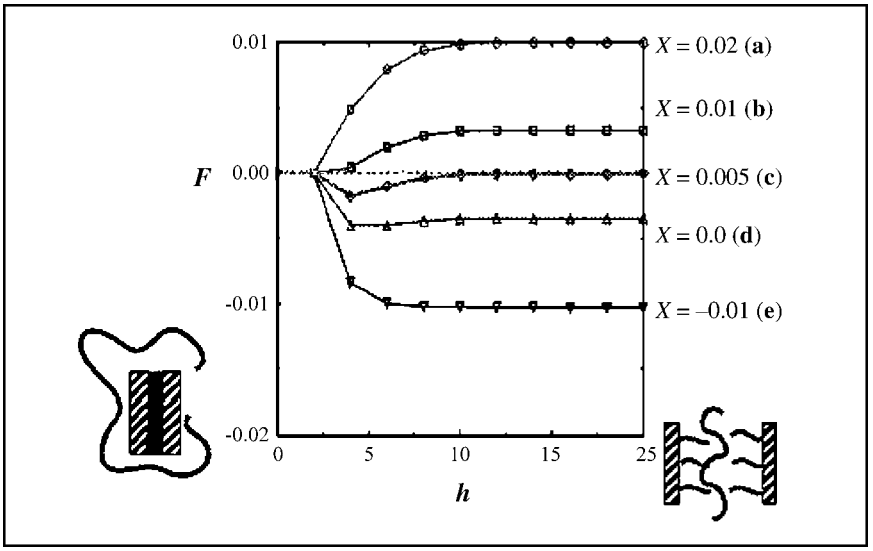

Figure 15.5 SCF-calculated free energy profiles for several model polymer–organoclay systems with varying polymer–surfactant Flory parameter χ. (From Reference 31 with permission from the American Chemical Society.) See text for more details.

For $\chi_{PS} > 0$ (cases (a) and (b)), $F(h) > 0$ and, consequently, the corresponding mixture would be immiscible. For $\chi_{PS} \cong 0$ (cases (c) and (d)), the plots show distinct local minima with $F(h_{min}) < 0$. Such local minima indicate that the mixture forms an ''intercalated'' structure (29). For $\chi_{PS} < 0$ (case (e)), the plot indicates that there is a global minimum at large (infinite) separations. Such plots point to an ''exfoliated'' structure (29), where the sheets are effectively separated from each other and dispersed within the melt. Thus, from a purely thermodynamic argument, we see that increasing the attraction between the polymers and surfactants promotes the formation of stable composites and could result in the creation of exfoliated structures.

Increasing the length of the polymers (P) increases the disparity in the lengths of the free and grafted chains and increases the values of $F(h)$ relative to those in Fig. 15.5. Thus, increasing P promotes phase separation and requires more attractive χ_{PS} in order for the system to be miscible. One way of decreasing the disparity between the free and tethered chains is to increase the length of the surfactants. Figure 15.6 shows the free energy profiles at various surfactant lengths ($N_{gr} = 25, 50,$ and 100) for $\chi_{PS} = 0$, 0.01, and 0.02. The grafting density is fixed at $\rho_{gr} = 0.04$. For the $\chi_{PS} = 0$ case, increasing the length of the tethered chain alters the structure of the composite from intercalated to exfoliated. More dramatically, for $\chi = 0.01$, increasing N_{gr} drives an immiscible mixture to form a thermodynamically stable intercalated hybrid.

The interactions between the short surfactants and long polymers are characterized by a sharp, thin interface and little interpenetration between the

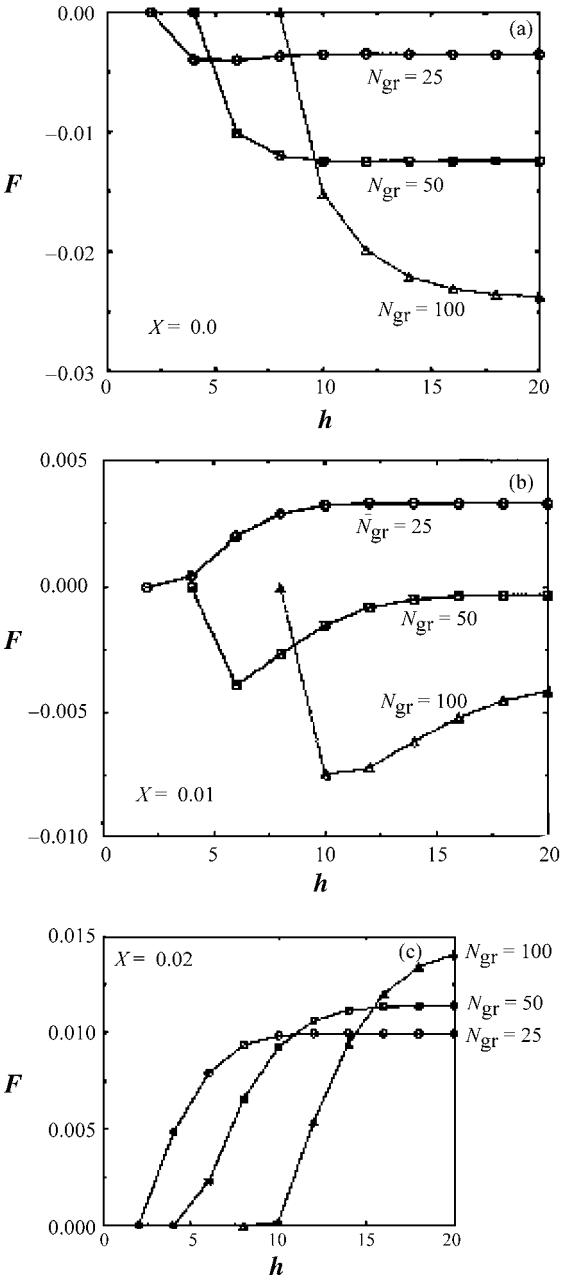

Figure 15.6 SCF-calculated free energy profiles for several model polymer–organoclay systems with varying surfactant lengths N_{gr}. (From Reference 31 with permission from the American Chemical Society.) See text for more details.

different chains (31). In contrast, when the polymer and surfactant are of the same length ($N_{gr} = P = 100$), the interaction between the species leads to a broad interface, or ''interphase,'' which allows the polymers more conformational degrees of freedom and, therefore, is more entropically favorable. As a result, the values of $F(h)$ are lower for the longer surfactants. Thus, within at least some finite range of polymer–surfactant interactions, the miscibility and morphology of the composite can be tailored by increasing the surfactant length. These observations are in agreement with recent experiments on the fabrication of nanocomposites with organically modified clays and polystyrene–polybutadiene block copolymers (42). The researchers found that increasing the length of the alkyl chains in the clay promoted insertion of the copolymer, whereas no insertion was observed with the shorter alkyl chains. They also noted that the longer the alkyl chain, the greater the compatibility with the polystyrene block and the greater the effective strength of the material.

Balazs et al. (31) also studied the role of increasing ρ_{gr} while keeping N_{gr} constant. It was shown that the dependence of the morphology on ρ_{gr} is not monotonic or trivial. At low ρ_{gr}, increasing surfactant density obviously favors intercalation or exfoliation. As the surfactant layer becomes denser, however, it becomes harder for the free chains to penetrate and intermix with the tethered species. At high ρ_{gr}, more attractive (negative) values of χ_{PS} are needed to promote polymer penetration into the interlayer. The comparison points to the fact that there is an optimal grafting density for forming polymer–clay composites. This conclusion was qualitatively supported by recent experimental studies of Galvin and coworkers (43) for various organoclay–polymer melt-compounded systems.

15.2.2.3 Functionalized Polymers

Yet another way of improving compatibility between polymer and clay is to modify the polymer by adding some ''stickers'' that have strong affinity to clay surface. Typical example of this is the use of maleated polypropylene or polyethylene; maleated chains can easily adsorb onto clay surfaces. For such systems, enthalpic gains due to adsorption can, ideally, overcome entropic losses due to chain confinement.

How many ''stickers'' per chain should there be? Intuitively, one could think that having more than one sticker per chain would increase the probability of intercalation, as the enthalpic driving force goes up. However, having more than one sticker also increases the probability of ''bridging intercalation.'' Indeed, using numerical and analytical SCF theory, Zhulina et al. (32) showed that two-sticker telechelic chains often could favor intercalated morphology over exfoliated one. Subsequent in-depth study by Kuznetsov and Balazs (34,35) suggested, however, that under the right conditions, telechelic chains could promote exfoliated morphology. In particular, it is necessary to have sufficiently large attraction between stickers and clay surfaces, as well as sufficiently large volume fraction of functionalized chains in the melt. It has to be noted, however, that even in those cases, modeling found metastable intercalated states that could dramatically slow down the exfoliation process.

The likelihood of having intercalated—rather than exfoliated—morphology would be even stronger for the case of multiple stickers on a single chain. Thus, the best-case scenario would be to have a single functional group attached at the end of some—or all—matrix chains. This was the case considered by Ginzburg and Balazs (44). Their model system consisted of organoclay, matrix homopolymer with chain length $P = 300$, and end-functionalized homopolymer with chain length $N = 100$. End-functionalized chains constituted a small fraction (5 wt% or 5 vol%) of the overall polymer present in the system. Using numerical SCF, researchers found the dependence of the stable morphology on the energy of sticker adsorption onto the clay surface, ε. For the particular case considered, transition from immiscible to exfoliated morphology was found at $\varepsilon \approx 4k_BT$—as adsorption of stickers becomes stronger, more and more chains prefer to adsorb onto clay surfaces and push the platelets apart.

15.2.3 Modeling Macroscopic Phase Behavior of Polymer–Clay Mixtures

In the studies discussed above, researchers determined conditions for clay exfoliation by studying the free energy profiles of polymers confined between two surfaces. In order to determine the equilibrium morphology of a given system, however, it is important to consider other factors, such as the clay volume fraction and the geometric characteristics of the clay sheets, such as aspect ratio, $A_f = D/H$, where D is the platelet diameter and H is the thickness. For this calculation, one must utilize more macroscopic models than the SCF. These models were based on the ideas developed in the theory of anisotropic colloidal particles dispersed in polymer melts or solutions.

The first model addressing the relationship between nanocomposite morphology, on the one hand, and platelet geometry, clay loading, polymer chain length, and clay–polymer interaction, on the other, was proposed by Lyatskaya and Balazs (45). That model considered the possibility of orientational ordering of the platelets. In a mean-field fashion, using Onsager-type model (46), researchers calculated free energy and chemical potentials for isotropic (orientationally disordered) and nematic (orientationally ordered) phases and also found two-phase coexistence region. The model correctly predicted, in particular, that in case when polymer–clay Flory–Huggins parameter, χ_{PC}, is positive, coexistence region expands dramatically (Fig. 15.7). Thus, at a finite clay loading, the system would be a mixture of clay-rich aggregates (''stacks'') and practically clay-free polymer. It was also shown that as the clay diameter increases, miscibility transition near $\chi_{PC} = 0$ becomes sharper, and the ''solubility'' of clay in polymer at any given positive χ_{PC} decreases dramatically.

The next step in modeling macroscopic phase behavior of polymer–clay systems was made by Ginzburg and Balazs (44,47,48), who developed a new density functional theory (DFT)-based formalism. Their treatment was based on the Somoza–Tarazona (49,50) DFT describing various mesophases of anisotropic hard bodies (Fig. 15.8).

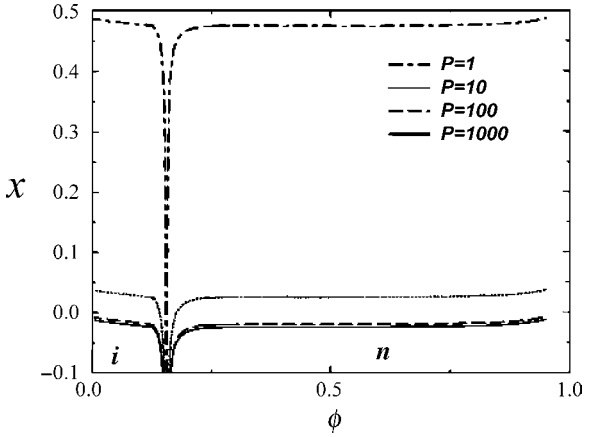

Figure 15.7 Phase diagram of polymer–disk mixture calculated using Onsager-type model. Here, ϕ is the volume fraction of disks and χ is the Flory parameter between the disk and the matrix. Phases: i, isotropic (orientationally disordered); n, nematic (orientationally ordered). Various coexistence curves correspond to varying matrix chain lengths: from $P = 1$ (monomer or solvent) to $P = 1000$ (ultrahigh molecular weight polymer). Region above a coexistence curve corresponds to the two-phase (immiscible) composites. (From Reference 45 with permission from the American Chemical Society.)

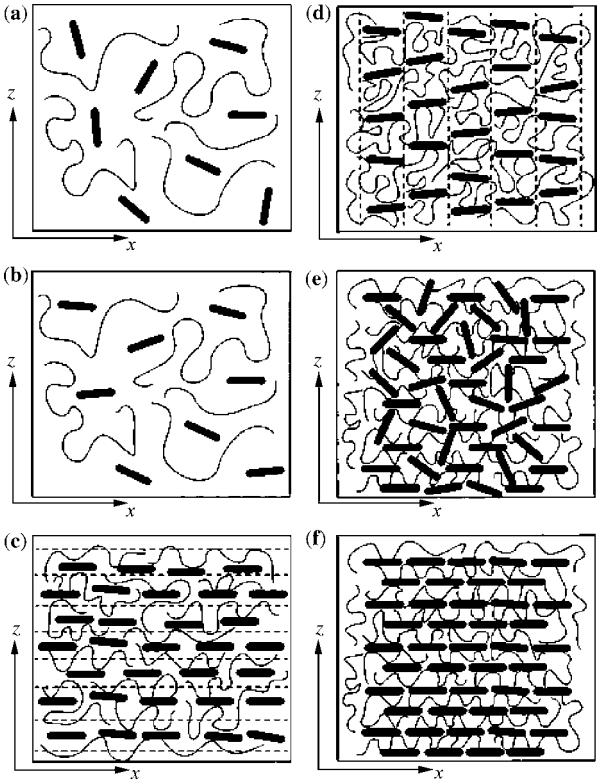

Figure 15.8 Mesophases of oblate uniaxial particles dispersed in polymer: (**a**) isotropic; (**b**) nematic; (**c**) layered smectic; (**d**) columnar; (**e**) isotropic gel; and (**f**) crystal. (From Reference 48 with permission from the American Chemical Society.)

In the Somoza–Tarazona approach, the free energy of a system of hard ellipsoids of revolution is written as a functional of the single-particle distribution function $\rho(\boldsymbol{r}, \boldsymbol{n})$, describing both positional and orientational ordering of the platelets. To this purely geometrical free energy, a perturbation term was added describing polymer-induced attraction or repulsion between the platelets. This term was evaluated by integrating the SCF-calculated free energy profile $F(h)$ over the platelet area (in the spirit of the well-known Derjaguin (51) approximation used in the theory of colloids). As illustrated in Fig. 15.9, this two-scale model allows one to directly predict morphology from formulation. In particular, it predicts that the presence of a small amount of end-functionalized chains in the melt (e.g., a few percent of maleated polypropylene added to polypropylene melt) can lead to the formation of favorable aligned and exfoliated structures, provided that the strength of adhesion of sticker to clay is tailored appropriately. These results are qualitatively in good agreement with various experimental observations (12,13), although it is somewhat difficult to make quantitative comparisons.

It is important to understand the limitations and approximations used in this model. It is assumed—implicitly—that (i) there is a thermodynamically stable polymer–inorganic hybrid phase and (ii) that clay platelets can be considered rigid bodies with little or no flexibility. Both assumptions are reasonably correct for small clays (laponite) but become somewhat inaccurate for larger clays like montmorrilonite or fluoromica. As the clay diameter increases, the likelihood of the formation of nonequilibrium structures becomes larger. The ultimate composite morphology would then depend substantially on the sample history and preparation conditions. As will be discussed later (Section 15.3), melt rheology plays an important role in determining the ultimate nanocomposite morphology upon solidification.

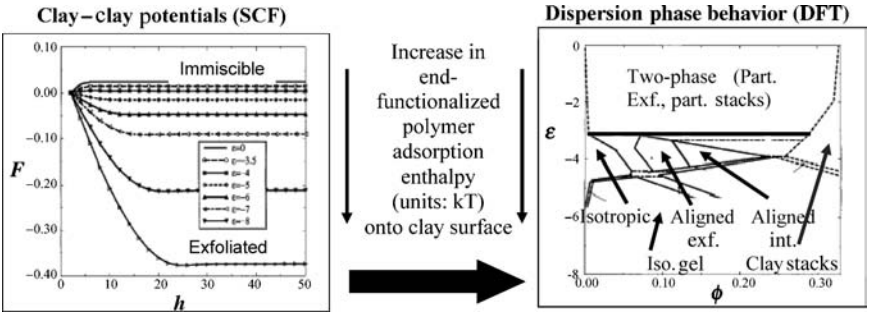

Figure 15.9 Example of a multiscale calculation combining SCF and DFT to predict thermodynamic behavior of polymer–clay nanocomposites. Polymer matrix consists of a homopolymer with chain length $P = 300$ and contains a small fraction ($\varphi = 0.05$) of end-functionalized chains with length $N = 100$. The energy of adhesion between the sticker and the clay surface, ε, is varied from 0 (no adhesion) to $-10k_BT$ (very strong adhesion). Clay platelets are modeled as oblate ellipsoids with $D = 30$ nm, $H = 1$ nm. Organic modifiers (surfactants) have length $N_{gr} = 5$, and grafting density $\rho_{gr} = 0.2$ chains per nm^2. All monomers are chemically identical ($\chi = 0$). For more details, see text. (From Reference 28 with permission from Taylor and Francis.)

15.2.4 Interpreting Morphology Using X-ray Scattering Data

As pointed above, most nanocomposite systems are only partially exfoliated even if thermodynamic conditions are favorable. The degree of exfoliation and the average number of layers per typical "stack" strongly depends on the sample history and processing conditions. Thus, it is important to be able to estimate these parameters experimentally.

It was emphasized by various authors (23,52–55) that no single experimental technique is sufficient to determine the degree of exfoliation in a nanocomposite. Typically, transmission electron microscopy (TEM) and wide-angle and small-angle X-ray scattering (WAXS and SAXS) are used to provide complementary information about a given sample. While TEM gives a qualitative picture of the clay platelet distribution in a given (and representative of the entire sample, hopefully) microscopic region, WAXS and SAXS provide volume-averaged information about the number density of scatterers and their geometry. If one can assume that clay platelets are the main sources of the X-ray scattering and that they are distributed uniformly through the sample, it is possible to develop a model relating WAXS and SAXS data to the statistics of clay platelets (single platelets versus multilayer stacks). Such a model was indeed developed by Vaia and coworkers (53–55). In this model, scattering intensity $I(q)$ is expressed as a function of the magnitude of the scattering vector $q = |\boldsymbol{q}| = (4\pi/\lambda)\sin(\Theta)$,

$$I(q) = KP(q)S'(q) \tag{15.1}$$

where K is the "normalization constant" (depending on the clay loading and the instrument characteristics), $P(q)$ is the single-particle form factor, and $S'(q)$ is the interference function. Based on the scattering theory of thin discs, Vaia and Liu (53) derive the following expressions for these functions:

$$P(q) = \int_0^{\pi/2} (\Delta\rho)^2 \left[\frac{\sin(qH\cos\beta)}{qH\cos\beta}\right]^2 \left[\frac{2J_1(qR\sin\beta)}{qR\sin\beta}\right]^2 \sin\beta d\beta \tag{15.2a}$$

$$S'(q) = f + (1-f)S(q) \tag{15.2b}$$

$$S(q) = \frac{1}{\langle N\rangle}\left[\langle N\rangle + 2\sum_{N=N_1}^{N=N_2}\sum_{n=1}^{n=N-1} p(N)(N-n)\exp\left\{-\frac{q^2\alpha^2 n}{4}\right\}\cos(qDn)\right] \tag{15.2c}$$

There are two types of parameters in Equation 15.2a–15.2c—those assumed to be known in advance (scattering contrast $\Delta\rho$, clay platelet thickness H, and radius R) and those describing mixture morphology (fraction of single layers, f; average number of layers per stack, $\langle N\rangle$; and degree of disorder within a stack, α). The probability distribution for the number of layers per stack, $p(N)$, can be assumed to be Gaussian, binomial, or some other—this could change the results slightly but not dramatically. Vaia and Liu used this model to evaluate the morphology of the dispersion of Cloisite 6A in toluene as function of clay loading. They obtained a fairly good agreement between experimental data and the best fit, especially in

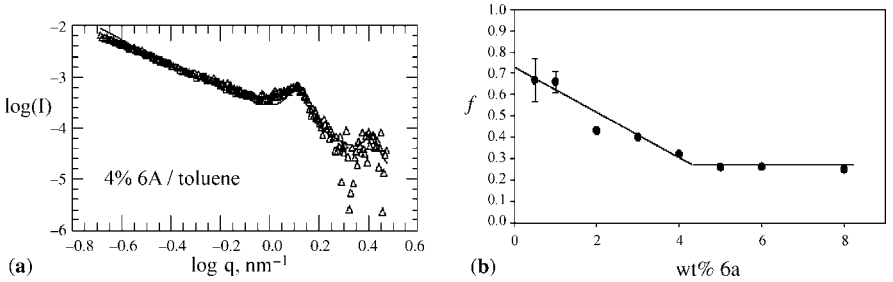

Figure 15.10 X-ray scattering analysis for polymer–clay nanocomposites. (**a**) X-ray scattering intensity data (triangles) and fit (line) for the toluene solution of organoclay Cloisite 6A; (**b**) calculated fraction of single layers, *f*, in Cloisite 6A–toluene solutions as function of organoclay weight percentage. See text for detailed description of the model used to calculate *f*. (From Reference 53 with permission from the authors.)

the wide-angle regime (Fig. 15.10a). In particular, they observed that the single-layer fraction *f* was a monotonically decreasing function of the clay loading (Fig. 15.10b), which is in a fair qualitative agreement with thermodynamic predictions. In their subsequent papers (54,55), Vaia and coworkers refined their model and applied it to explain additional WAXS and SAXS experiments in nanocomposites. Similar models were also proposed by various authors to describe small-angle neutron scattering (SANS) experiments. For example, Yoonessi et al. (56) applied a stacked-disk scattering model to estimate the degree of exfoliation and the average number of layers per stack in a poly(dicyclopentadiene)–montmorrilonite nanocomposite at several clay loadings. The results appeared to compare favorably with visual estimates from TEM and qualitatively agreed with the general trend that the degree of exfoliation decreases upon increasing clay loading.

It is important to emphasize again that the above models need to be used with some caution since they presume that nanocomposite is partially exfoliated and partially intercalated. If the scattering curve shows no peaks, this may be an indicator of a fully exfoliated nanocomposite—or a system with extremely poor miscibility, where a few macroscopic clay agglomerates are not contributing much to the scattering. To distinguish between these cases, additional examination by means of TEM is necessary; in many other cases, TEM analysis is still desired to ascertain the state of the nanocomposite, at least on a qualitative level. Combining the results from the scattering and microscopy experiments, one could obtain reasonable information about the degree of exfoliation and stacking; this information can then be used in predicting rheological and mechanical properties of polymer–clay mixtures.

15.3 NANOCOMPOSITE RHEOLOGY AND DYNAMICS

15.3.1 Intercalation Dynamics

It was recognized early on (57) that penetration of polymer into the galleries between clay sheets can be a complicated process. Dynamic behavior of polymers in confined geometries could be very different from that in the bulk, and mobility of the polymers

close to the clay surfaces could be strongly impacted by the polymer–clay interactions. As shown by Giannelis and coworkers (57,58), time dependence of the "degree of intercalation" $\chi(t)$, measured using SAXS technique, can be reasonably fitted assuming diffusive mechanism of polymer penetration into the galleries,

$$\chi(t) = 1 - \sum_{m=1}^{\infty} \frac{4}{\alpha_m} \exp\left[-\frac{D_{\text{eff}}}{R^2}\alpha_m t\right] \tag{15.3}$$

Here, D_{eff} is the diffusion constant of the polymer in the gallery, R is the platelet radius, and α_m is the mth positive root of the Bessel function of zeroth order, $J_0(\alpha) = 0$. Equation 15.3 has been very successful in describing wide variety of experimental data for the intercalation of polystyrene into organically modified clays (Fig. 15.11). Based on this, diffusion constant for the polymer penetration into the galleries could be estimated. It was found that (i) diffusion constant for polymers in the galleries, D_{eff}, was somewhat larger than bulk polymer self-diffusion constant, D_{self}; (ii) above entanglement molecular weight, D_{eff}, scales as P^{-1} as a function of the polymer chain length, P, while the bulk self-diffusion constant, D_{self}, scales as P^{-2}; and (iii) increasing affinity between the polymer and the clay surface (or surfactant chains on that surface) leads to the decrease in the effective diffusion constant. The last observation was especially important as it illustrated a major dilemma (formulated very succinctly by Balazs and coworkers (31,45))—increasing the attraction between polymer and clay surface is needed to provide thermodynamic stability of the exfoliated state, but it also dramatically slows down the diffusion of polymers into the galleries, as the polymers constantly get trapped into local energy minima.

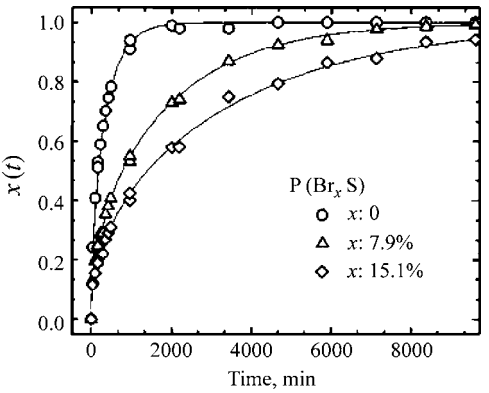

Figure 15.11 "Degree of intercalation", $\chi(t)$, measured by neutron scattering for a polystyrene–organoclay nanocomposite. Points illustrate experimental data; lines are best fits using Equation 15.3. For all three systems studied, polymer molecular weight, $M_w = 150\,\text{kg mol}^{-1}$, was kept constant, but the fraction of brominated segments (preferentially attracted to clay) was varied from 0% to 15%. As the "sticker" fraction increased, the diffusion constant correspondingly decreased. (From Reference 58 with permission from the American Chemical Society.)

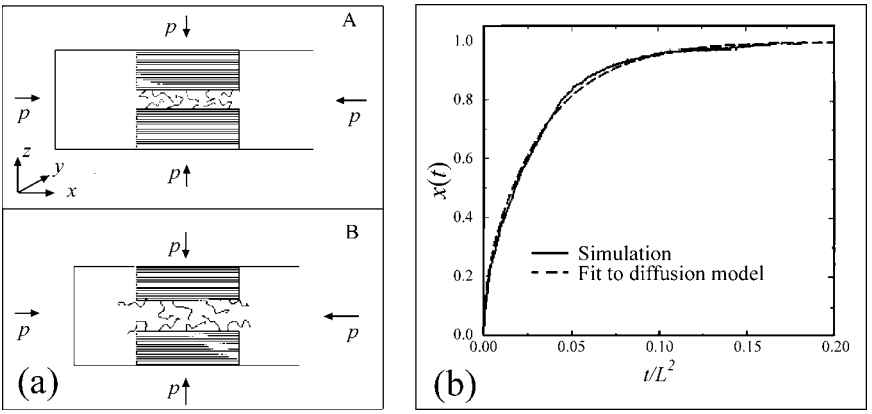

Figure 15.12 Molecular dynamic simulations of polymer intercalation into the galleries between adjacent clay platelets. (**a**) Schematic representation of the simulation setup. (**b**) Calculated "degree of intercalation" $\chi(t)$ for a diffusion of unentangled polymer into the slit. In the simulation, polymer chain length $P = 12$, while entanglement chain length $P_{ent} \sim 35$. Diffusion model derived by Lee and coworkers (39) is slightly different from Equation 15.3, but qualitative behavior is the same. (From References 39 and 40 with permission from American Institute of Physics.)

Diffusion of polymers into the galleries between two "solid" clay sheets was modeled in a series of papers by Baljon and coworkers (39–41). They utilized molecular dynamics (MD) technique and represented polymer chains using nonlinear bead–spring model of Kremer and Grest (59). Simulated geometry is shown in Fig. 15.12a, and a typical result depicting intercalation versus time is shown in Fig. 15.12b. Simulations clearly reproduce experimental trends fairly well. Baljon and coworkers (39,40) were able to reproduce several important experimental findings that intragallery diffusion can be faster than bulk diffusion and that increasing affinity between polymer and clay surface can inhibit the diffusion. In their subsequent study, Lee and et al. (41) also modeled the intercalation of diblock copolymers into the galleries.

Simulations of Baljon and coworkers assumed that the clay sheets were strictly rigid and parallel, with little or no flexibility. This assumption could be acceptable in cases of smaller clays (such as Laponite with $R \sim 30$ nm) but becomes inaccurate for larger clays like montmorrilonite ($R \sim 200$ nm) and fluoromica ($R \sim 1000$ nm). The issue of clay platelet flexibility was addressed by Ginzburg and coworkers (60,61). They proposed a "kink" mechanism of intercalation schematically shown in Fig. 15.13. Within their model, the gap between the two adjacent clay layers, $h(x,t)$, can be described by the following equation:

$$\xi \frac{\partial h}{\partial t} + EI \frac{\partial^4 h}{\partial x^4} + T \frac{\partial^2 h}{\partial x^2} + \frac{\delta F(h)}{\delta h} = 0 \tag{15.4}$$

where ξ is the friction coefficient (proportional to polymer bulk viscosity), E is the clay platelet Young's modulus, $I = H^3/12$ is the moment of inertia of a unit length of a clay sheet, T is the compressive force per unit length, and $F(h)$ is the

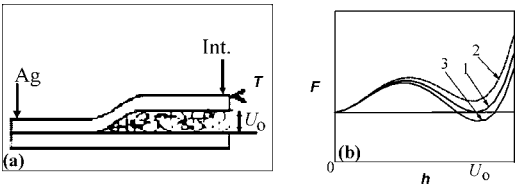

Figure 15.13 Model for the kink mechanism of intercalation. (**a**) Schematic depiction of the bending kink. (**b**) Model free energy profile $F(h)$ used to predict kink structure, energy, and threshold force for its appearance. Here, Ag corresponds to an ''agglomerated'' state, and Int corresponds to intercalated state; T is the external (shearing or compressing) force, and u_0 is the location of the free energy minimum (equilibrium gallery width) corresponding to the intercalated state. Various curves correspond to the situations when the energy of the intercalated state is equal to (1), higher than (2), or lower than (3) that of the agglomerated state. (From Reference 60 with permission from American Physical Society.)

effective clay–clay interaction potential per unit area. This equation can be solved—subject to appropriate initial and boundary conditions—to find ''kink''-like solutions. Such a kink would separate ''intercalated'' and ''closed'' regions on the same platelet. As the kink moves from the periphery to the center, the plate becomes more and more intercalated by the polymer. Although exact solutions could be found only in one-dimensional limit and only for specific functional forms of $F(h)$, one can solve Equation 15.4 numerically in two dimension for arbitrary potential and for various compressive force strengths T. As shown in Reference 60, in order for a kink to be formed, one needs to apply a compressive force $T > T^* = (2(EI)^{1/2}A^{1/2}/U_0)$ (threshold force); here, A and U_0 are parameters of the interaction potential $F(h)$ as shown in Fig. 15.13 $(A = 1/2(d^2F/dh^2)_{h=0})$. This threshold force T^* can be related to the threshold shear stress needed to initiate kink and separate the platelets. Our preliminary estimates showed this threshold shear stress to be on the order of 10^9–10^{10} Pa (unpublished work). This illustrates the need for strong shear in order to intercalate the clay platelets. However, further theoretical work is needed to better understand all aspects of intercalation, both in the melt and in solvent.

15.3.2 Nanocomposite Rheology

Melt rheology of nanocomposites has been studied extensively by experimentalists in the past two decades (62–67). In particular, the following were observed:

- Nanocomposites often lack time–temperature superposition that characterizes viscosity of most polymer melts.
- At low clay concentration, melts usually exhibit liquidlike behavior, while at higher clay concentration, there is a transition to solidlike behavior (Fig. 15.14a); this is very similar to the process of gelation (chemical or physical).
- Solidlike nanocomposite melts can become liquidlike following strong shear; they relax back to the solidlike state over the course of a very long relaxation process (hours or days).

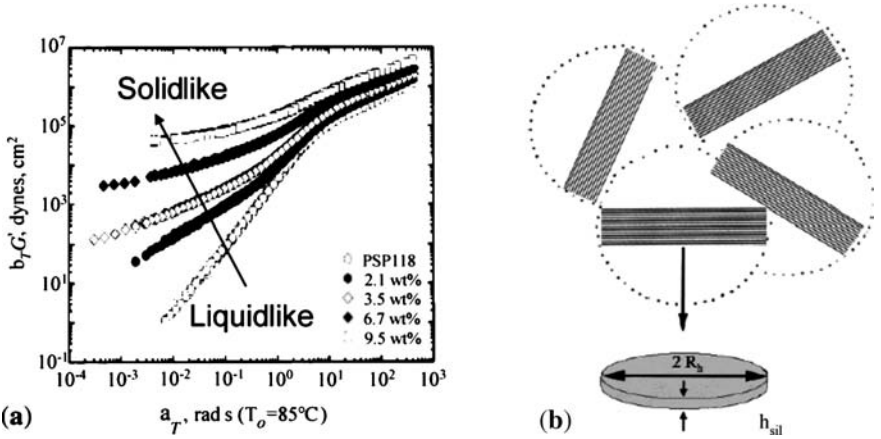

Figure 15.14 Nanocomposite rheology. (**a**) Experimental measurements of the time–temperature superimposed, frequency-dependent storage moduli, $G'(\omega)$, for nanocomposites of organically modified MMT with disordered PS-b-PI diblock copolymer. As the clay loading was increased, the rheological behavior of the melt transitioned smoothly from liquidlike to solidlike. Nanocomposite morphology was mainly intercalated for all cases. (**b**) Schematic representation of percolation model for the liquid–solid rheological transition. (From Reference 63 with permission from Taylor and Francis.)

Krishnamoorti and coworkers (62, 63, 67) proposed that most of these phenomena can be explained on the basis of the notion of percolation of the clay platelets (Fig. 15.14b). In case of disordered oblate ellipsoidal platelets, percolation threshold is given by (68):

$$p_c \approx \frac{9.875A_f^{-1} + A_f^{-2}}{7.742 + 14.61A_f^{-1} + 12.33A_f^{-1.5} + 1.763A_f^{-2} + 1.658A_f^{-3}}$$

where aspect ratio A_f is the diameter-to-thickness ratio (D/H). In the limit $A_f \gg 1$, $p_c \approx 1.275/A_f$. For oblate cylinders, the prefactor would be slightly different, but the linear dependence of percolation volume fraction on the aspect ratio would still remain. Thus, for clays with aspect ratio of ~ 200 (montmorrilonite), percolation threshold would correspond to ~ 0.5 vol%, assuming full exfoliation and no alignment. In case of partial exfoliation, percolation threshold would increase. Such simple estimates were indeed in reasonable agreement with experimental observations. It is also important to note that the above estimates assumed isotropic platelet orientation; in strong shear field, platelets can align and the percolation threshold would then increase.

While percolation arguments could qualitatively explain the changes observed in static (zero-shear) viscosity, explanation of the overall rheological spectra $G'(\omega)$, $G''(\omega)$ (oscillatory shear) or $\eta(d\gamma/dt)$ (steady shear) is still lacking. It appears that the nanofillers influence the behavior of $G'(\omega)$ and $G''(\omega)$ in both direct (formation of transient percolating nanofiller networks) and indirect (changing mobility of polymers near nanofiller surfaces) fashion. Recently, several computer simulations of nanocomposite melts were performed for in-depth analysis of both mechanisms (69–71). Detailed discussion of this topic is beyond the scope of our chapter.

The above discussion was primarily devoted to the understanding of nanocomposite behavior during preparation. We now turn our attention to the prediction of the properties of the nanocomposites themselves.

15.4 PREDICTION OF NANOCOMPOSITE PROPERTIES

15.4.1 Common Features Between Predictive Methods

The modeling of nanocomposite properties is an active topic of advanced research within the much broader area of the prediction of the morphologies and properties of multiphase materials. Bicerano (68) provides an overview where the prediction of nanocomposite properties is presented in this broader context.

All major methods for the prediction of the properties of polymer nanocomposites have certain common elements. In particular, they all require the input of certain key information about the relevant material properties of the matrix polymer and of the nanofiller; as well as information on the shape of the nanofiller, the morphology of the nanocomposite, and the nature of the interface between the polymer and the nanofiller.

The required input material properties depend on the nanocomposite property whose calculation is desired. For example, if one wishes to predict the elastic properties, the required input material properties normally include one of the elastic moduli (most commonly the elastic tensile modulus "E") and the Poisson's ratio "ν" for both the polymer and the nanofiller. If one wishes to predict the thermal expansion coefficients (α) of the nanocomposite in each of the principal axis directions, the values of E and ν for both the matrix polymer and the nanoplatelets are still required since the α values of a composite are "thermoelastic" properties that are affected by the elastic properties of the components, but in addition the α values of the matrix polymer and the nanoplatelets are also needed as additional input material parameters. However, if one wishes to predict the permeability of a nanocomposite to a particular type of gas, the permeability of the matrix polymer to that gas is generally the only required material parameter since the nanoplatelets are essentially impermeable to gases.

In the most elementary approaches, the shape of a nanoplatelet is characterized in terms of its "aspect ratio" A_f that indicates the extent of the characteristic anisotropy. For example, if a nanoplatelet is assumed to be shaped like a perfect thin disk, its shape can be described by the thickness/diameter ratio $(A_f \ll 1)$ or by the diameter/thickness ratio $(A_f \gg 1)$. Both of these alternative definitions of A_f are encountered in the literature. It is also possible for the shape to be far more complex, requiring the use of a more detailed description. For example, a nanoplatelet can have different "in-plane" principal axis directions, or it can be irregularly shaped. Furthermore, since a nanoplatelet only has a finite stiffness and it can be subjected to large bending moments during specimen preparation, it may end up in a "bent" or "wavy" shape in a nanocomposite. Finally, while the simpler predictive methods only consider the shape of a nanoplatelet but not its actual size, it is possible for

nanoplatelets (and/or their incompletely exfoliated stacks) to possess a range of sizes. Such more complex possible features of the nanoplatelet shape and size can only be accommodated by predictive methods of greater sophistication.

Similarly, the morphology of the nanocomposite itself can be described at many different levels of sophistication. At the simplest level of description, one can specify the volume fraction of nanoplatelets possessing identical A_f values that are assumed to all lie in the plane of the test specimen. This is the so called ''biaxial in-plane'' orientation. At more sophisticated levels of description, the morphology can be described in terms of the volume fractions of nanoplatelets possessing a distribution of A_f values, where the nanoplatelets may furthermore have a range of orientations within the specimen. In the most detailed levels of description, the possibility that the nanoplatelets may be bent or ''wavy,'' and the possibility that the nanoplatelets (or their stacks) may differ in size as well as in shape, may also be taken into account.

An issue of particular importance in modeling polyolefin nanocomposites is the fact that the matrix polymer is often semicrystalline. Consequently, the morphological features that are relevant to the prediction of nanocomposite properties are not limited to just the shape, size, volume fraction, distribution, and orientation of the nanoplatelets. It is also often important to consider the shape, size, volume fraction, distribution, and orientation of the crystallites, as well as the possibility that the crystallites and the nanoplatelets may interact and thus affect each other's distribution and orientation. In most predictive methods, these additional complications arising from crystallinity are neglected. In such methods, the so-called effective matrix approximation is used, whereby the semicrystalline polymer is approximated as a homogeneous matrix whose input material properties include the effects of the presence of a crystalline phase. In more advanced predictive methods, one can try to account for the presence of the crystalline phase explicitly by treating the nanocomposite as a triphasic system (consisting of an amorphous polymer phase, a crystalline polymer phase, and the nanoplatelets).

Another feature shared by all predictive methods is that they must address the issue of interfacial adhesion between the matrix polymer and the nanoplatelets. Most predictive methods make the approximation that there is perfect interfacial adhesion between the polymer and the nanoplatelets; so that, for example, there is 100% load transfer between these two phases upon mechanical deformation, and a gas molecule permeating the nanocomposite is diffusing entirely through the polymer phase. In fact, the assumption of perfect adhesion is so commonly made that many authors even neglect to mention that they have made this implicit assumption in their work. However, in many cases, this assumption may be inaccurate. For example, organically modified clays (where inorganic cations such as Na^+ or Ca^{2+} have been replaced by organic cations such as quarternary ammonium cations) are often used in nanocomposite fabrication in order to facilitate the dispersion of the nanoplatelets in the polymer matrix. The relatively small organic molecules incorporated into the nanocomposite as a result of the use of organically modified clays may disproportionately stay near the nanoplatelets in the nanocomposite. This type of behavior may weaken the interfacial adhesion between the matrix polymer and the nanoplatelets and may thus reduce the efficiency of load transfer. It may also create ''liquidlike''

paths of high permeability to gas molecules in the vicinity of the impermeable nanoplatelets. The most advanced predictive techniques can potentially account for such complexities to some extent. However, a truly realistic and accurate treatment of such effects is not possible at present since even the best model systems that can be built are still limited by the gaps in the current understanding of the fundamental physics of nanocomposites.

15.4.2 General Classes of Predictive Methods

As may be expected from the discussion in Section 15.4.1, methods for the prediction of the properties of nanocomposites are available at many different levels of complexity and detail. It is, however, possible to subdivide all of these methods into two general classes, namely, methods where the properties of a nanocomposite are predicted by using analytical (closed-form) model equations and methods where these properties are predicted by using numerical (most commonly, finite-element) simulations.

Methods based on analytical expressions have the advantage of greater simplicity since the equations can usually be solved by using a hand calculator or a simple spreadsheet program. Consequently, these methods can be applied with minimal effort and demand very little in terms of computational resources. This simplicity and ease of application, however, come at a price. The level of detail that can be taken into account and the accuracy of the predictions are both limited when analytical expressions are used. These limitations of models based on the analytical expressions of classical composite theory (or of adaptations of such models taking some of the unique aspects of nanocomposites into account at a rudimentary level) imply that such models are useful mainly for quick preliminary parametric screening studies, based on morphologies that are typically highly idealized compared with the true morphologies of the systems of interest. In attempting to use analytical expressions to predict the properties of nanocomposites, it is especially important to keep in mind that the inherent accuracy of such methods decreases both with increasing anisotropy and with increasing volume fraction of the nanofiller.

Detailed numerical simulations are required to make more accurate predictions based on models that are more realistic in their treatment of the relevant physics as well as in the extent to which the details of the nanocomposite morphology can be included in the description of the system of interest. For example, the results of detailed predictions of the morphology of a nanocomposite, obtained by means of simulations taking into account the thermodynamic and kinetic effects governing the fabrication process, can be "fed" directly as an input into software for the numerical simulation of the properties. The properties that can be predicted in this manner include the thermomechanical properties (and especially the properties describing the response to a small mechanical deformation and/or temperature change, such as the elastic moduli, compliances, and thermal expansion coefficients) and transport properties (and especially the gas permeability, gas diffusivity, thermal conductivity, electrical conductivity, and dielectric constant). It is also possible to construct

detailed model morphologies for actual nanocomposite samples directly by the automatic meshing of different two-dimensional electron micrographs (72) and use these highly realistic model morphologies to make detailed predictions of the properties. Finally, it is also possible to account for deviations from perfect adhesion at interfaces far more realistically in setting up the grids that will be used in numerical simulations than in deriving the equations of the analytical models.

Advances made in understanding and predicting the behavior of composite materials over the past half century have been instrumental in the exploitation of their immense technological potential (73). It can be anticipated that such advances will continue in the coming years, and that numerical simulation methods of increasing sophistication will play an important role as they are developed further and integrated more seamlessly with each other. In particular, when coupled more closely and used in combination with dynamic numerical simulation methods for morphology evolution (under development), numerical simulation techniques for nanocomposite properties will provide the opportunity to tailor the fabrication processes to obtain materials with morphologies that are most likely to provide the optimum properties.

Advances in computer hardware, and in particular the continued enhancement of the inexpensively available maximum central processor speeds and random access memory, have provided the ability to perform rapidly, on a well-equipped personal computer, numerical simulations that a decade ago may have required days of supercomputer time. Major developments in simulation software have also contributed to the enhancement of the power and accuracy of numerical simulation methods. In particular, ''adaptive meshing'' techniques, which enable the user to describe properly the morphologies of nanocomposites containing extremely anisotropic objects with sharp boundaries (such as thin nanoplatelets), have been essential in the advancement of the ability to simulate nanocomposite properties in a far more accurate and realistic manner than was possible by means of past meshing techniques that had been developed for representing the morphologies of conventional composites. The combined effect of all of these continuing advances is the gradually increasing the use of numerical simulations for the prediction of nanocomposite properties, at the expense of the use of simple but highly idealized analytical expressions. While the use of numerical simulations for the preliminary screening of candidate nanocomposite systems cannot yet be viewed as a routine product research and development approach as of the year 2006 when this chapter was written, it can be anticipated to become routine within the next 5–10 years.

It must be emphasized that the development of methods for the prediction of many other important properties of nanocomposites is still in its infancy because of the complexity of the governing physical phenomena. Such properties include the ultimate strength, the impact strength, and the ''toughness'' (total energy required to break a specimen), all of which are of course also functions of the mode and rate of deformation, and the ignition resistance. The development of appropriate models for the description and prediction of these properties is progressing slowly and gradually.

Examples of the use of both analytical expressions and numerical simulations will be provided in the next two subsections, in the contexts of the thermomechanical properties and the gas permeability respectively.

15.4.3 Thermoelastic Property Modeling

A general procedure based on analytical models, developed by Camacho et al. (74), can be used to predict roughly the thermoelastic properties of multiphase systems containing any number of components, of any shape, in any type of average orientation state, and of any number of layers.

1. The properties of a two-phase system consisting of a continuous ''matrix'' phase and a discontinuous ''filler'' phase are calculated in terms of the component properties and volume fractions. It is assumed that the thermoelastic properties within each phase domain are homogeneous and isotropic, and that there is perfect adhesion between adjacent phase domains. The shapes of the filler particles are assumed to have biaxial symmetry. Anisotropic filler particles (such as fibers or platelets) are oriented uniaxially at this stage of the calculation. Particle shape is described by the aspect ratio A_f (defined as the ratio of the largest dimension of the filler and its smallest dimension), and if $A_f \neq 1$ then also the filler may be fibrous (having one long and two short principal axis dimensions) or disklike (having two long and one short principal axis dimensions).
2. If another average orientation state besides uniaxial alignment is of interest for an anisotropic filler, orientation tensors are used to perform orientation averaging, as described by Advani and Tucker (75).
3. If there is more than one type of filler particle (differing in E, ν, α, and/or A_f), aggregate averaging is performed subsequently, in terms of the volume fractions of the components, to calculate the properties of the hybrid composite system.
4. If the composite system consists of more than one layer with different properties and/or orientations, lamination theory is used to predict the properties of this multilayer system as a function of the thicknesses, properties, and relative orientations of the layers.

The equations of Halpin and Kardos (76,77) (historically referred to as the ''Halpin–Tsai equations'') and Chow (78) are among the analytical models that are particularly useful and versatile when used in the first step of the modeling framework summarized above. The Halpin–Tsai equations have the advantage of greater simplicity. The Chow equations are far more complex and numerous, but they are sometimes more accurate.

Christensen (79) showed that platelets of high aspect ratio $(A_f \geq 100)$, when they are oriented randomly in three dimensions, should have roughly three times the stiffening effect of randomly oriented fibers.

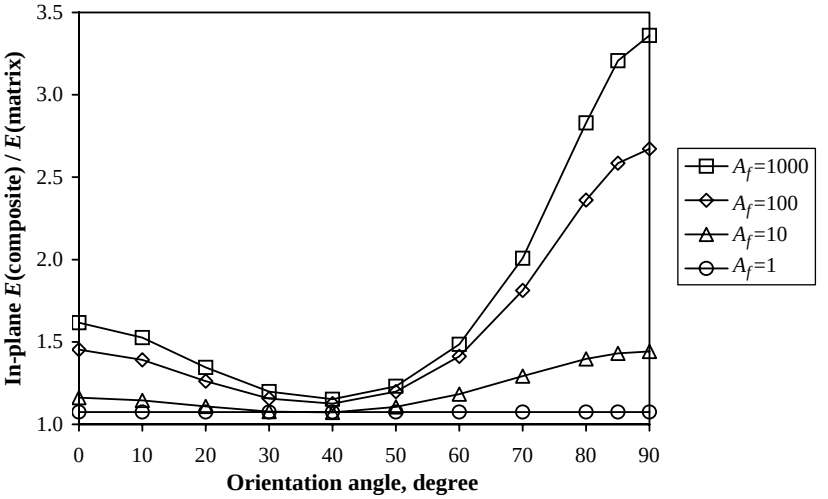

Figure 15.15 Effects of platelet orientation relative to the direction of deformation, predicted by using the model of Brune and Bicerano (80). The orientation angle is defined as the angle between the symmetry axis of the platelets and the direction of deformation, so that it is 90° if the platelets are aligned perfectly along the direction of deformation, while it is 0° if the platelets are aligned completely perpendicular to the direction of deformation. The curves are labeled by the platelet aspect ratio A_f. The platelet volume fraction was $\Phi = 0.025$, the platelets were assumed to have a Young's modulus of 100 times that of the matrix, and a Poisson's ratio of 0.4 was assumed for both the matrix polymer and the platelets in these calculations. (From Reference 68 with permission from Taylor and Francis.)

Brune and Bicerano (80) extended and refined some of the earlier models to account for the special morphological features of nanocomposites where the platelets are highly anisotropic, such as incomplete exfoliation and/or imperfect alignment that can both reduce the reinforcement efficiency significantly. For example, Fig. 15.15 shows that the off-plane deviations of the platelet orientation may cause large reductions in the in-plane Young's modulus. It is also seen that, because of the interplay between deformations in different directions as mediated by the anisotropic Poisson's ratio of the composite, the minimum reinforcement efficiency is predicted to occur at an intermediate orientation and not when the platelets are perfectly perpendicular to the deformation direction.

Fornes and Paul (81) used composite models to develop an improved understanding of the superior reinforcement observed for well-exfoliated nanocomposites relative to conventional glass fiber composites. Their work included an examination of the effects of incomplete exfoliation of the stacks of platelets in terms of reduction of reinforcement efficiency, with results that were similar to those obtained by Brune and Bicerano (80). More recently, Sheng et al. (82) reviewed the application of various micromechanical models to the prediction of polymer–clay nanocomposite modulus; special attention was paid to the determination of material parameters for

both clay and polymer matrix (e.g., the issue of crystallinity in polyolefin matrix was discussed at some length).

The work described above represents how far it has been possible to take analytical expressions in attempting to predict the thermoelastic properties of nanocomposites. As was discussed earlier, numerical simulation methods tailored to take into account the unique aspects of nanocomposite morphology are required in order to attain higher levels of realism and accuracy in predicting these properties. The state-of-the-art in the development of such techniques is represented by the work of Gusev (83) who developed a generic finite-element analysis (FEA) simulation method for the thermoelastic and transport properties of multiphase materials comprised of anisotropic phases that can be shaped and oriented arbitrarily. The consistent use of periodic boundary conditions in generating multi-inclusion Monte Carlo configurations, their division into morphology-adaptive quality meshes, and numerical solution for the overall properties, extracts accurate predictions of the properties of multiphase materials from remarkably small computer models. Examples of applications have been published for the moduli (83), coefficients of thermal expansion (83,85), dielectric constants (83), and gas permeabilities (84) of composite systems with polymeric matrices. The PALMYRA software package implementing this method can consider input morphologies approaching in complexity those extracted from analytical characterization data or multiscale simulations.

An example (28) of the application of PALMYRA to nanoplatelet-reinforced nanocomposites is provided in Fig. 15.16, which shows the Young's modulus

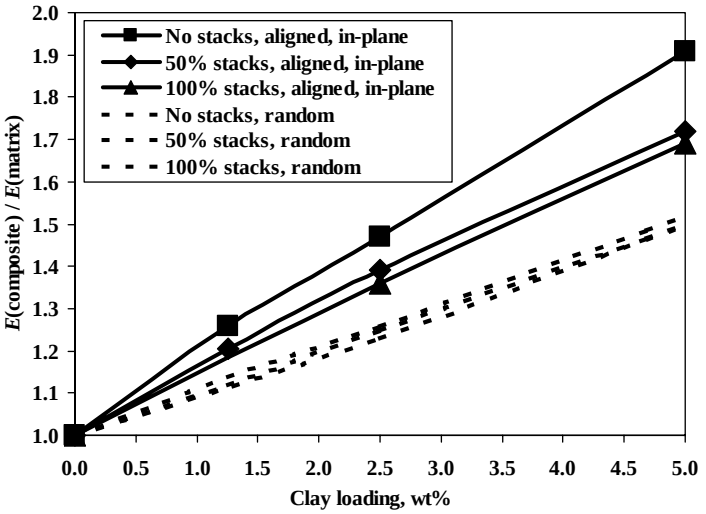

Figure 15.16 An example of the use of PALMYRA, showing the Young's modulus (E) predicted as a function of the extent of exfoliation and the orientation of the platelets. The platelets have a diameter of 60 nm and a thickness of 1 nm so that their aspect ratio is 1/60. The ratio of the moduli of the components of the composite is $(E_{\text{platelet}}/E_{\text{polymer}}) = 100$. There are five platelets per remaining stack. The distance between adjacent platelets in each remaining stack is 1 nm. (From Reference 28 with permission from Taylor and Francis.)

predicted as a function of the extent of exfoliation and the orientation of the platelets. Closed-form expressions from composite theory can be used in calculations of reasonable quality (such as those reported by Brune and Bicerano (80)) if the platelets are either all exfoliated completely or all located in stacks containing a certain number of platelets with a certain separation distance between adjacent platelets. On the contrary, the properties of composites where some platelets are exfoliated and others are still in stacks of various sizes can only be predicted by numerical simulations. It is seen that the modulus can depend strongly on platelet exfoliation and alignment and that the effects of these two factors are interdependent. In particular, the in-plane modulus should increase significantly with increased exfoliation if the platelets are aligned parallel to the plane of mechanical deformation, but the effects of exfoliation should be relatively small if the platelets are oriented isotropically in three dimensions.

We should note here that FEA is the most widely used, but not the only, method of simulating mechanical properties of composites. Recently, Buxton and Balazs (86) applied a somewhat different technique known as Lattice Spring Method (LSM) to predict modulus and other mechanical properties of nanocomposites. Their results were qualitatively similar to the ones obtained by Brune and Bicerano (80) or Gusev (83). Further investigations are needed to determine the accuracy and potential utility of LSM in predicting linear and nonlinear mechanical properties of nanocomposites.

15.4.4 Transport Property Modeling

Closed-form expressions from composite theory are also useful in correlating and predicting the transport properties (dielectric constant, electrical conductivity, magnetic susceptibility, thermal conductivity, gas diffusivity, and gas permeability) of multiphase materials. The models for these properties often utilize mathematical treatments (87,88) that are similar to those used for the thermoelastic properties, once the appropriate mathematical analogies (89,90) are made. Such analogies and the resulting composite models have been pursued quite extensively for both particulate-reinforced and fiber-reinforced composites where the filler phase consists of discrete entities dispersed in a continuous polymeric matrix.

For example, Fredrickson and Bicerano (91) showed that the previously developed equations for the permeability of oriented disk composites describe the limiting situations of the dilute and the semidilute concentration regimes and then developed an improved equation that is valid over a much wider concentration range. Predictions made by using their method are shown in Fig. 15.17, along with the predictions made by Gusev and Lusti (84), who used the numerical simulation method of Gusev (83) summarized in Section 15.4.3.

The two methods predict comparable improvement in the barrier properties (reductions in permeability) for A_f of up to 100, but the numerical simulations predict much greater potential improvements at $A_f \gg 100$ than expected based on the analytical model. Gusev and Lusti (84) proposed that such differences suggest that

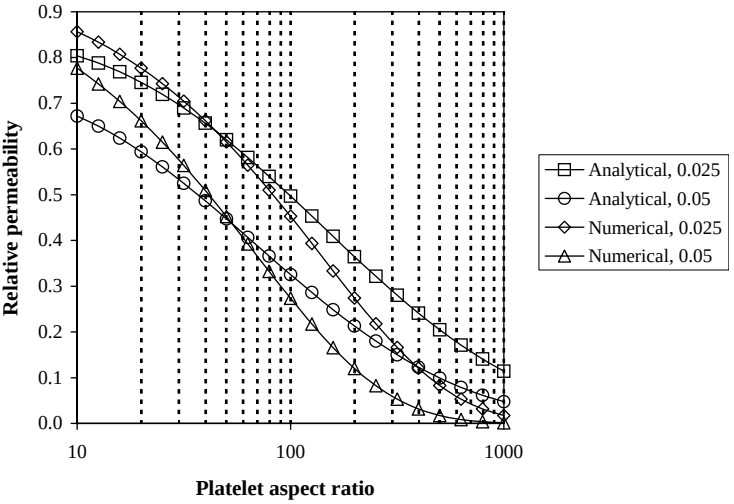

Figure 15.17 Predicted gas permeability of composites containing perfectly aligned disklike filler particles, relative to that of the matrix polymer. The number in each curve label denotes the filler volume fraction Φ. Results obtained by using the analytical equation of Fredrickson and Bicerano (91) are compared with results obtained by the numerical simulations of Gusev and Lusti (84), which suggest that relative permeability is a function of the product ΦA_f. (From Reference 68 with permission from Taylor and Francis.)

the potential improvements that can be obtained by incorporating highly anisotropic fillers in polymers are generally greater than suggested by previous work based on the use of analytical expressions.

15.5 CONCLUSIONS

We reviewed some of the theoretical and computational models developed to describe polymer–inorganic, and more specifically, polymer–clay, nanocomposites. These models address variety of issues, from preparation to structure to properties, and can be useful in designing new nanocomposite materials. At the same time, many challenges still remain, both in the development of the models and in a proper parameterization and comparison with experiment. Among the ones most critical for polyolefin–clay composites are those of proper accounting for (i) clay–clay electrostatic attraction and (ii) influence of polymer crystallinity on the clay exfoliation.

Our review touched on some—but not all—theoretical and numerical models aimed at understanding the nanocomposite behavior. Among the areas not discussed in the review are atomistic molecular simulations of structure and polymer chain configurations in nanocomposites (92–94), modeling of nanocomposite flame retardancy (95), or nonlinear mechanical properties such as fracture (96). Those models likely will be undergoing rapid development in the near future.

Despite all the difficulties, it is clear that polyolefin–clay nanocomposites will be utilized widely in industry. Today, their design is still as much an art as it is science, but more and more systematic understanding of their behavior and performance is being acquired. Models described in our review—as well as new ones that will be developed in years to come—will play an important role in helping develop new rules for nanocomposite design and, ultimately, to bring more and more nanocomposite-based products to the market.

ACKNOWLEDGMENT

V. Ginzburg wishes to acknowledge support from The Dow Chemical Company.

NOMENCLATURE

α	Coefficient of thermal expansion
γ	Shear strain
ε	Absorption energy of ''stickers'' onto clay surfaces
η	Viscosity
ρ_{gr}	Grafting density
ν	Poisson's ratio
Φ	Volume fraction
χ_{AB}	Flory–Huggins interaction parameter between species A and B
$\chi(t)$	Degree of intercalation as function of time
A or A_f	Aspect ratio of clay platelets
D	Diameter of clay platelets
D_{eff}	Diffusion constant of polymer in the gallery
D_{self}	Bulk diffusion constant of a polymer
DFT	Density functional theory
E	Young's modulus
F, $F(h)$	Free energy of polymer confined between clay platelets
f	Fraction of single layers in the nanocomposite
FEA	Finite-element analysis
G	Shear modulus
G'	Oscillatory shear storage modulus
G''	Oscillatory shear loss modulus
h	Distance between adjacent clay platelets
H	Thickness of clay platelets
$I(q)$	X-ray scattering intensity
k_B	Boltzmann's constant
LSM	Lattice spring model
N_{gr}	Degree of polymerization of grafted polymers or organic modifiers
N	Degree of polymerization of end-functionalized chains
P	Degree of polymerization of matrix polymer
$P(q)$	Single-particle form factor

P_c	Percolation threshold
PE	Polyethylene
PP	Polypropylene
PU	Polyurethane
q	Wavenumber
R	Clay platelet radius
$S'(q)$	Interference function
SAXS	Small-angle X-ray scattering
SCF	Self-consistent field theory
TEM	Transmission electron microscopy
WAXS	Wide-angle X-ray scattering

REFERENCES

1. K. Yano, A. Usuki, A. Okada, T. Kuraichi, and O. Kamigaito, *J. Polym. Sci. A Polym. Chem.*, **31**, 2493 (1993).
2. Y. Kojima, A. Usuki, M. Kawasumi, A. Okada, Y. Fukushima, T. Kurauchi, and O. Kamigaito, *J. Mater. Res.*, **8**, 1185 (1993).
3. P. B. Messersmith and E. P. Giannelis, *Chem. Mater.*, **5**, 1064 (1993).
4. T. Sun and J. M. Garcés, *Adv. Mater.*, **14**, 128 (2002).
5. K. Motha, U. Hippi, K. Hakala, M. Peltonen, V. Ojanperä, B. Löfgren, and J. Seppälä, *J. Appl. Polym. Sci.*, **94**, 1094 (2004).
6. N. Hasegawa, H. Okamoto, M. Kawasumi, M. Kato, A. Tsukigase, and A. Usuki, *Macromol. Mater. Eng.*, **280**, 76 (2000).
7. N. Hasegawa, M. Kawasumi, M. Kato, A. Usuki, and A. Okada, *J. Appl. Polym. Sci.*, **67**, 87 (1998).
8. J. Ma, Z. Qi, and Y. Hu, *J. Appl. Polym. Sci.*, **82**, 3611 (2001).
9. J. M. Garcés, D. J. Moll, J. Bicerano, R. F. Fibiger and D. G. McLeod, *Adv. Mater.*, **12**, 1835 (2000).
10. D. Garca-Lopez, O. Picazo, J. C. Merino and J. M. Pastor, *Eur. Polym. J.* **39**, 945 (2003).
11. T. G. Gopakumar, J. A. Lee, M. Kontopoulou, and J. S. Parent, *Polymer*, **43**, 5483 (2002).
12. C. M. Koo, H. T. Tam, S. O. Kim, K. H. Wang, I. J. Chung, D. C. Kim, and W. C. Zin, *Macromolecules*, **35**, 5116 (2002).
13. C. M. Koo, S. O. Kim, and I. J. Chung, *Macromolecules*, **36**, 2748 (2003).
14. Z. Wang and T. J. Pinnavaia, *Chem. Mater.*, **10**, 3769 (1998).
15. M. A. Osman, V. Mittal, V. Morbidelli, and U. W. Süter, *Macromolecules*, **36**, 9851 (2003).
16. C. Zilg, R. Mülhaupt, and J. Finter, *Macromol. Chem. Phys.*, **200**, 661 (1999).
17. M. A. Osman, V. Mittal, V. Morbidelli, and U. W. Süter, *Macromolecules*, **37**, 7250 (2004).
18. E. P. Giannelis, R. Krishnamoorti, and E. Manias, *Adv. Polym. Sci.*, **138**, 107 (1999), and references therein.
19. P. C. LeBaron, Z. Wang, T. J. Pinnavaia, *Appl. Clay Sci.*, **15**, 11 (1999), and references therein.
20. M. Alexandre, P. Dubois, *Mater. Sci. Eng. R*, **28**, 1 (2000), and references therein.
21. R. Krishnamoorti and R. Vaia (eds.), *Polymer Nanocomposites: Synthesis*, *Characterization*, *and Modeling*, Oxford University Press, Oxford, 2002.
22. T. Pinnavaia and G. Beall (eds.), *Polymer-Clay Nanocomposites*, Wiley, New York, 2000.
23. R. A. Vaia and E. P. Giannelis, *Mater. Res. Soc. Bull.*, 394–401 (May 2001), and references therein.
24. G. Kickelbick, *Prog. Polym. Sci.*, **28**, 83 (2003), and references therein.

25. S. Sinha Ray, M. Okamoto, *Prog. Polym. Sci.*, **28**, 1539 (2003), and references therein.
26. A. I. Taub, *Mater. Res. Soc. Bull.*, 336–343 (April 2006), and references therein.
27. A. C. Balazs, V. V. Ginzburg, Y. Lyatskaya, C. Singh, and E. Zhulina, Modeling the phase behavior of polymer–clay nanocomposites, in: *Polymer–Clay Nanocomposites*, T. G. Pinnavaia and G. W. Beall (eds.), Wiley, New York, 2000.
28. J. Bicerano, S. Balijepalli, A. Doufas, V. Ginzburg, J. Moore, M. Somasi, S. Somasi, J. Storer, and T. Verbrugge, *J. Macromol. Sci. Polym. Rev.*, **44**, 53 (2004).
29. R. A. Vaia and E. P. Giannelis, *Macromolecules*, **30**, 7990 (1997).
30. R. A. Vaia and E. P. Giannelis, *Macromolecules*, **30**, 8000 (1997).
31. A. C. Balazs, C. Singh, and E. Zhulina, *Macromolecules*, **31**, 8370 (1998).
32. E. Zhulina, C. Singh, and A. C. Balazs, *Langmuir*, **15**, 3935 (1999).
33. A. C. Balazs, C. Singh, E. Zhulina, and Y. Lyatskaya, *Acc. Chem. Res.*, **32**, 651 (1999).
34. D. Kuznetsov and A. C. Balazs, *J. Chem. Phys.*, **112**, 4365 (2000).
35. D. Kuznetsov and A. C. Balazs, *J. Chem. Phys.*, 113, 2479 (2000).
36. G. J. Fleer, M. A. Cohen Stuart, J. M. H. M. Scheutjens, T. Cosgrove, and B. Vincent, *Polymers at Interfaces*, Chapman & Hall, London, 1993.
37. J. M. H. M. Scheutjens and G. R. Fleer, *J. Phys. Chem.*, **83**, 1619 (1979).
38. J. M. H. M. Scheutjens and G. R. Fleer, *J. Phys. Chem.*, **84**, 178 (1980).
39. J. Y. Lee, A. R. C. Baljon, R. F. Loring, and A. Z. Panagiotopoulos, *J. Chem. Phys.*, **109**, 10321 (1998).
40. A. R. C. Baljon, J. Y. Lee, and R. F. Loring, *J. Chem. Phys.*, **111**, 9068 (1999).
41. J. Y. Lee, A. R. C. Baljon, and R. F. Loring, *J. Chem. Phys.*, **111**, 9754 (1999).
42. M. Laus, O. Francescangeli, and F. Sandrolini, *J. Mater. Res.*, **12**, 3134 (1997).
43. M. Kurian, A. Dasgupta, M. E. Galvin, C. R. Ziegler, and F. L. Beyer, *Macromol.*, **39**, 1864 (2006).
44. V. V. Ginzburg and A. C. Balazs, *Adv. Mater.*, **12**, 1805 (2000).
45. Y. Lyatskaya and A. C. Balazs, *Macromolecules*, **31**, 6676 (1998).
46. L. Onsager, *Ann. N.Y. Acad. Sci.*, **51**, 627 (1949).
47. V. V. Ginzburg and A. C. Balazs, *Macromolecules*, **32**, 5681 (1999).
48. V. V. Ginzburg, C. Singh, and A. C. Balazs, *Macromolecules*, **33**, 1089 (2000).
49. P. Tarazona, *Phys. Rev. A*, **31**, 2673 (1985).
50. A. M. Somoza, P. Tarazona, *J. Chem. Phys.*, **91**, 517 (1989).
51. B. Derjaguin and L. Landau, *Acta Physicochim. (URSS)*, **14**, 633 (1941).
52. A. B. Morgan and J. W. Gilman, *J. Appl. Polym. Sci.*, **87**, 1329 (2003).
53. R. A. Vaia and W. Liu, *Polym. Mater. Sci. Eng.*, **85**, 14 (2001).
54. R. A. Vaia and W. Liu, *J. Polym. Sci. B*, **40**, 1590 (2002).
55. R. A. Vaia, W. Liu, and W. Koerner, *J. Polym. Sci. B*, **41**, 3214 (2003).
56. M. Yoonessi, H. Toghiani, T. L. Daulton, J. S. Lin, and C. U. Pittman, *Macromolecules*, **38**, 818 (2005).
57. R. A. Vaia, K. D. Jandt, E. J. Kramer, and E. P. Giannelis, *Macromolecules*, **28**, 8080 (1995).
58. E. Manias, H. Chen, R. Krishnamoorti, J. Genzer, E. J. Kramer, and E. P. Giannelis, *Macromolecules*, **33**, 7955 (2000).
59. K. Kremer and G. S. Grest, *J. Chem. Phys.*, **92**, 5057 (1990).
60. V. V. Ginzburg, O. V. Gendelman, and L. I. Manevitch, *Phys. Rev. Lett.*, **86**, 5073 (2001).
61. O. V. Gendelman, L. I. Manevitch, and O. L. Manevitch, *J. Chem. Phys.*, **119**, 1066 (2003).
62. R. Krishnamoorti and A. S. Silva, Rheological properties of polymer–clay nanocomposites, in: *Polymer–Clay Nanocomposites*, T. G. Pinnavaia and G. W. Beall (eds.), Wiley, New York, 2000.
63. J. Ren, A. S. Silva, and R. Krishnamoorti, *Macromolecules*, **33**, 3739 (2000).
64. R. Krishnamoorti and K. Yurekli, *Curr. Opin. Colloid Interf. Sci.*, **6**, 464 (2001), and references therein.

65. H. S. Jeon, J. K. Rameshwarama, G. Kimb, and D. H. Weinkauf, *Polymer*, **44**, 5749 (2003).
66. C. Mitchell and R. Krishnamoorti, *J. Polym. Sci. B Polym. Phys.*, **40**, 1434 (2002).
67. J. Ren, A. S. Silva, and R. Krishnamoorti, *Macromolecules*, **33**, 3739 (2000).
68. J. Bicerano, *Prediction of Polymer Properties*, 3rd edition, Marcel Dekker, New York (2002).
69. S. Salaniwal, S. K. Kumar, and J. F. Douglas, *Phys. Rev. Lett.*, **89**, 025801 (2002).
70. P. J. Dionne, R. Ozisik, and C. R. Picu, *Macromolecules*, **38**, 9351 (2005).
71. V. Pryamitsyn and V. Ganesan, *Macromolecules*, **39**, 844 (2006).
72. S. A. Langer, E. R. Fuller Jr., and W. C. Carter, *Comput. Sci. Eng.*, **3**(3), 15 (2001).
73. T. Kelly and B. Clyne, *Phys. Today*, **37** (1999).
74. C. W. Camacho, C. L. Tucker III, S. Yalvac, and R. L. McGee, *Polym. Comp.*, **11**, 229 (1990).
75. S. G. Advani and C. L. Tucker III, *J. Rheol.*, **31**, 751 (1987).
76. J. C. Halpin and J. L. Kardos, *J. Appl. Phys.*, **43**, 2235 (1972).
77. J. C. Halpin and J. L. Kardos, *Polym. Eng. Sci.*, **16**, 344 (1976).
78. T. S. Chow, *J. Mater. Sci.*, **15**, 1873 (1980). Readers wishing to use Chow's method should note a typographical error communicated to us by him. The correct version of the second equation in the appendix is "$\alpha_3 = 4\pi Q/3 - 4(I - \pi)R$", while there is an erroneous "+" sign between the two terms on the right-hand side as printed in the article.
79. R. M. Christensen, *J. Eng. Mater. Technol.*, **101**, 299 (1979).
80. D. A. Brune and J. Bicerano, *Polymer*, **43**, 369 (2002).
81. T. D. Fornes and D. R. Paul, *Polymer*, **44**, 4993 (2003).
82. N. Sheng, M. C. Boyce, D. M. Parks, G. C. Rutledge, J. I. Abes, and R. E. Cohen, *Polymer*, **45**, 487 (2004), and references therein.
83. A. A. Gusev, *Macromolecules*, **34**, 3081 (2001).
84. A. A. Gusev and H. R. Lusti, *Adv. Mater.*, **13**, 1641 (2001).
85. A. A. Gusev and J. J. M. Slot, *Adv. Eng. Mater.*, **3**, 427 (2001).
86. G. A. Buxton and A. C. Balazs, *J. Chem. Phys.*, **117**, 7649 (2002).
87. D. M. Bigg, *Polym. Compos.*, **7**, 125 (1986).
88. J. T. Mottram, in: Computer aided design in composite material technology, S. G. Advani, W. R. Blain, W. P. de Wilde, J. W. Gillespie Jr., and O. H. Griffin Jr. (eds.), *Computational Mechanics Publications*, Vol. III, Southampton, 1992, pp. 615–626.
89. Z. Hashin, *J. Appl. Mech.*, **46**, 543 (1979).
90. L. V. Gibiansky and S. Torquato, *Phys. Rev. Lett.*, **71**, 2927 (1993).
91. G. H. Fredrickson and J. Bicerano, *J. Chem. Phys.*, **110**, 2181 (1999).
92. E. Hackett, E. Manias, and E. P. Giannelis, *J. Chem. Phys.*, **108**, 7410 (1998).
93. E. Hackett, E. Manias, and E. P. Giannelis, *Chem. Mater.*, **12**, 2161 (2000).
94. V. Kuppa and E. Manias, *Chem. Mater.*, **14**, 2171 (2002).
95. M. R. Nyden and J. Gilman, *Comput. Theor. Polym. Sci.*, **7**, 191 (1997).
96. D. Gersappe, *Phys. Rev. Lett.*, **89**, 058301 (2002).

Chapter 16

Monte Carlo Modeling of Polyethylene Nanocomposites Using a High Coordination Lattice

Peter J. Dionne,[1] Rahmi Ozisik,[2] and Catalin R. Picu[1]

16.1 INTRODUCTION

Polymer nanocomposites have been the focus of research over the past several years due to a number of reasons. First, these materials have enhanced mechanical, electrical, and optical properties among others compared to traditional composites. Second, nanofillers enable the control of a combination of properties. Finally, there is the potential to control the properties of the material by adjusting the size, amount, shape, and surface chemistry of the filler. Based on their geometry, nanofillers can be divided into three groups: spherical, cylindrical, and layered. Carbon nanotubes (1) are examples of cylindrical nanofillers but most studies focused on layered fillers such as clays due to their low cost, barrier properties, low flammability, and high reinforcement capability (2). The current study, however, centers on spherical nanofillers such as silica, alumina, and zinc oxide. Spherical nanofillers (referred to as nanofillers or nanoparticles) are useful in many applications because they can be optically transparent, improve mechanical and rheological properties, and control optical, thermal properties, and electrical properties.

[1]Department of Mechanical, Aerospace and Nuclear Engineering, Rensselaer Polytechnic Institute, Troy, NY 12180, USA

[2]Department of Materials Science and Engineering, Rensselaer Polytechnic Institute, Troy, NY 12180, USA

Polyolefin Composites, Edited by Domasius Nwabunma and Thein Kyu

The focus of the current study is the mechanical response of the nanocomposite. In order to be able to create a model of these materials at the continuum scale, one needs to investigate the atomistic scale effects of nanofillers and then transfer this information to higher length- and timescales. The multiscale nature of this problem can get quickly very complicated if there exist phase transitions; therefore, the current study is limited to amorphous polymers. In addition, because nanofillers offer an increased surface area to volume ratio, our main focus is the interface between the nanofillers and the polymer chains. Therefore, we will limit ourselves to situations where the effects of interface are the strongest, and as a result, the two important parameters are the nanofiller concentration and the polymer–filler interaction.

Several experimental studies have shown the reinforcement effects of nanofillers (3–9). One study of particular relevance to the simulation presented here is the work performed by Zhang and Archer (5). These researchers examined the effect of chain length, filler volume fraction, thermal history, and polymer–particle interaction strength on viscoelastic properties. Their results indicate that poly(ethylene oxide)/silica nanocomposites containing 4% silica (by volume) exhibited a five order of magnitude increase in the low frequency storage modulus compared to the neat polymer subjected to oscillatory shear (see Fig. 16.1).

Several notable observations of Zhang and Archer can be summarized as follows. At low frequencies the impact of filler loading on storage and loss modulus is substantial, whereas at high frequencies the impact of filler loading is small. This suggests that fillers do not influence the plateau modulus, and therefore the entanglement dynamics, as much as they influence the stress relaxation. All samples tested show a two-step relaxation curve in the plot of relaxation modulus versus time, suggesting that there are at least two distinct relaxation mechanisms occurring. One step was attributed to the fast relaxation processes and was thought to correspond to the relaxation of the bulk polymer chains, and the other one was attributed to slow relaxation processes and was thought to be the result of the filler–chain network relaxation. Filler–chain network relaxation was proposed to be the result of the following three mechanisms: (i) an increase in the effective particle size due to an immobilized layer of polymer around the fillers; (ii) the formation of polymer bridges between the particles as a result of the polymer–particle interactions; and (iii) particle flocculation for which a strong particle–particle interaction contributes to reinforcement. However, reinforcement was not thought to be the result of particle aggregation, which is the main reinforcing mechanism in composites containing micron-sized and larger filler particles.

Another very relevant experimental work by Zhu et al. presents storage (G') and loss (G'') moduli as a function of frequency over a large frequency range for polybutadiene containing between 2% and 15% (by volume) of 15 nm silica particles (7). A double peak in both the G' and G'' versus frequency curves further strengthens the idea that there are at least two different relaxation times, a fast relaxation process associated with relaxation of the bulk polymer chains and a slower relaxation process associated with the filler–chain network relaxation.

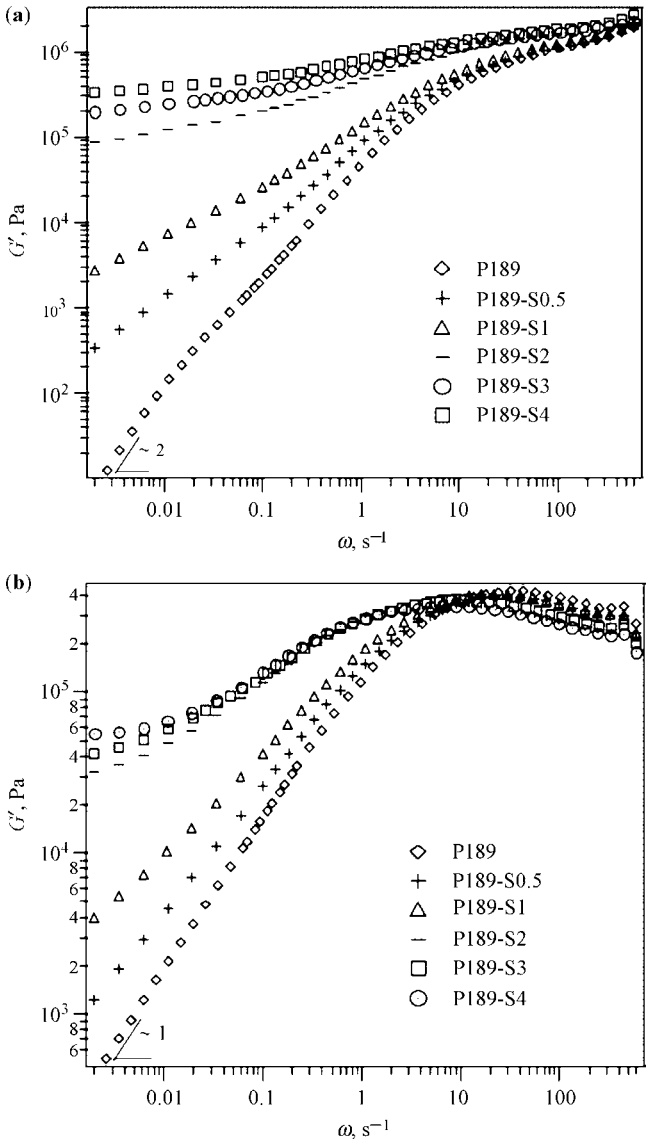

Figure 16.1 Storage (**a**) and loss (**b**) moduli for PEO/silica nanocomposites with volume fraction of filler varying from 0% (P189) to 4% (P189-S4). (From Reference 5 with permission from American Chemical Society.)

The nature of the polymer–particle interaction defines to a large extent the reinforcement and the viscoelastic properties of the nanocomposites (5,6). The interface can be controlled by adjusting the surface chemistry of the filler. Experimentally, it has been observed that when there was little or no adsorption of the

polymer to the particle, practically no difference was observed in the storage or loss modulus of the nanocomposite compared to the neat polymer (5). However, the storage modulus increased at least three orders of magnitude when there was strong adsorption (5).

Several theories based on molecular origins have been proposed for the observed reinforcement. Previous works on filled rubbers suggest that reinforcement is obtained once the filler agglomerates percolate (10). This notion contrasts with the experimental observation that polymer nanocomposites present enhanced properties once good filler dispersion is achieved. An attempt to adapt filler agglomeration idea for nonagglomerated filler structures was based on the assumption that the dynamics of polymer chains located near a surface was slowed down. This leads to a confined polymer layer next to the filler. The thickness of this confined layer was estimated to be on the order of one to two times the radius of gyration (R_g). It was conjectured that the percolation of these layers leads to the overall enhancement of properties, and under a critical strain, the softening (Payne effect) is a result of the lowering of T_g within the polymer layers adjacent to the fillers (8).

In contrast to this idea is the transient filler network theory, which states that fillers are connected by a network of adsorbed chains forming a ''secondary'' network (in addition to the entanglements). Simple calculations as well as molecular simulations estimated that the network forms once the average filler wall-to-wall distance was on the order of $2R_g$. This theory was able to qualitatively explain the nonlinear viscoelastic properties such as the Payne effect seen in nanocomposites (6).

If one considers the transient filler network theory, there are at least two different concepts in the literature that attempt to explain the enhanced material properties, specifically in the storage modulus. The first is the concept of trapped entanglements (6) that conjectures that chains in the neighborhood of the particle but not adsorbed on the particle are constrained more so than identical chains in a neat system. The constraint is believed to be the result of adsorbed chains containing loops, where a loop is formed between two chain beads that are adsorbed. The chains that are not adsorbed in the neighborhood of a particle are entangled with the loops in the adsorbed chain, thus causing the chain that is not adsorbed to be constrained in its diffusion through the system and hence display increased relaxation times.

The other concept used to explain the reinforcement within the context of the transient filler network theory is that any chain that is adsorbed on the surface of particle is not able to perform the reptative motion in order to relax after an applied deformation (11). Since the population of adsorbed chains at any given instant in the system is significant, the relaxation time of the entire system is affected by the adsorbed chains. Even though individual chains may continuously switch between being adsorbed and free due to thermal fluctuations, the average ratio of adsorbed chains and the total chains in the system remains constant in time at least for low to moderate strain rates. This idea assumes that chains that are not adsorbed will relax at the same rate as chains in a neat melt.

The simulation results presented here further support the latter theory of transient filler network and specifically the idea of reduced chain mobility due to adsorption as the molecular reason for the observed reinforcement in polymer nanocomposites. The simulation results show that chain structure and dynamics are changed by the presence of fillers and the nature of the interactions between chains and filler particles, and more complete understanding of how these changes occur is the goal of the simulation.

16.1.1 Computer Simulations of Spherical Nanocomposites

Computer simulations are very useful to study the effect of nanoparticles on the structure and dynamics of polymer chains because they provide information about polymer chain behavior near nanoparticle surface that is hard to obtain through experiments. Both molecular dynamics and Monte Carlo methods were employed in computer simulations and most studies focused on the structure and dynamics of polymer chains in the presence of nanoparticles. Vacatello performed molecular dynamics and Monte Carlo simulations (12–18) and studied the chain behavior near nanoparticles. Glotzer and coworkers (19–22) used molecular dynamics to study chain behavior near nanoparticles and clustering of nanoparticles. Mattice and coworkers (23,24) used Monte Carlo simulations to study the structure of polymer chains near nanoparticles, which were obtained by collapsing polymer chains. Mark and coworkers (25,26) investigated the effect of nanoparticle-induced deformations of polymer chains and its effect on reinforcement and properties. These and other simulations showed that many parameters contribute to the properties of nanocomposites: polymer–particle interactions (interface), amount of particles, particle clustering, polymer molecular weight, polymer chain chemistry (stiffness), and particle size and shape. Although some of these issues are polymer specific and have been studied extensively in the past, the presence of nanoparticles results in a large interfacial volume that affects the bulk properties. The systems studied so far are all amorphous because presence of polymer crystals would add more complications to an already complicated system. It is probably safe to assume that in the near future, heterogeneous systems will be studied, but we need to understand the underlying physics in amorphous systems in order to handle more complicated systems.

The material of interest in the current study is linear, monodisperse polyethylene chains with nanosized spherical fillers. The molecular weight of polyethylene is changed from short (unentangled) chains to chain lengths near the entanglement transition. The polyethylene in the current simulations remains amorphous and all simulations were performed above the glass transition temperature. The systems contained homogeneously dispersed spherical particles that were arranged in a close-packed structure and the distance between filler particles is comparable to chain size (R_g). Filler particles are spherical in shape and have a monodisperse size distribution. The material is viscoelastic in the melt state and flows at macroscopic timescales.

16.2 SIMULATION METHOD

In this section, we will give a detailed description of the second nearest neighbor diamond (SNND) lattice simulations. Most of the information presented here is available in the literature but we believe it is important to include a complete description. The second nearest neighbor diamond lattice, which was introduced in 1995 by Rapold and Mattice (27,28), has proven to be very useful in the simulation of polymers. This method provides various advantages that increase the observable time domain and the length scale of the simulation. SNND is an on-lattice simulation where the torsional angles are restricted to *trans* and two *gauche* states (for polyethylene), and therefore, the conformational space is limited to these three states only. Also, the SNND lattice is a coarse-grained lattice, where the number of degrees of freedom is decreased to achieve faster computation times. In most cases, coarse graining results in loss of physical reality, and it is not possible to recover the fully atomistic system. In SNND simulations, the coarse graining process is reversible for polyethylene and probably for other chains with saturated carbon backbones, but not for all chains, for example, polycarbonate. The fully atomistic system can be recovered at any time during the simulation, and therefore, coarse graining is used only as a tool to eliminate the unnecessary information from the system temporarily. Another advantage of the SNND simulation is the use of fast Metropolis Monte Carlo algorithm (29,30) to sample the conformational phase space effectively.

The energetic interactions of SNND simulations are introduced by short-(28) and long-range (28,31) interactions. Short-range interactions are derived from the rotational isomeric state (RIS) theory (32,33), and long-range interactions are derived from the second virial coefficient with a Lennard–Jones potential. The SNND lattice in combination with the short- and long-range interactions is used to simulate high molecular weight polymers at their bulk densities. Several examples of the SNND lattice simulations were performed in the past years and the method has been incrementally improved over the years (34–36). Properties include bulk dynamics (37), mixing of polypropylene and polyethylene (38), mixing of differing stereochemical polypropylenes (39), thin films (40), and others. Details of the simulation method and the potentials employed for polyethylene can be found in References 40 and 41.

16.2.1 Second Nearest Neighbor Diamond Lattice

The diamond lattice is a natural choice for the simulation of polyethylene and other vinyl polymer chains since the bond angle between three successive carbon atoms is approximately tetrahedral and the torsional angles (*trans* and *gauche* states) are separated by approximately 120°. The SNND lattice is derived from the diamond (tetrahedral) lattice by eliminating every other site on the lattice as shown in Fig. 16.2. The resulting coarse-grained lattice is well known and is identical to the closest packing of uniform hard spheres. The name ‘‘second nearest neighbor diamond lattice’’ is chosen because it conveys a crucial relationship to the underlying

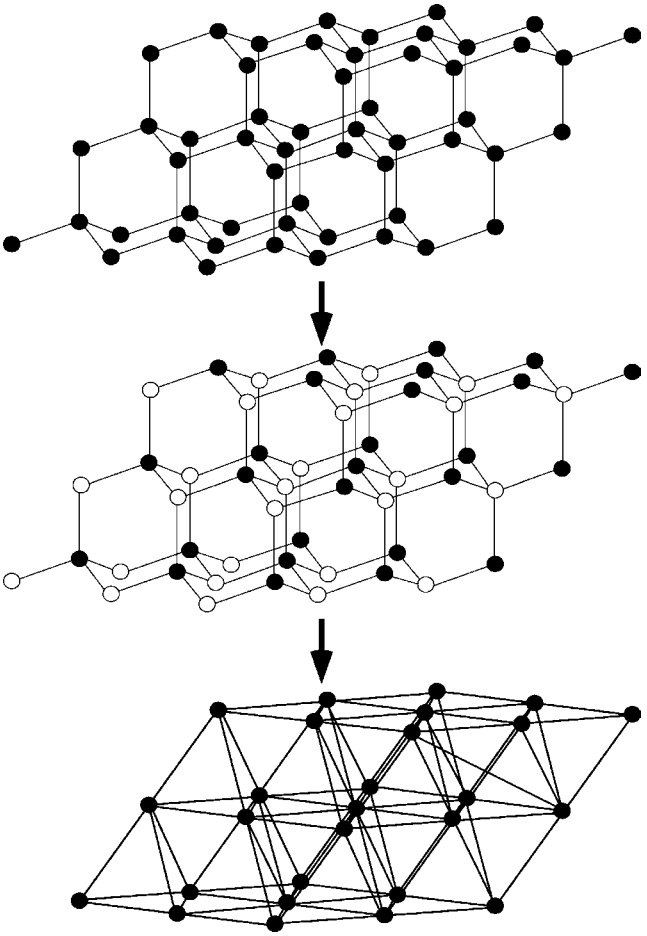

Figure 16.2 Transition from diamond lattice to SNND lattice. The eliminated (hidden) lattice sites are shown as open circles. The resulting SNND lattice is a distorted cubic lattice, and it is identical to the lattice obtained from the uniform packing of hard spheres (41).

diamond lattice that the ''uniform packing of hard spheres'' does not. The SNND lattice has a coordination number of 12 (see Fig. 16.3), whereas the diamond lattice has a coordination number of 4. The SNND unit cell is a cubic cell that is distorted in all directions, and the angle between any two axes is 60°. In the case of *n*-alkane simulations, each bead at a site on the SNND lattice represents two backbone carbon atoms and the hydrogen atoms bonded to them, that is, a ($-CH_2-CH_2-$) unit. Since the carbon–carbon bond length is 0.153 nm, the SNND lattice spacing is fixed at 0.25 nm. The SNND lattice is shown in Fig. 16.3, with the 12 nearest neighbors connected to the central bead with thick solid lines. The occupancy of the SNND lattice is quite low even at bulk densities since each lattice site represents two backbone carbon atoms.

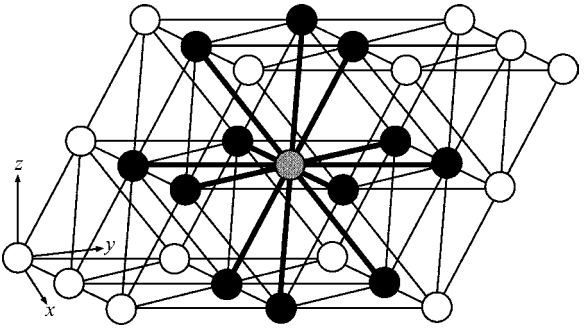

Figure 16.3 SNND lattice showing $2 \times 2 \times 2$ lattices. The 12 nearest neighbors (filled circles) of a central bead (gray circle) are also shown (41).

One of the advantages of the SNND simulations is that it is possible to reverse map and recover the fully atomistic detail at any time during the simulation. Reverse mapping is accomplished by adding the eliminated lattice sites onto the SNND lattice to recover the underlying diamond lattice. At this point, a choice is made between the two possible underlying diamond lattices (see Fig. 16.4). By choosing one of these, the coordinate system and the direction of filling are fixed. The existence of two underlying diamond lattices does not alter the outcome of the simulations in any way, and it is possible to choose one of these and carry this information all through the simulation.

16.2.1.1 Moves on the SNND Lattice

The Monte Carlo moves on the SNND lattice can either be global (42) or local. Both types of moves have been used on the SNND lattice with success. Global moves such as pivot move, where a large portion of the chain is rotated around a symmetry point, are used particularly during equilibration or calculation of static properties. Static properties can be calculated by adopting any type of move as long as the move samples the conformational space efficiently. This is not true if one needs to calculate dynamic properties. The type of moves that can be used for the calculation of dynamic properties is limited mainly because the moves should not alter the dynamics of the system. As a general rule, this complication can be avoided by adopting moves that are random, local (in order to mimic the thermally induced random molecular motions), and realistic.

The moves that are used on the SNND lattice in the current study are single bead moves, and the choice of the movement depends on the location of the two bonded neighbors. If the conformation of the three beads (two bonded neighbors and the central bead that is to be moved) corresponds to an extended conformation, then the bead cannot be moved. Otherwise, the beads can have either one or three choices of different locations to move.

The movement of the single bead on the SNND lattice can change the positions of either two or three consecutive carbon atoms on the underlying fully atomistic diamond lattice. Both of these possible moves are responsible for three different

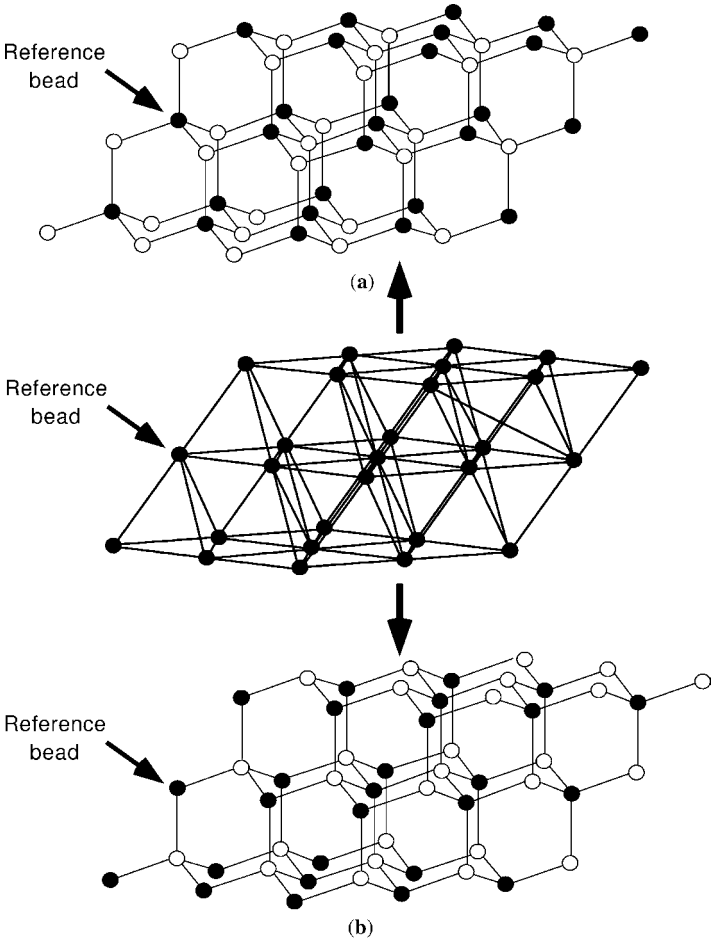

Figure 16.4 The underlying diamond lattice is recovered by adding the eliminated lattice sites back. Lattice sites can be added either above or below a reference SNND lattice site (marked with an arrow). By selecting one of these two addition methods, one of the underlying diamond lattices is recovered (41).

conformational changes each. The two displaced consecutive carbon atoms on the fully atomistic diamond lattice move from positions 2, 3 to 5, 6 of a cyclohexane ring, with the chain extending from this ring at positions 1 and 4. The initial positions of the carbon atoms before the move are 1, 2, 3, 4, and after the move they become 1, 6, 5, 4. Only one of the two carbon atoms that is moved is represented on the SNND lattice. The three displaced consecutive carbon atoms on the fully atomistic diamond lattice move from positions 2, 3, 4 to 6, 7, 8 of a cyclooctane ring, with the chain extending from positions 1 and 5. The initial chain positions of the carbon atoms before the move are 1, 2, 3, 4, 5, and after the move they become 1, 6, 7, 8, 5. Only the middle bead (position 3 before the move and position 7 after the move) is represented on the SNND lattice. More detailed information on the moves on the SNND lattice

and their corresponding changes on the fully atomistic diamond lattice is given by Doruker and Mattice (43).

Certain conformations on the SNND lattice do not have their counterparts on the fully atomistic diamond lattice. All of these conformations, which are called collapse conformations, arise due to not keeping track of every other backbone carbon atom on the SNND lattice. In certain cases, two beads of the atomistically detailed chain occupy the same location on the SNND lattice. It is also important to note that during reverse mapping from SNND lattice to diamond lattice, two distinct underlying diamond lattices are available but only one of these is chosen. And only one of these two diamond lattices gives a collapse conformation for the same three-bead conformation on the SNND lattice. Therefore, if the collapse conformations are to be restricted, one of these underlying diamond lattices should be chosen at the beginning of the simulation, and this information should be carried throughout the simulation. This way, only half of the three-bead conformations would form collapse conformations, and these can be restricted. Collapse conformations are represented with a statistical weight of $\sigma^2\omega$, and would be rare if the product $\sigma^2\omega \ll 1$. If the collapse conformations are available during the simulation, the efficiency and the speed of the simulation increase.

16.2.1.2 Metropolis Monte Carlo Algorithm

Since the introduction of the Metropolis algorithm (29) some 50 years ago, Monte Carlo sampling has become a widely used method in the simulation of polymeric systems. Combined with the integer arithmetic of the lattice models, on-lattice Monte Carlo can sample phase space with very high efficiency and speed. A simple Monte Carlo sampling algorithm would choose conformations randomly, and then weigh them with $e^{-\Delta E/kT}$. Metropolis algorithm chooses conformations with a probability of $e^{-\Delta E/kT}$, and then weighs them equally. The flow of the algorithm is given as follows:

$$\text{Attempt Move} \rightarrow \begin{cases} \Delta E < 0 \Rightarrow & \text{Accept Move} \\ \Delta E > 0 \Rightarrow & \begin{cases} \exp\left[-\frac{\Delta E}{kT}\right] > \lambda \Rightarrow & \text{Accept Move} \\ \exp\left[-\frac{\Delta E}{kT}\right] \leq \lambda \Rightarrow & \text{Deny Move} \end{cases} \end{cases} \tag{16.1}$$

where λ is a random number between 0 and 1.

16.2.1.3 Short-Range Interactions

The short-range interactions are calculated through an extended RIS formalism, which was formulated by Rapold and Mattice (28). The RIS formalism of Abe et al. (44) for polyethylene was used as a starting point for the extended description. The statistical weight matrix for polyethylene is given as follows:

$$U = \begin{bmatrix} 1 & \sigma & \sigma \\ 1 & \sigma & \sigma\omega \\ 1 & \sigma\omega & \sigma \end{bmatrix} \tag{16.2}$$

where σ and ω are the first-order and second-order interactions, respectively.

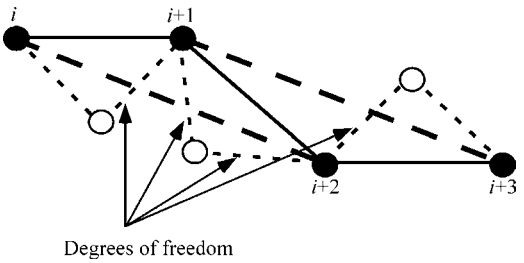

Figure 16.5 Representation of a polyethylene chain on the SNND lattice, and the corresponding detailed conformation on the diamond lattice. The solid lines represent the bonds on the SNND lattice, and the dashed lines represent the bonds on the detailed diamond lattice. The thick dashed lines represent the virtual vectors connecting the next nearest neighbors on the SNND lattice (41).

A one-to-one mapping of the RIS scheme onto the SNND lattice representation is possible only if the simulation uses vectors rather than distances, and one of the underlying diamond lattices is selected in advance (45). Since the torsion angles of the detailed (fully atomistic) model are not known on the coarse-grained SNND lattice (Fig. 16.5), the simulation is based on scalar distances; therefore, one-to-one mapping of the RIS scheme is not possible. To categorize the conformations on the SNND lattice, the distance between the second nearest neighbor segments (distance between beads i and $i+2$ on the SNND lattice) is used as a distinguishing factor. There are four different distances on the SNND lattice, and some of these correspond to more than one conformation on the fully atomistic diamond lattice (Table 16.1).

There are two degrees of freedom (torsion angles) on the detailed conformation that define the distance between second nearest neighbor segments on the SNND lattice (Fig. 16.5). In order to account for the interdependent bonds, two successive nearest neighbor segment bonds on the SNND lattice should be used. Such an arrangement describes four degrees of freedom in the atomistic detailed model as shown in Fig. 16.5 and corresponds to the description of *n*-heptane in the RIS model.

Table 16.1 The Coarse-Grained Conformations on the SNND Lattice with Respect to the Distances Between the Second Nearest Neighbors (on the SNND Lattice) and the Corresponding Detailed (Atomistic) Conformations.

SNND conformation	Distance, nm	Detailed conformations[a]
A	5.00	*tt*
B	4.33	$tg+, tg-, g+t, g-t$
C	3.53	$g+g+, g-g-$
D	2.50	$g+g-, g-g+$

SNND conformations B, C, and D correspond to more than one atomistic conformation.
[a] $t = trans, g+ = gauche+, g- = gauche-$.

An extension of the classical RIS model for polyethylene can be accomplished with the use of a 9×9 statistical weight matrix.

$$U^2 = \begin{bmatrix} 1 & \sigma & \sigma & \sigma & \sigma & \sigma^2 & \sigma^2 & \sigma^2\omega & \sigma^2\omega \\ 1 & \sigma & \sigma & \sigma & \sigma\omega & \sigma^2 & \sigma^2\omega & \sigma^2\omega & \sigma^2\omega^2 \\ 1 & \sigma & \sigma & \sigma\omega & \sigma & \sigma^2\omega & \sigma^2 & \sigma^2\omega^2 & \sigma^2\omega \\ 1 & \sigma & \sigma & \sigma & \sigma & \sigma^2 & \sigma^2 & \sigma^2\omega & \sigma^2\omega \\ 1 & \sigma & \sigma & \sigma & \sigma & \sigma^2 & \sigma^2 & \sigma^2\omega & \sigma^2\omega \\ 1 & \sigma & \sigma & \sigma & \sigma\omega & \sigma^2 & \sigma^2\omega & \sigma^2\omega & \sigma^2\omega^2 \\ 1 & \sigma & \sigma & \sigma\omega & \sigma & \sigma^2\omega & \sigma^2 & \sigma^2\omega^2 & \sigma^2\omega \\ 1 & \sigma & \sigma & \sigma\omega & \sigma & \sigma^2\omega & \sigma^2 & \sigma^2\omega^2 & \sigma^2\omega \\ 1 & \sigma & \sigma & \sigma & \sigma\omega & \sigma^2 & \sigma^2\omega & \sigma^2\omega & \sigma^2\omega^2 \end{bmatrix} \tag{16.3}$$

The rows represent the two torsion angles immediately before and after bead $i+1$ and the columns represent the two torsion angles immediately before and after bead $i+2$ as shown in Fig. 16.5. The sequence of the states of the rows and columns is $tt, tg+, tg-, g+t, g-t, g+g+, g-g-, g+g-, g-g+$. The statistical weight matrix U^2 is converted to its coarse-grained description by grouping the conformations that are indistinguishable on the SNND lattice. This new matrix is called the extended statistical weight matrix (U_{SNND}), and a, b, and c are the modified statistical weights that have to be assigned to obtain the coarse-grained description. The new extended statistical weight matrix can be reduced to a 4×4 matrix, where the rows now define the category of the vector connecting beads i and $i+2$, and the columns define the category of the vector connecting beads $i+1$ and $i+3$, with the sequence A, B, C, and D as defined in Table 16.1. This 4×4 matrix can be further reduced to a 3×3 matrix with the sequence A, B, and $(C+D)$.

$$U_{\text{SNND}} = \begin{bmatrix} 1 & \sigma & \sigma & \sigma & \sigma & \sigma^2 & \sigma^2 & \sigma^2\omega & \sigma^2\omega \\ 1 & a & a & a & a & \sigma b & \sigma b & \sigma\omega b & \sigma\omega b \\ 1 & a & a & a & a & \sigma b & \sigma b & \sigma\omega b & \sigma\omega b \\ 1 & a & a & a & a & \sigma b & \sigma b & \sigma\omega b & \sigma\omega b \\ 1 & a & a & a & a & \sigma b & \sigma b & \sigma\omega b & \sigma\omega b \\ 1 & b & b & b & b & c & c & \omega c & \omega c \\ 1 & b & b & b & b & c & c & \omega c & \omega c \\ 1 & b & b & b & b & c & c & \omega c & \omega c \\ 1 & b & b & b & b & c & c & \omega c & \omega c \end{bmatrix} \tag{16.4}$$

where a, b, and c are evaluated as the geometric average of the elements in each block,

$$\begin{aligned} a &= \sigma\omega^{1/8} \\ b &= \sigma\omega^{1/4} \\ c &= \sigma^2\omega^{1/2} \end{aligned} \tag{16.5}$$

and with regrouping according to the SNND conformations, the final statistical weight matrix becomes

$$U_{\mathrm{SNND}} = \begin{bmatrix} 1 & 4\sigma & 2\sigma & 2\sigma^2 \\ 1 & 4a & 2\sigma b & 2\sigma\omega b \\ 1 & 4b & 2c & 2\omega c \\ 1 & 4b & 2c & 2\omega c \end{bmatrix} = \begin{bmatrix} 1 & 4\sigma & 2\sigma^2(1+\omega) \\ 1 & 4a & 2\sigma b(1+\omega) \\ 1 & 4b & 2c(1+\omega) \end{bmatrix} \tag{16.6}$$

The new states on the extended statistical weight matrix correspond to a single conformation on the SNND lattice, but to more than one conformation on the fully atomistic diamond lattice with the exception of *tt* conformation. A more detailed description of the construction of the extended statistical weight matrix is given by Rapold and Mattice (28).

16.2.1.4 Long-Range Interactions

The long-range interactions were derived from the imperfect gas theory by Cho and Mattice (31). The basic idea behind the derivation process is that the interaction parameters between two monomers can be derived from the considerations of the second virial coefficient,

$$B_2 = \frac{\int \left[e^{-u(r)/kt} - 1 \right] dr}{2} = -\frac{\int f dr}{2} \tag{16.7}$$

where B_2 is the second virial coefficient, $u(r)$ is the Lennard–Jones potential, and f is the Mayer function. The interparticle potential is defined as a truncated Lennard–Jones potential with a hard core. The two parameters, σ and ε, should be optimized to have the best fit to certain selected properties. These parameters were taken from the literature (46) for a $CH_2{=}CH_2$ molecule instead of the unknown $-CH_2-CH_2-$ segment of a polyethylene chain.

$$u(r) = \begin{cases} 4\varepsilon\left[\left(\frac{\sigma}{r}\right)^{12} - \left(\frac{\sigma}{r}\right)^{6}\right], & r \geq 0.25\,\mathrm{nm} \\ \text{Hard}, & r < 0.25\,\mathrm{nm} \end{cases} \tag{16.8}$$

For the SNND lattice, B_2 is rewritten in a discretized form by separating the integral into subintegrals for each lattice cell, and regrouping them for each neighbor:

$$B_2 = -\frac{1}{2}\left[-\int_{\mathrm{cell}} dr + \sum_{1\mathrm{st}} \int_{\mathrm{cell}} f\, dr + \cdots \right] = \frac{V_c}{2}\left[1 - \sum_{1\mathrm{st}} \langle f \rangle_{1\mathrm{st}} - \cdots \right] \tag{16.9}$$

where the volume element $\int_{\mathrm{cell}} dr$ is the volume V_c of one lattice cell of the SNND lattice. The cell average Mayer function $\langle f \rangle$ is defined as follows:

$$\langle f \rangle = \frac{\int_{\mathrm{cell}} f\, dr}{\int_{\mathrm{cell}} dr} \tag{16.10}$$

In the calculation of the average Mayer function, the center of one monomer is allowed to be anywhere in the given lattice cell, whereas the other monomer is fixed at the origin. The second virial coefficient equation can be further manipulated to include the coordination number of each neighbor (z_i).

$$B_2 = \frac{V_c}{2}[1 - z_1\overline{f}_{1st} - z_2\overline{f}_{2nd} - z_3\overline{f}_{3rd} - \cdots] \tag{16.11}$$

The first three coordination numbers are 12, 42, and 92 (calculated by $10i^2 + 2$), respectively, and the overall average Mayer function ($\overline{f}_{i\text{th}}$) for the ith neighbor is the arithmetic mean of all $\langle f \rangle$ values. The overall average Mayer function is given by the equation

$$\overline{f}_{i\text{th}} = e^{-u_i/kT} - 1 \tag{16.12}$$

In the simulations, the effective interaction parameters (u_i) are used between nonbonded beads. The cohesive energy per monomer calculated from this method yields a range of values depending on the tail correction (number of interaction shells included during the calculation), and the experimental value (calculated from the solubility parameters at room temperature (47)) is between 8 and 9 kJ mol^{-1}. The calculation procedure is given in detail by Cho and Mattice (31).

16.2.1.5 Limits of the Simulation Model

The choice of the fundamental step size can have a major impact on the dynamics of the system. This issue can be avoided by adopting moves that are random, local, and realistic (physically acceptable). By making the moves random and local, the thermally induced random molecular motions are mimicked, and by making the moves realistic, the dynamics of the system are preserved, and the results resemble those of a system found in nature.

In a simulation where a continuous space is used, there is no lower limit for how much the beads can move. However, in a simulation that is performed on a lattice, like the one used in the current study, the coordinate system is simplified and only certain coordinate points are used, and therefore, each bead moves a fixed distance. The SNND lattice has a lattice spacing of 0.25 nm. This lattice spacing is also the distance that each bead moves when an attempt to move a bead succeeds. Collection of these moves, 0.25 nm at a time, results in the movement of the whole chain. If the fundamental step size of the SNND chain interferes with the dynamics of the chain, the results can be untrustworthy. One way of analyzing the impact of the fundamental step size on the dynamics of the chain is to compare the size of the chain to the fundamental step size. In Fig. 16.6, the fundamental step size is compared to the radius of gyration of the RIS chains. It is seen that the fundamental step size is comparable to the radius of gyration of the chain at low molecular weights. The ratio of the radius of gyration ($\langle R_g^2 \rangle^{1/2}$) to the fundamental step size (L_{SNND}) increases as the molecular weight of the chain increases. The value of $\langle R_g^2 \rangle^{1/2}/L_{SNND}$ is small at low molecular weights (see Fig. 16.6); therefore, the jump distance of a bead on the SNND lattice is comparable to the size of these chains. If the moves are required to be

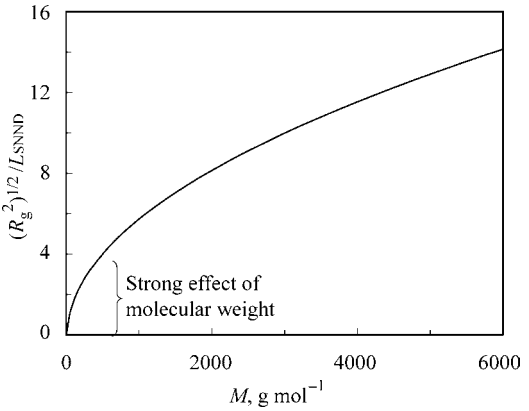

Figure 16.6 The radius of gyration of rotational isomeric state chains normalized by the fundamental step size (0.25 nm) as a function of molecular weight (41).

realistic and not interfere with the dynamics of the system, then a fundamental step size of 0.25 nm cannot be viewed as a realistic jump distance at low molecular weights.

Although the concept of fundamental step size is useful in establishing a lower limit for the SNND simulations with respect to molecular weight, it does not establish an upper limit. Therefore, the real aim of the SNND method, which is to simulate high molecular weight systems at a lower cost of computer time, is still valid. The low molecular weight systems can be simulated with the more accurate molecular dynamics simulations. It is the high molecular weight systems that force the limits of the computers, and therefore they are considered more important for the current study.

16.2.2 Simulation Setup

All of the simulations in this study are performed at 200°C (473 K), which is higher than the melting temperature. Each lattice unit on the SNND lattice corresponds to 0.25 nm, which is determined by the distance between next neighbor carbon atoms (with a bond length of 0.153 nm and a bond angle of 109.5°). The parameters of the various models studied are listed in Table 16.2 with respect to filler volume fraction (second to last column) and polymer–particle energetic interaction (last column). It must be noted that polyethylene in this model remained amorphous at all times; hence, the issue of how the presence of fillers affected the degree of crystallinity, although important, is not addressed in this work.

Each system was equilibrated for at least 15 million Monte Carlo steps (MCS), and production runs of at least 20 million MCS were performed. When the mean-square displacement of the representative chain center of mass reaches or exceeds R_g^2, the systems were assumed to have reached equilibrium. Three different and independent simulations were performed for most systems to improve statistics.

Table 16.2 Description of All Systems Investigated in the Current Study.

System identifier	Simulation cell size (L), lattice units[a]	Simulation cell size to R_g ratio (L/R_g)	Coarse-grained chain length (N)	Number of chains (N_c)	Number of particles (N_f)	Particle diameter (D_f/R_g)	Wall-to-wall distance (d/R_g)	Melt density (ρ), g cm^{-3}	Volume fraction of filler (φ), %	Monomer–particle interaction prefactor (w)
S14	21 × 22 × 22	6.37	6	252	0	—	—	0.628	—	—
S16	15 × 15 × 15	3.09	40	15	0	—	—	0.749	—	—
S1	19 × 18 × 18	2.53	80	14	0	—	—	0.767	—	—
S15	21 × 20 × 20	2.75	220	7	0	—	—	0.773	—	—
S6	22 × 22 × 22	3.09	80	24	1	0.70	2.39	0.767	0.87	1
S7	21 × 21 × 21	2.95	80	20	1	0.70	2.25	0.736	1.00	1
S3	18 × 18 × 18	2.53	80	13	1	0.70	1.83	0.764	1.59	0.1
S4	18 × 18 × 18	2.53	80	13	1	0.70	1.83	0.764	1.59	1
S5	18 × 18 × 18	2.53	80	13	1	0.70	1.83	0.764	1.59	2
S17	18 × 18 × 18	2.53	80	13	1	0.70	1.83	0.764	1.59	4
S18	18 × 18 × 18	2.53	80	13	1	0.70	1.83	0.764	1.59	6
S19	18 × 18 × 18	2.53	80	13	1	0.70	1.83	0.764	1.59	8
S9	31 × 31 × 31	2.75	220	24	1	0.90	1.86	0.767	2.56	1
S8	27 × 27 × 27	3.79	80	43	8	0.70	1.19	0.766	3.78	1
S2	18 × 18 × 18	2.53	80	12	1	1.30	1.21	0.776	10.6	1
S10	21 × 21 × 21	2.95	80	20	1	1.30	1.63	0.781	6.65	1

[a]Each lattice unit is 0.25 nm in length.

Discrete simulations can suffer from image effects due to small simulation cell size and periodic boundary conditions resulting in chains that unrealistically interact with themselves and produce erroneous results. The image effects were minimized here by setting the simulation cell size in all three coordinate directions larger than twice the polyethylene chain radius of gyration in all cases.

Monte Carlo simulations do not evolve in real time unlike molecular dynamics (MD) simulations where a time step directly corresponds to real physical time. Monte Carlo simulations, however, are comprised of many (on the order of tens of millions) steps called Monte Carlo steps, and each step represents a possible conformation of the system. The Monte Carlo method used here is based upon the Metropolis algorithm, which samples the conformational space effectively. In addition, each MCS uses only single bead moves that are random, physically realistic, and result in only local conformation changes, and because of this the progress of the system mimics the random thermal motions of molecules in the real polymer system. This allows us to make a relative comparison of the dynamic properties between chains in the bulk and chains near the filler particles. The particular Monte Carlo method used in this study has been compared to molecular dynamics simulations and to experiments to ensure compatibility (48).

In the Monte Carlo simulations, each polymer chain is represented by a series of beads, where each bead represents a segment of the polymer. Polyethylene chains were used as the matrix polymer and each bead corresponds to a polyethylene repeat unit. To represent a polyethylene melt the remaining lattice sites were filled until melt density at the simulation temperature was reached. Melt density values were obtained from an empirical equation proposed by von Meerwall et al. (49).

16.2.2.1 Representation of the Fillers

The filler particle is also made up of beads; however, unlike the polymer beads they are densely packed (close packing of spherical fillers in space). Spherical nanoparticles were added to the system by creating a volume consisting of beads that were uniquely specified as being of filler type. These sites were not accessible to the polymers. The particles were created by identifying all the sites within a specified radius; therefore, the shape of the filler particle was approximately spherical. The fillers were fixed in space during the simulation. This approximation was considered acceptable because the mass of the filler was much larger than that of the polymer beads, making it unlikely that the particle would move over the duration of the simulation.

The distance between fillers depends on the filler size and the filler volume fraction. The wall-to-wall distance d, which was defined as the smallest distance between two points located on the surface of two neighboring fillers, ranged from $1.2R_g$ to $2.4R_g$. In most simulations, one filler particle per simulation cell was considered. In these systems, the wall-to-wall distance is the surface-to-surface distance between the original filler and its nearest neighbor image (there are 12 nearest neighbors, all of which are exactly the same distance away from the original particle). Several larger systems with eight fillers per simulation cell were also

considered. In these cases, the fillers were arranged as a $2 \times 2 \times 2$ matrix within the SNND cell and the (center-to-center) distance between two fillers along a given axis is equal to half the lattice size along that axis. The results from the larger systems were indistinguishable from those obtained with systems with one filler per cell. The space occupied by the polymer was filled to a density of $\sim 0.76\,\mathrm{g\,cm^{-3}}$, as appropriate for polyethylene melt at 200°C. The filler radius and the distance between fillers were both comparable to the radius of gyration of polyethylene chains in the neat melt, which was consistent with prior research (50,51).

16.2.2.2 Polymer–Filler Energetic Interactions

The chemical makeup of filler particle is not explicitly modeled; however, the polymer–filler interaction is modeled and can represent the range of interactions including both physical and chemical adsorption. The range over which the polymer–filler interaction is varied in the current study represents physical adsorption. The energetic interaction between polymer beads and particle beads was defined using the same Lennard–Jones potential used for the polymer–polymer interactions, except it was multiplied by a prefactor w, as shown in Equation 16.13. In this equation, ε is the well depth, σ is the location of the well, and r is the distance between polymer and filler bead centers. No energetic interactions between filler beads were considered in the simulations.

$$u(r) = \begin{cases} 4w\varepsilon\left[\left(\frac{r}{\sigma}\right)^{12} - \left(\frac{r}{\sigma}\right)^{6}\right], & r \geq 0.25\,\mathrm{nm} \\ \text{Hard}, & r < 0.25\,\mathrm{nm} \end{cases} \tag{16.13}$$

The value of w is considered to be an important parameter affecting the viscoelastic properties of the material, and therefore, a range of values between $w = 0.1$ and $w = 8.0$ were investigated. When the value of w is less than, equal to, and greater than 1.0, the systems represent repulsive, neutral, and attractive polymer–particle interactions, respectively. The $w = 1.0$ case represented the physical situation when short polymer chains are grafted to the surface of the particle such that the polymer–filler and the polymer–polymer interactions are identical. Figure 16.7 shows the solvation energy or the difference in energy of a bead located at a specified distance r from the filler surface and its energy in the neat bulk. The depth of the well of the three curves indicates the meaning of the terms repulsive, neutral, and attractive used in the current study.

16.3 SIMULATION RESULTS

A series of Monte Carlo simulations of polyethylene nanocomposites were performed. The effects of several variables were investigated, including chain length, filler-to-filler distance, filler radius, and polymer–filler interaction. However, the two main variables considered were wall-to-wall distance d between filler particles and polymer–particle interaction prefactor w. The volume fraction of filler in the system

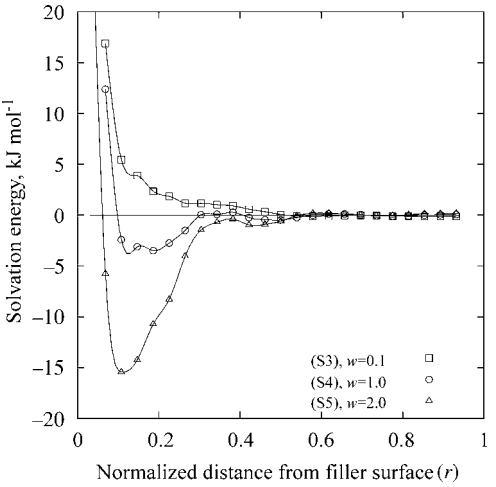

Figure 16.7 Energy difference between a bead located at distance r from the surface of the filler and a bead in the neat bulk. The distance r is normalized by half of the wall-to-wall distance ($d/2$). Three energetic interactions are shown: (i) $w = 0.1$, repulsive; (ii) $w = 1.0$, neutral; and (iii) $w = 2.0$, attractive. (From Reference 52 with permission from American Chemical Society.)

is determined by both d and the filler radius. The analysis performed can be grouped into three categories: static chain structures (52), dynamic properties (52), and chain adsorption/desorption dynamics (53). These will be discussed next.

16.3.1 Chain Structure (Static Properties)

The static chain structure analysis considers both subchain segments and the entire chain. The subchain segments include (i) bridges that connect two neighboring fillers, (ii) dangling ends that connect to the filler at one end while the other end is free, (iii) loops that begin and end on the surface of the same filler, and (iv) train segments that lie on the surface of a filler. Figure 16.8 illustrates the various types of chain segments investigated. A chain is considered attached to a filler particle when at least one of its monomers is within the cutoff distance of the filler particle. This selection of subchains is considered due to the role they are assumed to play in the viscoelasticity of the material. Bridges and dangling segments are particularly important, since bridges form the secondary network and dangling segments are expected to play a significant role in setting the viscosity.

Insight into the structure can be obtained by viewing the statistics for the whole chain. If chains that form bridges are the only chains selected, distribution of the end-to-end vector of the chain, $R_{ee}/(LN^{1/2})$, is slightly shifted to the right compared with the distribution in the neat melt, therefore, indicating a minor stretch. This obviously is an effect of the presence of the bridge. However, when the whole population of chains is considered, the end-to-end distribution is identical to that in the neat melt, to

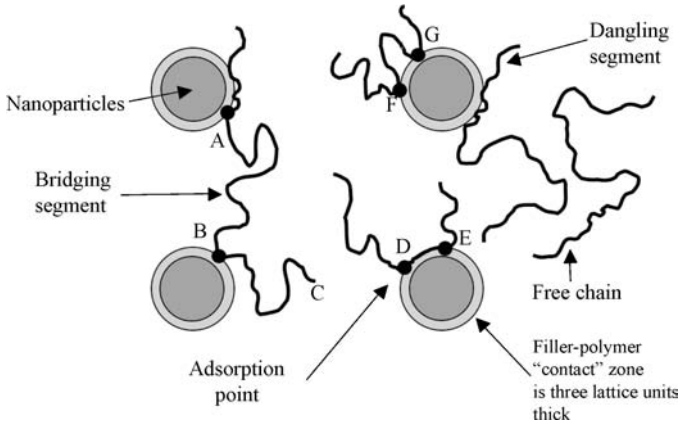

Figure 16.8 Definitions of the subchain structures that were investigated. (From Reference 52 with permission from American Chemical Society.)

within the accuracy of the present calculations. As have been observed for non-chemically specific bead-spring systems (50,51,54), the presence of the fillers does not change the structure of the chains if the wall-to-wall distance is larger than R_g, but rather chains' end-to-end vector distribution remains Gaussian.

The conclusion that chains preserve their neat melt structure is reinforced by the evaluation of R_g, as well as that of the eigenvalues of the gyration tensor λ_1, λ_2, and λ_3. Similar to the end-to-end distance, these quantities also are insensitive to d and w for the range of parameters considered. It is expected that if d becomes smaller than R_g, the chain size will decrease, as found for bead-spring systems. The ratios of the three eigenvalues of the gyration tensor $(\lambda_1/\lambda_3 : \lambda_2/\lambda_3 : \lambda_3/\lambda_3)$ are found not to be a function of distance from the particle. This ratio was found to be approximately 14:3:1 for the neat (S1) system. A change in these ratios in the composite systems would imply a change in the shape of the average chain. Again, no change was observed in these ratios as a function of distance from the surface of particle.

To further support the conclusion that chains preserve their neat melt structure, the chain orientation was also investigated by calculating the second Legendre polynomial of the angle between the major semiaxis of the chain and the vector normal to the filler surface passing through the chain center of mass. There is no significant difference in the average orientation of the major semiaxis of the chain ellipsoid as a function of distance from the surface of the particle.

16.3.1.1 Subchain Segment Statistics

An aspect that deserves attention is how frequent various subchain segments appear in various realizations of the system considered. This information is presented in Table 16.3, which includes the fraction of chains in the systems that form bridges, average number of bridges per filler, fraction of adsorbed beads per chain, and the

Table 16.3 Summary of the Chain Structures Formed in the Filled Systems.

System identifier	Average number of segments per filler particle				Number of monomers in segment normalized by the chain length (n/N)				Average fraction of chains forming at least one bridge	Average number of bridges per chain that forms bridges	Average fraction of chains with at least one bead adsorbed	Average fraction of adsorbed beads per chain
	Bridge	Dangling	Loop	Train	Bridge	Dangling	Loop	Train				
S2	18.5	16.1	16.1	34.0	0.21	0.16	0.12	0.12	0.86	1.79	1.00	0.37
S3	4.4	18.7	8.3	18.7	0.42	0.37	0.16	0.07	0.31	1.10	0.87	0.14
S4	4.2	19.1	7.7	17.2	0.42	0.36	0.15	0.10	0.30	1.09	0.87	0.17
S5	4.1	19.7	9.2	17.7	0.40	0.34	0.14	0.11	0.29	1.09	0.88	0.19
S6	1.3	24.8	7.9	17.3	0.54	0.43	0.16	0.10	0.05	1.01	0.59	0.13
S7	1.8	23.0	7.2	16.7	0.49	0.41	0.16	0.10	0.09	1.02	0.66	0.14
S9	5.5	33.9	26.9	38.7	0.42	0.36	0.08	0.04	0.21	1.07	0.77	0.10
S10	10.5	30.2	18.7	35.0	0.35	0.29	0.14	0.12	0.45	1.17	0.95	0.24
S17	3.7	20.1	8.2	19.0	0.38	0.32	0.13	0.15	0.27	1.07	0.89	0.26
S18	3.1	21.0	7.7	18.4	0.35	0.29	0.13	0.21	0.22	1.05	0.90	0.34
S19	3.6	19.8	9.8	18.8	0.36	0.27	0.12	0.20	0.26	1.07	0.95	0.39

fraction of chains that have at least one bead adsorbed (which is equal to 1 minus the fraction of free chains). Because these various systems have different values of d/R_g and w, data in Table 16.3 indicate the effect of confinement and stickiness to the filler on these quantities.

The following observations are made by comparing systems S2, S4, and S6, which are described by the same parameters, except the wall-to-wall distance, d/R_g, which increases from S2 to S6:

- The number of bridges decreases rapidly with increasing d. In fact, when $d \geq 3R_g$, no bridges form between fillers.
- As d increases, the number of dangling segments increases, which is associated with the decrease in number of bridges. Note that the filler coverage, the fraction of sites on the filler surface occupied by polymer beads, is similar in all systems.
- The number of loops and trains remain constant when $d \geq 1.83R_g$.
- While in S2, at the smallest d, all chains form bridges and a large fraction of beads are attached; in S6, 40% of the chains in the system are free.

The effect of the monomer–particle interaction prefactor w can be observed by comparing systems S3–S5 and S17–S19. Results indicate that this parameter has little effect on the number and length of subchain segments. However, an increase in the fraction of adsorbed polymer beads per chain is observed.

16.3.1.2 Subchain Segment Distributions

The chain segment structure is represented by the probability distribution function (PDF) of the number of monomers, n, in the segment and the PDF of the end-to-end vector length R_{ee}. The distributions of the number of monomers per bridge, dangling end, loop, and train segments normalized by N versus the number of monomers in the subchain segment, $P(n/N)$, are shown in Fig. 16.9. Data from systems S2, S3, S4, S5, and S6 are compared in each figure. Systems S2, S4, and S6 have the same monomer–particle interaction prefactor of $w = 1.0$ (neutral) but have a varying wall-to-wall distance d between particles, whereas systems S3–S5 and S17–S19 have varying w but the same d.

The bridge and dangling end distributions change substantially as the wall-to-wall distance d varies but are essentially independent of the interaction prefactor w (see Fig. 16.9a and b, respectively). As expected, the bridge distribution changes from a broad distribution where the mean number of monomers per bridge is approximately one half of the overall chain ($N/2$) to a sharp distribution of bridge segments containing a small number of monomers. The dangling end segment distribution changes from a nearly constant probability of having any number of monomers between 1 and N form a dangling end to a highly skewed distribution where there is a high probability of having dangling end segments having $N/2$ or less monomers. Again, this is consistent with the effect of confinement, because in S2 no long dangling ends may exist as they would form bridges.

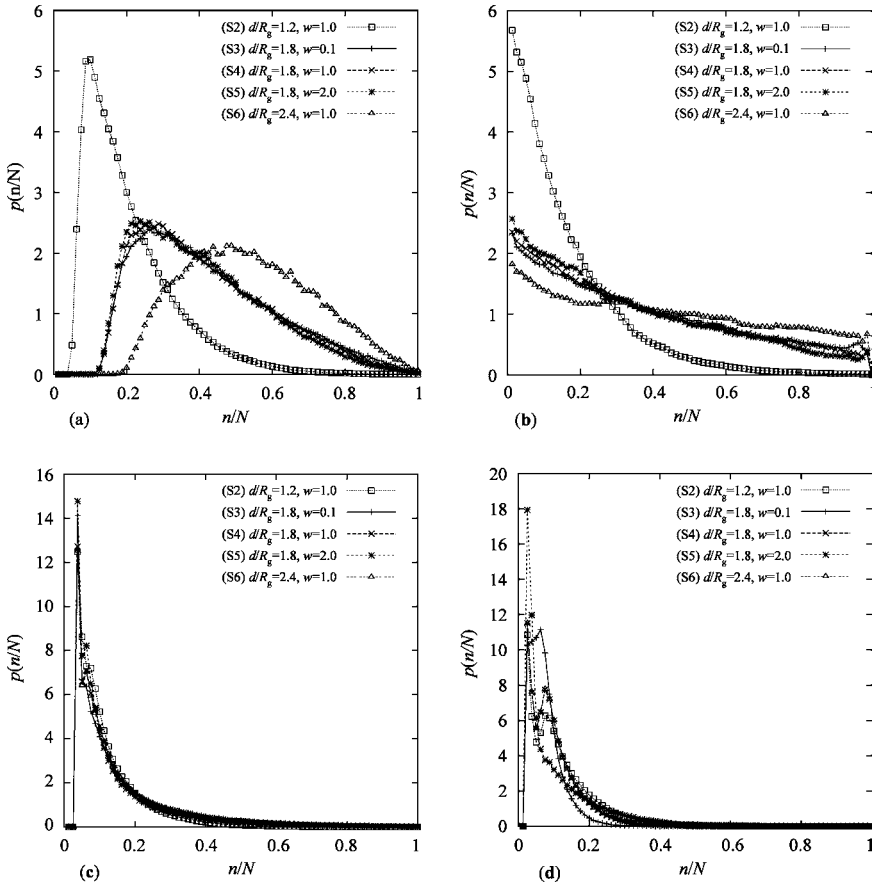

Figure 16.9 (**a**) Bridge, (**b**) dangling end, (**c**) loop, and (**d**) train segment probability distribution functions. (From Reference 52 with permission from American Chemical Society.)

As can be seen in Fig. 16.9c and d, there is very little variation in the distribution of loop and train segments as the wall-to-wall distance and the monomer–particle interaction prefactor change. This can be explained by the fact that loop and train segments are structures local to the surface of the particle. On average they form with less than $N/6$ monomers in a chain, and therefore do not feel the effect of the neighboring particles that are approximately twice as far away as their length.

The question of whether or not the equilibrium subchain structure changes as a result of the presence of nanoparticles is considered next. The issue is studied by probing the PDF of the end-to-end vector length of bridge segments. The probability distribution of bridge lengths in the nanocomposite is compared to the probability distribution of subchain segments in the neat melt. The following observations are made:

- The PDF of bridge segments are Gaussian and when properly normalized they are identical to the PDF of the entire chains that form bridges. This means that

chains forming bridges do not have subsegments that are more or less stretched than that of the entire chain.

- As the wall-to-wall distance d increases, keeping everything else constant, the bridge segments become more stretched than chains in the bulk and the variation in the number of beads per bridge decreases. Since stretched chains are stiffer than relaxed chains, due to the loss of entropy, this implies filled systems are stiffer than neat systems merely due to the presence of these stretched bridges. However, significant stretching is observed only when the wall-to-wall distance becomes larger that $2R_g$, situations in which the number of bridges per filler is very small (see Table 16.2). Hence, although an overall stiffening effect exists, it is not expected to be significant.
- As the polymer–particle energetic interaction factor w increases, no changes in the PDF of bridge segments are observed. This is because the interaction is local and does not change the chain structure on length scales equal to the chain size; however, the interaction does have a large effect on the dynamics due to an energy penalty imposed during chain detachment from the fillers.

Figure 16.10 presents various chain types as a function of w at a constant volume filler fraction of 1.59%. As can be seen, all three chain types are nearly independent of the polymer–particle interaction energy. There appears to be a slight increase in the fraction of dangling chains and a corresponding decrease in the fraction of bridges while the fraction of free chains remains constant over the entire range of w up to and including $w = 6$. This observation suggests that an increased monomer density near the surface of the filler particle may preclude bridge segments. There is also a slight decrease in the number of free chains as w increases beyond 6.

Figure 16.11 shows a very different picture of the fraction of chain types as a function of filler volume fraction and at a constant $w = 1$. The fraction of free chains

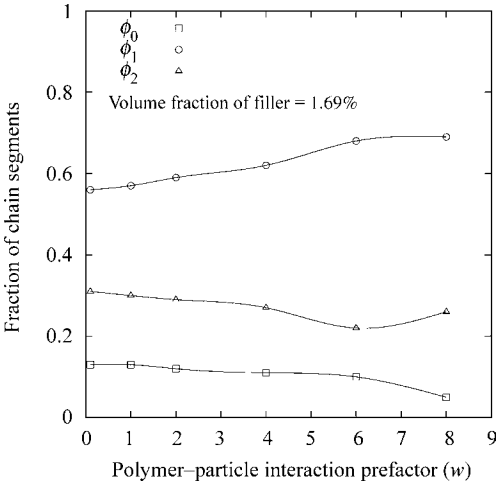

Figure 16.10 Fraction of chain types as a function of polymer–particle interaction prefactor w.

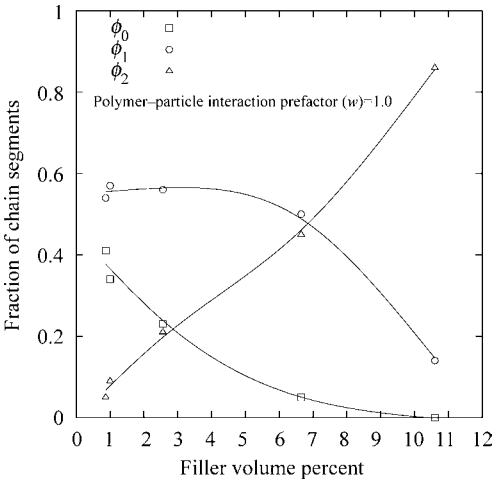

Figure 16.11 Fraction of chain types as a function of filler volume fraction.

increases quickly from zero as the volume fraction of fillers decreases. The fraction of dangling chains also increases but appears to plateau as the volume filler fraction approaches zero. The number of bridges on the contrary decreases approximately linearly to zero as the filler volume fraction decreases toward zero.

16.3.2 Chain Dynamics

The dynamics of the polyethylene chains is investigated by examining the Rouse modes and mean-square displacement of the chain center of mass, $g_3(t)$, as a function of the number of Monte Carlo steps.

16.3.2.1 Self-Diffusion

The dynamics is analyzed by evaluating the mean-square displacement of the chain center of mass, $g_3(t)$,

$$g_3(t) = \langle [r_{\text{cm}}(t) - r_{\text{cm}}(0)]^2 \rangle \tag{16.14}$$

where time t is represented by the number of MC steps and r_{cm} is the position vector of the chain center of mass. The results are shown in Fig. 16.12. The horizontal axis is normalized by the Rouse time in the neat system. Figure 16.12a demonstrates the effect of confinement ($w = 1.0$ in all these cases)—increased confinement slows down the dynamics. Various g_3 curves are parallel to each other suggesting that confinement preserves the nature of the diffusion, but changes the diffusivity.

Figure 16.12b shows the effect of the filler–polymer interaction prefactor w. The curve corresponding to the neutral interaction case ($w = 1.0$) has a slope of 1.0 beyond the Rouse time; that is, the behavior follows simple diffusion. The system

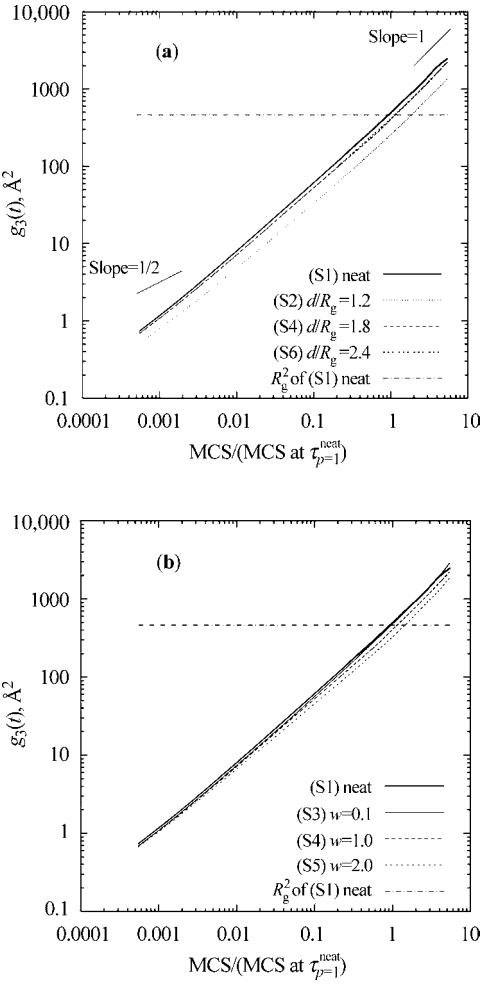

Figure 16.12 (**a**) Effect of wall-to-wall distance and (**b**) polymer–filler interaction prefactor on mean-square displacement of the center of mass of polyethylene chains. (From Reference 52 with permission from American Chemical Society.)

with repulsive interaction ($w = 0.1$) is superdiffusive, while the one with attractive interactions ($w = 2.0$) is subdiffusive (the slope is smaller than 1.0).

These findings suggest that if the polymer–filler interaction is attractive, the representative bead spends more time at the wall than in any other site of the lattice. If the interaction is repulsive, the interaction between chains and fillers pushes the chains away from the filler surface leading to the creation of a low density polymer layer in the immediate vicinity of the wall (50). As the number of occupied sites is smaller in the depleted layer than in the bulk, the residence time in these sites is shorter, which leads to the superdiffusive behavior.

16.3.2.2 Rouse Modes

The characteristic relaxation times of the system are determined in the usual way by computing the autocorrelation function of the normal modes. Figure 16.13 shows the autocorrelation function of the longest relaxation mode ($p = 1$) for various systems (see Table 16.2). Figure 16.13a displays the effect of confinement by comparing systems S2, S4, and S6 for which $w = 1.0$. As long as d is larger than $\sim 1.5R_g$ (S4 and S6), confinement is too weak to influence relaxation. Slowing down is evidenced in

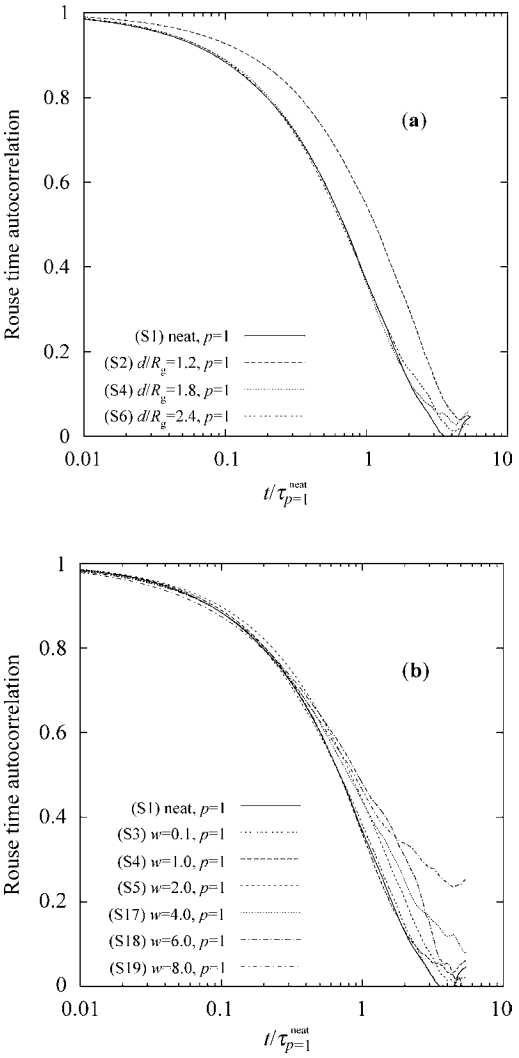

Figure 16.13 (**a**) Effect of wall-to-wall distance and (**b**) polymer–filler interaction prefactor on Rouse time. (From Reference 52 with permission from American Chemical Society.)

system S2 for which $d = 1.2R_g$. The relaxation of the neat system (S1) is plotted for reference. The effect of the prefactor w is shown in Fig. 16.13b in which the wall-to-wall distance d is held constant (systems S3, S4, and S5). As expected, increasing polymer–filler adhesion leads to an additional slowdown.

Next, the issue of whether there is a length scale below which the confinement has no effect on Rouse relaxation is investigated. The idea is rooted in the presumption that fillers will only affect relaxation modes with wavelengths comparable to the characteristic length scale of the microstructure, for example, the wall-to-wall distance. In the limit, one might expect that the motion of a single monomer would not be affected by the presence of a particle that is much larger than the chain itself. To test this hypothesis, all Rouse modes were evaluated. The results are shown in Fig. 16.14 in which the normalization of the two axes reflects the expected Rouse scaling of the relaxation times (55):

$$\tau_p = \tau_0 \left(\frac{N}{p}\right)^2 \tag{16.15}$$

A straight line with a slope of 2 and a y-axis intercept of τ_0 is predicted by this relationship and agrees with curves shown in Fig. 16.14, although the fit is better at large p for all systems including the neat system. The data for the given system align with each other, which suggests that the Rouse scaling is followed. The lines are shifted in the vertical direction, which is a manifestation of the slowing down shown in Fig. 16.13a. Interestingly, the assumption made above seems to be false: confinement affects all relaxation modes in the same way independent of their wavelength. The conclusion remains valid for the data in Fig. 16.13b; the slowing down due to w is similar for all modes. This observation has implications on the modeling of the rheology of the material at larger scales. It implies that the effect of fillers on

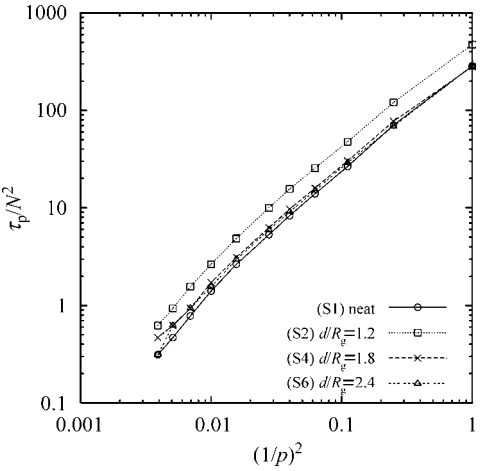

Figure 16.14 The Rouse relaxation times τ_p versus $(1/p)^2$. (From Reference 52 with permission from American Chemical Society.)

dynamics (at least Rouse dynamics) may be represented in a mean field sense by an increase in the average friction the monomer feels. The effective friction coefficient may be calibrated from the intercept of the vertical axis in Fig. 16.14. This mean field view was taken in the rheological model presented in Reference.

16.3.3 Adsorption–Desorption Dynamics

A study of the dependence of the chain–filler particle adsorption time t_{ad} on various system parameters is presented here. This information is crucial in modeling the dynamic behavior of the nanocomposite on larger scales (11). Previously, the polymer–filler affinity was described as having an important role in the viscoelastic properties of the polymer nanocomposite, and the chain dynamics (but not the chain structure) were shown to depend on this interaction. The polymer–particle interaction controls the adsorption time of chains to fillers. To illustrate this point consider two extremes. First, when the interaction is highly repulsive resulting in the characteristic adsorption time being zero, there is no bridging or secondary network formed, and experimental studies (6) have shown that in this case no reinforcement is seen. Second, at the other extreme of the adsorption time spectrum an infinitely long adsorption time created by permanent chemical bonds between filler and polymer results in cross-linked polymers that are highly reinforced.

To study the adsorption time, the length of the chain segment interacting with the filler particle (N_1) was measured throughout a series of simulations (53). The definition of the measure N_1 is shown in Fig. 16.15. The value of N_1 is the number of chain beads between (and including) the first and the last bead in contact with the filler particle on a given chain. The adsorption zone is defined by the range of the polymer–filler potential and contains three lattice sites in the radial direction. Note that N_1 may include loops.

The two measures N_a and N_1 exhibit a high frequency oscillation overlapped on lower frequency components. A chain may come in contact with the filler, build up contacts, and then diffuse away from the filler. The lower frequency process is of

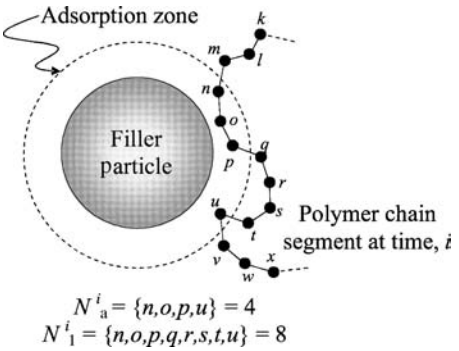

Figure 16.15 Definition of the measures of chain adsorption, N_a^i and N_1^i. (From Reference 53 with permission from American Chemical Society.)

interest here. An adsorption–desorption event is defined as a span of the simulation in which N_a is continuously greater than zero. The duration of the adsorption–desorption event is equal to the residence time of that chain, t_{ad}. From these data, it is possible to estimate the averages of the two fluctuating functions over each t_{ad},

$$\overline{N}_a = \overline{N}_a(t_{ad}) = \frac{1}{n_{ad}} \sum_{j=1}^{n_{ad}} \frac{1}{t_{ad}} \sum_{i=1}^{t_{ad}} N_a^i \tag{16.16}$$

$$\overline{N}_l = \overline{N}_l(t_{ad}) = \frac{1}{n_{ad}} \sum_{j=1}^{n_{ad}} \frac{1}{t_{ad}} \sum_{i=1}^{t_{ad}} N_l^i \tag{16.17}$$

where n_{ad} is the number of adsorption–desorption events whose duration is equal to t_{ad} and the overbar represents both time and replica averaging. Another similar measure is N_a^{max}, defined as the maximum value of N_a during an adsorption–desorption event of length t_{ad}. Its average, $\overline{N_a^{max}}$, is also a function of t_{ad}. The overbar represents a replica average over all n_{ad}.

The relationship between $\overline{N_a}$, $\overline{N_l}$, and t_{ad} is shown in Fig. 16.16. The adsorption time is normalized here by the Rouse relaxation time in the neat polymer, τ_R^{neat}. The two functions are well described over a broad range of t_{ad} by power laws of powers 0.5 for $\overline{N_l}$ and 0.25 for $\overline{N_a}$. It is also observed that the curves shift downward as the polymer–particle interaction increases from $w = 0.1$ to $w = 8$. At long residence times, a transient to a plateau is observed. The plateau is more obvious in Fig. 16.16b and becomes even more apparent when smaller chain lengths are considered.

It is interesting to note that the curve for the neat system (S1) has the same shape and slope as the systems containing filler particles, the only difference being a vertical shift of the curves corresponding to S1 relative to the other systems. The data for the neat system were collected considering a virtual filler of the same size as that used in the model of the composite. The chain was considered to be ''attached'' as long as at least one of its beads was present in an annular zone around the virtual filler, where the zone is identical to that used to define attachment in the filled systems (Fig. 16.15). The similarity between (S1) and the filled systems shown in Fig. 16.16 indicates that the general shape of the function is controlled by the geometry of the problem. Note that the Gaussian statistics of the chain conformations are not affected by the excluded volume of the filler.

The attachment–detachment process involves two distinct physical phenomena: (i) the random walk of the chain in the close neighborhood of the filler, which is well described by the Rouse model, and (ii) diffusion of chains to/from the filler on longer time- and spatial scales (57,58). The linear portion of the curves in Fig. 16.16b is due to the Rouse motion of the adsorbed chain segments. To illustrate the Rouse scaling, consider the Rouse time for mode p (see Eq. 16.18, where ζ is the friction coefficient, b is the Kuhn segment length, N is the number of Kuhn segments in a chain, k is the Boltzman constant, and T is the temperature).

$$\tau_p = \frac{\zeta b^2}{3\pi^2 kT} \left(\frac{N}{p}\right)^2 \tag{16.18}$$

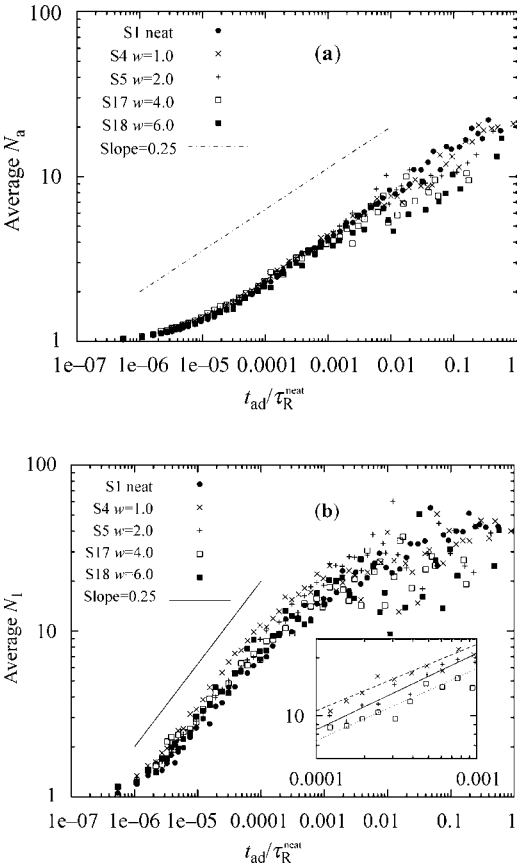

Figure 16.16 (**a**) Average number of adsorbed beads per chain versus chain residence time, and (**b**) average length of adsorbed segment versus chain residence time for $w = 1$, 2, 4, and 6. (From Reference 53 with permission from American Chemical Society.)

Identifying $N/p = \overline{N_l}$ and $\tau_p = t_{ad}$, one may write the following:

$$\log(\overline{N_l}) = \tfrac{1}{2}\log(t_{ad}) - \tfrac{1}{2}\log\left(\frac{\zeta b^2}{3\pi^2 kT}\right) \tag{16.19}$$

This justifies the observed slope of 0.5 at small and moderate t_{ad} in Fig. 16.16b.

The vertical shift of the curves in Fig. 16.16b with increasing w is due to the increase of the local apparent friction of the chains induced by the energetic interaction with fillers. This is represented by the second term on the right-hand side of Equation 16.19. This issue was studied in detail in the previous work (53), where the variation of the effective, system average ζ with respect to w was determined.

Deviation from the initial slope value of 0.5 in Fig. 16.16b to the plateau is conjectured to be purely geometric in nature and not related to excluded volume

interactions with the filler. This is supported by the observation that the transition has similar width whether the filled or the neat systems are considered. In the simulations described here the chains cannot cross one another, and hence, effects due to chain entanglement should be seen. To eliminate the effects of entanglements, a system of phantom chains was examined. The deviation from the initial slope of 0.5 is observed in the phantom chain simulations too. Therefore, the deviation is not a result of entanglements between polymer chains. The possibility that the deviation is a result of the highly adsorbed chains with conformations different from the average chain in the system was also investigated. For this reason, chains that stay adsorbed on the filler for extended periods were selected and their end-to-end vectors were computed. It was concluded that the conformations of these chains are not different from all other chains in the same system (and from those in the bulk, for that matter). This conclusion is similar to that obtained from a previous study (50), where it was shown that the statistics of chain conformations were not affected by the presence of filler particles.

The dynamics of the adsorption–desorption processes described by the data in Fig. 16.16 is not sensitive to the position of the center of mass of the respective chain relative to the surface of the filler. This issue was investigated by analyzing chain statistics with respect to their distance from the filler surface. This distance is divided into equal length shells (bins) and a plot similar to that shown in Fig. 16.16 was prepared for each bin. Plots of different bins showed similar results.

An estimate of the overall average of the adsorption time τ_{ad} for a given system is desirable. The obvious procedure for finding this quantity would be to find the mean of the PDF function of t_{ad} determined from the simulation. However, this distribution is dominated by very short lifetimes. Recent investigations found similarly that the dynamics of desorbing chains can be grouped into rapid and slow events (58). Clearly, viscoelasticity is controlled by the slow events; hence, in computing the average it is desirable to filter out high frequency fluctuations. A simple procedure by which this can be accomplished is to compute the average attachment time as $\tau_{ad} = t_{ad}(w, N_a = \langle N_a \rangle)$, where $\langle N_a \rangle$ is the ensemble average of the number of beads adsorbed per chain and taking $\langle N_a \rangle \approx \overline{N_a}$ one obtains $\tau_{ad} = \overline{t_{ad}} = t_{ad}(w, \overline{N_a})$, where the overbar represents time averaging. The resulting values of τ_{ad} for various values of w are shown in Fig. 16.17.

The relationship between the system average adsorption time and the polymer–filler affinity parameter w suggests an Arrhenius dependence of the form

$$\tau_{ad}(\mathrm{w}) = c_1 e^{c_2 w} \tag{16.20}$$

where c_1 and c_2 are constants. The slight deviation of the data points for $w = 6.0$ and $w = 8.0$ is most likely a result of insufficient statistics. Interestingly, the information about the geometry and the chain size is contained in the preexponential parameter c_1. The dependence of c_1 on chain size can be determined using data from the neat systems and the virtual filler approach described above. The parameter c_1 is found to

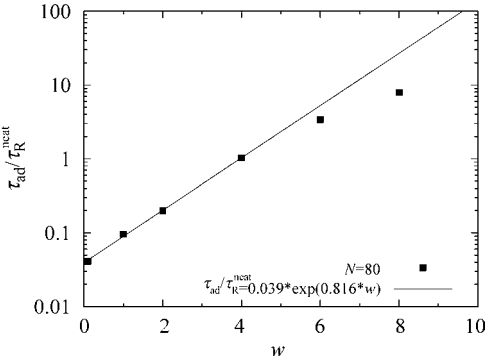

Figure 16.17 Characteristic adsorption/desorption time as a function of polymer–particle interaction parameter w. (From Reference 53 with permission from American Chemical Society.)

be an exponentially increasing function of the chain length N, as shown in Fig. 16.18. The constant c_2 is inversely proportional to the temperature, as observed from simulations at various temperatures. When this relation is used in molecular models aimed at capturing the rheology of the composite, the two constants must be determined for the respective system from this type of chemically specific simulations. The expression for the average attachment time determined for the systems investigated is given as follows:

$$\tau_{\mathrm{ad}}(\mathrm{w}) = 0.039\tau_{\mathrm{R}}^{\mathrm{neat}} e^{0.816w} \tag{16.21}$$

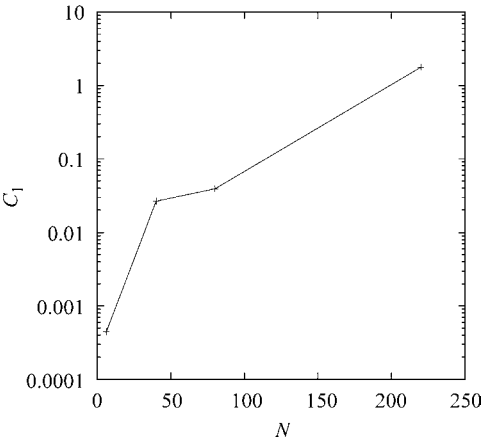

Figure 16.18 The preexponential parameter c_1 described in Equation 16.9 as a function of chain length N.

16.4 CONCLUSIONS

A number of conclusions about polymer nanocomposites can be drawn from the current work. At the discrete scale, a series of on-lattice Monte Carlo simulations were performed representing systems of polyethylene chains containing spherical nanoparticles. The relative fraction of chain segment types (free, dangling, and bridge) found in polymer nanocomposites can only be determined from the discrete scale simulations and are important input parameters to any mesoscale rheological model. The fraction of chain segment types was found to be weakly dependent on the polymer–particle interaction and strongly dependent on the volume fraction of filler.

Other general conclusions drawn from the discrete model about the chain structure are as follows. The segment length probability distribution of bridge and dangling end segments changes drastically as the distance between particles decreases but the segment length probability distribution of loop and train segments does not. For all chain segment types investigated, the length distribution did not change significantly as a result of varying the energetic interaction between monomer and particle.

The static chain structure of polyethylene nanocomposites is investigated by examining three chain measures: average size, average shape, and average chain orientation, between the composite systems and the comparable neat system. For all three measures, no significant variation is observed between values found for the composite systems and those found for the neat system. In addition, no significant variations were found in these measures as a function of distance from the particle for all composite systems investigated. Bridge segments become more stretched relative to neat chain segments containing the same number of monomers as the distance between fillers increases.

The static chain structure investigation using the chemically specific SNND model for polyethylene did not show any differences compared to previous simulations (11,50) that used a generic bead-spring model. Nearly identical probability distribution functions for the various chain structures are found using either the polyethylene model or the generic bead-spring model. This finding supports the utility of faster, more generic models to investigate chain structures at length scales comparable to the chain radius of gyration.

The dynamics of polyethylene chains is found to be different in the composite systems compared to the neat polyethylene. The Rouse relaxation time τ_R of the entire chain increased rather suddenly as the distance between fillers decreased below $\sim 1.5R_g$. In addition, τ_R also increased for systems with attractive monomer–particle interactions compared to the systems with neutral and repulsive interactions. The Rouse dynamics is slowed in all subsections of the chain, no matter how small the subsection is, suggesting that on average every monomer feels the confinement of the filler particles.

The dynamics of the attachment/detachment process of chains to/from spherical fillers was also investigated using the SNND model. It was observed that attachment time scales with the number of attached beads following a power law. The physical explanation for this behavior resides in the Rouse motion of the chains and the Rouse

scaling holds for many decades in time. The system average attachment time follows an Arrhenius dependence on the magnitude of the energetic interaction between polymers and filler.

NOMENCLATURE

b	Kuhn segment length
B_2	Second virial coefficient
d	Wall-to-wall distance between filler particles
D_f	Filler diameter
E	Energy
f	Mayer function
G'	Storage modulus
G''	Loss modulus
g_3	Mean-square displacement of the center of mass
k	Boltzman constant
L_{SNND}	Unit lattice size, fundamental step size
MCS	Monte Carlo time step
MD	Molecular dynamics
N	Chain length
n_{ad}	Number of adsorption–desorption events
N_l	Chain segment length interacting with filler
N_a	Chain segment length adsorbed on filler
$\overline{N_a^{max}}$	Average of N_a^{max}
$\overline{N_l}$	Average of N_l
$\overline{N_a}$	Average of N_a
N_a^{max}	Maximum value of N_a^i during an adsorption–desorption event
p	Rouse relaxation mode index
PDF	Probability distribution function
r	Radial distance
r_{cm}	Center of mass position vector
R_{ee}	End-to-end vector length
R_g	Radius of gyration
SNND	Second nearest neighbor diamond
T	Temperature
t	Time
t_{ad}	Adsorption time
T_g	Glass transition temperature
U	Statistical weight matrix
$u(r)$	Lennard–Jones potential energy function
V_c	Volume of one SNND lattice cell
w	Lennard–Jones interaction energy prefactor
z	Coordination number
ζ	Friction coefficient

λ	Random number
$\lambda_1, \lambda_2, \lambda_3$	Eigenvalues of the gyration tensor
π	Pi number
ρ	Density
σ	First-order statistical weight
σ, ε	Lennard–Jones parameters
τ	Relaxation time constant
τ_0	Monomer relaxation time constant
φ	Filler volume fraction
ω	Second-order statistical weight

REFERENCES

1. P. Ajayan, L. S. Schadler, and P. V. Braun, *Nanocomposite Science and Technology*, Wiley, New York, 2003.
2. T. J. Pinnavaia and G. W. Beall (eds.), *Polymer–Clay Nanocomposites*, Wiley, New York, 2000.
3. L. Wei, T. Tang, and B. Huang, *J. Polym. Sci. A*, **42**, 941 (2004).
4. Q. Zhang and L. Archer, *Macromolecules*, **37**, 1928 (2004).
5. Q. Zhang and L. Archer, *Langmuir*, **18**, 10435 (2002).
6. S. S. Sternstein and A. Zhu, *Macromolecules*, **35**, 7262 (2002).
7. Z. Zhu, T. Thompson, S. Q. Wang, E. D. von Meerwall, and A. Halasa, *Macromolecules*, **38**, 8816–8824 (2005).
8. H. Montes, F. Lequeux, and J. Berriot, *Macromolecules*, **36**, 8107 (2003).
9. R. Ozisik, J. Zheng, P. J. Dionne, C. R. Picu, and E. D. von Meerwall, *J. Chem. Phys.*, **123**, 134901 (2005).
10. G. Heinrich and M. Kluppel, *Adv. Polym. Sci.*, **160**, 1 (2002).
11. A. S. Sarvestani and R. C. Picu, *Rheol. Acta*, **45**, 132 (2005).
12. M. Vacatello, *Macromolecules*, **34**, 1946 (2001).
13. M. Vacatello, *Macromol. Theory Simul.*, **10**, 187 (2001).
14. M. Vacatello, *Macromol. Theory Simul.*, **11**, 53 (2002).
15. M. Vacatello, *Macromol. Theory Simul.*, **11**, 757 (2002).
16. M. Vacatello, *Macromol. Theory Simul.*, **12**, 86 (2003).
17. M. Vacatello, *Macromolecules*, **36**, 3411 (2003).
18. M. Vacatello, *Macromol. Theory Simul.*, **15**, 303 (2006).
19. F. W. Starr, T. B. Schroder, and S. C. Glotzer, *Phys. Rev. E*, **64**, 021802 (2001).
20. Y. Gebremichael, T. B. Schroder, F. W. Starr, and S. C. Glotzer, *Phys. Rev. E*, **64**, 051503 (2001).
21. F. W. Starr, T. B. Schroder, and S. C. Glotzer, *Macromolecules*, **35**, 4481 (2002).
22. F. W. Starr, J. F. Douglas, and S. C. Glotzer, *J. Chem. Phys.*, **119**, 1777 (2003).
23. H. Lin, F. Erguney, and W. L. Mattice, *Polymer*, **46**, 6154 (2005).
24. F. M. Erguney, H. Lin, and W. L. Mattice, *Polymer*, **47**, 3689 (2006).
25. J. E. Mark, R. Abou-Hussein, T. Z. Sen, and A. Kloczkowski, *Polymer*, **46**, 8894 (2005).
26. M. A. Sharaf, A. Kloczkowski, T. Z. Sen, K. I. Jacob, and J. E. Mark, *Eur. Polym. J.*, **42**, 796 (2006).
27. R. F. Rapold and W. L. Mattice, *J. Chem. Soc. Faraday Trans.*, **16**, 2435 (1995).
28. R. F. Rapold and W. L. Mattice, *Macromolecules*, **29**, 2457 (1996).

29. N. Metropolis, A. W. Rosenbluth, M. N. Rosenbluth, A. H. Teller, and E. Teller, *J. Chem. Phys.*, **21**, 1087 (1953).
30. M. P. Allen and D. J. Tildesley, *Computer Simulation of Liquids*, Oxford University Press, New York, 1987.
31. J. Cho and W. L. Mattice, *Macromolecules*, **30**, 637 (1997).
32. P. J. Flory, *Statistical Mechanics of Chain Molecules*, Wiley, New York, 1969.
33. W. L. Mattice and U. W. Suter, *Conformational Theory of Large Molecules: The Rotational Isomeric State Model in Macromolecular Systems*, Wiley, New York, 1994.
34. R. F. Rapold and W. L. Mattice, *Macromolecules*, **29**, 2457 (1996).
35. J. Cho and W. L. Mattice, *Macromolecules*, **30**, 637 (1997).
36. P. Doruker and W. L. Mattice, *Macromol. Theory Simul.*, **8**, 463 (1999).
37. R. Ozisik, P. Doruker, W. L. Mattice, and E. D. von Meerwall, *Comput. Theor. Polym. Sci.*, **10**, 411 (2000).
38. T. C. Clancy, M. Putz, J. D. Weinhold, J. G. Curro, and W. L. Mattice, *Macromolecules*, **33**, 9452 (2000).
39. T. C. Clancy and W. L. Mattice, *Chem. Phys.*, **115**, 8221 (2001).
40. G. Xu, H. Lin, and W. L. Mattice, *J. Chem. Phys.*, **119**, 6736 (2003).
41. R. Ozisik, Ph.D. dissertation, University of Akron, Akron, Ohio, 1999.
42. T. Haliloglu, T. Cho, and W. L. Mattice, *Macromol. Theory Simul.* **7**, 613 (1998).
43. P. Doruker and W. L. Mattice, *Macromolecules*, **30**, 5520 (1997).
44. A. Abe, R. L. Jernigan, and P. J. Flory, *J. Am. Chem. Soc.*, **88**, 631 (1966).
45. T. Halioglu and W. L. Mattice, *J. Chem. Phys.*, **108**, 6989 (1998).
46. J. O. Hirschfelder, C. F. Curtiss, and B. B. Bird, *Molecular Theory of Gases and Liquids*, Wiley, New York, 1954.
47. D. W. van Krevelan, *Properties of Polymers*, Elsevier Science Publishers, Amsterdam, Netherlands, 1990.
48. P. Doruker and W. L. Mattice, *Macromol. Symp.*, **133**, 47 (1998).
49. E. von Meerwall, E. Beckman, J. Jang, and W. L. Mattice, *Chem. Phys.*, **108**, 4299 (1998).
50. M. S. Ozmusul and R. C. Picu, *Polymer*, **43**, 4657 (2002).
51. M. S. Ozmusul, R. C. Picu, S. S. Sternstein, and S. Kumar, *Macromolecules*, **38**, 4495 (2005).
52. P. J. Dionne, R. Ozisik, and C. R. Picu, *Macromolecules*, **38**, 9351 (2005).
53. P. J. Dionne, C. R. Picu, and R. Ozisik, *Macromolecules*, **39**, 3089 (2006).
54. R. C. Picu and M. S. Ozmusul, *J. Chem. Phys.*, **118**, 11239 (2003).
55. M. Rubinstein and R. Colby, *Polymer Physics*, Oxford University Press, New York, 2003.
56. A. S. Sarvestani and R. C. Picu, *Polymer*, **45**, 7779 (2004).
57. Y. Wang, R. Rajagopalan, and W. L. Mattice, *Phys. Rev. Lett.*, **74**, 2503 (1995).
58. K. Smith, M. Vladkov, and J. L. Barrat, *Macromolecules*, **38**, 571 (2005).

Chapter 17

Characteristics of Multiwall Carbon Nanotube and Polyethylene Composites Prepared by Gelation/ Crystallization from Solutions

Masaru Matsuo,[1] Yuezhen Bin,[1] Qingyun Chen,[1] and Atsuko Yamanaka[1]

17.1 INTRODUCTION

Since their discovery, carbon nanotubes (CNTs) have attracted great interest. CNTs are long and slender fibers with hexagonal carbon (graphite structure) walls, which are often capped at the two ends. CNTs possess superior mechanical, thermal, and electrical properties and so offer tremendous opportunities for developing new fundamental material systems (1–3).

Much effort has already been made to produce polymer–nanotube composites with significantly improved mechanical (4–6) and electrical (7) properties. Salvetat et al. (8) studied the effect of CNT dispersions on the mechanical properties of polymer/CNT composites, and found that poor dispersion and ropelike entanglement of CNTs led to drastic weakening of the composites.

The processing of CNT/polymer composites is still in its infancy. Significant issues about the purification and dispersion of CNTs and the bulk processing of these materials still remain. The ability to disperse CNTs into a polymer may be the most critical processing parameter for controlling the properties of the composites. The

[1]Department of Clothing and Apparel Science, Nara Women's University, Nara 630-8263, Japan

Polyolefin Composites, Edited by Domasius Nwabunma and Thein Kyu

most popular method for preparing CNT/polymer composites involves the direct mixing of the CNTs into the polymer with a twin-screw melt mixer (9,10). However, this method is limited for less viscose polymer materials.

The dispersion of CNTs in solvents or polymers in the presence of surfactants is another important method that does not require reaction. Dispersion has been achieved using a number of methods, including sonication of the nanotubes in a solvent, chemical modification of the nanotube surface with the aid of surfactants (11), functionalization of the end caps with long aliphatic amines (12), or functionalization of the sidewalls with fluorine (13) or alkanes (14), all resulting in stable suspensions of CNTs. None of these methods, however, is ideal for composite processing. The use of surfactants results in impurities in the composite, and is also limited to water-soluble polymers or polymers in latex form. Functionalizing the CNT end caps subsequently limits further chemical modification for controlling bonding with the matrix, while modification of the sidewalls can affect the mechanical and electrical properties (15). Certain solvents such as *N*-methylpyrrolidone, dimethyl formamide, hexamethylphosphoramide, cyclopentane, tetramethylene sulfoxide, and ε-caprolactone have been identified as suitable solvents for the direct dispersion of CNTs. These solvents are all strong Lewis bases without hydrogen donors, although not all solvents with these characteristics are good solvent for CNTs.

On the contrary, ultrahigh molecular weight polyethylene (UHMWPE) prepared by gelation/crystallization from dilute decalin solutions possesses superior drawability (16). CNT is impossible to disperse uniformly into UHMWPE using a melt mixer due to its high melting viscosity. Zhang et al. reported a new method for dispersing single-wall carbon nanotubes (SWNT) bundles in UHMWPE by spraying an aqueous solution of these SWNTs containing sodium dodecylbenzene sulfate as surfactant onto UHMWPE powder, and then a composite film was prepared from the UHMWPE powder dissolved in xylene (17).

This chapter mainly introduces the gelation/crystallization method for preparing UHMWPE–CNT composites. The morphology of UHMWPE–CNT composite gel films prepared with different multiwall carbon nanotube (MWNT) contents, and their corresponding drawabilities were investigated (18). The mechanical properties, electrical properties, and the temperature dependencies of the composites were studied in detail.

Here, it should be noted that the polymer–MWNT interactions include (a) multicontacts between the polymer chains on the surface of the MWNTs (physiosorption), (b) reactions of the MWNTs with polymers (chemisorption), and (c) mechanical chain entanglements and covalent carbon–carbon cross-links within the polymer matrix (19, 20). These interactions obviously influence the electrical conductivity and mechanical properties of the composites. The uniform mixing of MWNTs into UHMWPE by gelation/crystallization from a solution depends on the structure of the curved graphene sheets of the MWNTs. MWNTs with few defects in the curved graphene sheets induce hard dispersion into the UHMWPE matrix. To pursue uniform mixing of UHMWPE and MWNTs, comixing of other polymers together with UHMWPE and MWNTs in cosolvent must be taken into consideration. The ethylene–methyl methacrylate (EMMA) copolymer is one of the suitable

comixing polymers for UHMWPE, since there are polar side groups (—C=O) in the alkyl main chains. The dispersion of MWNTs in the UHMWPE/EMMA matrix could be improved drastically. Of course, the uniform mixing of MWNTs (having a number of defects) into UHMWPE can be easily achieved by the described gelation/crystallization method.

17.2 CHARACTERISTICS OF UHMWPE, EMMA, AND TWO KINDS OF MWNTs

The characteristics of UHMWPE and EMMA used in this chapter are listed in Table 17.1.

Figures 17.1a and b shows Raman spectra for two kinds of MWNTs, revealing two prominent peaks at approximately 1562 and 1334 cm^{-1}, respectively. The former peak, termed as the G-band, is associated with the Raman-allowed phonon mode E_{2g}, and the latter termed as the D-band, corresponds to the disorder-induced phonon mode due to the infinite size of the crystals and defects. Accordingly, the MWNTs for Fig. 17.1a comprise curved graphene sheets with a number of defects, in which the diameters of the MWNTs are in the range of 12–17 nm. On the contrary, the MWNTs in Fig. 17.1b are composed of ordered graphene sheets with few defects, in which the diameters and lengths of the MWNTs are in the ranges of 10–50 nm and 10–20 μm, respectively.

In our experiment, as shown in Table 17.1, UHMWPE (Hercules 19000/90189) had an average viscosity molecular weight ($\overline{M}_v = 6 \times 10^6$), while the fibrous-type MWNTs were formed using imperfect graphene sheets with a number of defects. To make homogeneous blend gels, MWNTs were first ultrasonicated in decalin solvent for more than 10 h at room temperature. Then, UHMWPE was loaded into the solution, and the mixture was stirred and heated at a mild heating rate up to 140°C, where it was maintained for 1 h. The final concentration of UHMWPE was determined to be 1 g/100 ml decalin, which was higher than the optimum concentration of UHMWPE, and the concentration of decalin was found to be

Table 17.1 Some Properties of the Used Polymers.

Specimen	MMA, mol%	mp, °C	$\overline{M}_n^a$	$\overline{M}_v^b$	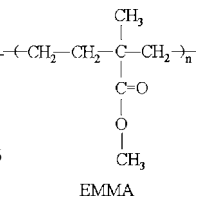
EMMA	14.6	64	3.1×10^4		
UHMWPE		142		6×10^6	

From Reference 19 with permission from the American Chemical Society.

[a] $\overline{M}_n$ = average number molecular weight.

[b] $\overline{M}_v$ = average viscosity molecular weight.

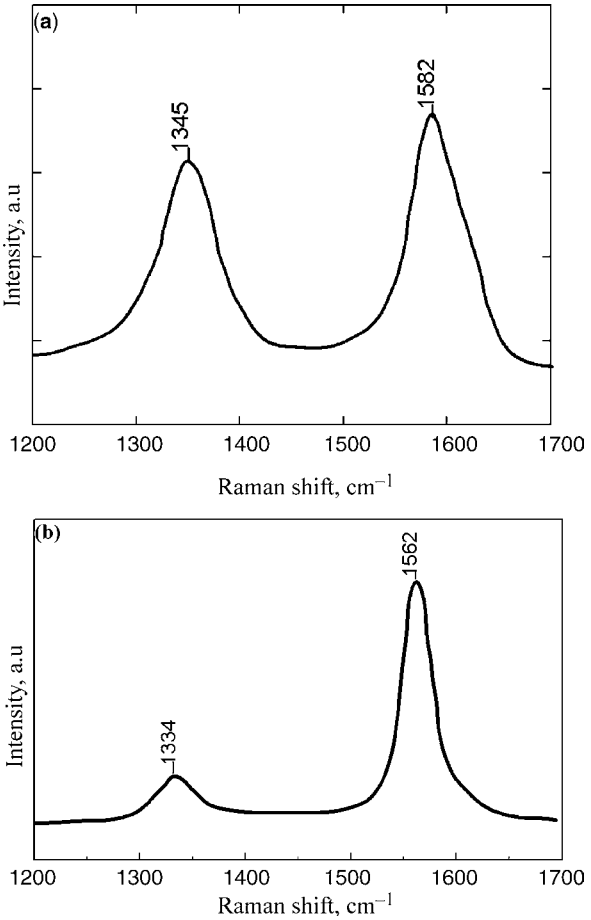

Figure 17.1 Raman spectra for two kinds of MWNTs.

0.4 g/100 ml for maximum drawability (21). However, this high concentration resulted in a highly viscous solution, and provided strong shear forces for making CNTs disperse well in the solution. The volume of solution was controlled to obtain films with thicknesses of 700–800 μm. The hot homogenized solution was quenched by pouring it into a glass dish at room temperature, thus generating a gel. The solvent decalin was evaporated from the gel under room temperature or 60°C. The strip was clamped in a manual stretching device and stretched in a hot oven at 135°C.

17.3 ADVANTAGE OF PREPARING UHMWPE–MWNT COMPOSITE BY GELATION/CRYSTALLIZATION

Figure 17.2a shows the electrical conductivity as a function of the content of conductive fillers, carbon black (CB), and MWNTs used in the UHMWPE-based

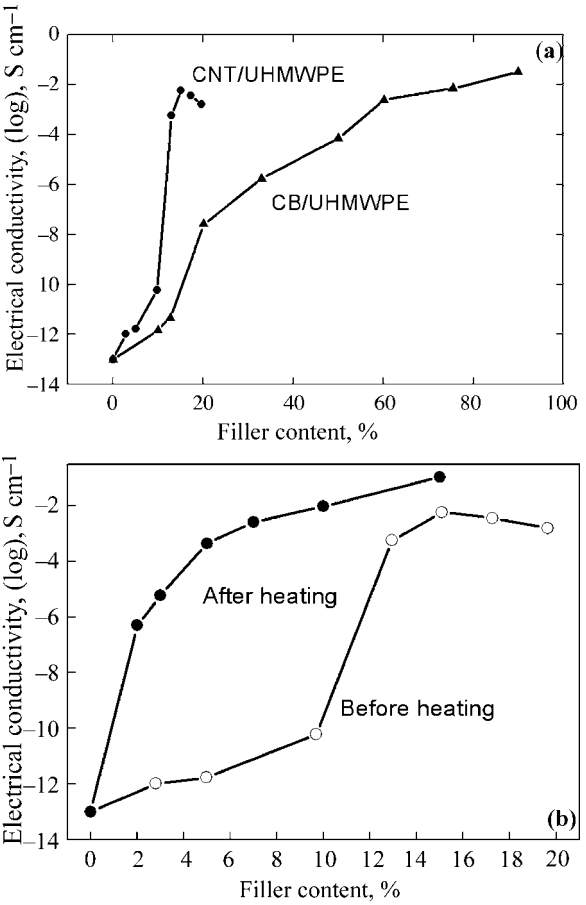

Figure 17.2 Electrical conductivity of composites. (**a**) UHMWPE–MWNT and UHMWPE–CB composites as a function of filler content. (From Reference 18 with permission from the American Chemical Society.) (**b**) Original dry UHMWPE–MWNT composites and treated by heating up to 140°C and cooling down to room temperature.

composites, which were dried at room temperature. The MWNTs discussed in Section 17.3 and 17.4 have a number of defects in the graphene sheets, as shown in the Raman spectrum in Fig. 17.1a. The electrical conductivity values of the composite films increased 11 orders of magnitude from 10^{-13} to 10^{-2} S cm^{-1} with increasing MWNT content. This indicated a typical percolation transition behavior. It is clearly seen that the percolation threshold of the composites of MWNTs is much lower than that of the UHMWPE–CB composites. This should be attributed to the high aspect ratio of the MWNTs, relating to overlapping of the carbon fillers. MWNTs appear to be a typical example of a highly structured and extended material. Incidentally, the CB employed as a raw material was Black Pearl 880 (Cabot Co. Ltd.), which had an average diameter of 16 nm.

Figure 17.2b shows an enlargement of the UHMWPE–MWNT curve for the original dry composites, and an additional curve for the composites obtained after first heating to 140°C and then cooling back down to room temperature. The conductivity of each composite increased drastically as a result of the heat treatment, and the conductivity attained 10^{-6} S cm^{-1} when the MWNT content was beyond 10%. Furthermore, the conductivity reached 10^{-1} S cm^{-1} at an MWNT content of 15%. To study such drastic increases in conductivity at low MWNT content, SEM images were observed for the composite before and after heat treatment.

Figure 17.3 shows SEM images of (a) the original MWNTs and (b) the original UHMWPE–MWNT composite (without heat treatment). The SEM observations were performed for the cross-sectional area of the UHMWPE composite with a 3 wt% MWNT content. The diameter of the MWNTs after heat treatment is in the range 12–17 nm, as compared to a diameter of 38–45 nm before heat treatment. This is due to the fact that the MWNTs are now coated with UHMWPE such that their diameters are much thicker than the original diameters. Judging from the change in diameter, most of the UHMWPE chains were crystallized on the surface of the MWNTs. This means that the uniform mixing of MWNTs and UHMWPE by the gelation/crystallization method is a very easy technique. When the original UHMWPE–MWNT composite was heated to 140°C and then cooled to room temperature, the SEM observation revealed that most of the UHMWPE chains were not crystallized on the surfaces of the MWNTs, and the average diameter of the dispersed MWNTs in the UHMWPE matrix was shorter, finally becoming the same size as the original MWNTs after three heating cycles as shown in Fig. 17.3a. Accordingly, the electrical

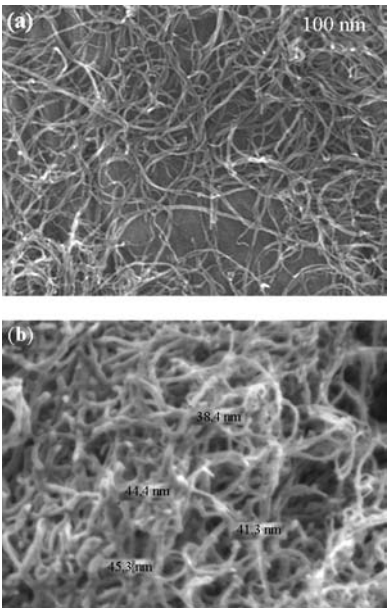

Figure 17.3 SEM images of (**a**) MWNTs and (**b**) UHMWPE–MWNT.

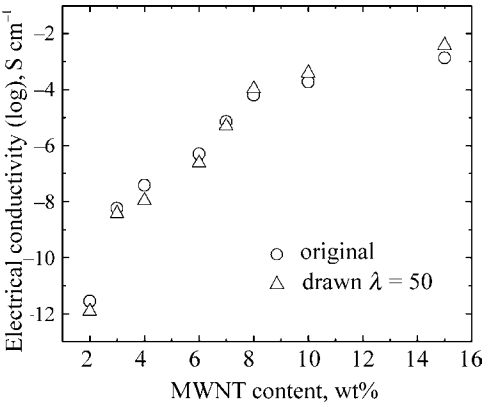

Figure 17.4 Electrical conductivity of composites with different MWNT contents.

conductivity increased drastically for composites with a low content of MWNTs, as shown in Fig. 17.2b. For example, the electron transfer between adjacent MWNTs coated by UHMWPE is less active in comparison to the transfer between MWNTs themselves

Figure 17.4 showed the electrical conductivity as a function of the MWNT content for UHMWPE–MWNT composites dried at 60°C. The percolation threshold shifted to a lower content than that of the original composite in Fig. 17.2b. The value of the electrical conductivity tended to level off at around an MWNT content of 8 wt%, which is similar to that of the composite after heat treatment (see Fig. 17.2b). According to the traditional percolation theory (22), the percolation threshold of the UHMWPE–MWNT composite was 3 wt%, which corresponds to volume fraction of approximately 1.52 % and is much lower than that of normal polyethylene composites with carbon black or carbon fibers (23). This should be attributed to the greater aspect ratio for the MWNTs compared to that for carbon black or carbon fibers. As the mass fraction increased to the percolation threshold, the conductivity increased sharply as conductive paths begin to form. As the MWNT content reached values of more than 8 wt%, the electric conductivity reached 10^{-2} S cm^{-1}, and this further increase in MWNT content to afford an overlap of MWNTs did not improve the electrical conductivity over a wide range of MWNT content.

The most important property for UHMWPE gel films is the superior drawability. Gel films of the UHMWPE homopolymer could be stretched by more than 300-fold, making the molecular chains highly oriented along the stretching direction, where the thus obtained Young's modulus and tensile strength are higher than 200 and 6 GPa, respectively (24–26). The composites of UHMWPE–MWNT also possess excellent drawability. The maximum draw ratio reached 100-fold, while the MWNT content was less than 15 wt%.

As shown in Fig. 17.4, the electrical conductivity values of composites with different MWNT contents were compared with respect to their drawn ($\lambda = 50$) and undrawn films. Obviously, the drawing of the film could influence the conductivity of

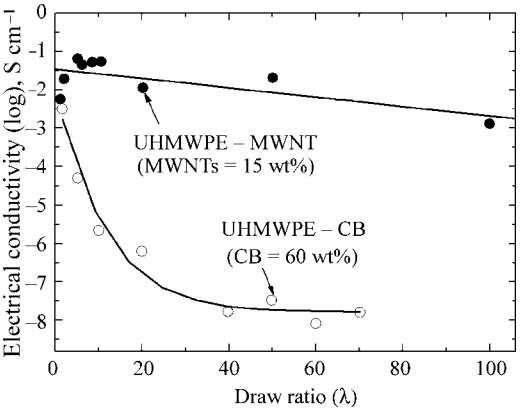

Figure 17.5 Electrical conductivity against draw ratio measured for two kinds of composites, UHMWPE–MWNT and UHMWPE–CB. (From Reference 18 with permission from the American Chemical Society.)

the composite. When the content of the MWNTs was below 8 wt%, the conductivity of the corresponding drawn composite was slightly lower than that of the undrawn composite. In this case, the possibility of fiber–fiber contacts was reduced, and this could lead to the slight decrease in conductivity. In contrast, the conductivity of the drawn composites with MWNT content over 8 wt% was slightly higher than that of the undrawn film. This very small increase in conductivity is due to a slight increase in crystallinity associated with electronic transitions, since electrons transfer easily within crystallites with short chain distances, as compared to electron transfer in amorphous regions. This shall be discussed later in Section 17.5.

Figure 17.5 shows the electrical conductivity against draw ratio measured for two kinds of composite, UHMWPE–MWNT and UHMWPE–CB. The MWNT content for UHMWPE–MWNT was 15 wt%. The electrical conductivity values obtained for the composites in an undrawn state ($\lambda = 1$) were plotted after the first heating run. The content of CB particles was chosen to be 60 wt%, which gave almost the same conductivity as that for the UHMWPE–MWNT composite in its undrawn state. The maximum draw ratios for the UHMWPE–MWNT and UHMWPE–CB composites were 100- and 70-fold, respectively. When stretching, the electrical conductivity of the UHMWPE–CB composites decreases by more than $10^{-3}\,\mathrm{S\,cm^{-1}}$ while being drawn 20-fold, and this value decreased slowly to $10^{-8}\,\mathrm{S\,cm^{-1}}$ where it tends to level off during further elongation. As contrasted with UHMWPE–CB composites, the conductivity of the UHMWPE–MWNT composites decreases slightly with increasing draw ratio, and maintains a value of about $10^{-3}\,\mathrm{S\,cm^{-1}}$ even after stretching by 100-fold. In normal cases, the stretching of carbon filler and polyethylene composites causes the separation of conductive particles from each other (27), such that a number of conductive paths are cut off. That is, the total number of contacting areas between conductive fillers decreases, so the electrical conductivity increases drastically.

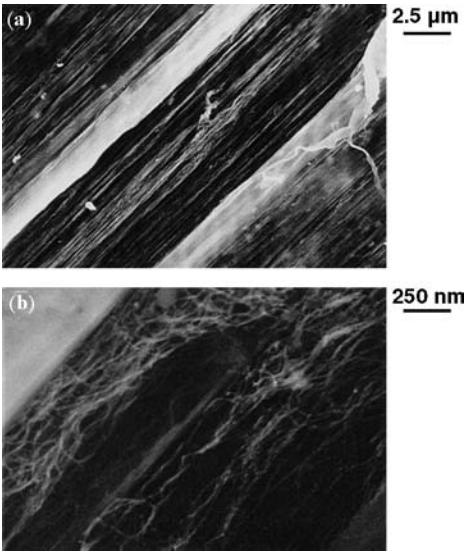

Figure 17.6 SEM images observed on the surface of UHMWPE–MWNT composite (MWNTs = 15 wt%) drawn up to 100-fold ((**b**) is the magnification of (**a**)). (From Reference 18 with permission from the American Chemical Society.)

Figure 17.6 shows SEM images of the surfaces of composites containing 15 wt% of MWNTs with a draw ratio of 100-fold. The high orientation of the PE fibrils and the alignment of MWNTs in the stretching direction can be observed from the image in (a). Image (b) represents the magnification of a part of image (a), where the continuous three-dimensional networks of MWNTs can be clearly observed. These networks of MWNTs are highly aligned together with the polyethylene fibrils oriented along the elongation direction. The continuous networks of MWNTs formed the most effective conductive paths in the composite materials. These SEM images reveal a good compatibility between UHMWPE and MWNTs prepared by the gelation/crystallization method. These two components are assembled and entangled with each other in these composites. This assembly explains why the ultradrawing beyond 100-fold did not cause a large decrease in electrical conductivity in the elongation direction.

17.4 CHARACTERISTICS OF UHMWPE–MWNT COMPOSITES

17.4.1 Morphology of the Drawn UHMWPE–MWNT Composite Film

Many authors reported (28–31) the preparation of polymer composites with SWNTs or MWNTs by mixing them in the melting state or dispersing the fillers in solution.

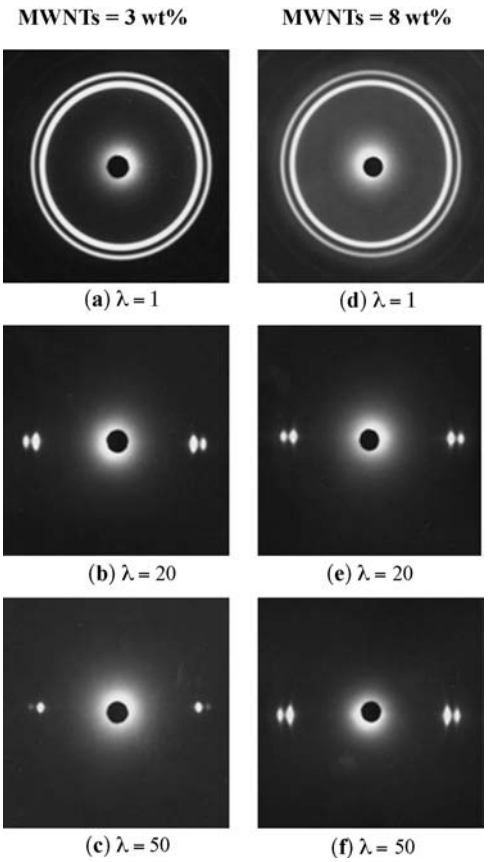

Figure 17.7 WAXD patterns (through view) for the composites at different draw ratio.

The resulting composites could not be ultradrawn to improve the mechanical properties. In the present case, the UHMWPE–MWNT composite films prepared by the gelation/crystallization method could be stretched to more than 100-fold. However, the results showed that the electrical conductivity of these composite films did not decrease evidently even though the films were stretched by up to 100-fold. Hence, the morphology of the composites and the influence of MWNTs on the UHMWPE crystal structure during elongation were investigated.

Figure 17.7 shows the WAXD patterns (through view) for the UHMWPE–MWNT elongated composites with 3 and 8 wt% MWNT contents. Here, as the draw ratio was increased, the diffraction from the (110) and (200) planes of UHMWPE crystallites became narrow arcs or sharp spots indicating a high degree of orientation of the *c*-axis with respect to the stretching direction. Comparing with the composite film containing 3 wt% MWNT, the diffraction arcs observed for the composite film containing 8 wt% MWNT at $\lambda = 50$ indicated an insufficient orienta-

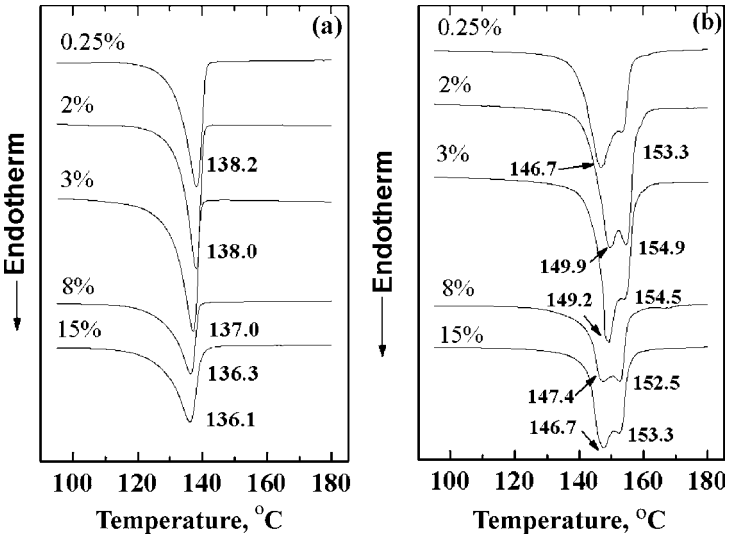

Figure 17.8 DSC curves for the undrawn (**a**) and drawn (**b**) UHMWPE–MWNT ($\lambda = 50$) composite films.

tion of the *c*-axis. This means that the large amounts of MWNTs hampered the predominant orientation of the *c*-axis of UHMWPE. Diffraction peaks relating to the MWNTs were not observed, since the number of MWNTs within the X-ray irradiated area was few, even in the undrawn state ($\lambda = 1$).

The DSC curves for the UHMWPE–MWNT composites with different MWNT contents were shown for the undrawn and drawn states in Fig. 17.8a and b, respectively. In Fig. 17.8a, it can be seen that the endothermic peak associated with the melting point for the undrawn composites was slightly shifted to a lower temperature, and the endothermic peaks became broader as the MWNT content increased. This suggested that the MWNTs hampered the crystallization of UHMWPE. The crystallinity of the composite film with different MWNTs will be discussed later.

Thermal analysis of the ultradrawn composites ($\lambda = 50$) was measured and the results were shown in Fig. 17.8b. Comparing with the profiles of the undrawn composites, as shown in Fig. 17.8a, the endothermic peaks of the UHMWPE crystallites became sharper, and the melting points shifted about 10°C to a higher temperature, attributed to the orientation crystallization of the UHMWPE crystallites. The melting points measured for the drawn films were higher than the equilibrium melting point (145.5°C) reported by Flory and Vrij (32). The abnormally high melting point was thought to be due to the fact that the polymer chains in the melting state retained an extended-chain arrangement. This entropy in fusion was obviously smaller than the value calculated for a random coil in the melting state. The corresponding crystallinity calculated from the DSC measurement for the undrawn and drawn films is shown in Fig. 17.9.

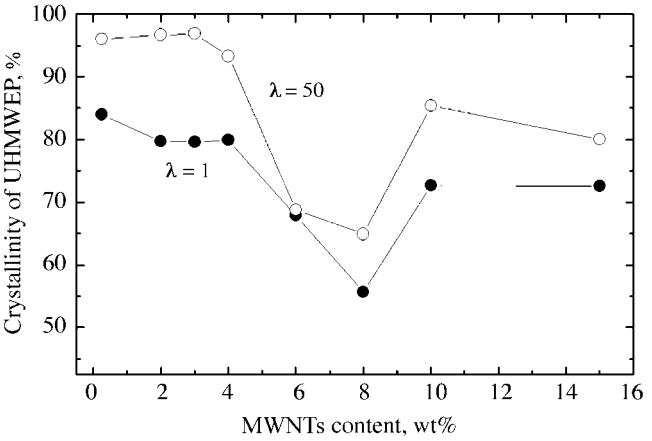

Figure 17.9 Crystallinity degree of the composite films at $\lambda = 1$ and 50 calculated from DSC measurements.

The crystallinity values were calculated from the ratio of measured Δh to Δh_f of a 100% crystalline polyethylene (245.3 J g^{-1}) (33). The crystallinity of the undrawn composite film decreased slightly when the MWNT content was below 4 wt%, and then sharply decreased due to the MWNTs hampering the crystallization of UHMWPE. In this respect, it seemed there existed a critical content influencing the crystallization.

Similar to the percolation threshold of conductivity, the crystallinity decreased slowly below the critical content. While over this critical content, the form of the continuous networks of MWNTs disturbed the crystallization of the polymer and caused the crystallinity to decrease quickly. Furthermore, it was noticed that the crystallinity began to increase when the MWNT content was more than 8 wt%. It is suggested that the addition of excessive MWNTs led to aggregation of the MWNT networks. The aggregated MWNTs easily separated from the polymer matrix causing the crystal domains and crystallinity to increase. This phenomenon was confirmed by the SEM images.

17.4.2 Mechanical Property of the Undrawn and Drawn Composite Films

The temperature dependence of the storage modulus (E') and loss modulus (E'') were measured for the UHMWPE–MWNT composites containing 15 wt% MWNT content in their undrawn and ultradrawn states. The results are shown in Fig. 17.10. E' increases with increasing draw ratios. In comparison with the Young's modulus of the undrawn film (1.5 GPa at 20°C), the values reached 49 and 58 GPa with elongations up to 50- and 100-fold, respectively. The E' value of the composite with $\lambda = 100$ at 20°C is close to the Young's modulus of aluminum. This is due to an increase in the

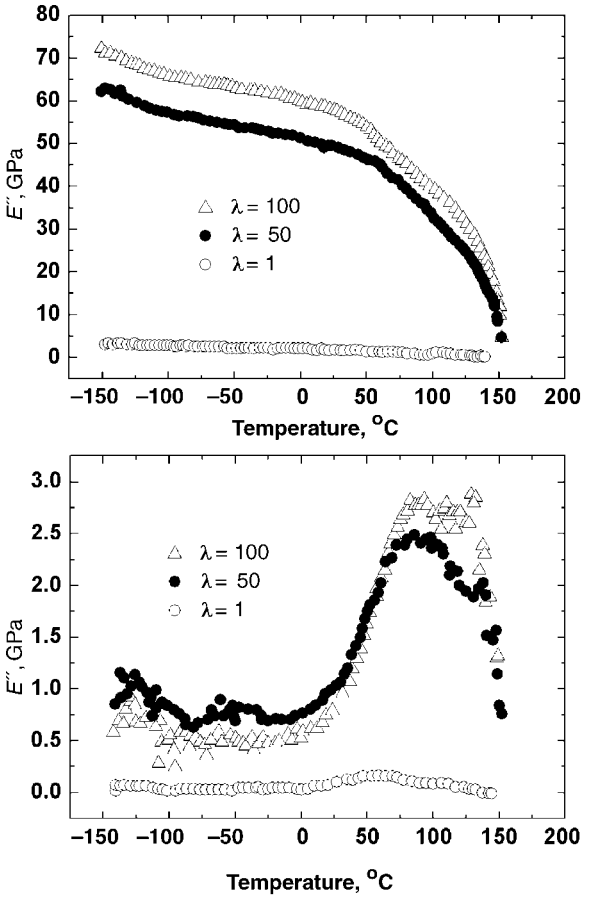

Figure 17.10 Temperature dependence of the storage modulus (E') and loss modulus (E'') for UHMWPE–MWNT composites (MWNTs = 15 wt%) at $\lambda = 1, 50$, and 100. (From Reference 18 with permission from the American Chemical Society.)

degree of orientation of the UHMWPE crystallites. Because of the increase in crystallinity of UHMWPE with draw ratio, the temperature dependence of E'' reveals that the magnitude of the β relaxation peak around $-50°C$ associated with the amorphous dispersion (34) is very small. The peak position of the α relaxation associated with the crystal dispersion (35), which appears around 50–100°C, slightly shifts to a higher temperature with increasing λ, indicating the growth of crystallites by oriented crystallization.

In the composite systems with highly orientated UHMWPE matrices and fillers, two factors may influence the mechanical properties of the drawn UHMWPE–MWNT composite film. One is the predominant orientation of MWNTs and UHMWPE; the other is an increase in crystallinity of UHMWPE. The following experimental results should confirm this speculation. Figure 17.11 compares the

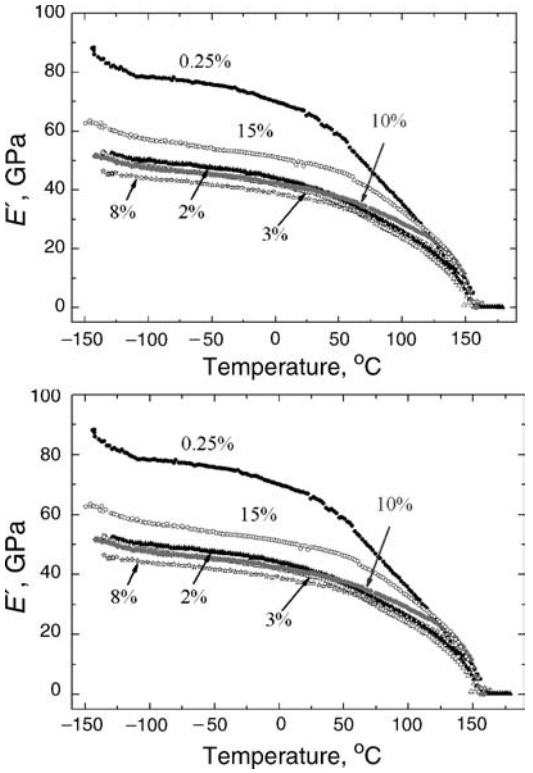

Figure 17.11 Temperature dependence of storage modulus (E') and loss modulus (E'') of drawn films ($\lambda = 50$).

temperature dependence on E' and E'' moduli for the composites with different MWNT contents at the drawn ratio of 50-fold. For composites with an MWNT content lower than 8 wt%, the E' value decreased with increasing MWNT content, while a reversed trend occurred for the composites containing more than 8 wt% MWNTs. As shown in Fig. 17.9, the crystallinity of the composite film with 8 wt% MWNTs was the lowest, which could lead to the smallest E'. In this case, the highest storage modulus at room temperature was 66 GPa for the composite film with 0.25 wt% MWNTs. For all composites, the storage modulus was higher than 37 GPa at room temperature.

17.4.3 Electrical Conductivity of UHMWPE–MWNT Composite Films Dependent on the Temperature

As is well known, based on the electrical conductivity of carbon polymers, the corresponding composites are very sensitive to temperature (36–39). Figure 17.12 shows the electrical conductivity measured against temperature for UHMWPE–MWNT gel films with 5 and 10 wt% MWNT contents in their undrawn states. The

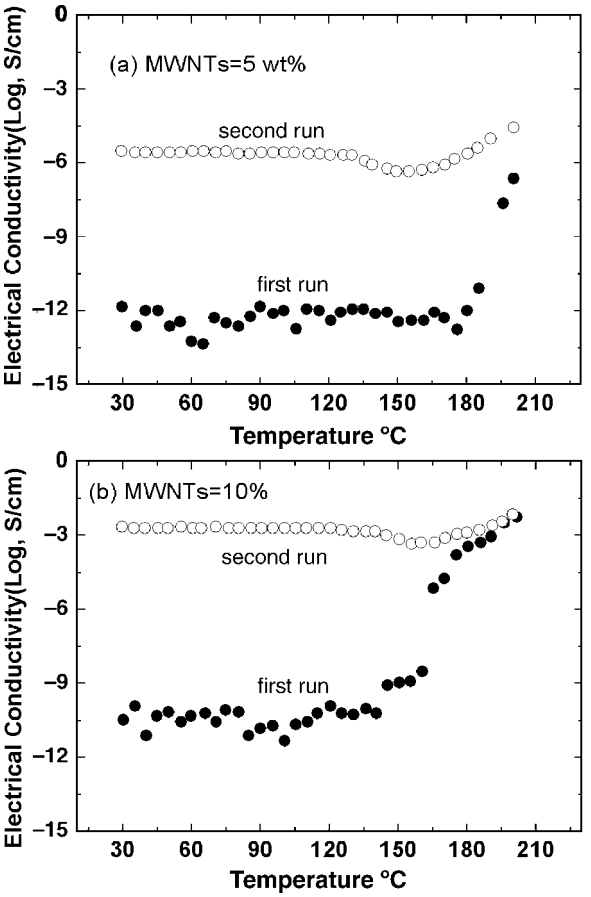

Figure 17.12 Temperature dependence of electrical conductivity measured for the undrawn UHMWPE–MWNT composites during two thermal cycles. The content of MWNT was (**a**) 5 wt% and (**b**) 10 wt%. (From Reference 18 with permission from the American Chemical Society.)

measurements were done for two thermal cycles. For the first cycle, the electrical conductivity increases gradually with increasing temperature, which suddenly increases further for more than five orders of magnitude when the melting point of PE is reached. This sudden change occurs at 170 and 160°C for the composites with 5 and 10wt% MWNT contents, respectively. After the first heating cycle, the specimen was cooled to room temperature. During the second cycle, the electrical conductivity was maintained constant during the heating process up to 130°C and was found to decrease slightly. However, these electrical conductivity values increase again beyond 160°C. Such thermal behavior of the UHMWPE–MWNT composite is considered to be due to the fact that the considerable mobility of the UHMWPE chains beyond the melting point causes the active movement and the rearrangement of the MWNTs, providing an increase in the number of contact points between

MWNTs. However, the thermal expansion of UHMWPE is not significant enough to cause the separation of the contacted MWNTs, so conductive paths for charge transportation are maintained. On the contrary, the thermal expansion of MWNTs is almost zero and the mobility of the polymer was controlled by the MWNTs. The conductivity for the UHMWPE–MWNT composite in the second thermal cycle shows almost constant values at temperatures $< 130°C$, indicating that the adhesion between MWNTs becomes tighter than the thermal expansion of UHMWPE after the first heat treatment cycle.

Figure 17.13 shows the electrical conductivity measured against temperature for the UHMWPE–MWNT composite with 15 wt% MWNT content. These measurements were performed for the undrawn and drawn composites with $\lambda = 50$ and 100. The results for three heat cycles are represented as first, second, and third runs in this figure. For the first run, the conductivity of the undrawn composite increases gradually with increasing temperature, and increases by more than one order of magnitude beyond 140°C. The conductivity of the films with $\lambda = 50$ and 100 shows a similar tendency, but this sudden increase is less pronounced than that of the undrawn composite. Of course, the conductivity did not change under the cooling process for the two specimens. However, the amplitude of varying conductivity during the heating cycle is much lower than the case for the specimens containing 5 and 10 wt% MWNTs, as shown in Fig. 17.12. This indicates that the optimum content of MWNTs assures the most stable form. At the second and third runs, the conductivity was found to increase slightly with temperature, but this tendency is much smaller in comparison with that of the first run. The increase in conductivity with temperature is due to the active electron transfer associated with electronic transitions. Beyond the fourth run, the route of the temperature dependence was confirmed to be similar to that of the third run, which indicates the achievement of more stable electrical properties by heat treatment. The conductivity of the undrawn composite was in the range from $10^{-1.8}$ to $10^{-0.7}\,S\,cm^{-1}$, while that of the drawn composite is from $10^{-1.3}$ to $10^{-1.1}\,S\,cm^{-1}$. This extraordinary stability in electrical conductivity for the UHMWPE–MWNT composites is completely different from that of normal carbon–polymer composites (40). This means that the UHMWPE–MWNT composites with 15 wt% of MWNTs drawn up to $\lambda = 100$ are absolutely conductive materials with good thermal stability and high stiffness.

17.4.4 Effect of Iodine Doping on the Electrical and Thermal Properties of UHMWPE–MWNT Composites

Iodine doping has been studied to improve the electrical conductivity of several polymers (41–44). Iodine doping of ion-implanted polyethylene results in an immediate increase in the sheet conductivity by three to four orders (45). Furthermore, doping of carbon nanotubes with suitable donor or acceptor dopants (46–48) facilitates the charge transfer between the dopants and the nanotubes.

In order to improve the electrical conductivity of the composites, iodine doping was carried out for the highly oriented UHMWPE–MWNT composites. The drawn

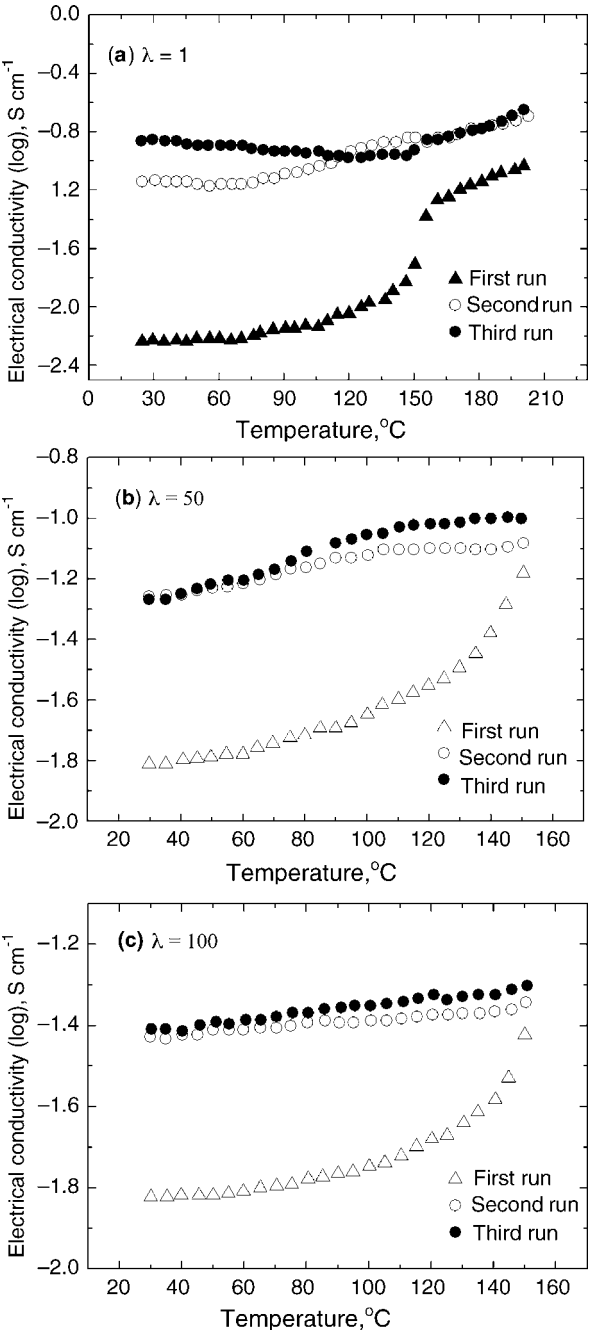

Figure 17.13 Temperature dependence of electrical conductivity of UHMWPE–MWNT composites with 15 wt% MWNTs: (**a**) undrawn ($\lambda = 1$), (**b**) $\lambda = 50$, and (**c**) $\lambda = 100$ (From Reference 18 with permission from the American Chemical Society.)

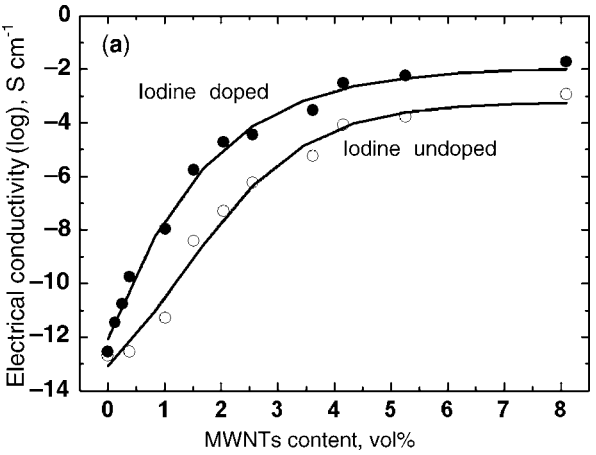

Figure 17.14 Electrical conductivity by iodine doping for the ultradrawn UHMWPE–MWNT composites at $\lambda = 50$.

composites were set in a desiccator containing iodine crystals. After being degassed, the desiccator was heated to 80°C at 5°C min^{-1} and saturated by iodine vapor. The samples were kept in the saturated iodine vapor at 80°C for 6 h. Then the samples were removed and washed with ethanol until the solvent extracts were colorless, and then vacuum dried for 24 h. The electrical conductivity was measured soon after vacuum drying.

Figure 17.14 shows the change of electrical conductivity by iodine doping for the oriented MWNT/UHMWPE composites ($\lambda = 50$) with different MWNT contents. The conductivity of the iodine-doped UHMWPE–MWNT composites was improved by one to four orders of magnitude compared with the undoped composites, but the trend of the conductivity versus MWNT content was hardly affected by iodine doping. Furthermore, it was found that the conductivity of neat UHMWPE showed little change by iodine doping.

To better understand this increase in conductivity, Raman spectra were used to investigate the mechanism. Figure 17.15 shows the Raman spectra of iodine measured for the iodine-doped composites with 3 wt% MWNT content, namely (a) pristine and (b) the iodine-doped UHMWPE–MWNT composite kept in a desiccator for 2 months. As shown in Fig. 17.15b, the strong and broad peak at about 175 cm^{-1} and the very weak peak at 110 cm^{-1} were observed. These peaks were assigned, respectively, to the I_5^- and I_3^- polyiodine chains, in accordance with similar cases reported for iodine-doped single-wall carbon nanotubes (49). No Raman peak (typically at 215 cm^{-1}) due to the existence of neutral or dissociative molecular iodine (I_2^0) (50) was observed. This indicates that no excessive iodine existed in the sample. Judging from the low intensity of the I_3^- band, the increase in the electrical conductivity is attributed mainly to the I_5^- band that takes the role of charge carriers to form the charge exchange complex.

Figure 17.16 shows the Raman scattering spectra of (a) pristine and (b) iodine-doped UHMWPE–MWNT composites kept in desiccator for 2 months, in which

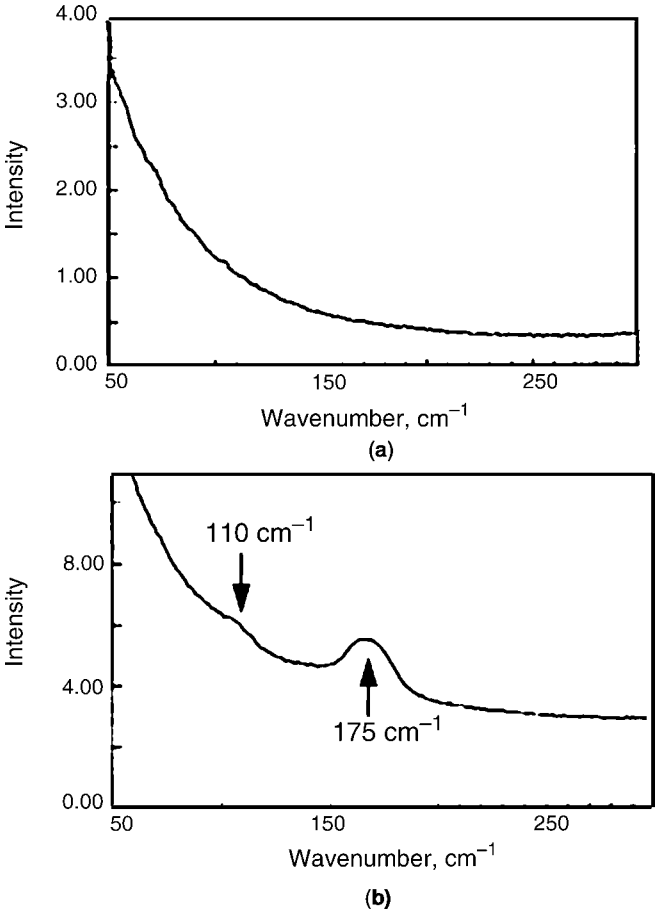

Figure 17.15 Raman spectrum of iodine for the iodine-doped composite composites with 3 wt% MWNTs using a 514.5 nm excitation: (**a**) pristine and (**b**) 2 months after doping.

(ZZ) and (ZX) represent the intensities of the polarization components of the chain axis parallel and perpendicular to the drawing direction, respectively. The intensity of the (ZX) component is much lower than that of the (ZZ) component, indicating that most of the MWNTs in the composites are oriented along the chain axis. For the pristine sample, the peaks at 1060, 1129, 1130, and 1418 cm^{-1} correspond to those of polyethylene. When the composites were doped with iodine, the peak at approximately 1130 cm^{-1} due to the C—C stretching mode became broader, and a new peak appearing at approximately 1460 cm^{-1} is associated with the CH_2 bending mode. This difference confirmed that the crystallinity of UHMWPE decreased and the amorphous regions increased. Iodine, being highly electronegative, can interact with the lattice and produce distortions and stresses within the crystallites, thereby leading to structural modifications.

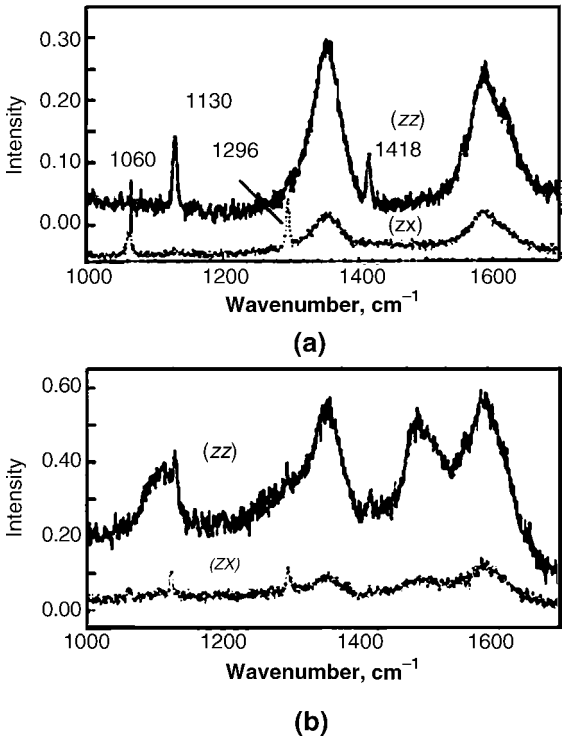

Figure 17.16 Raman spectra of the composite films with 3 wt% MWNTs-doped iodine measured using a 514.5 nm excitation: (**a**) pristine and (**b**) 2 months after doping.

The peaks at about 1345 cm^{-1} and 1582 cm^{-1} were assigned to the D- and G-bands of the MWNTs, respectively. Comparing Fig. 17.16a and b, it was found that the G-band was upshifted by 5 cm^{-1} after iodine doping. This result was in good agreement with the study of Cambedouzou et al. (51). The outer tube vibrations were affected by the iodine doping. According to the reports by Michel et al. (52) and Zhou et al. (53), the adsorption of iodine occurred on the surface of the MWNTs. Therefore, the content of MWNTs and the crystallinity of UHMWPE influenced the concentration of doped iodine, and then the increase in the conductivity was slightly different, which is shown in Fig. 17.14.

The temperature dependence of electrical conductivity for the undoped and doped UHMWPE–MWNT composites drawn up to 50-fold was investigated. The results for three heat cycles at the temperature range of 25 to 150°C were shown in Figs. 17.17 and 17.18 as first, second, and third run. For the composites with 3 wt% MWNT content, the electrical conductivity of undoped composites was irregular for three cycles, indicating that the charge transfer did not occur smoothly. In this case, the MWNT content was the critical value for the formation of conductive networks. This indicates that the thermally induced electron-hopping transport between the disconnected (or weakly connected) parts of the networks was unstable. After iodine

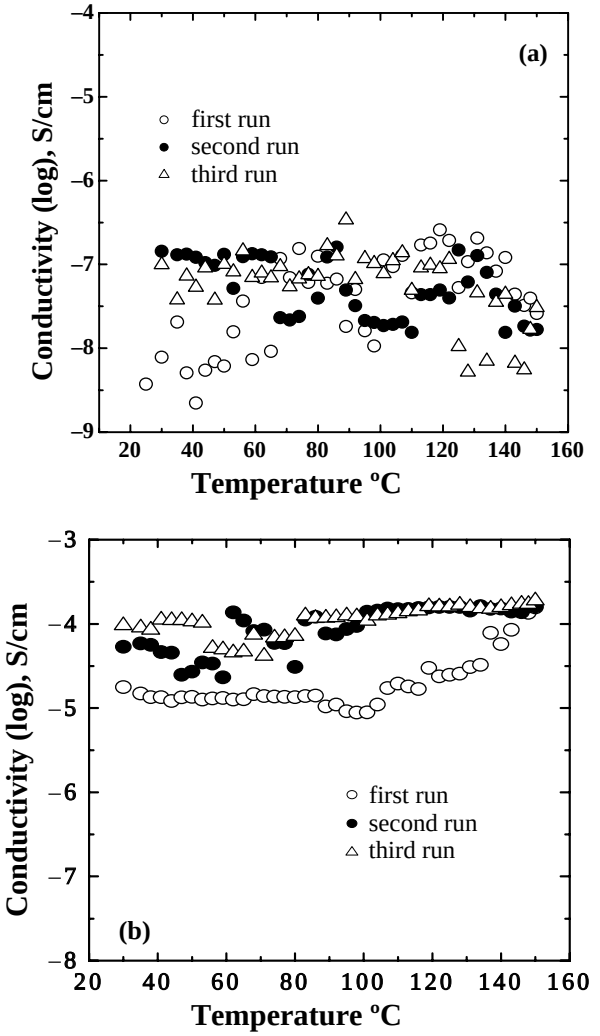

Figure 17.17 Electrical conductivity for the composite films ($\lambda = 50$) with 3 wt% MWNTs during three heat cycles: (**a**) pristine and (**b**) iodine doped.

doping, the conductivity became regular, indicating that the I_5^- may take the role of a bridge between the separate or nearby nanotubes so that the charge can flow via a shorter pathway. For the first heating run, near the melting point of UHMWPE, the conductivity suddenly increased. In the second and third runs, the conductivity was a little higher than that of the first run. Furthermore, comparing with the undoped composites, the iodine-doped films show that the stability against the temperature was promoted for all three heat runs. Beyond the fourth run, the route of the temperature dependence was confirmed to be similar to the third run, which indicated the establishment of more stable electrical properties by heat treatment.

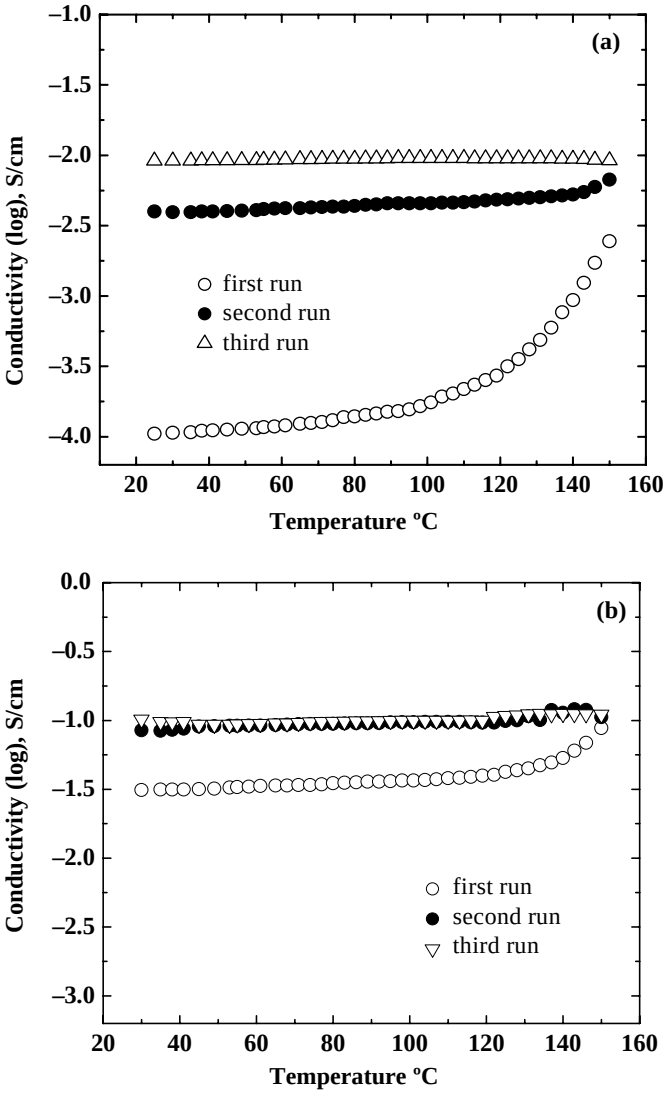

Figure 17.18 Electrical conductivity for the composites films ($\lambda = 50$) with 8 wt% MWNTs during three heat cycles: (**a**) pristine and (**b**) iodine doped.

For the composite with 8 wt% MWNT content with enough conductive paths, the conductivity increases slowly from 25 to 120°C. When the temperature was over 120°C for the first run, the conductivity increased drastically. However, for the second run, the conductivity maintains almost a constant value during the heating process up to 130°C and tends to increase only slightly. Such thermal behavior of the UHMWPE–MWNT composite is thought to be due to the fact that the considerable

mobility of the UHMWPE chains beyond the melting point causes the active movement and rearrangement of the MWNTs, thus providing an increase in the number of contact points between the MWNTs. However, the thermal expansion of UHMWPE is not significant enough to cause the separation of the contacted MWNTs, so conductive paths for charge transportation are maintained. The conductivity of the UHMWPE–MWNT composite in the second cycle shows almost constant values at temperatures $< 130°C$, indicating that the adhesion between adjacent MWNTs becomes stronger than the thermal expansion of UHMWPE after the first heating run. Like the doped composite with 3 wt% MWNT content, the conductivity of the doped composite was enhanced. Moreover, the conductivity afforded by the second and third runs was extraordinary stable.

Figure 17.19 shows the temperature dependence of E' and E'' measured for the UHMWPE–MWNT composites with 3 and 8 wt% MWNT contents in the three states: pristine, iodine-doped, and heat-treated at 150°C for 30 min after iodine doping. As shown in Fig. 17.19a and b, the storage modulus of the composite with 3 wt% MWNT content was a little higher than that of the film with 8 wt% MWNT content. This is thought to be due to the fact that the networks of MWNTs are obstacles to the orientation of UHMWPE. The storage modulus of the composite with 8 wt% MWNT content is lower than that of the pristine composite after doping

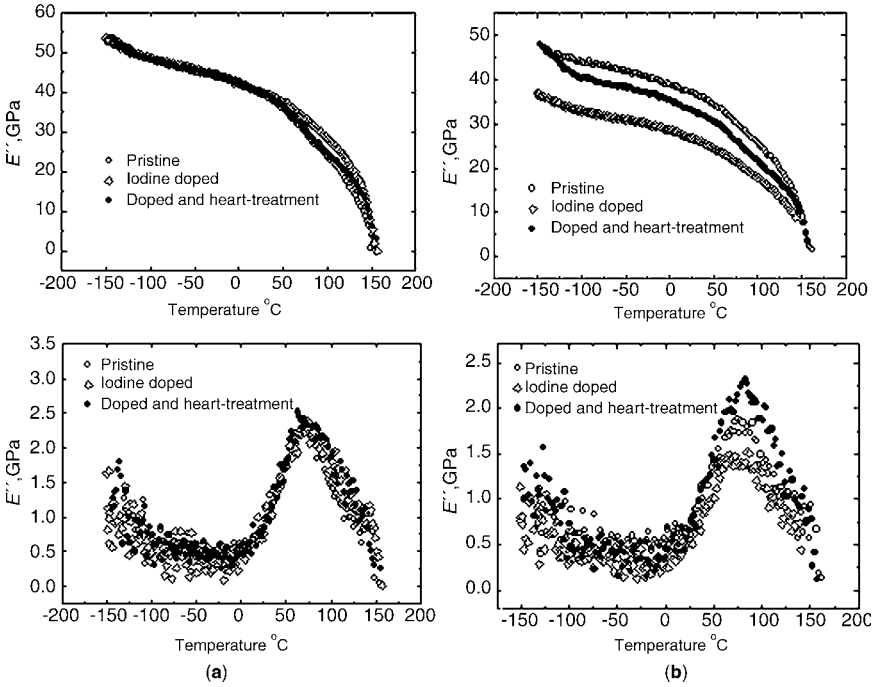

Figure 17.19 Temperature dependence of storage modulus of composites at 50-fold: (**a**) with 3 wt% MWNTs and (**b**) with 8 wt% MWNTs.

in the given temperature range, but further heat treatment made the storage modulus closer to that of the pristine composite. For the samples containing 3 wt% MWNT content, no significant change was observed after heat treatment. For all composites, the α-dispersion peak shows no obvious change. As explained in Fig. 17.17–17.19, heat treatment of the doped composites is helpful for the stability of the electrical and thermal properties. Therefore, it is evident that iodine doping and heat treatment play an important role in promoting the electrical conductivity and thermal stability for the highly elongated PE–MWNT composites.

17.5 UNIFORM MIXING OF UHMWPE AND RIGID MWNTs WITH ORDERED GRAPHENE SHEETS

The MWNTs used in this section have a higher degree of graphitization than the previous MWNTs, as shown in the Raman spectrum in Fig. 17.1b. When the present MWNTs with high order curved graphene sheets were used as fillers, the uniform dispersion of MWNTs into the UHMWPE matrix was slightly difficult, and so small amounts of EMMA, whose characteristics are shown in Table 17.1, were admixed into the UHMWPE. The resulting composite was termed as UHMWPE/EMMA.

In preparing the homogeneous UHMWPE/EMMA–MWNT composites, the concentration of UHMWPE against decalin was fixed as 1 g/100 ml decalin. Through trial and error, it was found that this concentration was the optimum condition to assure a uniform dispersion of MWNTs in the mixed UHMWPE and EMMA solution. First of all, the MWNTs in decalin were ultrasonically treated for more than 24 h by batch operation with treatment occurring at 20 min intervals (treated for 15 min and stopped for 5 min) at room temperature. After, UHMWPE and EMMA were added into the decalin solvent containing MWNTs and the mixture was stirred for 30 min at room temperature. The mixture was heated to 150°C at a mild heating rate of 2–3°C min^{-1}, and maintained by stirring for 40 min at 150°C. The hot homogenized solution was quenched by pouring it into an aluminum tray at room temperature, thus generating a gel. The decalin was allowed to evaporate from the gel under ambient condition. The nearly dry gels were vacuum dried for 24 h to remove residual traces of decalin. The dried blend film was cut into strips of length 30 mm and width 10 mm. The strip was clamped in a manual stretching device and stretched in a hot oven at 135°C under an argon atmosphere.

Figure 17.20 shows the electrical conductivity of EMMA (0/1), UHMWPE (1/0), and the 6/1 composite as a function of the content of MWNTs measured at room temperature. The measurements were carried out to investigate the effect of EMMA on electrical conductivity. The electrical conductivity increased with increasing MWNT content and tended to level off, indicating the formation of sufficient conductive paths. The conductivity of the EMMA matrix at the platform was the highest among the three specimens, and this value tended to level off at about 3 wt% MWNT content. In contrast, the electrical conductivity value for UHMWPE at the platform was the lowest, with an optimum MWNT content of about 13 wt%.

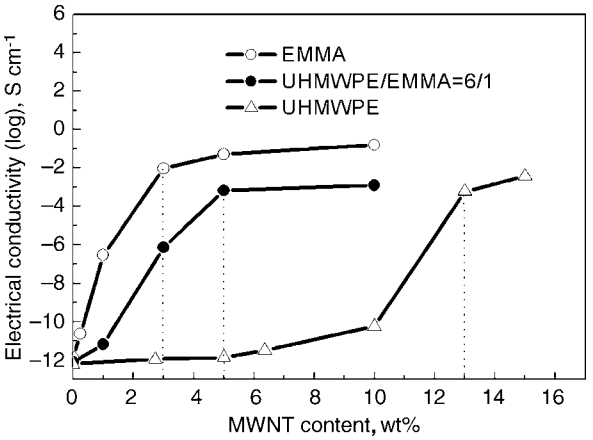

Figure 17.20 Electrical conductivity of composites as a function of the content of MWNTs. Note: MWNTs in UHMWPE is different from those in EMMA and UHMWPE–EMMA. (From Reference 19 with permission from the American Chemical Society.)

The corresponding platform value for the 6/1 blend was a composite with 5 wt% MWNT content. On the basis of the saturation conductivities against the MWNT content for the EMMA and 6/1 composites, the MWNT content in the following experiments was fixed to 5 wt%.

Fig. 17.21a and d shows the temperature dependence of the electrical conductivity measured for the EMMA–MWNT and UHMWPE/EMMA–MWNT composites, respectively, in which the content of the MWNTs is 5 wt%. The heating of the samples was carried out for three cycles, namely the first, second, and third runs. As shown in Fig. 17.21a, it is seen that the electrical conductivity of the EMMA–MWNT composite increased slightly at temperatures beyond 70°C during the first heating run. However, the values obtained during the second and third runs were almost equal to those of the first run. Incidentally, the temperature dependence of the EMMA film with 10 wt% MWNT content showed similar behavior, since 5 wt% MWNT was deemed to be the saturation value for conductivity, as shown in Fig. 17.20. The temperature dependence of this MWNT sheet is shown together with those of the EMMA–MWNT composite in this figure. The electrical conductivity of the MWNTs was tested on a loose MWNT sheet, which was prepared by mixing the MWNTs in methanol and then filtering. Here, it should be noted that the measured conductivities of the sheet are much lower than the theoretical values reported elsewhere (54, 55). This is due to the defects in the curved graphene sheets of the MWNTs containing amorphous carbon regions, which provides the flexibility of the MWNTs to form entanglements. If the MWNTs had no defects, the MWNTs must be straight tubes. In spite of the entanglements of the MWNTs, the conductivity of the MWNT sheet was much higher than those of the EMMA–MWNT composites. This indicates the possibility that the dispersed MWNTs, covered with a very thin layer of EMMA chains and active charge carriers between the adjacent MWNTs were hampered by this layer.

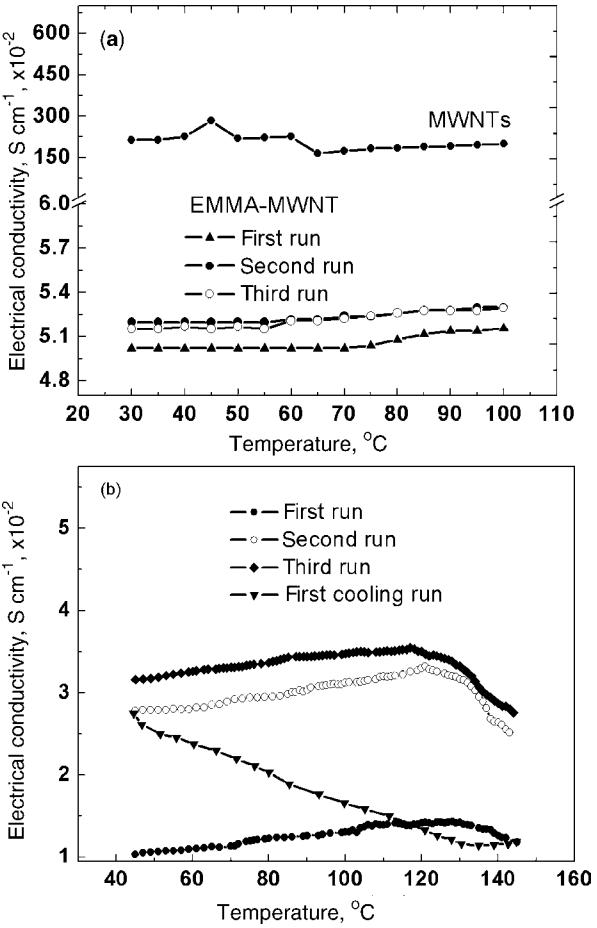

Figure 17.21 Temperature dependence of electrical conductivity measured for composites with 5% MWNTs: (**a**) EMMA and (**b**) UHMWPE/EMMA (6/1). (From Reference 19 with permission from the American Chemical Society.)

Figure 17.21b shows the temperature dependence of the conductivity under the repeated heating cycles measured for the 6/1 composite containing 5 wt% MWNT. Here, the conductivity increased with the elevating temperature and tended to decrease with further heating beyond 120°C. After the first heating run, the composite was cooled to room temperature. In the cooling process, the conductivity increased. This is quite different from the behavior of the UHMWPE–MWNT composites shown in Figs. 17.12 and 17.13. The conductivity slightly increased with elevating temperature during the second heating run and decreased beyond 120°C. Such behavior was also observed during the third heating run. The same tendency was also confirmed for the 2/1 and 1/1 composites containing 5 wt% MWNTs. Under SEM observation, it was confirmed that the average thickness (diameter) of the UHMWPE/EMMA layer on the MWNT surface became thinner

with further heating runs, and a drastic decrease occurred after the first heating run. This indicated that the recrystallization of the melted UHMWPE/EMMA chains under the cooling process did not occur on the MWNT surface.

As discussed in Sections 17.3 and 17.4 for UHMWPE–MWNT containing 5 wt% MWNT content, the conductivity increased from 10^{-12} to 10^{-5} S cm^{-1} by heating. For the first cycle, the conductivity increased with increasing temperature, when the composite was heated to the melting point of the UHMWPE. After cooling, the conductivity of the heat-treated composite was higher than that of the original composites. During the second heating, the conductivity maintained constant values up to 130°C and tended to decrease slightly. In the second run, the temperature dependence of the electrical conductivity of the UHMWPE–MWNT composite was similar to the behavior of the UHMWPE/EMMA–MWNT, although the conductivity of the present UHMWPE/EMMA–MWNT composite was higher than that of the UHMWPE–MWNT composite in the given temperature range.

The question of why the conductivity increased with elevating temperature up to 120°C, independent of the repeated heating run, but decreased beyond 120°C, exists. Such behavior has never been observed, but the inverse results have been reported for the carbon black–UHMWPE composites (24, 40). To obtain more detailed information, temperature dependence of X-ray diffraction curves for the 6/1 composite containing 5 wt% MWNT were shown in Fig. 17.22a and b. Under the heating process, the diffraction peak intensities were almost constant up to 100°C. In this temperature region, the electrical conductivity increased with elevating temperature as shown in Fig. 17.21b. The X-ray diffraction peak decreased drastically at 120°C corresponding to the starting point of the decrease of the electrical conductivity (see Fig. 17.21b) as well as the starting point of the melting of the crystallites (see Fig. 17.22c). Further increases in temperature up to 135°C caused drastic decreases in the X-ray peak intensities, which are also related to the drastic decrease in electrical conductivity. Under the cooling process from 140 to 27°C, which were shown in Fig. 17.22b. The peak intensity increased with decreasing temperature but an increase in the magnitude of the diffraction intensity peak associated with recrystallization by the cooling was much lower than the peak magnitude of the original film at the corresponding temperature. For example, it was obvious that the sample after the first heating had morphology different from the original film prepared by gelation/crystallization, in which the morphology was obviously thought to be similar to that of the melted film. Such behavior of X-ray diffraction intensity satisfied the thermal properties estimated by DSC curves shown in Fig. 17.22c. The DSC curves correspond to the above heating cycles. For example, the endothermic peak at the first heating showed a large peak indicating high crystallinity of the original film, but the exothermic peak under the first cooling showed a small peak indicating that the crystallinity of the film prepared by cooling the original film was lower than that of the original film. Certainly, the endothermic peaks under the second heating was much smaller than that of the original film, which supported the behavior of the X-ray diffraction curves under the first cooling. Of course, the recrystallization of the UHMWPE/EMMA did not occur on the MWNT surface and the thickness of the UHMWPE/

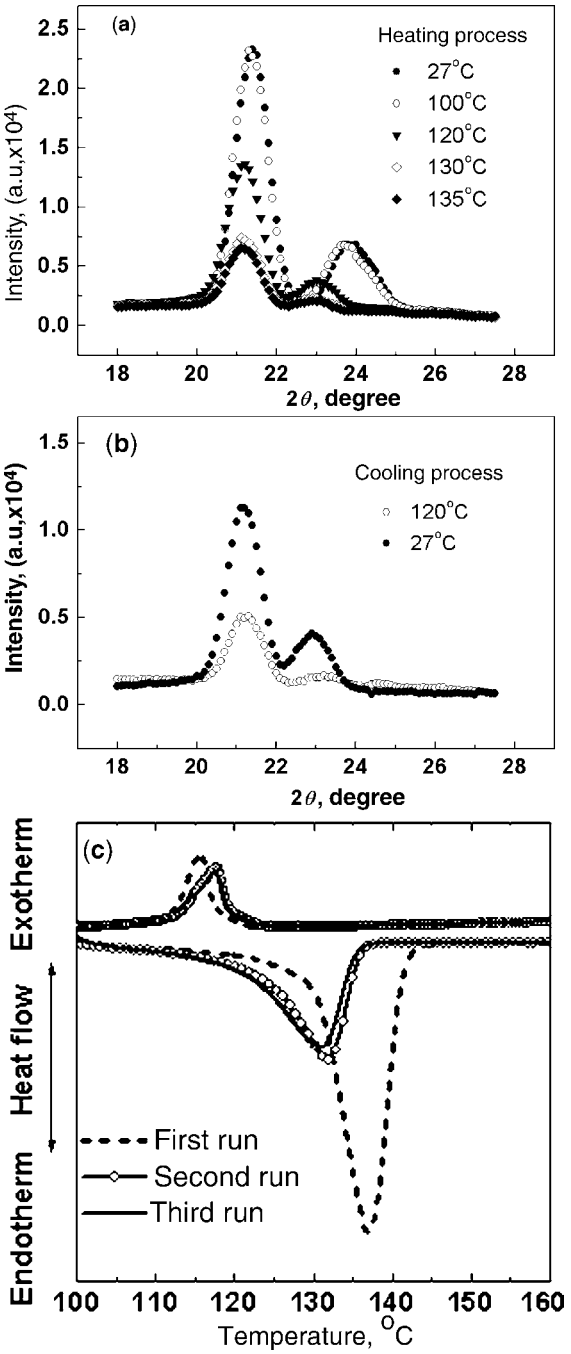

Figure 17.22 Temperature dependence of X-ray diffraction curves for the undrawn composites (6/1) with 5% MWNTs: (**a**) heating process, (**b**) cooling process, and (**c**) DSC analysis. (From Reference 19 with permission from the American Chemical Society.)

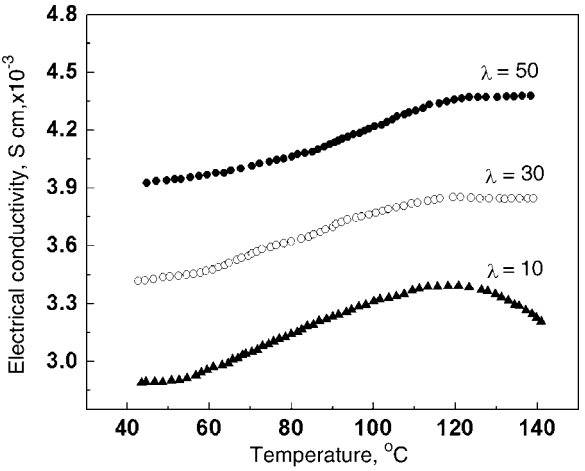

Figure 17.23 Temperature dependence of electrical conductivity measured for composites (6/1) with 5% MWNT content as the function of draw ratio. (From Reference 19 with permission from the American Chemical Society.)

EMMA layer became very thin and then the conductivity increased by the first heating and cooling cycle.

Figure 17.23 shows the temperature dependence of the drawn UHMWPE/EMMA–MWNT (6/1) composites. Interestingly, the conductivity slightly increased with draw ratio, and also increased with elevating temperature in the given range from room temperature to 140°C. This was quite different from the results of the UHMWPE–MWNT composites containing 5 and 15 wt% MWNT contents reported already (18). According to the report (18), the conductivity of the UHMWPE–MWNT composite with 5 wt% MWNT decreased drastically and became an insulator when the sample was stretched beyond 20 times. Only for the composite with 15 wt% MWNT content, the decrease of conductivity by the elongation up to 100 times could be prevented. The decrease in the conductivity was attributed to the disappearance of electrical conductive paths due to the disruption of three-dimensional networks by the tension along the stretching direction. On the contrary, the conductivity of UHMWPE/EMMA composite with the 5 wt% MWNT content was much higher than that of UHMWPE–MWNT with the same MWNT content. Interestingly, the conductivities of the composites with $\lambda = 30$ and 50 tended to level off beyond 120°C, which was different from the decrease in conductivity for the undrawn composite beyond 120°C as shown in Fig. 17.22b. To investigate this phenomenon, X-ray diffraction and DSC measurements were carried out for the composite with $\lambda = 50$.

Figure 17.24a shows the temperature dependence of the X-ray diffraction curves for the 6/1 composite containing 5% MWNT with $\lambda = 50$ obtained during heating. The diffraction intensity maintained almost the same magnitude up to 140°C, but this peak disappeared suddenly at 150°C, and replaced by an amorphous halo that appeared around 19.8° indicating the melting of the crystallites. In support of the

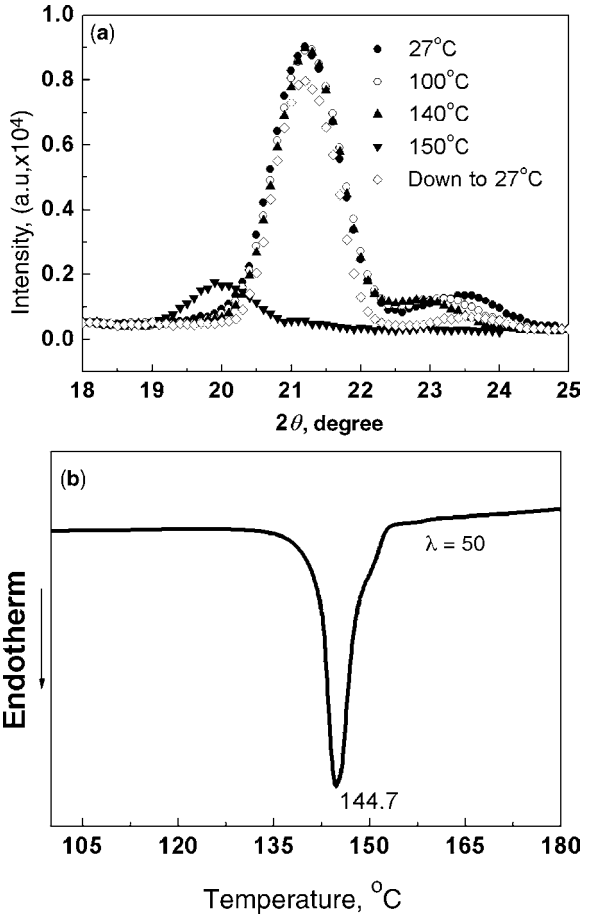

Figure 17.24 Temperature dependence of X-ray diffraction curves for composites (6/1) containing 5% MWNTs with $\lambda = 50$ under (**a**) heating processes and (**b**) DSC analysis. (From Reference 19 with permission from the American Chemical Society.)

above analysis, the corresponding DSC curve shown in Fig. 17.25b reveals that partial melting started at 135.0°C and the corresponding endothermic peak maximum occurred at 144.7°C. This behavior supports the drastic decrease in the X-ray diffraction peak magnitude in the temperature range 140–150°C in Fig. 17.24a

Here, it should be noted that the diffraction intensity measured again at 27°C after cooling recovered a similar peak profile close to the intensity magnitude of the original composite. This means that when extended crystallites formed extended amorphous chains by melting, perfect recovery from the extended amorphous chains to the extended crystallites occurred on cooling. For example, the amorphous chains in the melt state were obliged to retain the extended chain arrangement, since the specimen was fixed at a constant length under the heating process to assure the X-ray diffraction geometry. The crystallinities were almost constant in the temperature

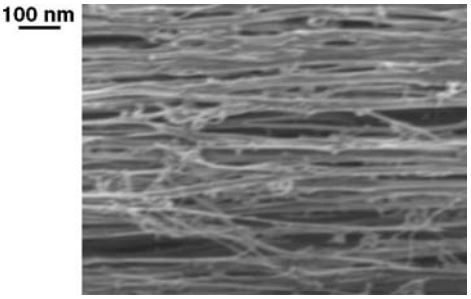

Figure 17.25 SEM image on the film surface of composite (6/1) containing 5% MWNT with $\lambda = 50$. (From Reference 19 with permission from the American Chemical Society.)

range from 27 to 140°C, and the corresponding electrical conductivity assured a slight increase beyond 120°C (see Fig. 17.23). In contrast, as discussed in Fig. 17.21b, the drastic decrease in the conductivity beyond 120°C was confirmed for the undrawn composite, and the corresponding crystallinity also decreased. Accordingly, it is evident that no decrease in crystallinity was afforded beyond 120°C, provided there was a slight increase in the electrical conductivity for the drawn composite with $\lambda = 50$. A series of experiments indicates that the increase in conductivity with increasing crystallinity is attributed to the electronic transition, where the electrons transfer more easily within the crystallites with short chain distances rather than within the amorphous region. Then, the conductivities of the drawn films with $\lambda = 30$ and 50 are considered to be higher than that of the undrawn film. This is quite different from the results obtained for the UHMWPE–MWNT system (18). As shown in Fig. 17.24b, the DSC peak of the UHMWPE/EMMA composite containing 5% MWNT at $\lambda = 50$ appeared at a temperature (144.7°C) lower than that (145.8°C) of the neat UHMWPE film with the same draw ratio (18). These results indicate the cocrystallization of the EMMA and UHMWPE chains under elongation and cooling processes. If cocrystallization of the EMMA and UHMWPE chains within the blend film did not occur under elongation, then the large peak must appear at the same temperature (145.8°C) as observed for the neat UHMWPE film, reflecting only the melting of the UHMWPE crystallites. Judging from the melting point of the EMMA being much lower than that of UHMWPE, the mechanism of cocrystallization under elongation is thought to be due to an epitaxial nucleation surface for the oriented ethylene sequences of the oriented EMMA chains during cooling to room temperature after elongation. That is, the ethylene sequences of the melted EMMA were oriented by the shear stress leading to the orientation of the UHMWPE chains with respect to the stretching direction, and these promoted the growth of crystallites on the surface of the extended crystal chains of UHMWPE during the cooling process. This means that most of the extended amorphous EMMA chains cocrystallized with the extended UHMWPE chains at the boundary. The cocrystallization of EMMA and UHMWPE chains provided a small lattice fluctuation leading to the slightly lower melting point of the cocrystallites in comparison to the melting point of the neat UHMWPE crystallites. Incidentally, it was confirmed

that the magnitude of the endothermic peak of the composite with $\lambda = 50$ was highest among the three specimens ($\lambda = 10, 30$, and 50), and the corresponding melting point, 144.7°C, was the highest. This means that the crystallinity of the composite with $\lambda = 50$ was highest among the three composites.

Figure 17.25 shows the SEM image of the surface of the 6/1 composite containing 5 wt% MWNT with $\lambda = 50$. This observation reveals that most of the UHMWPE fibrils were oriented with respect to the stretching direction, but some of the fibrils formed continuous networks. Of course, it was confirmed that the corresponding WAXD patterns showed very sharp spots from the (110) and (200) planes, indicating highly orientated crystallites with respect to the stretching direction. In Fig. 17.25, the average width (diameter) of the fibrils was in the range of 50–100 nm and no MWNTs could be observed. This indicates that each MWNT, or each bundle of aggregated MWNTs, was covered by thin UHMWPE–EMMA layers, and the neighboring MWNT or bundle covered by this layer did not contact each other directly. Together with another two SEM images of the specimens with $\lambda = 10$ and 20 (not shown in the present chapter), it is confirmed that the average width (diameter) of the fibrils became thinner as the draw ratio increased. Accordingly, it may be expected that the transfer of electrons between nearest MWNTs by hopping became easier with increasing draw ratio, and the conductivity of the film with $\lambda = 50$ became slightly higher than those with $\lambda = 10$ and 30. Of course, the electron transfer process may be active at elevated temperature because of the increase in conductivity, as shown in Fig. 17.23. However, when the crystallinity of the layer became lower with elevating temperature beyond 140°C, as shown in Fig. 17.24a, the electric conductivity of the film became lower. This is probably due to the fact that the electron transfer between adjoining MWNTs due to the electron transition mechanism became less active with a decreasing number of crystal regions with overlapped electron clouds.

Figure 17.26 shows the temperature dependence of the storage modulus E' and loss modulus E'' measured for the 6/1 composites with 5 wt% MWNT. Here, the storage modulus increased with increasing draw ratio. Even though E' for the specimen with $\lambda = 50$ was lower than E' for neat UHMWPE, as reported elsewhere (25–27), it is of interest that the E' values beyond 37 GPa are close to the crystal lattice modulus of polypropylene along the crystal chain direction (56), indicating successful results for preparing polymeric materials with high modulus and high conductivity.

The temperature dependence of E'' is sensitive to the draw ratio. Three dispersion peaks termed as α, β, and γ relaxations from the higher temperature side are observed for the undrawn film. The α dispersion is essentially associated with the crystal relaxation of the cocrystallites of UHMWPE and EMMA, and this peak becomes larger with increasing draw ratio, shifting to a higher temperature range indicating an increase in crystallinity. The α relaxation appeared at around -25°C.

In accordance with the reports of the relaxation mode for UHMWPE (57) and UHMWPE–EMMA blends (58) in terms of mechanical and positron annihilation methods, it is concluded that the β relaxation is not assigned as a glassy transition but is associated with a large motion of the amorphous chains. The β relaxation peak

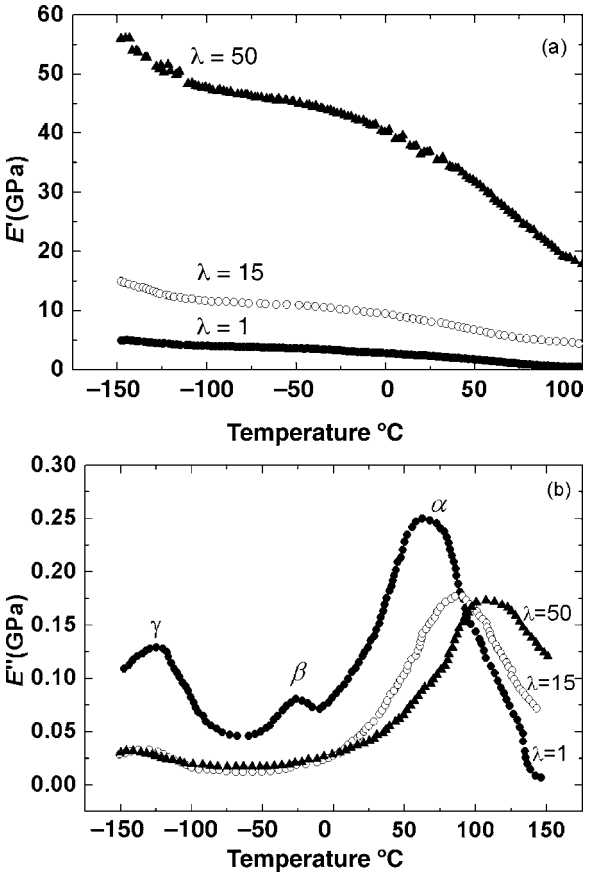

Figure 17.26 Temperature dependence of (**a**) the storage modulus E' (**b**) and loss modulus E'' measured for composites (6/1) with 5% MWNTs. (From Reference 19 with permission from the American Chemical Society.)

magnitude disappeared by elongation up to 15 times. This disappearance is thought to be due to the effect of the epitaxial nucleation surface of the ethylene sequences of the EMMA chains. That is, the EMMA chains crystallized on the surface of the UHMWPE crystallites behave as a crystalline mode different from the large motion associated with amorphous chains, when the EMMA content is much less than the UHMWPE content. However, when the blend film with 50% EMMA content (1/1 composition) was stretched up to 100 times, the β relaxation peak appeared indicating that most of the oriented EMMA chains within the 1/1 blend exist in an amorphous state with highly ordered arrangement and/or unstable state with large fluctuation of the lattice distance (58). In the present case, the ethylene sequences of the EMMA chains crystallize mainly together with the UHMWPE chains on the MWNT surfaces, as shown in Fig. 17.26. Hence, the γ relaxation, associated with the local chain in the amorphous phase, was observed for the undrawn composite at

around −130°C, but the peak disappeared at $\lambda = 15$. This is in good agreement with the behavior of the β relaxation.

Finally, we must emphasize that a series of experimental results must be taken into consideration on the basis of recent concepts (59–62) concerning conductive polymers in terms of charge carriers. In doing so, more detailed information about the polymer and MWNT composite materials must be needed in terms of the change in electric current density against voltage.

17.6 CONCLUSIONS

Based on a series of experiments, gelation/crystallization from solution was found to be an effective method for preparing electrically conductive materials with high modulus by adding MWNTs into UHMWPE. This effect was dependent on the structure of the curved graphene sheets of the MWNTs. The uniform mixing of MWNTs with a number of defects into UHMWPE can be achieved easily by the gelation/crystallization method. On the contrary, MWNTs with curved graphene sheets having few defects induced hard dispersion of MWNTs into the UHMWPE matrix. The EMMA copolymer was adopted as a suitable comixing polymer for UHMWPE, due to the large number of polar (—C=O) side groups in the alkyl main chains. The dispersion of MWNTs in the UHMWPE/EMMA matrix could be improved drastically.

As for the MWNTs with a number of defects in curved graphene sheets, uniform mixing could be realized by controlling both the optimum concentration of UHMWPE and the heating rate of the solution after ultrasonic treatment. The dried composites of UHMWPE–MWNT could be elongated up to more than 100-fold ($\lambda = 100$). The electrical conductivity and Young's modulus reached 10^{-3} S cm^{-1} and 58 GPa at room temperature, respectively, for the composite with 15 wt% MWNT content. The results showed that MWNTs were dispersed uniformly in the UHMWPE matrix, and that continuous networks of MWNTs were formed in the composite film. Furthermore, the networks of MWNTs were highly aligned with the oriented polyethylene fibrils along the elongation direction. The mechanical properties of the elongated UHMWPE–MWNT composite were affected by the orientation of the MWNTs, and the destruction of the fibril structure and the UHMWPE crystallites. For the electrical conductivity, the percolation threshold occurred at an MWNT content of approximately 3 wt%, corresponding to a volume ratio of 1.52%. The conductivity of the UHMWPE–MWNT composite around this percolation threshold was scattered without the regularity in the temperature range from 25 to 150°C during heating cycles. However, the conductivity of the UHMWPE composite containing more than 8 wt% MWNT changed orderly in the given temperature range.

Iodine doping further promoted the electrical conductivity of the UHMWPE–MWNT composite. The conductivity increased by one to four orders of magnitude, as compared to that of the original composite, and became stable and ordered in the temperature range of 25 to 150°C after iodine doping. The corresponding Raman

spectrum results indicated that the doped iodine (occurring as I_5^-) existed in the drawn UHMWPE–MWNT composite, which induced an increase in the electrical conductivity. The iodine doping also caused a decrease in the crystallinity of UHMWPE, as confirmed by DSC measurements. The storage modulus of the doped composite was maintained at a similarly high value to that of the original composite. The storage modulus of the iodine-doped composite reached 42 GPa at room temperature.

As for MWNTs of curved graphene sheets with few defects, the corresponding UHMWPE/EMMA composites containing these MWNTs were also prepared by the gelation/crystallization method. EMMA, like UHMWPE, is also an insulator, but the observed drastic increase in electrical conductivity could be realized by admixing 5 wt% MWNT content. Such a drastic increase in conductivity could not be confirmed even for the UHMWPE–MWNT composite whose MWNT content was 15 wt%. The admixture of EMMA into the UHMWPE matrix also provided a drastic increase in conductivity when the MWNT content was 5 wt%. The conductivity increased with elevating temperature, but decreased when the temperature was close to the melting point of the UHMWPE/EMMA cocrystallites, due to the decrease in the number of crystal regions. This indicated that the band gap became longer as a result of an increase in fluctuation of the ordered chains. Accordingly, it turned out that electron transfer between adjoining MWNTs is due to an electronic transition mechanism, and that the electron transfer process becomes easier with an increasing number of crystal regions with overlapped electron clouds. On stretching up to 50 times, the Young's modulus of the 6/1 blend film containing 5 wt% MWNT reached 37 GPa. Therefore, it may be concluded that the present method is one of a number of successful techniques for preparing composite materials with high electrical conductivity and high modulus.

NOMENCLATURE

CNTs	Carbon nanotubes
UHMWPE	Ultrahigh molecular weight polyethylene
EMMA	Ethylene–methyl methacrylate copolymer
SWNTs	Single-wall carbon nanotubes
MWNTs	Multiwall carbon nanotubes
ZZ	Intensities of the polarization components of the chain axis parallel to the drawing direction
ZX	Intensities of the polarization components perpendicular to the drawing direction
$\overline{M}_n$	Average number molecular weight
$\overline{M}_v$	Average viscosity molecular weight
λ	Draw ratio
E'	Storage modulus
E''	Loss modulus
α, β, γ	Relaxation peaks

REFERENCES

1. M. S. P. Shaffer and A. H. Windle, *Adv. Mater.*, **11**, 937 (1999).
2. M. J. Treacy, T. W. Ebbesen, and T. M. Gibson, *Nature*, **381**, 680 (1996).
3. E. W. Wong, P. E. Sheenan, and C. M. Lieber, *Science*, **277**, 1971 (1997).
4. A. B. Dalton, S. Collins, E. Munoz, J. M. Razal, V. H. Ebron, J. P. Ferraris, J. N. Coleman, B. G. Kim, and R. H. Baughman, *Nature*, **423**, 703 (2003).
5. M. Cadek, J. N. Coleman, V. Barron, K. Hedicke, and W. J. Blau, *Appl. Phys. Lett.*, **81**, 5123 (2002).
6. M. J. Biercuk, M. Llaguno, M. Radosavljevic, J. K. Hyun, A. T. Johnson, and J. E. Fischer, *Appl. Phys. Lett.*, **80**, 2767 (2002).
7. B. E. Kilbride, J. N. Coleman, P. Fournet, M. Cadek, A. Drury, and W. J. Blau, *J. Appl. Phys*., **92**, 4024 (2002).
8. J. P. Salvetat, J. M. Bonard, N. H. Thomson, A. J. Kulik, L. Forro, W. Benoit, and L. Zuppiroli, *Appl. Phys. A*, **69**, 255 (1999).
9. A. R. Bhattacharyya, P. Pötschke, M. Abdel-Goad, and D. Fischer, *Chem. Phys. Lett*., **392**, 28 (2004).
10. T. McNally, P. Pötschke, P. Halley, M. Murphy, D. Martin, S. E. J. Bell, G. P. Brennan, D. Bein, P. Lemoine, and J. P. Quinn, *Polymer*, **46**, 8222 (2005).
11. J. Liu, A. G. Rinzler, H. Dai, J. H. Hafner, R. K. Bradley, P. J. Boul, A. Lu, T. Iverson, K. Shelimov, C. B. Huffman, F. Rodriguez-Macias, Y. Shon, T. R. Lee, D. T. Colbert, and R. E. Smalley, *Science*, **280**, 1253 (1998).
12. J. Chen, M. A. Hamon, H. Hu, Y. Chen, A. M. Rao, P. C. Eklund, and R. C. Haddon, *Science*, **282**, 95 (1998).
13. E. T. Mickelson, I. W. Chiang, J. L. Zimmerman, P. J. Boul, J. Lozano, J. Liu, R. E. Smalley, R. H. Hauge, and J. L. Margrave, *J. Phys. Chem. B.*, **103**, 4318 (1999).
14. P. J. Boul, J. Liu, E. T. Mickelson, C. B. Huffman, L. M. Ericson, I. W. Chiang, K. A. Smith, D. T. Colbert, R. H. Hauge, J. L. Margrave, and R. E. Smalley, *Chem. Phys. Lett.*, **310**, 367 (1999).
15. K. D. Ausman, R. Piner, O. Lourie, R. S. Ruoff, and M. Korobov, *J. Phys. Chem. B.*, **104**, 8911 (2000).
16. P. Smith, and P. J. Lemstra, *J. Mater. Sci.*, **15**, 505 (1980).
17. Q. Zhang, D. R. Lippits, and S. Rastogi, *Macromolecules*, **39**, 658 (2006).
18. Y. Bin, M. Kitanaka, D. Zhu, and M. Matsuo, *Macromolecules*, **36**, 6213 (2003).
19. Q. Chen, Y. Bin, and M. Matsuo, *Macromolecules*, **39**, 6528 (2006).
20. G. W. Peng, F. Qiu, V. V. Ginzburg, D. Jasnow, and A. Balazs, *Science*, **288**, 1802 (2000).
21. M. Matsuo, C. Sawatari, and T. Ohhata, *Macromolecules*, **21**, 1317 (1988).
22. D. Stauffer and A. Aharony (eds.), *Introduction to Percolation Theory*, Taylor and Francis, London, 1994
23. M. Weber and M. R. Kamal, *Polym. Compos.*, **18**, 711 (1997).
24. C. Xu, Y. Agari, and M. Matsuo, *Polym. J.*, **30**, 372 (1998).
25. M. Matsuo, K. Inoue, and N. Abumiya, *Sen-i-Gakkaishi (Fiber)*, **36**, 696 (1983).
26. M. Matsuo and C. Sawatari, *Macromolecules*, **19**, 2036 (1986).
27. M. Matsuo and C. Sawatari, *Macromolecules*, **21**, 1653 (1988).
28. Y. Shieh and Y. Yang, *Eur. Polym. J.*, **42**, 3162 (2006).
29. R. E. Gibson, E. O. Ayorinde, and Y. Wen, *Compos. Sci. Technol.*, **67**, 1 (2007).
30. J. N. Coleman, U. Khan, W. J. Blau, and Y. K. Gunko, *Carbon*, **44**, 1624 (2006).
31. Z. M. Li, S. N. Li, M. B. Yang, and R. Huang, *Carbon*, **43**, 2413 (2005).
32. P. J. Flory and A. Vrij, *J. Am. Chem. Soc.*, **85**, 3548 (1963).

33. J. Brandrup, E. H. Immergut, and E. A. Grulke (eds.). *Polymer Handbook*, 4th edition Wiley, New York, 1999.
34. M. Matsuo and R. S. J. Manley, *Macromolecules*, **16**, 1500 (1983).
35. G. R. Ranade, V. M. Nadgir, C. A. Plank, and W. L. S. Laukhuf, *Polym. Eng. Rev.*, **23**, 6 (1983).
36. M. Narkis, A. Ram, and Z. J. Stein, *Appl. Polym. Sci.*, **25**, 1515 (1980).
37. C. Xu, Y. Bin, Y. Agari, and M. Matsuo, *Colloid Polym. Sci.*, **276**, 669 (1998).
38. Y. Bin, C. Xu, D. Zhu, and M. Matsuo, *Carbon*, **40**, 195 (2002).
39. Y. Xi, H. Ishikawa, Y. Bin, and M. Matsuo, *Carbon*, **42**, 1699 (2004).
40. Y. Bin, C. Xu, Y. Agari, and M. Matsuo, *Colloid Polym. Sci.*, **277**, 452 (1999).
41. S. L. A. da Silva, M. L. A. Temperini, and G. G. de Barros, *J. Appl. Polym. Sci.*, **87**, 939 (2003).
42. X. Zeng and T. J. Ko, *Polym. Sci. B.*, **35**, 1933 (1997).
43. G. G. de Barros, M. J. A. Sales, and A. R. F. de Britto, *Polym. Eng. Sci.*, **36**, 1125 (1996).
44. J. N. Mutuku and P. K. Karanja, *J. Polym. Mater.*, **20**, 445 (2003).
45. T. J. Lewis and D. M. Taylor, *J. Phys. D Appl. Phys.*, **5**, 1664 (1972).
46. M. S. Dresselhause and P. C. Eklund, *Adv. Phys.*, **49**, 705 (2000).
47. T. Michel, L. Alvarez, J. L. Sauvajol, R. Almairac, R. Aznar, O. Mathon, J. L. Bantignies, and E. J. Flahaut, *J. Phys. Chem. Solid*, **67**, 1190 (2006).
48. A. M. Rao, P. C. Eklund, S. Bandow, A. Thess, and R. E. Smalley, *Nature*, **388**, 257 (1997).
49. L. Grigorian, K. Williams, A. S. Fang, G. U. Sumanasekera, A. L. Loper, E. C. Dickey, S. J. Pennycook, and P. C. Eklund, *Phys. Rev. Lett.*, **80**, 5560 (1998).
50. R. C. Teitelbaum, S. L. Ruby, and T. J. Marks, *J. Am. Chem. Soc.*, **101**, 7568 (1979).
51. J. Cambedouzou, J. L. Sauvajol, A. Rahmani, E. Flahaut, A. Peigney, and C. Laurent, *Phys. Rev. B*, **69**, 235422 (2004).
52. T. Michel, L. Alvarez, J. L. Sauvajol, R. Almairac, R. Aznar, O. Mathon, J. L. Bantignies, and E. Flahaut, *J. Phys. Chem. Solid*, **67**, 1190 (2006).
53. W. Zhou, S. Xie, L. Sun, D. Tang, Y. Li, Z. Liu, L. Ci, X. Zou, and G. Wang, *Appl. Phys. Lett.*, **80**, 2553 (2002).
54. D. J. Yang, S. G. Wang, Q. Zhang, P. J. Sellin, and G. Chen, *Phys. Lett. A*, **329**, 207 (2004).
55. W. F. Hoenlein, G. S. Duesberg, A. P. Graham, M. Liebau, R. Seidel, and E. Unger, *Mater. Sci. Eng.*, **C23**, 663 (2003).
56. C. Sawatari and M. Matsuo, *Macromolecules*, **19**, 2653 (1986).
57. M. Matsuo, L. Ma, M. Azuma, C. He, and T. Suzuki, *Macromolecules*, **35**, 3059 (2002).
58. L. Ma, M. Azuma, C. He, T. Suzuki, Y. Bin, and M. Matsuo, *Macromolecules*, **37**, 7673 (2004).
59. S. V. Novikov, D. H. Dunlap, V. M. Kenkre, P. E. Parris, and A. V. Vannikov, *Phys. Rev. Lett.*, **81**, 4472 (1998).
60. S. V. Novikov, *J. Polym. Sci. B Polym. Phys.*, **41**, 2584 (2003).
61. C. Tanase, E. J. Meijer, P. W. M. Blom, and D. M. de Leeuw, *Phys. Rev. Lett.*, **91**, 216601 (2003).
62. W. F. Pasveer, J. Cottaar, C. Tanase, R. Coehoom, P. A. Bobbert, P. W. M. Blom, *Phys. Rev. Lett.*, **94**, 206601 (2005).

Chapter 18

Crystallization Behavior of Polyethylene/Carbon Nanotube Composites

Lingyu Li,[1] Bing Li,[1] Steve L. Kodjie,[2] and Christopher Y. Li[1]

18.1 INTRODUCTION

18.1.1 Structure and Properties of Carbon Nanotubes

In 1991, Iijima discovered carbon nanotube (CNT) in the form of elongated fullerenes (1). Similar to graphite, CNT comprises of interconnected six-membered rings or hexagons of carbon atoms spanning the entire surface of the nanotube. The ends of the tubes are formed from half-dome-shaped fullerene molecules as a result of topological defects such as pentagonal and heptagonal defects near the tube ends that aids in their closure (2). In CNTs the graphene sheet rolls up in such a way that the graphene lattice vector $\mathbf{C}_h = n\mathbf{a}_1 + m\mathbf{a}_2$ becomes the circumference of the tube as shown in Fig. 18.1, where n and m are integers and $\mathbf{a}_1$ and $\mathbf{a}_2$ are unit cell vectors of the planar graphene sheet (3). The spatial orientation of the hexagons in the planar graphene sheet with respect to the CNT length is not fixed and can lead to chiral and achiral arrangements. In the achiral-type CNT, the honeycomb lattice of hexagons is parallel to the tube axis and this type of configuration leads to the formation of armchair and zigzag types of CNTs. All other CNT configurations in which the C—C bond makes an angle $\theta, 0 < \theta < 30^\circ$, to the tube axis are known as chiral type. Figure 18.1b shows the three CNT classifications, namely armchair, zigzag, and chiral type CNTs (4).

[1]A. J. Drexel Nanotechnology Institute and Department of Materials Science and Engineering, Drexel University, Philadelphia, PA 19104, USA
[2]Arkema Inc., Analytical & Systems Research, King of Prussia, PA 19406, USA

Polyolefin Composites, Edited by Domasius Nwabunma and Thein Kyu

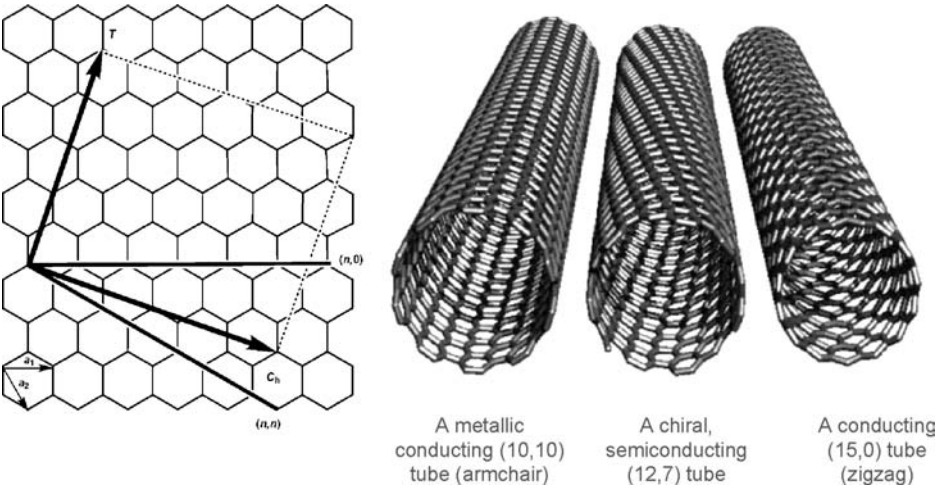

Figure 18.1 Schematic representations of rolling of graphene sheets (**a**) and three types of carbon nanotubes (**b**).

Theoretical studies have shown that CNTs possess interesting and potentially useful structural and electronic properties. The unique electronic properties have been suggested to be caused by quantum confinement of the electrons normal to the tube axis and as such electrons can propagate only along the tube axis (4). Depending on the chirality, CNTs are either metallic or semiconducting. When the difference between the chiral integers $(n - m)$ is a multiple of three, metallic single-walled carbon nanotube (SWNT) results; however, if the difference $(n - m)$ is not a multiple of three, semiconducting nanotubes are obtained. Experimental work carried out to date provides insights into the unique properties of CNTs. Scanning tunneling microscopy (STM) and spectroscopy techniques have confirmed the electronic properties of CNTs (3). The conductivity of SWNTs has also been measured, paving the way for their application in field-effect transistors (5,6). Investigation of the emission properties of CNTs (7–9) has revealed high field-emission current density of CNTs at a low emission threshold, which can be taken advantage of in flat panel displays and electron guns for various applications (10–12). The electronic, chemical, and mechanical properties of CNTs make them ideal candidates for applications as probes for STM and atomic force microscopy (AFM) (3,13). CNT could also be functionalized making it possible for applications in drug delivery and chemical patterning (14,15). The use of CNT for the production and the storage of energy is also very promising; CNTs have been proposed for the fabrication of lithium rechargeable batteries (16,17). Capillary forces may exist in the CNTs that are strong enough to hold gases or fluids (18) and the hollow tube can be used as a template for making nanowires and nanocapsule (19).

Though the reported values of stiffness and strength of CNTs vary widely, the excellent mechanical properties have been attributed to the strong in-plane carbon–carbon bonds in the graphene layer (20–25). Treacy reported that the Young's

modulus of SWNTs was approximately 1.25 TPa (12). Experimental studies carried out by Yu also showed that Young's modulus of SWNTs is approximately 1 TPa and the maximum tensile strength is approximately 30 GPa (15). Despite the high Young's modulus of CNTs, AFM measurements indicate that CNTs are flexible, tough, and capable of undergoing reversible deformation (26).

18.1.2 Carbon Nanotube Nanocomposites

Owning to the excellent properties of CNTs, they can be incorporated into polymers as fillers for fabricating polymer/CNT nanocomposites (PCN). In industry, the potential application of PCNs in conductivity enhancement, electrostatic dissipation, and aerospace structural materials have been highly recognized (27–29). It is perceived by developing PCNs that the attractive properties of CNTs would offer a way of transforming the mechanical, electrical, and optical properties from nano- to macroscales. PCN can exhibit properties that differ substantially from those of the pristine polymer matrix and of particular interest is the use of CNTs as reinforcing agents due to their high aspect ratio and extraordinary mechanical properties (20).

Depending on the targeted properties, a variety of polymers have been explored to form nanocomposites with CNTs. These include amorphous polymers such as polystyrene (30–32), poly(methyl methacrylate) (33–36), rigid-rod polymers such as poly(*p*-phenylene benzobisoxazole) (37), cross-linkable polymers such as epoxy (38–40), and conducting polymers such as polyaniline, and polypyrrole (41–44). Recently, PCNs formed by CNTs and semicrystalline polymers such as iPP (45–49), PE (50), polyvinyl alcohol (PVA) (51), polyacrylonitrile (PAN) (52–54), thermoplastic polyimide (55), conjugated organic polymer (56), as well as thermoplastic elastomers such as polyurethane systems (57–59) have been studied. Using differential scanning calorimetry (DSC) nonisothermal and isothermal techniques, it has been found that $t_{1/2}$ decreases with increasing CNT content in PCNs. Crystallization behavior of iPP/CNT PCNs was most extensively studied. Grady et al. reported that upon mixing with CNTs, β-form of iPP content increases, while Assouline et al. showed that multiwalled carbon nanotube (MWNTs) could act as α-nucleation agents (28,48). Kelarakis et al. studied the crystallization behavior of ethylene/propylene (EP) random copolymer (84.3 wt% P) in the mixture with modified carbon nanofibers (MCNF) (47). The MCNF was found to nucleate α form of iPP. They also reported that the highly stretched PCN exhibited a higher amount of unoriented crystals, a lower degree of crystal orientation, and a higher amount of γ crystals, indicating the effective load transfer from the matrix to MCNF. Chang et al. reported β-form of iPP crystals in the iPP/SWNT PCN under strain (45). In a series of thermoplastic elastomers (Morthane)/CNT PCNs, it has been found that the strain-induced–crystallization was enhanced with the addition of CNT (for 1–5 vol%), which led to the increase in the rubbery modulus by a factor of 2–5 and to the improvement in shape fixity (57,59). Near IR was used to ''heat'' CNTs, leading to the melting of the physical cross-linking points (polymer crystals), and 50% more recovery stress than the pristine resin was reported (59).

Winey and colleagues investigated the nucleation of PE by SWNTs (60). The crystallization kinetics of PE/SWNT nanocomposite prepared by solution blending followed by coagulation to form precipitates was studied and analyzed by Avrami equation from which it was shown that SWNTs provided nucleation sites as well as accelerated PE crystal growth rate. A two-dimensional crystal growth was reported for the nanocomposite compared to the three-dimensional spherulite growth of PE. McNally et al. (61) investigated the morphology and dispersion of MWNTs in melt-processed MWNT/PE nanocomposites by scanning electron microscope (SEM), wide-angle X-ray diffraction (WAXD), and Raman spectroscopy. In this chapter, we shall focus on the crystallization behavior of PE in the PE/CNT hybrid systems. Morphology, structure, and properties of PE/CNT PCN will be discussed.

18.2 EXPERIMENTAL

18.2.1 Materials

CNTs were purchased from Aldrich and Carbon Nanotechnologies Inc., and they are listed in Table 18.1. CNTs were washed with 2.4 M nitric acid for 30 min. The resulting CNTs were then centrifuged, collected, and dried in a vacuum oven. Linear polyethylene (MFI = 12 g/10 min), *p*-xylene, 1,2-dichlorobenzene (DCB), and glycerin were purchased from Aldrich and used as received.

18.2.2 Experimental Procedure

Functionalized CNTs were obtained via solution crystallization using CNTs as seeds. For PE solution crystallization, both *p*-xylene and DCB were used as solvent. 0.5 mg PE was dissolved in 4 g *p*-xylene at 120°C. 0.1 mg MWNT-10 and 1 g *p*-xylene solution was sonicated for 2–3 h at 45°C and then added to PE/*p*-xylene solution. The

Table 18.1 Source of CNTs.

Category	Synthetic method	Vendor	Outer diameter, nm	Length, μm
SWNT	HiPCO	Carbon Nanotechnology Inc.	0.8–1.3	~1
MWNT-10 (Product #406074)	Arc discharge	Sigma	5–15	1–10
MWNT-25 (Product #1240XH)	CVD	Nanostructured & Amorphous Materials, Inc.	20–30	0.5–2
CNF (PR-19-HHT)	CVD	Applied Science Inc.	100–300	30–100

mixture was then quenched to the preset crystallization temperature ($T_c = 103°C$). The crystallization time was controlled to be 0.5–3 h. Sample was isothermally filtered after crystallization to remove the uncrystallized materials. When DCB was used as the solvent of PE crystallization, SWNT concentration was varied from 0.01 to 0.1 wt%. T_c was varied from 80 to 91°C. TEM experiments were conducted using a JEOL-2000 FX microscope with an accelerating voltage of 120 kV. Nanohybrid shish-kebab (NHSK) suspensions were collected on a carbon-coated TEM grid. Both Pt-shadowed and nonshadowed samples were used. SEM experiments were carried out using a FEI/Phillips XL30 field emission environmental SEM and the acceleration voltage was 15 kV. NHSK suspensions were collected on a glass slide. After solvent evaporation, NHSKs were sputtered with Pt for 25 s before SEM observation. Differential scanning calorimetry (DSC) was carried out using a Perkin-Elmer DSC7 at a heating and cooling rate of 10°C min^{-1} under a nitrogen atmosphere. Sample with a mass of 3.6 mg was encapsulated in sealed aluminum pans. The temperature and heat flow were calibrated using standard materials (Indium) at different cooling and heating rates between 5 and 40°C min^{-1}. TGA was carried out using Perkin-Elmer TGA 7 under air and nitrogen (N_2) atmosphere with a flow rate of 40 ml min^{-1}. About 3–6 mg of the sample was heated from 30 to 600°C at a heating rate of 10°C min^{-1}.

18.3 RESULTS AND DISCUSSIONS

18.3.1 PE/CNT Nanohybrid Shish-Kebabs Via Solution Crystallization

Most of the studies regarding to the semicrystalline polymer/CNT hybrid materials focused on the nanocomposite crystallization behavior. It should also be noted that carbon materials, such as carbon fibers (CFs), which are $\sim 10\ \mu m$ in diameter, have been used to induce polymer crystallization (transcrystallization). A number of polymers have been investigated including iPP, PE, polyhexamethylene adipamide (Nylon 66), poly(phenylene sulfide), polyether ether ketone, and so on (62–64). In the case of iPP/CF composite, the pitch-based CF induces a dense population of iPP crystal nuclei along its surface (62). As these nuclei grow, they impinge upon one another such that crystals essentially grow perpendicular to the fiber axis. This leads to oriented growth of iPP lamellae away from the fiber outward into the thermoplastic matrix, thus forming a transcrystalline layer (62). Epitaxial growth of polymers such as PE, Nylon 6, and polyethers on graphite surface has also been confirmed using STM and TEM techniques (65,66). All these suggest that CNT might be an efficient nucleation agent for crystalline polymers.

Recently, we employed a polymer solution crystallization technique to study the PE/CNT crystallization behavior. *p*-Xylene was used as the solvent for controlled solution crystallization (67). Figure 18.2 shows two TEM images of PE-decorated SWNTs after solution crystallization at 104°C for 30 min. The relatively high T_c, which is higher than the clearing temperature of PE in *p*-xylene, was chosen so that

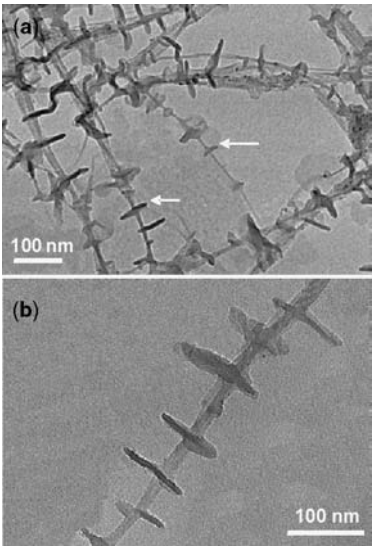

Figure 18.2 TEM micrograph of SWNTs periodically modified with PE lamellae crystals produced by crystallization of PE on SWNTs at 104°C in *p*-xylene for 0.5 h (**a**). The PE and SWNT concentrations are 0.01 and 0.002 wt%, respectively. SWNT bundles can be seen in NHSK (**b**).

homogenous nucleation of PE was prohibited and all the PE crystals grown at this condition were initiated by CNTs via a heterogeneous nucleation mechanism. It is evident from the figure that CNTs are decorated with disk-shaped objects (arrows), which are PE single-crystal lamellae (edge-on views). The crystalline nature of the disk-shaped objects was also confirmed by DSC and WAXD experiments. The average lateral dimension of the lamellae is ~50–80 nm. It is of great interest that these PE lamellae were strung together by SWNTs with the average periodicity of ~40–50 nm. This fibril-linked-disk structure is similar to the classic ''shish-kebab'' polymer crystals formed under shear field, as first observed in 1960s by Geil, Reneker (''Hedgerow'') (67) and Pennings (68). A shish-kebab polymer crystal usually consists of a central fibril (shish) and disk-shaped folded-chain lamellae (kebab) oriented perpendicularly to the shish as shown in Fig. 18.3a. Figure 18.3b shows the schematic representation of the structure in Fig. 18.2. A few similarities between these two structures can be found from this figure: (a) Both structures possess a central fibril core and the diameter of the core is approximately one to a few tens of nanometers, (b) the central cores in both structures are wrapped with disk-shaped single crystals with the lamellar thickness of a few tens of nanometers, (c) single-crystal lamellae are perpendicular to the shish axis, and (d) these lamellae are periodically located on the central one-dimensional (1D) cores. Since the central shish is CNT while the kebabs are formed by PE single crystals as in Fig. 18.3b, we name this novel structure nanohybrid shish-kebab.

Conventional polymer shish-kebab structure is formed in polymer solution/melt under an external shear field. For a polymer solution (i.e., 5% polyethylene/xylene) under an extension/shear flow, polymer chains that normally possess a coil confor-

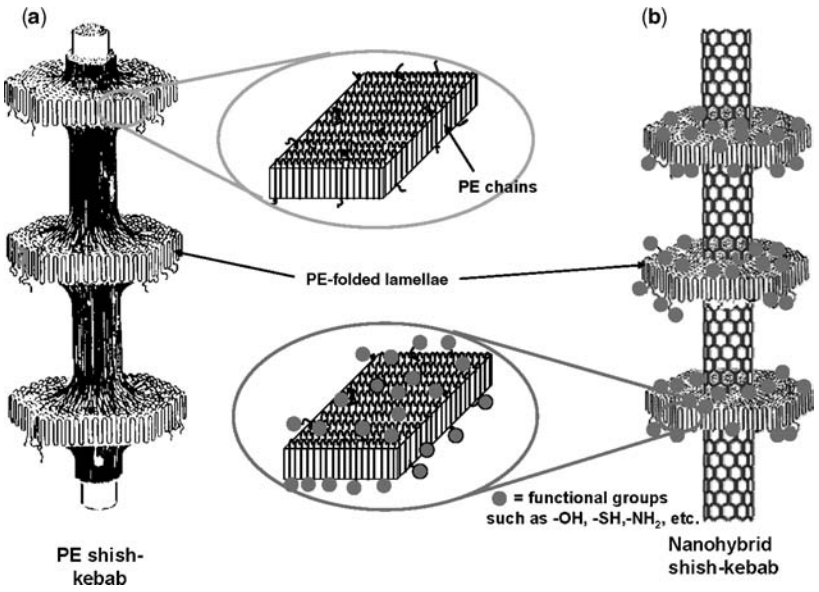

Figure 18.3 Schematic representations of (**a**) polymer shish-kebab crystals; (**b**) PE CNT nanohybrid shish-kebab structure. Periodic patterning of different functionalities can be achieved by crystallizing polymers with different end groups such as –OH, –SH, and $–NH_2$. These end groups are ''defects'' for the polymer single crystals and will most likely be excluded onto the crystal surfaces (**b**). The degree of functionalization can be easily controlled by tuning polymer crystal sizes.

mation might undergo a coil-to-stretch transition (69). If the chain is longer than a critical molecular weight (M^*), the stretched polymer chains aggregate to form extended chain fibrillar crystals (70). The remaining coil polymer chains could then crystallize upon the fibrillar crystals in a folded periodic fashion, forming the shish-kebab morphology. The stretched polymers are the shish and the folded lamellae are kebabs. In this study, the SWNT/PE solution was not under extension or shear flow during crystallization. Since the nanofibrillar structure of SWNT provides a 1D nucleation surface, shear is not needed in the CNT-induced crystallization and the formation of NHSK was observed. It is noticeable that some of SWNTs are in the form of small bundles. This is because as the polymer chains started to nucleate on SWNTs due to the poor solubility of SWNT in *p*-xylene, SWNTs were not completely exfoliated. A fraction of the SWNTs was still in the bundle state and PE crystallized/wrapped the bundle, which in turn captured the ''state of the CNT agglomeration'' in *p*-xylene solution.

The observation of NHSK opens the gateway to periodically functionalized CNTs. Periodic functionalization of CNTs is an attractive field of research and it provides a unique opportunity to pattern 1D CNTs to create functional, ordered structures for electrical and optical applications. Periodic functionalization of CNTs, on the contrary, is an extremely challenging task due to their small size. Very few reported CNT functionalization research works have been dedicated to studying how the functional groups arrange on the CNT surface. Worsley et al. carefully investi-

gated the structure of the CNTs functionalized by the Bingel reaction (71). The authors were able to identify long-range, regular patterns of the functional groups on the individual CNT surfaces. When functionalized, the formation of the sp^3 cyclopropane structure results in the disruption in the sp^2 lattice, altering the electronic properties of the nanotube and leading to a larger band gap depending on the degree of functionalization. Well-resolved images of individual functional groups on a nanotube bundle were reported with a clear periodicity of ~ 4.6 nm. In the present NHSK case, it is evident that polymer crystallization-driven CNT functionalization (PCCF) also led to periodic functionalization of CNTs. Furthermore, compared to the previous reported techniques, PCCF is unique since (1) it provides periodic functionalization and the periodicity is tunable from 20 to 150 nm, as opposed to 4.6 nm in the Bingel reaction-induced periodic functionalization, (2) it belongs to the noncovalent functionalization type and CNT integrity remained, (3) a variety of functional groups could be introduced on the chain ends and then brought to the vicinity of the CNT, and (4) the degree of functionalization could be easily controlled by increasing the kebab size.

In order to demonstrate the generality of this method, different kinds of CNTs were also employed. MWNTs synthesized by arc discharge and CVD methods as well as carbon nanofibers (CNF) were successfully used to functionalize CNTs. First, MWNTs synthesized by arc discharge and CVD methods were used. The diameters of these MWNTs were reported as 5–15 nm and 20–30 nm, respectively. They are thus denoted as MWNT-10 and MWNT-25. Figure 18.4a shows the TEM image of the resulting PE functionalized MWNT-10s after solution crystallization in *p*-xylene at 103°C for 30 min and the PE concentration was 0.01 wt%. It is evident that the disk-shaped PE single-crystal lamellae are periodically located along the tube axis, and they are mostly perpendicular to the tube axis. A larger periodicity (the average periodicity is about 50–70 nm) is observed compared to that in SWNTs and the diameter of kebab is about 50–70 nm. NHSK with better dispersed MWNT-10 can also be achieved by using DCB as the solvent, which will be discussed in the following section.

Figure 18.4b shows PE functionalized MWNT-25s (*p*-xylene was the solvent and $T_c = 97°C$). The tubes are slightly curvy and possess more defects as opposed to

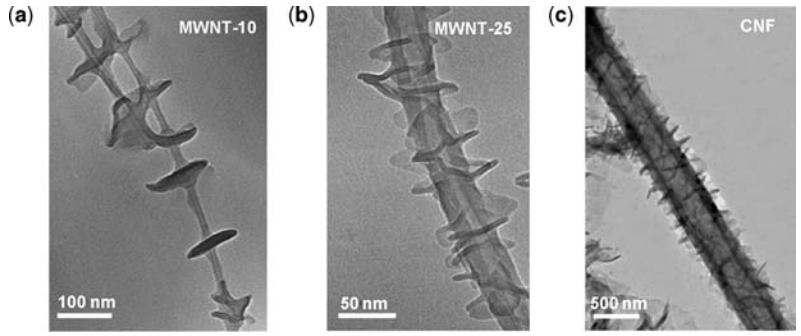

Figure 18.4 TEM images of PE/MWNT-10 NHSK (**a**), PE/MWNT-25 NHSK (**b**), and PE/CNF NHSK structures produced by crystallization of PE on different CNTs and CNF in *p*-xylene for 0.5 h at 103, 97, and 97°C. The PE and SWNT concentrations are 0.01 and 0.002 wt%, respectively.

MWNTs synthesized by the arc discharge method and HiPCO SWNTs. However, NHSK structure is clearly seen from the figure. The outer diameter of MWNT-25 is about 30 nm. The disk-shaped PE single-crystal lamellae are located along the tube axis and are not as uniform as those on MWNT-10s, which is probably due to the defects on the MWNT-25 surface and/or relatively lower T_c. Less perfect sidewall structure is also believed to be the reason that the kebab periodicity was not as well formed as in MWNT-10.

To further demonstrate the generality of this method, much larger size CNFs were used. CNFs are attractive from the practical point of view due to their relatively low cost. These CNFs have an outer diameter of 100–300 nm, a hollow core, and a length on the order of 30–100 μm. Figure 18.4c shows a TEM image of the PE NHSK with CNF shish. *p*-Xylene was used and T_c was 97°C. It is clear that PE forms single-crystal lamellae on the central CNF. The PE lamellae in this case are large; the diameter is about 500 nm. From these three figures, it is evident that PE was successfully used to form NHSK structure with CNTs having diameters ranging from less than 1 to ~300 nm.

Forming NHSK on CNTs is intriguing. One key observation in PE/SWNT NHSK is that the polymer chains in the kebabs are parallel to the shish axis, leading to the orthogonal orientation between the lamellar surface and the shish axis. Two possible factors that affect NHSK growth were proposed: first, epitaxial growth of PE on CNT. Second, geometric confinement by the CNT also plays a role. Owning to their small diameters, CNTs themselves can be considered as rigid macromolecules and polymer chains might preferably align along the tube axis regardless of the lattice matching between the polymer chain and the graphitic sheet. This mechanism can be attributed to ''soft epitaxy,'' in which strict lattice matching is not required. The growth mechanism might involve both and is size dependent as shown in Fig. 18.5. A typical polymer possesses a radius of gyration of ~10 nm (74). As a

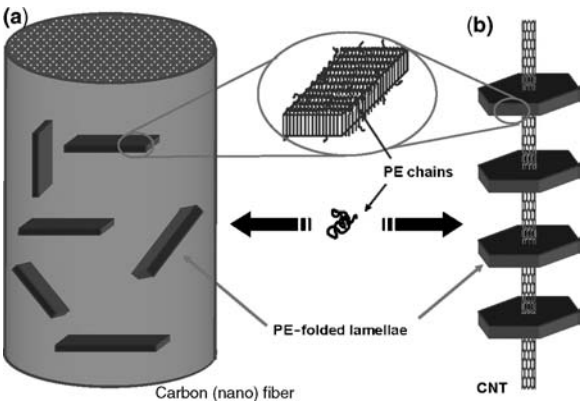

Figure 18.5 Schematic representation of the proposed ''size dependent soft epitaxy'' mechanism. For large-diameter CNFs, PE lamellae are randomly orientated on the fiber surface (**a**), while for small diameter CNTs, soft epitaxy dictates the parallel orientation between PE chains and the CNT axis, leading to a orthogonal orientation between CNT and PE lamellar surface (**b**).

macromolecule of such a size diffuses to the fiber/tube surface and crystallizes, the diameter of the fiber/tube plays a critical role in crystal formation. For larger diameter fibers (i.e., CF, 10 μm in diameter), the surface curvature is small and the polymer behaves as if it is on a flat surface. Strict lattice match and epitaxy should be the main growth mechanisms. For smaller fibers, as the fiber diameter approaches R_g of the polymer chain, the fiber surface is ''molecularly curvy.'' This curvy surface substantially affects the stability of the crystals if the polymer chain and the fiber axis do not match, which would lead to curved crystals with distorted lattice. Therefore, as a polymer starts to crystallize on this surface two scenarios could occur (using PE as an example, in which case epitaxy requires the PE chain $\langle 001 \rangle$ to be parallel with $\langle 2{-}1{-}10 \rangle$ graphite) (75, 76): (1) if the lattice of the graphitic sheet orients in such a way that $\langle 2{-}1{-}10 \rangle$ is parallel to the CNT axis [an (n, n) tube], both the lattice matching and the geometric confinement dictate the polymer chain to be parallel with the CNT axis and (2) if $\langle 2{-}1{-}10 \rangle$ is not parallel to the CNT axis [an (n, m) tube, $n \neq m$], lattice matching and geometric confinement, therefore, compete with each other and the dominant factor should determine the chain orientation. Since the geometric confinement becomes more significant as the fiber diameter decreases, one can envisage that for CNTs with small fiber diameter, geometric confinement would be the major factor and polymer chains should be exclusively parallel to the CNT axis, disregarding the CNT chirality. As a consequence, kebab crystal lamellae should be perpendicular to the CNT axis and orthogonal orientation was obtained. For larger diameter CNFs, geometric confinement is weak and lattice matching might play the major role and dictate the orientation of the polymer chain. Since a variety of graphitic sheet orientations exist for CNFs, epitaxial growth of the polymer crystals would lead to different orientations of the polymer chains/lamellar normal.

In order to confirm this hypothesis, TEM and SEM experiments were conducted to study the detailed lamellar orientation on the CNT/CNF surface. Figure 18.2 clearly shows that PE lamellae are perpendicular to SWNT axis, indicating that the polymer chains are parallel to the CNT axis. On the contrary, Fig. 18.6 shows the SEM image of CNF/PE NHSKs. Interestingly, PE lamellae possess multiple

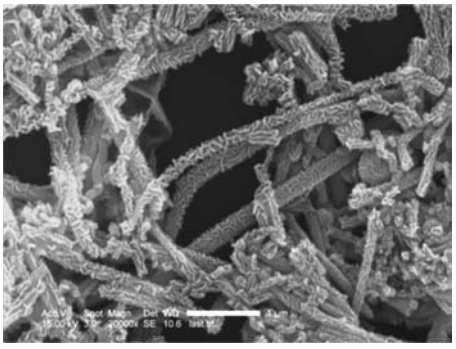

Figure 18.6 SEM micrograph of PE periodically functionalized CNFs produced by crystallization of PE on CNTs at 97°C in *p*-xylene for 0.5 h. Random orientation of PE lamellae can be clearly seen on CNF surface. The PE and CNF concentrations are 0.01 and 0.002 wt%, respectively.

orientations: the lamellar normals are parallel, perpendicular, or oblique to the CNF axis. This observation indicates that in CNF samples since the fiber diameter is relatively large (100–300 nm), the curvature of CNF is not significant for PE macromolecules and lattice epitaxy is therefore the major factor as CNF-induced crystallization occurs. Thus, SEM observations clearly support the size-dependent mechanism.

18.3.2 PE CNT Nanohybrid Shish-Kebabs Via Physical Vapor Deposition

The previously mentioned NHSK is a 3D structure and is an ideal reinforcing materials for nanocomposite application. For nanodevice applications, however, 2D nanostructure is more desirable. In order to achieve 2D NHSK structure, a physical vapor deposition (PVD) method was recently developed. A small drop of SWNT/DCB solution was first placed on a carbon-coated cover glass or a TEM grid using a spin coater. The spin speed and time were 3000 rpm and 60 s, respectively. These SWNTs dispersed TEM girds or carbon-coated cover glass were then coated by PE vapor using the physical vapor deposition method (77). Figure 18.7 shows a TEM micrograph of a PE-coated film. The sample was shadowed with a thin layer of Pt/Pd to enhance the contrast. Many small ''islands'' with an average height of ~ 10 nm can be seen on the substrate (the height was estimated using the shadowing angle; it can also be confirmed by AFM experiments, see the following section). Of interest is that numerous ''centipedelike'' objects can be seen from the image, as indicated by the arrows. The careful examination of the image shows that these ''centipedes'' are PE-coated SWNTs (or small SWNT bundles): the SWNTs seemingly form the ''body of the centipedes,'' while PE forms the ''feet.'' These ''feet'' are rod-shaped objects (about 120 nm in length and 10 nm in width). Unlike the rest

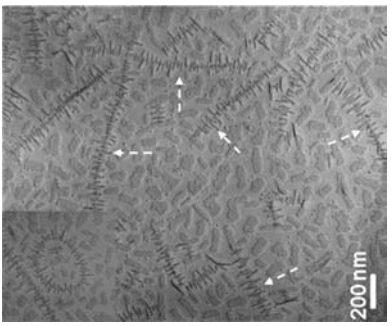

Figure 18.7 TEM image of PE decorated SWNTs. Arrows indicate the ''nanocentipedelike'' 2D nanostructure, which is named as 2D nanohybrid shish-kebabs. SWNTs form the central shish (the ''body of the centipede'') and PE rods form the kebabs (''centipede'' feet). PE crystalline rods are perpendicular to the SWNT axes. Inset shows a ''nanonecklace'' formed by PE decorating on a SWNT loop. Note that PE rods are locally perpendicular to the SWNT axis.

of the PE ''islands'' formed on the carbon film, PE rods attaching to SWNTs show uniform orientation and their long axes are perpendicular to the SWNT axes. This peculiar morphology resembles the previously discussed NHSK. One obvious difference is that NHSK formed in solution crystallization is 3D in nature, while in the present case, both PE rods and SWNTs are 1D objects and the resulting centipedelike hybrid structure is two dimensional. 2D NHSK was thus adopted to name this unique structure. CNTs form the shish, while PE rods form the kebabs.

The formation mechanism of these 2D NHSK is intriguing. In PVD, PE chain scission occurs upon heating under vacuum (typically 10^{-4}–10^{-5} Torr) and the resulting vaporized materials have a molecular weight (M_W) on the order of 1300 g mol^{-1} (78,79). Upon deposition on the solid surface, these PE oligomers crystallize, resulting in the previously mentioned rod-shaped objects, which are extended chain PE crystals with the PE axis being perpendicular to the rod long axis. Each PE rod having a width of about 10 nm that corresponds to M_W of $\sim$ 1300 g mol^{-1} provided the extended chain configuration. Most importantly, these PE crystals rods are relatively periodically arranged on individual SWNTs and have a periodicity of $\sim 37.4 \pm 7.9$ nm. Although a few of the PE nanorods are slightly oblique from axis normal, most rods are perpendicular to the SWNT axis. The inset of Fig. 18.7 shows a TEM image of a ''nano-necklace'' structure formed by PE decoration on a SWNT loop. Although the SWNT possesses an elliptical shape with a long axis of $\sim$200 nm and a short axis of $\sim$110 nm, rod-shaped PE crystals are formed on the SWNT loop as well with their long axes being locally perpendicular to the SWNT axis. This suggests that the present PVD method can be adapted for patterning on complex CNT arrays, and the orientation of PE rods is determined by the local CNT axis direction.

The 2D NHSK feature can be characterized by AFM experiments. Figure 18.8 shows the AFM tapping mode images of PE decoration on SWNTs. The 5-μm (a) and 2.5-μm (b) scans show that the surface of PE-decorated SWNTs is flat. PE decoration is uniform and all the SWNTs are decorated with PE crystal rods. Figure 18.8c, d, and f are 1 μm scan of the height, amplitude, and top view images, respectively. PE rods relatively periodically span along SWNT. AFM height profile along the SWNT is shown in Fig. 18.8e. The average height measured from three different spots on one PE decorated SWNT (indicated by green, red, and white arrows in Fig. 18.8e and f) is 12.4 nm, while the height in the pure SWNT area is $\sim$2.4 nm. The relatively large diameter indicates small SWNT bundle formation (two to four SWNTs for each bundle), which is not surprising since aggregation of SWNTs in the present case is dictated by the degree of exfoliation of SWNTs in DCB (more concentrated SWNT solution tends to induce more/larger SWNT bundles). 2D NHSK can also be formed on single SWNTs as shown in the lower left corner of Fig. 18.8c. AFM height profile indicates the tube diameter is $\sim$1.2 nm, indicating the absence of SWNT agglomeration. Hence, formation of the 2D NHSK is not significantly affected by SWNT aggregation. In all these images, PE rods were formed on the top of these SWNTs (bundles) and were orthogonally oriented with respect to the tube axis.

The orientation of the PE rods obtained in PVD has been used as a marker to determine chain folding direction in polymer single crystals (78,80,81). In the

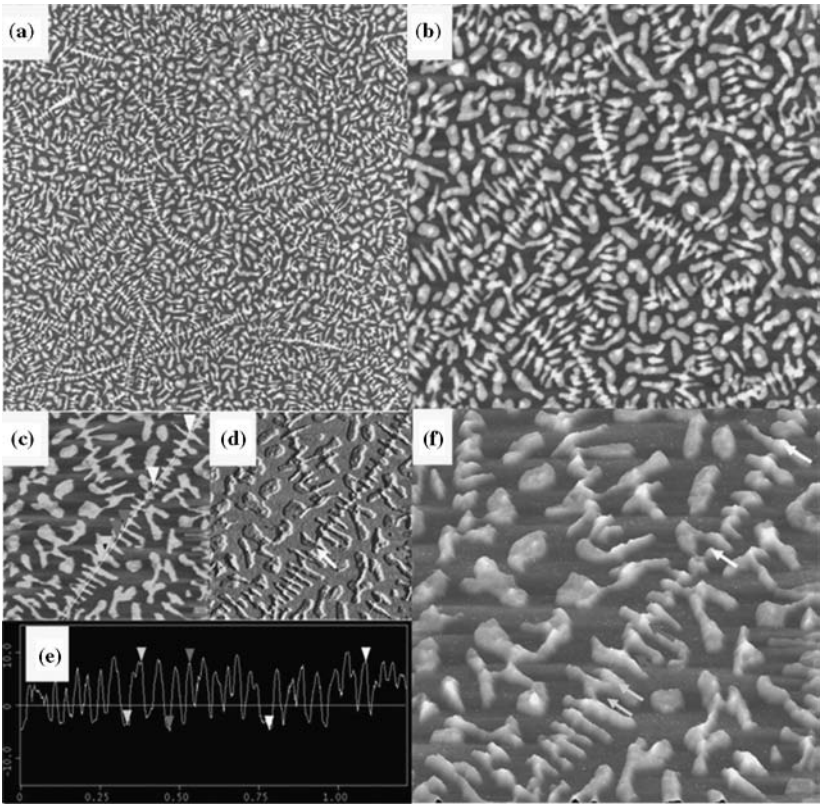

Figure 18.8 AFM tapping mode images of the PE decorated SWNTs. (**a**) and (**b**) Height images of the 5 and 2.5 μm scans, respectively. (**c**,**d**, and **f**) Height, amplitude, and top view images of 1 μm scan, respectively. (**e**) Height profile of the 2D NHSK along the SWNT axis.

present case, orthogonal orientation of the rods and CNTs suggests that most of the PE oligomers are parallel to the CNT surface. As discussed previously, since the HiPco SWNT was used in this study and a variety of chiral configurations exists in these SWNTs (82,83), the uniform PE orientation suggests that epitaxy is not the determining factor for PE orientation. This might also be due to the small diameter of the SWNTs: as the diameter of the CNTs is small, there are two factors that determine the orientation of the PE chain: epitaxy and geometry effect. Epitaxy requires a $\langle 001 \rangle_{PE} // \langle 2\text{–}1\text{–}10 \rangle_{graphite}$ orientation. For CNTs with different chirality, following strict epitaxy, PE chain should have different orientations (parallel or oblique to the tube axis). However, since SWNT possesses an extremely small diameter and the tube surface is thus curvy, geometry effect requires the PE chain to be parallel to the SWNT axis disregarding the SWNT chirality (84). Observation of the exclusive orthogonal orientation between SWNT and PE rods suggests that geometry effect plays the major role in determining PE chain orientation. Since

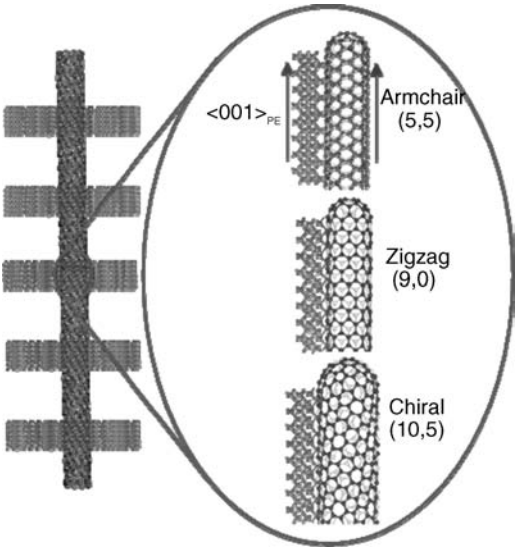

Figure 18.9 (**a**) Schematic representation of the 2D NHSK. A SWNT forms the central stem (shish). PE forms elongated, extended chain single crystals. PE chain axes are perpendicular to the PE rod crystals, while they are also parallel to the SWNT axis. (**b**, **c**, and **d**) The PE chain orientation on CNTs with different chirality. Irreepective of whether the CNT possess an armchair (**b**), a zigzag (**c**), or a chiral configuration, PE chains are always parallel to the CNT axis, suggesting a soft epitaxy growth mechanism.

strict lattice matching is not required, we name this growth mechanism as soft epitaxy. Figure 18.9 shows the schematics of the 2D NHSK structure. In armchair, zigzag, and chiral SWNTs, $\langle 001 \rangle_{PE}$ or PE chain orientation is always parallel to the SWNT axis.

Since the rods in 2D NHSK are PE oligomer crystals, two steps might be involved in the 2D NHSK formation process. In the first step, decomposed PE oligomers ($M_W \sim 1300\,g\,mol^{-1}$) deposit on the solid surface, forming a thin layer on the substrate. During this step, PE oligomers uniformly coat on the substrate regardless of the surface chemistry. In the second step, these oligomers self-organize to form single crystals. If the substrate is amorphous carbon, random orientation of PE crystals is formed. In the CNT case, however, CNT could serve as the nucleation sites. Nuclei formed on CNT and PE oligomers diffuse/crystallize upon these nuclei. The orientation of the nuclei dictates the final orthogonal orientation between PE rods and the CNT axis. Hence, the second step clearly involves surface diffusion and crystallization. In order to prove this two-step formation hypothesis, we design an experiment to decouple these two steps by using a lacey carbon grid as the substrate to conduct the PVD experiment. A lacey carbon grid consists of a ''broken'' amorphous carbon film with numerous ''holes'' (~3–5 μm) to allow high resolution TEM (HRTEM) observation. By decorating PE on CNT coated lacey carbon grids, since some of the CNTs dangle on the ''holes'' and thus are detached from the solid surface, PE oligomers cannot diffuse onto these CNTs to further grow into single

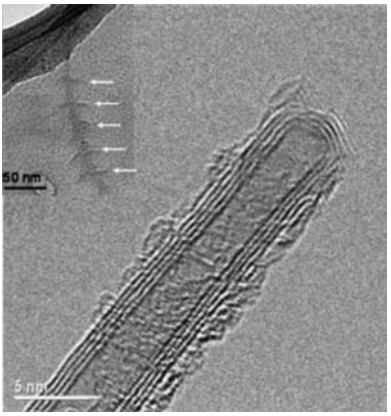

Figure 18.10 A HRTEM image of a PE decorated AD-MWNT. The MWNT was located in the hole region of a lacey carbon grid. This image captured the intermediate state of the PE decoration process. A thin layer of PE molecules were deposited on the MWNT surface. PE crystals did not grow on the CNT since the MWNT was detached from the substrate; diffusion of PE oligomers onto the CNT surface was thus prohibited. Inset shows a TEM image of a PE decorated AD-MWNT on the continuous carbon film area. White arrows indicate PE crystals.

crystals. Therefore, for all the CNTs dangling on the ''holes'' of lacey carbon grids, 2D NHSK should not form. Indeed, 2D NHSK was not observed in the ''hole'' region of the grids, and Fig. 18.10 shows an HRTEM image of such a MWNT. Three layers of the graphene sheets form the MWNT wall and a layer of PE coating can be clearly seen, as indicated by the arrows, on the MWNT surface. The PE coating appears to be continuous and has an average thickness of about ~1–2 nm. This continuous PE coating appears to be formed at the very beginning of this PVD process (step 1). Since CNTs are detached from the substrate, PE oligomers could not diffuse and further grow on the CNT surface. The PE oligomers already absorbed on the CNTs in step 1 also could not diffuse away from the CNT surface. The present image therefore captured the intermediate state of the 2D NHSK formation process. On the continuous carbon film area of this grid, the second step is allowed; hence, 2D NHSK structures were formed (inset of Fig. 18.10). The two-step formation mechanism can therefore be confirmed.

18.3.3 PE/CNT Nanocomposites

SWNTs and MWNTs have been used to prepare polymer nanocomposites with attractive properties using minimum concentration of CNTs in the polymer matrix. Despite the various attempts by researchers, a major challenge to the development of polymer/CNT nanocomposites is that CNTs are organized in bundles or agglomerates, making it difficult to disperse into individual tubes and in most polymeric matrices. Methods to modify CNT surface to overcome the tube–tube interaction and render them more compatible with polymers have been developed (85–92), and several processing techniques of polymer nanocomposite processing that aim at

obtaining homogeneous dispersion of CNTs in polymer matrices have been reported (60,61,93–97). These are as follows:

1. Melt mixing of CNTs and polymers (61,93,94).
2. Solution blending of CNTs with dissolved polymers (60,92,95,96).
3. *In situ* polymerization of monomer and CNTs (98,99).

The melt-mixing process makes use of high processing temperatures and shear forces in an extruder or compounder to mix and disperse the CNTs within the polymer resin. The solution processing technique involves the dispersion of the CNTs in a suitable solvent by ultrasonication followed by mixing with the polymer solution and casting or precipitating process to form the nanocomposite. For the *in situ* polymerization process CNTs are initially dispersed in solvents in the presence of surfactants prior to polymerization with the monomer.

Solution blending of polymers and CNTs has been employed in our study since it should provide better CNT exfoliation compared to the melt-blending method. Two types of precursors were utilized: pristine CNTs and PE single-crystal decorated CNTs (PE NHSK), leading to CP-PCN (CP denotes co precipitate) and N-PCN (N stands for NHSK) samples, respectively. Figure 18.11 shows PLM micrographs of

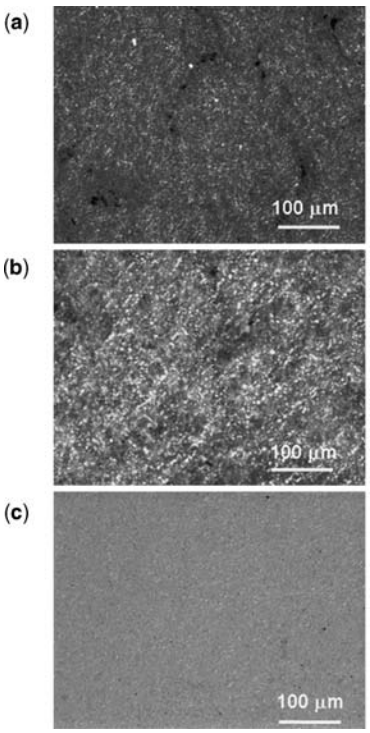

Figure 18.11 PLM of PE/CNT PCNs (**a**) 0.5% SWNT CP-PCN, (**b**) 0.25% SWNT N-PCN, and (**c**) 0.25% MWNT N-PCN.

the CP-PCN and N-PCN from both SWNTs and MWNTs. The samples were sandwiched between two glass slides, melt pressed at 190°C, and then quenched to 110°C for observation. It is evident that (1) CNTs were uniformly dispersed in the PE matrix and large size agglomeration was absent, indicating that solution blending leads to better CNT dispersion compared to melt blending. (2) PE spherulites were not observed in all cases, a common case in crystalline PCN since CNTs (or other inorganic fillers such as nanoclay) prevent PE from growing into large size spherulites. The crystalline nature of the PCN is, however, evident by the strong overall birefringence. The detailed morphology of the PCN is revealed by SEM micrographs shown in Fig. 18.12. Note that these samples were not melt pressed. Figure 18.11a shows the CP-PCN sample. Rounded PE aggregates can be clearly seen, which is due to the precipitation/phase separation process. The surface of the PE spheres is rough; small lamellae were formed within the precipitated spheres. The lamellae are relatively densely packed in each sphere. The average size of the spheres is ~2–3 μ. It should be noted that these spheres are similar to the PE "globs" observed by Garber and Geil by rapid quenching of 0.05% of PE (Marlex 6050) in xylene to temperature of 86 and 70°C. These authors suggested that the formation of the globs

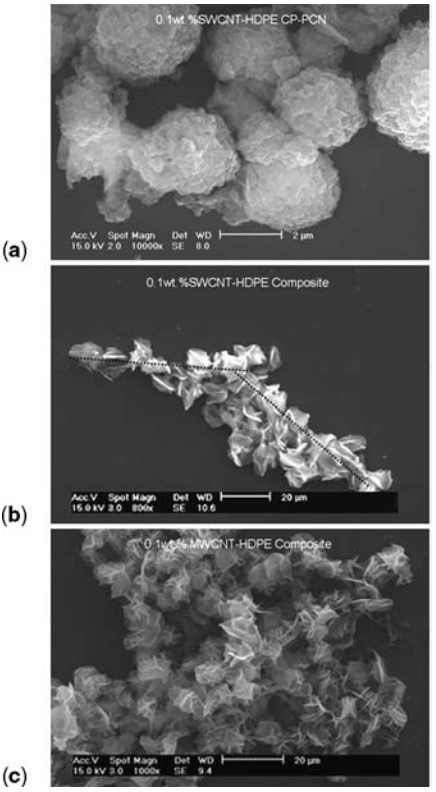

Figure 18.12 SEM of PE/CNT PCNs (**a**) 0.1% SWNT CP-PCN, (**b**) 0.1% SWNT N-PCN, and (**c**) 0.1% MWNT N-PCN.

was due to the phase separation occurred during the quenching process (100). In the present case, CNTs are not evident in the micrograph, indicating that the fast precipitation kinetics leads to rapid phase separation of PE from the solution. Microspheres were formed and CNTs might be buried inside the PE spheres. Figure 18.12b and c shows the N-PCN samples of 0.1% CNT content. Figure 18.12b is from SWNT sample, while Fig. 18.12c shows MWNT PCN. The morphology is clearly different from CP-PCN. CNTs are wrapped with a layer of PE single crystals. Although CNTs cannot be directly seen, it is evident that in N-PCNs, PE lamellae were formed on CNTs and the dotted lines in Fig. 18.12b represent the orientation of the CNTs. Prominent PE single-crystal lamellae can be seen perpendicular/oblique to the CNT axis. Figure 18.12b and c could thus be viewed as the overgrowth from NHSK.

Nonisothermal crystallization behaviors of PE and PE/CNT PCN were studied using DSC. PE, CP-PCNs, and N-PCNs were cooled from 200 to 30°C at 10°C min^{-1} and heated up at the same rate; the results are presented in Fig. 18.13 and the values (T_{on}, T_{peak}, ΔH_f, and crystallinity) are listed in Tables 18.2 and 18.3. The cooling curves show that pure PE crystallized at 110.8°C and the inclusion of SWNT did not significantly change the crystallization temperature (T_c). The 1.0 wt% composite increased the onset of crystallization by about 3°C. The increase of T_c is attributed to the heterogeneous nucleation induced by CNTs. The corresponding heat release during crystallization was reduced by 11 J g^{-1}, corresponding to a reduction in percentage crystallinity of about 4%. Figure 18.13b shows the second heating curve. Pure PE undergoes crystal melting at 125°C; it was observed that the melting points of the composites did not change much and were recorded as 125.2, 127.4, 127.7, and 126.2°C, respectively, corresponding to the 0.1, 0.25, 0.5, and 1.0 wt% samples. The corresponding heat of fusion that depends on the crystallinity was recorded as 176.2 J g^{-1} for PE and 173.0, 173.2, 174.6, and 169.3 J g^{-1} for the 0.1, 0.25, 0.5, and 1.0 wt% PCNs. The observed reduction in percentage crystallinity is different

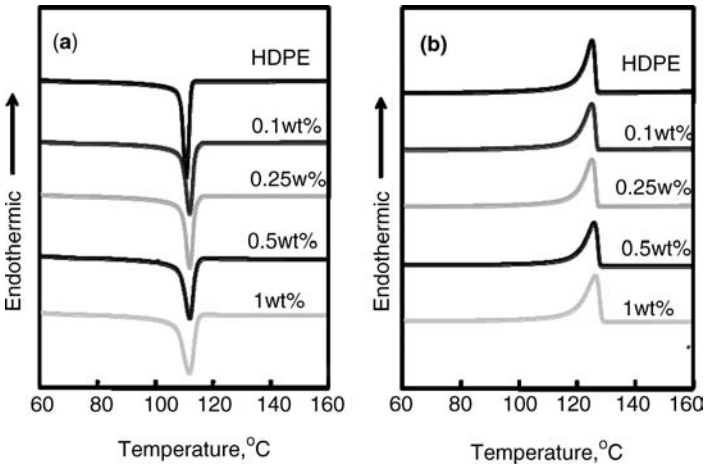

Figure 18.13 DSC thermograms of PE/CNT N-PCNs (**a**) first cooling and (**b**) second heating.

Table 18.2 DSC Data of PE CP-PCNs.

Sample	Cycle	T_{on}, °C	T_{peak}, °C	Heat of fusion ($\bullet H$), J g^{-1}	Crystallinity, %
PE	First heating	116.6	123.0	203.5	69.0
	Cooling	112.5	110.8	157.5	54.0
	Second heating	120.2	125.2	176.2	60.0
0.1 wt% SWCNT–PE	First heating	116.6	124.3	189.2	64.4
	Cooling	112.6	109.1	151.1	55.6
	Second heating	121.0	125.2	173.0	59.1
0.25 wt% SWCNT–PE	First heating	119.7	127.4	173.3	59.1
	Cooling	114.7	112.0	151.4	51.5
	Second heating	119.7	127.4	173.2	59.1
0.5 wt% SWCNT–PE	First heating	121.5	127.7	186.9	63.3
	Cooling	113.2	110.1	155.2	55.4
	Second heating	120.6	127.7	174.5	59.3
1 wt% SWCNT–PE	First heating	120.4	127.2	170.6	58.0
	Cooling	115.2	112.6	148.1	50.5
	Second heating	117.9	126.2	169.3	57.6

from that of some of the reported data, in which case, an increase in polymer crystallinity was claimed by adding CNTs (28). In the present case, we suggest that the reduction of the crystallinity is because the CNTs can break the continuity of the polymer matrix and large, uniform lamellae cannot be formed, as evidenced in Fig. 18.12. More grain boundaries as well as defects are formed in the case of PCNs, leading to the crystallinity reduction. From the DSC data, it should also be noted that the PE sample used might contain small amount of branches per chain since the melting temperature as well as the crystallinity are relatively low compared to linear PE.

For the N-PCN samples that were prepared from PE-NHSK, similar T_c and T_m were observed. One noticeable difference is that the heat of fusion of the first heating is much higher compared to the second heating, while the T_m is lower. This could be attributed to the fact that the first heating curve shows the melting of solution crystallized/precipitated samples, while the second heating curve shows the melting of nonisothermal meltcrystallized samples. Compared to melt crystallization, solution crystallization/precipitation occurred in a more dilute environment, leading to more complete crystallization (thus higher ΔH_f). Most of the crystals in solution crystallized/precipitated samples, however, were formed

Table 18.3 DSC Data of PE N-PCNs.

Sample	Cycle	T_{on}, °C	T_{peak}, °C	Heat of fusion ($\bullet H$), J g^{-1}	Crystallinity, %
PE	First heating	116.6	123	203.5	69
	Cooling	112.5	110.8	157.5	54
	Second heating	120.2	125.2	176.2	60
0.1 wt% SWNT–PE	First heating	113.9	121.5	206.5	70.1
	Cooling	114.0	112.0	157.4	54.1
	Second heating	119.2	125.0	175.8	60.1
0.25 wt% SWNT–PE	First heating	115.9	121.2	207.5	70.2
	Cooling	115.0	112.0	157.2	53.3
	Second heating	119.3	125.2	176.6	60.2
0.5 wt% SWNT–PE	First heating	117.0	122.8	206.0	70.4
	Cooling	114.3	112.1	155.9	53.3
	Second heating	119.7	125.9	175.2	60.0
1 wt% SWNT–PE	First heating	118.9	127.8	181.2	61.6
	Cooling	114.7	112.0	153.6	52.5
	Second heating	119.2	126.4	174.5	59.4

during precipitation or crystallization at 80°C. T_c is relatively low compared to nonisothermal melt crystallization; a relatively lower T_m was thus observed in the first heating curves. Note that the differences tend to diminish as the CNT contents increase, possibly due to the fact that CNT network provides nano confinement effect (T_m increases with increasing CNT contents, while crystallinity decreases with increasing CNT contents).

Compared to CP-PCN, there were no significant changes in crystallization and melting temperatures in the case of N-PCN except that a slightly lower impact on crystallinity was observed with increasing SWNT. This is probably due to the more open morphology of the PE/CNT hybrid structure as shown in Fig. 18.12. Since the lamellae in the NHSK PCNs are perpendicular/oblique to the CNT axis, this open structure leads to more free space for PE crystal growth and the crystallinity reduction due to the CNT confinement was therefore limited.

Isothermal crystallization was also carried out, and Fig. 18.14 shows the isothermal crystallization of PE and PCNs at 115°C and the plots of $t_{1/2}$ with respect to CNT content. It is evident that crystallization occurred at a much faster rate, for both CP-PCN and N-PCN. $t_{1/2}$ decreased dramatically, from 233 to 69 s for CP-PCN and 77 s for N-PCN sample. Again, the slightly higher $t_{1/2}$ of N-PCN compared to

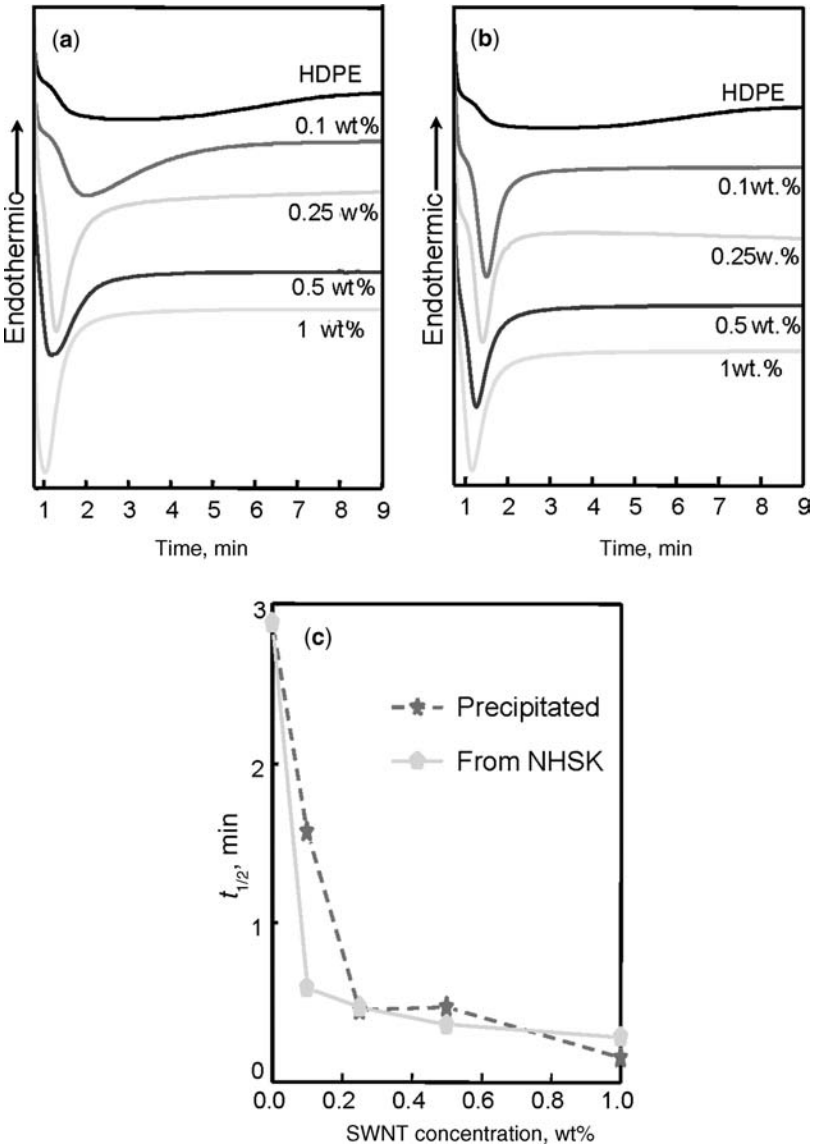

Figure 18.14 Isothermal crystallization at 115°C (**a**) CP-PCNs and (**b**) N-PCNs. (**c**) The plot of $t_{1/2}$ with respect to SWNT contents.

that of CP-PCN might be due to the open structure of N-PCN. Interestingly, the Avrami exponent n does not change much for the CP-PCN, while it increases slightly for N-PCN (1.59 for PE, 1.55 for 1% CP-PCN, and 1.78 for 1% N-PCN), indicating that the growth dimension of the PE crystal was not significantly affected by CNTs. Comparing the isothermal curve shapes, one can immediately tell that the pure PE

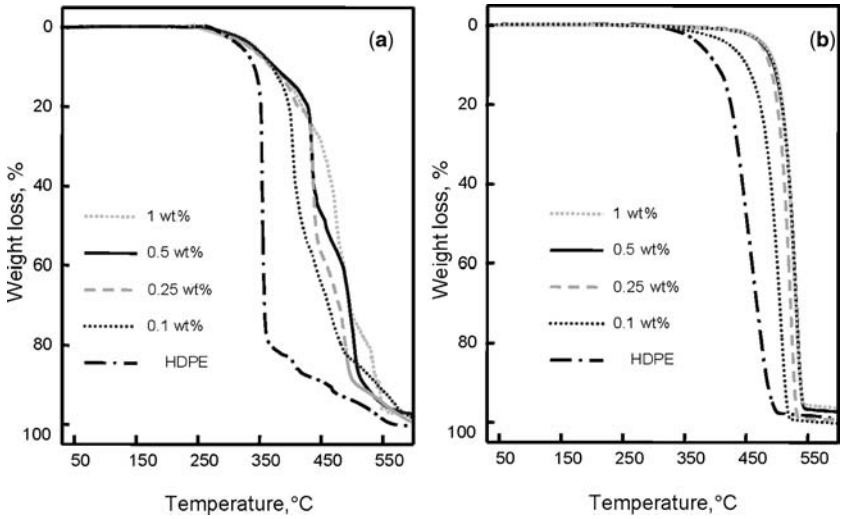

Figure 18.15 TGA of CP-PCNs in (**a**) air and (**b**) N_2.

curve is very broad, indicating multiple crystallization behavior, possibly due to the high polydispersity as well as the nonlinearity of the sample. The isothermal curve of the PCNs, however, is much narrower and uniform, suggesting that the heterogeneous nucleation is the overwhelming crystallization mechanism, and crystallization occurred at the same time, leading to the narrow distribution of the isotherm curve. Another feature of the isothermal crystallization is that the crystallinity of the PCNs is lower than that of the pure PE, suggesting again that the CNT network has dramatically hindered the crystal growth.

The degradation of pure PE as well as composites was analyzed in air and N_2 atmosphere. TGA curves of PE and CP-PCN specimens in air and N_2 are shown in Fig. 18.15, while the N-PCNs sample in air and N_2 are depicted in Fig. 18.16. In air, PE maintained a constant weight till about 240°C, and 346.9°C was recorded as the onset of maximum weight loss (T_{on}). The differential curves showed a single peak at 350.8°C which can be correlated to the temperature of maximum weight loss (T_{max}) of the neat polymer (not shown). The temperature of 5% sample weight loss ($T_{5\%}$) was found to be ~315.6°C. In N_2, the T_{on}, $T_{5\%}$, and T_{max} were found to be at 405.8, 369.0, and 446.9°C, respectively, which is much higher than that recorded in air atmosphere. At temperatures above 490°C, PE had completely degraded and the weight of the residue remained constant. For both CP-PCNs and N-PCN samples, in air or N_2, it is evident that the T_{on}, $T_{5\%}$, and T_{max} have been dramatically increased. Figure 18.17 shows the plots of T_{on}, $T_{5\%}$, and T_{max} with respect to the CNT contents for CP-PCN and N-PCN in N_2 and air. All three temperatures were dramatically increased with small amount of CNT, and they then tended to reach a plateau. In air, the T_{max} was increased by ~115°C for the

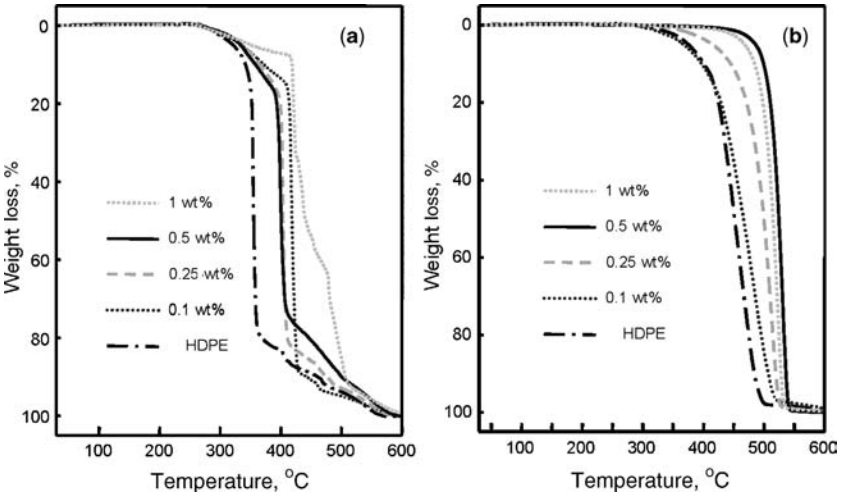

Figure 18.16 TGA of N-PCNs in (**a**) air and (**b**) N_2.

CP-PCN, while the increase was ~65°C for N-PCN. For all the samples in air atmosphere, the differential curves of the decomposition process showed several peaks, indicating that the degradation process involves a multistaged process of separate chemical reactions as a result of carbon–oxygen bond formation and

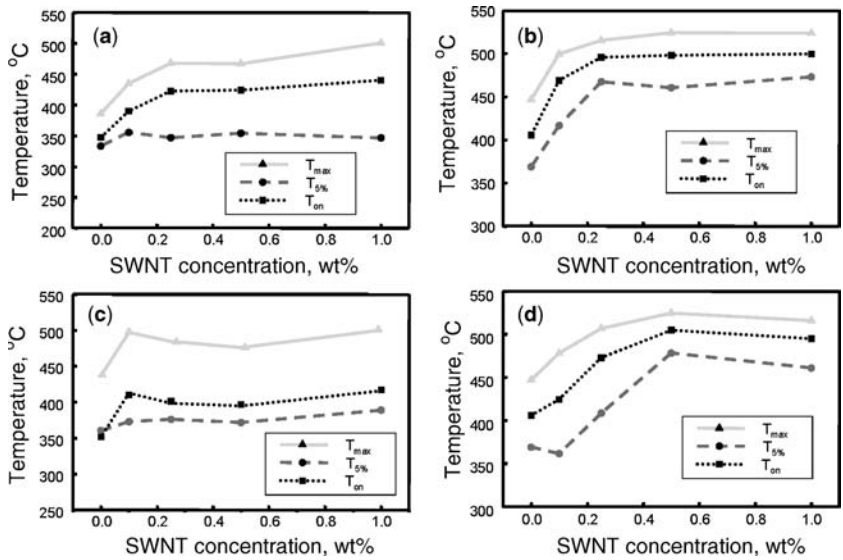

Figure 18.17 T_{on}, $T_{5\%}$, and T_{max} versus CNT contents for CP-PCNs in (**a**) air (**b**) N_2, and for N-PCNs in (**c**) air and (**d**) N_2.

subsequent decomposition of the bonds at higher temperatures to form carbon monoxide and carbon dioxide. Regardless of this multistage process, ~65–115°C increase in the degradation temperature is evident. Single peaks were found for the derivatives of the TGA curves for the PCNs in N_2 (not shown). With the increasing CNT contents, the degradation temperature shifted to higher end for both CP-PCN and N-PCN. As much as 70°C increase has been achieved for both samples in N_2 atmosphere.

It is known that the thermal degradation of PE occurs by random chain scission to form radicals of alkyl and alkyl peroxyl that are susceptible to inhibition reagents capable of trapping the radicals. CNTs have high electron affinities similar to C_{60} and have been as such proposed to act as scavengers of free radicals (101). By incorporating CNTs in polymers, the thermal stability of polymers could be enhanced. Watts et al. recently reported ~18°C increase in the degradation temperature of PE in N_2 at a much higher CNT content (~14% CNT) (101). In the present case, as high as 70°C improvements were achieved. The difference could be attributed to two factors: (1) MWNT was used in Watts' study, while SWNT has been used in our case and (2) melt blending was used in the previous study and solution blending technique was used in our case. In order to further confirm which is the major reason for the thermal stability enhancement, MWNT was also used. It has been found that for 0.25% MWNT/PE N-PCN in N_2, a T_{max} of 505°C has been achieved, indicating a ~59°C increase, which is much higher than the previously reported 18°C improvement. Therefore, more complete CNT exfoliation might hold the key to the present observation of the high PCN thermal stability.

Solution-blending technique ensures more complete CNT exfoliation and less CNT bundle formation in the PCNs. The radical scavenging efficiency can therefore be dramatically enhanced at very low CNT content. Figure 18.17 indicates that T_{on}, $T_{5\%}$, and T_{max} increases dramatically as small amount of CNT is added. The temperatures then reached a plateau. This indicates that the percolative network of CNTs was achieved and further increase in CNTs therefore did not alter the degradation behavior significantly. The threshold CNT content is ~0.2%, a very low value due to the high CNT aspect ratio.

It should be noted that T_{on}, $T_{5\%}$, and T_{max} of coprecipitated CP-PCN samples are slightly higher than that of the N-PCNs from NHSK (difference of few degrees). This could be attributed to two possible reasons: (1) Since the CP-PCN were prepared immediately after sonication, CNTs might be dispersed more uniformly, while in N-PCNs, 0.5–1 h crystallization time was allowed, which might result in certain CNT agglomeration. (2) It is evident that N-PCNs possess a more ''open'' morphology and PE therefore is not as intimately contacted with CNT as in CP-PCN. The radical scavenging efficiency might be relatively low, which could lead to a slightly lower degradation temperature. It is therefore again clear that uniform dispersion of SWNT holds the key to the thermal property enhancement, and we are currently investigating the use of other solvents (such as 1,2 dichlorobenzene, which is a better solvent for SWNT) to achieve better CNT exfoliation. Even higher degradation temperature of PE PCN is envisaged.

18.4 CONCLUSIONS

In conclusion, we have demonstrated that controlled polymer solution crystallization can be used to synthesize polymer single crystal–CNT hybrid materials. Lamellar crystals were formed, periodically spaced along entire CNTs. Novel NHSK structure was observed. A variety of CNTs and PE were used for NHSK formation. The formation mechanism of the NHSK was attributed to a ''size dependent soft epitaxy.'' For small diameter CNTs, geometric confinement dictates the polymer chain orientation in the kebabs and exclusively orthogonal orientation between lamellar surface and CNT axis was observed. As the diameter increases, normal epitaxy growth plays a major role and multiple orientations of PE lamellae were observed. PE/SWNT PCNs were prepared using solution-blending technique. Both pristine SWNT and the unique NHSKs were used as precursors for PCN preparation. Uniform SWNT dispersion was achieved in both cases. SEM shows that CP-PCNs from the pristine SWNT possess denser structures, while in N-PCNs from NHSK precursors, single-crystal lamellae are perpendicular/oblique to the CNT axis, creating an ''open'' space in the PCNs. A slight increase observed in the crystallization temperatures and a decrease in the $t_{1/2}$ in isothermal crystallization both suggest that CNTs initiated PE crystallization. Thermal stability of PE was dramatically enhanced, and as much as 115°C increases in T_{max} were achieved. The thermal stability enhancement was attributed to the formation of the radical scavenging SWNT network.

ACKNOWLEDGMENT

This work was supported by the NSF CAREER award (DMR-0239415), NSF DMI-0508407, 3M and DuPont.

NOMENCLATURE

AFM	Atomic force microscopy
CF	Carbon fibers
CNF	Carbon nanofibers
CNT	Carbon nanotube
CP–PCNs	Polymer/CNT nanocomposites prepared by coprecipitate method
CVD	Chemical vapor deposition
DCB	Dichlorobenzene
DSC	Differential scanning calorimetry
NHSK	Nanohybrid shish-kebab
HiPCO	High pressure CO conversion
HRTEM	High resolution transmission electron microscope
iPP	Isotactic polypropylene
MCNF	Modified carbon nanofibers
MFI	Melt flow index

MW	Molecular weight
MWNT	Multiwalled carbon nanotube
N–PCNs	Polymer/CNT nanocomposites prepared by using NHSK
PAN	Polyacrylonitrile
PCCF	Polymer crystallization driven CNT functionalization
PCN	Polymer/CNT nanocomposites
PE	Polyethylene
PLM	Polarized light microscope
PVA	Polyvinyl alcohol
PVD	Physical vapor deposition
SEM	Scanning electron microscope
STM	Scanning tunneling microscopy
SWNT	Single-walled carbon nanotube
TEM	Transmission electron microscope
TGA	Thermogravimetric analysis
WAXD	Wide-angle X-ray diffraction
$t_{1/2}$	Half-time of crystallization
T_c	Crystallization temperature
T_m	Melting temperature
T_{max}	Temperature of maximum weight loss
T_{on}	Onset temperature
T_{peak}	Peak temperature
$T_{5\%}$	Temperature of 5% sample weight loss
1D	One dimensional
2D	Two dimensional
3D	Three dimensional
ΔH_f	Heat of fusion

REFERENCES

1. S. Iijima, *Nature*, **354**, 56–58. (1991).
2. P. J. Harris, *Carbon Nanotubes and Related Structures*, Cambridge University Press, Cambridge, 1999.
3. T. W. Odom, J. L. Huang, and C. M. Lieber, *Nature*, **391**, 62 (1998).
4. R. Saito, G. Dresselhaus, and M. S. Dresselhaus, *Physical Properties of Carbon Nanotubes*, London and Imperial College Press, London, 1998.
5. A. Noy, C. H. Sanders, D. V. Vezenov, S. S. Wong, and C. M. Lieber, *Langmuir*, **14**, 1508 (1998).
6. S. S. Wong, J. D. Harper, P. T. J. Lansbury, and C. M. Lieber, *J. Am. Chem. Soc.*, **120**, 603 (1998).
7. B. Gao, A. Kleinhammes, X. P. Tang, C. Bower, L. Fleming, Y. Wu, and O. Zhou, *Chem. Phys. Lett.*, **307**, 153 (1999).
8. E. Frackowiak, S. Gautier, H. Gaucher, S. Bonnamy, and F. Beguin, *Carbon*, **37**, 61 (1999).
9. M. R. Pederson and J. Q. Broughton, *Phys. Rev. Lett.*, **69**, 2689 (1992).
10. P. M. Ajayan and O. Z. Zhou, *Top. Appl. Phys.*, **80**, 391 (2001).
11. D. H. Robertson, D. W. Brenner, and J. W. Mintmire, *Phys. Rev. B*, **45**, 12592 (1992)

12. M. M. J. Treacy, T. W. Ebbesen, and J. M. Gilson, *Nature*, **381**, 678 (1996).
13. A. Krishnan, E. Dujardin, T. W. Ebbesen, P. N. Yianilos, and M. M. J. Treacy, *Phys. Rev. B*, **58**, 14013 (1998).
14. E. W. Wong, P. E. Sheedan, and C. M. Lieber, *Science*, **277**, 1971 (1997).
15. M. F. Yu, O. Lourie, M. J. Dyer, K. Moloni, and R. S. Ruoff, *Science*, **287**, 637 (2000).
16. M. R. Falvo, *Nature*, **389**, 582 (1997).
17. Y. Maniwa and H. Suematsu, *Phys. Rev. B*, **64**, 241402 (2001).
18. P. Kim, L. Shi, and P. L. McEuen, *Phys. Rev. Lett.*, **87**, 215502 (2001).
19. J. Hone, M. Whitney, and A. Zettle, *Synth. Met.*, **103**, 2498 (2003).
20. J. C. Charlier, T. W. Ebbesen, and P. Lambin, *Phys. Rev. B*, **53**, 11108 (1996).
21. T. W. Ebbesen, H. J. Lezec, H. Hiura, J. W. Bennett, H. F. Ghaemi, and T. Thio, *Nature*, **382**, 54 (1996).
22. S. J. Tans, M. H. Devoret, M. H. Dai, A. Thess, R. E. Smalley, J. Geerligs, and C. Dekker, *Nature*, **386**, 474 (1997).
23. R. Martel, T. Schmidt, H. R. Shea, T. Hertel, and P. Avouris, *Appl. Phys. Lett.*, **73**, 2447 (1998).
24. A. Y. Kasumov, R. Deblock, M. Kociak, B. Reulet, H. B. Ouchiat, I. I. Khodos, Y. B. Gorbatov, V. T. Volkov, C. Journet, and M. Burghard, *Science*, **284**, 1508 (1999).
25. A. G. Rinzler, J. H. Hafner, P. Nikolaev, L. Lou, S. G. Kim, D. Tománek, P. Nordlander, D. T. Colbert, and R. E. Smalley, *Science*, **269**, 1550 (1995).
26. P. M. Ajayan, O. Stephan, C. Colliex, and D. Trauth, *Science*, **265**, 1212 (1994).
27. R. H. Baughman, A. A. Zakhidov, and W. A. de Heer, *Science*, **297**, 787 (2002).
28. A. Allaoui, S. Bai, H. M. Cheng, and J. B. Bai, *Compos. Sci. Technol*, **62**, 1993 (2002).
29. Z. Jin, K. P. Pramoda, G. Xu, and S. H. Goh, *Chem. Phys. Lett.*, **337**, 43 (2001).
30. B. M. Besancon and P. F. Green, *Macromolecules*, **38**, 110 (2005).
31. Y. Sabba and E. L. Thomas, *Macromolecules*, **37**, 4815 (2004).
32. D. E. Hill, Y. Lin, A. M. Rao, L. F. Allard, and Y. P. Sun *Macromolecules*, **35**, 9466 (2002).
33. T. Kashiwagi, F. M. Du, K. I. Winey, K. A. Groth, J. R. Shields, S. P. Bellayer, H. Kim, and J. F. Douglas, *Polymer*, **46**, 471 (2005).
34. F. M. Du, R. C. Scogna, W. Zhou, S. Brand, J. E. Fischer, and K. I. Winey, *Macromolecules*, **37**, 9048 (2004).
35. F. M. Du, J. E. Fischer, and K. I.Winey, *J. Polym. Sci. Polym. Phys.*, **41**, 3333 (2003).
36. R. Haggenmueller, H. H. Gommans, A. G. Rinzler, J. E. Fischer, and K. I.Winey, *Chem. Phys. Lett.*, **330**, 219 (2000).
37. S. Kumar, T. D. Dang, F. E. Arnold, A. R. Bhattacharyya, B. G. Min, X. F. Zhang, R. A. Vaia, C. Park, W. W. Adams, R. H. Hauge, R. E. Smalley, S. Ramesh, and P. A. Willis, *Macromolecules*, **35**, 9039 (2002).
38. G. Pecastaings, P. Delhaes, A. Derre, H. Saadaoui, F. Carmona, and S. Cui, *J. Nanosci. Nanotechnol.*, **4**, 838 (2004).
39. A. Eitan, K. Y. Jiang, D. Dukes, R. Andrews, and L. S. Schadler, *Chem. Mater.*, **15**, 3198 (2003).
40. X. J. Xu, M. M. Thwe, C. Shearwood, and K. Liao, *Appl. Phys. Lett.*, **81**, 2833 (2002).
41. G. Z. Chen, M. S. P. Shaffer, D. Coleby, G. Dixon, W. Z. Zhou, D. J. Fray, and A. H. Windle, *Adv. Mater.*, **12**, 522 (2000).
42. J. H. Chen, W. Z. Li, D. Z. Wang, S. X. Yang, J. G. Wen, and Z. F. Ren, *Carbon*, **40**, 1193 (2002).
43. X. T. Zhang, J. Zhang, R. M. Wang, and Z. F. Liu, *Carbon*, **42**, 1455 (2004).
44. X. T. Zhang, J. Zhang, R. M. Wang, T. Zhu, and Z. F. Liu, *Chem. Phys. Chem.*, **5**, 998 (2004).
45. T. E. Chang, L. R. Jensen, A. Kisliuk, R. B. Pipes, R. Pyrz, and A. P. Sokolov, *Polymer*, **46**, 439 (2005).

46. B. P. Grady, F. Pompeo, R. L. Shambaugh, and D. E. Resasco, *J. Phys. Chem. B*, **106**, 5852 (2002).
47. A. Kelarakis, K. W. Yoon, I. Sics, R. H. Somani, B. S. Hsiao, and B. Chu, *Polymer*, **46**, 5103 (2005).
48. E. Assouline, A. Lustiger, A. H. Barber, C. A. Cooper, E. Klein, E. Wachtel, and H. D. Wagner, *J. Polym. Sci. Polym. Phys.*, **41**, 520 (2003).
49. A. R. Bhattacharyya, T. V. Sreekumar, T. Liu, S. Kumar, L. M. Ericson, R. H. Hauge, and R. E. Smalley, *Polymer*, **44**, 2373 (2003).
50. R. Haggenmueller, W. Zhou, J. E. Fischer, and K. I. Winey, *J. Nanosci. Nanotechnol.*, **3**, 105 (2003).
51. M. S. P. Shaffer and A. H. Windle, *Adv. Mater.*, **11**, 937 (1999).
52. J. J. Ge, H. Q. Hou, Q. Li, M. J. Graham, A. Greiner, D. H. Reneker, F. W. Harris, and S. Z. D. Cheng, *J. Am. Chem. Soc.*, **126**, 15754 (2004).
53. H. H. Ye, H. Lam, N. Titchenal, Y. Gogotsi, and F. Ko, *Appl. Phys. Lett.*, **85**, 1775 (2004).
54. F. Ko, Y. Gogotsi, A. Ali, N. Naguib, H. H. Ye, G. L. Yang, C. Li, and P. Willis, *Adv. Mater.*, **15**, 1161 (2003).
55. V. E. Yudin, V. M. Svetlichnyi, A. N. Shumakov, D. G. Letenko, A. Y. Feldman, and G. Marom, *Macromol. Rapid Commun.*, **26**, 885 (2005).
56. K. P. Ryan, S. M. Lipson, A. Drury, M. Cadek, M. Ruether, S. M. O'Flaherty, V. Barron, B. McCarthy, H. J. Byrne, W. J. Blau, and J. N. Coleman, *Chem. Phys. Lett.*, **391**, 329 (2004).
57. H. Koerner, W. D. Liu, M. Alexander, P. Mirau, H. Dowty, and R. A. Vaia, *Polymer*, **46**, 4405 (2005).
58. J. W. Cho, J. W. Kim, Y. C. Jung, and N. S. Goo, *Macromol. Rapid Commun.*, **26**, 412 (2005).
59. H. Koerner, G. Price, N. A. Pearce, M. Alexander, and R. A. Vaia, *Nat. Mater.*, **3**, 115 (2004).
60. R. Haggenmueller, J. E. Fischer, and K. I. Winey, *Macromolecules*, **39**, 2964 (2006).
61. T. McNally, P. Potschke, P. Halley, M. Murphy, D. Martin, S. E. J. Bell, P. B. Brennan, D. Bein, P. Lemoine, and J. P. Quinn, *Polymer*, **46**, 8222 (2005).
62. D. M. Dean, L. Rebenfeld, R. A. Register, and B. S. Hsiao, *J. Mater. Sci.*, **33**, 4797 (1998).
63. F. Khoury, *Proc. SPE*, 1261 (1990).
64. N. Klein and G. Marom, *Compos Sci. Technol.*, **25**, 706 (1994).
65. M. Sano, D. Y. Sasaki, and T. Kunitake, *Science*, **258**, 441 (1992).
66. M. Sano, D. Y. Sasaki, S. Yoshimura, and T. Kunitake, *Faraday Discuss.*, **98**, 307 (1994).
67. P. H. Geil, in: *Polymer Single Crystals*, Robert E. Krieger Publisher, Juntington, NY, 1973.
68. A. J. Pennnings and A. M. Kiel, *Kolloid Z. Z. Polym.*, **205**, 160 (1965).
69. P. G. De Gennes, *J. Chem. Phys.*, **60**, 5030 (1970).
70. R. H. Somani, B. S. Hsiao, A. Nogales, H. Fruitwala, S. Srinivas, and A. H. Tsou, *Macromolecules*, **34**, 5902 (2001).
71. K. A. Worsley, K. R. Moonoosawmy, and P. Kruse, *Nano Lett.*, **4**, 1541 (2004).
72. M. Sano, D. Y. Sasaki, and T. Kunitake, *Science*, **258**, 441 (1992).
73. W. W. Cai, C. Y. Li, L. Y. Li, B. Lotz, M. N. Keating, and D. Marks, *Adv. Mater.*, **16**, 600 (2004).
74. P. J. Flory, *Principles of Polymer Chemistry*, Cornell University Press, Ithaca, 1953.
75. F. Tuinstra, E. Baer, *Polym. Lett.*, **8**, 861 (1970).
76. Y. Takenaka, H. Miyaji, A. Hoshino, A. Tracz, J. K. Jeszka, and I. Kucinska, *Macromolecules*, **37**, 9667 (2004).
77. L. Li, Y. Yang, G. Yang, X. M. Chen, B. S. Hsiao, B. Chu, J. E. Spanier, and C. Y. Li, *Nano Lett.*, **6**, 1007 (2006).
78. J. C. Wittmann and B. Lotz, *J. Polym. Sci. Polym. Phys. Ed.*, **23**, 205 (1985).
79. M. Satou, Y. Watanabe, and H. Hayashi, *J. Polym. Sci. A-2*, **10**, 835 (1972).
80. C. Y. Li, S. Z. D. Cheng, J. J. Ge, F. Bai, J. Z. Zhang, I. K. Mann, F. W. Harris, L. C. Chien, D. H. Yan, T. B. He, and B. Lotz, *Phys. Rev. Lett.*, **83**, 4558 (1999).

81. C. Y. Li, J. J. Ge, F. Bai, B. H. Calhoun, F. W. Harris, S. Z. D. Cheng, L. C. Chien, B. Lotz, and H. D. Keith, *Macromolecules*, **34**, 3634 (2001).
82. R. Saito, G. Dresselhaus, and M. S. Dresselhaus, *Physical Properties of Carbon Nanotubes*, Imperial College Press, London, 1998.
83. P. J. F. Harris, *Carbon Nanotubes and Related Structures*, Cambridge University Press, Cambridge, 1999.
84. L. Li, C. Y. Li, and C. Ni, *J. Am. Chem. Soc.*, **128**, 1692 (2006).
85. E. T. Mickelson, I. W. Chiang, J. L. Zimmerman, P. J. Boul, J. Lozano, R. E. Smalley, R. H. Hauge, and J. L. Margrave, *J. Phys. Chem. B*, **103**, 4318 (1999).
86. P. J. Boul, J. Liu, E. T. Mickelson, L. M. Ericson, I. W. Chiang, K. A. Smith, D. T. Colbert, R. H. Hauge, J. L. Margrave, and R. E. Smalley, *Chem. Phys. Lett.*, **310**, 367 (1999).
87. L. Feng, A. K. Sadana, P. Asghar, J. Chattopadhyay, G. Zhenning, R. H. Hauge, and W. E. Billups, *Nano Lett.*, **4**, 1257 (2004).
88. H. Hiura, T. W. Ebbesen, and K. Tanigaki, *Adv. Mater.*, **7**, 275 (1995).
89. M. Holzinger, J. P. Abraham, R. Whelan, and F. Hennrich, *J. Am. Chem. Soc.*, **125**, 8566 (2003).
90. M. Holzinger, J. Steinmetz, D. Samaille, M. Glerup, M. Paillet, and P. Bernier, *Carbon*, **42**, 941 (2004).
91. K. Kamaras, M. E. Itkis, H. Hu, and R. C. Haddon, *Science*, **301**, 1501 (2003).
92. C. Y. Li, L. Li, W. Cai, S. L. Kodjie, and K. Tenneti, *Adv. Mater.*, **17**, 1198 (2005).
93. A. R. Bhattacharyya, T. V. Sreekumar, T. Liu, S. Kumar, L. M. Ericson, R. H. Hauge, and R. E. Smalley, *Polymer*, **44**, 2373 (2003).
94. T. Liu, I. Y. Phang, L. Shen, S. Y. Chow, and W. D. Zhang, *Macromolecules*, **37**, 7214 (2004).
95. M. S. P. Shaffer and A. H. Windle, *Adv. Mater.*, **11**, 937 (1999).
96. E. Assouline, A. Lustiger, A. H. Barber, C. A. Cooper, E. Klein, E. Wachtel, and H. D. Wagner, *J. Polym. Sci. Polym. Phys.*, **41**, 520 (2003).
97. B. P. Grady, F. Pompeo, R. L. Shambaugh, and D. E. Resasco, *J. Phys. Chem. B*, **106**, 5852 (2002).
98. C. Park, Z. Ounaies, K. A. Watson, R. E. Crooks, J. Smith, S. E. Lowther, J. W. Connell, E. J. Siochi, J. S. Harrison, and T. L. Clair, *Chem. Phys. Lett.*, **364**, 303 (2002).
99. R. Haggenmueller, D. Faming, J. E. Fischer, and K. I. Winey, *Polymer*, **47**, 2381 (2006).
100. C. A. Garber and P. H. Geil, *Die Makromol. Chem.*, **98**, 304 (1966).
101. P. C. P. Watts, P. K. Fearon, W. K. Hsu, N. C. Billingham, H. W. Kroto, and D. R. M. Walton, *J. Mater. Chem.*, **13**, 491 (2003).

Chapter 19

Formation of Shish-Kebab Structures in Ultrahigh Molecular Weight Polyethylene (UHMWPE)/ Low Molecular Weight Polyethylene (LMWPE) Composites Under Shear Flow

Toshiji Kanaya,[1] Go Matsuba,[1] and Koji Nishida[1]

19.1 INTRODUCTION

Molten polymers are subjected to various kinds of flows and temperature histories during processing such as spinning, injection molding, and extrusion, and semicrystalline polymers crystallize during and/or after the flow and the properties are strongly influenced by the final crystalline structure (1–3). Therefore, extensive studies have been carried out on polymer crystallization under various flows such as shear flow and elongational flow both from scientific and industrial points of view

[1]Institute for Chemical Research, Kyoto University, Uji, Kyoto-fu 611-0011, Japan

Polyolefin Composites, Edited by Domasius Nwabunma and Thein Kyu

to elucidate the crystallization mechanism under flows (4). It is well known that the so-called shish-kebab structure is often formed when semicrystalline polymers are crystallized under flows, which consists of long central fiber core (shish) surrounded by lamellar crystalline structure (kebab) periodically attached along the shish, and it is believed that the shish-kebab structure is a structure origin of ultrahigh strength and ultrahigh modulus fibers (4–9). This is also one of the reasons why such many studies have been performed on polymer crystallization under flows. On the basis of recent development of advanced characterization techniques, extensive studies have been performed on polymer crystallization under various kinds of flows using time-resolved small-angle and wide-angle X-ray scattering (SAXS and WAXS) (10–20), time-resolved small-angle light scattering (SALS) (21–26), and optical measurements, (27–29) providing fruitful information on the formation mechanism of shish-kebab structure.

Among them some papers reported effects of high molecular weight (HMW) component or long chain on the crystallization under flow (20,30–34). Most of the results indicated that the presence of HMW component or long chain enhanced the crystallization in the rate and the orientation. Kornfield and coworkers (34) have studied the effects of the HMW component using model blends of HMW isotactic polypropyrene ($M_w = 923,000$) and low molecular weight (LMW) isotactic polypropyrene ($M_w = 186,000$), and found that the role of the HMW component in shear-induced crystallization is cooperative, enhanced by the entanglements among the long chains. Hsiao and coworkers (20) also demonstrated the role of the HMW component in blends of noncrystallizing low molecular weight polyethylenes ($M_w = 50,000$ and 100,000) and crystallizing HMW polyethylene (PE) ($M_w = 250,000$) using time-resolved SAXS and WAXS techniques. The results indicated that HMW component dominates the formation of crystallization of precursor structures in the blend under shear flow, and the viscosity of the matrix (LMW component) plays an important role in influencing the formation of crystallization precursor structure of the HMW component.

As for the size of shish-kebab structure it is not still fully understood. About 30 years ago, Keller and coworkers observed shish-kebab structure in polyethylene (PE) using transmission electron microscope (TEM) (7–9,35), showing shish of $\sim$10 nm in diameter and several microns in length. This has been assigned to extended chain crystal. However, in some polymers (22,26), large and long objects with diameter of several microns aligned along the flow direction are often observed using optical microscope (OM), even at very low shear rates (36). This long object is apparently similar to the shish structure but the spatial scale is very different. It must include the kebab inside, judging from the spatial scale. These observations suggest that shish-kebab has hierarchic structure in a wide spatial scale. However, few papers have dealt with the hierarchic structure of the shish-kebab structure. One of the reasons is the difficulty to study the shish-kebab structure in a wide spatial range simultaneously. In addition, kebab structure is overlapped on the shish structure so that it is not easy to distinguish the shish from the kebab.

In this work, therefore, we have investigated the crystallization process of composites or blends of ultra high molecular weight (UHMW) PE and LMW PE

under shear flow, focusing on the effects of UHMW PE using time-resolved depolarized light scattering (DPLS) and SAXS techniques in order to cover a wide spatial scale from 0.1 nm to several tens microns. We can observe large and long objects in micron scale aligned along the flow direction in DPLS measurements and the kebab formation or kebab spacing in SAXS measurements. In addition, we also employed small-angle neutron scattering (SANS) technique to see selectively the structure formed by the UHMW component.

19.2 EXPERIMENTAL

19.2.1 Materials

For DPLS and SAXS measurements, we used UHMW PEs with weight-average molecular weight $M_w = 2,000,000$ and polydispersity $M_w/M_n = 12$ and LMW PEs with $M_w = 58,600$ and $M_w/M_n = 8.01$, where M_n is number-average molecular weight. The nominal melting temperatures of the LMW and UHMW PEs determined by DSC measurements were 134 and 135°C, respectively, at a heating rate of 20°C min^{-1}. Two kinds of polyethylenes were blended in a solution to ensure the intimate mixing at the molecular level. The mixture of UHMW and LMW PEs with a given concentration of the UHMW PE (0.2–3 wt%) was dissolved in xylene with anitoxidant regent (2,6-*tert*-butyl-*p*-cresole) to form a homogeneous solution at 130°C under nitrogen atmosphere. After keeping the solution at 130°C for 1 h, it was quenched into ice water to precipitate as a gel, filtered from xylene and washed with methanol several times. The gel was vacuum-dried at 70°C for 2 days and then hot-pressed at 165°C for 5 min and quenched rapidly to ice water to get a thin film ~0.3 mm thick. The LMW PE film was prepared under the same procedure as a control sample.

For the SANS measurements, we used UHMW PE and LMW deuterated PE with $M_w = 200,000$ and $M_w/M_n = 5$, respectively. The UHMW PE is the same PE as in the DPLS and SAXS measurements. Strips of the blend film of UHMW hydrogenated PE (2.8 wt%) and LMW deuterated PE (97.2 wt%), which was prepared in the same procedure as the DPLS samples, were elongated about six times at 133°C just below the nominal melting temperature (= 135°C) and quenched into ice water. These elongated strips were aligned on a SANS cell window. It is noted that the quenching of the blends was done as rapidly as possible to avoid the segregation (37–39). However, in this work, we did not check the segregation directly.

19.2.2 DPLS Measurements

Two-dimensional (2D) DPLS measurements were carried out using a home-made apparatus with He–Ne laser (80 mW, wavelength $\lambda = 633$ nm) as a light source and a CCD camera with 2D screen as a detector system. The range of length of scattering vector Q in this experiment is 4×10^{-5} to 2.6×10^{-4} $Å^{-1}$, where Q is given by $Q = 4\pi \sin\theta/n\lambda$ (2θ and n being the scattering angle and the refractive index, respectively).

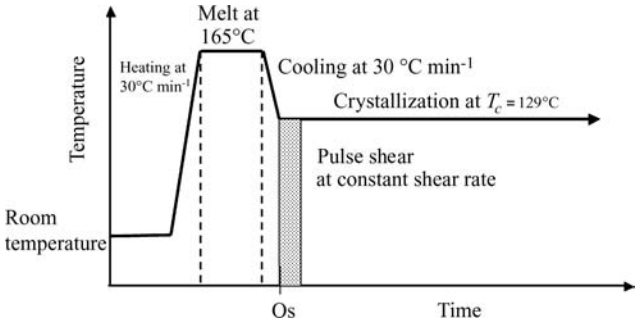

Figure 19.1 Temperature protocol for crystallization process of PE blend. (From Reference 25 with permission from Elsevier.)

A Linkam CSS-450 high temperature shear cell was used for the DPLS measurements to control the temperature and the shear conditions. The thin-film sample was placed between two quartz plates for the DPLS measurements, and the thickness was 0.3 mm for all the measurements. The temperature protocol for the DPLS experiments is shown in Fig. 19.1: (a) heat up the polymer sample from room temperature to 165°C at a rate of 30°C min^{-1}, (b) hold at 165°C for 5 min, (c) cool down to the crystallization temperature, $T_c = 129$°C at a rate of 30°C min^{-1}, and (d) hold the temperature at 129°C for the DPLS measurements. The polymer melt was subjected to pulse shear just after reaching the crystallization temperature T_c of 129°C.

19.2.3 SAXS Measurements

SAXS measurements were carried out using apparatus at the beam line BL45XU (40) in the synchrotron radiation facility, SPring-8, Nishiharima, and apparatus at the beam line BL-15A in Photon Factory, KEK, Tsukuba, and the incident wavelength was 0.9 and 1.54 Å, respectively. A CCD camera (C4880: Hamamatsu Photonics K.K.) with an image intensifier was used as a detector system for the SAXS measurements. In the measurements, we covered a Q range of 6×10^{-3} to 2×10^{-1} $Å^{-1}$. Here, Q is given by $Q = 4\pi \sin\theta/\lambda$. We also used U-SAXS machine with Bonse–Hart-type camera (TRY-HV) in a low Q range of 1×10^{-5} to 8×10^{-3} $Å^{-1}$.

A Linkam CSS-450 high temperature shear cell was also used for the SAXS measurements to control the temperature and the shear conditions. The thin film sample 0.3 mm thick was placed between two stainless plates with Kapton windows 50 μm thick. The temperature protocol was the same as in the DPLS measurements, but the pulse shear was applied at 30°C above the crystallization temperature T_c.

19.2.4 SANS Measurements

SANS measurements were performed using three spectrometers. One is F-SANS spectrometer at JRR-3 reactor in Tokai with neutron focusing lens made of MgF_2

with diameter 30 mm, curvature radius 25, and thickness 10.5 mm. Using F-SANS, we can perform two-dimensional measurements in a very low Q range from 1×10^{-4} to 10^{-2} Å^{-1}. We also used SANS-U spectrometer (41) at JRR-3 reactor in Tokai. In the SANS-U measurements, the scattering vector Q range was from 6×10^{-3} to 7×10^{-2} Å^{-1}. In addition, we used time-of-flight (TOF) SANS spectrometer SWAN (42) installed at a spallation pulse cold neutron source at KENS, Tsukuba, in order to extend the Q range up to 3 Å^{-1}. In this spectrometer, we measure the scattering intensity as a function of neutron wavelength λ as well as scattering angle 2θ. Hence, we can cover a very wide Q range from 10^{-2} to 3 Å^{-1} in the measurements. Combining all the data by three spectrometers, we can cover a Q range from 10^{-4} to 3 Å^{-1} in this study. This wide Q range is a distinct feature of this experiment.

19.3 RESULTS AND DISCUSSION

19.3.1 Depolarized Light Scattering Measurements

We first examined the structure development of the LMW PE (matrix PE) during the crystallization process after applying pulse shear by DPLS. This will give a basis for interpretation of the results of the PE blends.

Figure 19.2 shows examples of the time evolution of 2D DPLS patterns for the LMW PE during the crystallization process after pulse shear with the shear rates of 1, 8, and 16 s^{-1}.

The shear strain was 3200% for all the measurements. After a certain induction period for the structure formation, we observed an isotropic 2D DPLS pattern for the

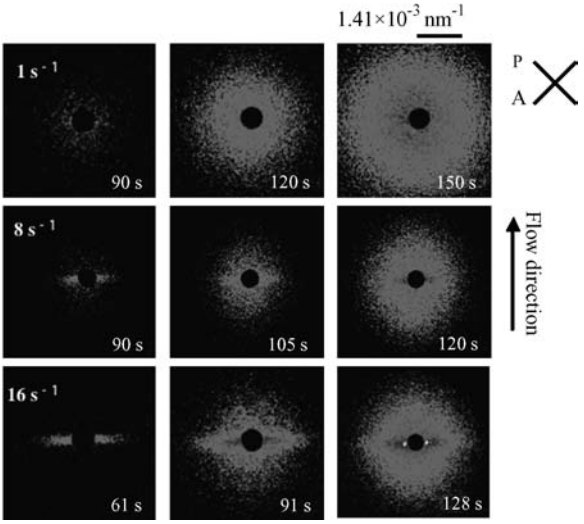

Figure 19.2 Time evolution of 2D DPLS patters form the matrix PE (LMW PE) during the crystallization process at 129°C after pulse shear with shear rates $\dot{\gamma}$ of 1, 8, and 16 s^{-1} from top to bottom. The shear strain ε was 3200%. (From Reference 25 with permission from Elsevier.)

shear rate $\dot{\gamma}$ of $1\,s^{-1}$. The induction period becomes shorter with increasing shear rate, although the 2D pattern is isotropic, showing the acceleration of the crystallization rate with increasing shear rate. As the shear rate increases further, the anisotropic 2D patterns were observed above about $\dot{\gamma} = 6\,s^{-1}$. For example, the 2D pattern for $\dot{\gamma} = 16\,s^{-1}$ shows a streaklike scattering normal to the flow direction in the early stage as seen in the lowest row in Fig. 19.2. The streaklike scattering means that long scattering objects are aligned along the flow direction. Keller and coworkers (7–9,35) observed the shish-kebab structure in polyethylene by TEM and found long shish with diameter of about 10 nm, which was assigned to extended chain crystal. The long object observed here is much larger in diameter than the shish, suggesting that it is not the shish (extended chain crystal) but a precursor of the shish. This problem will be discussed later. This large and long object is termed the ''row structure'' in this chapter hereafter.

On further annealing, the isotropic scattering emerges and covers the anisotropic scattering. The isotropic scattering has been assigned to spherulites and confirmed by the OM measurements. In order to evaluate the anisotropy of the 2D scattering patterns quantitatively, we have defined a measure for the anisotropy. A typical 2D anisotropic scattering pattern is shown in Fig. 19.3a and the scattering intensities normal and parallel to the flow direction are plotted against Q in Fig. 19.3b, respectively.

The scattering intensities are very weak in the high Q range, while they begin to increase at a certain onset Q value in the low Q range, depending on the scattering direction. We have defined the ratio of the onset Q value normal and parallel to the flow direction ($=Q_{\perp}/Q_{\parallel}$) as the measure of anisotropy for DPLS, and termed it as the degree of anisotropy R_{ani} in this chapter. The degree of anisotropy R_{ani} is time dependent: it has a maximum in the early stage and decreases with annealing time. We have employed the maximum value of R_{ani} for the discussion of the degree of anisotropy in this chapter. It is obvious that R_{ani} depends on length scale probed by Q. In the DPLS measurements, R_{ani} represents the degree anisotropy in micron scale.

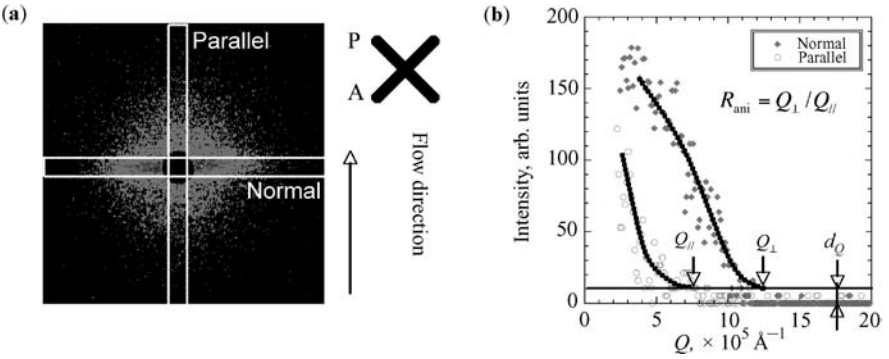

Figure 19.3 (**a**) Typical 2D DPLS pattern. (**b**) The definitions of the degree of anisotropy $R_{\mathrm{ani}}(=Q_{\perp}/Q_{\parallel})$ for DPLS.

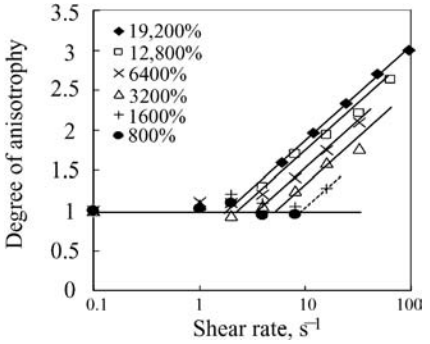

Figure 19.4 Shear rate dependence of the degree of anisotropy R_{ani} for the matrix PE (LMW PE) at various shear strains ε from 800% to 19,200%. (From Reference 25 with permission from Elsevier.)

The maximum value of the degree of anisotropy R_{ani} is plotted as a function of shear rate $\dot{\gamma}$ at various shear strains in Fig. 19.4 for the matrix PE.

In the low shear rate region, the value of R_{ani} is unity, meaning that the scattering is isotropic and begins to increase at a critical shear rate, which depends on the shear strain. For example, the degree of anisotropy R_{ani} is unity below the shear rate of 6 s^{-1} and begins to increase at around 6 s^{-1} for the shear strain ε of 3200%. On the basis of the results, we adopted such shear condition for the experiments of the PE blend that the matrix PE does not show anisotropic scattering pattern. If we observe anisotropic scattering pattern in the PE blend under such shear condition, we can directly attribute it to the effects of the UHMW PE.

Figure 19.5 shows the time evolution of 2D DPLS patterns of the matrix PE and the PE blend including 3 wt% UHMW PE during the crystallization process after the pulse shear at 129°C.

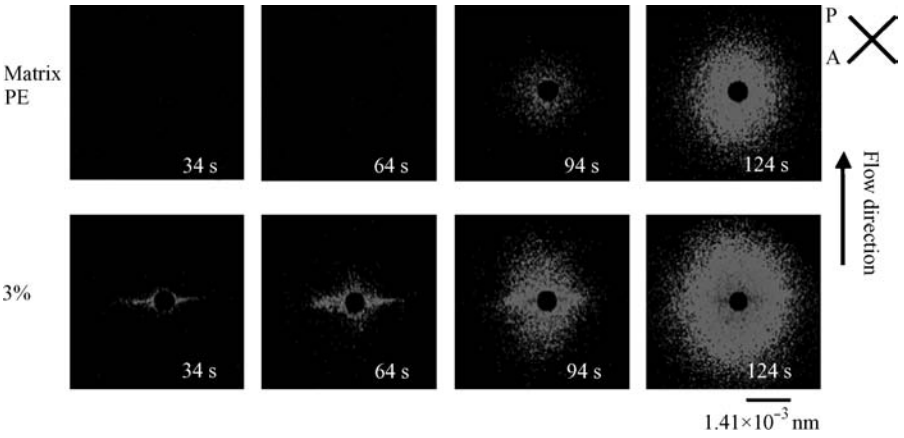

Figure 19.5 Time evolution of 2D DPLS patters for the matrix PE (LMW PE) and the PE blend including 3 wt% UHMW PE during the crystallization process at 129°C after pulse shear. The shear rate and the strain were 4 s^{-1} and 1600%, respectively. (From Reference 25 with permission from Elsevier.)

The shear rate $\dot{\gamma}$ and the shear stain ε are $4\,s^{-1}$ and 1600%, respectively. In the case of the matrix PE, an isotropic scattering pattern appears at around 80 s after applying the pulse shear and increases in intensity with annealing time. On the contrary, the 3% blend shows a very sharp streaklike scattering normal to the flow direction, which appears at around 30 s after the pulse shear, corresponding to the ''row structure.'' At about 80 s in the late stage, isotropic scattering appears to cover the anisotropic scattering. The onset time of the isotropic component in the 3% blend is very close to that in the matrix PE, suggesting that the isotropic scattering in the blend is coming from the matrix PE. However, it is evident that the streaklike scattering is due to the UHMW PE because the matrix PE does not show any anisotropic scattering under this shear condition. From these observations, we can directly conclude that the UHMW component enhances the formation of the ''row structure.'' We performed preliminary WAXS measurements on the ''row structure'' but did not observe any signs of crystallization, suggesting that the ''row structure'' observed here is not a crystal. However, the ''row structure'' can be detected in OM observations.

We also examined the effects of the concentration of the UHMW PE C_{HMPE}. Figure 19.6 shows the 2D scattering patterns of the PE blends at 68 and 98 s after the pulse shear as a function of the concentration C_{HMPE}.

The shear rate and the shear strain were $4\,s^{-1}$ and 3200%, respectively. Anisotropic scattering patterns were not observed when the concentration C_{HMPE} of the UHMW PE was less than 0.5 wt%. At around $C_{HMPE} = 0.5$ wt%, a very weak anisotropic scattering was observed at 68 s after the pulse shear as seen in Fig. 19.6 and the 2D scattering intensity increases in the anisotropy with the concentration C_{HMPE}, suggesting that there is a critical concentration C^*_{ani} for the anisotropic scattering at around $C_{HMPE} = 0.5$ wt%. In Fig. 19.7, the degree of anisotropy R_{ani} at 68 s after the pulse shear is plotted against the concentration of the UHMW PE C_{HMPE} for three shear conditions, under which the matrix PE does not show the anisotropic scattering pattern.

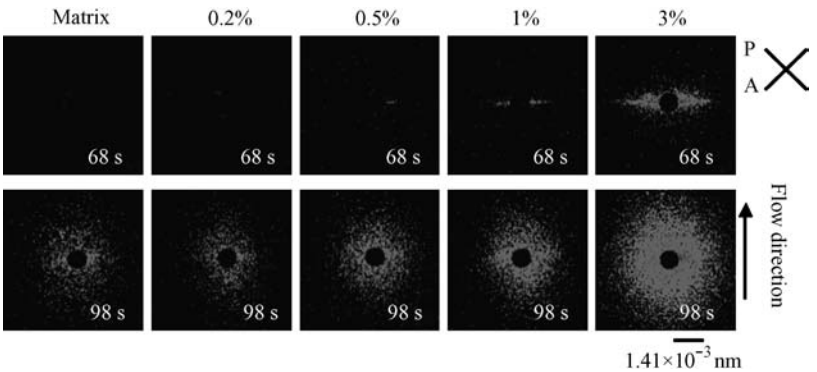

Figure 19.6 2D DPLS patters of the PE blends with various concentrations of the UHMW PE from 0 to 3 wt% at 68 and 98 s after pulse shear. The shear rate and the strain were $4\,s^{-1}$ and 1600%, respectively. (From Reference 25 with permission from Elsevier.)

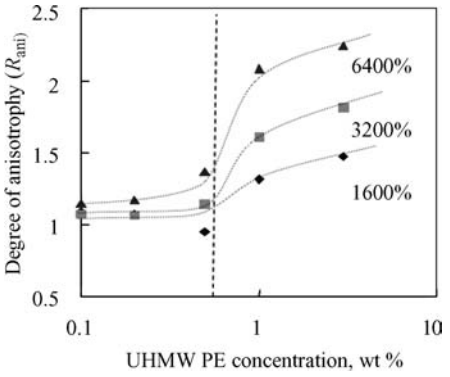

Figure 19.7 Degree of anisotropy R_{ani} as a function of the concentration of UHMW PE for various shear strains ε, 1600%, 3200%, and 6400%. Shear rate $\dot{\gamma}$ was $4\,s^{-1}$. (From Reference 25 with permission from Elsevier.)

It is obvious that the degree of anisotropy is almost unity below $C_{HMPE} = 0.5 - 0.6$ wt%, while it abruptly increases above this concentration, showing that the critical concentration for the anisotropy C^*_{ani} is 0.5–0.6 wt%.

We compare the critical concentration C^*_{ani} to the chain overlap concentration C^*_{Rg} of the UHMW PE. The overlap concentration of polymer chains with radius of gyration R_g is given by

$$C^*_{Rg} = \frac{M_w}{\frac{4}{3}\pi\langle R_g^2\rangle^{3/2} N_A} \tag{19.1}$$

where $\langle R_g^2\rangle$ is the mean square radius of gyration of the polymer chain, which is given by Equation 19.2 under the Gaussian chain approximation with molecular weight distribution $U = M_w/M_n - 1$ (43)

$$\langle R_g^2\rangle = \frac{bL(2U+1)}{3(U+1)} \tag{19.2}$$

where b and L are the persistence length and the contour length, respectively. Taking the literature data $[\langle R_g^2\rangle/M_w]^{1/2} = 0.46$ (39), we have calculated the overlap concentration C^*_{Rg} to be $0.178\,g\,cm^{-3}$ or 0.209 wt%, which is smaller than the critical concentration C^*_{ani}. The ratio of the critical concentration and the overlap concentration, C^*_{ani}/C^*_{Rg}, is 2.5–3, strongly suggesting that entanglements of the UHMW PE are very important for the formation of the ''row structure.'' This result agrees with the finding of Kornfield and coworkers (34) that the role of the long chains in the shear-induced crystallization is cooperative rather than a single-chain event. This result may be understood in the following picture. In order to produce the ''row structure'' or the precursor of shish, the polymer chains must be extended due to the shear. Suppose that the UHMW PE are isolated in the blend, they are somewhat extended by the shear flow; however, it does not lead to the anisotropic structure formation. On the contrary, when the concentration of UHMW PE is above the

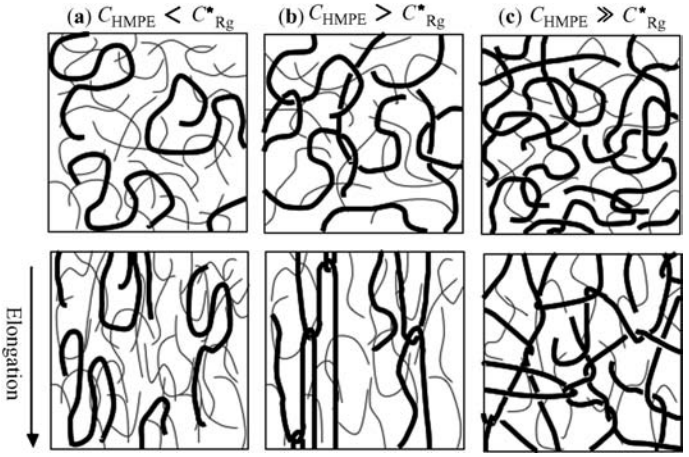

Figure 19.8 Schematic illustrations of the role of UHMW PE in formation of ''row structure.'' Thin and thick curves represent UHMW and LMW PEs, respectively. (**a**) $C_{HMPE} < C^*_{Rg}$: UHMW PE chains are isolated and slightly extended by the shear; (**b**) $C_{HMPE} > C^*_{Rg}$: UHMW PE chains are entangled and extended due to the connectivity as polymer network is deformed; and (**c**) $C_{HMPE} \gg C^*_{Rg}$: too many cross-linking points (or entanglements) prevent extension of HMW PE chains. (Reprinted from Reference 25 with permission from Elsevier.)

critical value for the entanglements, the chains must be extended due to the connectivity as polymer network is deformed. The critical concentration for the anisotropy C^*_{ani} must correspond to the critical concentration for the effective entanglements. This is schematically illustrated in Fig. 19.8a and b.

These pictures remind us of the gel spinning technique (44–47) that is used to produce ultrahigh strength and ultrahigh modulus fiber of PE, although all of the situations are not the same. In this procedure, PE chains are extremely extended because the tension is transmitted though the cross-linking points in the gel network. However, in order to obtain the ultrahigh strength fiber, the number of cross-linking points should be as small as possible because too many cross-linking points prevent the extension of polymer chains. In the crystallization of the PE blend under the shear, the formation of the ''row structure'' or the precursor of shish is therefore expected to be depressed at a rather high concentration of the UHMW PE above C^*_{ani} because the polymer chains cannot be extended due the shear because of too many entanglements, as illustrated in Fig. 19.8c.

19.3.2 Small-Angle X-Ray Scattering Measurements

In DPLS measurements, we observe structure formation in micron scale during crystallization of the PE blends, especially the ''row structure'' or the precursor of shish. In order to see the formation of kebab, however, we have to go to nanometer scale. Therefore, we performed SAXS measurements on crystallization process of

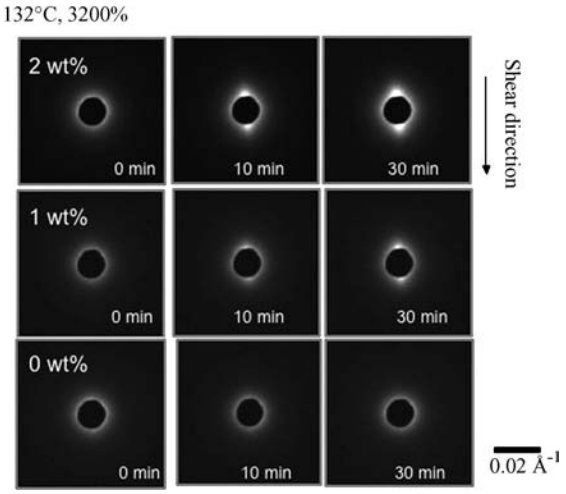

Figure 19.9 Time evolution of 2D SAXS patterns during crystallization process of PE blends with UHMW PE concentration of 0, 1, and 2 wt% at crystallization temperature 132°C.

the PE blends under the same shear condition as that in DPLS measurements except for the temperature at which the pulse shear was applied. In the SAXS experiments, the pulse shear was applied at 30°C above the crystallization temperature T_c. Figure 19.9 shows an example of time evolution of 2D SAXS profiles for the PE blends including 0, 1, and 2 wt% UHMW PE during the crystallization process at $T_c = 132°C$ after applying shear flow.

In the case of 0 wt%, only isotropic scattering patterns were observed. However, the 1 and 2 wt% blends show two-spot scattering parallel to the shear direction, and the spots became stronger in intensity with annealing time, showing that the UHMW PE enhances the anisotropic structure formation. These orientated features must be due to the kebab structures, which are oriented perpendicularly to the shear direction, and the spot position corresponds to the so-called long period between kebabs. The spot scattering appeared at around 3 min after reaching T_c for the 2 wt% blend, while it appeared at ~10 min for the 1 wt% blend. This means that the crystallization rate in the PE blend increases with the UHMW PE concentration. As shown in the previous section, we found that the UHMW PE enhanced the formation of the ''row structure'' or the precursor of shish, and there was a critical concentration of UHMW PE for the formation. The present results suggest that the UHMW PE also enhances the kebab structure formation and there is a critical concentration for the kebab formation. It should be noted that streaklike scattering normal to the flow direction was not observed for all UHMW PE concentrations in the SAXS measurements. Such streaklike scattering patterns are usually interpreted as a sign of shish structure (22,48–50). In the previous section, however, we showed that the ''row structure'' or the precursor of shish in micron scale was observed as streaklike scattering normal to the flow direction in 2D DPLS measurements under the temperature and shear conditions similar to those in the SAXS measurements. This result suggests that there

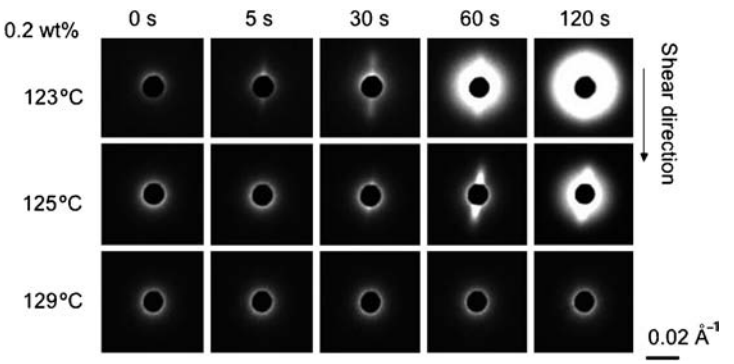

Figure 19.10 Time evolution of 2D SAXS patterns during crystallization process of PE blends with UHMW PE concentration of 0.2 wt% at various crystallization temperatures, 123, 125, and 129°C.

should be the ''row structure'' or the precursor of shish even though streaklike scattering normal to the flow was not observed in the SAXS measurements. Therefore, we will discuss the SAXS results assuming that ''row structure'' or the precursor of shish is formed in the experiments.

We also examined the crystallization temperatures T_c dependence of the time-resolved SAXS data. Figure 19.10 shows the time evolution of 2D SAXS images of the PE blend with UHMW PE concentration of 0.2 wt% for various crystallization temperatures T_c.

In a temperature range below about 127°C, two strong spots parallel to the shear direction were observed after a certain induction time and followed by isotropic scattering due to the spherulite formation. As the crystallization temperature decreases, the onset time of the anisotropic scattering becomes shorter. This is due to the increase in degree of supercooling (or quenching depth), which is a driving force of crystallization in this temperature region (51). On the contrary, the spot scattering parallel to the shear direction was not observed above about 129°C, at least during the annealing period of 1 h. Note that the two spots were observed even above ~129°C for the concentrations of UHMW PE higher than 0.2 wt%, showing that the critical UHMW PE concentration for the anisotropy exists and depends on the crystallization temperature.

In order to analyze the anisotropic scattering patterns, we defined the degree of anisotropy for the SAXS data. Figure 19.11 shows a typical anisotropic 2D SAXS pattern for the 0.2 wt% PE blend crystallized at $T_c = 125$°C for 40 s after applying pulse shear.

We calculated the ratio of intensity in the parallel direction, $I_{\parallel}$, and in the normal direction, $I_{\perp}$ in a range of $0.008\text{Å}^{-1} < Q < 0.02\text{Å}^{-1}$, which is shown by dashed lines in Fig. 19.11. The ratio of $I_{\parallel}$ and $I_{\perp}$ is a function of the annealing time and has a maximum in the early stage of crystallization and decreases with time due to growth of isotropic spherulite. We defined the maximum of the ratio as the degree of anisotropy for SAXS in this chapter and plotted it in Fig. 19.12 against logarithm of the UHMW PE concentration for various crystallization temperatures T_c.

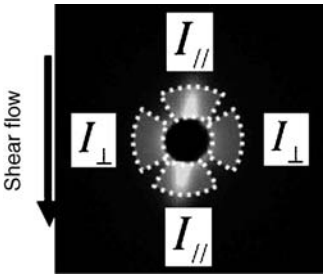

Figure 19.11 Typical 2D SAXS pattern for PE blend with UHMW PE concentration 0.2 wt%. Area for intensity integration is shown by dotted lines.

In the low concentration range, the degree of anisotropy is almost unity at each T_c, but it begins to increase at a certain critical concentration, depending on the crystallization temperature T_c. Extrapolating the linear relationship to unity, we have evaluated the critical UHMW PE concentration C^*_{SAXS} for the anisotropy. The critical UHMW PE concentration C^*_{SAXS} thus obtained is plotted against the crystallization temperature in Fig. 19.13.

In the previous section, we showed that the critical concentration for the ''row structure'' or the precursor of shish was about 0.5–0.6 wt% at $T_c = 129°C$, which is almost identical with the C^*_{SAXS} value determined from the kebab formation. This result supports the idea that the entanglements of UHMW PE also play an important role in kebab formation. In this experiment, however, we observed that the critical concentration C^*_{SAXS} decreased with the crystallization temperature T_c, and reached a constant value of ~0.1 wt%, which is about half of the chain overlap concentration

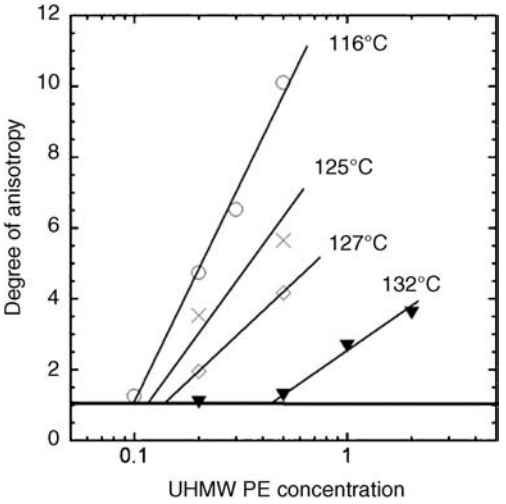

Figure 19.12 Degree of anisotropy against UHMW PE concentration at various crystallization temperatures.

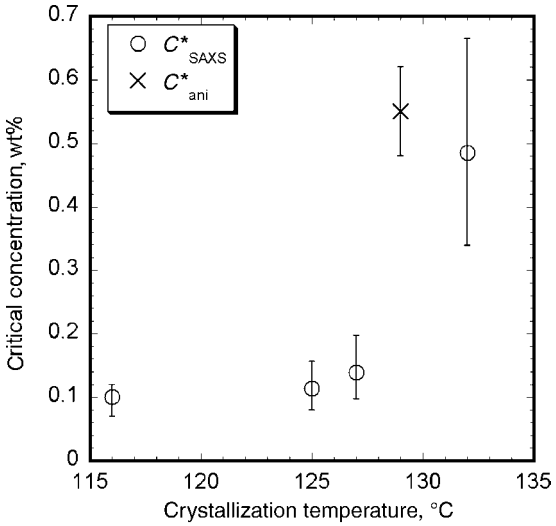

Figure 19.13 Critical concentration C^*_{SAXS} of UHMW PE for anisotropy in SAXS pattern against crystallization temperature T_c. Cross (×) shows critical concentration C^*_{ani} for anisotropic structure formation in DPLS.

C^*_{Rg}. Does this result mean that the critical concentration is not related to entanglements? Seki et al. (34) studied a critical concentration for the anisotropic structure formation in isotactic polypropylene blend including small amount of UHMW component and found that it was lower than the overlap concentration C^*_{Rg}, a result that is similar to the present result at the low crystallization temperatures below about 127°C. In order to understand their results and our results, we have to consider the molecular weight distribution of UHMW PE. The longer chains in UHMW PE could be entangled at concentration lower than that for the average molecular weight, and hence more oriented than the shorter ones. Therefore, the critical concentration lower than the overlap concentration is not so surprising for polymers with molecular weight distribution.

We briefly discuss the temperature dependence of the critical concentration for the anisotropy. In this discussion, we consider two processes in the crystallization under shear flow separately. One is the orientation process of polymer chains by applying shear and the other is the successive crystallization process, both of which must compete with the orientation relaxation of polymer chains. In order to produce the shish-kebab structure, the UHMW PE must be extended and oriented due to the shear. If UHMW PE is isolated in the blend without entanglements, they are somewhat extended by the shear flow; however, not so remarkably because the shear stress is not transmitted through the entanglements. On the contrary, when the concentration of UHMW PE is above a threshold for entanglements, the chains must be extended due to the connectivity as polymer network is deformed. The threshold for the anisotropy must correspond to the concentration above which entanglements work effectively. The above discussion is the same as

that for the critical concentration C^*_{ani} for anisotropic structure formation in DPLS measurements at a given temperature. In order to discuss the temperature dependence, we have to consider the relaxation process because the orientation process competes with the relaxation of UHMW PE. If the relaxation rate is faster than the shear rate, the polymer chains cannot be extended or oriented by the shear. This relaxation process must be the so-called reptation motion (52), whose relaxation time is give by

$$\tau_r = \tau_e Z^{3.4} = \tau_e \left(\frac{M_w}{M_e}\right)^{3.4} \tag{19.3}$$

where τ_e and M_e are the relaxation time of bond orientation and the molecular weight between molecular entanglements, respectively. The relaxation time of the reptation motion for PE with $M_w = 2,000,000$ at 116°C was calculated to be ~400 s on the basis of the reported data by Raju et al. (53). The relaxation rate for the reptation motion or the inverse of relaxation time ($0.0025\ s^{-1}$) is very slow compared with the shear rate ($32\ s^{-1}$), meaning that the relaxation process does not produce significant effects on the orientation process. It is therefore expected that the initial orientation of UHMW PE is dominated by the shear rate rather than the chain relaxation, at least under the present shear and temperature conditions.

After the initial orientation by the shear, the extended chains must crystallize before the chain relaxation to form the anisotropic structure such as the shish and the kebab. Both the crystallization rate (especially, crystal nucleation rate) and the relaxation rate depend on temperature. The temperature dependence of crystal nucleation rate ν_{nuc} could be described as (54)

$$\nu_{nuc} \sim \exp\left(\frac{ks^3 v_m^2}{kT(\Delta h_m^f)^2 (T_m^\infty - T)^2}\right) \tag{19.4}$$

where σ, v_m, Δh_m^f, and T_m denote the excess free energy per unit area of the surface of the nucleus, the monomer volume, the heat fusion per monomer, and the equilibrium melting temperature, respectively. Assuming that all parameters in Equation 19.4 are independent of temperature, the equation predicts that the crystal nucleation rate is very slow near the equilibrium melting temperature ($T_m^\infty = 142$°C) (55,56), while it increases rapidly as we more away from the equilibrium melting temperature. In this experiment, the crystal nucleation rate at 116°C is faster than that at 132°C by a factor ~10^3. The temperature dependence of the relaxation rate (or the inverse of relaxation time) due to the reptation can be described by Williams–Landel–Ferry (WLF) equation (54),

$$\frac{1}{\tau_r} = \frac{1}{\tau_0} \exp\left[\frac{2.303 C_1 (T - T_0)}{T - T_0 + C_2}\right] \tag{19.5}$$

The temperature dependence of the relaxation rate is not so large in the temperature range of this experiment. Taking the reference temperature $T_0 = 148$K (57), the relaxation rate at 132°C is only 1.33 times faster than that at 116°C. On the

basis of the temperature dependence of the crystal nucleation rate as well as the relaxation rate, we can give the following picture for the crystallization of PE in a temperature range between 116 and 132°C under the shear flow. At low temperatures near 116°C, where the crystal nucleation rate is very fast and the relaxation rate is slightly slow compared with 132°C, the extended polymer chains can crystallize immediately after the initial orientation. In such temperature range, the anisotropic structure formation depends only on the initial orientation that is mainly determined by the shear rate and the UHMW PE concentration but not by the crystallization temperature. Hence, the critical concentration of UHMW PE is independent of temperature in this range.

As the crystallization temperature increases, for example, from 116 to 132°C, the crystallization rate decreases very rapidly and the relaxation rate increases slowly, and hence extended polymer chains would relax before crystallization at around the critical concentration C^*_{SAXS} at a high crystallization temperature (~0.5 wt% at 132°C), meaning that no anisotropic structure is observed at ~0.5 wt% at 132°C. In order to form the anisotropic structure at a high crystallization temperature (132°C), the initial orientation must be high and the relaxation must be slow. This condition can be obtained by increasing the UHMW PE concentration; as the UHMW PE concentration increases, the number of entanglements increases, leading to enhancement of initial orientation and decrease in the relaxation rate. Therefore, at a high temperature (132°C), anisotropic structure is formed at a higher concentration than at a low temperature (116°C). In other words, the critical concentration of UHMW PE for the formation of the anisotropic structure increases with temperature. This picture qualitatively explains the present result that the critical concentration increases with crystallization temperature near the melting temperature.

19.3.3 Small-Angle Neutron Scattering Measurements

In the DPLS measurements, we showed that the ''row structure'' or the precursor of shish has a diameter in micron scale. However, as mentioned in Section 19.1, the TEM observations showed that shish (extended chain crystal) has a diameter of ~10 nm (7–9,35). These observations suggest that shish-kebab has hierarchic structure in a wide spatial scale. In this section, we studied the hierarchic structure using SANS in a very wide Q range. For this purpose, we used hydrogen/deuterium (H/D) labeling method in SANS. We briefly explain the basic idea of the SANS measurements. It is well known that in SANS the scattering contrast between hydrogenated and deterated PEs is very large (57), so if the ''row structure'' is formed from UHMW h-PE, we could observe it due to the high scattering contrast. On the contrary, in SAXS, the scattering contrast arises from the electron density difference, which corresponds to the mass density difference in one-component systems. Therefore, in the case that the ''row structure'' and/or the shish structure are formed from UHMW h-PE, we expect very large difference between the SANS and SAXS profiles (see Fig. 19.14a and c).

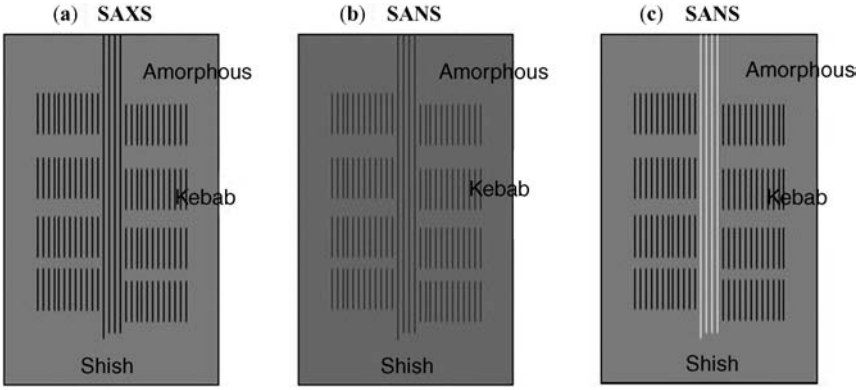

Figure 19.14 Schematic illustration of scattering contrast in SAXS and SANS. (**a**) SAXS contrast for the shish-kebab. (**b**) SANS contrast for homogeneous distribution of UHME PE. (**c**) SANS contrast for localization of UHMW PE in shish.

However, if the UHMW h-PE chains are homogeneously distributed in the shish and the kebab structure, the SANS contrast in the small-angle region arises mainly from the density difference similar to that in the SAXS (see Fig. 19.14a and b). In this case, we expect that the scattering patterns are almost identical in both the SANS and SAXS. Hence, we can see whether or not the ''row structure'' is mainly formed from the UHMW h-PE by comparing the SANS data to the SAXS data. On the basis of this idea we, have performed SANS and SAXS measurements on the elongated blend of UHMW h-PE and LMW d-PE (2.8/97.2). In the SANS data in Fig. 19.15a, we clearly see the streaklike scattering normal to the elongation direction in addition to the two-spot pattern along the elongation direction.

The former and the latter must correspond to the ''row structure'' and the kebab structure (or kebab spacing). However, we only see the two-spot pattern along the elongation direction in the SAXS result (Fig. 19.15b), corresponding to the kebab structure. The results directly show that the ''row structure'' is mainly formed from the UHMW h-PE, although the Q range is not enough to estimate the form factor of the ''row structure.'' In order to evaluate the form factor, we have extended the Q range in this work using F-SANS and SWAN spectrometers. Figure 19.16a shows the

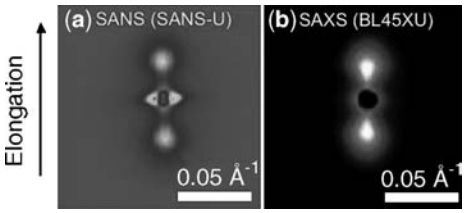

Figure 19.15 2D SANS (**a**) and SAXS (**b**) patterns of elongated PE blend of low molecular weight deuterated PE (LMW d-PE) and ultrahigh molecular weight hydrogenated polyethylene (UHMW h-PE). Weight fraction of UHMW h-PE is 2.8%.

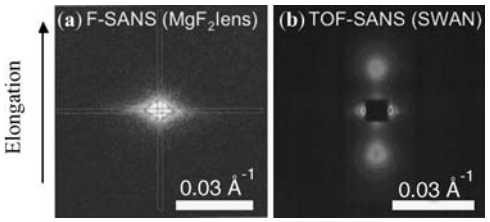

Figure 19.16 2D SANS patterns of elongated PE blend of LMW d-PE and UHMW h-PE: (**a**) measured by F-SANS and (**b**) measured by SWAN (TOF-SANS machine.)

F-SANS data in a Q range of 1×10^{-4} to 1×10^{-2} Å^{-1}, which shows the anisotropic scattering pattern as expected from the SANS-U data (Fig. 19.15a).

After subtracting the background, the one-dimensional intensities have been calculated and plotted in Fig. 19.17 in parallel and normal directions, where SANS-U data are also plotted in parallel and normal directions. Figure 19.16b shows the 2D SWAN (TOF SANS machine) data in low angle counters for neutron wavelength $\lambda = 11$ Å. Here we again observed streaklike scattering in the direction normal to the elongation. After correcting the data for the background scattering, counter efficiency, the wavelength distribution of incident neutron intensity, and the transmittance, we have calculated one-dimensional scattering intensities in the parallel and normal directions and plotted in Fig. 19.17. The data were shifted so that the data are smoothly connected.

As mentioned above, the SANS contrast in the present sample arises from two causes: scattering length density difference due to mass density difference and scattering length difference between H and D. We assume that the mass density correlation function and the H/D density correlation function could be decoupled because the fraction of UHMW h-PE is very small (2.8 wt%). In SAXS measurements, h-PE and d-PE cannot be distinguished, and the scattering contribution due to the mass density fluctuations $I_{\text{den}}(Q)$ can be observed in SAXS. Therefore, in order to

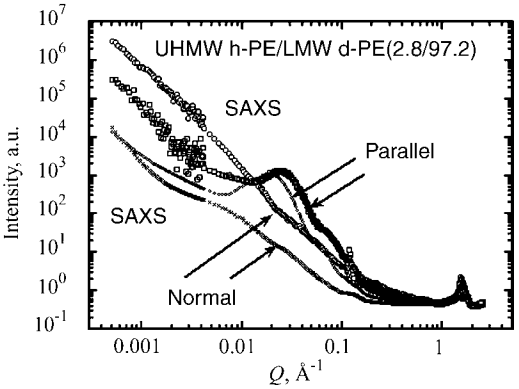

Figure 19.17 1D SANS and SAXS profiles of elongated PE blend of LMW d-PE and UHMW h-PE in directions normal and parallel to the elongation direction.

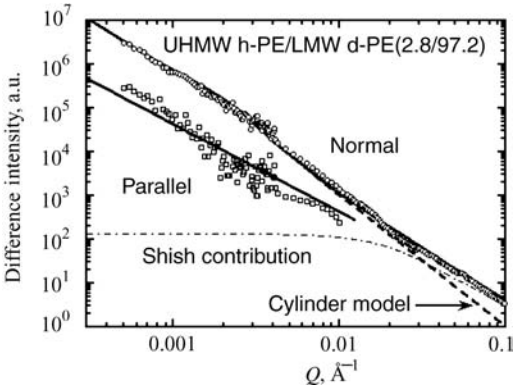

Figure 19.18 1D SANS difference intensities in directions normal and parallel to the elongation direction after subtraction of contributions of density fluctuations which were evaluated from SAXS data. Thick solid lines are the results of fit to multicore–shell cylinder model and thin chain line is a contribution of the core (or the shish (extended chain crystal)). Thick dashed line is the result of fit to the cylinder model.

evaluate the scattering contribution due to the mass density fluctuations $I_{\text{den}}(Q)$, we carried out WAXS, SAXS, and U-SAXS measurements on the same sample, and the results are plotted in Fig. 19.17 together with the neutron data. The X-ray intensity was adjusted so that the intensity ratio of WAXS and WANS is equal to the calculated ratio and subtracted from the neutron intensity in both the directions, and the difference intensities are plotted in Fig. 19.18.

The difference intensities approximately correspond to the form factors of the ''row structure.'' Note that the subtraction did not work well in the parallel direction in a Q range of 0.1–0.01 Å^{-1} corresponding to the long period because the long period due to the H/D contrast is slightly longer than that in X-ray scattering. Therefore, we omitted the data in this Q range for the further analysis.

In the low Q range between 3×10^{-3} and 2×10^{-2}, the scattering intensity in the normal direction can be described by a power law with an exponent of $-3, I(Q) \sim Q^{-3}$, corresponding to the asymptotic behavior of scattering from a cylinder in the normal direction to long axis, and hence we have first employed a cylinder model. The form factor of an oriented cylinder with a length of $2H$ and radius of R has been reported by Shibayama et al. (59). According to the report, we have calculated the form factor in the normal direction, taking into account the distributions of the radius R and the polar angle α of cylinder axis with respect to the elongation direction, and fitted to the observed scattering intensity after convoluted with the resolution functions of the spectrometers. We found that the R distribution is not negligible but the angular distribution is very small, and hence the α distribution was neglected in the fits. The result of fit is shown by a dotted line in Fig. 19.18, which is almost behind the data points (or a thick line) in the Q range above about 0.02 Å^{-1}. This means that the cylinder model can describe the ''row structure'' only in the large scale above about 300 Å, and the evaluated radius was $\sim$1 μm. This large radius certainly is not an extended chain crystal because it is large

enough to include kebab inside, but it must be the bundle of the shish-kebab. In the Q range above about 0.02 Å^{-1}, however, the observed data in the normal direction show excess scattering, suggesting some extra structure that is not included in the cylinder model. As mentioned in Section 19.1, Keller and coworkers (7–9,35) reported shish structure with diameter of ~10 nm, which must correspond to extended chain crystal (the shish). We have assigned the excess scattering intensity above about 0.02 Å^{-1} to the shish structure. In order to describe this contribution, we employed a core–shell cylinder model (60), in which the core and shell describe the extended chain crystal (the shish) and the ''row structure'' in micron scale, respectively. Calculating the scattering intensity of the core–shell cylinder model, we fitted to the observed one in the normal direction. However, it was found that the contribution of the core scattering in this model is too small to reproduce the observed intensity above about 0.02 Å^{-1}. Then we further assume that several extended chain crystals (shishs) are included in the large shell cylinder. Neglecting the cross-terms between core and core and between core and shell, the scattering intensity could be approximated by

$$I_{\text{core-shell}}(Q) = [V_{\text{shell}}(\rho_{\text{shell}} - \overline{\rho}_{\text{D}})F(Q, R_{\text{shell}}, H)]^2 + n_{\text{c}}[V_{\text{core}}(\rho_{\text{core}} - \rho_{\text{shell}})F(Q, R_{\text{core}}, H)] \tag{19.6}$$

where $F(Q, R, H)$ is the scattering amplitude of a cylinder with a length of $2H$ and a radius of R, V_{shell}, V_{core}, R_{shell}, and R_{core} are the shell and core volumes and the shell and core radii, respectively, and ρ_{shell}, ρ_{core}, and $\overline{\rho}_{\text{D}}$ are the scattering length densities of the shell, core, and d-PE matrix, respectively, and n_{c} is the number of the core cylinders in a shell cylinder. In the calculation of Equation 19.6 we assumed that ρ_{core} was the same as the scattering length densities of d-PE in crystalline region, and ρ_{shell} was calculated assuming that UHMW h-PE was homogeneously distributed in the shell with degree of crystallinity of 0.68 and the volume fraction of 0.3, which were determined by the SAXS data. $\overline{\rho}_{\text{D}}$ was calculated under an assumption that the matrix consisted of only LMW d-PE. The calculated scattering intensity $I_{\text{core-shell}}(Q)$ was fitted to the data. The result of the fit is shown by a thick solid line in Fig. 19.18 where the core contribution was also indicated by a chain line. The fitness is very good, showing that the present model, which is termed multicore–shell cylinder model, is appropriate to describe the shish structure and the ''row structure.'' The evaluated radii of the shell and the core are ~1 μm and 4.5 nm, respectively, and the number of core cylinders is about 3, meaning that only three extended chain crystals are in the ''row structure.'' This very small number of the shish is one of the reasons why we did not observe the extended chain crystals in the SAXS measurements. The results provide us a picture that the ''row structure'' with radius of ~1 μm includes about three extended chain crystals (shish) with diameter of 4.5 nm. The ''row structure'' must a bundle of the shish-kebab structure. If we assume that the three different shish-kebab structures equally shear the large bundle (or the ''row structure'') with radius of ~1 μm, the radius of the kebab would be about 500 nm. We estimated the dispersions of the radius for the shell and the core, which were about $30 \pm 5\%$ and ~5%, respectively. The latter is rather small, showing that the diameter of the extended chain crystals is rather uniform.

We also calculated the form factor in the parallel direction, but it was impossible to fit to the observed data in the Q range in the present experiment because the cylinder was too long. The ratio of scattering intensity in the parallel direction and in the normal direction is a function of the cylinder length in this Q range. Hence, fixing all the geometrical parameters in the multicore–shell cylinder model except for the length, we calculated the intensity in the parallel direction and fitted to the observed data to reproduce the ratio of the intensity in the parallel direction and in the normal direction. The result is shown by a thick solid line in Fig. 19.18, and the estimated length of the cylinder $2H$ was $\sim$12 μm. This length is comparable to the length of the shish observed by Keller and coworkers by TEM (7–9,35).

In the previous section, we found that the ''row structure'' or the precursor of shish in micron scale appeared in a very early stage of crystallization. This precursor is very similar to the ''row structure'' in size observed here for the elongated PE. We also found that the ''row structure'' or the precursor formation is enhanced by addition of high molecular weight component above a certain critical concentration, suggesting that entanglements of high molecular weight component play an important role in the ''row structure'' formation. In other words, the ''row structure'' is formed from deformation of polymer network due to entanglements, and hence we proposed a gel spinning-like formation mechanism for the ''row structure'' in an earlier section (25). Recent experiment on isotactic polystyrene (iPS) showed that ''row structure'' (precursor) in micron scale aligned along the shear flow appeared even above the nominal melting temperature T_m (61). In the SANS experiment, it was shown that the elongated PE has ''row structure'' similar to that of the precursor, although the crystallization mechanism between the pulse shear crystallization and the elongation crystallization is quite different. The finding may imply that the network of UHMW PE due to entanglements plays an important role in the ''row structure'' formation in both the crystallization processes. The large oriented network (or the ''row structure'') may enhance the formation of the shish structure (or the extended chain crystal).

19.4 CONCLUSIONS

We have studied the crystallization process of PE blends of UHMW PE and LMW PE using DPLS, SAXS, and SANS in a wide spatial scale of 0.1 nm to several microns. We observed the large and long objects (''row structure'') in micron scale aligned along the flow direction in the early stage of crystallization as well as in the elongated PE blend. The DPLS and SAXS results suggested that the network of UHMW PEs due to entanglements is the origin of the ''row structure,'' and the SANS results revealed that the ''row structure'' has radius of $\sim$1 μm and length of 12 μm and there are three shishs (extended chain crystals) with radius of 4.5 nm in the ''row structure.'' In addition to the structural information of the ''row structure'' and the shish-kebab, the critical concentration of UHMW PE for the anisotropic structure formation suggested that the entanglements of UHMW PE are very important for the chain extension, and the temperature dependence of critical concentration predicted that

the crystallization rate must be faster than the orientation relaxation rate of polymer chains for the shish-kebab formation.

NOMENCLATURE

C^*_{ani}	Critical concentration of ultrahigh molecular weight polyethylene for anisotropy from DPLS measurement
C^*_{Rg}	Chain overlap concentration
C^*_{SAXS}	Critical concentration of ultrahigh molecular weight polyethylene for anisotropy from SAXS measurement
C_1, C_2	Parameters in Williams–Landel–Ferry equation
C_{HMPE}	Concentration of ultrahigh molecular weight polyethylene
d-PE	Deuterated polyethylene
DPLS	Depolarized light scattering
DSC	Differential scanning calorimetry
$F(Q,R,H)$	Scattering amplitude of a cylinder with radius R and height $2H$
H	A half length of cylinder
HMW	High molecular weight
h-PE	Protonated polyethylene
$I_{\mathrm{den}}(Q)$	Scattering intensity from density fluctuations
$I_{\parallel}$	Integrated scattering intensity parallel to the flow direction
$I_{\perp}$	Integrated scattering intensity normal to the flow direction
LMW	Low molecular weight
M_{e}	Molecular weight between entanglements
n	Refractive index
n_{c}	Number of core cylinders in multicore–shell model
N_{A}	Avogadro's number
OM	Optical microscope
Q	Length of scattering vector
$Q_{\parallel}$	Onset Q value parallel to the flow direction
$Q_{\perp}$	Onset Q value normal to the flow direction
R	Radius of a cylinder
R_{ani}	Degree of anisotropy ($= Q_{\parallel}/Q_{\perp}$)
R_{g}	Radius of gyration of a polymer chain
$\langle R_{\mathrm{g}}^2 \rangle$	Mean-square radius of gyration of a polymer chain
SALS	Small-angle light scattering
SANS	Small-angle neutron scattering
SAXS	Small-angle X-ray scattering
T_0	Reference temperature in Williams–Landel–Ferry equation
T_{c}	Crystallization temperature
TEM	Transmission electron microscope
T_{m}	Melting temperature
T_m^{∞}	Equilibrium melting temperature
TOF	Time-of-flight

U	Index of molecular weight distribution ($= M_w/M_n - 1$)
UHMW	Ultrahigh molecular weight
U-SAXS	Ultrasmall-angle X-ray scattering
v_m	Monomer volume
WAXS	Wide-angle X-ray scattering
α	Polar angle for cylinder model
$\dot{\gamma}$	Shear rate
Δh_m^f	Heat fusion per volume
ε	Shear strain
θ	Half of scattering angle
λ	Wavelength
ν_{nuc}	Growth rate of nuclear
$\overline{\rho}_D$	Density of deuterated polyethylene
σ	Surface free energy
τ_0	Relaxation time at reference temperature
τ_e	Relaxation time for bond orientation
τ_r	Relaxation time for reptation motion

REFERENCES

1. I. M. Ward, *Structure and Properties of Oriented Polymers*, Wiley, New York, 1975.
2. A. Ziabicki, *Fundamentals of Fiber Formation*, Wiley, New York, 1976.
3. Z. K. Walczak, *Processes of Fiber Formation*, Elsevier, Amsterdam, 2002.
4. A. Keller and J. W. H. Kolnaar, in: *Processing of Polymers*, H. E. H. Meijer (ed.), VCH, New York, 1997, pp. 189–268.
5. A. J. Pennings and A. M. Kiel. *Colloid. Z. Z. Polym.*, **205**, 160–162 (1965).
6. A. J. Pennings, *J. Polym. Sci. C Polym. Symp.*, **59**, 55–86 (1977).
7. J. A. Odell, D. T. Grubb, and A. Keller, *Polymer*, **19**, 617–626 (1978).
8. Z. Bashir, J. A. Odell, and A. Keller, *J. Mater. Sci.*, **19**, 3713–3725 (1984).
9. Z. Bashir, J. A. Odell, and A. Keller, *J. Mater. Sci.*, **21**, 3993–4002 (1986).
10. J. M. Samon, J. M. Schultz, B. S. Hsiao, S. Seifert, N. Stribeck, I. Gurke, G. Collins, and C. Saw, *Macromolecules*, **32**, 8121–8132 (1999).
11. J. M. Samon, J. M. Schultz, J. Wu, B. S. Hsiao, F. Yeh, and R. Kolb, *J. Polym. Sci. B Polym. Phys.*, **37**, 1277–1287 (1999).
12. R. H. Somani, B. S. Hsiao, A. Nogales, S. Srinivas, A. H. Tsuo, I. Sics, J. Balta-Calleja, and T. A. Ezquerra, *Macromolecules*, **33**, 9385–9394 (2000).
13. J. M. Schultz, B. S. Hsiao, and J. M. Samon, *Polymer*, **41**, 8887–8895 (2000).
14. J. M. Samon, J. M. Schultz, B. S. Hsiao, J. Wu, and S. Khot, *J. Polym. Sci. B Polym. Phys.*, **38**, 1872–1882 (2000).
15. J. M. Samon, J. M. Schultz, B. S. Hsiao, S. Khot, and H. R. Johnson, *Polymer*, **42**, 1547–1559 (2001).
16. A. Nogales, R. H. Somani, B. S. Hsiao, S. Srinivas, A. H. Tsuo, J. Balta-Calleja, and T. A. Ezquerra, *Polymer*, **42**, 5247–5256 (2001).
17. R. H. Somani, B. S. Hsiao, A. Nogales, H. Fruitwala, S. Srinivas, and A. H. Tsuo, *Macromolecules*, 34, 5902–5909 (2001).

18. R. H. Somani, L. Yang, P. K. Agarwal, H. Fruitwala, and A. H. Tsuo, *Macromolecules*, **35**, 9096–9104 (2002).
19. R. H. Somani, L. Yang, and B. S. Hsiao, *Physica A*, **304**, 145–157 (2002).
20. L. Yang, R. H. Somani, I. Sics, B. S. Hsiao, R. Kolb, H. Fruitwala, and C. Ong, *Macromolecules*, **37**, 4845–4859 (2004).
21. S. K. Siddiquee, J. W. v. Egmond, and H. H. Winter, *Macromolecules*, **32**, 1167–1174 (1999).
22. N. V. Pogodina, V. P. Lavrenko, S. Srinivas, and, H. H. Winter, *Polymer*, **42**, 9031–9043 (2001).
23. A. Elmoumni, H. H. Winter, A. J. Waddon, and H. Fruitwala, *Macromolecules*, **36**, 6453–6461 (2003).
24. H. Fukushima, Y. Ogino, G. Matsuba, K. Nishida, and T. Kanaya, *Polymer*, **46**, 1878–1885 (2005).
25. Y. Ogino, H. Fukushima, G. Matsuba, N. Takahashi, K. Nishida, and T. Kanaya, *Polymer*, **47**, 5669–5677 (2006).
26. Y. Ogino, H. Fukushima, G. Matsuba, K. Nishida, and T. Kanaya, *Macromolecules*, **39**, 7617–7642 (2006).
27. G. Kumaraswamy, A. M. Issaian, and J. A. Kornfield, *Macromolecules*, **32**, 7537–7547 (1999).
28. G. Kumaraswamy, R. K. Verma, A. M. Issaian, P. Wang, J. A. Kornfield, F. Yeh, B. S. Hsiao, and R. H. Olley, *Polymer*, **41**, 8934–8940 (2000).
29. G. Kumaraswamy, J. A. Kornfield, F. Yeh, and B. S. Hsiao, *Macromolecules*, **35**, 1762–1769 (2002).
30. C. H. Sherwood, F. P. Price, and R. S. Stein, *J. Polym. Sci. Polym. Symp.*, **63**, 77–94 (1978).
31. R. R. Lagasse and B. Maxwell, *Polym. Eng. Sci.*, **16**, 189–203 (1976).
32. S. Vleeshouwers and H. Meijer, *Rheol. Acta*, **35**, 391–399 (1996).
33. A. Keller and J. A. Odell, *Colloid Polym. Sci.*, **263**, 181–201 (1985).
34. M. Seki, D. W. Thurman, J. P. Oberhauser, and J. Kornfield, *Macromolecules*, **35**, 2583–2594 (2002).
35. Z. Bashir, M. J. Hill, and A. Keller, *J. Mater. Sci. Lett.*, **5**, 876–878 (1986).
36. C. Zhang, H. Hu, D. Wang, S. Yang, C. C. Han, *Polymer*, **46**, 8157–8161 (2005).
37. J. Schelten, G. D. Wignall, and D. G. H. Ballard, *Polymer*, **15**, 682–685 (1974).
38. J. Schelten, G. D. Wignall, D. G. H. Ballard, and W. Schmatz, *Colloid Polym. Sci.*, **252**, 749–752 (1974).
39. J. Schelten, D. G. H. Ballard, G. D. Wignall, G. Longman, and W. Schmatz, *Polymer*, **17**, 751–757 (1976).
40. T. Fujisawa, K. Inoue, T. Oka, H. Iwamoto, T. Uruga, T. Kumasaka, Y. Inoko, N. Yagi, M. Yamamoto, and T. Ueki, *J. Appl. Cryst.*, **33**, 797–800 (2000).
41. Y. Ito, M. Imai, and S. Takahashi, *Physica B*, **213/214**, 889–891 (1995).
42. T. Otomo, M. Furusaka, S. Satoh, S. Itoh, T. Adachi, S. Shimizu, and M. Takeda, *J. Phys. Chem. Solids*, **60**, 1579–1582 (1999).
43. R. C. Oberthuer, *Makromol. Chem.*, **179**, 2693–2706 (1978).
44. P. Smith, P. J. Lemstra, B. Kalb, and A. J. Pennings, *Polym. Bull.*, **1**, 733–736 (1979).
45. P. Smith and P. J. Lemstra, *J. Mater. Sci.*, **15**, 505–514 (1980).
46. P. J. Lemstra, N. A. J. M. v. Aerle, and C. W. M. Bastiaansen, *Polym. J.*, **19**, 85–98 (1987).
47. C. W. M. Bastiaansen, *J. Polym. Sci. Polym. Phys.*, **28**, 1475–1482 (1990).
48. B. S. Hsiao, A. D. Kennedy, R. A. Leach, B. Chu, and P. Hemey, *J. Appl. Cryst.*, **30**, 1084–1095 (1997).
49. S. Ran, C. Burger, D. Feng, X. Zong, S. Crug, B. Chu, B. S. Hsiao, R. A. Bubeck, K. Yabuki, Y. Teramoto, D. C. Martin, M. A. Johnson, and P. M. Cunniff, *Macromolecules*, **35**, 433–439 (2002).
50. R. H. Somani, L. Yang, L. Zhu, and B. S. Hsiao, *Polymer*, **46**, 8587–8623 (2005).
51. L. Mandelkern, *Crystallization of Polymers — Kinetics and Mechanisms*, Cambridge University Press, Cambridge, 2002.
52. M. Doi and S. F. Edwards, *The Theory of Polymer Dynamics*, Clarendon Press, Oxford, 1986.

53. V. R. Raju, G. G. Smith, G. Martin, J. R. Knox, and W. W. Graessley, *J. Polym. Sci. Polym. Phys. Ed.*, **17**, 1183–1195 (1979).
54. G. Strobl, *The Physics of Polymers — Concepts for Understanding their Structures and Behavior*, Springer, Berlin, 1996.
55. M. H. Kim, P. J. Phillips, and J. S. Lin, *J. Polym. Sci. B Polym. Phys.*, **38**, 154–170 (2000).
56. J. Wegner and P. J. Phillips, *Polymer*, **42**, 8999–9013 (2001).
57. J. Brandup, E. H. Immergu, and E. A. Grulke (eds.), *Polymer Handbook*, Wiley Interscience, New York, 1999.
58. G. E. Bacon, *Neutron Diffraction*, Clarendon Press, Oxford, 1975.
59. M. Shibayama, S. Nomura, T. Hashimoto, and E. L. Thomas, *J. Appl. Phys.*, **66**, 4188–4197 (1989).
60. M. Nakano, H. Matsuoka, H. Yamaoka, A. Roppe, and D. Richter, *Macromolecules*, **32**, 697–703 (1999).
61. T. Kanaya, Y. Takayama, Y. Ogino, G. Matsuba, and K. Nishida, in: *Progress of Understanding of Polymer Crystallization, Lecture Notes in Physics*, G. Reiter and G. Strobl (eds.), Springer, Berlin, pp. 91–99, 2006.

Chapter 20

Template Crystallization of Ultrahigh Molecular Weight Polypropylene Induced by Chain Orientation of Cocrystallized Ultrahigh Molecular Weight Polyethylene

Rockliffe St. J. Manley[1] and Thein Kyu[2]

20.1 INTRODUCTION

Polyolefins, notably polyethylene (PE) and polypropylene (PP), are the largest commodity thermoplastics in the market place (1–5). It is therefore natural that interest in these blends of polyolefins has increased over the years. In the literature, the blends of PE and PP are known to be immiscible, exhibiting a two-phase morphology composed of spherulitic morphology of both constituents (6–9). Needless to say, the properties and end uses of these polyolefin blends are critically dependent on the nature and arrangement of the two-phase structures that in turn are influenced strongly by the preparation conditions. Several aspects of polyolefin

[1]Department of Chemistry, McGill University, Montreal, Quebec, Canada H3A 2A7
[2]Department of Polymer Engineering, University of Akron, Akron, OH 44325-0301, USA

Polyolefin Composites, Edited by Domasius Nwabunma and Thein Kyu

blends such as crystal1ization, phase diagrams, morphological features, mechanical properties, among others have been investigated using blends prepared by solution mixing, melt blending, or melting pressing of the premixed sample (4,5). These methods of sample preparation normally have led to the development of phase-separated structures as well as spherulitic morphology of the constituents.

Among various types of polyethylene, ultrahigh molecular weight polyethylene (UHMWPE) is attractive due to its unique properties such as ultrahigh modulus and strength. The molecular weight of UHMWPE is extremely high, which prevents the melt processability by the conventional extrusion or injection molding. Consequently, its application is limited to compression molding and/or solid-state extrusion (5). However, the viscosity of UHMWPE can be lowered by mixing with decalin (a high boiling solvent) or paraffin oil (10–16). UHMWPE can form gels in the presence of solvent and this has facilitated gel spinning to afford ultrahigh strength and modulus fibers. Consequently, gelation crystallization has received immense interest.

Another idea that deserves attention is the dilution of UHMWPE with conventional polyethylene to lower the melt viscosity of the blends (17,18), thereby improving the melt processability that eventually improves the mechanical and physical properties of conventional PE. This concept is similar to industrial practice, that is, many polyolefin manufacturers have overcome the problem faced when using high viscosity of linear low density polyethylene by melt blending with conventional low density polyethylene. The miscibility among various polyethylene analogs becomes a critical issue because of the crystallization behavior of one or both constituents (19–21). Four scenarios can be envisaged. The crystalline polymer pair may be miscible in their melt state and also form cocrystals upon solidification (crystallization). An example of such a case is the blend of high density polyethylene (HDPE) and linear low density polyethylene (LLDPE) blends. A second possibility is that the binary crystalline polymers may be miscible in the melt (amorphous) state, but separate crystals are formed during solidification. The blends of poly(ethylene terephthalate)/poly(butylene terephthalate) and LLDPE/LDPE (low density polyethylene) fall into this category (19,20). The third category is the case where the two components are not miscible in the melt, but they may form cocrystals, that is, one crystal component acts like a nucleus so that the other can crystallize epitaxially on it. The last is when the polymer pair is not miscible in the amorphous state and forms separate crystals in the solid state. Recently, theoretical treatments for phase equilibria of binary crystalline polymer blends have been introduced by Matkar and Kyu (22,23) by incorporating the crystal–amorphous, amorphous–crystal, and crystal–crystal interactions in addition to the Flory–Huggins interaction parameters that describes the amorphous–amorphous segmental interactions (7,8).

In the case of ultrahigh molecular weight polyolefin blends including UHMWPE and UHMWPP (ultrahigh molecular weight polypropylene), there is virtually no miscibility between the constituents (24–26). Moreover, the conventional method of blend preparation, that is, melt blending, is not feasible because of the very high viscosities that inhibit the melt flow, even at very high temperatures. For instance, UHMWPE powder fusion is only partial in compression-molding experiments at

temperatures as high as 210°C. Hence, these blends have to be prepared by the method of gelation/crystallization from dilute solution (14).

In view of their inherent immiscibility, it is appropriate to regard them as polyolefin composites that give a very fine dispersion of each component in the continuum of the other. The method involves quenching a dilute solution of UHMW polyolefins from a high temperature (usually about 150–160°C) to 0°C. Upon evaporation of the solvent, the polyolefin gels form a dry film, having lamellar single crystal type morphology with remarkable drawability. The purpose of the work to be discussed here was to investigate the *in situ* crystallization of the constituents in gelation crystallized UHMWPE/UHMWPP mixtures. It will be seen that *in situ* template crystallization of UHMWPP is induced by the chain orientation of gelation crystallized UHMWPE.

20.2 MATERIALS AND METHODS

20.2.1 Sample Preparation

The polyethylene sample used was ultrahigh molecular weight polyethylene (Hercules 1900 resin; $M_w = 6 \times 10^6$). The UHMWPP used was isotactic type supplied by Hercules Inc. under the trade name Profax 786223. The nominal intrinsic viscosity was 16.8 dl g^{-1} that corresponds to a molecular weight (M_W) of approximately 3.4×10^6 as estimated from the viscosity–molecular weight relation of Kinsinger et al. (15). Decalin, the common solvent, was used without further purification. Irganox-l076 Ciba-Geigy Company) was added as an antioxidant (0.5 w/w of polymer).

Dry gel films of pure PP were produced by a method similar to that of Cannon (27). The mixture of polymer, solvent, and antioxidant (containing 1% w/v of polymer) was degassed for 1 h under vacuum. The solution was prepared by refluxing under nitrogen with vigorous stirring at close to the solvent boiling temperature (185–190°C) for 45 min. The hot solution was transferred to an open beaker maintained at 90°C. The clear solution was stirred with a stainless steel spatula until the onset of gelation, as detected by a sudden increase in solution viscosity. At this point stirring was stopped, the heat was turned off, and the solution was allowed to cool slowly to room temperature. Within a few hours the solution turned turbid and the gel thickened and shrank while expelling some solvent by syneresis, and subsequently it was pipetted out. Finally the gel was pressed between filter papers on a laboratory press at 300 psi for half an hour. At this stage, a clear film approximately 0.45–1 mm in thickness was obtained. The remaining solvent was allowed to evaporate in an air current for several weeks.

Gelation crystallized samples of pure PE and blends of PE/PP were prepared by following the procedure described by Matsuo and Manley (14), with minor modification. The polymer was dissolved in decalin by vigorous mechanical stirring at 165–175°C for 30–40 min under nitrogen circulation. The hot solution (the total polymer concentration ranging from 0.4% to 1.0% w/v) was then

transferred to an aluminum tray held at 0°C in an ice water bath. The initially clear solution turned turbid and formed a gel on standing, indicating the onset of gelation. Decalin expelled through syneresis was pipetted out, and the remaining decalin was allowed to evaporate under air current in a laboratory fume hood for several weeks. The dried gel film was then placed in ethanol to remove the residual decalin, if any.

The average thickness of the dry film is 0.3–1.0 mm. The thickness of the stacked gelation-crystallized UHMWPE films by wide-angle X-ray diffraction (WAXD) and small-angle X-ray scattering (SAXS) experiments were about 300 μm, but a single dry gel film having a thickness of 10 μm was used for small-angle light scattering (SALS) and optical microscopic investigations (28, 29).

20.2.2 Characterization

WAXD pictures were taken using a 12-kW Rigaku X-ray generator operated at 40 kV and 150 mA. SAXS isointensity contours were acquired on the Oak Ridge National Laboratory (ORNL) 10-m SAXS camera equipped with a two-dimensional position-sensitive camera having a detector area of 20 cm × 20 cm. The sample-to-detector distance was fixed at 5.126 m to cover the magnitude of scattering vector, $\mathbf{q}$, in the range of $\mathbf{q} = 0.008$–$0.10\ \text{A}^{-1}$, where $\mathbf{q} = (4\pi/\lambda)\sin\theta/2$ with θ being the scattering angle and λ the wavelength of the incident X-rays.

SALS pictures under various polarization geometries were photographed using a Polaroid camera (Land film holder 545). The parallel polarization is called V_v for vertical polarizer with vertical analyzer or H_h for the case where both polarizers are in the horizontal directions. On the same token, the cross-polarization is termed as H_v to signify the horizontal polarizer with the vertical analyzer. A 2-mW He–Ne laser with the wavelength of 632.8 nm was used as a light source. The morphology of recrystallized UHMWPE films was characterized using a Leitz microscope (Laborlux 12 Pol). Polarized microscope pictures were taken under the cross-polarizers at a magnification of 400 times (28, 29).

The crystallization and melting behavior of the gelation-crystallized ultrahigh molecular weight polyolefin films were analyzed by means of differential scanning calorimetry (DSC) using a DuPont calorimeter (Model 910) equipped with a thermal analyzer (DuPont 9900). An indium standard was used for temperature calibration. A sample of approximately 10 mg was encapsulated in an aluminum pan. The DSC scans were undertaken under nitrogen circulation at a rate of $10°\text{C min}^{-1}$ unless indicated otherwise.

Densities were measured by the density gradient method using carbon tetrachloride and *p*-xylene as a mixed solvent. Prior to measurement, the samples were ultrasonicated in one of the solvents to remove any bubbles adhering to the film surface (24).

Dynamic mechanical properties were studied using a Rheovibron spectrometer (DDV-IIc, Tokyo Baldwin Co., Japan) at 110 Hz unless indicated otherwise. The experiments were performed in the temperature range of −160°C to softening point

of the samples at a heating rate of about 1°C min^{-1}. The softening point is reached when a constant tension on the sample cannot be sustained for the dynamic measurements. The onset of softening occurs at a few degrees below the melting transition temperature.

20.3 RESULTS AND DISCUSSION

20.3.1 Thermal Characterization of Melting Transitions of Gelation-Crystallized UHMW Polyolefins

Melting transition of gelation-crystallized UHMWPE was determined by means of DSC at a rate of 10°C min^{-1}. As shown in Fig. 20.1, the melting temperature peak of the dry gel UHMWPE film is located in the vicinity of 145°C. In the cooling run, the crystallization exotherm appears at about 115°C. Upon recrystallization from the melt in the second heating cycle, the melting peak is reduced to about 140°C, while the area under the peak declines relative to the gel film. These observations suggest reduction in crystal perfection or a possible structural change or a combination of both mechanisms during recrystallization from the melt.

As depicted in Fig. 20.2, the DSC scan of the gelation-crystallized 50/50 UHMWPE/UHMWPP blends reveals two distinct peaks in the intermediate blends corresponding to those of their constituents. The melting peak of UHMWPP shows a trend of slight depression from 165 to 160°C with increasing UHMWPE content up

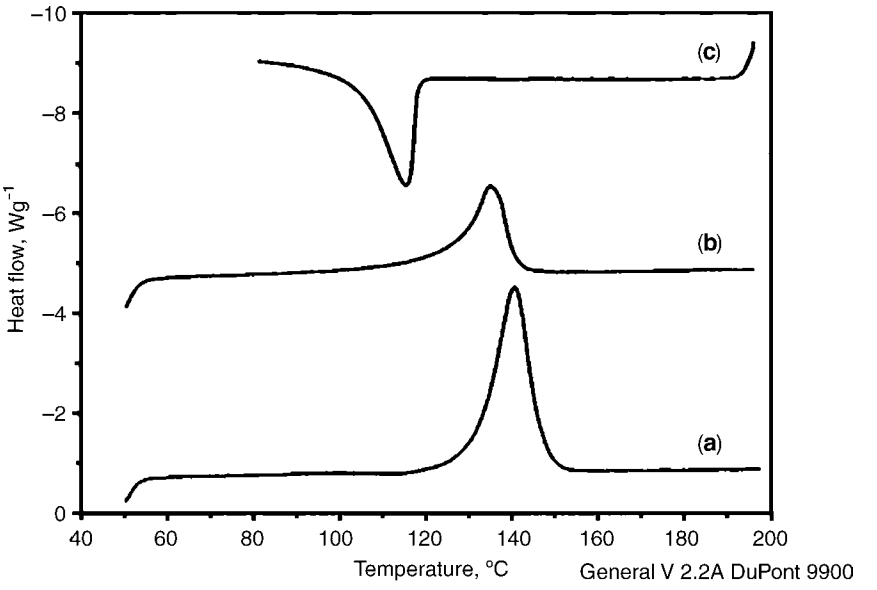

Figure 20.1 DSC thermograms of gel films of pure UHMWPE during (**a**) first heating, (**b**) second heating, and (**c**) cooling cycles. The heating and cooling rates were 10°C min^{-1}.

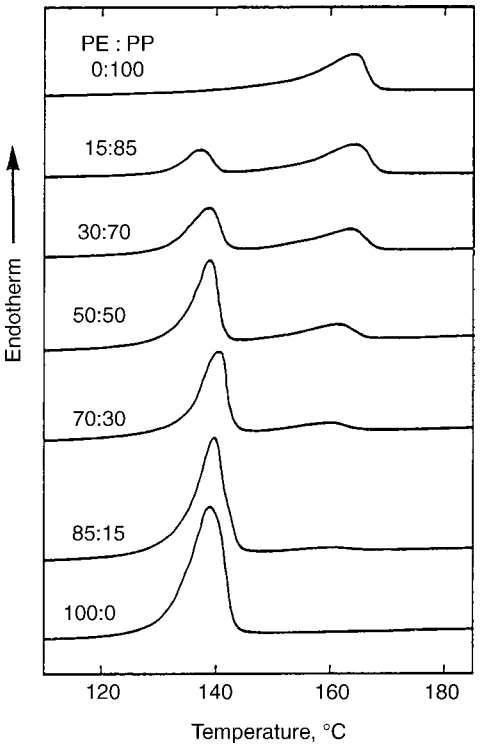

Figure 20.2 DSC scans of the UHMWPE, UHMWPP, and their gelation-crystallized blends as a function of blend composition, showing a slight depression of the PP crystals suggestive of little or no miscibility of the pair.

to the 70:30 ratio. However, the melting temperature of UHMWPE shows little or no change. The slight depression of UHMWPP melting due to the incorporation of UHMWPE suggests partial miscibility of the pair in the gelation crystallized film, that is, in the dry gel state. Upon recrystallization from the melt, the two melting peaks of UHMWPE and UHMWPP no longer change with composition, implying the immiscibility character of the pair in the solid crystalline state. The observed slight depression of the UHMWPE melting peaks with composition in the gelation-crystallized blends is seemingly lost in the melt-recrystallized UHMWPE/UHMWPP samples.

To further verify the partial miscibility of the gelation-crystallized UHMWPE/UHMWPP blends, dynamic mechanical experiments have been conducted as a function of blend compositions of the dry gel films of UHMWPE/UHMWPP. As shown in Fig. 20.3, the loss tangent of the neat UHMWPE at 110 Hz shows three distinct peaks corresponding to the α, β, and γ relaxations in the descending order of temperature (5, 30, 31). The highest temperature α peak is assigned to the crystalline phase, but occasionally two overlapping α peaks, called α_1 and α_2, are observed,

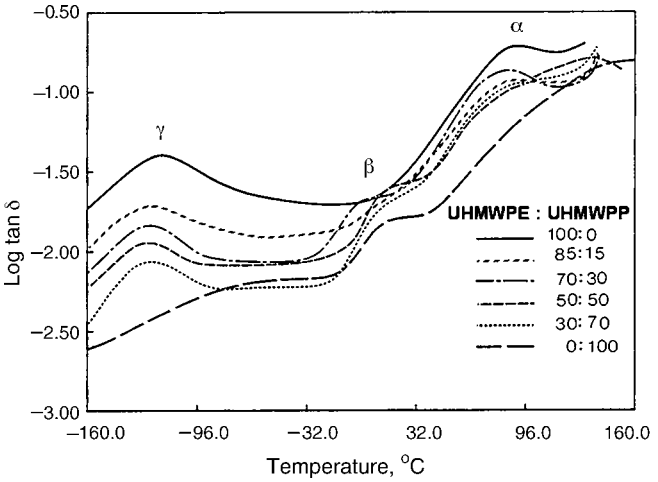

Figure 20.3 Dynamic mechanical studies of gelation-crystallized UWMWPE/UHMWPP as a function of blend ratios, showing multiple tan δ relaxation peaks in which the broad β peak exhibits a systematic movement with composition.

which may be attributed to the intercrystalline grain boundary relaxation and intracrystalline chain motions, respectively (5). The lowest temperature γ peak is generally assigned to the local mode motion such as crankshaft motion of the CH_2 bonds (30, 31). The assignment of β peak is controversial; possibly this may be associated with the glass transition temperature of interlamellar amorphous chains of PE. The presence of the crystalline phase, especially high crystallinity polyethylene, makes the present assignment ambiguous as the amorphous chains are highly constrained between the successive lamellae. In the case of pure UHMWPP, there are two distinct peaks called α and β relaxation. The former is associated with the crystalline phase, whereas the latter is attributed unambiguously to the glass transition peak of PP (30, 31). Upon varying the blend concentration, the crystalline α and γ peaks remain fairly unchanged, but there is a definitive movement of the β peak. If the β peak were truly associated with the glass transition temperature of PE and PP, the systematic movement of the observed single β peak would indicate possible miscibility between the PE and PP constituents at least in the dry gel form. In view of the broad nature the β peaks, the gelation crystallized PE/PP may be characterized as a partially miscible blend.

It should be pointed out that these dry gel films of the UHMWPE/UHMWPP blends at all compositions were optically clear and polarized optical microscopy showed no spherulitic structure. The transparent appearance of these gel films implies that despite immiscibility between the two polyolefins, this method of blend preparation affords intimate mixing giving rise to a very fine dispersion of respective phase domains, or the emerged crystalline structures would have unique characteristics such as single crystal mats with the crystal chain axis (c-axis), orienting perpendicular to the film surface, that is, homeotropic alignment of the chains,

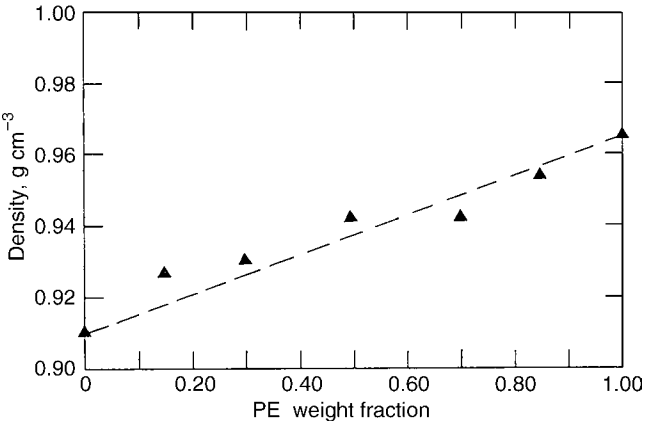

Figure 20.4 Change of bulk densities as a function of various UHMWPE/UHMWPP blend compositions.

thereby pointing toward the direction of the viewer so that the film may appear transparent. This behavior may be contrasted with the blends of conventional melt-crystallized PE/PP that show distinctive phase domains (e.g., spherulitic PP islands in the PE matrix or vice versa) with the spherulites having diameters of several micrometers (23).

The noninteractive nature of this polyolefin pair is also evident from Fig. 20.4 in which the variation of the density with UHMWPE composition is shown. The density increases linearly with increasing UHMWPE concentration. Once again, the existence of specific interaction between PE and PP would have resulted in the existence of nonzero ''excess volume of mixing'' (either positive or negative), giving rise to nonlinear density variation with PE composition. Teh (32) also found from DSC and density measurements that no identifiable specific interaction exists in the melt-crystallized spherulitic PE/PP blend. In view of the immiscible nature of the blends of the UHMWPE/UHMWPP, we shall regard this pair as polyolefin composites. While the above DSC and density investigations afford useful information with regard to the immiscibility character of the UHMW polyolefin blends, these techniques are incapable of correlating with the internal domain structure or crystalline morphology. This situation has led to the subsequent investigations of domain morphology and crystalline structures using X-ray and light scattering.

20.3.2 Structure of Gelation-Crystallized UHMWPE

SAXS scans of gelation crystallized UHMWPE films after drying were acquired from the through view (i.e., normal to the film surface) and the edge view (i.e., from the edge of the stacked films). As can be seen in Fig. 20.5, there are appreciable differences in the scattering patterns along the through and edge views.

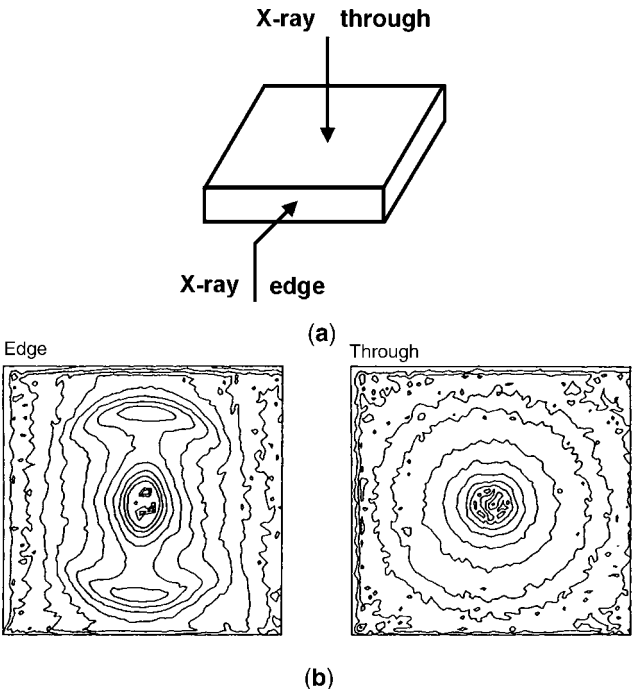

Figure 20.5 (**a**) Direction of incident X-rays with respect to the through and edge view geometries of the gel film, and (**b**) two-dimensional SAXS isointensity contour plots for the edge and through views of the dry gelation-crystallized UHMWPE films.

The isointensity contour in the through view reveals isotropic rings suggestive of random orientation of the crystals. In the edge view, a twofold symmetrical SAXS pattern emerges that indicates the development of the oriented lamellar stack structure during gelation crystallization of UHMWPE (28, 29).

Figure 20.6 shows a plot of SAXS intensity versus scattering wavenumber q. A distinct SAXS intensity maximum can be discerned clearly in the edge view, whereas a small shoulder appears in the through view in the vicinity of $q = 0.005\,\text{nm}^{-1}$. The scattered intensity of the former is one order of magnitude greater relative to the latter case. It should be pointed out that this small SAXS peak in the through view could be completely eliminated if there was no external disturbance during the preparation of gel films. This shoulder peak becomes more pronounced if the gels were slightly pressed during gelation crystallization. The long period as estimated from those SAXS peaks is approximately 12 nm.

The same dry gel films were further investigated by means of wide-angle X-ray diffraction. As can be seen in Fig. 20.7, the WAXD picture in the through view is isotropic without any indication of crystal orientation. However, in the edge view, the (110) and (200) arcs can be discerned in the equatorial direction indicating the preferential crystal c-axis orientation normal to the film surface. The WAXD results

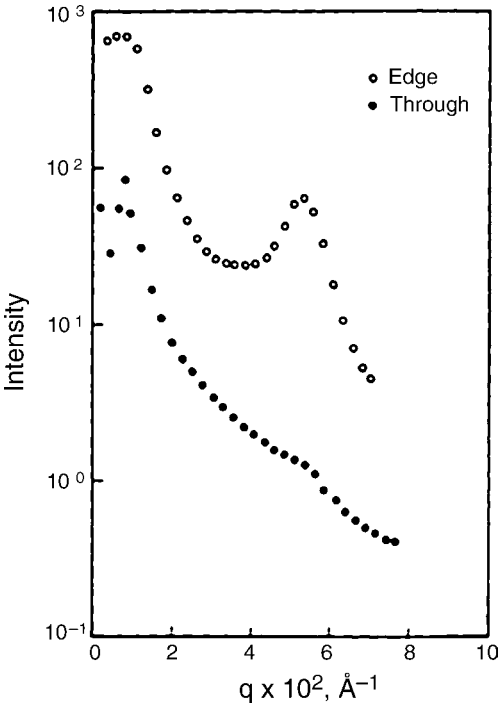

Figure 20.6 The corresponding SAXS scans of the dry gel UHMWPE film showing the distinct peak in the edge view corresponding to the lamellar long period, and a minor shoulder in the through view.

in combination with the aforementioned SAXS patterns of the dry gel films strongly indicate that the structure of the gelation crystallized film is a reminiscent of single crystal mats. Such preferential orientation of PE chains in the gelation-crystallized films is consistent with the reports by Matsuo and Manley (14) and by others (33–36).

Once it is melted at 200°C, the oriented single-crystal structure disappeared completely. Instead, a well-grown truncated spherulitic structure developed upon cooling from the melt temperature of 200°C. Fig. 20.8 shows the development of

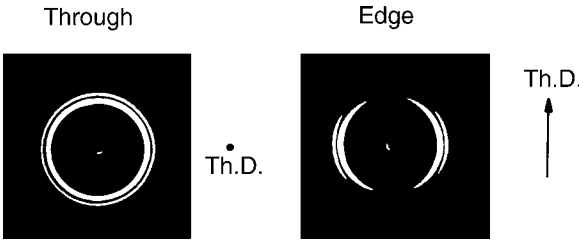

Figure 20.7 Wide-angle X-ray diffraction pictures of gelation-crystallized UHMWPE dry films (**a**) in the through view and (**b**) along the edge view, showing the oriented (110) and (200) arcs.

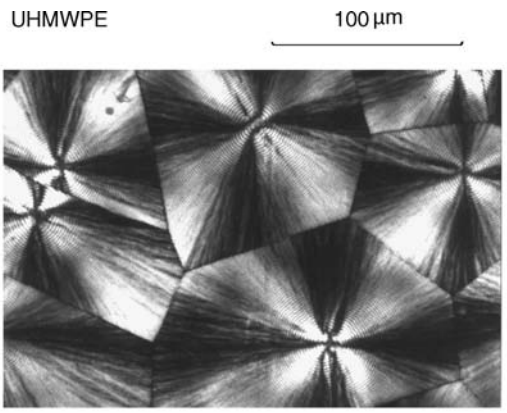

Figure 20.8 The development of banded spherulite structures of the gelation-crystallized UHMWPE films after recrystallization from the melt at 200°C.

well-defined banded spherulites showing Maltese cross-pattern with multiple concentric rings. The spherulitic sizes range from 80 to 200 μm in diameter. The emergence of such large spherulitic morphology is unusual for the melt-crystallized polyethylene, in general, and for the melt-crystallized UHMWPE, in particular. One possible account, although by means of a proof, is that the chain entanglement may be significantly reduced in the gelation-crystallized sample as compared with the melt-crystallized UHMWPE, which probably supports the development of larger spherulites.

In the corresponding SALS studies, the four-lobe scattering and two-lobe scattering profiles can be discerned in the H_v and V_v or H_h configurations, respectively. The four arcs were developed in the wide-angle light scattering under the H_v polarization, while two very diffuse arc patterns can be seen in the vertical direction of the V_v geometry, and the two arcs in the horizontal direction of the H_h configuration are too diffuse to be seen clearly (Fig. 20.9). These arcs correspond to the periodicity of the concentric fringes of the optical micrographs of spherulites shown in Fig. 20.8. The present arcs imply the development of lamellar twisting from a common center of the spherulite.

20.3.3 Characterization of Gelation-Crystallized UHMWPP

The crystalline structure of gelation-crystallized UHMWPP was investigated by means of the WAXD technique in the through and edge views. As can be seen in Fig. 20.10, the (110), (040), (130), and (060) Debye–Scherrer rings are discernible in the through view of the dry gel UHMWPP film (23). Unlike the UHMWPE gel film, the edge view reveals only the unoriented Debye–Scherrer rings corresponding to these crystallographic planes. On the contrary, no preferential orientation was

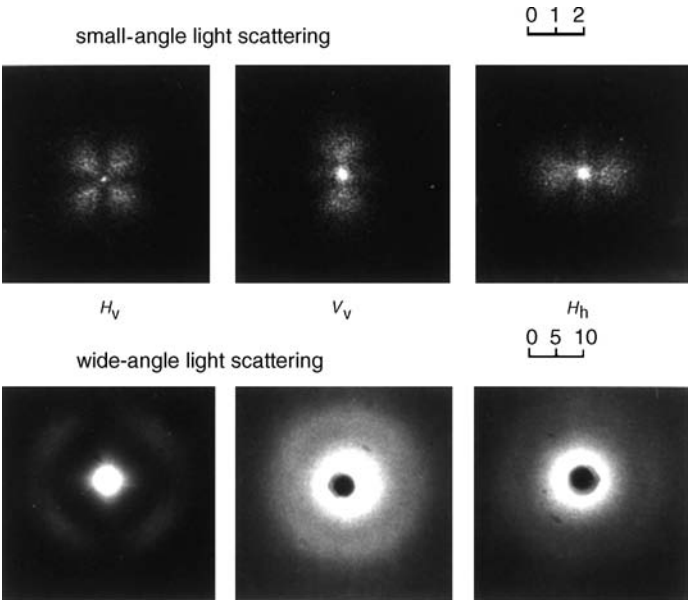

Figure 20.9 Small-angle and wide-angle light scattering patterns of the melt-crystallized UHMWPE gel films under the H_v, V_v, and H_h polarizations.

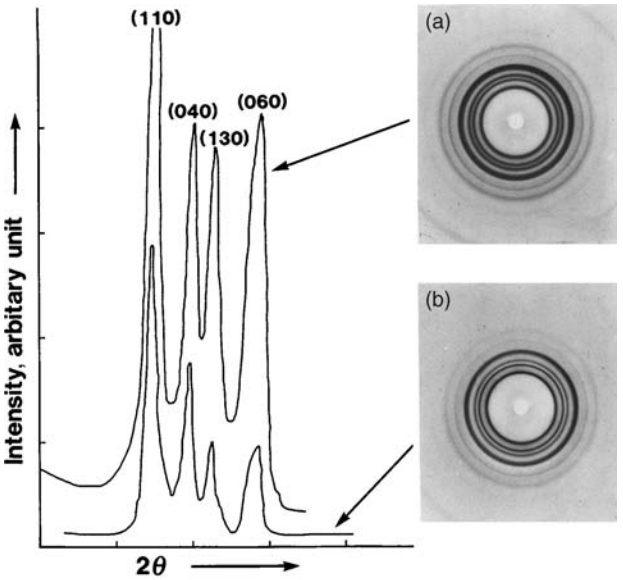

Figure 20.10 Wide-angle X-ray diffraction patterns of gelation-crystallized UHMWPP dry films (**a**) in the through view and (**b**) along the edge view, showing no preferred crystal orientation in both through and edge directions.

observed for pure UHMWPP gel films in both through and edge views, which implies that the PP crystallites are randomly oriented. Cannon (27) also observed that crystallites of the pure PP gel films did not show preferred orientation.

20.3.4 *In Situ* Template Crystallization of Gelation-Crystallized UHMWPE–UHMWPP Blends

In Fig. 20.11, wide-angle X-ray diffraction patterns of the 50:50 UHMWPE/UHMWPP dry gel film are shown as a function of the viewing angles. The WAXD patterns in the through view reveal random crystallite orientation of both PE and PP crystals in the plane of the film (Fig. 20.11a), whereas the preferential orientations of the (110), (200), and (020) diffraction peaks of UHMWPE crystallites are evident in the edge view (Fig. 20.11b). The striking observation is that the (040) and (060) planes of UHMWPP exhibit arcs in the same equatorial direction (Fig. 20.11b) as in the case of the (110) and (200) peaks of UHMWPE in the blends showing oriented arcs. The WAXD result for UHMWPE is expected because pure PE gel is known to form a stacked lamellar-type structure with the crystal *c*-axis oriented perpendicular to the film surface. However, as for PP this orientational feature is unique when compared with the gel of the pure homopolymer PP gel films, which shows no preferential orientation. Analysis of the patterns in Fig. 20.11b shows that the (040) and (060) reflections of PP appear as arcs on the equator, indicating preferred orientation of the crystal *b*-axis parallel to the film surface. However, the (110) and (130) arcs spread more along the Azimuthal direction, so much so that these reflections appear like rings. However, there are two broad arcs in the meridian direction that correspond to the (002) PE crystals and the other belongs to (00ℓ) planes of the PP crystal. In view of the monoclinic nature of the PP unit cell, the c^*-axis of the PP crystals may be oriented perpendicular to the film surface, that is, the crystal *c*-axis may be slightly off from the film thickness direction.

This remarkable observation implies that the PP crystal chains are more or less orientated along the same direction of the orientation of the crystal *c*-axis of the UHMWPE single crystal mats as illustrated schematically in Fig. 20.12. This preferential orientation of the PP chains is probably induced by the oriented PE single crystal acting as templates during gelation crystallization, hereafter called ''*in situ* template crystallization''. The aforementioned crystallization of UHMWPP on the oriented UHMWPE gel template is similar to the work by Hsaio and co-workers (37–39), who reported that the UHMWPE-oriented melt serves as a shish-like template upon which isotactic polypropylene (iPP) kebab grows in their 10/90 UHMWPE/iPP blends. This oriented growth of the shish-kebab structure is possible due to the long-chain nature and therefore the long relaxation time of the UHMWPE melt, despite the immiscibility of the UHMWPE/iPP pair. These authors further investigated the shear-induced crystallization in the 5/95 blends of long-chain atactic polypropylene (aPP) and iPP (40). Although aPP chains are not expected to undergo crystallization, the great length of the aPP chains enhanced nucleation and also expedited the crystallization kinetics of iPP upon shearing the blend just below the equilibrium melting temperature of iPP crystals.

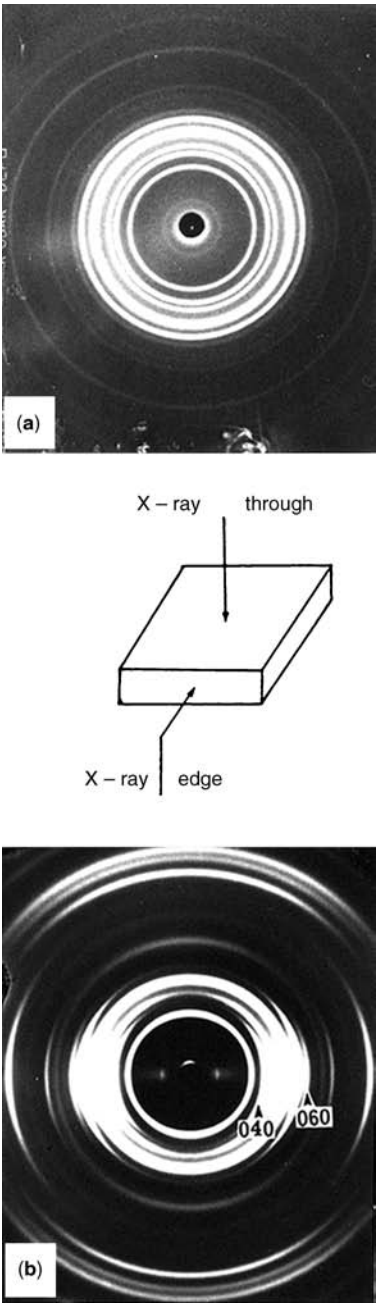

Figure 20.11 Wide-angle X-ray diffraction patterns of a 50:50 UHMWPE/UHMWPP gel film in the (**a**) through and (**b**) edge views, respectively. In the edge view, the observed (040) and (060) arcs of UHMWPP indicated by arrows in (**b**) suggest the template crystallization induced by the oriented UHMWPE lamellar crystals.

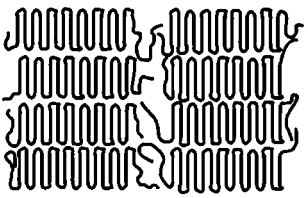

(a) Gelation - crystallized UHMWPE

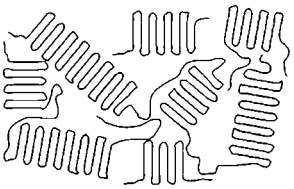

(b) Gelation - crystallized UHMWPP

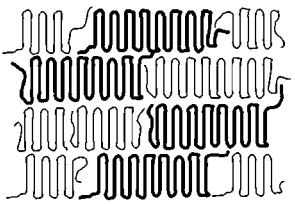

(c) Gelation - crystallized UHMWPE−PP

Figure 20.12 Schematic illustration of gelation-crystallized ultrahigh molecular weight polyolefins: (**a**) the stacked lamellar structures of UHMWPE, (**b**) random orientation of UHMWPP lamellae, and (**c**) oriented lamellae of UHMWPP induced by the chain orientation of the UHMWPE templates in the edge view.

Another possibility is that PP crystallizes faster than PE in their blends at a given elevated crystallization temperature (e.g., close to melting temperature of PE) by virtue of the differences in the supercoolings. However, if the isothermal crystallization of the PP/PE blends were performed from the melt to below 100°C, the trend reverses, that is, the PE chains crystallize faster as compared to that of PP at such low crystallization temperatures. It is thus possible that PP chains, which are rejected to the interlamellar regions of the already developed PE-oriented crystals, can undergo template crystallization on the oriented UHMWPE even in the wet gel state. Figure 20.12 illustrates a pictorial explanation in the edge view as to how UHMWPP gels crystallize epitaxially in the preformed UHMWPE single-crystal mats. As evidenced in the WAXD studies, these gelation-crystallized PE crystals are stacked and form single crystal mats with their *c*-axis in the direction of the film thickness, and thus the PP chains can undergo crystallization on the surface of the existing orientated PE crystals, which serves as a template (Fig. 20.12). The reason why PP

crystal chains oriented in the same direction as PE crystal chains may be attributed to the *in situ* template crystallization effect reported by Hsaio et al. (37–39). The aforementioned observations are analogous to the strain-induced crystallization of the UHMWPE/conventional linear PE composites containing extremely low concentration of UHMWPE (< 1 wt%) in which the linear chain PE kebabs grow on the UHMWPE shish during and/or after cessation of shear (41). The molecular weight of UHMWPE is an order of magnitude higher than that of the linear PE, and thus its relaxation of time is much slower. Upon shearing, the oriented UHMWPE chains serve as nucleating cites (e.g., shish) for PE kebabs to grow.

Once the gelation-cocrystallized UHMWPE/UHMWPP single-crystal mats are melted and recrystallized from the melt, spherulitic morphology usually develops. At a high crystallization temperature or small undercooling, the PP spherulite will develop first in which the PE crystallization occurs epitaxially at the interspherulitic regions or interlamellar regions. Given the immiscibility nature of these two polymers, it is likely that UHMWPE would crystallize at the interstitial boundaries of UHMWPP spherulites. This scenario can be expected even if the concentration of UHMWPP is minor, for example, 10 wt%. It may be speculated that the UHMWPP spherulites will fill the whole sample space first, and then UHMWPE will crystallize within the open-interlamellar regions of these UHMWPP spherulites. A similar observation has been made by Stein and coworkers in the crystallization of HDPE/LLDPE and HDPE/LDPE blends from the melt (19–21). From the SAXS and WAXD experiments, they found that the HDPE and LLDPE cocrystallized in all blend compositions. However, in the case of HDPE/LDPE, the skeleton of HDPE spherulite forms first and subsequently the LDPE crystallizes within the interlamellar as well as interspherulitic regions, showing separate crystallization.

The present template crystallization seems to be a more general phenomenon that shares a common ground to surface-induced epitaxial crystallization reported by Lotz et al. (42, 43) and Liu et al. (44) on polycaprolactone on the oriented PE melt template, as well as by Minus et al. (45) on the polyvinyl alcohol/single-wall carbon nanotube (SWCNT) nanofibrils. Recent numerical studies by Pakula (46) as well as by Bashnagel and Binder (47) revealed that even a neutral substrate could induce orientational ordering of polymer chains near the substrate surface. The segmental mobility of polymer chains can be enhanced in the parallel direction to the substrate, and vice versa it is reduced in the perpendicular direction of the substrate. Petra and Muthukumar found that polymer chains, when approaching the surface, usually follow the surface pattern if the surface interaction were sufficiently strong (48, 49).

The soft epitaxy of the carbon nanotube (CNT)/PE nanocomposite was demonstrated by Li and coworkers who revealed that the oriented CNT upon shearing acts like a shish overgrown by the PE kebabs (50, 51). Their finding is conceptually similar to the templating effect shown in the present work of UHMWPE/UHMWPP system as well as in the UHMWPE/iPP shish-kebab by Hsaio et al. (37–39) and also the UHMWPE/linear PE nanocomposites by Kanaya et al. (41). The hybrid shish-kebab of the CNT/PE system along with UHMWPE/conventional PP or PE has become a vibrant field in the nanocomposite area, but their physical (e.g., electrical, optical, or mechanical) performance is yet to be explored. Suspension or solution

blending of CNT/polyolefins suffices to give good dispersion of CNT at a much larger scales, but the melt blending appears to be more difficult since it has to be carried out at high temperatures and high shear-rate conditions (52). The gelation crystallization of UHMWPE/multiwall carbon nanotubes (MWCNT) has also emerged as a promising route for achieving microcomposites to nanocomposites (53). Oriented template crystallization has also been observed in the sulfuric acid doped SWCNT systems in which highly oriented solvent molecules form cylindrical shells rapping around the CNT fibers (54). Recently, templated crystallization has been observed in the injection molding of the SWCNT/poly(butylene terephthalate) composite (55). It may be envisaged that the template crystallization induced by the substrate or surfaces shares a common ground with the soft epitaxy hitherto reported.

20.4 CONCLUSIONS

It has been shown that gelation crystallization of UHMWPE exhibited the formation of single-crystal mats with the crystal *c*-axis orientation perpendicular to the film surface, whereas the dry gel films of UHMWPP showed no preferential orientation. However, when UHMWPP was gelation crystallized *in situ* with UHMWPE in their 50:50 blends, the PP crystal chains were found to orient along the same direction of the *c*-axis of the oriented UHMWPE single-crystal mats. A possible reason for the PP crystal chains to orient in the same direction as that of the PE crystal chains may be attributed to ''*in situ* template crystallization'' of oriented PP chains induced by the orientated PE single crystal acting as a template. The present template crystallization of the gelation-cocrystallized UHMWPE/UHMWPP shares a common ground to that of the development of the shish-kebab nanocomposite structure of UHMWPE/PE as well as the hybrid shish-kebab structure of the CNT/PE nanocomposites systems. The soft epitaxy induced by the substrate or surfaces including the template crystallization has become a well-accepted phenomenon, which presents new opportunity for development of unique composite structures in coming years.

ACKNOWLEDGMENT

This work is dedicated to late Dr. Soroj K. Roy without whose contribution the present paper would not have materialized.

NOMENCLATURES

UHMWPE	Ultrahigh molecular weight polyethylene
UHMWPP	Ultrahigh molecular weight polypropylene
HDPE	High density polyethylene
LDPE	Low density polyethylene
LLDPE	Linear low density polyethylene
WAXD	Wide-angle X-ray diffraction

SAXS	Small-angle X-ray scattering
SALS	Small-angle light scattering
H_v	Horizontal polarizer with vertical analyzer
V_v	Vertical polarizer with vertical analyzer
H_h	Horizontal polarizer with horizontal analyzer
DSC	Differential scanning calorimetry
q	Scattering wavenumber
θ	Scattering angle
λ	Wavelength of incident X-rays

REFERENCES

1. J. Peterman, *Polypropylene: Structure*, *Blends*, *and Composites*, Chapman & Hall, London 1995.
2. D. J. Lohse and W. W. Graessley, Thermodynamics of polyolefin blends, in: *Polymer Blends. Vol. 1: Formulation*, D. R. Paul and C. B. Bucknall (eds.), Wiley, New York, 2000.
3. K. Harutun (ed.), *Handbook of Polypropylene and Polypropylene Composites*, Marcel Dekker, New York, 2003.
4. J. L. White, *Polyolefins*, Hanser, Munich, 2005.
5. A. E. Zachariades and R. S. Porter (eds.), *The Strength and Stiffness of Polymers*, Marcel Dekker, New York, 1983.
6. J. A. Mason and L. H. Sperling, *Polymer Blends and Composites*, Plenum Press, New York, 1976.
7. D. R. Paul and S. Newman, *Polymer Blends*, Vols. 1 and 2, Academic Press, New York, 1978.
8. O. Olabisi, L. M. Robeson, and M. T. Shaw, *Polymer–Polymer Miscibility*, Academic Press, New York, 1979.
9. S. Krause, *J. Macromol. Sci. Rev. Macromol. Chem.*, **7**, 250 (1972).
10. P. Smith and P. J. Lamstra, *Makromol. Chem.*, **180**, 2983 (1979).
11. P. Smith and P. J. Lamstra, *J. Mater. Sci.*, **15**, 505 (1980).
12. P. Smith and J. A. Pennings, *J. Polym. Sci. Polym. Phys. Ed.*, **15**, 523–540 (1977).
13. P. Smith and R. St. J. Manley, *Macromolecules*, **12**, 483–491 (1979).
14. M. Matsuo and R. St. J. Manley, *Macromolecules*, **15**, 985 (1982).
15. J. B. Kinsinger and R. E. Hughes, *J. Phys. Chem.*, **63**, 2002 (1959).
16. J. C. Wittmann and R. St. J. Manley, *J. Polym. Sci. Polym. Phys. Ed.*, **15**, 1089 (1977).
17. T. Kyu and P. Vadhar, *J. Appl. Polym. Sci.*, **32**, 5575 (1986)
18. P. Vadhar and T. Kyu, *Polym. Eng. Sci.*, **27**, 202 (1987)
19. T. Kyu, S. R. Hu, and R. S. Stein, *J. Polym. Sci. Polym. Phys. Ed.*, **25**, 71 (1987)
20. S. R. Hu, T. Kyu, and R. S. Stein, *J. Polym. Sci. Polym. Phys. Ed.* **25**, 89 (1987)
21. M. Ree, T. Kyu, and R. S. Stein, *J. Polym. Sci. Polym. Phys. Ed.* **25**, 105 (1987)
22. R. A. Matkar and T. Kyu, *J. Phys. Chem. B*, **110**, 12728 (2006)
23. R. A. Matkar and T. Kyu, *J. Phys. Chem. B*, **110**, 16059, (2006)
24. S. K. Roy, PhD dissertation, McGill University, Montreal, Canada, 1986.
25. S. K. Roy, T. Kyu, and R. St. J. Manley, *Macromolecules*, **21**, 499 (1988).
26. S. K. Roy, T. Kyu, and R. St. J. Manley, *Macromolecules*, **21**, 1741 (1988).
27. C. G. Cannon, *Polymer*, **23**, 1123 (1984).
28. T. Kyu, K. Fujita, M. H. Cho, T. Kikutani, and J. S. Lin, *Macromolecules*, **22**, 2238 (1989)
29. M. H. Cho, T. Kyu, J. S. Lin, K. Saijo, and T. Hashimoto, *Polymer*, **33**, 4152 (1992)

30. N. G. McCrum, B. E. Read, and G. Williams, *Anelastic and Dielectric Effects in Polymeric Solids*, Wiley, New York, 1967.
31. I. M. Ward, *Mechanical Properties of Solid Polymers*, 2nd edition, Wiley Interscience, New York, 1983.
32. J. W. Teh, *J. Appl. Polym. Sci.*, **28**, 605 (1983).
33. B. Gross and J. Peterman, *J. Mater. Sci.*, **19**, 105 (1984).
34. R. M. Gohil, *J. Polym. Sci. Polym. Phys. Ed.*, **23**, 1713 (1985).
35. T. Takahashi, H. Mizuno, and E. L. Thomas, *J. Macromol. Sci. Phys. B*, **22**, 425 (1983).
36. Y. Nishio, T. Yamane, and T. Takahashi, *J. Macromol. Sci. Phys. B*, **23**, 17 (1984).
37. D. Dikovsky, G. Marom, C. A. Avila-Ortez, R. H. Somani, and B. S. Hsaio, *Polymer*, **46**, 3096 (2005).
38. B. S. Hsaio, L. Yang, R. H. Somani, C. A. Avila-Orta, L. Zhu, *Phys. Rev. Lett.*, **94**, 117802 (2005).
39. R. H. Somani, L. Yang, B. S. Hsaio, and H. Fruitwala, *J. Macromol. Sci. Phys. B*, **42**, 515 (2003).
40. C. A. Avila-Orta, C. Burger, R. Somani, L. Yang, G. Marom, F. J. Medellin-Rodriguez, and B. S. Hsiao, *Polymer*, **46**, 8859 (2005).
41. Y. Ogino, H. Fukushima, N. Takahashi, G. Matsuba, K. Nishida, and T. Kanaya, *Polymer*, **47**, 5669 (2006).
42. J. C. Wittmann and B. Lotz, *Prog. Polym. Sci.*, **15**, 909 (1990).
43. J. Zhang, D. Yang, A. Thierry, J. C. Wittmann, and B. Lotz., *Macromolecules*, **34**, 6261 (2001).
44. J. Liu, H. Li, S. Yan, Q. Xiao, and J. Petermann, *Colloid Polym. Sci.*, **281**, 601 (2003)
45. M. L. Minus, H. G. Chae, and S. Kumar, *Polymer*, **47**, 3705 (2006).
46. T. Pakula, *J. Chem. Phys.*, **95**, 4685 (1991).
47. J. Bashnagel and K. Binder, *Macromolecules*, **28**, 6808 (1995).
48. D. Petra and M. Muthukumar, *J. Chem. Phys.*, **107**, 9640 (1997).
49. D. Petra and M. Muthukumar, *J. Chem. Phys.*, **109**, 5101 (1998).
50. C. Y. Li, L. Li, W. Cai, S. L. Kodjie, and K. Tenneti, *Adv. Mater.*, **17**, 1198 (2005).
51. L. Li, C. Y. Li, and C. Ni, *J. Am. Chem. Soc.*, **128**, 1692 (2006).
52. M. Moniruzzaman and K. I. Winey, *Macromolecules*, **39**, 5194 (2006).
53. Q. Chen, Y. Bin, and M. Matsuo, *Macromolecules*, **39**, 6528 (2006).
54. W. Zhou, J. E. Fischer, P. A. Heiney, H. Fan, V. A. Davis, M. Pasquali, and R. E. Smalley, *Phys. Rev. B*, **72**, 045440 (2005).
55. M. C. Garcia-Gutierrez, A. Nogles, D. R. Rued, C. Domingo, J. V. Garcia-Ramos, and G. Broza, *Polymer*, **47**, 341 (2006).

Index

Absolute scattered intensity, 356
Acrylic acid, 208
Activation energy, 301
Adsorption–desorption events, 477, 478, 480, 483
AFM, *see* Atomic force microscopy
Agglomerates, 349, 355–358
Alkyl amine, 212
Alkyl ammonium, 215, 220, 230
Aluminum
  alkyl, 209, 219
  bronze, 220
  trihydroxide (ATH), 216, 224
D-Anhydroglucopyranose, 47
Annealing, 557, 559, 562, 563
Ansa-indenyl zirconocene catalysts, 212
Ansa-metallocene catalyst, 232
Antimony trioxide (AO), 277, 279
Average
  amorphous thickness, 348
  crystal thickness, 348
  distance between crystal, 348
  radius of gyration, 356
Avrami
  constant, 325
  equation, 244, 319, 321, 335
  exponent, 319, 321, 322, 331, 342
  Ozawa equation, 320
  Ozawa exponent, 320, 329
  theory, 319, 322, 325, 342

Barrel temperature, 261
Barrier effect, 326, 334
Barrier model mechanism, 302
$BaTiO_3$, 314, 335, 336, 338, 342
Bicyclic olefin, 210
Birefringence, 265
Bowyer and Bader model, 68
Bragg's relation, 254, 352
Bubble-stretching model, 285
Butyl acrylate, 212

Calcium sulfate, 220
ε-Caprolactam monomer, 232
Carbonaceous char, 276
Carbon black, 220, 489, 492, 512
Carbon nanofiber, 220, 525, 530, 547
Carbon nanotubes, 327
Cationic exchange capacity (CEC), 228
Cationic palladium complex, 233
Cetylpyridinium chloride (CPC), 232
Chain
  concentration, 560, 564
  fibrillar crystals, 529
  orientation, 579, 591
  scission, 272
Chemical vapor deposition, 327
Chirality, 524, 532, 535, 536
Clay delamination, 261
Clay–polystyrene nanocomposite, 350
Clostridium, 46
Co-rotating twin screw extruder, 291
CO_2 yield, 239
Coefficient of thermal expansion (CTE), 241
Cold rolling, 312
Compatibility, 255, 261, 270
Compatibilizer, 212, 257, 286, 291, 292, 295–297, 300, 306–307, 316
Compatibilizing agents, 95
Complex viscosity, 246, 295–296
Compression, 264
Conductivity, 140, 141–143
Cone calorimetry, 239
Configuration, 261
Conversion, 301

Polyolefin Composites, Edited by Domasius Nwabunma and Thein Kyu

Core–shell cylinder model, 570, 571, 572
Cross hatched lamellae, 266
Crystal nucleation rate, 566, 567
Crystalline forms, 312, 331
Crystallinity, 218, 298, 300, 306, 308, 322, 328, 496, 497, 512, 516, 519, 540–542, 544
Crystallization, 299, 298–300
  peak temperature, 318, 328

Decabromodiphynyl oxide (DB), 277
Decalin, 487, 489, 509
Decenol, 223
Degree of intercalation, 432, 433
Delamination, 196
Density fluctuation, 356
Depolarized light scattering, 554, 556, 573
Dicyclopentadienyl zirconium dichloride, 220
Die swell, 138
Diene, 209, 210
Differential scanning calorimetry, 268, 525, 527, 547, 580
Dioctadecyldiethylammonium chloride modified montmorillonite (DOM), 236
Disordered exfoliation, 231
Dispersion, 349, 352, 354, 355, 358, 359–360
Dispersity, 220
Divinylbenzene, 209, 210
DSC, *see* Differential scanning calorimetry
Dynamic mechanical analysis, 236, 267, 325, 332, 338, 342
Dynamic oscillatory shearing, 295
Dynamic packing injection molding (DPIM), 263
Dynamic simulation, 423, 433

Electrical conductivity temperature dependence, 489–493, 509–516
Enthalpic factor, 257, 262
Entropic factor, 257
Essential work of fracture (EWF), 271
Ethylene propylene diene methylene rubber (EPDM), 229
Exfoliated, 420, 421, 423, 424, 426, 427, 429–432, 437, 441, 443
  exfoliation, 255, 258, 259, 261, 262
  nanocomposite, 254, 350
  structure, 214, 317, 352

Fatigue strength, 268
Feasibility, 257
Feeding speed, 261
Fiber attrition, 156
Fibrillation, 272
Flame retardant, 214, 235, 285, 305–307
Flammability, 214, 239, 241, 242, 276
Flexural moduli, 268, 270
Flory–Huggins interaction parameter, 422, 423, 427
Fluorohectorite, 233
Form factor, 568, 570, 572
Fourier transfer infrared spectra (FTIR), 223, 232, 238
Fractographic analysis, 271
Fracture, 304
  toughness, 271
Free radical
  initiator, 263
  grafting, 208
Fullerenes, 523

Galleries, 228
Gamma radiation, 95
Gas permeability, 229, 237
Gel
  crystallization, 578–593
  spinning, 561, 572
  permeation chromatography (GPC), 233
Glass
  bead, 220
  fiber, 222, 223
  transition temperature (T_g), 236, 267
Graphene sheet, 523, 524, 537
Graphite, 220, 327
Growth rate, 319
Guinier
  law, 356
  prefactor, 357

Half-time, 320, 332, 341, 342
HDPE/clay, 235, 236
HDPE/LDH nanocomposite, 286, 292, 294, 302, 304

HDPE/OMT, 231, 238, 245
HDPE-g-MAH, 295–296
Heat
  distortion temperature (HDT), 274, 275
  flux, 239
  of fusion, 323, 324, 331, 337
  release rate (HRR), 239
Hectorite, 232, 365, 367
Hemicellulose, 180, 184
Heterogeneous nucleation, 318, 323, 340
High resolution TEM, 536, 537
Hoffman–Weeks plot, 268
Homogeneous nucleation, 321
Hydrophilic, 255, 258
Hydrotalcite, 284–285, 287–288, 290, 302
Hydroxyapatite, 95
Hydroxyl-functionalized
  polypropylene, 212
  polypropylene copolymer, 215–216

Impact
  behavior, 166
  strength, 268
In situ
  chain transfer, 211
  intercalative polymerization, 229
  polymerization, 219–222, 231, 243
Intercalated, 420, 421, 424, 426, 427, 431, 434, 435
  nanocomposite, 253, 316, 350
  structures, 317, 342, 349, 452
Interfacial adhesion, 179
Interfibrillar, 266
Intergallery ions, 315
Interlayer, 228
Iodine doping, 501–509
Ion-exchange capacity, 315
Irradiation resistance property, 243
Isomorphic substitution, 228
Isopropyltriisostearoyl titanate, 90
Isothermal
  crystallization, 313–315, 319, 321, 322, 328, 329, 335, 336, 340
  crystallization kinetics, 328
  crystallization parameters, 328

Kaolin, 220

Labyrinth effect, 216, 238
Lamellar, 347–349
Layered
  double hydroxide, 283, 287–290, 306
  nanofiller domains, 359
  silicates, 116, 283
LDH, *see* Layered double hydroxide
LDPE silicate nanocomposite, 231
LDPE/MgAl LDH nanocomposite, 285, 295
LDPE/OMT, 241
Lewis acidic borane, 209
Light scattering, 266, 355–356, 359
Lignin, 107
Lignocellulosic, 150, 152, 153, 187
Living polymerization, 211
LLDPE
  g-MAH, 296, 298
  MgAl LDH nanocomposite, 285, 302, 304
  PE-g-MAH, 234
  ZnAl LDH nanocomposite, 286, 301
LOI value, 285, 305
Loss modulus, 236, 246, 272, 497–499, 517, 518

Macro composite, 229
Magnesium hydroxide, 220
MAH, 208, 230
  grafted linear low density polyethylene (LLDPE-g-MAH)/OMT, 231
  g-SBS, 272
  modified polyolefin, 231
  maleic anhydride grafted polypropylene (PP-g-MA)
  modified PP (MAPP), 215, 217
Maltese cross, 323
MAO co-catalyst, 232
Mean-field statistical lattice model, 230
Melt
  compounding, 257
  flow index, MFI, 259, 300, 305
  intercalation, 229, 230, 316–317
  solidification, 264
  temperature, 219, 220, 268
Metallocene catalysts, 208, 209, 219, 220, 232
  catalyzed polyethylene (m-PE), 232
Methacrylate, 208

Methylaluminoxane (MAO), 232, 233
p-Methyl styrene, 209, 210
MAO co-catalyst, 209, 219, 220
Metropolis algorithm, 454, 458, 465
Microcomposites, 313, 316
Microstructure, 208
Miscibility, 258
Molar mass, 208
Monte Carlo simulations, 453, 465, 466, 482
Montmorillonite, 116, 228, 237, 242, 252, 315, 365–410
Montmorillonite/silica hybrid (MT-Si), 233
Morphology, 222
  draw ratio, 494, 495
Multiwall carbon nanotubes, 220, 314, 327, 340–342
MWCNTs, *see* Multiwall carbon nanotubes

Nafion/LDH membranes, 285
Nano
  clay, 315
  fibers, 347
  fillers, 211, 313, 340–342, 346, 351, 352, 354, 356, 357, 359
  hybrid shish-kebab, 527–528
  particles, 211, 346–351
  scale organic–inorganic hybrid material, 228
Network theory, 452
Nonisothermal
  crystallization, 315, 318, 328, 340–342
  crystallization kinetics, 319–320, 328
  crystallization parameters
Novel hybrid copolymer, 223
Nucleating activity, 321, 329, 336, 340, 342
Nucleating agents, 218, 313, 337
Nylon, 318
Nylon, 6/montmorillonite nanocomposite, 228
Nylon–clay nanocomposite, 350

Octahedral sheet, 228, 252
Ogden equation, 136
Optical microscopy, 323, 329, 337, 342
Ordered exfoliation, 231
Organic ion, 230
Organically modified montmorillonite, 230, 242, 243
Organo
  aluminum compound, 209
  clay, 217, 218, 255, 263, 267
  modified clays, 315
Organophilic, 212, 218, 255, 258
Oriented crystallization, 186
Oscillatory deformation, 236, 239
Oxophilicity, 211
Oxygen transmission rate, OTR, 305

PA6/LDH nanocomposite, 285
PB/$BaTiO_3$ nanocomposite, 334, 336–340, 342
PB/clay nanocomposite, 314–315, 317–318, 321–323, 326, 327, 332, 342
PB/MWCNT nanocomposite, 327–331, 333–334, 341–342
Pendant styrenic moieties, 210
Percolation threshold, 220
Permeability, 277
Phase separated microcomposite, 253, 254, 350, 353
Phase transformation, 312, 331, 332, 337, 338, 340, 342
Phenylsilane group, 210
Photodegradable, 150
Photooxidative degradation, 240, 241
Phyllosilicates, 116, 228, 365, 367, 371, 384
Physical adsorption, 334
Plant fiber
  cellulose, 47
  cellulose microfibrils, 48
  chemical coupling, 54
  chemical modification, 50
  chemical treatment, 50
  corona treatment, 51
  esterification, 55
  etherification, 55
  fibrillar structure, 49
  fringed micelle structure, 49
  graft copolymerization, 61
Plastic crack growth, 304
Plastic strain, 304
PMMA/LDH nanocomposite, 284
Polarity, 278
Polarized light microscope, 548

Poly(butylenes terephthalate), 230
Poly(ethylene-*co*-vinyl acetate) (EVA), 230
Poly(methyl methacrylate), 230
Polyamide, 220
Polyethylene nanocomposite, 349, 355, 358, 359
Polyethylene
  aluminum trihydroxide, 212
  clay nanocomposite, 350
  magnesium hydroxide (PE/MH), 212
  metal hydroxide composite, 212
  nanoparticles systems, 348
  octene copolymer (POE), 272
Polyhedral oligomeric silsesquioxane (POSS), 223
Polyimide, 230
Polymer
  melt intercalation, 350
  clay nanocomposite, 351
  layered silicate nanocomposite, 228, 229, 230, 234, 245
Polymerization-filling technique (PFT), 219, 233
Polymorphic form, 312, 323
Polyolefin, 207
Polyolefin natural fiber composites
  applications, 63
  cardanol derivative of toluene diisocyanate, 64
  c-axis slip, 66
  dynamic mechanical properties, 71
  electrical properties, 73
  Hirsch model, 68
  interface, 68
  interfacial shear strength, 70
  mechanical properties, 71
  nanocomposite, 76
  processing, 74
  rheological properties, 72
  thermo analytical properties, 72
  water absorption, 76
Polyolefin/ATH/nanoclay, 217
Polyolefin/MMT, 306
Polypropylene (PP), 229, 251, 258
  aluminum, 212
  glass laminate, 212
  microsilica, 214
  silica nanocomposite, 351
Polypropylene cellulosic fiber composite
  application, 32
  crystallization, 32
  mechanical properties, 36
  modification, 36
  morphology, 38
Preparation technique, 33
Polyvinylidine fluoride, 318
Power law, 357, 358
Power law prefactor, 358
PP/clay nanocomposite (PPCNs), 251, 252, 255, 257–259, 261–265, 267, 270, 272, 275, 276
  LDH nanocomposite, 283, 305
PB blend, 313
  clay, 378, 392–394
  g-MA, 258, 264, 270, 272, 278
  vermiculite nanocomposite, 263
PPC/MgAl LDH nanocomposite, 302, 304
Pulse shear, 555, 556, 558, 559, 562, 563, 572

Radical scavenging efficiency, 546
Radical, condensation, and ring-opening polymerization, 223
Radius of gyration, 560
Raman spectroscopy, 526
Reactive compounding, 262
Relaxation time, 566
Residence time, 261
Rheology, 229
Romero–Garcia model, 117
Rotational isomeric state (RIS), 454, 463
Rouse mode, 473, 475, 476, 478
Rouse relaxation time, 476, 478, 482

SALS, *see* Small-angle light scattering
SANS, *see* Small-angle neutron scattering
Saponite, 365, 367
SAXS, *see* Small angle X-ray scattering
Scanning electron microscopy, 358, 360
Scanning tunneling microscopy, 524
Scattering profiles, 353
Scattering wave vector, 356
Second nearest neighbor diamond lattice (SNND), 454
Self-consistent field theory (SCF), 454
SEM, *see* Scanning electron microscopy
Semicrystalline polymer, 264, 274

Semifluorinated surfactant, 257
Shear
  induced crystallization, 525
  modulus, 221, 235
  rate, 262, 553, 556, 557, 558, 559, 560, 566, 567
  strain, 556, 558, 559, 560
  thinning exponent (n), 297–298
  viscosity, 259
Shish-kebab, 528, 529, 553, 557, 565, 567, 568, 571
Silane, 209, 210
Silane coupling agent, 180
Silica
  nanoparticles, 351
  polyethylene composite dispersions, 352
  tetrahedral sheet, 228
Silicate layers, 349
Single-component palladium-based complex, 233
Sisal fiber, 118, 188
Slurry compounding, 263
Small-angle neutron scattering, 354, 431, 554, 567
Small-angle light scattering, 348, 360
Small-angle X-ray scattering, 348, 354, 360, 561, 573
Soft epitaxy, 531, 536
Solution compounding, 257
Spatial-orientational correlations, 347
Specific extinction areas (SEA), 239
Spherical nanoparicles, 347, 351, 356
Spherulitic morphology, 315, 323, 329, 337, 341, 342
Stearic acid, 211, 213
Storage modulus, 236, 272, 273, 274, 298–299, 325, 326, 332, 338, 339
Styrene–butadiene–styrene copolymer (SBS), 272
Supercooling, 563
Surface modification, 90
Surface modifiers, 88

Tacticity, 208
Tactoid, 254
tan δ, 236, 246, 272, 325, 332–333
TEM, 229–231, 233, 234, 242, 254, 262, 271, 370, 371, 375–377, 380, 382, 384, 385, 390, 392, 398, 410, 527, 528, 530–534, 553, 557, 567, 572
Template crystallization, 577, 579, 589, 591–593
Template synthesis, 229
Tensile, 220
  ductility, 369, 384, 389, 393, 394, 398, 409, 410
  modulus, 234
  property, 234, 235
  strength, 302, 304, 306, 365, 389–391, 393–397
Themophysical property, 241
Thermal
  conductivity, 241
  degradation, 242
  gravimetric analysis, 157, 238, 315, 326, 334, 339, 342
  oxidative degradation, 300, 302
  stability, 228, 238, 286–287, 294, 300, 302, 305, 307, 326, 334, 339, 340, 342
TiO_2 nanoparticles, 351, 358
Tortuous path, 237
Transverse micro cracking, 181
Triisobutylaluminum, 221
Trimethylchlorosilane modified montmorillonite (TMD), 236

Ultra small-angle X-ray scattering, 348, 356
Ultrasonic extrusion technology, 263
USAXS, *see* Ultra small angle X-ray scattering

Van der Waals interaction, 212, 228, 252
Vapor phase fire retardants, 277
Vicat softening temperature, 300, 305
Vinyl
  acetate, 208
  benzylmethacrylate, 257
Viscosity, 276
Volume-weighted particle size distribution, 354–355

WAXD, 232, 495, 517
WAXS, *see* Wide-angle X-ray scattering
Wide-angle X-ray scattering, 348, 553, 559, 570

William–Landel–Ferry (WLF) equation, 566
Wollastonite, 220

Xe-NMR spectroscopy, 131
X-ray diffraction, 215, 220, 229–231, 233, 234, 254, 262, 266, 349, 352, 353, 366, 370, 372, 374–376, 378–381, 387, 388
X-ray microanalysis, 223
XRD, *see* X-ray diffraction

Young's modulus, 187, 234, 268–270, 302, 304, 492, 497

Zicronates, 89
Ziegler–Natta catalysts, 207, 210, 219, 233
Zinc powder, 220
Zirconocene catalyst, 233